

# Petroleum Production Engineering

**Second Edition**

# Petroleum Production Engineering

**Second Edition**

**Boyun Guo, PhD**  
**Xinghui Liu, PhD**  
**Xuehao Tan, PhD**



**Gulf Professional Publishing**

An imprint of Elsevier  
elsevier.com



Gulf Professional Publishing is an imprint of Elsevier  
50 Hampshire Street, 5th Floor, Cambridge, MA 02139, United States  
The Boulevard, Langford Lane, Kidlington, Oxford, OX5 1GB, United Kingdom

Copyright © 2017 Elsevier Inc. All rights reserved.

No part of this publication may be reproduced or transmitted in any form or by any means, electronic or mechanical, including photocopying, recording, or any information storage and retrieval system, without permission in writing from the publisher. Details on how to seek permission, further information about the Publisher's permissions policies and our arrangements with organizations such as the Copyright Clearance Center and the Copyright Licensing Agency, can be found at our website: [www.elsevier.com/permissions](http://www.elsevier.com/permissions).

This book and the individual contributions contained in it are protected under copyright by the Publisher (other than as may be noted herein).

#### **Notices**

Knowledge and best practice in this field are constantly changing. As new research and experience broaden our understanding, changes in research methods, professional practices, or medical treatment may become necessary.

Practitioners and researchers must always rely on their own experience and knowledge in evaluating and using any information, methods, compounds, or experiments described herein. In using such information or methods they should be mindful of their own safety and the safety of others, including parties for whom they have a professional responsibility.

To the fullest extent of the law, neither the Publisher nor the authors, contributors, or editors, assume any liability for any injury and/or damage to persons or property as a matter of products liability, negligence or otherwise, or from any use or operation of any methods, products, instructions, or ideas contained in the material herein.

#### **British Library Cataloguing-in-Publication Data**

A catalogue record for this book is available from the British Library

#### **Library of Congress Cataloguing-in-Publication Data**

A catalog record for this book is available from the Library of Congress

ISBN: 978-0-12-809374-0

For Information on all Gulf Professional Publishing  
visit our website at <https://www.elsevier.com/books-and-journals>



**Working together  
to grow libraries in  
developing countries**

[www.elsevier.com](http://www.elsevier.com) • [www.bookaid.org](http://www.bookaid.org)

*Publisher:* Joe Hayton  
*Senior Acquisition Editor:* Katie Hammon  
*Senior Editorial Project Manager:* Kattie Washington  
*Production Project Manager:* Kiruthika Govindaraju  
*Cover Designer:* Harris Greg

Typeset by MPS Limited, Chennai, India

# Dedication

*This book is dedicated to my wife Huimei Wang for her understanding  
and encouragement that were as responsible as the experience  
and knowledge that have been inscribed herein.*

*—Boyun Guo*

# List of Figures

Figure 1.1	A sketch of a simple petroleum production system	4
Figure 1.2	A sketch of a typical flowing oil well	5
Figure 1.3	A sketch of a wellhead	5
Figure 1.4	A sketch of a casing head	6
Figure 1.5	A sketch of a tubing head	7
Figure 1.6	A sketch of a “Christmas tree”	7
Figure 1.7	A sketch of a surface valve	8
Figure 1.8	A sketch of a wellhead choke	8
Figure 1.9	Uses of offshore flowlines and pipelines	10
Figure 1.10	Safety device symbols	12
Figure 1.11	Safety system designs for surface wellhead flowlines	13
Figure 1.12	Safety system designs for underwater wellhead flowlines	15
Figure 1.13	Safety system design for pressure vessel	15
Figure 1.14	Safety system design for pipeline pumps	16
Figure 1.15	Safety system design for other pumps	16
Figure 3.1	A sketch of a radial flow reservoir model: (A) lateral view, (B) top view	38
Figure 3.2	A sketch of a reservoir with a constant-pressure boundary	39
Figure 3.3	A sketch of a reservoir with no-flow boundaries	40
Figure 3.4	(A): Shape factors for closed drainage areas with low-aspect ratios. (B): Shape factors for closed drainage areas with high-aspect ratios	41
Figure 3.5	Relationship between fracture conductivity and equivalent skin factor	44
Figure 3.6	A reservoir section drained by a multifractured horizontal wellbore	47
Figure 3.7	Fluid flow in a fracture to a horizontal wellbore	47
Figure 3.8	Schematic of a typical root well	50
Figure 3.9	Schematic of a reservoir section drained by a fishbone well	51
Figure 3.10	A typical IPR curve for an oil well	54
Figure 3.11	Transient IPR curve for Example Problem 3.2	56
Figure 3.12	Steady-state IPR curve for Example Problem 3.2	56
Figure 3.13	Pseudo-steady-state IPR curve for Example Problem 3.2	57
Figure 3.14	IPR curve for Example Problem 3.3	60
Figure 3.15	Generalized Vogel IPR model for partial two-phase reservoirs	60
Figure 3.16	IPR curve for Example Problem 3.4	62
Figure 3.17	IPR curves for Example Problem 3.5, Well A	64
Figure 3.18	IPR curves for Example Problem 3.5, Well B	65
Figure 3.19	IPR curves for Example Problem 3.6	67
Figure 3.20	IPR curves of individual layers in Example Problem 3.7	71
Figure 3.21	Composite IPR curve for all the layers open to flow in Example Problem 3.7	72
Figure 3.22	Composite IPR curve for Group 2 (Layers B4, C1, and C2) in Example Problem 3.7	72
Figure 3.23	Composite IPR curve for Group 3 (Layers B1, A4, and A5) in Example Problem 3.7	73
Figure 3.24	IPR curves for Example Problem 3.8	75

Figure 3.25	IPR curves for Example Problem 3.9	78
Figure 4.1	Flow along a tubing string	84
Figure 4.2	Darcy—Wiesbach friction factor diagram	86
Figure 4.3	Calculated tubing pressure profile for the Example Problem 4.2	91
Figure 4.4	Flow regimes in gas-liquid flow	96
Figure 4.5	Pressure traverse given by Hagedorn Brown Correltion.xls for Example Problem 4.6	106
Figure 5.1	A typical choke performance curve	112
Figure 5.2	Choke flow coefficient for nozzle-type chokes	113
Figure 5.3	Choke flow coefficient for orifice-type chokes	114
Figure 6.1	Nodes in an oil and gas production system	130
Figure 6.2	Nodal analysis for the Example Problem 6.1	134
Figure 6.3	Nodal analysis for Example Problem 6.4	140
Figure 6.4	Nodal analysis for Example Problem 6.6	145
Figure 6.5	Nodal analysis for Example Problem 6.8	148
Figure 6.6	Nodal analysis for Example Problem 6.9	152
Figure 6.7	Nodal analysis for Example Problem 6.10	153
Figure 6.8	Nodal analysis for Example Problem 6.11	156
Figure 6.9	Nodal analysis for Example Problem 6.12	158
Figure 6.10	Nodal analysis for Example Problem 6.13	160
Figure 6.11	A simplified well structure for root type multilateral wells	162
Figure 6.12	Symbols used to describe a root type multilateral well	162
Figure 7.1	Nodal analysis plot for Example Problem 7.1	181
Figure 7.2	Production forecast for Example Problem 7.1	181
Figure 7.3	Nodal analysis plot for Example Problem 7.2	184
Figure 7.4	Production forecast for Example Problem 7.2	185
Figure 7.5	Production forecast for Example Problem 7.3	189
Figure 7.6	Result of production forecast for Example Problem 7.4	192
Figure 7.7	Completion models of a multi-stage fractured horizontal oil well in the Upper Eagle Ford: (A) one fracture created from each cluster of perforations, and (B) three fractures/branches created from each cluster of perforations	193
Figure 7.8	Production forecast by reservoir simulation for a multi-stage fractured horizontal well in a shale oil reservoir	193
Figure 8.1	A semi-log plot of $q$ versus $t$ indicating an exponential decline	204
Figure 8.2	A plot of $N_p$ versus $q$ indicating an exponential decline	205
Figure 8.3	A plot of $\log(q)$ versus $\log(t)$ indicating a harmonic decline	205
Figure 8.4	A plot of $N_p$ versus $\log(q)$ indicating a harmonic decline	206
Figure 8.5	A plot of relative decline rate versus production rate	206
Figure 8.6	Procedure for determining $a$ - and $b$ -values	207
Figure 8.7	A plot of $\log(q)$ versus $t$ showing an exponential decline	208
Figure 8.8	Relative decline rate plot showing exponential decline	209
Figure 8.9	Projected production rate by an exponential decline model	209
Figure 8.10	Relative decline rate plot showing harmonic decline	210
Figure 8.11	Projected production rate by a harmonic decline model	211
Figure 8.12	Relative decline rate plot showing hyperbolic decline	212

Figure 8.13	Relative decline rate shot showing hyperbolic decline	212
Figure 8.14	Projected production rate by a hyperbolic decline model	213
Figure 9.1	Wellhead-tubing-packer relation	220
Figure 9.2	Effect of tension stress on tangential stress	223
Figure 9.3	Tubing–packer relation	228
Figure 9.4	(A) Ballooning and (B) buckling effects	229
Figure 9.5	Teeth on mechanical packers	233
Figure 9.6	Schematic of a tension packer	234
Figure 9.7	A sketch of a compression packer	234
Figure 9.8	Wireline-set tubing retrievable packer. Left: set with plug in place; Right: set with tubing connected and plug retrieved	235
Figure 9.9	Tension/compression-set versatile landing	236
Figure 9.10	Sketch of a hydraulic-set single-string packer	237
Figure 9.11	An oil-swellable packer is being run in a casing string	238
Figure 9.12	Typical packer-rating envelope	240
Figure 10.1	A typical vertical separator	245
Figure 10.2	A typical horizontal separator	246
Figure 10.3	A typical horizontal double-tube separator	246
Figure 10.4	A typical horizontal three-phase separator	247
Figure 10.5	A typical spherical low-pressure separator	248
Figure 10.6	Water content of natural gases	260
Figure 10.7	Flow diagram of a typical solid desiccant dehydration plant	262
Figure 10.8	Flow diagram of a typical glycol dehydrator	264
Figure 10.9	Gas capacity of vertical inlet scrubbers based on 0.7-specific gravity at 100°F	267
Figure 10.10	Gas capacity for trayed glycol contactors based on 0.7-specific gravity at 100°F	269
Figure 10.11	Gas capacity for packed glycol contactors based on 0.7-specific gravity at 100°F	270
Figure 10.12	The required minimum height of packing of a packed contactor, or the minimum number of trays of a trayed contactor	271
Figure 11.1	Double-action stroke in a duplex pump	276
Figure 11.2	Single-action stroke in a triplex pump	276
Figure 11.3	Elements of a typical reciprocating compressor	281
Figure 11.4	Cross-section of a centrifugal compressor	282
Figure 11.5	Basic pressure–volume diagram	283
Figure 11.6	Flow diagram of a two-stage compression unit	288
Figure 11.7	Fuel consumption of prime movers using three types of fuel	290
Figure 11.8	Fuel consumption of prime movers using natural gas as fuel	291
Figure 11.9	Effect of elevation on prime mover power	291
Figure 11.10	Darcy-Wiesbach friction factor chart	299
Figure 11.11	Stresses generated by internal pressure $p$ in a thin-wall pipe, $D/t > 20$	310
Figure 11.12	Stresses generated by internal pressure $p$ in a thick-wall pipe, $D/t < 20$	310
Figure 11.13	Calculated temperature profiles with a polyethylene layer of 0.0254 M (1 in.)	319

Figure 11.14	Calculated steady-flow temperature profiles with polyethylene layers of various thicknesses	320
Figure 11.15	Calculated temperature profiles with a polypropylene layer of 0.0254 M (1 in.)	321
Figure 11.16	Calculated steady-flow temperature profiles with polypropylene layers of various thicknesses	321
Figure 11.17	Calculated temperature profiles with a polyurethane layer of 0.0254 M (1 in.)	322
Figure 11.18	Calculated steady-flow temperature profiles with polyurethane layers of four thicknesses	322
Figure 12.1	Temperature and spinner flowmeter-derived production profile	330
Figure 12.2	Notations for a horizontal wellbore	332
Figure 12.3	Measured bottom-hole pressures and oil production rates during a pressure drawdown test	336
Figure 12.4	Log-log diagnostic plot of test data	337
Figure 12.5	Semi-log plot for vertical radial flow analysis	337
Figure 12.6	Square-root time plot for pseudo-linear flow analysis	338
Figure 12.7	Semi-log plot for horizontal pseudo-radial flow analysis	338
Figure 12.8	Match between measured and model calculated pressure data	339
Figure 12.9	Gas production due to channeling behind the casing	340
Figure 12.10	Gas production due to preferential flow through high-permeability zones	340
Figure 12.11	Gas production due to gas coning	341
Figure 12.12	Temperature and noise logs identifying gas channeling behind casing	341
Figure 12.13	Temperature and fluid density logs identifying a gas entry zone	342
Figure 12.14	Water production due to channeling behind the casing	342
Figure 12.15	Preferential water flow through high-permeability zones	343
Figure 12.16	Water production due to water coning	343
Figure 12.17	Prefracture and postfracture temperature logs identifying fracture height	344
Figure 12.18	Spinner flowmeter log identifying a watered zone at bottom	345
Figure 12.19	Calculated minimum flow rates with the Turner et al. model and test flow rates	346
Figure 12.20	The minimum flow rates given by the Guo et al. model and the test flow rates	352
Figure 12.21	Schematic of formation damage due to fines migration	353
Figure 12.22	Region of formation damage around a wellbore	360
Figure 12.23	Region of formation damage around a hydraulic fracture	360
Figure 13.1	Typical acid response curves	372
Figure 13.2	Wormholes created by acid dissolution of limestone	377
Figure 13.3	PVbt curves	378
Figure 13.4	Conductivity of Acid fractures	382
Figure 13.5	Example of pre- and post-treatment PLT data	385
Figure 14.1	Illustration of the hydraulic fracturing process	390
Figure 14.2	Rock deformation under uniaxial loading	391
Figure 14.3	Three fracture modes	393
Figure 14.4	General state of stress in 3D space	395

Figure 14.5	Concept of effective stress applied to rock grains	397
Figure 14.6	Common fault regimes	398
Figure 14.7	Schematic view of various hydraulic fracture types	401
Figure 14.8	Schematic of fracturing fluid leakoff regions	403
Figure 14.9	The PKN fracture geometry	409
Figure 14.10	The KGD fracture geometry	412
Figure 14.11	Typical fracture geometry predicted by a lumped-parameter model	416
Figure 14.12	Fracture geometry predicted by two types of P3D models	417
Figure 14.13	Fracture height migration from a P3D fracture model	417
Figure 14.14	Stress variation vs distance away from a semi-infinite crack	420
Figure 14.15	Potential stress shadowing effects on fracture propagation in a stage with 3 perforation clusters from a horizontal well: (A) without stress shadowing and (B) with stress shadowing	420
Figure 14.16	Complex fracture network simulated by an unconventional fracture model	421
Figure 14.17	Nonplanar fracture geometry	422
Figure 14.18	Surface treating pressure responses from a typical fracturing treatment	429
Figure 14.19	Net pressure response based on the Nolte-Smith analysis	430
Figure 14.20	Illustration of fracture tortuosity and multiple fractures in the near-wellbore area	433
Figure 14.21	Schematic of a typical rate step-down test	434
Figure 14.22	Illustration of a typical step-rate test	435
Figure 14.23	A typical minifrac test	436
Figure 14.24	A sample plot of pressure vs square root of time	438
Figure 14.25	A sample plot of pressure vs time on log-log scale	439
Figure 14.26	A sample plot of pressure vs G-function time	440
Figure 14.27	A typical borate crosslinked gel sample	445
Figure 14.28	Apparent viscosity vs time at different shear rates for a typical borate crosslinked gel	448
Figure 14.29	Visual chart for evaluating the roundness and sphericity of particle grains	450
Figure 14.30	Effect of effective closure stress on proppant pack conductivity for various types of proppants	451
Figure 14.31	Photo of 20/40-mesh proppant samples	452
Figure 14.32	Schematic of equipment layout for a typical fracturing treatment	453
Figure 14.33	Photo of a typical high-pressure pump	454
Figure 14.34	Photo of a typical blender	455
Figure 14.35	Photo of a typical manifold trailer	456
Figure 14.36	Photo of a typical data van	457
Figure 14.37	Proppant silos	457
Figure 14.38	Photo of fracturing equipment layout at well site	458
Figure 14.39	Up close view of fracturing equipment layout at well site	458
Figure 14.40	Relationship between fracture conductivity and equivalent skin factor	461
Figure 14.41	An illustration of the propped and unpropped fractures	465
Figure 14.42	An illustration of stress calibration	467
Figure 14.43	An illustration of fracture growth in width and length and proppant placement	469

Figure 14.44	Iteration procedure to determine the pumping time	472
Figure 14.45	Calculated slurry concentration	474
Figure 14.46	An illustration of treatment cost, posttreatment production and NPV vs treatment size	479
Figure 14.47	Typical components of a frac-pack completion	481
Figure 14.48	A typical frac plug	484
Figure 14.49	Illustration of multistage completion using the plug and perf method	485
Figure 14.50	A typical frac sleeve system	486
Figure 14.51	Typical net pressure matching with a pseudo-3D fracture model	491
Figure 14.52	Four flow regimes that can occur in hydraulically fractured reservoirs	492
Figure 14.53	Earth deformation created from a hydraulic fracture	493
Figure 14.54	Illustration of microseisms induced during hydraulic fracturing	494
Figure 14.55	Effects of horizontal well spacing and orientation on reservoir drainage	494
Figure 15.1	Nomenclature of a tubing string in a horizontal well	506
Figure 15.2	Calculated tension profiles in the workover string for Example Problem 15.1	508
Figure 16.1	A diagrammatic drawing of a sucker rod pumping system	516
Figure 16.2	Sketch of three types of pumping units: (A) conventional unit; (B) Lufkin Mark II Unit; (C) air-balanced unit	517
Figure 16.3	The pumping cycle: (A) plunger moving down, near the bottom of the stroke; (B) plunger moving up, near the bottom of the stroke; (C) plunger moving up, near the top of the stroke; (D) plunger moving down, near the top of the stroke	518
Figure 16.4	Two types of plunger pumps. (A) Tubing pump and (B) Rod pump	519
Figure 16.5	Polished rod motion for (A) conventional pumping unit and (B) air-balanced unit	519
Figure 16.6	Definitions of conventional pumping unit API geometry dimensions	522
Figure 16.7	Approximate motion of connection point between pitman arm and walking beam	523
Figure 16.8	Sucker rod pumping unit selection chart	538
Figure 16.9	A sketch of pump dynagraph	542
Figure 16.10	Pump dynagraph cards: (A) ideal card; (B) gas compression on down-stroke; (C) gas expansion on upstroke; (D) fluid pound; (E) vibration due to fluid pound; (F) gas lock	543
Figure 16.11	Surface dynamometer card: (A) ideal card (stretch and contraction); (B) ideal card (acceleration); (C) three typical cards	545
Figure 16.12	Strain-gage-type dynamometer chart	546
Figure 16.13	Surface to down hole cards derived from surface dynamometer card	546
Figure 17.1	Configuration of a typical gas lift well	550
Figure 17.2	A simplified flow diagram of a closed rotary gas lift system for single intermittent well	551
Figure 17.3	A sketch of continuous gas lift	553
Figure 17.4	Pressure relationship in a continuous gas lift	553
Figure 17.5	System analysis plot given by GasLiftPotential.xls for the unlimited gas injection case	556
Figure 17.6	System analysis plot given by GasLiftPotential.xls for the limited gas injection case	557
Figure 17.7	Well unloading sequence. (A) initial condition, (B) gas enters the first valve, (C) gas enters the second valve, (D) gas enters the last valve, and (E) unloaded condition	575
Figure 17.8	Flow characteristics of orifice-type valves	576



Figure 17.9	Unbalanced bellows valve at its closed condition	577
Figure 17.10	Unbalanced bellows valve at its open condition	578
Figure 17.11	Flow characteristics of unbalanced valves	578
Figure 17.12	A sketch of a balanced pressure valve	579
Figure 17.13	A sketch of a pilot valve	580
Figure 17.14	A sketch of a throttling pressure valve	580
Figure 17.15	A sketch of a fluid-operated valve	581
Figure 17.16	A sketch of a differential valve	582
Figure 17.17	A sketch of combination valve	583
Figure 17.18	A flow diagram to illustrate procedure of valve spacing	584
Figure 17.19	Illustrative plot of BHP of an intermittent flow	592
Figure 17.20	Intermittent flow gradient at midpoint of tubing	592
Figure 17.21	Example Problem 17.8 schematic and BHP buildup for slug flow	594
Figure 17.22	Three types of gas lift installations. (A) open installation, (B) semi-closed installation, and (C) closed installation	595
Figure 17.23	Sketch of a standard two-packer chamber. (A) full system sketch, and (B) sketch of standing valve	596
Figure 17.24	A sketch of an insert chamber	597
Figure 17.25	A sketch of a reserve flow chamber	597
Figure 18.1	A sketch of an ESP installation	604
Figure 18.2	An internal schematic of centrifugal pump	605
Figure 18.3	A sketch of a multistage centrifugal pump	605
Figure 18.4	A typical characteristic chart for a 100-stage ESP	607
Figure 18.5	A sketch of a hydraulic piston pump	611
Figure 18.6	Sketch of a PCP system	616
Figure 18.7	Rotor and stator geometry of PCP	617
Figure 18.8	Four flow regimes commonly encountered in gas wells	620
Figure 18.9	A sketch of a plunger lift system	622
Figure 18.10	Sketch of a hydraulic jet pump installation	630
Figure 18.11	Working principle of a hydraulic jet pump	631
Figure 18.12	Example jet pump performance chart	632
Figure 19.1	Schematic of a typical subsea pipeline system	640
Figure 19.2	Typical flooding, cleaning, and gauging pig train	641
Figure 19.3	Typical dewatering pig train	644
Figure 19.4	Typical vacuum drying pressure plot	645
Figure 20.1	Hydrate forming conditions of natural gases	650
Figure 20.2	Water content of natural gases	653
Figure 20.3	Gas hydrate curve with different amount of methanol inhibition	655
Figure 20.4	Methanol in gas phase as a function of methanol in liquid phase	657
Figure 21.1	Pressure dependence of asphaltene solubility in crude oil	673
Figure 21.2	Laser power as a function of pressure	675
Figure 21.3	Schematic diagram of refractometer	676
Figure 21.4	Relationship between solubility parameter and RI ( $K = \frac{RI^2 - 1}{RI^2 + 2}$ ) for n-alkanes and aromatics	677

Figure 21.5	Live oil RI changes as a function of pressure	678
Figure 21.6	de Boer crude oil supersaturation plot	679
Figure 21.7	Schematic of the corrosion process	686
Figure 21.8	Schematic of classical severe slugging formation process. (A) Liquid fall back, (B) liquid slug accumulation and production, (C) gas enters the riser, and (D) gas blowdown.	691
Figure 21.9	Pipeline inlet pressure as a function of time for severe slugging flow	692
Figure 21.10	Pipeline outlet pressure as a function of time for severe slugging flow	693
Figure 21.11	Outlet gas mass flowrate as a function of time for severe slugging flow	693
Figure 21.12	Upwards and downwards inclined pipeline profiles	694
Figure 21.13	Required total gas flow for stable flow in flowline for different water cut	695
Figure 22.1	Pipeline deposits that could obstruct or retard flow through a pipeline	702
Figure 22.2	Some spheres used in the pipeline pigging operations	703
Figure 22.3	(A) A foam pig (B) An ideal foam pig cleaning the pipeline	704
Figure 22.4	Some mandrel pigs used in pipeline pigging operations	705
Figure 22.5	Some solid cast pigs used in pipeline pigging operations	705
Figure 22.6	An ultrasonic inspection tool	706
Figure 22.7	Application of gel pigs in pipeline pigging operations	707
Figure 22.8	A typical configuration of pig launcher for liquid services	708
Figure 22.9	A typical configuration of pig receiver for liquid services	708
Figure 22.10	A typical configuration of pig launcher for gas services	709
Figure 22.11	A typical configuration of pig receiver for gas services	709
Figure 22.12	Some mandrel pigs used in pipeline pigging operations	711
Figure 22.13	Some bi-directional pigs used in pipeline pigging operations	712
Figure 22.14	Pig with multilipped conical cups	713
Figure 22.15	A special pig for spraying corrosion inhibitor	714

# List of Tables

Table 2.1	Result Given by the Spreadsheet Program OilProperties.xls	23
Table 2.2	Results Given by the Spreadsheet Program MixingRule.xls	24
Table 2.3	Results Given by the Spreadsheet Carr-Kobayashi-Burrows-GasViscosity.xls	27
Table 2.4	Results Given by the Spreadsheet Program Brill-Beggs-Z.xls	29
Table 2.5	Results Given by the Spreadsheet Program Hall-Yarborough-z-Density.xls	30
Table 2.6	Coefficients of Correlations for Parachors of Hydrocarbons	33
Table 3.1	Summary of Test Points for Nine Oil Layers	70
Table 3.2	Comparison of Commingled and Layer-Grouped Productions	73
Table 4.1	Spreadsheet AverageTZ.xls: The Input Data and Result Sections	90
Table 4.2	Spreadsheet Cullender-Smith.xls: The Input Data and Result Sections	92
Table 4.3	Result Given by Guo-GhalamborBHP.xls for Example Problem 4.3	95
Table 4.4	Result Given by Poettmann-CarpenterBHP.xls for Example Problem 4.2	101
Table 4.5	Result Given by HagedornBrownCorrelation.xls for Example Problem 4.6	105
Table 5.1	Solution Given by the Spreadsheet Program GasUpChokePressure.xls	119
Table 5.2	Solution Given by the Spreadsheet Program GasDownChokePressure.xls	120
Table 5.3	A Summary of $C$ , $m$ , and $n$ Values Given by Different Researchers	121
Table 5.4	An Example Calculation with Sachdeva's Choke Model	124
Table 6.1	Result Given by BottomHoleNodalGas.xls for Example Problem 6.1	133
Table 6.2	Result Given by BottomHoleNodalOil-PC.xls for Example Problem 6.2	136
Table 6.3	Result Given by BottomHoleNodalOil-GG.xls for Example Problem 6.2	138
Table 6.4	Solution Given by BottomHoleNodalOil-HB.xls	139
Table 6.5	Solution Given by WellheadNodalGas-SonicFlow.xls	142
Table 6.6	Solution Given by WellheadNodalOil-PC.xls	144
Table 6.7	Solution Given by WellheadNodalOil-GG.xls	147
Table 6.8	Results Given by Spreadsheet Program for Example Problem 6.14	161
Table 6.9	Reservoir Property Data	164
Table 6.10	Fluid Property Data	165
Table 6.11	Well Data for Vertical Sections	165
Table 6.12	Well Data for Curved Sections	165
Table 6.13	Well Data for Horizontal Sections	166
Table 6.14	Summary of Calculated Lateral and Well Production Rates for Sample Problem 6.15	166
Table 6.15	Well Data for Sample Problem 6.16	167
Table 6.16	Summary of Calculated Lateral and Well Production Rates for Sample Problem 6.16	167
Table 6.17	Well Data for Sample Problem 6.17	168
Table 6.18	Summary of Calculated Lateral and Well Production Rates for Sample Problem 6.17	168
Table 6.19	Well Data for Sample Problem 6.18	169
Table 6.20	Summary of Calculated Lateral and Well Production Rates for Sample Problem 6.18	169
Table 7.1	Production Forecast Given by TransientProductionForecast.xls	181
Table 7.2	Production Forecast for Example Problem 7.2	184
Table 7.3	Oil Production Forecast for $N = 1$	187

Table 7.4	Gas Production Forecast for $N = 1$	188
Table 7.5	Production Schedule Forecast	189
Table 7.6	Result of Production Forecast for Example Problem 7.4	191
Table 8.1	Production Data for Example Problem 8.2	208
Table 8.2	Production Data for Example Problem 8.3	210
Table 8.3	Production Data for Example Problem 8.4	211
Table 9.1	API Tubing Tensile Requirements	220
Table 10.1	$K$ Values Used for Selecting Separators	253
Table 10.2	Retention Time Required Under Various Separation Conditions	254
Table 10.3	Settling Volumes of Standard Vertical High-Pressure Separators (230–2000 psi Working Pressure)	255
Table 10.4	Settling Volumes of Standard Vertical Low-Pressure Separators (125 psi Working Pressure)	256
Table 10.5	Settling Volumes of Standard Horizontal High-Pressure Separators (230–2000 psi Working Pressure)	256
Table 10.6	Settling Volumes of Standard Horizontal Low-Pressure Separators (125 psi Working Pressure)	257
Table 10.7	Settling Volumes of Standard Spherical High-Pressure Separators (230–3000 psi Working Pressure)	258
Table 10.8	Settling Volumes of Standard Spherical Low-Pressure Separators (125 psi)	258
Table 10.9	Temperature Correction Factors for Trayed Glycol Contactors	268
Table 10.10	Specific Gravity Correction Factors for Trayed Glycol Contactors	268
Table 10.11	Temperature Correction Factors for Packed Glycol Contactors	268
Table 10.12	Specific Gravity Correction Factors for Packed Glycol Contactors	269
Table 11.1	Typical Values of Pipeline Efficiency Factors	308
Table 11.2	Design and Hydrostatic Pressure Definitions and Usage Factors for Oil Lines	311
Table 11.3	Design and Hydrostatic Pressure Definitions and Usage Factors for Gas Lines	311
Table 11.4	Thermal Conductivities of Materials Used in Pipeline Insulation	315
Table 11.5	Typical Performance of Insulated Pipelines	316
Table 11.6	Base Data for Pipeline Insulation Design	319
Table 11.7	Calculated Total Heat Losses for the Insulated Pipelines ( $kW$ )	323
Table 12.1	Basic Parameter Values for Example Problem 12.1	351
Table 12.2	Result Given by the Spreadsheet Program GasWellLoading.xls	351
Table 13.1	Primary Chemical Reactions in Acid Treatments	369
Table 13.2	Recommended Acid Type and Strength for Sandstone Acidizing	371
Table 13.3	Recommended Acid Type and Strength for Carbonate Acidizing	377
Table 14.1	Main Features of Hydraulic Fracture Models	427
Table 14.2	Net Pressure Response Modes Based on the Nolte-Smith Analysis	430
Table 14.3	Characteristics of Commonly Used Crosslinkers	444
Table 14.4	Calculated Slurry Concentration	474
Table 14.5	Design Treatment Schedule for Example 14.5	476
Table 16.1	Conventional Pumping Unit API Geometry Dimensions	520
Table 16.2	Solution Given by Computer Program SuckerRodPumpingLoad.xls	532
Table 16.3	Solution Given by SuckerRodPumpingFlowrate&Power.xls	537

Table 16.4	Design Data for API Sucker Rod Pumping Units	539
Table 17.1	Result Given by Computer Program CompressorPressure.xls	563
Table 17.2	Result Given by Computer Program ReciprocatingCompressorPower.xls for the First-Stage Compression	569
Table 17.3	Result Given by the Computer Program CentrifugalCompressorPower.xls	573
Table 17.4	<i>R</i> Values for Otis Spreadmaster Valves	588
Table 17.5	Summary of Results for Example Problem 17.7	591
Table 18.1	Result Given by the Computer Spreadsheet ESPdesign.xls	610
Table 18.2	Solution Given by HydraulicPistonPump.xls	615
Table 18.3	Summary of Calculated Parameters	629
Table 18.4	Solution Given by Spreadsheet Program PlungerLift.xls	629
Table 20.1	Hydrate Forming Conditions of Natural Gases	650
Table 20.2	Water Content of Typical Natural Gas (lb <sub>m</sub> H <sub>2</sub> O/MMcf @60°F, 14.7 psia)	652
Table 20.3	Correlation Coefficients in Eq. (20.6)	658
Table 21.1	Summary of Major Factors Impacting Scale Precipitations	682
Table 22.1	Recommended Pigging Pressures and Flow Rates	718

# Preface

The advances in digital computing technology in the last two decades have revolutionized the petroleum industry. Using modern computer technologies, today's petroleum production engineers work much more efficiently than ever before in their daily activities, including analyzing and optimizing the performance of their existing production systems and designing new production systems. During several years of teaching the production engineering courses in academia and in the industry, the authors realized that there is a need for a textbook that reflects the current practice of what the modern production engineers do. Currently available books fail to provide adequate information about how the engineering principles are applied to solving petroleum production engineering problems with modern computer technologies. These facts motivated the authors to write the second edition of this book. In addition to updating materials in the chapters in the first edition of the book, the second edition was completed by adding new chapters mainly in two areas: (1) productivity of oil and gas wells with modern completion methods such as multi-fractured horizontal wells and multi-lateral wells, and (2) flow assurance.

This book is written primarily for production engineers and college students of senior level as well as graduate level. It is not authors' intention to simply duplicate general information that can be found from other books. This book gathers authors' experiences gained through years of teaching courses of petroleum production engineering in universities and in the petroleum industry. The mission of the book is to provide production engineers a handy guideline to designing, analyzing, and optimizing petroleum production systems. The original manuscript of this book has been used as a textbook for college students of undergraduate and graduate levels in Petroleum Engineering.

This book was intended to cover the full scope of petroleum production engineering. Following the sequence of oil and gas production process, this book presents its contents in eighteen chapters covered in five parts.

Part I contains chapters covering petroleum production engineering fundamentals as the first course for the entry-level production engineers and undergraduate students. Part II includes chapters presenting principles and rules of designing and selecting surface and downhole equipment. These chapters are also written for entry-level production engineers and undergraduate students. Part III consists of three chapters introducing well stimulation and workover as the second course for the entry-level production engineers and undergraduate students. Part IV is composed of chapters addressing artificial lift methods. They are designed for production engineers with some experience, and for graduate students. Part V is prepared for production and pipeline engineers specializing in flow assurance.

Since the substance of this book is virtually boundless in depth, knowing what to omit was the greatest difficulty with its editing. The authors believe that it requires many books to describe the foundation of knowledge in petroleum production engineering. To counter any deficiency that might arise from the limitations of space, the book provides a reference list of books and papers at the end of each chapter so that readers should experience little difficulty in pursuing each topic beyond the presented scope.

Regarding presentation, this book focuses on presenting and illustrating engineering principles used for designing and analyzing petroleum production systems rather than in-depth theories. Derivation of mathematical models is beyond the scope of this book, except for some special

topics. Applications of the principles are illustrated by solving example problems. While the solutions to some simple problems not involving iterative procedures are demonstrated with stepwise calculations, complicated problems are solved with computer spreadsheet programs. The programs can be downloaded from the publisher's website (<https://www.elsevier.com/books-and-journals/book-companion/9780128093740>). The combination of the book and the computer programs provides a perfect tool kit to petroleum production engineers for performing their daily work in a most efficient manner. All the computer programs were written in spreadsheet form in MS Excel that is available in most computer platforms in the petroleum industry. These spreadsheets are accurate and very easy to use. Although the U.S. field units are used in the companion book, options of using U.S. field units and SI units are provided in the spreadsheet programs.

This book is based on numerous documents including reports and papers accumulated through years of work in the University of Louisiana at Lafayette, a major energy producer, and a major service company in the oil and gas industry. The authors are grateful to the university for permissions of publishing the materials. Contributions of Dr. Shanhong Song in Flow Assurance is acknowledged. Special thanks go to the Chevron Corporation for providing Chevron Professorships in Petroleum Engineering throughout editing of this book. On the basis of the collective experiences of authors, we expect this book to be of value to the production engineers in the petroleum industry.

**Dr. Boyun Guo**

*Chevron Endowed Professor in Petroleum Engineering,  
University of Louisiana at Lafayette, Lafayette, LA, United States  
June 10, 2016.*

# List of Symbols

$A$	area, ft <sup>2</sup>
$A_b$	total effective bellows area, in. <sup>2</sup>
$A_{eng}$	net cross-sectional area of engine piston, in. <sup>2</sup>
$A_{fb}$	total firebox surface area, ft <sup>2</sup>
$A'_i$	inner area of tubing sleeve, in. <sup>2</sup>
$A'_o$	outer area of tubing sleeve, in. <sup>2</sup>
$A_p$	valve seat area, gross plunger cross-sectional area, or inner area of packer, in. <sup>2</sup>
$A_{pump}$	net cross-sectional area of pump piston, in. <sup>2</sup>
$A_r$	cross-sectional area of rods, in. <sup>2</sup>
$A_t$	tubing inner cross-sectional area, in. <sup>2</sup>
$^{\circ}\text{API}$	API gravity of stock tank oil
$B$	formation volume factor of fluid, rb/stb
$b$	constant $1.5 \times 10^{-5}$ in SI units
$B_o$	formation volume factor of oil, rb/stb
$B_w$	formation volume factor of water, rb/bbl
$C_A$	drainage area shape factor
$C_a$	weight fraction of acid in the acid solution
$C_c$	choke flow coefficient
$C_D$	choke discharge coefficient
$C_g$	correction factor for gas-specific gravity
$C_i$	productivity coefficient of lateral $i$
$C_l$	clearance, fraction
$C_m$	mineral content, volume fraction
$C_s$	structure unbalance, lb <sub>f</sub>
$C_t$	correction factor for operating temperature
$c_t$	total compressibility, psi <sup>-1</sup>
$\underline{C}_p$	specific heat of gas at constant pressure, lb <sub>f</sub> -ft/lb <sub>m</sub> -R
$\overline{C}_p$	specific heat under constant pressure evaluated at cooler
$C_{wi}$	water content of inlet gas, lb <sub>m</sub> H <sub>2</sub> O/MMscf
$D$	outer diameter, in., or depth, ft, or non-Darcy flow coefficient, d/Mscf, or molecular diffusion coefficient, m <sup>2</sup> /s
$d$	diameter, in.
$d_1$	upstream pipe diameter, in.
$d_2$	choke diameter, in.
$d_b$	barrel inside diameter, in.
$D_{ci}$	inner diameter of casing, in.
$d_f$	fractal dimension constant 1.6
$D_h$	hydraulic diameter, in.
$D_H$	hydraulic diameter, ft
$D_i$	inner diameter of tubing, in.
$D_o$	outer diameter, in.
$d_p$	plunger outside diameter, in.
$D_{pump}$	minimum pump depth, ft
$D_r$	length of rod string, ft



## xxxiv List of Symbols

$E$	rotor/stator eccentricity, in., or Young's modulus, psi
$E_v$	volumetric efficiency, fraction
$e_v$	correction factor
$e_p$	efficiency
$F_b$	axial load, lb <sub>f</sub>
$F_{CD}$	fracture conductivity, dimensionless
$F_F$	fanning friction factor
$F_{gs}$	modified Foss and Gaul slippage factor
$f_{hi}$	flow performance function of the vertical section of lateral $i$
$f_{Li}$	inflow performance function of the horizontal section of lateral $i$
$f_M$	Darcy-Wiesbach (Moody) friction factor
$F_{pump}$	pump friction-induced pressure loss, psia
$f_{Ri}$	flow performance function of the curvic section of lateral $i$
$f_{sl}$	slug factor, 0.5 to 0.6
$G$	shear modulus, psia
$g$	gravitational acceleration, 32.17 ft/s <sup>2</sup>
$G_b$	pressure gradient below the pump, psi/ft
$g_c$	unit conversion factor, 32.17 lb <sub>m</sub> - ft/lb <sub>f</sub> - s <sup>2</sup>
$G_{fd}$	design unloading gradient, psi/ft
$G_i$	initial gas-in-place, scf
$G_p$	cumulative gas production, scf
$G_p^1$	cumulative gas production per stb of oil at the beginning of the interval, scf
$G_s$	static (dead liquid) gradient, psi/ft
$G_2$	mass flux at downstream, lb <sub>m</sub> /ft <sup>2</sup> /sec
$GLR_{fm}$	formation oil GLR, scf/stb
$GLR_{inj}$	injection GLR, scf/stb
$GLR_{min}$	minimum required GLR for plunger lift, scf/bbl
$GLR_{opt,o}$	optimum GLR at operating flow rate, scf/stb
$GOR$	producing gas-oil ratio, scf/stb
$GWR$	glycol to water ratio, gal TEG/lb <sub>m</sub> H <sub>2</sub> O
$H$	depth to the average fluid level in the annulus, ft, or dimensionless head
$h$	reservoir thickness, ft, or pumping head, ft
$h_f$	fracture height, ft
$HP$	required input power, hp
$HP_{MM}$	required theoretical compression power, hp/MMcfd
$H_t$	total heat load on reboiler, Btu/h
$\Delta h$	depth increment, ft
$\Delta HP_m$	mechanical power losses, hp
$\nabla_{hi}$	pressure gradient in the vertical section of lateral $i$ , psi/ft
$J$	productivity of fractured well, stb/d-psi
$J_i$	productivity index of lateral $i$ .
$J_o$	productivity of nonfractured well, stb/d-psi
$K$	empirical factor, or characteristic length for gas flow in tubing, ft
$k$	permeability of undamaged formation, md, or specific heat ratio
$k_f$	fracture permeability, md
$k_H$	the average horizontal permeability, md
$k_h$	the average horizontal permeability, md
$k_i$	liquid/vapor equilibrium ratio of compound $i$

$k_p$	a constant
$k_{ro}$	the relative permeability to oil
$k_v$	vertical permeability, md
$L$	length, ft, or tubing inner capacity, ft/bbl
$L_g$	length of gas distribution line, mile
$L_N$	net lift, ft
$L_p$	length of plunger, in.
$M$	total mass associated with 1 stb of oil
$M_2$	mass flow rate at downstream, lb <sub>m</sub> /sec
$MW_a$	molecular weight of acid
$MW_m$	molecular weight of mineral
$N$	pump speed, spm, or rotary speed, rpm
$n$	number of layers, or polytropic exponent for gas
$N_{Ac}$	acid capillary number, dimensionless
$N_{Cmax}$	maximum number of cycles per day
$n_G$	number of lb-mole of gas
$N_i$	initial oil in place in the well drainage area, stb
$n_i$	productivity exponent of lateral $i$
$n_L$	number of mole of fluid in the liquid phase
$N_{max}$	maximum pump speed, spm
$n_p$	number of pitches of stator
$N_p^1$	cumulative oil production per stb of oil in place at the beginning of the interval
$N_p^f$	forecasted annual cumulative production of fractured well for year $n$
$N_p^{nf}$	predicted annual cumulative production of nonfractured well for year $n$
$N_p^{no}$	predicted annual cumulative production of non-optimized well for year $n$
$N_p^{op}$	forecasted annual cumulative production of optimized system for year $n$
$N_{Re}$	Reunolds number
$N_s$	number of compression stages required
$N_{st}$	number of separation stages – 1
$n_v$	number of mole of fluid in the vapor phase
$N_w$	number of wells
$\Delta N_{p,n}$	predicted annual incremental cumulative production for year $n$
$P$	pressure, lb/ft <sup>2</sup>
$p$	pressure, psia
$p_b$	base pressure, psia
$p_{bd}$	formation breakdown pressure, psia
$P_c$	casing pressure, psig
$p_c$	critical pressure, psia, or required casing pressure, psia, or the collapse pressure with no axial load, psia
$p_{cc}$	the collapse pressure corrected for axial load, psia
$P_{cd2}$	design injection pressure at valve 2, psig
$P_{Cmin}$	required minimum casing pressure, psia
$p_{c,s}$	casing pressure at surface, psia
$p_{c,v}$	casing pressure at valve depth, psia
$P_d$	pressure in the dome, psig
$p_d$	final discharge pressure, psia
$p_{eng,d}$	engine discharge pressure, psia
$p_{eng,i}$	pressure at engine inlet, psia

**xxxvi** List of Symbols

$p_f$	frictional pressure loss in the power fluid injection tubing, psi
$P_h$	hydraulic power, hp
$p_h$	hydrostatic pressure of the power fluid at pump depth, psia
$p_{hf}$	wellhead flowing pressure, psia
$p_{hfi}$	flowing pressure at the top of lateral $i$ , psia
$p_L$	pressure at the inlet of gas distribution line, psia
$p_i$	initial reservoir pressure, psia, or pressure in tubing, psia, or pressure at stage $i$ , psia $p_{kdi}$ kick-off pressure opposite the first valve, psia
$p_{kfi}$	flowing pressure at the kick-out-point of lateral $i$ , psia
$p_L$	pressure at the inlet of the gas distribution line, psia
$P_{lf}$	flowing liquid gradient, psi/bbl slug
$P_{lh}$	hydrostatic liquid gradient, psi/bbl slug
$p_{Lmax}$	maximum line pressure, psia
$p_o$	pressure in the annulus, psia
$p_{out}$	output pressure of the compression station, psia
$P_p$	$W_p/A_t$ , psia
$p_p$	pore pressure, psi
$p_{pc}$	pseudocritical pressure, psia
$p_{pump,i}$	pump intake pressure, psia
$p_{pump,d}$	pump discharge pressure, psia
$P_r$	pitch length of rotor, ft
$p_r$	pseudoreduced pressure
$P_s$	pitch length of stator, ft, or shaft power, ft–lb <sub>f</sub> /sec
$p_s$	surface operating pressure, psia, or suction pressure, psia, or stock-tank pressure, psia
$p_{sc}$	standard pressure, 14.7 psia
$p_{sh}$	slug hydrostatic pressure, psia
$p_{si}$	surface injection pressure, psia
$p_{suction}$	suction pressure of pump, psia
$P_t$	tubing pressure, psia
$p_{tf}$	flowing tubing head pressure, psig
$p_{up}$	pressure upstream the choke, psia
$P_{vc}$	valve closing pressure, psig
$P_{vo}$	valve opening pressure, psig
$p_{wh}$	upstream (wellhead) pressure, psia
$p_{wf}$	flowing bottom hole pressure, psia
$p_{wfi}$	the average flowing bottom-lateral pressure in lateral $i$ , psia
$p_{wfo}$	dynamic bottom hole pressure because of cross-flow between, psia
$p_{wf}^c$	critical bottom hole pressure maintained during the production decline, psia
$p_{up}$	upstream pressure at choke, psia
$P_1$	pressure at point 1 or inlet, lb <sub>f</sub> /ft <sup>2</sup>
$P_2$	pressure at point 2 or outlet, lb <sub>f</sub> /ft <sup>2</sup>
$p_1$	upstream/inlet/suction pressure, psia
$p_2$	downstream/outlet/discharge pressure, psia
$\bar{p}$	average reservoir pressure, psia
$\bar{p}_f$	reservoir pressure in a future time, psia
$\bar{p}_0$	average reservoir pressure at decline time zero, psia
$\bar{p}_t$	average reservoir pressure at decline time $t$ , psia
$\Delta P$	pressure drop, lb <sub>f</sub> /ft <sup>2</sup>

$\Delta p$	pressure increment, psi
$\delta_p$	head rating developed into an elementary cavity, psi
$\Delta p_f$	frictional pressure drop, psia
$\Delta p_h$	hydrostatic pressure drop, psia
$\Delta p_{i \text{ avg}}$	the average pressure change in the tubing, psi
$\Delta p_{o \text{ avg}}$	the average pressure change in the annulus, psi
$\Delta p_{sf}$	safety pressure margin, 200 to 500 psi
$\Delta p_v$	pressure differential across the operating valve (orifice), psi
$Q$	volumetric flow rate
$q$	volumetric flow rate
$Q_c$	pump displacement, bbl/day
$q_{eng}$	flow rate of power fluid, bbl/day
$Q_G$	gas production rate, Mscf/day
$q_G$	glycol circulation rate, gal/hr
$q_g$	gas production rate, scf/day
$q_{g,inj}$	the lift gas injection rate (scf/day) available to the well
$q_{gM}$	gas flow rate, Mscf/d
$q_{g,total}$	total output gas flow rate of the compression station, scf/day
$q_h$	injection rate per unit thickness of formation, m <sup>3</sup> /sec-m
$q_i$	flow rate from/into layer $i$ , or pumping rate, bpm
$q_{i,max}$	maximum injection rate, bbl/min
$q_L$	liquid capacity, bbl/day
$Q_o$	oil production rate, bbl/day
$q_o$	oil production rate, bbl/day
$q_{pump}$	flow rate of the produced fluid in the pump, bbl/day
$Q_s$	leak rate, bbl/day, or solid production rate, ft <sup>3</sup> /day
$q_s$	gas capacity of contactor for standard gas (0.7 specific gravity) at standard temperature (100°F), MMscfd, or sand production rate, ft <sup>3</sup> /day
$q_{sc}$	gas flow rate, Mscf/day
$q_{st}$	gas capacity at standard conditions, MMscfd
$q_{total}$	total liquid flow rate, bbl/day
$Q_w$	water production rate, bbl/day
$q_w$	water production rate, bbl/d
$q_{wh}$	flow rate at wellhead, stb/day
$R$	producing gas-liquid ratio, Mcf/bbl, or dimensionless nozzle area, or area ratio $A_p/A_b$ , or the radius of fracture, ft, or gas constant, 10.73 ft <sup>3</sup> -psia/lbmol-R
$r$	distance between the mass center of counterweights and the crank shaft, ft or cylinder compression ratio
$r_a$	radius of acid treatment, ft
$R_c$	radius of hole curvature, in.
$r_e$	drainage radius, ft
$r_{eH}$	radius of drainage area, ft
$R_p$	pressure ratio
$R_s$	solution gas-oil ratio, scf/stb
$r_w$	radius of wellbore, ft
$r_{wh}$	desired radius of wormhole penetration, m
$R^2$	$A_o/A_i$
$\nabla_{Ri}$	vertical pressure gradient in the curvic section of lateral $i$ , psi/ft

## xxxviii List of Symbols

$S$	skin factor, or choke size, 1/64 in.
$S_A$	axial stress at any point in the tubing string, psi
$S_f$	specific gravity of fluid in tubing, water = 1, or safety factor
$S_g$	specific gravity of gas, air = 1
$S_o$	specific gravity of produced oil, fresh water = 1
$S_s$	specific gravity of produced solid, fresh water = 1
$S_t$	equivalent pressure caused by spring tension, psig
$S_w$	specific gravity of produced water, fresh water = 1
$T$	temperature, °R
$t$	temperature, °F, or time, hour, or retention time, min
$T_{av}$	average temperature, °R
$T_{avg}$	average temperature in tubing, °F
$T_b$	base temperature, °R, or boiling point, °R
$T_c$	critical temperature, °R
$T_{ci}$	critical temperature of component $i$ , °R
$T_d$	temperature at valve depth, °R
$TF_1$	maximum upstroke torque factor
$TF_2$	maximum downstroke torque factor
$T_m$	mechanical resistant torque, lb <sub>r</sub> -ft
$t_r$	retention time $\approx$ 5.0 min
$T_{sc}$	standard temperature, 520°R
$T_{up}$	upstream temperature, °R
$T_v$	viscosity resistant torque, lb <sub>r</sub> -ft
$T_1$	suction temperature of the gas, °R
$\bar{T}$	average temperature, °R
$u$	fluid velocity, ft/s
$u_m$	mixture velocity, ft/s
$u_{SL}$	superficial velocity of liquid phase, ft/s
$u_{SG}$	superficial velocity of gas phase, ft/s
$V$	volume of the pipe segment, ft <sup>3</sup>
$v$	superficial gas velocity based on total cross-sectional area $A$ , ft/s
$V_a$	the required minimum acid volume, ft <sup>3</sup>
$V_{fg}$	plunger falling velocity in gas, ft/min
$V_{fl}$	plunger falling velocity in liquid, ft/min
$V_g$	required gas per cycle, Mscf
$V_{gas}$	gas volume in standard condition, scf
$V_{G1}$	gas specific volume at upstream, ft <sup>3</sup> /lb <sub>m</sub>
$V_{G2}$	gas specific volume at downstream, ft <sup>3</sup> /lb <sub>m</sub>
$V_h$	required acid volume per unit thickness of formation, m <sup>3</sup> /m
$V_L$	specific volume of liquid phase, ft <sup>3</sup> /mol—lb, or volume of liquid phase in the pipe segment, ft <sup>3</sup> , or liquid settling volume, bbl, or liquid specific volume at upstream, ft <sup>3</sup> /lb <sub>m</sub>
$V_m$	volume of mixture associated with 1 stb of oil, ft <sup>3</sup> , or volume of minerals to be removed, ft <sup>3</sup>
$V_0$	pump displacement, ft <sup>3</sup>
$V_P$	initial pore volume, ft <sup>3</sup>
$V_r$	plunger rising velocity, ft/min
$V_{res}$	oil volume in reservoir condition, rb
$V_s$	required settling volume in separator, gal
$V_{slug}$	slug volume, bbl

$V_{st}$	oil volume in stock tank condition, stb
$V_t$	$A_t(D - V_{slug}L)$ , gas volume in tubing, Mcf
$V_{Vsc}$	specific volume of vapor phase under standard condition, scf/mol-lb
$V_1$	inlet velocity of fluid to be compressed, ft/sec
$V_2$	outlet velocity of compressed fluid, ft/sec
$v_1$	specific volume at inlet, ft <sup>3</sup> /lb
$v_2$	specific volume at outlet, ft <sup>3</sup> /lb
$w$	fracture width, ft, or theoretical shaft work required to compress the gas, ft-lb <sub>f</sub> /lb <sub>m</sub>
$W_{air}$	weight of tubing in air, lb/ft
$W_c$	total weight of counterweights, lb <sub>f</sub>
$W_f$	weight of fluid, lb <sub>f</sub>
$W_{fi}$	weight of fluid inside tubing, lb/ft
$W_{fo}$	weight of fluid displaced by tubing, lb/ft
<b>WOR</b>	producing water-oil ratio, bbl/stb
$W_p$	plunger weight, lb <sub>f</sub>
$W_s$	mechanical shaft work into the system, ft-lb <sub>f</sub> per lb of fluid
$w_w$	fracture width at wellbore, in.
$\bar{w}$	average width, in.
$X$	volumetric dissolving power of acid solution, ft <sup>3</sup> mineral/ ft <sup>3</sup> solution
$x_f$	fracture half-length, ft
$x_i$	mole fraction of compound $i$ in the liquid phase
$x_1$	free gas quality at upstream, mass fraction
$y_a$	actual pressure ratio
$y_c$	critical pressure ratio
$y_i$	mole fraction of compound $i$ in the vapor phase
$y_L$	liquid hold up, fraction
$Z$	gas compressibility factor in average tubing condition
$Z$	gas compressibility factor
$z_b$	gas deviation factor at $T_b$ and $p_b$
$z_d$	gas deviation factor at discharge of cylinder, or gas compressibility factor at valve depth condition
$z_s$	gas deviation factor at suction of the cylinder
$z_1$	compressibility factor at suction conditions
$\bar{z}$	the average gas compressibility factor
$\Delta Z$	elevation increase, ft

---

## GREEK SYMBOLS

$\alpha$	Biot's poroelastic constant, approximately 0.7
$\beta$	gravimetric dissolving power of acid solution, lb <sub>m</sub> mineral/lb <sub>m</sub> solution
$\epsilon'$	pipe wall roughness, in.
$\varphi$	porosity, fraction
$\eta$	pump efficiency
$\gamma$	1.78 = Euler's constant
$\gamma_a$	acid specific gravity, water = 1.0
$\gamma_g$	gas-specific gravity, air = 1
$\gamma_L$	specific gravity of production fluid, water = 1

## xi List of Symbols

$\gamma_m$	mineral specific gravity, water = 1.0
$\gamma_o$	oil specific gravity, water = 1
$\gamma_{oST}$	specific gravity of stock-tank oil, water = 1
$\gamma_S$	specific weight of steel (490 lb/ft <sup>3</sup> )
$\gamma_s$	specific gravity of produced solid, water = 1
$\gamma_w$	specific gravity of produced water, fresh water = 1
$\mu$	viscosity
$\mu_a$	viscosity of acid solution, cp
$\mu_{od}$	viscosity of dead oil, cp
$\mu_f$	viscosity of the effluent at the inlet temperature, cp
$\mu_G$	gas viscosity, cp
$\mu_g$	gas viscosity at in-situ temperature and pressure, cp
$\mu_L$	liquid viscosity, cp
$\mu_o$	viscosity of oil, cp
$\mu_s$	viscosity of the effluent at the surface temperature, cp
$\nu$	Poisson's ratio
$\nu_a$	stoichiometry number of acid
$\nu_m$	stoichiometry number of mineral
$\nu_{pf}$	viscosity of power fluid, centistokes
$\theta$	inclination angle, deg., or dip angle from horizontal direction, deg.
$\rho$	fluid density lb <sub>m</sub> /ft <sup>3</sup>
$\rho_1$	mixture density at top of tubing segment, lb <sub>f</sub> /ft <sup>3</sup>
$\rho_2$	mixture density at bottom of segment, lb <sub>f</sub> /ft <sup>3</sup>
$\rho_a$	density of acid, lb <sub>m</sub> /ft <sup>3</sup>
$\rho_{air}$	density of air, lb <sub>m</sub> /ft <sup>3</sup>
$\rho_G$	in-situ gas density, lb <sub>m</sub> /ft <sup>3</sup>
$\rho_L$	liquid density, lb <sub>m</sub> /ft <sup>3</sup>
$\rho_m$	density of mineral, lb <sub>m</sub> /ft <sup>3</sup>
$\rho_{m2}$	mixture density at downstream, lb <sub>m</sub> /ft <sup>3</sup>
$\rho_{o,st}$	density of stock tank oil, lb <sub>m</sub> /ft <sup>3</sup>
$\rho_w$	density of fresh water, 62.4 lb <sub>m</sub> /ft <sup>3</sup>
$\rho_{wh}$	density of fluid at wellhead, lb <sub>m</sub> /ft <sup>3</sup>
$\rho_i$	density of fluid from/into layer <i>i</i> , lb <sub>m</sub> /ft <sup>3</sup>
$\rho$	average mixture density (specific weight), lb <sub>f</sub> /ft <sup>3</sup>
$\sigma$	liquid-gas interfacial tension, dyne/cm
$\sigma_1$	axial principal stress, psi,
$\sigma_2$	tangential principal stress, psi
$\sigma_3$	radial principal stress, psi
$\sigma_b$	bending stress, psi
$\sigma_v$	overburden stress, psi
$\sigma'_v$	effective vertical stress, psi

# WELL PRODUCTIVITY

# I

*The upstream of the petroleum industry involves itself in the business of oil and gas exploration and production (E & P) activities. While the exploration activities find oil and gas reserves, the production activities deliver oil and gas to the downstream of the industry (i.e., processing plants). The petroleum production is definitely the heart of the petroleum industry.*

*Petroleum production engineering is that part of petroleum engineering that attempts to maximize oil and gas production in a cost-effective manner. To achieve this objective, production engineers need to have a thorough understanding of the petroleum production systems with which they work. To perform their job correctly, production engineers should have a solid background and sound knowledge about the properties of fluids they produce, and working principles of all the major components of producing wells and surface facilities. This part of the book provides graduating production engineers with fundamentals of petroleum production engineering. Materials are presented in the following eight chapters:*

Chapter 1: Well Components 1/3

Chapter 2: Properties of Petroleum Fluids 2/19

Chapter 3: Reservoir Deliverability 3/37



Chapter 4: Wellbore Flow Performance	4/83
Chapter 5: Choke Performance	5/111
Chapter 6: Well Deliverability	6/129
Chapter 7: Forecast of Well Production	7/179
Chapter 8: Production Decline Analysis	8/197

# WELL COMPONENTS

# 1

## 1.1 INTRODUCTION

Role of a production engineer is to maximize oil and gas production in a cost-effective manner. Familiarization and understanding of oil and gas wells are essential to the engineers. This chapter provides graduating production engineers with some basic knowledge about petroleum production wells. More engineering principles are discussed in the later chapters.

Wells fall into categories of oil, condensate, and gas wells depending on the producing gas–oil ratio (GOR). Gas wells are wells with producing GOR being greater than 100,000 scf/stb; condensate wells are those with producing GOR being less than 100,000 scf/stb but greater than 5000 scf/stb; and wells with producing GOR being less than 5000 scf/stb are classified as oil wells.

Fig. 1.1 shows a simple oil production system where a well provides a link between an oil reservoir and surface facilities. The well consists of a wellbore, a wellhead, and a flowline leading the produced fluids to separators.

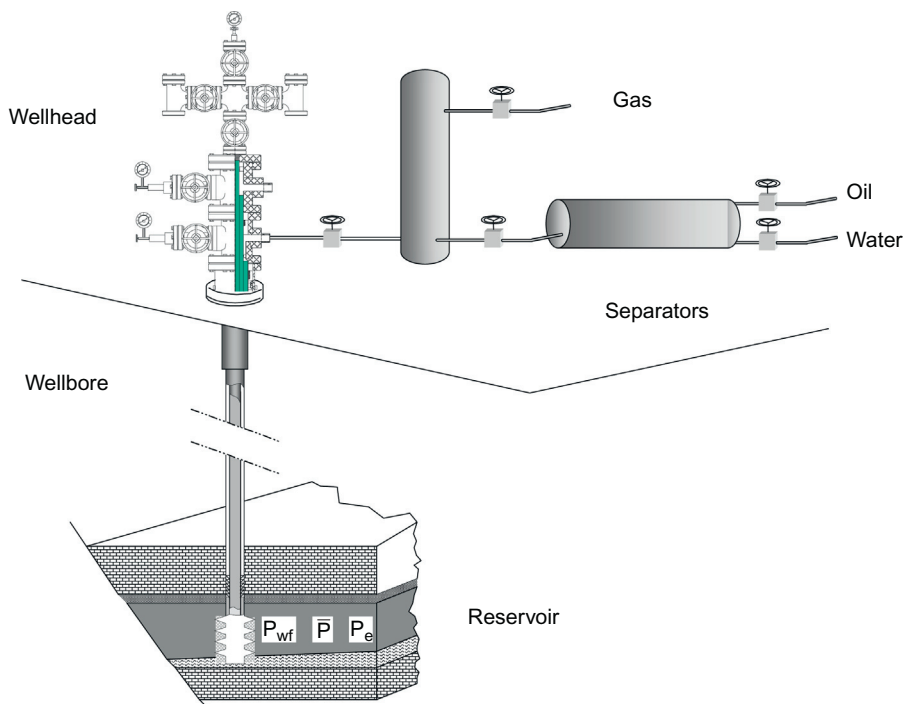
## 1.2 WELLBORE

Fig. 1.2 shows a typical flowing oil well, defined as a well producing solely because of the natural pressure of the reservoir. It is composed of casings, tubing, packers, down-hole chokes (optional), wellhead, Christmas tree, and surface chokes.

Oil and gas wellbores are constructed like an upside-down telescope. The large-diameter borehole section is at the top of the well. Each section is cased to the surface, or a liner is placed in the well that laps over the last casing in the well. Each casing or liner is cemented into the well (usually up to at least where the cement overlaps the previous cement job).

The last casing in the well is the production casing (or production liner). Once the production casing has been cemented into the well, the production tubing is run into the well. Usually a packer is used near the bottom of the tubing to isolate the annulus between the outside of the tubing and the inside of the casing. Thus, the produced fluids are forced to move out of the perforation into the bottom of the well and then into the inside of the tubing. Packers can be actuated by either mechanical or hydraulic mechanisms. The production tubing is often (particularly during initial well flow) provided with a bottom-hole choke to control the initial well flow (i.e., to restrict overproduction and loss of reservoir pressure).

Most wells produce oil through tubing strings, mainly because a tubing string provides good sealing performance and allows the use of gas expansion to lift oil. The American Petroleum Institute (API) defines tubing size using nominal diameter and weight (API, 1987a). The nominal



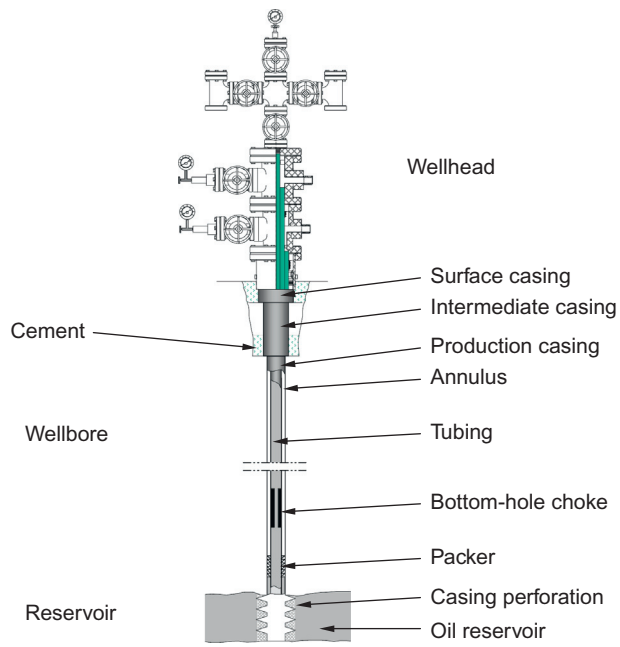
**FIGURE 1.1**

A sketch of a simple petroleum production system.

diameter is based on the internal diameter of the tubing body. The weight of tubing determines the tubing outer diameter. Steel grades of tubing are designated H-40, J-55, C-75, L-80, N-80, C-90, and P-105, where the digits represent the minimum yield strength in 1000 psi. The minimum performance properties of tubing are given in Chapter 9 and Appendix B.

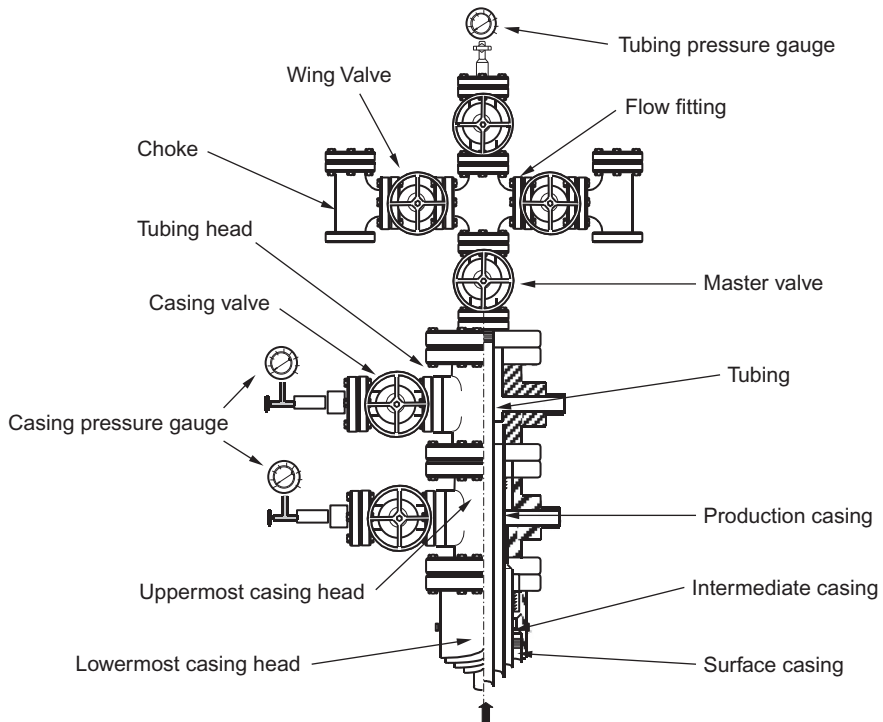
### 1.3 WELLHEAD

The “wellhead” is defined as the surface equipment set below the master valve. As we can see in Fig. 1.3, it includes casing heads and a tubing head. The casing head (lowermost) is threaded onto the surface casing. This can also be a flanged or studded connection. A “casing head” is a mechanical assembly used for hanging a casing string (Fig. 1.4). Depending on casing programs in well drilling, several casing heads can be installed during well construction. The casing head has a bowl that supports the casing hanger. This casing hanger is threaded onto the top of the production casing (or uses friction grips to hold the casing). As in the case of the production tubing, the production casing is landed in tension so that the casing hanger actually supports the production casing



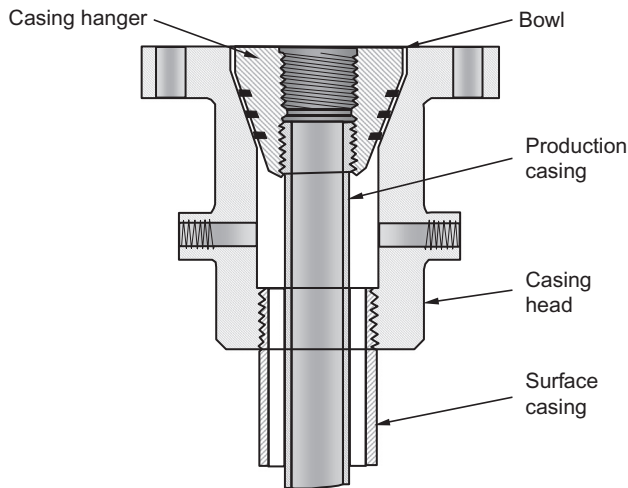
**FIGURE 1.2**

A sketch of a typical flowing oil well.



**FIGURE 1.3**

A sketch of a wellhead.



**FIGURE 1.4**

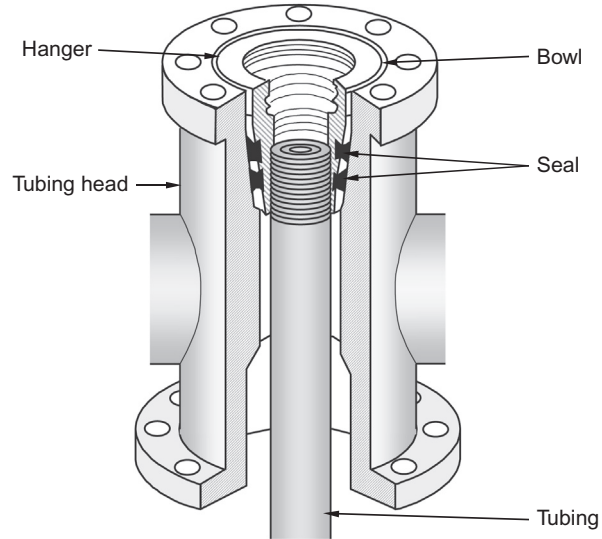
A sketch of a casing head.

(down to the freeze point). In a similar manner, the intermediate casing(s) are supported by their respective casing hangers (and bowls). All of these casing head arrangements are supported by the surface casing, which is in compression and cemented to the surface. A well completed with three casing strings has two casing heads. The uppermost casing head supports the production casing. The lowermost casing head sits on the surface casing (threaded to the top of the surface casing).

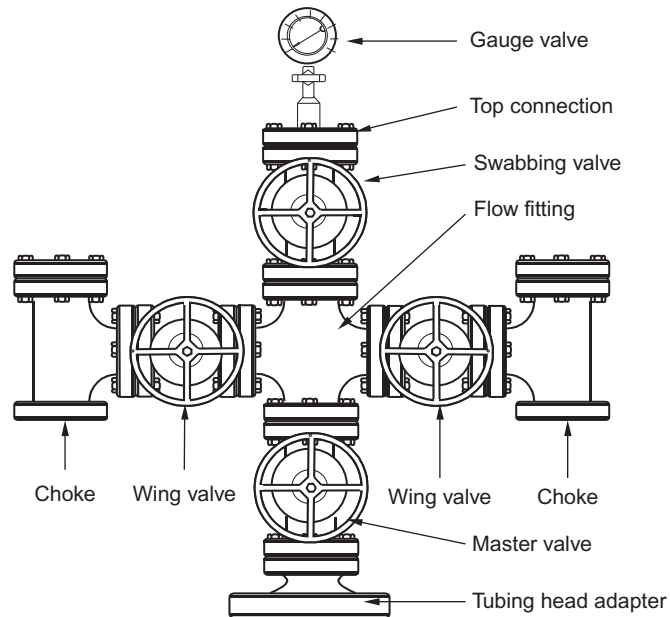
Most flowing wells are produced through a string of tubing run inside the production casing string. At the surface, the tubing is supported by the tubing head (i.e., the tubing head is used for hanging tubing string on the production casing head (Fig. 1.5)). The tubing head supports the tubing string at the surface (this tubing is landed on the tubing head so that it is in tension all the way down to the packer).

The equipment at the top of the producing wellhead is called a “Christmas tree” (Fig. 1.6) and it is used to control flow. The Christmas tree is installed above the tubing head. An “adaptor” is a piece of equipment used to join the two. The Christmas tree may have one flow outlet (a tee) or two flow outlets (a cross). The master valve is installed below the tee or cross. To replace a master valve, the tubing must be plugged. A Christmas tree consists of a main valve, wing valves, and a needle valve. These valves are used for closing the well when needed. At the top of the tee structure (on the top of the Christmas tree), there is a pressure gauge that indicates the pressure in the tubing. The wing valves and their gauges allow access (for pressure measurements and gas or liquid flow) to the annulus spaces (Fig. 1.7).

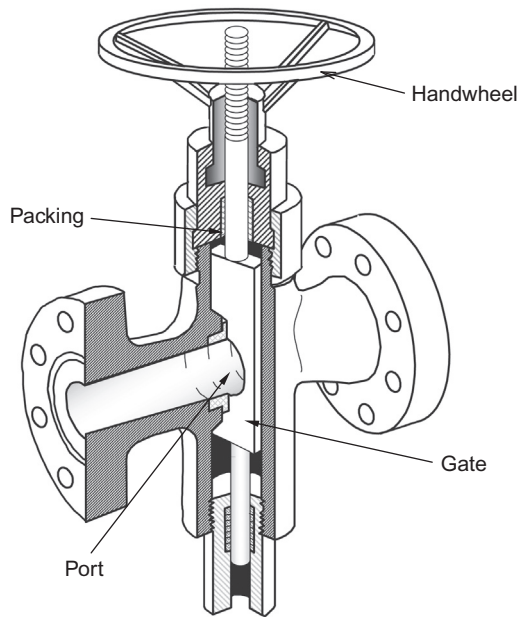
“Surface choke” is a piece of equipment used to control the flow rate (Fig. 1.8). In most flowing wells, the oil production rate is altered by adjusting the choke size. The choke causes back-pressure in the line. The back-pressure (caused by the chokes or other restrictions in the flowline) increases the bottom-hole flowing pressure. Increasing the bottom-hole flowing pressure decreases the

**FIGURE 1.5**

A sketch of a tubing head.

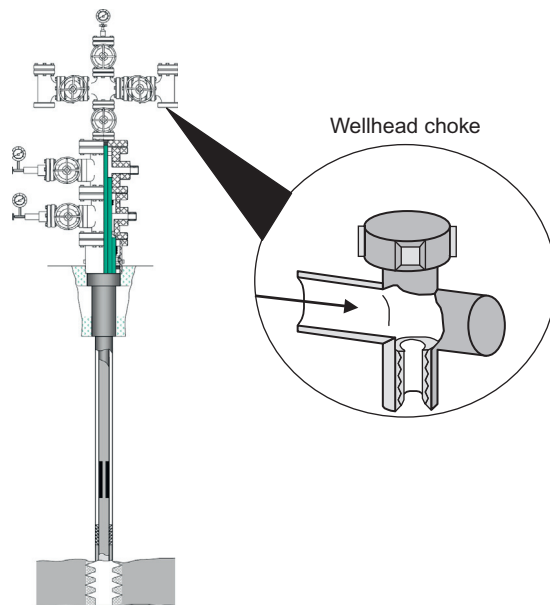
**FIGURE 1.6**

A sketch of a "Christmas tree."



**FIGURE 1.7**

A sketch of a surface valve.



**FIGURE 1.8**

A sketch of a wellhead choke.

pressure drop from the reservoir to the wellbore (pressure drawdown). Thus, increasing the back-pressure in the wellbore decreases the flow rate from the reservoir. In some wells, chokes are installed in the lower section of tubing strings. This choke arrangement reduces wellhead pressure and enhances oil production rate as a result of gas expansion in the tubing string. For gas wells, use of down-hole chokes minimizes the gas hydrate problem in the well stream. A major disadvantage of using down-hole chokes is that replacing a choke is costly.

Certain procedures must be followed to open or close a well. Before opening, check all the surface equipment such as safety valves, fittings, and so on. The burner of a line heater must be lit before the well is opened. This is necessary because the pressure drop across a choke cools the fluid and may cause gas hydrates or paraffin to deposit out. A gas burner keeps the involved fluid (usually water) hot. Fluid from the well is carried through a coil of piping. The choke is installed in the heater. Well fluid is heated both before and after it flows through the choke. The upstream heating helps melt any solids that may be present in the producing fluid. The downstream heating prevents hydrates and paraffins from forming at the choke (Guo and Ghalambor, 2012).

Surface vessels should be open and clear before the well is allowed to flow. All valves that are in the master valve and other downstream valves are closed. Then follow the following procedure to open a well:

1. The operator barely opens the master valve (just a crack), and escaping fluid makes a hissing sound. When the fluid no longer hisses through the valve, the pressure has been equalized, and then the master valve is opened wide.
2. If there are no oil leaks, the operator cracks the next downstream valve that is closed. Usually, this will be either the second (backup) master valve or a wing valve. Again, when the hissing sound stops, the valve is opened wide.
3. The operator opens the other downstream valves the same way.
4. To read the tubing pressure gauge, the operator must open the needle valve at the top of the Christmas tree. After reading and recording the pressure, the operator may close the valve again to protect the gauge.

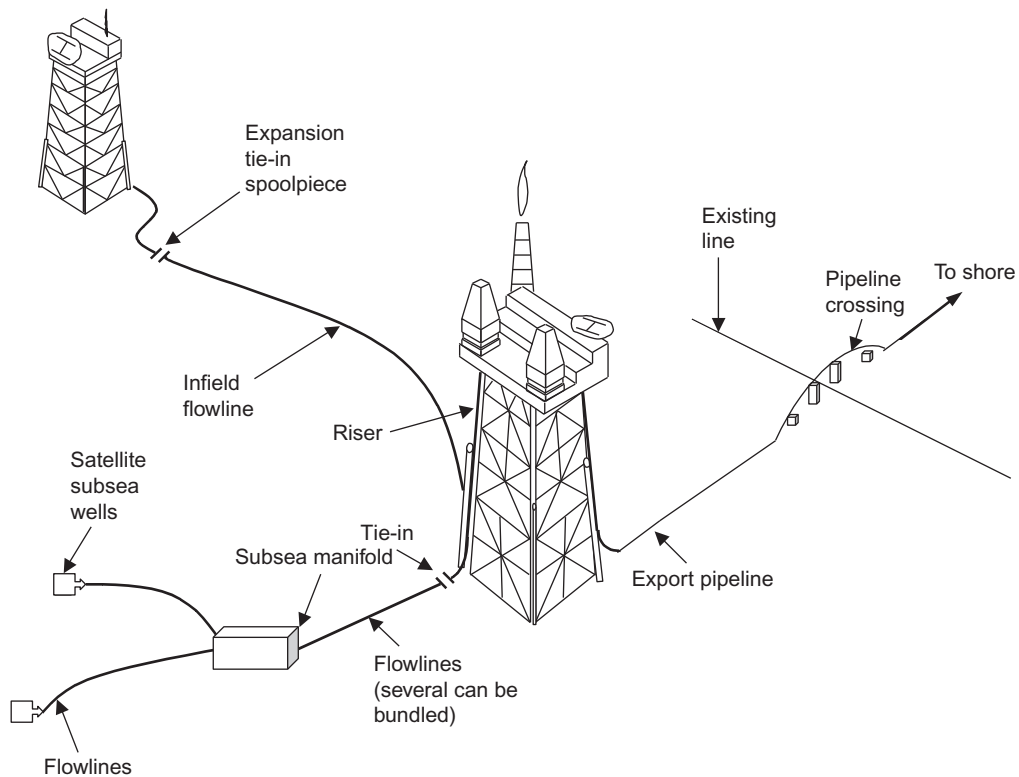
The procedure for “shutting-in” a well is the opposite of the procedure for opening a well. In shutting-in the well, the master valve is closed last. Valves are closed rather rapidly to avoid wearing of the valve (to prevent erosion). At least two valves must be closed.

---

## 1.4 FLOWLINE

A flowline is a segment of steel pipe conveying the produced fluids from a wellhead, through a production manifold as necessary, to a fluid separator of a surface facility. Fig. 1.9 shows applications of flowlines in offshore operations. It indicates flowlines transporting oil and/or gas from satellite subsea wells to subsea manifolds, flowlines transporting oil and/or gas from subsea manifolds to production facility platforms, infield flowlines transporting oil and/or gas from between production facility platforms, and export pipelines transporting oil and/or gas from production facility platforms to shore.



**FIGURE 1.9**

Uses of offshore flowlines and pipelines (Guo et al., 2013).

## 1.5 SAFETY CONTROL SYSTEM

The purpose of safety systems is to protect personnel, the environment, and the facility. The major objective of the safety system is to prevent the release of hydrocarbons from the process and to minimize the adverse effects of such releases if they occur. This can be achieved through the following:

1. Preventing undesirable events
2. Shutting-in the process
3. Recovering released fluids
4. Preventing ignition

The modes of safety system operation include:

1. Automatic monitoring by sensors
2. Automatic protective action
3. Emergency shutdown

Protection concepts and safety analysis are based on undesirable events, which include:

1. Overpressure caused by:
  - a. Increased input flow due to upstream flow-control device failure
  - b. Decreased output flow due to blockage
  - c. Heating of closed system
2. Leak caused by:
  - a. Corrosion
  - b. Erosion
  - c. Mechanical failure due to temperature change, overpressure and underpressure, and external impact force
3. Liquid overflow caused by:
  - a. Increased input flow due to upstream flow-control device failure
  - b. Decreased output flow due to blockage in the liquid discharge
4. Gas blow-by caused by:
  - a. Increased input flow due to upstream flow-control device failure
  - b. Decreased output flow due to blockage in the gas discharge
5. Underpressure caused by:
  - a. Outlet flow-control device (e.g., choke) failure
  - b. Inlet blockage
  - c. Cooling of closed system
6. Excess temperature caused by:
  - a. Overfueling of burner
  - b. External fire
  - c. Spark emission

Fig. 1.10 presents some symbols used in safety system design. Some API-recommended safety devices are shown in Figs. 1.11 through 1.15 (API, 1987b).

---

## 1.6 SUMMARY

This chapter provided a brief introduction to the components of petroleum production wells. Working principles, especially flow performances, of the components are described in later chapters.

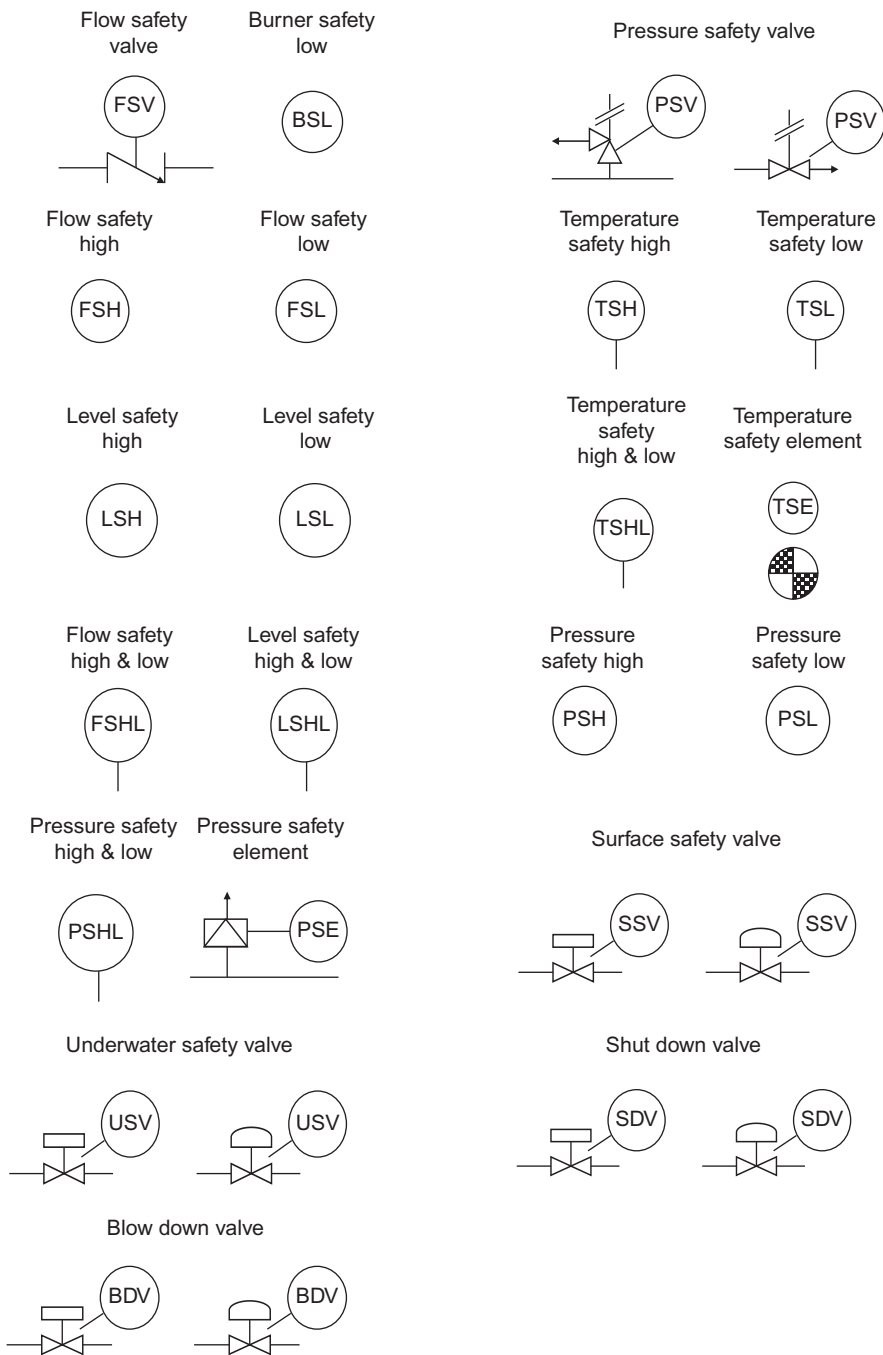
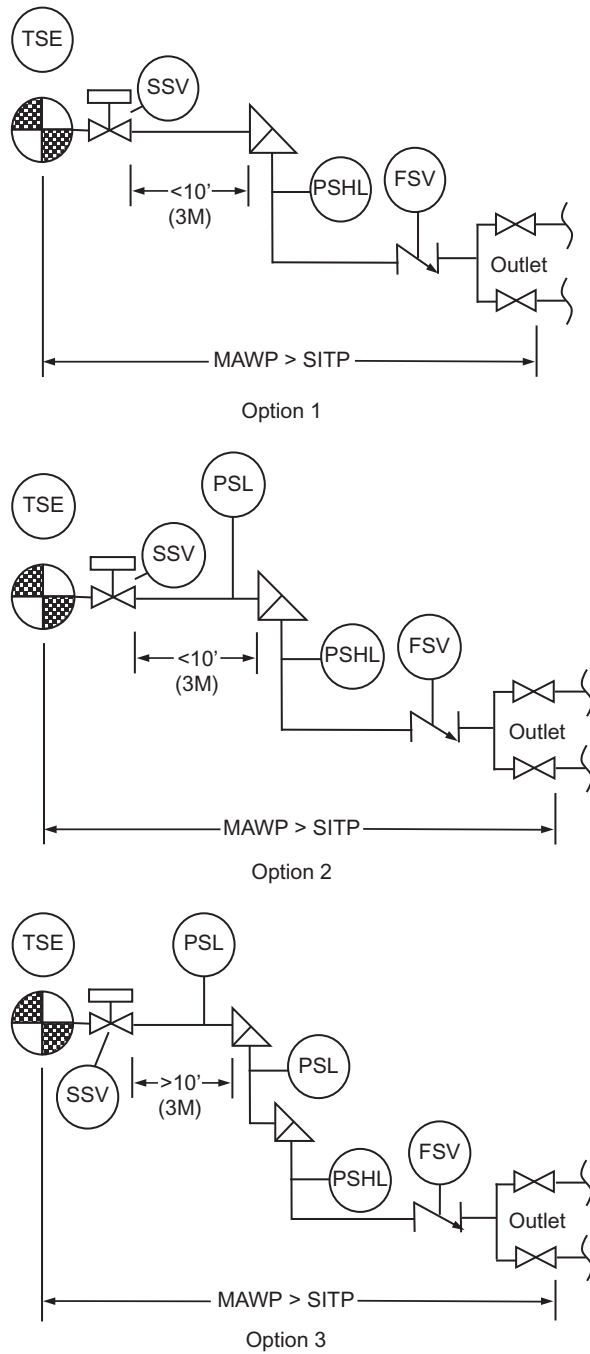


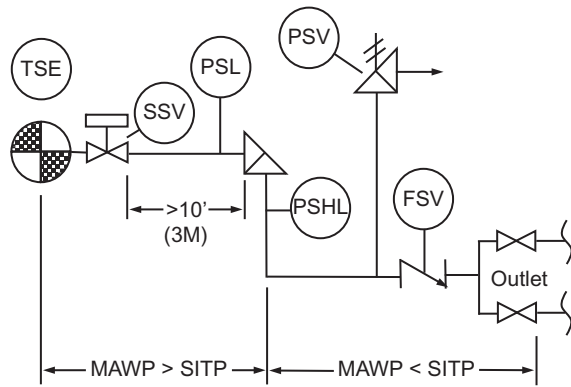
FIGURE 1.10

Safety device symbols.

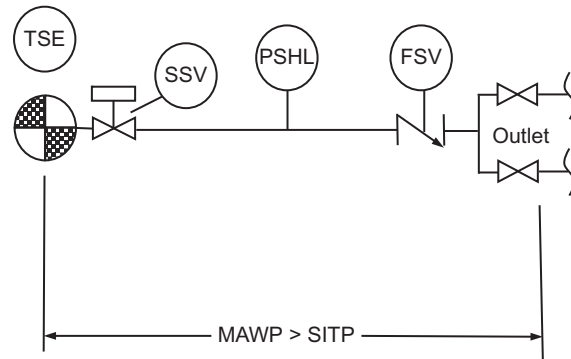


**FIGURE 1.11**

Safety system designs for surface wellhead flowlines.



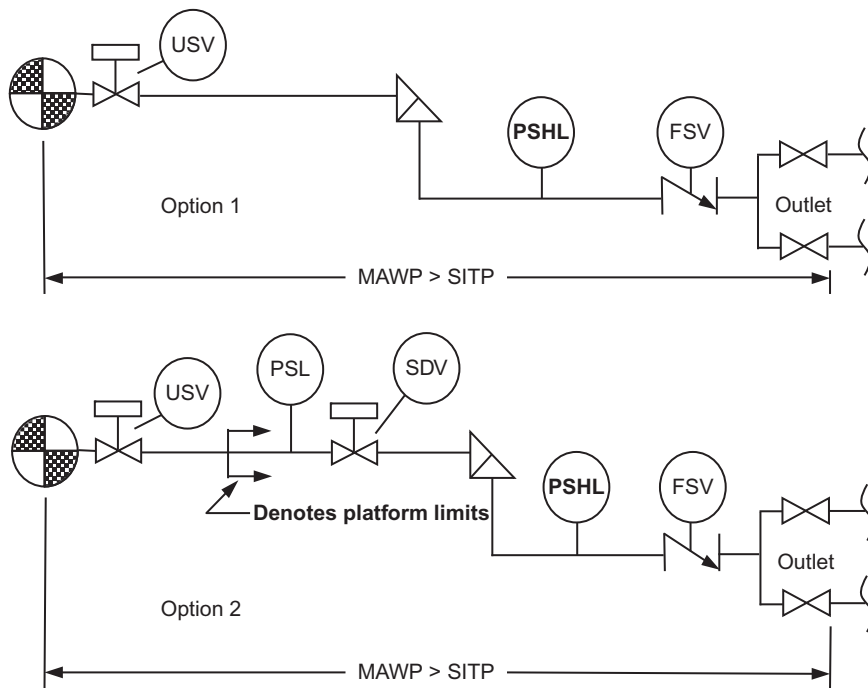
Option 4



Option 5

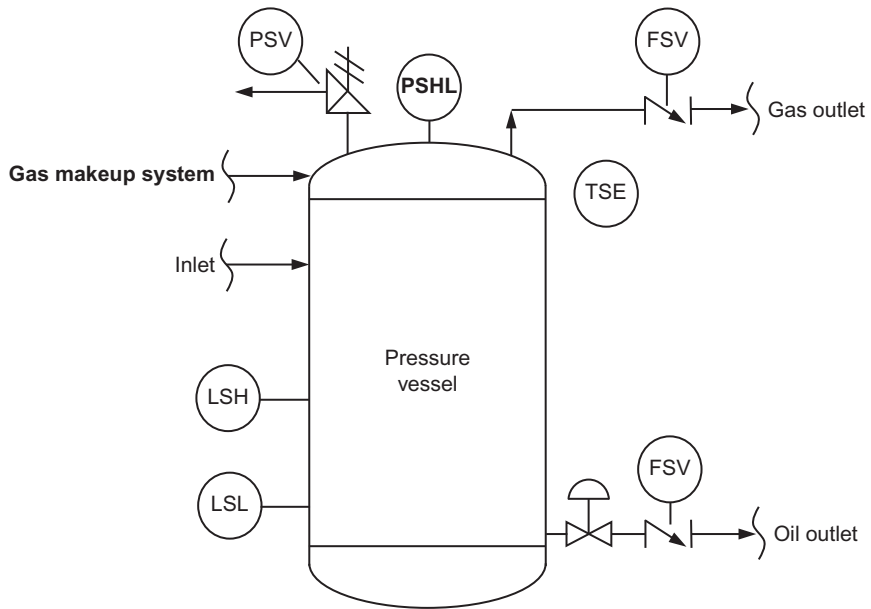
**FIGURE 1.11**

(Continued).



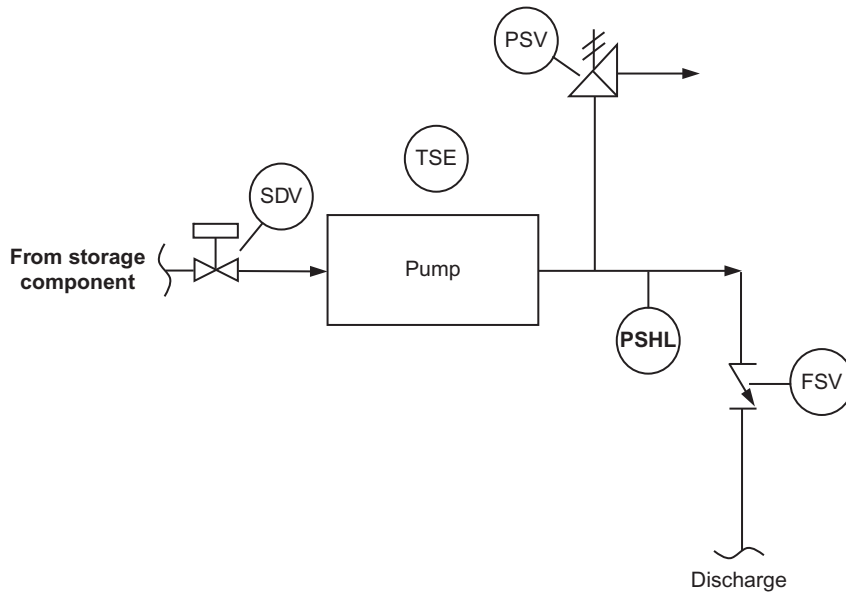
**FIGURE 1.12**

Safety system designs for underwater wellhead flowlines.

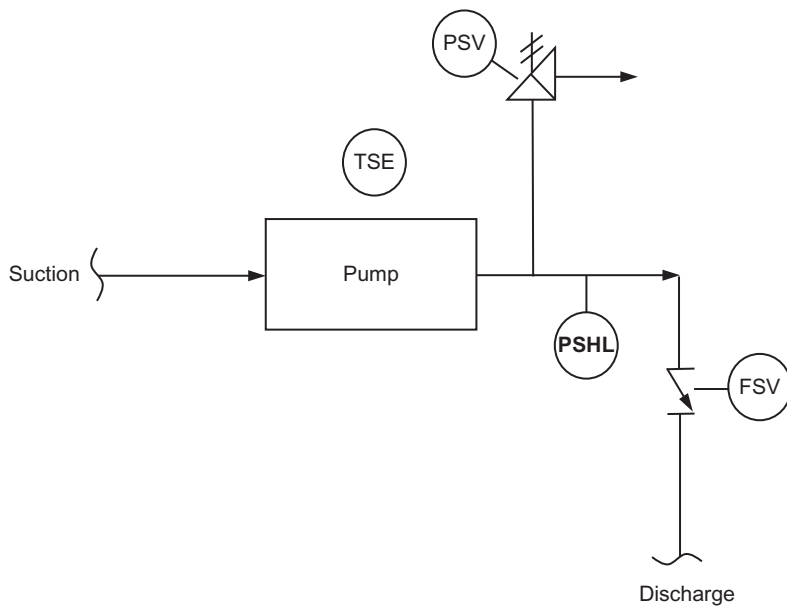


**FIGURE 1.13**

Safety system design for pressure vessel.



**FIGURE 1.14**  
Safety system design for pipeline pumps.



**FIGURE 1.15**  
Safety system design for other pumps.

---

## REFERENCES

- American Petroleum Institute (API), 1987a. API Bulletin 5C2, May 31. Bulletin on Performance Properties of Casing, Tubing, and Drill Pipe. twentieth ed. American Petroleum Institute, Washington, DC.
- American Petroleum Institute (API), 1987b. API Bulletin 14C, May 31. Recommended Practice for Analysis, Design, Installation, and Testing of Basic Surface Safety Systems for Offshore Production Platforms. twentieth ed. American Petroleum Institute, Washington, DC.
- Guo, B., Ghalambor, A., 2012. Natural Gas Engineering Handbook. second ed. Gulf Publishing Company, Houston.
- Guo, B., Song, S., Ghalambor, A., Lin, T., 2013. Offshore Pipelines. second ed. Elsevier, Amsterdam.

---

## PROBLEMS

- 1.1. What is the role of an oil production engineer?
- 1.2. Is the tubing nominal diameter closer to tubing outside diameter or tubing inside diameter?
- 1.3. What do the digits in the tubing specification represent?
- 1.4. What is a wellhead choke used for?
- 1.5. What are the benefits and disadvantages of using down-hole chokes over wellhead chokes?
- 1.6. What is the temperature safety element used for?



# PROPERTIES OF PETROLEUM FLUIDS

## 2.1 INTRODUCTION

Properties of crude oil, natural gas, and produced water are fundamental for designing and analyzing oil and gas production systems in petroleum engineering. This chapter presents definitions of these fluid properties and some means of obtaining these property values other than experimental measurements. Applications of the fluid properties appear in subsequent chapters.

## 2.2 PROPERTIES OF OIL

Oil properties include solution gas–oil ratio (GOR), density, formation volume factor, viscosity, and compressibility. The latter four properties are interrelated through solution GOR.

### 2.2.1 SOLUTION GAS–OIL RATIO

“Solution GOR” is defined as the amount of gas (in standard condition) that will dissolve in unit volume of oil when both are taken down to the reservoir at the prevailing pressure and temperature; that is,

$$R_s = \frac{V_{gas}}{V_{oil}}, \quad (2.1)$$

where  $R_s$  = solution GOR (in scf/stb);  $V_{gas}$  = gas volume in standard condition (scf);  $V_{oil}$  = oil volume in stock tank condition (stb)

The “standard condition” is defined as 14.7 psia and 60 °F in most states in the United States. At a given reservoir temperature, solution GOR remains constant at pressures above bubble-point pressure. It drops as pressure decreases in the pressure range below the bubble-point pressure.

Solution GOR is measured in PTV laboratories. Empirical correlations are also available based on data from PVT labs. One of the correlations is,

$$R_s = \gamma_g \left[ \frac{p}{18} \frac{10^{0.0125(^{\circ}API)}}{10^{0.00091t}} \right]^{1.2048} \quad (2.2)$$

where  $\gamma_g$  and  $^{\circ}API$  are defined in the latter sections, and  $p$  and  $t$  are pressure and temperature in psia and °F, respectively.

Solution GOR factor is often used for volumetric oil and gas calculations in reservoir engineering. It is also used as a base parameter for estimating other fluid properties such as density of oil.

### 2.2.2 DENSITY OF OIL

“Density of oil” is defined as the mass of oil per unit volume, or  $\text{lb}_m/\text{ft}^3$  in U.S. Field unit. It is widely used in hydraulics calculations, e.g., wellbore flow and pipeline flow performance calculations (see Chapters 4 and 11).

Because of gas content, density of oil is pressure dependent. The density of oil at standard condition (stock tank oil) is evaluated by API gravity. The relationship between the density of stock tank oil and API gravity is given through the following relations:

$$^\circ API = \frac{141.5}{\gamma_o} - 131.5 \quad (2.3)$$

and

$$\gamma_o = \frac{\rho_{o,st}}{\rho_w}, \quad (2.4)$$

where  $^\circ API$  = API gravity of stock tank oil;  $\gamma_o$  = specific gravity of stock tank oil, 1 for freshwater;  $\rho_{o,st}$  = density of stock tank oil,  $\text{lb}_m/\text{ft}^3$ ;  $\rho_w$  = density of freshwater,  $62.4 \text{ lb}_m/\text{ft}^3$

The density of oil at elevated pressures and temperatures can be estimated on empirical correlations developed by a number of investigators. [Ahmed \(1989\)](#) gives a summary of correlations. Engineers should select and validate the correlations carefully with measurements before adopting any correlations.

[Standing \(1981\)](#) proposed a correlation for estimating the oil formation volume factor as a function of solution GOR, specific gravity of stock tank oil, specific gravity of solution gas, and temperature. By coupling the mathematical definition of the oil formation volume factor with Standing’s correlation, [Ahmed \(1989\)](#) presented the following expression for the density of oil:

$$\rho_o = \frac{62.4\gamma_o + 0.0136R_s\gamma_g}{0.972 + 0.000147 \left[ R_s \sqrt{\frac{\gamma_g}{\gamma_o}} + 1.25t \right]^{1.175}}, \quad (2.5)$$

where  $t$  = temperature,  $^\circ\text{F}$ ;  $\gamma_g$  = specific gravity of gas, 1 for air.

### 2.2.3 FORMATION VOLUME FACTOR OF OIL

“Formation volume factor of oil” is defined as the volume occupied in the reservoir at the prevailing pressure and temperature by volume of oil in stock tank, plus its dissolved gas; that is,

$$B_o = \frac{V_{res}}{V_{st}}, \quad (2.6)$$

where  $B_o$  = formation volume factor of oil (rb/stb);  $V_{res}$  = oil volume in reservoir condition (rb);  $V_{st}$  = oil volume in stock tank condition (stb)

Formation volume factor of oil is always greater than unity because oil dissolves more gas in reservoir condition than in stock tank condition. At a given reservoir temperature, oil formation volume factor remains nearly constant at pressures above bubble-point pressure. It drops as pressure decreases in the pressure range below the bubble-point pressure.

Formation volume factor of oil is measured in PTV labs. Numerous empirical correlations are available based on data from PVT labs. One of the correlations is

$$B_o = 0.9759 + 0.00012 \left[ R_s \sqrt{\frac{\gamma_g}{\gamma_o}} + 1.25t \right]^{1.2} \quad (2.7)$$

Formation volume factor of oil is often used for oil volumetric calculations and well-inflow calculations. It is also used as a base parameter for estimating other fluid properties.

### 2.2.4 VISCOSITY OF OIL

“Viscosity” is an empirical parameter used for describing the resistance to flow of fluid. The viscosity of oil is of interest in well-inflow and hydraulics calculations in oil production engineering. While the viscosity of oil can be measured in PVT labs, it is often estimated using empirical correlations developed by a number of investigators including [Beal \(1946\)](#), [Beggs and Robinson \(1975\)](#), [Standing \(1981\)](#), [Glaso \(1985\)](#), [Khan \(1987\)](#), and [Ahmed \(1989\)](#). A summary of these correlations is given by [Ahmed \(1989\)](#). Engineers should select and validate a correlation with measurements before it is used. [Standing’s \(1981\)](#) correlation for dead oil is expressed as

$$\mu_{od} = \left( 0.32 + \frac{1.8 \times 10^7}{APJ^{4.53}} \right) \left( \frac{360}{t+200} \right)^A, \quad (2.8)$$

where

$$A = 10^{(0.43 + \frac{8.33}{APJ})} \quad (2.9)$$

and  $\mu_{od}$  = viscosity of dead oil (cp).

[Standing’s \(1981\)](#) correlation for saturated crude oil is expressed as

$$\mu_{ob} = 10^a \mu_{od}^b, \quad (2.10)$$

where  $\mu_{ob}$  = viscosity of saturated crude oil in cp and

$$a = R_s(2.2 \times 10^{-7} R_s - 7.4 \times 10^{-4}), \quad (2.11)$$

$$b = \frac{0.68}{10^c} + \frac{0.25}{10^d} + \frac{0.062}{10^e}, \quad (2.12)$$

$$c = 8.62 \times 10^{-5} R_s, \quad (2.13)$$

$$d = 1.10 \times 10^{-3} R_s, \quad (2.14)$$

and

$$e = 3.74 \times 10^{-3} R_s, \quad (2.15)$$

[Standing’s \(1981\)](#) correlation for unsaturated crude oil is expressed as

$$\mu_o = \mu_{ob} + 0.001(p - p_b) \left( 0.024 \mu_{ob}^{1.6} + 0.38 \mu_{ob}^{0.56} \right). \quad (2.16)$$

### 2.2.5 OIL COMPRESSIBILITY

“Oil compressibility” is defined as

$$c_o = -\frac{1}{V} \left( \frac{\partial V}{\partial p} \right)_T, \quad (2.17)$$

where  $T$  and  $V$  are temperature and volume, respectively. Oil compressibility is measured from PVT labs. It is often used in modeling well-inflow performance and reservoir simulation.

**Example Problem 2.1** The solution GOR of a crude oil is 600 scf/stb at 4475 psia and 140 °F. Given the following PVT data, estimate density and viscosity of the crude oil at the pressure and temperature:

Bubble-point pressure:	2745 psia
Oil gravity:	35 °API
Gas-specific gravity:	0.77 air = 1

**Solution** Example Problem 2.1 can be quickly solved using the spreadsheet program *OilProperties.xls* where Standing’s correlation for oil viscosity was coded. The input and output of the program is shown in [Table 2.1](#).

## 2.3 PROPERTIES OF NATURAL GAS

Gas properties include gas-specific gravity, gas psuedo-critical pressure and temperature, gas viscosity, gas compressibility factor, gas density, gas formation volume factor, and gas compressibility. The first two are composition dependent. The latter four are pressure dependent.

### 2.3.1 SPECIFIC GRAVITY OF GAS

“Specific gravity gas” is defined as the ratio of the apparent molecular weight of the gas to that of air. The molecular weight of air is usually taken as equal to 28.97 (~79% nitrogen and 21% oxygen). Therefore, the gas-specific gravity is

$$\gamma_g = \frac{MW_a}{28.97}, \quad (2.18)$$

where  $MW_a$  is the apparent molecular weight of gas, which can be calculated on the basis of gas composition. Gas composition is usually determined in a laboratory and reported in mole fractions of components in the gas. Let  $y_i$  be the mole fraction of component  $i$ , and the apparent molecular weight of the gas can be formulated using a mixing rule such as

$$MW_a = \sum_{i=1}^{N_c} y_i MW_i, \quad (2.19)$$

where  $MW_i$  is the molecular weight of component  $i$ , and  $N_c$  is number of components. The molecular weights of compounds ( $MW_i$ ) can be found in textbooks on organic chemistry or petroleum fluids such as that by [Ahmed \(1989\)](#). Gas-specific gravity varies between 0.55 and 0.9.

**Table 2.1 Result Given by the Spreadsheet Program OilProperties.xls**

*OilProperties.xls*

*Description:* This spreadsheet calculates density and viscosity of a crude oil.

*Instruction:* (1) Click a unit-box to choose a unit system; (2) update parameter values in the Input data section; (3) view result in the Solution section and charts.

<i>Input data</i>	<i>U.S. Field units</i>	<i>SI units</i>
Pressure ( <i>p</i> ):	4475 psia	
Temperature ( <i>t</i> ):	140 °F	
Bubble point pressure ( <i>p<sub>b</sub></i> ):	2745 psia	
Stock tank oil gravity:	35 °API	
Solution gas–oil ratio ( <i>R<sub>s</sub></i> ):	600 scf/stb	
Gas specific gravity ( <i>γ<sub>g</sub></i> ):	0.77 air = 1	
<i>Solution</i>		
$\gamma_o = \frac{141.5}{\text{°API} + 131.5}$	= 0.8498 H <sub>2</sub> O = 1	
$\rho_o = \frac{62.4\gamma_o + 0.0136R_s\gamma_g}{0.972 + 0.000147 \left[ R_s \sqrt{\frac{\gamma_g}{\gamma_o}} + 1.25t \right]^{1.175}}$	= 44.90 lb <sub>m</sub> /ft <sup>3</sup>	
$A = 10^{(0.43+8.33/\text{API})}$	= 4.6559	
$\mu_{od} = \left( 0.32 + \frac{1.8 \times 10^7}{\text{API}^{4.53}} \right) \left( \frac{360}{t+200} \right)^A$	= 2.7956 cp	
$a = R_s(2.2 \times 10^{-7}R_s - 7.4 \times 10^{-4})$	= -0.3648	
$c = 8.62 \times 10^{-5}R_s$	= 0.0517	
$d = 1.10 \times 10^{-3}R_s$	= 0.6600	
$e = 3.74 \times 10^{-3}R_s$	= 2.2440	
$b = \frac{0.68}{10^c} + \frac{0.25}{10^d} + \frac{0.062}{10^e}$	= 0.6587	
$\mu_{ob} = 10^a \mu_{od}^b$	= 0.8498 cp	0.0008 Pa-s
$\mu_o = \mu_{ob} + 0.001(p - p_b)(0.024\mu_{ob}^{1.6} + 0.38\mu_{ob}^{0.56})$	= 1.4819 cp	0.0015 Pa-s

### 2.3.2 GAS PSEUDO-CRITICAL PRESSURE AND TEMPERATURE

Similar to gas apparent molecular weight, the critical properties of a gas can be determined on the basis of the critical properties of compounds in the gas using the mixing rule. The gas critical properties determined in such a way are called “pseudo-critical properties.” Gas pseudo-critical pressure (*p<sub>pc</sub>*) and pseudo-critical temperature (*T<sub>pc</sub>*) are, respectively, expressed as

$$p_{pc} = \sum_{i=1}^{N_c} y_i p_{ci} \tag{2.20}$$

and

$$T_{pc} = \sum_{i=1}^{N_c} y_i T_{ci}, \tag{2.21}$$

where *p<sub>ci</sub>* and *T<sub>ci</sub>* are critical pressure and critical temperature of component *i*, respectively.

**Example Problem 2.2** For the gas composition given in the following text, determine apparent molecular weight, specific gravity, pseudo-critical pressure, and pseudo-critical temperature of the gas.

Component	Mole Fraction
C <sub>1</sub>	0.775
C <sub>2</sub>	0.083
C <sub>3</sub>	0.021
i-C <sub>4</sub>	0.006
n-C <sub>4</sub>	0.002
i-C <sub>5</sub>	0.003
n-C <sub>5</sub>	0.008
C <sub>6</sub>	0.001
C <sub>7+</sub>	0.001
N <sub>2</sub>	0.050
CO <sub>2</sub>	0.030
H <sub>2</sub> S	0.020

**Solution** Example Problem 2.2 is solved with the spreadsheet program *MixingRule.xls*. Results are shown in Table 2.2.

Table 2.2 Results Given by the Spreadsheet Program <i>MixingRule.xls</i>							
<i>MixingRule.xls</i>							
<i>Description:</i> This spreadsheet calculates gas apparent molecular weight, specific gravity, pseudo-critical pressure, and pseudo-critical temperature.							
<i>Instruction:</i> (1) Update gas composition data ( $y_i$ ); (2) read result.							
Compound	$y_i$	$MW_i$	$y_i MW_i$	$p_{ci}$ (psia)	$y_i p_{ci}$ (psia)	$T_{ci}$ (°R)	$y_i T_{ci}$ (°R)
C <sub>1</sub>	0.775	1e.04	12.43	673	521.58	344	266.60
C <sub>2</sub>	0.083	30.07	2.50	709	58.85	550	45.65
C <sub>3</sub>	0.021	44.10	0.93	618	12.98	666	13.99
i-C <sub>4</sub>	0.00e	58.12	0.35	530	3.18	733	4.40
n-C <sub>4</sub>	0.002	58.12	0.12	551	1.10	766	1.53
i-C <sub>5</sub>	0.003	72.15	0.22	482	1.45	830	2.49
n-C <sub>5</sub>	0.008	72.15	0.58	485	3.88	847	6.78
C <sub>6</sub>	0.001	8e.18	0.09	434	0.43	915	0.92
C <sub>7+</sub>	0.001	114.23	0.11	361	0.36	1024	1.02
N <sub>2</sub>	0.050	28.02	1.40	227	11.35	492	24.60
CO <sub>2</sub>	0.030	44.01	1.32	1,073	32.19	548	16.44
H <sub>2</sub> S	0.020	34.08	0.68	1306	13.45	672	26.12
	1.000	$MW_a =$	20.71	$p_{pc} =$	673	$T_{pc} =$	398
		$\gamma_g =$	0.71				

If the gas composition is not known but gas-specific gravity is given, the pseudo-critical pressure and temperature can be determined from various charts or correlations developed based on the charts. One set of simple correlations is

$$p_{pc} = 709.604 - 58.718\gamma_g \quad (2.22)$$

$$T_{pc} = 170.491 + 307.344\gamma_g, \quad (2.23)$$

which are valid for  $H_2S < 3\%$ ,  $N_2 < 5\%$ , and total content of inorganic compounds less than 7%.

Corrections for impurities in sour gases are always necessary. The corrections can be made using either charts or correlations such as the [Wichert and Aziz \(1972\)](#) correction expressed as follows:

$$A = y_{H_2S} + y_{CO_2} \quad (2.24)$$

$$B = y_{H_2S} \quad (2.25)$$

$$\varepsilon_3 = 120(A^{0.9} - A^{1.6}) + 15(B^{0.5} - B^{4.0}) \quad (2.26)$$

$$T_{pc'} = T_{pc} - \varepsilon_3 \quad (2.27)$$

$$P_{pc'} = \frac{P_{pc} T_{pc'}}{T_{pc} + B(1 - B)\varepsilon_3} \quad (2.28)$$

Correlations with impurity corrections for mixture pseudo-criticals are also available ([Ahmed, 1989](#)):

$$p_{pc} = 678 - 50(\gamma_g - 0.5) - 206.7y_{N_2} + 440y_{CO_2} + 606.7y_{H_2S} \quad (2.29)$$

$$T_{pc} = 326 + 315.7(\gamma_g - 0.5) - 240y_{N_2} - 83.3y_{CO_2} + 133.3y_{H_2S}. \quad (2.30)$$

Applications of the pseudo-critical pressure and temperature are normally found in petroleum engineering through pseudo-reduced pressure and temperature defined as

$$p_{pr} = \frac{p}{p_{pc}} \quad (2.31)$$

$$T_{pr} = \frac{T}{T_{pc}}. \quad (2.32)$$

### 2.3.3 VISCOSITY OF GAS

Dynamic viscosity ( $\mu_g$ ) in centipoises (cp) is usually used in petroleum engineering. Kinematic viscosity ( $\nu_g$ ) is related to the dynamic viscosity through density ( $\rho_g$ ),

$$\nu_g = \frac{\mu_g}{\rho_g} \quad (2.33)$$

Kinematic viscosity is not typically used in natural gas engineering.

Direct measurements of gas viscosity are preferred for a new gas. If gas composition and viscosities of gas components are known, the mixing rule can be used to determine the viscosity of the gas mixture:

$$\mu_g = \frac{\sum (\mu_{gi} y_i \sqrt{MW_i})}{\sum (y_i \sqrt{MW_i})} \quad (2.34)$$

Viscosity of gas is very often estimated with charts or correlations developed based on the charts. Gas viscosity correlation of Carr et al., 1954 involves a two-step procedure: The gas viscosity at temperature and atmospheric pressure is estimated first from gas-specific gravity and inorganic compound content. The atmospheric value is then adjusted to pressure conditions by means of a correction factor on the basis of reduced temperature and pressure state of the gas. The atmospheric pressure viscosity ( $\mu_1$ ) can be expressed as

$$\mu_1 = \mu_{1HC} + \mu_{1N_2} + \mu_{1CO_2} + \mu_{1H_2S}, \quad (2.35)$$

where

$$\mu_{1HC} = 8.188 \times 10^{-3} - 6.15 \times 10^{-3} \log(\gamma_g) + (1.709 \times 10^{-5} - 2.062 \times 10^{-6} \gamma_g)T, \quad (2.36)$$

$$\mu_{1N_2} = [9.59 \times 10^{-3} + 8.48 \times 10^{-3} \log(\gamma_g)]y_{N_2}, \quad (2.37)$$

$$\mu_{1CO_2} = [6.24 \times 10^{-3} + 9.08 \times 10^{-3} \log(\gamma_g)]y_{CO_2}, \quad (2.38)$$

$$\mu_{1H_2S} = [3.73 \times 10^{-3} + 8.49 \times 10^{-3} \log(\gamma_g)]y_{H_2S}, \quad (2.39)$$

Dempsey (1965) developed the following relation:

$$\begin{aligned} \mu_r &= \ln \left( \frac{\mu_g}{\mu_1} T_{pr} \right) \\ &= a_0 + a_1 p_{pr} + a_2 p_{pr}^2 + a_3 p_{pr}^3 + T_{pr}(a_4 + a_5 p_{pr} \\ &\quad + a_6 p_{pr}^2 + a_7 p_{pr}^3) + T_{pr}^2(a_8 + a_9 p_{pr} + a_{10} p_{pr}^2 \\ &\quad + a_{11} p_{pr}^3) + T_{pr}^3(a_{12} + a_{13} p_{pr} + a_{14} \\ &\quad + a_{15} p_{pr}^3), \end{aligned} \quad (2.40)$$

where  $a_0 = -2.46211820$ ;  $a_1 = 2.97054714$ ;  $a_2 = -0.28626405$ ;  $a_3 = 0.00805420$ ;  $a_4 = 2.80860949$ ;  $a_5 = -3.49803305$ ;  $a_6 = 0.36037302$ ;  $a_7 = -0.01044324$ ;  $a_8 = -0.79338568$ ;  $a_9 = 1.39643306$ ;  $a_{10} = -0.14914493$ ;  $a_{11} = 0.00441016$ ;  $a_{12} = 0.08393872$ ;  $a_{13} = -0.18640885$ ;  $a_{14} = 0.02033679$ ;  $a_{15} = -0.00060958$

Thus, once the value of  $\mu_r$  is determined from the right-hand side of this equation, gas viscosity at elevated pressure can be readily calculated using the following relation:

$$\mu_g = \frac{\mu_1}{T_{pr}} e^{\mu_r} \quad (2.41)$$

Other correlations for gas viscosity include that of Dean and Stiel (1958) and Lee et al. (1966).

**Example Problem 2.3** A 0.65-specific gravity natural gas contains 10% nitrogen, 8% carbon dioxide, and 2% hydrogen sulfide. Estimate viscosity of the gas at 10,000 psia and 180 °F.

**Solution** Example Problem 2.3 is solved with the spreadsheet *Carr-Kobayashi-Burrows-GasViscosity.xls*, which is attached to this book. The result is shown in Table 2.3.



**Table 2.3 Results Given by the Spreadsheet Carr-Kobayashi-Burrows-GasViscosity.xls**

<i>Carr-Kobayashi-Burrows-GasViscosity.xls</i>		
<i>Description:</i> This spreadsheet calculates gas viscosity with correlation of Carr et al.		
<i>Instruction:</i> (1) Select a unit system; (2) update data in the Input data section; (3) review result in the Solution section.		
<i>Input data</i>	<i>U.S. Field units</i>	<i>SI units</i>
Pressure:	10,000 psia	
Temperature:	180 °F	
Gas-specific gravity:	0.65 air = 1	
Mole fraction of N <sub>2</sub> :	0.1	
Mole fraction of CO <sub>2</sub> :	0.08	
Mole fraction of H <sub>2</sub> S:	0.02	
<i>Solution</i>		
Pseudo-critical pressure	= 697.164 psia	
Pseudo-critical temperature	= 345.357 °R	
Uncorrected gas viscosity at 14.7 psia	= 0.012174 cp	
N <sub>2</sub> correction for gas viscosity at 14.7 psia	= 0.000800 cp	
CO <sub>2</sub> correction for gas viscosity at 14.7 psia	= 0.000363 cp	
H <sub>2</sub> S correction for gas viscosity at 14.7 psia	= 0.000043 cp	
Corrected gas viscosity at 14.7 psia ( $\mu_1$ )	= 0.013380 cp	
Pseudo-reduced pressure	= 14.34	
Pseudo-reduced temperature	= 1.85	
$\ln(\mu_g/\mu_1 * T_{pr})$	= 1.602274	
Gas viscosity	= 0.035843 cp	

### 2.3.4 GAS COMPRESSIBILITY FACTOR

Gas compressibility factor is also called “deviation factor” or “z-factor.” Its value reflects how much the real gas deviates from the ideal gas at a given pressure and temperature. Definition of the compressibility factor is expressed as

$$z = \frac{V_{actual}}{V_{ideal\ gas}} \tag{2.42}$$

Introducing the z-factor to the gas law for ideal gas results in the gas law for real gas as

$$pV = nzRT, \tag{2.43}$$

where  $n$  is the number of moles of gas. When pressure  $p$  is entered in psia, volume  $V$  in ft<sup>3</sup>, and temperature in  $R$ , the gas constant  $R$  is equal to  $10.73 \frac{psia \cdot ft^3}{mole \cdot ^\circ R}$ .

Gas compressibility factor can be determined on the basis of measurements in PVT laboratories. For a given amount of gas, if temperature is kept constant and volume is measured at 14.7 psia and an elevated pressure  $p_1$ , z-factor can then be determined with the following formula:

$$z = \frac{p_1 V_1}{14.7 V_0} \quad (2.44)$$

where  $V_0$  and  $V_1$  are gas volumes measured at 14.7 psia and  $p_1$ , respectively.

Very often the z-factor is estimated with the chart developed by [Standing and Katz \(1954\)](#). This chart has been set up for computer solution by a number of individuals. [Brill and Beggs \(1974\)](#) yield z-factor values accurate enough for many engineering calculations. Brill and Beggs' z-factor correlation is expressed as follows:

$$A = 1.39(T_{pr} - 0.92)^{0.5} - 0.36T_{pr} - 0.10, \quad (2.45)$$

$$B = (0.62 - 0.23T_{pr})p_{pr} + \left( \frac{0.066}{T_{pr} - 0.86} - 0.037 \right) p_{pr}^2 + \frac{0.32p_{pr}^6}{10^E}, \quad (2.46)$$

$$C = 0.132 - 0.32\log(T_{pr}), \quad (2.47)$$

$$D = 10^F, \quad (2.48)$$

$$E = 9(T_{pr} - 1), \quad (2.49)$$

$$F = 0.3106 - 0.49T_{pr} + 0.1824T_{pr}^2, \quad (2.50)$$

and

$$z = A + \frac{1-A}{e^B} + Cp_{pr}^D, \quad (2.51)$$

**Example Problem 2.4** For the natural gas described in Example Problem 2.3, estimate z-factor at 5000 psia and 180 °F.

**Solution** Example Problem 2.4 is solved with the spreadsheet program *Brill-Beggs-Z.xls*. The result is shown in [Table 2.4](#).

[Hall and Yarborough \(1973\)](#) presented a more accurate correlation to estimate z-factor of natural gas. This correlation is summarized as follows:

$$t_r = \frac{1}{T_{pr}} \quad (2.52)$$

$$A = 0.06125t_r e^{-1.2(1-t_r)^2} \quad (2.53)$$

$$B = t_r(14.76 - 9.76t_r + 4.58t_r^2) \quad (2.54)$$

$$C = t_r(90.7 - 242.2t_r + 42.4t_r^2) \quad (2.55)$$

$$D = 2.18 + 2.82t_r \quad (2.56)$$

and

$$z = \frac{Ap_{pr}}{Y} \quad (2.57)$$

<b>Table 2.4 Results Given by the Spreadsheet Program Brill-Beggs-Z.xls</b>		
<i>Brill-Beggs-Z.xls</i>		
<i>Description:</i> This spreadsheet calculates gas compressibility factor based on the Brill and Beggs correlation.		
<i>Instruction:</i> (1) Select a unit system; (2) update data in the Input data section; (3) review result in the Solution section.		
<i>Input data</i>	<i>U.S. Field units</i>	<i>SI units</i>
Pressure:	5000 psia	
Temperature:	180 °F	
Gas specific gravity:	0.65 air = 1	
Mole fraction of N <sub>2</sub> :	0.1	
Mole fraction of CO <sub>2</sub> :	0.08	
Mole fraction of H <sub>2</sub> S:	0.02	
<i>Solution</i>		
Pseudo-critical pressure	= 697 psia	
Pseudo-critical temperature	= 345 °R	
Pseudo-reduced pressure	= 7.17	
Pseudo-reduced temperature	= 1.95	
A	= 0.6063	
B	= 2.4604	
C	= 0.0395	
D	= 1.1162	
Gas compressibility factor z	= 0.9960	

where  $Y$  is the reduced density to be solved from

$$f(Y) = \frac{Y + Y^2 + Y^3 - Y^4}{(1 - Y)^3} - Ap_{pr} - BY^2 + CY^D = 0. \quad (2.58)$$

If the Newton and Raphson iteration method is used to solve Eq. (2.58) for  $Y$ , the following derivative is needed:

$$\frac{df(Y)}{dY} = \frac{1 + 4Y + 4Y^2 - 4Y^3 + Y^4}{(1 - Y)^4} - 2BY + CDY^{D-1} \quad (2.59)$$

### 2.3.5 DENSITY OF GAS

Because gas is compressible, its density depends on pressure and temperature. Gas density can be calculated from gas law for real gas with good accuracy:

$$\rho_g = \frac{m}{V} = \frac{MW_a p}{zRT}, \quad (2.60)$$

**Table 2.5 Results Given by the Spreadsheet Program Hall-Yarborough-z-Density.xls**
*Hall-Yarborough-z-Density.xls*
*Description:* This spreadsheet computes gas compressibility factor with the Hall–Yarborough method.

*Instruction:* (1) Select a unit system; (2) update data in the Input data section; (3) click Solution button; (4) view result.

Input data	U.S. Field units	SI units
Temperature:	200 °F	
Pressure:	2000 psia	
Gas-specific gravity:	0.7 air = 1	
Nitrogen mole fraction:	0.05	
Carbon dioxide fraction:	0.05	
Hydrogen sulfite fraction:		
<i>Solution</i>	0.02	
$T_{pc} = 326 + 315.7(\gamma_g - 0.5) - 240y_{N_2} - 83.3y_{CO_2} + 133.3y_{H_2S}$	= 375.641 °R	
$p_{pc} = 678 - 50(\gamma_g - 0.5) - 206.7y_{N_2} + 4440y_{CO_2} + 606.7y_{H_2S}$	= 691.799 psia	
$T_{pr} = \frac{T}{T_{pc}}$	= 1.618967	
$t_r = \frac{1}{T_{pr}}$	= 0.617678	
$p_{pr} = \frac{p}{p_{pc}}$	= 2.891013	
$A = 0.06125t_r e^{-1.2(1-t_r)^2}$	= 0.031746	
$B = t_r(14.76 - 9.76t_r + 4.58t_r^2)$	= 6.472554	
$C = t_r(90.7 - 242.2t_r + 42.4t_r^2)$	= -26.3902	
$D = 2.18 + 2.82t_r$	= 3.921851	
$Y = \text{ASSUMED}$	= 0.109759	
$f(Y) = \frac{Y = Y^2 + Y^3 - Y^4}{(1-Y)^3} - Ap_{pr} - BY^2 + CY^D = 0$	= 4.55E-06	
$z = \frac{Ap_{pr}}{Y}$	= 0.836184	
$\rho_g = \frac{2.7\gamma_g p}{zT}$	= 6.849296 lb <sub>m</sub> /ft <sup>3</sup>	

where  $m$  is mass of gas and  $\rho_g$  is gas density. Taking air molecular weight 29 and  $R = 10.73 \frac{\text{psia} \cdot \text{ft}^3}{\text{mole} \cdot \text{°R}}$ , Eq. (2.60) is rearranged to yield

$$\rho_g = \frac{2.7\gamma_g p}{zT}, \quad (2.61)$$

where the gas density is in lb<sub>m</sub>/ft<sup>3</sup>.

**Example Problem 2.5** A gas from oil has a specific gravity of 0.65, estimate z-factor and gas density at 5000 psia and 180 °F.

**Solution** Example Problem 2.5 is solved with the spreadsheet program *Hall-Yarborough-z-Density.xls*. The result is shown in Table 2.5.

### 2.3.6 FORMATION VOLUME FACTOR OF GAS

Gas formation volume factor is defined as the ratio of gas volume at reservoir condition to the gas volume at standard condition, that is,

$$B_g = \frac{V}{V_{sc}} = \frac{p_{sc}}{p} \frac{T}{T_{sc}} \frac{z}{z_{sc}} = 0.0283 \frac{zT}{p}, \quad (2.62)$$

where the unit of formation volume factor is ft<sup>3</sup>/scf. If expressed in rb/scf, it takes the form

$$B_g = 0.00504 \frac{zT}{p}. \quad (2.63)$$

Gas formation volume factor is frequently used in mathematical modeling of gas well-inflow performance relationship (IPR).

Another way to express this parameter is to use gas expansion factor defined, in scf/ft<sup>3</sup>, as

$$E = \frac{1}{B_g} = 35.3 \frac{P}{ZT} \quad (2.64)$$

or

$$E = 198.32 \frac{P}{zT}, \quad (2.65)$$

in scf/rb. It is normally used for estimating gas reserves.

### 2.3.7 GAS COMPRESSIBILITY

Gas compressibility is defined as

$$c_g = -\frac{1}{V} \left( \frac{\partial V}{\partial p} \right)_T. \quad (2.66)$$

Because the gas law for real gas gives  $V = \frac{nzRT}{p}$ ,

$$\left( \frac{\partial V}{\partial p} \right) = nRT \left( \frac{1}{p} \frac{\partial z}{\partial p} - \frac{z}{p^2} \right). \quad (2.67)$$

Substituting Eq. (2.67) into Eq. (2.66) yields

$$c_g = \frac{1}{p} - \frac{1}{z} \frac{\partial z}{\partial p}. \quad (2.68)$$

Since the second term in the right-hand side is usually small, gas compressibility is approximately equal to the reciprocal of pressure.

## 2.4 PROPERTIES OF PRODUCED WATER

Water properties that are frequently used in oil and gas field management include density, specific gravity, salinity, viscosity, formation volume factor, and compressibility. These properties are easy to measure in laboratories.

### 2.4.1 DENSITY, SPECIFIC GRAVITY, AND SALINITY

The density of pure water (H<sub>2</sub>O) is 62.4 lbm/ft<sup>3</sup> at STP. The density of produced water is higher than this value due to impurities, mostly salts. Water specific gravity is defined as the ratio of density of the produced water to that of pure water. In practice, the water density, specific gravity, and salinity are inter-convertible, as their relationships depend on the types of salts dissolved in the water. For typical oil-field brines, the data from [McCain \(1973\)](#) provides the following correlation:

$$\rho_w = 62.4 + 0.48C_s \quad (2.69)$$

where,  $\rho_w$  = density of brine (lb<sub>m</sub>/ft<sup>3</sup>);  $C_s$  = total dissolved solids (%)

### 2.4.2 WATER VISCOSITY

The viscosity of water is affected by its salinity, dissolved gas content, pressure, and temperature, with temperature being the most significant factor. For typical oil-field brines, the data from [McCain \(1973\)](#) provides the following correlation:

$$\mu_w = \frac{70.42}{t} \quad (2.70)$$

where,  $\mu_w$  = viscosity of brine, cp;  $t$  = temperature, °F

### 2.4.3 WATER FORMATION VOLUME FACTOR

Like oil, the formation volume factor of produced water is defined as the volume occupied in the reservoir at the prevailing reservoir pressure and temperature, divided by the volume of water plus its dissolved gas at surface conditions (STP), expressed as:

$$B_w = \frac{V_{res}}{V_{st}} \quad (2.71)$$

where,  $B_w$  = formation volume factor of water (rb/stb);  $V_{res}$  = water volume in reservoir condition (rb);  $V_{st}$  = water volume at surface conditions (STP, stb)

For typical oil-field brines, formation volume factors are very close to one.

### 2.4.4 WATER COMPRESSIBILITY

Water compressibility is defined as:

$$c_w = -\frac{1}{V} \left( \frac{\partial V}{\partial p} \right)_T \quad (2.72)$$

Water compressibility is measured in laboratories, with values in the order of 10<sup>-6</sup> psi<sup>-1</sup>. Water compressibility is often used in modeling well-inflow performance and in reservoir simulation.

## 2.5 INTERFACIAL TENSION

The interfacial tension (IFT) between liquid (oil or water) and gas phases is an important parameter in multiphase flow calculations for wellbore and pipeline design. For a given pair of fluids, IFT is a function of pressure and temperature. [Schechter and Guo \(1998\)](#) proposed the following relation for estimating IFT of hydrocarbons based on modern physics:

$$\sigma = \left[ \sum_{i=1}^n P_i \left( x_i \frac{\rho_l}{M_l} - y_i \frac{\rho_v}{M_v} \right) \right]^{3.88} \quad (2.73)$$

where,  $\sigma$  = interfacial tension (dyne/cm<sup>2</sup>);  $n$  = number of compounds in the system;  $i$  = index of compound;  $P_i$  = Parachor of compound  $i$ , dimensionless;  $x_i$  = mole fraction of compound  $i$  in the liquid phase;  $y_i$  = mole fraction of compound  $i$  in the vapor phase;  $\rho_l$  = density of liquid phase (g/cm<sup>3</sup>);  $\rho_v$  = density of vapor phase (g/cm<sup>3</sup>);  $M_l$  = apparent molecular weight of the liquid phase;  $M_v$  = apparent molecular weight of the vapor phase

[Schechter and Guo \(1998\)](#) presented values for Parachor for single compounds and oil cuts. They also proposed the following correlation for mixtures of compounds:

$$P = aM + b \quad (2.74)$$

where  $M$  is apparent molecular weight of fluid mixture. The correlation coefficients  $a$  and  $b$  are given in [Table 2.6](#).

The IFT between water and gas phases is a strong function of temperature and weak function of pressure. [Lyons et al. \(2009\)](#) presented the following correlation for IFT for temperatures between 74°F and 280°F:

$$\sigma = \sigma_{74} - \frac{(\sigma_{74} - \sigma_{280})(t - 74)}{206} \quad (2.74)$$

where the temperature  $t$  is in °F, or

$$\sigma = \sigma_{74} - \frac{(\sigma_{74} - \sigma_{280})(1.8t_C - 42)}{206} \quad (2.75)$$

where temperature  $t_C$  is in °C. The IFT at 74°F is given by

$$\sigma_{74} = 75 - 1.108p^{0.349} \quad (2.76)$$

**Table 2.6 Coefficients of Correlations for Parachors of Hydrocarbons**

Hydrocarbons	A	b	SEOE <sup>a</sup>
Normal Paraffins	2.9799	18.1763	4.617
Alkanes	2.987	11.7344	5.884
Alkanes, alkenes, and alkadienes	2.9792	12.7057	10.022
Alkanes, alkenes, alkadienes, and alkynes	2.9769	11.3715	12.594
Alkanes, alkenes, alkadienes, alkynes, and cyclic compounds	2.9764	5.06389	16.022
Alkanes, alkenes, alkadienes, alkynes, cyclic, and aromatic compounds	2.9518	3.71917	21.941

<sup>a</sup>SEOE = Standard Error of Estimate for Parachor.

and the IFT at 280°F is given by

$$\sigma_{280} = 53 - 0.1048p^{0.637} \quad (2.77)$$

where pressure  $p$  is in psi, or

$$\sigma_{74} = 75 - 6.323p_{MPa}^{0.349} \quad (2.78)$$

and

$$\sigma_{280} = 53 - 2.517p_{MPa}^{0.637} \quad (2.79)$$

where pressure  $p_{MPa}$  is in MPa.

## 2.6 SUMMARY

This chapter presented definitions and properties of crude oil, natural gas, and produced water. It also provided a few empirical correlations for determining the value of these properties. These correlations are coded in spreadsheet programs that are available with this book. Applications of these fluid properties are found in the later chapters.

## REFERENCES

- Ahmed, T., 1989. *Hydrocarbon Phase Behavior*. Gulf Publishing Company, Houston.
- Beal, C., 1946. The viscosity of air, water, natural gas, crude oils and its associated gases at oil field temperatures and pressures. *Trans. AIME* 165, 94–112.
- Beggs, H.D., Robinson, J.R., 1975. Estimating the viscosity of crude oil systems. *J. Petrol. Technol.* 1140–1141.
- Brill, J.P., Beggs, H.D., 1974. Two-phase flow in pipes. INTERCOMP course. Hague.
- Carr, N.L., Kobayashi, R., Burrows, D.B., 1954. Viscosity of hydrocarbon gases under pressure. *Trans. AIME* 201, 264–272.
- Dean, D.E., Stiel, L.I., 1958. The viscosity of non-polar gas mixtures at moderate and high pressures. *AIChE J.* 4, 430–436.
- Dempsey, J.R., 1965. Computer routine treats gas viscosity as a variable. *Oil Gas J.* 63, p. 141.
- Glaso, O., 1985. Generalized pressure-volume-temperature correlations. *J. Petrol. Technol.* 785–795.
- Hall, K.R., Yarborough, L., 1973. A new equation of state for Z-factor calculations. *Oil Gas J.* 71, 82–92.
- Khan, S.A., Viscosity correlations for Saudi Arabian crude oils. Presented at the 50th Middle East Conference and Exhibition held 7–10 March 1987, in Manama, Bahrain. Paper SPE 15720.
- Lee, A.L., Gonzalez, M.H., Eakin, B.E., 1966. The viscosity of natural gases. *J. Petrol. Technol.* 997–1000.
- Lyons, W.C., Guo, B., Graham, R.L., Hawley, G.D., 2009. *Air and Gas Drilling Manual*. third ed. Elsevier Publishing Company, Amsterdam.
- Mccain Jr., W.D., 1973. *Properties of Petroleum Fluids*. PennWell Books, Tulsa.
- Schechter, D.S., Guo, B., 1998. Parachors Based on Modern Physics and Their Uses in IFT Prediction of Reservoir Fluids. *SPE Reserv. Eval. Eng. J.*
- Standing, M.B., 1981. *Volume and Phase Behavior of Oil Field Hydrocarbon Systems*. ninth ed. Society of Petroleum Engineers, Dallas.



Standing, M.B., Katz, D.L., 1954. Density of natural gases. Trans. AIME 146, 140–149.  
 Wichert, E., Aziz, K., 1972. Calculate Zs for sour gases. Hydrocarbon Process 51 (May), 119.

**PROBLEMS**

- 2.1 Estimate the density of a 25-API gravity dead oil at 100 °F.
- 2.2 The solution GOR of a crude oil is 800 scf/stb at 3000 psia and 120 °F. Given the following PVT data:

Bubble-point pressure: 2500 psia  
 Oil gravity: 35 °ApI  
 Gas-specific gravity: 0.77 (air = 1),

estimate densities and viscosities of the crude oil at 120 °F, 2500 psia, and 3000 psia.

- 2.3 For the gas composition given below, determine apparent molecular weight, specific gravity, pseudo-critical pressure, and pseudo-critical temperature of the gas:

Component	Mole Fraction
C <sub>1</sub>	0.765
C <sub>2</sub>	0.073
C <sub>3</sub>	0.021
i-C <sub>4</sub>	0.006
n-C <sub>4</sub>	0.002
i-C <sub>5</sub>	0.003
n-C <sub>5</sub>	0.008
C <sub>6</sub>	0.001
C <sub>7+</sub>	0.001
N <sub>2</sub>	0.060
CO <sub>2</sub>	0.040
H <sub>2</sub> S	0.020

- 2.4 Estimate gas viscosities of a 0.70-specific gravity gas at 200 °F and 100 psia, 1000 psia, 5000 psia, and 10,000 psia.
- 2.5 Calculate gas compressibility factors and densities of a 0.65-specific gravity gas at 150 °F and 50 psia, 500 psia, and 5000 psia with the Hall–Yarborough method. Compare the results with that given by the Brill and Beggs correlation. What is your conclusion?
- 2.6 For a 0.65-specific gravity gas at 250 °F, calculate and plot pseudo-pressure in a pressure range from 14.7 and 8000 psia. Under what condition is the pseudopressure linearly proportional to pressure?
- 2.7 Estimate the density of a 0.8-specific gravity dead oil at 40°C.

- 2.8** The solution GOR of a crude oil is  $4000 \text{ sm}^3/\text{m}^3$  at 20 MPa and  $50^\circ\text{C}$ . Given the following PVT data:

Bubble-point pressure:	15 MPa
Oil-specific gravity:	0.8 water = 1
Gas-specific gravity:	0.77 air = 1,

estimate densities and viscosities of the crude oil at  $50^\circ\text{C}$ , 15 MPa, and 20 MPa.

- 2.9** For the gas composition given below, determine apparent molecular weight, specific gravity, pseudo-critical pressure, and pseudo-critical temperature of the gas.

Component	Mole Fraction
C <sub>1</sub>	0.755
C <sub>2</sub>	0.073
C <sub>3</sub>	0.011
i-C <sub>4</sub>	0.006
n-C <sub>4</sub>	0.002
i-C <sub>5</sub>	0.003
n-C <sub>5</sub>	0.008
C <sub>6</sub>	0.001
C <sub>7+</sub>	0.001
N <sub>2</sub>	0.070
CO <sub>2</sub>	0.050
H <sub>2</sub> S	0.020

- 2.10** Estimate gas viscosities of a 0.70-specific gravity gas at  $90^\circ\text{C}$  and 1 MPa, 5 MPa, 10 MPa, and 50 MPa.
- 2.11** Calculate gas compressibility factors and densities of a 0.65-specific gravity gas at  $80^\circ\text{C}$  and 1 MPa, 5 MPa, 10 MPa, and 50 MPa with the Hall–Yarborough method. Compare the results with that given by the Brill and Beggs correlation. What is your conclusion?
- 2.12** For a 0.65-specific gravity gas at  $110^\circ\text{C}$ , calculate and plot pseudo-pressures in a pressure range from 0.1 to 30 MPa. Under what condition is the pseudo-pressure linearly proportional to pressure?

## RESERVOIR DELIVERABILITY

## 3

---

### 3.1 INTRODUCTION

Reservoir deliverability is defined as the oil or gas production rate achievable from reservoir at a given bottom-hole pressure. It is a major factor affecting well deliverability. Reservoir deliverability determines types of completion and artificial lift methods to be used. A thorough knowledge of reservoir productivity is essential for production engineers.

Reservoir deliverability depends on several factors including the following:

- Reservoir pressure
- Pay zone thickness and permeability
- Reservoir boundary type and distance
- Wellbore radius
- Reservoir fluid properties
- Near-wellbore condition
- Reservoir relative permeabilities
- Well completion method (vertical, horizontal, fracturing, and multilateral wells)

Reservoir deliverability can be mathematically modeled on the basis of flow regimes such as transient flow, steady-state flow, and pseudo-steady state flow. An analytical relation between bottom-hole pressure and production rate can be formulated for a given flow regime. The relation is called “inflow performance relationship” (IPR). This chapter addresses the procedures used for establishing IPR of different types of reservoirs and well completions.

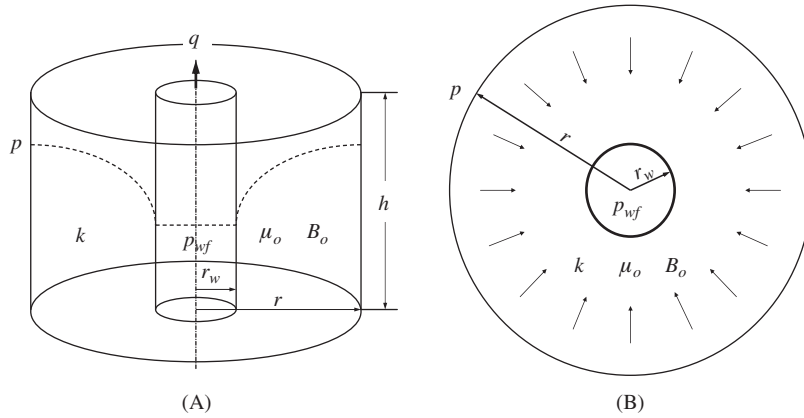
---

### 3.2 VERTICAL WELLS

When a vertical well is open to produce oil at production rate  $q$ , it creates a pressure funnel of radius  $r$  around the wellbore, as illustrated by the dotted line in Fig. 3.1A. In this reservoir model, the  $h$  is the reservoir thickness,  $k$  is the effective horizontal reservoir permeability to oil,  $\mu_o$  is viscosity of oil,  $B_o$  is oil formation volume factor,  $r_w$  is wellbore radius,  $p_{wf}$  is the flowing bottom-hole pressure, and  $p$  is the pressure in the reservoir at the distance  $r$  from the wellbore center line. The flow stream lines in the cylindrical region form a horizontal radial flow pattern are depicted in Fig. 3.1B.

#### 3.2.1 TRANSIENT FLOW

“Transient flow” is defined as a flow regime where/when the radius of pressure wave propagation from wellbore has not reached any boundaries of the reservoir. During transient flow, the



**FIGURE 3.1**

A sketch of a radial flow reservoir model: (A) lateral view, (B) top view.

developing pressure funnel is small relative to the reservoir size. Therefore, the reservoir acts like an infinitely large reservoir from transient pressure analysis point of view.

Assuming single-phase oil flow in the reservoir, several analytical solutions have been developed for describing the transient flow behavior. They are available from classic textbooks such as that of [Dake \(1978\)](#). A constant rate solution expressed by [Eq. \(3.1\)](#) is frequently used in production engineering:

$$p_{wf} = p_i - \frac{162.6qB_o\mu_o}{kh} \times \left( \log t + \log \frac{k}{\phi\mu_o c_t r_w^2} - 3.23 + 0.87S \right), \quad (3.1)$$

where  $p_{wf}$  = flowing bottom-hole pressure, psia;  $P_i$  = initial reservoir pressure, psia;  $q$  = oil production rate, stb/day;  $\mu_o$  = viscosity of oil, cp;  $k$  = effective horizontal permeability to oil, md;  $h$  = reservoir thickness, ft;  $t$  = flow time, hour;  $\phi$  = porosity, fraction;  $c_t$  = total compressibility,  $\text{psi}^{-1}$ ;  $r_w$  = wellbore radius to the sand face, ft;  $S$  = skin factor;  $\text{Log} = 10$ -based logarithm  $\log_{10}$

Because oil production wells are normally operated at constant bottom-hole pressure because of constant wellhead pressure imposed by constant choke size, a constant bottom-hole pressure solution is more desirable for well-inflow performance analysis. With an appropriate inner boundary condition arrangement, [Earlougher \(1977\)](#) developed a constant bottom-hole pressure solution, which is similar to [Eq. \(3.1\)](#):

$$q = \frac{kh(p_i - p_{wf})}{162.6B_o\mu_o \left( \log t + \log \frac{k}{\phi\mu_o c_t r_w^2} - 3.23 + 0.87S \right)}, \quad (3.2)$$

which is used for transient well performance analysis in production engineering.

[Eq. \(3.2\)](#) indicates that oil rate decreases with flow time. This is because the radius of the pressure funnel, over which the pressure drawdown ( $p_i - p_{wf}$ ) acts, increases with time, that is, the overall pressure gradient in the reservoir drops with time.

For gas wells, the transient solution is

$$q_g = \frac{kh[m(p_i) - m(p_{wf})]}{1.638T \left( \log t + \log \frac{k}{\phi \mu_o c_t r_w^2} - 3.23 + 0.87S \right)}, \quad (3.3)$$

where  $q_g$  is production rate in Mscf/d,  $T$  is temperature in °R, and  $m(p)$  is real gas pseudopressure defined as

$$m(p) = \int_{p_b}^p \frac{2p}{\mu z} dp. \quad (3.4)$$

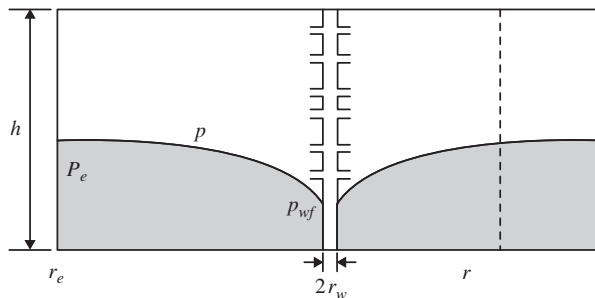
The real gas pseudo-pressure can be readily determined with the spreadsheet program *PseudoPressure.xls*.

### 3.2.2 STEADY-STATE FLOW

“Steady-state flow” is defined as a flow regime where the pressure at any point in the reservoir remains constant over time. This flow condition prevails when the pressure funnel shown in Fig. 3.1 has propagated to a constant-pressure boundary. The constant-pressure boundary can be an aquifer or a water injection well. A sketch of the reservoir model is shown in Fig. 3.2, where  $p_e$  represents the pressure at the constant-pressure boundary. Assuming single-phase flow, the following theoretical relation can be derived from Darcy’s law for an oil reservoir under the steady-state flow condition due to a circular constant-pressure boundary at distance  $r_e$  from wellbore:

$$q = \frac{kh(p_e - p_{wf})}{141.2B_o\mu_o \left( \ln \frac{r_e}{r_w} + S \right)}, \quad (3.5)$$

where “ln” denotes 2.718-based natural logarithm  $\log_e$ . Derivation of Eq. (3.5) is left to readers for an exercise.



**FIGURE 3.2**

A sketch of a reservoir with a constant-pressure boundary.

### 3.2.3 PSEUDO-STEADY-STATE FLOW

“Pseudo-steady-state” flow is defined as a flow regime where the pressure at any point in the reservoir declines at the same constant rate over time. This flow condition prevails after the pressure funnel shown in Fig. 3.1 has propagated to all no-flow boundaries. A no-flow boundary can be a sealing fault, pinch-out of pay zone, or boundaries of drainage areas of production wells. A sketch of the reservoir model is shown in Fig. 3.3, where  $p_e$  represents the pressure at the no-flow boundary at time  $t_4$ . Assuming single-phase flow, the following theoretical relation can be derived from Darcy’s law for an oil reservoir under pseudo-steady-state flow condition due to a circular no-flow boundary at distance  $r_e$  from wellbore:

$$q = \frac{kh(p_e - p_{wf})}{141.2B_o\mu_o \left( \ln \frac{r_e}{r_w} - \frac{1}{2} + S \right)}. \quad (3.6)$$

The flow time required for the pressure funnel to reach the circular boundary can be expressed as

$$t_{pss} = 1,200 \frac{\phi\mu_o c_t r_e^2}{k}. \quad (3.7)$$

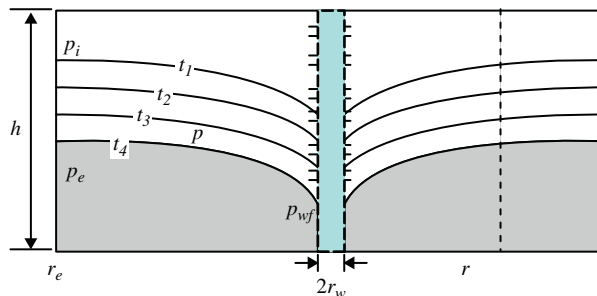
Because the  $p_e$  in Eq. (3.6) is not known at any given time, the following expression using the average reservoir pressure is more useful:

$$q = \frac{kh(\bar{p} - p_{wf})}{141.2B_o\mu_o \left( \ln \frac{r_e}{r_w} - \frac{3}{4} + S \right)}, \quad (3.8)$$

where  $p$  is the average reservoir pressure in psia. Derivations of Eqs. (3.6) and (3.8) are left to readers for exercises.

If the no-flow boundaries delineate a drainage area of noncircular shape, the following equation should be used for analysis of pseudo-steady-state flow:

$$q = \frac{kh(\bar{p} - p_{wf})}{141.2B_o\mu_o \left( \frac{1}{2} \ln \frac{4A}{\gamma C_A r_w^2} + S \right)}, \quad (3.9)$$



**FIGURE 3.3**

A sketch of a reservoir with no-flow boundaries.

where  $A$  = drainage area,  $\text{ft}^2$ ;  $\gamma = 1.78$  = Euler's constant;  $C_A$  = drainage area shape factor, 31.6 for a circular boundary.

The value of the shape factor  $C_A$  can be found from Fig. 3.4.

For a gas well located at the center of a circular drainage area, the pseudo-steady-state solution is

$$q_g = \frac{kh[m(\bar{p}) - m(p_{wf})]}{1,424T \left( \ln \frac{r_e}{r_w} - \frac{3}{4} + S + Dq_g \right)}, \tag{3.10}$$

where  $D$  = non-Darcy flow coefficient,  $\text{d/Mscf}$ .


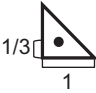
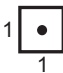
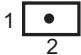

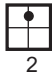


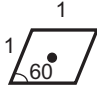

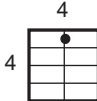

(A)	Reservoir shape & well location	Shape factor $C_A$	Reservoir shape & well location	Shape factor $C_A$
		31.6		21.9
		30.9		22.6
		31.6		12.9
		27.6		4.5
		27.1	In water-drive reservoirs 	19.1
		3.39	In reservoirs of unknown production character 	25

FIGURE 3.4

(A): Shape factors for closed drainage areas with low-aspect ratios. (B): Shape factors for closed drainage areas with high-aspect ratios.

From Dietz, D.N., 1965. Determination of average reservoir pressure from build-up surveys. *J. Pet. Tech.*, Dietz, 1965.

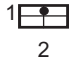

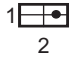
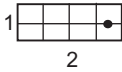
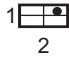
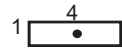

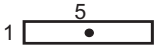

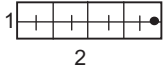


(B)	Reservoir shape & well location	Shape factor $C_A$	Reservoir shape & well location	Shape factor $C_A$
		10.8		3.13
		4.86		0.607
		2.07		5.38
		2.72		2.36
		0.232		0.111
		0.115		0.098

FIGURE 3.4

(Continued).

### 3.2.4 HYDRAULIC-FRACTURED WELLS

Hydraulically created fractures receive fluids from the reservoir matrix and provide channels for it to flow into the wellbore. Apparently, the productivity of fractured wells depends on two stages: (1) receiving fluids from the formation by the fractures, and (2) transporting the received fluid to wellbore along the fractures. Usually one of the stages is a limiting factor that controls well production rate. The efficiency of the first stage depends on fracture dimension (length and height), and the efficiency of the second stage depends on fracture permeability. The relative importance of each can be analyzed using the concept of fracture conductivity (Argawal et al., 1979; Cinco-Ley and Samaniego, 1981) defined as:

$$F_{CD} = \frac{k_f w}{k x_f} \tag{3.11}$$

where,  $F_{CD}$  = fracture conductivity (dimensionless);  $k_f$  = fracture permeability (md);  $w$  = fracture width (ft);  $x_f$  = fracture half-length (ft)



In situations where the fracture length is much small compared to the drainage area of the well, the long-term productivity of a fractured well can be estimated assuming pseudo-radial flow in the reservoir. In that case, the inflow equation for steady-state flow around an oil well can be expressed as:

$$q = \frac{kh(p_e - p_{wf})}{141.2B\mu \left( \ln \frac{r_e}{r_w} + S_f \right)} \quad (3.12)$$

where  $S_f$  is the equivalent skin factor for the fractured well, and takes negative values. The factor of increase in reservoir deliverability can be expressed as:

$$\frac{J}{J_o} = \frac{\ln \frac{r_e}{r_w}}{\ln \frac{r_e}{r_w} + S_f} \quad (3.13)$$

where,  $J$  = productivity of fractured well (stb/d-psi);  $J_o$  = productivity of nonfractured well (stb/d-psi)

The inflow equation for steady-state flow around a gas well can be expressed as:

$$q_g = \frac{kh(m(p_e) - m(p_{wf}))}{1424T \left( \ln \frac{r_e}{r_w} + S_f + Dq_g \right)} \quad (3.14)$$

The effective skin factor  $S_f$  can be determined based on fracture conductivity based on the chart shown in Fig. 3.5 prepared by Cinco-Ley and Samaniego (1981). Valko et al. (1997) converted Cinco-Ley and Samaniego's (1981) chart to the following correlation:

$$S_f + \ln(x_f/r_w) = \frac{1.65 - 0.328u + 0.116u^2}{1 + 0.180u + 0.064u^2 + 0.05u^3} \quad (3.15)$$

where  $u = \ln(F_{CD})$ .

**Example Problem 3.1** An oil reservoir has a permeability of 1 md. A vertical well with a radius of 0.328 ft drains a reservoir area of 160 acres. If the well is hydraulically fractured to create a 2000 ft long, 0.12 inch wide fracture of 200,000 md permeability around the center of the drainage area, what is the expected factor of increase in reservoir deliverability?

**Solution**

Radius of the drainage area:

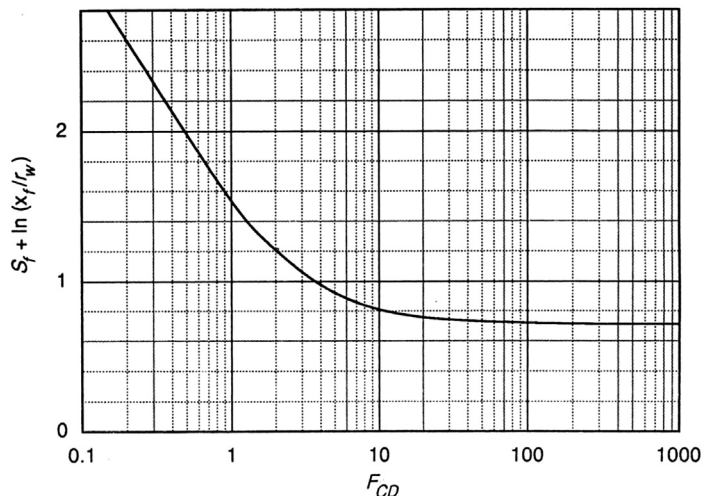
$$r_e = \sqrt{\frac{A}{\pi}} = \sqrt{\frac{(43,560)(160)}{\pi}} = 1,490 \text{ ft}$$

Fracture conductivity:

$$F_{CD} = \frac{k_f w}{k x_f} = \frac{(200,000)(0.12/12)}{(1)(2,000/2)} = 2$$

Eq. (3.15) yields:

$$S_f + \ln(x_f/r_w) \approx 1.2$$


**FIGURE 3.5**

Relationship between fracture conductivity and equivalent skin factor.

From Cinco-Ley, H., Samaniego, F., 1981. *Transient pressure analysis for fractured wells*, J. Petrol. Technol., Cinco-Ley and Samaniego, 1981.

which gives:

$$S_f \approx 1.2 - \ln(x_f/r_w) = 1.2 - \ln(1,000/0.328) = -6.82$$

The factor of increase in reservoir deliverability is therefore:

$$\frac{J}{J_o} = \frac{\ln \frac{r_e}{r_w}}{\ln \frac{r_e}{r_w} + S_f} = \frac{\ln \frac{1,490}{0.328}}{\ln \frac{1,490}{0.328} - 6.82} = 5.27.$$

The above principle is also valid for pseudosteady flow, in which the average reservoir pressure should be used. In that case, Eq. (3.12) becomes:

$$q = \frac{kh(\bar{p} - p_{wf})}{141.2B_o\mu_o \left( \frac{1}{2} \ln \frac{4A}{\gamma C_A r_w^2} + S_f \right)} \quad (3.16)$$

The corresponding equation for gas wells is:

$$q_g = \frac{kh(m(\bar{p}) - m(p_{wf}))}{1424T \left( \frac{1}{2} \ln \frac{4A}{\gamma C_A r_w^2} + S_f + Dq_g \right)} \quad (3.17)$$

Eq. (3.12) assumes radial flow, and may result in significant error if used in situations where the fracture length is comparable to the drainage area of the well ( $x_f > 0.5 r_e$ ). In these cases,

long-term reservoir deliverability may be estimated assuming bilinear flow in the reservoir and fracture. An analytical solution for estimating the factor of increase in reservoir deliverability was presented by Guo and Schechter (1999), as follows:

$$\frac{J}{J_o} = \frac{0.72 \left( \ln \frac{r_e}{r_w} - \frac{3}{4} + S_o \right)}{z_e \sqrt{c} \left( \frac{1}{1 - e^{-\sqrt{c}y}} - \frac{1}{2x\sqrt{c}} \right)}, \quad (3.18)$$

where  $c = \frac{2k}{z_e w k_f}$  and,  $J$  = productivity index of fractured well (stb/d-psi);  $J_o$  = productivity index of nonfractured well (stb/d-psi);  $S_o$  = skin factor of the nonfractured well (dimensionless);  $z_e$  = distance between the fracture and the flow boundary (ft)

### 3.3 HORIZONTAL WELLS

The transient flow, steady-state flow, and pseudo-steady-state flow can also exist in reservoirs penetrated by horizontal wells. Different mathematical models are available from literature. Equations for steady-state flow conditions are presented in this section.

#### 3.3.1 NONFRACTURED WELLS

Joshi (1988) presented the following relationship considering steady-state flow of oil in the horizontal plane and pseudo-steady-state flow in the vertical plane:

$$q = \frac{k_H h (p_e - p_{wf})}{141.2 B \mu \left\{ \ln \left[ \frac{a + \sqrt{a^2 - (L/2)^2}}{L/2} \right] + \frac{I_{ani} h}{L} \ln \left[ \frac{I_{ani} h}{r_w (I_{ani} + 1)} \right] + s \right\}} F_o \quad (3.19)$$

where

$$a = \frac{L}{2} \sqrt{\frac{1}{2} + \sqrt{\left[ \frac{1}{4} + \left( \frac{r_{eH}}{L/2} \right)^4 \right]}}, \quad (3.20)$$

and

$$I_{ani} = \sqrt{\frac{k_H}{k_V}}, \quad (3.21)$$

and  $k_H$  = the average horizontal permeability, md;  $k_V$  = vertical permeability, md;  $r_{eH}$  = radius of drainage area, ft;  $L$  = length of horizontal wellbore ( $L/2 < 0.9r_{eH}$ ), ft.

For gas wells, Eq. (3.19) takes the form of

$$q_g = \frac{k_H h [m(p_e) - m(p_{wf})]}{1424 T \left\{ \ln \left[ \frac{a + \sqrt{a^2 - (L/2)^2}}{L/2} \right] + \frac{I_{ani} h}{L} \ln \left[ \frac{I_{ani} h}{r_w (I_{ani} + 1)} \right] + s + D q_g \right\}} F_g \quad (3.22)$$

The  $F_o$  and  $F_g$  in Eqs. (3.19) and (3.22) are correction factors for wellbore friction. They are given by Guo et al. (2008) for high productivity wells.

### 3.3.2 SINGLE-FRACTURED WELLS

Reservoir deliverability through a single-fractured horizontal well depends on the orientation of the fracture relative to the wellbore. If the horizontal wellbore is drilled in the direction perpendicular to the minimum horizontal in-situ stress, a longitudinal fracture is expected to form. Eq. (3.12) can be utilized for predicting reservoir deliverability. If the horizontal wellbore is drilled in the direction of the minimum horizontal in-situ stress, a transverse fracture is created. The same equation can be adopted with modification to the skin factor due to the choking effect around the wellbore. This is further described in the following section for multistage fractured wells.

### 3.3.3 MULTISTAGE FRACTURED WELLS

Multistage fractured horizontal wells are widely used for producing oil and gas from low-permeability reservoirs such as shale gas/oil and tight sand reservoirs. Due to the interference between drainages of multifractures, reservoir simulators are usually employed in prediction of reservoir productivity. This section presents an analytical model for quick estimates of reservoir productivity.

Horizontal wells drilled in the direction not parallel to the minimum horizontal stress in the formation allows multiple transverse fractures to be hydraulically created for enhancing productivity. Linear flow may exist initially before fractures begin to influence each other. Radial flow may prevail later if the drainage area is sufficiently large compared to the fractured region of the reservoir.

Raghavan and Joshi (1993) presented a mathematical model that can predict the productivities of horizontal wells with multiple transverse fractures. The model uses the effective wellbore radius (in radial flow) to simulate fluid flow toward the fractured well. Flow within the fracture itself was not considered.

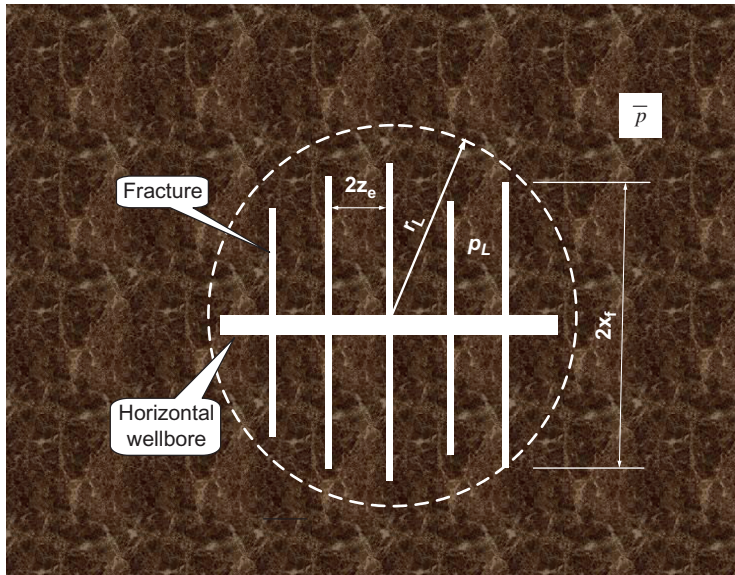
Li et al. (1996) presented an analytical model for predicting productivities of horizontal wells with multiple transverse fractures. The model incorporates:

- Linear flow from the fractured reservoir region to the fractures
- Linear flow within the fractures
- Radial flow within the fractures to the horizontal wellbore
- Flow from the fractured region directly to the horizontal wellbore.

Most fractured horizontal wells are drilled in low-permeability reservoirs, in which fluid flow from the unfractured regions directly to the horizontal wellbore is often negligible. As demonstrated by Guo and Yu (2008), predictions of the long-term productivity of multifractured horizontal wells must consider the following sequence:

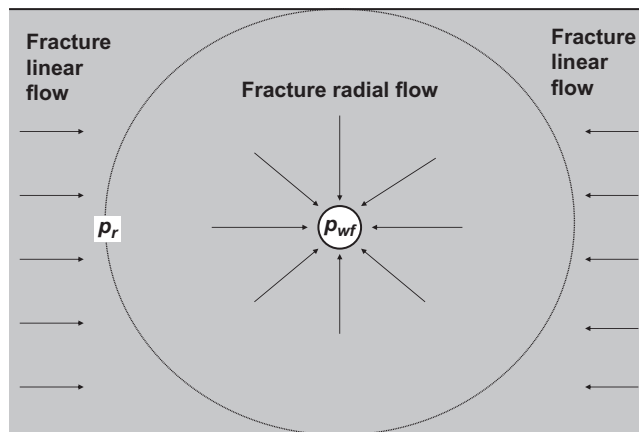
1. Reservoir radial flow within the drainage boundary to the fractured region of reservoir
2. Reservoir linear flow between fractures in the reservoir to the fracture faces
3. Fracture linear flow in the fracture to the near-wellbore region
4. Wellbore radial flow in the fracture to the wellbore, where a “choking” effect occurs.

Fig. 3.6 shows two regions of the reservoir. The inner region is the fractured region, and the outer region is the nonfractured region. Fig. 3.7 illustrates flow in the fracture. Consider a reservoir



**FIGURE 3.6**

A reservoir section drained by a multifracted horizontal wellbore (Guo et al., 2008).



**FIGURE 3.7**

Fluid flow in a fracture to a horizontal wellbore (Guo et al., 2008).

characterized by pseudo-steady-state radial flow in the outer region. The total oil flow rate can then be described by:

$$q = \frac{7.08 \times 10^{-3} k_H h (\bar{p} - p_L)}{B_o \mu_o \left( \frac{1}{2} \ln \frac{4A}{\gamma C_A r_L^2} \right)} \quad (3.23)$$

where  $p_L$  is defined as the pressure at the outer boundary of the inner region, and  $r_L$  is the equivalent radius of the inner region, that can be estimated by:

$$r_L = \sqrt{\frac{4n\bar{z}_e\bar{x}_f}{\pi}} \quad (3.24)$$

where  $\bar{z}_e$  and  $\bar{x}_f$  are the average half-distances between fractures and the average fracture half-length, respectively.

If the multifractured well is used to drain an entire reservoir characterized by physical no-flow boundaries, the drainage area shape factor  $C_A$  can be estimated, based on reservoir shape and the location of the reservoir's inner region. If the multifractured well is employed to drain a portion of a reservoir, then the  $C_A$  should be estimated based on the shape of the drainage area, with the location of the inner region centered in the drainage area.

The reservoir-fracture cross-flow model of [Guo and Schechter \(1999\)](#) links reservoir linear flow and fracture linear flow. For uniformly distributed fractures, according to this model, the deliverability of  $n$  fractures can be expressed as:

$$q = \sum_{i=1}^n \frac{4.5 \times 10^{-3} h}{B_o \mu_o \sqrt{c_i} \left[ \frac{(z_{ei} - z_{si})}{k_H} + \frac{z_{si}}{k_{si}} \right]} (1 - e^{-\sqrt{c_i} x_{fi}}) (p_L - p_r) \quad (3.25)$$

where  $c_i = \frac{24}{k_{fi} w_i \left[ \frac{(z_{ei} - z_{si})}{k_H} + \frac{z_{si}}{k_{si}} \right]}$ ,  $z_{ei}$  is half the distance between the  $i$ th and  $(i+1)$ th fractures,  $z_{si}$  is the depth of the altered zone near the surface of fracture  $i$ ,  $k_{si}$  is the permeability of the altered zone near the surface of fracture  $i$ , and  $p_r$  represents the pressure in the fracture before the onset of flow convergence to wellbore ([Fig. 3.7](#)).

The linear-radial flow model of [Furui et al. \(2003\)](#) can be used to couple the fracture linear flow and the fracture radial flow. According to this model, well deliverability through  $n$  uniformly distributed fractures can be expressed as:

$$q = \sum_{i=1}^n \frac{5.9 \times 10^{-4} k_{fwi} w_{wi} (p_r - p_{wf})}{\mu_o B_o \left\{ \ln \left[ \frac{h}{2r_{wi}} \right] + \pi - (1.224 - s_i - Dq) \right\}} \quad (3.26)$$

where  $p_{wf}$  is the flowing bottom-hole pressure. The  $k_{fwi}$  is fracture permeability in the near-wellbore region, and  $w_{wi}$  is the width of the  $i$ th fracture in the near-wellbore region. These two parameters, plus the non-Darcy flow coefficient  $D$ , can be used to simulate choked fractures.

Combining [Eqs. \(3.23\), \(3.25\), and \(3.26\)](#) gives the reservoir deliverability equation:

$$q = \frac{1}{\left( \frac{1}{J_R} + \frac{1}{J_L} + \frac{1}{J_r} \right)} (\bar{p} - p_{wf}) \quad (3.27)$$

where,

$$J_R = \frac{7.08 \times 10^{-3} k_H h}{B_o \mu_o \left( \frac{1}{2} \ln \frac{4A}{\gamma C_A r_L^2} \right)} \quad (3.28)$$

$$J_L = \sum_{i=1}^n \frac{4.5 \times 10^{-3} h}{B_o \mu_o \sqrt{c_i} \left[ \frac{(z_{ei} - z_{si})}{k_H} + \frac{z_{si}}{k_{si}} \right]} (1 - e^{-\sqrt{c_i} x_{fi}}) \quad (3.29)$$

$$J_r = \sum_{i=1}^n \frac{5.9 \times 10^{-4} k_{fwi} w_{wi}}{\mu_o B_o \left\{ \ln \left[ \frac{h}{2r_{wi}} \right] + \pi - (1.224 - s_i - Dq) \right\}}. \quad (3.30)$$

The mathematical model for multifracted horizontal gas wells is similar to that for oil wells. The pseudo-steady-state radial flow in the outer region of the reservoir (Fig. 3.6) can be described by:

$$q_g = \frac{k_H h (\bar{p}^2 - p_L^2)}{1424 \bar{z} \bar{\mu}_g T \left( \frac{1}{2} \ln \frac{4A}{\gamma C_A r_L^2} \right)} \quad (3.31)$$

When applied to gas reservoirs, the reservoir-fracture cross-flow model of Guo and Schechter (1999) gives:

$$q_g = \sum_{i=1}^n \frac{4.475 \times 10^{-4} h}{\bar{\mu}_g \bar{z} T \sqrt{c_i} \left[ \frac{(z_{ei} - z_{si})}{k_H} + \frac{z_{si}}{k_{si}} \right]} (1 - e^{-\sqrt{c_i} x_{fi}}) (p_L^2 - p_r^2) \quad (3.32)$$

When the linear-radial flow model of Furui et al. (2003) is used, the well deliverability through  $n$  uniformly distributed fractures can be expressed as:

$$q_g = \sum_{i=1}^n \frac{5.85 \times 10^{-5} k_{fwi} w_{wi} (p_r^2 - p_{wf}^2)}{\bar{z} \bar{\mu}_g T \left\{ \ln \left[ \frac{h}{2r_{wi}} \right] + \pi - (1.224 - s_i - Dq_g) \right\}} \quad (3.33)$$

Combining Eqs. (3.31) through (3.33) yields a reservoir deliverability equation, expressed as:

$$q_g = \frac{1}{\left( \frac{1}{J_R} + \frac{1}{J_L} + \frac{1}{J_r} \right)} (\bar{p}^2 - p_{wf}^2) \quad (3.34)$$

where,

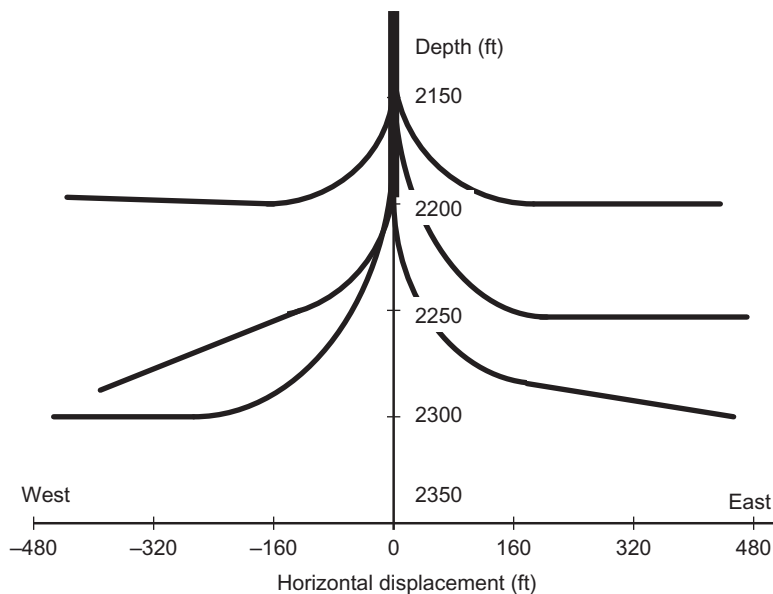
$$J_R = \frac{k_H h}{1424 \bar{z} \bar{\mu}_g T \left( \frac{1}{2} \ln \frac{4A}{\gamma C_A r_L^2} \right)} \quad (3.35)$$

$$J_L = \sum_{i=1}^n \frac{4.475 \times 10^{-4} h}{\bar{\mu}_g \bar{z} T \sqrt{c_i} \left[ \frac{(z_{ei} - z_{si})}{k_H} + \frac{z_{si}}{k_{si}} \right]} (1 - e^{-\sqrt{c_i} x_{fi}}) \quad (3.36)$$

$$J_r = \sum_{i=1}^n \frac{5.85 \times 10^{-5} k_{fwi} w_{wi}}{\bar{z} \mu_g T \left\{ \ln \left[ \frac{h}{2r_{wi}} \right] + \pi - (1.224 - s_i - Dq_g) \right\}} \quad (3.37)$$

### 3.4 MULTILATERAL WELLS

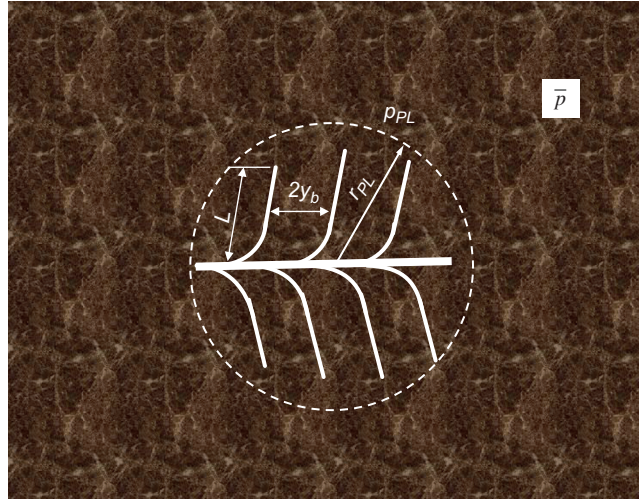
A multilateral well is defined, in general, as a well with multiple branches in the lower bore hole targeting oil and gas reserves in the same or in different strata. These branches are called “laterals.” The primary, or main wellbore, from which the laterals are drilled out, can be vertical or horizontal. Lateral bores extending from vertical wellbores are usually used to reach different pay zones, while the laterals drilled out from horizontal wellbores are usually intended to reach different areas of the same pay zone. In this book, multilateral wells with laterals drilled from vertical main wellbores are called “root wells” (Fig. 3.8). Multilateral wells with the laterals drilled out from horizontal main wellbores are called “fishbone wells” (Fig. 3.9). The prediction of fishbone well productivity is relatively simple because all laterals (rib holes) share approximately the same pressure in the main wellbore (backbone hole). Prediction of root well productivity is more complicated because the pressures in the laterals can be significantly different, and wellbore hydraulics plays an important role. This is further discussed in Chapter 6, Well Deliverability.



**FIGURE 3.8**

Schematic of a typical root well (Guo et al., 2008).





**FIGURE 3.9**  
Schematic of a reservoir section drained by a fishbone well (Guo et al., 2008).

The initial flow regime in a fishbone well may be pseudolinear, before the rib holes begin to interfere with each other. Radial flow may prevail later, if the drainage area is large in proportion to the drilled region of the reservoir.

Raghavan and Joshi (1993) presented a mathematical model that can be used to predict the productivities of root wells. The model uses effective wellbore radius (horizontal radial flow) to simulate fluid flow to the horizontal drain holes. Retnanto and Economides (1996) published a simple formulation of multilateral well productivity for pseudo-steady-state flow. They derived their formulation by combining a one-dimensional linear-flow model with a two-dimensional radial flow model, to cover the whole drainage area. Larsen (1996) proposed a mathematical model, similar to that of Raghavan and Joshi (1993) in the sense that horizontal drain holes are simulated by vertical wellbores located at the midpoints of the well elements.

A pseudo-linear-radial-combined model is described in this section. The model assumes two regions within the reservoir-- an inner, drilled region, and an outer nondrilled region. The model assumes the inner region to be dominated by pseudo-steady-state pseudo-linear flow between the rib holes, and the outer region to be dominated by pseudo-steady-state radial flow.

Following Furui et al. (2003), for uniformly distributed rib holes in the inner region, the deliverability of  $n$  rib holes is expressed as:

$$q = \sum_{i=1}^n \frac{7.08 \times 10^{-3} k_H L_i (p_{PL} - p_{wf})}{\mu_o B_o \left\{ I_{ani} \ln \left[ \frac{h I_{ani}}{r_{wi} (I_{ani} + 1)} \right] + \frac{\pi y_{bi}}{h} - I_{ani} (1.224 - s_i) \right\}} \quad (3.38)$$

for oil reservoirs, where  $L_i$ ,  $r_{wi}$ ,  $y_{bi}$  and  $s_i$  are length, radius, drainage distance, and skin factor of rib hole  $i$ , respectively. For gas reservoirs the reservoir deliverability equation is expressed as:

$$q_g = \sum_{i=1}^n \frac{k_H L_i (p_{PL}^2 - p_w^2)}{1424 \bar{\mu}_g \bar{z} T \left\{ I_{ani} \ln \left[ \frac{h I_{ani}}{r_{wi} (I_{ani} + 1)} \right] + \frac{\pi y_{bi}}{h} - I_{ani} (1.224 - (s_i + Dq_g)) \right\}} \quad (3.39)$$

The permeability anisotropy  $I_{ani}$  is defined as  $\sqrt{\frac{k_H}{k_V}}$ . The  $p_{PL}$  is defined as the average pressure at the edge of the inner region. The radial flow in the outer region can be described by:

$$q = \frac{k_H h (\bar{p} - p_{PL})}{141.2 B_o \mu_o \left( \frac{1}{2} \ln \frac{4A}{\gamma C_A r_{PL}^2} \right)} \quad (3.40)$$

for oil reservoirs, and:

$$q_g = \frac{k_H h (\bar{p}^2 - p_{PL}^2)}{1424 \bar{\mu}_g \bar{z} T \left( \frac{1}{2} \ln \frac{4A}{\gamma C_A r_{PL}^2} \right)} \quad (3.41)$$

for gas reservoirs. Solving these equations for production rates gives:

$$q = \frac{1}{\left( \frac{1}{J_{PL}} + \frac{1}{J_R} \right)} (\bar{p} - p_{wf}) \quad (3.42)$$

for oil reservoirs, and:

$$q = \frac{1}{\left( \frac{1}{J_{PL}} + \frac{1}{J_R} \right)} (\bar{p}^2 - p_{wf}^2) \quad (3.43)$$

for gas reservoirs, where:

$$J_{PL} = \sum_{i=1}^n \frac{7.08 \times 10^{-3} k_H L_i}{\mu_o B_o \left\{ I_{ani} \ln \left[ \frac{h I_{ani}}{r_{wi} (I_{ani} + 1)} \right] + \frac{\pi y_{bi}}{h} - I_{ani} (1.224 - s_i) \right\}} \quad (3.44)$$

for oil reservoirs, and:

$$J_{PL} = \sum_{i=1}^n \frac{k_H L_i}{1424 \bar{\mu}_g \bar{z} T \left\{ I_{ani} \ln \left[ \frac{h I_{ani}}{r_{wi} (I_{ani} + 1)} \right] + \frac{\pi y_{bi}}{h} - I_{ani} (1.224 - (s_i + Dq)) \right\}} \quad (3.45)$$

for gas reservoirs, and:

$$J_R = \frac{k_H h}{141.2 B_o \mu_o \left( \frac{1}{2} \ln \frac{4A}{\gamma C_A r_{PL}^2} \right)}. \quad (3.46)$$

for oil reservoirs, and:

$$J_R = \frac{k_H h}{1424 \bar{\mu}_g \bar{z} T \left( \frac{1}{2} \ln \frac{4A}{\gamma C_A r_{PL}^2} \right)} \quad (3.47)$$

for gas reservoirs. The equivalent radius of the inner region may be estimated by:

$$r_{PL} = \sqrt{\frac{2(n+1)\bar{y}_b \bar{L}}{\pi}} \quad (3.48)$$

where  $\bar{y}_b$  and  $\bar{L}$  are the average rib hole drainage distance and rib hole length, respectively. If the fishbone well is used to drain an entire reservoir with physical no-flow boundaries, the drainage area shape factor  $C_A$  can be estimated based on the reservoir shape and the location of the inner region in the reservoir. If the fishbone well is employed to drain only a portion of a reservoir, the  $C_A$  should be estimated based on the shape of the drainage area, with the location of the inner region at the center of the drainage area. Because all the above equations are deterministic, they can be used for predicting actual well IPR.

### 3.5 INFLOW PERFORMANCE RELATIONSHIP

IPR is used for evaluating reservoir deliverability in production engineering. The IPR curve is a graphical presentation of the relation between the flowing bottom-hole pressure and liquid production rate. A typical IPR curve is shown in Fig. 3.10. The magnitude of the slope of the IPR curve is called the “productivity index” (PI or  $J$ ), that is,

$$J = \frac{q}{(p_e - p_{wf})}, \quad (3.49)$$

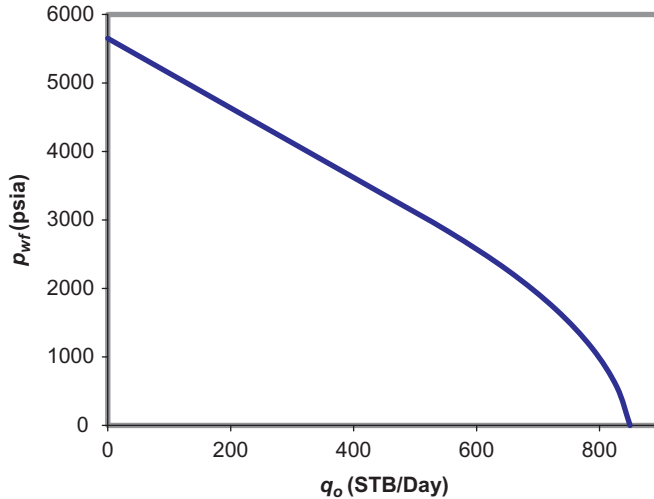
where  $J$  is the productivity index. Apparently  $J$  is not a constant in the two-phase flow region.

Well IPR curves are usually constructed using reservoir inflow models, which can be from either a theoretical basis or an empirical basis. It is essential to validate these models with test points in field applications.

#### 3.5.1 IPR FOR SINGLE (LIQUID)-PHASE RESERVOIRS

All oil reservoir inflow models represented in the previous sections were derived on the basis of the assumption of single-phase flow. This assumption is valid for oil reservoirs with undersaturated oil, or reservoir portions where the pressure is above the bubble-point pressure. These equations define the productivity index ( $J^*$ ) for flowing bottom-hole pressures above the bubble-point pressure as follows:

$$J^* = \frac{q}{(p_i - p_{wf})} = \frac{kh}{162.6 B_o \mu_o \left( \log t + \log \frac{k}{\phi \mu_o c_t r_w^2} - 3.23 + 0.87S \right)} \quad (3.50)$$


**FIGURE 3.10**

A typical IPR curve for an oil well.

for radial transient flow around a vertical well,

$$J^* = \frac{q}{(p_e - p_{wf})} = \frac{kh}{141.2B_o\mu_o \left( \ln \frac{r_e}{r_w} + S \right)} \quad (3.51)$$

for radial steady-state flow around a vertical well,

$$J^* = \frac{q}{(\bar{p} - p_{wf})} = \frac{kh}{141.2B_o\mu_o \left( \frac{1}{2} \ln \frac{4A}{\gamma C_A r_w^2} + S \right)} \quad (3.52)$$

for pseudo-steady-state flow around a vertical well, and

$$\begin{aligned} J^* &= \frac{q}{(p_e - p_{wf})} \\ &= \frac{k_H h}{141.2B\mu \left\{ \ln \left[ \frac{a + \sqrt{a^2 - (L/2)^2}}{L/2} \right] + \frac{I_{ani} h}{L} \ln \left[ \frac{I_{ani} h}{I_{ani} + 1} \right] \right\}} \end{aligned} \quad (3.53)$$

for steady-state flow around a nonfractured horizontal well.

Since the productivity index ( $J^*$ ) above the bubble-point pressure is independent of production rate, the IPR curve for a single (liquid)-phase reservoir is simply a straight line drawn from the reservoir pressure to the bubble-point pressure. If the bubble-point pressure is 0 psig, the absolute open flow (AOF) is the productivity index ( $J^*$ ) times the reservoir pressure.

**Example Problem 3.2** Construct IPR of a vertical well in an oil reservoir. Consider (1) transient flow at 1 month, (2) steady-state flow, and (3) pseudo-steady-state flow. The following data are given:

Porosity:	$\phi = 0.19$
Effective horizontal permeability:	$k = 8.2$ md
Pay zone thickness:	$h = 53$ ft
Reservoir pressure:	$p_e$ or $\bar{p} = 5,651$ psia
Bubble-point pressure:	$p_b = 50$ psia
Fluid formation volume factor:	$B_o = 1.1$
Fluid viscosity:	$\mu_o = 1.7$ cp
Total compressibility:	$c_r = 0.0000129$ psi <sup>-1</sup>
Drainage area:	$A = 640$ acres ( $r_e = 2980$ ft)
Wellbore radius:	$r_w = 0.328$ ft
Skin factor:	$S = 0$

**Solution**

1. For transient flow, calculated points are:

$$\begin{aligned}
 J^* &= \frac{kh}{162.6B\mu \left( \log t + \log \frac{k}{\phi\mu c_r r_w^2} - 3.23 \right)} \\
 &= \frac{(8.2)(53)}{162.6(1.1)(1.7) \left( \log[(30)(24)] + \log \frac{(8.2)}{(0.19)(1.7)(0.0000129)(0.328)^2} - 3.23 \right)} \\
 &= 0.2075 \text{ STB}/d\text{-psi}
 \end{aligned}$$

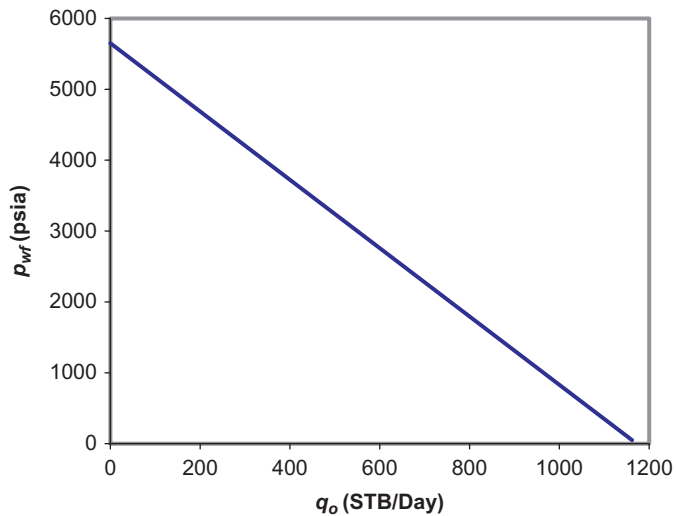
Calculated points are:

$P_{wf}$ (psi)	$q_o$ (sb/day)
50	1162
5651	0

Transient IPR curve is plotted in Fig. 3.11.

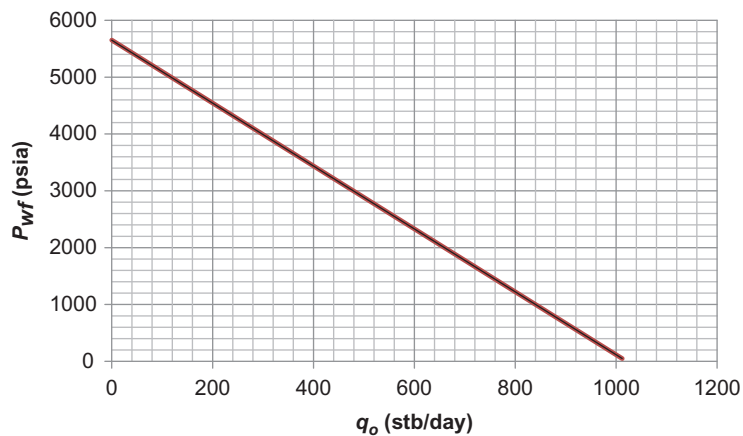
2. For steady-state flow:

$$\begin{aligned}
 J^* &= \frac{kh}{141.2B\mu \left( \ln \frac{r_e}{r_w} + S \right)} \\
 &= \frac{(8.2)(53)}{141.2(1.1)(1.7) \ln \left( \frac{2,980}{0.328} \right)} \\
 &= 0.1806 \text{ STB}/d\text{-psi}
 \end{aligned}$$



**FIGURE 3.11**

Transient IPR curve for Example Problem 3.2.



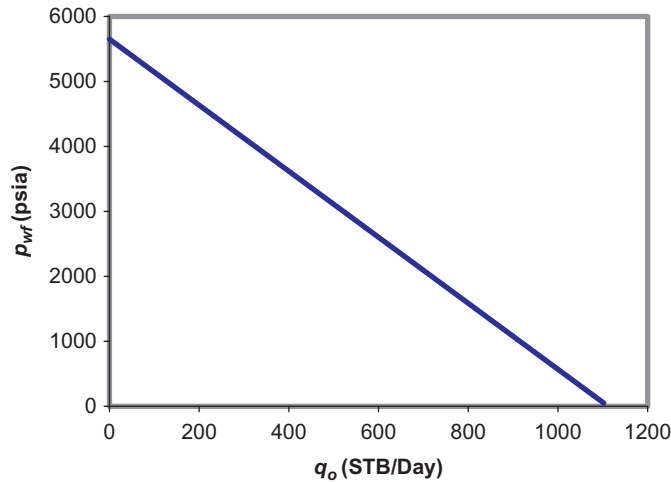
**FIGURE 3.12**

Steady-state IPR curve for Example Problem 3.2.

Calculated points are:

$P_{wf}$ (psi)	$q_o$ (sb/day)
50	1012
5651	0

Steady state IPR curve is plotted in Fig. 3.12.

**FIGURE 3.13**

Pseudo-steady-state IPR curve for Example Problem 3.2.

3. For pseudo-steady-state flow:

$$\begin{aligned}
 J^* &= \frac{kh}{141.2B\mu \left( \ln \frac{r_e}{r_w} - \frac{3}{4} + S \right)} \\
 &= \frac{(8.2)(53)}{141.2(1.1)(1.7) \left( \ln \frac{2,980}{0.328} - 0.75 \right)} \\
 &= 0.1968 \text{ STB/d-psi}
 \end{aligned}$$

Calculated points are:

$P_{wf}$ (psi)	$q_o$ (stb/day)
50	1102
5651	0

Pseudo-steady-state IPR curve is plotted in Fig. 3.13.

### 3.5.2 IPR FOR TWO-PHASE RESERVOIRS

The linear IPR model presented in the previous section is valid for pressure values as low as bubble-point pressure. Below the bubble-point pressure, the solution gas escapes from the oil and becomes free gas. The free gas occupies some portion of pore space, which reduces flow of oil. This effect is

quantified by the reduced relative permeability. Also, oil viscosity increases as its solution gas content drops. The combination of the relative permeability effect and the viscosity effect results in lower oil production rate at a given bottom-hole pressure. This makes the IPR curve deviate from the linear trend below bubble-point pressure, as shown in Fig. 3.10. The lower the pressure, the larger the deviation. If the reservoir pressure is below the initial bubble-point pressure, oil and gas two-phase flow exists in the whole reservoir domain and the reservoir is referred as a “two-phase reservoir.”

Only empirical equations are available for modeling IPR of two-phase reservoirs. These empirical equations include Vogel’s (1968) equation extended by Standing (1971), the Fetkovich (1973) equation, Bandakhlia and Aziz’s (1989) equation, Chang’s (1992) equation, and Retnanto and Economides’ (1998) equation. Vogel’s equation is still widely used in the industry. It is written as

$$q = q_{\max} \left[ 1 - 0.2 \left( \frac{p_{wf}}{\bar{p}} \right) - 0.8 \left( \frac{p_{wf}}{\bar{p}} \right)^2 \right] \quad (3.54)$$

or

$$p_{wf} = 0.125\bar{p} \left[ \sqrt{81 - 80 \left( \frac{q}{q_{\max}} \right) - 1} \right], \quad (3.55)$$

where  $q_{\max}$  is an empirical constant and its value represents the maximum possible value of reservoir deliverability, or AOF. The  $q_{\max}$  can be theoretically estimated based on reservoir pressure and productivity index above the bubble-point pressure. The pseudo-steady-state flow follows that

$$q_{\max} = \frac{J^* \bar{p}}{1.8}. \quad (3.56)$$

Derivation of this relation is left to the reader for an exercise.

Fetkovich’s equation is written as

$$q = q_{\max} \left[ 1 - \left( \frac{p_{wf}}{\bar{p}} \right)^2 \right]^n \quad (3.57)$$

or

$$q = C(\bar{p}^2 - p_{wf}^2)^n, \quad (3.58)$$

where  $C$  and  $n$  are empirical constants and is related to  $q_{\max}$  by  $C = q_{\max}/\bar{p}^{2n}$ .

**Example Problem 3.3** Construct IPR of a vertical well in a saturated oil reservoir using Vogel’s equation. The following data are given:

Porosity:	$\phi = 0.19$
Effective horizontal permeability:	$k = 8.2$ md
Pay zone thickness:	$h = 53$ ft
Reservoir pressure:	$\bar{p} = 5,651$ psia
Bubble-point pressure:	$p_b = 5651$ psia
Fluid formation volume factor:	$B_o = 1.1$
Fluid viscosity:	$\mu_o = 1.7$ cp
Total compressibility:	$c_t = 0.0000129$ psi <sup>-1</sup>
Drainage area:	$A = 640$ acres ( $r_e = 2980$ ft)
Wellbore radius:	$r_w = 0.328$ ft
Skin factor:	$S = 0$



**Solution**

$$\begin{aligned}
 J^* &= \frac{kh}{141.2B\mu \left( \ln \frac{r_e}{r_w} - \frac{3}{4} + S \right)} \\
 &= \frac{(8.2)(53)}{141.2(1.1)(1.7) \left( \ln \frac{2,980}{0.328} - 0.75 \right)} \\
 &= 0.1968 \text{ STB/d} - \text{psi} \\
 q_{\max} &= \frac{J^* \bar{p}}{1.8} = \frac{(0.1968)(5,651)}{1.8} = 618 \text{ stb/day}
 \end{aligned}$$

Calculated points are:

$p_{wf}$ (psi)	$q_o$ (stb/day)
5651	0
5000	122
4500	206
4000	283
3500	352
3000	413
2500	466
2000	512
1500	550
1000	580
500	603
0	618

The IPR curve is plotted in Fig. 3.14.

### 3.5.3 IPR FOR PARTIAL TWO-PHASE OIL RESERVOIRS

If the reservoir pressure is above the bubble-point pressure and the flowing bottom-hole pressure is below the bubble-point pressure, a generalized IPR model can be formulated. This can be done by combining the straight-line IPR model for single-phase flow with Vogel's IPR model for two-phase flow. Fig. 3.15 helps to understand the formulation.

According to the linear IPR model, the flow rate at bubble-point pressure is

$$q_b = J^*(\bar{p} - p_b), \quad (3.59)$$

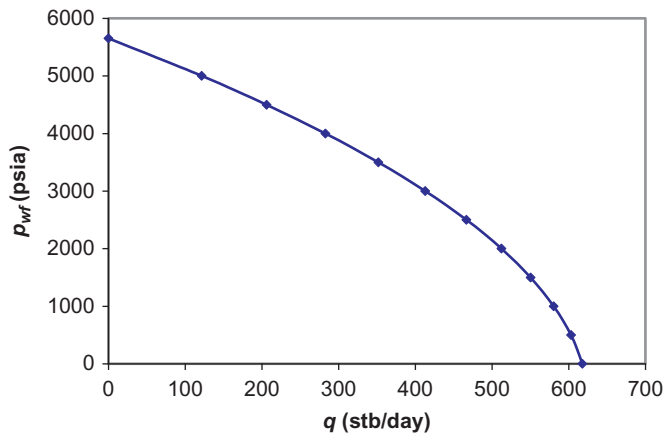


FIGURE 3.14

IPR curve for Example Problem 3.3.

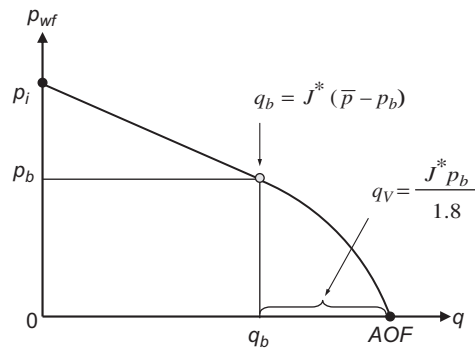


FIGURE 3.15

Generalized Vogel IPR model for partial two-phase reservoirs.

Based on Vogel’s IPR model, the additional flow rate caused by a pressure below the bubble-point pressure is expressed as

$$\Delta q = q_v \left[ 1 - 0.2 \left( \frac{p_{wf}}{p_b} \right) - 0.8 \left( \frac{p_{wf}}{p_b} \right)^2 \right]. \quad (3.60)$$

Thus, the flow rate at a given bottom-hole pressure that is below the bubble-point pressure is expressed as

$$q = q_b + q_v \left[ 1 - 0.2 \left( \frac{p_{wf}}{p_b} \right) - 0.8 \left( \frac{p_{wf}}{p_b} \right)^2 \right]. \quad (3.61)$$

Because

$$q_v = \frac{J^* p_b}{1.8}, \tag{3.62}$$

we have

$$q = J^*(\bar{p} - p_b) = \frac{J^* p_b}{1.8} \times \left[ 1 - 0.2 \left( \frac{p_{wf}}{p_b} \right) - 0.8 \left( \frac{p_{wf}}{p_b} \right)^2 \right]. \tag{3.63}$$

**Example Problem 3.4** Construct IPR of a vertical well in an undersaturated oil reservoir using the generalized Vogel equation. The following data are given:

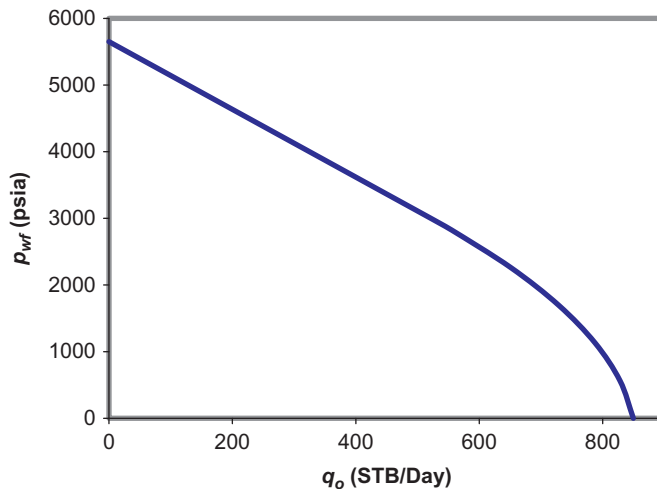
Porosity:	$\phi = 0.19$
Effective horizontal permeability:	$k = 8.2$ md
Pay zone thickness:	$h = 53$ ft
Reservoir pressure:	$\bar{p} = 5,651$ psia
Bubble-point pressure:	$p_b = 3000$ psia
Fluid formation volume factor:	$B_o = 1.1$
Fluid viscosity:	$\mu_o = 1.7$ cp
Total compressibility:	$c_t = 0.0000129$ psi <sup>-1</sup>
Drainage area:	$A = 640$ acres ( $r_e = 2980$ ft)
Wellbore radius:	$r_w = 0.328$ ft
Skin factor:	$S = 0$

**Solution**

$$\begin{aligned} J^* &= \frac{kh}{141.2B\mu \left( \ln \frac{r_e}{r_w} - \frac{3}{4} + S \right)} \\ &= \frac{(8.2)(53)}{141.2(1.1)(1.7) \left( \ln \frac{2,980}{0.328} - 0.75 \right)} \\ &= 0.1968 \text{ STB/d - psi} \end{aligned}$$

$$\begin{aligned} q_b &= J^*(\bar{p} - p_b) \\ &= (0.1968)(5,651 - 3,000) \\ &= 522 \text{ sbt/day} \end{aligned}$$

$$\begin{aligned} q_v &= \frac{J^* p_b}{1.8} \\ &= \frac{(0.1968)(3,000)}{1.8} \\ &= 328 \text{ stb/day} \end{aligned}$$

**FIGURE 3.16**

IPR curve for Example Problem 3.4.

Calculated points are

$P_{wf}$ (psi)	$q_o$ (stb/day)
0	850
565	828
1130	788
1695	729
2260	651
2826	555
3000	522
5651	0

The IPR curve is plotted in [Fig. 3.16](#).

### 3.6 CONSTRUCTION OF IPR CURVES USING TEST POINTS

It has been shown in the previous section that well IPR curves can be constructed using reservoir parameters including formation permeability, fluid viscosity, drainage area, wellbore radius, and well skin factor. These parameters determine the constants (e.g., productivity index) in the IPR model. However, the values of these parameters are not always available. Thus, test points (measured values of production rate and flowing bottom-hole pressure) are frequently used for constructing IPR curves.

Constructing IPR curves using test points involves backing-calculation of the constants in the IPR models. For a single-phase (unsaturated oil) reservoir, the model constant  $J^*$  can be determined by

$$J^* = \frac{q_1}{(\bar{p} - p_{wf1})}, \tag{3.64}$$

where  $q_1$  is the tested production rate at tested flowing bottom-hole pressure  $p_{wf1}$ .

For a partial two-phase reservoir, model constant  $J^*$  in the generalized Vogel equation must be determined based on the range of tested flowing bottom-hole pressure. If the tested flowing bottom-hole pressure is greater than bubble-point pressure, the model constant  $J^*$  should be determined by

$$J^* = \frac{q_1}{(\bar{p} - p_{wf1})}. \tag{3.65}$$

If the tested flowing bottom-hole pressure is less than bubble-point pressure, the model constant  $J^*$  should be determined using

$$J^* = \frac{q_1}{\left( (\bar{p} - p_b) + \frac{p_b}{1.8} \left[ 1 - 0.2 \left( \frac{p_{wf1}}{p_b} \right) - 0.8 \left( \frac{p_{wf1}^2}{p_b^2} \right) \right] \right)}. \tag{3.66}$$

**Example Problem 3.5** Construct IPR of two wells in an undersaturated oil reservoir using the generalized Vogel equation. The following data are given:

Reservoir pressure:	$\bar{p} = 5,000$ psia
Bubble-point pressure:	$p_b = 3000$ psia
Tested flowing bottom-hole pressure in Well A:	$p_{wf1} = 4000$ psia
Tested production rate from Well A:	$q_1 = 300$ stb/day
Tested flowing bottom-hole pressure in Well B:	$p_{wf1} = 2000$ psia
Tested production rate from Well B:	$q_1 = 900$ stb/day

**Solution**  
**Well A:**

$$\begin{aligned} J^* &= \frac{q_1}{(\bar{p} - p_{wf1})} \\ &= \frac{300}{(5,000 - 4,000)} \\ &= 0.3000 \text{ stb/day - psi} \end{aligned}$$

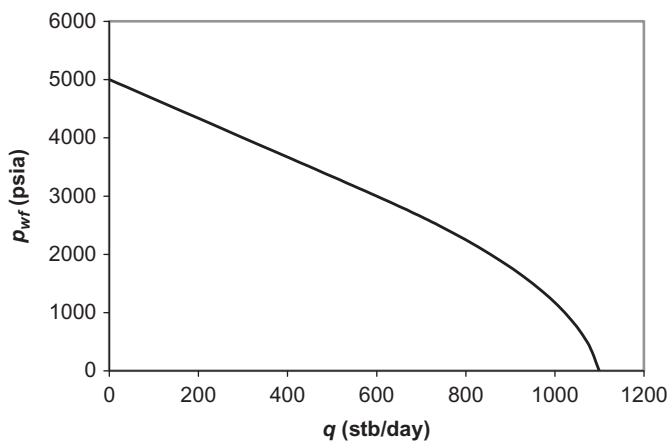
Calculated points are:

$p_{wf}$ (psia)	$q$ (stb/day)
0	1100
500	1072
1000	1022
1500	950
2000	856
2500	739
3000	600
5000	0

The IPR curve is plotted in Fig. 3.17.

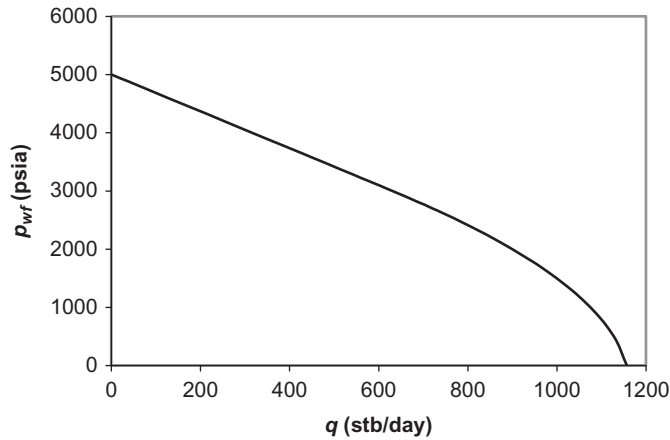
**Well B:**

$$\begin{aligned}
 J^* &= \frac{q_1}{\left( (\bar{p} - p_b) + \frac{p_b}{1.8} \left[ 1 - 0.2 \left( \frac{p_{wf1}}{p_b} \right) - 0.8 \left( \frac{p_{wf1}}{p_b} \right)^2 \right] \right)} \\
 &= \frac{900}{\left( (5000 - 3000) + \frac{3000}{1.8} \left[ 1 - 0.2 \left( \frac{2000}{3000} \right) - 0.8 \left( \frac{2000}{3000} \right)^2 \right] \right)} \\
 &= 0.3156 \text{ stb/day} - \text{psi}
 \end{aligned}$$



**FIGURE 3.17**

IPR curves for Example Problem 3.5, Well A.

**FIGURE 3.18**

IPR curves for Example Problem 3.5, Well B.

Calculated points are:

$p_{wf}$ (psia)	$q$ (stb/day)
0	1157
500	1128
1000	1075
1500	999
2000	900
2500	777
3000	631
5000	0

The IPR curve is plotted in Fig. 3.18.

For a two-phase (saturated oil) reservoir, if the Vogel equation is used for constructing the IPR curve, the model constant  $q_{max}$  can be determined by

$$q_{max} = \frac{q_1}{1 - 0.2(p_{wf1}/\bar{p}) - 0.8(p_{wf1}/\bar{p})^2}. \quad (3.67)$$

The productivity index at and above bubble-point pressure, if desired, can then be estimated by

$$J^* = 1.8q_{max}\bar{p}. \quad (3.68)$$

If Fetkovich's equation is used, two test points are required for determining the values of the two model constant, that is,

$$n = \frac{\log\left(\frac{q_1}{q_2}\right)}{\log\left(\frac{\bar{p}^2 - p_{wf1}^2}{\bar{p}^2 - p_{wf2}^2}\right)} \quad (3.69)$$

and

$$C = \frac{q_1}{(\bar{p}^2 - p_{wf1}^2)^n}, \quad (3.70)$$

where  $q_1$  and  $q_2$  are the tested production rates at tested flowing bottom-hole pressures  $p_{wf1}$  and  $p_{wf2}$ , respectively.

**Example Problem 3.6** Construct IPR of a well in a saturated oil reservoir using both Vogel's equation and Fetkovich's equation. The following data are given:

Reservoir pressure:	$\bar{p} = 3,000$ psia
Tested flowing bottom-hole pressure:	$p_{wf1} = 2000$ psia
Tested production rate at $p_{wf1}$ :	$q_1 = 500$ stb/day
Tested flowing bottom-hole pressure:	$p_{wf2} = 1000$ psia
Tested production rate at $p_{wf2}$ :	$q_2 = 800$ stb/day

**Solution**

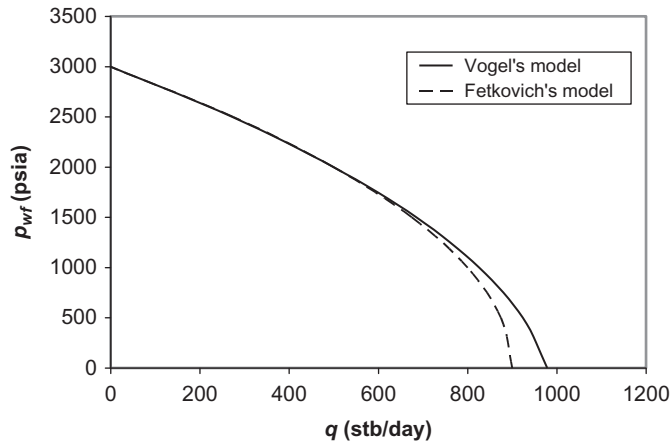
Vogel's equation:

$$\begin{aligned} q_{\max} &= \frac{q_1}{1 - 0.2 \left( \frac{p_{wf1}}{\bar{p}} \right) - 0.8 \left( \frac{p_{wf1}}{\bar{p}} \right)^2} \\ &= \frac{500}{1 - 0.2 \left( \frac{2000}{3000} \right) - 0.8 \left( \frac{2000}{3000} \right)^2} \\ &= 978 \text{ stb/day} \end{aligned}$$

Calculated data points are:

$p_{wf}$ (psia)	$q$ (stb/day)
0	978
500	924
1000	826
1500	685
2000	500
2500	272
3000	0





**FIGURE 3.19**

IPR curves for Example Problem 3.6.

Fetkovich's equation:

$$n = \frac{\log\left(\frac{q_1}{q_2}\right)}{\log\left(\frac{\bar{p}^2 - p_{wf1}^2}{\bar{p}^2 - p_{wf2}^2}\right)} = \frac{\log\left(\frac{500}{800}\right)}{\log\left(\frac{(3,000)^2 - (2,000)^2}{(3,000)^2 - (1,000)^2}\right)} = 1.0$$

$$C = \frac{q_1}{(\bar{p}^2 - p_{wf1}^2)^n}$$

$$= \frac{500}{((3,000)^2 - (2,000)^2)^{1.0}}$$

$$= 0.0001 \text{ stb/day} - \text{psi}^{2n}$$

Calculated data points are:

$p_{wf}$ (psia)	$q$ (stb/day)
0	900
500	875
1000	800
1500	675
2000	500
2500	275
3000	0

The IPR curves are plotted in Fig. 3.19, which indicates that Fetkovich's equation with two constants catches more details than Vogel's equation.

### 3.7 COMPOSITE IPR OF STRATIFIED RESERVOIRS

Nearly all producing formations are stratified to some extent. This means that the vertical borehole in the production zone has different layers having different reservoir pressures, permeabilities, and producing fluids. If it is assumed that there is no other communication between these formations (other than the wellbore), the production will come mainly from the higher permeability layers.

As the well's rate of production is gradually increased, the less consolidated layers will begin to produce one by one (at progressively lower GOR), and so the overall ratio of production will fall as the rate is increased. If, however, the most highly depleted layers themselves produce at high ratios because of high free gas saturations, the overall GOR will eventually start to rise as the rate is increased and this climb will be continued (after the most permeable zone has come onto production). Thus, it is to be expected that a well producing from a stratified formation will exhibit a minimum GOR as the rate of production is increased.

One of the major concerns in a multilayer system is that interlayer cross-flow may occur if reservoir fluids are produced from commingled layers that have unequal initial pressures. This cross-flow greatly affects the composite IPR of the well, which may result in an optimistic estimate of production rate from the commingled layers.

El-Banbi and Wattenbarger (1996, 1997) investigated productivity of commingled gas reservoirs based on history matching to production data. However, no information was given in the papers regarding generation of IPR curves.

#### 3.7.1 COMPOSITE IPR MODELS

The following assumptions are made in this section:

1. Pseudo-steady-state flow prevails in all the reservoir layers.
2. Fluids from/into all the layers have similar properties.
3. Pressure losses in the wellbore sections between layers are negligible (these pressure losses are considered in Chapter 6, Well Deliverability, where multilateral wells are addressed).
4. The IPR of individual layers is known.

On the basis of Assumption 1, under steady-flow conditions, the principle of material balance dictates

$$\begin{aligned} & \text{net mass flow rate from layers to the well} \\ & = \text{mass flow rate at well head} \end{aligned}$$

or

$$\sum_{i=1}^n \rho_i q_i = \rho_{wh} q_{wh}, \quad (3.71)$$

where  $\rho_i$  = density of fluid from/into layer  $i$ ;  $q_i$  = flow rate from/into layer  $i$ ;  $\rho_{wh}$  = density of fluid at wellhead;  $q_{wh}$  = flow rate at wellhead, and;  $n$  = number of layers.

Fluid flow from wellbore to reservoir is indicated by negative  $q_i$ . Using Assumption 2 and ignoring density change from bottom hole to well head, Eq. (3.71) degenerates to

$$\sum_{i=1}^n q_i = q_{wh} \tag{3.72}$$

or

$$\sum_{i=1}^n J_i(\bar{p}_i - p_{wf}) = q_{wh}, \tag{3.73}$$

where  $J_i$  is the productivity index of layer  $i$ .

### 3.7.1.1 Single-Phase Liquid Flow

For reservoir layers containing undersaturated oils, if the flowing bottom-hole pressure is above the bubble-point pressures of oils in all the layers, single-phase flow in all the layers is expected. Then Eq. (3.73) becomes

$$\sum_{i=1}^n J_i^*(\bar{p}_i - p_{wf}) = q_{wh}, \tag{3.74}$$

where  $J_i^*$  is the productivity index of layer  $i$  at and above the bubble-point pressure. Eq. (3.74) represents a linear composite IPR of the well. A straight-line IPR can be drawn through two points at AOF and shut-in bottom-hole pressure ( $p_{wfo}$ ). It is apparent from Eq. (3.74) that

$$AOF = \sum_{i=1}^n J_i^* \bar{p}_i = \sum_{i=1}^n AOF_i \tag{3.75}$$

and

$$p_{wfo} = \frac{\sum_{i=1}^n J_i^* \bar{p}_i}{\sum_{i=1}^n J_i^*}. \tag{3.76}$$

It should be borne in mind that  $p_{wfo}$  is a dynamic bottom-hole pressure because of cross-flow between layers.

### 3.7.1.2 Two-Phase Flow

For reservoir layers containing saturated oils, two-phase flow is expected. If Vogel’s IPR model is used, inflow model becomes

$$\sum_{i=1}^n \frac{J_i^* \bar{p}_i}{1.8} \left[ 1 - 0.2 \left( \frac{p_{wf}}{\bar{p}_i} \right) - 0.8 \left( \frac{p_{wf}}{\bar{p}_i} \right)^2 \right] = q_{wh}, \tag{3.77}$$

which gives

$$AOF = \sum_{i=1}^n \frac{J_i^* \bar{p}_i}{1.8} = \sum_{i=1}^n AOF_i \tag{3.78}$$

and

$$p_{wfo} = \frac{\sqrt{80 \sum_{i=1}^n J_i^* \bar{p}_i \sum_{i=1}^n \frac{J_i^*}{\bar{p}_i} + \left(\sum_{i=1}^n J_i^*\right)^2 - \sum_{i=1}^n J_i^*}}{8 \sum_{i=1}^n \frac{J_i^*}{\bar{p}_i}} \quad (3.79)$$

Again,  $p_{wfo}$  is a dynamic bottom-hole pressure because of cross-flow between layers.

### 3.7.1.3 Partial Two-Phase Flow

The generalized Vogel IPR model can be used to describe well-inflow from multilayer reservoirs where reservoir pressures are greater than oil bubble pressures and the wellbore pressure is below these bubble-point pressures. Inflow equation takes the form

$$\sum_{i=1}^n J_i^* \times \left\{ (\bar{p}_i - p_{bi}) + \frac{p_{bi}}{1.8} \left[ 1 - 0.2 \left( \frac{p_{wf}}{p_{bi}} \right) - 0.8 \left( \frac{p_{wf}}{p_{bi}} \right)^2 \right] \right\} = q_{wh}, \quad (3.80)$$

which gives

$$AOF = \sum_{i=1}^n J_i^* (\bar{p}_i - 0.44 p_{bi}) = \sum_{i=1}^n AOF_i \quad (3.81)$$

and

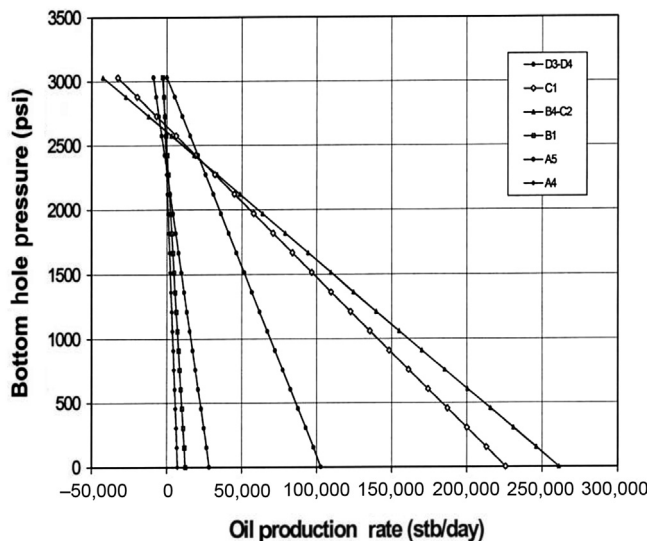
$$p_{wfo} = \frac{\sqrt{147 [0.56 \sum_{i=1}^n J_i^* p_{bi} + \sum_{i=1}^n J_i^* (\bar{p}_i - p_{bi})] \sum_{i=1}^n \frac{J_i^*}{p_{bi}} + \left(\sum_{i=1}^n J_i^*\right)^2 - \sum_{i=1}^n J_i^*}}{8 \sum_{i=1}^n \frac{J_i^*}{p_{bi}}}. \quad (3.82)$$

Again,  $p_{wfo}$  is a dynamic bottom-hole pressure because of cross-flow between layers.

**Example Problem 3.7** An exploration well in the South China Sea penetrated eight oil layers with unequal pressures within a short interval. These oil layers were tested in six groups. Layers B4 and C2 were tested together and Layers D3 and D4 were tested together. Test data and calculated productivity index ( $J_i^*$ ) are summarized in Table 3.1. The IPR curves of the individual layers

**Table 3.1 Summary of Test Points for Nine Oil Layers**

Layer No.	D3-D4	C1	B4-C2	B1	A5	A4
Layer pressure (psi)	3030	2648	2606	2467	2302	2254
Bubble point (psi)	26.3	4.1	4.1	56.5	31.2	33.8
Test rate (bopd)	3200	3500	3510	227	173	122
Test pressure (psi)	2936	2607	2571	2422	2288	2216
$J^*$ (bopd/psi)	34	85.4	100.2	5.04	12.4	3.2



**FIGURE 3.20**

IPR curves of individual layers in Example Problem 3.7.

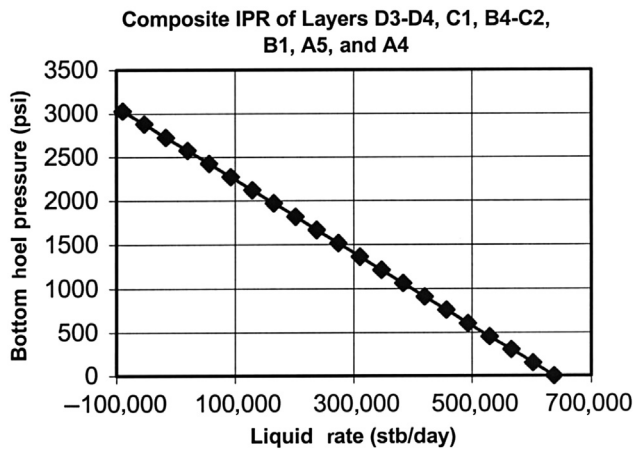
are shown in Fig. 3.20. It is seen from this figure that productivities of Layers A4, A5, and B1 are significantly lower than those of other layers. It is expected that wellbore cross-flow should occur if the bottom pressure is above the lowest reservoir pressure of 2254 psi. Layers B4, C1, and C2 should be the major thief zones because of their high injectivities (assuming to be equal to their productivities) and relatively low pressures.

The composite IPR of these layers is shown in Fig. 3.21 where the net production rate from the well is plotted against bottom-hole pressure. It is seen from this figure that net oil production will not be available unless the bottom-hole pressure is reduced to below 2658 psi.

Fig. 3.20 suggests that the eight oil layers be produced separately in three layer groups:

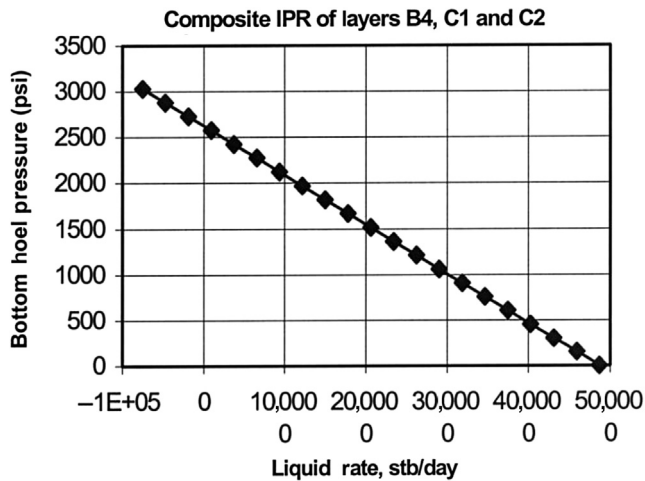
- Group 1: Layers D3 and D4
- Group 2: Layers B4, C1, and C2
- Group 3: Layers B1, A4, and A5

The composite IPR for Group 1 (D3 and D4) is the same as shown in Fig. 3.20 because these two layers were the commingle-tested. Composite IPRs of Group 2 and Group 3 are plotted in Figs. 3.22 and 3.23. Table 3.2 compares production rates read from Figs. 3.21–3.23 at some pressures. This comparison indicates that significant production from Group 1 can be achieved at bottom-hole pressures higher than 2335 psi, while Group 2 and Group 3 are shut-in. A significant production from Group 1 and Group 2 can be achieved at bottom-hole pressures higher than 2625 psi while Group 3 is shut-in. The grouped-layer production will remain beneficial until bottom-hole pressure is dropped to below 2335 psi where Group 3 can be open for production.



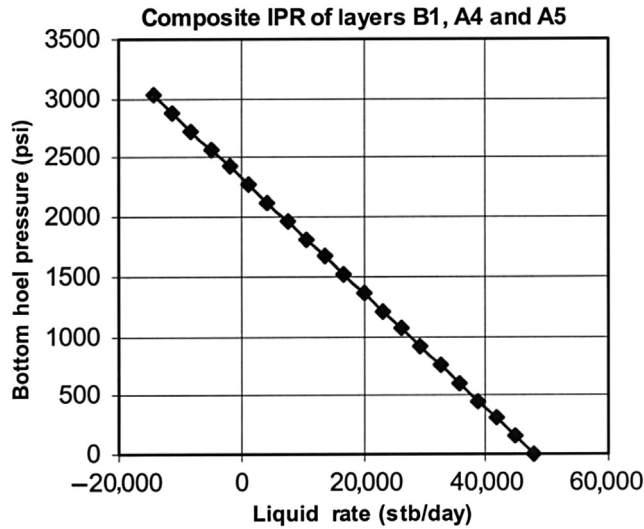
**FIGURE 3.21**

Composite IPR curve for all the layers open to flow in Example Problem 3.7.



**FIGURE 3.22**

Composite IPR curve for Group 2 (Layers B4, C1, and C2) in Example Problem 3.7.



**FIGURE 3.23**

Composite IPR curve for Group 3 (Layers B1, A4, and A5) in Example Problem 3.7.

Table 3.2 Comparison of Commingled and Layer-Grouped Productions					
		Production rate (stb/day)			
		Grouped Layers			
Bottom-hole pressure (psi)	All layers commingled	Group 1	Group 2	Group 3	Total
2658	0	12,663	Shut-in	Shut-in	12,663
2625	7866	13,787	0	Shut-in	13,787
2335	77,556	23,660	53,896	0	77,556
2000	158,056	35,063	116,090	6903	158,056

### 3.8 FUTURE IPR

Reservoir deliverability declines with time. During transient flow period in single-phase reservoirs, this decline is because the radius of the pressure funnel, over which the pressure drawdown ( $p_i - p_{wf}$ ) acts, increases with time, i.e., the overall pressure gradient in the reservoir drops with time. In two-phase reservoirs, as reservoir pressure depletes, reservoir deliverability drops due to reduced relative permeability to oil and increased oil viscosity. Future IPR can be predicted by both Vogel's method and Fetkovich's method.

### 3.8.1 VOGEL'S METHOD

Let  $J_p^*$  and  $J_f^*$  be the present productivity index and future productivity index, respectively. The following relation can be derived:

$$\frac{J_f^*}{J_p^*} = \frac{\left(\frac{k_{ro}}{B_o\mu_o}\right)_f}{\left(\frac{k_{ro}}{B_o\mu_o}\right)_p} \quad (3.83)$$

or

$$J_f^* = J_p^* \frac{\left(\frac{k_{ro}}{B_o\mu_o}\right)_f}{\left(\frac{k_{ro}}{B_o\mu_o}\right)_p} \quad (3.84)$$

Thus,

$$q = \frac{J_f^* \bar{p}_f}{1.8} \left[ 1 - 0.2 \frac{p_{wf}}{\bar{p}_f} - 0.8 \left( \frac{p_{wf}}{\bar{p}_f} \right)^2 \right], \quad (3.85)$$

where  $\bar{p}_f$  is the reservoir pressure in a future time.

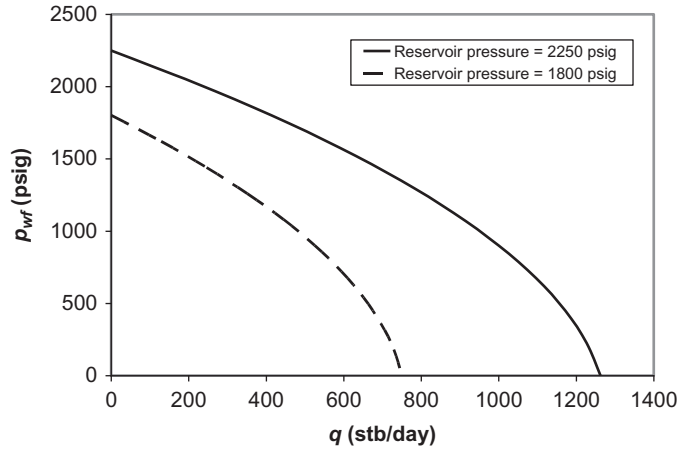
**Example Problem 3.8** Determine the IPR for a well at the time when the average reservoir pressure will be 1800 psig. The following data are obtained from laboratory tests of well fluid samples:

Reservoir properties	Present	Future
Average pressure (psig)	2250	1800
Productivity index $J^*$ (stb/day-psi)	1.01	
Oil viscosity (cp)	3.11	3.59
Oil formation volume factor (rb/stb)	1.173	1.150
Relative permeability to oil	0.815	0.685

**Solution**

$$\begin{aligned} J_f^* &= J_p^* \frac{\left(\frac{k_{ro}}{B_o\mu_o}\right)_f}{\left(\frac{k_{ro}}{B_o\mu_o}\right)_p} \\ &= 1.01 \frac{\left(\frac{0.685}{3.59(1.150)}\right)}{\left(\frac{0.815}{3.11(1.173)}\right)} \\ &= 0.75 \text{ stb/day - psi} \end{aligned}$$





**FIGURE 3.24**

IPR curves for Example Problem 3.8.

Vogel’s equation for future IPR:

$$q = \frac{J_f^* \bar{p}_f}{1.8} \left[ 1 - 0.2 \frac{p_{wf}}{\bar{p}_f} - 0.8 \left( \frac{p_{wf}}{\bar{p}_f} \right)^2 \right]$$

$$= \frac{(0.75)(1,800)}{1.8} \left[ 1 - 0.2 \frac{p_{wf}}{1,800} - 0.8 \left( \frac{p_{wf}}{1,800} \right)^2 \right]$$

Calculated data points are as follows:

Present and future IPR curves are plotted in Fig. 3.24.

Reservoir pressure = 2250 psig		Reservoir pressure = 1800 psig	
$p_{wf}$ (psig)	$q$ (stb/day)	$p_{wf}$ (psig)	$q$ (stb/day)
2250	0	1800	0
2025	217	1620	129
1800	414	1440	246
1575	591	1260	351
1350	747	1080	444
1125	884	900	525
900	1000	720	594
675	1096	540	651
450	1172	360	696
225	1227	180	729
0	1263	0	750

### 3.8.2 FETKOVICH'S METHOD

The integral form of reservoir inflow relationship for multiphase flow is expressed as

$$q = \frac{0.007082kh}{\ln\left(\frac{r_e}{r_w}\right)} \int_{p_{wf}}^{p_e} f(p) dp, \quad (3.86)$$

where  $f(p)$  is a pressure function. The simplest two-phase flow case is that of constant pressure  $p_e$  at the outer boundary ( $r_e$ ), with  $p_e$  less than the bubble-point pressure so that there is two-phase flow throughout the reservoir.

Under these circumstances,  $f(p)$  takes on the value  $\frac{k_{ro}}{\mu_o B_o}$ , where  $k_{ro}$  is the relative permeability to oil at the saturation conditions in the formation corresponding to the pressure  $p$ . In this method, Fetkovich makes the key assumption that to a good degree of approximation, the expression  $\frac{k_{ro}}{\mu_o B_o}$  is a linear function of  $p$ , and is a straight line passing through the origin. If  $p_i$  is the initial formation pressure (i.e.,  $\sim p_e$ ), then the straight-line assumption is

$$\frac{k_{ro}}{\mu_o B_o} = \left(\frac{k_{ro}}{\mu_o B_o}\right)_i \frac{p}{p_i}. \quad (3.87)$$

Substituting Eq. (3.87) into Eq. (3.86) and integrating the latter gives

$$q_o = \frac{0.007082kh}{\ln\left(\frac{r_e}{r_w}\right)} \left(\frac{k_{ro}}{\mu_o B_o}\right)_i \frac{1}{2p_i} (p_i^2 - p_{wf}^2) \quad (3.88)$$

or

$$q_o = J'_i (p_i^2 - p_{wf}^2), \quad (3.89)$$

where

$$J'_i = \frac{0.007082kh}{\ln\left(\frac{r_e}{r_w}\right)} \left(\frac{k_{ro}}{\mu_o B_o}\right)_i \frac{1}{2p_i}. \quad (3.90)$$

The derivative of Eq. (3.89) with respect to the flowing bottom-hole pressure is

$$\frac{dq_o}{dp_{wf}} = -2J'_i p_{wf}. \quad (3.91)$$

This implies that the rate of change of  $q$  with respect to  $p_{wf}$  is lower at the lower values of the inflow pressure.

Next, we can modify Eq. (3.91) to take into account that in practice  $p_e$  is not constant but decreases as cumulative production increases. The assumption made is that  $J'_i$  will decrease in proportion to the decrease in average reservoir (drainage area) pressure. Thus, when the static pressure is  $p_e$  ( $< p_i$ ), the IPR equation is

$$q_o = J'_i \frac{p_e}{p_i} (p_e^2 - p_{wf}^2) \quad (3.92)$$

or, alternatively,

$$q_o = J'(p_e^2 - p_{wf}^2), \tag{3.93}$$

where

$$J' = J'_i \frac{p_e}{p_i}. \tag{3.94}$$

These equations may be used to extrapolate into the future.

**Example Problem 3.9** Using Fetkovich’s method plot the IPR curves for a well in which  $p_i$  is 2000 psia and  $J'_i = 5 \times 10^{-4}$  stb/day – psia<sup>2</sup>. Predict the IPRs of the well at well shut-in static pressures of 1500 and 1000 psia.

**Solution**

The value of  $J'_o$  at 1500 psia is

$$\begin{aligned} J'_o &= 5 \times 10^{-4} \left( \frac{1,500}{2,000} \right) \\ &= 3.75 \times 10^{-4} \text{ stb/day (psia)}^2, \end{aligned}$$

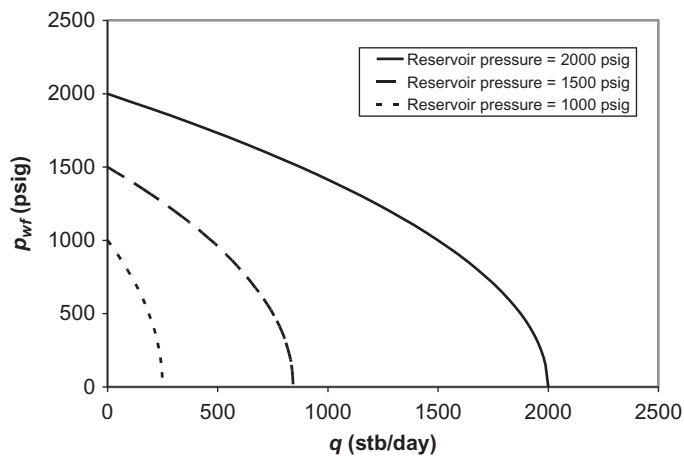
and the value of  $J'_o$  at 1000 psia is

$$J'_o = 5 \times 10^{-4} \left( \frac{1,000}{2,000} \right) = 2.5 \times 10^{-4} \text{ stb/day(psia)}^2.$$

Using the above values for  $J'_o$  and the accompanying  $p_e$ , the following data points are calculated:

$p_e = 2000$ psig		$p_e = 1500$ psig		$p_e = 1000$ psig	
$p_{wf}$ (psig)	$q$ (stb/day)	$p_{wf}$ (psig)	$q$ (stb/day)	$p_{wf}$ (psig)	$q$ (stb/day)
2000	0	1500	0	1000	0
1800	380	1350	160	900	48
1600	720	1200	304	800	90
1400	1020	1050	430	700	128
1200	1280	900	540	600	160
1000	1500	750	633	500	188
800	1680	600	709	400	210
600	1820	450	768	300	228
400	1920	300	810	200	240
200	1980	150	835	100	248
0	2000	0	844	0	250

IPR curves are plotted in Fig. 3.25.



**FIGURE 3.25**

IPR curves for Example Problem 3.9.

### 3.9 SUMMARY

This chapter presented and illustrated various mathematical models for estimating deliverability of oil and gas reservoirs. Production engineers should make selections of the models based on the best estimate of his/her reservoir conditions, that is, flow regime, pressure level, and well completion method. The selected models should be validated with actual well production rate and bottom-hole pressure. At least one test point is required to validate a straight-line (single-liquid flow) IPR model. At least two test points are required to validate a curve (single-gas flow or two-phase flow) IPR model.

### REFERENCES

- Argawal, R.G., Carter, R.D., Pollock, C.B., 1979. Evaluation and prediction of performance of low-permeability gas wells stimulated by massive hydraulic fracturing, *JPT* (March 1979), *Trans. AIME* 267, 362–372.
- Bandakhlia, H., Aziz, K. Inflow performance relationship for solution-gas drive horizontal wells. Presented at the 64th SPE Annual Technical Conference and Exhibition held 8–11 October 1989, in San Antonio, Texas. Paper SPE 19823.
- Chang, M. Analysis of inflow performance simulation of solution-gas drive for horizontal/slant vertical wells. Presented at the SPE Rocky Mountain Regional Meeting held 18–21 May 1992, in Casper, Wyoming. Paper SPE 24352.
- Cinco-Ley, H., Samaniego, F., September 1981. Transient pressure analysis for fractured wells. *J. Petrol. Technol.*

- Dietz, D.N., 1965 August. Determination of average reservoir pressure from build-up surveys. *J. Pet. Tech.*
- Dake, L.P., 1978. *Fundamentals of Reservoir Engineering*. Elsevier, New York, NY.
- Earlougher, R.C., 1977. *Advances in Well Test Analysis*. Society of Petroleum Engineers, Dallas.
- El-Banbi, A.H., Wattenbarger, R.A. Analysis of commingled tight gas reservoirs. Presented at the SPE Annual Technical Conference and Exhibition held 6–9 October 1996, in Denver, Colorado. Paper SPE 36736.
- El-Banbi, A.H., Wattenbarger, R.A. Analysis of commingled gas reservoirs with variable bottom-hole flowing pressure and non-Darcy flow. Presented at the SPE Annual Technical Conference and Exhibition held 5–8 October 1997, in San Antonio, Texas. Paper SPE 38866.
- Fetkovich, M.J. The isochronal testing of oil wells. Presented at the SPE Annual Technical Conference and Exhibition held 30 September–3 October 1973, Las Vegas, Nevada. Paper SPE 4529.
- Furui, K., Zhu, D., Hill, A.D., 2003. A rigorous formation damage skin factor and reservoir inflow model for a horizontal well. *SPERE* 151.
- Guo, B., Schechter, D.S., 1999. A simple and rigorous IPR equation for vertical and horizontal wells intersecting long fractures. *J. Can. Petrol. Technol.* 207–218.
- Guo, B., Sun, K., Ghalambor, A., 2008. *Well Productivity Handbook*. Gulf Publishing Company, Houston, pp. 321–328.
- Guo, B., Yu, X. A Simple and Accurate Mathematical Model for Predicting Productivity of Multifractured Horizontal Wells, Paper SPE 114452 Presented at the CIPC/SPE Gas Technology Symposium 2008 Joint Conference held 16–19 June 2008 in Calgary, Canada.
- Joshi, S.D., 1988. Augmentation of well productivity with slant and horizontal wells. *J. Petrol. Technol.* 729–739.
- Larsen, L. Productivity Computations for Multilateral, Branched, and Other Generalized and Extended Well Concepts, Paper SPE 36754 Presented at the SPE Annual Technical Conference & Exhibition held 6–9 October 1996 in Denver, Colorado.
- Li, H., Jia, Z., Wei, Z. A New Method to Predict Performance of Fractured Horizontal Wells, Paper SPE 37051 Presented at the SPE International Conference on Horizontal Well Technology held 18–20 November 1996 in Calgary, Canada.
- Raghavan, R., Joshi, S.D., 1993. Productivity of multiple drainholes or fractured horizontal wells. *SPE Formation Eval.* 11–16.
- Retnanto, A., Economides, M.J., 1996. Performance of multilateral horizontal well laterals in low-permeability reservoirs. *SPE Reservoir Eng* 67–77.
- Retnanto, A., Economides, M. Inflow performance relationships of horizontal and multibranch wells in a solution gas drive reservoir. Presented at the 1998 SPE Annual Technical Conference and Exhibition held 27–30 September 1998, in New Orleans, Louisiana. Paper SPE 49054.
- Standing, M.B., 1971. Concerning the calculation of inflow performance of wells producing from solution gas drive reservoirs. *J. Petrol. Technol.* 1141–1142.
- Valko, P., Oligney, R.E., Economides, M.J., 1997. High permeability fracturing of gas wells. *Gas TIPS* 3, 31–34-E.
- Vogel, J.V., 1968. Inflow performance relationships for solution gas drive wells. *J. Petrol. Technol.* 83–92.

---

**PROBLEMS**

- 3.1.** Construct IPR of a vertical well in an oil reservoir. Consider (1) transient flow at 1 month, (2) steady-state flow, and (3) pseudo-steady-state flow. The following data are given:

Porosity	$\phi = 0.25$
Effective horizontal permeability	$k = 10$ md
Pay zone thickness	$h = 50$ ft
Reservoir pressure	$\bar{p}_e$ or $p = 5000$ psia
Bubble-point pressure	$p_b = 100$ psia
Fluid formation volume factor	$B_o = 1.2$
Fluid viscosity	$\mu_o = 1.5$ cp
Total compressibility	$c_t = 0.0000125$ psi <sup>-1</sup>
Drainage area	$A = 640$ acres ( $r_e = 2980$ ft)
Wellbore radius	$r_w = 0.328$ ft
Skin factor	$S = 5$

- 3.2.** Construct IPR of a vertical well in a saturated oil reservoir using Vogel's equation. The following data are given:

Porosity	$\phi = 0.2$
Effective horizontal permeability	$k = 80$ md
Pay zone thickness	$h = 55$ ft
Reservoir pressure	$\bar{p} = 4,500$ psia
Bubble-point pressure	$p_b = 4500$ psia
Fluid formation volume factor	$B_o = 1.1$
Fluid viscosity	$\mu_o = 1.8$ cp
Total compressibility	$c_t = 0.000013$ psi <sup>-1</sup>
Drainage area	$A = 640$ acres ( $r_e = 2980$ ft)
Wellbore radius	$r_w = 0.328$ ft
Skin factor	$S = 2$

- 3.3.** Construct IPR of a vertical well in an unsaturated oil reservoir using generalized Vogel's equation. The following data are given:

Porosity	$\phi = 0.25$
Effective horizontal permeability	$k = 100$ md
Pay zone thickness	$h = 55$ ft
Reservoir pressure	$\bar{p} = 5,000$ psia
Bubble-point pressure	$p_b = 3000$ psia
Fluid formation volume factor	$B_o = 1.2$
Fluid viscosity	$\mu_o = 1.8$ cp
Total compressibility	$c_t = 0.000013$ psi <sup>-1</sup>
Drainage area	$A = 640$ acres ( $r_e = 2980$ ft)
Wellbore radius	$r_w = 0.328$ ft
Skin factor	$S = 5.5$

- 3.4. Construct IPR of two wells in an unsaturated oil reservoir using generalized Vogel’s equation. The following data are given:

Reservoir pressure	$\bar{p} = 5,500$ psia
Bubble-point pressure	$p_b = 3500$ psia
Tested flowing bottom-hole pressure in Well A	$p_{wf1} = 4000$ psia
Tested production rate from Well A	$q_1 = 400$ stb/day
Tested flowing bottom-hole pressure in Well B	$p_{wf1} = 2000$ psia
Tested production rate from Well B	$q_1 = 1000$ stb/day

- 3.5. Construct IPR of a well in a saturated oil reservoir using both Vogel’s equation and Fetkovich’s equation. The following data are given:

Reservoir pressure	$\bar{p} = 3,500$ psia
Tested flowing bottom-hole pressure	$p_{wf1} = 2500$ psia
Tested production rate at $p_{wf1}$	$q_1 = 600$ stb/day
Tested flowing bottom-hole pressure	$p_{wf2} = 1500$ psia
Tested production rate at $p_{wf2}$	$q_2 = 900$ stb/day

- 3.6. Determine the IPR for a well at the time when the average reservoir pressure will be 1500 psig. The following data are obtained from laboratory tests of well fluid samples:

Reservoir properties	Present	Future
Average pressure (psig)	2200	1500
Productivity index $J^*$ (stb/day-psi)	1.25	
Oil viscosity (cp)	3.55	3.85
Oil formation volume factor (rb/stb)	1.20	1.15
Relative permeability to oil	0.82	0.65

- 3.7. Using Fetkovich’s method, plot the IPR curve for a well in which  $p_i$  is 3000 psia and  $J'_o = 4 \times 10^{-4}$  stb/day- $\text{psia}^2$ . Predict the IPRs of the well at well shut-in static pressures of 2500 psia, 2000 psia, 1500 psia, and 1000 psia.

## WELLBORE FLOW PERFORMANCE

## 4

## 4.1 INTRODUCTION

Chapter 3, Reservoir Deliverability described reservoir deliverability. However, the achievable oil production rate from a well is determined by wellhead pressure and the flow performance of production string; that is, tubing, casing, or both. The flow performance of production string depends on geometries of the production string and properties of fluids being produced. The fluids in oil wells include oil, water, gas, and sand. Wellbore performance analysis involves establishing a relationship between tubular size, wellhead and bottom-hole pressure, fluid properties, and fluid production rate. Understanding wellbore flow performance is vitally important to production engineers for designing oil well equipment and optimizing well production conditions.

Oil can be produced through tubing, casing, or both in an oil well, depending on which flow path has better performance. Producing oil through tubing is a better option in most cases to take the advantage of gas-lift effect. The traditional term *tubing performance relationship* (TPR) is used in this book (other terms such as *vertical lift performance* have been used in the literature). However, the mathematical models are also valid for casing flow and casing-tubing annular flow as long as hydraulic diameter is used. This chapter focuses on determination of TPR and pressure traverse along the well string. Both single-phase and multiphase fluids are considered. Calculation examples are illustrated with hand calculations and computer spreadsheets that are provided with this book.

## 4.2 SINGLE-PHASE LIQUID FLOW

Single-phase liquid flow exists in an oil well only when the wellhead pressure is above the bubble-point pressure of the oil, which is usually not a reality. However, it is convenient to start from single-phase liquid for establishing the concept of fluid flow in oil wells where multiphase flow usually dominates.

Consider a fluid flowing from point 1 to point 2 in a tubing string of length  $L$  and height  $\Delta z$  (Fig. 4.1). The first law of thermodynamics yields the following equation for pressure drop:

$$\Delta P = P_1 - P_2 = \frac{g}{g_c} \rho \Delta z + \frac{\rho}{2g_c} \Delta u^2 + \frac{2f_F \rho u^2 L}{g_c D} \quad (4.1)$$

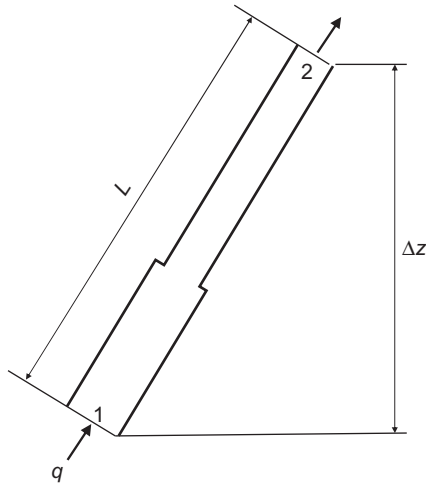
where

$\Delta P$  = pressure drop, lb<sub>f</sub>/ft<sup>2</sup>

$P_1$  = pressure at point 1, lb<sub>f</sub>/ft<sup>2</sup>

$P_2$  = pressure at point 2, lb<sub>f</sub>/ft<sup>2</sup>






---

**FIGURE 4.1**

Flow along a tubing string.

- $g$  = gravitational acceleration,  $32.17 \text{ ft/s}^2$   
 $g_c$  = unit conversion factor,  $32.17 \text{ lb}_m\text{-ft/lb}_f\text{-s}^2$   
 $\rho$  = fluid density,  $\text{lb}_m/\text{ft}^3$   
 $\Delta z$  = elevation increase, ft  
 $u$  = fluid velocity, ft/s  
 $f_F$  = Fanning friction factor  
 $L$  = tubing length, ft  
 $D$  = tubing inner diameter, ft

The first, second, and third terms in the right-hand side of the equation represent pressure drops due to changes in elevation, kinetic energy, and friction, respectively.

The Fanning friction factor ( $f_F$ ) can be evaluated based on Reynolds number and relative roughness. Reynolds number is defined as the ratio of inertial force to viscous force. The Reynolds number is expressed in consistent units as

$$N_{\text{Re}} = \frac{D u \rho}{\mu} \quad (4.2)$$

or in U.S. field units as

$$N_{\text{Re}} = \frac{1.48 q \rho}{d \mu} \quad (4.3)$$

where

- $N_{\text{Re}}$  = Reynolds number  
 $q$  = fluid flow rate, bbl/day  
 $\rho$  = fluid density,  $\text{lb}_m/\text{ft}^3$   
 $d$  = tubing inner diameter, in.  
 $\mu$  = fluid viscosity, cp

For laminar flow where  $N_{Re} < 2000$ , the  $f_F$  is inversely proportional to the Reynolds number, or

$$f_F = \frac{16}{N_{Re}} \quad (4.4)$$

For turbulent flow where  $N_{Re} > 2100$ , the  $f_F$  can be estimated using empirical correlations. Among numerous correlations developed by different investigators, [Chen's \(1979\)](#) correlation has an explicit form and gives similar accuracy to the Colebrook–White equation ([Gregory and Fogarasi, 1985](#)) that was used for generating the friction factor chart used in the petroleum industry. Chen's correlation takes the following form:

$$\frac{1}{\sqrt{f_F}} = -4 \times \log \left\{ \frac{\varepsilon}{3.7065} - \frac{5.0452}{N_{Re}} \log \left[ \frac{\varepsilon^{1.1098}}{2.8257} + \left( \frac{7.149}{N_{Re}} \right)^{0.8981} \right] \right\} \quad (4.5)$$

where the relative roughness is defined as  $\varepsilon = \frac{\delta}{d}$ , and  $\delta$  is the absolute roughness of pipe wall.

The  $f_F$  can also be obtained based on Darcy–Wiesbach friction factor shown in [Fig. 4.2](#). The Darcy–Wiesbach friction factor is also referred to as the *Moody friction factor* ( $f_M$ ) in some literatures. The relation between the Moody and the  $f_F$  is expressed as

$$f_F = \frac{f_M}{4}. \quad (4.6)$$

**Example Problem 4.1** Suppose that 1000 bbl/day of 40 °API, 1.2 cp oil is being produced through  $2\frac{7}{8}$ -in., 8.6-lb<sub>m</sub>/ft tubing in a well that is 15° from vertical. If the tubing wall relative roughness is 0.001, calculate the pressure drop over 1000 ft of tubing.

**Solution** Oil-specific gravity:

$$\begin{aligned} \gamma_0 &= \frac{141.5}{^\circ\text{API} + 131.5} \\ &= \frac{141.5}{40 + 131.5} \\ &= 0.825 \end{aligned}$$

Oil density:

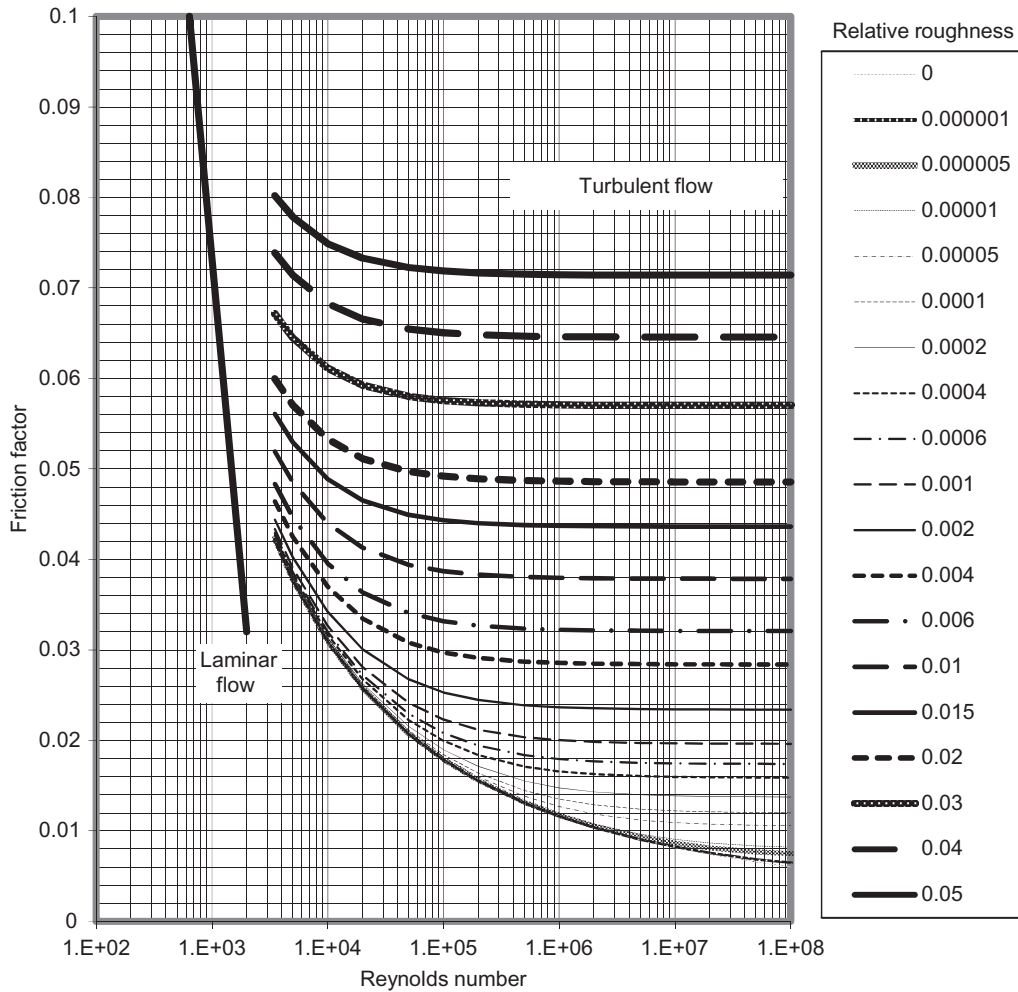
$$\begin{aligned} \rho &= 62.4\gamma_0 \\ &= (62.4)(0.825) \\ &= 51.57 \text{ lb}_m/\text{ft}^3 \end{aligned}$$

Elevation increase:

$$\begin{aligned} \Delta Z &= \cos(\alpha)L \\ &= \cos(15)(1,000) \\ &= 966 \text{ ft} \end{aligned}$$

The  $2\frac{7}{8}$ -in., 8.6-lb<sub>m</sub>/ft tubing has an inner diameter of 2.259 in. Therefore,

$$\begin{aligned} D &= \frac{2.259}{12} \\ &= 0.188 \text{ ft.} \end{aligned}$$



**FIGURE 4.2**  
Darcy–Wiesbach friction factor diagram.

*After Moody, 1944.*

Fluid velocity can be calculated accordingly:

$$\begin{aligned}
 u &= \frac{4q}{\pi D^2} \\
 &= \frac{4(5.615)(1,000)}{\pi(0.188)^2(86,400)} \\
 &= 2.34 \text{ ft/s.}
 \end{aligned}$$

Reynolds number:

$$\begin{aligned} N_{\text{Re}} &= \frac{1.48qp}{d\mu} \\ &= \frac{1.48(1000)(51.57)}{(2.259)(1.2)} \\ &= 28,115 > 2100, \text{ turbulent flow} \end{aligned}$$

Chen's correlation gives

$$\begin{aligned} \frac{1}{\sqrt{f_F}} &= -4 \log \left\{ \frac{\varepsilon}{3.7065} - \frac{5.0452}{N_{\text{Re}}} \log \left[ \frac{\varepsilon^{1.1098}}{2.8257} + \left( \frac{7.149}{N_{\text{Re}}} \right)^{0.8981} \right] \right\} \\ &= 12.3255 \\ f_F &= 0.006583 \end{aligned}$$

If Fig. 4.2 is used, the chart gives a  $f_M$  of 0.0265. Thus, the  $f_F$  is estimated as

$$\begin{aligned} f_F &= \frac{0.0265}{4} \\ &= 0.006625 \end{aligned}$$

Finally, the pressure drop is calculated:

$$\begin{aligned} \Delta P &= \frac{g}{g_c} \rho \Delta z + \frac{\rho}{2g_c} \Delta u^2 = \frac{2f_F \rho u^2 L}{g_c D} \\ &= \frac{32.17}{32.17} (51.57)(966) = \frac{51.57}{2(32.17)} (0)^2 = \frac{2(0.006625)(51.57)(2.34)^2(1000)}{(32.17)(0.188)} \\ &= 50,435 \text{ Ib}_f/\text{ft}^2 \\ &= 350 \text{ psi} \end{aligned}$$

### 4.3 SINGLE-PHASE GAS FLOW

The first law of thermodynamics (conservation of energy) governs gas flow in tubing. The effect of kinetic energy change is negligible because the variation in tubing diameter is insignificant in most gas wells. With no shaft work device installed along the tubing string, the first law of thermodynamics yields the following mechanical balance equation:

$$\frac{dP}{\rho} + \frac{g}{g_c} dZ + \frac{f_M v^2 dL}{2g_c D_i} = 0 \quad (4.7)$$

Because  $dZ = \cos \theta dL$ ,  $\rho = \frac{29\gamma_g P}{ZRT}$ , and  $v = \frac{4q_{sc} z P_{sc} T}{\pi D_i^2 T_{sc} P}$ , Eq. (4.7) can be rewritten as

$$\frac{zRT}{29\gamma_g} \frac{dP}{P} + \left\{ \frac{g}{g_c} \cos \theta + \frac{8f_M Q_{sc}^2 P_{sc}^2}{\pi^2 g_c D_i^5 T_{sc}^2} \left[ \frac{zT}{P} \right]^2 \right\} dL = 0, \quad (4.8)$$

which is an ordinary differential equation governing gas flow in tubing. Although the temperature  $T$  can be approximately expressed as a linear function of length  $L$  through geothermal gradient, the compressibility factor  $z$  is a function of pressure  $P$  and temperature  $T$ . This makes it difficult to solve the equation analytically. Fortunately, the pressure  $P$  at length  $L$  is not a strong function of temperature and compressibility factor. Approximate solutions to Eq. (4.8) have been sought and used in the natural gas industry.

### 4.3.1 AVERAGE TEMPERATURE AND COMPRESSIBILITY FACTOR METHOD

If single average values of temperature and compressibility factor over the entire tubing length can be assumed, Eq. (4.8) becomes

$$\frac{\bar{z}R\bar{T}}{29\gamma_g} \frac{dP}{P} + \left\{ \frac{g}{g_c} \cos \theta + \frac{8f_M Q_{sc}^2 P_{sc}^2 \bar{z}^2 \bar{T}^2}{\pi^2 g_{ci}^5 T_{sc}^2 P^2} \right\} dL = 0. \quad (4.9)$$

By separation of variables, Eq. (4.9) can be integrated over the full length of tubing to yield

$$P_{wf}^2 = \text{Exp}(s)P_{hf}^2 + \frac{8f_M[\text{Exp}(s) - 1]Q_{sc}^2 P_{sc}^2 \bar{z}^2 \bar{T}^2}{\pi^2 g_{ci}^5 D_i^5 T_{sc}^2 \cos \theta}, \quad (4.10)$$

where

$$s = \frac{58\gamma_g g L \cos \theta}{g_c R \bar{z} \bar{T}}. \quad (4.11)$$

Eqs. (4.10) and (4.11) take the following forms when U.S. field units ( $q_{sc}$  in Mscf/d), are used (Katz et al., 1959):

$$P_{wf}^2 = \text{Exp}(s)P_{hf}^2 + \frac{6.67 \times 10^{-4}[\text{Exp}(s) - 1]f_M q_{sc}^2 \bar{z}^2 \bar{T}^2}{d_i^5 \cos \theta} \quad (4.12)$$

and

$$s = \frac{0.0375\gamma_g L \cos \theta}{\bar{z} \bar{T}} \quad (4.13)$$

The Darcy–Wiesbach (Moody) friction factor  $f_M$  can be found in the conventional manner for a given tubing diameter, wall roughness, and Reynolds number. However, if one assumes fully turbulent flow, which is the case for most gas wells, then a simple empirical relation may be used for typical tubing strings (Katz and Lee, 1990):

$$f_M = \frac{0.01750}{d_i^{0.224}} \quad \text{for } d_i \leq 4.277 \text{ in.} \quad (4.14)$$

$$f_M = \frac{0.01603}{d_i^{0.164}} \quad \text{for } d_i > 4.277 \text{ in.} \quad (4.15)$$

Guo and Ghalambor (2002) used the following Nikuradse friction factor correlation for fully turbulent flow in rough pipes:

$$f_M = \left[ \frac{1}{1.74 - 2 \log \left( \frac{2\epsilon}{d_i} \right)} \right]^2 \tag{4.16}$$

Because the average compressibility factor is a function of pressure itself, a numerical technique such as Newton–Raphson iteration is required to solve Eq. (4.12) for bottom-hole pressure. This computation can be performed automatically with the spreadsheet program *Average TZ.xls*. Users need to input parameter values in the Input data section and run Macro Solution to get results.

**Example Problem 4.2** Suppose that a vertical well produces 2 MMscf/d of 0.71 gas-specific gravity gas through a 2<sup>7</sup>/<sub>8</sub> in. tubing set to the top of a gas reservoir at a depth of 10,000 ft. At tubing head, the pressure is 800 psia and the temperature is 150°F; the bottom-hole temperature is 200°F. The relative roughness of tubing is about 0.0006. Calculate the pressure profile along the tubing length and plot the results.

**Solution** Example Problem 4.2 is solved with the spreadsheet program *AverageTZ.xls*. Table 4.1 shows the appearance of the spreadsheet for the Input data and Result sections. The calculated pressure profile is plotted in Fig. 4.3.

### 4.3.2 CULLENDER AND SMITH METHOD

Eq. (4.8) can be solved for bottom-hole pressure using a fast numerical algorithm originally developed by Cullender and Smith (Katz et al., 1959). Eq. (4.8) can be rearranged as

$$\frac{\frac{P}{zT} dp}{\frac{g}{g_c} \cos \theta \left( \frac{P}{zT} \right)^2 + \frac{8f_M Q_{sc}^2 P_{sc}^2}{\pi^2 g_c D_i^5 T_{sc}^2}} = - \frac{29\gamma_g}{R} dL \tag{4.17}$$

that takes an integration form of

$$\int_{P_{hf}}^{P_{wf}} \left[ \frac{\frac{P}{zT}}{\frac{g}{g_c} \cos \theta \left( \frac{P}{zT} \right)^2 + \frac{8f_M Q_{sc}^2 P_{sc}^2}{\pi^2 g_c D_i^5 T_{sc}^2}} \right] dp = \frac{29\gamma_g L}{R}. \tag{4.18}$$

In U.S. field units ( $q_{msc}$  in MMscf/d), Eq. (4.18) has the following form:

$$\int_{P_{hf}}^{P_{wf}} \left[ \frac{\frac{P}{zT}}{0.001 \cos \theta \left( \frac{P}{zT} \right)^2 + 0.6666 \frac{f_M q_{msc}^2}{d_i^5}} \right] dp = 18.75 \gamma_g L \tag{4.19}$$

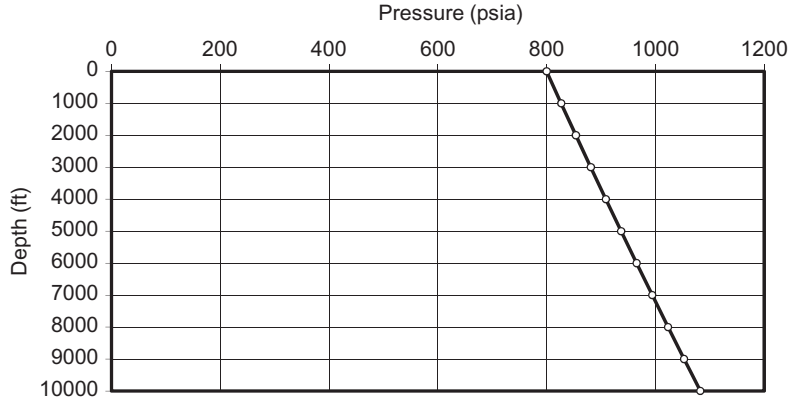
<b>Table 4.1 Spreadsheet AverageTZ.xls: The Input Data and Result Sections</b>			
<i>AverageTZ.xls</i>			
<i>Description:</i> This spreadsheet calculates tubing pressure traverse for gas wells.			
<i>Instructions:</i> (1) Input your data in the Input data section; (2) Click “Solution” button to get results; and (3) View results in table and in graph sheet “Profile”.			
<b>Input Data</b>			
$\gamma_g =$	0.71		
$d =$	2.259 in.		
$\varepsilon/d =$	0.0006		
$L =$	10,000 ft		
$\theta =$	0°		
$p_{hf} =$	800 psia		
$T_{hf} =$	150°F		
$T_{wf} =$	200°F		
$q_{sc} =$	2000 Mscf/d		
<b>Solution</b>			
$f_M =$	0.017396984		
Depth (ft)	$T$ (°R)	$p$ (psia)	$Z_{av}$
0	610	800	0.9028
1000	615	827	0.9028
2000	620	854	0.9027
3000	625	881	0.9027
4000	630	909	0.9026
5000	635	937	0.9026
6000	640	965	0.9026
7000	645	994	0.9026
8000	650	1023	0.9027
9000	655	1053	0.9027
10,000	660	1082	0.9028

If the integrant is denoted with symbol  $I$ , that is,

$$I = \frac{\frac{p}{zT}}{0.001 \cos \theta \left(\frac{p}{zT}\right)^2 + 0.6666 \frac{f_M q_{sc}^2}{d_i^5}}, \tag{4.20}$$

Eq. (4.19) becomes

$$\int_{p_{hf}}^{p_{wf}} I dp = 1875 \gamma_g L. \tag{4.21}$$



**FIGURE 4.3**  
 Calculated tubing pressure profile for the Example Problem 4.2.

In the form of numerical integration, Eq. (4.21) can be expressed as

$$\frac{(p_{mf} - p_{hf})(I_{mf} - I_{hf})}{2} + \frac{(p_{wf} - p_{mf})(I_{wf} - I_{mf})}{2} = 18.75\gamma_g L, \tag{4.22}$$

where  $p_{mf}$  is the pressure at the mid-depth. The  $I_{hf}$ ,  $I_{mf}$ , and  $I_{wf}$  are integrant is evaluated at  $p_{hf}$ ,  $p_{mf}$ , and  $p_{wf}$ , respectively. Assuming the first and second terms in the right-hand side of Eq. (4.22) each represents half of the integration, that is,

$$\frac{(p_{mf} - p_{hf})(I_{mf} - I_{hf})}{2} = \frac{18.75\gamma_g L}{2} \tag{4.23}$$

$$\frac{(p_{wf} - p_{mf})(I_{wf} - I_{mf})}{2} = \frac{18.75\gamma_g L}{2}, \tag{4.24}$$

the following expressions are obtained:

$$p_{mf} = p_{hf} + \frac{18.75\gamma_g L}{I_{mf} + I_{hf}} \tag{4.25}$$

$$p_{wf} = p_{mf} + \frac{18.75\gamma_g L}{I_{wf} + I_{mf}} \tag{4.26}$$

Because  $I_{mf}$  is a function of pressure  $p_{mf}$  itself, a numerical technique such as Newton–Raphson iteration is required to solve Eq. (4.25) for  $p_{mf}$ . Once  $p_{mf}$  is computed,  $p_{wf}$  can be solved numerically from Eq. (4.26). These computations can be performed automatically with the spreadsheet



<b>Table 4.2 Spreadsheet Cullender-Smith.xls: The Input Data and Result Sections</b>					
<i>Cullender-SmithBHP.xls</i>					
<i>Description:</i> This spreadsheet calculates bottom-hole pressure with the Cullender–Smith method.					
<i>Instructions:</i> (1) Input your data in the Input data section; and (2) Click Solution button to get results.					
<b>Input Data</b>					
$\gamma_g$	= 0.71				
$D$	= 2.259 in.				
$\varepsilon/d$	= 0.0006				
$L$	= 10,000 ft				
$\Theta$	= 0°				
$p_{hf}$	= 800 psia				
$T_{hf}$	= 150°F				
$T_{wf}$	= 200°F				
$q_{msc}$	= 2 MMscf/d				
<b>Solution</b>					
$f_M$	= 0.017397				
Depth (ft)	$T$ (°R)	$p$ (psia)	$Z$	$p/ZT$	$I$
0	610	800	0.9028	1.45263	501.137
5000	635	937	0.9032	1.63324	472.581
10,000	660	1082	0.9057	1.80971	445.349

program *Cullender-Smith.xls*. Users need to input parameter values in the *Input Data* section and run Macro Solution to get results.

**Example Problem 4.3** Solve the problem in Example Problem 4.2 with the Cullender and Smith Method.

**Solution** Example Problem 4.3 is solved with the spreadsheet program *Cullender-Smith.xls*. Table 4.2 shows the appearance of the spreadsheet for the Input data and Result sections. The pressures at depths of 5000 ft and 10,000 ft are 937 psia and 1082 psia, respectively. These results are exactly the same as that given by the Average Temperature and Compressibility Factor Method.

### 4.3.3 FLOW OF IMPURE GAS

The average temperature average  $z$ -factor method and the Cullender and Smith method were derived on the basis of pure gas flow. In reality, almost all gas wells produce certain amount of liquids (oil and water) and sometimes solid particles (sand and coal). The volume fractions of these liquids and solids are low but their effect on pressure can be significant due to their densities being much higher than the density of gas.

A gas-oil-water-sand four-phase flow model was proposed by Guo and Ghalambor (2005) to describe the flow impure gas. The model takes a closed (integrated) form, which makes it easy to use. The Guo–Ghalambor model can be expressed as follows:

$$\begin{aligned}
 & b(P - P_{top}) + \frac{1 - 2bM}{2} \ln \left| \frac{(P+M)^2 + N}{(P_{top}+M)^2 + N} \right| \\
 & - \frac{M + \frac{b}{c}N - bM^2}{\sqrt{N}} \\
 & \times \left[ \tan^{-1} \left( \frac{P+M}{\sqrt{N}} \right) - \tan^{-1} \left( \frac{P_{top}+M}{\sqrt{N}} \right) \right] \\
 & = aL(\cos \theta + d^2e)
 \end{aligned} \tag{4.27}$$

where the group parameters are defined as

$$a = \frac{0.0765\gamma_g q_g + 350\gamma_o q_o + 350\gamma_w q_w + 62.4\gamma_s q_s}{4.07T_{av}q_g}, \tag{4.28}$$

$$b = \frac{5.615q_o + 5.615q_w + q_s}{4.07T_{av}Q_g}, \tag{4.29}$$

$$c = 0.00678 \frac{T_{av}Q_g}{A}, \tag{4.30}$$

$$d = \frac{0.00166}{A} (5.615q_o + 5.615q_w + q_s), \tag{4.31}$$

$$e = \frac{f_M}{2gD_H}, \tag{4.32}$$

$$M = \frac{cde}{\cos \theta + d^2e}, \tag{4.33}$$

$$N = \frac{c^2e \cos \theta}{(\cos \theta + d^2e)^2}, \tag{4.34}$$

where

$A$  = cross-sectional area of conduit, in.<sup>2</sup>

$D_H$  = hydraulic diameter, ft

$f_M$  = Darcy–Wiesbach friction factor (Moody factor)

$g$  = gravitational acceleration, 32.17 ft/s<sup>2</sup>

$L$  = conduit length, ft

$P$  = pressure, lb<sub>f</sub>/ft<sup>2</sup>

$P_{top}$  = flowing pressure at section top, lb<sub>f</sub>/ft<sup>2</sup>

$q_g$  = gas production rate, scf/d

$q_o$  = oil production rate, bbl/d

$q_s$  = sand production rate, ft<sup>3</sup>/day

$q_w$  = water production rate, bbl/d

$T_{av}$  = average temperature, °R

$\gamma_g$  = specific gravity of gas, air = 1

$\gamma_o$  = specific gravity of produced oil, freshwater = 1

$\gamma_s$  = specific gravity of produced solid, fresh water = 1

$\gamma_w$  = specific gravity of produced water, fresh water = 1

The Darcy–Wiesbach friction factor ( $f_M$ ) can be obtained from diagram (Fig. 4.2) or based on  $f_F$  obtained from Eq. (4.16). The required relation is  $f_M = 4f_F$ . The Guo–Ghalambor can also be used for describing mist flow in oil wells (Guo et al., 2008).

Because iterations are required to solve Eq. (4.18) for pressure, a computer spreadsheet program *Guo-Ghalambor BHP.xls* has been developed.

**Example Problem 4.4** For the following data, estimate bottom-hole pressure with the Guo–Ghalambor method:

Total measured depth:	7000 ft
The average inclination angle:	20°
Tubing inner diameter:	1.995 in.
Gas production rate:	1 MMscfd
Gas-specific gravity:	0.7 air = 1
Oil production rate:	1000 stb/d
Oil-specific gravity:	0.85 H <sub>2</sub> O = 1
Water production rate:	300 bbl/d
Water-specific gravity:	1.05 H <sub>2</sub> O = 1
Solid production rate:	1 ft <sup>3</sup> /d
Solid-specific gravity:	2.65 H <sub>2</sub> O = 1
Tubing head temperature:	100°F
Bottom-hole temperature:	224°F
Tubing head pressure:	300 psia

**Solution** This example problem is solved with the spreadsheet program *Guo-GhalamborBHP.xls*. The result is shown in Table 4.2, and Table 4.3.

---

## 4.4 MULTIPHASE FLOW IN OIL WELLS

In addition to oil, almost all oil wells produce a certain amount of water, gas, and sometimes sand. These wells are called *multiphase oil wells*. The TPR equation for single-phase flow is not valid for multiphase oil wells. To analyze TPR of multiphase oil wells rigorously, a multiphase flow model is required.

Multiphase flow is much more complicated than single-phase flow because of the variation of flow regime (or flow pattern). Fluid distribution changes greatly in different flow regimes, which significantly affects pressure gradient in the tubing.

**Table 4.3 Result Given by Guo-GhalamborBHP.xls for Example Problem 4.3***Guo-GhalamborBHP.xls*

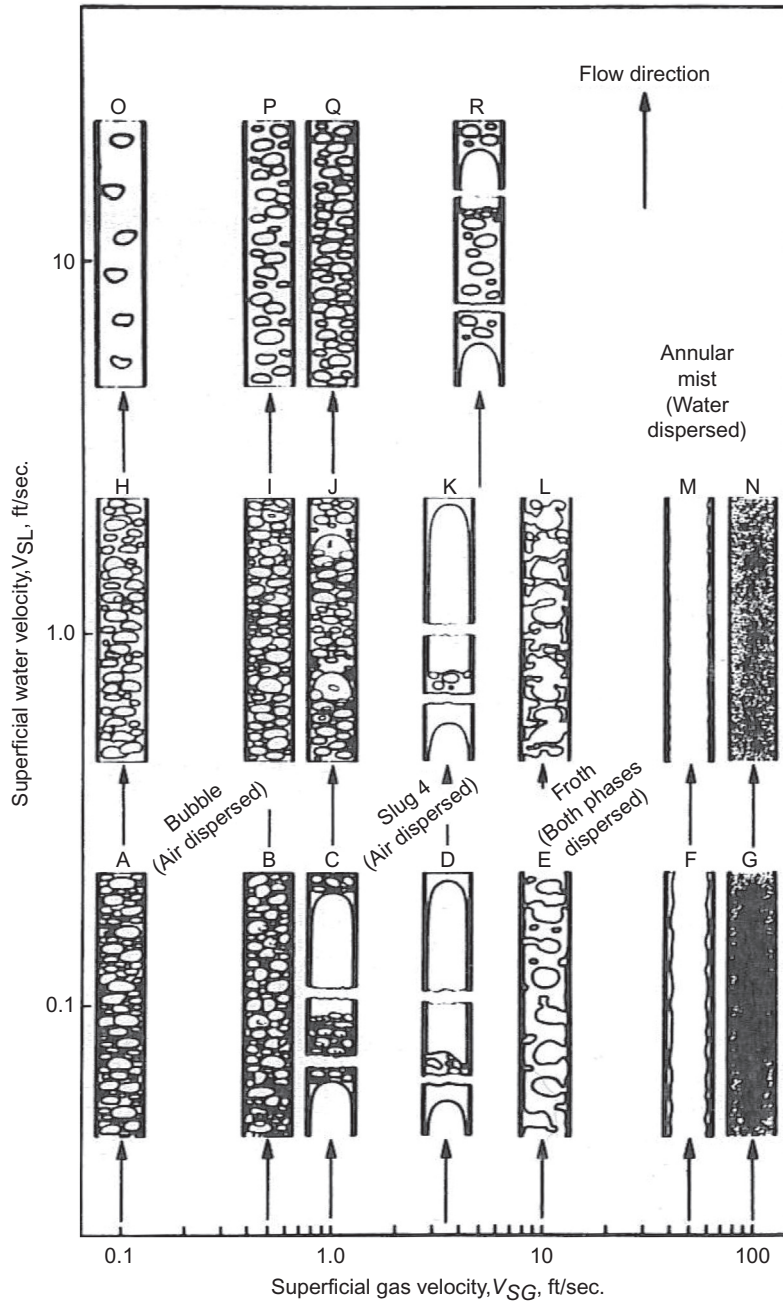
*Description:* This spreadsheet calculates flowing bottom-hole pressure based on tubing head pressure and tubing flow performance using the Guo–Ghalambor method.

*Instruction:* (1) Select a unit system; (2) update parameter values in the Input data section; (3) click “Solution” button; and (4) view result in the Solution section.

Input Data	U.S. Field Units	SI Units
Total measured depth:	7000 ft	
Average inclination angle:	20°	
Tubing inside diameter:	1.995 in.	
Gas production rate:	1,000,000 scfd	
Gas-specific gravity:	0.7 air = 1	
Oil production rate:	1000 stb/d	
Oil-specific gravity:	0.85 H <sub>2</sub> O = 1	
Water production rate:	300 bbl/d	
Water-specific gravity:	1.05 H <sub>2</sub> O = 1	
Solid production rate:	1 ft <sup>3</sup> /d	
Solid-specific gravity:	2.65 H <sub>2</sub> O = 1	
Tubing head temperature:	100°F	
Bottom-hole temperature:	224°F	
Tubing head pressure:	300 psia	
<b>Solution</b>		
$A =$	3.1243196 in. <sup>2</sup>	
$D =$	0.16625 ft	
$T_{av} =$	622 °R	
$\cos(\theta) =$	0.9397014	
$(D\rho v) =$	40.908853	
$f_M =$	0.0415505	
$a =$	0.0001713	
$b =$	2.884E-06	
$c =$	1349785.1	
$d =$	3.8942921	
$e =$	0.0041337	
$M =$	20447.044	
$N =$	6.669E + 09	
Bottom-hole pressure, $p_{wf} =$	1682 psia	

#### 4.4.1 FLOW REGIMES

As shown in Fig. 4.4, at least four flow regimes have been identified in gas-liquid two-phase flow. They are bubble, slug, churn, and annular flow. These flow regimes occur as a progression with



**FIGURE 4.4**

Flow regimes in gas-liquid flow.

After Goier, G.W., Aziz, K., 1977. *The Flow of Complex Mixtures in Pipes*. Robert E. Drieger Publishing Co, Huntington, NY.

increasing gas flow rate for a given liquid flow rate. In bubble flow, gas phase is dispersed in the form of small bubbles in a continuous liquid phase. In slug flow, gas bubbles coalesce into larger bubbles that eventually fill the entire pipe cross-section. Between the large bubbles are slugs of liquid that contain smaller bubbles of entrained gas. In churn flow, the larger gas bubbles become unstable and collapse, resulting in a highly turbulent flow pattern with both phases dispersed. In annular flow, gas becomes the continuous phase, with liquid flowing in an annulus, coating the surface of the pipe and with droplets entrained in the gas phase.

#### 4.4.2 LIQUID HOLDUP

In multiphase flow, the amount of the pipe occupied by a phase is often different from its proportion of the total volumetric flow rate. This is due to density difference between phases. The density difference causes dense phase to slip down in an upward flow (i.e., the lighter phase moves faster than the denser phase). Because of this, the in-situ volume fraction of the denser phase will be greater than the input volume fraction of the denser phase (i.e., the denser phase is “held up” in the pipe relative to the lighter phase). Thus, liquid “holdup” is defined as

$$y_L = \frac{V_L}{V}, \quad (4.35)$$

where

$y_L$  = liquid holdup, fraction

$V_L$  = volume of liquid phase in the pipe segment, ft<sup>3</sup>

$V$  = volume of the pipe segment, ft<sup>3</sup>

Liquid holdup depends on flow regime, fluid properties, and pipe size and configuration. Its value can be quantitatively determined only through experimental measurements.

#### 4.4.3 TPR MODELS

Numerous TPR models have been developed for analyzing multiphase flow in vertical pipes. [Brown \(1977\)](#) presents a thorough review of these models. TPR models for multiphase flow wells fall into two categories: (1) homogeneous-flow models and (2) separated-flow models. Homogeneous models treat multiphase as a homogeneous mixture and do not consider the effects of liquid holdup (no-slip assumption). Therefore, these models are less accurate and are usually calibrated with local operating conditions in field applications. The major advantage of these models comes from their mechanistic nature. They can handle gas-oil-water three-phase and gas-oil-water-sand four-phase systems. It is easy to code these mechanistic models in computer programs.

Separated-flow models are more realistic than the homogeneous-flow models. They are usually given in the form of empirical correlations. The effects of liquid holdup (slip) and flow regime are considered. The major disadvantage of the separated-flow models is that it is difficult to code them in computer programs because most correlations are presented in graphic form.

##### 4.4.3.1 Homogeneous-flow models

Numerous homogeneous-flow models have been developed for analyzing the TPR of multiphase wells since the pioneering works of [Poettmann and Carpenter \(1952\)](#). Poettmann–Carpenter’s model uses empirical two-phase friction factor for friction pressure loss calculations without

considering the effect of liquid viscosity. The effect of liquid viscosity was considered by later researchers including Cicchitti (1960) and Dukler et al. (1964). A comprehensive review of these models was given by Hasan and Kabir (2002). Guo and Ghalambor (2005) presented work addressing gas-oil-water-sand four-phase flow.

Assuming no slip of liquid phase, Poettmann and Carpenter (1952) presented a simplified gas-oil-water three-phase flow model to compute pressure losses in wellbores by estimating mixture density and friction factor. According to Poettmann and Carpenter, the following equation can be used to calculate pressure traverse in a vertical tubing when the acceleration term is neglected:

$$\Delta p = (\bar{\rho} + \bar{k}/\bar{\rho}) \frac{\Delta h}{144} \quad (4.36)$$

where

$\Delta p$  = pressure increment, psi

$\bar{\rho}$  = average mixture density (specific weight), lb/ft<sup>3</sup>

$\Delta h$  = depth increment, ft

and

$$\bar{k} = \frac{f_{2F} q_o^2 M^2}{7.4137 \times 10^{10} D^5} \quad (4.37)$$

where

$f_{2F}$  = Fanning friction factor for two-phase flow

$q_o$  = oil production rate, stb/day

$M$  = total mass associated with 1 stb of oil

$D$  = tubing inner diameter, ft

The average mixture density  $\bar{\rho}$  can be calculated by

$$\bar{\rho} = \frac{\rho_1 + \rho_2}{2} \quad (4.38)$$

where

$\rho_1$  = mixture density at top of tubing segment, lb/ft<sup>3</sup>

$\rho_2$  = mixture density at bottom of segment, lb/ft<sup>3</sup>

The mixture density at a given point can be calculated based on mass flow rate and volume flow rate:

$$\rho = \frac{M}{V_m} \quad (4.39)$$

where

$$M = 350.17(\gamma_o + WOR\gamma_w) + GOR\rho_{air}\gamma_g \quad (4.40)$$

$$V_m = 5.615(B_o + WOR B_w) + (GOR - R_s) \left( \frac{14.7}{p} \right) \left( \frac{T}{520} \right) \left( \frac{z}{1.0} \right) \quad (4.41)$$

and where

- $\gamma_o$  = oil-specific gravity, 1 for freshwater
- $WOR$  = producing water–oil ratio, bbl/stb
- $\gamma_w$  = water-specific gravity, 1 for freshwater
- $GOR$  = producing gas–oil ratio, scf/stb
- $\rho_{air}$  = density of air, lb<sub>m</sub>/ft<sup>3</sup>
- $\gamma_g$  = gas-specific gravity, 1 for air
- $V_m$  = volume of mixture associated with 1 stb of oil, ft<sup>3</sup>
- $B_o$  = formation volume factor of oil, rb/stb
- $B_w$  = formation volume factor of water, rb/bbl
- $R_s$  = solution gas–oil ratio, scf/stb
- $p$  = in-situ pressure, psia
- $T$  = *in situ* temperature, °R
- $z$  = gas compressibility factor at  $p$  and  $T$ .

If data from direct measurements are not available, solution gas–oil ratio and formation volume factor of oil can be estimated using the following correlations:

$$R_s = \gamma_g \left[ \frac{p}{18} \frac{10^{0.0125API}}{10^{0.00091t}} \right]^{1.2048} \quad (4.42)$$

$$B_o = 0.9759 + 0.00012 \left[ R_s \left( \frac{\gamma_g}{\gamma_o} \right)^{0.5} + 1.25t \right]^{1.2} \quad (4.43)$$

where  $t$  is in-situ temperature in °F. The two-phase friction factor  $f_{2F}$  can be estimated from a chart recommended by Poettmann and Carpenter (1952). For easy coding in computer programs, Guo and Ghalambor (2002) developed the following correlation to represent the chart:

$$f_{2F} = 10^{1.444 - 2.5 \log(D\rho v)}, \quad (4.44)$$

where  $(D\rho v)$  is the numerator of Reynolds number representing inertial force and can be formulated as

$$(D\rho v) = \frac{1.4737 \times 10^{-5} M q_o}{D}. \quad (4.45)$$

Because the Poettmann–Carpenter model takes a finite-difference form, this model is accurate for only short-depth incremental  $\Delta h$ . For deep wells, this model should be used in a piecewise manner to get accurate results (i.e., the tubing string should be “broken” into small segments and the model is applied to each segment).

Because iterations are required to solve Eq. (4.36) for pressure, a computer spreadsheet program *Poettmann-CarpenterBHP.xls* has been developed. The program is available from the attached CD.

**Example Problem 4.5** For the following given data, calculate bottom-hole pressure:

Tubing head pressure:	500 psia
Tubing head temperature:	100°F
Tubing inner diameter:	1.66 in.
Tubing shoe depth (near bottom hole):	5000 ft



Bottom-hole temperature:	150°F
Liquid production rate:	2000 stb/day
Water cut:	25%
Producing GLR:	1000 scf/stb
Oil gravity:	30 °API
Water-specific gravity:	1.05 1 for freshwater
Gas-specific gravity:	0.65 1 for air

**Solution** This problem can be solved using the computer program *Poettmann-CarpenterBHP.xls*. The result is shown in Table 4.4.

#### 4.4.3.2 Separated-flow models

A number of separated-flow models are available for TPR calculations. Among many others are the Lockhart and Martinelli correlation (1949), the Duns and Ros correlation (1963), and the Hagedorn and Brown method (1965). Based on comprehensive comparisons of these models, Ansari et al. (1994) and Hasan and Kabir (2002) recommended the Hagedorn–Brown method with modifications for near-vertical flow.

The modified Hagedorn–Brown (mH-B) method is an empirical correlation developed on the basis of the original work of Hagedorn and Brown (1965). The modifications include using the no-slip liquid holdup when the original correlation predicts a liquid holdup value less than the no-slip holdup and using the Griffith correlation (Griffith and Wallis, 1961) for the bubble flow regime.

The original Hagedorn–Brown correlation takes the following form:

$$\frac{dP}{dz} = \frac{g}{g_c} \bar{\rho} + \frac{2f_F \bar{\rho} u_m^2}{g_c D} + \bar{\rho} \frac{\Delta(u_m^2)}{2g_c \Delta z}, \quad (4.46)$$

which can be expressed in U.S. field units as

$$144 \frac{dp}{dz} = \bar{\rho} + \frac{f_F M_t^2}{7.413 \times 10^{10} D^5 \bar{\rho}} + \bar{\rho} \frac{\Delta(u_m^2)}{2g_c \Delta z}, \quad (4.47)$$

where

$M_t$  = total mass flow rate, lb<sub>m</sub>/d  
 $\bar{\rho}$  = in-situ average density, lb<sub>m</sub>/ft<sup>3</sup>  
 $u_m$  = mixture velocity, ft/s

and

$$\bar{\rho} = y_L \rho_L + (1 - y_L) \rho_G, \quad (4.48)$$

$$u_m = u_{SL} + u_{SG}, \quad (4.49)$$

where

$\rho_L$  = liquid density, lb<sub>m</sub>/ft<sup>3</sup>  
 $\rho_G$  = in-situ gas density, lb<sub>m</sub>/ft<sup>3</sup>  
 $u_{SL}$  = superficial velocity of liquid phase, ft/s  
 $u_{SG}$  = superficial velocity of gas phase, ft/s

<p><b>Table 4.4 Result Given by Poettmann-CarpenterBHP.xls for Example Problem 4.2</b></p>	
<p><i>Poettmann–CarpenterBHP.xls</i></p> <p><i>Description:</i> This spreadsheet calculates flowing bottom-hole pressure based on tubing head pressure and tubing flow performance using the Poettmann–Carpenter method.</p> <p><i>Instruction:</i> (1) Select a unit system; (2) update parameter values in the Input data section; (3) Click “Solution” button; and (4) view result in the Solution section.</p>	
Input Data	U.S. Field Units
Tubing ID:	1.66 in
Wellhead pressure:	500 psia
Liquid production rate:	2000 stb/d
Producing gas–liquid ratio (GLR):	1000 scf/stb
Water cut (WC):	25%
Oil gravity:	30 °API
Water-specific gravity:	1.05 freshwater = 1
Gas-specific gravity:	0.65 1 for air
N <sub>2</sub> content in gas:	0 mole fraction
CO <sub>2</sub> content in gas:	0 mole fraction
H <sub>2</sub> S content in gas:	0 mole fraction
Formation volume factor for water:	1.0 rb/stb
Wellhead temperature:	100°F
Tubing shoe depth:	5000 ft
Bottom-hole temperature:	150°F
Solution	
Oil-specific gravity	= 0.88 freshwater = 1
Mass associated with 1 stb of oil	= 495.66 lb
Solution gas ratio at wellhead	= 78.42 scf/stb
Oil formation volume factor at wellhead	= 1.04 rb/stb
Volume associated with 1 stb oil @ wellhead	= 45.12 cf
Fluid density at wellhead	= 10.99 lb/cf
Solution gas–oil ratio at bottom hole	= 301.79 scf/stb
Oil formation volume factor at bottom hole	= 1.16 rb/stb
Volume associated with 1 stb oil @ bottom hole	= 17.66 cf
Fluid density at bottom hole	= 28.07 lb/cf
The average fluid density	= 19.53 lb/cf
Inertial force ( $D\rho v$ )	= 79.21 lb/day-ft
Friction factor	= 0.002
Friction term	= 293.12 (lb/cf) <sup>2</sup>
Error in depth	= 0.00 ft
Bottom-hole pressure	= 1699 psia

The superficial velocity of a given phase is defined as the volumetric flow rate of the phase divided by the pipe cross-sectional area for flow. The third term in the right-hand side of Eq. (4.47) represents pressure change due to kinetic energy change, which is in most instances negligible for oil wells.

Obviously, determination of the value of liquid holdup  $y_L$  is essential for pressure calculations. The mH-B correlation uses liquid holdup from three charts using the following dimensionless numbers:

Liquid velocity number,  $N_{vL}$ :

$$N_{vL} = 1.938u_{SL}^4 \sqrt{\frac{\rho_L}{\sigma}} \quad (4.50)$$

Gas velocity number,  $N_{vG}$ :

$$N_{vG} = 1.938u_{SG}^4 \sqrt{\frac{\rho_L}{\sigma}} \quad (4.51)$$

Pipe diameter number,  $N_D$ :

$$N_D = 120.872D \sqrt{\frac{\rho_L}{\sigma}} \quad (4.52)$$

Liquid viscosity number,  $N_L$ :

$$N_L = 0.15726\mu_L^4 \sqrt{\frac{1}{\rho_L \sigma^3}}, \quad (4.53)$$

where

$D$  = conduit inner diameter, ft

$\sigma$  = liquid–gas interfacial tension, dyne/cm

$\mu_L$  = liquid viscosity, cp

$\mu_G$  = gas viscosity, cp

The first chart is used for determining parameter ( $CN_L$ ) based on  $N_L$ . We have found that this chart can be replaced by the following correlation with acceptable accuracy:

$$(CN_L) = 10^Y, \quad (4.54)$$

where

$$Y = -2.69851 + 0.15841X_1 - 0.55100X_1^2 + 0.54785X_1^3 - 0.12195X_1^4 \quad (4.55)$$

and

$$X_1 = \log(N_L) + 3. \quad (4.56)$$

Once the value of parameter ( $CN_L$ ) is determined, it is used for calculating the value of the group  $\frac{N_{vL} p^{0.1} (CN_L)}{N_{vG}^{0.575} p_a^{0.1} N_D}$ , where  $p$  is the absolute pressure at the location where pressure gradient is to be calculated, and  $p_a$  is atmospheric pressure. The value of this group is then used as an entry in

the second chart to determine parameter ( $y_L/\psi$ ). We have found that the second chart can be represented by the following correlation with good accuracy:

$$\begin{aligned} \frac{y_L}{\psi} = & -0.10307 + 0.61777[\log(X_2) + 6] \\ & - 0.63295[\log(X_2) + 6]^2 + 0.29598[\log(X_2) + 6]^3 \\ & - 0.0401[\log(X_2) + 6]^4, \end{aligned} \quad (4.57)$$

where

$$X_2 = \frac{N_{vL}P^{0.1}(CN_L)}{N_{vG}^{0.575}P_a^{0.1}N_D}. \quad (4.58)$$

According to Hagedorn and Brown (1965), the value of parameter  $\psi$  can be determined from the third chart using a value of group  $\frac{N_{vG}N_L^{0.38}}{N_D^{2.14}}$ .

We have found that for  $\frac{N_{vG}N_L^{0.38}}{N_D^{2.14}} > 0.01$  the third chart can be replaced by the following correlation with acceptable accuracy:

$$\begin{aligned} \psi = & 0.91163 - 4.82176X_3 + 1,232.25X_3^2 \\ & - 22,253.6X_3^3 + 116174.3X_3^4, \end{aligned} \quad (4.59)$$

where

$$X_3 = \frac{N_{vG}N_L^{0.38}}{N_D^{2.14}}. \quad (4.60)$$

However,  $\psi = 1.0$  should be used for  $\frac{N_{vG}N_L^{0.38}}{N_D^{2.14}} \leq 0.01$ .

Finally, the liquid holdup can be calculated by

$$y_L = \psi \left( \frac{y_L}{\psi} \right). \quad (4.61)$$

The Reynolds number for multiphase flow can be calculated by

$$N_{Re} = \frac{2.2 \times 10^{-2} m_t}{D \mu_L^{y_L} \mu_G^{(1-y_L)}}, \quad (4.62)$$

where  $m_t$  is mass flow rate. The modified mH-B method uses the Griffith correlation for the bubble-flow regime. The bubble-flow regime has been observed to exist when

$$\lambda_G < L_B, \quad (4.63)$$

where

$$\lambda_G = \frac{u_{sG}}{u_m} \quad (4.64)$$

and

$$L_B = 1.071 - 0.2218 \left( \frac{u_m^2}{D} \right), \quad (4.65)$$

which is valid for  $L_B \geq 0.13$ . When the  $L_B$  value given by Eq. (4.65) is less than 0.13,  $L_B = 0.13$  should be used.

Neglecting the kinetic energy pressure drop term, the Griffith correlation in U.S. field units can be expressed as

$$144 \frac{dp}{dz} = \bar{p} + \frac{f_F m_L^2}{7.413 \times 10^{10} D^5 \rho_L y_L^2}, \quad (4.66)$$

where  $m_L$  is mass flow rate of liquid only. The liquid holdup in Griffith correlation is given by the following expression:

$$y_L = 1 - \frac{1}{2} \left[ 1 + \frac{u_m}{u_s} - \sqrt{\left(1 + \frac{u_m}{u_s}\right)^2 - 4 \frac{u_s G}{u_s}} \right], \quad (4.67)$$

where  $\mu_s = 0.8$  ft/s. The Reynolds number used to obtain the friction factor is based on the in-situ average liquid velocity, that is,

$$N_{Re} = \frac{2.2 \times 10^{-2} m_L}{D \mu_L}. \quad (4.68)$$

To speed up calculations, the Hagedorn–Brown correlation has been coded in the spreadsheet program *Hagedorn Brown Correlation.xls*.

**Example Problem 4.6** For the data given below, calculate and plot pressure traverse in the tubing string:

Tubing shoe depth:	9700 ft
Tubing inner diameter:	1.995 in.
Oil gravity:	40 °API
Oil viscosity:	5 cp
Production GLR:	75 scf/bbl
Gas-specific gravity:	0.7 air = 1
Flowing tubing head pressure:	100 psia
Flowing tubing head temperature:	80°F
Flowing temperature at tubing shoe:	180°F
Liquid production rate:	758 stb/day
Water cut:	10%
Interfacial tension:	30 dynes/cm
Specific gravity of water:	1.05 H <sub>2</sub> O = 1

**Solution** This example problem is solved with the spreadsheet program *HagedornBrownCorrelation.xls*. The result is shown in Table 4.5 and Fig. 4.5.

## 4.5 SUMMARY

This chapter presented and illustrated different mathematical models for describing wellbore/tubing performance. Among many models, the mH-B model has been found to give results with good

**Table 4.5 Result Given by HagedornBrownCorrelation.xls for Example Problem 4.6**

*HagedornBrownCorrelation.xls*

*Description:* This spreadsheet calculates flowing pressures in tubing string based on tubing head pressure using the Hagedorn–Brown correlation.

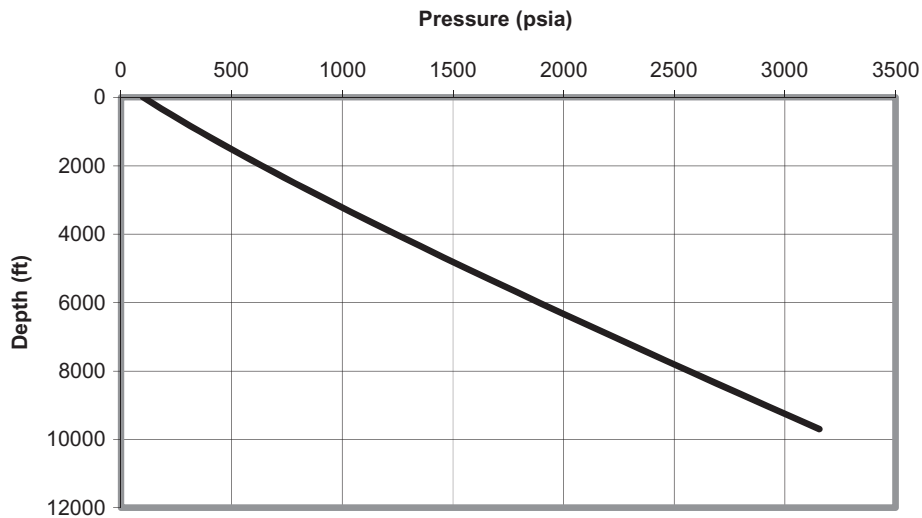
*Instruction:* (1) Select a unit system; (2) update parameter values in the Input data section; (3) click “Solution” button; and (4) view result in the Solution section and charts.

Input Data	U.S. Field Units	SI Units	
Depth ( $D$ ):	9700 ft		
Tubing inner diameter ( $d_{ti}$ ):	1.995 in.		
Oil gravity (API):	40 °API		
Oil viscosity ( $\mu_o$ ):	5 cp		
Production GLR (GLR):	75 scf/bbl		
Gas-specific gravity ( $\gamma_g$ ):	0.7 air = 1		
Flowing tubing head pressure ( $p_{hf}$ ):	100 psia		
Flowing tubing head temperature ( $t_{hf}$ ):	80°F		
Flowing temperature at tubing shoe ( $t_{wf}$ ):	180°F		
Liquid production rate ( $q_L$ ):	758 stb/day		
Water cut (WC):	10%		
Interfacial tension ( $\sigma$ ):	30 dynes/cm		
Specific gravity of water ( $\gamma_w$ ):	1.05 H <sub>2</sub> O = 1		
<b>Solution</b>			
Depth (ft)	(m)	Pressure (psia)	(MPa)
0	0	100	0.68
334	102	183	1.24
669	204	269	1.83
1003	306	358	2.43
1338	408	449	3.06
1672	510	543	3.69
2007	612	638	4.34
2341	714	736	5.01
2676	816	835	5.68
3010	918	936	6.37
3345	1020	1038	7.06
3679	1122	1141	7.76
4014	1224	1246	8.48
4348	1326	1352	9.20
4683	1428	1459	9.93
5017	1530	1567	10.66
5352	1632	1676	11.40
5686	1734	1786	12.15
6021	1836	1897	12.90
6355	1938	2008	13.66

(Continued)

**Table 4.5 Result Given by HagedornBrownCorrelation.xls for Example Problem 4.6**  
*Continued*

6690	2040	2121	14.43
7024	2142	2234	15.19
7359	2243	2347	15.97
7693	2345	2461	16.74
8028	2447	2576	17.52
8362	2549	2691	18.31
8697	2651	2807	19.10
9031	2753	2923	19.89
9366	2855	3040	20.68
9700	2957	3157	21.48



**FIGURE 4.5**

Pressure traverse given by Hagedorn Brown Correlation.xls for Example Problem 4.6.

accuracy. The industry practice is to conduct a flow gradient (FG) survey to measure the flowing pressures along the tubing string. The FG data are then employed to validate one of the models and tune the model if necessary before the model is used on a large scale.

## REFERENCES

Ansari, A.M., Sylvester, N.D., Sarica, C., Shoham, O., Brill, J.P., 1994. A comprehensive mechanistic model for upward two-phase flow in wellbores. SPE Production and Facilities (May 1994). Trans. AIME 297.

- Brown, K.E., 1977. *The Technology of Artificial Lift Methods*, Vol. 1. Penn Well Books, Tulsa, OK, pp. 104–158.
- Chen, N.H., 1979. An explicit equation for friction factor in pipe. *Ind. Eng. Chem. Fund.* 18, 296.
- Cicchitti, A., 1960. Two-phase cooling experiments—pressure drop, heat transfer and burnout measurements. *Energia Nucleare* 7 (6), 407.
- Dukler, A.E., Wicks, M., Cleveland, R.G., 1964. Frictional pressure drop in two-phase flow: a comparison of existing correlations for pressure loss and hold-up. *AIChE J* 38–42.
- Duns, H., Ros, N.C.J. Vertical flow of gas and liquid mixtures in wells. In: *Proceedings of the 6th World Petroleum Congress*, Tokyo, 1963.
- Goier, G.W., Aziz, K., 1977. *The Flow of Complex Mixtures in Pipes*. Robert E. Drieger Publishing Co, Huntington, NY.
- Gregory, G.A., Fogarasi, M., 1985. Alternate to standard friction factor equation. *Oil Gas J.* 83, 120–127.
- Griffith, P., Wallis, G.B., 1961. Two-phase slug flow. *Trans. ASME* 83 (Ser. C), 307–320.
- Guo, B., Ghalambor, A., 2002. Gas Volume Requirements for Underbalanced Drilling Deviated Holes. PennWell Corporation, Tulsa, OK, pp. 132–133.
- Guo, B., Ghalambor, A., 2005. *Natural Gas Engineering Handbook*. Gulf Publishing Company, Houston, TX, pp. 59–61.
- Guo, B., Sun, K., Ghalambor, A., 2008. *Well Productivity Handbook*. Gulf Publishing Company, Houston, TX.
- Hagedorn, A.R., Brown, K.E., 1965. Experimental study of pressure gradients occurring during continuous twophase flow in small-diameter conduits. *J. Petroleum Technol* 475.
- Hasan, A.R., Kabir, C.S., 2002. *Fluid Flow and Heat Transfer in Wellbores*. Society of Petroleum Engineers, Richardson, TX, pp. 10–15.
- Katz, D.L., Cornell, D., Kobayashi, R., Poettmann, F.H., Vary, J.A., Elenbaas, J.R., 1959. *Handbook of Natural Gas Engineering*. McGraw-Hill Publishing Company, New York.
- Katz, D.L., Lee, R.L., 1990. *Natural Gas Engineering—Production and Storage*. McGraw-Hill Publishing Company, New York.
- Lockhart, R.W., Martinelli, R.C., 1949. Proposed correlation of data for isothermal two-phase, twocomponent flow in pipes. *Chem. Eng. Prog.* 45, 39.
- Moody, L.F., 1944. Friction factor for pipe flow. *Trans. ASME* 66, 671–685.
- Poettmann, F.H., Carpenter, P.G., 1952. The multiphase flow of gas, oil, and water through vertical string. *Proceedings of the API Drilling and Production Practice Conference held in Dallas, TX*, 257–263.

---

## PROBLEMS

- 4.1.** Suppose that 1000 bbl/day of 16 °API, 5-cp oil is being produced through 2 $\frac{7}{8}$ -in., 8.6-lb<sub>m</sub>/ft tubing in a well that is 3° from vertical. If the tubing wall relative roughness is 0.001, assuming no free gas in tubing string, calculate the pressure drop over 1000 ft of tubing.
- 4.2.** For the following given data, calculate bottom-hole pressure using the Poettmann–Carpenter method:

Tubing head pressure:	300 psia
Tubing head temperature:	100°F
Tubing inner diameter:	1.66 in.
Tubing shoe depth (near bottom hole):	8000 ft



Bottom-hole temperature:	170°F
Liquid production rate:	2000 stb/day
Water cut:	30%
Producing GLR:	800 scf/stb
Oil gravity:	40 °API
Water-specific gravity:	1.05 1 for freshwater
Gas-specific gravity:	0.70 1 for air

4.3. For the data given below, estimate bottom-hole pressure with the Guo–Ghalambor method.

Total measured depth:	8000 ft
The average inclination angle:	5°
Tubing inner diameter:	1.995 in.
Gas production rate:	0.5 MMscfd
Gas-specific gravity:	0.75 air = 1
Oil production rate:	2000 stb/d
Oil-specific gravity:	0.85 H <sub>2</sub> O = 1
Water production rate:	500 bbl/d
Water-specific gravity:	1.05 H <sub>2</sub> O = 1
Solid production rate:	4 ft <sup>3</sup> /d
Solid-specific gravity:	2.65 H <sub>2</sub> O = 1
Tubing head temperature:	100°F
Bottom-hole temperature:	170°F
Tubing head pressure:	500 psia
Tubing shoe depth:	6000 ft
Tubing inner diameter:	1.995 in.
Oil gravity:	30 °API
Oil viscosity:	2 cp
Production GLR:	500 scf/bbl
Gas-specific gravity:	0.65 air = 1
Flowing tubing head pressure:	100 psia
Flowing tubing head temperature:	80°F
Flowing temperature at tubing shoe:	140°F
Liquid production rate:	1500 stb/day
Water cut:	20%
Interfacial tension:	30 dynes/cm
Specific gravity of water:	1.05 H <sub>2</sub> O = 1

4.4. For the data given below, calculate and plot pressure traverse in the tubing string using the Hagedorn–Brown correlation:

4.5. Suppose 3 MMscf/d of 0.75 specific gravity gas is produced through a 3<sup>1</sup>/<sub>2</sub>-in. tubing string set to the top of a gas reservoir at a depth of 8000 ft. At the tubing head, the pressure is 1000 psia and the temperature is 120°F; the bottom-hole temperature is 180°F. The relative roughness of

- tubing is about 0.0006. Calculate the flowing bottom-hole pressure with three methods: (1) the average temperature and compressibility factor method; (2) the Cullender–Smith method; and (3) the four-phase flow method. Make comments on your results.
- 4.6.** Solve Problem 4.5 for gas production through a K-55, 17-lb/ft, 5<sup>1</sup>/<sub>2</sub>-in casing.
- 4.7.** Suppose 2 MMscf/d of 0.65 specific gravity gas is produced through a 2<sup>7</sup>/<sub>8</sub>-in. (2.259-in. inside diameter) tubing string set to the top of a gas reservoir at a depth of 5000 ft. Tubing head pressure is 300 psia and the temperature is 100°F; the bottom-hole temperature is 150°F. The relative roughness of tubing is about 0.0006. Calculate the flowing bottom pressure with the average temperature and compressibility factor method.

# CHOKER PERFORMANCE

# 5

## 5.1 INTRODUCTION

Wellhead chokes are used to limit production rates for regulations, protect surface equipment from slugging, avoid sand problems due to high drawdown, and control flow rate to avoid water or gas coning. Two types of wellhead chokes are used. They are (1) positive (fixed) chokes and (2) adjustable chokes.

Placing a choke at the wellhead means fixing the wellhead pressure and, thus, the flowing bottom-hole pressure and production rate. For a given wellhead pressure, by calculating pressure loss in the tubing the flowing bottom-hole pressure can be determined. If the reservoir pressure and productivity index is known, the flow rate can then be determined on the basis of inflow performance relationship (IPR).

## 5.2 SONIC AND SUBSONIC FLOW

Pressure drop across well chokes is usually very significant. There is no universal equation for predicting pressure drop across the chokes for all types of production fluids. Different choke flow models are available from the literature, and they have to be chosen based on the gas fraction in the fluid and flow regimes, that is, subsonic or sonic flow.

Both sound waves and pressure waves are mechanical waves. When the fluid flow velocity in a choke reaches the traveling velocity of sound in the fluid under the in-situ condition, the flow is called “sonic flow.” Under sonic flow conditions, the pressure wave downstream of the choke cannot go upstream through the choke because the medium (fluid) is traveling in the opposite direction at the same velocity. Therefore, a pressure discontinuity exists at the choke, that is, the downstream pressure does not affect the upstream pressure. Because of the pressure discontinuity at the choke, any change in the downstream pressure cannot be detected from the upstream pressure gauge. Of course, any change in the upstream pressure cannot be detected from the downstream pressure gauge either. This sonic flow provides a unique choke feature that stabilizes well production rate and separation operation conditions.

Whether a sonic flow exists at a choke depends on a downstream-to-upstream pressure ratio. If this pressure ratio is less than a critical pressure ratio, sonic (critical) flow exists. If this pressure ratio is greater than or equal to the critical pressure ratio, subsonic (subcritical) flow exists. The critical pressure ratio through chokes is expressed as

$$\left(\frac{p_{outlet}}{p_{up}}\right)_c = \left(\frac{2}{k+1}\right)^{\frac{k}{k-1}}, \quad (5.1)$$

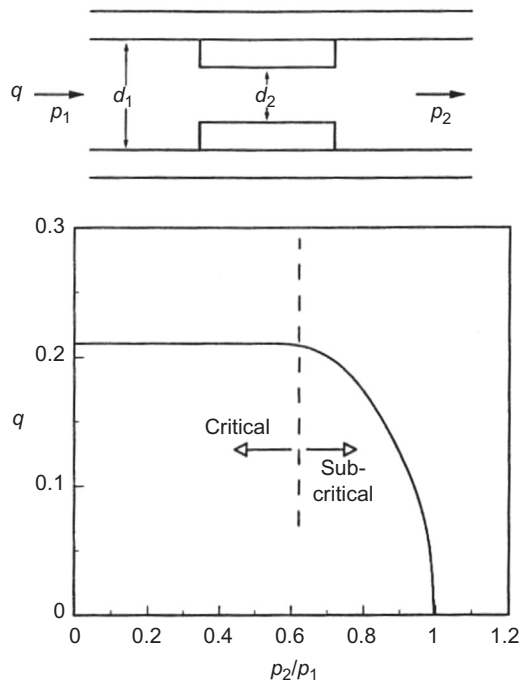


FIGURE 5.1

A typical choke performance curve.

where  $p_{outlet}$  is the pressure at choke outlet,  $p_{up}$  is the upstream pressure, and  $k = C_p/C_v$  is the specific heat ratio. The value of the  $k$  is about 1.28 for natural gas. Thus, the critical pressure ratio is about 0.55 for natural gas. A similar constant is used for oil flow. A typical choke performance curve is shown in Fig. 5.1.

### 5.3 SINGLE-PHASE LIQUID FLOW

The pressure drop across a choke is mainly due to kinetic energy change. For single-phase liquid flow, the second term in the right-hand side of Eq. (4.1) can be rearranged as

$$q = C_D A \sqrt{\frac{2g_c \Delta P}{\rho}}, \quad (5.2)$$

where

$q$  = flow rate, ft<sup>3</sup>/s

$C_D$  = choke discharge coefficient

$A$  = choke area, ft<sup>2</sup>

$g_c$  = unit conversion factor, 32.17 lb<sub>m</sub>-ft/lb<sub>f</sub>-s<sup>2</sup>

$\Delta P$  = pressure drop, lb<sub>f</sub>/ft<sup>2</sup>

$\rho$  = fluid density, lb<sub>m</sub>/ft<sup>3</sup>

If U.S. field units are used, Eq. (5.2) is expressed as

$$q = 8074 C_D d_2^2 \sqrt{\frac{\Delta p}{\rho}}, \quad (5.3)$$

where

$q$  = flow rate, bbl/d

$d_2$  = choke diameter, in.

$\Delta p$  = pressure drop, psi

The choke discharge coefficient  $C_D$  can be determined based on Reynolds number and choke/pipe diameter ratio (Figs. 5.2 and 5.3). The following correlation has been found to give reasonable accuracy for Reynolds numbers between  $10^4$  and  $10^6$  for nozzle-type chokes (Guo and Ghalambor, 2005):

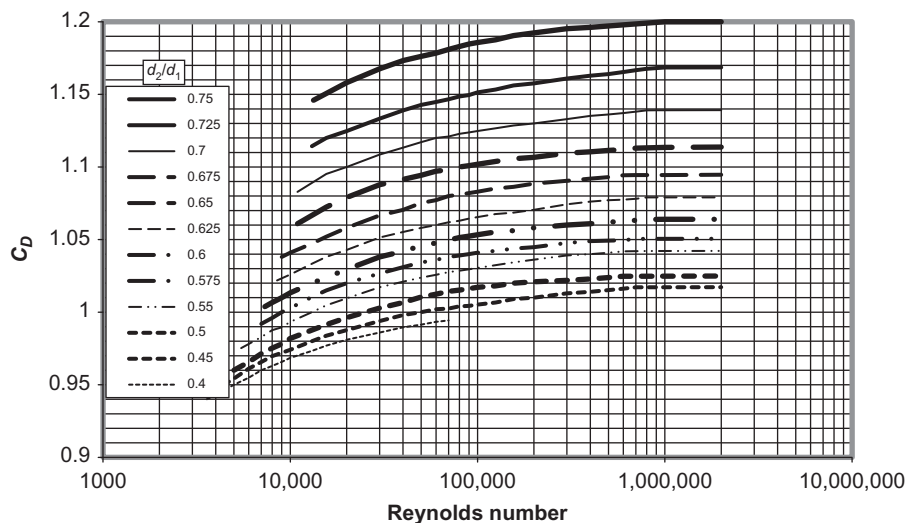
$$C_D = \frac{d_2}{d_1} + \frac{0.3167}{\left(\frac{d_2}{d_1}\right)^{0.6}} + 0.025[\log(N_{Re}) - 4], \quad (5.4)$$

where

$d_1$  = upstream pipe diameter, in.

$d_2$  = choke diameter, in.

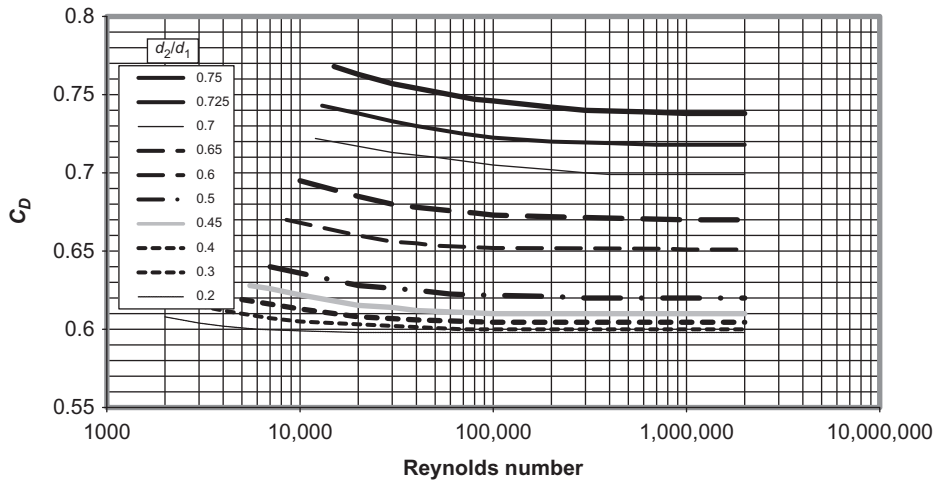
$N_{Re}$  = Reynolds number based on  $d_2$



**FIGURE 5.2**

Choke flow coefficient for nozzle-type chokes.

After Crane Co. *Flow of fluids through valves, fittings, and pipe. Technical paper No. 410. Chicago, IL, 1957.*



**FIGURE 5.3**

Choke flow coefficient for orifice-type chokes.

*After Crane Co. Flow of fluids through valves, fittings, and pipe. Technical paper No. 410. Chicago, IL, 1957.*

## 5.4 SINGLE-PHASE GAS FLOW

Pressure equations for gas flow through a choke are derived based on an isentropic process. This is because there is no time for heat to transfer (adiabatic) and the friction loss is negligible (assuming reversible) at chokes. In addition to the concern of pressure drop across the chokes, temperature drop associated with choke flow is also an important issue for gas wells, because hydrates may form that may plug flow lines.

### 5.4.1 SUBSONIC FLOW

Under subsonic flow conditions, gas passage through a choke can be expressed as

$$q_{sc} = 1248 C_D A_2 p_{up} \sqrt{\frac{k}{(k-1)\gamma_g T_{up}} \left[ \left( \frac{p_{dn}}{p_{up}} \right)^{\frac{2}{k}} - \left( \frac{p_{dn}}{p_{up}} \right)^{\frac{k+1}{k}} \right]}, \quad (5.5)$$

where

- $q_{sc}$  = gas flow rate, Mscf/d
- $p_{up}$  = upstream pressure at choke, psia
- $A_2$  = cross-sectional area of choke, in.<sup>2</sup>
- $T_{up}$  = upstream temperature, °R
- $g$  = acceleration of gravity, 32.2 ft/s<sup>2</sup>
- $\gamma_g$  = gas-specific gravity related to air

The Reynolds number for determining  $C_D$  is expressed as

$$N_{Re} = \frac{20q_{sc}\gamma_g}{\mu d_2}, \quad (5.6)$$

where  $\mu$  is gas viscosity in cp.

Gas velocity under subsonic flow conditions is less than the sound velocity in the gas at the in-situ conditions:

$$v = \sqrt{v_{up}^2 + 2g_c C_p T_{up} \left[ 1 - \frac{z_{up}}{z_{dn}} \left( \frac{P_{down}}{P_{up}} \right)^{\frac{k-1}{k}} \right]}, \quad (5.7)$$

where  $C_p$  = specific heat of gas at constant pressure (187.7 lbf-ft/lbm-R for air).

### 5.4.2 SONIC FLOW

Under sonic flow conditions, the gas passage rate reaches its maximum value. The gas passage rate is expressed in the following equation for ideal gases:

$$Q_{sc} = 879 C_D A p_{up} \sqrt{\left( \frac{k}{\gamma_g T_{up}} \right) \left( \frac{2}{k+1} \right)^{\frac{k+1}{k-1}}} \quad (5.8)$$

The choke flow coefficient  $C_D$  is not sensitive to the Reynolds number for Reynolds number values greater than  $10^6$ . Thus, the  $C_D$  value at the Reynolds number of  $10^6$  can be assumed for  $C_D$  values at higher Reynolds numbers.

Gas velocity under sonic flow conditions is equal to sound velocity in the gas under the in-situ conditions:

$$v = \sqrt{v_{up}^2 + 2g_c C_p T_{up} \left[ 1 - \frac{z_{up}}{z_{outlet}} \left( \frac{2}{k+1} \right) \right]} \quad (5.9)$$

or

$$v \approx 44.76 \sqrt{T_{up}} \quad (5.10)$$

### 5.4.3 TEMPERATURE AT CHOKE

Depending on the upstream-to-downstream pressure ratio, the temperature at choke can be much lower than expected. This low temperature is due to the Joule–Thomson cooling effect, that is, a sudden gas expansion below the nozzle causes a significant temperature drop. The temperature can easily drop to below ice point, resulting in ice-plugging if water exists. Even though the temperature still can be above ice point, hydrates can form and cause plugging problems. Assuming an isentropic process for gas flowing through chokes, the temperature at the choke downstream can be predicted using the following equation:

$$T_{dn} = T_{up} \frac{z_{up}}{z_{outlet}} \left( \frac{P_{outlet}}{P_{up}} \right)^{\frac{k-1}{k}} \quad (5.11)$$

The outlet pressure is equal to the downstream pressure in subsonic flow conditions.

## 5.4.4 APPLICATIONS

Eqs. (5.5) through (5.11) can be used for estimating

- Downstream temperature
- Gas passage rate at given upstream and downstream pressures
- Upstream pressure at given downstream pressure and gas passage
- Downstream pressure at given upstream pressure and gas passage

To estimate the gas passage rate at given upstream and downstream pressures, the following procedure can be taken:

**Step 1.** Calculate the critical pressure ratio with Eq. (5.1).

**Step 2.** Calculate the downstream-to-upstream pressure ratio.

**Step 3.** If the downstream-to-upstream pressure ratio is greater than the critical pressure ratio, use Eq. (5.5) to calculate gas passage. Otherwise, use Eq. (5.8) to calculate gas passage.

**Example Problem 5.1** A 0.6 specific gravity gas flows from a 2-in. pipe through a 1-in. orifice-type choke. The upstream pressure and temperature are 800 psia and 75°F, respectively. The downstream pressure is 200 psia (measured 2 ft from the orifice). The gas-specific heat ratio is 1.3. (1) What is the expected daily flow rate? (2) Does heating need to be applied to ensure that the frost does not clog the orifice? (3) What is the expected pressure at the orifice outlet?

**Solution**

a.

$$\left(\frac{P_{outlet}}{P_{up}}\right) = \left(\frac{2}{k+1}\right)^{\frac{k}{k-1}} = \left(\frac{2}{1.3+1}\right)^{\frac{1.3}{1.3-1}} = 0.5459$$

$$\frac{P_{dn}}{P_{up}} = \frac{200}{800} = 0.25 < 0.5459 \quad \text{Sonic flow exists.}$$

$$\frac{d_2}{d_1} = \frac{1''}{2''} = 0.5$$

Assuming  $N_{Re} > 10^6$ , Fig. 5.2 gives  $C_D = 0.62$ .

$$q_{sc} = 879 C_D A P_{up} \sqrt{\left(\frac{k}{\gamma_g T_{up}}\right) \left(\frac{2}{k+1}\right)^{\frac{k+1}{k-1}}}$$

$$q_{sc} = (879)(0.62) [\pi(1)^2/4] (800) \sqrt{\left(\frac{1.3}{(0.6)(75 + 460)}\right) \left(\frac{2}{1.3+1}\right)^{\frac{1.3+1}{1.3-1}}}$$

$$q_{sc} = 12,743 \text{ Mscf/d}$$

Check  $N_{Re}$ :

$\mu = 0.01245$  cp by the Carr–Kobayashi–Burrows correlation.

$$N_{Re} = \frac{20 q_{sc} \gamma_g}{\mu d_2} = \frac{(20)(12,743)(0.6)}{(0.01245)(1)} = 1.23 \times 10^7 > 10^6$$



b.

$$T_{dn} = T_{up} \frac{z_{up}}{z_{outlet}} \left( \frac{P_{outlet}}{P_{up}} \right)^{\frac{k-1}{k}} = (75 + 460)(1)(0.5459)^{\frac{1.3-1}{1.3}}$$

$$= 465^\circ\text{R} = 5^\circ\text{F} < 32^\circ\text{F}$$

Therefore, heating is needed to prevent icing.

c.

$$P_{outlet} = P_{up} \left( \frac{P_{outlet}}{P_{up}} \right) = (800)(0.5459) = 437 \text{ psia}$$

**Example Problem 5.2** A 0.65 specific gravity natural gas flows from a 2-in. pipe through a 1.5-in. nozzle-type choke. The upstream pressure and temperature are 100 psia and 70°F, respectively. The downstream pressure is 80 psia (measured 2 ft from the nozzle). The gas-specific heat ratio is 1.25. (1) What is the expected daily flow rate? (2) Is icing a potential problem? (3) What is the expected pressure at the nozzle outlet?

**Solution**

a.

$$\left( \frac{P_{outlet}}{P_{up}} \right) = \left( \frac{2}{K+1} \right)^{\frac{k}{k-1}} = \left( \frac{2}{1.25+1} \right)^{\frac{1.25}{1.25-1}} = 0.5549$$

$$\frac{P_{dn}}{P_{up}} = \frac{80}{100} = 0.8 > 0.559 \quad \text{Subsonic flow exists.}$$

$$\frac{d_2}{d_1} = \frac{1.5''}{2''} = 0.75$$

Assuming  $N_{Re} > 10^6$ , Fig. 5.1 gives  $C_D = 1.2$ .

$$q_{sc} = 1248 C_D A P_{up} \sqrt{\frac{k}{(k-1)\gamma_g T_{up}} \left[ \left( \frac{P_{dn}}{P_{up}} \right)^{\frac{2}{k}} - \left( \frac{P_{dn}}{P_{up}} \right)^{\frac{k+1}{k}} \right]}$$

$$q_{sc} = (1248)(1.2) [\pi(1.5)^2/4] (100)$$

$$\times \sqrt{\frac{1.25}{(1.25-1)(0.65)(530)} \left[ \left( \frac{80}{100} \right)^{\frac{2}{1.25}} - \left( \frac{80}{100} \right)^{\frac{1.25+1}{1.25}} \right]}$$

$$q_{sc} = 5572 \text{ Mscf/d}$$

Check  $N_{Re}$ :

$\mu = 0.0108$  cp by the Carr–Kobayashi–Burrows correlation.

$$N_{Re} = \frac{20 q_{sc} \gamma_g}{\mu d} = \frac{(20)(5,572)(0.65)}{(0.0108)(1.5)} = 4.5 \times 10^6 > 10^6$$

b.

$$T_{dn} = T_{up} \frac{z_{up}}{z_{outlet}} \left( \frac{P_{outlet}}{P_{up}} \right)^{\frac{k-1}{k}} = (70 + 460)(1)(0.8)^{\frac{1.25-1}{1.25}}$$

$$= 507^{\circ}\text{R} = 47^{\circ}\text{F} > 32^{\circ}\text{F}$$

Heating may not be needed, but the hydrate curve may need to be checked.

c.

$$P_{outlet} = P_{dn} = 80 \text{ psia}$$

for subcritical flow.

To estimate upstream pressure at a given downstream pressure and gas passage, the following procedure can be taken:

- Step 1.** Calculate the critical pressure ratio with Eq. (5.1).
- Step 2.** Calculate the minimum upstream pressure required for sonic flow by dividing the downstream pressure by the critical pressure ratio.
- Step 3.** Calculate gas flow rate at the minimum sonic flow condition with Eq. (5.8).
- Step 4.** If the given gas passage is less than the calculated gas flow rate at the minimum sonic flow condition, use Eq. (5.5) to solve upstream pressure numerically. Otherwise, Eq. (5.8) to calculate upstream pressure.

**Example Problem 5.3** For the following given data, estimate upstream pressure at choke:

Downstream pressure:	300 psia
Choke size:	32 1/64 in.
Flowline ID:	2 in.
Gas production rate:	5000 Mscf/d
Gas-specific gravity:	0.75 1 for air
Gas-specific heat ratio:	1.3
Upstream temperature:	110°F
Choke discharge coefficient:	0.99

**Solution** Example Problem 5.3 is solved with the spreadsheet program *GasUpChokePressure.xls*. The result is shown in Table 5.1.

Downstream pressure cannot be calculated on the basis of given upstream pressure and gas passage under sonic flow conditions, but it can be calculated under subsonic flow conditions. The following procedure can be followed:

- Step 1.** Calculate the critical pressure ratio with Eq. (5.1).
- Step 2.** Calculate the maximum downstream pressure for minimum sonic flow by multiplying the upstream pressure by the critical pressure ratio.
- Step 3.** Calculate gas flow rate at the minimum sonic flow condition with Eq. (5.8).
- Step 4.** If the given gas passage is less than the calculated gas flow rate at the minimum sonic flow condition, use Eq. (5.5) to solve downstream pressure numerically. Otherwise, the downstream pressure cannot be calculated. The maximum possible downstream pressure for sonic flow can be estimated by multiplying the upstream pressure by the critical pressure ratio.

<b>Table 5.1 Solution Given by the Spreadsheet Program GasUpChokePressure.xls</b>	
<i>GasUpChokePressure.xls</i>	
<i>Description:</i> This spreadsheet calculates upstream pressure at choke for dry gases.	
<i>Instructions:</i> (1) Update parameter values in blue; (2) click Solution button; (3) view results.	
<b>Input Data</b>	
Downstream pressure:	300 psia
Choke size:	32 1/64 in.
Flowline ID:	2 in.
Gas production rate:	5000 Mscf/d
Gas-specific gravity:	0.75 1 for air
Gas-specific heat ratio ( <i>k</i> ):	1.3
Upstream temperature:	110°F
Choke discharge coefficient:	0.99
<b>Solution</b>	
Choke area:	0.19625 in. <sup>2</sup>
Critical pressure ratio:	0.5457
Minimum upstream pressure required for sonic flow:	549.72 psia
Flow rate at the minimum sonic flow condition:	3029.76 Mscf/d
Flow regime (1 = sonic flow; -1 = subsonic flow):	1
Upstream pressure given by sonic flow equation:	907.21 psia
Upstream pressure given by subsonic flow equation:	1088.04 psia
Estimated upstream pressure:	907.21 psia

**Example Problem 5.4** For the following given data, estimate downstream pressure at choke:

Upstream pressure:	600 psia
Choke size:	32 1/64 in.
Flowline ID:	2 in.
Gas production rate:	2500 Mscf/d
Gas-specific gravity:	0.75 1 for air
Gas-specific heat ratio:	1.3
Upstream temperature:	110°F
Choke discharge coefficient:	0.99

**Solution** Example Problem 5.4 is solved with the spreadsheet program *GasDownChokePressure.xls*. The result is shown in [Table 5.2](#).

**Table 5.2 Solution Given by the Spreadsheet Program GasDownChokePressure.xls***GasDownChokePressure.xls**Description:* This spreadsheet calculates upstream pressure at choke for dry gases.*Instructions:* (1) Update values in the Input data section; (2) click Solution button; (3) view results.**Input Data**

Upstream pressure:	700 psia
Choke size:	32 1/64 in.
Flowline ID:	2 in.
Gas production rate:	2500 Mscf/d
Gas-specific gravity:	0.75 1 for air
Gas-specific heat ratio ( <i>k</i> ):	1.3
Upstream temperature:	110°F
Choke discharge coefficient:	0.99

**Solution**

Choke area:	0.19625 in. <sup>2</sup>
Critical pressure ratio:	0.5457
Minimum downstream pressure for minimum sonic flow:	382 psia
Flow rate at the minimum sonic flow condition:	3857 Mscf/d
Flow regime (1 = sonic flow; -1 = subsonic flow):	-1
The maximum possible downstream pressure in sonic flow:	382 psia
Downstream pressure given by subsonic flow equation:	626 psia
Estimated downstream pressure:	626 psia

## 5.5 MULTIPHASE FLOW

When the produced oil reaches the wellhead choke, the wellhead pressure is usually below the bubble-point pressure of the oil. This means that free gas exists in the fluid stream flowing through choke. Choke behaves differently depending on gas content and flow regime (sonic or subsonic flow).

### 5.5.1 CRITICAL (SONIC) FLOW

Tangren et al. (1947) performed the first investigation on gas-liquid two-phase flow through restrictions. They presented an analysis of the behavior of an expanding gas-liquid system. They showed that when gas bubbles are added to an incompressible fluid, above a critical flow velocity, the medium becomes incapable of transmitting pressure change upstream against the flow. Several empirical choke flow models have been developed in the past half century. They generally take the following form for sonic flow:

$$p_{wh} = \frac{CR^m q}{S^n}, \quad (5.12)$$

<b>Correlation</b>	<b><math>C</math></b>	<b><math>m</math></b>	<b><math>n</math></b>
Gilbert	10	0.546	1.89
Ros	17.4	0.5	2
Baxendell	9.56	0.546	1.93
Achong	3.82	0.65	1.88
Pilehvari	46.67	0.313	2.11

where

- $p_{wh}$  = upstream (wellhead) pressure, psia  
 $q$  = gross liquid rate, bbl/day  
 $R$  = producing gas-liquid ratio, Scf/bbl  
 $S$  = choke size,  $\frac{1}{64}$  in.

and  $C$ ,  $m$ , and  $n$  are empirical constants related to fluid properties. On the basis of the production data from Ten Section Field in California, [Gilbert \(1954\)](#) found the values for  $C$ ,  $m$ , and  $n$  to be 10, 0.546, and 1.89, respectively. Other values for the constants were proposed by different researchers including [Baxendell \(1957\)](#), [Ros \(1960\)](#), [Achong \(1961\)](#), and [Pilehvari \(1980\)](#). A summary of these values is presented in [Table 5.3](#). [Poettmann and Beck \(1963\)](#) extended the work of [Ros \(1960\)](#) to develop charts for different API crude oils. [Omana et al. \(1969\)](#) derived dimensionless choke correlations for water-gas systems.

### 5.5.2 SUBCRITICAL (SUBSONIC) FLOW

Mathematical modeling of subsonic flow of multiphase fluid through choke has been controversial over decades. [Fortunati \(1972\)](#) was the first investigator who presented a model that can be used to calculate critical and subcritical two-phase flow through chokes. [Ashford \(1974\)](#) also developed a relation for two-phase critical flow based on the work of [Ros \(1960\)](#). [Gould \(1974\)](#) plotted the critical–subcritical boundary defined by Ashford, showing that different values of the polytropic exponents yield different boundaries. [Ashford and Pierce \(1975\)](#) derived an equation to predict the critical pressure ratio. Their model assumes that the derivative of flow rate with respect to the downstream pressure is zero at critical conditions. One set of equations was recommended for both critical and subcritical flow conditions. [Pilehvari \(1980, 1981\)](#) also studied choke flow under subcritical conditions. [Sachdeva et al. \(1986\)](#) extended the work of [Ashford and Pierce \(1975\)](#) and proposed a relationship to predict critical pressure ratio. He also derived an expression to find the boundary between critical and subcritical flow. [Surbey et al. \(1988, 1989\)](#) discussed the application of multiple orifice valve chokes for both critical and subcritical flow conditions. Empirical relations were developed for gas and water systems. [Al-Attar and Abdul-Majeed \(1988\)](#) made a comparison of existing choke flow models. The comparison was based on data from 155 well tests. They indicated that the best overall comparison was obtained

with the Gilbert correlation, which predicted measured production rate within an average error of 6.19%. On the basis of energy equation, Perkins (1990) derived equations that describe isentropic flow of multiphase mixtures through chokes. Osman and Dokla (1990) applied the least-square method to field data to develop empirical correlations for gas condensate choke flow. Gilbert-type relationships were generated. Applications of these choke flow models can be found elsewhere (Wallis, 1969; Perry, 1973; Brown and Beggs, 1977; Brill and Beggs, 1978; Ikoku, 1980; Nind, 1981; Bradley, 1987; Beggs, 1991; Saberi, 1996).

Sachdeva's multiphase choke flow mode is representative of most of these works and has been coded in some commercial network modeling software. This model uses the following equation to calculate the critical–subcritical boundary:

$$y_c = \left\{ \frac{\frac{k}{k-1} + \frac{(1-x_1)V_L(1-y_c)}{x_1V_{G1}}}{\frac{k}{k-1} + \frac{n}{2} + \frac{n(1-x_1)V_L}{x_1V_{G2}} + \frac{n}{2} \left[ \frac{(1-x_1)V_L}{x_1V_{G2}} \right]^2} \right\}^{\frac{k}{k-1}}, \quad (5.13)$$

where

$y_c$  = critical pressure ratio

$k = C_p/C_v$ , specific heat ratio

$n$  = polytropic exponent for gas

$x_1$  = free gas quality at upstream, mass fraction

$V_L$  = liquid-specific volume at upstream, ft<sup>3</sup>/lbm

$V_{G1}$  = gas-specific volume at upstream, ft<sup>3</sup>/lbm

$V_{G2}$  = gas-specific volume at downstream, ft<sup>3</sup>/lbm.

The polytropic exponent for gas is calculated using

$$n = 1 + \frac{x_1(C_p - C_v)}{x_1C_v + (1-x_1)C_L}. \quad (5.14)$$

The gas-specific volume at upstream ( $V_{G1}$ ) can be determined using the gas law based on upstream pressure and temperature. The gas-specific volume at downstream ( $V_{G2}$ ) is expressed as

$$V_{G2} = V_{G1}y_c^{-\frac{1}{k}}. \quad (5.15)$$

The critical pressure ratio  $y_c$  can be solved from Eq. (5.13) numerically.

The actual pressure ratio can be calculated by

$$y_a = \frac{p_2}{p_1}, \quad (5.16)$$

where

$y_a$  = actual pressure ratio

$p_1$  = upstream pressure, psia

$p_2$  = downstream pressure, psia

If  $y_a < y_c$ , critical flow exists, and the  $y_c$  should be used ( $y = y_c$ ). Otherwise, subcritical flow exists, and  $y_a$  should be used ( $y = y_a$ ).

The total mass flux can be calculated using the following equation:

$$G_2 = C_D \left\{ 288 g_c p_1 \rho_{m2}^2 \left[ \frac{(1-x_1)(1-y)}{\rho_L} + \frac{x_1 k}{k-1} (V_{G1} - y V_{G2}) \right] \right\}^{0.5}, \quad (5.17)$$

where

$G_2$  = mass flux at downstream, lbm/ft<sup>2</sup>/s

$C_D$  = discharge coefficient, 0.62–0.90

$\rho_{m2}$  = mixture density at downstream, lbm/ft<sup>3</sup>

$\rho_L$  = liquid density, lbm/ft<sup>3</sup>

The mixture density at downstream ( $\rho_{m2}$ ) can be calculated using the following equation:

$$\frac{1}{\rho_{m2}} = x_1 V_{G1} y^{-\frac{1}{k}} + (1-x_1) V_L \quad (5.18)$$

Once the mass flux is determined from Eq. (5.17), mass flow rate can be calculated using the following equation:

$$M_2 = G_2 A_2, \quad (5.19)$$

where

$A_2$  = choke cross-sectional area, ft<sup>2</sup>

$M_2$  = mass flow rate at down stream, lbm/s

Liquid mass flow rate is determined by

$$M_{G2} = x_2 M_2. \quad (5.20)$$

At typical velocities of mixtures of 50–150 ft/s flowing through chokes, there is virtually no time for mass transfer between phases at the throat. Thus,  $x_2 = x_1$  can be assumed. Liquid volumetric flow rate can then be determined based on liquid density.

Gas mass flow rate is determined by

$$M_{G2} = x_2 M_2. \quad (5.21)$$

Gas volumetric flow rate at choke downstream can then be determined using gas law based on downstream pressure and temperature.

The major drawback of Sachdeva's multiphase choke flow model is that it requires free gas quality as an input parameter to determine flow regime and flow rates, and this parameter is usually not known before flow rates are known. A trial-and-error approach is, therefore, needed in flow rate computations. Table 5.4 shows an example calculation with Sachdeva's choke model. Guo et al. (2002) investigated the applicability of Sachdeva's choke flow model in southwest Louisiana gas condensate wells. A total of 512 data sets from wells in southwest Louisiana were gathered for this study. Out of these data sets, 239 sets were collected from oil wells and 273 from condensate wells. Each of the data sets includes choke size, gas rate, oil rate, condensate rate, water rate, gas–liquid ratio, upstream and downstream pressures, oil API gravity, and gas deviation factor ( $z$ -factor). Liquid and gas flow rates from these wells were also calculated using Sachdeva's choke model. The overall performance of the model was studied in predicting the gas flow rate from both oil and gas condensate wells. Out of the 512 data sets, 48 sets failed to comply with the model.

<b>Table 5.4 An Example Calculation with Sachdeva's Choke Model</b>	
<b>Input Data</b>	
Choke diameter ( $d_2$ ):	24 1/64 in.
Discharge coefficient ( $C_D$ ):	0.75
Downstream pressure ( $p_2$ ):	50 psia
Upstream pressure ( $p_1$ ):	80 psia
Upstream temperature ( $T_1$ ):	100°F
Downstream temperature ( $T_2$ ):	20°F
Free gas quality ( $x_1$ ):	0.001 mass fraction
Liquid-specific gravity:	0.9 water = 1
Gas-specific gravity:	0.7 air = 1
Specific heat of gas at constant pressure ( $C_p$ ):	0.24
Specific heat of gas at constant volume ( $C_v$ ):	0.171429
Specific heat of liquid ( $C_L$ ):	0.8
<b>Precalculations</b>	
Gas-specific heat ratio ( $k = C_p/C_v$ ):	1.4
Liquid-specific volume ( $V_L$ ):	0.017806 ft <sup>3</sup> /lbm
Liquid density ( $P_L$ ):	56.16 lb/ft <sup>3</sup>
Upstream gas density ( $p_{G1}$ ):	0.27 lb/ft <sup>3</sup>
Downstream gas density ( $p_{G2}$ ):	0.01 lb/ft <sup>4</sup>
Upstream gas-specific volume ( $V_{G1}$ ):	3.70 ft <sup>3</sup> /lbm
Polytropic exponent of gas ( $n$ ):	1.000086
<b>Critical Pressure Ratio Computation</b>	
$k/(k-1) =$	3.5
$(1-x_1)/x_1 =$	999
$n/2 =$	0.500043
$V_L/V_{G1} =$	0.004811
Critical pressure ratio ( $y_c$ ):	0.353134
$V_{G2} =$	7.785109 ft <sup>3</sup> /lbm
$V_L/V_{G2} =$	0.002287
Equation residue (goal seek 0 by changing $y_c$ ):	0.000263
<b>Flow Rate Calculations</b>	
Pressure ratio ( $y_{actual}$ ):	0.625
Critical flow index:	-1
Subcritical flow index:	1
Pressure ratio to use ( $y$ ):	0.625
Downstream mixture density ( $\rho_{m2}$ ):	43.54 lb/ft <sup>3</sup>
Downstream gas-specific volume ( $V_{G2}$ ):	5.178032



**Table 5.4 An Example Calculation with Sachdeva's Choke Model**  
*Continued*

Choke area ( $A_2$ ) =	0.000767 ft <sup>2</sup>
Mass flux ( $G_2$ ) =	1432.362 lbm/ft <sup>2</sup> /s
Mass flow rate ( $M$ ) =	1.098051 lbm/s
Liquid mass flow rate ( $M_L$ ) =	1.096953 lbm/s
Liquid glow rate =	300.5557 bbl/d
Gas mass flow rate ( $M_G$ ) =	0.001098 lbm/s
Gas flow rate =	0.001772 MMscfd

Mathematical errors occurred in finding square roots of negative numbers. These data sets were from the condensate wells where liquid densities ranged from 46.7 to 55.1 lb/ft<sup>3</sup> and recorded pressure differential across the choke less than 1100 psi. Therefore, only 239 data sets from oil wells and 235 sets from condensate wells were used. The total number of data sets is 474. Different values of discharge coefficient  $C_D$  were used to improve the model performance. Based on the cases studied, [Guo et al. \(2002\)](#) draw the following conclusions:

1. The accuracy of Sachdeva's choke model can be improved by using different discharge coefficients for different fluid types and well types.
2. For predicting liquid rates of oil wells and gas rates of gas condensate wells, a discharge coefficient of  $C_D = 1.08$  should be used.
3. A discharge coefficient  $C_D = 0.78$  should be used for predicting gas rates of oil wells.
4. A discharge coefficient  $C_D = 1.53$  should be used for predicting liquid rates of gas condensate wells.

---

## 5.6 SUMMARY

This chapter presented and illustrated different mathematical models for describing choke performance. While the choke models for gas flow have been well established with fairly good accuracy in general, the models for two-phase flow are subject to tuning to local oil properties. It is essential to validate two-phase flow choke models before they are used on a large scale.

---

## REFERENCES

- Achong, I.B., 1961. Revised bean and performance formula for lake maracaibo wells, Shell Internal Report.
- Al-Attar, H.H., Abdul-Majeed, G., 1988. Revised bean performance equation for east Baghdad oil wells. *SPE Prod. Eng.* 3, 127–131.
- Ashford, F.E., 1974. An evaluation of critical multiphase flow performance through wellhead chokes. *J. Petroleum Technol.* 26 (August), 843–848.
- Ashford, F.E., Pierce, P.E., 1975. Determining multiphase pressure drop and flow capabilities in down hole safety valves. *J. Petroleum Technol.* 27 (September), 1145–1152.
- Baxendell, P.B., 1957. Bean performance-lake wells. Shell Internal Report.

- Beggs, H.D., 1991. *Production Optimization Using Nodal Analysis*. OGTC Publications, Tulsa, OK.
- Bradley, H.B., 1987. *Petroleum Engineering Handbook*. Society of Petroleum Engineers, Richardson, TX.
- Brill, J.P., Beggs, H.D., 1978. *Two-Phase Flow in Pipes*. The University of Tulsa Press, Tulsa, OK.
- Brown, K.E., Beggs, H.D., 1977. *The Technology of Artificial Lift Methods*. PennWell Books, Tulsa, OK.
- Crane, Co., 1957. Flow of fluids through valves, fittings, and pipe. Technical paper No. 410. Chicago.
- Fortunati, F. Two-phase flow through wellhead chokes. Presented at the SPE European Spring Meeting held 16–18 May 1972 in Amsterdam, the Netherlands. SPE paper 3742.
- Gilbert, W.E., 1954. Flowing and gas-lift well performance. *API Drill. Prod. Pract.* 20, 126–157.
- Gould, T.L., 1974. Discussion of an evaluation of critical multiphase flow performance through wellhead chokes. *J. Petroleum Technol.* 26 (August), 849–850.
- Guo, B., Al-Bemani, A., Ghalambor, A. Applicability of Sachdeva's choke flow model in southwest Louisiana gas condensate wells. Presented at the SPE Gas technology Symposium held 30 April–2 May 2002 in Calgary, Canada. Paper SPE 75507.
- Guo, B., Ghalambor, A., 2005. *Natural Gas Engineering Handbook*. Gulf Publishing Company, Houston, TX.
- Ikoku, C.U., 1980. *Natural Gas Engineering*. Penn-Well Books, Tulsa, OK.
- Nind, T.E.W., 1981. *Principles of Oil Well Production*. second ed McGraw-Hill Book Co, New York.
- Omana, R., Houssiere, C., Jr., Brown, K.E., Brill, J.P., Thompson, R.E. Multiphase flow through chokes. Presented at the SPE 44th Annual Meeting held 28–31 September 1969 in Denver, CO. SPE paper 2682.
- Osman, M.E., Dokla, M.E. Has condensate flow through chokes. Presented at 23 April 1990. SPE paper 20988.
- Perkins, T.K. Critical and subcritical flow of multiphase mixtures through chokes. Presented at the SPE 65th Annual Technical Conference and Exhibition held 23–26 September 1990 in New Orleans, LA. SPE paper 20633.
- Perry, R.H., 1973. *Chemical Engineers' Handbook*. fifth ed McGraw-Hill Book Co., New York.
- Pilehvari, A.A., 1980. Experimental Study of Subcritical Twophase Flow through Wellhead Chokes. University of Tulsa Fluid Flow Projects Report, Tulsa, OK.
- Pilehvari, A.A., 1981. Experimental Study of Critical Two-Phase Flow through Wellhead Chokes. University of Tulsa Fluid Flow Projects Report, Tulsa, OK.
- Poettmann, F.H., Beck, R.L., 1963. New charts developed to predict gas-liquid flow through chokes. *World Oil* 95–101.
- Ros, N.C.J., 1960. An analysis of critical simultaneous gas/liquid flow through a restriction and its application to flow metering. *Appl. Sci. Res. Section A* (9), 374–389.
- Saberi, M., 1996. A Study on Flow through Wellhead Chokes and Choke Size Selection, MS thesis. University of Southwestern Louisiana, Lafayette, LA, pp. 78–89.
- Sachdeva, R., Schmidt, Z., Brill, J.P., Blais, R.M. Two-phase flow through chokes. Paper presented at the SPE 61st Annual Technical Conference and Exhibition held 5–8 October 1986 in New Orleans, LA. SPE paper 15657.
- Surbey, D.W., Kelkar, B.G., Brill, J.P., 1988. Study of subcritical flow through multiple orifice valves. *SPE Prod. Eng.* 3, 103–108.
- Surbey, D.W., Kelkar, B.G., Brill, J.P., 1989. Study of multiphase critical flow through wellhead chokes. *SPE Prod. Eng.* 4, 142–146.
- Tangren, R.F., Dodge, C.H., Seifert, H.S., 1947. Compressibility effects in two-phase flow. *J. Appl. Phys.* 20, 637–645.
- Wallis, G.B., 1969. *One Dimensional Two-Phase Flow*. McGraw-Hill Book Co., New York.

---

**PROBLEMS**

- 5.1.** A well is producing 40 °API oil at 200 stb/d and no gas. If the beam size is 1 in., pipe size is 2 in., temperature is 100°F, estimate pressure drop across a nozzle-type choke.
- 5.2.** A well is producing at 200 stb/d of liquid along with a 900 scf/stb of gas. If the beam size is ½ in., assuming sonic flow, calculate the flowing wellhead pressure using Gilbert's formula.
- 5.3.** A 0.65 specific gravity gas flows from a 2-in. pipe through a 1-in. orifice-type choke. The upstream pressure and temperature are 850 psia and 85°F, respectively. The downstream pressure is 210 psia (measured 2 ft from the orifice). The gas-specific heat ratio is 1.3.  
(1) What is the expected daily flow rate? (2) Does heating need to be applied to ensure that the frost does not clog the orifice? (3) What is the expected pressure at the orifice outlet?
- 5.4.** A 0.70 specific gravity natural gas flows from a 2-in. pipe through a 1.5-in. nozzle-type choke. The upstream pressure and temperature are 120 psia and 75°F, respectively. The downstream pressure is 90 psia (measured 2 ft from the nozzle). The gas-specific heat ratio is 1.25. (1) What is the expected daily flow rate? (2) Is icing a potential problem? (3) What is the expected pressure at the nozzle outlet?
- 5.5.** For the following given data, estimate upstream gas pressure at choke:

Downstream pressure:	350 psia
Choke size:	32 <sup>1</sup> / <sub>64</sub> in.
Flowline ID:	2 in.
Gas production rate:	4000 Mscf/d
Gas-specific gravity:	0.70 1 for air
Gas-specific heat ratio:	1.25
Upstream temperature:	100°F
Choke discharge coefficient:	0.95

- 5.6.** For the following given data, estimate downstream gas pressure at choke:

Upstream pressure:	620 psia
Choke size:	32 <sup>1</sup> / <sub>64</sub> in.
Flowline ID:	2 in.
Gas production rate:	2200 Mscf/d
Gas-specific gravity:	0.65 1 for air
Gas-specific heat ratio:	1.3
Upstream temperature:	120°F
Choke discharge coefficient:	0.96

5.7. For the following given data, assuming subsonic flow, estimate liquid and gas production rate:

Choke diameter:	32 <sup>1</sup> / <sub>64</sub> in.
Discharge coefficient:	0.85
Downstream pressure:	60 psia
Upstream pressure:	90 psia
Upstream temperature:	120°F
Downstream temperature:	30°F
Free gas quality:	0.001 mass fraction
Liquid-specific gravity:	0.85 water = 1
Gas-specific gravity:	0.75 air = 1
Specific heat of gas at constant pressure:	0.24
Specific heat of gas at constant volume:	0.171429
Specific heat of liquid:	0.8

# WELL DELIVERABILITY

# 6

## 6.1 INTRODUCTION

Well deliverability is determined by the combination of well inflow performance (see Chapter 3: Reservoir Deliverability) and wellbore flow performance (see Chapter 4: Wellbore Flow Performance). Whereas the former describes the deliverability of the reservoir, the latter presents the resistance to flow of well. This chapter focuses on prediction of achievable fluid production rates from reservoirs with specified production well characteristics. The technique of analysis is called “Nodal analysis” (a Schlumberger patent). Calculation examples are illustrated with computer spreadsheets that are provided with this book.

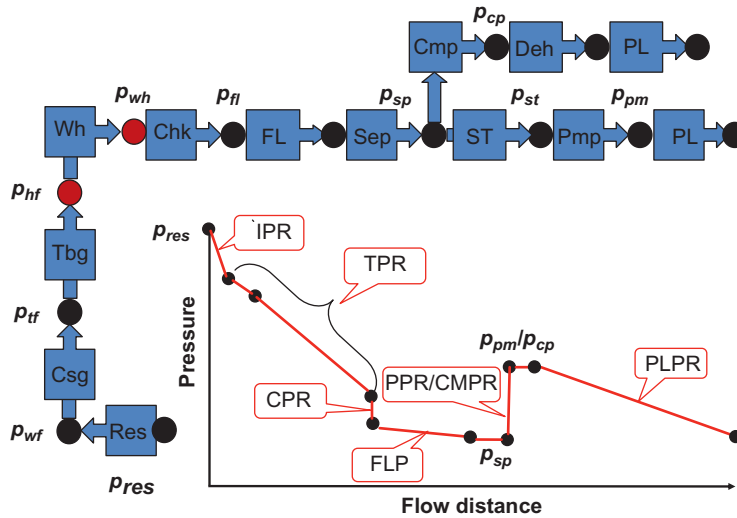
## 6.2 PRINCIPLE OF NODAL ANALYSIS

The system analysis for determination of fluid production rate and pressure is called “Nodal analysis” in petroleum engineering. It is widely used in petroleum production engineering to solve problems involving multiphase flow in wellbores and pipelines.

Fluid properties change with the location-dependent pressure and temperature in the oil and gas production system. To simulate the fluid flow in the system, it is necessary to “break” the system into discrete nodes that separate system elements (equipment sections). Fluid properties at the elements are evaluated locally.

Fig. 6.1 illustrates the nodes in an oil and gas production system and pressure trend along the flow path. Abbreviations for elements are defined as follows:

Res	= reservoir
Csg	= casing
Tbg	= tubing
Wh	= wellhead
Chk	= choke
FL	= flowline
Sep	= separator
ST	= stock tank
Pmp	= pump
PL	= Pipeline
Cmp	= compressor
Deh	= dehydrator



**FIGURE 6.1**  
Nodes in an oil and gas production system.

Flow performance relations of elements are denoted by:

- IPR = inflow performance relationship
- TPR = tubing performance relationship
- CPR = choke performance relationship
- FLP = flowline performance relationship
- PPR = pump performance relationship
- CMPR = compressor performance relationship
- PLPR = pipeline performance relationship

Pressures at nodes are denoted by:

- $p_{res}$  = reservoir pressure
- $p_{wf}$  = wellbore flowing pressure at bottom-hole
- $p_{hf}$  = wellhead flowing pressure
- $p_{wh}$  = wellhead flowing pressure
- $p_{fl}$  = flowline pressure
- $p_{sp}$  = separator pressure
- $p_{st}$  = stock tank pressure
- $p_{pm}$  = pump pressure
- $p_{cp}$  = compressor pressure

Nodal analysis is performed on the principle of pressure continuity, that is, there is only one unique pressure value at a given node regardless of whether the pressure is evaluated from the performance of upstream equipment or downstream equipment. The performance curve (pressure–rate relation) of upstream equipment is called “inflow performance curve”; the performance curve of downstream equipment is called “outflow performance curve.” The intersection of the two performance curves defines the operating point, that is, operating flow rate and pressure, at the specified node. The following section illustrates the principle of Nodal analysis with simplified tubing string geometries (i.e., single-diameter tubing strings) and single-phase flow in vertical wells.

## 6.3 DELIVERABILITY OF VERTICAL WELLS

This section demonstrates how to predict deliverability of gas and oil wells using bottom-hole and wellhead as the solution nodes. Different inflow and outflow performance relationships are considered. The materials are presented in the order of increasing complexity of inflow and outflow models.

### 6.3.1 ANALYSIS WITH THE BOTTOM-HOLE NODE

When the bottom-hole is used as a solution node in Nodal analysis, the inflow performance is the well inflow performance relationship (IPR) and the outflow performance is the tubing performance relationship (TPR), if the tubing shoe is set to the top of the pay zone. Well IPR can be established with different methods presented in Chapter 3, Reservoir Deliverability. TPR can be modeled with various approaches as discussed in Chapter 4, Wellbore Flow Performance.

Traditionally, Nodal analysis at the bottom-hole is carried out by plotting the IPR and TPR curves and graphically finding the solution at the intersection point of the two curves. With modern computer technologies, the solution can be computed quickly without plotting the curves, although the curves are still plotted for visual verification.

#### 6.3.1.1 Gas well

Consider the bottom-hole node of a gas well. If the IPR of the well is defined by

$$q_{sc} = C(\bar{p}^2 - p_{wf}^2)^n, \quad (6.1)$$

and if the outflow performance relationship of the node (i.e., the TPR) is defined by

$$p_{wf}^2 = \text{Exp}(s)p_{hf}^2 + \frac{6.67 \times 10^{-4} [\text{Exp}(s) - 1] f_M q_{sc}^2 \bar{z}^2 \bar{T}^2}{d_i^5 \cos \theta}, \quad (6.2)$$

then the operating flow rate  $q_{sc}$  and pressure  $p_{wf}$  at the bottom-hole node can be determined graphically by plotting Eqs. (6.1) and (6.2) and finding the intersection point.

The operating point can also be solved analytically by combining Eqs. (6.1) and (6.2). In fact, Eq. (6.1) can be rearranged as

$$p_{wf}^2 = \bar{p}^2 - \left(\frac{q_{sc}}{C}\right)^{\frac{1}{n}} \quad (6.3)$$

Substituting Eq. (6.3) into Eq. (6.2) yields

$$\begin{aligned} \bar{p}^2 - \left(\frac{q_{sc}}{C}\right)^{\frac{1}{n}} - \text{Exp}(s)p_{wf}^2 \\ - \frac{6.67 \times 10^{-4} [\text{Exp}(s) - 1] f_M q_{sc}^2 \bar{z}^2 \bar{T}^2}{D_i^5 \cos \theta} = 0, \end{aligned} \quad (6.4)$$

which can be solved with a numerical technique such as the Newton-Raphson iteration for gas flow rate  $q_{sc}$ . This computation can be performed automatically with the spreadsheet program *BottomHoleNodalGas.xls*.

**Example Problem 6.1** Suppose that a vertical well produces 0.71 specific gravity gas through a 2<sup>7</sup>/<sub>8</sub>-in. tubing set to the top of a gas reservoir at a depth of 10,000 ft. At tubing head, the pressure is 800 psia and the temperature is 150°F, whereas the bottom-hole temperature is 200°F. The relative roughness of tubing is about 0.0006. Calculate the expected gas production rate of the well using the following data for IPR:

Reservoir pressure:	2000 psia
IPR model parameter $C$ :	0.01 Mscf/d-psi <sup>2n</sup>
IPR model parameter $n$ :	0.8

**Solution** Example Problem 6.1 is solved with the spreadsheet program *BottomHoleNodalGas.xls*. Table 6.1 shows the appearance of the spreadsheet for the Input data and Result sections. It indicates that the expected gas flow rate is 1478 Mscf/d at a bottom-hole pressure of 1059 psia. The inflow and outflow performance curves plotted in Fig. 6.2 confirm this operating point.

### 6.3.1.2 Oil well

Consider the bottom-hole node of an oil well. As discussed in Chapter 3, Reservoir Deliverability, depending on reservoir pressure range, different IPR models can be used. For instance, if the reservoir pressure is above the bubble-point pressure, a straight-line IPR can be used:

$$q = J^*(\bar{p} - p_{wf}) \quad (6.5)$$

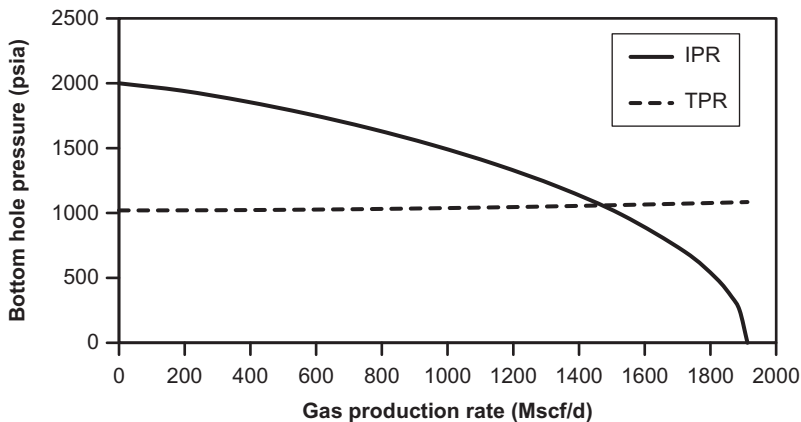
The outflow performance relationship of the node (i.e., the TPR) can be described by a different model. The simplest model would be Poettmann–Carpenter model defined by Eq. (6.8), that is,

$$p_{wf} = p_{wh} + \left(\bar{\rho} + \frac{\bar{k}}{\bar{\rho}}\right) \frac{L}{144} \quad (6.6)$$

where  $p_{wh}$  and  $L$  are tubing head pressure and well depth, respectively, then the operating flow rate  $q$  and pressure  $p_{wf}$  at the bottom-hole node can be determined graphically by plotting Eqs. (6.5) and (6.6) and finding the intersection point.



<b>Table 6.1 Result Given by BottomHoleNodalGas.xls for Example Problem 6.1</b>		
<i>BottomHoleNodalGas.xls</i>		
<i>Description:</i> This spreadsheet calculates gas well deliverability with bottom-hole node.		
<i>Instructions:</i> (1) Input your data in the Input data section; (2) click Solution button; (3) view results in table and in graph sheet "Plot."s		
<b>Input Data</b>		
Gas-specific gravity ( $\gamma_g$ ):	0.71	
Tubing inside diameter ( $D$ ):	2.259 in.	
Tubing relative roughness ( $e/D$ ):	0.0006	
Measured depth at tubing shoe ( $L$ ):	10,000 ft	
Inclination angle ( $\Theta$ ):	0°	
Wellhead pressure ( $p_{hf}$ ):	800 psia	
Wellhead temperature ( $T_f$ ):	150°F	
Bottom-hole temperature ( $T_{wf}$ ):	200°F	
Reservoir pressure ( $p \sim$ ):	2000 psia	
C-constant in back-pressure IPR model:	0.01 Mscf/d-psi <sup>2n</sup>	
n-exponent in back-pressure IPR model:	0.8	
<b>Solution</b>		
$T_{av} =$	635°R	
$Z_{av} =$	0.8626	
$s =$	0.486062358	
$e^s =$	1.62590138	
$f_M =$	0.017396984	
AOF =	1912.705 Mscf/d	
$q_{sc}$ (Mscf/d)	<i>IPR</i>	<i>TPR</i>
0	2000	1020
191	1943	1021
383	1861	1023
574	1764	1026
765	1652	1031
956	1523	1037
1148	1374	1044
1339	1200	1052
1530	987	1062
1721	703	1073
1817	498	1078
1865	353	1081
1889	250	1083
1913	0	1084
Operating flow rate	= 1470 Mscf/d	
Residual of objective function	= -0.000940747	
Operating pressure	= 1059 psia	



**FIGURE 6.2**

Nodal analysis for the Example Problem 6.1.

The operating point can also be solved analytically by combining Eqs. (6.5) and (6.6). In fact, substituting Eq. (6.6) into Eq. (6.5) yields

$$q = J^* \left[ \bar{p} - p_{wh} - \left( \bar{\rho} + \frac{\bar{k}}{\bar{\rho}} \right) \frac{L}{144} \right], \quad (6.7)$$

which can be solved with a numerical technique such as the Newton–Raphson iteration for liquid flow rate  $q$ . This computation can be performed automatically with the spreadsheet program *BottomHoleNodalOil-PC.xls*.

**Example Problem 6.2** For the data given in the following table, predict the operating point:

Reservoir pressure:	3000 psia
Tubing ID:	1.66 in.
Wellhead pressure:	500 psia
Productivity index above bubble point:	1 stb/d-psi
Producing gas-liquid ratio (GLR):	1000 scf/stb
Water cut (WC):	25%
Oil gravity:	30 °API
Water-specific gravity:	1.05 1 for fresh-water
Gas-specific gravity:	0.65 1 for air
N <sub>2</sub> content in gas:	0 mole fraction
CO <sub>2</sub> content in gas:	0 mole fraction
H <sub>2</sub> S content in gas:	0 mole fraction
Formation volume factor of oil:	1.2 rb/stb
Wellhead temperature:	100°F
Tubing shoe depth:	5000 ft
Bottom-hole temperature:	150°F

**Solution** Example Problem 6.2 is solved with the spreadsheet program *BottomHoleNodalOil-PC.xls*. Table 6.2 shows the appearance of the spreadsheet for the Input data and Result sections. It indicates that the expected oil flow rate is 1127 stb/d at a bottom-hole pressure of 1873 psia.

If the reservoir pressure is below the bubble-point pressure, Vogel’s IPR can be used

$$q = q_{\max} \left[ 1 - 0.2 \left( \frac{p_{wf}}{\bar{p}} \right) - 0.8 \left( \frac{p_{wf}}{\bar{p}} \right)^2 \right] \tag{6.8}$$

or

$$p_{wf} = 0.125 p_b \left[ \sqrt{21 - 80 \left( \frac{q}{q_{\max}} \right)} - 1 \right] \tag{6.9}$$

If the outflow performance relationship of the node (i.e., the TPR) is described by the Guo-Ghalambor model for mist flow in oil or gas wells, that is,

$$\begin{aligned} & b(P - P_{top}) + \frac{1 - 2bM}{2} \ln \left| \frac{(P + M)^2 + N}{(P_{top} + M)^2 + N} \right| \\ & M + \frac{b}{c} N - bM^2 \\ & - \frac{\phantom{M + \frac{b}{c} N - bM^2}}{\sqrt{N}} \\ & \times \left[ \tan^{-1} \left( \frac{P + M}{\sqrt{N}} \right) - \tan^{-1} \left( \frac{P_{top} + M}{\sqrt{N}} \right) \right] \\ & = aL(\cos \theta + d^2 e) \end{aligned} \tag{6.10}$$

substituting Eq. (6.9) into Eq. (6.10) will give an equation to solve for liquid production rate  $q$ . The equation can be solved with a numerical technique such as the Newton-Raphson iteration. This computation is performed automatically with the spreadsheet program *BottomHoleNodalOil-GG.xls*.

**Example Problem 6.3** For the data given in the following table, predict the operating point:

Reservoir pressure:	3000 psia
Total measured depth:	7000 ft
Average inclination angle:	20°
Tubing ID:	1.995 in.
Gas production rate:	1,000,000 scfd
Gas-specific gravity:	0.7 air = 1
Oil-specific gravity:	0.85 H <sub>2</sub> O = 1
Water cut:	30%
Water-specific gravity:	1.05 H <sub>2</sub> O = 1
Solid production rate:	1 ft <sup>3</sup> /d
Solid-specific gravity:	2.65 H <sub>2</sub> O = 1
Tubing head temperature:	100°F
Bottom-hole temperature:	160°F
Tubing head pressure:	300 psia
Absolute open flow (AOF):	2000 bbl/d

**Table 6.2 Result Given by BottomHoleNodalOil-PC.xls for Example Problem 6.2**

*BottomHoleNodalOil-PC.xls*

*Description:* This spreadsheet calculates the operating point using the Poettmann–Carpenter method with bottom-hole node.

*Instruction:* (1) Select a unit system; (2) update parameter values in the Input data section; (3) click Solution button; and (4) view result in the Solution section.

Input Data	U.S. Field Units	SI Units
Reservoir pressure:	3000 psia	
Tubing ID:	1.66 in.	
Wellhead pressure:	500 psia	
Productivity index above bubble point:	1 stb/d-psi	
Producing gas–liquid ratio (GLR):	1000 scf/stb	
Water cut:	25%	
Oil gravity:	30 °API	
Water-specific gravity:	1.05, 1 for water	
Gas-specific gravity:	0.65, 1 for air	
N <sub>2</sub> content in gas:	0 mole fraction	
CO <sub>2</sub> content in gas:	0 mole fraction	
H <sub>2</sub> S content in gas:	0 mole fraction	
Formation volume factor of oil:	1.2 rb/stb	
Wellhead temperature:	100°F	
Tubing shoe depth:	5000 ft	
Bottom-hole temperature:	150°F	
<b>Solution</b>		
Oil-specific gravity	= 0.88, 1 for water	
Mass associated with 1 stb of oil	= 495.66 lb	
Solution–gas ratio at wellhead	= 78.42 scf/stb	
Oil formation volume factor at wellhead	= 1.04 rb/stb	
Volume associated with 1 stb of oil at wellhead	= 45.12 cf	
Fluid density at wellhead	= 10.99 lb/cf	
Solution gas–oil ratio at bottom-hole	= 339.39 scf/stb	
Oil formation volume factor at bottom-hole	= 1.18 rb/stb	
Volume associated with 1 stb of oil at bottom-hole	= 16.56 cf	
Fluid density at bottom-hole	= 29.94 lb/cf	
The average fluid density	= 20.46 lb/cf	
Inertial force ( $D\rho v$ )	= 44.63 lb/day-ft	
Friction factor	= 0.0084	
Friction term	= 390.50 (lb/cf) <sup>2</sup>	
Error in liquid rate	= 0.00 stb/d	
Bottom-hole pressure	= 1873 psia	
Liquid production rate:	= 1127 stb/d	

**Solution** Example Problem 6.3 is solved with the spreadsheet program *BottomHoleNodalOil-GG.xls*. Table 6.3 shows the appearance of the spreadsheet for the Input data and Result sections. It indicates that the expected oil flow rate is 1400 stb/d at a bottom-hole pressure of 1500 psia.

If the reservoir pressure is above the bubble-point pressure, but the flowing bottom-hole pressure is in the range of below bubble-point pressure, the generalized Vogel's IPR can be used:

$$q = q_b + q_v \left[ 1 - 0.2 \left( \frac{P_{wf}}{P_b} \right) - 0.8 \left( \frac{P_{wf}}{P_b} \right)^2 \right] \quad (6.11)$$

If the outflow performance relationship of the node (i.e., TPR) is described by Hagedorn-Brown correlation, Eq. (4.47) can be used for generating the TPR curve. Combining Eqs. (6.11) and Eq. (4.47) can be solved with a numerical technique such as the Newton–Raphson iteration for liquid flow rate  $q$ . This computation can be performed automatically with the spreadsheet program *BottomHoleNodalOil-HB.xls*.

**Example Problem 6.4** For the data given in the following table, predict the operating point:

Depth:	9850 ft
Tubing inner diameter:	1.995 in.
Oil gravity:	45 °API
Oil viscosity:	2 cp
Production GLR:	500 scf/bbl
Gas-specific gravity:	0.7 air = 1
Flowing tubing head pressure:	450 psia
Flowing tubing head temperature:	80°F
Flowing temperature at tubing shoe:	180°F
Water cut:	10%
Reservoir pressure:	5000 psia
Bubble-point pressure:	4000 psia
Productivity index above bubble point:	1.5 stb/d-psi

**Solution** Example Problem 6.4 is solved with the spreadsheet program *BottomHoleNodalOil-HB.xls*. Table 6.4 shows the appearance of the spreadsheet for the Input data and Result sections. Fig. 6.3 indicates that the expected gas flow rate is 2200 stb/d at a bottom-hole pressure of 3500 psia.

### 6.3.2 ANALYSIS WITH WELLHEAD NODE

When the wellhead is used as a solution node in Nodal analysis, the inflow performance curve is the “wellhead performance relationship” (WPR), which is obtained by transforming the IPR to wellhead through the TPR. The outflow performance curve is the wellhead choke performance relationship (CPR). Some TPR models are presented in Chapter 4, Wellbore Flow Performance. CPR models are discussed in Chapter 5, Choke Performance.

**Table 6.3 Result Given by BottomHoleNodalOil-GG.xls for Example Problem 6.2**

*BottomHoleNodalOil-GG.xls*

*Description:* This spreadsheet calculates flowing bottom-hole pressure based on tubing head pressure and tubing flow performance using the Guo-Ghalambor method.

*Instruction:* (1) Select a unit system; (2) update parameter values in the Input data section; (3) click Result button; and (4) view result in the Result section.

Input Data	U.S. Field Units	SI Units
Reservoir pressure:	3000 psia	
Total measured depth:	7000 ft	
Average inclination angle:	20°	
Tubing ID:	1.995 in.	
Gas production rate:	1,000,000 scfd	
Gas-specific gravity:	0.7 air = 1	
Oil-specific gravity:	0.85 H <sub>2</sub> O = 1	
Water cut:	30%	
Water-specific gravity:	1.05 H <sub>2</sub> O = 1	
Solid production rate:	1 ft <sup>3</sup> /d	
Solid-specific gravity:	2.65 H <sub>2</sub> O = 1	
Tubing head temperature:	100°F	
Bottom-hole temperature:	160°F	
Tubing head pressure:	300 psia	
Absolute open flow (AOF):	2000 bbl/d	
Pipe roughness:	0.0018 in.	
<b>Solution</b>		
$A$	= 3.1243196 in. <sup>2</sup>	
$D$	= 0.16625 ft	
$T_{av}$	= 622°R	
$\cos(\theta)$	= 0.9397014	
$2\varepsilon/d$	= 0.0018045	
$f_M$	= 0.0191448	
$a$	= 0.0001955	
$b$	= 3.274E-06	
$c$	= 1,280,343	
$d$	= 4.1937058	
$e$	= 0.0019047	
$M$	= 9895.3756	
$N$	= 2.923E + 09	
Liquid production rate, $q$	= 1400 bbl/d	
Bottom-hole pressure, $p_{wf}$	= 1500 psia	

Table 6.4 Solution Given by BottomHoleNodalOil-HB.xls			
<i>BottomHoleNodalOil-HB.xls</i>			
<p><i>Description:</i> This spreadsheet calculates operating point using the Hagedorn-Brown correlation.  <i>Instruction:</i> (1) Select a unit system; (2) update parameter values in the Input data section; (3) click Solution button; and (4) view result in the Result section and charts.</p>			
Input Data	U.S. Field Units	SI Units	
Depth ( $D$ ):	9850 ft		
Tubing inner diameter ( $d_{ti}$ ):	1.995 in.		
Oil gravity (API):	45 °API		
Oil viscosity ( $\mu_o$ ):	2 cp		
Production GLR (GLR):	500 scf/bbl		
Gas-specific gravity ( $\gamma_g$ ):	0.7 air = 1		
Flowing tubing head pressure ( $p_{hf}$ ):	450 psia		
Flowing tubing head temperature ( $t_{hf}$ ):	80°F		
Flowing temperature at tubing shoe ( $t_{wf}$ ):	180°F		
Water cut:	10%		
Reservoir pressure ( $p_e$ ):	5000 psia		
Bubble-point pressure ( $p_b$ ):	4000 psia		
Productivity index above bubble point ( $J^*$ ):	1.5 stb/d-psi		
Solution			
US Field units:			
$q_b$	= 1500		
$q_{max}$	= 4833		
	$q$ (stb/d)	$p_{wf}$ (psia)	
		IPR	TPR
	0	4908	
	537	4602	2265
	1074	4276	2675
	1611	3925	3061
	2148	3545	3464
	2685	3125	3896
	3222	2649	4361
	3759	2087	4861
	4296	1363	5397
	4833	0	5969

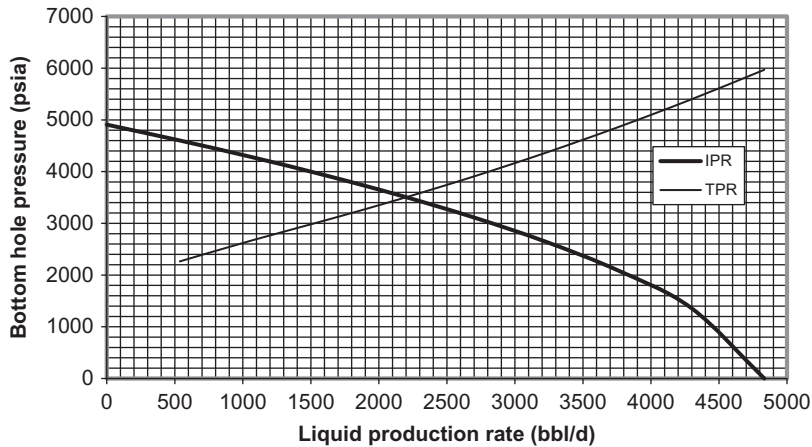


FIGURE 6.3

Nodal analysis for Example Problem 6.4.

Nodal analysis with wellhead being a solution node is carried out by plotting the WPR and CPR curves and finding the solution at the intersection point of the two curves. Again, with modern computer technologies, the solution can be computed quickly without plotting the curves, although the curves are still plotted for verification.

### 6.3.2.1 Gas well

If the IPR of a well is defined by Eq. (6.1) and the TPR is represented by Eq. (6.2), substituting Eq. (6.2) into Eq. (6.1) gives

$$q_{sc} = C \left[ \bar{p}^2 - \left( \text{Exp}(s) p_{hf}^2 + \frac{6.67 \times 10^{-4} [\text{Exp}(s) - 1] f_M q_{sc}^2 \bar{z}^2 \bar{T}^2}{d_i^5 \cos \theta} \right) \right]^n, \quad (6.12)$$

which defines a relationship between wellhead pressure  $p_{hf}$  and gas production rate  $q_{sc}$ , that is, WPR. If the CPR is defined by Eq. (6.8), that is,

$$q_{sc} = 879 C_D A p_{hf} \sqrt{\left( \frac{k}{\gamma_g Y_{up}} \right) \left( \frac{2}{k+1} \right)^{\frac{k+1}{k-1}}}, \quad (6.13)$$

then the operating flow rate  $q_{sc}$  and pressure  $p_{hf}$  at the wellhead node can be determined graphically by plotting Eqs. (6.12) and (6.13) and finding the intersection point.

The operating point can also be solved numerically by combining Eqs. (6.12) and (6.13). In fact, Eq. (6.13) can be rearranged as

$$p_{hf} = \frac{q_{sc}}{879 C_D A \sqrt{\left( \frac{k}{\gamma_g T_{up}} \right) \left( \frac{2}{k+1} \right)^{\frac{k+1}{k-1}}}}. \quad (6.14)$$



Substituting Eq. (6.14) into Eq. (6.12) gives

$$q_{sc} = C \left[ \bar{p}^2 - \left( \text{Exp}(s) \left[ \frac{q_{sc}}{879 C_D A \sqrt{\left(\frac{k}{\gamma_g T_{up}}\right) \left(\frac{2}{k+1}\right)^{\frac{k+1}{k}}}} \right]^2 + \frac{6.67 \times 10^{-4} [\text{Exp}(s) - 1] f_M q_{sc}^2 \bar{z}^2 T^2}{d_i^5 \cos \theta} \right) \right]^n, \quad (6.15)$$

which can be solved numerically for gas flow rate  $q_{sc}$ . This computation can be performed automatically with the spreadsheet program *WellheadNodalGas-SonicFlow.xls*.

**Example Problem 6.5** Use the data given in the following table to estimate gas production rate of a gas well:

Gas-specific gravity:	0.71
Tubing inside diameter:	2.259 in.
Tubing wall relative roughness:	0.0006
Measured depth at tubing shoe:	10,000 ft
Inclination angle:	0°
Wellhead choke size:	161/644 in.
Flowline diameter:	2 in.
Gas-specific heat ratio:	1.3
Gas viscosity at wellhead:	0.01 cp
Wellhead temperature:	150°F
Bottom-hole temperature:	200°F
Reservoir pressure:	2000 psia
C-constant in IPR model:	0.01 Mscf/ d-psi <sup>2n</sup>
n-exponent in IPR model:	0.8

**Solution** Example Problem 6.5 is solved with the spreadsheet program *WellheadNodalGas-SonicFlow.xls*. Table 6.5 shows the appearance of the spreadsheet for the Input data and Result sections. It indicates that the expected gas flow rate is 1478 Mscf/d at a bottom-hole pressure of 1050 psia.

### 6.3.2.2 Oil well

As discussed in Chapter 3, Reservoir Deliverability, depending on reservoir pressure range, different IPR models can be used. For instance, if the reservoir pressure is above the bubble-point pressure, a straight-line IPR can be used:

$$q = J^* (\bar{p} - p_{wf}) \quad (6.16)$$

If the TPR is described by the Poettmann–Carpenter model defined by Eq. (6.8), that is,

$$p_{wf} = p_{wh} + \left( \bar{\rho} + \frac{\bar{k}}{\bar{\rho}} \right) \frac{L}{144} \quad (6.17)$$

substituting Eq. (6.17) into Eq. (6.16) gives

$$q = J^* \left[ \bar{p} - \left( p_{wh} + \left( \bar{\rho} + \frac{\bar{k}}{\bar{\rho}} \right) \frac{L}{144} \right) \right], \quad (6.18)$$

<b>Table 6.5 Solution Given by WellheadNodalGas-SonicFlow.xls</b>			
<i>WellheadNodalGas-SonicFlow.xls</i>			
<i>Description:</i> This spreadsheet calculates well deliverability with wellhead node.			
<i>Instructions:</i> (1) Input your data in the Input data section; (2) Click Solution button to get results; and (3) View results in table and in the plot graph sheet.			
<b>Input Data</b>			
Gas-specific gravity ( $\gamma_g$ ):	0.71		
Tubing inside diameter ( $D$ ):	2.259 in.		
Tubing relative roughness ( $\varepsilon/D$ ):	0.0006		
Measured depth at tubing shoe ( $L$ ):	10,000 ft		
Inclination angle ( $\theta$ ):	0°		
Wellhead choke size ( $D_{ck}$ ):	16 1/64 in.		
Flowline diameter ( $D_{fl}$ ):	2 in.		
Gas-specific heat ratio ( $k$ ):	1.3		
Gas viscosity at wellhead ( $\mu_g$ ):	0.01 cp		
Wellhead temperature ( $T_{hf}$ ):	120°F		
Bottom-hole temperature ( $T_{wf}$ ):	180°F		
Reservoir pressure ( $\bar{p}$ ):	2000 psia		
C-constant in back-pressure IPR model:	0.01 Mscf/d-psi <sup>2n</sup>		
n-exponent in back-pressure IPR model:	0.8		
<b>Solution</b>			
$T_{av}$	= 610°R		
$Z_{av}$	= 0.8786		
$s$	= 0.4968		
$e^s$	= 1.6434		
$f_m$	= 0.0174		
AOF	= 1913 Mscf/d		
$D_{ck}/D_{fi}$	= 0.125		
$Re$	= 8,348,517		
$C_{ck}$	= 1.3009 in. <sup>2</sup>		
$A_{ck}$	= 0.0490625		
	$q_{sc}$ (Mscf/d)	WPR	CPR
	0	1600	0
	191	1554	104
	383	1489	207
	574	1411	311
	765	1321	415
	956	1218	518
	1148	1099	622
	1339	960	726
	1530	789	830

**Table 6.5 Solution Given by WellheadNodalGas-SonicFlow.xls Continued**

	1721	562	933
	1817	399	985
	1865	282	1011
	1889	200	1024
	1913	1	1037
Operating flow rate = 1470 Mscf/d			
Operating pressure = 797 psia			

which describes inflow for the wellhead node and is called the WPR. If the CPR is given by Eq. (6.12), that is,

$$p_{wh} = \frac{CR^m q}{S^n}, \quad (6.19)$$

the operating point can be solved analytically by combining Eqs. (6.18) and (6.19). In fact, substituting Eq. (6.19) into Eq. (6.18) yields

$$q = J^* \left[ \bar{p} - \left( \frac{CR^m q}{S^n} + \left( \bar{p} + \frac{\bar{k}}{\bar{\rho}} \right) \frac{L}{144} \right) \right], \quad (6.20)$$

which can be solved with a numerical technique. Because the solution procedure involves loop-in-loop iterations, it cannot be solved in MS Excel in an easy manner. A special computer program is required. Therefore, a computer-assisted graphical solution method is used in this text.

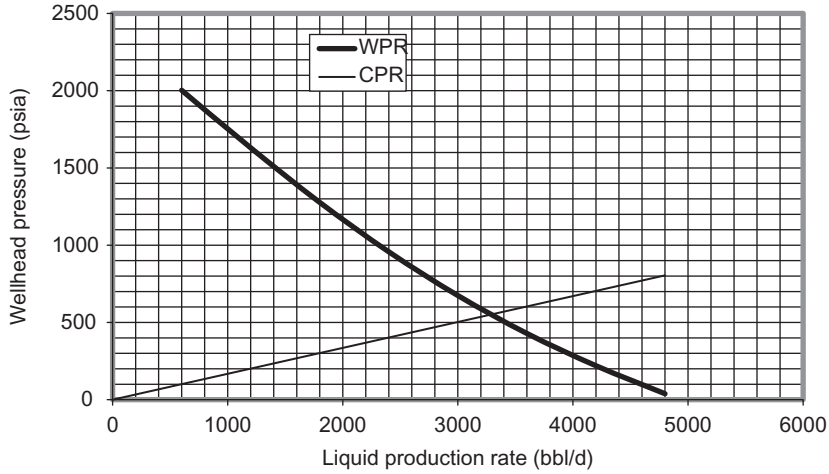
The operating flow rate  $q$  and pressure  $p_{wh}$  at the wellhead node can be determined graphically by plotting Eqs. (6.18) and (6.19) and finding the intersection point. This computation can be performed automatically with the spreadsheet program *WellheadNodalOil-PC.xls*.

**Example Problem 6.6** Use the following data to estimate the liquid production rate of an oil well:

Reservoir pressure:	6000 psia
Tubing ID:	3.5 in.
Choke size:	64 1/64 in.
Productivity index above bubble point:	1 stb/d-psi
Producing gas-liquid ratio (GLR):	1000 scf/stb
Water cut:	25%
Oil gravity:	30 °API
Water-specific gravity:	1.05 1 for freshwater
Gas-specific gravity:	0.65 1 for air
Choke constant:	10
Choke GLR exponent:	0.546
Choke-size exponent:	1.89
Formation volume factor of oil:	1 rb/stb
Wellhead temperature:	100°F
Tubing shoe depth:	12,000 ft
Bottom-hole temperature:	150°F

**Solution** Example Problem 6.6 is solved with the spreadsheet program *WellheadNodalOil-PC.xls*. Table 6.6 shows the appearance of the spreadsheet for the Input data and Result sections. The inflow and outflow performance curves are plotted in Fig. 6.4, which indicates that the expected oil flow rate is 3280 stb/d at a wellhead pressure of 550 psia.

Table 6.6 Solution Given by WellheadNodalOil-PC.xls				
<i>WellheadNodalOil-PC.xls</i>				
<i>Description:</i> This spreadsheet calculates operating point using the Poettmann-Carpenter method with wellhead node.				
<i>Instruction:</i> (1) Select a unit system; (2) update parameter values in the Input data section; (3) click Solution button; and (4) view result in the Solution section and charts.				
Input Data	U.S. Field Units	SI Units		
Reservoir pressure:	6000 psia			
Tubing ID:	3.5 in.			
Choke size:	64 1/64 in.			
Productivity index above bubble point:	1 stb/d-psi			
Producing gas–liquid ratio:	1000 scf/stb			
Water cut:	25%			
Oil gravity:	30 °API			
Water-specific gravity:	1.05 1 for fresh-water			
Gas-specific gravity:	0.65 1 for air			
Choke constant:	10			
Choke gas–liquid ratio exponent:	0.546			
Choke-size exponent:	1.89			
Formation volume factor for water:	1 rb/stb			
Wellhead temperature:	100°F			
Tubing shoe depth:	12,000 ft			
Bottom-hole temperature:	150°F			
<b>Solution:</b>				
	$q$ (stb/d)	$p_{wf}$ (psia)	$p_{wh}$ (psia) WPR	CPR
	0	6000		0
	600	5400	2003	101
	1200	4800	1630	201
	1800	4200	1277	302
	2400	3600	957	402
	3000	3000	674	503
	3600	2400	429	603
	4200	1800	220	704
	4800	1200	39	805



**FIGURE 6.4**

Nodal analysis for Example Problem 6.6.

If the reservoir pressure is below the bubble-point pressure, Vogel’s IPR can be rearranged to be

$$p_{wf} = 0.125\bar{p} \left[ \sqrt{81 - 80 \left( \frac{q}{q_{max}} \right)} - 1 \right] \tag{6.21}$$

If the TPR is described by the Guo–Ghalambor model for mist flow in oil and gas wells, that is,

$$\begin{aligned} & b(P - P_{top}) + \frac{1 - 2bM}{2} \ln \left| \frac{(P + M)^2 + N}{(P_{top} + M)^2 + N} \right| \\ & - \frac{M + \frac{b}{c}N - bM^2}{\sqrt{N}} \\ & \times \left[ \tan^{-1} \left( \frac{P + M}{\sqrt{N}} \right) - \tan^{-1} \left( \frac{P_{top} + M}{\sqrt{N}} \right) \right] \\ & = aL(\cos \theta + d^2e) \end{aligned} \tag{6.22}$$

and the CPR is given by Eq. (6.12), that is,

$$p_{hf} = \frac{CR^m q}{S^u}, \tag{6.23}$$

solving Eqs. (6.21)–(6.23) simultaneously will give production rate  $q$  and wellhead pressure  $p_{hf}$ . The solution procedure has been coded in the spreadsheet program *WellheadNodalOil-GG.xls*.

**Example Problem 6.7** Use the following data to estimate the liquid production rate of an oil well:

Choke size:	64 1/64 in.
Reservoir pressure:	3000 psia
Total measured depth:	7000 ft
Average inclination angle:	20°
Tubing ID:	1.995 in.
Gas production rate:	1,000,000 scfd
Gas-specific gravity:	0.7 air = 1
Oil-specific gravity:	0.85 H <sub>2</sub> O = 1
Water cut:	30%
Water-specific gravity:	1.05 H <sub>2</sub> O = 1
Solid production rate:	1 ft <sup>3</sup> /d
Solid-specific gravity:	2.65 H <sub>2</sub> O = 1
Tubing head temperature:	100°F
Bottom-hole temperature:	160°F
Absolute open flow (AOF):	2000 bbl/d
Choke flow constant:	10
Choke GLR exponent:	0.546
Choke-size exponent:	1.89

**Solution** Example Problem 6.7 is solved with the spreadsheet program *WellheadNodalOil-GG.xls*. Table 6.7 shows the appearance of the spreadsheet for the *Data Input* and *Result* sections. It indicates that the expected oil flow rate is 1494 stb/d at a wellhead pressure of 201 psia.

If the reservoir pressure is above the bubble-point pressure, but the flowing bottom-hole pressure is in the range of below bubble-point pressure, the generalized Vogel's IPR can be used:

$$q = q_b + q_v \left[ 1 - 0.2 \left( \frac{p_{wf}}{p_b} \right) - 0.8 \left( \frac{p_{wf}}{p_b} \right)^2 \right] \quad (6.24)$$

Hagedorn–Brown correlation, Eq. (6.27), can be used for translating the IPR to the WPR. Again, if the CPR is given by Eq. (6.12), that is,

$$p_{hf} = \frac{CR^m q}{S^n}, \quad (6.25)$$

solving Eqs. (6.24), (4.27), and (6.25) simultaneously will give production rate  $q$  and wellhead pressure  $p_{hf}$ . Because the solution procedure involves loop-in-loop iterations, it cannot be solved in MS Excel in an easy manner. A special computer program is required. Therefore, a computer-assisted graphical solution method is used in this text.

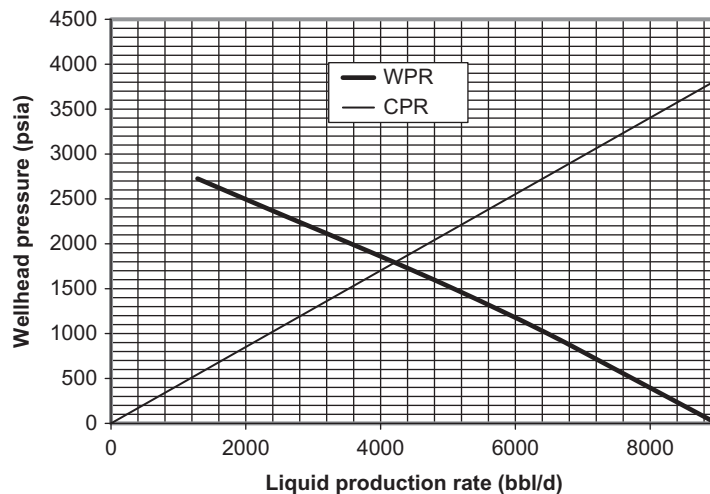
The operating flow rate  $q$  and pressure  $p_{hf}$  at the wellhead node can be determined graphically. This computation can be performed automatically with the spreadsheet program *WellheadNodalOil-HB.xls*.

Table 6.7 Solution Given by WellheadNodalOil-GG.xls		
<i>WellheadNodalOil-GG.xls</i>		
<i>Description:</i> This spreadsheet calculates operating point based on CPR and Guo-Ghalambor TPR.		
<i>Instruction:</i> (1) Select a unit system; (2) update parameter values in the Input data section; (3) click Solution button; and (4) view result in the Solution section.		
Input Data	U.S. Field Units	SI Units
Choke size:	64 1/64 in.	
Reservoir pressure:	3000 psia	
Total measured depth:	7000 ft	
Average inclination angle:	20°	
Tubing ID:	1.995 in.	
Gas production rate:	1,000,000 scfd	
Gas-specific gravity:	0.7 air = 1	
Oil-specific gravity:	0.85 H <sub>2</sub> O = 1	
Water cut:	30%	
Water-specific gravity:	1.05 H <sub>2</sub> O = 1	
Solid production rate:	1 ft <sup>3</sup> /d	
Solid-specific gravity:	2.65 H <sub>2</sub> O = 1	
Tubing head temperature:	100°F	
Bottom-hole temperature:	160°F	
Absolute open flow (AOF):	2000 bbl/d	
Choke flow constant:	10	
Choke GLR exponent:	0.546	
Choke-size exponent:	1.89	
Pipe roughness ( $\epsilon$ ):	0.0018 in.	
Solution		
$A$	= 3.1243196 in. <sup>2</sup>	
$D$	= 0.16625 ft	
$T_{av}$	= 622°R	
$\cos(\theta)$	= 0.9397014	
$2\epsilon/d$	= 0.0018045	
$f_M$	= 0.0191448	
$a$	= 0.0001965	
$b$	= 3.313E-06	
$c$	= 1349785.1	
$d$	= 4.4742645	
$e$	= 0.0019047	
$M$	= 11,080.32	
$N$	= 3.22E + 09	
Liquid production rate, $q$	= 1494 bbl/d	237 m <sup>3</sup> /d
Bottom-hole pressure, $p_{wf}$	= 1354 psia	9.21 MPa
Wellhead pressure, $p_{hf}$	= 201 psia	1.37 MPa

**Example Problem 6.8** For the following data, predict the operating point:

Depth:	7000 ft
Tubing inner diameter:	3.5 in.
Oil gravity:	45 °API
Oil viscosity:	0.5 cp
Production gas–liquid ratio (GLR):	500 scf/bbl
Gas-specific gravity:	0.7 air = 1
Choke size:	32 1/64 in.
Flowing tubing head temperature:	80°F
Flowing temperature at tubing shoe:	150°F
Water cut:	10%
Reservoir pressure:	4000 psia
Bubble-point pressure:	3800 psia
Productivity index above bubble point:	5 stb/d-psi
Choke flow constant:	10.00
Choke GLR exponent:	0.546
Choke-size exponent:	1.89

**Solution** Example Problem 6.8 is solved with the spreadsheet program *WellheadNodalOil-HB.xls*. Figure 6.5 indicates that the expected oil flow rate is 4200 stb/d at a wellhead pressure of 1800 psia.



**FIGURE 6.5**

Nodal analysis for Example Problem 6.8.



Deliverability of fractured vertical wells can be predicted with the same method as that for the non-fractured wells except that the productivity index  $J^*$  should be estimated by Eq. (3.12) for oil wells and the  $C$  and  $n$  values should be estimated by Eq. (3.13) for gas wells.

## 6.4 DELIVERABILITY OF HORIZONTAL WELLS

Deliverability of horizontal wells depends on well completion method, namely non-fractured and hydraulically fractured wells. Well IPR curve is constructed with different models described in Chapter 3, Reservoir Deliverability. Well TPR curve is generated for multiphase flow in deviated well trajectory.

### 6.4.1 NON-FRACTURED HORIZONTAL WELLS

The initial deliverability of non-fractured horizontal wells may be estimated on the basis of IPR models presented in Chapter 3, Reservoir Deliverability. For oil wells, the IPR model is

$$q = \frac{k_H h (p_e - p_{wf})}{141.2 B \mu \left\{ \ln \left[ \frac{a + \sqrt{a^2 - (L/2)^2}}{L/2} \right] + \frac{I_{ani} h}{L} \ln \left[ \frac{I_{ani} h}{r_w (I_{ani} + 1)} \right] + s \right\}} F_o \quad (6.26)$$

For gas wells, the IPR model is

$$q_g = \frac{k_H h [m(p_e) - m(p_{wf})]}{1424 T \left\{ \ln \left[ \frac{a + \sqrt{a^2 - (L/2)^2}}{L/2} \right] + \frac{I_{ani} h}{L} \ln \left[ \frac{I_{ani} h}{r_w (I_{ani} + 1)} \right] + s + D q_g \right\}} F_g \quad (6.27)$$

where  $p_{wf}$  is the flowing pressure at the heel of the horizontal well. Oil well TPR curve is constructed by Hagedorn-Brown correlation for multiphase flow in deviated well trajectory. Gas well TPR curve is constructed by the Average-Temperature-Average-Z-Factor Method in deviated well trajectory.

Guo (2010) showed that neglecting the frictional pressure loss in the horizontal wellbore can result in very significant over-prediction of well productivity within large ranges of variable values. The amount of the over-prediction increases nonlinearly with the ratio of horizontal wellbore pressure drop to production drawdown. When the wellbore pressure drop reaches to 18% of production drawdown at heel, the production rate can be over-predicted by 10%. The effect of frictional pressure loss in the horizontal wellbore on well productivity is more pronounced for small-diameter, long horizontal wells in high-permeability, thick oil and gas reservoirs. Compared to reservoir permeability, hole diameter, and hole length, the pay zone thickness of oil and gas reservoirs has less effect on prediction of well productivity. The effect of wellbore flow friction on well deliverability is considered in the correction factors  $F_o$  and  $F_g$ . Guo et al. (2008) provides a complete set of equations for determining these factors. Computer programs *Correction Factor Fo.xls* and *Correction Factor Fg.xls* are used in this section.

**Example Problem 6.9** The following data are given for a horizontal oil well. Predict the initial well production rate:

Pay zone thickness ( $h$ ):	48 ft
Effective horizontal permeability ( $k_h$ ):	68 md
Effective vertical permeability ( $k_v$ ):	17 md
Reservoir pressure ( $p_r$ ):	4053 psia
Oil formation volume factor ( $B_o$ ):	1.1 rb/stb
Well drainage area ( $A$ ):	640 acres
Horizontal wellbore length ( $L$ ):	2000 ft
Radius of curvature (ROC):	1000 ft
Total measured well depth ( $H$ ):	8500 ft
Tubing inner diameter ( $d$ ):	2.441 in.
Oil gravity (API):	42 °API
Oil viscosity ( $\mu_o$ ):	1.5 cp
Producing GLR (GLR):	550 scf/bbl
Gas-specific gravity ( $\gamma_g$ ):	0.7 air = 1
Flowing tubing head pressure ( $p_{hf}$ ):	500 psia
Flowing tubing head temperature ( $t_{hf}$ ):	125°F
Flowing temperature at tubing shoe ( $t_{wf}$ ):	210°F
Water cut (WC):	10%
Oil-gas interfacial tension ( $\sigma$ ):	30 dynes/cm
Specific gravity of water ( $\gamma_w$ ):	1.07
Wellbore radius ( $r_w$ ):	0.328 ft

Hole inclination data are as follows:

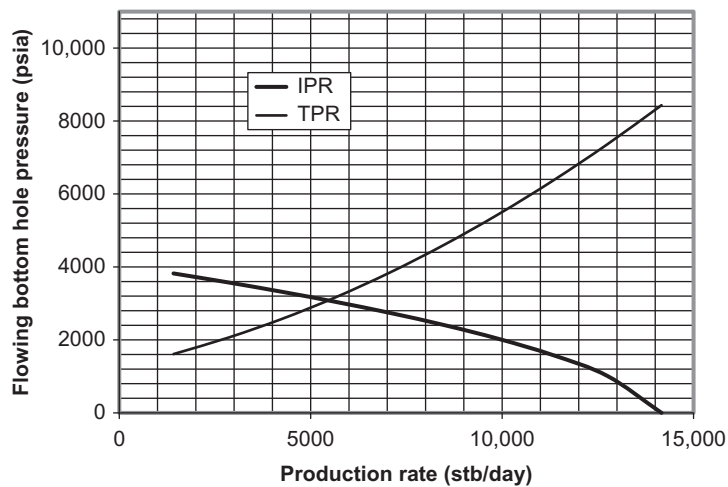
Depth (ft)	Inclination (°)
0	0
293	0
586	0
879	0
1172	0
1466	0
1759	0
2052	0
2345	0
2638	0
2931	0
3224	0
3517	0
3810	0

<i>Continued</i>	
Depth (ft)	Inclination (°)
4103	0
4397	0
4690	0
4983	2
5276	15
5569	30
5862	45
6155	60
6448	75
6741	90
7034	90
7328	90
7621	90
7914	90
8207	90
8500	90

**Solution** Example Problem 6.9 is solved with spreadsheet programs. Assuming 4 in. completion string, program *Correction Factor Fo.xls* gives  $F_o = 0.9$ . Program *Pseudo-Steady-2Phase Horizontal Well Production.xls* outputs a Nodal analysis plot shown in Fig. 6.6 which indicates that the expected oil flow rate is 5500 stb/d at a bottom-hole pressure of 3100 psia.

**Example Problem 6.10** The following data are given for a horizontal gas well. Predict the initial well production rate:

Pay zone thickness ( $h$ ):	20 ft
Horizontal permeability ( $k_h$ ):	1 md
Vertical permeability ( $k_v$ ):	0.2 md
Reservoir pressure ( $p_e$ ):	3458 psia
Reservoir temperature ( $T$ ):	200°F
Gas-specific gravity ( $\gamma_g$ ):	0.7 air = 1
Gas viscosity ( $\mu_g$ ):	0.02 cp
Drainage area ( $A$ ):	320 acres
Wellbore radius ( $r_w$ ):	0.328 ft
Horizontal wellbore length ( $L$ ):	1000 ft
Total well depth (TD):	9000 ft
Kick-off-point (KOP):	6000 ft
Tubing diameter ( $d$ ):	2.441 in
Tubing relative roughness ( $e/d$ ):	0.0006
Tubing head pressure ( $p_{hf}$ ):	1500 psia
Tubing head temperature ( $T_{hf}$ ):	150°F



**FIGURE 6.6**

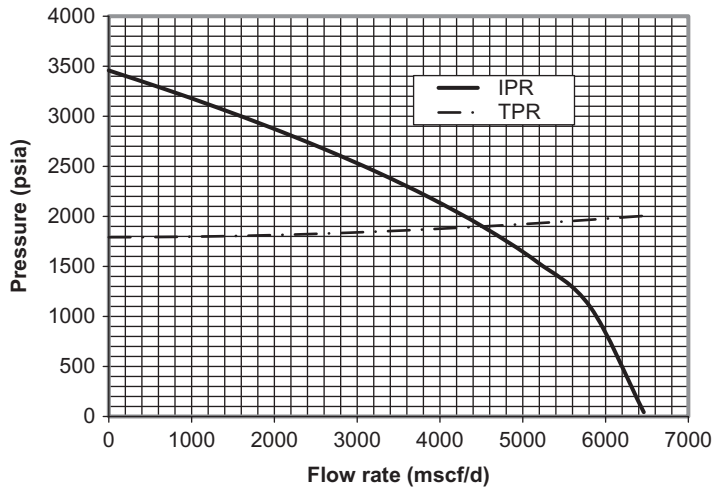
Nodal analysis for Example Problem 6.9.

Well deviation data are given as follows:

Measured Depth (ft)	Inclination (°)
0	0.00
300	0.00
600	0.00
900	0.00
1200	0.00
1500	0.00
1800	0.00
2100	0.00
2400	0.00
2700	0.00
3000	0.00
3300	0.00
3600	0.00
3900	0.00
4200	0.00
4500	0.00
4800	0.00
5100	0.00

<i>Continued</i>	
Measured Depth (ft)	Inclination (°)
5400	0.00
5700	0.00
6000	0.00
6300	5.00
6600	15.00
6900	30.00
7200	45.00
7500	60.00
7800	75.00
8100	90.00
8400	90.00
8700	90.00
9000	90.00

**Solution** Example Problem 6.10 is solved with spreadsheet programs. Assuming 4 in. completion string, program *Correction Factor Fo.xls* gives  $F_g = 1$ . Program *Horizontal Dry Gas Well Production.xls* outputs a Nodal analysis plot shown in Fig. 6.7 which indicates that the expected oil flow rate is 4500 Mscf/d at a bottom-hole pressure of 1900 psia.



**FIGURE 6.7**

Nodal analysis for Example Problem 6.10.

### 6.4.2 SINGLE-FRACTURED HORIZONTAL WELLS

Deliverability of single-fractured horizontal wells can be predicted with the same method as for the non-fractured wells except that the inflow equation should be changed to Eq. (3.12) for oil wells and the  $C$  and  $n$  values should be estimated by Eq. (3.13) for gas wells. Hagedorn-Brown correlation can be employed to generate oil well TPR. Guo-Ghalambor's model can be utilized in a piecewise manner to construct gas well TPR.

### 6.4.3 MULTI-STAGE-FRACTURED HORIZONTAL WELLS

Deliverability of multi-stage-fractured horizontal well is controlled by many factors including the scale of stage-fracturing and the number of stages. A numerical reservoir simulator linked to a wellbore hydraulics simulator is required to better predict well deliverability. This section provides an analytical, approximate approach to solving the problem. This approach uses the IPR model presented by Eq. (3.27) for oil wells and Eq. (3.34) for gas wells. Hagedorn-Brown correlation can be employed to generate oil well TPR. Guo-Ghalambor's model for mist flow can be utilized in a piecewise manner to construct gas well TPR.

**Example Problem 6.11** The following data are given for a multi-stage fractured horizontal oil well. Predict the initial well production rate:

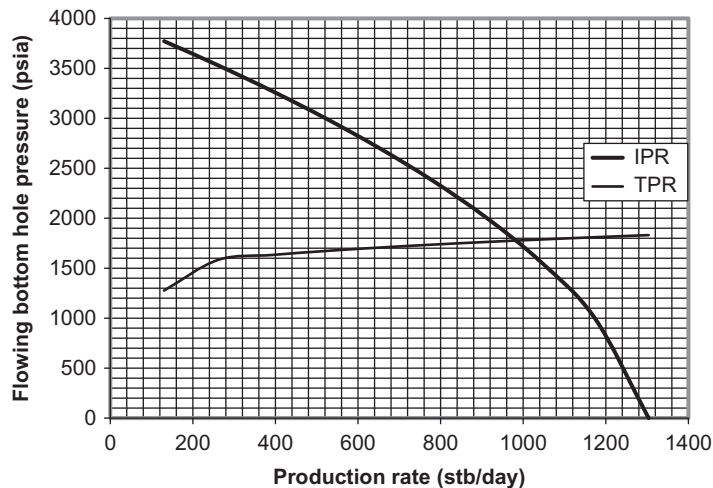
Fracture spacing ( $2z_e$ ):	1000 ft
Fracture half length ( $x_f$ ):	1000 ft
Fracture permeability ( $k_f$ ):	50,000 md
Oil bubble-point pressure ( $p_b$ ):	5000 psia
Effective horizontal permeability ( $k$ ):	10 md
Pay zone thickness ( $h$ ):	60 ft
Average reservoir pressure ( $\bar{p}$ ):	4000 psia
Oil formation volume factor ( $B_o$ ):	1.2 rb/stb
Well drainage area ( $A$ ):	320 acres
Well radius ( $r_w$ ):	0.33 ft
Fracture width ( $w$ ):	0.30 in.
Well vertical depth ( $H$ ):	8000 ft
Tubing inner diameter ( $d$ ):	4 in.
Oil gravity (API):	40 °API
Oil viscosity ( $\mu_o$ ):	1.5 cp
Producing GLR (GLR):	500 scf/bbl
Gas-specific gravity ( $\gamma_g$ ):	0.7 air = 1
Flowing tubing head pressure ( $p_{hf}$ ):	800 psia
Flowing tubing head temperature ( $t_{hf}$ ):	150°F
Flowing temperature at tubing shoe ( $t_{wf}$ ):	180°F
Water cut (WC):	10%
Near-wellbore fracture width ( $w_w$ ):	0.2 in.

Drainage shape factor ( $C_A$ ):	5
Number of fractures ( $n$ ):	20
Near wellbore fracture permeability ( $k_{fwi}$ ):	2500 md

Well inclination data:

Measured Depth (ft)	Inclination Angle (°)
0	0
276	0
552	0
828	0
1103	0
1379	0
1655	0
1931	0
2207	0
2483	0
2759	0
3034	0
3310	0
3586	0
3862	0
4138	10
4414	20
4690	30
4966	40
5241	50
5517	60
5793	70
6069	80
6345	90
6621	90
6897	90
7172	90
7448	90
7724	90
8000	90

Example Problem 6.11 is solved with spreadsheet program *Multi-Fractured Horizontal Oil Well Production.xls*. The Nodal analysis plot is shown in Fig. 6.8 which indicates that the expected oil flow rate is 890 stb/d at a bottom-hole pressure of 1770 psia.

**FIGURE 6.8**

Nodal analysis for Example Problem 6.11.

**Example Problem 6.12** The following data are given for a multi-stage fractured horizontal gas well. Predict the initial well production rate:

Drainage area:	640 acres
Pay zone thickness:	50 ft
Horizontal permeability:	0.1 md
Fracture width:	0.02 in.
Skin factor near wellbore in fracture:	1
Wellbore radius:	0.328 ft
Reservoir pressure:	4565 psia
Reservoir depth:	10,000 ft
Fracture face damaged permeability:	0.05 md
Gas-specific gravity:	0.65 air = 1
Gas viscosity:	0.022 cp
Gas $z$ -factor:	0.958
Oil production rate:	5 stb/day
Oil-specific gravity:	0.85 H <sub>2</sub> O = 1
Water cut:	20%
Water-specific gravity:	1.05 H <sub>2</sub> O = 1
Solid production rate:	1 ft <sup>3</sup> /d
Solid-specific gravity:	2.65 H <sub>2</sub> O = 1
Tubing head temperature:	100°F
Bottom-hole temperature:	180°F
Tubing head pressure:	1500 psia
Fracture width near wellbore:	0.01 in.
Pipe wall roughness:	0.01 in.



Number of fractures: 10  
 Average fracture half length: 500 ft  
 Average fracture spacing ( $2z_e$ ): 200 ft  
 Fracture permeability: 100,000 md  
 Fracture permeability near wellbore: 50,000 md  
 Non-Darcy flow coefficient: 0.001 d/Mscf  
 Fracture face invasion depth: 0.5 ft

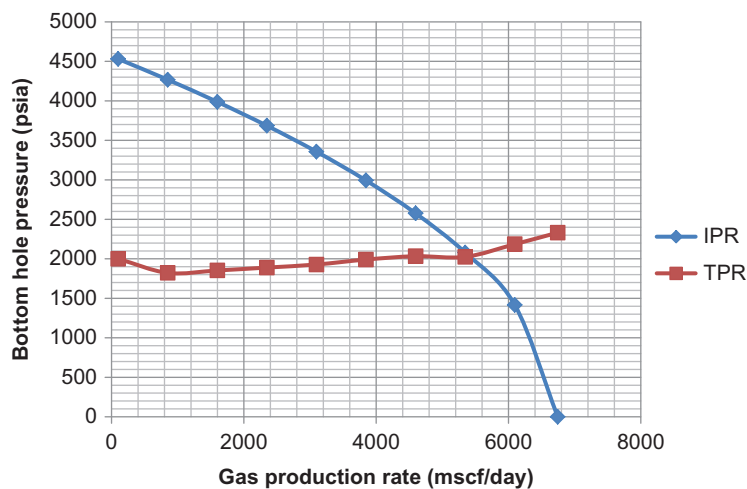
Well tubing and inclination data:

Depth (ft)	Tubing ID (in.)	Inclination (°)
0	2.441	0
250	2.441	0
500	2.441	0
750	2.441	0
1000	2.441	0
1250	2.441	0
1500	2.441	0
1750	2.441	0
2000	2.441	0
2250	2.441	0
2500	2.441	0
2750	2.441	0
3000	2.441	0
3250	2.441	0
3500	2.441	0
3750	2.441	0
4000	2.441	0
4250	2.441	0
4500	2.441	0
4750	2.441	0
5000	2.441	0
5250	2.441	0
5500	2.441	0
5750	2.441	0
6000	2.441	0
6250	2.441	0
6500	2.441	0
6750	2.441	0
7000	2.441	0
7250	2.441	0
7500	2.441	0
7750	2.441	0
8000	2.441	0

(Continued)

<i>Continued</i>		
Depth (ft)	Tubing ID (in.)	Inclination (°)
8250	2.441	0
8500	2.441	0
8750	2.441	0
9000	2.441	10
9250	2.441	20
9500	2.441	30
9750	2.441	40
10,000	2.441	50
10,250	2.441	60
10,500	2.441	70
10,750	2.441	80
11,000	2.441	88
11,250	2.441	88
11,500	2.441	88
11,750	2.441	88
12,000	2.441	88
12,250	2.441	88
12,500	2.441	88

Example Problem 6.12 is solved with spreadsheet program *Multi-Fractured Horizontal Gas Well Production.xls*. The Nodal analysis plot is shown in Fig. 6.9 which indicates that the expected oil flow rate is 5500 Mscf/day at a bottom-hole pressure of 2000 psia.



**FIGURE 6.9**

Nodal analysis for Example Problem 6.12.

## 6.5 DELIVERABILITY OF MULTILATERAL WELLS

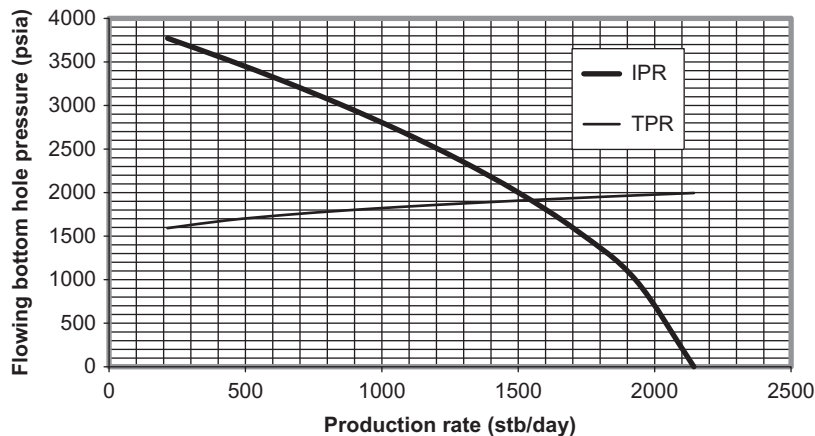
Inflow equations for both fishbone type and root type multilateral wells are described in Chapter 3, Reservoir Deliverability. Different wellbore flow performance equations presented in Chapter 4, Wellbore Flow Performance are used for oil and gas wells.

### 6.5.1 FISHBONE WELLS

For construction of wellbore flow performance curves in oil wells, Hagedorn-Brown correlation is utilized for fishbone type wells and Poettmann–Carpenter model is used for root type wells. The Guo-Ghalambor model is employed to generate TPR for gas wells. For simplicity of computations, it is assumed that the set of fishbone laterals are directly linked to the main vertical wellbore. This assumption should over-estimate the deliverability of well due to neglecting the flow friction in the angle-building section.

**Sample Problem 6.13** The following data are given for a fishbone type oil well. Assuming tubing string is set just above the pay zone, predict the pseudosteady-state liquid production rate.

Average rib hole spacing ( $2y_b$ ):	1000 ft
Average rib hole length ( $L$ ):	1000 ft
Average rib hole skin factor ( $s$ ):	5
Oil bubble point pressure ( $p_b$ ):	5000 psia
Effective horizontal permeability ( $k_H$ ):	10 md
Pay zone thickness ( $h$ ):	50 ft
Average reservoir pressure ( $\bar{p}$ ):	4000 psia
Oil formation volume factor ( $B_o$ ):	1.2 rb/stb
Well drainage area ( $A$ ):	320 acres
Average rib hole radius ( $r_w$ ):	0.328 ft
Vertical permeability ( $k_v$ ):	2 md
Well vertical depth ( $H$ ):	8000 ft
Tubing inner diameter ( $d$ ):	4 in.
Oil gravity (API):	30 °API
Oil viscosity ( $\mu_o$ ):	1.5 cp
Producing GLR (GLR):	500 scf/bbl
Gas-specific gravity ( $\gamma_g$ ):	0.7 air = 1
Flowing tubing head pressure ( $p_{hf}$ ):	800 psia
Flowing tubing head temperature ( $t_{hf}$ ):	150°F
Flowing temperature at tubing shoe ( $t_{wf}$ ):	180°F
Water cut (WC):	10%
Oil-gas interfacial tension ( $\sigma$ ):	30 dynes/cm
Specific gravity of water ( $\gamma_w$ ):	1.05
Number of rib holes ( $n$ ):	7
Drainage area shape factor ( $C_A$ ) based on aspect ratio:	5.38



**FIGURE 6.10**

Nodal analysis for Example Problem 6.13.

Example Problem 6.13 is solved with spreadsheet program *Pseudosteady Production of Fishbone Oil Well.xls*. Fig. 6.10 indicates that the expected liquid production rate is 1540 stb/day, at a flowing bottom-hole pressure of 1905 psia. Using this spreadsheet, it can be shown that the productivity of fishbone wells does not increase in proportion to the number of rib holes. The solution to this problem is left to the reader as an exercise in using the spreadsheet.

**Sample Problem 6.14** The following data are given for a fishbone type gas well. Assuming tubing string is set just above the pay zone, predict the pseudosteady-state gas production rate.

Pay zone thickness:	30 ft
Horizontal permeability:	1 md
Wellbore radius:	0.328 ft
Average Darcy skin factor:	5
Non-Darcy skin coefficient:	0.001 day/Mscf
Reservoir pressure:	4613 psia
Total measured depth:	7000 ft
Average inclination angle:	0°
Tubing ID:	3.5 in.
Gas-specific gravity:	0.65 air = 1
Gas viscosity:	0.022 cp
Gas z-factor:	0.958
Oil production rate:	1 stb/day
Oil-specific gravity:	0.85 H <sub>2</sub> O = 1

Water cut:	10%
Water-specific gravity:	1.05 H <sub>2</sub> O = 1
Solid production rate:	1 ft <sup>3</sup> /d
Solid-specific gravity:	2.65 H <sub>2</sub> O = 1
Tubing head temperature:	100°F
Bottom-hole temperature:	180°F
Tubing head pressure:	2000 psia
Drainage area:	640 acres
Average wall roughness:	0.01 in.
Number of rib holes:	4
Average rib hole length:	500 ft
Average rib hole spacing (2y <sub>b</sub> ):	1000 ft
Vertical permeability:	0.25 md

Example Problem 6.14 is solved with spreadsheet program *Pseudosteady Production of Fishbone Gas Well.xls*. Table 6.8 indicates that the expected liquid production rate is 12,092 Mscf/d, at a flowing bottom-hole pressure of 2427 psia.

### 6.5.2 ROOT WELLS

The lower section of a root well is an integration of several horizontal wells. However, because of pressure drops in the wellbore sections, the productivity of a root well is not simply the sum of the productivities of the individual laterals, unless the IPRs of all the laterals are properly integrated with an understanding of the wellbore hydraulics.

Fig. 6.11 shows a generalized root well structure. The root well can be viewed as a few well branches linked in series, each having three sections: vertical, curved, and horizontal sections. The

$f_M =$	2.58E-02	$I_{ana} =$	2	
$a =$	2.04E-05	$r_{PL} =$	892	ft
$b =$	2.45E-10	$J_{PL} =$	0.00115	Mscf/d-psi <sup>2</sup>
$c =$	5.12E + 06	$J_R =$	0.00250	Mscf/d-psi <sup>2</sup>
$d =$	1.25E-03	$J =$	0.00079	Mscf/d-psi <sup>2</sup>
$e =$	1.37E-03			
$M =$	8.82E + 00			
$N =$	3.60E + 10			
	Gas production rate, $q =$		12,092	Mscf/d
	Bottom-hole pressure, $p_{wf} =$		2427	psia

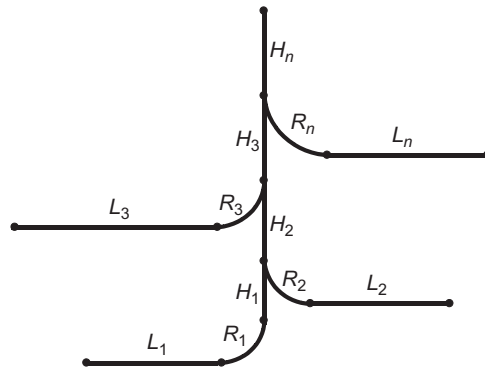


FIGURE 6.11

A simplified well structure for root type multilateral wells.

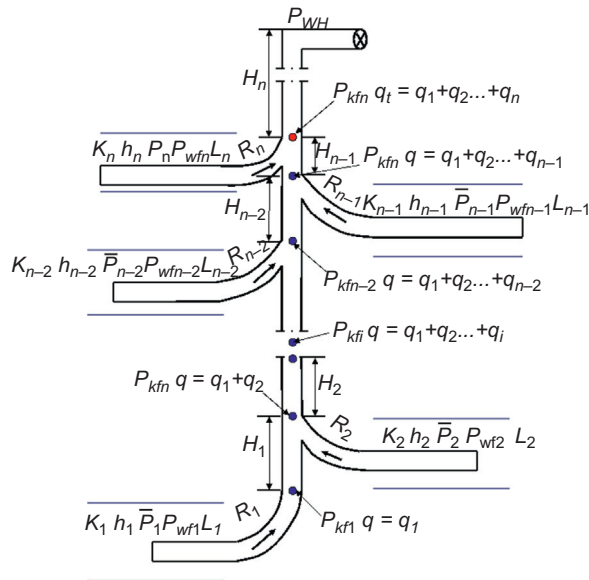


FIGURE 6.12

Symbols used to describe a root type multilateral well.

symbols  $H$ ,  $R$ , and  $L$  stand for the vertical length, the radius-of-curvature, and the length of the vertical, curved, and horizontal sections, respectively.

Fig. 6.12 illustrates the parameters used to characterize a root well. The notations  $K$ ,  $h$ , and  $\bar{P}$  represent the respective permeability, thickness, and the average pressure in the reservoir area

drained by a lateral branch. The pressures at heel and kick-out point are denoted by  $P_{wf}$  and  $P_{kf}$ , respectively. The symbols  $P_{hf}$  and  $q$  represent wellhead pressure and well production rate. The following trial-and-error procedure can be used to predict the productivity of a root well with  $n$  roots.

1. At the given wellhead flowing pressure  $p_{hf_n}$ , assume a value of the total well flow rate  $q_t$ , and calculate the pressure at the kick-out-point of lateral  $n$ ,  $p_{kf_n}$ , using the TPR function  $\mathfrak{F}_n$ :

$$p_{kf_n} = \mathfrak{F}_n(p_{hf_n}, q_t) \quad (6.28)$$

2. Perform an inflow-outflow analysis for lateral  $n$ , to calculate the production rate. Do this by combining the TPR of the curved section and the IPR of the horizontal section, by solving for  $q_n$  from the following two relations:

$$p_{wf_n} = \mathfrak{N}_n(\bar{p}_n, q_n) \quad (6.29)$$

$$p_{wf_n} = \mathfrak{R}_n(p_{kf_n}, q_n) \quad (6.30)$$

where  $\mathfrak{N}_n$  and  $\mathfrak{R}_n$  are IPR and TPR (curved section) functions for the lateral  $n$ .

3. Calculate the flowing pressure at the kick-out-point of lateral  $n - 1$ ,  $p_{kf_{n-1}}$ , using the TPR function of the vertical section, with flow rate  $(q_t - q_n)$ , that is:

$$p_{kf_{n-1}} = \mathfrak{F}_{n-1}(p_{kf_n}, q_t - q_n) \quad (6.31)$$

4. Perform an inflow-outflow analysis for lateral  $n - 1$ , to calculate the production rate from that lateral. This is done by combining the TPR of the curved section and the IPR of the horizontal section, that is, solving for  $q_{n-1}$  from the following two relations:

$$p_{wf_{n-1}} = \mathfrak{N}_{n-1}(\bar{p}_{n-1}, q_{n-1}) \quad (6.32)$$

$$p_{wf_{n-1}} = \mathfrak{R}_{n-1}(p_{kf_{n-1}}, q_{n-1}) \quad (6.33)$$

5. Calculate the flowing pressure at the kick-out-point of lateral  $n - 2$ ,  $p_{kf_{n-2}}$ , using the TPR function of the vertical section, with flow rate  $(q_t - q_n - q_{n-1})$ , that is:

$$p_{kf_{n-2}} = \mathfrak{F}_{n-2}(p_{kf_{n-1}}, q_t - q_n - q_{n-1}) \quad (6.34)$$

6. Perform an inflow-outflow analysis for lateral  $n - 2$ , to calculate the production rate from that lateral. Do this by combining the TPR of the curved section and the IPR of the horizontal section, by solving for  $q_{n-2}$  from the following two relations:

$$p_{wf_{n-2}} = \mathfrak{N}_{n-2}(\bar{p}_{n-2}, q_{n-2}) \quad (6.35)$$

$$p_{wf_{n-2}} = \mathfrak{R}_{n-2}(p_{kf_{n-2}}, q_{n-2}) \quad (6.36)$$

7. Repeat the procedure shown in steps 3 through 6, until the flow rate from lateral 1 ( $q_1$ ) is calculated.
8. Compare the calculated total flow rate  $(q_1 + q_2 + \dots + q_n)$  with the assumed total flow rate  $q_t$ . If the  $(q_1 + q_2 + \dots + q_n) - q_t >$  specified tolerance, use the value of  $(q_1 + q_2 + \dots + q_n)$  as a new assumption for the total flow rate  $q_t$ , and repeat steps 1–6. If  $(q_1 + q_2 + \dots + q_n) - q_t <$  the specified tolerance, exit the loop. Then the  $q_t$  is a prediction of production rate of the root well.

For oil wells, either the Hagedorn-Brown correlation or the Peotmann-Carpenter model presented in Chapter 4, Wellbore Flow Performance can be employed to generate the tubing performance functions  $\mathfrak{F}$  and  $\mathfrak{R}$ . The lateral IPR function  $\mathfrak{N}_n$  can be chosen from different IPR models.

For gas wells, either the Guo-Ghalambor's mist-flow model or the Average-Temperature Average  $z$ -Factor methods presented in Chapter 4, Wellbore Flow Performance can be employed to generate the tubing performance functions  $\mathfrak{F}$  and  $\mathfrak{R}$ . The lateral IPR function  $\mathfrak{N}_n$  can be chosen from different IPR models.

One of the difficulties in predicting the productivity of root wells lies in accommodating the mixed properties of fluids (oil, water, and gas) from all roots in the hydraulic computations for different wellbore sections. The mixing rule can be applied to all stages of the trial-and-error procedure.

**Sample Problem 6.15** A planned root well has 10 roots penetrating 10 reservoir sections. From the data given in Tables 6.9 through 6.13, predict the pseudosteady-state oil production rate using Hagedorn-Brown correlation for wellbore performance.

Example Problem 6.15 is solved with spreadsheet program *Multilateral Oil Well Deliverability-HB.xls*. The result is presented in Table 6.14.

**Sample Problem 6.16** A planned root well has 4 roots penetrating 4 reservoir sections. From the data given in Table 6.15, predict the pseudosteady-state oil production rate using Peotmann-Carpenter model for wellbore performance.

Example Problem 6.16 is solved with spreadsheet program *Multilateral Oil Well Deliverability-PC.xls*. The result is presented in Table 6.16. It indicates that layer steals production due to its low pressure. This problem can be solved by lowering the well head pressure. Exercises are left the reader to run the program with reduced wellhead pressures.

**Sample Problem 6.17** A planned root well has 4 roots penetrating 4 reservoir sections. From the data given in Table 6.17, predict the initial gas production rate using reservoir properties to model IPR.

**Table 6.9 Reservoir Property Data**

Lateral No.	Reservoir Pressure (psia)	Temperature (°F)	Horizontal Permeability (md)	Vertical Permeability (md)	Thickness (ft)
1	1200	120	5	1.67	50
2	1400	125	6	2.00	51
3	1600	130	7	2.33	52
4	1800	135	8	2.67	53
5	2000	140	9	3.00	54
6	2200	145	10	3.33	55
7	2400	150	11	3.67	56
8	2600	155	12	4.00	57
9	2800	160	13	4.33	58
10	3000	165	14	4.67	59



**Table 6.10 Fluid Property Data**

Lateral No.	Oil Gravity (API)	Oil Viscosity (cp)	Oil Formation Volume Factor (rb/stb)	Solution Gas Ratio (scf/stb)	Water Cut (%)
1	65	0.5	1.4	5000	33
2	60	1	1.35	4000	34
3	55	1.5	1.3	3000	35
4	50	2	1.25	2000	36
5	45	2.5	1.2	1000	37
6	40	3	1.15	500	38
7	35	3.5	1.13	300	39
8	30	4	1.1	200	40
9	25	4	1.07	100	60
10	20	4	1.05	50	80

**Table 6.11 Well Data for Vertical Sections**

Lateral No.	Kick-off Point (ft)	Inclination Angle (°)	Tubing Diameter (in.)	Wall Roughness (in.)
1	3000	0	9	0.0001
2	3500	0	6	0.0001
3	4000	0	6	0.0001
4	4500	0	6	0.0001
5	5000	0	6	0.0001
6	5500	0	6	0.0001
7	6000	0	6	0.0001
8	6500	0	6	0.0001
9	7000	0	6	0.0001
10	7500	0	6	0.0001

**Table 6.12 Well Data for Curved Sections**

Lateral No.	Radius of Curvature (ft)	Plane Inclination Angle (°)	Tubing Diameter (in.)	Wall Roughness (in.)
1	500	0	4	0.0001
2	550	0	4	0.0001
3	600	0	4	0.0001
4	650	0	4	0.0001
5	700	0	4	0.0001
6	750	0	4	0.0001
7	800	0	4	0.0001
8	850	0	4	0.0001
9	900	0	4	0.0001
10	950	0	4	0.0001

**Table 6.13 Well Data for Horizontal Sections**

Lateral No.	Lateral Length (ft)	Inclination Angle (°)	Tubing Diameter (in.)	Wall Roughness (in.)	Openhole Radius (ft)	Drainage Area (acres)
1	2000	90	4	0.0001	0.328	160
2	1900	90	4	0.0001	0.328	160
3	1800	90	4	0.0001	0.328	160
4	1700	90	4	0.0001	0.328	160
5	1600	90	4	0.0001	0.328	160
6	1500	90	4	0.0001	0.328	160
7	1400	90	4	0.0001	0.328	160
8	1300	90	4	0.0001	0.328	160
9	1200	90	4	0.0001	0.328	160
10	1100	90	4	0.0001	0.328	160

**Table 6.14 Summary of Calculated Lateral and Well Production Rates for Sample Problem 6.15**

Lateral No.	Heel Pressure (psi)	Liquid Production Rate (stb/day)	Oil Production Rate (stb/day)	Water Production Rate (bbl/day)	Gas Production Rate (Mscf/day)
1	808	743	498	245	2489
2	1020	443	292	151	1170
3	1224	346	225	121	675
4	1424	298	191	107	381
5	1623	265	167	98	167
6	1842	227	141	86	70
7	2065	182	111	71	33
8	2299	132	79	53	16
9	2556	104	42	62	4
10	2818	56	11	45	1
Total:		2796	1756	1040	5006

Example Problem 6.17 is solved with spreadsheet program *Multilateral Gas Well Deliverability (Radial Flow IPR).xls*. The result is presented in Table 6.18. This spreadsheet was coded with a linear IPR model, allowing for inter-layer cross-flow from high-pressure layers to lower-pressure thief layers. The reader can run the model at higher wellhead pressures to see the cross-flow. It can be shown that layer 3 will become a thief layer when the well is operated with a wellhead pressure higher than 1430 psia in this well.

<b>Table 6.15 Well Data for Sample Problem 6.16</b>					
<b>Wellhead Condition:</b>					
Pressure ( $p_{wh}$ )	1800	psia			
Temperature ( $T_{wh}$ )	100	°F			
<b>Horizontal Sections:</b>					
Lateral No.:	1	2	3	4	
Reservoir pressure ( $\bar{p}$ )	3700	3500	3300	2800	psia
Oil formation factor ( $B_o$ )	1.20	1.15	1.10	1.1	stb/rb
Water formation factor ( $B_w$ )	1.00	1.00	1.00	1.00	stb/rb
Bottom-hole temperature ( $T$ )	270	260	250	230	°F
Gas compressibility factor ( $z$ )	0.85	0.90	0.95	0.98	
Gas-specific gravity ( $\gamma_g$ )	0.85	0.83	0.80	0.75	air = 1
Oil-specific gravity ( $\gamma_o$ )	0.80	0.78	0.87	0.85	water = 1
Water-specific gravity ( $\gamma_w$ )	1.07	1.06	1.05	1.04	water = 1
Water oil ratio (WOR)	0.10	0.40	0.20	0.30	stb/stb
Gas-oil ratio (GOR)	1000	1500	2000	2500	scf/stb
Solution gas oil ratio ( $R_s$ )	800	1200	1500	2000	scf/stb
Productivity index ( $J$ )	1	0.8	0.7	0.6	stb/d/psi
<b>Curve Sections:</b>					
Lateral No.:	1	2	3	4	
Radius of curve ( $R$ )	200	200	200	200	ft
Inclination angle ( $\theta$ )	45	45	45	45	°
Tubing diameter ( $d_i$ )	3	3	3	3	in
Pipe Roughness ( $e$ )	0.0018	0.0018	0.0018	0.0018	in
<b>Vertical Sections:</b>					
Lateral No.:	1	2	3	4	
Interval length ( $H$ )	500	400	300	3000	ft
Tubing diameter ( $d_i$ )	3	3	3	3	in
Pipe roughness ( $e$ )	0.0018	0.0018	0.0018	0.0018	in
Temperature ( $T$ )	265	250	240	230	°F

<b>Table 6.16 Summary of Calculated Lateral and Well Production Rates for Sample Problem 6.16</b>		
$q_{total}$	973	stb/d
$q_1$	451	stb/d
$q_2$	324	stb/d
$q_3$	237	stb/d
$q_4$	(39)	stb/d

<b>Table 6.17 Well Data for Sample Problem 6.17</b>					
<b>Wellhead Condition:</b>					
Pressure ( $p_{wh}$ )	1200	psia			
Temperature ( $T_{wh}$ )	100	°F			
<b>Horizontal Sections:</b>					
Lateral No.:	1	2	3	4	
Length of horizontal section ( $L$ )	500	600	700	400	ft
Horizontal permeability ( $k$ )	0.10	0.20	0.30	0.40	md
Net pay thickness ( $h$ )	20	20	20	20	ft
Reservoir pressure ( $\bar{p}$ )	3700	3500	1800	2800	psia
Radius of drainage ( $r_{eh}$ )	2000	2500	1700	2100	ft
Gas viscosity ( $\mu_g$ )	0.02	0.02	0.02	0.02	cp
Wellbore diameter ( $D_i$ )	8.00	8.00	8.00	8.00	in
Bottom-hole temperature ( $T$ )	270	260	250	230	°F
Gas compressibility factor ( $z$ )	0.85	0.90	0.95	0.98	
Gas-specific gravity ( $\gamma_g$ )	0.85	0.83	0.80	0.75	air = 1
<b>Curve Sections:</b>					
Lateral No.:	1	2	3	4	
Radius of curve ( $R$ )	250	300	200	270	ft
Average inclination angle ( $\theta$ )	45	45	45	45	°
Tubing diameter ( $d_i$ )	3	3	3	3	in
Pipe roughness ( $e$ )	0.0018	0.0018	0.0018	0.0018	in
<b>Vertical Sections:</b>					
Lateral No.:	1	2	3	4	
Interval length ( $H$ )	250	300	200	8000	ft
Tubing diameter ( $d_i$ )	3	3	3	3	in
Pipe roughness ( $e$ )	0.0018	0.0018	0.0018	0.0018	in
Kick off points:	1	2	3	4	

**Table 6.18 Summary of Calculated Lateral and Well Production Rates for Sample Problem 6.17**

$q_{total}$	2834	Mscf/d
$q_1$	633	Mscf/d
$q_2$	1039	Mscf/d
$q_3$	157	Mscf/d
$q_4$	1005	Mscf/d

Table 6.19 Well Data for Sample Problem 6.18					
<b>Wellhead Condition:</b>					
Pressure ( $p_{wh}$ )	800	psia			
Temperature ( $T_{wh}$ )	100	°F			
<b>Horizontal Sections:</b>					
Lateral No.:	1	2	3	4	
Reservoir pressure ( $p_r$ )	3700	3500	3000	2800	psia
Bottom-hole temperature ( $T$ )	270	260	250	230	°F
Gas compressibility factor ( $z$ )	0.90	0.90	0.95	0.98	
Gas-specific gravity ( $\gamma_g$ )	0.85	0.83	0.80	0.75	air = 1
IPR coefficient ( $C$ )	0.04	0.035	0.03	0.02	
IPR coefficient ( $n$ )	0.6	0.6	0.6	0.6	
<b>Curve Sections:</b>					
Lateral No.:	1	2	3	4	
Radius of curve ( $R$ )	200	200	200	200	ft
Inclination angle ( $\theta$ )	45	45	45	45	°
Tubing diameter ( $d_i$ )	5	5	5	5	in
Pipe Roughness ( $e$ )	0.0018	0.0018	0.0018	0.0018	in
<b>Vertical Sections:</b>					
Lateral No.:	1	2	3	4	
Interval length ( $H$ )	250	300	200	3000	ft
Tubing diameter ( $d_i$ )	5	5	5	5	in
Pipe roughness ( $e$ )	0.0018	0.0018	0.0018	0.0018	in

**Table 6.20 Summary of Calculated Lateral and Well Production Rates for Sample Problem 6.18**

$q_{total}$	2022	Mscf/d
$q_1$	739	Mscf/d
$q_2$	602	Mscf/d
$q_3$	423	Mscf/d
$q_4$	258	Mscf/d

**Sample Problem 6.18** A planned root well has 4 roots penetrating 4 reservoir sections. From the data given in Table 6.19, predict gas production rate using an empirical correlation ( $C$ - $n$  model) to analyze IPR.

Example Problem 6.18 is solved with spreadsheet program *Multilateral Gas Well Deliverability (C-n IPR).xls*. The result is presented in Table 6.20. This spreadsheet was coded with a nonlinear IPR model ( $C$ - $n$  model). It does not allow for modeling inter-layer cross-flow

from high-pressure layers to lower-pressure thief layers because the iteration procedure in computations may create a condition of taking square-root of a negative number. The reader can run the model at higher wellhead pressures to see the error message. It can be shown that layer 4 will become a thief layer when the well is operated with a wellhead pressure higher than 2560 psia in this well.

---

## 6.6 SUMMARY

This chapter illustrated principles of predicting deliverability of wells with various configurations of completion. These wells are non-fractured and fractured vertical wells, non-fractured and multi-fractured horizontal wells, and multilateral wells of fishbone type, and root type. Different IPR and TPR models are used for both oil and gas wells. The illustrations are made with spreadsheet programs coded with simple IPR models mostly for single-phase flow. It is recommended that reservoir simulators coupled with wellbore hydraulics be utilized in real engineering projects to consider multiphase flow in reservoirs.

---

## REFERENCES

- Guo, B., 2010. Corrections to horizontal drainhole productivity equations for wellbore friction effect. *J. Petroleum Sci. Eng.* 70 (3–4), 344–349.
- Guo, B., Sun, K., Ghalambor, A., 2008. *Well Productivity Handbook*. Gulf Publishing Company, Houston, pp. 321–328.

---

## PROBLEMS

- 6.1.** Suppose that a vertical well produces 0.65 specific gravity gas through a 2 $\frac{1}{8}$ -in. tubing set to the top of a gas reservoir at a depth of 8000 ft. At tubing head, the pressure is 600 psia and the temperature is 120°F, and the bottom-hole temperature is 180°F. The relative roughness of tubing is about 0.0006. Calculate the expected gas production rate of the well using the following data for IPR:

Reservoir pressure:	1800 psia
IPR model parameter $C$ :	0.15 Mscf/d-psi <sup>2<math>n</math></sup>
IPR model parameter $n$ :	0.82

**6.2.** For the data given in the following table, predict the operating point using the bottom-hole as a solution node:

Reservoir pressure:	3200 psia
Tubing ID:	1.66 in.
Wellhead pressure:	600 psia
Productivity index above bubble point:	1.5 stb/d-psi
Producing gas–liquid ratio (GLR):	800 scf/stb
Water cut (WC):	30%
Oil gravity:	40° API
Water-specific gravity:	1.05 1 for freshwater
Gas-specific gravity:	0.75 1 for air
N <sub>2</sub> content in gas:	0.05 mole fraction
CO <sub>2</sub> content in gas:	0.03 mole fraction
H <sub>2</sub> S content in gas:	0.02 mole fraction
Formation volume factor for water:	1.25 rb/stb
Wellhead temperature:	110°F
Tubing shoe depth:	6000 ft
Bottom-hole temperature:	140°F

**6.3.** For the data given in the following table, predict the operating point using the bottom-hole as the solution node:

Reservoir pressure:	3500 psia
Total measured depth:	8000 ft
Average inclination angle:	10°
Tubing ID:	1.995 in.
Gas production rate:	500,000 scfd
Gas-specific gravity:	0.7 air = 1
Oil-specific gravity:	0.82 H <sub>2</sub> O = 1
Water cut:	20%
Water-specific gravity:	1.07 H <sub>2</sub> O = 1
Solid production rate:	2 ft <sup>3</sup> /d
Solid-specific gravity:	2.65 H <sub>2</sub> O = 1
Tubing head temperature:	120°F
Bottom-hole temperature:	160°F
Tubing head pressure:	400 psia
Absolute open flow (AOF):	2200 bbl/d

**6.4.** For the data given in the following table, predict the operating point using the bottom-hole as the solution node:

Depth:	9500 ft
Tubing inner diameter:	1.995 in.

Oil gravity:	40°
API Oil viscosity:	3 cp
Production gas—liquid ratio:	600 scf/bbl
Gas-specific gravity:	0.75 air = 1
Flowing tubing head pressure:	500 psia
Flowing tubing head temperature:	90°F
Flowing temperature at tubing shoe:	190°F
Water cut:	20%
Reservoir pressure:	5250 psia
Bubble-point pressure:	4200 psia
Productivity above bubble point:	1.2 stb/d-psi

**6.5.** Use the following data to estimate the gas production rate of a gas well:

Gas-specific gravity:	0.75
Tubing inside diameter:	2.259 in.
Tubing wall relative roughness:	0.0006
Measured depth at tubing shoe:	8000 ft
Inclination angle:	0°
Wellhead choke size:	24 1/64 in.
Flowline diameter:	2 in.
Gas-specific heat ratio:	1.3
Gas viscosity at wellhead:	0.01 cp
Wellhead temperature:	140°F
Bottom-hole temperature:	180°F
Reservoir pressure:	2200 psia
C-constant in backpressure IPR model:	0:01 Mscf d-psi <sup>2n</sup>
n-exponent in backpressure IPR model:	0.84

**6.6.** Use the following data to estimate liquid production rate of an oil well:

Reservoir pressure:	6500 psia
Tubing ID:	3.5 in
Choke size:	64 1/64 in.
Productivity index above bubble point:	1.2 stb/d-psi
Producing gas—liquid ratio:	800 scf/stb
Water cut:	35%
Oil gravity:	40 °API
Water-specific gravity:	1.05 1 for freshwater
Gas-specific gravity:	0.75 1 for air
Choke constant:	10
Choke gas—liquid ratio exponent:	0.546
Choke-size exponent:	1.89
Formation volume factor for water:	1 rb/stb



Wellhead temperature:	110°F
Tubing shoe depth:	10,000 ft
Bottom-hole temperature:	200°F

**6.7.** Use the following data to estimate the liquid production rate of an oil well:

Choke size:	48 1/64 in.
Reservoir pressure:	3200 psia
Total measured depth:	7000 ft
Average inclination angle:	10°
Tubing ID:	1.995 in.
Gas production rate:	600,000 scfd
Gas-specific gravity:	0.7 air = 1
Oil-specific gravity:	0.85 H <sub>2</sub> O = 1
Water cut:	20%
Water-specific gravity:	1.05 H <sub>2</sub> O = 1
Solid production rate:	0.5 ft <sup>3</sup> /d
Solid-specific gravity:	2.65 H <sub>2</sub> O = 1
Tubing head temperature:	120°F
Bottom-hole temperature:	180°F
Absolute open flow (AOF):	2200 bbl/d
Choke flow constant:	10
Choke gas–liquid ratio exponent:	0.546
Choke size exponent:	1.89

**6.8.** For the following data, predict the oil production rate:

Depth:	7500 ft
Tubing inner diameter:	3.5 in.
Oil gravity:	40 °API
Oil viscosity:	0.8 cp
Production GLR:	700 scf/bbl
Gas-specific gravity:	0.7 air = 1
Choke size:	48 1/64 in.
Flowing tubing head temperature:	90°F
Flowing temperature at tubing shoe:	160°F
Water cut:	20%
Reservoir pressure:	4200 psia
Bubble-point pressure:	4000 psia
Productivity above bubble point:	4 stb/d-psi
Choke flow constant:	10
Choke gas-liquid ratio exponent:	0.546
Choke-size exponent:	1.89

6.9. For the following data, predict the gas production rate against 1200 psia wellhead pressure and 90°F wellhead temperature:

Horizontal Sections				
<i>Lateral no.:</i>	1	2	3	
Length of horizontal section ( $L$ )	1000	1100	1200	ft
Horizontal permeability ( $k$ )	8	5	4	md
Net pay thickness ( $h$ )	40	50	30	ft
Reservoir pressure ( $\bar{p}$ )	3500	3450	3400	psia
Radius of drainage area ( $r_{eh}$ ) 2000	2200	2400	ft	
Gas viscosity ( $\mu_g$ )	0.02	0.02	0.02	cp
Wellbore diameter ( $D_i$ )	6.00	6.00	6.00	in.
Bottom-hole temperature ( $T$ )	150	140	130	°F
Gas compressibility factor ( $z$ )	0.95	0.95	0.95	
Gas-specific gravity ( $\gamma_g$ )	0.80	0.80	0.80	air = 1
Curvic Sections				
<i>Lateral no.:</i>	1	2	3	
Radius of curve ( $R$ )	333	400	500	ft
Average inclination angle ( $\theta$ )	45	45	45	degrees
Tubing diameter ( $d_i$ )	1.995	1.995	1.995	in.
Pipe roughness ( $e$ )	0.0018	0.0018	0.0018	in.
Vertical Sections				
<i>Lateral no.:</i>	1	2	3	
Interval length ( $H$ )	500	500	6000	ft
Tubing diameter ( $d_i$ )	1.995	1.995	1.995	in.
Pipe roughness ( $e$ )	0.0018	0.0018	0.0018	in.

6.10. For the following data, predict the gas production rate against 2000 psia wellhead pressure and 80°F wellhead temperature:

Horizontal Sections					
<i>Lateral no.:</i>	1	2	3	4	
Reservoir pressure ( $\bar{p}$ )	3500	3300	3100	2900	psia
Oil formation factor ( $B_o$ )	1.25	1.18	1.19	1.16	stb/rb
Water formation factor ( $B_w$ )	1.00	1.00	1.00	1.00	stb/rb
Bottom-hole temperature ( $T$ )	170	160	150	130	°F
Gas compressibility factor ( $z$ )	0.9	0.90	0.90	0.90	
Gas-specific gravity ( $\gamma_g$ )	0.75	0.73	0.70	0.75	air = 1
Oil-specific gravity ( $\gamma_o$ )	0.85	0.88	0.87	0.8	6 water = 1
Water-specific gravity ( $\gamma_w$ )	1.07	1.06	1.05	1.0	4 water = 1
Water-oil ratio (WOR)	0.30	0.20	0.10	0.1	0 stb/stb

Gas–oil ratio (GOR)	1000	1200	1500	2000	scf/stb
Solution–gas–oil ratio ( $R_s$ )	600	1000	1200	1800	scf/stb
Productivity index ( $J$ )	2	1.8	1.7	1.6	stb/d/psi
<b>Curvic Sections</b>					
<i>Lateral no.:</i>	1	2	3	4	
Radius of curve ( $R$ )	400	400	400	400	ft
Average inclination angle ( $\theta$ )	45	45	45	45	degrees
Tubing diameter ( $d_t$ )	2.441	2.441	2.441	2.441	in.
Pipe roughness ( $e$ )	0.0018	0.0018	0.0018	0.0018	in.
<b>Vertical Sections</b>					
<i>Lateral no.:</i>	1	2	3	4	
Interval length ( $H$ )	100	100	100	5000	ft
Tubing diameter ( $d_t$ )	2.441	2.441	2.441	2.441	in.
Pipe roughness ( $e$ )	0.0018	0.0018	0.0018	0.0018	in.

- 6.11. From the data given below, and assuming that the tubing string is set just above the pay zone, the predict pseudosteady-state production rate.

Fracture spacing ( $2z_e$ ):	1200 ft
Fracture half length ( $x_f$ ):	800 ft
Fracture permeability ( $k_f$ ):	40,000 md
Oil bubble point pressure ( $p_b$ ):	4000 psia
Effective horizontal permeability ( $k$ ):	20 md
Pay zone thickness ( $h$ ):	40 ft
Average reservoir pressure ( $\bar{p}$ ):	3000 psia
Oil formation volume factor ( $B_o$ ):	1.2 rb/stb
Well drainage area ( $A$ ):	320 acres
Well radius ( $r_w$ ):	0.328 ft
Fracture width ( $w$ ):	0.3 in.
Well vertical depth ( $H$ ):	6000 ft
Tubing inner diameter ( $d$ ):	3.5 in.
Oil gravity (API):	40 °API
Oil viscosity ( $\mu_o$ ):	1.2 cp
Producing GLR (GLR):	800 scf/bbl
Gas-specific gravity ( $\gamma_g$ ):	0.65 air = 1
Flowing tubing head pressure ( $p_{hf}$ ):	600 psia
Flowing tubing head temperature ( $t_{hf}$ ):	120°F
Flowing temperature at tubing shoe ( $t_{wf}$ ):	150°F
Water cut (WC):	15%
Near-wellbore fracture width ( $w_w$ ):	0.2 in.
Total skin factor ( $S$ ):	1
Number of fractures ( $n$ ):	5
Near-wellbore fracture permeability ( $k_{fw}$ ):	50,000 md

6.12. A planned fishbone well will have 10 laterals penetrating 10 reservoir sections. From the data given in the following tables, predict the pseudosteady-state oil production rate.

Reservoir Property Data					
Lateral No.	Reservoir Pressure (psia)	Temperature (°F)	Horizontal Permeability (md)	Vertical Permeability (md)	Thickness (ft)
1	1200	120	5	2	50
2	1400	125	5	2	50
3	1600	130	5	2	50
4	1800	135	5	2	50
5	2000	140	5	2	50
6	2200	145	10	4	55
7	2400	150	10	4	55
8	2600	155	10	4	55
9	2800	160	10	4	55
10	3000	165	10	4	55

Fluid Property Data					
Lateral No.	Oil Gravity (API)	Oil Viscosity (cp)	Oil Formation Volume Factor (rb/stb)	Solution Gas Ratio (scf/stb)	Water Cut (%)
1	65	0.5	1.4	5000	30
2	60	1	1.35	4000	30
3	55	1.5	1.3	3000	35
4	50	2	1.25	2000	35
5	45	2.5	1.2	1000	35
6	40	3	1.15	500	38
7	35	3.5	1.13	300	38
8	30	4	1.1	200	40
9	25	4	1.07	100	50
10	20	4	1.05	50	60

Well Data for the Vertical Sections				
Lateral No.	Kick-off Point (ft)	Inclination Angle (°)	Tubing Diameter (in.)	Wall Roughness (in.)
1	3000	0	7	0.0001
2	3500	0	4	0.0001
3	4000	0	4	0.0001
4	4500	0	4	0.0001

<i>Continued</i>						
Well Data for the Vertical Sections						
Lateral No.	Kick-off Point (ft)	Inclination Angle (°)	Tubing Diameter (in.)	Wall Roughness (in.)		
5	5000	0	4	0.0001		
6	5500	0	4	0.0001		
7	6000	0	4	0.0001		
8	6500	0	4	0.0001		
9	7000	0	4	0.0001		
10	7500	0	4	0.0001		
Data for the Curve Sections						
Lateral No.	Radius of Curvature (ft)	Plane Inclination Angle (°)	Tubing Diameter (in.)	Wall Roughness (in.)		
1	500	0	4	0.0001		
2	500	0	4	0.0001		
3	600	0	4	0.0001		
4	600	0	4	0.0001		
5	700	0	4	0.0001		
6	700	0	4	0.0001		
7	800	0	4	0.0001		
8	800	0	4	0.0001		
9	900	0	4	0.0001		
10	900	0	4	0.0001		
Well Data for the Horizontal Sections						
Lateral No.	Lateral Length (ft)	Inclination Angle (°)	Tubing Diameter (in.)	Wall Roughness (in.)	Openhole Radius (ft)	Drainage Area (acres)
1	2100	90	4	0.0001	0.328	160
2	2000	90	4	0.0001	0.328	160
3	1900	90	4	0.0001	0.328	160
4	1800	90	4	0.0001	0.328	160
5	1700	90	4	0.0001	0.328	160
6	1600	90	4	0.0001	0.328	160
7	1500	90	4	0.0001	0.328	160
8	1400	90	4	0.0001	0.328	160
9	1300	90	4	0.0001	0.328	160
10	1200	90	4	0.0001	0.328	160

## FORECAST OF WELL PRODUCTION

## 7

## 7.1 INTRODUCTION

With the knowledge of Nodal analysis, it is possible to forecast well production, that is, future production rate and cumulative production of oil and gas. Combined with information of oil and gas prices, the results of a production forecast can be used for field economics analyses.

A production forecast is performed on the basis of principle of material balance. The remaining oil and gas in the reservoir determine the future inflow performance relationship (IPR) and, therefore, production rates of wells. Production rates are predicted using IPR (see Chapter 3: Reservoir Deliverability) and tubing performance relationship (TPR) (see Chapter 4: Wellbore Flow Performance) in the future times. Cumulative productions are predicted by integrations of future production rates.

A complete production forecast should be carried out in different flow periods identified on the basis of flow regimes and drive mechanisms. For a volumetric oil reservoir, these periods include the following:

- Transient flow period
- Pseudo-steady one-phase flow period
- Pseudo-steady two-phase flow period

## 7.2 OIL PRODUCTION DURING TRANSIENT FLOW PERIOD

The production rate during the transient flow period can be predicted by Nodal analysis using transient IPR and steady flow TPR. The length of the transient flow depends on reservoir properties and well configuration/completion including vertical well, horizontal well, fractured well, and multilateral well, etc. For the purpose of demonstration, only vertical wells are considered in this chapter. IPR model for oil wells is given by Eq. (3.2), that is,

$$q = \frac{kh(p_i - p_{wf})}{162.6B_o\mu_o \left( \log t + \log \frac{k}{\phi\mu_o c_t r_w^2} - 3.23 + 0.87S \right)} \quad (7.1)$$

Eq. 7.1 can be used for generating IPR curves for future time  $t$  before any reservoir boundary is reached by the pressure wave from the wellbore. After all reservoir boundaries are reached, either pseudo-steady-state flow or steady-state flow should prevail depending on the types of reservoir boundaries. The time required for the pressure wave to reach a circular reservoir boundary can be

calculated with  $t_{pss} \approx 1200 \frac{\phi\mu c_t r_e^2}{k}$ .

The same TPR is usually used in the transient flow period, assuming fluid properties remain the same in the well over the period. Depending on the producing gas–liquid ratio (GLR), the TPR model can be chosen from simple ones such as Poettmann–Carpenter and sophisticated ones such as the modified Hagedorn–Brown. It is essential to validate the selected TPR model based on measured data such as flow gradient survey from local wells.

**Example Problem 7.1** Suppose a reservoir can produce oil under transient flow for the next 6 months. Predict oil production rate and cumulative oil production over the 6 months using the following data:

Reservoir porosity ( $\phi$ ):	0.2
Effective horizontal permeability ( $k$ ):	10 md
Pay zone thickness ( $h$ ):	50 ft
Reservoir pressure ( $p_i$ ):	5500 psia
Oil formation volume factor ( $B_o$ ):	1.2 rb/stb
Total reservoir compressibility ( $c_r$ ):	0.000013 psi <sup>-1</sup>
Wellbore radius ( $r_w$ ):	0.328 ft
Skin factor ( $S$ ):	0
Well depth ( $H$ ):	10,000 ft
Tubing inner diameter ( $d$ ):	2.441
Oil gravity (API):	30 API
Oil viscosity ( $\mu_o$ ):	1.5 cp
Producing GLR (GLR):	300 scf/bbl
Gas-specific gravity ( $\gamma_g$ ):	0.7 air = 1
Flowing tubing head pressure ( $p_f$ ):	800 psia
Flowing tubing head temperature ( $T_{hf}$ ):	150°F
Flowing temperature at tubing shoe ( $T_{wf}$ ):	180°F
Water cut:	10%
Interfacial tension ( $\sigma$ ):	30 dynes/cm
Specific gravity of water ( $\gamma_w$ ):	1.05

**Solution** To solve Example Problem 7.1, the spreadsheet program *TransientProductionForecast.xls* was used to perform Nodal analysis for each month. Operating points are shown in Fig. 7.1. The production forecast result is shown in Table 7.1, which also includes calculated cumulative production at the end of each month. The data in Table 7.1 are plotted in Fig. 7.2.

### 7.3 OIL PRODUCTION DURING PSEUDO—STEADY FLOW PERIOD

It is generally believed that oil production during a pseudo-steady-state flow period is due to fluid expansion in undersaturated oil reservoirs and solution-gas drive in saturated oil reservoirs. An undersaturated oil reservoir becomes a saturated oil reservoir when the reservoir pressure drops to below the oil bubble-point pressure. Single-phase flow dominates in undersaturated oil reservoirs and two-phase flow prevails in saturated oil reservoirs. Different mathematical models have been

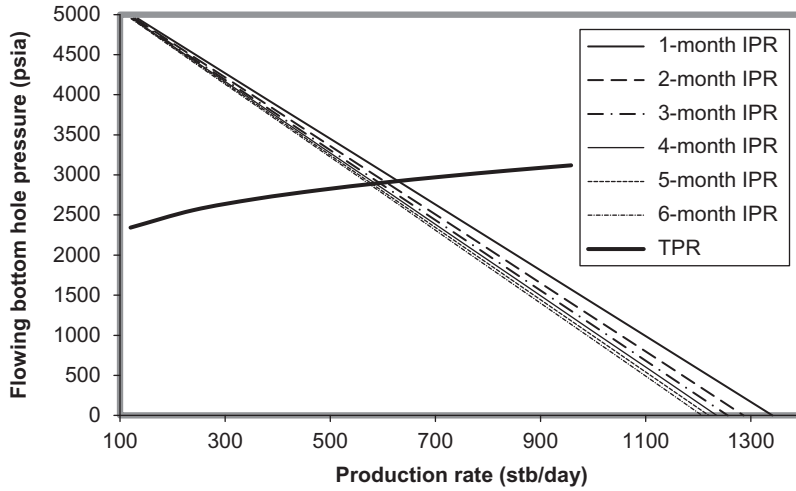


FIGURE 7.1

Nodal analysis plot for Example Problem 7.1.

**Table 7.1 Production Forecast Given by TransientProductionForecast.xls**

Time (Mo)	Production Rate (stb/day)	Cumulative Production (stb)
1	639	19,170
2	618	37,710
3	604	55,830
4	595	73,680
5	588	91,320
6	583	108,795

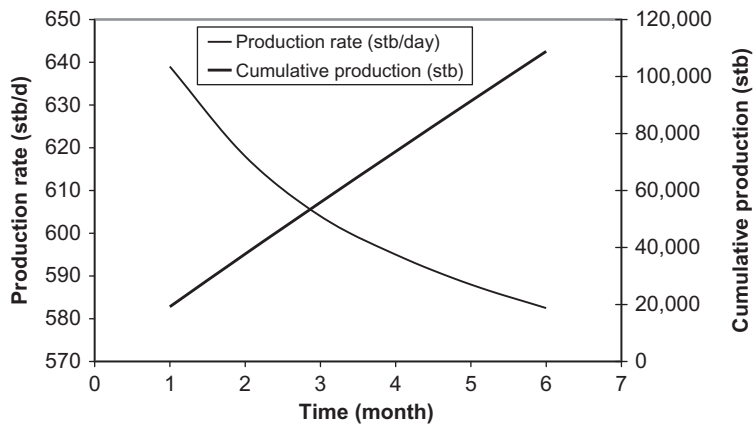


FIGURE 7.2

Production forecast for Example Problem 7.1.



used for time projection in production forecast for these two types of reservoirs, or the same reservoir at different stages of development based on reservoir pressure. IPR changes over time due to the changes in gas saturation and fluid properties.

### 7.3.1 OIL PRODUCTION DURING SINGLE-PHASE FLOW PERIOD

Following a transient flow period and a transition time, oil reservoirs continue to deliver oil through single-phase flow under a pseudo-steady-state flow condition. The IPR changes with time because of the decline in reservoir pressure, while the TPR may be considered constant because fluid properties do not significantly vary above the bubble-point pressure. The TPR model can be chosen from simple ones such as Poettmann–Carpenter and sophisticated ones such as the modified Hagedorn–Brown. The IPR model for vertical wells is given by Eq. (3.9), in Chapter 3, Reservoir Deliverability that is,

$$q = \frac{kh(\bar{p} - p_{wf})}{141.2B_o\mu_o \left( \frac{1}{2} \ln \frac{4A}{\gamma C_A r_w^2} + S \right)}. \quad (7.2)$$

The driving mechanism above the bubble-point pressure is essentially the oil expansion because oil is slightly compressible. The isothermal compressibility is defined as

$$c = -\frac{1}{V} \frac{\partial V}{\partial p}, \quad (7.3)$$

where  $V$  is the volume of reservoir fluid and  $p$  is pressure. The isothermal compressibility  $c$  is small and essentially constant for a given oil reservoir. The value of  $c$  can be measured experimentally. By separating variables, integration of Eq. (7.3) from the initial reservoir pressure  $p_i$  to the current average-reservoir pressure  $\bar{p}$  results in

$$\frac{V}{V_i} = e^{c(p_i - \bar{p})}, \quad (7.4)$$

where  $V_i$  is the reservoir volume occupied by the reservoir fluid. The fluid volume  $V$  at lower pressure  $\bar{p}$  includes the volume of fluid that remains in the reservoir (still  $V_i$ ) and the volume of fluid that has been produced, that is,

$$V = V_i + V_p. \quad (7.5)$$

Substituting Eq. (7.5) into Eq. (7.4) and rearranging the latter gives

$$r = \frac{V_p}{V_i} = e^{c(p_i - \bar{p})} - 1, \quad (7.6)$$

where  $r$  is the recovery ratio. If the original oil in place (OOIP)  $N$  is known, the cumulative recovery (cumulative production) is simply expressed as  $N_p = rN$ .

For the case of an undersaturated oil reservoir, formation water and rock also expand as reservoir pressure drops. Therefore, the compressibility  $c$  should be the total compressibility  $c_t$ , that is,

$$c_t = c_o S_o + c_w S_w + c_f, \quad (7.7)$$

where  $c_o$ ,  $c_w$ , and  $c_f$  are the compressibilities of oil, water, and rock, respectively, and  $S_o$  and  $S_w$  are oil and water saturations, respectively.

The following procedure is taken to perform the production forecast during the single-phase flow period:

1. Assume a series of average-reservoir pressure  $\bar{p}$  values between the initial reservoir pressure  $p_i$  and oil bubble-point pressure  $p_b$ . Perform Nodal analyses to estimate production rate  $q$  at each average-reservoir pressure and obtain the average production rate  $\bar{q}$  over the pressure interval.
2. Calculate recovery ratio  $r$ , cumulative production  $N_p$  at each average-reservoir pressure, and the incremental cumulative production  $\Delta N_p$  within each average-reservoir pressure interval.
3. Calculate production time  $\Delta t$  for each average-reservoir pressure interval by  $\Delta t = \Delta N_p / \bar{q}$  and the cumulative production time by  $t = \Sigma \Delta t$ .

**Example Problem 7.2** Suppose the reservoir described in Example Problem 7.1 begins to produce oil under pseudo-steady-state flow conditions immediately after the 6-month transient flow. If the bubble-point pressure is 4500 psia, predict the oil production rate and cumulative oil production over the time interval before the reservoir pressure declines to bubble-point pressure.

**Solution** Based on the transient flow IPR, Eq. (7.1), the productivity index will drop to 0.2195 stb/d-psi and production rate will drop to 583 stb/day at the end of the 6 months. If a pseudo-steady-state flow condition assumes immediately after the 6-month transient flow, the same production rate should be given by the pseudo-steady-state flow IPR, Eq. (7.2). The average pressure within the production funnel is given by  $\bar{p} = p_i - 35.3 \frac{B_{oi}}{kh}$  (Dake, 1978), or

$$\bar{p} = (5500) - (35.3) \frac{(1.2)(583)(1.5)}{(10)(50)} = 5426 \text{ psia}$$

Substituting this and other values of parameters into Eq. (7.2) gives a drainage area of 1458 acres. Assuming an initial water saturation of 0.35, the OOIP in the drainage area is estimated to be 87,656,581 stb.

Using these additional data, Nodal analyses were performed with spreadsheet program *Pseudo-Steady-1Phase ProductionForecast.xls* at 10 average-reservoir pressures from 5426 to bubble-point pressure of 4500 psia. Operating points are shown in Fig. 7.3. The production forecast result is shown in Table 7.2. The production rate and cumulative production data in Table 7.2 are plotted in Fig. 7.4.

### 7.3.2 OIL PRODUCTION DURING TWO-PHASE FLOW PERIOD

When the average-reservoir pressure drops to below bubble-point pressure, some solution gas becomes free gas in the reservoir, and solution-gas drive becomes a dominating mechanism of fluid production. The gas–oil two-phase pseudo-steady-state flow begins to prevail the reservoir. Both IPR and TPR change with time because of the significant variations of fluid properties, relative permeabilities, and GLR. The Hagedorn–Brown correlation should be used to model the TPR. The IPR can be described with Vogel’s model by Eq. (3.19), in Chapter 3, Reservoir Deliverability that is,

$$q = \frac{J^* \bar{p}}{1.8} \left[ 1 - 0.2 \left( \frac{p_{wf}}{\bar{p}} \right) - 0.8 \left( \frac{p_{wf}}{\bar{p}} \right)^2 \right]. \quad (7.8)$$

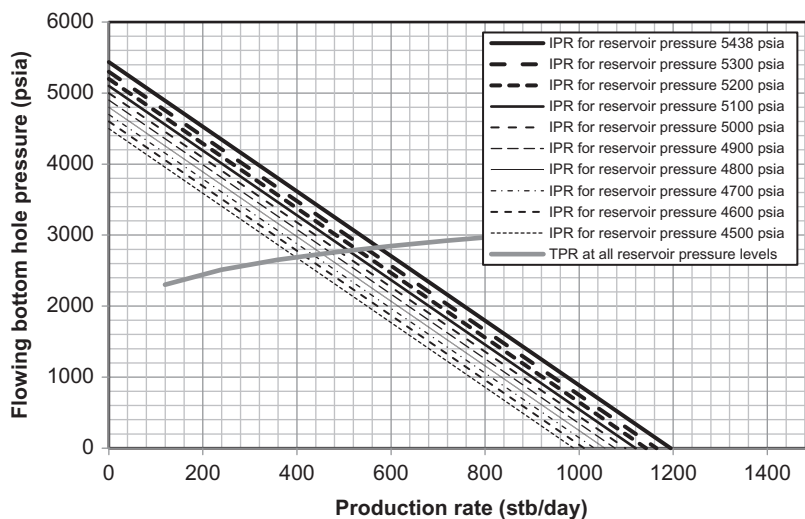


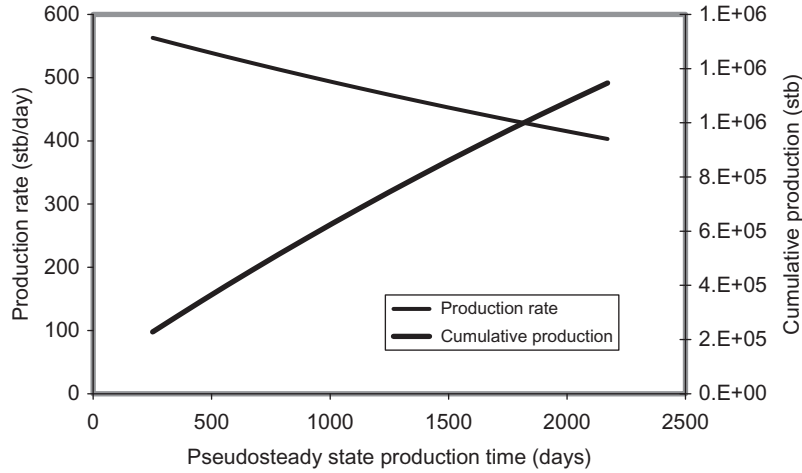
FIGURE 7.3

Nodal analysis plot for Example Problem 7.2.

Table 7.2 Production Forecast for Example Problem 7.2

Reservoir Pressure (psia)	Production Rate (stb/day)	Recovery Ratio	Cumulative Production (stb)	Incremental Production (stb)	Incremental Production Time (days)	Pseudo-Steady-State Production Time (days)
5426	583	0.0010	84,366			0
5300	563	0.0026	228,204	143,837	251	251
5200	543	0.0039	342,528	114,325	207	458
5100	523	0.0052	457,001	114,473	215	673
5000	503	0.0065	571,624	114,622	223	896
4900	483	0.0078	686,395	114,771	233	1,129
4800	463	0.0091	801,315	114,921	243	1,372
4700	443	0.0105	916,385	115,070	254	1,626
4600	423	0.0118	1,031,605	115,220	266	1,892
4500	403	0.0131	1,146,975	115,370	279	2,171

To perform production forecast for solution-gas drive reservoirs, material balance models are used for establishing the relation of the cumulative production to time. The commonly used material balance model is found in [Craft and Hawkins \(1991\)](#), which was based on the original work of [Tarnier \(1944\)](#).



**FIGURE 7.4**  
Production forecast for Example Problem 7.2.

The following procedure is taken to carry out a production forecast during the two-phase flow period:

- Step 1: Assume a series of average-reservoir pressure  $\bar{p}$  values between the bubble-point pressure  $p_b$  and abandonment reservoir pressure  $p_a$ .
  - Step 2: Estimate fluid properties at each average-reservoir pressure, and calculate incremental cumulative production  $\Delta N_p$  and cumulative production  $N_p$  within each average-reservoir pressure interval.
  - Step 3: Perform Nodal analyses to estimate production rate  $q$  at each average-reservoir pressure.
  - Step 4: Calculate production time  $\Delta t$  for each average-reservoir pressure interval by  $\Delta t = \Delta N_p / q$  and the cumulative production time by  $t = \sum \Delta t$ .
- Step 2 is further described in the following procedure:

1. Calculate coefficients  $\Phi_n$  and  $\Phi_g$  for the two pressure values that define the pressure interval, and obtain average values  $\bar{\Phi}_n$  and  $\bar{\Phi}_g$  in the interval. The  $\Phi_n$  and  $\Phi_g$  are calculated using

$$\Phi_n = \frac{B_o - R_s B_g}{(B_o - B_{oi}) + (R_{si} - R_s) B_g}, \tag{7.9}$$

$$\Phi_g = \frac{B_g}{(B_o - B_{oi}) + (R_{si} - R_s) B_g}, \tag{7.10}$$

where  $B_g$  should be in rb/scf if  $R_s$  is in scf/stb.

2. Assume an average gas-oil ratio  $\bar{R}$  in the interval, and calculate incremental oil and gas production per stb of oil in place by

$$\Delta N_p^1 = \frac{1 - \bar{\Phi}_n N_p^1 - \bar{\Phi}_g G_p^1}{\bar{\Phi}_n + \bar{R} \bar{\Phi}_g}, \tag{7.11}$$

$$\Delta G_p^1 = \Delta N_p^1 \bar{R}, \tag{7.12}$$

where  $N_p^1$  and  $G_p^1$  are the cumulative oil and gas production per stb of oil in place at the beginning of the interval.

3. Calculate cumulative oil and gas production at the end of the interval by adding  $\Delta N_p^1$  and  $\Delta G_p^1$  to  $N_p^1$  and  $G_p^1$ , respectively.
4. Calculate oil saturation by

$$S_o = \frac{B_o}{B_{oi}}(1 - S_w)(1 - N_p^1). \quad (7.13)$$

5. Obtain the relative permeabilities  $k_{rg}$  and  $k_{ro}$  based on  $S_o$ .
6. Calculate the average gas–oil ratio by

$$\bar{R} = R_s + \frac{k_{rg}\mu_o B_o}{k_{ro}\mu_g B_g}, \quad (7.14)$$

where again  $B_g$  should be in rb/scf if  $R_s$  is in scf/stb.

7. Compare the calculated  $\bar{R}$  with the value assumed in Step 2. Repeat Steps 2 through 6 until  $\bar{R}$  converges.

**Example Problem 7.3** For the oil reservoir described in Example Problem 7.2, predict the oil production rate and cumulative oil production over the time interval during which reservoir pressure declines from bubble-point pressure to abandonment reservoir pressure of 2500. The following additional data are given:

Reservoir pressure (psia)	$B_o$ (rb/stb)	$B_g$ (rb/scf)	$R_s$ (rb/scf)	$\mu_g$ (cp)
4500	1.200	6.90E-04	840	0.01
4300	1.195	7.10E-04	820	0.01
4100	1.190	7.40E-04	770	0.01
3900	1.185	7.80E-04	730	0.01
3700	1.180	8.10E-04	680	0.01
3500	1.175	8.50E-04	640	0.01
3300	1.170	8.90E-04	600	0.01
3100	1.165	9.30E-04	560	0.01
2900	1.160	9.80E-04	520	0.01
2700	1.155	1.00E-03	480	0.01
2500	1.150	1.10E-03	440	0.01

$$k_{ro} = 10^{-(4.8455S_g + 0.301)}$$

$$k_{rg} = 0.730678S_g^{1.892}$$

**Solution** Example Problem 7.3 is solved using spreadsheets *Pseudo-Steady-2PhaseProductionForecast.xls* and *Pseudosteady2PhaseForecastPlot.xls*. The former computes operating points and the latter performs material balance calculations. The results are shown in Tables 7.3–7.5. Production forecast curves are given in Fig. 7.5.

**Table 7.3 Oil Production Forecast for  $N = 1$** 

$\bar{p}$ (psia)	$B_o$ (rb/stb)	$B_g$ (rb/scf)	$R_s$ (rb/scf)	$\Phi_n$	$\Phi_g$	$R_{av}$ (rb/scf)	$\Delta N_p^1$ (stb)	$\Delta N_p^1$ (stb)
4500	1.200	6.9E-04	840					
4300	1.195	7.1E-04	820	66.61	0.077	859	7.52E-03	7.52E-03
								7.52E-03
4100	1.190	7.4E-04	770	14.84	0.018	1176	2.17E-02	2.92E-02
								2.92E-02
3900	1.185	7.8E-04	730	8.69	0.011	1666	1.45E-02	4.38E-02
								4.38E-02
3700	1.180	8.1E-04	680	5.74	0.007	2411	1.41E-02	5.79E-02
								5.79E-02
3500	1.175	8.5E-04	640	4.35	0.006	3122	9.65E-03	6.76E-02
								6.76E-02
3300	1.170	8.9E-04	600	3.46	0.005	3877	8.18E-03	7.57E-02
								7.57E-02
3100	1.165	9.3E-04	560	2.86	0.004	4658	7.05E-03	8.28E-02
								8.28E-02
2900	1.160	9.8E-04	520	2.38	0.004	5436	6.43E-03	8.92E-02
								8.92E-02
2700	1.155	1.0E-03	480	2.07	0.003	6246	5.47E-03	9.47E-02
								9.47E-02
2500	1.150	1.1E-03	440	1.83	0.003	7066	4.88E-03	9.96E-02
								9.96E-02

## 7.4 GAS PRODUCTION DURING TRANSIENT FLOW PERIOD

Similar to oil production, the gas production rate during a transient flow period can be predicted by Nodal analysis using transient IPR and steady-state flow TPR. The IPR model for gas wells is described in Chapter 3, Reservoir Deliverability that is,

$$q = \frac{kh[m(p_i) - m(p_{wf})]}{1638T \left( \log t + \log \frac{k}{\phi \mu_o c_t r_w^2} - 3.23 + 0.875S \right)}. \quad (7.15)$$

Eq. (7.15) can be used for generating IPR curves for future time  $t$  before any reservoir boundary is “felt.” After all reservoir boundaries are reached, a pseudo-steady-state flow should prevail for a volumetric gas reservoir. For a circular reservoir, the time required for the pressure wave to reach the reservoir boundary can be estimated with  $t_{pss} \approx 1200 \frac{\phi \mu c_t r_e^2}{k}$ .

The same TPR is usually used in the transient flow period assuming fluid properties remain the same in the well over the period. The average temperature–average  $z$ -factor method can be used for constructing TPR.

**Table 7.4 Gas Production Forecast for  $N = 1$** 

$\bar{p}$ (psia)	$\Delta G_p^1$ (scf)	$\Delta G_p^1$ (scf)	$S_o$	$S_g$	$k_{ro}$	$k_{rg}$	$R_{av}$ (rb/scf)
4500	6.46E + 00	6.46E + 00	0.642421	0.007579	0.459492	7.11066E-05	859
4300	2.55E + 01	3.20E + 01	0.625744	0.024256	0.381476	0.000642398	1176
4100	2.42E + 01	5.62E + 01	0.61378	0.03622	0.333809	0.001371669	1666
3900	3.41E + 01	9.03E + 01	0.602152	0.047848	0.293192	0.002322907	2411
3700	3.01E + 01	1.20E + 02	0.593462	0.056538	0.266099	0.003185377	3122
3500	3.17E + 01	1.52E + 02	0.585749	0.064251	0.244159	0.004057252	3877
3300	3.28E + 01	1.85E + 02	0.578796	0.071204	0.225934	0.004927904	4658
3100	3.50E + 01	2.20E + 02	0.572272	0.077728	0.210073	0.005816961	5436
2900	3.41E + 01	2.54E + 02	0.566386	0.083614	0.19672	0.006678504	6246
2700	3.45E + 01	2.89E + 02	0.560892	0.089108	0.185024	0.007532998	7066
2500							

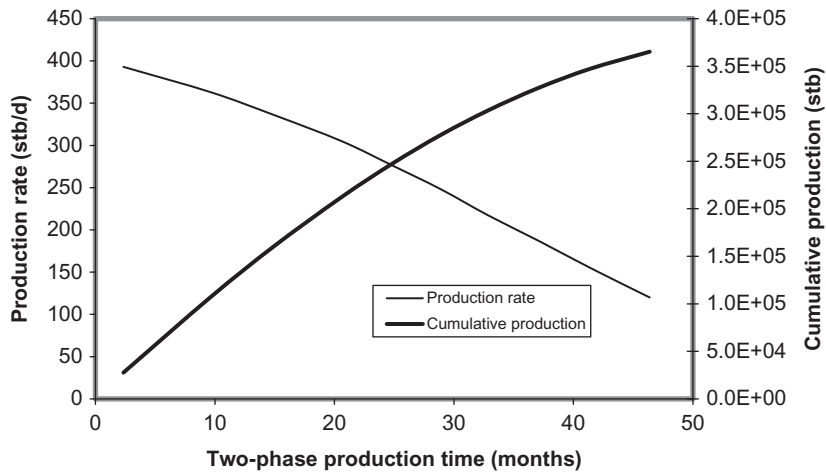
## 7.5 GAS PRODUCTION DURING PSEUDO—STEADY-STATE FLOW PERIOD

Gas production during pseudo-steady-state flow period is due to gas expansion. The IPR changes over time due to the change in reservoir pressure. An IPR model is described in Chapter 3, Reservoir Deliverability that is,

$$q = \frac{kh[m(\bar{p}) - m(p_{wf})]}{1424T \left( \ln \frac{r_e}{r_w} - \frac{3}{4} + S + Dq \right)} \quad (7.16)$$

**Table 7.5 Production Schedule Forecast**

$\bar{p}$ (psia)	$q_o$ (stb/day)	$\Delta N_p$ (stb)	$N_p$ (stb)	$\Delta G_p$ (scf)	$G_p$ (scf)	$\Delta t$ (day)	$t$ (day)
4500	393	2.8E + 04		2.37E + 07		70	
4300	363	8.0E + 04	27,601	9.36E + 07	2.37E + 07	219	7.02E + 01
4100	336	5.3E + 04	107,217	8.89E + 07	1.17E + 08	159	2.90E + 02
3900	305	5.2E + 04	160,565	1.25E + 08	2.06E + 08	170	4.48E + 02
3700	276	3.5E + 04	212,442	1.10E + 08	3.31E + 08	128	6.18E + 02
3500	248	3.0E + 04	247,824	1.16E + 08	4.42E + 08	121	7.47E + 02
3300	217	2.6E + 04	277,848	1.21E + 08	5.58E + 08	119	8.68E + 02
3100	187	2.4E + 04	303,716	1.28E + 08	6.79E + 08	126	9.87E + 02
2900	155	2.0E + 04	327,302	1.25E + 08	8.07E + 08	129	1.11E + 03
2700	120	1.8E + 04	347,354	1.27E + 08	9.32E + 08	149	1.24E + 03
2500			365,268		1.06E + 09		1.39E + 03



**FIGURE 7.5**

Production forecast for Example Problem 7.3.



Constant TPR is usually assumed if liquid loading is not a problem and the wellhead pressure is kept constant over time.

The gas production schedule can be established through the material balance equation,

$$G_p = G_i \left( \frac{\bar{p}}{z_i} \right), \quad (7.17)$$

where  $G_p$  and  $G_i$  are the cumulative gas production and initial “gas in place,” respectively.

If the gas production rate is predicted by Nodal analysis at a given reservoir pressure level and the cumulative gas production is estimated with Eq. (7.17) at the same reservoir pressure level, the corresponding production time can be calculated and, thus, production forecast can be carried out.

**Example Problem 7.4** Use the following data and develop a forecast of a well production after transient flow until the average reservoir pressure declines to 2000 psia:

Reservoir depth:	10,000 ft
Initial reservoir pressure:	4613 psia
Reservoir temperature:	180°F
Pay zone thickness:	78 ft
Formation permeability:	0.17 md
Formation porosity:	0.14
Water saturation:	0.27
Gas-specific gravity:	0.7 air = 1
Total compressibility:	$1.5 \times 10^{-4} \text{ ps}^{-1}$
Darcy skin factor:	0
Non-Darcy flow coefficient:	0
Drainage area:	40 acres
Wellbore radius:	0.328 ft
Tubing inner diameter:	2.441 in.
Desired flowing bottom-hole pressure:	1500 psia

**Solution** The spreadsheet program *Carr-KobayashiBurrows-GasViscosity.xls* gives a gas viscosity value of 0.0251 cp at the initial reservoir pressure of 4613 psia and temperature of 180°F for the 0.7 specific gravity gas. The spreadsheet program *Hall-Yarborough-z.xls* gives a  $z$ -factor value of 1.079 at the same conditions. Formation volume factor at the initial reservoir pressure is calculated with Eq. (2.62):

$$B_{gi} = 0.0283 \frac{(1.079)(180 + 460)}{4613} = 0.004236 \text{ ft}^3/\text{scf}$$

The initial “gas in place” within the 40 acres is

$$G_i = \frac{(43,560)(40)(78)(0.14)(1 - 0.27)}{0.004236} = 3.28 \times 10^9 \text{ scf.}$$

Assuming a circular drainage area, the equivalent radius of the 40 acres is 745 ft. The time required for the pressure wave to reach the reservoir boundary is estimated as

$$\begin{aligned} t_{pss} &\approx 1200 \frac{(0.14)(0.0251)(1.5 \times 10^{-4})(745)^2}{0.17} \\ &= 2065 \text{ hours} = 86 \text{ days.} \end{aligned}$$

The spreadsheet program *PseudoPressure.xls* gives

$$m(p_i) = m(4613) = 1.27 \times 10^9 \text{ psi}^2/\text{cp}$$

$$m(p_{wf}) = m(1500) = 1.85 \times 10^8 \text{ psi}^2/\text{cp}$$

Substituting these and other given parameter values into Eq. (7.15) yields

$$q = \frac{(0.17)(78)[1.27 \times 10^9 - 1.85 \times 10^8]}{1638(180 + 460) \left( \log(2065) + \log \frac{0.17}{(0.14)(0.0251)(1.5 \times 10^{-4})(0.328)^2} - 3.23 \right)}$$

$$= 2092 \text{ Mscf/day.}$$

Substituting  $q = 2092$  Mscf/day into Eq. (7.16) gives

$$2092 = \frac{(0.17)(78)[m(\bar{p}) - 1.85 \times 10^8]}{1424(180 + 460) \left( \ln \frac{745}{0.328} - \frac{3}{4} + 0 \right)},$$

which results in  $m(\bar{p}) = 1.19 \times 10^9 \times \text{psi}^2/\text{cp}$ . The spreadsheet program *PseudoPressure.xls* gives  $\bar{p} = 4409$  at the beginning of the pseudo–steady-state flow period.

If the flowing bottom-hole pressure is maintained at a level of 1500 psia during the pseudo–steady-state flow period (after 86 days of transient production), Eq. (7.16) is simplified as

$$q = \frac{(0.17)(78)[m(\bar{p}) - 1.85 \times 10^8]}{1424(180 + 460) \left( \ln \frac{745}{0.328} - \frac{3}{4} + 0 \right)}$$

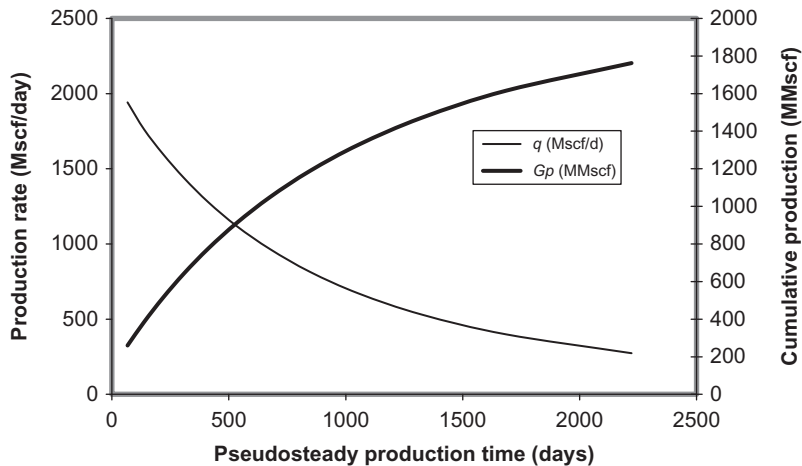
or

$$q = 2.09 \times 10^{-6} [m(\bar{p}) - 1.85 \times 10^8],$$

which, combined with Eq. (7.17), gives the production forecast shown in Table 7.6, where  $z$ -factors and real gas pseudo–pressures were obtained using spreadsheet programs *Hall-Yarborough-z.xls* and *PseudoPressure.xls*, respectively. The spreadsheet performing gas production forecast is *GasWellProductionForecast.xls*. The production forecast result is plotted in Fig. 7.6.

**Table 7.6 Result of Production Forecast for Example Problem 7.4**

Reservoir pressure (psia)	$z$	Pseudopressure ( $10^8 \text{ psi}^2/\text{cp}$ )	$G_p$ (MMscf)	$\Delta G_p$ (MMscf)	$q$ (Mscf/day)	$\Delta t$ (day)	$t$ (day)
4409	1.074	11.90	130				
4200	1.067	11.14	260	130	1942	67	67
4000	1.060	10.28	385	125	1762	71	138
3800	1.054	9.50	514	129	1598	81	218
3600	1.048	8.73	645	131	1437	91	309
3400	1.042	7.96	777	132	1277	103	413
3200	1.037	7.20	913	136	1118	122	534
3000	1.032	6.47	1050	137	966	142	676
2800	1.027	5.75	1188	139	815	170	846
2600	1.022	5.06	1328	140	671	209	1055
2400	1.018	4.39	1471	143	531	269	1324
2200	1.014	3.76	1615	144	399	361	1686
2000	1.011	3.16	1762	147	274	536	2222

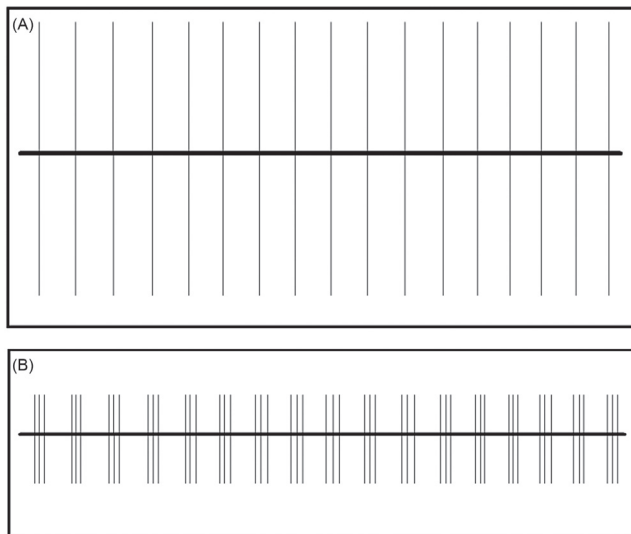
**FIGURE 7.6**

Result of production forecast for Example Problem 7.4.

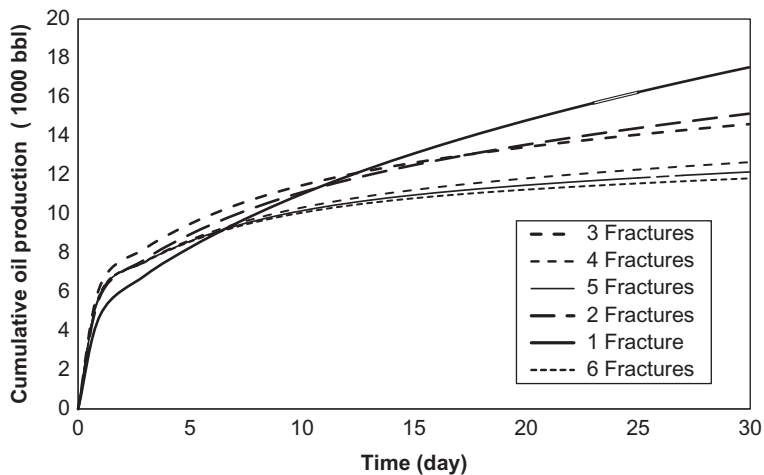
## 7.6 PRODUCTION FORECAST THROUGH RESERVOIR SIMULATION

Reservoir simulation has become an industry standard practice in production forecast at well level, facility level, and field level. Classical reservoir simulators allow for simulation of multiphase flow in heterogeneous reservoirs with special variations of reservoir properties including pay zone thickness, fluid saturation, porosity, permeability, and in inclusion of faults and multiple wells. Modern reservoir simulators allow inclusion of multi-stage fractures. Reservoir simulators linked with wellbore flow simulators allow for using wellhead pressure/flow rate to specify operating conditions.

Reservoir simulators are widely employed for optimization of well completion design for maximizing well productivity and field production performance. For instance, Fig. 7.7 shows two completion models of a multi-stage fractured horizontal oil well in the Upper Eagle Ford shale. Option (A) illustrates a scenario of one fracture created from each cluster of perforations, and option (B) shows a scenario of three fractures/branches created from each cluster of perforations. Fig. 7.8 demonstrates the result of production forecast given by a reservoir simulation run for the multi-stage fractured horizontal well with different fracturing scenarios including (A) and (B). The curves in the figure indicate that short multi-fractures/branches from each perforation cluster will increase short-term (<13 years) production volume while long single-fractures from each cluster will yield high production performance in the long-term (>13 years).

**FIGURE 7.7**

Completion models of a multi-stage fractured horizontal oil well in the Upper Eagle Ford: (A) one fracture created from each cluster of perforations, and (B) three fractures/branches created from each cluster of perforations.

**FIGURE 7.8**

Production forecast by reservoir simulation for a multi-stage fractured horizontal well in a shale oil reservoir.

---

## 7.7 SUMMARY

This chapter illustrated how to perform production forecast using the principle of Nodal analysis and material balance. Accuracy of the forecast strongly depends on the quality of fluid property data, especially for the two-phase flow period. It is always recommended to use fluid properties derived from PVT lab measurements in production forecast calculations. Reservoir simulators should be used for forecasting production performance of wells with complex configurations such as multi-stage fractured horizontal wells and multi-lateral wells.

---

## REFERENCES

- Craft, B.C., Hawkins, M., 1991. *Applied Petroleum Reservoir Engineering*. second ed Prentice Hall, Englewood Cliffs, NJ.
- Dake, L.P., 1978. *Fundamentals of Reservoir Engineering*. Elsevier Science Publishing Company, New York.
- Tarner, J., 1944. How different size gas caps and pressure maintenance programs affect amount of recoverable oil. *Oil Weekly* 144, 32–34.

---

## PROBLEMS

- 7.1. Suppose an oil reservoir can produce under transient flow for the next 1 month. Predict oil production rate and cumulative oil production over the 1 month using the following data:

Reservoir porosity ( $\phi$ ):	0.25
Effective horizontal permeability ( $k$ ):	50 md
Pay zone thickness ( $h$ ):	75 ft
Reservoir pressure ( $p_i$ ):	5000 psia
Oil formation volume factor ( $B_o$ ):	1.3 rb/stb
Total reservoir compressibility ( $c_r$ ):	0.000012 psi <sup>-1</sup>
Wellbore radius ( $r_w$ ):	0.328 ft
Skin factor ( $S$ ):	0
Well depth ( $H$ ):	8000 ft
Tubing inner diameter ( $d$ ):	2.041
Oil gravity (API):	35 API
Oil viscosity ( $\mu_o$ ):	1.3 cp
Producing gas–liquid ratio:	400 scf/bbl
Gas-specific gravity ( $\gamma_g$ ):	0.7 air = 1
Flowing tubing head pressure ( $p_{hf}$ ):	500 psia
Flowing tubing head temperature ( $T_{hf}$ ):	120°F
Flowing temperature at tubing shoe ( $T_{wf}$ ):	160°F
Water cut:	10%
Interfacial tension ( $\sigma$ ):	30 dynes/cm
Specific gravity of water ( $\gamma_w$ ):	1.05

- 7.2. Suppose the reservoir described in Problem 7.1 begins to produce oil under a pseudo–steady-state flow condition immediately after the 1-month transient flow. If the bubble-point pressure is 4000 psia, predict oil production rate and cumulative oil production over the time interval before reservoir pressure declines to bubble-point pressure.

Reservoir pressure (psia)	$B_o$ (rb/stb)	$B_g$ (rb/scf)	$R_s$ (rb/scf)	$\mu_g$ (cp)
4000	1.300	6.80E–04	940	0.015
3800	1.275	7.00E–04	920	0.015
3600	1.250	7.20E–04	870	0.015
3400	1.225	7.40E–04	830	0.015
3200	1.200	8.00E–04	780	0.015
3000	1.175	8.20E–04	740	0.015
2800	1.150	8.50E–04	700	0.015
2600	1.125	9.00E–04	660	0.015
2400	1.120	9.50E–04	620	0.015
2200	1.115	1.00E–03	580	0.015
2000	1.110	1.10E–03	540	0.015

- 7.3. For the oil reservoir described in Problem 7.2, predict oil production rate and cumulative oil production over the time interval during which reservoir pressure declines from bubble-point pressure to abandonment reservoir pressure of 2000. The following additional data are given:

$$k_{ro} = 10^{-(4.5S_g + 0.3)}$$

$$k_{rg} = 0.75S_g^{1.8}$$

- 7.4. Assume that a 0.328-ft radius well in a gas reservoir drains gas from an area of 40 acres at depth 8000 ft through a 2.441 inside diameter (ID) tubing against a wellhead pressure 500 psia. The reservoir has a net pay of 78 ft, porosity of 0.14, permeability of 0.17 md, and water saturation of 0.27. The initial reservoir pressure is 4613 psia. Reservoir temperature is 180°F. Gas-specific gravity is 0.65. The total system compressibility is 0.00015 psi<sup>-1</sup>. Both Darcy and non-Darcy skin are negligible. Considering both transient and pseudo-steady-state flow periods, generate a gas production forecast until the reservoir pressure drops to 3600 psia.
- 7.5. Use the following data and develop a forecast of a gas well production during the transient flow period:

Reservoir depth:	9000 ft
Initial reservoir pressure:	4400 psia
Reservoir temperature:	170°F
Pay zone thickness:	60 ft
Formation permeability:	0.25 md
Formation porosity:	0.15
Water saturation:	0.30
Gas-specific gravity:	0.7 air = 1
Total compressibility:	1.6 × 10 <sup>-4</sup> psi <sup>-1</sup>

Darcy skin factor:	0
Non-Darcy flow coefficient:	0
Drainage area:	40 acres
Wellbore radius:	0.328 ft
Tubing inner diameter:	2.441 in.
Desired flowing bottom-hole pressure:	1100 psia

**7.6.** Use the following data and develop a forecast of a gas well production after transient flow until the average reservoir pressure declines to 2000 psia:

Reservoir depth:	8000 ft
Initial reservoir pressure:	4300 psia
Reservoir temperature:	160°F
Pay zone thickness:	50 ft
Formation permeability:	0.20 md
Formation porosity:	0.15
Water saturation:	0.30
Gas-specific gravity:	0.7 air = 1
Total compressibility:	$1.6 \times 10^{-4} \text{ psi}^{-1}$
Darcy skin factor:	0
Non-Darcy flow coefficient:	0
Drainage area:	160 acres
Wellbore radius:	0.328 ft
Tubing inner diameter:	1.995 in.
Desired flowing bottom-hole pressure:	1200 psia

**7.7.** Use the following data and develop a forecast of a gas well production after transient flow until the average reservoir pressure declines to 2000 psia:

Reservoir depth:	8000 ft
Initial reservoir pressure:	4300 psia
Reservoir temperature:	160°F
Pay zone thickness:	50 ft
Formation permeability:	0.20 md
Formation porosity:	0.15
Water saturation:	0.30
Gas-specific gravity:	0.7 air = 1
Total compressibility:	$1.6 \times 10^{-4} \text{ psi}^{-1}$
Darcy skin factor:	0
Non-Darcy flow coefficient:	0
Drainage area:	160 acres
Wellbore radius:	0.328 ft
Tubing inner diameter:	1.995 in.
Desired flowing wellhead pressure:	800 psia

## PRODUCTION DECLINE ANALYSIS

## 8

## 8.1 INTRODUCTION

Production decline analysis is a traditional means of identifying well production problems and predicting well performance and life based on real production data. It uses empirical decline models that have little fundamental justification. These models include the following:

- Exponential decline (constant fractional decline)
- Harmonic decline
- Hyperbolic decline

Although the hyperbolic decline model is more general, the other two models are degenerations of the hyperbolic decline model. These three models are related through the following relative decline rate equation (Arps, 1945):

$$\frac{1}{q} \frac{dq}{dt} = -bq^d, \quad (8.1)$$

where  $b$  and  $d$  are empirical constants to be determined based on production data. When  $d = 0$ , Eq. (8.1) degenerates to an exponential decline model, and when  $d = 1$ , Eq. (8.1) yields a harmonic decline model. When  $0 < d < 1$ , Eq. (8.1) derives a hyperbolic decline model. The decline models are applicable to both oil and gas wells.

## 8.2 EXPONENTIAL DECLINE

The relative decline rate and production rate decline equations for the exponential decline model can be derived from volumetric reservoir model. Cumulative production expression is obtained by integrating the production rate decline equation (Golan and Whitson, 1986).

### 8.2.1 RELATIVE DECLINE RATE

Consider an oil well drilled in a volumetric oil reservoir. Suppose the well's production rate starts to decline when a critical (lowest permissible) bottom-hole pressure is reached. Under the pseudo-steady-state flow condition, the production rate at a given decline time  $t$  can be expressed as



$$q = \frac{kh(\bar{p}_t - p_{wf}^c)}{141.2B_o\mu \left[ \ln \left( \frac{0.472r_e}{r_w} \right) + s \right]}, \quad (8.2)$$

where

$\bar{p}_t$  = average reservoir pressure at decline time  $t$ ,

$p_{wf}^c$  = the critical bottom-hole pressure maintained during the production decline.

The cumulative oil production of the well after the production decline time  $t$  can be expressed as

$$N_p = \int_0^t \frac{kh(\bar{p}_t - p_{wf}^c)}{141.2B_o\mu \left[ \ln \left( \frac{0.472r_e}{r_w} \right) + s \right]} dt. \quad (8.3)$$

The cumulative oil production after the production decline upon decline time  $t$  can also be evaluated based on the total reservoir compressibility:

$$N_p = \frac{c_t N_i}{B_o} (\bar{p}_0 - \bar{p}_t), \quad (8.4)$$

where

$c_t$  = total reservoir compressibility,

$N_i$  = initial oil in place in the well drainage area,

$\bar{p}_0$  = average reservoir pressure at decline time zero.

Substituting Eq. (8.3) into Eq. (8.4) yields

$$\int_0^t \frac{kh(\bar{p}_t - p_{wf}^c)}{141.2B_o\mu \left[ \ln \left( \frac{0.472r_e}{r_w} \right) + s \right]} dt = \frac{c_t N_i}{B_o} (\bar{p}_0 - \bar{p}_t). \quad (8.5)$$

Taking derivative on both sides of this equation with respect to time  $t$  gives the differential equation for reservoir pressure:

$$\frac{kh(\bar{p}_t - p_{wf}^c)}{141.2\mu \left[ \ln \left( \frac{0.472r_e}{r_w} \right) + s \right]} = -c_t N_i \frac{d\bar{p}_t}{dt} \quad (8.6)$$

Because the left-hand side of this equation is  $q$  and Eq. (8.2) gives

$$\frac{dq}{dt} = \frac{kh}{141.2B_o\mu \left[ \ln \left( \frac{0.472r_e}{r_w} \right) + s \right]} \frac{d\bar{p}_t}{dt}, \quad (8.7)$$

Eq. (8.6) becomes

$$q = \frac{-141.2c_t N_i \mu \left[ \ln \left( \frac{0.472r_e}{r_w} \right) + s \right]}{kh} \frac{dq}{dt} \quad (8.8)$$

or the relative decline rate equation of

$$\frac{1}{q} \frac{dq}{dt} = -b, \quad (8.9)$$

where

$$b = \frac{kh}{141.2\mu c_t N_i \left[ \ln \left( \frac{0.472r_e}{r_w} \right) + s \right]}. \quad (8.10)$$

### 8.2.2 PRODUCTION RATE DECLINE

Eq. (8.6) can be expressed as

$$-b(\bar{p}_t - p_{wf}^c) = \frac{d\bar{p}_t}{dt}. \quad (8.11)$$

By separation of variables, Eq. (8.11) can be integrated,

$$-\int_0^t b dt = \int_{\bar{p}_0}^{\bar{p}_t} \frac{d\bar{p}_t}{(\bar{p}_t - p_{wf}^c)}, \quad (8.12)$$

to yield an equation for reservoir pressure decline:

$$\bar{p}_t = p_{wf}^c + (\bar{p}_0 - p_{wf}^c) e^{-bt} \quad (8.13)$$

Substituting Eq. (8.13) into Eq. (8.2) gives the well production rate decline equation:

$$q = \frac{kh(\bar{p}_0 - p_{wf}^c)}{141.2B_o\mu \left[ \ln \left( \frac{0.472r_e}{r_w} \right) + s \right]} e^{-bt} \quad (8.14)$$

or

$$q = \frac{bc_t N_i}{B_o} (\bar{p}_0 - p_{wf}^c) e^{-bt}, \quad (8.15)$$

which is the exponential decline model commonly used for production decline analysis of solution-gas-drive reservoirs. In practice, the following form of Eq. (8.15) is used:

$$q = q_i e^{-bt}, \quad (8.16)$$

where  $q_i$  is the production rate at  $t = 0$ .

It can be shown that  $\frac{q_2}{q_1} = \frac{q_3}{q_2} = \dots = \frac{q_n}{q_{n-1}} = e^{-b}$ . That is, the fractional decline is constant for exponential decline. As an exercise, this is left to the reader to prove.

### 8.2.3 CUMULATIVE PRODUCTION

Integration of Eq. (8.16) over time gives an expression for the cumulative oil production since decline of

$$N_p = \int_0^t q dt = \int_0^t q_i e^{-bt} dt, \quad (8.17)$$

that is,

$$N_p = \frac{q_i}{b} (1 - e^{-bt}). \quad (8.18)$$

Since  $q = q_i e^{-bt}$ , Eq. (8.18) becomes

$$N_p = \frac{1}{b} (q_i - q). \quad (8.19)$$

### 8.2.4 DETERMINATION OF DECLINE RATE

The constant  $b$  is called the *continuous decline rate*. Its value can be determined from production history data. If production rate and time data are available, the  $b$  value can be obtained based on the slope of the straight line on a semi-log plot. In fact, taking logarithm of Eq. (8.16) gives

$$\ln(q) = \ln(q_i) - bt, \quad (8.20)$$

which implies that the data should form a straight line with a slope of  $-b$  on the  $\log(q)$  versus  $t$  plot, if exponential decline is the right model. Picking up any two points,  $(t_1, q_1)$  and  $(t_2, q_2)$ , on the straight line will allow analytical determination of  $b$  value because

$$\ln(q_1) = \ln(q_i) - bt_1 \quad (8.21)$$

and

$$\ln(q_2) = \ln(q_i) - bt_2 \quad (8.22)$$

give

$$b = \frac{1}{(t_2 - t_1)} \ln\left(\frac{q_1}{q_2}\right). \quad (8.23)$$

If production rate and cumulative production data are available, the  $b$  value can be obtained based on the slope of the straight line on an  $N_p$  versus  $q$  plot. In fact, rearranging Eq. (8.19) yields

$$q = q_i - bN_p. \quad (8.24)$$

Picking up any two points,  $(N_{p1}, q_1)$  and  $(N_{p2}, q_2)$ , on the straight line will allow analytical determination of the  $b$  value

$$b = \frac{q_1 - q_2}{N_{p2} - N_{p1}}. \quad (8.25)$$

Depending on the unit of time  $t$ , the  $b$  can have different units such as  $\text{month}^{-1}$  and  $\text{year}^{-1}$ . The following relation can be derived:

$$b_a = 12b_m = 365b_d, \quad (8.26)$$

where  $b_a$ ,  $b_m$ , and  $b_d$  are annual, monthly, and daily decline rates, respectively.

### 8.2.5 EFFECTIVE DECLINE RATE

Because the exponential function is not easy to use in hand calculations, traditionally the effective decline rate has been used. Since  $e^{-x} \approx 1 - x$  for small  $x$ -values based on Taylor's expansion,  $e^{-b} \approx 1 - b$  holds true for small values of  $b$ . The  $b$  is substituted by  $b'$ , the effective decline rate, in field applications. Thus, Eq. (8.16) becomes

$$q = q_i(1 - b')^t. \quad (8.27)$$

Again, it can be shown that  $\frac{q_2}{q_1} = \frac{q_3}{q_2} = \dots = \frac{q_n}{q_{n-1}} = 1 - b'$ .

Depending on the unit of time  $t$ , the  $b'$  can have different units such as  $\text{month}^{-1}$  and  $\text{year}^{-1}$ . The following relation can be derived:

$$(1 - b'_a) = (1 - b'_m)^{12} = (1 - b'_d)^{365}, \quad (8.28)$$

where  $b'_a$ ,  $b'_m$ , and  $b'_d$  are annual, monthly, and daily effective decline rates, respectively. The following relations are obtained by integration:

$$N_p = \int_{t_0}^t q dt = \int_{t_0}^t q_i(1 - b')^t dt = \frac{q_i}{\ln(1 - b')} [(1 - b')^t - (1 - b')^{t_0}]. \quad (8.29)$$

Substituting Eq. (8.27) into Eq. (8.29) gives

$$N_p = \frac{1}{\ln(1 - b')} [q - q_i]. \quad (8.30)$$

**Example Problem 8.1** Given that a well has declined from 100 stb/day to 96 stb/day during a 1-month period, use the exponential decline model to perform the following tasks:

1. Predict the production rate after 11 more months
2. Calculate the amount of oil produced during the first year
3. Project the yearly production for the well for the next 5 years

#### Solution

1. Production rate after 11 more months:

$$\begin{aligned} b_m &= \frac{1}{(t_{1m} - t_{0m})} \ln \left( \frac{q_{0m}}{q_{1m}} \right) \\ &= \left( \frac{1}{1} \right) \ln \left( \frac{100}{96} \right) = 0.04082/\text{month} \end{aligned}$$

Rate at end of 1 year:

$$q_{1m} = q_{0m} e^{-b_m t} = 100 e^{-0.04082(12)} = 61.27 \text{ stb/day}$$

If the effective decline rate  $b'$  is used,

$$b'_m = \frac{q_{0m} - q_{1m}}{q_{0m}} = \frac{100 - 96}{100} = 0.04/\text{month}.$$

From

$$1 - b'_y = (1 - b'_m)^{12} = (1 - 0.04)^{12},$$

one gets

$$b'_y = 0.3875/\text{yr}$$

Rate at end of 1 year:

$$q_1 = q_0(1 - b'_y) = 100(1 - 0.3875) = 61.27 \text{ stb/day}$$

2. The amount of oil produced during the first year:

$$b_y = 0.04082(12) = 0.48986/\text{year}$$

$$N_{p,1} = \frac{q_0 - q_1}{b_y} = \left( \frac{100 - 61.27}{0.48986} \right) 365 = 28,858 \text{ stb}$$

Or

$$b_d = \left[ \ln \left( \frac{100}{96} \right) \right] \left( \frac{1}{30.42} \right) = 0.001342 \frac{1}{\text{day}}$$

$$N_{p,1} = \frac{100}{0.001342} (1 - e^{-0.001342(365)}) = 17,681 \text{ stb}$$

3. Yearly production for the next 5 years:

$$N_{p,2} = \frac{61.27}{0.001342} (1 - e^{-0.001342(365)}) = 17,681 \text{ stb}$$

$$q_2 = q_1 e^{-bt} = 100 e^{-0.04082(12)(2)} = 37.54 \text{ stb/day}$$

$$N_{p,3} = \frac{37.54}{0.001342} (1 - e^{-0.001342(365)}) = 10,834 \text{ stb}$$

$$q_3 = q_2 e^{-bt} = 100 e^{-0.04082(12)(3)} = 23.00 \text{ stb/day}$$

$$N_{p,4} = \frac{23.00}{0.001342} (1 - e^{-0.001342(365)}) = 6639 \text{ stb}$$

$$q_4 = q_3 e^{-bt} = 100 e^{-0.04082(12)(4)} = 14.09 \text{ stb/day}$$

$$N_{p,5} = \frac{14.09}{0.001342} (1 - e^{-0.001342(365)}) = 4061 \text{ stb}$$

In summary,

Year	Rate at End of Year (stb/day)	Yearly Production (stb)
0	100.00	—
1	61.27	28,858
2	37.54	17,681
3	23.00	10,834
4	14.09	6639
5	8.64	4061

### 8.3 HARMONIC DECLINE

When  $d = 1$ , Eq. (8.1) yields differential equation for a harmonic decline model:

$$\frac{1}{q} \frac{dq}{dt} = -bq, \quad (8.31)$$

which can be integrated as

$$q = \frac{q_0}{1 + bt}, \quad (8.32)$$

where  $q_0$  is the production rate at  $t = 0$ .

Expression for the cumulative production is obtained by integration:

$$N_p = \int_0^t q dt,$$

which gives

$$N_p = \frac{q_0}{b} \ln(1 + bt). \quad (8.33)$$

Combining Eqs. (8.32) and (8.33) gives

$$N_p = \frac{q_0}{b} [\ln(q_0) - \ln(q)]. \quad (8.34)$$

### 8.4 HYPERBOLIC DECLINE

When  $0 < d < 1$ , integration of Eq. (8.1) gives

$$\int_{q_0}^q \frac{dq}{q^{1+d}} = - \int_0^t b dt, \quad (8.35)$$

which results in

$$q = \frac{q_0}{(1 + bdt)^{1/d}} \quad (8.36)$$

or

$$q = \frac{q_0}{\left(1 + \frac{b}{a}t\right)^a}, \quad (8.37)$$

where  $a = 1/d$ .

Expression for the cumulative production is obtained by integration:

$$N_p = \int_0^t q dt,$$

which gives

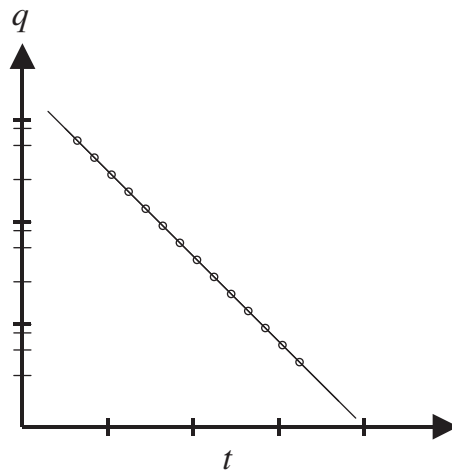
$$N_p = \frac{aq_0}{b(a-1)} \left[ 1 - \left( 1 + \frac{b}{a}t \right)^{1-a} \right]. \quad (8.38)$$

Combining Eqs. (8.37) and (8.38) gives

$$N_p = \frac{a}{b(a-1)} \left[ q_0 - q \left( 1 + \frac{b}{a}t \right) \right]. \quad (8.39)$$

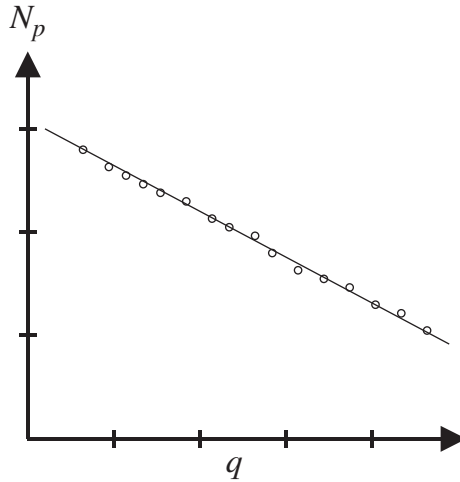
## 8.5 MODEL IDENTIFICATION

Production data can be plotted in different ways to identify a representative decline model. If the plot of  $\log(q)$  versus  $t$  shows a straight line (Fig. 8.1), according to Eq. (8.20), the decline data follow an exponential decline model. If the plot of  $q$  versus  $N_p$  shows a straight line (Fig. 8.2), according to Eq. (8.24), an exponential decline model should be adopted. If the plot of  $\log(q)$  versus  $\log(t)$  shows a straight line (Fig. 8.3), according to Eq. (8.32), the decline data follow a harmonic decline model. If the plot of  $N_p$  versus  $\log(q)$  shows a straight line (Fig. 8.4), according to Eq. (8.34), the harmonic decline model should be used. If no straight line is seen in these plots, the hyperbolic decline model may be verified by plotting the relative decline rate defined by Eq. (8.1). Fig. 8.5 shows such a plot. This work can be easily performed with the computer program *UcomS.exe*.

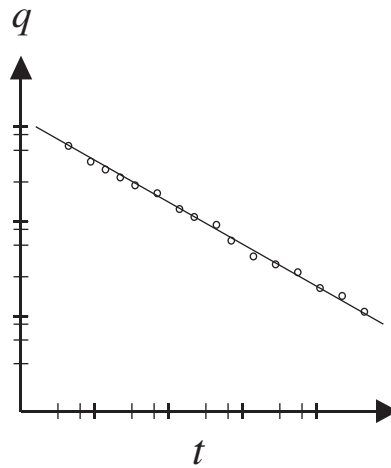


**FIGURE 8.1**

A semi-log plot of  $q$  versus  $t$  indicating an exponential decline.

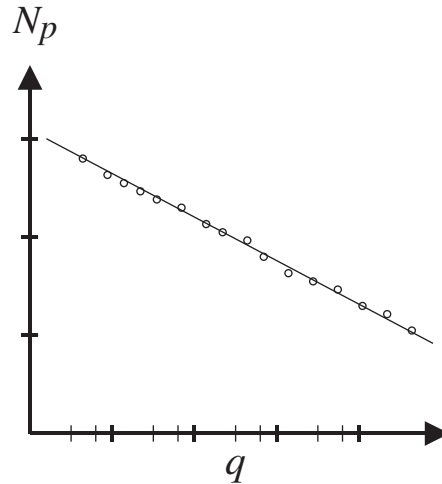
**FIGURE 8.2**

A plot of  $N_p$  versus  $q$  indicating an exponential decline.

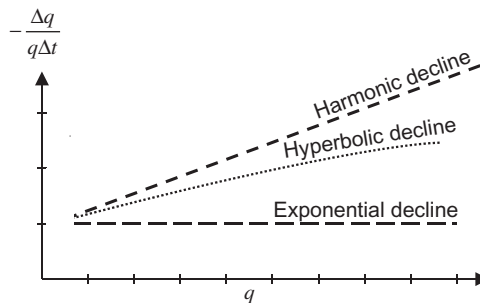
**FIGURE 8.3**

A plot of  $q$  versus  $\log(t)$  indicating a harmonic decline.



**FIGURE 8.4**

A plot of  $N_p$  versus  $\log(q)$  indicating a harmonic decline.

**FIGURE 8.5**

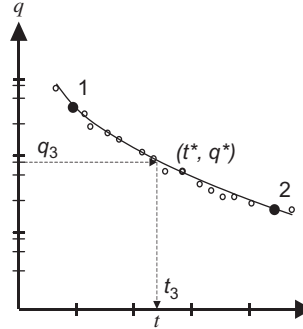
A plot of relative decline rate versus production rate.

## 8.6 DETERMINATION OF MODEL PARAMETERS

Once a decline model is identified, the model parameters  $a$  and  $b$  can be determined by fitting the data to the selected model. For the exponential decline model, the  $b$  value can be estimated on the basis of the slope of the straight line in the plot of  $\log(q)$  versus  $t$  Eq. (8.23). The  $b$  value can also be determined based on the slope of the straight line in the plot of  $q$  versus  $N_p$  Eq. (8.27).

For the harmonic decline model, the  $b$  value can be estimated on the basis of the slope of the straight line in the plot of  $\log(q)$  versus  $\log(t)$  or Eq. (8.32):

1. Select points  $(t_1, q_1)$  and  $(t_2, q_2)$
2. Read  $t_3$  at  $q_3 = \sqrt{q_1 q_2}$
3. Calculate  $\left(\frac{b}{a}\right) = \frac{t_1 + t_2 - 2t_3}{t_3^2 - t_1 t_2}$
4. Find  $q_0$  at  $t = 0$
5. Pick up any point  $(t^*, q^*)$
6. Use  $q_0 = \frac{q_0}{\left(1 + \left(\frac{b}{a}\right)t^*\right)^a} \Rightarrow a = \frac{\log\left(\frac{q_0}{q^*}\right)}{\log\left(1 + \left(\frac{b}{a}\right)t^*\right)}$
7. Finally  $b = \left(\frac{b}{a}\right)a$



**FIGURE 8.6**

Procedure for determining  $a$ - and  $b$ -values.

$$b = \frac{q_0 - 1}{t_1} \tag{8.40}$$

The  $b$  value can also be estimated based on the slope of the straight line in the plot of  $N_p$  versus  $\log(q)$  Eq. (8.34).

For the hyperbolic decline model, determination of  $a$  and  $b$  values is somewhat tedious (Economides et al., 1994). The procedure is shown in Fig. 8.6.

The computer program *UcomS.exe* can be used for both model identification and model parameter determination, as well as production rate prediction.

## 8.7 ILLUSTRATIVE EXAMPLES

**Example Problem 8.2** For the data given in Table 8.1, identify a suitable decline model, determine model parameters, and project production rate until a marginal rate of 25 stb/day is reached.

**Solution** A plot of  $\log(q)$  versus  $t$  is presented in Fig. 8.7, which shows a straight line. According to Eq. (8.20), the exponential decline model is applicable. This is further evidenced by the relative decline rate shown in Fig. 8.8.

Select points on the trend line:

$$\begin{aligned} t_1 &= 5 \text{ months,} & q_1 &= 607 \text{ stb/day} \\ t_2 &= 20 \text{ months,} & q_2 &= 135 \text{ stb/day} \end{aligned}$$

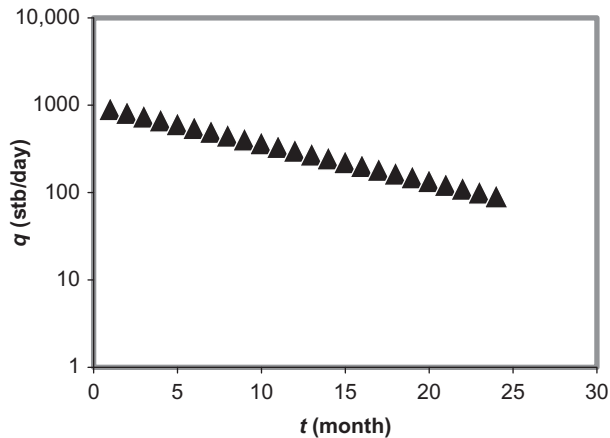
Decline rate is calculated with Eq. (8.23):

$$b = \frac{1}{(5 - 20)} \ln\left(\frac{135}{607}\right) = 0.11/\text{month}$$

Projected production rate profile is shown in Fig. 8.9.

**Table 8.1 Production Data for Example Problem 8.2**

$t$ (mo)	$q$ (stb/day)	$t$ (mo)	$q$ (stb/day)
1.00	904.84	13.00	272.53
2.00	818.73	14.00	246.60
3.00	740.82	15.00	223.13
4.00	670.32	16.00	201.90
5.00	606.53	17.00	182.68
6.00	548.81	18.00	165.30
7.00	496.59	19.00	149.57
8.00	449.33	20.00	135.34
9.00	406.57	21.00	122.46
10.00	367.88	22.00	110.80
11.00	332.87	23.00	100.26
12.00	301.19	24.00	90.720

**FIGURE 8.7**

A plot of  $\log(q)$  versus  $t$  showing an exponential decline.

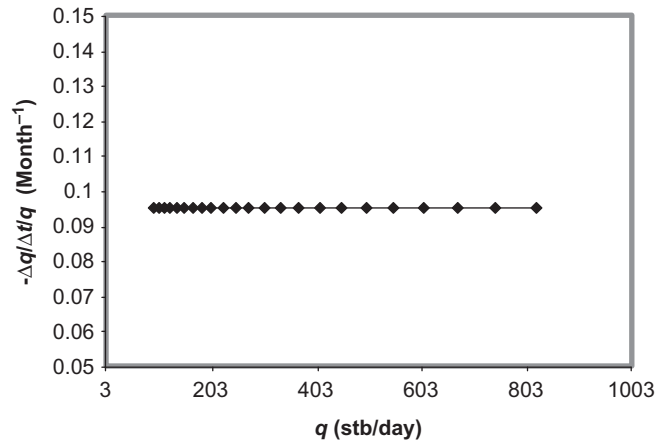
**Example Problem 8.3** For the data given in Table 8.2, identify a suitable decline model, determine model parameters, and project production rate until the end of the fifth year.

**Solution** A plot of relative decline rate is shown in Fig. 8.10, which clearly indicates a harmonic decline model.

On the trend line, select

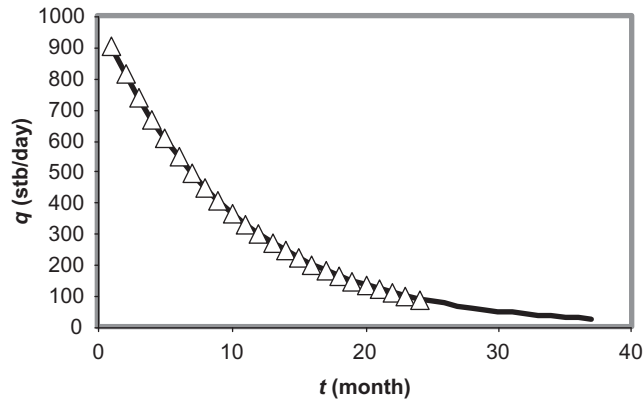
$$q_0 = 10,000 \text{ stb/day at } t = 0$$

$$q_1 = 5680 \text{ stb/day at } t = 2 \text{ years.}$$



**FIGURE 8.8**

Relative decline rate plot showing exponential decline.



**FIGURE 8.9**

Projected production rate by an exponential decline model.

Therefore, Eq. (8.40) gives

$$b = \frac{\frac{10,000}{5680} - 1}{2} = 0.38 \text{ 1/yr.}$$

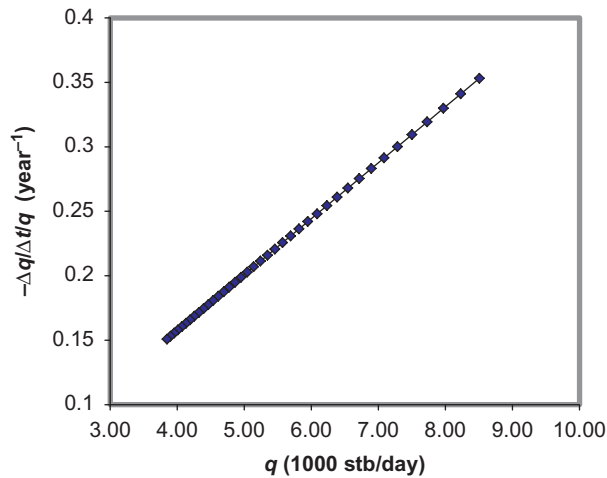
Projected production rate profile is shown in Fig. 8.11.

**Example Problem 8.4** For the data given in Table 8.3, identify a suitable decline model, determine model parameters, and project production rate until the end of the fifth year.

**Solution** A plot of relative decline rate is shown in Fig. 8.12, which clearly indicates a hyperbolic decline model.

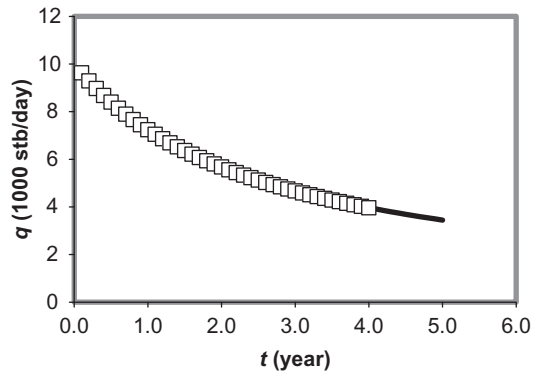
**Table 8.2 Production Data for Example Problem 8.3**

$t$ (yr)	$q$ (1000 stb/day)	$t$ (yr)	$q$ (1000 stb/day)
0.20	9.29	2.10	5.56
0.30	8.98	2.20	5.45
0.40	8.68	2.30	5.34
0.50	8.40	2.40	5.23
0.60	8.14	2.50	5.13
0.70	7.90	2.60	5.03
0.80	7.67	2.70	4.94
0.90	7.45	2.80	4.84
1.00	7.25	2.90	4.76
1.10	7.05	3.00	4.67
1.20	6.87	3.10	4.59
1.30	6.69	3.20	4.51
1.40	6.53	3.30	4.44
1.50	6.37	3.40	4.36
1.60	6.22	3.50	4.29
1.70	6.08	3.60	4.22
1.80	5.94	3.70	4.16
1.90	5.81	3.80	4.09
2.00	5.68	3.90	4.03



**FIGURE 8.10**

Relative decline rate plot showing harmonic decline.



**FIGURE 8.11**

Projected production rate by a harmonic decline model.

**Table 8.3 Production Data for Example Problem 8.4**

$t$ (yr)	$q$ (1000 stb/day)	$t$ (yr)	$q$ (1000 stb/day)
0.10	9.63	2.10	5.18
0.20	9.28	2.20	5.05
0.30	8.95	2.30	4.92
0.40	8.64	2.40	4.80
0.50	8.35	2.50	4.68
0.60	8.07	2.60	4.57
0.70	7.81	2.70	4.46
0.80	7.55	2.80	4.35
0.90	7.32	2.90	4.25
1.00	7.09	3.00	4.15
1.10	6.87	3.10	4.06
1.20	6.67	3.20	3.97
1.30	6.47	3.30	3.88
1.40	6.28	3.40	3.80
1.50	6.10	3.50	3.71
1.60	5.93	3.60	3.64
1.70	5.77	3.70	3.56
1.80	5.61	3.80	3.49
1.90	5.46	3.90	3.41
2.00	5.32	4.00	3.34

Select points

$$t_1 = 0.2 \text{ year, } q_1 = 9280 \text{ stb/day}$$

$$t_2 = 3.8 \text{ years, } q_2 = 3490 \text{ stb/day}$$

$$q_3 = \sqrt{(9280)(3490)} = 5670 \text{ stb/day}$$

$$\left(\frac{b}{a}\right) = \frac{0.2 + 3.8 - 2(1.75)}{(1.75)^2 - (0.2)(3.8)} = 0.217$$

Read from decline curve (Fig. 8.13)  $t_3 = 1.75$  years at  $q_3 = 5670$  stb/day.

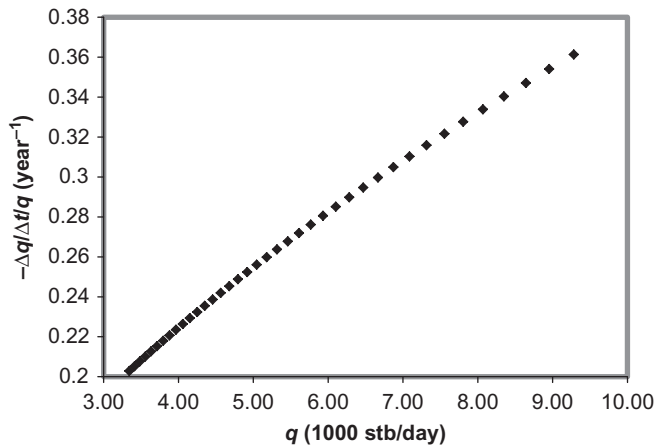


FIGURE 8.12

Relative decline rate plot showing hyperbolic decline.

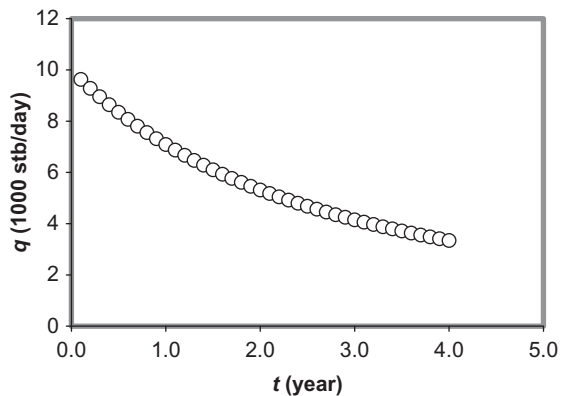
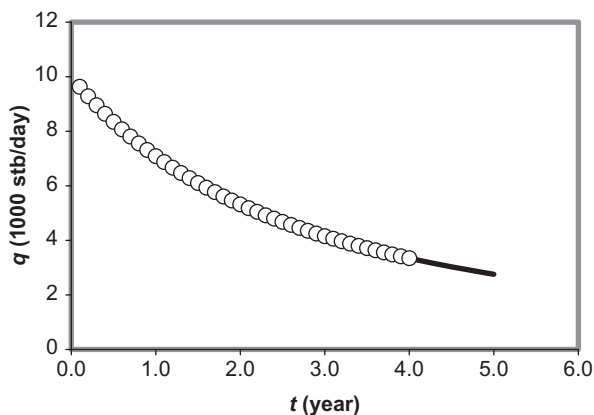


FIGURE 8.13

Relative decline rate shot showing hyperbolic decline.



**FIGURE 8.14**

Projected production rate by a hyperbolic decline model.

Read from decline curve (Fig. 8.13)  $q_0 = 10,000$  stb/day at  $t_0 = 0$ .

Pick up point ( $t^* = 1.4$  years,  $q^* = 6280$  stb/day).

$$a = \frac{\log\left(\frac{10,000}{680}\right)}{\log(1 + (0.217)(1.4))} = 1.75$$

$$b = (0.217)(1.758) = 0.38$$

Projected production rate profile is shown in Fig. 8.14.

## 8.8 SUMMARY

This chapter presents empirical models and procedure for using the models to perform production decline data analyses. Computer program *UcomS.exe* can be used for model identification, model parameter determination, and production rate prediction.

## REFERENCES

- Arps, J.J., 1945. Analysis of decline curves. *Trans. AIME* 160, 228–247.
- Golan, M., Whitson, C.M., 1986. *Well Performance*. International Human Resource Development Corp, Upper Saddle River, NJ.
- Economides, M.J., Hill, A.D., Ehlig-Economides, C., 1994. *Petroleum Production Systems*. Prentice Hall PTR, Upper Saddle River, NJ.



---

**PROBLEMS**

- 8.1.** For the data given in the following table, identify a suitable decline model, determine model parameters, and project production rate until the end of the 10th year. Predict yearly oil productions:
- 8.2.** For the data given in the following table, identify a suitable decline model, determine model parameters, predict the time when the production rate will decline to a marginal value of 500 stb/day, and the reserves to be recovered before the marginal production rate is reached:

Time (yr)	Production Rate (1000 stb/day) for Problem 8.1	Production Rate (1000 stb/day) for Problem 8.2
0.1	9.63	9.63
0.2	9.29	9.28
0.3	8.98	8.95
0.4	8.68	8.64
0.5	8.4	8.35
0.6	8.14	8.07
0.7	7.9	7.81
0.8	7.67	7.55
0.9	7.45	7.32
1	7.25	7.09
1.1	7.05	6.87
1.2	6.87	6.67
1.3	6.69	6.47
1.4	6.53	6.28
1.5	6.37	6.1
1.6	6.22	5.93
1.7	6.08	5.77
1.8	5.94	5.61
1.9	5.81	5.46
2	5.68	5.32
2.1	5.56	5.18
2.2	5.45	5.05
2.3	5.34	4.92
2.4	5.23	4.8
2.5	5.13	4.68
2.6	5.03	4.57
2.7	4.94	4.46
2.8	4.84	4.35
2.9	4.76	4.25
3	4.67	4.15
3.1	4.59	4.06
3.2	4.51	3.97
3.3	4.44	3.88
3.4	4.36	3.8

- 8.3.** For the data given in the following table, identify a suitable decline model, determine model parameters, predict the time when the production rate will decline to a marginal value of 50 Mscf/day, and the reserves to be recovered before the marginal production rate is reached:

Time (mo)	Production Rate (Mscf/day)
1	904.84
2	818.73
3	740.82
4	670.32
5	606.53
6	548.81
7	496.59
8	449.33
9	406.57
10	367.88
11	332.87
12	301.19
13	272.53
14	246.6
15	223.13
16	201.9
17	182.68
18	165.3
19	149.57
20	135.34
21	122.46
22	110.8
23	100.26
24	90.72

- 8.4.** For the data given in the following table, identify a suitable decline model, determine model parameters, predict the time when the production rate will decline to a marginal value of 50 stb/day, and yearly oil productions:

Time (mo)	Production Rate (stb/day)
1	1810
2	1637
3	1482
4	1341
5	1213
6	1098
7	993
8	899

(Continued)

*Continued*

Time (mo)	Production Rate (stb/day)
9	813
10	736
11	666
12	602
13	545
14	493
15	446
16	404
17	365
18	331
19	299
20	271
21	245
22	222
23	201
24	181

# SURFACE AND DOWNHOLE EQUIPMENT

# II

*The role of a petroleum production engineer is to maximize oil and gas production in a cost-effective manner. Design and selection of the right equipment for production systems is essential for a production engineer to achieve his or her job objective. To perform their design work correctly, production engineers should have a thorough knowledge of the principles and rules used in the industry for equipment design and selection. This part of the book provides graduating production engineers with principles and rules used in the petroleum production engineering practice. Materials are presented in the following three chapters:*

Chapter 9: Well Tubing and Packers 9/219

Chapter 10: Separation Systems 10/243

Chapter 11: Transportation Systems 11/275

---

# WELL TUBING AND PACKERS

# 9

---

## 9.1 INTRODUCTION

Most oil wells produce reservoir fluids through tubing strings. This is mainly because tubing strings provide good sealing performance and allow the use of gas expansion to lift oil. Gas wells produce gas through tubing strings to reduce liquid loading problems.

Tubing strings are designed considering tension, collapse, and burst loads under various well operating conditions to prevent loss of tubing string integrity including mechanical failure and deformation due to excessive stresses and buckling. This chapter describes wellhead-tubing-packer relation, presents properties of the American Petroleum Institute (API) tubing and special considerations in designing tubing strings.

---

## 9.2 WELLHEAD-TUBING-PACKER RELATION

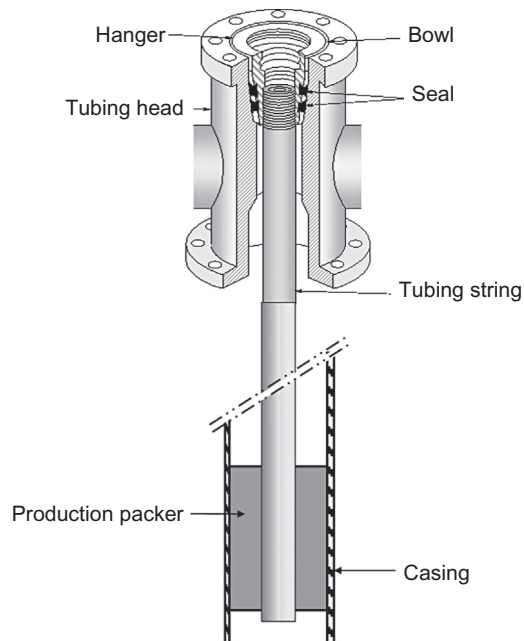
Tubing string is hanged to the tubing head in the wellhead at top and usually anchored to casing at bottom with production packer. Fig. 9.1 shows the wellhead-tubing-packer relation. Sometimes the tubing string is not anchored to the casing where the packer only provides a seal to the annular space between tubing and casing. When the tubing string is anchored to the casing, the packer is called a restraining packer, otherwise it is called a nonrestraining packer. If a restraining packer is used, the tubing string is set to the wellhead head in a tension load greater than the weight of the tubing string so that the string will not buckle during fluid production due to thermal expansion. When a well is subjected to treatment operations such as cement squeezing, acidizing, hydraulic fracturing, and workover, tubing tension is adjusted on the basis of treatment conditions. Calculation of required tension load is illustrated in the section that follows.

---

## 9.3 TUBING DESIGN

Tubing string is the most important equipment of oil and gas wells. It ensures efficient transport of production fluids (oil, water, and gas) from bottom hole to surface. Safe operation of wells requires proper design of tubing string considering various possible well conditions during fluid production and well treatment.

The API defines “tubing size” using nominal diameter and weight (per foot). The nominal diameter is based on the internal diameter of tubing body. The weight of tubing determines the tubing

**FIGURE 9.1**

Wellhead-tubing-packer relation.

Tubing Grade	Yield strength (psi)		Minimum Tensile Strength (psi)
	Minimum	Maximum	
H-40	40,000	80,000	60,000
J-55	55,000	80,000	75,000
C-75	75,000	90,000	95,000
L-80	80,000	95,000	95,000
N-80	80,000	110,000	100,000
C-90	90,000	105,000	100,000
P-105	105,000	135,000	120,000

outer diameter (OD). Steel grades of tubing are designated to H-40, J-55, C-75, L-80, N-80, C-90, and P-105, where the digits represent the minimum yield strength in 1000 psi. Table 9.1 gives the tensile requirements of API tubing. The minimum performance properties of API tubing are listed in Appendix B of this book. The tubing collapse strength data listed in Appendix B do not reflect the effect of biaxial stress. The effect of tension on the collapse resistance is analyzed as follows.

Consider a simple uniaxial test of a metal specimen. Hooke's Law applies to the elastic portion before yield point:

$$\sigma = E\varepsilon, \tag{9.1}$$

where  $\sigma$ ,  $\varepsilon$ , and  $E$  are stress, strain, and Young's modulus, respectively. The energy in the elastic portion of the test is

$$U_u = \frac{1}{2}\sigma\varepsilon = \frac{1}{2}\frac{P}{A}\frac{\Delta l}{L} = \frac{1}{2}\frac{(P \cdot \Delta l)}{V}$$

$$U_u = \frac{1}{2}\frac{W}{V}, \tag{9.2}$$

where  $P$ ,  $A$ ,  $L$ ,  $V$ , and  $\Delta l$  are force, area, length, volume, and length change, respectively. However, using Hooke's Law, we have

$$U_u = \frac{1}{2}\sigma\varepsilon = \frac{1}{2}\sigma\left(\frac{\sigma}{E}\right) = \frac{1}{2}\frac{\sigma^2}{E}. \tag{9.3}$$

To assess whether a material is going to fail, we use various material failure criteria. One of the most important is the Distortion Energy Criteria. This is for 3D and is

$$U = \frac{1}{2}\left(\frac{1+\nu}{3E}\right)[(\sigma_1 - \sigma_2)^2 + (\sigma_2 - \sigma_3)^2 + (\sigma_3 - \sigma_1)^2], \tag{9.4}$$

where

- $\nu$  = Poison's ratio
- $\sigma_1$  = axial principal stress, psi
- $\sigma_2$  = tangential principal stress, psi
- $\sigma_3$  = radial principal stress, psi.

For our case of the uniaxial test, we would have

$$\begin{aligned} \sigma_1 &= \sigma \\ \sigma_2 &= 0. \\ \sigma_3 &= 0 \end{aligned} \tag{9.5}$$

Then from Eq. (9.4), we would get

$$U = \frac{1}{2}\left(\frac{1+\nu}{3E}\right)[\sigma^2 + \sigma^2]$$

$$U = \left(\frac{1+\nu}{3E}\right)\sigma^2. \tag{9.6}$$

If the failure of a material is taken to be when the material is at the yield point, then Eq. (9.6) is written

$$U_f = \left(\frac{1+\nu}{3E}\right)\sigma_y^2, \tag{9.7}$$

where  $\sigma_y$  is yield stress. The definition of an “equivalent stress” is the energy level in 3D, which is equivalent to the criteria energy level. Thus,

$$\left(\frac{1+\nu}{3E}\right)\sigma_e^2 = \left(\frac{1+\nu}{3E}\right)\sigma_y^2$$

and

$$\sigma_e = \sigma_y, \quad (9.8)$$

where  $\sigma_e$  is the equivalent stress. The collapse pressure is expressed as

$$p_c = 2\sigma_y \left[ \frac{\left(\frac{D}{t}\right) - 1}{\left(\frac{D}{t}\right)^2} \right], \quad (9.9)$$

where  $D$  is the tubing OD and  $t$  is wall thickness.

For the 3D case, we can consider

$$U = \left(\frac{1+\nu}{3E}\right)\sigma_e^2, \quad (9.10)$$

where  $\sigma_e$  is the equivalent stress for the 3D case of

$$\left(\frac{1+\nu}{3E}\right)\sigma_e^2 = \frac{1}{2} \left(\frac{1+\nu}{3E}\right) [(\sigma_1 - \sigma_2)^2 + (\sigma_2 - \sigma_3)^2 + (\sigma_3 - \sigma_1)^2]; \quad (9.11)$$

thus,

$$\sigma_e^2 = \frac{1}{2} \{(\sigma_1 - \sigma_2)^2 + (\sigma_2 - \sigma_3)^2 + (\sigma_3 - \sigma_1)^2\}. \quad (9.12)$$

Consider the case in which we have only tensile axial loads, and compressive pressure on the outside of the tubing, then Eq. (9.12) reduces to

$$\sigma_e^2 = \frac{1}{2} \{(\sigma_1 - \sigma_2)^2 + (\sigma_2)^2 + (-\sigma_1)^2\} \quad (9.13)$$

$$\sigma_e^2 = \sigma_1^2 - \sigma_1\sigma_2 + \sigma_2^2. \quad (9.14)$$

Further, we can define

$$\begin{aligned} \sigma_1 &= \frac{W}{A} \\ \frac{\sigma_2}{Y_m} &= -\frac{p_\alpha}{p_c}, \end{aligned} \quad (9.15)$$

where

$Y_m$  = minimum yield stress

$p_{cc}$  = the collapse pressure corrected for axial load

$p_c$  = the collapse pressure with no axial load.

$\sigma_e = -Y_m$



Thus, Eq. (9.14) becomes

$$Y_m^2 = \left(\frac{W}{A}\right)^2 + \left(\frac{W}{A}\right) \frac{p_{cc}}{p_c} \cdot Y_m + \left(\frac{p_{cc}}{p_c}\right)^2 Y_m^2 \tag{9.16}$$

$$\left(\frac{p_{cc}}{p_c}\right)^2 + \frac{W}{AY_m} \cdot \left(\frac{p_{cc}}{p_c}\right) + \left(\frac{W}{AY_m}\right)^2 - 1 = 0. \tag{9.17}$$

We can solve Eq. (9.17) for the term  $\frac{p_{cc}}{p_c}$ . This yields

$$\frac{p_{cc}}{p_c} = \frac{-\frac{W}{AY_m} \pm \sqrt{\left(\frac{W}{AY_m}\right)^2 - 4\left(\frac{W}{AY_m}\right)^2 + 4}}{2} \tag{9.18}$$

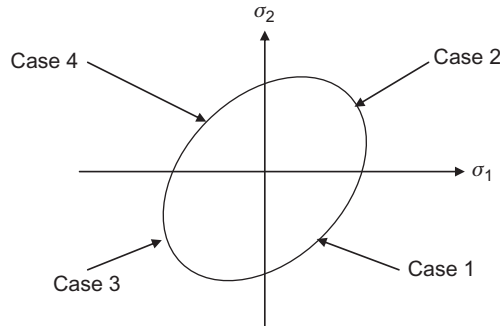
$$p_{cc} = p_c \left\{ \sqrt{1 - 0.75\left(\frac{S_A}{Y_m}\right)^2} - 0.5\left(\frac{S_A}{Y_m}\right) \right\}, \tag{9.19}$$

where  $S_A = \frac{W}{A}$  is axial stress at any point in the tubing string.

In Eq. (9.19), it can be seen that as  $W$  (or  $S_A$ ) increases, the corrected collapse pressure resistance decreases (from the nonaxial load case).

In general, there are four cases, as shown in Fig. 9.2:

- Case 1: Axial tension stress ( $\sigma_1 > 0$ ) and collapse pressure ( $\sigma_2 < 0$ )
- Case 2: Axial tension stress ( $\sigma_1 > 0$ ) and burst pressure ( $\sigma_2 > 0$ )
- Case 3: Axial compression stress ( $\sigma_1 < 0$ ) and collapse pressure ( $\sigma_2 < 0$ )
- Case 4: Axial compression stress ( $\sigma_1 < 0$ ) and burst pressure ( $\sigma_2 > 0$ )



**FIGURE 9.2**

Effect of tension stress on tangential stress.

**Example Problem 9.1** Calculate the collapse resistance for a section of 2 $\frac{7}{8}$  in. API 6.40 lb/ft, Grade J-55, nonupset tubing near the surface of a 10,000-ft string suspended from the surface in a well that is producing gas.

**Solution** Appendix B shows an inner diameter of tubing of 2.441 in., therefore,

$$t = (2.875 - 2.44)/2 = 0.217 \text{ in.}$$

$$\frac{D}{t} = \frac{2.875}{0.217} = 13.25$$

$$p_c = 2(55,000) \left[ \frac{13.25 - 1}{(13.25)^2} \right] = 7675.3 \text{ psi,}$$

which is consistent with the rounded value of 7680 psi listed in Appendix B.

$$A = \pi t(D - t) = \pi(0.217)(2.875 - 0.217) = 1.812 \text{ in.}^2$$

$$S_A = \frac{6.40(10,000)}{1.812} = 35,320 \text{ psi.}$$

Using Eq. (9.19), we get

$$p_\infty = 7675.3 \left\{ \sqrt{1 - 0.75 \left( \frac{35,320}{55,000} \right)^2} - 0.5 \left( \frac{35,320}{55,000} \right) \right\}$$

$$= 3914.5 \text{ psi.}$$

Tubing design should consider tubing failure due to tension, collapse, and burst loads under various well operating conditions. Forces affecting tubing strings include the following:

1. Axial tension due to weight of tubing and compression due to buoyancy
2. External pressure (completion fluids, oil, gas, formation water)
3. Internal pressure (oil, gas, formation water)
4. Bending forces in deviated portion of well
5. Forces due to lateral rock pressure
6. Other forces due to thermal gradient or dynamics

### 9.3.1 TENSION, COLLAPSE, AND BURST DESIGN

The last three columns of the tables in Appendix B present tubing collapse resistance, internal yield pressure, and joint yield strength. These are the limiting strengths for a given tubing joint without considering the biaxial effect shown in Fig. 9.2. At any point should the net external pressure, net internal pressure, and buoyant tensile load not be allowed to exceed tubing's axial load-corrected collapse resistance, internal yield pressure, and joint yield strength, respectively. Tubing strings should be designed to have strengths higher than the maximum expected loads with safety factors

greater than unity. In addition, bending stress should be considered in tension design for deviated and horizontal wells. The tensile stress due to bending is expressed as

$$\sigma_b = \frac{ED_o}{2R_c}, \quad (9.20)$$

where

$\sigma_b$  = bending stress, psi

$E$  = Young's modulus, psi

$R_c$  = radius of hole curvature, in.

$D_o$  = OD of tubing, in.

Because of the great variations in well operating conditions, it is difficult to adopt a universal tubing design criterion for all well situations. Probably the best design practice is to consider the worst loading cases for collapse, burst, and tension loads that are possible for the well to experience during the life of the well. It is vitally important to check the remaining strengths of tubing in a subject well before any unexpected well treatment is carried out. Some special considerations in well operations that affect tubing string integrity are addressed in the sections that follow.

### 9.3.2 BUCKLING PREVENTION DURING PRODUCTION

A completion fluid is in place in the annular space between the tubing and the casing before a well is put into production. The temperature at depth is  $T = T_{sf} + G_T D$ , where  $G_T$  is geothermal gradient. When the oil is produced, the temperature in the tubing will rise. This will expand (thermal) the tubing length, and if there is not sufficient landing tension, the tubing will buckle. The temperature distribution in the tubing can be predicted on the basis of the work of [Ramey \(1962\)](#), [Hasan and Kabir \(2002\)](#), and [Guo et al. \(2005\)](#). The latter is described in Chapter 11, Transportation Systems. A conservative approach to temperature calculations is to assume the maximum possible temperature in the tubing string with no heat loss to formation through annulus.

**Example Problem 9.2** Consider a 2½ in. API, 6.40 lb/ft Grade P-105 nonupset tubing anchored with a packer set at 10,000 ft. The crude oil production through the tubing from the bottom of the hole is 1000 stb/day (no gas or water production). A completion fluid is in place in the annular space between the tubing and the casing (9.8 lb/gal KCl water). Assuming surface temperature is 60°F and geothermal gradient of 0.01°F/ft, determine the landing tension to avoid buckling.

**Solution** The temperature of the fluid at the bottom of the hole is estimated to be

$$T_{10,000} = 60 + 0.01(10,000) = 160^\circ\text{F}.$$

The average temperature of the tubing before oil production is

$$T_{av1} = \frac{60 + 160}{2} = 110^\circ\text{F}.$$

The maximum possible average temperature of the tubing after oil production has started is

$$T_{av2} = \frac{160 + 160}{2} = 160^\circ\text{F}.$$

This means that the approximate thermal expansion of the tubing in length will be

$$\Delta L_T \approx \beta(\Delta T_{avg})L,$$

where  $\beta$  is the coefficient of thermal expansion (for steel, this is  $\beta_s = 0.0000065$  per  $^{\circ}\text{F}$ ). Thus,

$$\Delta L_T \approx 0.0000065[160 - 110]10,000 = 3.25 \text{ ft.}$$

To counter the above thermal expansion, a landing tension must be placed on the tubing string that is equivalent to the above. Assuming the tubing is a simple uniaxial element, then

$$A \approx \pi t(D - t) = \pi(0.217)(2.875 - 0.217) = 1.812 \text{ in.}^2$$

$$\sigma = E\varepsilon$$

$$\frac{F}{A} = E \cdot \frac{\Delta L}{L}$$

$$F = \frac{AE}{L} \Delta L = \frac{(1.812)(30 \times 10^6)(3.25)}{10,000} = 17,667 \text{ lb}_f.$$

Thus, an additional tension of 17,667  $\text{lb}_f$  at the surface must be placed on the tubing string to counter the thermal expansion.

It can be shown that turbulent flow will transfer heat efficiently to the steel wall and then to the completion fluid and then to the casing and out to the formation. Laminar flow will not transfer heat very efficiently to the steel then out to the formation. Thus, the laminar flow situations are the most likely to have higher temperature oil at the exit. Therefore, it is most likely the tubing will be hotter via simple conduction. This effect has been considered in the work of [Hasan and Kabir \(2002\)](#). Obviously, in the case of turbulent flow, landing tension beyond the buoyancy weight of the tubing may not be required, but in the case of laminar flow, the landing tension beyond the buoyancy weight of the tubing is usually required to prevent buckling of tubing string. In general, it is good practice to calculate the buoyant force of the tubing and add approximately 4000–5000  $\text{lb}_f$  of additional tension when landing.

### 9.3.3 CONSIDERATIONS FOR WELL TREATMENT AND STIMULATION

Tubing strings are designed to withstand the harsh conditions during wellbore treatment and stimulation operations such as hole cleaning, cement squeezing, gravel packing, frac-packing, acidizing, and hydraulic fracturing. Precautionary measures to take depend on tubing–packer relation. If the tubing string is set through a nonrestraining packer, the tubing is free to move. Then string buckling and tubing–packer integrity will be major concerns. If the tubing string is set on a restraining packer, the string is not free to move and it will apply force to the packer.

The factors to be considered in tubing design include the following:

- Tubing size, weight, and grade
- Well conditions
  - Pressure effect
  - Temperature effect

- Completion method
  - Cased hole
  - Open hole
  - Multitubing
  - Packer type (restraining, nonrestraining)

### 9.3.3.1 Temperature effect

As discussed in Example Problem 9.2, if the tubing string is free to move, its thermal expansion is expressed as

$$\Delta L_T = \beta L \Delta T_{avg}. \quad (9.21)$$

If the tubing string is not free to move, its thermal expansion will generate force. Since Hook's Law gives

$$\Delta L_T = \frac{L \Delta F}{AE}, \quad (9.22)$$

substitution of Eq. (9.22) into Eq. (9.21) yields

$$\Delta F \approx AE \beta \Delta T_{avg} \approx 207A \Delta T_{avg} \quad (9.23)$$

for steel tubing.

### 9.3.3.2 Pressure effect

Pressures affect tubing string in different ways including piston effect, ballooning effect, and buckling effect. Consider the tubing–pack relation shown in Fig. 9.3. The total upward force acting on the tubing string from internal and external pressures is expressed as

$$F_{up} = p_i(A_p - A'_i) + p_o(A_o - A'_o), \quad (9.24)$$

where

- $p_i$  = pressure in the tubing, psi
- $p_o$  = pressure in the annulus, psi
- $A_p$  = inner area of packer, in.<sup>2</sup>
- $A'_i$  = inner area of tubing sleeve, in.<sup>2</sup>
- $A'_o$  = outer area of tubing sleeve, in.<sup>2</sup>

The total downward force acting on the tubing string is expressed as

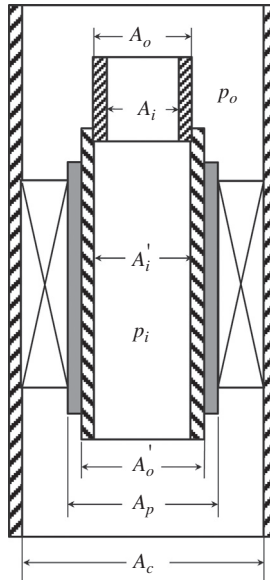
$$F_{down} = p_i(A_i - A'_i) + p_o(A_p - A'_o), \quad (9.25)$$

where  $A_i$  is the inner area of tubing. The net upward force is then

$$F = F_{up} - F_{down} = p_i(A_p - A_i) - p_o(A_p - A_o). \quad (9.26)$$

During a well treatment operation, the change (increase) in the net upward force is expressed as

$$\Delta F = [\Delta p_i(A_p - A_i) - \Delta p_o(A_p - A_o)]. \quad (9.27)$$



**FIGURE 9.3**

Tubing–packer relation.

If the tubing string is anchored to a restraining packer, this force will be transmitted to the packer, which may cause packer failure. If the tubing string is free to move, this force will cause the tubing string to shorten by

$$\Delta L_P = \frac{L\Delta F}{AE}, \quad (9.28)$$

which represents tubing string shrinkage due to piston effect.

As shown in Fig. 9.4A, the ballooning effect is due to the internal pressure being higher than the external pressure during a well treatment. The change in tensile force can be expressed as

$$\Delta F_B = 0.6[\Delta p_{i \text{ avg}} A_i - \Delta p_{o \text{ avg}} A_o]. \quad (9.29)$$

If the tubing string is set through a restraining packer, this force will be transmitted to the packer, which may cause packer failure. If the tubing string is free to move, this force will cause the tubing string to shorten by

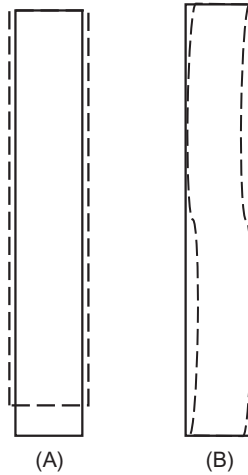
$$\Delta L_B = \frac{2L}{10^8} \left[ \frac{\Delta p_{i \text{ avg}} - R^2 \Delta p_{o \text{ avg}}}{R^2 - 1} \right], \quad (9.30)$$

where

$\Delta p_{i \text{ avg}}$  = the average pressure change in the tubing, psi

$\Delta p_{o \text{ avg}}$  = the average pressure change in the annulus, psi

and  $R^2 = A_o/A_i$ .

**FIGURE 9.4**

(A) Ballooning and (B) buckling effects.

As illustrated in Fig. 9.4B, the buckling effect is caused by the internal pressure being higher than the external pressure during a well treatment. The tubing string buckles when  $F_{BK} = A_p(p_i - p_o) > 0$ . If the tubing end is set through a restraining packer, this force will be transmitted to the packer, which may cause packer failure. If the tubing string is not restrained at bottom, this force will cause the tubing string to shorten by

$$\Delta L_{BK} = \frac{r^2 F_{BK}^2}{8RIW}, \quad (9.31)$$

which holds true only if  $F_{BK}$  is greater than 0, and

$$r = \frac{D_{ci} - D_o}{2}$$

$$I = \frac{\pi}{64} (D_o^4 - D_i^4)$$

$$W = W_{air} + W_{fl} - W_{fo},$$

where

$D_{ci}$  = inner diameter of casing, in.

$D_i$  = inner diameter of tubing, in.

$D_o$  = OD of tubing, in.

$W_{air}$  = weight of tubing in air, lb/ft

$W_{fl}$  = weight of fluid inside tubing, lb/ft

$W_{fo}$  = weight of fluid displaced by tubing, lb/ft

**9.3.3.3 Total effect of temperature and pressure**

The combination of Eqs. (9.22), (9.28), (9.30), and (9.31) gives

$$\Delta L = \Delta L_T + \Delta L_P + \Delta L_B + \Delta L_{BK}, \quad (9.32)$$

which represents the tubing shortening with a nonrestraining packer. If a restraining packer is used, the total tubing force acting on the packer is expressed as

$$\Delta F = \frac{AE\Delta L}{L}. \quad (9.33)$$

**Example Problem 9.3** The following data are given for a cement squeezing job:

Tubing:	2½ in., 6.5 lb/ft (2.441-in. ID)
Casing:	7 in., 32 lb/ft (6.094-in. ID)
Packer:	Bore size $D_p = 3.25$ in., set at 10,000 ft
Initial condition:	Tubing and casing are full of 30 API oil (S.G. = 0.88)
Operation:	Tubing is displaced with 15 ppg cement with an injection pressure 5000 psi and casing pressure 1000 psi. The average temperature drop is 20°F

1. Calculate tubing movement if the tubing is not restrained by the packer, and discuss solutions to the possible operation problems.
2. Calculate the tubing force acting on a restraining packer.

**Solution**

Temperature Effect:

$$\Delta L_T = \beta L \Delta T_{avg} = (6.9 \times 10^{-6})(10,000)(20) = 1.38 \text{ ft}$$

Piston Effect:

$$\begin{aligned} \Delta p_i &= (0.052)(10,000)[15 - (0.88)(8.33)] + 5000 \\ &= 8988 \text{ psi} \end{aligned}$$

$$\Delta p_o = 1000 \text{ psi}$$

$$A_p = 3.14(3.25)^2/4 = 8.30 \text{ in.}^2$$

$$A_i = 3.14(2.441)^2/4 = 4.68 \text{ in.}^2$$

$$A_o = 3.14(2.875)^2/4 = 6.49 \text{ in.}^2$$

$$\begin{aligned} \Delta F &= [\Delta p_i(A_p - A_i) - \Delta p_o(A_p - A_o)] \\ &= [(8988)(8.30 - 4.68) - (1000)(8.30 - 6.49)] \\ &= 30,727 \text{ lb}_f \end{aligned}$$

$$\Delta L_P = \frac{L\Delta F}{AE} = \frac{(10,000)(30,727)}{(6.49 - 4.68)(30,000,000)} = 5.65 \text{ ft}$$



Ballooning Effect:

$$\begin{aligned}\Delta P_{i, avg} &= (10,000/2)(0.052)[15 - (0.88)(8.33)] + 5000 \\ &= 6994 \text{ psi}\end{aligned}$$

$$\Delta P_{o, avg} = 1000 \text{ psi}$$

$$R^2 = 6.49/4.68 = 1.387$$

$$\begin{aligned}\Delta L_B &= \frac{2L}{10^8 \left[ \frac{\Delta P_{i, avg} - R^2 \Delta P_{o, avg}}{R^2 - 1} \right]} \\ &= \frac{2(10,000)}{10^8} \left[ \frac{6994 - 1.387(1000)}{1.387 - 1} \right] = 2.898 \text{ ft}\end{aligned}$$

Since the tubing internal pressure is higher than the external pressure during the cement squeezing, tubing string buckling should occur.

$$p_i = 5000 + (0.052)(15)(10,000) = 12,800 \text{ psi}$$

$$p_o = 1000 + (0.88)(0.433)(10,000) = 4810 \text{ psi}$$

$$r = (6.094 - 2.875)/2 = 1.6095 \text{ in.}$$

$$F_{BK} = A_p(p_i - p_o) = (8.30)(12,800 - 4800) = 66,317 \text{ lb}_f$$

$$I = \frac{\pi}{64} ((2.875)^4 - (2.441)^4) = 1.61 \text{ in.}^4$$

$$W_{air} = 6.5 \text{ lb}_f/\text{ft}$$

$$W_{\bar{f}} = (15)(7.48)(4.68/144) = 3.65 \text{ lb}_f/\text{ft}$$

$$W_{fo} = (0.88)(62.4)(6.49/144) = 2.48 \text{ lb}_f/\text{ft}$$

$$W = 6.5 + 3.65 - 2.48 = 7.67 \text{ lb}_f/\text{ft}$$

$$\begin{aligned}\Delta L_{BK} &= \frac{r^2 F_{BK}^2}{8EIW} \\ &= \frac{(1.6095)^2 (66,317)^2}{(8)(30,000,000)(1.61)(7.67)} = 3.884 \text{ ft}\end{aligned}$$

1. Tubing is not restrained by the packer. The tubing shortening is

$$\begin{aligned}\Delta L &= \Delta L_T + \Delta L_P + \Delta L_B + \Delta L_{BK} \\ &= 1.38 + 5.65 + 2.898 + 3.844 = 13.77 \text{ ft.}\end{aligned}$$

Buckling point from bottom:

$$\begin{aligned} L_{BK} &= \frac{F_{BK}}{W} \\ &= \frac{66,317}{7.67} \\ &= 8646 \text{ ft} \end{aligned}$$

To keep the tubing in the packer, one of the following measures needs to be taken:

- a. Use a sleeve longer than 13.77 ft
  - b. Use a restraining packer
  - c. Put some weight on the packer (slack-hook) before treatment. Buckling due to slacking off needs to be checked.
2. Tubing is restrained by the packer. The force acting on the packer is

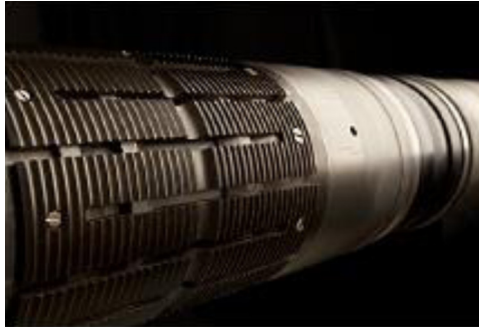
$$\begin{aligned} \Delta F &= \frac{AE\Delta L}{L} = \frac{(6.49 - 4.68)(30,000,000)(13.77)}{(10,000)} \\ &= 74,783 \text{ lb}_f. \end{aligned}$$

---

## 9.4 PRODUCTION PACKERS

A packer is a sealing device that isolates and contains produced fluids and pressures within the wellbore to protect the casing and other formations above or below the producing zone. Other functions of packers include preventing downhole movement of the tubing string, supporting some of the weight of the tubing, improving well flow and production rate, protecting casing from corrosion from the produced fluids and high pressures, limiting well control to the tubing at the surface for safety purposes, and holding well-servicing fluid (kill fluids, packer fluids) in the casing annulus.

Production packers can be classified as conventional packers and swellable packers. Conventional packers are set mechanically or by hydraulics (Patton and Abbott, 1985; Allen and Roberts, 1998). Fluid-swellable packers have been used in recent years. Mechanical type packers have four key elements (Giacomi and Rowe, 1992): slip, cone, packing-element system, and body or mandrel. The slip is a wedge-shaped device with wickers (or teeth) on its face, which penetrate and grip the casing wall when the packer is set (Fig. 9.5). The cone is beveled to match the back of the slip and forms a ramp that drives the slip outward and into the casing wall when setting force is applied to the packer. Once the slips have anchored into the casing wall, additional applied setting force energizes the packing-element system and creates a seal between the packer body and the inside diameter of the casing. Swellable packers inflate in principle by reacting with different types of fluids such as water and oil.



**FIGURE 9.5**

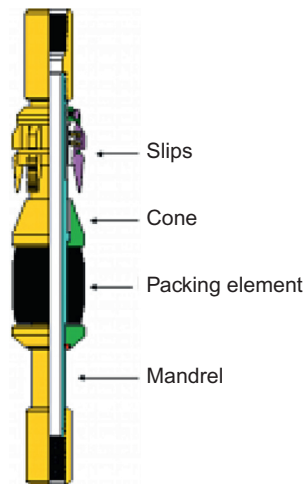
Teeth on mechanical packers (Patton and Abbott, 1985).

### 9.4.1 CONVENTIONAL PACKERS

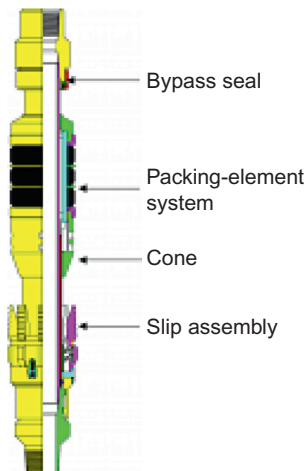
Conventional packers can be classified into two groups: (1) permanent packers, and (2) retrievable packers. Permanent packers can be removed from the wellbore only by milling. The retrievable packer may or may not be resettable, but removal from the wellbore normally does not require milling. Retrieval is usually accomplished by some form of tubing manipulation. This may necessitate rotation or require pulling tension on the tubing string. The permanent packer is fairly simple and generally offers higher performance in both temperature and pressure ratings than does the retrievable packer. In most instances, it has a smaller outside diameter, offering greater running clearance inside the casing string than do retrievable packers. The smaller OD and the compact design of the permanent packer help the tool negotiate through tight spots and deviations in the wellbore. The permanent packer also offers the largest inside diameter to make it compatible with larger-diameter tubing strings and monobore completions. The retrievable packer can be very basic for low pressure/low temperature applications or very complex in high-pressure/high temperature applications. Because of this design complexity in high-end tools, a retrievable packer offering performance levels similar to those of a permanent packer will invariably cost more. However, the ease of removing the packer from the wellbore as well as features, such as reset ability and being able to reuse the packer often, may outweigh the added cost.

Retrievable packers fall into two categories: (1) tension packers, and (2) compression packers. As shown in Fig. 9.6, a tension packer has a single set of unidirectional slips that grip only the casing when the tubing is pulled in tension. Constant tubing tension must be maintained to keep the packer set and the packing element energized. Tension packers, typically, are set mechanically and are released by means of tubing rotation. Most models also have an emergency shear-release feature should the primary release method fail. Tension packers are usually used in medium- to shallow-depth production or injection applications.

Depicted in Fig. 9.7 is a compression packer with a fluid-bypass valve. It prevents setting by means of a mechanical interlock while it is being run in the hole. Once the packer has been run to the desired depth, the tubing string is rotated to initiate the setting sequence. As the tubing is being rotated, the drag blocks on the packer hold the packer in place and provide the resistance to set it. Once the interlock system is released, the tubing string is lowered to close the bypass seal and set

**FIGURE 9.6**

Schematic of a tension packer (Patton and Abbott, 1985).

**FIGURE 9.7**

A sketch of a compression packer (Patton and Abbott, 1985).

the slips. The continued application of slackoff force energizes the packing-element system and creates a seal. The packer is released by simply picking up on the tubing string. The addition of the integral bypass valve assists equalization of pressures in the tubing and annulus and aids in releasing the packer. The valve can be opened by picking up on the tubing string without releasing the packer. Compression packer is recommended for low- to medium-pressure/medium-temperature oil- or gas-production applications.

Compression packer with additional set of hold-down slips, or an anchor system above the packing-element system, sets and releases in much the same manner as the compression packer described in Fig. 3. However, the addition of the hold-down slip helps to keep the packoff force and bypass valve locked in place when pressure below the tool is greater than the pressure in the annulus. This variation can be used in limited treating operations, in gas lift applications, or in production applications in which tubing pressures are greater than annular pressures. There are limitations to the ability of the anchor to keep the bypass closed, and any operational modes that will result in loss of set-down weight must be planned carefully (Baker Oil Tools, 1992).

There are several retrievable packers designed to be installed in the wellbore on electric wireline and retrieved on the tubing string. Fig. 9.8 demonstrates a wireline-set tubing retrievable packer. On the top of the packer is located a special nipple. The nipple has a polished seal surface on its OD and has j-lugs that are used to anchor a seal housing or washover shoe in place. The polished nipple also has a landing nipple profile in its inner diameter. This allows the installation of a slick-line retrievable blanking plug if desired.

The packer is first run and set on electric wireline. The electric wireline setting tool provides the force necessary to anchor the slips in the casing wall and energize the packing element. Once the packer is installed and the wireline is retrieved, a seal housing is run in the hole on the bottom of the production tubing. The housing has internal seals that, when landed on the polished nipple, create a seal between the tubing and the annulus. The housing also has an internal j-profile that engages the lugs of the nipple and anchors the tubing string to the packer. The tubing string can be retrieved from the wellbore at any time without disturbing the packer by unjaying the seal housing from the polished nipple, or the packer can be released and retrieved mechanically with the tubing.



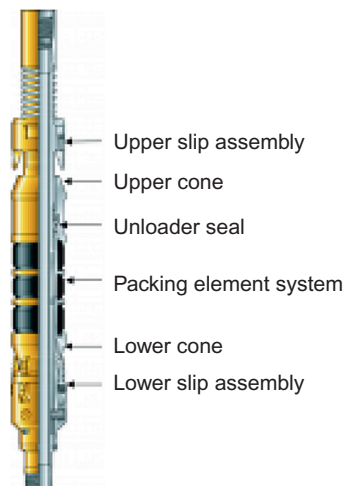
**FIGURE 9.8**

Wireline-set tubing retrievable packer. Left: set with plug in place; Right: set with tubing connected and plug retrieved (Allen and Roberts, 1998).

The main advantage of this system is that it can be run and set under pressure on electric wireline in a live oil or gas well. Once the packer is set, the electric line is removed, and the pressure above the packer can be bled off. With the plug in place, the packer will act as a temporary bridge plug for well control while the tubing string and seal housing are run and landed. Because the plug is located near the top of the packer assembly, it can be circulated free of any debris before landing the tubing. Once the tree has been installed, the plug is removed with slickline, and the well is placed on production. Common applications are for completion of the well after a high-rate fracture is performed down the casing or after underbalanced perforating with a casing gun. This underbalanced completion method is especially useful in applications in which formation damage may occur if kill-weight fluid is introduced into the wellbore.

Fig. 9.9 illustrates a tension/compression-set versatile landing packer that is the most common types of mechanical-set retrievable packers run today. Tension- or compression-set packers that allow the tubing to be landed in tension, compression, or neutral. This group of mechanical-set retrievable packers varies greatly in design and performance and may require tension, compression, or a combination of both to set and pack off the element. The exact setting method depends on the design of the tool. Various packing-element systems and differential ratings are available, making this type of packer suitable for a large number of applications—up to and including some high-pressure/high temperature completions.

One of the common features found in this style of packer is that, once the element is sealed off and the packoff force is mechanically locked in place, the tubing string may be landed in compression, tension, or neutral. Slips located above and below the packing element are designed to hold axial tubing loads from either direction to keep the packer anchored in place. An internal lock system mechanically traps the packoff force and keeps the elements energized until the packer is released. A bypass valve is present to aid in equalization and the release of the packer. It is locked



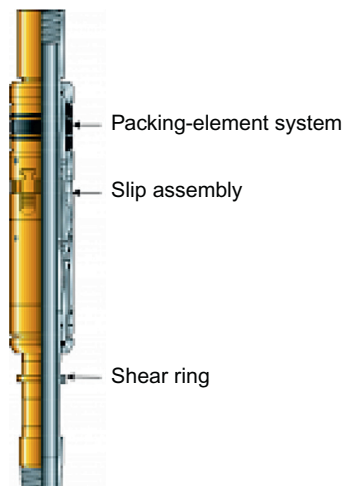
**FIGURE 9.9**

Tension/compression-set versatile landing (Giacomi and Rowe, 1992).

from accidentally opening until the packer-releasing sequence has been initiated. Because the packer does not rely on constant tubing forces to maintain its packoff, this tool is much more versatile in application. It can be used in production or injection applications, as well as in completions for which well stimulation is planned, and it is almost universal in application. The only constraint is in deep deviated wells, where tubing manipulation or getting packoff force to the tool may present a problem. Extreme shallow depth setting is achievable in models that allow the elements to be energized with tension.

Fig. 9.10 demonstrates a hydraulic-set packer. It has a bidirectional slip system that is actuated by a predetermined amount of hydraulic pressure applied to the tubing string. To achieve a pressure differential at the packer and set it, a temporary plugging device must be run in the tailpipe below the packer. The applied hydraulic pressure acts against a piston chamber in the packer. The force created by this action sets the slips and packs the element off. Some models have an atmospheric setting chamber and use the hydrostatic pressure of the well to boost the packoff force. Regardless of design, all of the force generated during the setting process is mechanically locked in place until the packer is later released. Once the packer is set, the tubing may be landed in tension, compression, or neutral. Because no tubing manipulation is required to set a hydraulic packer, it can be set easily after the wellhead has been flanged up and the tubing has been displaced. This promotes safety and allows better control of the well while displacing tubing and annulus fluids. The hydraulic-set packer can be run in a single-packer installation, and because no packer body movement occurs during the setting process, it can be run in tandem as an isolation packer in single-string multiple-zone production wells. The hydraulic-set single-string packer is ideal for highly deviated wells in which conditions are not suitable for mechanical-set packers.

While retrieval of the hydraulic-set single-string packer is possible by pulling tension with the tubing string to shear a shear ring, or shear pins, located within the packer, most models have a



**FIGURE 9.10**

Sketch of a hydraulic-set single-string packer (Baker Oil Tools, 1992).

built-in bypass system that allows the pressures in the tubing and annulus to equalize, or balance, as the packer is released. The tension load required to release the packer must be considered carefully in the initial completion design and in the selection of the shear-ring value. The shear-release value must not be set too high so that it will not be beyond the tensile capabilities of the tubing string, yet it must be high enough so that the packer will not release prematurely during any of the planned operational modes over the life of the completion. A variation of the hydraulic-set single-string retrievable packer, which can be furnished without the shear-release feature, is available for the larger-size casing and tubing combinations commonly used in big monobore completions. This design is better described as a “removable” packer because it is not retrieved by conventional means. The running and the hydraulic setting procedure remain the same, but to remove the packer from the wellbore, the inner mandrel of the packer must be cut. This is done either with a chemical cutter on electric wireline or by a mechanical cutter on drill pipe or coiled tubing. Once the mandrel is cut, retrieval is accomplished by picking up on the tubing string or the top of the packer. The packer is also designed to be millable should the cut-to-release feature fail. The elimination of the shear ring enables the packer to achieve higher tensile and differential pressure ratings. This permits well-treating and well-injection operations to occur that were not possible with the conventional shear-release hydraulic-set packer.

#### 9.4.2 SWELLABLE PACKERS

Swellable packers are not mechanically or hydraulically set. It is due to swelling of packer element on contact with specific type of fluid, i.e., oil or water. A packer with element expanding on contact with hydrocarbons is called an oil-swellable packer. A water-swellable packer has element that expands on contact with water. They are used for sealing wellbore for blocking oil flow and water flow, respectively. Bonded-to-pipe and slip-on, oil- and water-swellable, low- and high-pressure packers are used the energy industry (Fig. 9.11).



**FIGURE 9.11**

An oil-swellable packer is being run in a casing string (Fothergill, 2003).



Slip swellable slip-on packers consist of an elastomer that swells on contact with wellbore fluids (water or oil). The expansion seals the annulus around the pipe in both open and cased holes. With no moving parts, these packers provide a simple, one-trip solution for effective zonal isolation, saving rig time and costs. Swellable packers are engineered from complex polymers that are suitable for high-pressure applications, such as multistage fracturing, and also for sealing in flowing wells, such as when inflow control devices (ICDs) are used. At the same time, the polymers are pliant enough to accommodate washouts and irregular wellbores. Packers undergo full-scale highly accelerated lifecycle testing. Elastomers are tested in high concentrations of hydrogen sulfide ( $H_2S$ ), hydrochloric acid (HCl), and carbon dioxide ( $CO_2$ ) at simulated downhole temperatures and pressures.

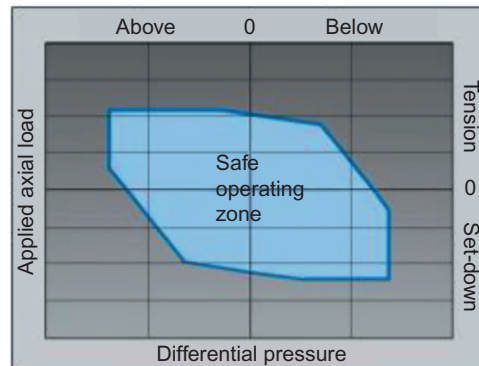
Oil-swellable packers prevent premature setting without the need for any additional exterior coating. Swelling starts immediately after contact with wellbore fluids and progresses in very small increments, enabling the packer to reach the setting depth safely, where it continues to swell and seal. Oil-swellable packers are available for temperatures up to 365°F (185°C) and differential pressures up to 15,000 psi (103 MPa).

In water-swellable packers reactive fillers are integrated into the elastomer to prevent the loss of strength and deswelling effects seen in conventional water-swellable packers, thereby maximizing long-term reliability. Some swellable bonded-to-pipe packers overcome the main weakness of conventional water-swellable packers, which rely solely on osmosis for swelling. Osmosis can reverse over time, causing other packers to deswell and leak. The proprietary reactive technology, however, is based on an irreversible chemical reaction that mechanically reinforces the elastomer and enables higher differential pressures to be withstood by shorter lengths. Superior compounding and mechanical design ensure greater reliability and temperature and differential pressure capabilities with shorter lengths of element. Water-swellable packers are available for temperatures of up to 270°F (133°C) and differential pressures of up to 10,000 psi (69 MPa).

### 9.4.3 SELECTION OF PACKERS

Before selecting any pack, it is important to consider the performance and features of each design, as well as the application in which it will be used. Perhaps in some instances, the permanent packer is the only option, as may be the case in some HP/HT applications. However, in those instances in which either will suffice, the operator must decide which features offer the best return over the life of the well. When selecting a packer for a cased-hole completion, the differential pressure and temperature requirements of the application must be considered. The well depth, deployment and setting method desired, and final tubing landing conditions are also factors that come into play. The various operational modes (flowing, shut-in, injection, and stimulation) that are anticipated over the life of the well are critical and must be considered carefully in the design phase. The changes in the operational modes that influence changes in temperature, differential pressure, and axial loads all have a direct impact on the packer. Understanding the uses and constraints of the different types of packers will help clarify the factors to consider when making a selection.

The envelope is a graph consisting of two axis lines. On the “X” axis, negative values represent tension, and positive values equal compression (Fig. 9.12). The values of the “Y” axis depict differential pressure from above the packer as negative and below the packer as positive. The maximum



**FIGURE 9.12**

Typical packer-rating envelope (Fothergill, 2003).

tested packer ratings under the all-combined load conditions are plotted on the graph and connected by boundary lines that more or less take the shape of a box. Any combinations of pressure and axial loads that fall within the box are considered safe and within the tested limits of the packer.

To use the rating envelope effectively, tubing-movement calculations must be done to determine the packer tubing loads and differential pressures to be encountered in any of the production, shut-in, injection, or treating modes to which the completion will be subjected. These points are then plotted on the rating envelope to see if the applications fall within the safe operating limits of the packer. If they do not, an alternate packer must be selected, or the operation must be tailored to suit the limits of the packer.

## 9.5 SUMMARY

This chapter presents strength of API tubing that can be used for designing tubing strings for oil and gas wells. Tubing design should consider operating conditions in individual wells. Special care should be taken for tubing strings before a well undergoes a treatment or stimulation.

## REFERENCES

- Allen, T., Roberts, A.P., Production operations, four ed. I and II. 1998.
- Baker Oil Tools., Packer calculations handbook. 1992.
- Fothergill, J., Ratings standardization for production packers. In: Paper SPE 80945 presented at the SPE Production and Operations Symposium, Oklahoma City, OK, 22–25 March, 2003.
- Giacomi, A., Rowe, C., Inflatable packer fundamentals. In: Proceedings of International Drilling Conference held in Perth Western Australia, 12–14 October, 1992.
- Guo, B., Song, S., Chacko, J., Ghalambor, A., 2005. *Offshore Pipelines*. Gulf Professional Publishing, Burlington, USA.

- Hasan, R., Kabir, C.S., 2002. Fluid Flow and Heat Transfer in Wellbores. SPE, Richardson, TX, pp. 79–89.
- Patton, L.D., Abbott, W.A., 1985. Well Completions and Workovers: The Systems Approach. second ed Energy Publications, Dallas, TX, pp. 57–67.
- Ramey, Jr., H.J., 1962. Wellbore heat transmission. Trans. AIME 14, 427.

---

## PROBLEMS

- 9.1.** Calculate the collapse resistance for a section of 3-in. API 9.20 lb/ft, Grade J-55, nonupset tubing near the surface of a 12,000-ft string suspended from the surface in a well that is producing gas.
- 9.2.** Consider a 2 $\frac{7}{8}$ -in. API, 6.40 lb/ft Grade J-55 nonupset tubing anchored with a packer set at 8000 ft. The crude oil production through the tubing from the bottom of the hole is 1500 stb/day (no gas or water production). A completion fluid is in place in the annular space between the tubing and the casing (9.6 lb/gal KCl water). Assuming surface temperature is 80°F and geothermal gradient of 0.01°F/ft, determine the landing tension to avoid buckling.
- 9.3.** The following data are given for a frac-packing job:

Tubing:	2 $\frac{7}{8}$ in., 6.5 lb/ft (2.441 in. ID)
Casing:	7 in., 32 lb/ft (6.094 in. ID)
Packer:	Bore size $D_p = 3.25$ in., set at 8000 ft
Initial condition:	Tubing and casing are full of 30 API oil (S.G. = 0.88)
Operation:	Tubing is displaced with 12 ppg cement with an injection pressure 4500 psi and casing pressure 1200 psi. The average temperature drop is 30°F.

1. Calculate tubing movement if the tubing is not restrained by the packer, and discuss solutions to the possible operation problems.
2. Calculate the tubing force acting on a restraining packer.

---

# SEPARATION SYSTEMS

# 10

---

## 10.1 INTRODUCTION

Oil and gas produced from wells are normally complex mixtures of hundreds of different compounds. A typical well stream is a turbulent mixture of oil, gas, water, and sometimes solid particles. The well stream should be processed as soon as possible after bringing it to the surface. Field separation processes fall into two categories: (1) separation of oil, water, and gas; and (2) dehydration that removes condensable water vapor and other undesirable compounds, such as hydrogen sulfide or carbon dioxide. This chapter focuses on the principles of separation and dehydration and selection of required separators and dehydrators.

---

## 10.2 SEPARATION SYSTEM

Separation of well stream gas from free liquids is the first and most critical stage of field-processing operations. Composition of the fluid mixture and pressure determine what type and size of separator are required. Separators are also used in other locations such as upstream and downstream of compressors, dehydration units, and gas sweetening units. At these locations, separators are referred to as scrubbers, knockouts, and free liquid knockouts. All these vessels are used for the same purpose: to separate free liquids from the gas stream.

### 10.2.1 PRINCIPLES OF SEPARATION

Separators work on the basis of gravity segregation and/or centrifugal segregation. A separator is normally constructed in such a way that it has the following features:

1. It has a centrifugal inlet device where the primary separation of the liquid and gas is made.
2. It provides a large settling section of sufficient height or length to allow liquid droplets to settle out of the gas stream with adequate surge room for slugs of liquid.
3. It is equipped with a mist extractor or eliminator near the gas outlet to coalesce small particles of liquid that do not settle out by gravity.
4. It allows adequate controls consisting of level control, liquid dump valve, gas backpressure valve, safety relief valve, pressure gauge, gauge glass, instrument gas regulator, and piping.

The centrifugal inlet device makes the incoming stream spin around. Depending on the mixture flow rate, the reaction force from the separator wall can generate a centripetal acceleration of up to

500 times the gravitational acceleration. This action forces the liquid droplets together where they fall to the bottom of the separator into the settling section. The settling section in a separator allows the turbulence of the fluid stream to subside and the liquid droplets to fall to the bottom of the vessel due to gravity segregation. A large open space in the vessel is required for this purpose. Use of internal baffling or plates may produce more liquid to be discharged from the separator. However, the product may not be stable because of the light ends entrained in it. Sufficient surge room is essential in the settling section to handle slugs of liquid without carryover to the gas outlet. This can be achieved by placing the liquid level control in the separator, which in turn determines the liquid level. The amount of surge room required depends on the surge level of the production steam and the separator size used for a particular application.

Small liquid droplets that do not settle out of the gas stream due to little gravity difference between them and the gas phase tend to be entrained and pass out of the separator with the gas. A mist eliminator or extractor near the gas outlet allows this to be almost eliminated. The small liquid droplets will hit the eliminator or extractor surfaces, coalesce, and collect to form larger droplets that will then drain back to the liquid section in the bottom of the separator. A stainless steel woven-wire mesh mist eliminator can remove up to 99.9% of the entrained liquids from the gas stream. Cane mist eliminators can be used in areas where there is entrained solid material in the gas phase that may collect and plug a wire mesh mist eliminator.

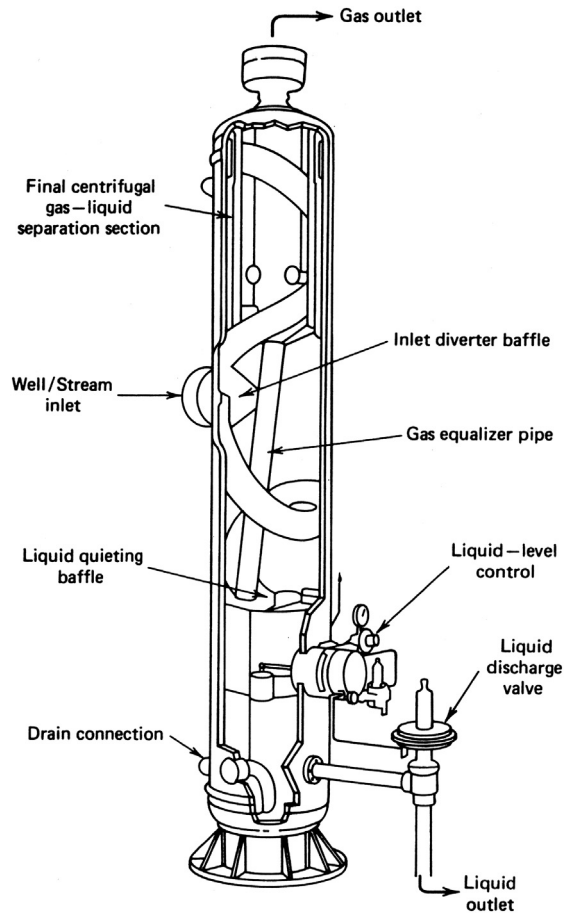
## 10.2.2 TYPES OF SEPARATORS

Three types of separators are generally available from manufacturers: vertical, horizontal, and spherical separators. Horizontal separators are further classified into two categories: single tube and double tube. Each type of separator has specific advantages and limitations. Selection of separator type is based on several factors including characteristics of production steam to be treated, floor space availability at the facility site, transportation, and cost.

### 10.2.2.1 Vertical separators

Fig. 10.1 shows a vertical separator. The inlet diverter baffle is a centrifugal inlet device making the incoming stream spin around. This action forces the liquid droplets to stay together and fall to the bottom of the separator along the separator wall due to gravity. Sufficient surge room is available in the settling section of the vertical separator to handle slugs of liquid without carryover to the gas outlet. A mist eliminator or extractor near the gas outlet allows the entrained liquid in the gas to be almost eliminated.

Vertical separators are often used to treat low to intermediate gas–oil ratio (GOR) well streams and streams with relatively large slugs of liquid. They handle greater slugs of liquid without carryover to the gas outlet, and the action of the liquid level control is not as critical. Vertical separators occupy less floor space, which is important for facility sites such as those on offshore platforms where space is limited. Because of the large vertical distance between the liquid level and the gas outlet, the chance for liquid to revaporize into the gas phase is limited. However, because of the natural upward flow of gas in a vertical separator against the falling droplets of liquid, adequate separator diameter is required. Vertical separators are more costly to fabricate and ship in skid-mounted assemblies.



**FIGURE 10.1**

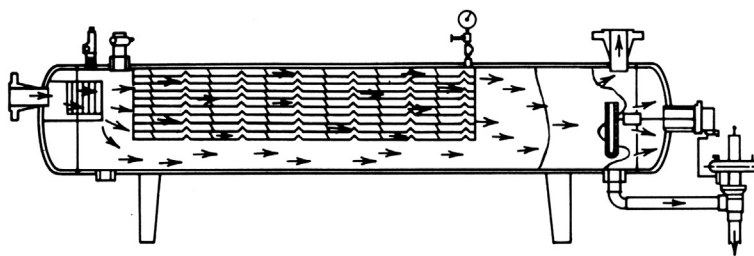
A typical vertical separator.

*Courtesy Petroleum Extension Services.*

### 10.2.2.2 Horizontal separators

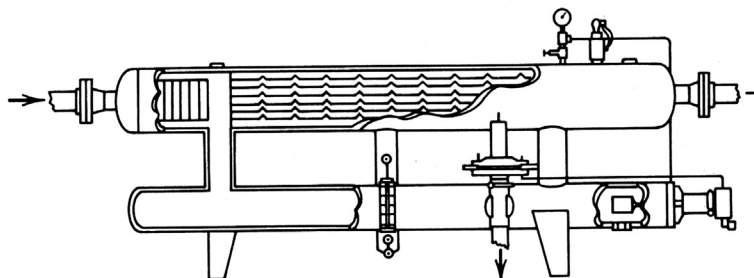
Fig. 10.2 presents a sketch of a horizontal separator. In horizontal separators, gas flows horizontally while liquid droplets fall toward the liquid surface. The moisture gas flows in the baffle surface and forms a liquid film that is drained away to the liquid section of the separator. The baffles need to be longer than the distance of liquid trajectory travel. The liquid level control placement is more critical in a horizontal separator than in a vertical separator because of limited surge space.

Horizontal separators are usually the first choice because of their low costs. They are most widely used for high GOR well streams, foaming well streams, or liquid-from-liquid separation. They have much greater gas-liquid interface because of a large, long, baffled gas separation

**FIGURE 10.2**

A typical horizontal separator.

*Courtesy Petroleum Extension Services.*

**FIGURE 10.3**

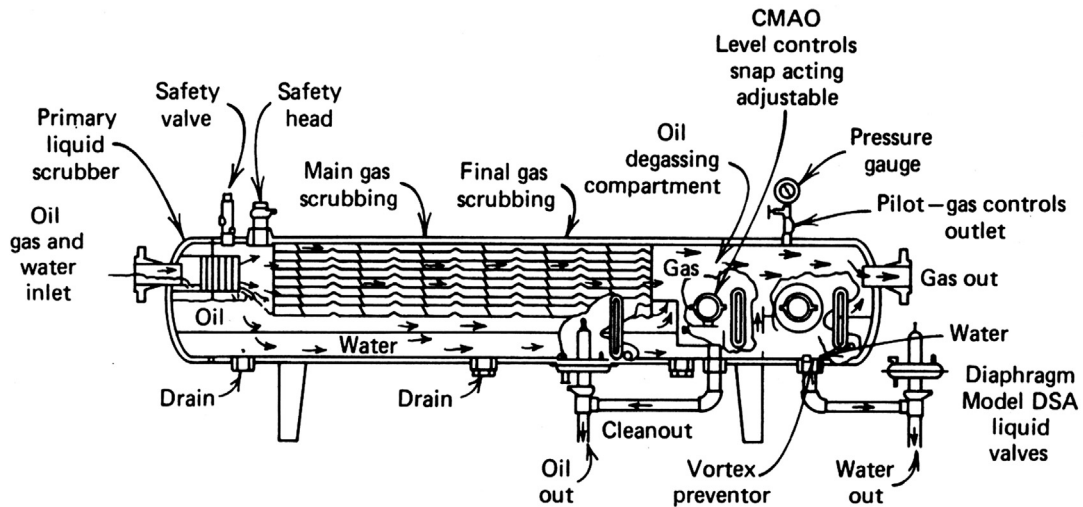
A typical horizontal double-tube separator.

*Courtesy Petroleum Extension Services.*

section. Horizontal separators are easier to skid-mount and service and require less piping for field connections. Individual separators can be stacked easily into stage separation assemblies to minimize space requirements.

Fig. 10.3 demonstrates a horizontal double-tube separator consisting of two tube sections. The upper tube section is filled with baffles, gas flows straight through and at higher velocities, and the incoming free liquid is immediately drained away from the upper tube section into the lower tube section. Horizontal double-tube separators have all the advantages of normal horizontal single-tube separators, plus much higher liquid capacities.

Fig. 10.4 illustrates a horizontal oil–gas–water three-phase separator. This type of separator is commonly used for well testing and in instances where free water readily separates from the oil or condensate. Three-phase separation can be accomplished in any type of separator. This can be achieved by installing either special internal baffling to construct a water leg or water siphon arrangement. It can also be achieved by using an interface liquid level control. In three-phase operations, two liquid dump valves are required.



**FIGURE 10.4**

A typical horizontal three-phase separator.

*Courtesy Petroleum Extension Services.*

### 10.2.2.3 Spherical separators

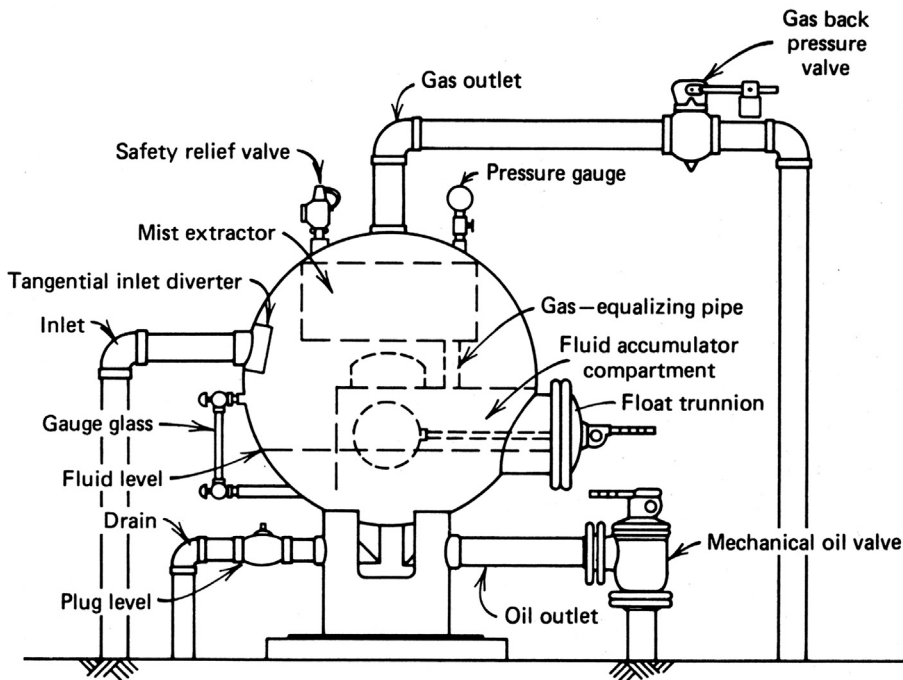
A spherical separator is shown in Fig. 10.5. Spherical separators offer an inexpensive and compact means of separation arrangement. Because of their compact configurations, this type of separator has a very limited surge space and liquid settling section. Also, the placement and action of the liquid level control in this type of separator is very critical.

## 10.2.3 FACTORS AFFECTING SEPARATION

Separation efficiency is dominated by separator size. For a given separator, factors that affect separation of liquid and gas phases include separator operating pressure, separator operating temperature, and fluid stream composition. Changes in any of these factors will change the amount of gas and liquid leaving the separator. An increase in operating pressure or a decrease in operating temperature generally increases the liquid covered in a separator. However, this is often not true for gas condensate systems in which an optimum pressure may exist that yields the maximum volume of liquid phase. Computer simulation (flash vaporization calculation) of phase behavior of the well stream allows the designer to find the optimum pressure and temperature at which a separator should operate to give maximum liquid recovery. However, it is often not practical to operate at the optimum point. This is because storage system vapor losses may become too great under these optimum conditions.

In field separation facilities, operators tend to determine the optimum conditions for them to maximize revenue. As the liquid hydrocarbon product is generally worth more than the gas, high liquid recovery is often desirable, provided that it can be handled in the available storage system.





**FIGURE 10.5**

A typical spherical low-pressure separator (Sivalls, 1977).

The operator can control operating pressure to some extent by use of backpressure valves. However, pipeline requirements for Btu content of the gas should also be considered as a factor affecting separator operation.

It is usually unfeasible to try to lower the operating temperature of a separator without adding expensive mechanical refrigeration equipment. However, an indirect heater can be used to heat the gas before pressure reduction to pipeline pressure in a choke. This is mostly applied to high-pressure wells. By carefully operating this indirect heater, the operator can prevent overheating the gas stream ahead of the choke. This adversely affects the temperature of the downstream separator.

### 10.2.3.1 Stage separation

Stage separation is a process in which hydrocarbon mixtures are separated into vapor and liquid phases by multiple equilibrium flashes at consecutively lower pressures. A two-stage separation requires one separator and a storage tank, and a three-stage separation requires two separators and a storage tank. The storage tank is always counted as the final stage of vapor-liquid separation. Stage separation reduces the pressure a little at a time, in steps or stages, resulting in a more stable stock-tank liquid. Usually a stable stock-tank liquid can be obtained by a stage separation of not more than four stages.

In high-pressure gas-condensate separation systems, a stepwise reduction of the pressure on the liquid condensate can significantly increase the recovery of stock tank liquids. Prediction of the performance of the various separators in a multistage separation system can be carried out with compositional computer models using the initial well stream composition and the operating temperatures and pressures of the various stages.

Although three to four stages of separation theoretically increase the liquid recovery over two-stage separation, the incremental rarely pay out the cost of the additional separators. It has been generally recognized that two stages of separation plus the stock tank are practically optimum. The increase in liquid recovery for two-stage separation over single-stage separation usually varies from 2% to 12%, although 20% to 25% increases in liquid recoveries have been reported.

The first-stage separator operating pressure is generally determined by the flow line pressure and operating characteristics of the well. The pressure usually ranges from 600 to 1200 psi. In situations where the flow line pressure is greater than 600 psi, it is practical to let the first-stage separator ride the line or operate at the flow line pressure. Pressures at low-stage separations can be determined based on equal pressure ratios between the stages (Campbell, 1976):

$$R_p = \left( \frac{p_1}{p_s} \right)^{\frac{1}{N_{st}}} \quad (10.1)$$

where

$R_p$  = pressure ratio

$N_{st}$  = number of stages -1

$p_1$  = first-stage or high-pressure separator pressure, psia

$p_s$  = stock tank pressure, psia.

Pressures at the inter mediate stages can be then designed with the following formula:

$$p_i = \frac{p_1^{i-1}}{R_p^i} \quad (10.2)$$

where

$p_i$  = pressure at stage  $i$ , psia.

### 10.2.3.2 Flash calculation

Based on the composition of well stream fluid, the quality of products from each stage of separation can be predicted by flash calculations, assuming phase equilibriums are reached in the separators. This requires the knowledge of equilibrium ratio defined as:

$$k_i = \frac{y_i}{x_i} \quad (10.3)$$

Where

$k_i$  = liquid-vapor equilibrium ratio of compound  $i$ ,

$y_i$  = mole fraction of compound  $i$  in the vapor phase,

$x_i$  = mole fraction of compound  $i$  in the liquid phase.

Accurate determination of  $k_i$  values requires computer simulators solving the Equation of State (EoS) for hydrocarbon systems. Ahmed (1989) presented a detailed procedure for solving the EoS. For pressures lower than 1000 psia, a set of equations presented by Standing (1979) provides an easy and accurate means of determining  $k_i$  values. According to Standing,  $k_i$  can be calculated by:

$$k_i = \frac{1}{p} 10^{a+cF_i} \quad (10.4)$$

where

$$a = 1.2 + 4.5 \times 10^{-4}p + 1.5 \times 10^{-8}p^2 \quad (10.5)$$

$$c = 0.89 - 1.7 \times 10^{-4}p - 3.5 \times 10^{-8}p^2 \quad (10.6)$$

$$F_i = b_i \left( \frac{1}{T_{bi}} - \frac{1}{T} \right) \quad (10.7)$$

$$b_i = \frac{\log\left(\frac{P_{ci}}{14.7}\right)}{\frac{1}{T_{bi}} - \frac{1}{T_{ci}}} \quad (10.8)$$

where

$p_c$  = critical pressure, psia

$T_b$  = boiling point, °R

$T_c$  = critical temperature, °R.

Consider 1 mole of fed-in fluid, the following equation holds true on the basis of mass balance:

$$n_L + n_V = 1. \quad (10.9)$$

where

$n_L$  = number of mole of fluid in the liquid phase,

$n_V$  = number of mole of fluid in the vapor phase.

For compound  $i$ ,

$$z_i = x_i n_L + y_i n_V. \quad (10.10)$$

where  $z_i$  is the mole fraction of compound  $i$  in the fed-in fluid.

Combining Eqs. (10.3) and (10.10) gives:

$$z_i = x_i n_L + k_i x_i n_V \quad (10.11)$$

which yields:

$$x_i = \frac{z_i}{n_L + k_i n_V}. \quad (10.12)$$

Mass balance applied to Eq. (7.16) requires:

$$\sum_{i=1}^{N_c} x_i = \sum_{i=1}^{N_c} \frac{z_i}{n_L + k_i n_V} = 1. \quad (10.13)$$

where  $N_c$  is the number of compounds in the fluid.

Combining Eqs. (10.3) and (10.10) also gives:

$$z_i = \frac{y_i}{k_i} n_L + y_i n_V \quad (10.14)$$

which yields:

$$y_i = \frac{z_i k_i}{n_L + k_i n_V}. \quad (10.15)$$

Mass balance applied to Eq. (10.15) requires:

$$\sum_{i=1}^{N_c} y_i = \sum_{i=1}^{N_c} \frac{z_i k_i}{n_L + k_i n_V} = 1. \quad (10.16)$$

Subtracting Eq. (10.16) from Eq. (10.13) gives:

$$\sum_{i=1}^{N_c} \frac{z_i}{n_L + k_i n_V} - \sum_{i=1}^{N_c} \frac{z_i k_i}{n_L + k_i n_V} = 0 \quad (10.17)$$

which can be rearranged to obtain:

$$\sum_{i=1}^{N_c} \frac{z_i (1 - k_i)}{n_L + k_i n_V} = 0. \quad (10.18)$$

Combining Eqs. (10.18) and (10.9) results in:

$$\sum_{i=1}^{N_c} \frac{z_i (1 - k_i)}{n_V (k_i - 1) + 1} = 0. \quad (10.19)$$

If values of  $k_i$  are known, Eq. (10.19) can be used to solve for the number of mole of fluid in the vapor phase. Then,  $x_i$  and  $y_i$  can be calculated with Eqs. (10.12) and (10.15), respectively. The apparent molecular weights of liquid phase ( $MW_a^L$ ) and vapor phase ( $MW_a^V$ ) can be calculated by

$$MW_a^L = \sum_{i=1}^{N_c} x_i MW_i \quad (10.20)$$

$$MW_a^V = \sum_{i=1}^{N_c} y_i MW_i. \quad (10.21)$$

where  $MW_i$  is the molecular weight of compound  $i$ . With the apparent molecular weight of vapor phase known, the specific gravity of the vapor phase can be determined, and the density of the vapor phase in  $\text{lb}_m/\text{ft}^3$  can be calculated by

$$\rho_V = \frac{MW_a^V P}{zRT}. \quad (10.22)$$

The liquid phase density in  $\text{lb}_m/\text{ft}^3$  can be estimated by mixing rule:

$$\rho_L = \sum_{i=1}^{N_c} x_i \rho_{Li}. \quad (10.23)$$

Then the volumes of vapor and liquid phases can be calculated by:

$$V_{Vsc} = \frac{zn_V RT_{sc}}{p_{sc}} \quad (10.24)$$

$$V_L = \frac{n_L MW_a^L}{5.615 \rho_L} \quad (10.25)$$

where

$V_{Vsc}$  = volume of vapor phase under standard condition, scf

$R$  = gas constant,  $10.73 \text{ ft}^3\text{-psia/lb mol-R}$

$T_{sc}$  = standard temperature,  $520^\circ\text{R}$

$p_{sc}$  = standard pressure,  $14.7 \text{ psia}$

$V_L$  = volume of liquid phase, bbl.

Finally, GOR can be calculated by dividing Eq. (10.24) by Eq. (10.25).

**Example Problem 10.1** For the following fluid composition, perform flash calculation under 1000 psia and  $100^\circ\text{F}$ :

C <sub>1</sub>	0.6599
C <sub>2</sub>	0.0869
C <sub>3</sub>	0.0591
i-C <sub>4</sub>	0.0239
n-C <sub>4</sub>	0.0278
i-C <sub>5</sub>	0.0157
n-C <sub>5</sub>	0.0112
C <sub>6</sub>	0.0181
C <sub>7+</sub>	0.0601
N <sub>2</sub>	0.0194
CO <sub>2</sub>	0.0121
H <sub>2</sub> S	0.0058

### Solution

The flash calculation can be carried out using the spreadsheet program LP-Flash.xls attached to this book. The result is

Apparent molecular weight of liquid phase:	54.88	
Apparent molecular weight of vapor phase:	19.79	
Specific gravity of vapor phase:	0.68	air = 1
Density of liquid phase:	36.38	lb <sub>m</sub> /ft <sup>3</sup>
Specific gravity of liquid phase:	0.58	water = 1
Density of vapor phase:	3.43	lb <sub>m</sub> /ft <sup>3</sup>
Volume of liquid phase:	0.08	bbl
Volume of vapor phase:	253.71	scf
GOR:	3109	scf/bbl.

### 10.2.4 SELECTION OF SEPARATORS

Petroleum engineers normally do not perform detailed designing of separators but carry out selection of separators suitable for their operations from manufacturers' product catalogs. This section addresses how to determine separator specifications based on well stream conditions. The specifications are used for separator selections.

#### 10.2.4.1 Gas capacity

The following empirical equations proposed by Souders-Brown are widely used for calculating gas capacity of oil/gas separators:

$$v = K \sqrt{\frac{\rho_L - \rho_g}{\rho_g}} \quad (10.26)$$

and

$$q = Av, \quad (10.27)$$

where

- $A$  = total cross-sectional area of separator, ft<sup>2</sup>
- $v$  = superficial gas velocity based on total cross-sectional area  $A$ , ft/sec
- $q$  = gas flow rate at operating conditions, ft<sup>3</sup>/sec
- $\rho_L$  = density of liquid at operating conditions, lb<sub>m</sub>/ft<sup>3</sup>
- $\rho_g$  = density of gas at operating conditions, lb<sub>m</sub>/ft<sup>3</sup>
- $K$  = empirical factor

Table 10.1 presents  $K$  values for various types of separators. Also listed in the table are  $K$  values used for other designs such as mist eliminators and trayed towers in dehydration or gas sweetening units.

Separator Type	$K$	Remarks
Vertical separators	0.06–0.35	
Horizontal separators	0.40–0.50	
Wire mesh mist eliminators	0.35	
Bubble cap trayed columns	0.16	24-in. spacing

Substituting Eq. (10.26) into Eq. (10.27) and applying real gas law gives

$$q_{st} = \frac{2.4D^2K_p}{z(T+460)} \sqrt{\frac{\rho_L - \rho_g}{\rho_g}}, \quad (10.28)$$

where

- $q_{st}$  = gas capacity at standard conditions, MMscfd  
 $D$  = internal diameter of vessel, ft  
 $p$  = operation pressure, psia  
 $T$  = operating temperature, °F  
 $z$  = gas compressibility factor

It should be noted that Eq. (10.28) is empirical. Height differences in vertical separators and length differences in horizontal separators are not considered. Field experience has indicated that additional gas capacity can be obtained by increasing height of vertical separators and length of horizontal separators. The separator charts (Sivalls, 1977; Ikoku, 1984) give more realistic values for the gas capacity of separators. In addition, for single-tube horizontal vessels, corrections must be made for the amount of liquid in the bottom of the separator. Although one-half full of liquid is more or less standard for most single-tube horizontal separators, lowering the liquid level to increase the available gas space within the vessel can increase the gas capacity.

#### 10.2.4.2 Liquid capacity

Retention time of the liquid within the vessel determines liquid capacity of a separator. Adequate separation requires sufficient time to obtain an equilibrium condition between the liquid and gas phase at the temperature and pressure of separation. The liquid capacity of a separator relates to the retention time through the settling volume:

$$q_L = \frac{1440 V_L}{t} \quad (10.29)$$

where

- $q_L$  = liquid capacity, bbl/day  
 $V_L$  = liquid settling volume, bbl  
 $t$  = retention time, min

Table 10.2 presents  $t$  values for various types of separators tested in fields. It is shown that temperature has a strong impact on three-phase separations at low pressures.

Separation Condition	$T$ (°F)	$t$ (min)
Oil/gas separation		1
High-pressure oil/gas/water separation		2–5
Low-pressure oil/gas/water separation	>100	5–10
	90	10–15
	80	15–20
	70	20–25
	60	25–30

Size (D × H)	$V_L$ (bbl)	
	Oil/Gas Separators	Oil/Gas/Water Separators
16" × 5'	0.27	0.44
16" × 7½'	0.41	0.72
16" × 10'	0.51	0.94
20" × 5'	0.44	0.71
20" × 7½'	0.65	1.15
20" × 10'	0.82	1.48
24" × 5'	0.66	1.05
24" × 7½'	0.97	1.68
24" × 10'	1.21	2.15
30" × 5'	1.13	1.76
30" × 7½'	1.64	2.78
30" × 10'	2.02	3.54
36" × 7½'	2.47	4.13
36" × 10'	3.02	5.24
36" × 15'	4.13	7.45
42" × 7½'	3.53	5.80
42" × 10'	4.29	7.32
42" × 15'	5.80	10.36
48" × 7½'	4.81	7.79
48" × 10'	5.80	9.78
48" × 15'	7.79	13.76
54" × 7½'	6.33	10.12
54" × 10'	7.60	12.65
54" × 15'	10.12	17.70
60" × 7½'	8.08	12.73
60" × 10'	9.63	15.83
60" × 15'	12.73	22.03
60" × 20'	15.31	27.20

Tables 10.3–10.8 present liquid-settling volumes with the conventional placement of liquid level controls for typical oil/gas separators.

Proper sizing of a separator requires the use of both Eq. (10.28) for gas capacity and Eq. (10.29) for liquid capacity. Experience shows that for high-pressure separators used for treating high GOR well streams, the gas capacity is usually the controlling factor for separator selection. However, the reverse may be true for low-pressure separators used on well streams with low GORs.



**Table 10.4 Settling Volumes of Standard Vertical Low-Pressure Separators (125 psi Working Pressure)**

Size (D × H)	$V_L$ (bbl)	
	Oil/Gas Separators	Oil/Gas/Water Separators
24" × 5'	0.65	1.10
24" × 7½'	1.01	1.82
30" × 10'	2.06	3.75
36" × 5'	1.61	2.63
36" × 7½'	2.43	4.26
36" × 10'	3.04	5.48
48" × 10'	5.67	10.06
48" × 15'	7.86	14.44
60" × 10'	9.23	16.08
60" × 15'	12.65	12.93
60" × 20'	15.51	18.64

**Table 10.5 Settling Volumes of Standard Horizontal High-Pressure Separators (230–2000 psi Working Pressure)**

Size (D × L)	$V_L$ (bbl)		
	½ Full	⅓ Full	¼ Full
12¾" × 5'	0.38	0.22	0.15
12¾" × 7½'	0.55	0.32	0.21
12¾" × 10'	0.72	0.42	0.28
16" × 5'	0.61	0.35	0.24
16" × 7½'	0.88	0.50	0.34
16" × 10'	1.14	0.66	0.44
20" × 5'	0.98	0.55	0.38
20" × 7½'	1.39	0.79	0.54
20" × 10'	1.80	1.03	0.70
24" × 5'	1.45	0.83	0.55
24" × 7½'	2.04	1.18	0.78
24" × 10'	2.63	1.52	1.01
24" × 15'	3.81	2.21	1.47
30" × 5'	2.43	1.39	0.91
30" × 7½'	3.40	1.96	1.29
30" × 10'	4.37	2.52	1.67
30" × 15'	6.30	3.65	2.42
36" × 7½'	4.99	2.87	1.90
36" × 10'	6.38	3.68	2.45

**Table 10.5 Settling Volumes of Standard Horizontal High-Pressure Separators (230–2000 psi Working Pressure) *Continued***

Size (D × L)	VL(bbl)		
	½ Full	⅓ Full	¼ Full
36" × 15'	9.17	5.30	3.54
36" × 20'	11.96	6.92	4.63
42" × 7½'	6.93	3.98	2.61
42" × 10'	8.83	5.09	3.35
42" × 15'	12.62	7.30	4.83
42" × 20'	16.41	9.51	6.32
48" × 7½'	9.28	5.32	3.51
48" × 10'	11.77	6.77	4.49
48" × 15'	16.74	9.67	6.43
48" × 20'	21.71	12.57	8.38
54" × 7½'	12.02	6.87	4.49
54" × 10'	15.17	8.71	5.73
54" × 15'	12.49	12.40	8.20
54" × 20'	27.81	16.08	10.68
60" × 7½'	15.05	8.60	5.66
60" × 10'	18.93	10.86	7.17
60" × 15'	26.68	15.38	10.21
60" × 20'	34.44	19.90	13.24

**Table 10.6 Settling Volumes of Standard Horizontal Low-Pressure Separators (125 psi Working Pressure)**

Size (D × L)	V <sub>L</sub> (bbl)		
	½ Full	⅓ Full	¼ Full
24" × 5'	1.55	0.89	0.59
24" × 7½'	2.22	1.28	0.86
24" × 10'	2.89	1.67	1.12
30" × 5'	2.48	1.43	0.94
30" × 7½'	3.54	2.04	1.36
30" × 10'	4.59	2.66	1.77
36" × 10'	6.71	3.88	2.59
36" × 15'	9.76	5.66	3.79
48" × 10'	12.24	7.07	4.71
48" × 15'	17.72	10.26	6.85
60" × 10'	19.50	11.24	7.47
60" × 15'	28.06	16.23	10.82
60" × 20'	36.63	21.21	14.16

**Table 10.7 Settling Volumes of Standard Spherical High-Pressure Separators (230–3000 psi Working Pressure)**

Size (OD)	$V_L$ (bbl)
24"	0.15
30"	0.30
36"	0.54
42"	0.88
48"	1.33
60"	2.20

**Table 10.8 Settling Volumes of Standard Spherical Low-Pressure Separators (125 psi)**

Size (OD)	$V_L$ (bbl)
41"	0.77
46"	1.02
54"	1.60

**Example Problem 10.2** Calculate the minimum required size of a standard oil/gas separator for the following conditions. Consider both vertical and horizontal separators.

Gas flow rate:	5.0 MMscfd
Gas-specific gravity:	0.7
Condensate flow rate:	20 bbl/MMscf
Condensate gravity:	60 °API
Operating pressure:	800 psia
Operating temperature:	80°F

**Solution** The total required liquid flow capacity is  $(5)(20) = 100$  bbl/day. Assuming a 20-in.  $\times$  7½-ft vertical separator, Table 10.1 suggests an average  $K$  value of 0.205. The spreadsheet program *Hall-Yarborough-z.xls* gives  $z = 0.8427$  and  $\rho_g = 3.38$  lb<sub>m</sub>/ft<sup>3</sup> at 800 psig and 80°F. Liquid density is calculated as

$$\rho_L = 62.4 \frac{141.5}{131.5 + 60} = 46.11 \text{ lb}_m/\text{ft}^3.$$

Eq. (10.28) gives

$$q_{st} = \frac{(2.4)(20/12)^2(0.205)(800)}{(0.8427)(80 + 460)} \sqrt{\frac{46.11 - 3.38}{3.38}}$$

$$= 8.70 \text{ MMscfd.}$$

Sivalls's chart gives 5.4 MMscfd.

From Table 10.3, a 20-in.  $\times$  7½-ft separator will handle the following liquid capacity:

$$q_L = \frac{1440(0.65)}{1.0} = 936 \text{ bbl/day,}$$

which is much higher than the liquid load of 100 bbl/day.

Consider a 16-in.  $\times$  5-ft horizontal separator and Eq. (10.28) gives

$$\begin{aligned} q_{st} &= \frac{(2.4)(16/12)^2(0.45)(800)}{(0.8427)(80 + 460)} \sqrt{\frac{46.11 - 3.38}{3.38}} \\ &= 12.22 \text{ MMscfd.} \end{aligned}$$

If the separator is one-half full of liquid, it can still treat 6.11 MMscfd of gas. Sivalls's chart indicates that a 16-in.  $\times$  5-ft horizontal separator will handle 5.1 MMscfd.

From Table 10.5, a half-full, 16-in.  $\times$  5-ft horizontal separator will handle

$$q_L = \frac{1440(0.61)}{1.0} = 878 \text{ bbl/day,}$$

which again is much higher than the liquid load of 100 bbl/day.

This example illustrates a case of high GOR well streams where the gas capacity is the controlling factor for separator selection. It suggests that a smaller horizontal separator would be required and would be more economical. The selected separator should have at least a 1000 psig working pressure.

## 10.3 DEHYDRATION SYSTEMS

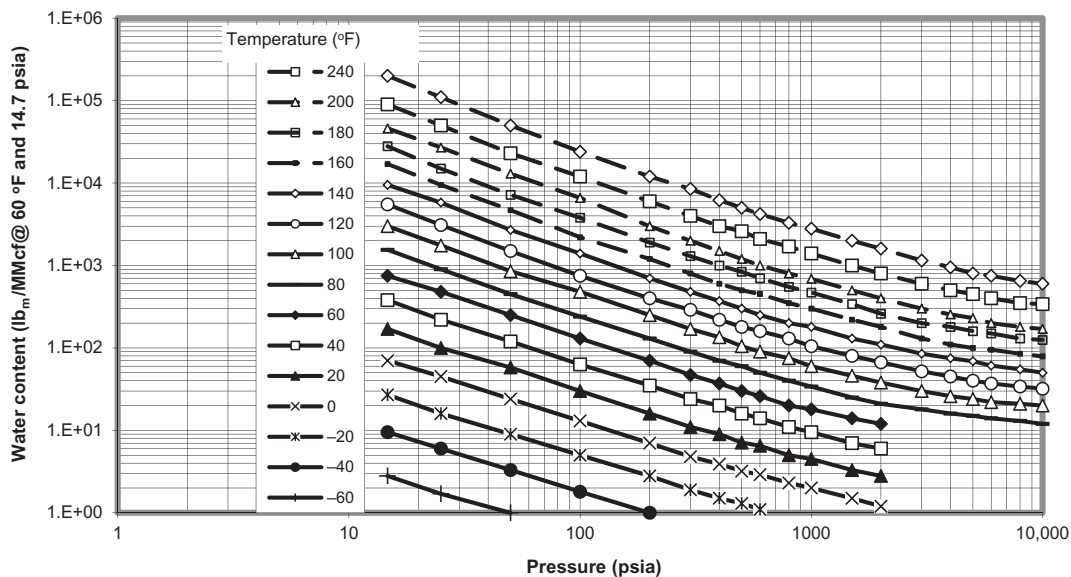
All natural gas downstream from the separators still contain water vapor to some degree. Water vapor is probably the most common undesirable impurity found in the untreated natural gas. The main reason for removing water vapor from natural gas is that water vapor becomes liquid water under low-temperature and/or high-pressure conditions. Specifically, water content can affect long-distance transmission of natural gas because of the following facts:

1. Liquid water and natural gas can form hydrates that may plug the pipeline and other equipment.
2. Natural gas containing CO<sub>2</sub> and/or H<sub>2</sub>S is corrosive when liquid water is present.
3. Liquid water in a natural gas pipeline potentially causes slugging flow conditions resulting in lower flow efficiency of the pipeline.
4. Water content decreases the heating value of natural gas being transported.

Dehydration systems are designed for further separating water vapor from natural gas before the gas is transported by pipeline.

### 10.3.1 WATER CONTENT OF NATURAL GAS STREAMS

Solubility of water in natural gas increases with temperature and decreases with pressure. The presence of salt in the liquid water reduces the water content of the gas. Water content of untreated



**FIGURE 10.6**

Water content of natural gases (Guo and Ghalambor, 2005).

natural gases is normally in the magnitude of a few hundred pounds of water per million standard cubic foot of gas ( $\text{lb}_m/\text{MMscf}$ ); while gas pipelines normally require water content to be in the range of 6–8  $\text{lb}_m/\text{MMscf}$  and even lower for offshore pipelines.

The water content of natural gas is indirectly indicated by the “dew point,” defined as the temperature at which the natural gas is saturated with water vapor at a given pressure. At the dew point, natural gas is in equilibrium with liquid water; any decrease in temperature or increase in pressure will cause the water vapor to begin condensing. The difference between the dew point temperature of a water-saturated gas stream and the same stream after it has been dehydrated is called “dew-point depression.”

It is essential to accurately estimate the saturated water vapor content of natural gas in the design and operation of dehydration equipment. Several methods are available for this purpose including the correlations of McCarthy et al. (1950) and McKetta and Wehe (1958). Dalton’s law of partial pressures is valid for estimating water vapor content of gas at near-atmospheric pressures. Readings from the chart by McKetta and Wehe (1958) were re-plotted in Fig. 10.6 by Guo and Ghalambor (2005).

**Example Problem 10.3** Estimate water content of a natural gas at a pressure of 3000 psia and temperature of  $150^\circ\text{F}$ .

**Solution** The chart in Fig. 10.6 gives water contents of

$$\begin{aligned} C_{w140F} &= 84 \text{ lb}_m/\text{MMcf} \\ C_{w160F} &= 130 \text{ lb}_m/\text{MMcf} \end{aligned}$$

Linear interpolation yields:

$$C_{w150F} = 107 \text{ lb}_m/\text{MMcf}$$

## 10.3.2 METHODS OF DEHYDRATION

Dehydration techniques used in the petroleum industry fall into four categories in principle: (1) direct cooling, (2) compression followed by cooling, (3) absorption, and (4) adsorption. Dehydration in the first two methods does not result in sufficiently low water contents to permit injection into a pipeline. Further dehydration by absorption or adsorption is often required.

### 10.3.2.1 Dehydration by cooling

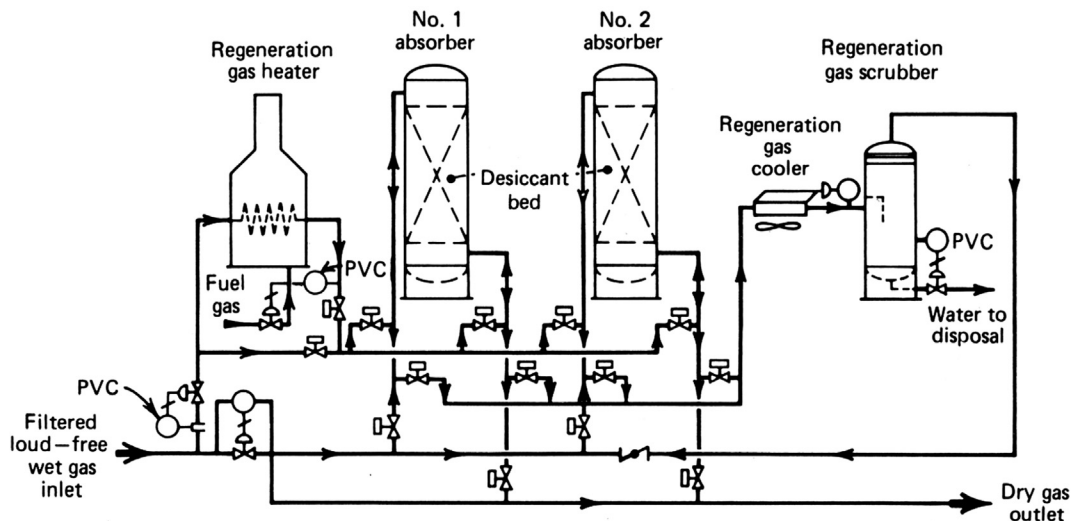
The ability of natural gas to contain water vapor decreases as the temperature is lowered at constant pressure. During the cooling process, the excess water in the vapor state becomes liquid and is removed from the system. Natural gas containing less water vapor at low-temperature is output from the cooling unit. The gas dehydrated by cooling is still at its water dew point unless the temperature is raised again or the pressure is decreased. Cooling for the purpose of gas dehydration is sometimes economical if the gas temperature is unusually high. It is often a good practice that cooling is used in conjunction with other dehydration processes.

Gas compressors can be used partially as dehydrators. Because the saturation water content of gases decreases at higher pressure, some water is condensed and removed from gas at compressor stations by the compressor discharge coolers. Modern lean oil absorption gas plants use mechanical refrigeration to chill the inlet gas stream. Ethylene glycol is usually injected into the gas chilling section of the plant, which simultaneously dehydrates the gas and recovers liquid hydrocarbons, in a manner similar to the low-temperature separators.

### 10.3.2.2 Dehydration by adsorption

“Adsorption” is defined as the ability of a substance to hold gases or liquids on its surface. In adsorption dehydration, the water vapor from the gas is concentrated and held at the surface of the solid desiccant by forces caused by residual valiancy. Solid desiccants have very large surface areas per unit weight to take advantage of these surface forces. The most common solid adsorbents used today are silica, alumina, and certain silicates known as *molecular sieves*. Dehydration plants can remove practically all water from natural gas using solid desiccants. Because of their great drying ability, solid desiccants are employed where higher efficiencies are required.

Depicted in Fig. 10.7 is a typical solid desiccant dehydration plant. The incoming wet gas should be cleaned preferably by a filter separator to remove solid and liquid contaminants in the gas. The filtered gas flows downward during dehydration through one adsorber containing a desiccant bed. The down-flow arrangement reduces disturbance of the bed caused by the high gas velocity during the adsorption. While one adsorber is dehydrating, the other adsorber is being regenerated by a hot stream of inlet gas from the regeneration gas heater. A direct-fired heater, hot oil, steam, or an indirect heater can supply the necessary regeneration heat. The regeneration gas usually flows upward through the bed to ensure thorough regeneration of the bottom of the bed, which is the last area contacted by the gas being dehydrated. The hot regenerated bed is cooled by shutting off or bypassing the heater. The cooling gas then flows downward through the bed so that any water adsorbed from the cooling gas will be at the top of the bed and will not be desorbed into the gas during the dehydration step. The still-hot regeneration gas and the cooling gas flow through the regeneration gas cooler to condense the desorbed water. Power-operated valves activated by a timing device switch the adsorbers between the dehydration, regeneration, and cooling steps.



**FIGURE 10.7**

Flow diagram of a typical solid desiccant dehydration plant (Guenther, 1979).

Under normal operating conditions, the usable life of a desiccant ranges from 1 to 4 years. Solid desiccants become less effective in normal use because of loss of effective surface area as they age. Abnormally fast degradation occurs through blockage of the small pores and capillary openings lubricating oils, amines, glycols, corrosion inhibitors, and other contaminants, which cannot be removed during the regeneration cycle. Hydrogen sulfide can also damage the desiccant and reduce its capacity.

The advantages of solid-desiccant dehydration include the following:

- Lower dew point, essentially dry gas (water content  $< 1.0$  lb/MMcf) can be produced
- Higher contact temperatures can be tolerated with some adsorbents
- Higher tolerance to sudden load changes, especially on start up
- Quick start up after a shutdown
- High adaptability for recovery of certain liquid hydrocarbons in addition to dehydration functions

Operating problems with the solid-desiccant dehydration include the following:

- Space adsorbents degenerate with use and require replacement

Dehydrating tower must be regenerated and cooled for operation before another tower approaches exhaustion. The maximum allowable time on dehydration gradually shortens because desiccant loses capacity with use.

Although this type of dehydrator has high adaptability to sudden load changes, sudden pressure surges should be avoided because they may upset the desiccant bed and channel the gas stream resulting in poor dehydration. If a plant is operated above its rated capacity, high-pressure loss may introduce some attrition to occur. Attrition causes fines, which may in turn cause excessive pressure loss and result in loss of capacity.

Replacing the desiccant should be scheduled and completed ahead of the operating season. To maintain continuous operation, this may require discarding the desiccant before its normal operating life is reached. To cut operating costs, the inlet part of the tower can be recharged and the remainder of the desiccant retained because it may still possess some useful life. Additional service life of the desiccant may be obtained if the direction of gas flow is reversed at a time when the tower would normally be recharged.

### 10.3.2.3 Dehydration by absorption

Water vapor is removed from the gas by intimate contact with a hygroscopic liquid desiccant in absorption dehydration. The contacting is usually achieved in packed or trayed towers. Glycols have been widely used as effective liquid desiccants. Dehydration by absorption with glycol is usually economically more attractive than dehydration by solid desiccant when both processes are capable of meeting the required dew point.

Glycols used for dehydrating natural gas are ethylene glycol (EG), diethylene glycol (DEG), triethylene glycol (TEG), and tetraethylene glycol (T<sub>4</sub>EG). Normally a single type of pure glycol is used in a dehydrator, but sometimes a glycol blend is economically attractive. TEG has gained nearly universal acceptance as the most cost effective of the glycols because of its superior dew-point depression, operating cost, and operation reliability. TEG has been successfully used to dehydrate sweet and sour natural gases over wide ranges of operating conditions. Dew-point depression of 40–140°F can be achieved at a gas pressure ranging from 25 to 2500 psig and gas temperature between 40 and 160°F. The dew-point depression obtained depends on the equilibrium dew-point temperature for a given TEG concentration and contact temperature. Increased glycol viscosity may cause problems at lower contact temperature. Thus, heating of the natural gas may be desirable. Very hot gas streams are often cooled before dehydration to prevent vaporization of TEG.

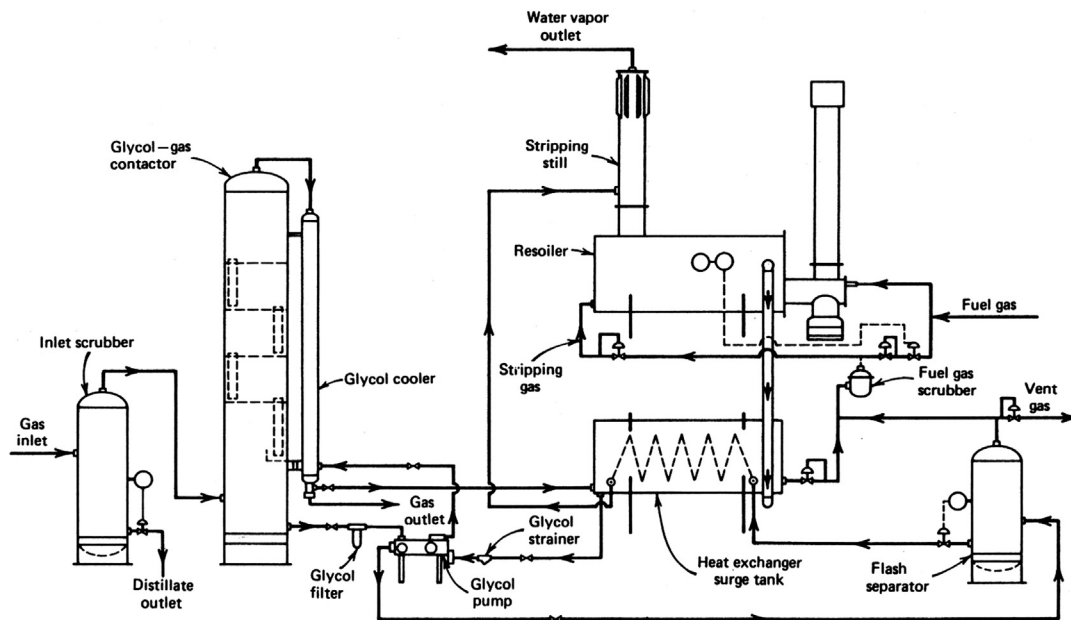
The feeding-in gas must be cleaned to remove all liquid water and hydrocarbons, wax, sand, drilling muds, and other impurities. These substances can cause severe foaming, flooding, higher glycol losses, poor efficiency, and increased maintenance in the dehydration tower or absorber. These impurities can be removed using an efficient scrubber, separator, or even a filter separator for very contaminated gases. Methanol, injected at the wellhead as hydrate inhibitor, can cause several problems for glycol dehydration plants. It increases the heat requirements of the glycol regeneration system. Slugs of liquid methanol can cause flooding in the absorber. Methanol vapor vented to the atmosphere with the water vapor from the regeneration system is hazardous and should be recovered or vented at nonhazardous concentrations.

#### 10.3.2.3.1 Glycol dehydration process

Illustrated in Fig. 10.8 shows the process and flow through a typical glycol dehydrator. The dehydration process can be described as follows:

1. The feeding-in gas stream first enters the unit through an inlet gas scrubber to remove liquid accumulations. A two-phase inlet scrubber is normally required.
2. The wet gas is then introduced to the bottom of the glycol-gas contactor and allowed to flow upward through the trays, while glycol flows downward through the column. The gas contacts the glycol on each tray and the glycol absorbs the water vapor from the gas steam.





**FIGURE 10.8**

Flow diagram of a typical glycol dehydrator (Sivalls, 1977).

3. The gas then flows down through a vertical glycol cooler, usually fabricated in the form of a concentric pipe heat exchanger, where the outlet dry gas aids in cooling the hot regenerated glycol before it enters the contactor. The dry gas then leaves the unit from the bottom of the glycol cooler.
4. The dry glycol enters the top of the glycol-gas contactor from the glycol cooler and is injected onto the top tray. The glycol flows across each tray and down through a downcomer pipe onto the next tray. The bottom tray downcomer is fitted with a seal pot to hold a liquid seal on the trays.
5. The wet glycol, which has now absorbed the water vapor from the gas stream, leaves the bottom of the glycol-gas contactor column, passes through a high-pressure glycol filter, which removes any foreign solid particles that may have been picked up from the gas stream, and enters the power side of the glycol pump.
6. In the glycol pump, the wet high-pressure glycol from the contactor column pumps the dry regenerated glycol into the column. The wet glycol stream flows from the glycol pump to the flash separator, which allows for the release of the entrained solution gas.
7. The gas separated in the flash separator leaves the top of the flash separator vessel and can be used to supplement the fuel gas required for the reboiler. Any excess vent gas is discharged through a backpressure valve. The flash separator is equipped with a liquid level control and diaphragm motor valve that discharges the wet glycol stream through a heat exchange coil in the surge tank to preheat the wet glycol stream.

8. The wet glycol stream leaves the heat exchange coil in the surge tank and enters the stripping still mounted on top of the reboiler at the feed point in the still. The stripping still is packed with a ceramic intalox saddletype packing, and the glycol flows downward through the column and enters the reboiler. The wet glycol passing downward through the still is contacted by hot rising glycol and water vapors passing upward through the column. The water vapors released in the reboiler and stripped from the glycol in the stripping still pass upward through the still column through an atmospheric reflux condenser that provides a partial reflux for the column. The water vapor then leaves the top of the stripping still column and is released to the atmosphere.
9. The glycol flows through the reboiler in essentially a horizontal path from the stripping still column to the opposite end. In the reboiler, the glycol is heated to approximately 350–400°F to remove enough water vapor to re-concentrate it to 99.5% or higher. In field dehydration units, the reboiler is generally equipped with a direct-fired firebox, using a portion of the natural gas stream for fuel.
10. The re-concentrated glycol leaves the reboiler through an overflow pipe and passes into the shell side of the heat exchanger/surge tank. In the surge tank, the hot re-concentrated glycol is cooled by exchanging heat with the wet glycol stream passing through the coil. The surge tank also acts as a liquid accumulator for feed for the glycol pump. The re-concentrated glycol flows from the surge tank through a strainer and into the glycol pump. From the pump, it passes into the shell side of the glycol cooler mounted on the glycol-gas contactor. It then flows upward through the glycol cooler where it is further cooled and enters the column on the top tray.

#### 10.3.2.3.2 Advantages and limitations

Glycol dehydrators have several advantages including the following:

- Low initial equipment cost
- Low-pressure drop across absorption towers
- Continuous operation
- Makeup requirements may be added readily
- Recharging of towers presents no problems
- Plant may be used satisfactorily in the presence of materials that would cause fouling of some solid adsorbents

Glycol dehydrators also present several operating problems including the following:

- Suspended matter, such as dirt, scale, and iron oxide, may contaminate glycol solutions.
- Overheating of solution may produce both low and high boiling decomposition products.
- The resultant sludge may collect on heating surfaces, causing some loss in efficiency, or in severe cases, complete flow stoppage.
- When both oxygen and hydrogen sulfide are present, corrosion may become a problem because of the formation of acid material in glycol solution.
- Liquids (e.g., water, light hydrocarbons, or lubrication oils) in inlet gas may require installation of an efficient separator ahead of the absorber. Highly mineralized water entering the system with inlet gas may, over long periods, crystallize and fill the reboiler with solid salts.

- Foaming of solution may occur with a resultant carry over of liquid. The addition of a small quantity of antifoam compound usually remedies this problem.
- Some leakage around the packing glands of pumps may be permitted because excessive tightening of packing may result in the scouring of rods. This leakage is collected and periodically returned to the system.
- Highly concentrated glycol solutions tend to become viscous at low temperatures and, therefore, are hard to pump. Glycol lines may solidify completely at low temperatures when the plant is not operating. In cold weather, continuous circulation of part of the solution through the heater may be advisable. This practice can also prevent freezing in water coolers.
- To start a plant, all absorber trays must be filled with glycol before good contact of gas and liquid can be expected. This may also become a problem at low circulation rates because weep holes on trays may drain solution as rapidly as it is introduced.
- Sudden surges should be avoided in starting and shutting down a plant. Otherwise, large carryover losses of solution may occur.

#### 10.3.2.3.3 Sizing glycol dehydrator unit

Dehydrators with TEG in trays or packed-column contactors can be sized from standard models by using the following information:

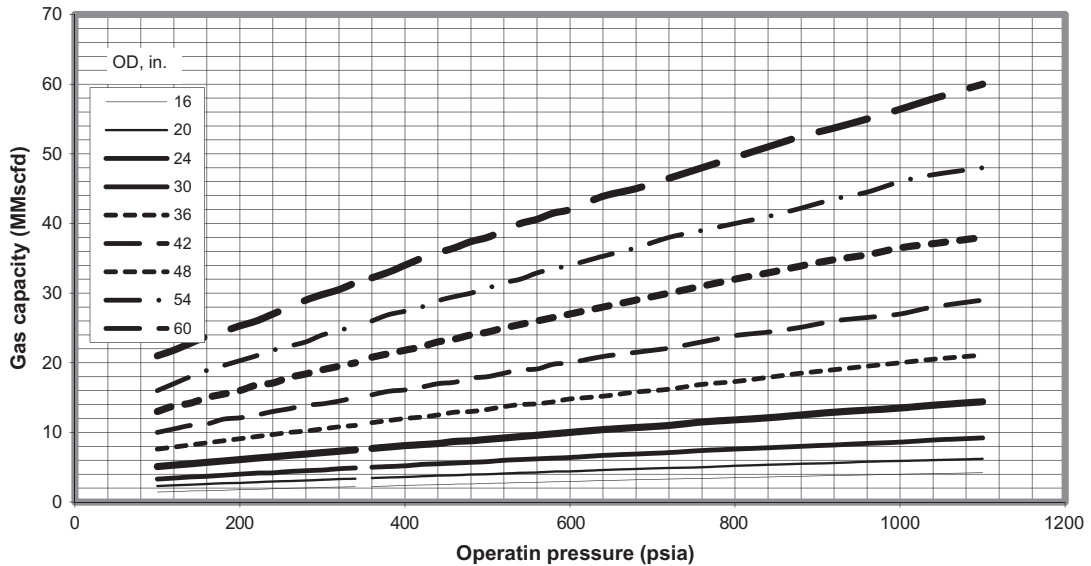
- Gas flow rate
- Specific gravity of gas
- Operating pressure
- Maximum working pressure of contact
- Gas inlet temperature
- Outlet gas water content required

One of the following two design criteria can be employed:

1. Glycol/water ratio (GWR): A value of 2–6 gal TEG/lb<sub>m</sub> H<sub>2</sub>O removed is adequate for most glycol dehydration requirements. Very often 2.5–4 gal TEG/lb<sub>m</sub> H<sub>2</sub>O is used for field dehydrators.
2. Lean TEG concentration from re-concentrator. Most glycol re-concentrators can output 99.0%–99.9% lean TEG. A value of 99.5% lean TEG is used in most designs.

**Inlet scrubber.** It is essential to have a good inlet scrubber for efficient operation of a glycol dehydrator unit. Two-phase inlet scrubbers are generally constructed with 7½-ft shell heights. The required minimum diameter of a vertical inlet scrubber can be determined based on the operating pressure and required gas capacity using Fig. 10.9, which was prepared by Guo and Ghaleb (2005) based on Sivalls's data (1977).

**Glycol-gas contactor.** Glycol contactors are generally constructed with a standard height of 7½ ft. The minimum required diameter of the contactor can be determined based on the gas capacity of the contactor for standard gas of 0.7 specific gravity at standard temperature 100°F. If the gas is



**FIGURE 10.9**

Gas capacity of vertical inlet scrubbers based on 0.7-specific gravity at 100°F (Guo and Ghalambor, 2005).

not the standard gas and/or the operating temperature is different from the standard temperature, a correction should be first made using the following relation:

$$q_s = \frac{q}{C_t C_g}, \quad (10.30)$$

where

$q$  = gas capacity of contactor at operating conditions, MMscfd

$q_s$  = gas capacity of contactor for standard gas (0.7 specific gravity) at standard temperature (100°F), MMscfd

$C_t$  = correction factor for operating temperature

$C_g$  = correction factor for gas-specific gravity

The temperature and gas-specific gravity correction factors for trayed glycol contactors are given in Tables 10.9 and 10.10, respectively. The temperature and specific gravity factors for packed glycol contactors are contained in Tables 10.11 and 10.12, respectively.

Once the gas capacity of the contactor for standard gas at standard temperature is calculated, the required minimum diameter of a trayed glycol contactor can be calculated using Fig. 10.10. The required minimum diameter of a packed glycol contactor can be determined based on Fig. 10.11.

Operating Temperature (°F)	Correction Factor ( $C_t$ )
40	1.07
50	1.06
60	1.05
70	1.04
80	1.02
90	1.01
100	1.00
110	0.99
120	0.98

*Used, with permission, from Sivalls, C.R., 1977. Fundamentals of oil and gas separation. In: Proceedings of the Gas Conditioning Conference, University of Oklahoma, Norman, OK.*

Gas-Specific Gravity (air = 1)	Correction Factor ( $C_g$ )
0.55	1.14
0.60	1.08
0.65	1.04
0.70	1.00
0.75	0.97
0.80	0.93
0.85	0.90
0.90	0.88

*Used, with permission, from Sivalls, C.R., 1977. Fundamentals of oil and gas separation. In: Proceedings of the Gas Conditioning Conference, University of Oklahoma, Norman, OK.*

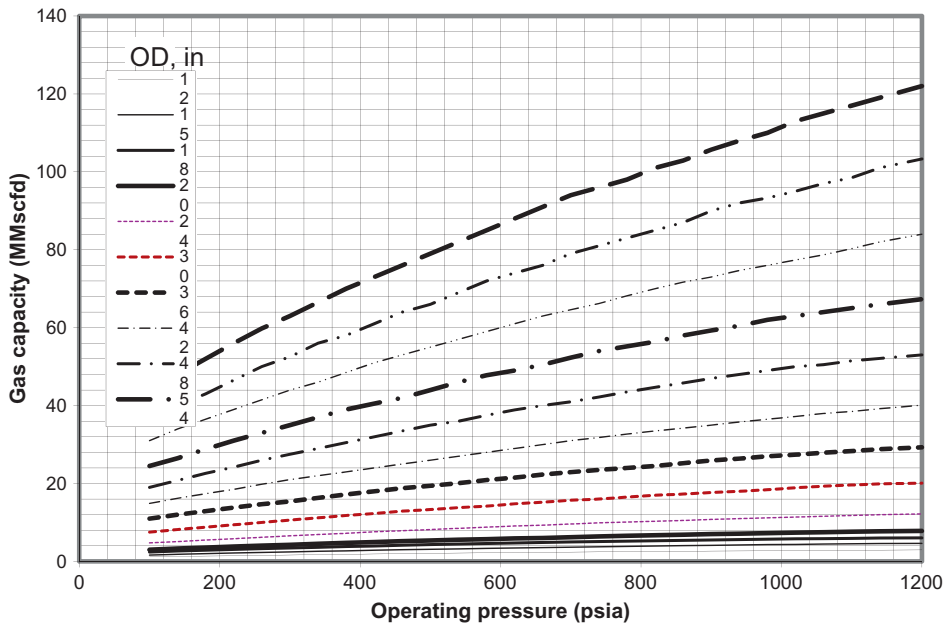
Operating Temperature (°F)	Correction Factor ( $C_t$ )
50	0.93
60	0.94
70	0.96
80	0.97
90	0.99
100	1.00
110	1.01
120	1.02

*Used, with permission, from Sivalls, C.R., 1977. Fundamentals of oil and gas separation. In: Proceedings of the Gas Conditioning Conference, University of Oklahoma, Norman, OK.*

**Table 10.12 Specific Gravity Correction Factors for Packed Glycol Contactors**

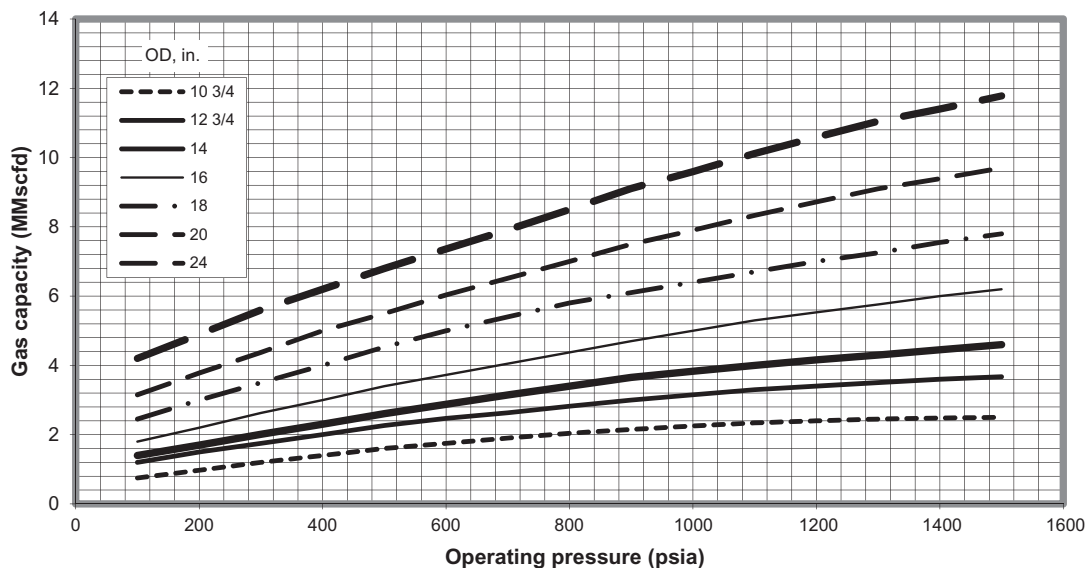
Gas-Specific Gravity (air = 1)	Correction Factor ( $C_g$ )
0.55	1.13
0.60	1.08
0.65	1.04
0.70	1.00
0.75	0.97
0.80	0.94
0.85	0.91
0.90	0.88

*Used, with permission, from Sivalis, C.R., 1977. Fundamentals of oil and gas separation. In: Proceedings of the Gas Conditioning Conference, University of Oklahoma, Norman, OK.*



**FIGURE 10.10**

Gas capacity for trayed glycol contactors based on 0.7-specific gravity at 100°F (Sivalis, 1977).



**FIGURE 10.11**

Gas capacity for packed glycol contactors based on 0.7-specific gravity at 100°F (Sivalls, 1977).

The required minimum height of packing of a packed contactor, or the minimum number of trays of a trayed contactor, can be determined based on Fig. 10.12.

**Example Problem 10.2** Size a trayed-type glycol contactor for a field installation to meet the following requirements:

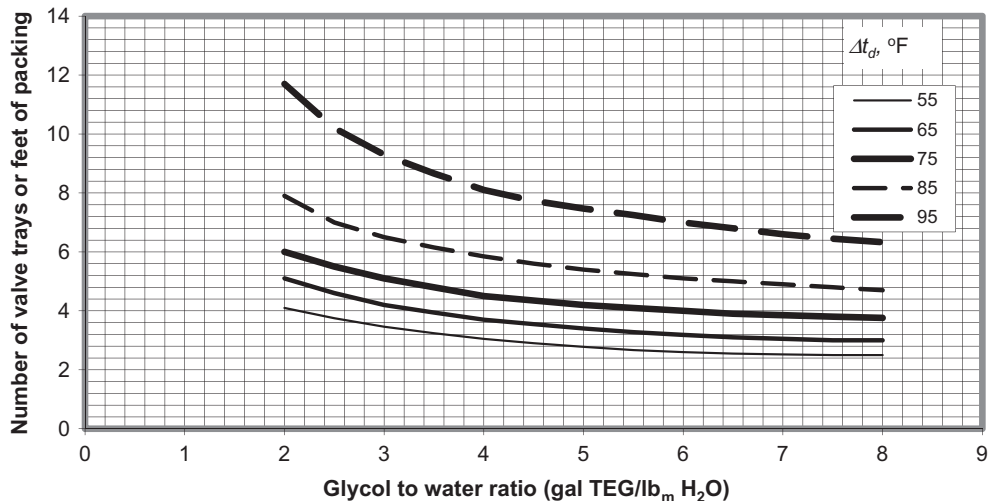
Gas flow rate:	12 MMscfd
Gas-specific gravity:	0.75
Operating line pressure:	900
Maximum working pressure of contactor:	1440 psig
Gas inlet temperature:	90°F
Outlet gas water content:	6 lb H <sub>2</sub> O/MMscf
Design criteria:	GWR = 3 gal TEG/lb <sub>m</sub> H <sub>2</sub> O with 99.5% TEG

**Solution** Because the given gas is not a standard gas and the inlet temperature is not the standard temperature, corrections need to be made. Tables 10.9 and 10.10 give  $C_t = 1.01$  and  $C_g = 0.97$ . The gas capacity of contactor is calculated with Eq. (10.30):

$$q_s = \frac{12}{(1.01)(0.97)} = 12.25 \text{ MMscfd.}$$

Fig. 10.10 gives contactor diameter  $D_C = 30$  in.

Fig. 10.6 gives water content of inlet gas:  $C_{wi} = 50 \text{ lb}_m/\text{MMscf}$ .



**FIGURE 10.12**

The required minimum height of packing of a packed contactor, or the minimum number of trays of a trayed contactor (Sivalls, 1977).

The required water content of outlet gas determines the dew-point temperature of the outlet gas through Fig. 10.6:  $t_{do} = 28^\circ\text{F}$ .

Therefore, the dew-point depression is  $\Delta t_d = 90 - 28 = 62^\circ\text{F}$ .

Based on  $\text{GWR} = 3 \text{ gal TEG/lb}_m \text{ H}_2\text{O}$  and  $\Delta t_d = 62^\circ\text{F}$ , Fig. 10.12 gives the number of trays rounded off to be four.

**Glycol re-concentrator.** Sizing the various components of a glycol re-concentrator starts from calculating the required glycol circulation rate:

$$q_G = \frac{(\text{GWR})C_{wi}q}{24}, \quad (10.31)$$

where

$q_G$  = glycol circulation rate, gal/hr

$\text{GWR}$  = GWR, gal TEG/lb<sub>m</sub> H<sub>2</sub>O

$C_{wi}$  = water content of inlet gas, lb<sub>m</sub> H<sub>2</sub>O/MMscf

$q$  = gas flow rate, MMscfd

**Reboiler.** The required heat load for the reboiler can be approximately estimated from the following equation:

$$H_t = 2000 q_G, \quad (10.32)$$

where

$H_t$  = total heat load on reboiler, Btu/hr



Eq. (10.32) is accurate enough for most high-pressure glycol dehydrator sizing. A more detailed procedure for determination of the required reboiler heat load can be found from Ikoku (1984). The general overall size of the reboiler can be determined as follows:

$$A_{fb} = \frac{H_t}{7000}, \quad (10.33)$$

where  $A_{fb}$ , is the total firebox surface area in squared feet.

**Glycol circulating pump.** The glycol circulating pump can be sized using the glycol circulation rate and the maximum operating pressure of the contactor. Commonly used glycol-powered pumps use the rich glycol from the bottom of the contactor to power the pump and pump the lean glycol to the top of the contactor. The manufacturers of these pumps should be consulted to meet the specific needs of the glycol dehydrator.

**Glycol flash separator.** A glycol flash separator is usually installed downstream from the glycol pump to remove any entrained hydrocarbons from the rich glycol. A small 125-psi vertical two-phase separator is usually adequate for this purpose. The separator should be sized based on a liquid retention time in the vessel of at least 5 minutes.

$$V_s = \frac{q_G t_r}{60}, \quad (10.34)$$

where

$V_s$  = required settling volume in separator, gal

$q_G$  = glycol circulation rate, gph

$t_r$  = retention time approximately 5 minute

Liquid hydrocarbon is not allowed to enter the glycol-gas contactor. If this is a problem, a three-phase glycol flash separator should be used to keep these liquid hydrocarbons out of the reboiler and stripping still. Three-phase flash separators should be sized with a liquid retention time of 20–30 minutes. The hydrocarbon gas released from the flash separator can be piped to the reboiler to use as fuel gas and stripping gas. Based on the glycol circulation rate and the operating pressure of the contactor, the amount of gas available from the glycol pump can be determined.

**Stripping still.** The size of the packed stripping still for the glycol re-concentrator can be determined based on the glycol-to-water circulation rate (gas TEG/lb<sub>m</sub> H<sub>2</sub>O) and the glycol circulation rate (gph). The required diameter for the stripping still is normally based on the required diameter at the base of the still using the vapor and liquid loading conditions at the base point. The vapor load consists of the water vapor and stripping gas flowing up through the still. The liquid load consists of the rich glycol stream and reflux flowing downward through the still column. One tray is normally sufficient for most stripping still requirements for TEG dehydration units. The amount of stripping gas required to re-concentrate the glycol is approximately 2–10 ft<sup>3</sup> per gal of glycol circulated.

---

## 10.4 SUMMARY

This chapter gives a brief introduction to fluid separation and gas dehydration systems. Effects of pressure and temperature on separation performance are illustrated with a flash calculation example. A guideline to selection of system components is also presented. Operators need to consult with equipment providers in designing their separation systems.

---

## REFERENCES

- Ahmed, T., 1989. *Hydrocarbon Phase Behavior*. Gulf Publishing Company, Houston, TX.
- Campbell, J.M., 1976. *Gas Conditioning and Processing*. Campbell Petroleum Services, Norman, OK.
- Guenther, J.D., Natural gas dehydration. In: Paper presented at the Seminar on Process Equipment and Systems on Treatment Platforms, April 26, 1979, Taastrup, Denmark.
- Guo, B., Ghalambor, A., 2005. *Natural Gas Engineering Handbook*. Gulf Publishing Company, Houston, TX.
- Ikoku, C.U., 1984. *Natural Gas Production Engineering*. John Wiley & Sons, New York.
- McCarthy, E.L., Boyd, W.L., Reid, L.S., 1950. The water vapor content of essentially nitrogen-free natural gas saturated at various conditions of temperature and pressure. *Trans. AIME* 189, 241–243.
- McKetta, J.J., Wehe, W.L., 1958. Use this chart for water content of natural gases. *Pet. Refin.* 37, 153–154.
- Sivalls, C.R., 1977. *Fundamentals of oil and gas separation*. Proceedings of the Gas Conditioning Conference. University of Oklahoma, Norman, OK.
- Standing, M.B., 1979. A set of equations for computing equilibrium ratios of a crude oil/natural gas system at pressures below 1,000 psia. *Trans. AIME* 31, 1193.

---

## PROBLEMS

10.1. For the following fluid compositione, run flash calculation under 800 psia and 80°F:

C <sub>1</sub>	0.6099
C <sub>2</sub>	0.0569
C <sub>3</sub>	0.0391
i-C <sub>4</sub>	0.0249
n-C <sub>4</sub>	0.0268
i-C <sub>5</sub>	0.0357
n-C <sub>5</sub>	0.0412
C <sub>6</sub>	0.0381
C <sub>7+</sub>	0.0901
N <sub>2</sub>	0.0244
CO <sub>2</sub>	0.0101
H <sub>2</sub> S	0.0028

- 10.2.** Calculate the minimum required size of a standard oil/gas separator for the following conditions (consider vertical, horizontal, and spherical separators):

Gas flow rate:	4.0 MMscfd
Gas-specific gravity:	0.7
Condensate-gas ratio (CGR):	15 bbl/MMscf
Condensate gravity:	65 °API
Operating pressure:	600 psig
Operating temperature:	70°F

- 10.3.** A three-stage separation is proposed to treat a well stream at a flowline pressure of 1000 psia. Calculate pressures at each stage of separation.
- 10.4.** Estimate water contents of a natural gas at a pressure of 2000 psia and temperatures of 40, 80, 120, 160, 200, and 240°F.
- 10.5.** Design a glycol contactor for a field dehydration installation to meet the following requirements. Consider both trayed-type and packed-type contactors.

Gas flow rate:	10 MMscfd
Gas-specific gravity:	0.65
Operating line pressure:	1000 psig
Maximum working pressure of contactor:	1440 psig
Gas inlet temperature:	90°F
Outlet gas water content:	7 lb H <sub>2</sub> O/MMscf
Design criteria with gal 99.5% TEG:	GWR = 3 TEG/lb <sub>m</sub> H <sub>2</sub> O

## 11.1 INTRODUCTION

Crude oil and natural gas are transmitted over short and long distances mainly through pipelines. Pumps and compressors are used for providing pressures required for the transportation. This chapter presents principles of pumps and compressors and techniques that are used for selecting these equipments. Pipeline design criteria and fluid flow in pipelines are also discussed. Flow assurance issues are addressed.

## 11.2 PUMPS

Reciprocating piston pumps (also called “slush pumps” or “power pumps”) are widely used for transporting crude oil through pipelines. There are two types of piston strokes: the single-action piston stroke and the double-action piston stroke. These are graphically shown in Figs. 11.1 and 11.2. The double-action stroke is used for duplex (two pistons) pumps. The single-action stroke is used for pumps with three or more pistons (e.g., triplex pump). Normally, duplex pumps can handle higher flow rate and triplex pumps can provide higher pressure.

### 11.2.1 TRIPLEX PUMPS

The work per stroke for a single piston is expressed as

$$\bar{W}_1 = P \left( \frac{\pi D^2}{4} \right) L (\text{ft} - \text{lbs}).$$

The work per one rotation of crank is

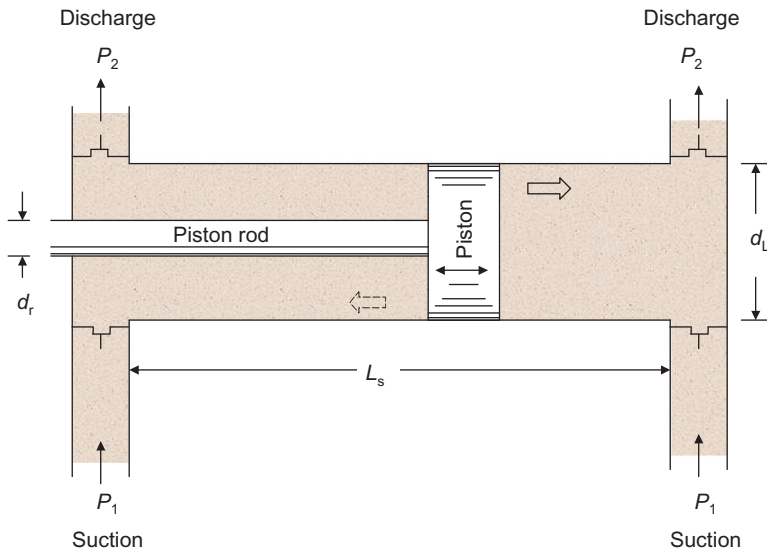
$$\bar{W}_2 = P \left( \frac{\pi D^2}{4} \right) L (1) \left( \frac{\text{ft} - \text{lbs}}{\text{rotation}} \right).$$

where

$P$  = pressure, lb/ft<sup>2</sup>

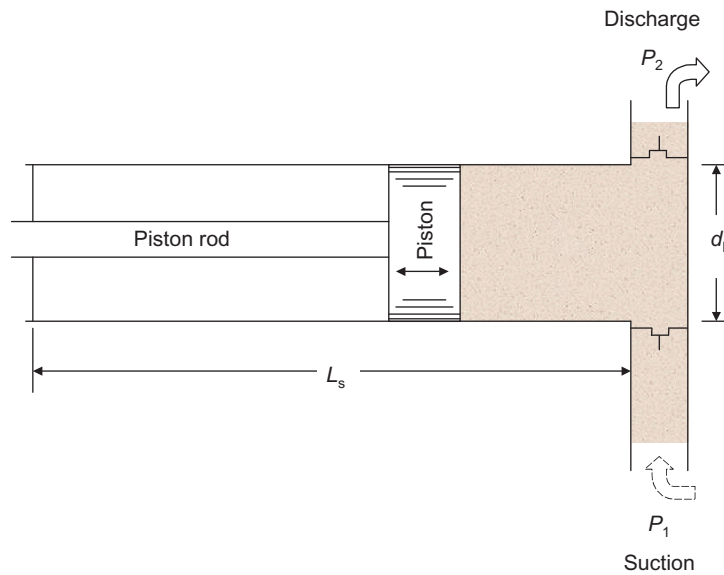
$L$  = stroke length, ft

$D$  = piston diameter, ft



**FIGURE 11.1**

Double-action stroke in a duplex pump.



**FIGURE 11.2**

Single-action stroke in a triplex pump.

Thus, for a triplex pump, the theoretical power is

$$\text{Power} = 3P \left( \frac{\pi D^2}{4} \right) LN \left( \frac{\text{ft} \cdot \text{lb}}{\text{min}} \right), \quad (11.1)$$

where  $N$  is pumping speed in strokes per minute. The theoretical horsepower is

$$HP_{th} = \frac{3P \left( \frac{\pi D^2}{4} \right)}{550(60)} LN(\text{hp}) \quad (11.2)$$

or

$$HP_{th} = \frac{3P \left( \frac{\pi D^2}{4} \right)}{33,000} LN(\text{hp}). \quad (11.3)$$

The input horsepower needed from the prime mover is

$$HP_i = \frac{3P \left( \frac{\pi D^2}{4} \right)}{33,000 e_m} LN(\text{hp}), \quad (11.4)$$

where  $e_m$  is the mechanical efficiency of the mechanical system transferring power from the prime mover to the fluid in the pump. Usually  $e_m$  is taken to be about 0.85.

The theoretical volume output from a triplex pump per revolution is

$$Q_{th} = 3 \left( \frac{\pi D^2}{4} \right) \frac{LN}{60} (\text{ft}^3/\text{sec}). \quad (11.5)$$

The theoretical output in bbl/day is thus

$$q_{th} = 604 LND^2 \left( \frac{\text{bbl}}{\text{day}} \right). \quad (11.6)$$

If we use inches (i.e.,  $d$  [in.] and  $l$  [in.]), for  $D$  and  $L$ , then

$$q_{th} = 0.35 lNd^2 \left( \frac{\text{bbl}}{\text{day}} \right). \quad (11.7)$$

The real output of the pump is dependent on how efficiently the pump can fill the chambers of the pistons. Using the volumetric efficiency  $e_v$  in Eq. 11.7 gives

$$q_r = 0.35 e_v lNd^2 \left( \frac{\text{bbl}}{\text{day}} \right) \quad (11.8)$$

or

$$q_r = 0.01 e_v d^2 lN(\text{gal}/\text{min}), \quad (11.9)$$

where  $e_v$  is usually taken to be 0.88–0.98.

As the above volumetric equation can be written in  $d$  and  $l$ , then the horsepower equation can be written in  $d$ ,  $l$ , and  $p$  (psi). Thus,

$$HP_i = \frac{3p \left( \frac{\pi d^2}{4} \right) \frac{1}{12} N}{33,000 e_m} \quad (11.10)$$

reduces to

$$HP_i = \frac{pd^2 l N}{168,067 e_m}. \quad (11.11)$$

### 11.2.2 DUPLEX PUMPS

The work per stroke cycle is expressed as

$$W_1 = P \left( \frac{\pi D_1^2}{4} \right) L + P \left[ \frac{\pi D_1^2}{4} - \frac{\pi D_2^2}{4} \right] L \text{ (ft-lbs)}. \quad (11.12)$$

The work per one rotation of crank is

$$W_2 = \left\{ P \left( \frac{\pi D_1^2}{4} \right) L + P \left[ \frac{\pi D_1^2}{4} - \frac{\pi D_2^2}{4} \right] L \right\} (1) \left( \frac{\text{ft-lbs}}{\text{rotation}} \right). \quad (11.13)$$

Thus, for a duplex pump, the theoretical power is

$$\text{Power} = 2 \times \left\{ P \left( \frac{\pi D_1^2}{4} \right) L + P \left[ \frac{\pi D_1^2}{4} - \frac{\pi D_2^2}{4} \right] L \right\} N \left( \frac{\text{ft-lbs}}{\text{min}} \right). \quad (11.14)$$

The theoretical horsepower is

$$HP_{th} = \frac{2 \left\{ P \left( \frac{\pi D_1^2}{4} \right) L + P \left[ \frac{\pi D_1^2}{4} - \frac{\pi D_2^2}{4} \right] L \right\} N}{550(60)} \text{ (hp)}$$

or

$$HP_{th} = \frac{2 \left\{ P \left( \frac{\pi D_1^2}{4} \right) L + P \left[ \frac{\pi D_1^2}{4} - \frac{\pi D_2^2}{4} \right] L \right\} N}{33,000}. \quad (11.15)$$

The input horsepower needed from the prime mover is

$$Q_{th} = \frac{2 \left\{ P \left( \frac{\pi D_1^2}{4} \right) L + P \left[ \frac{\pi D_1^2}{4} - \frac{\pi D_2^2}{4} \right] L \right\} N}{33,000 e_m} \text{ (hp)}. \quad (11.16)$$

The theoretical volume output from the double-acting duplex pump per revolution is

$$Q_{th} = 2 \left\{ \frac{\pi D_1^2}{4} L + \left[ \frac{\pi D_1^2}{4} - \frac{\pi D_2^2}{4} \right] L \right\} \frac{N}{60} \text{ (ft}^3/\text{sec)}. \quad (11.17)$$

The theoretical output in gals/min is thus

$$q_{th} = 2 \left\{ \frac{\pi D_1^2}{4} L + \left[ \frac{\pi D_1^2}{4} - \frac{\pi D_2^2}{4} \right] L \right\} \times \frac{N}{0.1337} \text{ (gal/min)}. \quad (11.18)$$

If we use inches (i.e.,  $d$  [in.] and  $l$  [in.]), for  $D$  and  $L$ , then

$$q_{th} = 2 \left\{ \frac{\pi d_1^2}{4} l + \left[ \frac{\pi d_1^2}{4} - \frac{\pi d_2^2}{4} \right] l \right\} \frac{N}{231} \text{ (gal/min)}. \quad (11.19)$$

The real output of the pump is

$$q_r = 2 \left\{ \frac{\pi d_1^2}{4} l + \left[ \frac{\pi d_1^2}{4} - \frac{\pi d_2^2}{4} \right] l \right\} \frac{N}{231} e_v \text{ (gal/min)}$$

or

$$q_r = 0.0068(2d_1^2 - d_2^2)lNe_v \text{ (gal/min)}, \quad (11.20)$$

that is,

$$q_r = 0.233(2d_1^2 - d_2^2)lNe_v \text{ (bbl/day)}. \quad (11.21)$$

As in the volumetric output, the horsepower equation can also be reduced to a form with  $p$ ,  $d_1$ ,  $d_2$ , and  $l$

$$HP_i = \frac{p(2d_1^2 - d_2^2)lN}{252,101e_m}. \quad (11.22)$$

Returning to Eq. (11.16) for the duplex double-action pump, let us derive a simplified pump equation. Rewriting Eq. (11.16), we have

$$HP_i = \frac{2 \left\{ P \left( \frac{\pi D_1^2}{4} \right) L + P \left[ \frac{\pi D_1^2}{4} - \frac{\pi D_2^2}{4} \right] L \right\} N}{33,000e_m}. \quad (11.23)$$

The flow rate is

$$Q_{th} = 2 \left\{ \frac{\pi D_1^2}{4} L + \left[ \frac{\pi D_1^2}{4} - \frac{\pi D_2^2}{4} \right] L \right\} N \text{ (ft}^3/\text{min)}, \quad (11.24)$$

so

$$HP_i = \frac{PQ_{th}}{33,000e_m} \quad (11.25)$$



The usual form of this equation is in  $p$  (psi) and  $q$  (gal/min):

$$HP_i = \frac{[p(12)^2] [q(0.1337)]}{33,000e_m}, \quad (11.26)$$

that is,

$$HP_i = \frac{pq}{1714e_m}. \quad (11.27)$$

The other form of this equation is in  $p$  (psi) and  $q_o$  (bbl/day) for oil transportation:

$$HP_i = \frac{pq_o}{58,766e_m}. \quad (11.28)$$

Eqs. (11.27) and (11.28) are valid for any type of pump.

**Example Problem 11.1** A pipeline transporting 5000 bbl/day of oil requires a pump with a minimum output pressure of 1000 psi. The available suction pressure is 300 psi. Select a triplex pump for this operation.

**Solution** Assuming a mechanical efficient of 0.85, the horsepower requirement is

$$HP_i = \frac{pq_o}{58,766e_m} = \frac{(1000)(5000)}{58,766(0.85)} = 100 \text{ hp.}$$

According to a product sheet of the Oilwell Plunger Pumps, the Model 336-ST Triplex with forged steel fluid end has a rated brake horsepower of 160 hp at 320 rpm. The maximum working pressure is 3180 psi with the minimum plunger (piston) size of 1¾ in. It requires a suction pressure of 275 psi. With 3-in. plungers, the pump displacement is 0.5508 gal/rpm, and it can deliver liquid flow rates in the range of 1889 bbl/day (55.08 gpm) at 100 rpm to 6046 bbl/day (176.26 gpm) at 320 rpm, allowing a maximum pressure of 1420 psi. This pump can be selected for the operation. The required operating rpm is

$$\text{RPM} = \frac{(5000)(42)}{(24)(60)(0.5508)} = 265 \text{ rpm.}$$

---

## 11.3 COMPRESSORS

When natural gas does not have sufficient potential energy to flow, a compressor station is needed. Five types of compressor stations are generally used in the natural gas production industry:

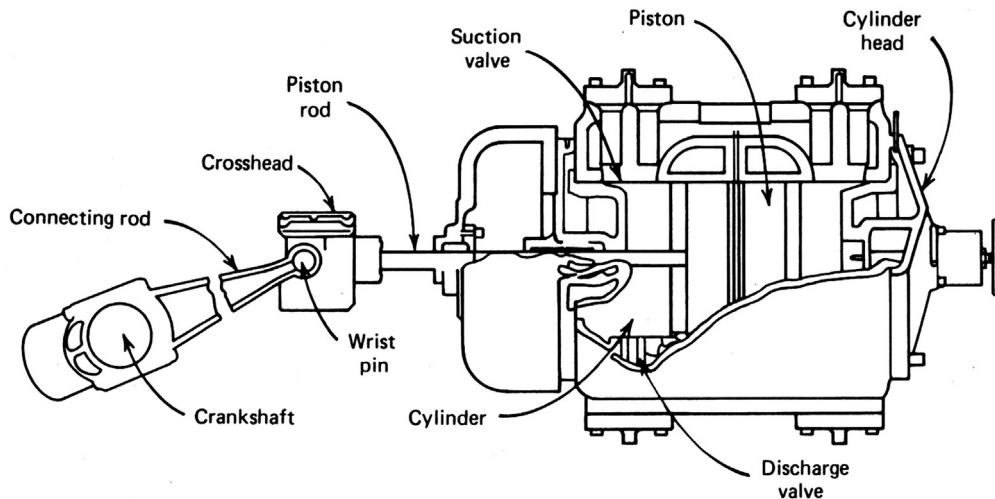
- Field gas-gathering stations to gather gas from wells in which pressure is insufficient to produce at a desired rate of flow into a transmission or distribution system. These stations generally handle suction pressures from below atmospheric pressure to 750 psig and volumes from a few thousand to many million cubic feet per day.
- Relay or main-line stations to boost pressure in transmission lines compress generally large volumes of gas at a pressure range between 200 and 1300 psig.
- Re-pressuring or recycling stations to provide gas pressures as high as 6000 psig for processing or secondary oil recovery projects.

- Storage field stations to compress trunk line gas for injection into storage wells at pressures up to 4000 psig.
- Distribution plant stations to pump gas from holder supply to medium- or high-pressure distribution lines at about 20–100 psig, or pump into bottle storage up to 2500 psig.

### 11.3.1 TYPES OF COMPRESSORS

The compressors used in today's natural gas production industry fall into two distinct types: reciprocating and rotary compressors. Reciprocating compressors are most commonly used in the natural gas industry. They are built for practically all pressures and volumetric capacities. As shown in Fig. 11.3, reciprocating compressors have more moving parts and, therefore, lower mechanical efficiencies than rotary compressors. Each cylinder assembly of a reciprocating compressor consists of a piston, cylinder, cylinder heads, suction and discharge valves, and other parts necessary to convert rotary motion to reciprocation motion. A reciprocating compressor is designed for a certain range of compression ratios through the selection of proper piston displacement and clearance volume within the cylinder. This clearance volume can be either fixed or variable, depending on the extent of the operation range and the percent of load variation desired. A typical reciprocating compressor can deliver a volumetric gas flow rate of up to 30,000 cubic feet per minute (cfm) at a discharge pressure of up to 10,000 psig.

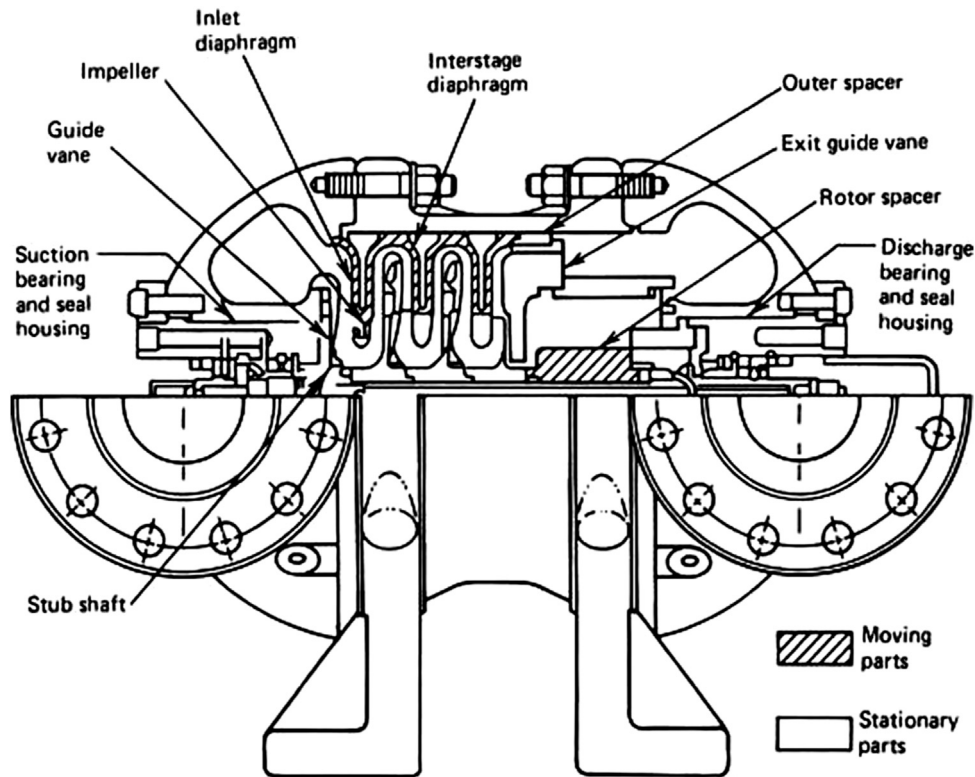
Rotary compressors are divided into two classes: the centrifugal compressor and the rotary blower. A centrifugal compressor (Fig. 11.4) consists of a housing with flow passages, a rotating shaft on which the impeller is mounted, bearings, and seals to prevent gas from escaping along the shaft. Centrifugal compressors have few moving parts because only the impeller and shaft rotate. Thus, its



**FIGURE 11.3**

Elements of a typical reciprocating compressor.

*Courtesy of Petroleum Extension Services.*



**FIGURE 11.4**

Cross-section of a centrifugal compressor.

*Courtesy of Petroleum Extension Services.*

efficiency is high and lubrication oil consumption and maintenance costs are low. Cooling water is normally unnecessary because of lower compression ratio and lower friction loss. Compression rates of centrifugal compressors are lower because of the absence of positive displacement. Centrifugal compressors compress gas using centrifugal force. In this type of compressor, work is done on the gas by an impeller. Gas is then discharged at a high velocity into a diffuser where the velocity is reduced and its kinetic energy is converted to static pressure. Unlike reciprocating compressors, all this is done without confinement and physical squeezing. Centrifugal compressors with relatively unrestricted passages and continuous flow are inherently high-capacity, low-pressure ratio machines that adapt easily to series arrangements within a station. In this way, each compressor is required to develop only part of the station compression ratio. Typically, the volume is more than 100,000 cfm and discharge pressure is up to 100 psig.

A rotary blower is built of a casing in which one or more impellers rotate in opposite directions. Rotary blowers are primarily used in distribution systems where the pressure differential between suction and discharge is less than 15 psi. They are also used for refrigeration and closed regeneration of adsorption plants. The rotary blower has several advantages: large quantities of low-pressure gas can be handled at comparatively low horsepower, it has small initial cost and low maintenance cost,

it is simple to install and easy to operate and attend, it requires minimum floor space for the quantity of gas removed, and it has almost pulsation-less flow. As its disadvantages, it cannot withstand high pressures, it has noisy operation because of gear noise and clattering impellers, it improperly seals the clearance between the impellers and the casing, and it overheats if operated above safe pressures. Typically, rotary blowers deliver a volumetric gas flow rate of up to 17,000 cfm and have a maximum intake pressure of 10 psig and a differential pressure of 10 psi.

When selecting a compressor, the pressure–volume characteristics and the type of driver must be considered. Small rotary compressors (vane or impeller type) are generally driven by electric motors. Large-volume positive compressors operate at lower speeds and are usually driven by steam or gas engines. They may be driven through reduction gearing by steam turbines or an electric motor. Reciprocation compressors driven by steam turbines or electric motors are most widely used in the natural gas industry as the conventional high-speed compression machine. Selection of compressors requires considerations of volumetric gas deliverability, pressure, compression ratio, and horsepower.

The following are important characteristics of the two types of compressors:

- Reciprocating piston compressors can adjust pressure output to backpressure.
- Reciprocating compressors can vary their volumetric flow-rate output (within certain limits).
- Reciprocating compressors have a volumetric efficiency, which is related to the relative clearance volume of the compressor design.
- Rotary compressors have a fixed pressure ratio, so they have a constant pressure output.
- Rotary compressors can vary their volumetric flow-rate output (within certain limits).

### 11.3.2 RECIPROCATING COMPRESSORS

Fig. 11.5 shows a diagram volume relation during gas compression. The shaft work put into the gas is expressed as

$$W_s = \frac{V_2^2}{2g} - \frac{V_1^2}{2g} + \left( P_2 v_2 - \int_1^2 P dv - P_1 v_1 \right), \quad (11.29)$$

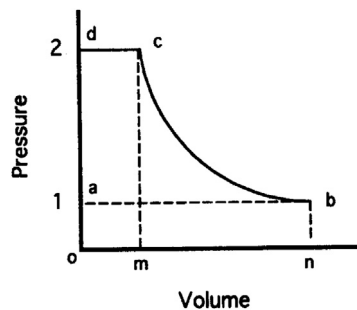


FIGURE 11.5

Basic pressure–volume diagram.

where

$W_s$  = mechanical shaft work into the system, ft-lbs per lb of fluid

$V_1$  = inlet velocity of fluid to be compressed, ft/sec

$V_2$  = outlet velocity of compressed fluid, ft/sec

$P_1$  = inlet pressure, lb/ft<sup>2</sup> abs

$P_2$  = outlet pressure, lb/ft<sup>2</sup> abs

$v_1$  = specific volume at inlet, ft<sup>3</sup>/lb

$v_2$  = specific volume at outlet, ft<sup>3</sup>/lb.

Note that the mechanical kinetic energy term  $\frac{V^2}{2g}$  is in ft  $\left(\frac{\text{lb}}{\text{lb}}\right)$  to get ft-lbs per lb.

Rewriting Eq. (11.29), we can get

$$W_s + \frac{V_1^2}{2g} - \frac{V_2^2}{2g} + P_1 v_1 - P_2 v_2 = - \int_1^2 P dv. \quad (11.30)$$

An isentropic process is usually assumed for reciprocating compression, that is,  $P_1 v_1^k = P_2 v_2^k = P v^k = \text{constant}$ , where  $k = \frac{c_p}{c_v}$ . Because  $P = \frac{P_1 v_1^k}{v^k}$ , the right-hand side of Eq. (11.30) is formulated as

$$\begin{aligned} - \int_1^2 p dv &= - \int_1^2 \frac{P_1 v_1^k}{v^k} dv = - P_1 v_1^k \int_1^2 \frac{dv}{v^k} \\ &= - P_1 v_1^k \left[ \frac{v^{1-k}}{1-k} \right]_1^2 = - \frac{P_1 v_1^k}{1-k} [v_2^{1-k} - v_1^{1-k}] \\ &= \frac{P_1 v_1^k}{1-k} \left( \frac{v_1^{1-k}}{v_1^{1-k}} \right) [v_2^{1-k} - v_1^{1-k}] \\ &= \frac{P_1 v_1}{1-k} \left[ \frac{v_2^{1-k}}{v_1^{1-k}} - 1 \right] \\ &= \frac{P_1 v_1}{1-k} \left[ \left( \frac{v_1}{v_2} \right)^{k-1} - 1 \right]. \end{aligned} \quad (11.31)$$

Using the ideal gas law

$$\frac{P}{\gamma} = RT, \quad (11.32)$$

where  $\gamma$  (lb/ft<sup>3</sup>) is the specific weight of the gas and  $T$  (°R) is the temperature and  $R = 53.36$  (lb-ft/lb-°R) is the gas constant, and  $v = \frac{1}{\gamma}$ , we can write Eq. (11.32) as

$$Pv = RT \quad (11.33)$$

or

$$P_1 v_1 = RT_1. \quad (11.34)$$

Using  $P_1 v_1^k = P_2 v_2^k = P v^k = \text{constant}$ , which gives

$$\left(\frac{v_1}{v_2}\right)^k = \frac{P_2}{P_1}$$

or

$$\frac{v_1}{v_2} = \left(\frac{P_2}{P_1}\right)^{\frac{1}{k}}. \quad (11.35)$$

Substituting Eqs. (11.35) and (11.34) into Eq. (11.31) gives

$$-\int_1^2 P dv = \frac{RT_1}{k-1} \left[ \left(\frac{P_2}{P_1}\right)^{\frac{k-1}{k}} - 1 \right]. \quad (11.36)$$

We multiply Eq. (11.33) by  $v^{k-1}$ , which gives

$$\begin{aligned} P v^{(k-1)} &= RT(v^{k-1}) \\ P v^k &= RT v^{k-1} = C_1 \\ \frac{P v^k}{R} &= T v^{k-1} = \frac{C_1}{R} = C'_1 \end{aligned}$$

Thus,

$$T v^{k-1} = C'_1. \quad (11.37)$$

Also we can rise  $P v^k = \text{constant}$  to the  $\left(\frac{k-1}{k}\right)$  power. This is

$$\begin{aligned} (P v^k)^{\frac{k-1}{k}} &= C_1^{\frac{k-1}{k}} \\ P^{\frac{k-1}{k}} v^{k-1} &= C_1^{\frac{k-1}{k}} \end{aligned}$$

or

$$v^{k-1} = \frac{C_1^{\frac{k-1}{k}}}{P^{\frac{k-1}{k}}} = \frac{C_1^{\frac{k-1}{k}}}{P^{\frac{k-1}{k}}}. \quad (11.38)$$

Substituting Eq. (11.38) into (11.37) gives

$$T \frac{C_1^{\frac{k-1}{k}}}{P^{\frac{k-1}{k}}} = C'_1$$

or

$$\frac{T}{P^{\frac{k-1}{k}}} = \frac{C'_1}{C_1^{\frac{k-1}{k}}} = C''_1 = \text{constant}. \quad (11.39)$$

Thus, Eq. (11.39) can be written as

$$\frac{T_1}{P_1^{\frac{k-1}{k}}} = \frac{T_2}{P_2^{\frac{k-1}{k}}}. \quad (11.40)$$

Thus, Eq. (11.40) is written

$$\left(\frac{P_2}{P_1}\right)^{\frac{k-1}{k}} = \frac{T_2}{T_1}. \quad (11.41)$$

Substituting Eq. (11.41) into (11.36) gives

$$\begin{aligned} -\int_1^2 P dv &= \frac{RT_1}{k-1} \left[ \frac{T_2}{T_1} - 1 \right] \\ -\int_1^2 P dv &= \frac{R}{k-1} (T_2 - T_1). \end{aligned} \quad (11.42)$$

Therefore, our original expression, Eq. (11.30), can be written as

$$W_s + \frac{V_1^2}{2g} - \frac{V_2^2}{2g} + P_1 v_1 - P_2 v_2 = \frac{R}{k-1} (T_2 - T_1)$$

or

$$W_s = \frac{R}{k-1} (T_2 - T_1) + P_2 v_2 - P_1 v_1 + \frac{(V_2^2 - V_1^2)}{2g}. \quad (11.43)$$

And because

$$P_1 v_1 = RT_1 \quad (11.44)$$

and

$$P_2 v_2 = RT_2, \quad (11.45)$$

Eq. (11.43) becomes

$$W_s = \frac{R}{k-1} (T_2 - T_1) + R(T_2 - T_1) + \frac{(V_2^2 - V_1^2)}{2g}, \quad (11.46)$$

but rearranging Eq. (11.46) gives

$$W_s = \frac{k}{k-1} RT_1 \left( \frac{T_2}{T_1} - 1 \right) + \frac{(V_2^2 - V_1^2)}{2g}.$$

Substituting Eq. (11.41) and (11.44) into the above gives

$$W_s = \frac{k}{k-1} P_1 v_1 \left[ \left( \frac{P_2}{P_1} \right)^{\frac{k-1}{k}} - 1 \right] + \frac{(V_2^2 - V_1^2)}{2g}. \quad (11.47)$$

Neglecting the kinetic energy term, we arrive at

$$W_s = \frac{k}{k-1} P_1 v_1 \left[ \left( \frac{p_2}{P_1} \right)^{\frac{k-1}{k}} - 1 \right], \quad (11.48)$$

where  $W_s$  is ft-lb/lb, that is, work done per lb.

It is convenient to obtain an expression for power under conditions of steady state gas flow. Substituting Eq. (11.44) into (11.48) yields

$$W_s = \frac{k}{k-1} RT_1 \left[ \left( \frac{p_2}{P_1} \right)^{\frac{k-1}{k}} - 1 \right]. \quad (11.49)$$

If we multiply both sides of Eq. (11.49) by the weight rate of flow,  $w_t$  (lb/sec), through the system, we get

$$P_s = \frac{k}{k-1} w_t RT_1 \left[ \left( \frac{p_2}{P_1} \right)^{\frac{k-1}{k}} - 1 \right], \quad (11.50)$$

where  $P_s = W_s w_t \frac{\text{ft-lb}}{\text{sec}}$  and is shaft power. However, the term  $w_t$  is

$$w_t = \gamma_1 Q_1 = \gamma_2 Q_2, \quad (11.51)$$

where  $Q_1$  (ft<sup>3</sup>/sec) is the volumetric flow rate into the compressor and  $Q_2$  (ft<sup>3</sup>/sec) would be the compressed volumetric flow rate out of the compressor. Substituting Eq. (11.32) and (11.51) into (11.50) yields

$$P_s = \frac{k}{k-1} P_1 Q_1 \left[ \left( \frac{p_2}{P_1} \right)^{\frac{k-1}{k}} - 1 \right]. \quad (11.52)$$

If we use more conventional field terms such as

$$P_1 = p_1(144) \text{ where } p_1 \text{ is in psia}$$

$$P_2 = p_2(144) \text{ where } p_2 \text{ is in psia}$$

and

$$Q_1 = \frac{q_1}{60} \text{ where } q_1 \text{ is in cfm,}$$

and knowing that 1 horsepower = 550 ft-lb/sec, then Eq. (11.52) becomes

$$HP = \frac{k}{k-1} \frac{p_1(144)q_1}{550(60)} \left[ \left( \frac{p_2}{p_1} \right)^{\frac{k-1}{k}} - 1 \right],$$

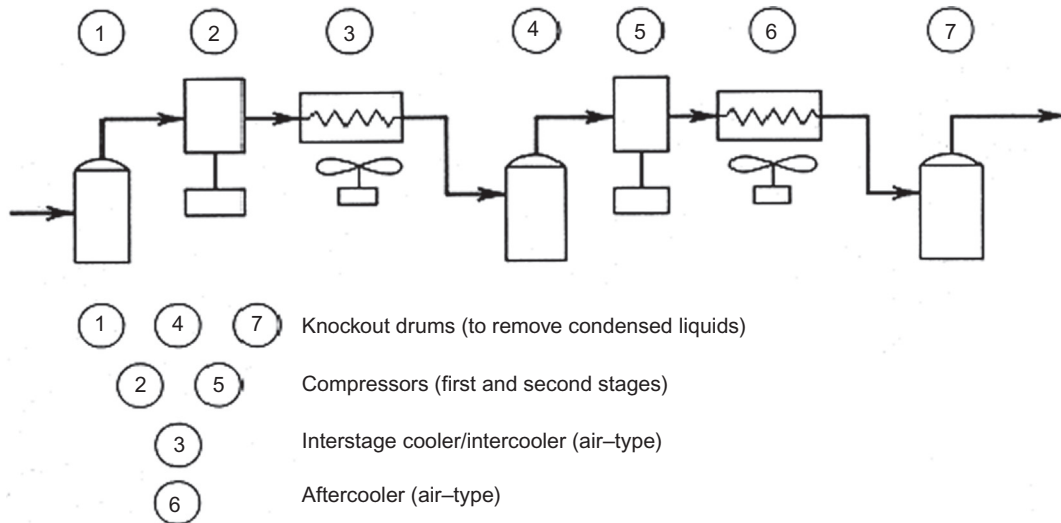
which yields

$$HP = \frac{k}{(k-1)229.2} \frac{p_1 q_1}{229.2} \left[ \left( \frac{p_2}{p_1} \right)^{\frac{k-1}{k}} - 1 \right]. \quad (11.53)$$

If the gas flow rate is given in  $Q_{MM}$  (MMscf/day) in a standard base condition at base pressure  $p_b$  (e.g., 14.7 psia) and base temperature  $T_b$  (e.g., 520 °R), since

$$q_1 = \frac{p_b T_1 Q_{MM}(1,000,000)}{p_1 T_b(24)}, \quad (11.54)$$




**FIGURE 11.6**

Flow diagram of a two-stage compression unit.

Eq. (11.53) becomes

$$HP = \frac{181.79 p_b T_1 Q_{MM}}{T_b} \frac{k}{(k-1)} \left[ \left( \frac{p_2}{p_1} \right)^{\frac{k-1}{k}} - 1 \right]. \quad (11.55)$$

It will be shown later that the efficiency of compression drops with increased compression ratio  $p_2/p_1$ . Most field applications require multistage compressors (two, three, and sometimes four stages) to reduce compression ratio in each stage. Fig. 11.6 shows a two-stage compression unit. Using compressor stages with perfect intercooling between stages gives a theoretical minimum power for gas compression. To obtain this minimum power, the compression ratio in each stage must be the same and the cooling between each stage must bring the gas entering each stage to the same temperature.

The compression ratio in each stage should be less than six to increase compression efficiency. The equation to calculate stage-compression ratio is

$$r_s = \left( \frac{P_{dis}}{P_{in}} \right)^{1/n_s}, \quad (11.56)$$

where  $P_{dis}$ ,  $P_{in}$ , and  $n_s$  are final discharge pressure, inlet pressure, and number of stages, respectively.

For a two-stage compression, the compression ratio for each stage should be

$$r_s = \sqrt{\frac{P_{dis}}{P_{in}}}. \quad (11.57)$$

Using Eq. (11.50), we can write the total power requirement for the two-stage compressor as

$$P_{total} = \frac{k}{k-1} w_t R T_{in1} \left[ \left( \frac{P_{dis1}}{P_{in1}} \right)^{\frac{k-1}{k}} - 1 \right] + \frac{k}{k-1} w_t R T_{in2} \left[ \left( \frac{P_{dis2}}{P_{in2}} \right)^{\frac{k-1}{k}} - 1 \right]. \quad (11.58)$$

The ideal intercooler will cool the gas flow stage one to stage two to the temperature entering the compressor. Thus, we have  $T_{in1} = T_{in2}$ . Also, the pressure  $P_{in2} = P_{dis1}$ . Eq. (11.58) may be written as

$$P_{total} = \frac{k}{k-1} w_t R T_{in1} \left[ \left( \frac{P_{dis1}}{P_{in1}} \right)^{\frac{k-1}{k}} - 1 \right] + \frac{k}{k-1} w_t R T_{in1} \left[ \left( \frac{P_{dis2}}{P_{in2}} \right)^{\frac{k-1}{k}} - 1 \right]. \quad (11.59)$$

We can find the value of  $P_{dis1}$  that will minimize the power required,  $P_{total}$ . We take the derivative of Eq. (11.59) with respect to  $P_{dis1}$  and set this equal to zero and solve for  $P_{dis1}$ . This gives

$$P_{dis1} = \sqrt{P_{in1} P_{dis2}},$$

which proves Eq. (11.57).

For the two-stage compressor, Eq. (11.59) can be rewritten as

$$P_{total} = \frac{2k}{k-1} w_t R T_1 \left[ \left( \frac{P_{dis2}}{P_{in1}} \right)^{\frac{k-1}{2k}} - 1 \right]. \quad (11.60)$$

The ideal intercooling does not extend to the gas exiting the compressor. Gas exiting the compressor is governed by Eq. (11.41). Usually there is an adjustable after-cooler on a compressor that allows the operators to control the temperature of the exiting flow of gas. For greater number of stages, Eq. (11.60) can be written in field units as

$$HP_t = \frac{n_s p_1 q_1}{229.2} \frac{k}{(k-1)} \left[ \left( \frac{p_2}{p_1} \right)^{\frac{k-1}{n_s k}} - 1 \right] \quad (11.61)$$

or

$$HP_t = \frac{181.79 n_s p_b T_1 Q_{MM}}{T_b} \frac{k}{(k-1)} \left[ \left( \frac{p_2}{p_1} \right)^{\frac{k-1}{n_s k}} - 1 \right]. \quad (11.62)$$

In the above,  $p_1$  (psia) is the intake pressure of the gas and  $p_2$  (psia) is the outlet pressure of the compressor after the final stage,  $q_1$  is the actual cfm of gas into the compressor,  $HP_t$  is the theoretical horsepower needed to compress the gas. This  $HP_t$  value has to be matched with a prime mover motor. The proceeding equations have been coded in the spreadsheet *ReciprocatingCompressor Power.xls* for quick calculations.

Reciprocating compressors have a clearance at the end of the piston. This clearance produces a volumetric efficiency  $e_v$ . The relation is given by

$$e_v = 0.96 \left\{ 1 - \varepsilon \left[ r_s^{\frac{1}{k}} - 1 \right] \right\}, \quad (11.63)$$

where  $\varepsilon$  is the clearance ratio defined as the clearance volume at the end of the piston stroke divided by the entire volume of the chamber (volume contacted by the gas in the cylinder).

In addition, there is a mechanical efficiency  $e_m$  of the compressor and its prime mover. This results in two separate expressions for calculating the required  $HP_t$  for reciprocating compressors and rotary compressors. The required minimum input prime mover motor to practically operate the compressor (either reciprocating or rotary) is

$$HP_{in} = \frac{HP_t}{e_v e_m}, \quad (11.64)$$

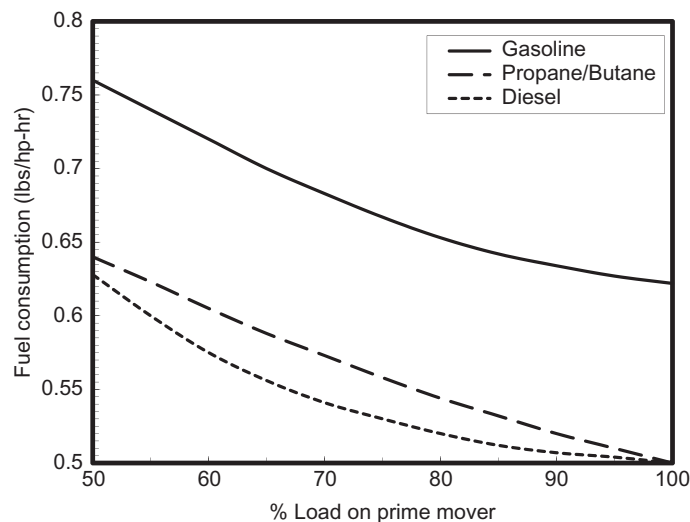
where  $e_v \approx 0.80-0.99$  and  $e_m \approx 0.80-0.95$  for reciprocating compressors, and  $e_v = 1.0$  and  $e_m \approx 0.70-0.75$  for rotary compressors.

Eq. (11.64) stands for the input power required by the compressor, which is the minimum power to be provided by the prime mover. The prime movers usually have fixed power  $HP_p$  under normal operating conditions. The usable prime mover power ratio is

$$PR = \frac{HP_{in}}{HP_p}. \quad (11.65)$$

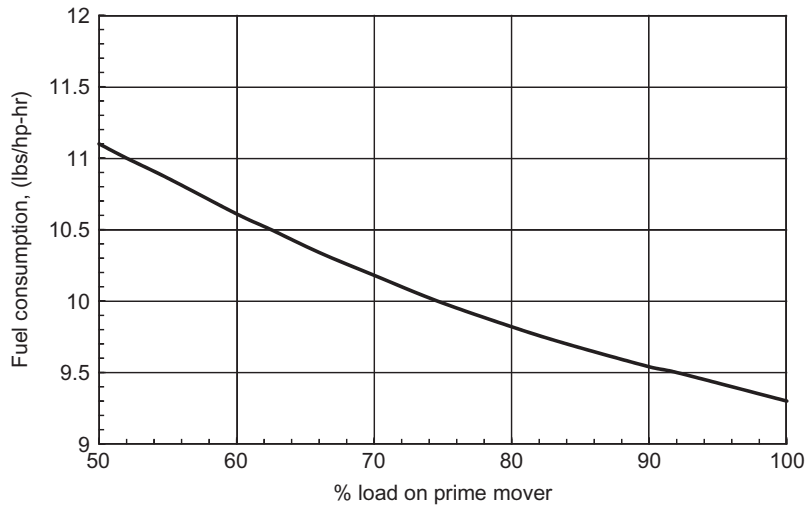
If the prime mover is not fully loaded by the compressor, its rotary speed increases and fuel consumption thus increases. Fig. 11.7 shows fuel consumption curves for prime movers using gasoline, propane/butane, and diesel as fuel. Fig. 11.8 presents fuel consumption curve for prime movers using natural gas as fuel. It is also important to know that the prime mover power drops with surface location elevation (Fig. 11.9).

**ExampleProblem 11.2** Consider a three-stage reciprocating compressor that is rated at  $q = 900$  scfm and a maximum pressure capability of  $p_{max} = 240$  psig (standard conditions at sea



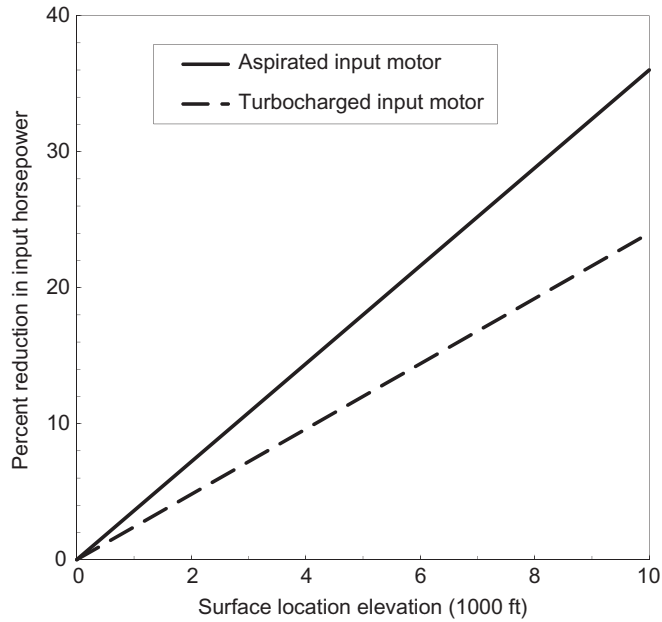
**FIGURE 11.7**

Fuel consumption of prime movers using three types of fuel.



**FIGURE 11.8**

Fuel consumption of prime movers using natural gas as fuel.



**FIGURE 11.9**

Effect of elevation on prime mover power.

level). The diesel prime mover is a diesel motor (naturally aspirated) rated at 300 horsepower (at sea-level conditions). The reciprocating compressor has a clearance ratio of  $\varepsilon = 0.06$  and  $e_m \approx 0.90$ . Determine the gallons/hr of fuel consumption if the working backpressure is 150 psig, and do for

- operating at sea level
- operating at 6000 ft.

**Solution**

- Operating at sea level:

$$r_s = \sqrt[3]{\frac{P_{dis}}{P_{in}}} = \sqrt[3]{\frac{150 + 14.7}{14.7}} = \sqrt[3]{\frac{164.7}{14.7}} = 2.24$$

$$e_v = 0.96 \left\{ 1 - 0.06 \left[ (2.24)^{\frac{1}{14}} - 1 \right] \right\} = 0.9151$$

Required theoretical power to compress the gas:

$$HP_t = (3) \frac{14.7(900)}{229.2} \left( \frac{1.4}{0.4} \right) \left[ \left( \frac{164.7}{14.7} \right)^{\frac{0.4}{3-(1.4)}} - 1 \right] = 156.8 \text{ hp}$$

Required input power to the compressor:

$$HP_r = \frac{HP_t}{e_m e_v} = \frac{156.8}{0.90(0.9151)} = 190.3 \text{ hp}$$

Since the available power from the prime mover is 300 hp, which is greater than  $HP_r$ , the prime mover is okay. The power ratio is

$$PR = \frac{190.3}{300.0} = 0.634 \text{ or } 63.4\%.$$

From Fig. 11.7, fuel usage is approximately 0.56 lb/hp-hr. The weight of fuel requirement is, therefore,

$$w_f(\text{lb/hr}) \approx 0.56(190.3) = 106.6 \text{ lb/hr.}$$

The volumetric fuel requirement is

$$q_f(\text{gallons/hr}) \approx \frac{106.6}{6.9} = 15.4 \text{ gallons/hr.}$$

- Operating at 6000 ft, the atmospheric pressure at an elevation of 6000 is about 11.8 psia (Lyons et al., 2001). Fig. 11.9 shows a power reduction of 22%.

$$r_s = \sqrt[3]{\frac{150 + 11.8}{11.8}} = 2.39$$

$$e_v = 0.96 \left\{ 1 - 0.06 \left[ (2.39)^{0.714} - 1 \right] \right\} = 0.9013$$

$$HP_t = (3) \frac{11.8(900)}{229.2} \left( \frac{1.4}{0.4} \right) \left[ \left( \frac{161.8}{11.8} \right)^{0.0952} - 2 \right] = 137.7 \text{ hp}$$

$$HP_r = \frac{137.7}{e_m e_v} = \frac{137.7}{0.90(0.9103)} = 168.1 \text{ hp}$$

$$HP_m = 300(1 - 0.22) = 234 \text{ hp} > 168.1 \text{ hp, so okay.}$$

$$PR = \frac{161.8}{234} = 0.718 \text{ or } 71.8\%$$

Fig. 11.7 shows that a fuel usage of 0.54 lb/hp-hr at 71.8% power ratio. Thus,

$$w_f(\text{lbs/hr}) \approx 0.54(168.1) = 90.8 \text{ lbs/hr}$$

$$q_f(\text{gallons/hr}) \approx \frac{90.8}{6.9} = 13.2 \text{ gallons/hr}$$

### 11.3.3 CENTRIFUGAL COMPRESSORS

Although the adiabatic compression process can be assumed in centrifugal compression, polytropic compression process is commonly considered as the basis for comparing centrifugal compressor performance. The process is expressed as

$$pV^n = \text{constan}, \quad (11.66)$$

where  $n$  denotes the polytropic exponent. The isentropic exponent  $k$  applies to the ideal frictionless adiabatic process, while the polytropic exponent  $n$  applies to the actual process with heat transfer and friction. The  $n$  is related to  $k$  through polytropic efficiency  $E_p$ :

$$\frac{n-1}{n} = \frac{k-1}{k} \times \frac{1}{E_p}. \quad (11.67)$$

The polytropic efficiency of centrifugal compressors is nearly proportional to the logarithm of gas flow rate in the range of efficiency between 0.7 and 0.75. The polytropic efficiency chart presented by Rollins (1973) can be represented by the following correlation:

$$E_p = 0.61 + 0.03 \log(q_1), \quad (11.68)$$

where

$q_1$  = gas capacity at the inlet condition, cfm.

There is a lower limit of gas flow rate, below which severe gas surge occurs in the compressor. This limit is called “surge limit.” The upper limit of gas flow rate is called “stone-wall limit,” which is controlled by compressor horsepower.

The procedure of preliminary calculations for selection of centrifugal compressors is summarized as follows:

1. Calculate compression ratio based on the inlet and discharge pressures:

$$r = \frac{p_2}{p_1} \quad (11.69)$$

2. Based on the required gas flow rate under standard condition ( $q$ ), estimate the gas capacity at inlet condition ( $q_1$ ) by ideal gas law:

$$q_1 = \frac{p_b T_1}{p_1 T_b} q \quad (11.70)$$

3. Find a value for the polytropic efficiency  $E_p$  from the manufacturer's manual based on  $q_1$ .  
4. Calculate polytropic ratio  $(n-1)/n$  using Eq. (11.67):

$$R_p = \frac{n-1}{n} = \frac{k-1}{k} \times \frac{1}{E_p} \quad (11.71)$$

5. Calculate discharge temperature by

$$T_2 = T_1 r^{R_p}. \quad (11.72)$$

6. Estimate gas compressibility factor values at inlet and discharge conditions.

7. Calculate gas capacity at the inlet condition ( $q_1$ ) by real gas law:

$$q_1 = \frac{z_1 p_b T_1}{z_2 p_1 T_b} q \quad (11.73)$$

8. Repeat Steps 2–7 until the value of  $q_1$  converges within an acceptable deviation.  
9. Calculate gas horsepower by

$$Hp_g = \frac{q_1 p_1}{229 E_p} \left( \frac{z_1 + z_2}{2 z_1} \right) \left( \frac{r^{R_p} - 1}{R_p} \right), \quad (11.74)$$

Some manufacturers present compressor specifications using polytropic head in  $\text{lb}_f\text{-ft}/\text{lb}_m$  defined as

$$H_g = RT_1 \left( \frac{z_1 + z_2}{2} \right) \left( \frac{r^{R_p} - 1}{R_p} \right), \quad (11.75)$$

where  $R$  is the gas constant given by  $1544/MW_a$  in  $\text{psia}\text{-ft}^3/\text{lb}_m\text{-}^\circ\text{R}$ . The polytropic head relates to the gas horsepower by

$$Hp_g = \frac{m_t H_g}{33,000 E_p}, \quad (11.76)$$

where  $m_t$  is mass flow rate in  $\text{lb}_m/\text{min}$ .

10. Calculate gas horsepower by:

$$Hp_b = Hp_g + \Delta Hp_m, \quad (11.77)$$

where  $\Delta Hp_m$  is mechanical power losses, which is usually taken as 20 horsepower for bearing and 30 horsepower for seals.

The proceeding equations have been coded in the spreadsheet *CentrifugalCompressorPower.xls* for quick calculations.

**Example Problem 11.3** Size a centrifugal compressor for the following given data:

Gas-specific gravity:	0.68
Gas-specific heat ratio:	1.24
Gas flow rate:	144 MMscfd at 14.7 psia and 60°F
Inlet pressure:	250 psia
Inlet temperature:	100°F
Discharge pressure:	600 psia
Polytropic efficiency:	$E_p = 0.61 + 0.03 \log(q_1)$

**Solution** Calculate compression ratio based on the inlet and discharge pressures:

$$r = \frac{600}{250} = 2.4$$

Calculate gas flow rate in scfm:

$$q = \frac{144,000,000}{(24)(60)} = 100,000 \text{ scfm}$$

Based on the required gas flow rate under standard condition ( $q$ ), estimate the gas capacity at inlet condition ( $q_1$ ) by ideal gas law:

$$q_1 = \frac{(14.7)(560)}{(250)(520)}(100,000) = 6332 \text{ cfm}$$

Find a value for the polytropic efficiency based on  $q_1$ :

$$E_p = 0.61 + 0.031 \log(6332) = 0.724$$

Calculate polytropic ratio  $(n-1)/n$ :

$$R_p = \frac{n-1}{n} = \frac{1.24-1}{1.24} \times \frac{1}{0.724} = 0.2673$$

Calculate discharge temperature:

$$T_2 = (560)(2.4)^{0.2673} = 707.7^\circ\text{R} = 247.7^\circ\text{F}$$

Estimate gas compressibility factor values at inlet and discharge conditions (spreadsheet program *Hall-Yaborough-z.xls* can be used):

$$z_1 = 0.97 \text{ at } 250 \text{ psia and } 100^\circ\text{F}$$

$$z_2 = 0.77 \text{ at } 600 \text{ psia and } 247.7^\circ\text{F}$$

Calculate gas capacity at the inlet condition ( $q_1$ ) by real gas law:

$$q_1 = \frac{(0.97)(14.7)(560)}{(0.77)(250)(520)}(100,000) = 7977 \text{ cfm}$$

Use the new value of  $q_1$  to calculate  $E_p$ :

$$E_p = 0.61 + 0.03 \log(7977) = 0.727$$



Calculate the new polytropic ratio  $(n-1)/n$ :

$$R_p = \frac{n-1}{n} = \frac{1.24-1}{1.24} \times \frac{1}{0.727} = 0.2662$$

Calculate the new discharge temperature:

$$T_2 = (560) (2.4)^{0.2662} = 707^\circ\text{R} = 247^\circ\text{F}$$

Estimate the new gas compressibility factor value:

$$z_2 = 0.77 \text{ at } 600 \text{ psia and } 247^\circ\text{F}$$

Because  $z_2$  did not change,  $q_1$  remains the same value of 7977 cfm.

Calculate gas horsepower:

$$\begin{aligned} Hp_g &= \frac{(7977)(250)}{(229)(0.727)} \left( \frac{0.97+0.77}{2(0.97)} \right) \left( \frac{2.4^{0.2662}-1}{0.2662} \right) \\ &= 10,592 \text{ hp} \end{aligned}$$

Calculate gas apparent molecular weight:

$$MW_a = (0.68)(29) = 19.72$$

Calculated gas constant:

$$R = \frac{1544}{19.72} = 78.3 \text{ psia} \cdot \text{ft}^3/\text{lb}_m \cdot ^\circ\text{R}$$

Calculate polytropic head:

$$\begin{aligned} H_g &= (78.3)(560) \left( \frac{0.97+0.77}{2} \right) \left( \frac{2.4^{0.2662}-1}{0.2662} \right) \\ &= 37,610 \text{ lb}_f \cdot \text{ft}/\text{lb}_m \end{aligned}$$

Calculate gas horsepower requirement:

$$Hp_b = 10,592 + 50 = 10,642 \text{ hp.}$$

## 11.4 PIPELINES

Transporting petroleum fluids with pipelines is a continuous and reliable operation. Pipelines have demonstrated an ability to adapt to a wide variety of environments including remote areas and hostile environments. With very minor exceptions, largely due to local peculiarities, most refineries are served by one or more pipelines, because of their superior flexibility to the alternatives.

Pipelines can be divided into different categories, including the following:

- Flowlines transporting oil and/or gas from satellite wells to manifolds
- Flowlines transporting oil and/or gas from manifolds to production facility
- Infield flowlines transporting oil and/or gas from between production facilities
- Export pipelines transporting oil and/or gas from production facilities to refineries/users

The pipelines are sized to handle the expected pressure and fluid flow on the basis of flow assurance analysis. This section covers the following topics:

1. Flow in oil and gas pipelines
2. Design of pipelines
3. Operation of pipelines.

### 11.4.1 FLOW IN PIPELINES

Designing a long-distance pipeline for transportation of crude oil and natural gas requires knowledge of flow formulas for calculating capacity and pressure requirements. Based on the first law of thermal dynamics, the total pressure gradient is made up of three distinct components:

$$\frac{dP}{dL} = \frac{g}{g_c} \rho \sin \theta + \frac{f_M \rho u^2}{2g_c D} + \frac{\rho u du}{g_c dL} \quad (11.78)$$

where

$\frac{g}{g_c} \rho \sin \theta$  = pressure gradient due to elevation or potential energy change

$\frac{f_M \rho u^2}{2g_c D}$  = pressure gradient due to frictional losses

$\frac{\rho u du}{g_c dL}$  = pressure gradient due to acceleration or kinetic energy change

$P$  = pressure, lbf/ft<sup>2</sup>

$L$  = pipe length, ft

$g$  = gravitational acceleration, ft/sec<sup>2</sup>

$g_c = 32.17$ , ft-lbm/lbf-sec<sup>2</sup>

$\rho$  = density lbm/ft<sup>3</sup>

$\theta$  = dip angle from horizontal direction, °

$f_M$  = Darcy–Wiesbach (Moody) friction factor

$u$  = flow velocity, ft/sec

$D$  = pipe inner diameter, ft

The elevation component is pipe-angle dependent. It is zero for horizontal flow. The friction loss component applies to any type of flow at any pipe angle and causes a pressure drop in the direction of flow. The acceleration component causes a pressure drop in the direction of velocity increase in any flow condition in which velocity changes occurs. It is zero for constant-area, incompressible flow. This term is normally negligible for both oil and gas pipelines.

The friction factor  $f_M$  in Eq. (11.78) can be determined based on flow regimes, that is, laminar flow or turbulent flow. Reynolds number ( $N_{Re}$ ) is used as a parameter to distinguish between laminar and turbulent fluid flow. Reynolds number is defined as the ratio of fluid momentum force to viscous shear force. The Reynolds number can be expressed as a dimensionless group defined as

$$N_{Re} = \frac{Du\rho}{\mu}, \quad (11.79)$$

where

- $D$  = pipe ID, ft
- $u$  = fluid velocity, f/sec
- $\rho$  = fluid density, lb<sub>m</sub>/ft<sup>3</sup>
- $\mu$  = fluid viscosity, lb<sub>m</sub>/ft-sec.

The change from laminar to turbulent flow is usually assumed to occur at a Reynolds number of 2100 for flow in a circular pipe. If U.S. field units of ft for diameter, ft/sec for velocity, lb<sub>m</sub>/ft<sup>3</sup> for density and centipoises for viscosity are used, the Reynolds number equation becomes

$$N_{Re} = 1488 \frac{Du\rho}{\mu}. \quad (11.80)$$

For a gas with specific gravity  $\gamma_g$  and viscosity  $\mu_g$  (cp) flowing in a pipe with an inner diameter  $D$  (in.) at flow rate  $q$  (Mcf/d) measured at base conditions of  $T_b$  (°R) and  $p_b$  (psia), the Reynolds number can be expressed as

$$N_{Re} = \frac{711p_b q \gamma_g}{T_b D \mu_g}. \quad (11.81)$$

The Reynolds number usually takes values greater than 10,000 in gas pipelines. As  $T_b$  is 520°R and  $p_b$  varies only from 14.4 to 15.025 psia in the United States, the value of  $711p_b/T_b$  varies between 19.69 and 20.54. For all practical purposes, the Reynolds number for natural gas flow problems may be expressed as

$$N_{Re} = \frac{20q\gamma_g}{\mu_g d}, \quad (11.82)$$

where

- $q$  = gas flow rate at 60°F and 14.73 psia, Mcfd
- $\gamma_g$  = gas-specific gravity (air = 1)
- $\mu_g$  = gas viscosity at in-situ temperature and pressure, cp
- $d$  = pipe diameter, in.

The coefficient 20 becomes 0.48 if  $q$  is in scfh.

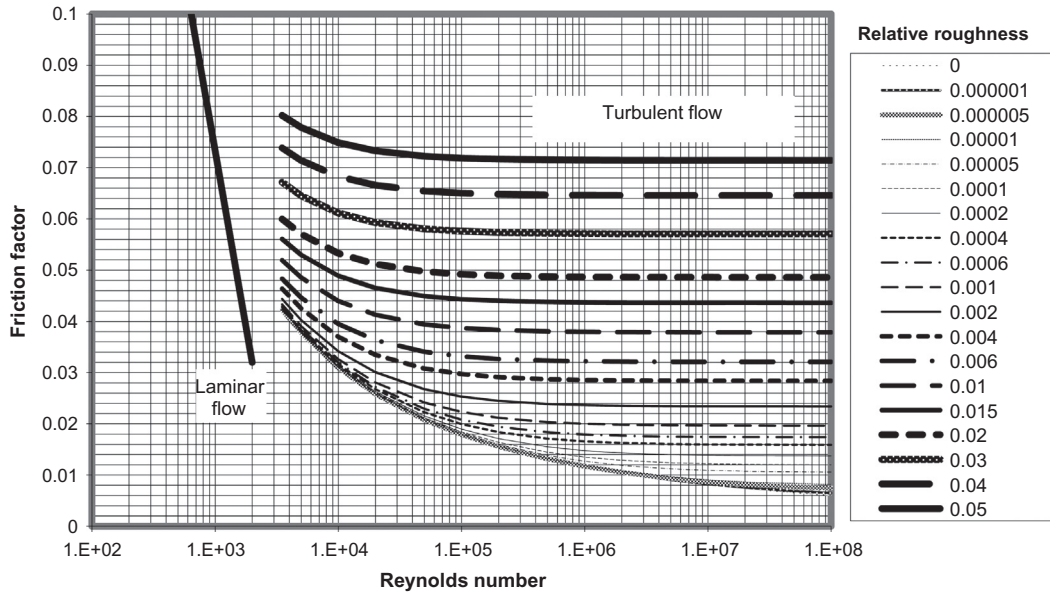
Fig. 11.10 is a friction factor chart covering the full range of flow conditions. It is a log-log graph of  $(\log f_M)$  versus  $(\log N_{Re})$ . Because of the complex nature of the curves, the equation for the friction factor in terms of the Reynolds number and relative roughness varies in different regions.

In the laminar flow region, the friction factor can be determined analytically. The Hagen–Poiseuille equation for laminar flow is

$$\left(\frac{dp}{dL}\right)_f = \frac{32\mu u}{g_c D^2}. \quad (11.83)$$

Equating the frictional pressure gradients given by Eqs. (11.78) and (11.83) gives

$$\frac{f_M \rho u^2}{2g_c D} = \frac{32\mu u}{g_c D^2}, \quad (11.84)$$


**FIGURE 11.10**

Darcy-Wiesbach friction factor chart (Moody, 1944).

which yields

$$f_M = \frac{64\mu}{du\rho} = \frac{64}{N_{Re}}. \quad (11.85)$$

In the turbulent flow region, a number of empirical correlations for friction factors are available. Only the most accurate ones are presented in this section.

For smooth wall pipes in the turbulent flow region, Drew et al. (1930) presented the most commonly used correlation:

$$f_M = 0.0056 + \frac{0.5}{N_{Re}^{0.32}}, \quad (11.86)$$

which is valid over a wide range of Reynolds numbers,  $3 \times 10^3 < N_{Re} < 3 \times 10^6$ .

For rough wall pipes in the turbulent flow region, the effect of wall roughness on friction factor depends on the relative roughness and Reynolds number. The Nikuradse (1933) friction factor correlation is still the best one available for fully developed turbulent flow in rough pipes:

$$\frac{1}{\sqrt{f_M}} = 1.74 - 2 \log(2e_D) \quad (11.87)$$

This equation is valid for large values of the Reynolds number where the effect of relative roughness is dominant. The correlation that is used as the basis for modern friction factor charts was proposed by Colebrook (1983):

$$\frac{1}{\sqrt{f_M}} = 1.74 - 2 \log \left( 2e_D + \frac{18.7}{N_{Re}\sqrt{f_M}} \right), \quad (11.88)$$

which is applicable to smooth pipes and to flow in transition and fully rough zones of turbulent flow. It degenerates to the Nikuradse correlation at large values of the Reynolds number. Eq. (11.88) is not explicit in  $f_M$ . However, values of  $f_M$  can be obtained by a numerical procedure such as Newton–Raphson iteration. An explicit correlation for friction factor was presented by Jain (1976):

$$\frac{1}{\sqrt{f_M}} = 1.14 - 2 \log \left( e_D + \frac{21.25}{N_{\text{Re}}^{0.9}} \right). \quad (11.89)$$

This correlation is comparable to the Colebrook correlation. For relative roughness between  $10^{-6}$  and  $10^{-2}$  and the Reynolds number between  $5 \times 10^3$  and  $10^8$ , the errors were reported to be within +1% when compared with the Colebrook correlation. Therefore, Eq. (11.89) is recommended for all calculations requiring friction factor determination of turbulent flow.

The wall roughness is a function of pipe material, method of manufacturing, and the environment to which it has been exposed. From a microscopic sense, wall roughness is not uniform, and thus, the distance from the peaks to valleys on the wall surface will vary greatly. The absolute roughness,  $\varepsilon$ , of a pipe wall is defined as the mean protruding height of relatively uniformly distributed and sized, tightly packed sand grains that would give the same pressure gradient behavior as the actual pipe wall. Analysis has suggested that the effect of roughness is not due to its absolute dimensions, but to its dimensions relative to the inside diameter of the pipe. Relative roughness,  $e_D$ , is defined as the ratio of the absolute roughness to the pipe internal diameter:

$$e_D = \frac{\varepsilon}{D}, \quad (11.90)$$

where  $\varepsilon$  and  $D$  have the same unit.

The absolute roughness is not a directly measurable property for a pipe, which makes the selection of value of pipe wall roughness difficult. The way to evaluate the absolute roughness is to compare the pressure gradients obtained from the pipe of interest with a pipe that is sand roughened. If measured pressure gradients are available, the friction factor and Reynolds number can be calculated and an effective  $e_D$  obtained from the Moody diagram. This value of  $e_D$  should then be used for future predictions until updated. If no information is available on roughness, a value of  $\varepsilon = 0.0006$  in. is recommended for tubing and line pipes.

#### 11.4.1.1 Oil flow

This section addresses flow of crude oil in pipelines. Flow of multiphase fluids is discussed in other literatures such as that of Guo et al. (2005).

Crude oil can be treated as an incompressible fluid. The relation between flow velocity and driving pressure differential for a given pipeline geometry and fluid properties is readily obtained by integration of Eq. (11.78) when the kinetic energy term is neglected:

$$P_1 - P_2 = \left( \frac{g}{g_c} \rho \sin \theta + \frac{f_M \rho u^2}{2g_c D} \right) L, \quad (11.91)$$

which can be written in flow rate as

$$P_1 - P_2 = \left( \frac{g}{g_c} \rho \sin \theta + \frac{f_M \rho q^2}{2g_c D A^2} \right) L, \quad (11.92)$$

where

$q$  = liquid flow rate, ft<sup>3</sup>/sec

$A$  = inner cross-sectional area, ft<sup>2</sup>

When changed to U.S. field units, Eq. (11.92) becomes

$$p_1 - p_2 = 0.433\gamma_o L \sin \theta + 1.15 \times 10^{-5} \times \frac{f_M \gamma_o Q^2 L}{d^5}, \quad (11.93)$$

where

$p_1$  = inlet pressure, psi

$p_2$  = outlet pressure, psi

$\gamma_o$  = oil-specific gravity, water = 1.0

$Q$  = oil flow rate, bbl/day

$d$  = pipe inner diameter, in.

**Example Problem 11.4** A 35 API gravity, 5 cp, oil is transported through a 6-in. (I.D.) pipeline with an uphill angle of 15° across a distance of 5 miles at a flow rate of 5000 bbl/day. Estimate the minimum required pump pressure to deliver oil at 50 psi pressure at the outlet. Assume  $e = 0.0006$  in.

**Solution**

Pipe inner area:

$$A = \frac{\pi}{4} \left( \frac{6}{12} \right)^2 = 0.1963 \text{ ft}^2$$

The average oil velocity in pipe:

$$u = \frac{(5000)(5.615)}{(24)(60)(0.1963)} = 1.66 \text{ ft/sec}$$

Oil-specific gravity:

$$\gamma_o = \frac{141.5}{131.5 + 35} = 0.85$$

Reynolds number:

$$N_{Re} = 1488 \frac{\left( \frac{6}{12} \right) (1.66) (0.85) (62.4)}{5} = 13,101 > 2100 \text{ turbulent flow}$$

Eq. (11.89) gives

$$\frac{1}{\sqrt{f_M}} = 1.14 - 2 \log \left( \left( \frac{0.0006}{6} \right) + \frac{21.25}{(13,101)^{0.9}} \right) = 5.8759,$$

which gives

$$f_M = 0.02896.$$

Eq. (11.93) gives

$$p_1 = 50 + 0.433(0.85)(5)(5280) \sin(15^\circ) + 1.15 \times 10^{-5} \times \frac{(0.02896)(0.85)(5000)^2(5)(5280)}{(6)^2}$$

$$= 2590 \text{ psi.}$$

### 11.4.1.2 Gas flow

Consider steady-state flow of dry gas in a constant-diameter, horizontal pipeline. The mechanical energy equation, Eq. (11.78), becomes

$$\frac{dp}{dL} = \frac{f_M \rho u^2}{2g_c D} = \frac{p(MW)_a}{zRT} \frac{f u^2}{2g_c D}, \quad (11.94)$$

which serves as a base for development of many pipeline equations. The difference in these equations originated from the methods used in handling the  $z$ -factor and friction factor. Integrating Eq. (11.94) gives

$$\int dp = \frac{(MW)_a f_M u^2}{2Rg_c D} \int \frac{p}{zT} dL. \quad (11.95)$$

If temperature is assumed constant at average value in a pipeline,  $\bar{T}$ , and gas deviation factor,  $\bar{z}$ , is evaluated at average temperature and average pressure,  $\bar{p}$ , Eq. (11.95) can be evaluated over a distance  $L$  between upstream pressure,  $p_1$ , and downstream pressure,  $p_2$ :

$$p_1^2 - p_2^2 = \frac{25\gamma_g Q^2 \bar{T} \bar{z} f_M L}{d^5}, \quad (11.96)$$

where

- $\gamma_g$  = gas gravity (air = 1)
- $Q$  = gas flow rate, MMscfd (at 14.7 psia, 60°F)
- $\bar{T}$  = average temperature, °R
- $\bar{z}$  = gas deviation factor at  $\bar{T}$  and  $\bar{p}$
- $\bar{p} = (p_1 + p_2)/2$
- $L$  = pipe length, ft
- $d$  = pipe internal diameter, in.
- $F$  = Moody friction factor

Eq. (11.96) may be written in terms of flow rate measured at arbitrary base conditions ( $T_b$  and  $p_b$ ):

$$q = \frac{CT_b}{p_b} \sqrt{\frac{(p_1^2 - p_2^2)d^5}{\gamma_g \bar{T} \bar{z} f_M L}}, \quad (11.97)$$

where  $C$  is a constant with a numerical value that depends on the units used in the pipeline equation. If  $L$  is in miles and  $q$  is in scfd,  $C = 77.54$ .

The use of Eq. (11.97) involves an iterative procedure. The gas deviation factor depends on pressure and the friction factor depends on flow rate. This problem prompted several investigators to develop pipeline flow equations that are noniterative or explicit. This has involved substitutions

for the friction factor  $f_M$ . The specific substitution used may be diameter-dependent only (Weymouth equation) or Reynolds number–dependent only (Panhandle equations).

#### 11.4.1.2.1 Weymouth equation for horizontal flow

Eq. (11.97) takes the following form when the unit of scfh for gas flow rate is used:

$$q_h = \frac{3.23T_b}{p_b} \sqrt{\frac{1}{f_M}} \sqrt{\frac{(p_1^2 - p_2^2)d^5}{\gamma_g \bar{T} z L}}, \quad (11.98)$$

where  $\sqrt{\frac{1}{f_M}}$  is called the “transmission factor.” The friction factor may be a function of flow rate and pipe roughness. If flow conditions are in the fully turbulent region, Eq. (11.89) degenerates to

$$f_M = \frac{1}{[1.14 - 2 \log(e_D)]^2}, \quad (11.99)$$

where  $f_M$  depends only on the relative roughness,  $e_D$ . When flow conditions are not completely turbulent,  $f_M$  depends on the Reynolds number also.

Therefore, use of Eq. (11.98) requires a trial-and-error procedure to calculate  $q_h$ . To eliminate the trial-and-error procedure, Weymouth proposed that  $f$  vary as a function of diameter as follows:

$$f_M = \frac{0.032}{d^{1/3}} \quad (11.100)$$

With this simplification, Eq. (11.98) reduces to

$$q_h = \frac{18.062T_b}{p_b} \sqrt{\frac{(p_1^2 - p_2^2)D^{16/3}}{\gamma_g \bar{T} z L}}, \quad (11.101)$$

which is the form of the Weymouth equation commonly used in the natural gas industry.

The use of the Weymouth equation for an existing transmission line or for the design of a new transmission line involves a few assumptions including no mechanical work, steady-flow, isothermal flow, constant compressibility factor, horizontal flow, and no kinetic energy change. These assumptions can affect accuracy of calculation results.

In the study of an existing pipeline, the pressure-measuring stations should be placed so that no mechanical energy is added to the system between stations. No mechanical work is done on the fluid between the points at which the pressures are measured. Thus, the condition of no mechanical work can be fulfilled.

Steady flow in pipeline operation seldom, if ever, exists in actual practice because pulsations, liquid in the pipeline, and variations in input or output gas volumes cause deviations from steady-state conditions. Deviations from steady-state flow are the major cause of difficulties experienced in pipeline flow studies.

The heat of compression is usually dissipated into the ground along a pipeline within a few miles downstream from the compressor station. Otherwise, the temperature of the gas is very near that of the containing pipe, and because pipelines usually are buried, the temperature of the flowing gas is not influenced appreciably by rapid changes in atmospheric temperature. Therefore, the gas flow can be considered isothermal at an average effective temperature without causing significant error in long-pipeline calculations.



The compressibility of the fluid can be considered constant and an average effective gas deviation factor may be used. When the two pressures  $p_1$  and  $p_2$  lie in a region where  $z$  is essentially linear with pressure, it is accurate enough to evaluate  $\bar{z}$  at the average pressure  $\bar{p} = (p_1 + p_2)/2$ . One can also use the arithmetic average of the  $z$ 's with  $\bar{z} = (z_1 + z_2)/2$ , where  $z_1$  and  $z_2$  are obtained at  $p_1$  and  $p_2$ , respectively. On the other hand, should  $p_1$  and  $p_2$  lie in the range where  $z$  is not linear with pressure (double-hatched lines), the proper average would result from determining the area under the  $z$ -curve and dividing it by the difference in pressure:

$$\bar{z} = \frac{\int_{p_1}^{p_2} z dp}{(p_1 - p_2)}, \quad (11.102)$$

where the numerator can be evaluated numerically. Also,  $\bar{z}$  can be evaluated at an average pressure given by

$$\bar{p} = \frac{2}{3} \left( \frac{p_1^3 - p_2^3}{p_1^2 - p_2^2} \right). \quad (11.103)$$

Regarding the assumption of horizontal pipeline, in actual practice, transmission lines seldom, if ever, are horizontal, so that factors are needed in Eq. (11.101) to compensate for changes in elevation. With the trend to higher operating pressures in transmission lines, the need for these factors is greater than is generally realized. This issue of correction for change in elevation is addressed in the next section.

If the pipeline is long enough, the changes in the kinetic energy term can be neglected. The assumption is justified for work with commercial transmission lines.

**Example Problem 11.5** For the following data given for a horizontal pipeline, predict gas flow rate in ft<sup>3</sup>/hr through the pipeline. Solve the problem using Eq. (11.101) with the trial-and-error method for friction factor and the Weymouth equation without the Reynolds number–dependent friction factor:

$$\begin{aligned} d &= 12.09 \text{ in.} \\ L &= 200 \text{ mi} \\ e &= 0.0006 \text{ in.} \\ T &= 80^\circ\text{F} \\ \gamma_g &= 0.70 \\ T_b &= 520^\circ\text{R} \\ p_b &= 14.7 \text{ psia} \\ p_1 &= 600 \text{ psia} \\ p_2 &= 200 \text{ psia} \end{aligned}$$

**Solution** The average pressure is

$$\bar{p} = (200 + 600)/2 = 400 \text{ psia.}$$

With  $\bar{p} = 400$  psia,  $T = 540^\circ\text{R}$  and  $\gamma_g = 0.70$ , *Brill-Beggs-Z.xls* gives

$$\bar{z} = 0.9188.$$

With  $\bar{p}$  400 psia,  $T = 540$  °R and  $\gamma_g = 0.70$ , *Carr-Kobayashi-BurrowsViscosity.xls* gives

$$\mu = 0.0099 \text{ cp.}$$

Relative roughness:

$$e_D = 0.0006/12.09 = 0.00005$$

**A.** Trial-and-error calculation:

First trial:

$$q_h = 500,000 \text{ scfh}$$

$$N_{\text{Re}} = \frac{0.48(500,000)(0.7)}{(0.0099)(12.09)} = 1,403,733$$

$$\frac{1}{\sqrt{f_M}} = 1.14 - 2 \log \left( 0.00005 + \frac{21.25}{(1,403,733)^{0.9}} \right)$$

$$f_M = 0.01223$$

$$q_h = \frac{3.23(520)}{14.7} \sqrt{\frac{1}{0.01223}} \sqrt{\frac{(600^2 - 200^2)(12.09)^5}{(0.7)(540)(0.9188)(200)}}$$

$$= 1,148,450 \text{ scfh}$$

Second trial:

$$q_h = 1,148,450 \text{ cfh}$$

$$N_{\text{Re}} = \frac{0.48(1,148,450)(0.7)}{(0.0099)(12.09)} = 3,224,234$$

$$\frac{1}{\sqrt{f_M}} = 1.14 - 2 \log \left( 0.00005 + \frac{21.25}{(3,224,234)^{0.9}} \right)$$

$$f_M = 0.01145$$

$$q_h = \frac{3.23(520)}{14.7} \sqrt{\frac{1}{0.01145}} \sqrt{\frac{(600^2 - 200^2)(12.09)^5}{(0.7)(540)(0.9188)(200)}}$$

$$= 1,186,759 \text{ scfh}$$

Third trial:

$$q_h = 1,186,759 \text{ scfh}$$

$$N_{\text{Re}} = \frac{0.48(1,186,759)(0.7)}{(0.0099)(12.09)} = 3,331,786$$

$$\frac{1}{\sqrt{f_M}} = 1.14 - 2 \log \left( 0.00005 + \frac{21.25}{(3,331,786)^{0.9}} \right)$$

$$f_M = 0.01143$$

$$q_h = \frac{3.23(520)}{14.7} \sqrt{\frac{1}{0.01143}} \sqrt{\frac{(600^2 - 200^2)(12.09)^5}{(0.7)(540)(0.9188)(200)}}$$

$$= 1,187,962 \text{ scfh}$$

which is close to the assumed 1,186,759 scfh.

**B.** Using the Weymouth equation:

$$q_h = \frac{18.062(520)}{14.7} \sqrt{\frac{(600^2 - 200^2)(12.09)^{16/3}}{(0.7)(540)(0.9188)(200)}}$$

$$= 1,076,035 \text{ scfh}$$

Problems similar to this one can be quickly solved with the spreadsheet program *PipeCapacity.xls*.

#### 11.4.1.2.2 Weymouth equation for nonhorizontal flow

Gas transmission pipelines are often nonhorizontal. Account should be taken of substantial pipeline elevation changes. Considering gas flow from point 1 to point 2 in a nonhorizontal pipe, the first law of thermal dynamics gives

$$\int_1^2 w dP + \frac{g}{g_c} \Delta Z + \int_1^2 \frac{f_M u^2}{2g_c D} dL = 0. \quad (11.104)$$

Based on the pressure gradient due to the weight of gas column,

$$\frac{dP}{dz} = \frac{\rho_g}{144}, \quad (11.105)$$

and real gas law,  $\rho_g = \frac{p(MW)_a}{zRT} = \frac{29\gamma_g p}{zRT}$ , **Weymouth (1912)** developed the following equation:

$$q_h = \frac{3.23T_b}{p_b} \sqrt{\frac{(p_1^2 - e^s p_2^2) d^5}{f_M \gamma_g \bar{T} \bar{z} L}}, \quad (11.106)$$

where

$$e = 2.718 \quad \text{and} \quad s = \frac{0.0375\gamma_g \Delta z}{\bar{T} \bar{z}}, \quad (11.107)$$

and  $\Delta z$  is equal to outlet elevation minus inlet elevation (note that  $\Delta z$  is positive when outlet is higher than inlet). A general and more rigorous form of the Weymouth equation with compensation for elevation is

$$q_h = \frac{3.23T_b}{p_b} \sqrt{\frac{(p_1^2 - e^s p_2^2) d^5}{f_M \gamma_g \bar{T} \bar{z} L_e}}, \quad (11.108)$$

where  $L_e$  is the effective length of the pipeline. For a uniform slope,  $L_e$  is defined as  $L_e = \frac{(e^s - 1)L}{s}$ .

For a nonuniform slope (where elevation change cannot be simplified to a single section of constant gradient), an approach in steps to any number of sections,  $n$ , will yield

$$L_e = \frac{(e^{S_1} - 1)}{S_1} L_1 + \frac{e^{S_1}(e^{S_2} - 1)}{S_2} L_2 + \frac{e^{S_1+S_2}(e^{S_3} - 1)}{S_3} L_3 + \dots + \sum_{i=1}^n \frac{\sum_{j=1}^{i-1} S_j}{S_i} (e^{S_i} - 1) L_i, \quad (11.109)$$

where

$$s_i = \frac{0.0375 \gamma_g \Delta z_i}{\bar{T} \bar{z}}. \quad (11.110)$$

#### 11.4.1.2.3 Panhandle-A equation for horizontal flow

The Panhandle-A pipeline flow equation assumes the following Reynolds number–dependent friction factor:

$$f_M = \frac{0.085}{N_{\text{Re}}^{0.147}} \quad (11.111)$$

The resultant pipeline flow equation is, thus,

$$q = 435.87 \frac{d^{2.6182}}{\gamma_g^{0.4604}} \left( \frac{T_b}{p_b} \right)^{1.07881} \left[ \frac{(p_1^2 - p_2^2)}{\bar{T} \bar{z} L} \right]^{0.5394}, \quad (11.112)$$

where  $q$  is the gas flow rate in scfd measured at  $T_b$  and  $p_b$ , and other terms are the same as in the Weymouth equation.

#### 11.4.1.2.4 Panhandle-B equation for horizontal flow (modified Panhandle)

The Panhandle-B equation is the most widely used equation for long transmission and delivery lines. It assumes that  $f_M$  varies as

$$f_M = \frac{0.015}{N_{\text{Re}}^{0.0392}}, \quad (11.113)$$

and it takes the following resultant form:

$$q = 737 d^{2.530} \left( \frac{T_b}{p_b} \right)^{1.02} \left[ \frac{(p_1^2 - p_2^2)}{\bar{T} \bar{z} L \gamma_g^{0.961}} \right]^{0.510} \quad (11.114)$$

#### 11.4.1.2.5 Clinedinst equation for horizontal flow

The Clinedinst equation rigorously considers the deviation of natural gas from ideal gas through integration. It takes the following form:

$$q = 3973.0 \frac{z_b p_b p_{pc}}{p_b} \times \sqrt{\frac{d^5}{\bar{T} f_M L \gamma_g} \left( \int_0^{p_{r1}} \frac{p_r}{z} dp_r \int_0^{p_{r2}} \frac{p_r}{z} dp_r \right)}, \quad (11.115)$$

where

- $q$  = volumetric flow rate, Mcfd
- $p_{pc}$  = pseudocritical pressure, psia

$d$  = pipe internal diameter, in.

$L$  = pipe length, ft

$p_r$  = pseudo-reduced pressure

$\bar{T}$  = average flowing temperature, °R

$\gamma_g$  = gas gravity, air = 1.0

$z_b$  = gas deviation factor at  $T_b$  and  $p_b$ , normally accepted as 1.0.

Based on Eqs. (2.29), (2.30), and (2.51), Guo and Ghalambor (2005) generated curves of the integral function  $\int_0^{p_r} \frac{p_r}{z} dp_r$  for various gas-specific gravity values.

#### 11.4.1.2.6 Pipeline efficiency

All pipeline flow equations were developed for perfectly clean lines filled with gas. In actual pipelines, water, condensates, sometimes crude oil accumulates in low spots in the line. There are often scales and even “junk” left in the line. The net result is that the flow rates calculated for the 100% efficient cases are often modified by multiplying them by an efficiency factor  $E$ . The efficiency factor expresses the actual flow capacity as a fraction of the theoretical flow rate. An efficiency factor ranging from 0.85 to 0.95 would represent a “clean” line. Table 11.1 presents typical values of efficiency factors.

### 11.4.2 DESIGN OF PIPELINES

Pipeline design includes determination of material, diameter, wall thickness, insulation, and corrosion protection measure. For offshore pipelines, it also includes weight coating and trenching for stability control. Bai (2001) provides a detailed description on the analysis-based approach to designing offshore pipelines. Guo et al. (2005) presents a simplified approach to the pipeline design.

The diameter of pipeline should be determined based on flow capacity calculations presented in the previous section. This section focuses on the calculations to design wall thickness and insulation.

#### 11.4.2.1 Wall thickness design

Wall thickness design for steel pipelines is governed by U.S. Code ASME/ANSI B32.8. Other codes such as Z187 (Canada), DnV (Norway), and IP6 (UK) have essentially the same requirements but should be checked by the readers.

Except for large-diameter pipes (>30 in.), material grade is usually taken as X-60 or X-65 (414 or 448 MPa) for high-pressure pipelines or in deepwater. Higher grades can be selected in special

**Table 11.1 Typical Values of Pipeline Efficiency Factors**

Type of Line	Liquid Content (gal/MMcf)	Efficiency $E$
Dry-gas field	0.1	0.92
Casing-head gas	7.2	0.77
Gas and condensate	800	0.6

cases. Lower grades such as X-42, X-52, or X-56 can be selected in shallow water or for low-pressure, large-diameter pipelines to reduce material cost or in cases in which high ductility is required for improved impact resistance. Pipe types include:

- Seamless
- Submerged arc welded (SAW or DSAW)
- Electric resistance welded (ERW)
- Spiral weld

Except in specific cases, only seamless or SAW pipes are to be used, with seamless being the preference for diameters of 12 in. or less. If ERW pipe is used, special inspection provisions such as full-body ultrasonic testing are required. Spiral weld pipe is very unusual for oil/gas pipelines and should be used only for low-pressure water or outfall lines.

#### 11.4.2.1.1 Design procedure

Determination of pipeline wall thickness is based on the design internal pressure or the external hydrostatic pressure. Maximum longitudinal stresses and combined stresses are sometimes limited by applicable codes and must be checked for installation and operation. However, these criteria are not normally used for wall thickness determination. Increasing wall thickness can sometimes ensure hydrodynamic stability in lieu of other stabilization methods (such as weight coating). This is not normally economical, except in deepwater where the presence of concrete may interfere with the preferred installation method. We recommend the following procedure for designing pipeline wall thickness:

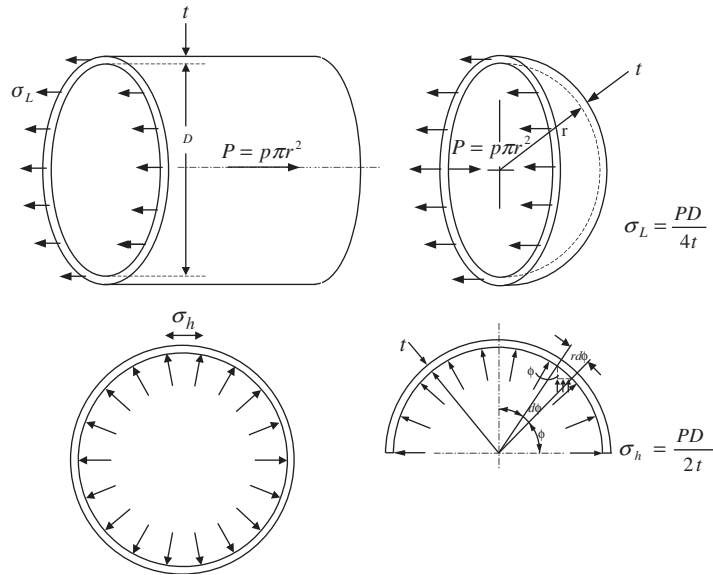
- Step 1: Calculate the minimum wall thickness required for the design internal pressure.
- Step 2: Calculate the minimum wall thickness required to withstand external pressure.
- Step 3: Add wall thickness allowance for corrosion if applicable to the maximum of the above.
- Step 4: Select next highest nominal wall thickness.
- Step 5: Check selected wall thickness for hydrotest condition.
- Step 6: Check for handling practice, that is, pipeline handling is difficult for  $D/t$  larger than 50; welding of wall thickness less than 0.3 in. (7.6 mm) requires special provisions.

Note that in certain cases, it may be desirable to order a nonstandard wall. This can be done for large orders.

Pipelines are sized on the basis of the maximum expected stresses in the pipeline under operating conditions. The stress calculation methods are different for thin-wall and thick-wall pipes. A thin-wall pipe is defined as a pipe with  $D/t$  greater than or equal to 20. Fig. 11.11 shows stresses in a thin-wall pipe. A pipe with  $D/t$  less than 20 is considered a thick-wall pipe. Fig. 11.12 illustrates stresses in a thick-wall pipe.

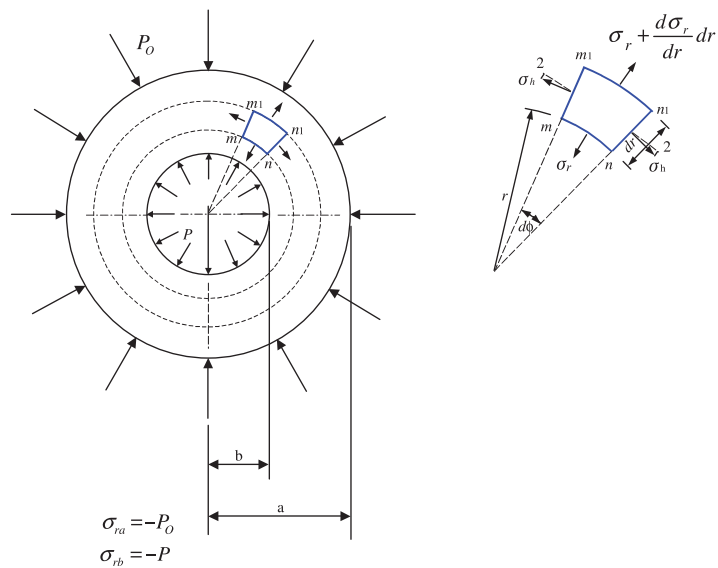
#### 11.4.2.1.2 Design for internal pressure

Three pipeline codes typically used for design are ASME B31.4 (ASME, 1989), ASME B31.8 (ASME, 1990), and DnV (1981). ASME B31.4 is for all oil lines in North America. ASME B31.8 is for all gas lines and two-phase flow pipelines in North America. DnV (1981) is for oil, gas, and two-phase flow pipelines in North Sea. All these codes can be used in other areas when no other code is available.



**FIGURE 11.11**

Stresses generated by internal pressure  $p$  in a thin-wall pipe,  $D/t > 20$ .



**FIGURE 11.12**

Stresses generated by internal pressure  $p$  in a thick-wall pipe,  $D/t < 20$ .

The nominal pipeline wall thickness ( $t_{NOM}$ ) can be calculated as follows:

$$t_{NOM} = \frac{P_d D}{2E_w \eta \sigma_y F_t} + t_a, \quad (11.116)$$

where  $P_d$  is the design internal pressure defined as the difference between the internal pressure ( $P_i$ ) and external pressure ( $P_e$ ),  $D$  is nominal outside diameter,  $t_a$  is thickness allowance for corrosion, and  $\sigma_y$  is the specified minimum yield strength. Eq. (11.116) is valid for any consistent units.

Most codes allow credit for external pressure. This credit should be used whenever possible, although care should be exercised for oil export lines to account for head of fluid and for lines that traverse from deep to shallow water.

ASME B31.4 and DnV (1981) define  $P_i$  as the maximum allowable operating pressure (MAOP) under normal conditions, indicating that surge pressures up to 110% MAOP is acceptable. In some cases,  $P_i$  is defined as wellhead shut-in pressure (WSIP) for flowlines or specified by the operators.

In Eq. (11.116), the weld efficiency factor ( $E_w$ ) is 1.0 for seamless, ERW, and DSAW pipes. The temperature de-rating factor ( $F_t$ ) is equal to 1.0 for temperatures under 250°F. The usage factor ( $\eta$ ) is defined in Tables 11.2 and 11.3 for oil and gas lines, respectively.

The under thickness due to manufacturing tolerance is taken into account in the design factor. There is no need to add any allowance for fabrication to the wall thickness calculated with Eq. (11.116).

**Table 11.2 Design and Hydrostatic Pressure Definitions and Usage Factors for Oil Lines**

Parameter	ASME B31.4, 1989 Edition	Dnv (Veritas, 1981)
Design internal pressure $P_d^a$	$P_i - P_e$ [401.2.2]	$P_i - P_e$ [4.2.2.2]
Usage factor $\eta$	0.72 [402.3.1(a)]	0.72 [4.2.2.1]
Hydrotest pressure $P_h$	1.25 $P_i^b$ [437.4.1(a)]	1.25 $P_d$ [8.8.4.3]

<sup>a</sup>Credit can be taken for external pressure for gathering lines or flowlines when the MAOP ( $P_i$ ) is applied at the wellhead or at the seabed. For export lines, when  $P_i$  is applied on a platform deck, the head fluid shall be added to  $P_i$  for the pipeline section on the seabed.

<sup>b</sup>If hoop stress exceeds 90% of yield stress based on nominal wall thickness, special care should be taken to prevent overstrain of the pipe.

**Table 11.3 Design and Hydrostatic Pressure Definitions and Usage Factors for Gas Lines**

Parameter	ASME B31.8, 1989 Edition, 1990 Addendum	DnV (Veritas, 1981)
$P_d^a$	$P_i - P_e$ [A842.221]	$P_i - P_e$ [4.2.2.2]
Usage factor $\eta$	0.72 [A842.221]	0.72 [4.2.2.1]
Hydrotest pressure $P_h$	1.25 $P_i^b$ [A847.2]	1.25 $P_d$ [8.8.4.3]

<sup>a</sup>Credit can be taken for external pressure for gathering lines or flowlines when the MAOP ( $P_i$ ) is applied at wellhead or at the seabed. For export lines, when  $P_i$  is applied on a platform deck, the head of fluid shall be added to  $P_i$  for the pipeline section on the seabed (particularly for two-phase flow).

<sup>b</sup>ASME B31.8 imposes  $P_h = 1.4 P_i$  for offshore risers but allows onshore testing of prefabricated portions.



## 11.4.2.1.3 Design for external pressure

Different practices can be found in the industry using different external pressure criteria. As a rule of thumb, or unless qualified thereafter, it is recommended to use propagation criterion for pipeline diameters under 16-in. and collapse criterion for pipeline diameters more than or equal to 16-in.

**Propagation criterion.** The propagation criterion is more conservative and should be used where optimization of the wall thickness is not required or for pipeline installation methods not compatible with the use of buckle arrestors such as reel and two methods. It is generally economical to design for propagation pressure for diameters less than 16-in. For greater diameters, the wall thickness penalty is too high. When a pipeline is designed based on the collapse criterion, buckle arrestors are recommended. The external pressure criterion should be based on nominal wall thickness, as the safety factors included below account for wall variations.

Although a large number of empirical relationships have been published, the recommended formula is the latest given by AGA.PRC (AGA, 1990):

$$P_p = 33S_y \left( \frac{t_{NOM}}{D} \right)^{2.46}, \quad (11.117)$$

which is valid for any consistent units. The nominal wall thickness should be determined such that  $P_p > 1.3 P_e$ . The safety factor of 1.3 is recommended to account for uncertainty in the envelope of data points used to derive Eq. (11.117). It can be rewritten as

$$t_{NOM} \geq D \left( \frac{1.3P_p}{33S_y} \right)^{\frac{1}{2.46}}. \quad (11.118)$$

For the reel barge method, the preferred pipeline grade is below X-60. However, X-65 steel can be used if the ductility is kept high by selecting the proper steel chemistry and microalloying. For deepwater pipelines,  $D/t$  ratios of less than 30 are recommended. It has been noted that bending loads have no demonstrated influence on the propagation pressure.

**Collapse criterion.** The mode of collapse is a function of  $D/t$  ratio, pipeline imperfections, and load conditions. The theoretical background is not given in this book. An empirical general formulation that applies to all situations is provided. It corresponds to the transition mode of collapse under external pressure ( $P_e$ ), axial tension ( $T_a$ ), and bending strain ( $\varepsilon_b$ ), as detailed elsewhere (Murphy and Langner, 1985; AGA, 1990).

The nominal wall thickness should be determined such that

$$\frac{1.3P_p}{P_C} + \frac{\varepsilon_b}{\varepsilon_B} \leq g_p, \quad (11.119)$$

where 1.3 is the recommended safety factor on collapse,  $B_B$  is the bending strain of buckling failure due to pure bending, and  $g$  is an imperfection parameter defined below.

The safety factor on collapse is calculated for  $D/t$  ratios along with the loads ( $P_e$ ,  $\varepsilon_b$ ,  $T_a$ ) and initial pipeline out-of-roundness ( $\delta_o$ ). The equations are

$$P_C = \frac{P_{el}P'_y}{\sqrt{P_{el}^2 + P'_y{}^2}}, \quad (11.120)$$

$$P'_y = P_y \left[ \sqrt{1 - 0.75 \left( \frac{T_a}{T_y} \right)^2} - \frac{T_a}{2T_y} \right], \quad (11.121)$$

$$P_{el} = \frac{2E}{1 - \nu^2} \left( \frac{t}{D} \right)^3, \quad (11.122)$$

$$P_y = 2S_y \left( \frac{t}{D} \right), \quad (11.123)$$

$$T_y = AS_y, \quad (11.124)$$

where  $g_p$  is based on pipeline imperfections such as initial out-of-roundness ( $\delta_o$ ), eccentricity (usually neglected), and residual stress (usually neglected). Hence,

$$g_p = \frac{\sqrt{1 + p^2}}{\sqrt{p^2 - \frac{1}{f_p^2}}}, \quad (11.125)$$

where

$$p = \frac{P'_y}{P_{el}}, \quad (11.126)$$

$$f_p = \sqrt{1 + \left( \delta_o \frac{D}{t} \right)^2} - \delta_o \frac{D}{t}, \quad (11.127)$$

$$\varepsilon_B = \frac{t}{2D}, \quad (11.128)$$

and

$$\delta_o = \frac{D_{\max} - D_{\min}}{D_{\max} + D_{\min}}. \quad (11.129)$$

When a pipeline is designed using the collapse criterion, a good knowledge of the loading conditions is required ( $T_a$  and  $\varepsilon_b$ ). An upper conservative limit is necessary and must often be estimated.

Under high bending loads, care should be taken in estimating  $\varepsilon_b$  using an appropriate moment-curvature relationship. A Ramberg Osgood relationship can be used as

$$K^* = M^* + AM^{*B}, \quad (11.130)$$

where  $K^* = K/K_y$  and  $M^* = M/M_y$ , with  $K_y = 2S_y/ED$  is the yield curvature and  $M_y = 2IS_y/D$  is the yield moment. The coefficients  $A$  and  $B$  are calculated from the two data points on stress-strain curve generated during a tensile test.

#### 11.4.2.1.4 Corrosion allowance

To account for corrosion when water is present in a fluid along with contaminants such as oxygen, hydrogen sulfide ( $H_2S$ ), and carbon dioxide ( $CO_2$ ), extra wall thickness is added. A review of standards, rules, and codes of practices (Hill and Warwick, 1986) shows that wall allowance is only one of several methods available to prevent corrosion, and it is often the least recommended.

For H<sub>2</sub>S and CO<sub>2</sub> contaminants, corrosion is often localized (pitting) and the rate of corrosion allowance ineffective. Corrosion allowance is made to account for damage during fabrication, transportation, and storage. A value of 1/16 in. may be appropriate. A thorough assessment of the internal corrosion mechanism and rate is necessary before any corrosion allowance is taken.

#### 11.4.2.1.5 Check for hydrotest condition

The minimum hydrotest pressure for oil and gas lines is given in Tables 11.2 and 11.3, respectively, and is equal to 1.25 times the design pressure for pipelines. Codes do not require that the pipeline be designed for hydrotest conditions but sometimes give a tensile hoop stress limit 90% SMYS, which is always satisfied if credit has not been taken for external pressure. For cases where the wall thickness is based on  $P_d = P_i - P_e$ , codes recommend not to overstrain the pipe. Some of the codes are ASME B31.4 (Clause 437.4.1), ASME B31.8 (no limit on hoop stress during hydrotest), and DnV (Clause 8.8.4.3).

For design purposes, condition  $\sigma_h \leq \sigma_y$  should be confirmed, and increasing wall thickness or reducing test pressure should be considered in other cases. For offshore pipelines connected to riser sections requiring  $P_h = 1.4P_i$ , it is recommended to consider testing the riser separately (for prefabricated sections) or to determine the hydrotest pressure based on the actual internal pressure experienced by the pipeline section. It is important to note that most pressure testing of subsea pipelines is done with water, but on occasion, nitrogen or air has been used. For low  $D/t$  ratios ( $<20$ ), the actual hoop stress in a pipeline tested from the surface is overestimated when using the thin wall equations provided in this chapter. Credit for this effect is allowed by DnV Clause 4.2.2.2 but is not normally taken into account.

**Example Problem 11.6** Calculate the required wall thickness for the pipeline in Example Problem 11.4 assuming a seamless still pipe of X-60 grade and onshore gas field (external pressure  $P_e = 14.65$  psia).

**Solution** The wall thickness can be designed based on the hoop stress generated by the internal pressure  $P_i = 2590$  psia. The design pressure is

$$P_d = P_i - P_e = 2590 - 14.65 = 2575.35 \text{ psi.}$$

The weld efficiency factor is  $E_w = 1.0$ . The temperature de-rating factor  $F_t = 1.0$ . Table 11.3 gives  $\eta = 0.72$ . The yield stress is  $\sigma_y = 60,000$  psi. A corrosion allowance 1/16 in. is considered. The nominal pipeline wall thickness can be calculated using Eq. (11.116) as

$$t_{NOM} = \frac{(2574.3)(6)}{2(1.0)(0.72)(60,000)(1.0)} + \frac{1}{16} = 0.2413 \text{ in.}$$

Considering that welding of wall thickness less than 0.3 in. requires special provisions, the minimum wall thickness is taken, 0.3 in.

#### 11.4.2.2 Insulation design

Oil and gas field pipelines are insulated mainly to conserve heat. The need to keep the product fluids in the pipeline at a temperature higher than the ambient temperature could exist, for reasons including the following:

- Preventing formation of gas hydrates
- Preventing formation of wax or asphaltenes

- Enhancing product flow properties
- Increasing cool-down time after shutting down

In liquefied gas pipelines, such as liquefied natural gas, insulation is required to maintain the cold temperature of the gas to keep it in a liquid state.

Designing pipeline insulation requires thorough knowledge of insulation materials and heat transfer mechanisms across the insulation. Accurate predictions of heat loss and temperature profile in oil- and gas-production pipelines are essential to designing and evaluating pipeline operations.

#### 11.4.2.2.1 Insulation materials

Polypropylene, polyethylene, and polyurethane are three base materials widely used in the petroleum industry for pipeline insulation. Their thermal conductivities are given in Table 11.4 (Carter et al., 2002). Depending on applications, these base materials are used in different forms, resulting in different overall conductivities. A three-layer polypropylene applied to pipe surface has a conductivity of 0.225 W/M-°C (0.13 btu/hr-ft-°F), while a four-layer polypropylene has a conductivity of 0.173 W/M-°C (0.10 btu/hr-ft-°F). Solid polypropylene has higher conductivity than polypropylene foam. Polymer syntactic polyurethane has a conductivity of 0.121 W/M-°C (0.07 btu/hr-ft-°F), while glass syntactic polyurethane has a conductivity of 0.156 W/M-°C (0.09 btu/hr-ft-°F). These materials have lower conductivities in dry conditions such as that in pipe-in-pipe (PIP) applications.

Because of their low thermal conductivities, more and more polyurethane foams are used in deepwater pipeline applications. Physical properties of polyurethane foams include density, compressive strength, thermal conductivity, closed-cell content, leachable halides, flammability, tensile strength, tensile modulus, and water absorption. Typical values of these properties are available elsewhere (Guo et al., 2005).

In steady-state flow conditions in an insulated pipeline segment, the heat flow through the pipe wall is given by

$$Q_r = IA_r \Delta T, \quad (11.131)$$

where  $Q_r$  is heat-transfer rate;  $U$  is overall heat-transfer coefficient (OHTC) at the reference radius;  $A_r$  is area of the pipeline at the reference radius;  $\Delta T$  is the difference in temperature between the pipeline product and the ambient temperature outside.

The OHTC,  $U$ , for a system is the sum of the thermal resistances and is given by (Holman, 1981):

$$U = \frac{1}{A_r \left[ \frac{1}{A_i h_i} + \sum_{m=1}^n \frac{\ln(r_{m+1}/r_m)}{2\pi L k_m} + \frac{1}{A_o h_o} \right]}, \quad (11.132)$$

**Table 11.4 Thermal Conductivities of Materials Used in Pipeline Insulation**

Material Name	Thermal Conductivity	
	W/M-°C	Btu/hr-ft-°F
Polyethylene	0.35	0.20
Polypropylene	0.22	0.13
Polyurethane	0.12	0.07

where  $h_i$  is film coefficient of pipeline inner surface;  $h_o$  is film coefficient of pipeline outer surface;  $A_i$  is area of pipeline inner surface;  $A_o$  is area of pipeline outer surface;  $r_m$  is radius of layer  $m$ ; and  $k_m$  is thermal conductivity of layer  $m$ .

Similar equations exist for transient-heat flow, giving an instantaneous rate for heat flow. Typically required insulation performance, in terms of OHTC ( $U$  value) of steel pipelines in water, is summarized in Table 11.5.

Pipeline insulation comes in two main types: dry insulation and wet insulation. The dry insulations require an outer barrier to prevent water ingress (PIP). The most common types of this include the following:

- Closed-cell polyurethane foam
- Open-cell polyurethane foam
- Poly-isocyanurate foam
- Extruded polystyrene
- Fiber glass
- Mineral wool
- Vacuum-insulation panels

Under certain conditions, PIP systems may be considered over conventional single-pipe systems. PIP insulation may be required to produce fluids from high-pressure/high-temperature ( $> 150^\circ\text{C}$ ) reservoirs in deepwater (Carmichael et al., 1999). The annulus between pipes can be filled with different types of insulation materials such as foam, granular particles, gel, and inert gas or vacuum.

A pipeline-bundled system—a special configuration of PIP insulation—can be used to group individual flowlines together to form a bundle (McKelvie, 2000); heat-up lines can be included in the bundle, if necessary. The complete bundle may be transported to site and installed with a considerable cost savings relative to other methods. The extra steel required for the carrier pipe and spacers can sometimes be justified (Bai, 2001).

Wet-pipeline insulations are those materials that do not need an exterior steel barrier to prevent water ingress, or the water ingress is negligible and does not degrade the insulation properties. The most common types of this are as follows:

- Polyurethane
- Polypropylene

**Table 11.5 Typical Performance of Insulated Pipelines**

Insulation Type	U-Value		Water Depth (M)	
	(Btu/hr-ft <sup>2</sup> -°F)	W/M <sup>2</sup> -K	Field Proven	Potential
Solid polypropylene	0.50	2.84	1600	4000
Polypropylene foam	0.28	1.59	700	2000
Syntactic polyurethane	0.32	1.81	1200	3300
Syntactic polyurethane foam	0.30	1.70	2000	3300
Pipe-in-pipe syntactic polyurethane foam	0.17	0.96	3100	4000
Composite	0.12	0.68	1000	3000
Pipe-in-pipe high efficiency	0.05	0.28	1700	3000
Glass syntactic polyurethane	0.03	0.17	2300	3000

- Syntactic polyurethane
- Syntactic polypropylene
- Multilayered

The main materials that have been used for deepwater insulations have been polyurethane and polypropylene based. Syntactic versions use plastic or glass matrix to improve insulation with greater depth capabilities. Insulation coatings with combinations of the two materials have also been used. [Guo et al. \(2005\)](#) gives the properties of these wet insulations. Because the insulation is buoyant, this effect must be compensated by the steel pipe weight to obtain lateral stability of the deepwater pipeline on the seabed.

#### 11.4.2.2.2 Heat transfer models

Heat transfer across the insulation of pipelines presents a unique problem affecting flow efficiency. Although sophisticated computer packages are available for predicting fluid temperatures, their accuracies suffer from numerical treatments because long pipe segments have to be used to save computing time. This is especially true for transient fluid-flow analyses in which a very large number of numerical iterations are performed.

[Ramey \(1962\)](#) was among the first investigators who studied radial-heat transfer across a well casing with no insulation. He derived a mathematical heat-transfer model for an outer medium that is infinitely large. [Miller \(1980\)](#) analyzed heat transfer around a geothermal wellbore without insulation. [Winterfeld \(1989\)](#) and [Almehaideb et al. \(1989\)](#) considered temperature effect on pressure-transient analyses in well testing. [Stone et al. \(1989\)](#) developed a numerical simulator to couple fluid flow and heat flow in a wellbore and reservoir. More advanced studies on the wellbore heat-transfer problem were conducted by [Hasan and Kabir \(1994, 2002\)](#), [Hasan et al. \(1997, 1998\)](#), and [Kabir et al. \(1996\)](#). Although multilayers of materials have been considered in these studies, the external temperature gradient in the longitudinal direction has not been systematically taken into account. Traditionally, if the outer temperature changes with length, the pipe must be divided into segments, with assumed constant outer temperature in each segment, and numerical algorithms are required for heat-transfer computation. The accuracy of the computation depends on the number of segments used. Fine segments can be employed to ensure accuracy with computing time sacrificed.

[Guo et al. \(2006\)](#) presented three analytical heat-transfer solutions. They are the transient-flow solution for startup mode, steady-flow solution for normal operation mode, and transient-flow solution for flow rate change mode (shutting down is a special mode in which the flow rate changes to zero).

**Temperature and heat transfer for steady fluid flow.** The internal temperature profile under steady fluid-flow conditions is expressed as

$$T = \frac{1}{\alpha^2} [\beta - \alpha\beta L - \alpha\gamma - e^{-\alpha(L+C)}], \quad (11.133)$$

where the constant groups are defined as

$$\alpha = \frac{2\pi Rk}{v\rho C_p sA}, \quad (11.134)$$

$$\beta = \alpha G \cos(\theta), \quad (11.135)$$

$$\gamma = -\alpha T_0, \quad (11.136)$$

and

$$C = -\frac{1}{\alpha} \ln(\beta - \alpha^2 T_s - \alpha\gamma), \quad (11.137)$$

where  $T$  is temperature inside the pipe,  $L$  is longitudinal distance from the fluid entry point,  $R$  is inner radius of insulation layer,  $k$  is the thermal conductivity of the insulation material,  $v$  is the average flow velocity of fluid in the pipe,  $\rho$  is fluid density,  $C_p$  is heat capacity of fluid at constant pressure,  $s$  is thickness of the insulation layer,  $A$  is the inner cross-sectional area of pipe,  $G$  is principal thermal-gradient outside the insulation,  $\theta$  is the angle between the principal thermal gradient and pipe orientation,  $T_0$  is temperature of outer medium at the fluid entry location, and  $T_s$  is temperature of fluid at the fluid entry point.

The rate of heat transfer across the insulation layer over the whole length of the pipeline is expressed as

$$q = -\frac{2\pi Rk}{s} \times \left( T_0 L - \frac{G \cos(\theta)}{2} L^2 - \frac{1}{\alpha^2} \left\{ (\beta - \alpha\gamma)L - \frac{\alpha\beta}{2} L^2 + \frac{1}{\alpha} [e^{-\alpha(L+C)} - e^{-\alpha C}] \right\} \right), \quad (11.138)$$

where  $q$  is the rate of heat transfer (heat loss).

**Transient temperature during startup.** The internal temperature profile after starting up a fluid flow is expressed as follows:

$$T = \frac{1}{\alpha^2} \{ \beta - \alpha\beta L - \alpha\gamma - e^{-\alpha[L+f(L+vt)]} \}, \quad (11.139)$$

where the function  $f$  is given by

$$f(L - vt) = -(L - vt) - \frac{1}{\alpha} \ln \{ \beta - \alpha\beta(L - vt) - \alpha\gamma - \alpha^2 [T_s - G \cos(\theta)(L - vt)] \} \quad (11.140)$$

and  $t$  is time.

**Transient temperature during flow rate change.** Suppose that after increasing or decreasing the flow rate, the fluid has a new velocity  $v'$  in the pipe. The internal temperature profile is expressed as follows:

$$T = \frac{1}{\alpha'^2} \{ \beta' - \alpha'\beta'L - \alpha'\gamma' - e^{-\alpha'[L+f(L-v't)]} \}, \quad (11.141)$$

where

$$\alpha' = \frac{2\pi Rk}{v'\rho C_p s A}, \quad (11.142)$$

$$\beta' = \alpha' G \cos(\theta), \quad (11.143)$$

$$\gamma' = -\alpha' T_0, \quad (11.144)$$

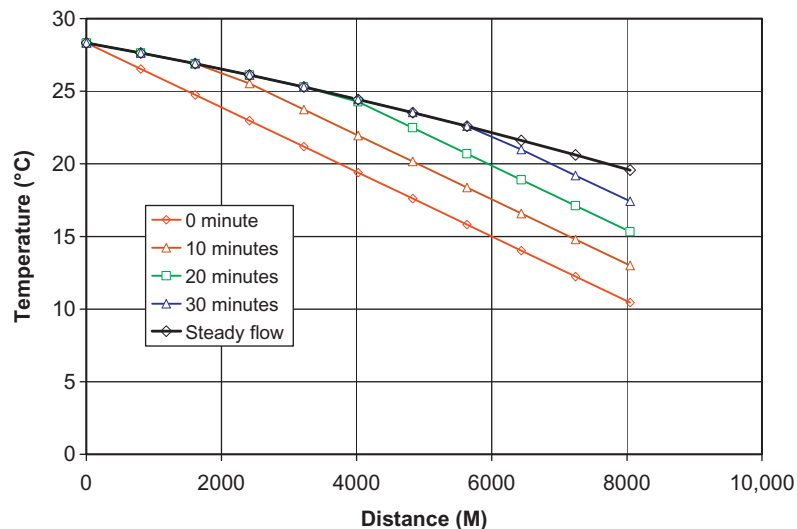
and the function  $f$  is given by

$$f(L - v't) = -(L - v't) - \frac{1}{\alpha'} \ln \{ \beta' - \alpha'\beta'(L - v't) - \alpha'\gamma' - \left( \frac{\alpha'}{\alpha} \right)^2 \{ \beta - \alpha\beta(L - v't) - \alpha\gamma - e^{-\alpha[(L-v't)C]} \} \}. \quad (11.145)$$

**Example Problem 11.7** A design case is shown in this example. Design base for a pipeline insulation is presented in Table 11.6. The design criterion is to ensure that the temperature at any point in the pipeline will not drop to less than 25°C, as required by flow assurance. Insulation materials considered for the project were polyethylene, polypropylene, and polyurethane.

**Solution** A polyethylene layer of 0.0254 M (1 in.) was first considered as the insulation. Fig. 11.13 shows the temperature profiles calculated using Eqs. (11.133) and (11.139). It indicates that at approximately 40 minutes after startup, the transient-temperature profile in the pipeline will approach the steady-flow temperature profile. The temperature at the end of the pipeline will be slightly lower than 20°C under normal operating conditions. Obviously, this insulation option does not meet design criterion of 25°C in the pipeline.

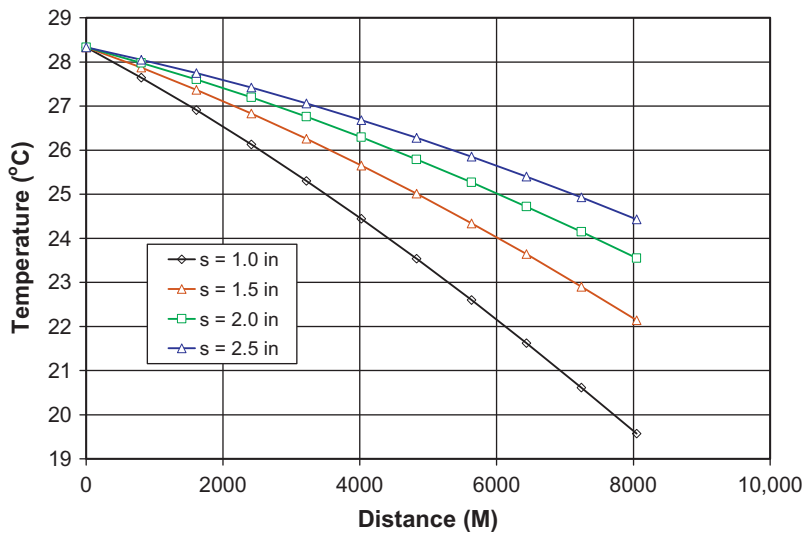
Length of pipeline:	8047	M
Outer diameter of pipe:	0.2032	M
Wall thickness:	0.00635	M
Fluid density:	881	kg/M <sup>3</sup>
Fluid specific heat:	2012	J/kg-°C
Average external temperature:	10	°C
Fluid temperature at entry point:	28	°C
Fluid flow rate:	7950	M <sup>3</sup> /day



**FIGURE 11.13**

Calculated temperature profiles with a polyethylene layer of 0.0254 M (1 in.).





**FIGURE 11.14**

Calculated steady-flow temperature profiles with polyethylene layers of various thicknesses.

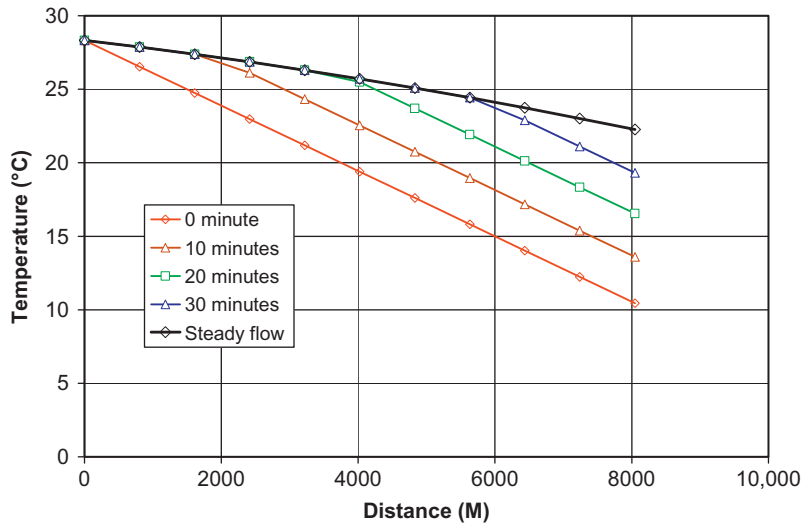
Fig. 11.14 presents the steady-flow temperature profiles calculated using Eq. (11.133) with polyethylene layers of four thicknesses. It shows that even a polyethylene layer 0.0635-M (2.5-in.) thick will still not give a pipeline temperature higher than 25°C; therefore, polyethylene should not be considered in this project.

A polypropylene layer of 0.0254 M (1 in.) was then considered as the insulation. Fig. 11.15 illustrates the temperature profiles calculated using Eq. (11.133) and (11.139). It again indicates that at approximately 40 minutes after startup, the transient-temperature profile in the pipe will approach the steady-flow temperature profile. The temperature at the end of the pipeline will be approximately 22.5°C under normal operating conditions. Obviously, this insulation option, again, does not meet design criterion of 25°C in the pipeline.

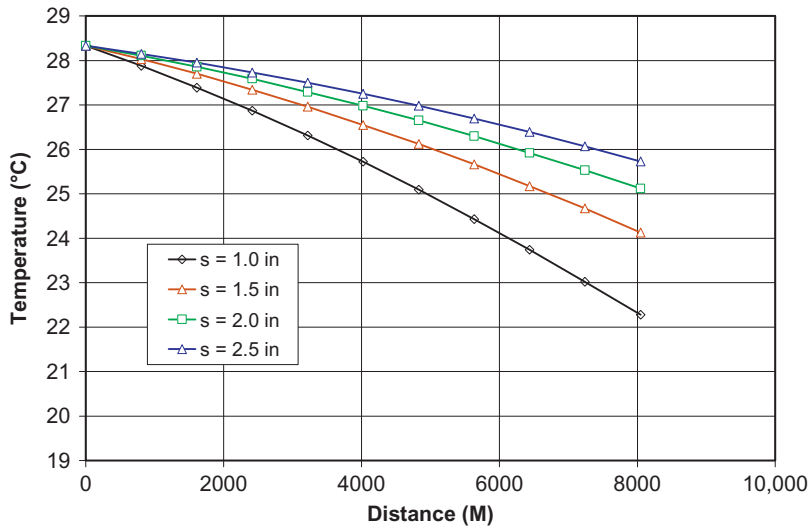
Fig. 11.16 demonstrates the steady-flow temperature profiles calculated using Eq. (11.133) with polypropylene layers of four thicknesses. It shows that a polypropylene layer of 0.0508 M (2.0 in.) or thicker will give a pipeline temperature of higher than 25°C.

A polyurethane layer of 0.0254 M (1 in.) was also considered as the insulation. Fig. 11.17 shows the temperature profiles calculated using Eqs. (11.133) and (11.139). It indicates that the temperature at the end of pipeline will drop to slightly lower than 25°C under normal operating conditions. Fig. 11.18 presents the steady-flow temperature profiles calculated using Eq. (11.133) with polyurethane layers of four thicknesses. It shows that a polyurethane layer of 0.0381 M (1.5 in.) is required to keep pipeline temperatures higher than 25°C under normal operating conditions.

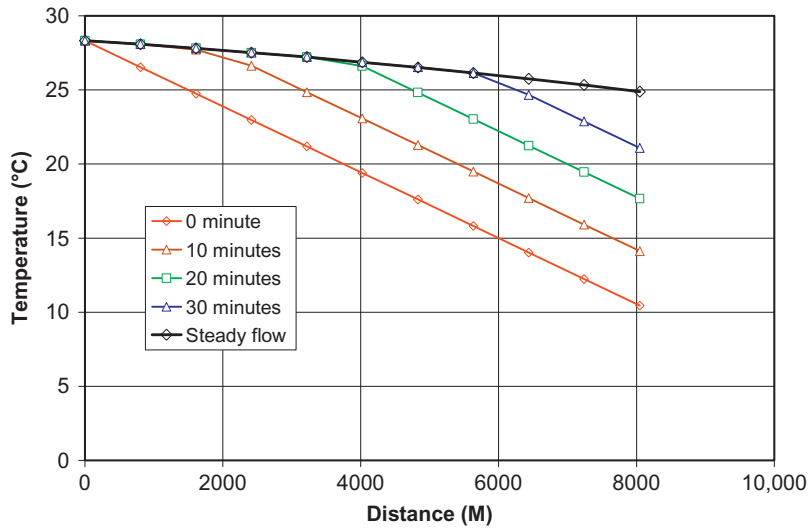
Therefore, either a polypropylene layer of 0.0508 M (2.0 in.) or a polyurethane layer of 0.0381 M (1.5 in.) should be chosen for insulation of the pipeline. Cost analyses can justify one of the options, which is beyond the scope of this example.



**FIGURE 11.15**  
 Calculated temperature profiles with a polypropylene layer of 0.0254 M (1 in.).

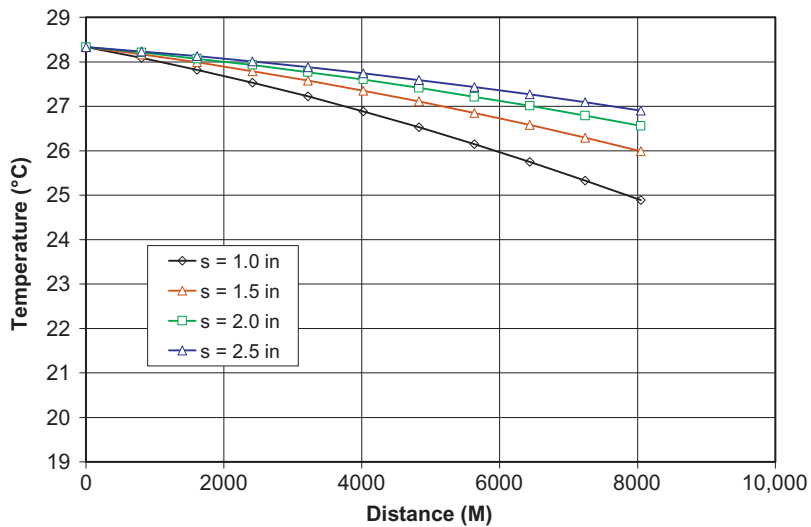


**FIGURE 11.16**  
 Calculated steady-flow temperature profiles with polypropylene layers of various thicknesses.



**FIGURE 11.17**

Calculated temperature profiles with a polyurethane layer of 0.0254 M (1 in.).



**FIGURE 11.18**

Calculated steady-flow temperature profiles with polyurethane layers of four thicknesses.

**Table 11.7 Calculated Total Heat Losses for the Insulated Pipelines (kW)**

Material Name	Insulation Thickness (M) 0.0254	0.0381	0.0508	0.0635
Polyethylene	1430	1,011	781	636
Polypropylene	989	685	524	424
Polyurethane	562	383	290	234

The total heat losses for all the steady-flow cases were calculated with Eq. (11.138). The results are summarized in Table 11.7. These data may be used for sizing heaters for the pipeline if heating of the product fluid is necessary.

---

## 11.5 SUMMARY

This chapter described oil and gas transportation systems. The procedure for selection of pumps and gas compressors were presented and demonstrated. Theory and applications of pipeline design were illustrated.

---

## REFERENCES

- Almehaideb, R.A., Aziz, K., Pedrosa, O.A., Jr., A reservoir/wellbore model for multiphase injection and pressure transient analysis. In: Presented at the 1989 SPE Middle East Oil Show, Bahrain, 11–14 March. Paper SPE 17941.
- American Gas Association, Collapse of Offshore Pipelines. Pipeline Research Committee, Seminar held 20 February, 1990, in Houston, Texas. American Society of Mechanical Engineers. Liquid transportation systems for hydrocarbons, liquid petroleum gas, anhydrous ammonia and alcohols. *ASME B31.4* 1989. Washington.
- American Society of Mechanical Engineers, Gas transmission and distribution piping systems, ASME code for pressure piping, B31.8-(1989 Edition and 1990 Addendum). Washington.
- Bai, Y., 2001. Pipelines and risers, *Ocean Engineering Book Series*, vol. 3. Elsevier, Amsterdam.
- Carmichael, R., Fang, J., Tam, C., Pipe-in-pipe systems for deepwater developments. In: Proceedings of the Deepwater Pipeline Technology Conference, in New Orleans, 1999.
- Carter, B., Gray, C., Cai, J., 2002 survey of offshore non-chemical flow assurance solutions. Poster published by *Offshore Magazine*, Houston, 2003.
- Colebrook, C.F.J., 1983. *Inst. Civil Eng.* 11, 133.
- Drew, T.B., Koo, E.C., McAdams, W.H., 1930. *Trans. Am. Inst. Chem. Eng.* 28, 56.
- Guo, B., et al., 2005. *Offshore Pipelines*. Gulf Professional Publishing, Burlington, USA.
- Guo, B., Ghalambor, A., 2005. *Natural Gas Engineering Handbook*. Gulf Publishing Company, Houston, TX.
- Guo, B., Duan, S., Ghalambor, A., 2006. A simple model for predicting heat loss and temperature profiles in insulated pipelines. *SPE Prod. Oper. J.* 21 (1).
- Hasan, A.R., Kabir, C.S., 1994. Aspects of wellbore heat transfer during two-phase flow. *SPEPF* 9 (2), 211–218.
- Hasan, A.R., Kabir, C.S., Wang, X., 1997. Development and application of a wellbore/reservoir simulator for testing oil wells. *SPEFE* 12 (3), 182–189.

- Hasan, A.R., Kabir, C.S., Wang, X., 1998. Wellbore twophase flow and heat transfer during transient testing. SPEJ 174–181.
- Hasan, R., Kabir, C.S., 2002. Fluid Flow and Heat Transfer in Wellbores. SPE, Richardson, TX.
- Hill, R.T., Warwick, P.C., Internal corrosion allowance for marine pipelines: a question of validity. OTC paper No. 5268, 1986.
- Holman, J.P., 1981. Heat Transfer. McGraw-Hill Book Co, New York.
- Jain, A.K., May 1976. An accurate explicit equation for friction factor, ASCE **102**, HY5 .J. *Hydraul. Div.*
- Kabir, C.S., et al., 1996. A wellbore/reservoir simulator for testing gas well in high-temperature reservoirs. SPEFE 11 (2), 128–135.
- Lyons, W.C., Guo, B., Seidel, F.A., 2001. Air and Gas Drilling Manual. McGraw-Hill, New York, pp. 4–5.
- Mckelvie, M., Bundles—design and construction, Integrated Graduate Development Scheme, Heriot-Watt U., 2000.
- Moody, L.F., 1944. Friction factor for pipe flow. Trans. ASME 66, 671.
- Miller, C.W., 1980. Wellbore storage effect in geothermal wells. SPEJ 20 (6), 555.
- Murphey, C.E., Langner, C.G. Ultimate pipe strength under bending, collapse, and fatigue. In: Proceedings of the OMAE Conference, 1985.
- Nikuradse, J., 1933. Forschungshelf 301.
- Ramey Jr., H.J., 1962. Wellbore heat transmission. Trans. AIME 14.
- Rollins, J.P., 1973. Compressed Air and Gas Handbook. Compressed Air and Gas Institute, New York.
- Stone, T.W., Edmunds, N.R., Kristoff, B.J., A comprehensive wellbore/reservoir simulator. In: Presented at the 1989 SPE Reservoir Simulation Symposium, 6–8 February, in Houston. Paper SPE 18419.
- Veritas, D.n., Rules for submarine pipeline systems. 1981.
- Winterfeld, P.H., 1989. Simulation of pressure buildup in a multiphase wellbore/reservoir system. SPEFE 4 (2), 247–252.
- Weymouth, T.R., 1912. Problems in natural gas engineering. Trans. ASME 34, 185.

---

## PROBLEMS

- 11.1** A pipeline transporting 10,000 bbl/day of oil requires a pump with a minimum output pressure of 500 psi. The available suction pressure is 300 psi. Select a triplex pump for this operation.
- 11.2** A pipeline transporting 8000 bbl/day of oil requires a pump with a minimum output pressure of 400 psi. The available suction pressure is 300 psi. Select a duplex pump for this operation.
- 11.3** For a reciprocating compressor, calculate the theoretical and brake horsepower required to compress 30 MMscfd of a 0.65 specific gravity natural gas from 100 psia and 70°F to 2000 psia. If intercoolers and end-coolers cool the gas to 90°F, what is the heat load on the coolers? Assuming the overall efficiency is 0.80.
- 11.4** For a centrifugal compressor, use the following data to calculate required input horsepower and polytropic head:

Gas-specific gravity:	0.70
Gas-specific heat ratio:	1.30
Gas flow rate:	50 MMscfd at 14.7 psia and 60°F
Inlet pressure:	200 psia Inlet temperature: 70°F
Discharge pressure:	500 psia
Polytropic efficiency:	$E_p = 061 + 003 \log (q_1)$

- 11.5** For the data given in Problem 11.4, calculate the required brake horsepower if a reciprocating compressor is used.
- 11.6** A 40-API gravity, 3-cp oil is transported through an 8-in. (I.D.) pipeline with a downhill angle of  $5^\circ$  across a distance of 10 miles at a flow rate of 5000 bbl/day. Estimate the minimum required pump pressure to deliver oil at 100 psi pressure at the outlet. Assume  $e = 0.0006$  in.
- 11.7** For the following data given for a horizontal pipeline, predict gas flow rate in cubic feet per hour through the pipeline. Solve the problem using Eq. (11.101) with the trial-and-error method for friction factor and the Weymouth equation without the Reynolds number–dependent friction factor:
- $d = 6$  in.
  - $L = 100$  mi
  - $e = 0.0006$  in.
  - $T = 70^\circ\text{F}$
  - $\gamma_g = 0.70$
  - $T_b = 520^\circ\text{R}$
  - $p_b = 14.65$  psia
  - $p_1 = 800$  psia
  - $p_2 = 200$  psia
- 11.8** Solve Problem 11.7 using
- a. Panhandle-A Equation
  - b. Panhandle-B Equation
- 11.9** Assuming a  $10^\circ$  uphill angle, solve Problem using the Weymouth equation.
- 11.10** Calculate the required wall thickness for a pipeline using the following data:
- Water depth 2000 ft offshore oil field
  - Water temperature  $45^\circ\text{F}$
  - 12.09 in. pipe inner diameter
  - Seamless still pipe of X-65 grade
  - Maximum pipeline pressure 3000 psia
- 11.11** Design insulation for a pipeline with the following given data:
- |                                   |  |
|-----------------------------------|--|
| Length of pipeline:               | 7000 M                                 |
| Outer diameter of pipe:           | 0.254 M                                |
| Wall thickness:                   | 0.0127 M                               |
| Fluid density:                    | $800 \text{ kg/M}^3$                   |
| Fluid specific heat:              | $2000 \text{ J/kg}\cdot^\circ\text{C}$ |
| Average external temperature:     | $15^\circ\text{C}$                     |
| Fluid temperature at entry point: | $30^\circ\text{C}$                     |
| Fluid flow rate:                  | $5000 \text{ M}^3/\text{day}$          |

# WELL STIMULATION AND WORKOVER

# III

*Good production engineers never stop looking for opportunities to improve the performance of their production systems. Performance enhancement ideas come from careful examinations and thorough analyses of production data to find the controlling factors affecting the performance. Part III of this book presents procedures taken in the petroleum industry for identifying well problems and means of solving the problems. Materials are presented in the following four chapters:*

Chapter 12: Well Problem Identification 12/329

Chapter 13: Acidizing 13/367

Chapter 14: Hydraulic Fracturing 14/389

Chapter 15: Well Workover 15/503

# WELL PROBLEM IDENTIFICATION 12

---

## 12.1 INTRODUCTION

The engineering work for sustaining and enhancing oil and gas production rates starts from identifying problems that cause low production rates of wells, quick decline of the desirable production fluid, or rapid increase in the undesirable fluids. For oil wells, these problems include:

- Low productivity
- Excessive gas production
- Excessive water production
- Sand production

For gas wells, the problems include:

- Low productivity
- Excessive water production
- Liquid loading
- Sand production

Although sand production is easy to identify, well testing and production logging are frequently needed to identify the causes of other well problems.

---

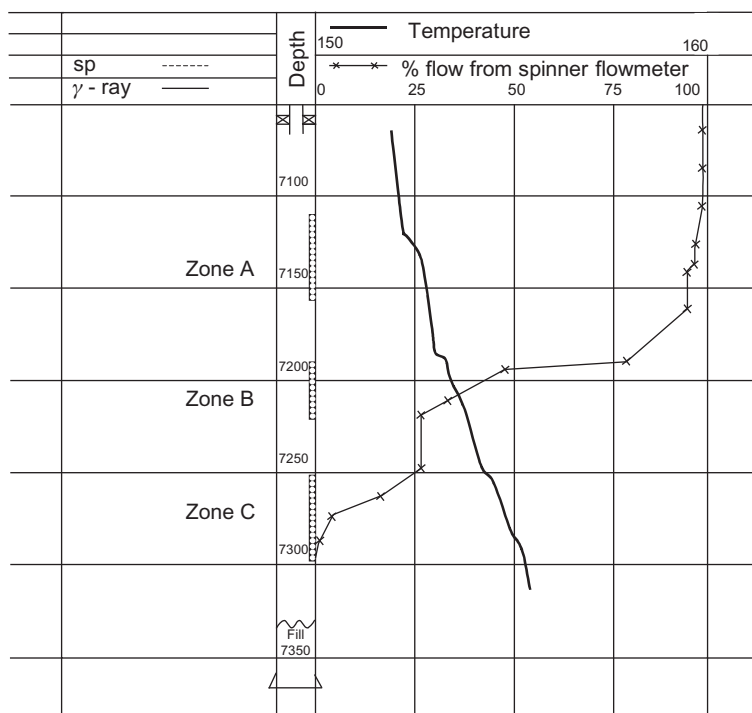
## 12.2 LOW PRODUCTIVITY

The lower than expected productivity of an oil or gas well is found on the basis of comparison of the well's actual production rate and the production rate that is predicted by Nodal analysis. If the reservoir inflow model used in the Nodal analysis is correct (which is often questionable), the lower than expected well productivity can be attributed to one or more of the following reasons:

- Overestimate of reservoir pressure
- Overestimate of reservoir permeability (absolute and relative permeabilities)
- Formation damage (mechanical and pseudo skins)
- Reservoir heterogeneity (faults, stratification, etc.)
- Completion ineffectiveness (limited entry, shallow perforations, low perforation density, etc.)
- Restrictions in wellbore (paraffin, asphaltane, scale, gas hydrates, sand, etc.)

The first five factors affect reservoir inflow performance, that is, deliverability of reservoir. They can be evaluated on the basis of pressure transient data analyses.





**FIGURE 12.1**

Temperature and spinner flowmeter-derived production profile (Economides et al., 1994).

The true production profile from different zones can be obtained based on production logging such as temperature and spinner flow meter logs. An example is presented in Fig. 12.1, which shows that Zone A is producing less than 10% of the total flow, Zone B is producing almost 70% of the total rate, and Zone C is contributing about 25% of the total production.

The last factor controls well deliverability. It can be evaluated using data from production logging such as flowing gradient survey (FGS). The depth interval with high-pressure gradient is usually the interval where the depositions of paraffins, asphaltanes, scales, or gas hydrates are suspected.

### 12.2.1 PRESSURE TRANSIENT DATA ANALYSIS

Pressure transient testing plays a key role in evaluating exploration and development prospects. Properly designed well tests can provide reservoir engineers with reservoir pressure, reserves (minimum economic or total), and flow capacity, all of which are essential in the reservoir evaluation process. Some of the results one can obtain from pressure transient testing include the following:

- Initial reservoir pressure
- Average reservoir pressure
- Directional permeability

- Radial effective permeability changes from the wellbore
- Gas condensate fallout effect on flow
- Near wellbore damage/stimulation
- Rate-dependent skin
- Boundary identification
- Partial penetration effect on flow
- Effective fracture length
- Effective fracture conductivity
- Dual-porosity characteristics (storativity and transmissivity ratios)

The theoretical basis of pressure transient data analysis is beyond the scope of this book. It can be found elsewhere (Chaudhry, 2004; Horne, 1995; Lee et al., 2003). Modern computer software packages are available for data analyses. These packages include PanSystem (EPS, 2004) and F.A. S.T. WellTest (Fekete, 2003). The following subsections briefly present some principles of data analyses that lead to deriving reservoir properties directly affecting well productivity.

### 12.2.1.1 Reservoir pressure

Reservoir pressure is a key parameter controlling well deliverability. A simple way to determine the magnitude of initial reservoir pressure may be the Horner plot of data from pressure buildup test if the reservoir boundary was not reached during the test. If the boundary effects are seen, the average reservoir pressure can be estimated on the basis of the extrapolated initial reservoir pressure from Horner plot and the MBH plot (Dake, 2002).

### 12.2.1.2 Effective permeability

The effective reservoir permeability that controls the well's deliverability should be derived from the flow regime that prevails in the reservoir for long-term production. To better understand the flow regimes, the commonly used equations describing flow in oil reservoirs are summarized first in this subsection. Similar equations for gas reservoirs can be found in Lee et al. (2003).

### 12.2.1.3 Horizontal radial flow

For vertical wells fully penetrating nonfractured reservoirs, the horizontal radial flow can be mathematically described in consistent units as

$$p_{wf} = p_i - \frac{qB\mu}{4\pi k_h h} \left[ \ln \left( \frac{k_h t}{\phi \mu c_i r_w^2} \right) + 2S + 0.80907 \right], \quad (12.1)$$

where

- $p_{wf}$  = flowing bottom-hole pressure
- $p_i$  = initial reservoir pressure
- $q$  = volumetric liquid production rate
- $B$  = formation volume factor
- $\mu$  = fluid viscosity
- $k_h$  = the average horizontal permeability
- $h$  = pay zone thickness

- $t$  = flow time
- $\phi$  = porosity
- $c_t$  = total reservoir compressibility
- $r_w$  = wellbore radius
- $S$  = total skin factor

### 12.2.1.4 Horizontal linear flow

For hydraulically fractured wells, the horizontal linear flow can be mathematically described in consistent units as

$$p_{wf} = p_i - \frac{qB\mu}{2\pi k_y h} \left[ \sqrt{\frac{\pi k_y t}{\phi \mu c_t x_f^2}} + S \right], \quad (12.2)$$

where  $x_f$  is fracture half-length and  $k_y$  is the permeability in the direction perpendicular to the fracture face.

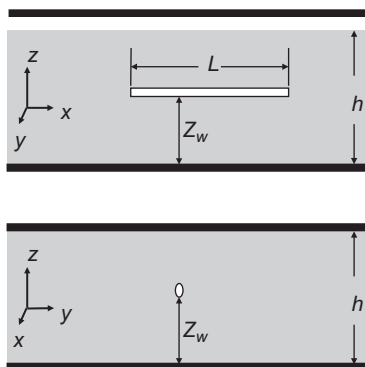
### 12.2.1.5 Vertical radial flow

For horizontal wells as depicted in Fig. 12.2, the early-time vertical radial flow can be mathematically described in consistent units as

$$p_{wf} = p_i - \frac{qB\mu}{4\pi k_{yz} L} \left[ \ln \left( \frac{k_{yz} t}{\phi \mu c_t r_w^2} \right) + 2S + 0.80907 \right], \quad (12.3)$$

where  $L$  is the horizontal wellbore length and  $k_{yz}$  is the geometric mean of horizontal and vertical permeabilities, that is,

$$k_{yz} = \sqrt{k_y k_z}. \quad (12.4)$$



**FIGURE 12.2**

Notations for a horizontal wellbore.

### 12.2.1.6 Horizontal Pseudo-linear flow

The pseudo-linear flow toward a horizontal wellbore can be mathematically described in consistent units as

$$p_{wf} = p_i - \frac{qB\mu}{2\pi k_y(h - Z_w)} \left[ \sqrt{\frac{4\pi k_y t}{\phi\mu c_i L^2}} + S \right]. \quad (12.5)$$

### 12.2.1.7 Horizontal Pseudo-radial flow

The pseudo-radial flow toward a horizontal wellbore can be mathematically described in consistent units as

$$p_{wf} = p_i - \frac{qB\mu}{4\pi k_h h} \left[ \ln \left( \frac{k_h t}{\phi\mu c_i r_w^2} \right) + 2S + 0.80907 \right]. \quad (12.6)$$

For vertical wells fully penetrating nonfractured reservoirs, it is usually the average (geometric mean) of horizontal permeabilities,  $kh$ , that dominates long-term production performance. This average horizontal permeability can be derived from the horizontal radial flow regime. For wells draining relatively small portions of hydraulically fractured reservoir segments, it is usually the permeability in the direction perpendicular to the fracture face that controls long-term production performance. This permeability can be derived from the horizontal linear flow regime. For horizontal wells draining relatively large portions of nonfractured reservoir segments, it is usually again the geometric mean of horizontal permeabilities that dominates long-term production performance. This average horizontal permeability can be derived from the pseudo-radial flow regime. For vertical wells partially penetrating nonfractured reservoirs, both horizontal and vertical permeabilities influence long-term production performance. These permeabilities can usually be derived from the hemispherical flow regime.

Flow regimes are usually identified using the diagnostic pressure derivative  $p'$  defined as

$$p' = \frac{d\Delta p}{d \ln(t)} = t \frac{d\Delta p}{dt}, \quad (12.7)$$

where  $t$  is time and  $\Delta p$  is defined as

$$\Delta p = p_i - p_{wf} \quad (12.8)$$

for drawdown tests, where  $p_i$  and  $p_{wf}$  are initial reservoir pressure and flowing bottom-hole pressure, respectively. For pressure buildup tests, the  $\Delta p$  is defined as

$$\Delta p = p_{sw} - p_{wfe}, \quad (12.9)$$

where  $p_{ws}$  and  $p_{wfe}$  are shut-in bottom-hole pressure and the flowing bottom-hole pressure at the end of flow (before shut-in), respectively.

For any type of radial flow (e.g., horizontal radial flow, vertical radial flow, horizontal pseudo-radial flow), the diagnostic derivative is derived from Eqs. (12.1), (12.3), and (12.6) as

$$p' = \frac{d\Delta p}{d \ln(t)} = \frac{qB\mu}{4\pi k H_R}, \quad (12.10)$$

where  $\bar{k}$  is the average permeability in the flow plane ( $k_h$  or  $k_{yz}$ ) and

$$k_h = \sqrt{k_x k_y}$$

$H_R$  is the thickness of the radial flow ( $h$  or  $L$ ). Apparently, the diagnostic derivative is constant over the radial flow time regime. The plot of  $p'$  versus  $t$  data should show a trend of straight line parallel to the  $t$ -axis.

For linear flow (e.g., flow toward a hydraulic fracture), the diagnostic derivative is derived from Eq. (12.2) as

$$p' = \frac{d\Delta p}{d \ln(t)} = \frac{qB}{4hx_f} \sqrt{\frac{\mu t}{\pi \phi c_t k_y}} \quad (12.12)$$

For pseudo-linear flow (e.g., flow toward a horizontal well), the diagnostic derivative is derived from Eq. (12.5) as

$$p' = \frac{d\Delta p}{d \ln(t)} = \frac{qB}{2L(h - z_w)} \sqrt{\frac{\mu t}{\pi \phi c_t k_y}} \quad (12.13)$$

Taking logarithm of Eqs. (12.12) and (12.13) gives

$$\log(p') = \frac{1}{2} \log(t) + \log\left(\frac{qB}{4hx_f} \sqrt{\frac{\mu}{\pi \phi c_t k_y}}\right) \quad (12.14)$$

and

$$\log(p') = \frac{1}{2} \log(t) + \log\left(\frac{qB}{2L(h - z_w)} \sqrt{\frac{\mu}{\pi \phi c_t k_y}}\right) \quad (12.15)$$

Eqs. (12.13) and (12.14) indicate that the signature of the linear flow regime is the  $\frac{1}{2}$  slope on the log-log plot of diagnostic derivative versus time.

Once the flow regimes are identified, permeabilities associated with the flow regime can be determined based on slope analyses. For any types of radial flow, Eqs. (12.1), (12.3), and (12.6) indicate that plotting of bottom-hole pressure versus time data on a semi-log scale will show a trend with a constant slope  $m_R$ , where

$$m_R = -\frac{qB\mu}{4\pi\bar{k}H_R} \quad (12.16)$$

Then the average permeability in the flow plane ( $k_h$  or  $k_{yz}$ ) can be estimated by

$$\bar{k} = -\frac{qB\mu}{4\pi H_R m_R} \quad (12.17)$$

For any types of linear flow, Eqs. (12.2) and (12.5) indicate that plotting of the bottom-hole pressure versus the square-root of time data will show a trend with a constant slope  $m_L$ , where

$$m_L = -\frac{qB}{H_L X_L} \sqrt{\frac{\mu}{\pi \phi c_t k_y}} \quad (12.18)$$

where  $H_L = h$  and  $X_L = 2x_f$  for linear flow, and  $H_L = h - Z_w$  and  $X_L = L$  for pseudo-linear flow, respectively. Then the permeability in the flow plane can be estimated by

$$k_y = \frac{\mu}{\pi \phi c_l} \left( \frac{qB}{m_L H_L X_L} \right)^2. \quad (12.19)$$

If a horizontal well is tested for a time long enough to detect the pseudo-radial flow, then it is possible to estimate other directional permeabilities by

$$k_x = \frac{k_h^2}{k_y} \quad (12.20)$$

and

$$k_z = \frac{k_{yz}^2}{k_y}. \quad (12.21)$$

Although  $k_x$  and  $k_z$  are not used in well productivity analysis, they provide some insight about reservoir anisotropy.

### 12.2.1.8 Skin factor

Skin factor is a constant that is used to adjust the flow equation derived from the ideal condition (homogeneous and isotropic porous media) to suit the applications in nonideal conditions. It is an empirical factor employed to consider the lumped effects of several aspects that are not considered in the theoretical basis when the flow equations were derived. The value of the skin factor can be derived from pressure transient test analysis with Eqs. (12.1)–(12.3), (12.5), and (12.6). But its value has different meanings depending on flow regime. A general expression of the skin factor is

$$S = S_D + S_{C+\theta} + S_p + \sum S_{PS}, \quad (12.22)$$

where  $S_D$  is damage skin during drilling, cementing, well completion, fluid injection, and even oil and gas production. Physically, it is due to plugging of pore space by external or internal solid particles and fluids. This component of skin factor can be removed or averted with well stimulation operations. The  $S_{C+\theta}$  is a skin component due to partial completion and deviation angle, which make the flow pattern near the wellbore deviate from ideal radial flow pattern. This skin component is not removable in water coning and gas coning systems. The  $S_p$  is a skin component due to the nonideal flow condition around the perforations associated with cased-hole completion. It depends on a number of parameters including perforation density, phase angle, perforation depth, diameter, compacted zone, and others. This component can be minimized with optimized perforating technologies. The  $\sum S_{PS}$  represents pseudo-skin components due to non-Darcy flow effect, multi-phase effect, and flow convergence near the wellbore. These components cannot be eliminated.

It is essential to know the magnitude of components of the skin factor  $S$  derived from the pressure transient test data analysis. Commercial software packages are available for decomposition of the skin factor on the basis of well completion method. One of the packages is WellFlo (EPS, 2005).

**Example Problem 12.1** A horizontal wellbore was placed in a 100-ft thick oil reservoir of 0.23 porosity. Oil formation volume factor and viscosity are 1.25 rb/stb and 1 cp, respectively. The total reservoir compressibility factor is  $10^{-5} \text{ psi}^{-1}$ . The well was tested following the schedule shown in Fig. 12.3. The measured flowing bottom-hole pressures are also presented in Fig. 12.3. Estimate directional permeabilities and skin factors from the test data.

**Solution** Fig. 12.4 presents a log-log diagnostic plot of test data. It clearly indicates a vertical radial flow at early time, a pseudo-linear flow at mid-time, and the beginning of a pseudo-radial flow at late time.

The semi-log analysis for the vertical radial flow is shown in Fig. 12.5, which gives  $k_{yz} = 0.9997 \text{ md}$  and near-wellbore skin factor  $S = -0.0164$ .

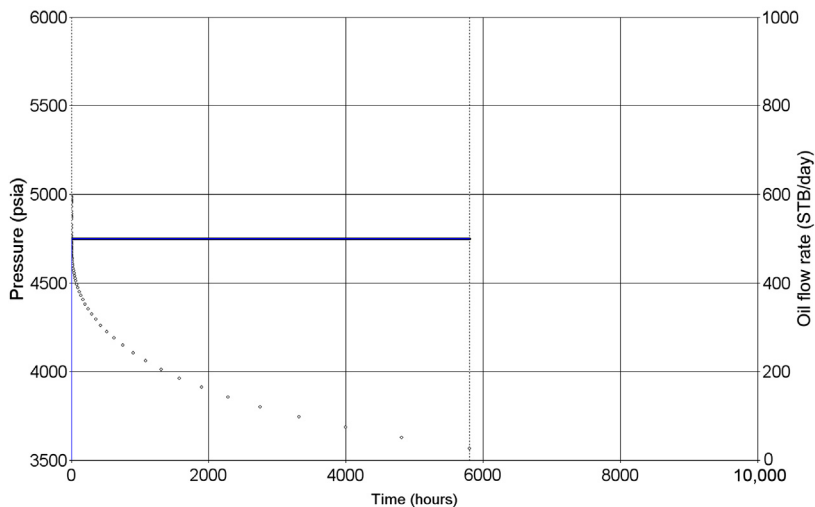
The square-root time plot analysis for the pseudo-linear flow is shown in Fig. 12.6, which gives the effective wellbore length of  $L = 1082.75 \text{ ft}$  and a skin factor due to convergence of  $S = 3.41$ .

The semi-log analysis for the horizontal pseudo-radial flow is shown in Fig. 12.7, which gives  $k_h = 1.43 \text{ md}$  and pseudo-skin factor  $S = -6.17$ .

Fig. 12.8 shows a match between the measured and model-calculated pressure responses given by an optimization technique. This match was obtained using the following parameter values:

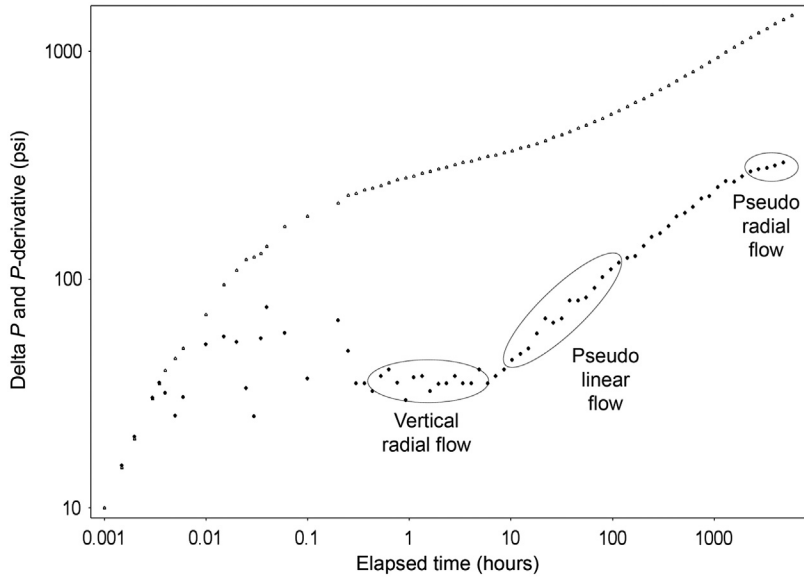
$$\begin{aligned}k_h &= 1.29 \text{ md} \\k_z &= 0.80 \text{ md} \\S &= 0.06 \\L &= 1243 \text{ ft}.\end{aligned}$$

To estimate the long-term productivity of this horizontal well, the  $k_h = 1.29 \text{ md}$  and  $S = 0.06$  should be used in the well inflow equation presented in Chapter 3, Reservoir Deliverability.



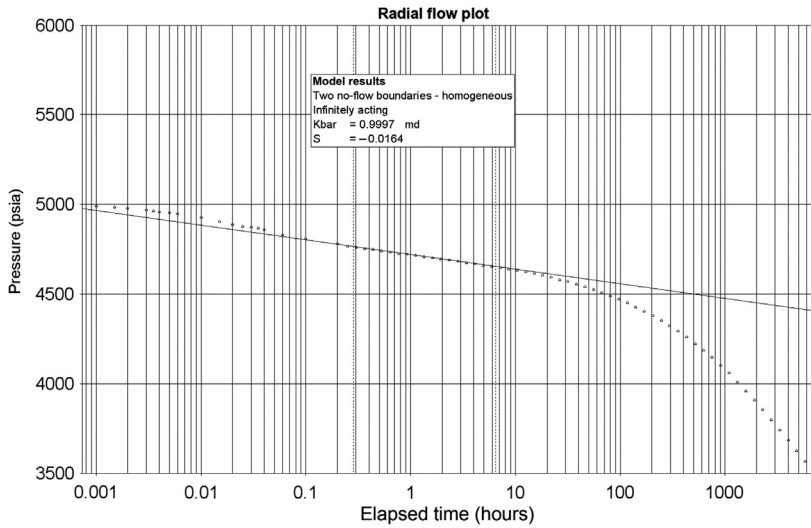
**FIGURE 12.3**

Measured bottom-hole pressures and oil production rates during a pressure drawdown test.



**FIGURE 12.4**

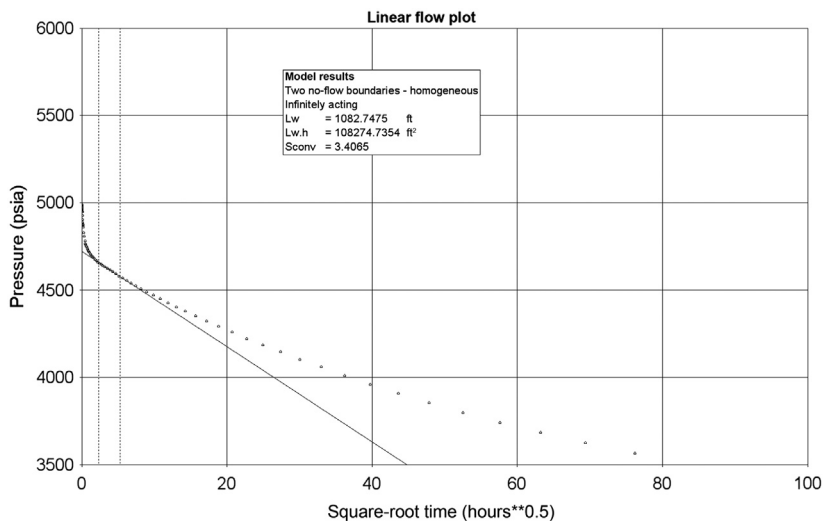
Log-log diagnostic plot of test data.



**FIGURE 12.5**

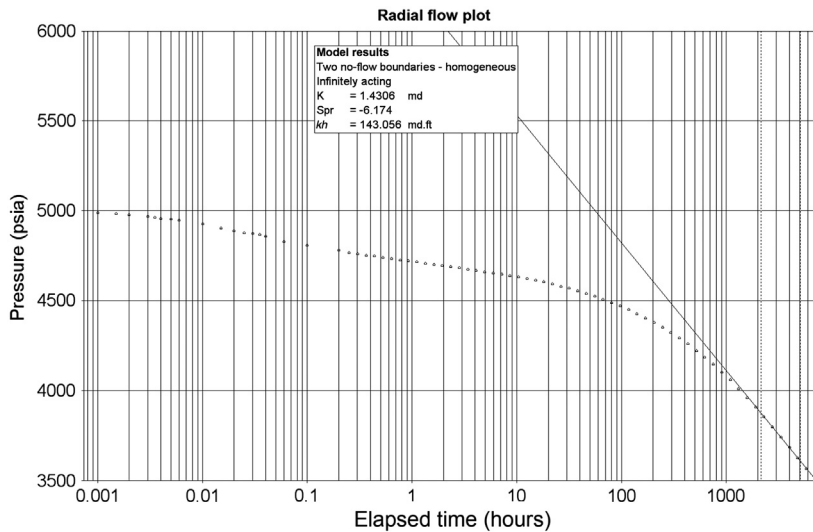
Semi-log plot for vertical radial flow analysis.





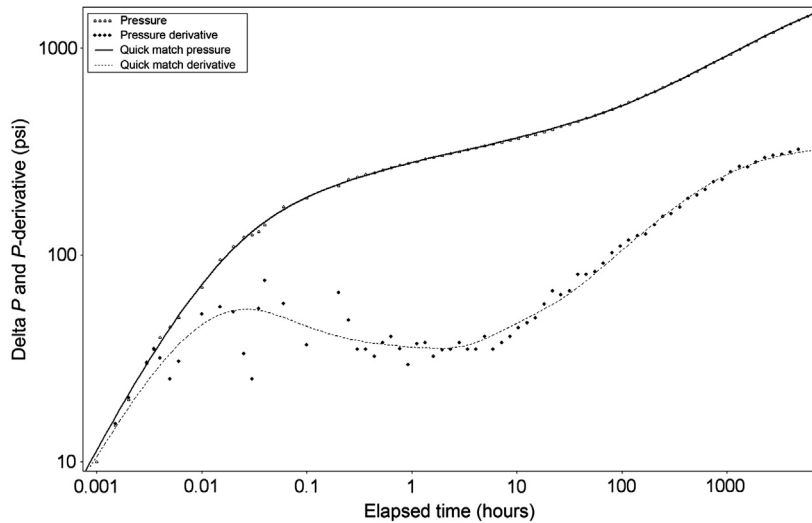
**FIGURE 12.6**

Square-root time plot for pseudo-linear flow analysis.



**FIGURE 12.7**

Semi-log plot for horizontal pseudo-radial flow analysis.



**FIGURE 12.8**

Match between measured and model calculated pressure data.

## 12.3 EXCESSIVE GAS PRODUCTION

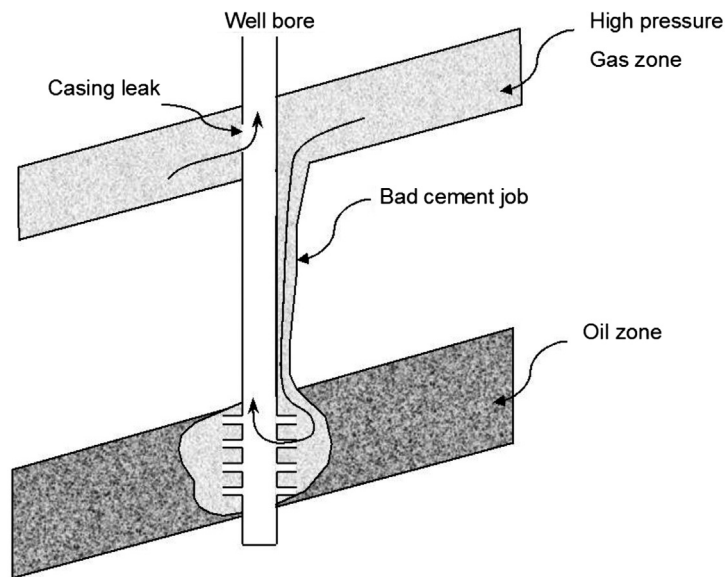
Excessive gas production is usually due to channeling behind the casing (Fig. 12.9), preferential flow through high-permeability zones (Fig. 12.10), gas coning (Fig. 12.11), and casing leaks (Clark and Schultz, 1956).

The channeling behind the casing and gas coning problems can be identified based on production logging such as temperature and noise logs. An example is depicted in Fig. 12.12, where both logs indicate that gas is being produced from an upper gas sand and channeling down to some perforations in the oil zone.

Excessive gas production of an oil well could also be due to gas production from unexpected gas zones. This can be identified using production logging such as temperature and density logs. An example is presented in Fig. 12.13, where both logs indicate gas production from the thief zone B.

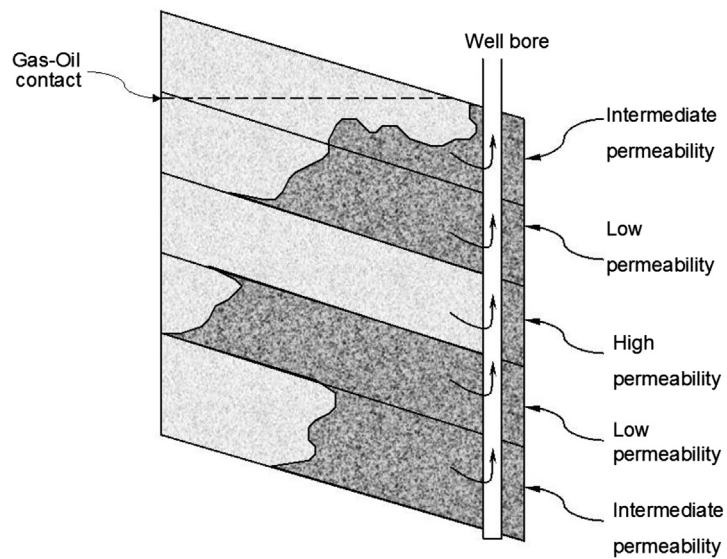
## 12.4 EXCESSIVE WATER PRODUCTION

Excessive water production is usually from water zones, not from the connate water in the pay zone. Water enters the wellbore due to channeling behind the casing (Fig. 12.14), preferential flow through high-permeability zones (Fig. 12.15), water coning (Fig. 12.16), hydraulic fracturing into water zones, and casing leaks.



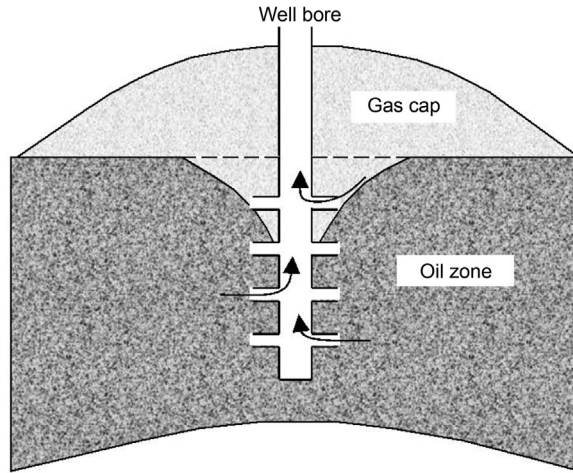
**FIGURE 12.9**

Gas production due to channeling behind the casing (Clark and Schultz, 1956).

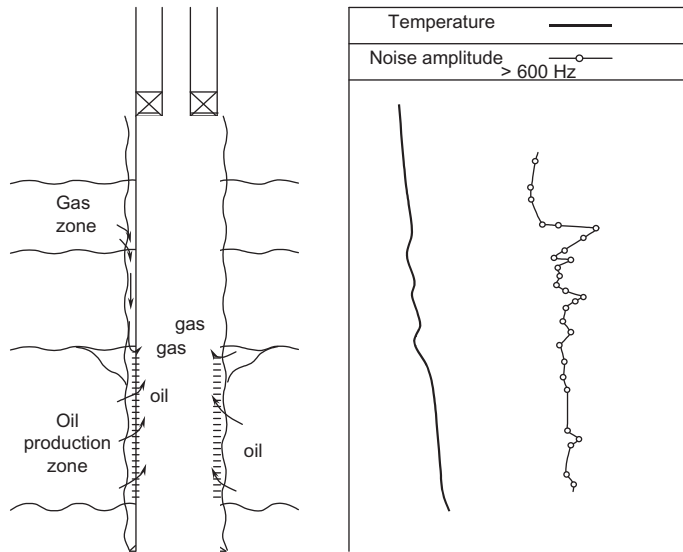


**FIGURE 12.10**

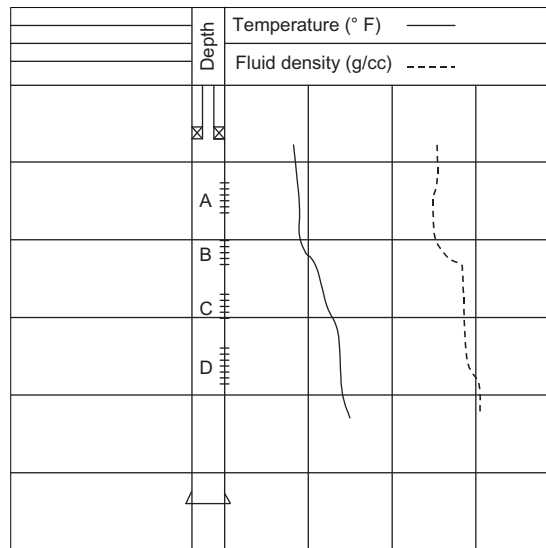
Gas production due to preferential flow through high-permeability zones (Clark and Schultz, 1956).



**FIGURE 12.11**  
Gas production due to gas coning (Clark and Schultz, 1956).

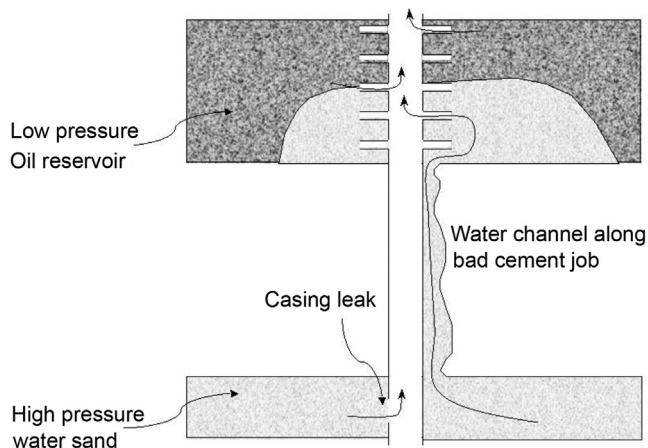


**FIGURE 12.12**  
Temperature and noise logs identifying gas channeling behind casing (Economides et al., 1994).



**FIGURE 12.13**

Temperature and fluid density logs identifying a gas entry zone (Economides et al., 1994).

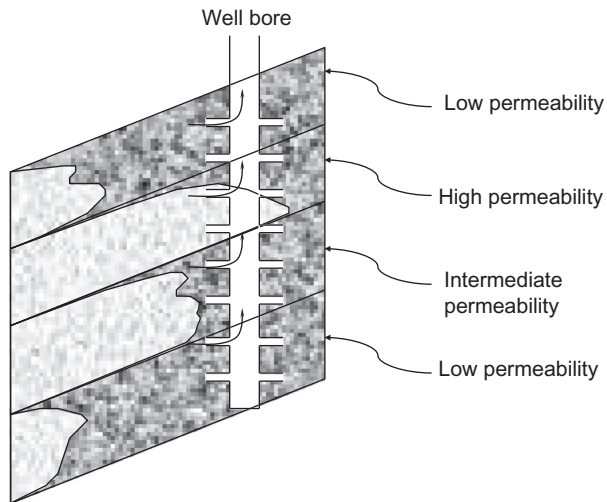


**FIGURE 12.14**

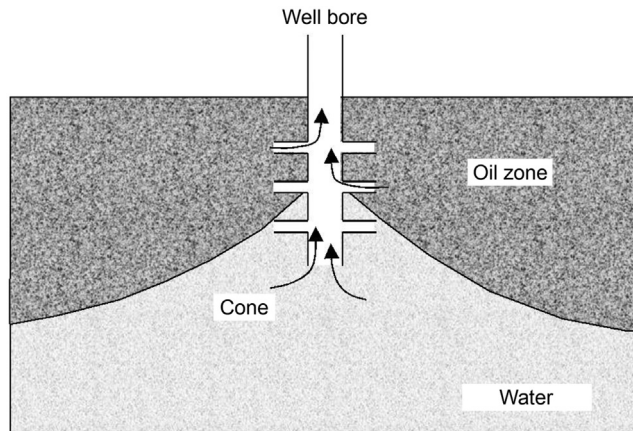
Water production due to channeling behind the casing.

Fig. 12.17 shows how to identify fracture height using prefracture and postfracture temperature logs to tell whether the hydraulic fracture has extended into a water zone.

In addition to those production logging tools that are mentioned in the previous section, other production logging tools can be used for identifying water-producing zones. Fluid density logs are

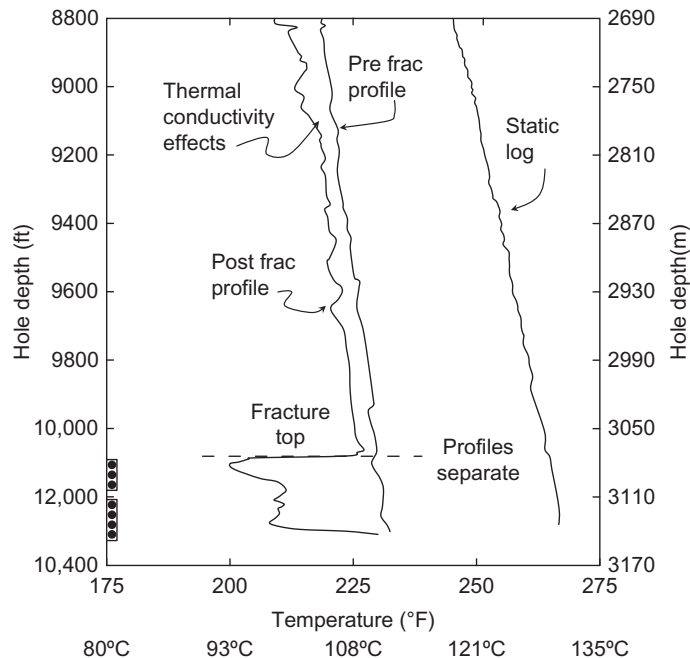
**FIGURE 12.15**

Preferential water flow through high-permeability zones.

**FIGURE 12.16**

Water production due to water coning.

especially useful for identifying water entries. Comparison between water-cut data and spinner flowmeter log can sometimes give an idea of where the water is coming from. Fig. 12.18 shows a spinner flowmeter log identifying a watered zone at the bottom of a well with a water-cut of nearly 50%.



**FIGURE 12.17**

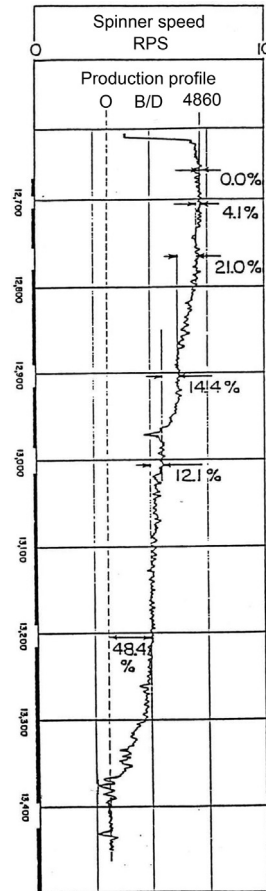
Prefracture and postfracture temperature logs identifying fracture height (Dobkins, 1981).

## 12.5 LIQUID LOADING OF GAS WELLS

Gas wells usually produce natural gas-carrying liquid water and/or condensate in the form of mist. As the gas flow velocity in the well drops because of reservoir pressure depletion, the carrying capacity of the gas decreases.

When the gas velocity drops to a critical level, liquids begin to accumulate in the well and the well flow can undergo an annular flow regime followed by a slug flow regime. The accumulation of liquids (liquid loading) increases the bottom-hole pressure, which reduces gas production rate. A low gas production rate will cause gas velocity to drop further. Eventually, the well will undergo a bubbly flow regime and cease producing.

Several measures can be taken to solve the liquid-loading problem. Foaming the liquid water can enable the gas to lift water from the well. Using smaller tubing or creating a lower wellhead pressure sometimes can keep mist flowing. The well can be unloaded by gas-lifting or pumping the liquids out of the well. Heating the wellbore can prevent oil condensation. Down-hole injection of water into an underlying disposal zone is another option. However, liquid-loading is not always obvious and recognizing the liquid-loading problem is not an easy task. A thorough diagnostic analysis of well data needs to be performed. The symptoms to look for include onset of liquid slugs at



**FIGURE 12.18**

Spinner flowmeter log identifying a watered zone at bottom.

the surface of well, increasing difference between the tubing and casing pressures with time, sharp changes in gradient on a flowing pressure survey, and sharp drops in production decline curve.

### 12.5.1 THE TURNER ET AL. METHOD

Turner et al. (1969) were the pioneer investigators who analyzed and predicted the minimum gas flow rate to prevent liquid-loading. They presented two mathematical models to describe the liquid-loading problem: the film-movement model and the entrained drop movement model. On the basis of analyses on field data, they concluded that the film-movement model does not represent the controlling liquid transport mechanism.



Turner et al.'s entrained drop movement model was derived on the basis of the terminal free settling velocity of liquid drops and the maximum drop diameter corresponding to the critical Weber number of 30. Turner et al.'s terminal slip velocity equation is expressed in U.S. field units as

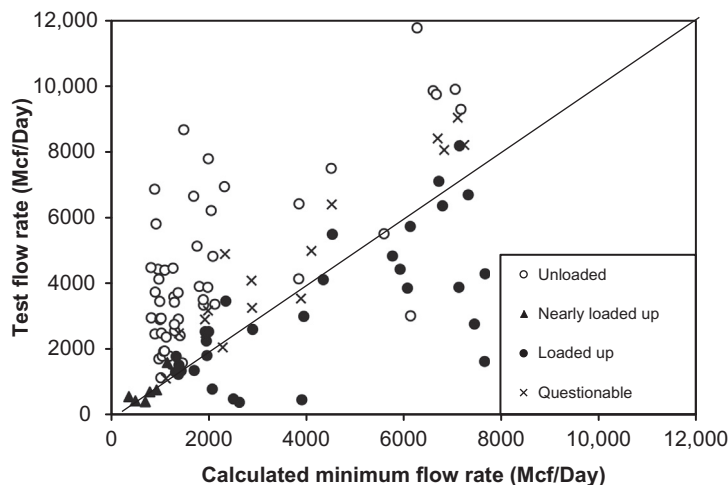
$$v_{sl} = \frac{1.3\sigma^{1/4}(\rho_L - \rho_g)^{1/4}}{C_d^{1/4} \rho_g^{1/2}} \quad (12.23)$$

According to Turner et al., gas will continuously remove liquids from the well until its velocity drops to below the terminal slip velocity. The minimum gas flow rate (in MMcf/D) for a particular set of conditions (pressure and conduit geometry) can be calculated using Eqs. (12.23) and (12.24):

$$Q_{gs/MM} = \frac{3.06pv_{sl}A}{T_z} \quad (12.24)$$

Fig. 12.19 shows a comparison between the results of Turner et al.'s entrained drop movement model. The map shows many loaded points in the unloaded region. Turner et al. recommended the equation-derived values be adjusted upward by approximately 20% to ensure removal of all drops. Turner et al. believed that the discrepancy was attributed to several factors including the use of drag coefficients for solid spheres, the assumption of stagnation velocity, and the critical Weber number established for drops falling in air, not in compressed gas.

The main problem that hinders the application of Turner et al.'s entrained drop model to gas wells comes from the difficulties of estimating the values of fluid density and pressure. Using an average value of gas-specific gravity (0.6) and gas temperature (120°F), Turner et al. derived an expression for gas density as 0.0031 times the pressure. However, they did not present a method for calculating the gas pressure in a multiphase flow wellbore. The spreadsheet program *TurnerLoading.xls* has been developed for quick calculation associated with this book.



**FIGURE 12.19**

Calculated minimum flow rates with the Turner et al. model and test flow rates.

Turner et al.'s entrained drop movement model was later modified by a number of authors. Coleman et al. (1991) suggested to use Eq. (12.23) with a lower constant value. Nosseir et al. (2000) expanded Turner et al.'s entrained drop model to more than one flow regime in a well. Lea and Nickens (2004) made some corrections to Turner et al.'s simplified equations. However, the original drawbacks (neglected transport velocity and multiphase flow pressure) with Turner et al.'s approach still remain unsolved.

## 12.5.2 THE GUO ET AL. METHOD

Starting from Turner et al.'s entrained drop model, Guo et al. (2006) determined the minimum kinetic energy of gas that is required to lift liquids. A four-phase (gas, oil, water, and solid particles) mist-flow model was developed. Applying the minimum kinetic energy criterion to the four-phase flow model resulted in a closed-form analytical equation for predicting the minimum gas flow rate.

### 12.5.2.1 Minimum kinetic energy

Kinetic energy per unit volume of gas can be expressed as

$$E_k = \frac{\rho_g v_g^2}{2g_c} \quad (12.25)$$

Substituting Eq. (12.23) into Eq. (12.25) gives an expression for the minimum kinetic energy required to keep liquid droplets from falling:

$$E_{ksl} = 0.026 \sqrt{\frac{\sigma(\rho_L - \rho_g)}{C_d}} \quad (12.26)$$

If the value of drag coefficient  $C_d = 0.44$  (recommended by Turner et al.) is used and the effect of gas density is neglected (a conservative assumption), Eq. (12.26) becomes

$$E_{ksl} = 0.04 \sqrt{\sigma \rho_L} \quad (12.27)$$

In gas wells producing water, typical values for water–gas interfacial tension and water density are 60 dynes/cm and 65 lb<sub>m</sub>/ft<sup>3</sup>, respectively. This yields the minimum kinetic energy value of 2.5 lb<sub>f</sub>-ft/ft<sup>3</sup>. In gas wells producing condensate, typical values for condensate–gas interfacial tension and condensate density are 20 dynes/cm and 45 lb<sub>m</sub>/ft<sup>3</sup>, respectively. This yields the minimum kinetic energy value of 1.2 lb<sub>f</sub>-ft/ft<sup>3</sup>.

The minimum gas velocity required for transporting the liquid droplets upward is equal to the minimum gas velocity required for floating the liquid droplets (keeping the droplets from falling) plus the transport velocity of the droplets, that is,

$$v_{gm} = v_{sl} + v_{tr} \quad (12.28)$$

The transport velocity  $v_{tr}$  may be calculated on the basis of liquid production rate, geometry of the conduit, and liquid volume fraction, which is difficult to quantify. Instead of trying to formulate an expression for the transport velocity  $v_{tr}$ , Guo et al. used  $v_{tr}$  as an empirical constant to lump the effects of nonstagnation velocity, drag coefficients for solid spheres, and the critical Weber number established for drops falling in air. On the basis of the work by Turner et al., the value of  $v_{tr}$  was taken as 20% of  $v_{sl}$  in this study. Use of this value results in

$$v_{gm} \approx 1.2v_{sl} \quad (12.29)$$

Substituting Eqs. (12.23) and (12.29) into Eq. (12.25) results in the expression for the minimum kinetic energy required for transporting the liquid droplets as

$$E_{km} = 0.0576\sqrt{\sigma\rho_L}. \quad (12.30)$$

For typical gas wells producing water, this equation yields the minimum kinetic energy value of 3.6 lb<sub>f</sub>-ft/ft<sup>3</sup>. For typical gas wells producing condensate, this equation gives the minimum kinetic energy value of 1.73 lb<sub>f</sub>-ft/ft<sup>3</sup>. These numbers imply that the required minimum gas production rate in water-producing gas wells is approximately twice that in condensate-producing gas wells.

To evaluate the gas kinetic energy  $E_k$  in Eq. (12.25) at a given gas flow rate and compare it with the minimum required kinetic energy  $E_{km}$  in Eq. (12.30), the values of gas density  $\rho_g$  and gas velocity  $v_g$  need to be determined. Expressions for  $\rho_g$  and  $v_g$  can be obtained from ideal gas law:

$$\rho_g = \frac{2.7S_g p}{T} \quad (12.31)$$

$$v_g = 4.71 \times 10^{-2} \frac{TQ_G}{A_i p} \quad (12.32)$$

Substituting Eqs. (12.31) and (12.32) into Eq. (12.25) yields

$$E_k = 9.3 \times 10^{-5} \frac{S_g T Q_G^2}{A_i^2 p}. \quad (12.33)$$

Eq. (12.33) indicates that the gas kinetic energy decreases with increased pressure, which means that the controlling conditions are bottom-hole conditions where gas has higher pressure and lower kinetic energy. This analysis is consistent with the observations from air drilling operations where solid particles accumulate at the bottom-hole rather than at the top-hole. However, this analysis is in contradiction with the results by Turner et al., which indicated that the wellhead conditions are, in most instances, controlling.

### 12.5.2.2 Four-phase flow model

To accurately predict the bottom-hole pressure  $p$  in Eq. (12.33), a gas-oil-water-solid four-phase mist-flow model was developed by Guo et al. (2006). According to the four-phase flow model, the flowing pressure  $p$  at depth  $L$  can be solved numerically from the following equation:

$$\begin{aligned} & 144b(p - p_{hf}) + \frac{1 - 2bm}{2} \ln \left| \frac{(144p + m)^2 + n}{(144p_{hf} + m)^2 + n} \right| \\ & b(P - P_{hf}) + \frac{1 - 2bm}{2} \ln \left| \frac{(144p + m)^2 + n}{(144p_{hf} + m)^2 + n} \right| \\ & - \frac{m + \frac{b}{c}n - bm^2}{\sqrt{n}} \left[ \tan^{-1} \left( \frac{144p + m}{\sqrt{n}} \right) - \tan^{-1} \left( \frac{144p_{hf} + m}{\sqrt{n}} \right) \right] \\ & = a(1 + d^2e)L, \end{aligned} \quad (12.34)$$

where

$$a = \frac{15.33S_sQ_s + 86.07S_wQ_w + 86.07S_oQ_o + 18.79S_gQ_G}{10^3T_{av}Q_G} \times \cos(\theta), \quad (12.35)$$

$$b = \frac{0.2456Q_s + 1.379Q_w + 1.379Q_o}{10^3T_{av}Q_G}, \quad (12.36)$$

$$c = \frac{6.785 \times 10^{-6}T_{av}Q_G}{A_i}, \quad (12.37)$$

$$d = \frac{Q_s + 5.615(Q_w + Q_o)}{600A_i}, \quad (12.38)$$

$$e = \frac{6f}{gD_h \cos(\theta)}, \quad (12.39)$$

$$f_M = \left[ \frac{1}{1.74 - 2 \log \left( \frac{2\epsilon'}{D_h} \right)} \right]^2, \quad (12.40)$$

$$m = \frac{cde}{1 + d^2e}, \quad (12.41)$$

and

$$n = \frac{c^2e}{(1 + d^2e)^2}, \quad (12.42)$$

where

- $A$  = cross-sectional area of conduit, ft<sup>2</sup>
- $D_h$  = hydraulic diameter, in.
- $f_M$  = Moody friction factor
- $g$  = gravitational acceleration, 32.17 ft/s<sup>2</sup>
- $L$  = conduit length, ft
- $p$  = pressure, psia
- $p_{hf}$  = wellhead flowing pressure, psia
- $Q_G$  = gas production rate, Mscf/day
- $Q_o$  = oil production rate, bbl/day
- $Q_s$  = solid production rate, ft<sup>3</sup>/day
- $Q_w$  = water production rate, bbl/day
- $S_g$  = specific gravity of gas, air = 1
- $S_o$  = specific gravity of produced oil, freshwater = 1
- $S_w$  = specific gravity of produced water, freshwater = 1
- $S_s$  = specific gravity of produced solid, freshwater = 1
- $T_{av}$  = the average temperature in the butting, °R
- $\epsilon'$  = pipe wall roughness, in.
- $\theta$  = inclination angle, °

### 12.5.2.3 Minimum required gas production rate

A logical procedure for predicting the minimum required gas flow rate  $Q_{gm}$  involves calculating gas density  $\rho_g$ , gas velocity  $v_g$ , and gas kinetic energy  $E_k$  at bottom-hole condition using an assumed gas flow rate  $Q_G$ , and compare the  $E_k$  with  $E_{km}$ . If the  $E_k$  is greater than  $E_{km}$ , the  $Q_G$  is higher than the  $Q_{gm}$ . The value of  $Q_G$  should be reduced and the calculation should be repeated until the  $E_k$  is very close to  $E_{km}$ . Because this procedure is tedious, a simple equation was derived by Guo et al. for predicting the minimum required gas flow rate in this section. Under the minimum unloaded condition (the last point of the mist flow regime), Eq. (12.33) becomes

$$E_{km} = 9.3 \times 10^{-5} \frac{S_g T_{bh} Q_{gm}^2}{A_i^2 p}, \quad (12.43)$$

which gives

$$p = 9.3 \times 10^{-5} \frac{S_g T_{bh} Q_{gm}^2}{A_i^2 E_{km}}. \quad (12.44)$$

Substituting Eq. (12.44) into Eq. (12.34) results in

$$144b\alpha_1 + \frac{1-2bm}{2} \ln \alpha_2 - \frac{m + \frac{b}{c}n - bm^2}{\sqrt{n}} \times [\tan^{-1}\beta_1 - \tan^{-1}\beta_2] = \gamma, \quad (12.45)$$

where

$$\alpha_1 = 9.3 \times 10^{-5} \frac{S_g T_{bh} Q_{gm}^2}{A_i^2 E_{km}} - p_{hf}, \quad (12.46)$$

$$\alpha_2 = \frac{\left(1.34 \times 10^{-2} \frac{S_g T_{bh} Q_{gm}^2}{A_i^2 E_{km}} + m\right)^2 + n}{(144p_{hf} + m)^2 + n}, \quad (12.47)$$

$$\beta_1 = \frac{1.34 \times 10^{-2} \frac{S_g T_{bh} Q_{gm}^2}{A_i^2 E_{km}} + m}{\sqrt{n}}, \quad (12.48)$$

$$\beta_2 = \frac{144p_{hf} + m}{\sqrt{n}}, \quad (12.49)$$

and

$$\gamma = a(1 + d^2 e)L. \quad (12.50)$$

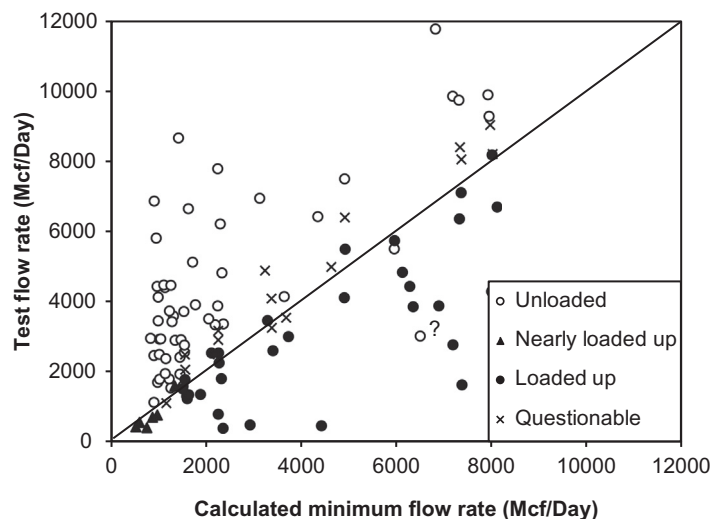
All the parameter values should be evaluated at  $Q_{gm}$ . The minimum required gas flow rate  $Q_{gm}$  can be solved from Eq. (12.45) with a trial-and-error or numerical method such as the Bisection method. It can be shown that Eq. (12.45) is a one-to-one function of  $Q_{gm}$  for  $Q_{gm}$  values greater than zero. Therefore, the Newton–Raphson iteration technique can also be used for solving  $Q_{gm}$ . Commercial software packages such as MS Excel can be used as solvers. In fact, the Goal Seek function built into MS Excel was used for generating solutions presented in this chapter. The spreadsheet program is named *GasWellLoading.xls*.

**Example Problem 12.2** To demonstrate how to use Eq. (12.45) for predicting the minimum unloading gas flow rate, consider a vertical gas well producing 0.70 specific gravity gas and 50 bbl/day condensate through a 2.441-in. inside diameter (ID) tubing against a wellhead pressure of 900 psia. Suppose the tubing string is set at a depth of 10,000 ft, and other data are given in Table 12.1.

**Solution** The solution given by the spreadsheet program *GasWellLoading.xls* is shown in Table 12.2.

Gas-specific gravity	0.7 (air = 1)
Hole inclination	0°
Wellhead temperature	60°
Geothermal gradient	0.01 °F/ft
Condensate gravity	60 °API
Water-specific gravity	1.05 (water = 1)
Solid-specific gravity	2.65 (water = 1)
Interfacial tension	20 dyne/cm
Tubing wall roughness	0.000015 in.

<b>Calculated Parameters</b>	
Hydraulic diameter	0.2034 ft
Conduit cross-sectional area	0.0325 ft <sup>2</sup>
Average temperature	570 °R
Minimum kinetic energy	1.6019 lb-ft/ft <sup>3</sup>
$a =$	2.77547E-05
$b =$	1.20965E-07
$c =$	875999.8117
$d =$	0.10598146
$e =$	0.000571676
$f_M =$	0.007481992
$m =$	53.07387106
$n =$	438684299.6
<b>Solution</b>	
Critical gas production rate	1059 Mscf/day
Pressure ( $p$ ) =	1189 psia
Objective function $f(Q_{gm}) =$	-1.78615E-05



**FIGURE 12.20**

The minimum flow rates given by the Guo et al. model and the test flow rates.

### 12.5.3 COMPARISON OF THE TURNER ET AL. AND THE GUO ET AL. METHODS

Fig. 12.20 illustrates Eq. (12.45)—calculated minimum flow rates mapped against the test flow rates for the same wells used in Fig. 12.19. This map shows six loaded points in the unloaded region, but they are very close to the boundary. This means the Guo et al. method is more accurate than the Turner et al. method in estimating the minimum flow rates.

## 12.6 FORMATION DAMAGE

Formation damage is generally referred to as permeability impairment in petroleum reservoirs, which can occur during almost every field operation, including drilling, completion, production and workover operations, stimulation and remedial treatments, as well as waterflooding, thermal and other enhanced recovery processes. When the productivity or injectivity of a well is lower than expected, it may be caused by formation damage. Some mechanical factors such as limited perforation or partial penetration may also be a factor. Understanding the causes of formation damage is the first step toward the successful control and prevention of formation damage. Various aspects of formation damage have been reviewed in detail by Krueger (1986) and Ameafule et al. (1988). In the following sections, damage sources, factors, and field operations that affect formation damage are discussed.

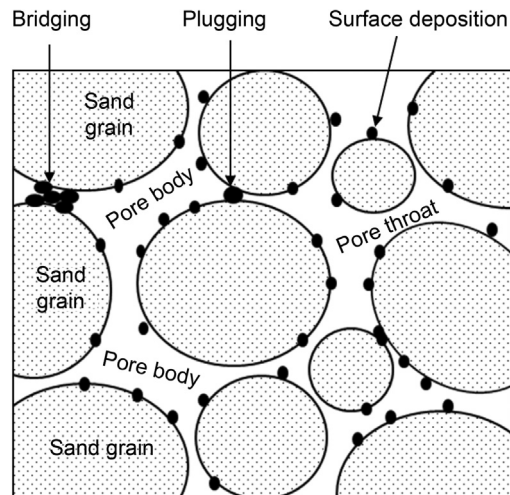
### 12.6.1 DAMAGE SOURCES

During reservoir development, any changes to rock-fluid and fluid-fluid equilibrium conditions can cause formation damage. Most of the most damage usually occurs in the near wellbore region or around the face of hydraulic fractures. Common sources of formation damage include fines migration, clay swelling, scale precipitation, organic precipitation, emulsion and water block, and wettability alteration, etc. It has been generally recognized that fines migration, clay swelling, scale precipitation, and organic precipitation are the most commonly occurring sources for formation damage.

#### 12.6.1.1 Fines migration

Porous media in typical petroleum reservoirs can be viewed to consist of pore throats and pore bodies. As fine particles travel along tortuous pore spaces, particle retention can take three forms: surface deposition, bridging, and plugging, as illustrated in Fig. 12.21 (Liu and Civan, 1995). Among these particle retention mechanisms, it is particle bridging and plugging that causes most damage to the formation. Fines that cause formation damage can be either externally introduced or in-situ generated.

When external particles enter the formation, they will fill and plug the pore spaces of the formation near the wellbore and severely reduce the formation permeability. The depth of invasion of fine particles from the wellbore into the formation is dependent on the structure and size of formation pores as well as the shape and size of the particles. Deeper invasion into the formation is favored by large pore size and small particle size. The depth of invasion can be significant if the formation is highly fractured. Once the formation near wellbore becomes totally filled or plugged by particles, a filter cake is established on the formation face, preventing additional particle



**FIGURE 12.21**

Schematic of formation damage due to fines migration.



invasion. Although the external particles usually cannot invade the formation deeply, such an invading process causes extremely severe damage in the formation near wellbore.

Formation fines can be easily generated in unconsolidated formations during production and reservoir depletion. The problem becomes more severe with larger drawdown pressures and higher production rates. The onset of water production can make the problem worse, as there is a lack of cementation between sand grains and water weakens the bond between grains. These fines will migrate and accumulate in the near wellbore area and inside the wellbore, causing formation damage, sand production, and damages to downhole equipment and surface facilities.

Nearly all petroleum-bearing, sedimentary formations contain fines and clay minerals. Formation fines are composed of quartz, silica, feldspar, mica, calcite, dolomite, siderite, and chloride. The clay minerals commonly found in reservoirs include smectite, kaolinite, chlorite, and illite. Clays and fine particles are attached to pore surfaces by various forces such as van der Waals, electrical double layer, and hydrodynamic forces. However, rock fluid interactions, high flow velocity, and low salinity of the injected fluids can counteract these forces and often lead to the mobilization of fines. These particles then migrate along the flow paths until they are captured in pore constrictions, and cause formation damage. Investigations by [Gray and Rex \(1966\)](#) and [Khilar and Fogler \(1983\)](#) indicate that formation damage in water-sensitive sandstone formations is predominately caused by clay particles. These clay minerals usually occur as loose pore-filling or pore-lining aggregates in the formations. A small proportion of clay particles in flowing fluids can make a relatively high contribution to formation damage due to their swelling, plastic, and colloidal properties as well as plate-shaped structures.

### **12.6.1.2 Clay minerals**

The presence of clays in petroleum reservoirs is a major factor for formation damage. In order to understand the effects of clays on formation damage, it is important to know their origin and crystal structure. Clays in sedimentary rocks may have two different origins: detrital and authigenic (diagenetic) clays ([Almon, 1977](#)). Detrital clays, which form an integral part of rock framework and are abundant in shale formations, usually do not cause damage to petroleum-bearing formations. Authigenic clays exist as deposits lined or filled in the pore system and do cause formation damage upon contact with various incompatible aqueous fluids during field operations. Clay minerals are composed of hydrous aluminum silicates of either tetrahedral or octahedral patterns. The crystals combine in sheets or layers. Clay minerals can be described according to the pattern of layering of the tetrahedral and octahedral sheets and are referred to as 1:1 or 2:1 type. A type 1:1 clay mineral contains layers of tetrahedral and octahedral crystals in a 1:1 ratio. A type 2:1 clay mineral contains two tetrahedral layers for every octahedral layer. The ratio affects the water adsorption potential of the clay mineral. The basic structure of clay minerals is commonly plate-shaped due to the layering phenomenon. However, elongated, hair-like, and fibrous forms also occur when crystal units combine in a less orderly fashion. The size of clay mineral ranges from a few micrometers down to 0.01 micrometers, which is similar to the size range of colloidal matter ([Brindley, 1981](#)). [Almon and Davies \(1981\)](#) and [Porter \(1989\)](#) describe four major types of clay minerals: kaolinite, smectite (montmorillonite), illite, and chlorite. Each type of clay exhibits a particular problem and has the tendency to cause formation damage.

Kaolinite is a 1:1 type clay composed of one tetrahedral sheet and one octahedral sheet bound together by strong hydrogen bonds. Kaolinite exhibits little or no swelling characteristics and occurs as platy structures. The maximum dimension of a kaolinite particle ranges between 2 to 4

microns. Kaolinites are usually attached loosely to the pore surfaces of the host rock and are released into aqueous fluids by fluid-fluid interactions.

Smectite is a 2:1 type clay composed of two tetrahedral and one octahedral layers bound together by weak interactive forces. Smectites and mixed-layer clays are referred to as swelling clays. Smectites in particular contain large amounts of sodium ions that cause the mineral to adsorb water and swell several times the original volume in the presence of fresh water. The swelling of smectites on pore surfaces reduces the porosity and permeability of the formation. Smectites can also be released from pore surfaces and migrate during swelling.

Illite is a hydrous mica and a typical example of the 2:1 type clay. Illite has several crystal structures and sometimes forms an irregular fibrous network in the pore space, reducing the capacity of fluid flow. Illite can also swell when it co-exists with smectite.

Chlorites are a group of 2:1 type clays and often contain large amounts of iron. During the treatment of hydrochloric acid, chlorites will readily dissolve and the iron will be liberated. When the acid has spent, the liberated iron will then re-precipitate as a gelatinous ferric hydroxide,  $\text{Fe}(\text{OH})_3$ , which has a large crystal size and plugs pore throats (Almon and Davies, 1981).

Factors that affect formation damage caused by fines and clays include particle and pore size distribution, mobilization and retention forces, salt concentrations, flow rates, pore pressure, and temperature, etc. Among these factors, salt concentrations and flow rates are the most important, and worth discussing in detail.

### **12.6.1.3 Salt concentrations**

The concentration of electrolytes in aqueous fluids has significant effects on clay particles, which are negatively charged due to isomorphous substitution of elements in the crystal lattice (Brindley, 1981). Pore walls of sandstone formations are similarly charged. When a charged surface is placed in an aqueous fluid, an electrical double layer is observed at the surface of the particle. The double layer consists of an inner layer of adsorbed ions (Stern layer) and an outer layer of diffusely held ions (diffuse layer). The electrical field near the charged surface decays exponentially with increasing distance from the particle surface. The thickness of the diffuse layer (Debye length) is inversely proportional to the square-root of the electrolyte concentration. A double layer is developed similarly at the pore wall. When the two charged surfaces approach each other, interactions of the two double layers occur (Hirasaki, 1991). Salinity has a marked effect on water-sensitive formations. Before fresh water is injected into a water-sensitive formation, clays are held on rock surfaces in the formation brine by the net attractive surface forces (van der Waals attractive and electrical double layer repulsive forces). In concentrated brine solution, the diffuse layers are compressed. Consequently, the double layer repulsive forces are less compared to van der Waals attractive forces and clay particles are kept on rock surfaces. As fresh water is injected into the formation, the salinity of the formation brine decreases, the double layers expand, and the double layer forces increase. When the net surface forces can no longer keep clay particles in place, they will be released, migrate, and then plug pore constrictions along the flow path. Khilar and Fogler (1983) determined that a critical salt concentration exists below which the release of clay particles occurs.

### **12.6.1.4 Flow rates**

Fine particles loosely attached on pore surfaces can also move if viscous drag promotes such movement. Gruesbeck and Collins (1982) studied the entrainment and deposition of fine particles in

porous media. A major finding was the observance of a critical velocity, below which entrainment of particles from pore surfaces cannot occur, and above which the rate of entrainment is proportional to the flow rate. Other researchers confirmed the existence of the critical velocity (Gabriel and Inamdar, 1983).

#### **12.6.1.5 Scale precipitation**

Changes in reservoir conditions and/or the mixing of formation water with incompatible injection fluids can lead to chemical reactions, cause some water-soluble chemicals to precipitate out of the aqueous solution as scales, and thus result in formation damage. Scale precipitation can cause both formation and facility damage as it can occur in the reservoir, inside the well and surface facilities. The injection fluids can also dissolve minerals on the pore surface of the formation. The dissolved minerals can then migrate with the injection fluids and precipitate deeper in the formation as reservoir conditions change. The precipitates can accumulate around pore throats and eventually block off flow paths, resulting in reduced permeability. The most common scales in oilfields are calcium carbonate, calcium sulfate, barium sulfate (Vetter, 1976); and other commonly occurring scales include iron scales, silica scales, sodium chloride, etc. Scale precipitation can occur due to any change to the fluid equilibrium conditions such as pressure drop, changes in temperature, hydrocarbon contents, and by other factors such as nucleation sites.

#### **12.6.1.6 Organic precipitation**

Asphaltenes and paraffins in crude oil are a source of potential organic precipitation (Chung et al., 1991). These organic compounds in crude oil can precipitate when the equilibrium is disturbed due to the changes in reservoir temperature and pressure as well as the change in the crude oil composition. These organic precipitates often occur on the tubing wall inside a well or around the near-wellbore area inside the reservoir. It can be quite expensive to treat organic precipitates (Ameaful et al., 1988). The mechanisms of organic precipitation are complex (Houchin and Hudson, 1986), but a change in temperature or pressure in the reservoir and/or the system is the main mechanism. Damage by organic scaling can not only cause plugging of formation pores but also alter the rock wettability. In the latter case, the rock tends to become more oil-wet, which reduces the relative permeability to oil.

#### **12.6.1.7 Wettability alteration**

Rock wettability is a major factor when determining the location and flow of fluids in a reservoir formation (Anderson, 1986). In a water-wet formation, water can contact the rock surfaces and occupy the smaller pore spaces. Similarly, in an oil-wet formation, oil can contact the pore surfaces and occupy the smaller pore spaces. Since sandstone formations were formed in aqueous environments, a water-wet condition is expected. However, when oil later migrated into sandstone formations, the oil displaced water from the larger pores, leaving a water film on the pore wall. If the water film broke, oil could contact the pore wall directly. The wettability of the pore wall was then altered by the adsorption of polar compounds or by the deposition of organic matter from the oil onto the rock surface. The degree of alteration in rock wettability is determined by the stability of the aqueous thin film, which depends on the composition of the oil, rock mineral surfaces, formation water, and surfactants introduced during field operation. When the rock surfaces of a formation exhibit oil-wet behavior, the surface area upon which water can come in contact is significantly

diminished. The transformation from water-wet to oil-wet in the near wellbore region is not advantageous for production of oil because it will cause a reduction in the relative permeability to oil.

Clays and fines present on the pore surfaces of a sedimentary rock are usually negatively charged and exhibit water-wet characteristics in their native state. Inorganic particles in injected water or water-based drilling and completion fluids are water-wet. Solids in oil-based and emulsion fluids are oil-wet or intermediately wet. The wettability of such particles plays an important role in formation damage occurring in multiphase systems. Muecke (1979) determined that particle wettability and interfacial tension strongly influence the movement of particles in multiphase flow systems. It was observed that fine particles remain in the wetting phase and therefore become mobile when the wetting phase moves. In addition, it was observed that fines of intermediate wettability are located at the interface of fluids.

The alteration of wettability to fines and rock surface affect both fine retention mechanisms and relative permeability values. In addition to these potential damages, formation damage can also be caused by the plugging of nonwetting droplets of liquid or gas at the pore throats due to adverse changes in rock wettability.

## 12.6.2 FORMATION DAMAGE FROM VARIOUS OILFIELD OPERATIONS

Although the occurrence of formation damage can vary from operation to operation, common field operations for chances of formation damage are briefly reviewed in this section. These operations include drilling, completion, production, stimulation, waterflooding, and enhanced oil recovery (EOR).

### 12.6.2.1 Drilling induced damage

Drilling mud pressure is usually maintained above formation pressure to prevent the reservoir fluid from flowing into wellbore, which can cause well blowout conditions. As a drillbit penetrates a petroleum bearing formation, the drilling mud invades the formation due to the positive differential pressure between the mud and reservoir fluids. Particles that are smaller in size than that of formation pores can enter the formation during mud spurt loss. They plug the formation around the wellbore and form an internal filter cake. Particles with a larger diameter than that of formation pores are either retained on the formation face, initiating the buildup of an external filter cake, or are entrained in the circulating mud by the shear forces exerted by the mud.

The formation of a low-permeability mud cake on the entire sand face effectively prevents additional drilling mud solids from entering the formation, but does not stop the mud filtrate. As the filtrate passes through the mud cake, the thickness of the mud cake increases by retaining the mud particles until a dynamic equilibrium is established. Under the equilibrium condition, the rate of deposition of mud particles on the mud cake by the fluid infiltration and rate of erosion of deposited particles by mud circulation are equalized and the cake thickness attains a constant value (Ferguson and Klotz, 1954). The plugging-off of the pore spaces of the formation around the wellbore and the complete formation of the low-permeability mud cake on the borehole wall eventually limits the mud filtrate invasion into the formation.

The mud solids and filtrate introduced into the reservoir during drilling operations can cause formation damage in the formation around the wellbore. Mud solids can reduce formation permeability by filling and plugging formation pores. Mud filtrate causes formation damage by

mobilizing formation fines, creating precipitates and altering rock wettability. Water based muds contain various chemicals that can react with the reservoir fluid and the formation resulting in precipitation. Oil based and invert emulsion muds that contain surfactants and emulsifiers can alter the wettability of the pore surface to oil wetness, which serves to reduce the effective permeability of the oil phase. The filtrate can mobilize the fine particles from pore surfaces into flowing fluids in the formation by colloidal and hydrodynamic forces. The mobilized fine particles then move along with the fluids until they are captured at pore constrictions or deposited on other pore surfaces thereby causing formation damage.

### ***12.6.2.2 Completion/Workover induced damage***

One of the major operations during well completion is cementing. The objective of a primary cementing operation is to seal the annulus between the casing and the formation. Cement slurry is usually pumped into a well through the casing in order to displace the drilling fluid from the pipe into the annulus. The cement filtrate invades the formation similarly to the mud filtrate, causing formation damage. The cementing operation does not last as long as the drilling. In addition, the cement slurry solidifies within hours. Therefore, the amount of cement filtrate invading the formation is believed to be very limited.

In order to improve the isolation between zones, turbulent flow, casing movements, and other mechanical means are used to remove the mud from the annulus. During this process, the mud cake can be destroyed or removed and the invasion of the cement filtrate will increase. Even so, the internal filter cake within the formation provides an effective barrier to excessive invasion of the cement filtrate. Various studies indicate that the cement slurry can cause formation damage due to interactions of the cement filtrate with formation fluids or minerals (Cunningham and Smith, 1968; Rahman and Marx, 1991).

Perforation can be another cause of formation damage. Detailed studies on this subject have been reported by Klotz et al. (1974). Although the rock around a perforation hole is pulverized during the perforating process, a damaged zone around the perforation tunnel about 1 cm thick is created with a permeability decrease up to 80% (Krueger, 1986). If perforation is performed under overbalanced pressure condition, completion fluids can invade the formation and cause additional damage. Completion and workover fluids damage is similar to drilling fluid damage and can be caused by both fluid and particle invasion.

### ***12.6.2.3 Production induced damage***

Formation damage associated with production operation includes sand or fines production, inorganic and organic scaling. In many cases, some wells are capable of high production rates, but do not perform as expected due to formation damage. Damage begins with fine particles that are loosely attached to pore walls, become mobilized at high flow rates, which can damage the formation as well as downhole and surface equipment. A high flow rate can also lead to an excessive reduction in the pore pressure, causing an increase in the effective stress and a decrease of permeability in consolidated formations. In addition, such excessive pressure drawdown can cause pore collapse in weakly consolidated sandstones, which promotes sand production.

Inorganic and organic scaling are common problems during production. Inorganic scales occur when the thermodynamic and chemical equilibrium of connate water is disturbed by changes in

reservoir temperature and pressure. Common inorganic scales are calcium carbonate, calcium sulfate, barium sulfate, and iron carbonate (Krueger, 1986).

#### **12.6.2.4 Stimulation induced damage**

A popular method to treat a damaged formation is to inject acids, such as hydrochloric and hydrofluoric acids, into the formation near the wellbore. Although the objective of acid stimulation is to remove damage and improve well productivity, acid treatments do not always increase well productivity. Occasionally, they may even reduce productivity. A solid understanding of damage mechanisms, formation mineralogy, and brine chemistry is necessary to obtain optimum results for acid treatments. For example, hydrofluoric acid can react with calcium compounds that are present in the formation, which can result in formation of insoluble precipitates. Calcium precipitates can be eliminated or reduced by the preflush of hydrochloric acid.

During acid treatment, some minerals are dissolved that may re-precipitate later. Fine particles loosely attached to pore surfaces can be mobilized during the acid treatment. Excessive acid treatment can dissolve the cementing materials of the formation, which will cause pore collapse and formation deconsolidation. Finally, surfactants that are used in acid treatment as corrosion inhibitors can change formation wettability to oil wetness.

Hydraulic fracturing, an effective means of increasing the productivity of a well, is also associated with formation damage. Electrical models and theoretical studies of steady-state and transient flow performance of fractured wells indicate that shallow damage to the formation immediately surrounding the fracture has little effect on the well productivity (Van Poollen, 1957; Cinco-Ley and Samaniego, 1981). If, for example, this damage is 3 in. deep and a 95% permeability reduction, the impairment to the well productivity can still be tolerated. However, damage within the fracture has a major effect on productivity reduction. The damage to the fracture flow capacity includes crosslinked gel plugging, proppant crushing, and formation fines plugging.

#### **12.6.2.5 Waterflooding and EOR induced damage**

Water quality control is important to the success of a waterflooding operation. As water is injected into the formation, suspensions in the water, such as solids, insoluble materials, bacteria, or emulsion droplets, will invade and plug the formation. The injected water can induce fines mobilization and form precipitates if it is incompatible with the formation brine or minerals.

Formation damage problems can be associated with various EOR processes. Chemical flooding, such as alkaline flooding, can lead to the dissolution of siliceous minerals in formations and the dissolved minerals can re-precipitate at a distance from the wellbore when conditions change. Yuan et al. (2001) presented a West Texas case study and showed the increased scale precipitation due to CO<sub>2</sub> flooding. Laboratory studies by Bennion et al. (1992) indicate that hot water injection and steam flooding have adverse effects on absolute permeability, relative permeability, wettability, and mineral composition of a clay-bearing sandstone reservoir. Polymer flooding can cause formation damage by polymer retention in the formation.

### **12.6.3 DAMAGE EVALUATION**

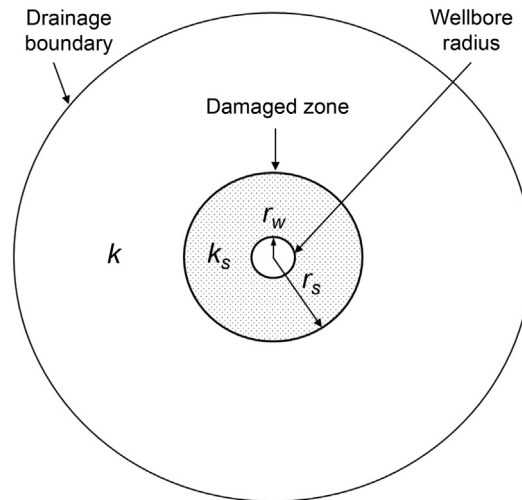
Hawkins (1956) first introduced the concept of skin factor to describe the effects of formation damage around a wellbore. A damaged region is represented as a zone of reduced permeability adjacent

to the wellbore. Fig. 12.22 represents the map view of a vertical well surrounded by a damaged zone in the near wellbore region. Based on a radial flow condition, Hawkins proposed the following equation to calculate the skin factor associated with this well:

$$s = \left( \frac{k}{k_s} - 1 \right) \ln \left( \frac{r_s}{r_w} \right) \quad (12.51)$$

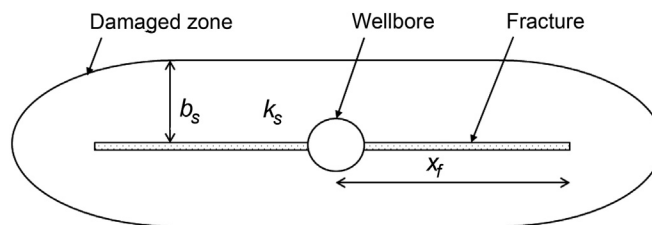
In this equation,  $r_w$  is the wellbore radius,  $r_s$  is the radius of the damaged zone with an average permeability  $k_s$ , and  $k$  is the reservoir permeability.

In a hydraulically fractured well, there is a similar skin factor that can be used to describe formation damage around a fracture, which is caused by fracturing fluid leak off. Fig. 12.23 illustrates the damaged zone around the fracture in a vertical well intersected by a vertical fracture, but the



**FIGURE 12.22**

Region of formation damage around a wellbore.



**FIGURE 12.23**

Region of formation damage around a hydraulic fracture.



reservoir is not shown here. [Cinco-Ley and Samaniego \(1981\)](#) provided an equation to quantify this skin damage factor as follows:

$$s_{fs} = \frac{\pi b_s}{2x_f} \left( \frac{k}{k_s} - 1 \right) \quad (12.52)$$

In this equation,  $b_s$  is the damage depth normal to the fracture face,  $k_s$  is the average permeability in the damaged zone,  $x_f$  is the fracture half-length, and  $k$  is the reservoir permeability.

In addition to the skin factors described above, there is another concept named pseudo-skin factor. The restriction to fluid flow in this case results from the low density and short distance of perforations and/or partial penetration/completion (i.e., a well is partially completed across the entire pay intervals). The pseudo-skin factor can be determined independently by other methods ([Hong, 1975](#); [Jones and Watts, 1971](#)). Once the pseudo-skin factor is calculated, it must be subtracted from the total skin factor obtained from the well test in order to obtain the skin factor from true formation damage.

Formation damage can be identified from field measurements and laboratory tests. Field measurements taken during well testing are used to calculate skin factors. A total skin factor obtained from the well test includes the effects of both true formation damage and pseudo-damage. Well testing is a powerful technique used to detect formation damage. It can provide an overall measure of formation damage, but not the radius and permeability of the damaged zone. Resistivity logs provide better information about the depth and degree of mud filtrate invasion, but filtrate invasion is not the same as formation damage. The well logs give qualitative indications of possible formation damage. Production history review and well performance analysis provide additional information that can be used to define formation damage.

Field measurements do not reveal the causes of formation damage, which is critical for successful control and remedy of formation damage. Causes of formation damage can be more fully defined in laboratory flow tests. Investigations of formation damage by means of conducting core tests are commonly used to determine the causes, degree, and extent of damage, as well as factors, such as critical velocity and critical salt concentration.

Petrographic evaluation of reservoir rocks provides another means of detecting formation damage. X-Ray fluoroscopy is used to determine the degree and extent of the invasion of drilling fluid solids into core samples, especially for unconsolidated and sleeved cores ([Ameafule et al., 1988](#)). X-Ray Computerized Tomography or CT Scanning provides detailed three-dimensional analyses of solids invasion, as well as fluid saturation, bulk density, and porosity. X-ray diffraction (XRD) analysis is widely used to determine the mineralogy of the bulk rock and clay minerals. Petrographic analyses of thin section rock samples provide information about the mineralogy of rock components and the morphology of pore systems. Scanning electron microscopy (SEM) is used to determine information about a rock sample, similar to thin section method.

#### 12.6.4 DAMAGE PREVENTION AND CONTROL

Formation damage is a constant theme faced by petroleum engineers, as it can cause a significant reduction in well productivity and economic return. In many cases, the cost of damage prevention is less costly than damage control or remedial actions. Every field operation can be a potential



source of formation damage. As a result, the aggregated damage is often a combination of complicated phenomena, with one or more damage mechanisms dominated under certain circumstances. Once the origins of formation damage are identified, appropriate remedial actions can be taken accordingly.

#### **12.6.4.1 Damage control by matrix acidizing**

Matrix acidizing is a commonly used technique for formation damage removal and control. Matrix acidizing is performed by injecting an acid fluid or a blend of acid fluids into the porous matrix of a formation with a bottom-hole pressure below the formation closure stress to prevent fracturing the formation. Hydrochloric acid (HCl) or organic acids are used for matrix acidizing in carbonate reservoirs, while a mixture of HCl and hydrofluoric acid (HF) is the main ingredient used for matrix acidizing in sandstone reservoirs. The goal of matrix acidizing is to remove flow restrictions caused by formation damage by dissolving some of the damaging materials and rock matrix in sandstone formations, or to bypass the damage by creating channels or wormholes in the carbonate rock matrix due to rapid reactions of acids with carbonate minerals.

Matrix acidizing is very effective to restore formation damage caused by invading solids, migrating fines, and swelling clays, in consolidated formations. Prevention of migrating fines and swelling clay minerals can be accomplished by using a clay-control process. Clay stabilizers are commonly used in completion and stimulation fluids to mitigate damage migrating fines and swelling clays. Matrix acidizing is not recommended to treat unconsolidated formations for a couple of reasons: (1) HF acid cannot dissolve a large amount of sand (quartz) in unconsolidated formations; and (2) acids will further weaken the formation. Additional chemicals are often added to the treating fluid system during matrix acidizing to remove organic damage, inhibit scale formation, and to reduce any potential side effects from the matrix treatment. The topic of matrix acidizing will be discussed in more detail in Chapter 13.

#### **12.6.4.2 Damage control by hydraulic fracturing**

When matrix acidizing is not effective, hydraulic fracturing can be used as an alternative for formation damage control. Regardless of damage origins or damage mechanisms, the objective of hydraulic fracturing is to bypass the damage in the near wellbore area rather than to remove it. The presence of a hydraulic fracture will change the flow pattern from radial flow to linear flow, increase the surface area for fluids to flow, and thus reduce flow velocities in the near wellbore region.

Formation damage tends to become worse in high-permeability reservoirs because higher production rate, higher pressure drawdown, and more rapid changes in reservoir conditions will make any potential damages more severe. High-permeability, high-porosity reservoirs are often associated with unconsolidated formations. To control sand production in unconsolidated formations, a process called frac-pack, which is a combination of hydraulic fracturing and gravel packing, is often used to reduce the drawdown around the wellbore, and thus mitigate the potential of sand production. In frac-pack treatments, the proper sizes of gravel and proppant are important as the goal is to stop sand production with the gravel pack and fracture created (Fischer et al., 2016). A number of products (Nguyen and Rickman, 2012; Christanti et al., 2011) are available in the industry that can be used to prevent fines production. These products are either resin or polymer based, and will create thin coating layers around the surfaces of formation fines and other particles to make them immobile.

In tight rock reservoirs, most wells cannot produce economically without massive hydraulic fracturing treatments. In these cases, fracturing will both stimulate the reservoir and bypass any near wellbore damage. However, hydraulic fracturing itself can also create various type of damage: damage in the reservoir due to fracturing fluid leak off and damage inside the fracture due to filter cake buildup, proppant embedment, proppant crushing, fines migration, and gel residue, etc. The topic of hydraulic fracturing will be discussed in more detail in Chapter 14.

#### **12.6.4.3 Scale control**

The treatment of scale problems can be achieved by either prevention or removal. It makes economic senses to prevent or mitigate scale formation in the first place, rather than to remove the scale after it has already caused production problems. In addition to potential production downtime, scale removal can be very costly.

Chemical inhibitors are available for oilfield applications and commonly used for prevention or after remediation treatments. Most of these inhibitors are phosphorous compounds (Ralston, 1973). A partial list of scale inhibitors includes inorganic phosphates, organic phosphonates, and organic polymers. In oilfield scale treatments, aqueous based scale inhibitor solutions are routinely injected or squeezed into the downhole location or the near wellbore region where scale problems occur. Solid scale inhibitor capsules can also be deployed downhole that will deliver a near constant level of inhibitor over a long time (Bourne et al., 2000).

If scale precipitation occurs inside the wellbore, remediation could be achieved either mechanically (via milling or jetting) or chemically via dissolution. Certain types of wellbore scales can be easily removed by chemical dissolution and often less expensive than mechanical removal. If scale precipitation occurs in the near wellbore region, chemical means are typically used.

Carbonate scales, such as  $\text{CaCO}_3$  and  $\text{FeCO}_3$ , are highly soluble in HCl acid, and can easily be dissolved by acid wash or matrix acidizing treatments. In general, sulfate scales are more difficult to remove chemically; however, gypsum ( $\text{CaSO}_4 \cdot 2\text{H}_2\text{O}$ ) and anhydrite ( $\text{CaSO}_4$ ) can be dissolved by ethylenediaminetetraacetic acid (EDTA). Other sulfate scales, such as barite ( $\text{BaSO}_4$ ) and celestite ( $\text{SrSO}_4$ ), are even more difficult to dissolve once they have formed, and are usually removed by mechanical means. Therefore, prevention through inhibitor treatments seems to be the best course of action for barium and strontium scale control. Sodium chloride ( $\text{NaCl}$ ) or halite scale can be easily dissolved with fresh water or weak acid solutions. When thick halite deposits occur inside the wellbore, mechanical action such as milling or water jetting can be effective.

#### **12.6.4.4 Organic precipitation control**

Organic compounds, such as paraffins and asphaltenes, can precipitate both inside the wellbore and in the near wellbore region. If organic precipitates occur inside the wellbore, they could be removed by several means, including mechanical scraping, heating with hot oil, or dissolution by using aromatic solvents, such as xylene and toluene. For organic damage beyond the wellbore, solvent treatments are more effective.

#### **12.6.4.5 Wettability alteration control**

The formation wettability in the near wellbore region is often altered by drilling, completion, and stimulation fluids. Mutual solvents can be used to restore the rock wettability, and surfactants can also be used to alter or maintain the rock wettability in a favorable condition. In fact, both mutual

solvents and surfactants are often used to avoid any adverse effects of rock-fluid and fluid-fluid interactions during matrix acidizing treatments.

---

## 12.7 SUMMARY

This chapter presents a guideline to identifying problems commonly encountered in oil and gas wells. Well test analysis provides a means of estimating properties of individual pay zones. Production logging analysis identifies fluid entries to the wellbore from different zones. The Guo et al. method is more accurate than the Turner et al. method for predicting liquid-loading problems in gas production wells. Formation damage is mainly due to fluid and solid particle invasion during well drilling, completion, and production operations. Acidizing and hydraulic fracturing can be used for removal of formation damage, which will be discussed in the chapters that follow.

---

## REFERENCES

- Almon, W.R., 1977. Sandstone diagenesis is stimulation design factor. *Oil Gas J* 56–59.
- Almon, W.R., Davies, D.K., 1981. Formation damage and the crystal chemistry of clays, Chapter 5. In: Longstaffe, F.J. (Ed.), *Clays and the Resource Geologist*. Mineralogical Association of Canada, pp. 81–103.
- Ameafule, J.O., Kersey, D.G., Norman, D.K., Shannon, P.M., Advances in formation damage assessment and control strategies, In: Presented at 39th Annual Technical Meeting of Petroleum Society of CIM and Canadian Gas Processors Association, Calgary, Alberta, June 12–16, 1988.
- Anderson, G.W., 1986. Wettability literature survey - Part 1: Rock/Oil/Brine interactions and the effects of core handling on wettability. *J. Pet. Technol.* 1125–1144.
- Bennion, D.B., Thomas, F.B., Sheppard, D.A., Formation damage due to mineral alteration and wettability changes during hot water and steam injection in clay-bearing sandstone reservoirs, In: Paper SPE 23783 presented at the SPE Intl. Symposium on Formation Damage Control, Lafayette, LA, 26–27 February 1992.
- Bourne, H.M., Heath, S.M., McKay, S., Fraser, J., Stott, L., Müller, S., 2000. Effective treatment of subsea wells with a solid scale inhibitor system. *Soc. Pet. Eng.* Available from: <http://dx.doi.org/10.2118/60207-MS>.
- Brindley, G.W., 1981. Structures and chemical composition of clay minerals, chapter 1. In: Longstaffe, F.J. (Ed.), *Clays and the Resource Geologist*. Mineralogical Association of Canada, Alberta, pp. 1–19.
- Chaudhry, A.C., 2004. *Oil Well Testing Handbook*. Gulf Professional Publishing, Burlington, USA.
- Christanti, Y., Ferrara, G., Ritz, T., Busby, B., Jeanpert, J., Abad, C., et al., 2011. A new technique to control fines migration in poorly consolidated sandstones—laboratory development and case histories. *Soc. Pet. Eng.* Available from: <http://dx.doi.org/10.2118/143947-MS>.
- Chung, F., Sarathi, P., Jones, R., Modeling of asphaltene and wax precipitation, In: DOE Topical Report (NIPER-498), Bartlesville, OK, January 1991.
- Cinco-Ley, H., Samaniego V.F., Transient pressure analysis: finite conductivity fracture case versus damaged fracture case, In: Paper SPE 10179 presented at the 56th SPE Annual Fall Technical Conference and Exhibition, San Antonio, TX, 5–7 October, 1981.
- Clark, N.J., Schultz, W.P., 1956. The analysis of problem wells. *Pet. Eng.* 28, B30–B38.

- Coleman, S.B., Clay, H.B., Mccurdy, D.O., Norris III, L.H., 1991. A new look at predicting gas well loading-up. JPT (March 1991) .Trans. AIME 291, 329.
- Cunningham, W.C., Smith, D.K., 1968. Effect of salt cement filtrate on subsurface formations. J. Pet. Technol. 259–264.
- Dake, L.P., 2002. Fundamentals of Reservoir Engineering. Elsevier, Amsterdam.
- Dobkins, T.A., 1981. Improved method to determine hydraulic fracture height. JPT 33 (4), 719–726, April.
- Economides, M.J., Hill, A.D., Ehlig-Economides, C., 1994. Petroleum Production Systems. Prentice Hall PTR, Upper Saddle River, NJ.
- E-Production Services, Inc, 2004. PanSystem User Manual. E-Production Services, Inc, Edinburgh.
- E-Production Services, Inc, 2005. FloSystem User Manual. E-Production Services, Inc, Edinburgh.
- Fekete, F.A.S.T., 2003. WellTest User Manual. Fekete Associates, Inc, Calgary.
- Ferguson, C.K., Klotz, J.A., 1954. Filtration from mud during drilling. J. Pet. Technol. 201, 29–42.
- Fischer, C., Constien, V., Vining, C., 2016. Gravel pack sizing criteria - It's time to re-evaluate. Soc. Pet. Eng. Available from: <http://dx.doi.org/10.2118/179023-MS>.
- Gabriel, G.A., Inamdar, G.R., An experimental investigation of fines migration in porous media, In: Paper SPE 12168, presented at 58th SPE Annual Technical Conference and Exhibition, San Francisco, CA, 5–8 October 1983.
- Gray, D.H., Rex, R.W., Formation damage in sandstones caused by clay dispersion and migration, In: Proceeding of the 14th National Conference on Clays and Clay Minerals, 1966, pp. 355–66.
- Gruesbeck, C., Collins, R.E., 1982. Entrainment and deposition of fines particles in porous media. Soc. Pet. Eng. J. 22, 847–856.
- Guo, B., Ghalambo, R.A., Xu, C., 2006. A systematic approach to predicting liquid loading in gas well. SPE Prod. Oper. J. 21 (1).
- Hawkins Jr., M.F., 1956. A note on the skin effect. Trans. AIME 207, 355–357.
- Hirasaki, G.A., 1991. Wettability: fundamentals and surface forces. SPE Formation Eval. 6, 217–226.
- Hong, K.C., 1975. Productivity of perforated completions in formations with and without damage. J. Pet. Technol. 27, 1027–1038.
- Horne, R.N., 1995. Modern Well Test Analysis: A Computer-Aided Approach. Petroway Publishing, New York.
- Houchin, L.R., Hudson, L.M., 1986. The prediction, evaluation, and treatment of formation damage caused by organic deposition. Soc. Pet. Eng. Available from: <http://dx.doi.org/10.2118/14818-MS>.
- Jones, L.G., Watts, J.W., 1971. Estimating skin effect in a partially completed damaged well. J. Pet. Technol. 23, 249–252.
- Khilar, K.C., Fogler, H.S., 1983. Water sensitivity of sandstones. Soc. Pet. Eng. J. 23, 55–64.
- Klotz, J.A., Krueger, R.F., Pye, D.S., 1974. Effect of perforation damage on well productivity. J. Pet. Technol. 26, 1303–1314.
- Krueger, R.F., 1986. An overview of formation damage and well productivity in oilfield operations. J. Pet. Technol. 39, 131–152.
- Lea, J.F., Nickens, H., 2004. Solving gas-well liquid-loading problems. SPE Prod. Facil. 56 (4), 30.
- Lee, J.W., Rollins, J.B., Spivey, J.P., 2003. Pressure Transient Testing. Society of Petroleum Engineers, Richardson, TX.
- Liu, X., Civan, F., Formation damage by fines migration including effects of filter cake, pore compressibility, and non-darcy flow - A modeling approach to scaling from core to field, In: Paper SPE 28980 presented at the SPE Intl. Symposium on Oilfield Chemistry held in San Antonio, TX, 14-17 February 1995.
- Muecke, T.W., 1979. Formation fines and factors controlling their movement in porous media. J. Pet. Technol. 31, 144–150.

- Nguyen, P.D., Rickman, R.D., 2012. Foaming aqueous-based curable treatment fluids enhances placement and consolidation performance. Soc. Pet. Eng. Available from: <http://dx.doi.org/10.2118/151002-MS>.
- Nosseir, M.A., Darwich, T.A., Sayyouh, M.H., Sallaly, M.E., 2000. A new approach for accurate prediction of loading in gas wells under different flowing conditions. SPE Prod. Facil. 15 (4), 245.
- Porter, K.E., 1989. An overview of formation damage. J. Petrol. Technol. 780–786.
- Rahman, S.S., Marx, C., 1991. Laboratory evaluation of formation damage caused by drilling fluids and cement slurry. J. Can. Pet. Technol. 30, 40–46.
- Ralston, P.H., 1973. Phosphonates - A chemical answer to oilfield water problems. Soc. Pet. Eng. Available from: <http://dx.doi.org/10.2118/4350-MS>.
- Turner, R.G., Hubbard, M.G., Dukler, A.E., 1969. Analysis and prediction of minimum flow rate for the continuous removal of liquids from gas wells, *JPT* November 1969. Trans. AIME 246, 1475.
- Van Poolen, H.K., 1957. Productivity vs. permeability damage in hydraulically produced fractures. API Drill. Prod. Prac. 103, 103–110. Available from: <http://dx.doi.org/10.2118/5879-PA>.
- Vetter, O.J., 1976. Oilfield scale---can we handle it? J. Pet. Technol. 1402–1408.
- Yuan, M., Mosley, J., Hyer, N., 2001. Mineral scale control in a CO<sub>2</sub> flooded oilfield. Soc. Pet. Eng. Available from: <http://dx.doi.org/10.2118/65029-MS>.

---

## PROBLEMS

- 12.1.** Consider a gas well producing 50 bbl/day of condensate and 0.1 cubic foot of sand through a 2.441-in. ID tubing against a wellhead pressure of 500 psia. Suppose the tubing string is set at a depth of 8000 ft, use the following data and estimate the minimum gas production rate before the gas well gets loaded. Gas-specific gravity: 0.75 (air = 1) Hole inclination: 0° Wellhead temperature: 60°F Geothermal gradient: 0.01°F/ft Condensate gravity: 60° API Water-specific gravity: 1.07 (water = 1) Solid-specific gravity: 2.65 (water = 1) Oil-gas interface tension: 20 dyne/cm Tubing wall roughness: 0.000015 in.
- 12.2.** Consider a gas well producing 50 bbl/day of water and 0.2 ft<sup>3</sup> of sand through a 2.441-in. ID tubing against a wellhead pressure of 600 psia and temperature of 80°F. Suppose the tubing string is set at a depth of 9000 ft and geothermal gradient is 0.01°F/ft, estimate the minimum gas production rate before the gas well gets loaded.
- 12.3.** Consider a gas well producing 80 bbl/day of water and 0.1 ft<sup>3</sup> of sand through a 1.995-in. ID tubing against a wellhead pressure of 400 psia and temperature of 70°F. Suppose the tubing string is set at a depth of 7000 ft and geothermal gradient is 0.01°F/ft, estimate the minimum gas production rate before the gas well gets loaded.
- 12.4.** Consider a gas well producing 70 bbl/day of oil and 0.1 ft<sup>3</sup> of sand through a 1.995-in. ID tubing against a wellhead pressure of 600 psia and temperature of 80°F. Suppose the tubing string is set at a depth of 6000 ft and geothermal gradient is 0.01°F/ft, estimate the minimum gas production rate before the gas well gets loaded.

---

## 13.1 INTRODUCTION

Acidizing treatments have been commonly applied in oilfield to remove the near-wellbore damage and slightly increase the productivity of formations. There are two different acidizing treatment types: matrix acidizing and acid fracturing, depending on the treatment pressure and if fractures are created in the formations. Matrix acidizing is also called acid matrix treatment. It is a technique to pump acid and other treatment fluids below the fracture pressure of formations, to stimulate wells for improving well inflow performance. In matrix acidizing treatments, acid solution is injected into the formation to dissolve some of the minerals to recover permeability of sandstones (removing skin) or increase permeability of carbonates near the wellbore (creating wormholes). Acid fracturing, on the other hand, is to create fractures in the formations first, followed by injecting acid into fractures. Due to the uneven etching of fractures' faces by acids, some small channels will stay open after fractures close, which will increase the permeability of the reservoir. After a brief introduction to acid types and acid–rock interaction, this chapter focuses on important issues on sandstone acidizing design, carbonate acidizing design and acid fracturing treatments.

---

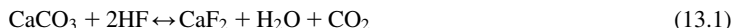
## 13.2 ACID TYPES

Currently, the main acid fluids used in acidizing treatments can be classified into three different types: mineral acids, organic acids and retarded acids. Different types of acids can be applied for different rock types and different treatment purposes.

### 13.2.1 MINERAL ACIDS

Hydrochloric acid (HCl) is commonly used acid for carbonate acidizing treatments, due to its low cost and fast reaction with carbonate rock types (limestone and dolomite). It is mostly used with the concentration of 15% (by weight) solution, to provide enough dissolving power of acid and limit the corrosion of well tubulars. For stimulations where acid dissolving power is not an issue, lower concentration of HCl can also be used to further reduce the corrosion. The main disadvantage of HCl is still its high corrosivity, especially at high downhole temperature (above 250°F), where the reaction rate between HCl and steel tubulars is even faster and more difficult to control. Therefore, the concentration of HCl depends on different stimulation treatments and wellbore conditions.

Hydrofluoric acid (HF), usually mixed with HCl, is mainly applied for sandstone acidizing. Typically, 15% HCl and 3% HF solution is prepared. If any calcite presents in the formation, calcium fluoride is the product due to the reaction between HF and calcite.



Calcium fluoride is insoluble in acid solutions, and may cause more damage to the porous space of the formations. Therefore, appropriate preflush with HCl and pumping HF with HCl is necessary to remove the carbonate minerals in sandstone formations and prevent the precipitating reaction between calcite and HF.

### 13.2.2 ORGANIC ACIDS

The advantage of organic acids is their lower corrosivity and slower reaction compared to mineral acids. When the contacting time between acid and well tubular is long or the wellbore downhole temperature is very high, organic acids can be used to control the corrosion. Meanwhile, the dissolving power of organic acids is also lower than mineral acids, resulting in less effective reaction between acid and minerals in the formation. The two main organic acids used in acidizing treatments are acetic acid and formic acids. Both acetic and formic acids are more expensive than HCl, and are often used as one component in retarded-acid systems or in the formations with high temperature.

### 13.2.3 RETARDED ACIDS

Due to the fast reaction between HCl and carbonate minerals, acid injected can be mostly spent at a very short distance from the wellbore without penetrating deep enough into the formation. Thus, to achieve deeper acid penetration and a successful acidizing treatment, it is necessary to retard acid reaction by adding extra components into the acid systems. The most commonly used retarded acid systems are gelled acids and emulsified acids.

By mixing gelling agents (polymers and surfactants) with acids, gelled acid systems can be achieved. By increasing the viscosity of acid systems, the transportation of acid from fluid stream to formation rocks is significantly reduced, and ultimately slows down the acid reaction. Thus, more acid can be transported deeper into the formation and increase the chance of a successful treatment. However, the stability of gelling agents are strongly dependent on the downhole temperature. At high temperature, many gelling agents can degrade causing the gelling acid system to lose its viscosity. It is recommended to use gelling acids at low-moderate bottom-hole temperature. Some other gelled acid systems depend on the pH value of the solution. Once the acid is spent and pH of fluids is high, the viscosity of gelled acid can be significantly increased. Meanwhile, due to the high viscosity of gelled acids, it can also be used as a diverter by temporarily blocking the high permeability zones and divert the acids to desired zones.

Emulsified acid can be prepared by mixing acid, oil phase and emulsifier together, which contains 20%–30% of oil phase. Droplets are formed by having the oil phase as an external film and having acid as the internal phase. The presence of external oil film reduces the diffusion rate

of acid phase to the rock surface, thus retarding the reaction rate between acid and rocks. Stability of emulsions are also dependent on downhole temperature.

### 13.3 CANDIDATE SELECTION

In general, acid will only penetrate several feet into the formation for matrix acidizing treatments, resulting in removal of near-wellbore damage or slight increase of permeability. On the other hand, acid fracturing will create fractures which can propagate much deeper into the formation. For sandstone formations, if the permeability is moderate to high, and damage is the main factor limiting the well production, matrix acidizing is recommended. However, if the permeability is low, such as tight gas reservoirs or shale reservoirs, hydraulic fracturing is recommended, since even all the damage is removed, the reservoir still cannot produce economically due to the low permeability. Similar rules also apply for carbonate formations. To remove or bypass the damage in the near-wellbore region in moderate or high permeability formations, the well should be stimulated by matrix acidizing. Otherwise, acid fracturing should be applied for low-perm carbonate formations.

## 13.4 ACID–ROCK INTERACTION

Minerals that are present in sandstone pores include montmorillonite (bentonite), kaolinite, calcite, dolomite, siderite, quartz, albite (sodium feldspar), orthoclase, and others. These minerals can be either from invasion of external fluid during drilling, cementing, and well completion, or from host materials that exist in the naturally occurring rock formations. The most commonly used acids for dissolving these minerals are HCl and HF.

### 13.4.1 CHEMICAL REACTIONS

Silicate minerals such as clays and feldspars in sandstone pores are normally removed using mixtures of HF and HCl, whereas carbonate minerals are usually attacked with HCl. The chemical reactions are summarized in [Table 13.1](#). The amount of acid required to dissolve a given amount of mineral is determined by the stoichiometry of the chemical reaction. For example, the simple

Table 13.1 Primary Chemical Reactions in Acid Treatments	
Montmorillonite (Bentonite)-HF/HCl:	$\text{Al}_4\text{Si}_8\text{O}_{20}(\text{OH})_4 + 40\text{HF} + 4\text{H}^+ \leftrightarrow 4\text{AlFt} + 8\text{SiF}_4 + 24\text{H}_2\text{O}$
Kaolinite-HF/HCl:	$\text{Al}_4\text{Si}_8\text{O}_{10}(\text{OH})_8 + 40\text{HF} + 4\text{H}^+ \leftrightarrow 4\text{AlF}_2 + 8\text{SiF}_4 + 18\text{H}_2\text{O}$
Albite-HF/HCl:	$\text{NaAlSi}_3\text{O}_8 + 14\text{HF} + 2\text{H}^+ \leftrightarrow \text{Na}^+ + \text{AlF}_2^+ + 3\text{SiF}_4 + 8\text{H}_2\text{O}$
Orthoclase-HF/HCl:	$\text{KAlSi}_3\text{O}_8 + 14\text{HF} + 2\text{H}^+ \leftrightarrow \text{K}^+ + \text{AlF}_2^+ + 3\text{SiF}_4 + 8\text{H}_2\text{O}$
Quartz-HF/HCl:	$\text{SiO}_2 + 4\text{HF} \leftrightarrow \text{SiF}_4 + 2\text{H}_2\text{O}$ $\text{SiF}_4 + 2\text{HF} \leftrightarrow \text{H}_2\text{SiF}_6$
Calcite-HCl:	$\text{CaCO}_3 + 2\text{HCl} \rightarrow \text{CaCl}_2 + \text{CO}_2 + \text{H}_2\text{O}$
Dolomite-HCl:	$\text{CaMg}(\text{CO}_3)_2 + 4\text{HCl} \rightarrow \text{CaCl}_2 + \text{MgCl}_2 + 2\text{CO}_2 + 2\text{H}_2\text{O}$
Siderite-HCl:	$\text{FeCO}_3 + 2\text{HCl} \rightarrow \text{FeCl}_2 + \text{CO}_2 + \text{H}_2\text{O}$



reaction between HCl and  $\text{CaCO}_3$  requires that 2 mol of HCl is needed to dissolve 1 mol of  $\text{CaCO}_3$ .

### 13.4.2 DISSOLVING POWER OF ACIDS

A more convenient way to express reaction stoichiometry is the dissolving power. The dissolving power on a mass basis is called *gravimetric dissolving power* and is defined as

$$\beta = C_a \frac{v_m MW_m}{v_a MW_a}, \quad (13.2)$$

where

$\beta$  = gravimetric dissolving power of acid solution,  $\text{lb}_m$  mineral/ $\text{lb}_m$  solution

$C_a$  = weight fraction of acid in the acid solution

$v_m$  = stoichiometry number of mineral

$v_a$  = stoichiometry number of acid

$MW_m$  = molecular weight of mineral

$MW_a$  = molecular weight of acid.

For the reaction between 15 wt% HCl solution and  $\text{CaCO}_3$ ,  $C_a = 0.15$ ,  $v_m = 1$ ,  $v_a = 2$ ,  $MW_m = 100.1$ , and  $MW_a = 36.5$ . Thus,

$$\begin{aligned} \beta_{15} &= (0.15) \frac{(1)(100.1)}{(2)(36.5)} \\ &= 0.21 \text{ lb}_m \text{CaCO}_3 / \text{lb}_m \text{15 wt\% HCl solution.} \end{aligned}$$

The dissolving power on a volume basis is called *volumetric dissolving power* and is related to the gravimetric dissolving power through material densities:

$$X = \beta \frac{\rho_a}{\rho_m}, \quad (13.3)$$

where

$X$  = volumetric dissolving power of acid solution,  $\text{ft}^3$  mineral/ $\text{ft}^3$  solution

$\rho_a$  = density of acid,  $\text{lb}_m/\text{ft}^3$

$\rho_m$  = density of mineral,  $\text{lb}_m/\text{ft}^3$

### 13.4.3 REACTION KINETICS

The acid–mineral reaction takes place slowly in the rock matrix being acidized. The reaction rate can be evaluated experimentally and described by kinetics models. Research work in this area has been presented by many investigators including Fogler et al. (1976), Lund et al. (1973, 1975), Hill et al. (1981), and Schechter (1992). Generally, the reaction rate is affected by the characteristics of the mineral, the properties of the acid, reservoir temperature, and the rates of acid transport to the mineral surface and removal of product from the surface. Detailed discussion of reaction kinetics is beyond the scope of this book.

## 13.5 SANDSTONE ACIDIZING DESIGN

The purpose of sandstone acidizing is to remove the damage to the sandstone near the wellbore that occurred during drilling and well completion processes. The acid treatment is only necessary when it is sure that formation damage is significant enough to affect well productivity. A major formation damage is usually indicated by a large positive skin factor derived from pressure transit test analysis in a flow regime of early time (see Chapter 12: Well Problem Identification).

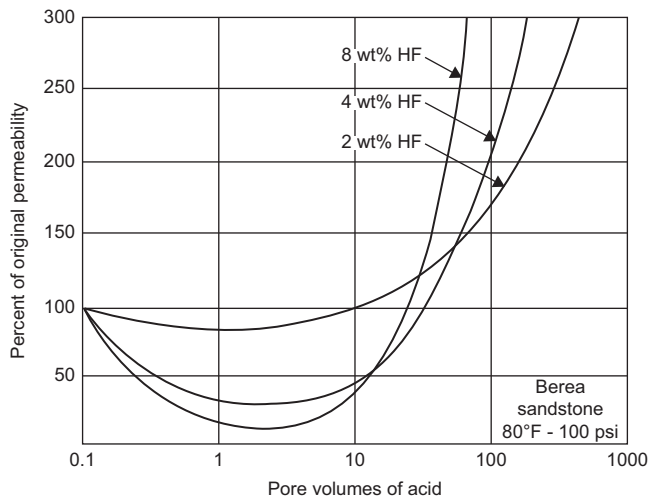
### 13.5.1 SELECTION OF ACID

The acid type and acid concentration used in acidizing treatments is selected on the basis of minerals in the formation and field experience. For sandstones, the typical treatments usually consist of a mixture of 3 wt% HF and 12 wt% HCl, preceded by a 15 wt% HCl preflush. McLeod (1984) presented a guideline to the selection of acid on the basis of extensive field experience. His recommendations for sandstone treatments are shown in Table 13.2. McLeod's recommendation should serve only as a starting point. When many wells are treated in a particular formation, it is worthwhile to conduct laboratory tests of the responses of cores to different acid strengths. Fig. 13.1 shows typical acid–response curves.

### 13.5.2 ACID VOLUME REQUIREMENT

The acid volume should be high enough to remove near-wellbore formation damage and low enough to reduce cost of treatment. Selection of an optimum acid volume is complicated by the competing effects. The volume of acid needed depends strongly on the depth of the damaged zone, which is seldom known. Also, the acid will never be distributed equally to all parts of the damaged

<b>Table 13.2 Recommended Acid Type and Strength for Sandstone Acidizing</b>	
<b>HCl Solubility &gt; 20%</b>	<b>Use HCl Only</b>
<b>High-perm Sand (<math>k &gt; 100</math> md)</b>	
High quartz (80%), low clay (<5%)	10% HCl-3% HF <sup>a</sup>
High feldspar (> 20%)	13.5% HCl-1.5% HF <sup>a</sup>
High clay (> 10%)	6.5% HCl-1% HF <sup>b</sup>
High iron chlorite clay	3% HCl-0.5% HF <sup>b</sup>
<b>Low-perm Sand (<math>k &lt; 10</math> md)</b>	
Low clay (<5%)	6% HCl-1.5% HF <sup>c</sup>
High chlorite	3% HCl-0.5% HF <sup>d</sup>
<sup>a</sup> Preflush with 15% HCl. <sup>b</sup> Preflush with sequestered 5% HCl. <sup>c</sup> Preflush with 7.5% HCl or 10% acetic acid. <sup>d</sup> Preflush with 5% acetic acid.	



**FIGURE 13.1**

Typical acid response curves (Smith and Henderickson, 1965).

formation. The efficiency of acid treatment and, therefore, acid volume also depends on acid injection rate. To ensure that an adequate amount of acid contacts most of the damaged formation, a larger amount of acid is necessary.

The acid preflush volume is usually determined on the basis of void volume calculations. The required minimum acid volume is expressed as

$$V_a = \frac{V_m}{X} + V_P + V_m, \quad (13.4)$$

where

$V_a$  = the required minimum acid volume,  $\text{ft}^3$

$V_m$  = volume of minerals to be removed,  $\text{ft}^3$

$V_P$  = initial pore volume,  $\text{ft}^3$

and

$$V_m = \pi(r_a^2 - r_w^2)(1 - \phi)C_m, \quad (13.5)$$

$$V_P = \pi(r_a^2 - r_w^2)\phi, \quad (13.6)$$

where

$r_a$  = radius of acid treatment, ft

$r_w$  = radius of wellbore, ft

$\phi$  = porosity, fraction

$C_m$  = mineral content, volume fraction.

**Example Problem 13.1** A sandstone with a porosity of 0.2 containing 10 v% calcite ( $\text{CaCO}_3$ ) is to be acidized with HF/HCl mixture solution. A preflush of 15 wt% HCl solution is to be injected ahead of the mixture to dissolve the carbonate minerals and establish a low-pH environment. If the HCl preflush is to remove all carbonates in a region within 1 ft beyond a 0.328-ft radius wellbore before the HF/HCl stage enters the formation, what minimum preflush volume is required in terms of gallon per foot of pay zone?

**Solution**

Volume of  $\text{CaCO}_3$  to be removed:

$$\begin{aligned} V_m &= \pi(r_a^2 - r_w^2)(1 - \phi)C_m \\ &= \pi(1.328^2 - 0.328^2)(1 - 0.2)(0.1) \\ &= 0.42 \text{ ft}^3 \text{CaCO}_3/\text{ft pay zone} \end{aligned}$$

Initial pore volume:

$$\begin{aligned} V_p &= \pi(r_a^2 - r_w^2)\phi \\ &= \pi(1.328^2 - 0.328^2)(0.2) = 1.05 \text{ ft}^3/\text{ft pay zone} \end{aligned}$$

Gravimetric dissolving power of the 15 wt% HCl solution:

$$\begin{aligned} \beta &= C_a \frac{v_m MW_m}{v_a MW_a} \\ &= (0.15) \frac{(1)(100.1)}{(2)(36.5)} \\ &= 0.21 \text{ lb}_m \text{CaCO}_3/\text{lb}_m \text{ 15 wt\% HCl solution} \end{aligned}$$

Volumetric dissolving power of the 15 wt% HCl solution:

$$\begin{aligned} X &= \beta \frac{\rho_a}{\rho_m} \\ &= (0.21) \frac{(1.07)(62.4)}{(169)} \\ &= 0.082 \text{ ft}^3 \text{CaCO}_3/\text{ft}^3 \text{ 15 wt\% HCl solution} \end{aligned}$$

The required minimum HCl volume

$$\begin{aligned} V_a &= \frac{V_m}{X} + V_p + V_m \\ &= \frac{0.42}{0.082} + 1.05 + 0.42 \\ &= 6.48 \text{ ft}^3 \text{ 15 wt\% HCl solution}/\text{ft pay zone} \\ &= (6.48)(7.48) \\ &= 48 \text{ gal 15 wt\% HCl solution}/\text{ft pay zone} \end{aligned}$$

The acid volume requirement for the main stage in a mud acid treatment depends on mineralogy and acid type and strength. Economides and Nolte (2000) provide a listing of typical stage

sequences and volumes for sandstone acidizing treatments. For HCl acid, the volume requirement increases from 50 to 200 gal/ft pay zone with HCl solubility of HF changing from less than 5%–20%. For HF acid, the volume requirement is in the range of 75–100 gal/ft pay zone with 3.0%–13.5% HCl and 0.5%–3.0% HF depending on mineralogy.

Numerous efforts have been made to develop a rigorous method for calculating the minimum required acid volume in the past two decades. The most commonly used method is the two-mineral model (Hekim et al., 1982; Hill et al., 1981; Taha et al., 1989). This model requires a numerical technique to obtain a general solution. Schechter (1992) presented an approximate solution that is valid for Damkohler number being greater than 10. This solution approximates the HF fast-reacting mineral front as a sharp front. Readers are referred to Schechter (1992) for more information.

Because mud acid treatments do not dissolve much of the formation minerals but dissolve the materials clogging the pore throats, Economides and Nolte (2000) suggest taking the initial pour volume (Eq. [13.6]) within the radius of treatment as the minimum required acid volume for the main stage of acidizing treatment. Additional acid volume should be considered for the losses in the injection tubing string.

### 13.5.3 ACID INJECTION RATE AND PRESSURE

Acid injection rate should be selected on the basis of mineral dissolution and removal and depth of damaged zone. Selecting an optimum injection rate is a difficult process because the damaged zone is seldom known with any accuracy and the competing effects of mineral dissolution and reaction product precipitation. Fortunately, research results have shown that acidizing efficiency is relatively insensitive to acid injection rate and that the highest rate possible yields the best results. McLeod (1984) recommends relatively low injection rates based on the observation that acid contact time with the formation of 2–4 hours appears to give good results. da Motta (1993) shows that with shallow damage, acid injection rate has little effect on the residual skin after 100 gal/ft of injection rate; and with deeper damage, the higher the injection rate, the lower the residual skin. Paccaloni et al. (1988) and Paccaloni and Tambini (1993) also report high success rates in numerous field treatments using the highest injection rates possible.

There is always an upper limit on the acid injection rate that is imposed by formation breakdown (fracture) pressure  $p_{bd}$ . Assuming pseudo-steady-state flow, the maximum injection rate limited by the breakdown pressure is expressed as

$$q_{i,\max} = \frac{4.917 \times 10^{-6} kh (p_{bd} - \bar{p} - \Delta p_{sf})}{\mu_a \left( \ln \frac{0.472 r_e}{r_w} + S \right)}, \quad (13.7)$$

where

- $q_i$  = maximum injection rate, bbl/min
- $k$  = permeability of undamaged formation, md
- $h$  = thickness of pay zone to be treated, ft
- $p_{bd}$  = formation breakdown pressure, psia

$\bar{p}$  = reservoir pressure, psia  
 $\Delta p_{sf}$  = safety margin, 200–500 psi  
 $\mu_a$  = viscosity of acid solution, cp  
 $r_e$  = drainage radius, ft  
 $r_w$  = wellbore radius, ft  
 $S$  = skin factor, ft.

The acid injection rate can also be limited by surface injection pressure at the pump available to the treatment. This effect is described in the next section.

In most acid treatment operations, only the surface tubing pressure is monitored. It is necessary to predict the surface injection pressure at the design stage for pump selection. The surface tubing pressure is related to the bottom-hole flowing pressure by

$$p_{si} = p_{wf} - \Delta p_h + \Delta p_f, \quad (13.8)$$

where

$p_{si}$  = surface injection pressure, psia  
 $p_{wf}$  = flowing bottom-hole pressure, psia  
 $\Delta p_h$  = hydrostatic pressure drop, psia  
 $\Delta p_f$  = frictional pressure drop, psia.

The second and the third term in the right-hand side of Eq. (13.8) can be calculated using Equations in Chapter 11, Transportation Systems. However, to avert the procedure of friction factor determination, the following approximation may be used for the frictional pressure drop calculation (Economides and Nolte, 2000):

$$\Delta p_f = \frac{518 \rho^{0.79} q^{1.79} \mu^{0.207}}{1000 D^{4.79}} L, \quad (13.9)$$

where

$\rho$  = density of fluid, g/cm<sup>3</sup>  
 $q$  = injection rate, bbl/min  
 $\mu$  = fluid viscosity, cp  
 $D$  = tubing diameter, in.  
 $L$  = tubing length, ft.

Eq. (13.9) is relatively accurate for estimating frictional pressures for Newtonian fluids at flow rates less than 9 bbl/min.

**Example Problem 13.2** A 60-ft thick, 50-md sandstone pay zone at a depth of 9500 ft is to be acidized with an acid solution having a specific gravity of 1.07 and a viscosity of 1.5 cp down a 2-in. inside diameter (ID) coil tubing. The formation fracture gradient is 0.7 psi/ft. The wellbore radius is 0.328 ft. Assuming a reservoir pressure of 4000 psia, drainage area radius of 1000 ft, and a skin factor of 15, calculate

1. the maximum acid injection rate using safety margin 300 psi.
2. the maximum expected surface injection pressure at the maximum injection rate.

**Solution**

1. The maximum acid injection rate:

$$\begin{aligned}
 q_{i,\max} &= \frac{4.917 \times 10^{-6} kh(p_{bd} - \bar{p} - \Delta p_{sf})}{\mu_a \left( \ln \frac{0.472 r_e}{r_w} + S \right)} \\
 &= \frac{4.917 \times 10^{-6} (50)(60)((0.7)(9,500) - 4,000 - 300)}{(1.5) \left( \ln \frac{0.472(1000)}{0.328} + 15 \right)} \\
 &= 1.04 \text{ bbl/min}
 \end{aligned}$$

2. The maximum expected surface injection pressure:

$$\begin{aligned}
 p_{wf} &= p_{bd} - \Delta p_{sf} = (0.7)(9500) - 300 = 6350 \text{ psia} \\
 \Delta p_h &= (0.433)(1.07)(9500) = 4401 \text{ psi} \\
 \Delta p_f &= \frac{518 \rho^{0.79} q^{1.79} \mu^{0.207}}{1000 D^{4.79}} L \\
 &= \frac{518(1.07)^{0.79} (1.04)^{1.79} (1.5)^{0.207}}{1000(2)^{4.79}} (9500) \\
 &= 218 \text{ psi} \\
 p_{si} &= p_{wf} - \Delta p_h + \Delta p_f \\
 &= 6350 - 4401 + 218 = 2167 \text{ psia}
 \end{aligned}$$

---

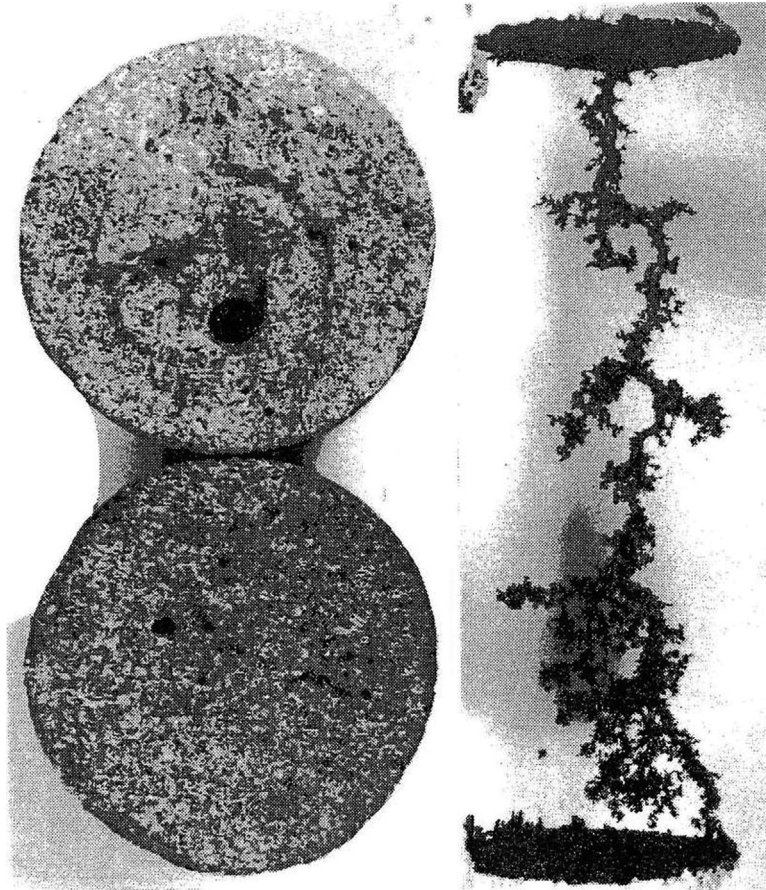
## 13.6 CARBONATE ACIDIZING DESIGN

The purpose of carbonate acidizing is not to remove the damage to the formation near the wellbore, but to create wormholes to bypass the damage region and through which oil or gas will be produced after stimulation. Fig. 13.2 shows wormholes created by acid dissolution of limestone in a laboratory (Hoefner and Fogler, 1988).

Carbonate acidizing is a more difficult process to predict than sandstone acidizing because the physics is much more complex. Because the surface reaction rates are very high and mass transfer often plays the role of limiting step locally, highly nonuniform dissolution patterns are usually created. The structure of the wormholes depends on many factors including flow geometry, injection rate, reaction kinetics, and mass transfer rates. Acidizing design relies on mathematical models calibrated by laboratory data.

### 13.6.1 SELECTION OF ACID

HCl is the most widely used acid for carbonate matrix acidizing. Weak acids are suggested for perforating fluid and perforation cleanup, and strong acids are recommended for other treatments. Table 13.3 lists recommended acid type and strength for carbonate acidizing (McLeod, 1984).

**FIGURE 13.2**

Wormholes created by acid dissolution of limestone (Hoefner and Fogler, 1988).

*Courtesy AIChE.*

**Table 13.3 Recommended Acid Type and Strength for Carbonate Acidizing**

Perforating fluid:	5% acetic acid
Damaged perforations:	9% formic acid
	10% acetic acid
	15% HCl
Deep wellbore damage:	15% HCl
	28% HCl
	Emulsified HCl

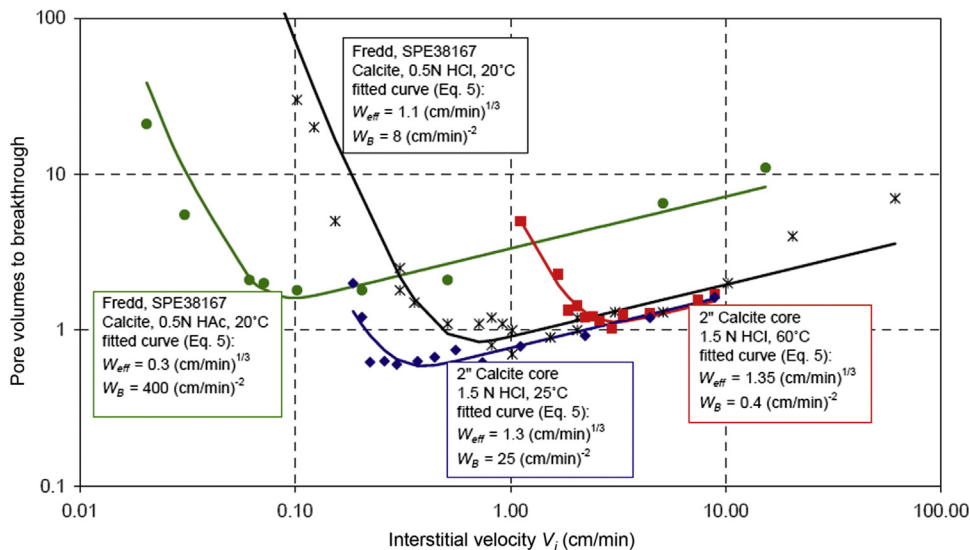


All theoretical models of wormhole propagation predict deeper penetration for higher acid strengths, so a high concentration of acid is always preferable.

### 13.6.2 WORMHOLE PENETRATION AND GROWTH

Wormholing is the phenomenon that complicates acidizing in carbonate formation and is also the key factor for a successful matrix acidizing treatment. Therefore, appropriately predicting wormhole growth and penetration is crucial for acidizing designs. Typically, to study the wormholing with different rock types and acid systems, core-flooding tests are introduced. Core samples from actual fields will be used in the lab, with diameter varying from 1 to 3 in., and length of 6 in. The acid systems will be injected at a constant rate from one end of the core samples and the pressure difference between two ends of the core samples will be recorded. Once the wormholes fully penetrate the core (break-through), the pressure difference will be significantly reduced, since the wormholes provide a low-resistance path for fluid to flow through. The volume of acid that has been injected to achieve this break-through will be recorded as a ratio to the total volume of pore space in this core sample, known as pore volume to break-through. These core-flooding tests with the same rock types and acid systems is repeated at different injection rates to generate a plot as shown in Fig. 13.3 (Buijse and Glasbergen, 2005). Also, to fully understand wormholing behavior of an acid, it is recommended to carry out core-flooding tests under different temperatures and using core samples with varying permeability.

Although core-flooding tests are still the most common tests to study wormholing, it has a different flowing pattern from the field application. In oil field wells, when acid is injected into the



**FIGURE 13.3**

PVbt curves (Buijse and Glasbergen, 2005).

formation rocks, flow is mainly in radial direction, while core-flooding tests are simulating liner flow. Therefore, some radial core-flooding tests were carried out to extend the understanding (McDuff et al., 2010; Valsecchi et al., 2012). Many times, by comparing the results from linear and radial core-flooding tests, a correction factor can be introduced, which will be applied in the worm-holing model.

Based on the core-flooding tests, wormhole propagation models can be established for field acidizing treatment design and evaluation. Daccord et al. (1989) presented a wormhole propagation model based on the fractal behavior of wormholes in the radial geometry as following equation:

$$r_{wh} = \left( \frac{bN_{Ac}V_h}{\pi\phi D^{2/3}d_h^{1/3}} \right)^{1/d_f} \quad (13.10)$$

where

$V_h$  = required acid volume per unit thickness of formation,  $m^3/m$

$\phi$  = porosity, fraction

$D$  = molecular diffusion coefficient,  $m^2/s$

$q_h$  = injection rate per unit thickness of formation,  $m^3/sec\text{-}m$

$r_{wh}$  = radius of wormhole penetration,  $m$

$d_f$  = 1.6, fractal dimension

$b$  =  $105 \times 10^{-5}$  in SI units

$N_{Ac}$  = acid capacity number, dimensionless,

where the acid capacity number is defined as

$$N_{Ac} = \frac{\phi\beta\gamma_a}{(1-\phi)\gamma_m}, \quad (13.11)$$

Where

$\gamma_a$  = acid specific gravity, water = 1.0

$\gamma_m$  = mineral specific gravity, water = 1.0.

Economides et al. (1994) presented a volumetric model by assuming a constant fraction of the rock will be dissolved by acid. The wormhole radius can be predicted by

$$r_{wh} = \left( \frac{V_h}{\pi\phi PV_{bt}} + r_w^2 \right)^{1/2} \quad (13.12)$$

where  $PV_{bt}$  is the number of pore volumes of acid injected at the time of wormhole breakthrough at the end of the core. Apparently, the volumetric model requires data from laboratory tests. The constant dissolving fraction  $\eta$  in volumetric model is defined as

$$\eta = N_{Ac}PV_{bt} \quad (13.13)$$

Buijse and Glasbergen (2005) developed an empirical correlation to capture wormhole propagation based on both experimental results and a near-wellbore simulator. Their model predicts the velocity of wormhole growth at the tip of wormholes as

$$V_{wh}(r_{wh}) = W_{eff} V_i(r_{wh})^{2/3} B(V_i(r_{wh})) \quad (13.14)$$

Where

- $V_{wh}$  = Growth rate of wormhole front, m/s  
 $W_{eff}$  = Constant from the optimum velocity and  $PV_{bt}$   
 $V_i$  = Interstitial acid velocity at wormhole front, m/s  
 $V_i$  = Interstitial acid velocity at wormhole front, m/s  
 $B(V_i)$  = B-function related to  $V_i$  at wormhole front

The interstitial acid velocity in radial geometry is defined as

$$V_i(r) = \frac{Q}{2\pi r h \phi} \quad (13.15)$$

where  $r$  is radial distance in the formation from the wellbore center, and  $h$  is the zone thickness. Therefore, the interstitial velocity at the wormhole front used in Eq. (13.14) is

$$V_i(r_{wh}) = \frac{Q}{2\pi r_{wh} h \phi} \quad (13.16)$$

The B-function in Eq. (13.14) can be expressed as

$$B(V_i) = (1 - \exp(-W_B V_i^2))^2 \quad (13.17)$$

$W_{eff}$  and in Eq. (13.14) and  $W_B$  in Eq. (13.17) can be calculated from the optimum interstitial velocity  $V_{i-opt}$  and optimum pore volume to break-through  $PV_{bt-opt}$ .

$$W_{eff} = \frac{V_{i-opt}^{1/3}}{PV_{bt-opt}} \quad (13.18)$$

$$W_B = \frac{4}{V_{i-opt}^2} \quad (13.19)$$

### 13.6.3 ACIDIZING DESIGN FOR CARBONATE

Acidizing design parameters include acid volume, injection rate, and injection pressure. The acid volume can be calculated with different methods as mentioned in Section 13.6.2, such as Daccord's wormhole propagation model or the volumetric model, on the basis of desired penetration of wormholes.

Based on the wormhole propagation model presented in Eq. (13.10) by Daccord et al. (1989), the required acid volume per unit thickness of formation can be estimated using the following equation:

$$V_h = \frac{\pi \phi D^{2/3} q_h^{1/3} r_{wh}^{df}}{b N_{Ac}} \quad (13.20)$$

On the other hand, based on the volumetric model, the required acid volume per unit thickness of formation can be estimated using the following equation:

$$V_h = \pi \phi (r_{wh}^2 - r_w^2) PV_{bt} \quad (13.21)$$

**Example Problem 16.3** A 28 wt% HCl is needed to propagate wormholes 3 ft from a 0.328-ft radius wellbore in a limestone formation (specific gravity 2.71) with a porosity of 0.15. The designed injection rate is 0.1 bbl/min-ft, the diffusion coefficient is  $10^{-9}$  m<sup>2</sup>/sec, and the density of the 28% HCl is 1.14 g/cm<sup>3</sup>. In linear core floods, 1.5 pore volume is needed for wormhole breakthrough at the end of the core. Calculate the acid volume requirement using (1) Daccord's model and (2) the volumetric model.

**Solution**

1. Daccord's model:

$$\begin{aligned}\beta &= C_a \frac{v_m MW_m}{v_a MW_a} = (0.28) \frac{(1)(100.1)}{(2)(36.5)} \\ &= 0.3836 \text{ lb}_m \text{CaCO}_3 / \text{lb}_m 28 \text{ wt}\% \text{ HCl solution.} \\ N_{Ac} &= \frac{\phi \beta \gamma_a}{(1 - \phi) \gamma_m} = \frac{(0.15)(0.3836)(1.14)}{(1 - 0.15)(2.71)} = 0.0285 \\ q_h &= 0.1 \text{ bbl/min-ft} = 8.69 \times 10^{-4} \text{ m}^3 / \text{sec-m} \\ r_{wh} &= 0.328 + 3 = 3.328 \text{ ft} = 1.01 \text{ m} \\ V_h &= \frac{\pi \phi D^{2/3} q_h^{1/3} r_{wh}^{d_f}}{b N_{Ac}} \\ &= \frac{\pi (0.15) (10^{-9})^{2/3} (8.69 \times 10^{-4})^{1/3} (1.01)^{1.6}}{(1.5 \times 10^{-5}) (0.0285)} \\ &= 0.107 \text{ m}^3 / \text{m} = 8.6 \text{ gal/ft}\end{aligned}$$

2. Volumetric model:

$$\begin{aligned}V_h &= \pi \phi (r_{wh}^2 - r_w^2) (PV)_{bt} \\ &= \pi (0.15) (3.328^2 - 0.328^2) (1.5) \\ &= 7.75 \text{ ft}^3 / \text{ft} = 58 \text{ gal/ft.}\end{aligned}$$

For Buijse and Glasbergen's model, numerical solution is needed to design acidizing treatments, by counting for the interstitial velocity at the tips of wormholes at each time step.

The maximum injection rate and pressure for carbonate acidizing can be calculated in the same way as that for sandstone acidizing. Models of wormhole propagation predict that wormhole velocity increases with injection rate to the power of  $\frac{1}{2}$  to 1. Therefore, the maximum injection rate is preferable. However, this approach may require more acid volume. If the acid volume is constrained, a slower injection rate may be preferable. If a sufficient acid volume is available, the maximum injection rate is recommended for limestone formations. However, a lower injection rate may be preferable for dolomites. This allows the temperature of the acid entering the formation to increase, and thus, the reaction rate increases. The designed acid volume and injection rate should be adjusted based on the real-time monitoring of pressure during the treatment.

### 13.6.4 ACID FRACTURING

Matrix acidizing in carbonate formation discussed in the previous sections targets the near-wellbore region, one to several feet into the formation, by injecting acid into the formation rocks below the fracturing pressure. In some of the carbonate formations, where the original permeability is low or the damage penetrates deeper into the formation, acid fracturing treatments can be applied. Unlike matrix acidizing, acid fracturing treatments are composed of several pumping steps. First, a pad stage containing high viscosity fluid will be pumped to create fractures inside the formation. Then acid is injected into the fractures, whose surfaces are etched by acid. Unlike hydraulic fracturing, proppant is not used to keep fractures open. Instead, when pumping stops, fractures will close. The conductivity of acid fractures depends on the nonuniform etching pattern of rock surfaces. Due to the acid distribution in the fracture and rock heterogeneity, the reaction and etching on rock surfaces can be uneven, which leads to small, open channels after fracture closure. These channels can provide higher conductivity compared to the original matrix permeability, as shown in Fig. 13.4.

The conductivity of acid fractures is decided by these open channels, which strongly depends on acid distribution in the fractures, acid penetration depth, acid leak-off through fractures' walls and reaction rate of acid with carbonate rock. In general, to achieve better performance of acid fracturing treatments, the design needs to allow acid to penetrate deeply into the fractures, enough time for acid to react with fracture surfaces and control leak-off acid through fracture surfaces.

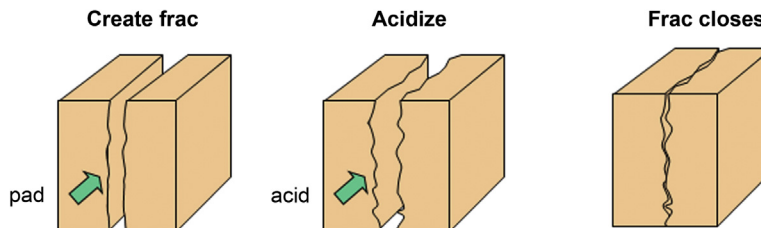
To predict the conductivity of acid fractures, [Nierode and Kruk \(1973\)](#) developed a correlation based on experimental results. The conductivity of acid fractures can be calculated by the following equations:

$$wk_f = C_1 \exp(-C_2 S) \quad (13.22)$$

$$C_1 = 0.265(\text{DREC})^{0.822} \quad (13.23)$$

$$C_2 \times 10^3 = \begin{cases} 19.9 - 1.3 \ln(\text{RES}), & 0 < \text{RES} < 20,000 \text{ psi} \\ 3.8 - 0.28 \ln(\text{RES}), & 20,000 < \text{RES} < 500,000 \text{ psi} \end{cases} \quad (13.24)$$

$wk_f$  is the acid fracture conductivity in md-in,  $S$  is the fracture closure stress in psi, DREC is the dissolved rock equivalent conductivity in md-in and RES is the rock embedment strength in psi. However, by comparing to field-measured conductivity, the disagreement between the *N-K* correlation and measured data sometimes is large, because the *N-K* correlation is based on experimental data from small core samples.



**FIGURE 13.4**

Conductivity of Acid fractures.

A new correlation to predict the conductivity of acid fractures was developed by [Deng et al. \(2012\)](#) based on statistical variations of the formation properties. The fracture conductivity at zero closure stress for permeability-distribution-dominant cases can be presented as

$$(wk_f)_0 = 4.48 \times 10^9 \bar{w}^3 \left[ 1 + (a_1 \operatorname{erf}(a_2(\lambda_{D,x} - a_3)) - a_4 \operatorname{erf}(a_5(\lambda_{D,z} - a_6))) \sqrt{(e^{\sigma_D} - 1)} \right] \quad (13.25)$$

$$a_1 = 1.82 \quad a_2 = 3.25 \quad a_3 = 0.12 \quad a_4 = 1.31 \quad a_5 = 6.71 \quad a_6 = 0.03$$

where  $\lambda_D$  is the normalized correlation length,  $\sigma_D$  is the normalized standard deviation, and  $\bar{w}$  is the average fracture width in inches.  $\lambda_D$  and  $\sigma_D$  can be quantified by using the semi-variogram model. For high leakoff coefficient ( $> 0.004 \text{ ft}/(\text{min})^{0.5}$ ), the average width can be predicted by

$$\bar{w} = 0.56 \operatorname{erf}(0.8\sigma_D) w_i^{0.83} \quad (13.26)$$

For the medium leakoff coefficient ( $\sim 0.001 \text{ ft}/(\text{min})^{0.5}$ ) with uniform mineralogy distribution,

$$\bar{w} = 0.2 \operatorname{erf}(0.78\sigma_D) w_i^{0.81} \quad (13.27)$$

Then the correlation for overall fracture

$$wk_f = \alpha \exp(-\beta \sigma_c)$$

$$\alpha = (wk_f)_0 \left[ 0.22 (\lambda_{D,x} \sigma_D)^{2.8} + 0.01 ((1 - \lambda_{D,z}) \sigma_D)^{0.4} \right]^{0.52} \quad (13.28)$$

$$\beta = [14.9 - 3.78 \ln(\sigma_D) - 6.81 \ln(E)] \times 10^{-4}$$

where  $\sigma_c$  is the closure stress in psi and E is Young's modulus in Mpsi.

## 13.7 ACID DIVERSION

Acid placement is the key factor for a successful acidizing treatment in multi-layered formations. Without any control, acid injected will flow through the path with least resistance. In other words, acid will flow into zones with higher permeability and lower damage skin, leaving zones with severe damage untreated. To evenly distribute acid among different zones, diversion is necessary. Diversion is a method to temporarily block zones that receive most acid, and force acid to flow into other zones. There are mainly two types of diversion methods: Mechanical diversion methods and chemical diversion methods.

### 13.7.1 MECHANICAL DIVERSION METHODS

Mechanical diversion is to plug or block the high-perm zones with mechanical methods, including ball sealers and fibers.

Ball sealers are a commonly used diversion method in acidizing treatments. It can be only applied in cased and perforated completion. During acid injection, balls will be dropped into the wellbore. These balls will flow with acid and try to seat on perforations in zones that are taking most acid. Once seated, ball sealers will block the acid flow into these zones and divert fluid flow

into other zones. Once the acidizing treatment is finished and wells are back on production, ball sealers will be unseated from perforations and flow back to surface. Thus, they will not affect production from the zones which are temporarily blocked.

Fibers can be mixed with acid or nonacid fluid and injected into the wellbore. Fibers will form a filter cake inside perforation tunnels for cased and perforated completion, or on the wall of wellbores for openhole completion. The filter cake has a designed permeability which adds extra resistance for acid to enter these zones. Fibers used for acidizing treatments are degradable, dependent on the downhole temperature and pH value of the fluid environment. Typically, fibers can be fully degraded at downhole environment with presence of acid in less than a day. Thus, fibers will not introduce extra damage for production.

### 13.7.2 CHEMICAL DIVERSION METHODS

Unlike mechanical diversion methods, chemical diversion methods are commonly dependent on viscosity of injected fluids. Gelling agents or surfactants are mixed with base fluid, either acid or nonacid, to create a chemical diverter. For some chemical diverter containing acids, the viscosity of the fluids depends on pH value. When acid injected into the high-perm zones is partially spent or pH value is higher, the fluid will viscosify and create more resistance in these zones, and force the acid to enter zones with low permeability or high damage skin. If wells are put back to production or acid is fully spent, the high viscosity fluid will be broken in contact with hydrocarbons or in even higher pH environment, allowing the high-perm zones to produce. The main disadvantage of chemical diversion is the potential risk of introducing extra damage to the formation. If the high viscosity fluid cannot be broken properly, production of the well will be affected.

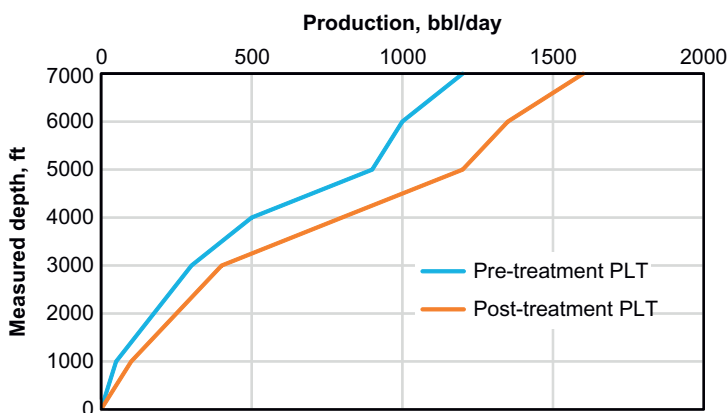
---

## 13.8 ACID PLACEMENT DIAGNOSIS

To execute an evaluation of an acidizing treatment or optimize the design of acidizing treatments, it is necessary to diagnosis acid placement in a multizone formation. The most common methods are to apply production logging tools (PLT) and distributed temperature sensing (DTS) tools.

Typically, a production logging tool will be deployed in the wellbore to measure the production contribution from each zone or layer before treatments. This data will provide information on damage skin factor for each zone if zone permeability and zone pressure are predetermined. After acidizing treatments, another PLT run will be carried out. By comparing the pre-treatment and post-treatment PLT data (Fig. 13.5), one can determine which zones have been treated successfully and contributing more production, and which zones need more acid injected. However, since this comparison can only be done after treatments, it can only benefit future acidizing treatment design for this particular well.

Most recently, distributed temperature sensor has been used in the oil fields for different purposes, including diagnosing acid distribution in the formations, either postjob or real-time. DTS can provide a continuous temperature measurement along wellbore with very small time intervals by using optical fibers, during acid injection, shut-in, and flow-back. DTS can be either installed



**FIGURE 13.5**

Example of pre- and post-treatment PLT data.

permanently inside completion or deployed by using coiled tubing whenever temperature measurements are needed. With DTS data and help of an optimization algorithm (Tan et al., 2012), one can determine acid distribution among different zones in the heterogeneous carbonate formation in real-time, which can help to improve the treatment design and optimize the injection rate/volume on the site or for better evaluation of treatment results after jobs.

## 13.9 SUMMARY

This chapter briefly presents the chemistry of matrix acidizing and offers a guideline to acidizing design for both sandstone and carbonate formations, as well as acid fracturing, diversion, and acid placement diagnosis. More in-depth materials can be found in McLeod (1984), Economides et al. (1994), and Economides and Nolte (2000).

## REFERENCES

- Buijse, M., Glasbergen, G., 2005. A semiempirical model to calculate wormhole growth in carbonate acidizing. In: Presented at the SPE Annual Technical Conference and Exhibition, Dallas, TX, 9–12 October. SPE-96892-MS.
- Daccord, G., Touboul, E., Lenormand, R., 1989. Carbonate acidizing: toward a quantitative model of the wormholing phenomenon. SPEPE 4 (1), 63–68.
- Da Motta, E.P., 1993. Matrix Acidizing of Horizontal Wells, Ph.D. Dissertation. University of Texas at Austin, Austin, TX.
- Deng, J., Mou, J., Hill, A.D., Zhu, D., 2012. A new correlation of acid-fracture conductivity subject to closure stress. SPE Prod. Oper. 27, 158–169.



- Economides, M.J., Hill, A.D., Ehlig-Economides, C., 1994. *Petroleum Production Systems*. Prentice Hall, Englewood Cliffs, NJ.
- Economides, M.J., Nolte, K.G., 2000. *Reservoir Stimulation*. third ed. John Wiley & Sons, New York.
- Fogler, H.S., Lund, K., Mccune, C.C., 1976. Predicting the flow and reaction of HCl/HF mixtures in porous sandstone cores, *SPEJ* Oct. 1976 . Trans. AIME 234, 248–260.
- Hekim, Y., Fogler, H.S., Mccune, C.C., 1982. The radial movement of permeability fronts and multiple reaction zones in porous media. *SPEJ* 2, 99–107.
- Hill, A.D., Lindsay, D.M., Silberberg, I.H., Schechter, R.S., 1981. Theoretical and experimental studies of sandstone acidizing. *SPEJ* 21, 30–42.
- Hoefner, M.L., Fogler, H.S., 1988. Pore evolution and channel formation during flow and reaction in porous media. *AIChE J.* 34, 45–54.
- Lund, K., Fogler, H.S., Mccune, C.C., 1973. Acidization I: the dissolution of dolomite in hydrochloric acid. *Chem. Eng. Sci.* 28, 691.
- Lund, K., Fogler, H.S., Mccune, C.C., Ault, J.W., 1975. Acidization II: the dissolution of calcite in hydrochloric acid. *Chem. Eng. Sci.* 30, 825.
- McDuff, D., Jackson, S., Schuchart, C., Postl, D., 2010. Understanding wormholes in carbonates: unprecedented experimental scale and 3D visualization. *JPT* 62 (10), 78–81.
- McLeod Jr., H.O., 1984. Matrix acidizing. *JPT* 36, 2055–2069.
- Nierode, D.D., Kruk, K.F., An evaluation of acid fluid loss additives, retarded acids, and acidized fracture conductivity. In: Paper SPE 4549 presented at the Fall Meeting of the SPE of AIME, Las Vegas, NV, 30 September–3 October, 1973.
- Paccaloni, G., Tambini, M., 1993. Advances in matrix stimulation technology. *JPT* 45, 256–263.
- Paccaloni, G., Tambini, M., Galoppini, M. Key factors for enhanced results of matrix stimulation treatment. In: Presented at the SPE Formation Damage Control Symposium held in Bakersfield, CA on 8–9 February, 1988. SPE Paper 17154.
- Schechter, R.S., 1992. *Oil Well Stimulation*. Prentice Hall, Englewood Cliffs, NJ.
- Smith, C.F., Henderickson, A.R., 1965. Hydrofluoric acid stimulation of sandstone reservoirs, *JPT* Feb. 1965 . Trans. AIME 234, 215–222
- Taha, R., Hill, A.D., Sepehrnoori, K., 1989. Sandstone acidizing design with a generalized model. *SPEPE* 4 (1), 49–55.
- Tan, X., Tabatabaei, M., Zhu, D., Hill, A.D., 2012. Diagnosis of acid placement from temperature profiles. *SPE Prod. Oper.* 284–293.
- Valsecchi, P., McDuff, D., Chang, D., Huang, H., Burdette, J., Long, T., et al., Simulation and visualization of near-well flow. In: Paper SPE 157028 presented at the SPE International Production and Operation Conference and Exhibition, Doha, Qatar, 14–18 May 2012.

---

## PROBLEMS

- 13.1.** For the reaction between 20 wt% HCl solution and calcite, calculate the gravimetric and volumetric dissolving power of the acid solution.
- 13.2.** For the reaction between 20 wt% HCl solution and dolomite, calculate the gravimetric and volumetric dissolving power of the acid solution.

- 13.3.** A sandstone with a porosity of 0.18 containing 8 v% calcite is to be acidized with HF/HCl mixture solution. A preflush of 15 wt% HCl solution is to be injected ahead of the mixture to dissolve the carbonate minerals and establish a low-pH environment. If the HCl preflush is to remove all carbonates in a region within 1.5 ft beyond a 0.328-ft-radius wellbore before the HF/HCl stage enters the formation, what minimum preflush volume is required in terms of gallon per foot of pay zone?
- 13.4.** A sandstone with a porosity of 0.15 containing 12 v% dolomite is to be acidized with HF/HCl mixture solution. A preflush of 15 wt% HCl solution is to be injected ahead of the mixture to dissolve the carbonate minerals and establish a low-pH environment. If the HCl preflush is to remove all carbonates in a region within 1.2 ft beyond a 0.328-ft-radius wellbore before the HF/HCl stage enters the formation, what minimum preflush volume is required in terms of gallon per foot of pay zone?
- 13.5.** A 30-ft thick, 40-md sandstone pay zone at a depth of 9000 ft is to be acidized with an acid solution having a specific gravity of 1.07 and a viscosity of 1.2 cp down a 2-in. ID coil tubing. The formation fracture gradient is 0.7 psi/ft. The wellbore radius is 0.328 ft. Assuming a reservoir pressure of 4000 psia, drainage area radius of 1500 ft and skin factor of 10, calculate
- The maximum acid injection rate using safety margin 200 psi.
  - The maximum expected surface injection pressure at the maximum injection rate.
- 13.6.** A 40-ft thick, 20-md sandstone pay zone at a depth of 8000 ft is to be acidized with an acid solution having a specific gravity of 1.07 and a viscosity of 1.5 cp down a 2-in. ID coil tubing. The formation fracture gradient is 0.65 psi/ft. The wellbore radius is 0.328 ft. Assuming a reservoir pressure of 3500 psia, drainage area radius of 1200 ft, and skin factor of 15, calculate
- The maximum acid injection rate using a safety margin of 400 psi.
  - The maximum expected surface injection pressure at the maximum injection rate.
- 13.7.** A 20 wt% HCl is needed to propagate wormholes 2 ft from a 0.328-ft radius wellbore in a limestone formation (specific gravity 2.71) with a porosity of 0.12. The designed injection rate is 0.12 bbl/min-ft, the diffusion coefficient is  $10^{-9}$  m<sup>2</sup>/sec, and the density of the 20% HCl is 1.11 g/cm<sup>3</sup>. In linear core floods, 1.2 pore volume is needed for wormhole breakthrough at the end of the core. Calculate the acid volume requirement using (1) Daccord's model and (2) the volumetric model.
- 13.8.** A 25 wt% HCl is needed to propagate wormholes 3 ft from a 0.328-ft radius wellbore in a dolomite formation (specific gravity 2.87) with a porosity of 0.16. The designed injection rate is 0.15 bbl/min-ft, the diffusion coefficient is  $10^{-9}$  m<sup>2</sup>/sec, and the density of the 25% HCl is 1.15 g/cm<sup>3</sup>. In linear core floods, 4 pore volumes is needed for wormhole breakthrough at the end of the core. Calculate the acid volume requirement using (1) Daccord's model and (2) the volumetric model.

## HYDRAULIC FRACTURING

## 14

**14.1 INTRODUCTION**

Hydraulic fracturing, as a well stimulation technique, is one of the most enduring technologies that the oil and gas industry has ever developed. Tens of thousands of oil and gas wells worldwide are stimulated using hydraulic fracturing every year. Commercial developments of unconventional resources would not be possible today without hydraulic fracturing. There are a wide range of applications for hydraulic fracturing, including unconventional development, production enhancement in low- and moderate-permeability reservoirs, bypassing near wellbore damage in high-permeability reservoirs, reducing sand production in loosely consolidated or unconsolidated sandstone reservoirs, and connecting the natural fractures in a formation to the wellbore.

Hydraulic fracturing is a process in which fluid is pumped into the wellbore, through a perforated or openhole interval, and into the targeted formation at pressures high enough to break the rock and create a fracture. As high-pressure fluid injection continues, some fluid leaks off into the formation and the rest of the fluid keeps the pressure inside the fracture high enough to allow the fracture propagation to continue. A clean fluid is typically pumped initially to create a fracture. Once the desired fracture dimensions are achieved, the pumping is switched from the clean fluid to a mixture of fluid and proppant. Upon the completion of the process, pumping is stopped, but the fluid inside the fracture continues leaking off into the formation until the fracture closes on proppant. The goal of hydraulic fracturing is to leave a fracture packed with proppant to create a conductive path from the wellbore deep into the formation. Part or all of the fracturing fluid remaining inside the fracture and in the reservoir around the fracture will flow back during the flowback and early production periods.

A hydraulic fracturing treatment is implemented at a well site using an array of specialized equipment, including high-pressure pumps, blenders, fluid tanks, proppant storage units, and ancillary equipment such as hoses, pipes, valves, manifolds, etc. [Fig. 14.1](#) provides a simplified view of the process, including the equipment, the equipment layout at surface, the wellbore, the fracture created, and the proppant placed. In oilfield terms, fracture and fracturing are often referred to as “frac”.

This chapter describes various aspects of hydraulic fracturing treatments in reasonable detail. For more information on this subject, the reader may refer to [Economides and Nolte \(2000\)](#), [Gidley et al. \(1989\)](#) and [Economides et al. \(1994\)](#).

This chapter focuses on the following topics:

- Basic rock mechanics
- Hydraulic fracture geometry overview
- Hydraulic fracture models

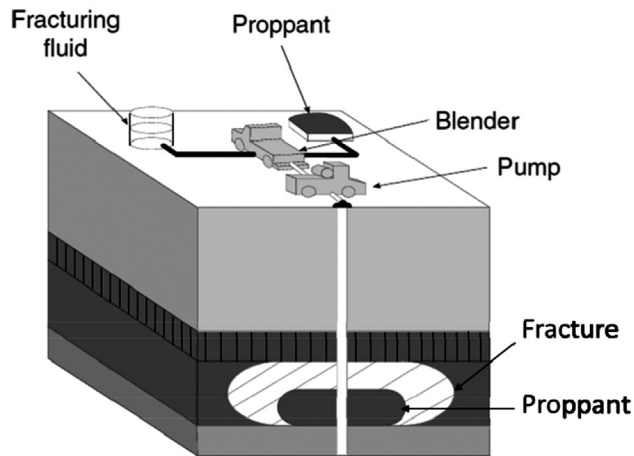
**FIGURE 14.1**

Illustration of the hydraulic fracturing process.

- Fracturing pressure analysis
- Fracturing materials and equipment
- Fractured well productivity
- Fracturing treatment design
- Frac-pack treatments
- Fracturing horizontal wells
- Fracturing treatment evaluation

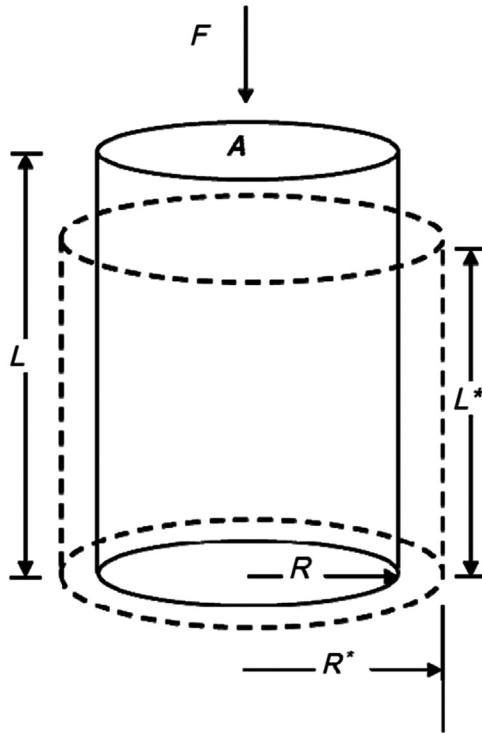
## 14.2 BASIC ROCK MECHANICS

### 14.2.1 BASIC DEFINITIONS

Consider a cylindrical rock sample with radius  $R$  and length  $L$ , as shown in Fig. 14.2. The rock sample deforms when a uniaxial force  $F$  is applied. Stress is defined as the ratio of a force to the cross-sectional area where the force is applied. The axial stress  $\sigma_L$  applied to the rock sample in this case is expressed as:

$$\sigma_L = \frac{F}{A}. \quad (14.1)$$

where  $A$  is the area, which equals  $\pi R^2$  in this example.

**FIGURE 14.2**

Rock deformation under uniaxial loading.

As uniaxial loading (compressional force) is applied in this example, the cylindrical rock body shrinks in the axial direction, but expands in the radial direction, which results in new dimensions  $L^*$  and  $R^*$  of the sample. Strain provides a measure of how a solid material deforms under stress, and is defined as the amount of deformation divided by the initial length of the material. There are two strains associated with this example. Strain in the axial direction is expressed as:

$$\varepsilon_L = \frac{L - L^*}{L}. \quad (14.2)$$

Strain in the radial direction is expressed as:

$$\varepsilon_R = \frac{R - R^*}{R}. \quad (14.3)$$

The Poisson's ratio is defined as the strain in the unloaded direction divided by the strain in the loaded direction:

$$\nu = -\frac{\varepsilon_R}{\varepsilon_L}. \quad (14.4)$$

The negative sign is included in the above equation to make sure that Poisson's ratio is a positive quantity. The Poisson's ratio is dimensionless and always less than 0.5. The Poisson's ratio for most rocks ranges from 0.15 to 0.35.

There are two types of deformation for solid materials: elastic and plastic deformation. In elastic deformation, all strain recovers when the applied stress is removed. Plastic deformation is permanent and occurs when the deformation passes beyond the elastic limit of a material. When linear elasticity is valid, there exists a linear and unique relationship between stress and strain, which is commonly known as Hooke's Law:

$$\sigma_L = E\varepsilon_L. \quad (14.5)$$

The linear coefficient  $E$  in Hooke's Law is Young's modulus of the material, which has the same unit as stress since strain is dimensionless. The values of Young's modulus are affected by rock type and rock fabrics. In general, as the formation gets deeper and tighter, the value of its Young's modulus tends to become larger. For most petroleum reservoirs, the values of Young's modulus can range from as low as  $50 \times 10^3$  psi to as high as  $10 \times 10^6$  psi. Coal, weak sandstone, soft chalk, and diatomite are among the rocks that have very low Young's modulus values.

When a material is subjected to shear force, shear stress and shear strain arise. A shear stress is defined as the component of stress arising from the force vector component parallel to the cross section of the material. Shear strain is defined as the length of deformation divided by the perpendicular length in the plane of the force applied. In elastic deformation, there also exists a linear and unique relationship between shear stress and shear strain. The proportionality coefficient between the shear stress and shear strain is defined as shear modulus. Instead of measuring it, the shear modulus,  $G$ , is readily calculated directly from the Young's modulus and Poisson's ratio:

$$G = \frac{E}{2(1 + \nu)}. \quad (14.6)$$

In fracture mechanics and fracture modeling, there is another modulus appearing often in equations, which is named the plane strain modulus,  $E'$ . The plane strain modulus is related to the Young's modulus and Poisson's ratio as follows:

$$E' = \frac{E}{1 - \nu^2} \quad (14.7)$$

The value of the plane strain modulus is very close to the value of the Young's modulus for most hydraulic fracturing applications as typical Poisson's ratio values for most petroleum-bearing rocks range from 0.15 to 0.25.

Like other solid materials, rock exhibits tensile and compressive strengths. The tensile strength of a material is defined as the maximum tensile load or force, divided by its cross-sectional area, to make it fail. Compressive strength is defined as the maximum compressive load, divided by its cross-sectional area, to make it fail. The strength of a rock sample obtained with uniaxial stress testing is called the uniaxial compressive strength (UCS). The tensile strengths of rocks are generally much lower than their compressive strengths. In contrast, most metals perform well both in tension and compression.

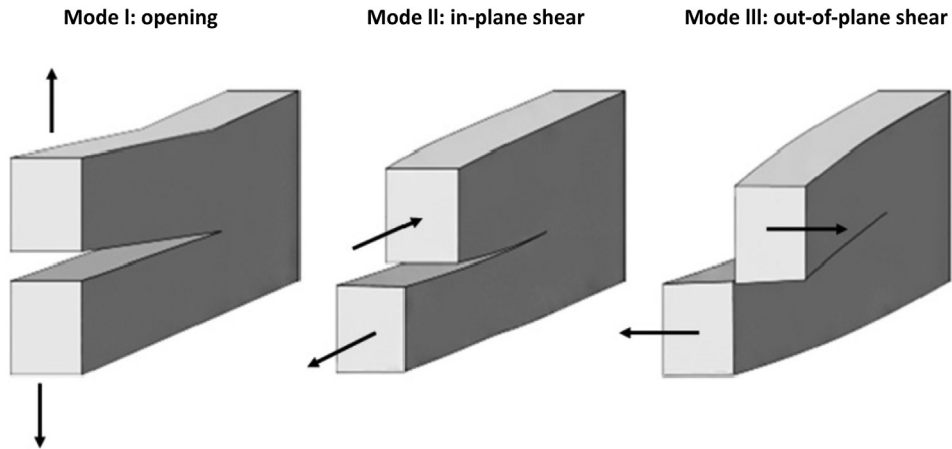


FIGURE 14.3

Three fracture modes.

### 14.2.2 FRACTURE MODES AND FRACTURE TOUGHNESS

Fracture is literally the cracking or breaking of a solid material. As shown in Fig. 14.3, there are three modes of fractures that can occur when a material fails by external loads:

- Mode I fracture, also known as the opening mode, which is caused by a tensile stress normal to the plane of the crack;
- Mode II fracture, also known as the sliding mode, which is caused by a shear stress acting parallel to the plane of the crack and perpendicular to the crack front;
- Mode III fracture, also known as the tearing mode, which is caused by a shear stress acting parallel to the plane of the crack and parallel to the crack front.

The opening mode that results in tensile fractures is usually concerned in hydraulic fracturing applications. Tensile fractures propagate in the direction perpendicular to the least principal stress.

Linear Elastic Fracture Mechanics (LEFM) is the basic theory of fracture, which was originally developed by Griffith (1921, 1924) and modified by Irwin (1957). LEFM assumes linear elastic deformation on the fracture surface. Griffith advanced the understanding of crack behavior by suggesting that low tensile strengths observed in some brittle materials such as glass were caused by the presence of preexisting microcracks. Griffith assumed that the microcracks were elliptical in shape and that the work performed during the extension of a crack was equal to the surface energy of the newly created crack surface. The work to extend a crack of half-length  $a$  by an amount of  $da$  is given by

$$dW = \frac{\pi\sigma^2}{E}ada, \quad (14.8)$$

where  $\sigma$  is the applied stress, and the work,  $dW$ , is equal to the newly released surface energy for two new faces of the crack:

$$dW = 2\gamma da, \quad (14.9)$$

where  $\gamma$  is the surface energy. The value of a critical stress required for crack propagation can be expressed as

$$\sigma_c = \sqrt{\frac{2E'\gamma}{\pi a}}. \quad (14.10)$$

Irwin (1957) found a method to relate the amount of energy available for a fracture to the stress and displacement fields around the crack tip and demonstrated that the magnitude of the stresses around the crack is inversely proportional to the square root of the radial distance  $r$  away from the crack tip:

$$\sigma_{ij} \approx \left( \frac{K_I}{\sqrt{2\pi r}} \right) f_{ij}(\theta) \quad (14.11)$$

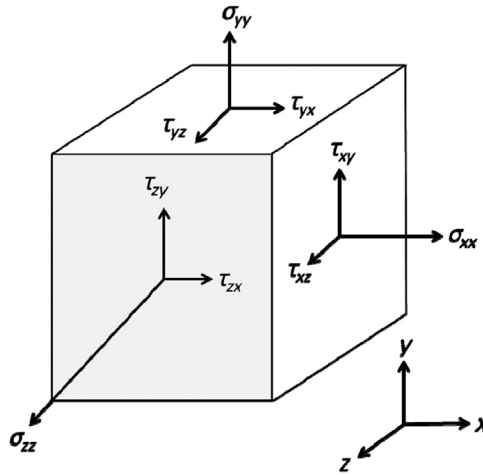
where  $\sigma_{ij}$  is any of the nine stress vector components that completely define the state of stress at any point inside a material,  $\theta$  is the angle referenced to the plane of the crack, and  $f_{ij}$  are functions that depend on the angle  $\theta$ . Irwin named the quantity  $K$  as the stress intensity factor, and the subscript  $I$  represents the opening mode of the crack deformation. Stress intensity factors are not limited to the opening mode, but also apply to other fracture modes. The unit of the stress intensity factor can be expressed in  $\text{MPa} \cdot \text{m}^{1/2}$  or  $\text{psi} \cdot \text{in}^{1/2}$  since the values of the function  $f_{ij}$  are dimensionless.

A fracture propagates when  $K_I$  reaches a critical value, known as the critical stress intensity factor  $K_{Ic}$ , which is more commonly referred to as *fracture toughness*. The stress intensity factor is a function of the crack geometry and loading conditions, but fracture toughness is a material property, and has to be evaluated experimentally. Fracture toughness ranges from 500 to 3500  $\text{psi} \cdot \text{in}^{1/2}$ , with a typical value of about 2000  $\text{psi} \cdot \text{in}^{1/2}$  for most rocks. Fracture toughness reflects the resistance of the rock to fracture propagation. In another word, fracture toughness represents the energy required to propagate the fracture at its tip. When the fracture length is small, it requires more energy to propagate the fracture. As the fracture becomes larger, the effect of fracture toughness becomes insignificant. Fracture toughness is a required input parameter for all realistic fracture simulators.

### 14.2.3 PRINCIPAL STRESSES

The stress described in Fig. 14.2 is under a uniaxial load and has only one component. When a material is subjected to triaxial loading, the state of stress becomes more complicated, which is the case for formation rocks in underground conditions. The stress in a three-dimensional (3D) space can be decomposed into and described by two types of stresses: normal and shear stresses. A shear stress, typically denoted as  $\tau$ , arises from the component of stress arising from the force vector component parallel to the material cross section. Normal stress, typically denoted as  $\sigma$ , arises from the force vector component perpendicular to the material cross section. 3D stress components for a material under loading in all directions are illustrated in Fig. 14.4.





**FIGURE 14.4**

General state of stress in 3D space.

As noticed in the above figure, there are 9 stress components in a 3D space. The 3D stress can be expressed with a  $3 \times 3$  matrix in the following stress tensor form:

$$\sigma = \begin{bmatrix} \sigma_{xx} & \tau_{xy} & \tau_{xz} \\ \tau_{yx} & \sigma_{yy} & \tau_{yz} \\ \tau_{zx} & \tau_{zy} & \sigma_{zz} \end{bmatrix}. \quad (14.12)$$

Among the 9 stress components, only six components are independent, as some shear stress components share the same value:  $\tau_{xy} = \tau_{yx}$ ,  $\tau_{xz} = \tau_{zx}$ , and  $\tau_{yz} = \tau_{zy}$ , due to symmetry. A 3D stress tensor can be transformed to its three principal directions in a new coordinate system, allowing all shear stress components to disappear and resulting in the following simpler form:

$$\sigma = \begin{bmatrix} \sigma'_x & & \\ & \sigma'_y & \\ & & \sigma'_z \end{bmatrix}. \quad (14.13)$$

The three new normal stresses in the above equation have now become three principal stresses, which are generally referred to as the maximum, intermediate, and minimum principal stresses, and are typically renamed in such a way that  $\sigma_1 \geq \sigma_2 \geq \sigma_3$ . A hydraulic fracture will initiate and propagate in a formation with the least energy. Since the least energy required to crack a rock is against the minimum principal stress, a hydraulic fracture generally propagates perpendicular to the direction of the minimum principal stress. The value and orientation of the minimum principal stress are very important to hydraulic fracturing as they control the treating pressure required for fracture initiation and propagation as well as the direction of the fracture. The shape and vertical extent of the fracture are also highly affected by the magnitude of the minimum principal stress at various depths. In a geological setting, these three principal stresses are neither isotropic nor homogeneous. Both the magnitude and orientation of these three principal stresses vary vertically and horizontally.

Because both stresses and strains are 3D, the relationship between these stresses and strains can be generalized to a 3D space. In three principal directions designated by  $x$ ,  $y$ , and  $z$ , Hooke's Law takes the following forms:

$$\varepsilon_x = \frac{\sigma_x}{E} - \frac{\nu}{E}(\sigma_y + \sigma_z), \quad (14.14a)$$

$$\varepsilon_y = \frac{\sigma_y}{E} - \frac{\nu}{E}(\sigma_x + \sigma_z), \quad (14.14b)$$

$$\varepsilon_z = \frac{\sigma_z}{E} - \frac{\nu}{E}(\sigma_x + \sigma_y). \quad (14.14c)$$

#### 14.2.4 OVERBURDEN, HORIZONTAL AND EFFECTIVE STRESSES

The overburden stress is caused by the weight of all the rocks above the point of interest and is always in the vertical direction. For a reservoir rock at depth  $H$  with variable density  $\rho$ , the overburden stress  $\sigma_v$  is calculated as

$$\sigma_v = \int_0^H \frac{\rho}{144} dh, \quad (14.15)$$

In this equation,  $\sigma_v$  is in psi,  $\rho$  is in  $\text{lb/ft}^3$ , and  $H$  is in ft.

In geological formations, the overburden stress is often the maximum principal stress, which leaves the other two principal stresses in the horizontal directions, often denoted as  $\sigma_{h,\text{max}}$  and  $\sigma_{h,\text{min}}$ . For the majority of hydraulic fracturing applications in petroleum reservoirs, the overburden stress is the maximum principal stress, and vertical fractures are created.

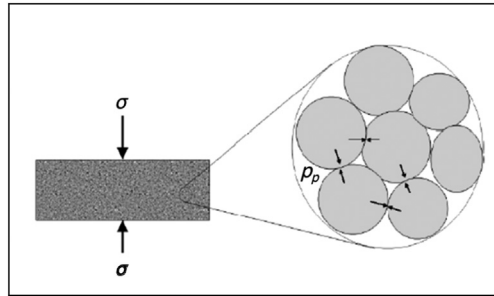
In order to derive a relationship between the horizontal and overburden stresses, elastic deformation in a homogenous and isotropic reservoir without tectonic influences from the outside is assumed. The above assumptions further imply the following two conditions: (1)  $\sigma_{h,\text{max}} = \sigma_{h,\text{min}} = \sigma_h$  because the stresses in the horizontal plane have to be symmetrical; and (2)  $\varepsilon_x = \varepsilon_y = 0$  because no deformation takes place in the horizontal plane. By applying the above two conditions to the stress-strain relations described in Eq. (14.14a) or (14.14b), the following relationship between the vertical and horizontal stresses can be obtained:

$$\sigma_h = \frac{\nu}{1-\nu} \sigma_v. \quad (14.16)$$

Eq. (14.16) indicates that the Poisson's ratio value of a formation can have a considerable influence on the horizontal stresses of the formation. In general, clay-rich shale formations tend to have larger Poisson's ratio values than these of clean sandstone formations. As a result, sandstones tend to be under lower stresses than shales. This explains why thick shale formations are often considered to be fracture barriers.

Both vertical and horizontal stresses for a reservoir rock underground are compressive in nature. The compressive stresses are interacted with the pore pressure of reservoir fluid because they support a portion of the total stress applied. To take the fluid pressure into consideration, the concept of effective stress is illustrated in Fig. 14.5, and the effective stress  $\sigma'$  is calculated as:

$$\sigma' = \sigma - \alpha p_p, \quad (14.17)$$



**FIGURE 14.5**

Concept of effective stress applied to rock grains.

where  $\alpha$  is Biot's poroelastic constant. The poroelastic constant describes how effectively the fluid pressure counteracts the total applied stress. By definition, it varies between 0 and 1, but typically between 0.7 and 1.0 for most petroleum reservoirs. Note that the concept of effective stress applies to both the overburden and horizontal stresses.

### 14.2.5 FAULTS AND TECTONIC STRESSES

The overburden stress is a principal stress, but not necessarily the maximum principal stress. There are situations where the vertical overburden stress of a reservoir formation is not the maximum principal stress. These situations may occur in shallow formations and some fault environments. For reservoirs typically less than 1000 ft in depth, the overburden stress can be lower than the horizontal stress. Fig. 14.6 illustrates three types of fault regimes (Anderson, 1951). For the case of a thrust fault environment, the overburden stress can be the present-day minimum principal stress. For the case of a strike-slip fault environment, the overburden stress can be the present-day intermediate principal stress. In these situations, horizontal or slant fractures and fractures with multiple orientations can be developed. The development of these fractures tends to have negative impacts on stimulation effectiveness as these types of fractures, especially horizontal fractures, are less effective to drain reservoir rocks in comparison with vertical fractures. In particular, horizontal fractures drain reservoir fluids in the vertical direction. The extent of a reservoir is usually much more limited in the vertical direction than that in the horizontal direction. Also, for many sedimentary rocks, vertical permeability values are much smaller than horizontal permeability values. In addition, treatment execution is often problematic in these reservoir environments as high treating pressure and failure to pump the treatment as planned is often encountered.

In a tectonic active region, the movement of a tectonic plate will give rise to both tectonic strains and stresses. Incremental tectonic strains in the horizontal plane can be decomposed into two components,  $d\varepsilon_{t,H}$  and  $d\varepsilon_{t,h}$ , with each component associated with its own horizontal principal direction. By assuming elastic deformation in an isotropic and homogenous rock and no variation in the overburden stress, the resulting tectonic stress components in the horizontal plane can be estimated as follows:

$$d\sigma_{t,h} \approx E' d\varepsilon_{t,h} + E' \nu d\varepsilon_{t,H}, \quad (14.18)$$

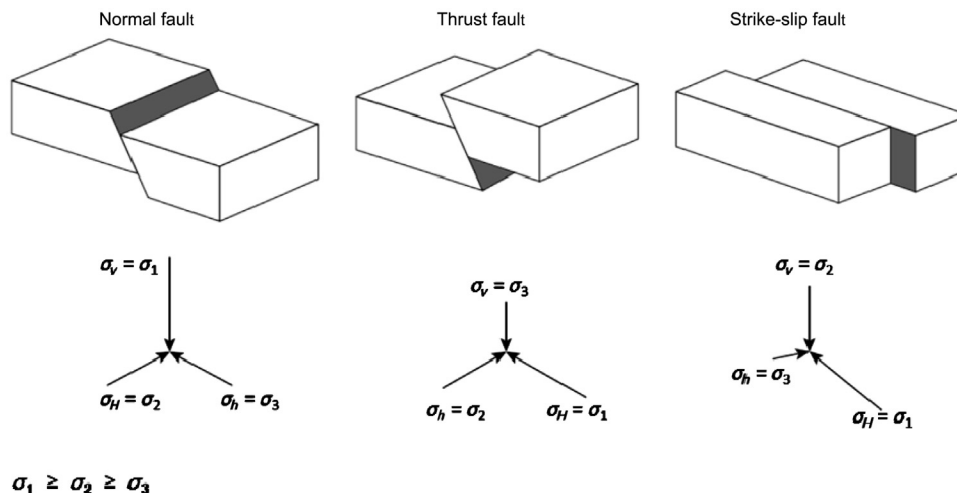


FIGURE 14.6

Common fault regimes (Anderson, 1951).

$$d\sigma_{t,H} \approx E' d\varepsilon_{t,H} + E' \nu d\varepsilon_{t,h}, \quad (14.19)$$

where  $d\sigma_{t,H}$  and  $d\sigma_{t,h}$  are the resulting tectonic stresses in each horizontal principal direction, respectively. The resulting tectonic stress increments,  $d\sigma_{t,H} > d\sigma_{t,h}$ , are not equal because of unequal tectonic strain increments. The direction of  $d\sigma_{t,H}$  is associated with the direction of the maximum horizontal principal direction while the direction of  $d\sigma_{t,h}$  is associated with the direction of the minimum horizontal principal direction. Both tectonic strains and stresses are very difficult to estimate.

## 14.2.6 MINIMUM HORIZONTAL STRESS

It is very important to include the effects of the pore fluid pressure for estimating the minimum horizontal stress. Effective stress calculated in Eq. (14.17) applies to stresses in any direction, including the overburden and horizontal stresses. By replacing the horizontal and overburden stresses in Eq. (14.10) with their effective stresses based on Eq. (14.17), the following relationship is obtained to correctly calculate horizontal stresses:

$$\sigma_h = \frac{\nu}{1-\nu}(\sigma_v - \alpha p_r) + \alpha p_r. \quad (14.20)$$

Eq. (14.20) assumes that the two horizontal stresses are the same because tectonic influences are not considered in Eq. (14.16). As demonstrated in Eq. (14.20), both the rock lithology (Poisson's ratio) and the pore fluid pressure strongly affect horizontal stresses. For the purpose of illustration, assume  $\nu = 0.25$  and  $\alpha = 1.0$ , Eq. (14.20) then becomes  $\sigma_h = 1/3 \sigma_v + 2/3 p_r$ , which indicates that any change in the pore fluid pressure will have huge impacts on horizontal stresses. The minimum horizontal stress varies at various depths due to the changes in the rock lithology and the pore fluid pressure in the vertical direction. The geometry of a vertical fracture is highly dependent on the horizontal stress profile along the vertical direction.

Generally speaking, sedimentary rocks are not isotropic, but exhibit anisotropic properties to some degree, including elastic properties such as Young's modulus and Poisson's ratio. The topic of anisotropy is beyond the scope of this book. However, both formation rock anisotropy and tectonic influences give rise to horizontal stress anisotropy and result in a difference between the two horizontal principal stresses. The two horizontal stresses can now be distinguished with the consideration of the above effects:

$$\sigma_{h,\min} = \frac{\nu}{1-\nu}(\sigma_v - \alpha p_r) + \alpha p_r + d\sigma_{t,h}. \quad (14.21)$$

$$\sigma_{h,\max} = \frac{\nu}{1-\nu}(\sigma_v - \alpha p_r) + \alpha p_r + d\sigma_{t,H}. \quad (14.22)$$

It is easier to obtain the minimum horizontal stress than the maximum horizontal stress. In practice, the minimum horizontal stress can be estimated by acoustic log data analysis or measured through diagnostic fracture testing. It is worth noting that stress estimation from acoustic log data must be validated and calibrated using stress measurements from diagnostic fracture testing, which will be discussed in [Section 14.8.4](#). The actual state of stress is much more complex due to the anisotropic and heterogeneous nature of rock formations. Furthermore, the magnitude and orientation of the in-situ stress field can also be altered locally due to reservoir development.

The two horizontal principal stresses can be related in a general form as follows:

$$\sigma_{h,\max} = a\sigma_{h,\min} + \Delta\sigma_h, \quad (14.23)$$

where  $a$  is the factor and  $\Delta\sigma_h$  is the stress offset. In a tectonically relaxed environment, the maximum horizontal principal stress is typically only a few percentages larger than the minimum horizontal principal stress.

For most hydraulic fracturing applications, the direction and magnitude of the minimum horizontal stress are more important than those of the maximum horizontal stress. Except for the near wellbore area, if a planar fracture is created, it will propagate perpendicular to the minimum horizontal stress direction. And the far-field fracture geometry is only affected by the values of the minimum horizontal stress. The fluid pressure inside a fracture has to be larger than the minimum principal stress in order for the fracture to continue propagating. For that, the minimum principal stress is often referred to as the "closure stress" or "closure pressure," below which the fracture will close between its two walls. In most cases, the minimum horizontal stress is the closure stress unless a thrust fault environment is encountered.

When the maximum principal stress is in the vertical direction, a vertical fracture will be created and propagate parallel to the  $\sigma_{h,\max}$  orientation and perpendicular to the  $\sigma_{h,\min}$  orientation. In tight rock and shale reservoir development, a common practice is to drill horizontal wells along the  $\sigma_{h,\min}$  orientation. As a result, hydraulic fractures from multistage fracture completion will become transverse to the horizontal lateral, which helps maximize reservoir exposure and drainage volume.

### 14.2.7 FORMATION BREAKDOWN AROUND THE WELLBORE

Drilling a borehole will induce large stress concentrations around the wellbore. The initiation of a fracture has to first overcome the in-situ stresses, the induced stresses, and the tensile strength of

the rock. The induced stresses around the wellbore are also affected by the in-situ stresses (minimum horizontal and maximum horizontal stresses). The breakdown pressure,  $p_{bd}$ , for fracture initiation at the wellbore can be estimated as follows (Hubbert and Willis, 1957):

$$p_{bd} = 3\sigma_{h,\min} - \sigma_{h,\max} + T_0 - p_p, \quad (14.24)$$

where  $T_0$  is the tensile strength of the rock.

The induced stresses around the wellbore only affect fracture initiation, but not propagation, because the induced stresses will diminish to zero when the fracture propagates away from the wellbore. Eq. (14.24) provides the upper boundary of the breakdown pressure only. Before a fracture initiates, the wellbore fluid first enters the formation through matrix flow and increases the pore pressure around the wellbore. The poroelastic effects of the wellbore fluid in the formation around the wellbore will reduce the breakdown pressure. In addition, if preexisting fractures (natural fractures or drilling induced fractures) exist, the breakdown pressure will also be lower because a fracture will initiate from the preexisting fracture and does not need to overcome the tensile strength of the rock.

By definition, a hydraulic fracture is created by fluid injection. For that, pressure and stress are interchangeable to describe fracture initiation and propagation. Due to the effects of the induced stresses around the wellbore, the breakdown pressure is larger than the fracture extension pressure (often simply called fracture pressure), which is the fluid pressure required to propagate the fracture through the formation, away from the influence of wellbore effects. The fracture pressure is affected by many factors, including the minimum stresses in various formation layers that the fracture covers, the contrast of minimum stresses between lithology, the contrast between the minimum and intermediate stresses, rock properties, fracturing fluid properties, and pumping rates, etc.

**Example Problem 14.1** A sandstone at a depth of 10,000 ft has a Poisson's ratio of 0.25 and a poroelastic constant of 0.72. The average density of the overburden formation is 165 lb/ft<sup>3</sup>. The pore pressure gradient in the sandstone is 0.38 psi/ft. Assume the difference between the maximum and minimum horizontal stresses of 1000 psi and a tensile strength of the sandstone of 500 psi, predict the breakdown pressure for the sandstone.

**Solution**

Overburden stress:

$$\sigma_v = \frac{\rho H}{144} = \frac{(165)(10,000)}{144} = 11,500 \text{ psi}$$

Pore pressure is:

$$p_p = (0.38)(10,000) = 3800 \text{ psi}$$

The effective vertical stress:

$$\sigma'_v = \sigma_v - \alpha p_p = 11,500 - (0.72)(3800) = 8800 \text{ psi}$$

The effective horizontal stress:

$$\sigma'_h = \frac{\nu}{1 - \nu} \sigma'_v = \frac{0.25}{1 - 0.25}(8800) = 2900 \text{ psi}$$

The minimum horizontal stress:

$$\sigma_{h,\min} = \sigma'_h + \alpha p_p = 2900 + (0.72)(3800) = 5700 \text{ psi}$$

The maximum horizontal stress:

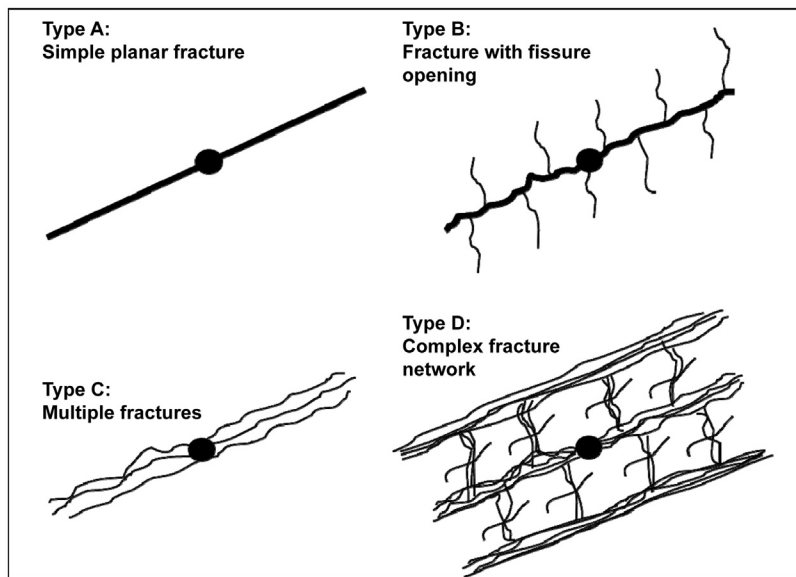
$$\sigma_{h,\max} = a\sigma_{h,\min} + \Delta\sigma_h = (1)5700 + 1000 = 6700 \text{ psi}$$

The breakdown pressure:

$$\begin{aligned} p_{bd} &= 3\sigma_{h,\min} - \sigma_{h,\max} + T_0 - p_p \\ &= 3(5700) - 6700 + 500 - 3800 = 7100 \text{ psi} \end{aligned}$$

### 14.3 HYDRAULIC FRACTURE GEOMETRY OVERVIEW

A planar fracture with bi-wings symmetrical at the wellbore has been often used to describe the shape of a vertical hydraulic fracture. However, [Warpinski et al. \(2008\)](#) presented a more realistic view of the types of fractures that can be envisioned in various petroleum reservoirs. The authors pointed out that some level of fracture complexity appears to occur in many reservoirs. [Fig. 14.7](#) shows a schematic map view of four types of vertical fractures, adapted and modified from [Warpinski et al. \(2008\)](#). Type A represents an ideal fracture developed in a homogenous reservoir. In high-permeability reservoirs with high porosity and very low Young's modulus, smaller fractures



**FIGURE 14.7**

Schematic view of various hydraulic fracture types ([Warpinski et al., 2008](#)).

are usually required to bypass near wellbore damage or to mitigate sand production. In these cases, relatively simple fractures are expected to develop from each set of perforation intervals in a planar fashion. Type B represents the scenario that a single hydraulic fracture is developed with natural fractures activated in a direction perpendicular to the hydraulic fracture. Type C represents the scenario that the orientations of hydraulic and natural fractures are about the same so that multiple hydraulic fractures may propagate along the orientation of the preexisting natural fractures. Type D represents the scenario that a complex fracture network is developed in reservoirs having two orthogonal sets of natural fractures. The Barnett shale is an example that the Type D fracture network tends to develop during hydraulic fracturing treatments. Hydraulic fracturing in shale reservoirs has often resulted in complex fracture network growth due to the interaction with natural fractures, as evidenced by laboratory studies and microseismic monitoring.

[Inui et al. \(2014\)](#) conducted tri-axial hydraulic fracturing experiments to investigate how the viscosity of fracturing fluid affects fracture propagation and fracture mode. The authors have drawn the following conclusions from their experimental studies: (1) the injection of a low viscosity fluid can generate complex fractures with multiple branches; (2) low viscosity fluids induce shear dominant fracture, while high viscosity fluids induce tensile dominant fracture.

[Warpinski et al. \(2005\)](#) presented a case study that two fracturing treatments were conducted on the same well in the Barnett shale. Cross-linked gel was used in the initial treatment and slickwater was used in the re-fracturing treatment. Microseismic monitoring results show that more complex fractures and larger SRV (stimulated rock volume) were generated from the refracturing treatment using slickwater. Note that the viscosity of typical crosslinked gel fluids is over a hundred times larger than the viscosity of typical slickwater.

Computer model simulation results by [Weng et al. \(2011\)](#) showed that stress anisotropy, natural fractures, and interfacial friction play critical roles in creating fracture network complexity. Decreasing stress anisotropy or interfacial friction can change the induced fracture geometry from a bi-wing fracture to a complex fracture network for the same initial natural fractures. The results presented illustrated the importance of rock fabrics and stresses on fracture complexity in unconventional reservoirs.

---

## 14.4 HYDRAULIC FRACTURE MODELS

The process of hydraulic fracturing involves fracture initiation and propagation, rock deformation, fluid flow in the fracture, fluid loss into the formation, and proppant transport, etc. Hydraulic fracture models are aimed to capture the above physics with various assumptions. A robust fracture model is useful for the following reasons: (1) predicting the fracture geometry and proppant placement achieved by a specified treatment design; (2) conducting sensitivity analysis of the effects of rock/reservoir properties and treatment design parameters such as fluid type, treatment size, and pumping rate, etc.; and (3) performing treatment optimization with costs, production performance and economics taking into considerations.

Hydraulic fracture models can be generally classified into three categories: 2D fracture models, 3D fracture models, and unconventional fracture models. 3D fracture models can be further grouped into pseudo 3D, planar 3D, and general 3D models. General 3D models make no



assumptions about the orientation of the fracture, and are most applicable in research environments. For that reason, the general 3D models will not be discussed. Except for that, all other types of fracture models are reviewed and discussed in this section.

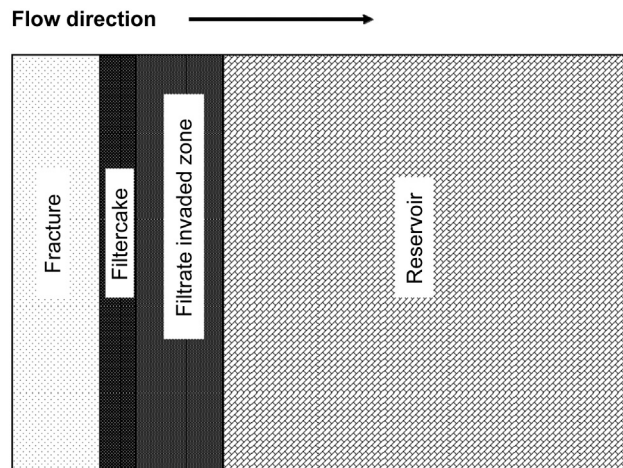
Before any fracture model is presented, let us first introduce a very important term “net pressure,” which is defined as the pressure inside the fracture minus the rock closure stress (i.e., the minimum stress against which the fracture opens):

$$p_{net} = p_f - \sigma_{min}, \quad (14.25)$$

where  $p_{net}$  is the net pressure,  $p_f$  is the fluid pressure inside the fracture, and  $\sigma_{min}$  is the minimum stress. Net pressure varies both spatially and temporally. In the theory of LEFM, the fracture width is directly proportional to net pressure. The product of net pressure and the fracture volume provides the total amount of energy available to propagate the fracture. The analysis of net pressure data during or post fracturing treatments is a very important technique for evaluating fracture growth behavior and estimating the fracture geometry.

### 14.4.1 FLUID LEAKOFF MODELS

During fracture propagation, the fracturing fluid pressure inside the fracture is larger than the minimum principal stress and much larger than the pore fluid pressure in the formation. Because of the fluid pressure differential between the fracture and the formation, some of the fracturing fluid will be squeezed out from the fracture into the formation, resulting in fluid loss. This process is often called fluid leakoff in hydraulic fracturing. As illustrated in Fig. 14.8, the leakoff process can be described by three different mechanisms in three regions: filtercake on the fracture face, filtrate invaded zone, and the rest of the reservoir. Flow in each region is governed by its own distinct mechanism. Howard and Fast (1957) and Carter (1957) recognized these three distinct processes



**FIGURE 14.8**

Schematic of fracturing fluid leakoff regions.

involved with fracturing leakoff and derived the basic equations to describe these mechanisms. The leakoff process is very important for fracture modeling and designs, as it is one of the critical factors affecting the ultimate fracture geometry and volume. In most fracture models, leakoff is considered as a one-dimensional (1D), linear flow perpendicular to the fracture face. For a planar fracture without the interference with other parallel fractures nearby, treating the leakoff process as a 1D linear flow is not a bad assumption in considerations of large fracture surface areas created in a short period of treatment time.

### 14.4.1.1 Filtercake

When a fluid containing suspensions enters a formation, larger particles that cannot penetrate the pore space in the formation will form an external filtercake immediately. Smaller particles that can enter the formation may plug the pore space and form an internal filtercake. Once the internal filtercake is established, an external filtercake will follow. Gelling agents and fluid loss additives used in fracturing fluids are usually difficult to enter the formation. As a result, an external filtercake will form on the fracture face. Initially, some fluid will leakoff without forming a filtercake, and the volume of the initial loss is called spurt loss.

The process of fluid leakoff through filtercake is governed by mass balance and Darcy's law. By assuming that the filtercake is incompressible, the filtercake thickness is proportional to the fluid volume lost through a unit surface area

$$L_c = V_L/\alpha, \quad (14.26)$$

$$\alpha = \frac{C}{(1 - \phi_c)\rho}, \quad (14.27)$$

where  $L_c$  is the filtercake thickness,  $V_L$  is the volume of fluid lost through a unit surface area,  $C$  is the mass concentration of suspensions, and  $\phi_c$  is the filtercake porosity, and  $\rho$  is the density of the suspensions. Based on Darcy's Law, the leakoff velocity can be given as follows:

$$u_L = \frac{dV_L}{dt} = \frac{k_c \Delta p_c}{\mu_f L_c} = \frac{k_c \alpha \Delta p_c}{\mu_f V_L}, \quad (14.28)$$

where  $u_L$  is the leakoff velocity,  $k_c$  is the filtercake permeability,  $\mu_f$  is the filtrate viscosity, and  $\Delta p_c$  is the pressure drop across the filtercake. Recognize that the above differential equation is valid only when a filtercake starts to form after the initial spurt loss. Assuming  $\Delta p_c$  is constant and integrating Eq. (14.28) with the condition that  $V_L = V_{sp}$  at  $t = t_{sp}$  will result in:

$$V_L = 2C_w(\sqrt{t - t_{sp}}) + V_{sp}, \quad (14.29)$$

$$u_L = \frac{C_w}{\sqrt{t - t_{sp}}}, \quad (14.30)$$

$$C_w = \sqrt{\frac{k_c \alpha \Delta p_c}{2\mu_f}}, \quad (14.31)$$

where  $C_w$  is the leakoff coefficient of the filtercake or often referred to as the wall-building coefficient,  $t_{sp}$  is the spurt loss time, and  $V_{sp}$  is the spurt loss volume.

Note that Eq. (14.31) is expressed in a consistent unit system. In oilfield units, the filtercake leakoff coefficient is in  $\text{ft}/\text{min}^{1/2}$  and the spurt loss volume is in  $\text{gal}/\text{ft}^2$ . In practice, the value of  $C_w$  is never estimated by Eqs. (14.27) and (14.31). Both the filtercake leakoff and the spurt loss volume for fracturing fluids are measured in the laboratory.

#### 14.4.1.2 Filtrate invaded zone

The leakoff process in the filtrate invaded zone also obeys Darcy's Law. With the assumptions that filtrate invasion is a piston-like displacement and that the rock and fluid are incompressible in the filtrate zone, the leakoff velocity can be described by the following equation:

$$u_L = \frac{dV_L}{dt} = \frac{k_f \Delta p_v}{\mu_f L_v} = \frac{k_f \Delta p_v}{\mu_f V_L / \phi}, \quad (14.32)$$

where  $k_f$  is the permeability in the filtrate zone,  $\Delta p_v$  is the pressure drop across the filtrate zone,  $L_v$  is the length of the filtrate zone, and  $\phi$  is the reservoir porosity. Assuming  $\Delta p_c$  is constant and integrating Eq. (14.32) results in the following equations:

$$V_L = 2C_v \sqrt{t}, \quad (14.33)$$

$$u_L = \frac{C_v}{\sqrt{t}}, \quad (14.34)$$

$$C_v = \sqrt{\frac{k_f \phi \Delta p_v}{2\mu_f}}, \quad (14.35)$$

where  $C_v$  is the leakoff coefficient of the filtrate zone. The filtrate can alter both the relative permeability and absolute permeability of the rock in the filtrate invaded zone. Eq. (14.35) is expressed in a consistent unit system, which in oilfield units is as follows:

$$C_v = 0.469 \sqrt{\frac{k_f \phi \Delta p_v}{\mu_f}}, \quad (14.36)$$

where  $C_v$  is in  $\text{ft}/\text{min}^{1/2}$ ,  $k_f$  is in Darcy,  $\phi$  is in fraction,  $\Delta p_v$  is in psi, and  $\mu_f$  is in cP.

#### 14.4.1.3 The reservoir region

Although the fracturing fluid does not go beyond the filtrate invaded zone, transient pressure responses in the uninvaded reservoir region are required to allow the leakoff process to develop. A transient flow solution can only be obtained in a compressible system. By assuming the total compressibility is constant and the reservoir is infinite, a 1D, linear transient solution to calculate the leakoff velocity in the uninvaded reservoir region is given by:

$$u_L = \frac{C_c}{\sqrt{t}}, \quad (14.37)$$

$$C_c = \sqrt{\frac{kc_t \phi}{\pi \mu} \Delta p_c}, \quad (14.38)$$

where  $C_c$  is the leakoff coefficient of the uninvaded reservoir region,  $k$  is the reservoir permeability,  $c_t$  is the total compressibility,  $\mu$  is the reservoir fluid viscosity, and  $\Delta p_c$  is the pressure drop across

the reservoir region. Eq. (14.38) is expressed in a consistent unit system, which in oilfield units becomes:

$$C_c = 0.0374 \sqrt{\frac{kc_t \phi}{\mu}} \Delta p_c, \quad (14.39)$$

where  $C_c$  is in  $\text{ft}/\text{min}^{1/2}$ ,  $k$  is in Darcy,  $c_t$  is in  $\text{psi}^{-1}$ ,  $\phi$  is in fraction,  $\Delta p_c$  is in psi, and  $\mu$  is in cP.

#### 14.4.1.4 Combined leakoff effects

In reality, all three leakoff processes occur simultaneously during any fracturing treatment. Among the three separate leakoff mechanisms, only the two mechanisms related to fracturing fluid properties can be controlled in treatment designs. The spurt loss can often be neglected. In this case, the total leakoff coefficient from the combined process can be calculated as follows (Williams et al., 1979):

$$C_L = \frac{2C_w C_v C_c}{C_w C_v + \sqrt{C_w^2 C_v^2 + 4C_c^2 (C_v^2 + C_w^2)}}, \quad (14.40)$$

where  $C_L$  is the total combined coefficient. In low-permeability reservoirs, the amount of fluid loss is very small and is dominated by reservoir leakoff. In this case, the reservoir leakoff coefficient is basically the total leakoff coefficient. A filtercake cannot form if water that does not contain any gelling agents or fluid loss additives is used as the fracturing fluid. In this case,  $C_w$  can be assumed to be infinitely large. Dividing the numerator and denominator of the right hand side of Eq. (14.40) by  $C_w$  and assuming  $(C_v^2 + C_w^2)/C_w^2 = 1$  will lead to a simpler equation for calculating  $C_L$ :

$$C_L = \frac{2C_v C_c}{C_v + \sqrt{C_v^2 + 4C_c^2}}, \quad (14.41)$$

The fluid leakoff mechanisms discussed in this section are generally credited to Carter (1957) for his pioneering work. These leakoff equations are often referred to as the ‘‘Carter 1D leakoff model’’.

### 14.4.2 TWO-DIMENSIONAL FRACTURE MODELS

There are three types of 2D fracture models, namely, the radial, Perkins-Kern-Nordgren (PKN) and Klerk fracture model (KGD) models. The first radial model was probably developed by Sneddon (1946) and Sneddon and Elliott (1946), which predicts the width and radial extent of a penny-shaped fracture. The PKN is named after its original developers, Perkins and Kern (1961) and Nordgren (1972). The KGD model is named after its original developers, Khristianovich and Zheltov (1955), and Geertsma and de Klerk (1969). Both the KGD and PKN models assume a fixed fracture height and predict the fracture width and length. General assumptions of these 2D fracture models include: (1) the formation is homogeneous and isotropic; (2) the deformation of the formation during fracture propagation is based on the linear elastic stress-strain relations; (3) fluid flow in the fracture is laminar; and (4) gravity effects are neglected.

For all these 2D fracture models, analytical solutions can be obtained when fluid losses are ignored or in special cases when fluid losses are extremely high. One advantage of analytical models is that the influence of an individual parameter can be analyzed in closed-form equations. Even

a 2D fracture model can become complicated and generally require numerical solutions when the effects of fluid leakoff are taken into consideration. The 2D fracture models for nonNewtonian fracturing fluids and turbulent conditions are not presented in this chapter. More in-depth discussions can be found from [Gidley et al. \(1989\)](#) and [Economides and Nolte \(2000\)](#).

#### 14.4.2.1 Radial models

A radial fracture occurs when the fracture is horizontal or when there are no stress barriers constraining height growth in the case of a vertical fracture. A simple radial (penny-shaped) crack/fracture was first presented by [Sneddon \(1946\)](#) and [Sneddon and Elliott \(1946\)](#). By assuming constant pressure, they showed that the width of a static circular fracture of radius  $R$  is expressed as:

$$w(r) = \frac{8(1-\nu^2)p_{net}R}{\pi E} \sqrt{1-(r/R)^2}. \quad (14.42)$$

For most realistic fracture sizes,  $r/R$  is negligible at the wellbore when  $r = r_w$ . Therefore, the fracture width at the wellbore can be approximated by:

$$w_w = \frac{8(1-\nu^2)p_{net}R}{\pi E}. \quad (14.43)$$

Note that [Eqs. \(14.42\) and \(14.43\)](#) are expressed in a consistent unit system.

Both [Perkins and Kern \(1961\)](#) and [Geertsma and de Klerk \(1969\)](#) developed radial fracture models with pressure drop along the fracture radius, but they differ in the assumptions on fluid pressure distribution and the condition at the fracture tip. Perkins and Kern did not consider the effects of fluid loss. The Perkins and Kern solution in oilfield units is given by:

$$w_w = 0.22 \left[ \frac{(1-\nu^2)\mu q_i R}{E} \right]^{\frac{1}{4}}. \quad (14.44)$$

where  $w_w$  is fracture width in in. at the wellbore,  $\mu$  is fluid viscosity in cP,  $q_i$  is pumping rate in bbl/min, and  $R$  is fracture radius in ft, and  $E$  is Young's modulus in psi. [Eq. \(14.44\)](#) indicates that the influence of Poisson's ratio on the fracture width is insignificant as Poisson's ratio values for most petroleum formation are between 0.2 and 0.3 and that the fracture width is proportional to the quarter root of the product of fluid viscosity and pumping rate. The average width in the fracture for the radial model derived by Perkins and Kern is given as:

$$\bar{w} = \left( \frac{2}{3} \right) w_w. \quad (14.45)$$

The fracture width at the wellbore for the case with no fluid loss in the radial fracture model derived by [Geertsma and de Klerk \(1969\)](#) is given as follows:

$$w_w = 0.33 \left[ \frac{(1-\nu^2)\mu q_i R}{E} \right]^{\frac{1}{4}}. \quad (14.46)$$

where  $w_w$  is fracture width in in. at the wellbore,  $\mu$  is fluid viscosity in cP,  $q_i$  is pumping rate in bbl/min, and  $R$  is fracture radius in ft, and  $E$  is Young's modulus in psi. The average width in the fracture for the radial model derived by Perkins and Kern is given as:

$$\bar{w} = \left( \frac{8}{15} \right) w_w. \quad (14.47)$$

The radial model from Perkins and Kern predicts narrower fractures than the radial model from Geertsma and de Klerk because the total fluid pressure drop in the fracture predicted by Perkins and Kern is smaller. A comparison between Eqs. (14.44) and (14.46) indicates that the fracture width predicted by Geertsma and de Klerk is approximately 50% larger than that by Perkins and Kern model. Radial fractures can occur in both the horizontal and vertical planes. Although vertical fractures are encountered for the majority of hydraulic fracturing treatments, a radial fracture will normally initiate and propagate until it reaches stress barriers in the vertical direction.

The fracture radius in Eq. (14.46) has to be obtained first before the fracture width at the wellbore can be predicted. The fracture radius from the Geertsma and de Klerk model can be approximated as follows for the case without fluid loss:

$$R = 8.38 \left[ \frac{Eq_i^3}{(1-\nu^2)\mu} \right]^{\frac{1}{9}} t^{4/9} \quad (14.48)$$

where  $R$  is fracture radius in ft,  $E$  is in psi,  $q_i$  is in bbl/min, and  $\mu$  is in cP, and  $t$  is the pumping time in min. When fluid loss effects are considered, the solution from the Geertsma and de Klerk model becomes more complicated. In cases of large fluid loss, an approximation for the radial length versus time is given by:

$$R = 0.75 \left[ \frac{q_i^2 t}{C_i^2} \right]^{\frac{1}{4}}, \quad (14.49)$$

where  $R$  is fracture radius in ft,  $q_i$  is in bbl/min,  $t$  is in min, and the total leakoff coefficient  $Ct$  is in ft/min<sup>1/2</sup>. It is interesting to note that when fluid loss is extremely large, the radial length of the fracture depends only on the pumping rate and the total leakoff coefficient.

#### 14.4.2.2 The PKN model

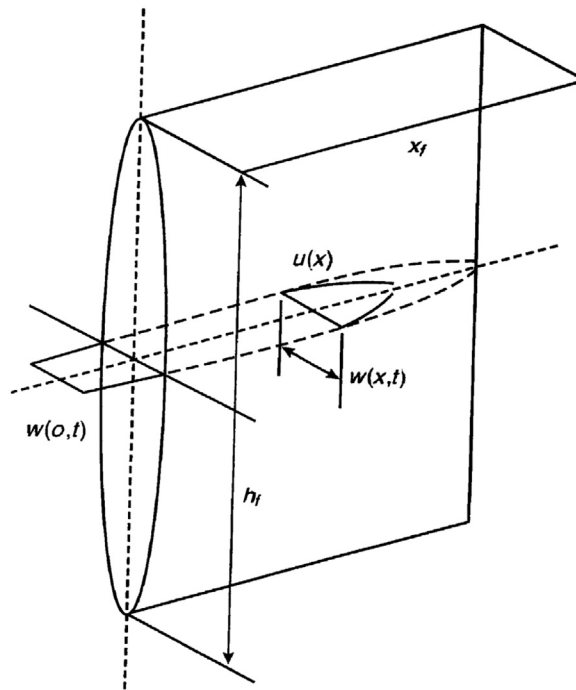
The PKN model was first developed by Perkins and Kern (1961) without the considerations of fluid loss and storage (rate of fracture volume change). Perkins and Kern derived an analytical solution for the propagation of a vertical fracture by assuming a fixed fracture height and elliptical cross-section in the vertical plane as illustrated in Fig. 14.9. They further assumed that only the maximum width of the elliptical width profile at any position along the fracture length is proportional to the net pressure at that position proposed by Sneddon and Elliott (1946):

$$w_{\max}(x) = \frac{2(1-\nu^2)p_{\text{net}}(x)h_f}{E} \quad (14.50)$$

where  $w_{\max}(x)$  is the maximum fracture width at position  $x$  along the fracture length,  $p_{\text{net}}(x)$  is the net pressure at position  $x$ , and  $h_f$  is the fixed fracture height. They also assumed that the net pressure at the tip of the fracture is zero, namely, the fluid pressure at the fracture tip equals the rock minimum stress. With that, a solution of the maximum fracture width at position  $x$  can be derived for a symmetric bi-wing fracture, which is expressed as:

$$w_{\max}(x) = 3 \left[ \frac{(1-\nu^2)\mu q_i (x_f - x)}{E} \right]^{\frac{1}{4}} \quad (14.51)$$

where  $x_f$  is the fracture half-length.



**FIGURE 14.9**

The PKN fracture geometry.

As noted in Eq. (14.50), the net pressure  $p_{net}(x)$  is a function of position  $x$  along the fracture. The maximum net pressure occurs at the wellbore ( $x=0$ ). A combination of Eqs. (14.50) and (14.51) yields the maximum net pressure occurs at the wellbore as follows:

$$p_{net,max} = \frac{3(\mu q_i x_f)^{\frac{1}{4}} [E/(1-\nu^2)]^{\frac{3}{4}}}{2h_f}. \quad (14.52)$$

Eq. (14.52) indicates that a formation having higher Young's modulus requires higher net pressure to achieve the same fracture dimensions (length and height) if everything else is equal. It is important to recognize that the net pressure at the wellbore is proportional to Young's modulus to the power of three quarters. Note that Eqs. (14.50) through (14.52) are expressed in a consistent unit system. The maximum fracture width at the wellbore ( $x=0$ ) in oilfield units is as follows:

$$w_w = 0.39 \left[ \frac{(1-\nu^2)\mu q_i L}{E} \right]^{\frac{1}{4}}, \quad (14.53)$$

where  $w_w$  is the maximum fracture width at the wellbore in in.,  $\mu$  is in cP,  $q_i$  in bbl/min,  $L$  is in ft,  $\nu$  is Poisson's ratio, and  $E$  is in psi.

Since the cross-section of the fracture is elliptical, the average width at the wellbore is  $(\pi/4)w_w$ . However, the average width in the entire fracture is given by:

$$\bar{w} = \left(\frac{\pi}{5}\right)w_w. \quad (14.54)$$

Eq. (14.53) indicates that the influence of Poisson's ratio on the fracture width is negligible for most rocks as Poisson's ratio values for most petroleum formation are between 0.2 and 0.3, and that the fracture width is proportional to the quarter root of the product of fluid viscosity and pumping rate. In order to create enough fracture width to allow proppant transport, it is much easier to increase the fluid viscosity than to increase the pumping rate. In order to double the pumping rate, doubling the horsepower with more equipment is required. In fracturing treatment designs, a switch from slickwater to a gelled fluid can increase fluid viscosity by over 100 times. Based on Eq. (14.53), doubling the pumping rate will only increase the fracture width by 19% while increasing the fluid viscosity by 100 times will lead to a width increment by 216%!

Nordgren (1972) added both fluid loss and storage to the Perkins and Kern model, which is now known as the PKN model, and derived a different set of solutions. The Nordgren model generally requires numerical solutions. Simple analytical solutions can be obtained for two limiting cases: the storage-dominated approximation without leakoff effects and the high-leakoff approximations. Even for the case without leakoff effects, the Nordgren model is slightly different from the Perkins and Kern model as the effects of storage (rate of fracture volume change) are included. The storage-dominated approximation of the Nordgren model, expressed in oilfield units, is given as:

$$x_f = 58.07 \left[ \frac{Eq_i^3}{(1-\nu^2)\mu h_f^4} \right]^{1/5} t^{4/5} \quad (14.55)$$

$$w_w = 0.99 \left[ \frac{(1-\nu^2)\mu q_i^2}{Eh_f} \right]^{1/5} t^{1/5} \quad (14.56)$$

where  $x_f$  is the fracture half-length in ft,  $w_w$  is the maximum fracture width at the wellbore in in.,  $E$  is in psi,  $q_i$  in bbl/min,  $\mu$  is in cP, and  $t$  is the pumping time in min.

The high-leakoff approximation of the Nordgren model, expressed in oilfield units, is given as:

$$x_f = 0.89 \frac{q_i t^{1/2}}{C_t h_f} \quad (14.57)$$

$$w_w = 0.34 \left[ \frac{(1-\nu^2)\mu q_i^2}{EC_t h_f} \right]^{1/4} t^{1/8} \quad (14.58)$$

where  $x_f$  is the fracture half-length in ft,  $q_i$  is in bbl/min,  $C_t$  is in  $\text{ft}/\text{min}^{1/2}$ ,  $h_f$  is the fracture height in ft,  $t$  is the pumping time in min,  $w_w$  is the maximum fracture width at the wellbore in in.,  $\mu$  is in cP, and  $E$  is in psi.

A fixed-height fracture can be valid in some cases if the stresses in the formations above and below the pay zone are large enough to prevent any fracture growth out of the pay zone. It is important to emphasize that even for contained fractures the PKN solution is only valid for longer fractures. A rule of thumb is that the fracture length has to be at least three times the height.



**Example Problem 14.2** Consider an oil reservoir with the following properties: Poisson's ratio of 0.2, Young's modulus of  $3.0 \times 10^6$  psi, payzone depth of 5000 ft, pore pressure gradient of 0.45 psi/ft, minimum stress gradient of 0.6 psi/ft, permeability of 0.01 Darcy (or 10 md), porosity of 0.2, pore fluid viscosity of 1.0 cP, total compressibility of  $1.0E-5$  psi<sup>-1</sup>. A fracturing fluid with a viscosity of 500 cP is pumped at 50 bbl/min for 60 minutes with an average net pressure of 250 psi during the treatment. Assume that a fixed fracture height equals 150 ft and that the leakoff mechanisms due to filtercake buildup and filtrate invasion are neglected. Calculate the fracture half-length and the fracture width at the wellbore using Nordgren's PKN model for both no-leakoff (storage-dominated) and high-leakoff cases.

**Solution**

For the storage-dominated case without leakoff, the fracture half-length is calculated from Eq. (14.55):

$$x_f = 58.07 \left[ \frac{(3.0E+6)(50)^3}{(1-0.2^2)(500)(150)^4} \right]^{1/5} 60^{4/5} = 1676 \text{ ft,}$$

For the storage-dominated case with no-leakoff, the fracture width at the wellbore is calculated from Eq. (14.56):

$$w_w = 0.99 \left[ \frac{(1-0.2^2)(500)(50)^2}{(3.0E+6)(150)} \right]^{1/5} 60^{1/5} = 0.69 \text{ in.}$$

The reservoir pressure is calculated from the pore pressure gradient given in this example:

$$p_r = (0.45) * (5000) = 2250 \text{ psi,}$$

The minimum stress is calculated from the minimum stress gradient given:

$$\sigma_{\min} = (0.6) * (5000) = 3000 \text{ psi,}$$

The fluid pressure inside the fracture is calculated from Eq. (4.25):

$$p_f = \sigma_{\min} + p_{\text{net}} = (3000) + (250) = 3250 \text{ psi,}$$

The pressure drop across the reservoir is calculated as follows:

$$\Delta p_c = p_f - p_r = (3250) - (2250) = 1000 \text{ psi,}$$

The total leakoff coefficient is calculated from Eq. (14.39):

$$C_t = C_c = 0.0374 \sqrt{\frac{(0.01)(1.0E-5)(0.2)}{(1.0)}} (1000) = 0.00529 \text{ ft}/\sqrt{\text{min}},$$

For the high-leakoff case, the fracture half-length is calculated from Eq. (14.57):

$$x_f = 0.89 \frac{(50)(60)^{1/2}}{(0.00529)(150)} = 434 \text{ ft,}$$

For the high-leakoff case, the fracture width at the wellbore calculated from Eq. (14.58):

$$w_w = 0.34 \left[ \frac{(1-0.2^2)(500)(50)^2}{(3.0E+6)(0.00529)(150)} \right]^{1/4} (60)^{1/8} = 0.48 \text{ in.}$$

This example indicates that a total leakoff coefficient of  $0.00529 \text{ ft}/\text{min}^{1/2}$  can reduce the fracture half-length by 286%. The total leakoff coefficient has a significant impact on the fracture geometry and is a critical parameter for fracturing design and modeling.

### 14.4.2.3 The KGD model

As shown in Fig. 14.10, Khristianovich and Zheltov (1955) first presented a model to describe this type of fractures. They assumed that the fracture height is constant, the periphery of the fracture is rectangular, and the shape of the fracture (or the width variation from the wellbore to the fracture tip) is elliptical. In order to derive an analytical solution, they further assumed particular fluid pressure distribution and boundary condition at the tip of the fracture: the pressure in the majority of the fracture body could be approximated as a constant, except for a small region near the tip with no fluid penetrated, and hence, zero value of fluid pressure there.

Geertsma and de Klerk (1969) solved the same problem described above. A boundary condition is required to solve the propagation of a fracture at its tip. The condition at the tip of the fracture was first suggested by Khristianovich and Zheltov (1955) and was later clarified by Barenblatt (1962). Barenblatt stated that the distribution of normal pressure exerted by the fracturing fluid on the fracture walls must meet such a condition that the fracture closes smoothly at the edges, which implies that  $dw/dx = 0$  at the fracture tip, where  $w$  is the fracture width and  $x$  is the fracture distance. This condition ensures that the normal stress at the tip is finite and equal to the tensile strength of the rock. In addition, the tensile strength can be assumed to be negligible for large fractures. The 2D vertical fracture model developed by Geertsma and de Klerk presented here is now referred to as the *KGD model*. Geertsma and de Klerk provided solutions for the cases with and without fluid leakoff.

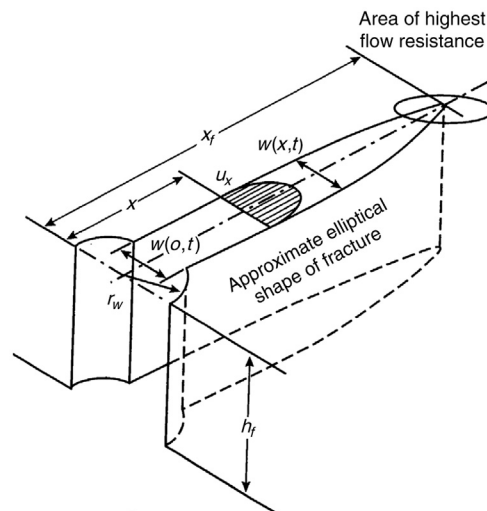


FIGURE 14.10

The KGD fracture geometry.

Similar to the PKN model expressed in Eq. (14.50), a relationship between the fracture width at the wellbore and other parameters for the KGD model can be obtained as follows:

$$w_w = \left[ \frac{84(1-\nu^2)\mu q_i L^2}{\pi E h_f} \right]^{\frac{1}{4}}, \quad (14.59)$$

where  $w_w$  is the fracture width at the wellbore. Eq. (14.59) is expressed in a consistent unit system. If expressed in oilfield units, Eq. (14.59) becomes:

$$w_w = 0.29 \left[ \frac{(1-\nu^2)\mu q_i L^2}{E h_f} \right]^{\frac{1}{4}}, \quad (14.60)$$

where  $w_w$  is in in.,  $\mu$  is in cP,  $q_i$  is in bbl/min,  $L$  is in ft,  $E$  is in psi, and  $h_f$  is in ft. Note that there is no maximum fracture width at the wellbore for the KGD model as the fracture is rectangular in cross section anywhere along the fracture length.

Although the periphery of the fracture in the KGD is rectangular, the width profile is elliptical from the wellbore to the fracture tip. The average width in the fracture is given by:

$$\bar{w} = \left( \frac{\pi}{4} \right) w_w. \quad (14.61)$$

The no-leakoff solution of the KGD model in oilfield units is given by:

$$x_f = 27.81 \left[ \frac{E q_i^3}{(1-\nu^2)\mu h_f^3} \right]^{\frac{1}{6}} t^{2/3}, \quad (14.62)$$

$$w_w = 1.54 \left[ \frac{(1-\nu^2)\mu q_i^3}{E h_f^3} \right]^{\frac{1}{6}} t^{1/3}. \quad (14.63)$$

where  $x_f$  is the fracture half-length in ft,  $w_w$  is the fracture width at the wellbore in in.,  $\mu$  is in cP,  $q_i$  is in bbl/min,  $E$  is in psi, and  $h_f$  is in ft. Note that Eq. (14.63) is equivalent to Eq. (14.61) if  $L$  from Eq. (14.62) is substituted into Eq. (14.61).

For the case where fluid leakoff is taken into account, a closed-form solution becomes more complex and is given by:

$$x_f = \frac{q_i w_w}{64 C_f^2 h_f} \left[ \exp(S^2) \operatorname{erfc}(S) + (2/\sqrt{\pi}) S - 1 \right], \quad (14.64)$$

$$S = \frac{8 C_f}{\sqrt{\pi} w_w} \sqrt{t}. \quad (14.65)$$

Note that Eqs. (14.64) and (14.65) are expressed in a consistent unit system. In order to obtain the fracture half-length and width at the wellbore, Eqs. (14.59), (14.64) and (14.65) have to be solved iteratively. However, for the case of high-leakoff, the approximation to calculate the fracture half-length given in Eq. (14.57) from the PKN model expressed in also applies to the KGD model.

The KGD model is valid for a vertical fracture with its height much greater than its length, which can only be achieved by injection over a large perforated interval to form a line source along the wellbore. Even in the case of injection over a large perforated interval, it is very unlikely in reality that a single tall fracture will propagate from the entire perforated interval; instead, multiple fractures are likely to propagate from various sections of the large perforated interval.

**Example Problem 14.3** Consider an oil reservoir with the following properties: Poisson's ratio of 0.2, Young's modulus of  $1.0 \times 10^6$  psi, payzone depth of 5000 ft, pore pressure gradient of 0.45 psi/ft, minimum stress gradient of 0.6 psi/ft, permeability of 0.01 Darcy, porosity of 0.2, pore fluid viscosity of 1.0 cP, total compressibility of  $1.0E-5$   $\text{psi}^{-1}$ . A fracturing fluid with a viscosity of 500 cP is pumped at 25 bbl/min for 15 minutes with an average net pressure of 250 psi during the treatment. Assume that a fixed fracture height equals 200 ft and that the leakoff mechanisms due to filtercake buildup and filtrate invasion are neglected. Calculate the fracture half-length and the fracture width at the wellbore using the KGD model for both the no-leakoff and high-leakoff cases.

**Solution**

For the no-leakoff case, the fracture half-length is calculated from Eq. (14.62):

$$x_f = 27.81 \left[ \frac{(1.0E+6)(25)^3}{(1-0.2^2)(500)(200)^3} \right]^{\frac{1}{6}} (15)^{2/3} = 214 \text{ ft},$$

For the no-leakoff case, the fracture width at the wellbore is calculated from Eq. (14.63):

$$w_w = 1.54 \left[ \frac{(1-0.2^2)(500)(25)^3}{(1.0E+6)(200)^3} \right]^{\frac{1}{6}} (15)^{1/3} = 0.38 \text{ in.}$$

For the high-leakoff case, the total leakoff coefficient is the same as Example Problem 14.2 and is  $0.00529$   $\text{ft}/\text{min}^{1/2}$ . The fracture half-length is calculated from Eq. (14.57):

$$x_f = 0.89 \frac{(25)(15)^{1/2}}{(0.00529)(200)} = 81 \text{ ft},$$

For the high-leakoff case, the fracture width at the wellbore calculated from Eq. (14.60):

$$w_w = 0.29 \left[ \frac{(1-0.2^2)(500)(25)(81)^2}{(1.0E+6)(200)} \right]^{\frac{1}{4}} = 0.23 \text{ in.}$$

A smaller pumping rate and a shorter pumping time are used in this example. This is because the KGD model is valid when the fracture height is much larger than the length. When the leakoff effect is taken into consideration, the fracture height is indeed much larger than the length.

Three types of 2D models discussed in this section only include solutions for laminar flow and Newtonian fluids. The extended solutions for turbulent flow and power law fluids are available and can be found in the literature. For all these 2D fracture models, analytical solutions are available when fluid losses are ignored or in special cases when fluid losses are extremely high. One advantage of analytical models is that the influence of an individual parameter can be analyzed in closed-form equations. These models are deviated with significant simplifying assumptions. First, planar fractures are assumed to propagate in a direction perpendicular to the minimum stress in continuous, homogeneous, isotropic, linear elastic solid materials. Other assumptions include that fluid flow inside the fracture is 1D along the length or radius of the fracture and that fluid leakoff is 1D and perpendicular to the fracture face on each side of the fracture. The KGD model assumes that the fracture height is much larger than the length while the PKN model assumes that the fracture height is much smaller than the length. Although the capabilities of these models are limited, they are useful for understanding the growth of hydraulic fractures.

### 14.4.3 THREE-DIMENSIONAL FRACTURE MODELS

The biggest limitation of the 2D models discussed in the previous section is that the fracture is assumed to be either of a fixed height or propagate in a penny-shape. Since the introduction of the 2D fracture models from the mid 1950s through early 1970s, numerous 3D fracture models have been developed to overcome the limitation of the 2D models. By definition, 3D fracture models are capable of predicting the fracture length, height and width. The development of 3D fracture models (Clifton and Abou-Sayed, 1979; Clifton and Abou-Sayed, 1981; Cleary, 1980; Barree, 1983; Cleary et al., 1983, Ahmed, 1984; Settari and Cleary, 1984; Meyer, 1986, etc.) proliferated during the late 1970s and 1980s, in part due to technology improvements in modern computers and the industry's need for realistic models.

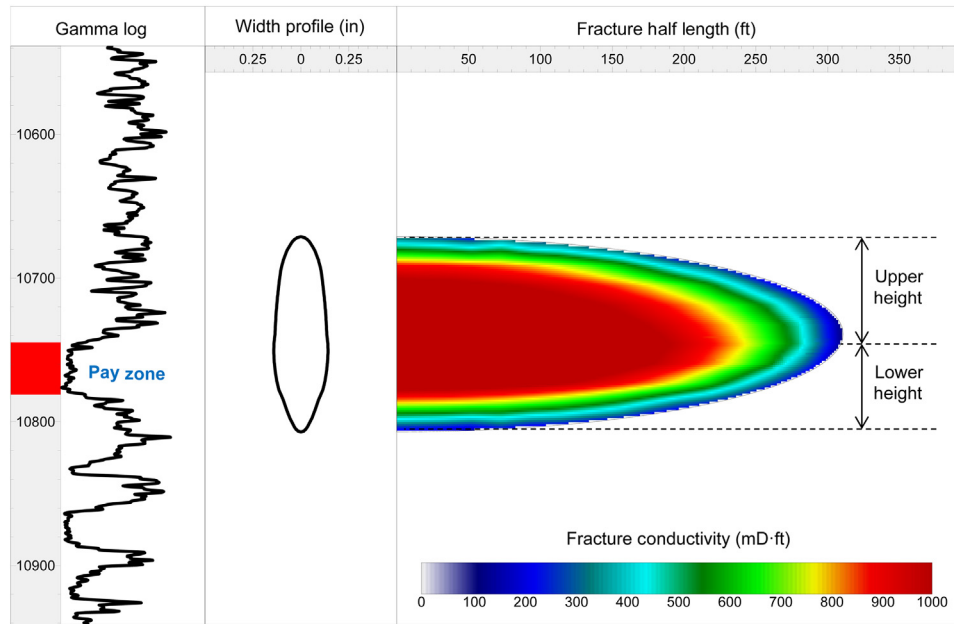
In this section, two types of 3D fracture models are briefly discussed, including pseudo-3D models and planar 3D models. Pseudo-3D models provide simplified solutions to planar 3D models, but are able to capture the essence of planar 3D models without solving the governing equations rigorously. Planar 3D models allow full 3D fracture propagation and two-dimensional (2D) fluid flow by solving the governing equations numerically. Since both pseudo-3D and planar 3D models assume that the fracture is planar and oriented perpendicular to the direction of far-field minimum in-situ stress, fracture complexities that result in deviations from this planar behavior are not accounted. Other fracture models, such as coupled geomechanical reservoir simulators (Dean and Schmidt, 2009), are beyond the scope of this book and not discussed in this chapter.

#### 14.4.3.1 Pseudo 3D models

Three basic relations govern the hydraulic fracturing process, which includes fluid flow in the fracture, material balance or conservation of mass, and rock elastic deformation. Although pseudo-3D models account for all the physics, simplified approaches are used to solve these equations. There are mainly two types of pseudo-3D models, which are generally referred to as *cell-based* and *lumped-parameter* models.

In cell-based models the fracture length is discretized into cells along the length of the fracture, but the fracture shape is not redefined. The fracture is treated as a series of connected cells, which are linked only via the fluid flow from cell to cell. By assuming that vertical fracture extension is sufficiently slow, the cross-sectional shape of the fracture is determined as a function of the net pressure. The height at any cross-section is calculated from the pressure in that cell, and fluid flow in the vertical direction is generally ignored. Fluid flow is calculated essentially as 1D along the length of the fracture because the fracture is discretized in one direction only. Cell-based models calculate the three dimensions (length, height and width) of planar fractures, but the model assumptions make them more applicable for relatively contained fractures, with the fracture half-length much greater than its height.

Lumped-parameter models were first introduced by Cleary (1980). As the author concluded in the paper, "The heart of the formulae can be extracted very simply by a nondimensionalization of the governing equations; the remainder just involves a good physico-mathematical choice of the undetermined coefficients." Therefore, it is very important to select appropriate coefficients and their values for the successful use of a lumped-parameter model. In lumped-parameter models, the partial differential equations in space and time that govern the hydraulic fracturing process are simplified by assuming a fracture shape and adopting a spatial averaging approach. This manipulation reduces the partial



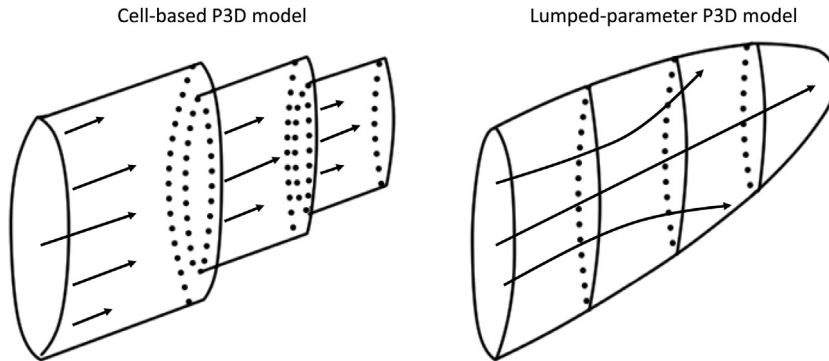
**FIGURE 14.11**

Typical fracture geometry predicted by a lumped-parameter model.

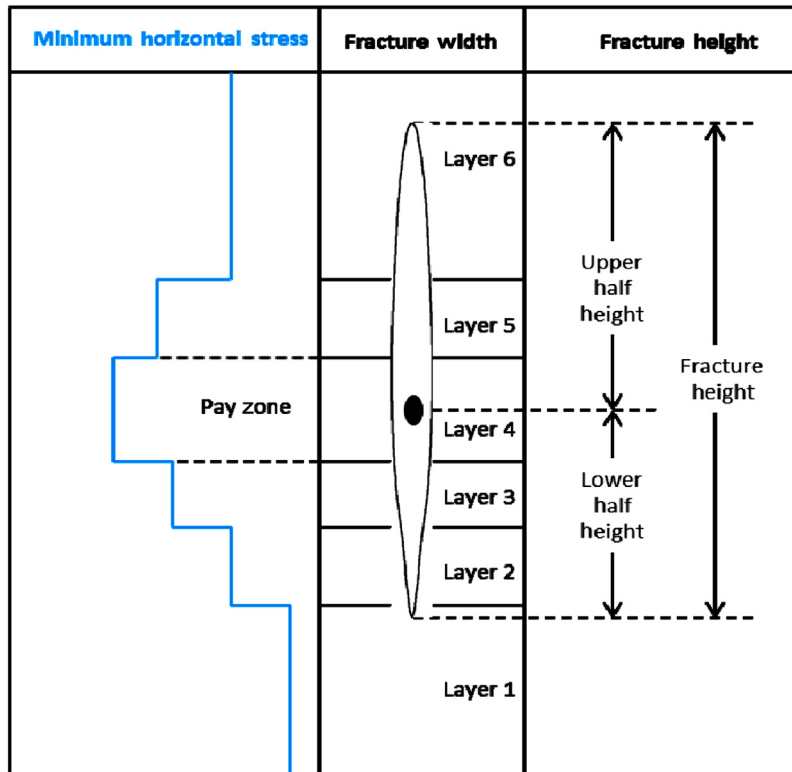
differential equations in space and time that govern the process to ordinary differential equations in time. The fracture shape is generally assumed to consist of two half-ellipses of equal horizontal extent, but with different vertical extent. The fracture half-length and lower and upper fracture heights at the wellbore are calculated at every time-step based on a set of lumped parameters. Fluid flow is generally assumed as streamlines from the perforated interval at the wellbore to the edge of the fracture, and the shape of the streamlines is derived from analytical solutions. The model then allows the calculation of fracture length, height, and width distributions under conditions of slow vertical spreading. Fig. 14.11 shows a typical fracture geometry predicted by a lumped-parameter P3D model.

Fig. 14.12 illustrates how the fracture shape and fluid flow are handled differently between the cell-based and lumped-parameter models. In this figure, the arrows represent the fluid direction. The vertical fluid flow is completely neglected in the cell-based model, but is only partially accounted for by assuming a streamline flow pattern in the lumped-parameter model.

Unlike a 2D fracture model, a pseudo-3D model is required to properly handle fracture height growth across various formation layers that have different minimum horizontal stress values and rock properties. A simple model proposed by [Simonson et al. \(1978\)](#) provides a solution to relate the fracture height migration at the wellbore with the stress contrast between layers, the net pressure, and fracture toughness for a symmetric three-layer case. [Fung et al. \(1987\)](#) derived a more general solution for nonsymmetric multilayer cases. Both models consist of a set of nonlinear equations that can be solved by an iteration technique. An illustration of fracture height growth in multiple formation layers is shown in Fig. 14.13. In this case, the fracture grows slightly upwards due to lower minimum horizontal stresses in the upper layers in a setting of six layers.



**FIGURE 14.12**  
Fracture geometry predicted by two types of P3D models.



**FIGURE 14.13**  
Fracture height migration from a P3D fracture model.

### 14.4.3.2 Planar 3D models

Basic equations that govern a hydraulic fracturing process include elastic-deformation equations that relate pressure and stress with the fracture width, equations for conservation of mass, and equations for conservation of momentum. Planar 3D models formulate the physics rigorously, consider planar fractures of arbitrary shape in a linearly elastic formation, and incorporate 2D fluid flow in the fracture and linear fracture mechanics for fracture propagation. Fluid leakoff is handled either by the Carter 1D leakoff model or more rigorously. The governing equations are solved numerically in space and time, using the finite element, finite difference, boundary element, or other numerical techniques. The geometry of a hydraulic fracture is determined by its width at each grid block. The width distribution and the overall shape change with time and depend on the pressure distribution, which is determined by the fluid flow within the fracture. The relation between pressure gradient and flow rate is very sensitive to fracture width, resulting in a tightly coupled calculation. Although the mechanics of these processes can be described separately, this close coupling complicates the solution of any fracture model. The nonlinear relation between width and pressure and the complexity of a moving-boundary problem further complicate numerical solutions.

Clifton and Abou-Sayed (1979) first reported a numerical implementation of a planar 3D model. The solution starts with a small fracture that initiated at the perforations. The fracture is divided into a number of equal elements, and the elements continue changing to fit the evolving fracture shape. As time continues, the elements can develop large aspect ratios and very small angles, which are not well handled by the numerical schemes typically used to solve the model. Barree (1983) developed a model that does not show grid distortion. The layered reservoir is divided into a grid system of equal-size rectangular elements, over the entire region that the fracture may cover.

Fracture simulators based on planar 3D models are much more computationally intensive than P3D-based simulators, because they solve the fully 2D fluid flow equations and couple this solution rigorously to the elastic-deformation equations. The elasticity equations are also solved more rigorously, using a 3D solution rather than 2D slices. Planar 3D models are more useful for cases whenever rock lithology and vertical stress profiles are very complex, or when a significant portion of the fracture grows outside the zone where the fracture initiates or where vertical fluid flow is significant. Leakoff behavior for hydraulic fractures created from long-term injections, such as water and steam flooding, usually deviates from the Carter 1D leakoff model. In these situations, an appropriate planar 3D model with robust leakoff modeling capability is required.

### 14.4.4 UNCONVENTIONAL FRACTURE MODELS

Unconventional reservoirs are extremely tight with permeability in the nano-Darcy ranges, heterogeneous, and highly complex. The development of unconventional reservoirs is uniquely challenging, which demands the application of many new and innovative technologies. Horizontal well drilling and completion with multistage hydraulic fracture stimulation have proven to be most economically effective in developing unconventional reservoirs. The interference between adjacent hydraulic fractures and the interactions of hydraulic fractures with natural fractures also play a key role in affecting stimulation effectiveness, well productivity, and ultimate recovery for unconventional reservoirs.



Until the recent shale revolution, all 3D fracture models commercially available in the industry were based on the assumptions that the fracture is planar and that there are no interactions with natural fractures and existing hydraulic fractures. The classical planar models have become inadequate for hydraulic fracturing applications in unconventional reservoirs. Numerous unconventional fracture models have been developed in recent years to account for these effects. Some of the models only address some geomechanics aspects such as interference between multiple fractures while the other models attempt to capture hydraulic fracture interference and the interaction with natural fractures.

#### 14.4.4.1 Stress shadowing effects

Horizontal wells in unconventional reservoirs are commonly completed with multiple transverse fractures that are typically vertical. To create transverse fractures, the horizontal wellbore must be drilled in the direction of the minimum horizontal principal stress. The fluid pressure required to propagate a hydraulic fracture also compresses the formation adjacent to it. Therefore, the fluid pressure required to initiate and propagate a subsequent fracture within the compressed region must be increased to accommodate the compression effects from the active fracture. The magnitude of pressure increase is affected by the distance between the two fractures, the net pressure and the overlap area between the two fractures. This pressure or stress increase is often referred to as “stress shadowing” effects. Stress shadowing affects fracture spacing and stimulation effectiveness in closely spaced multistage fracture completions.

Sneddon and Elliott (1946) developed an analytical model to calculate the perturbation of both normal and shear stresses for a semi-infinite crack in an infinite, 2D elastic material. For tensile fractures, stress shadowing effects on normal stresses in the principal directions are only concerned. Fig. 14.14 shows the changes in two horizontal principal stresses caused by stress shadowing based on the analytical model developed by Sneddon and Elliott (1946) using a Poisson’s ratio of 0.25. The vertical axis in this figure represents the changes in two principal stresses  $\sigma_{h,\min}$  and  $\sigma_{h,\max}$  divided by the net pressure  $p_{net}$ , and the horizontal axis represents the distance away from the fracture  $L$  divided by the fracture height  $H$ . At the fracture wall, the two principal stresses are increased exactly by the value of the net pressure  $p_{net}$ . However, as the distance away from the fracture increases, the change in the maximum horizontal stress reduces more quickly than that for the minimum horizontal stress. In fact, at some point away from the fracture, the change in the maximum horizontal stress becomes negative, which means that the effective maximum horizontal stress becomes less than its original value due to stress shadowing effects. When the condition is right, the original maximum horizontal stress may become the minimum horizontal stress and complex fractures will be created.

The stress perturbation due to stress shadowing effects will alter the orientations of the two horizontal principal stresses everywhere in the stress-perturbed region even if it is not large enough to cause a complete reversal between the two horizontal principal stresses. Fig. 14.15 shows a cross-sectional view of three equally spaced, transverse fractures created across a horizontal lateral section in a homogenous and isotropic reservoir for two scenarios. Case A represents the ideal case that three identical fractures are created simultaneously from the same treatment design without the consideration of stress shadowing effects. However, when the stress shadowing effects are considered, the two outer fractures in Case B will take more fracturing fluids, become larger and propagate in a nonplanar fashion while the fracture in the middle is still planar but becomes smaller and narrower due the stress shadowing effects from the two outer fractures. In reality, stress shadowing effects are more complex for multistage fracture stimulation in horizontal wells as the stress

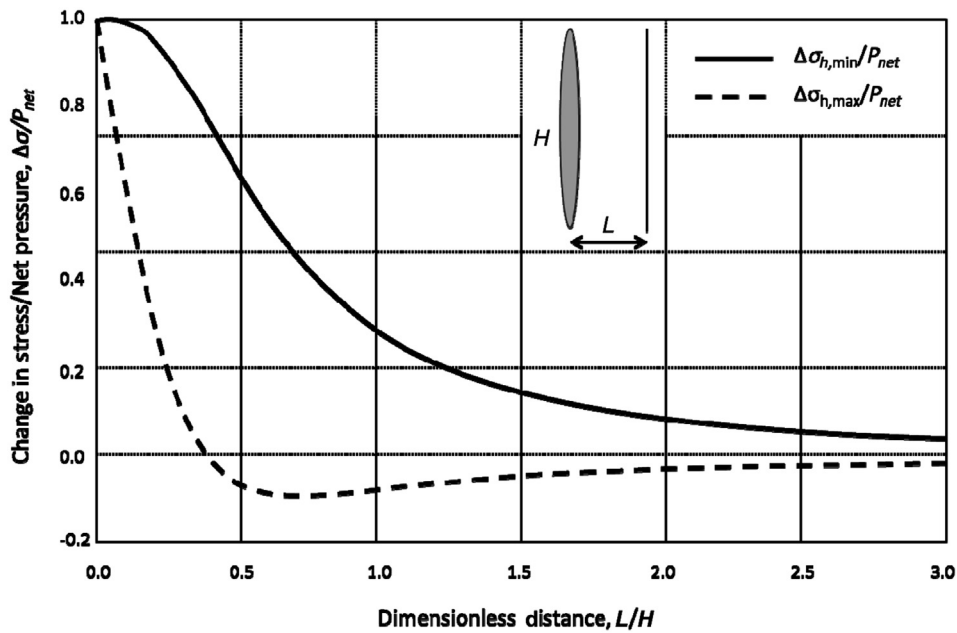


FIGURE 14.14

Stress variation vs distance away from a semi-infinite crack.

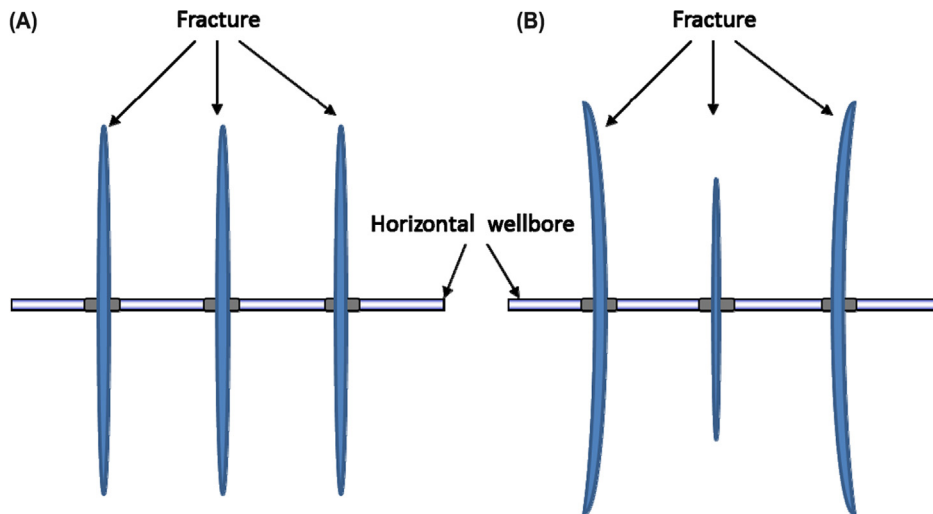


FIGURE 14.15

Potential stress shadowing effects on fracture propagation in a stage with 3 perforation clusters from a horizontal well: (A) without stress shadowing and (B) with stress shadowing.

perturbation resulted from the previous stages affect the propagation of fractures initiated from all perforation clusters in a subsequent stage. When the distance between the subsequent and previous stages is over three times the fracture height, the change in stress due to stress shadowing from the previous stage becomes less than 5%, based on the analytical model developed by [Sneddon and Elliott \(1946\)](#) as illustrated in [Fig. 14.14](#). However, the Sneddon and Elliot solution is only valid if parallel planar fractures are created and the fracture length is much larger than the fracture height.

#### 14.4.4.2 Unconventional fracture models

[Roussel and Sharma \(2011\)](#) presented a 3D numerical model and demonstrated that a transverse fracture initiated from a horizontal well may deviate away from the previous fracture due to the redistribution of local in-situ stresses. The extent of stress reversal and reorientation was investigated for fractured horizontal wells using a 3D numerical model of the stress interference induced by the creation of one or more propped fractures. The impact of stress reversal and reorientation on simultaneous and sequential fracturing of horizontal wells was analyzed.

[Weng et al. \(2011\)](#) presented a new hydraulic fracture model to simulate complex fracture network propagation in a formation with preexisting natural fractures. The model solves a system of equations governing fracture deformation, height growth, fluid flow, and proppant transport in a complex fracture network with multiple propagating fracture tips. The interaction between a hydraulic fracture and preexisting natural fractures is taken into account by using an analytical crossing model and is validated against experimental data. The model is able to predict whether a hydraulic fracture front crosses or is arrested by a natural fracture it encounters, which leads to complexity. The crossing model or criterion to determine whether a fracture crosses a preexisting fracture was presented in detail by [Gu et al. \(2012\)](#). The new hydraulic fracture model also considers the mechanical interaction among the adjacent fractures (i.e., the “stress shadow” effects). [Fig. 14.16](#) shows the geometry of a complex fracture network for a slickwater treatment simulated

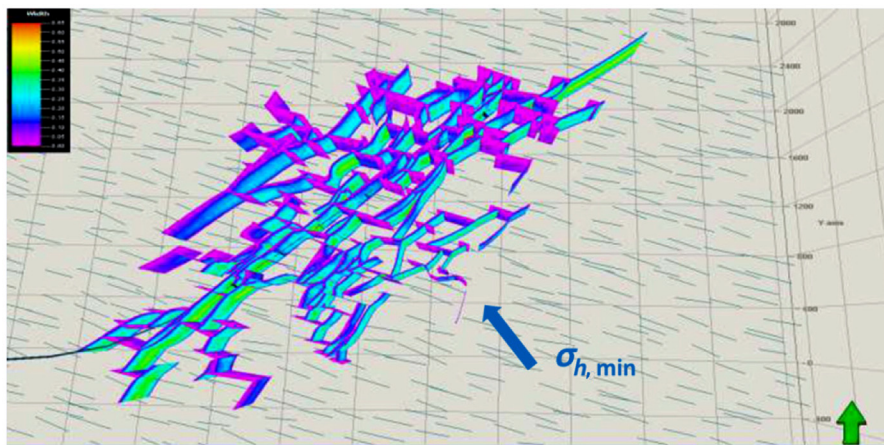
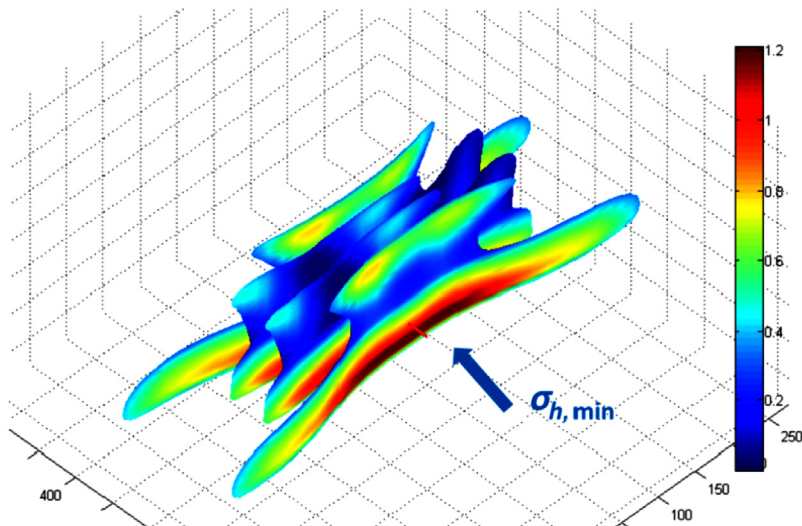


FIGURE 14.16

Complex fracture network simulated by an unconventional fracture model ([Kresse et al., 2013](#)).



**FIGURE 14.17**

Nonplanar fracture geometry.

*Image Courtesy of FracOptima, Inc.*

by an unconventional fracture model (Kresse et al., 2013). The simulation results indicate that the network extends shorter perpendicular to the minimum horizontal stress direction. The color-coded map also reveals complex fracture width profiles.

Xu and Wong (2013) presented a new 3D hydraulic fracture that describes nonplanar hydraulic fracture growth in heterogeneous formations. The model addresses the geomechanical interaction of multiple fractures. Examples presented demonstrated that the model can be used to provide insights into the growth of multiple fractures under the influence of geomechanical stress shadowing and serve as a valuable tool for optimization of multiple hydraulic fractures design. Fig. 14.17 illustrates the geometry of four nonplanar fractures initiated from a single stage with four perforation clusters simulated by an unconventional fracture model. The simulation results indicate that two outer fractures are larger and deviate from planar fashion and that complex fracture shapes in the height profiles are created due to complex stress profiles in the vertical direction. The color-coded map indicates that fracture widths are larger toward the lower central part of the fracture system. The complex fracture geometry cannot be predicted by a conventional 3D model.

Wu and Olson (2015) developed a novel fracture propagation model to simulate multiple-hydraulic-fracture propagation from a horizontal wellbore. The model generates physically realistic multiple-fracture geometries and nonplanar-fracture geometries that are consistent with physical-laboratory results and inferences drawn from microseismic diagnostic interpretations.

McClure et al. (2016) developed a hydraulic fracturing simulator that implicitly couples fluid flow with the stresses induced by fracture deformation in large, complex, 3D discrete-fracture networks (DFNs). The simulator can describe propagation of hydraulic fractures and opening and

shear stimulation of natural fractures. A crossing criterion was implemented that predicts whether propagating hydraulic fractures will cross natural fractures or terminate against them, depending on orientation and stress anisotropy. Limitations of the model are that all fractures are vertical and propagate a linearly elastic and homogeneous medium; proppant transport is not included.

There are numerous unconventional fracture models (Cottrell et al., 2013; Profit et al., 2015) that have been published or made available in recent years. Only some of these models are reviewed and presented in this section, and the models reviewed may not necessarily be the best among them.

#### 14.4.5 PROPPANT TRANSPORT MODELS

The objective of a hydraulic fracturing treatment is to create a conductive path connected the wellbore to the formation. Although the fluid pressure keeps the fracture open during injection, a propping material (small solid particles) is usually required to add to the fluid during the pumping. With proppant added, the fracture will close on proppant rather than close between the two fracture walls once the treatment is done and the fluid pressure is depleted.

In a typical pseudo 3D fracture model, proppant transport is generally handled via 1D flow along the fracture length direction, but includes the proppant settling and convection effects. In a typical planar 3D fracture model, proppant transport is generally handled via 2D flow. In many proppant transport models, a common assumption is that the average proppant velocity due to flow equals the average carrier fluid velocity, while the settling velocity is governed by Stokes' law. To accurately determine the placement of proppant in a fracture, it is necessary to rigorously account for many effects not included in the above assumptions. Blyton et al. (2015) used a coupled CFD-DEM (Computational Fluid Dynamics/Discrete Element Method) code to simulate the motion of particles flowing with a fluid between fracture walls.

For the purpose of illustration and scope of this book, a 1D proppant transport model along the fracture length direction in a 2D vertical fracture is presented here. The momentum equation for the 1D flow of Newtonian fluids can be written as:

$$u_x = \frac{-\bar{w}_x^2}{12\mu} \frac{\partial p}{\partial x}, \quad (14.66)$$

where  $u_x$  is the flow velocity along the fracture length direction,  $x$  is the distance from the wellbore along the fracture length direction,  $p$  is the fluid pressure,  $\mu$  is the fluid viscosity,  $\bar{w}_x$  is the average fracture width at location  $x$ . The negative sign in this equation is needed to make sure that the flow velocity is a positive quantity because fluid flows from high pressure to low pressure.

The continuity equation for incompressible fluids can be written as:

$$\frac{\partial((h_f - h_{bank})\bar{w}_x u_x)}{\partial x} + \frac{\partial((h_f - h_{bank})\bar{w}_x)}{\partial t} + 2h_f u_L = 0, \quad (14.67)$$

where  $t$  is the time,  $h_f$  is the fracture height,  $u_L$  is the leakoff velocity, and  $h_{bank}$  is the proppant bank height. The continuity equation for proppant transport can be written as:

$$\frac{\partial((h_f - h_{bank})\bar{w}_x u_x C_k)}{\partial x} + \frac{\partial((h_f - h_{bank})\bar{w}_x C_k)}{\partial t} + R_k = 0, \quad (14.68)$$

where  $C_k$  is the concentration of proppant type  $k$  and  $R_k$  is the source term representing the settling of proppant type  $k$  in the vertical direction to form a proppant bank. The settling velocity for proppant type  $k$  in a stagnant Newtonian fluid is given by Stokes law:

$$u_{set,k} = \frac{g(\rho_{prop,k} - \rho_f)d_{prop,k}^2}{18\mu}, \quad (14.69)$$

where  $u_{set,k}$  is the settling velocity for proppant type  $k$ ,  $\rho_{prop,k}$  is the density of proppant type  $k$ ,  $\rho_f$  is the density of the fluid, and  $d_{prop,k}$  is the average diameter of proppant type  $k$ . The proppant bank height  $h_{bank}$  is calculated by the accumulation of proppant settled at any point along the fracture length. Note that Eqs. (14.66) through (14.69) are expressed in a consistent unit system.

#### 14.4.6 ACID FRACTURING MODELS

Acid fracturing, also referred to as “fracture acidizing,” is a special case of hydraulic fracturing. An acid fracturing treatment typically requires a much larger volume of acids than a matrix acidizing treatment does. Acid fracturing is generally applicable in low- to moderate-permeability carbonate reservoirs. Matrix acidizing is sufficient to remove near wellbore damage and to stimulate high-permeability reservoirs. Commonly used acid types for acid fracturing include HCl, acetic, foamed HCl or emulsified HCl acids. Acid fracturing does not bode well in sandstone reservoirs for several reasons: the reaction rates of hydrofluoric acid (HF) with clays and quartz are too slow to create adequate acid-etched fracture conductivity; a huge amount of HF acid required for a typical acid fracturing treatment is simply too much to make economic sense; and additionally, the very low reaction rates of HF acid with clay minerals will result in most of the injected HF acid leaking off from inside the fracture into the formation and too much HF acid in the sandstone matrix will likely induce formation damage due to the precipitation of secondary and tertiary reaction products of HF acid with clay minerals. Successful acid fracturing treatments in sandstone reservoirs have been reported occasionally. In these rare cases, either high carbonate mineral contents or abundant natural fractures filled with carbonate minerals are present in the sandstone reservoirs treated by acid fracturing.

Similar to hydraulic fracturing treatments with proppants, a pad stage (clean fluids that do not contain acids) is first pumped into the formation to create a fracture. After that, instead of proppant slurry, an acid or a blend of acids is pumped into the fracture. The acid is consumed by reactions with carbonate rock minerals on fracture walls, thereby creating the etched width needed for production enhancement. Proper modeling of the acid fracturing process requires the fracture geometry and fluid flow calculations from a hydraulic fracture simulator in order to calculate acid transport and reactions. An acid fracturing model is usually a module of a typical hydraulic fracture simulator.

A number of acid fracturing models have been published in the literature (Nierode and Williams, 1971; Roberts and Guin, 1975; Lo and Dean, 1989; Settari, 1993; Settari et al., 2001; Zhu et al., 2013). Some early acid fracturing models (Nierode and Williams, 1971; Lo and Dean, 1989) had incorporated a gross assumption that the reaction of acid and rock minerals is infinite and the rate of acid spending is controlled by the rate of mass transfer of acid toward the fracture wall. This assumption means that all the acid molecules transferred to the fracture wall are spent instantaneously, i.e., the acid concentration at the wall is always zero, and therefore, the



information of reaction kinetics is not required. It is Roberts and Guin (1975) who first proposed and modeled the acid spending calculations by incorporating both mass transfer and reaction kinetics. At a high-temperature, the rate of reaction is fast and the spending process is controlled by mass transfer, and at a low temperature, the rate of reaction is slow and the spending process is controlled by reaction kinetics. For conditions of modest reaction rates, both mass transfer and reaction kinetics take place simultaneously. In newer acid fracturing models (Settari et al., 2001; Zhu et al., 2013), the equations that govern acid transport are discretized and solved along the fracture length and across the width directions. As a result a mass transfer coefficient to handle acid transport across the width direction in a lumped formulation is eliminated.

For the purpose of illustration and scope of this book, an acid fracturing model for 1D acid transport in a 2D vertical fracture is presented here. The 1D acid continuity equation is given as:

$$D \frac{\partial^2(\bar{w}_x \bar{C})}{\partial x^2} - \frac{\partial(\bar{w}_x u_x \bar{C})}{\partial x} - 2u_L C_w - 2R = \bar{w}_x \frac{\partial \bar{C}}{\partial t}, \quad (14.70)$$

where  $x$  is the distance from the wellbore along the fracture length direction,  $t$  is the time,  $D$  is the acid diffusivity coefficient,  $\bar{w}_x$  is the average fracture width at location  $x$ ,  $\bar{C}$  is the acid bulk (average) concentration,  $u_x$  is the average acid flow velocity along the fracture length direction,  $u_L$  is the leakoff velocity,  $R$  is the acid reaction rate at the fracture face, and  $C_w$  is the acid concentration at the fracture wall. Because there are two fracture walls, a factor of 2 is added to the two source terms, one for acid lost due to leakoff and the other for acid spent due to reaction. The fracture height  $h_f$ , average width  $\bar{w}_x$ , and the leakoff velocity  $u_L$  are obtained from a fracture model. Note that the fracture height  $h_f$  is not shown in the continuity equation, but will be needed later to calculate the acid-etched width.

The transport and spending of the acid creates acid concentration profiles both along the fracture length and across the fracture width. The continuity equation in Eq. (14.69) can only describe the transport behavior along the fracture length direction, but not across the fracture width. Roberts and Guin (1975) proposed two acid concentrations, bulk acid concentration and wall acid concentration, to describe the acid concentration profile across the width. The acid concentration gradient from the center of the fracture to the fracture wall is caused by acid reaction with rock mineral on the fracture wall. Based on reaction kinetics, the reaction rate at the fracture wall is given by:

$$R = kC_w^n, \quad (14.71)$$

where  $k$  is the acid reaction rate constant,  $n$  is the order of acid reaction with carbonate minerals. The rate of acid transfer from the center of the fracture to the fracture wall can be expressed as:

$$R = K_g(\bar{C} - C_w), \quad (14.72)$$

where  $K_g$  is the mass transfer coefficient for the acid. Because there is no mass accumulation along the fracture width direction, the mass transfer rate must equal the reaction rate. Therefore, the two acid concentrations are related as follows:

$$K_g(\bar{C} - C_w) = kC_w^n, \quad (14.73)$$

It is difficult to obtain the acid concentration at the fracture wall  $C_w$  directly from the above equation unless the reaction order is 2 or 0.5. However,  $C_w$  can be easily obtained using the Newton-Raphson iteration method.

The mass transfer coefficient  $K_g$  is commonly estimated from published correlations. A number of correlations are available in the literature to evaluate the mass transfer coefficient. The correlation by [Lee and Roberts \(1980\)](#) is commonly used for both turbulent and transitional flow. However, the correlation from [Settari \(1993\)](#) can be used for laminar flow.

Once the acid reaction rate at any grid block at any time is determined from the coupling between hydraulic fracturing and acid transport models, the acid etched width at grid block  $i$  at time step  $n$  can be readily calculated as follows:

$$w_e(i) = 2 \sum_1^n h_f(i) \Delta x(i) X R(i) \Delta t, \quad (14.74)$$

where  $w_e(i)$  is the acid etched width at grid block  $i$ ,  $h_f(i)$  is the fracture height at grid block  $i$ ,  $\Delta x(i)$  is the grid block length at grid block  $i$ ,  $X$  is the volumetric dissolving power of acid solution,  $R(i)$  is the acid reaction rate at grid block  $i$ ,  $\Delta t$  is the timestep size, and  $n$  is the total number of time steps. The factor 2 in the above equation reflects the fact that the acid reacts with minerals on two fracture walls. The volumetric dissolving power of acid solution  $X$  in [Eq. \(14.74\)](#) is calculated from [Eq. \(13.3\)](#) in Chapter 13, Acidizing. Note that [Eqs. \(14.71\)–\(14.74\)](#) are expressed in a consistent unit system.

When the acid etched width determined, the dissolved rock equivalent conductivity DREC is calculated as:

$$\text{DREC}(i) = 3.32 \times 10^9 w_e^3(i), \quad (14.75)$$

where  $\text{DREC}(i)$  is the dissolved rock equivalent conductivity in md-in at grid block  $i$ , and the acid etched width  $w_e(i)$  at grid block  $i$  is in inch. When the value of DREC at every grid block is available, the conductivity of the acid etched fracture at any at grid block can finally be calculated based on the conductivity correlations developed by [Nierode and Kruk \(1973\)](#) or [Deng et al. \(2012\)](#). These conductivity correlations for acid fracturing were discussed in detail in Chapter 13, Acidizing.

### 14.4.7 SUMMARY OF HYDRAULIC FRACTURE MODELS

Four types of fracture propagation models have been discussed so far, including 2D models, pseudo 3D models, planar 3D models, and unconventional fracture models. These fracture models are reviewed and discussed in this section. A summary of the main features of these fracture models in different categories is provided in [Table 14.1](#).

There will probably never be a fracture model that can capture the full physics of the hydraulic fracturing process. The physics of fracture initiation and propagation is difficult to fully understand, especially for unconventional reservoirs. In unconventional fracture models, the interaction between hydraulic and natural fractures is generally approximated by simple crossing criteria. Compromises are always made in model developments, and the compromised physics considered in each model depends on the nature of the problem and one's biases.

Fracture modeling is nonunique due to many reasons, including but not limited to the nonlinear nature of the process, formation heterogeneity, and compromised physics implemented in the model. Because of these reasons, a fracture model without calibration provides little value. The use of any computer models follows a very same rule: "garbage in, garbage out." For that, collecting



<b>Table 14.1 Main Features of Hydraulic Fracture Models</b>
<p><b>A. 2D fracture models</b></p> <p>Assume planar fractures</p> <p>Calculate two dimensions of a fracture by assuming a constant fracture height or a known fracture shape (radial)</p> <p>Analytical solutions available</p> <p>Useful for parametric evaluation</p> <p>Basics of fracture modeling</p>
<p><b>B. Pseudo-3D fracture models</b></p> <p>Assume planar fractures</p> <p>Capture the essence of 3D fractures (width, height and length) without significant computing requirements</p> <p>Moderate computation requirements</p> <p>Fluid flow and proppant transport are typically handled in one dimension along the fracture length direction</p> <p>Rock mechanical properties and minimum horizontal stresses from multiple layers are required</p> <p>Properties of commonly used fracturing fluids and proppants are generally provided</p> <p>Specialized for real-time and on-site applications</p>
<p><b>C. Planar 3D fracture models</b></p> <p>Assume planar fractures</p> <p>Three-dimensional fracture propagation is handled more rigorously</p> <p>Fluid flow and proppant transport are typically handled in two dimensions along the fracture length and height directions</p> <p>Properties of commonly used fracturing fluids and proppants are generally provided</p> <p>Computationally intensive, and not feasible for real-time or on-site applications</p>
<p><b>D. Unconventional fracture models</b></p> <p>Nonplanar fracture propagation</p> <p>Stress shadowing effects (interaction between adjacent hydraulic fractures)</p> <p>Interaction between hydraulic and natural fractures</p> <p>Fluid flow and proppant transport are typically handled either in one dimension along the fracture length direction or in two dimensions along the fracture length and height directions</p> <p>Computationally intensive, and not feasible for real-time or on-site applications</p> <p>Some models are research orientated</p> <p>Most models still under development at the time of this writing</p>

and entering proper data is as important as selecting a proper model. Regardless of which model is used to calculate the fracture geometry, limited data, such as pumping rates and treating pressures, collected during fracturing treatments alone, may not be sufficient to validate a fracture model used. Net pressure matching of treatment data is often performed using a fracture model of one's choice. The net pressure during a treatment is calculated from the minimum horizontal stress and bottom-hole treating pressure. Accurate minimum horizontal stress values are important from the viewpoints of both treatment design and posttreatment pressure analysis. The best way to obtain the minimum horizontal stress is through diagnostic injection testing. Often times, the bottom-hole treating pressures are not readily available and have to be calculated from surface treating pressures. The calculated bottom-hole treating pressures become less reliable as it is difficult to accurately estimate friction for turbulent flow, especially for crosslinked fluids.

Integrated studies may be an appropriate way to calibrate a fracture model. Once a simulator is selected, a model for a specific problem has to be built using reservoir and rock mechanics data available. The next step is to perform net pressure analysis on fracture treatments in offset wells in the area of interest. To reduce the likelihood that a nonunique solution is obtained, the model has to be calibrated by other measurements, including near-wellbore diagnostics such as tracers, PLT (production logging testing), DTS (distributed temperature sensing) and DAS (distributed acoustic sensing) using fiberoptic techniques, and far-field fracture diagnostics such as microseismic and tiltmeters monitoring techniques. The remaining step is to refine the model by pressure transient and/or rate transient analysis, production history analysis, and reservoir simulation studies.

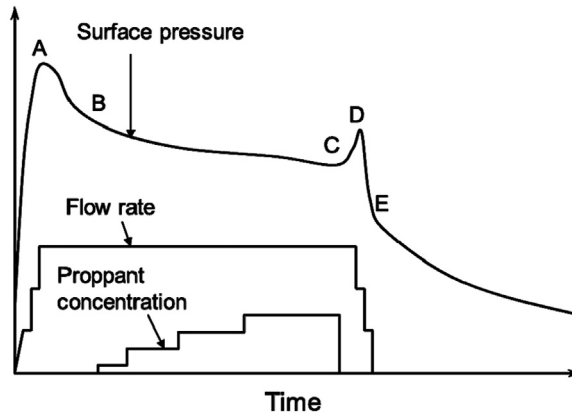
---

## 14.5 FRACTURING PRESSURE ANALYSIS

During and after a hydraulic fracturing treatment, the fluid pressure in the fracture is constantly changing until the fracture is closed and the fluid pressure around the fracture becomes equalized with the reservoir pressure. The evolution and history of the fluid pressure can be used to provide information on how the fracture propagates. Fracturing pressure analysis is analogous to the pressure transient analysis applied in reservoir engineering. However, the change in fluid pressure from hydraulic fracturing is more complex because the pressure responses are resulted from a coupling process of fracture mechanics and transient fluid flow. In this section, fracturing pressure characteristics and techniques to analyze fracture diagnostic tests are described.

### 14.5.1 FRACTURING PRESSURE CHARACTERISTICS

During a hydraulic fracturing treatment, a clean fluid is typically pumped initially to create a fracture. Once the desired fracture dimensions are achieved, the pumping is switched from the clean fluid to a mixture of fluid and proppant. Upon completion, pumping is stopped, but the fluid inside the fracture continues leaking off into the formation, and the fracture starts to close on proppants. Fig. 14.18 shows general surface pressure responses from a typical fracturing treatment with a given flow rate and a given proppant concentration profile during a proppant fracturing treatment. Once the pumping is started, the wellbore fluid begins to enter the formation matrix through a perforated or openhole interval as the injection rate and surface treating pressure are increased gradually. As explained in a previous section, a fracture initiates once the fluid pressure at the bottom-hole reaches the formation breakdown pressure, which is illustrated as the point A in the plot. As the pumping continues, proppant laden slurry starts to enter the wellbore, which is illustrated as the point B in the plot. As the proppant concentration increases, the hydrostatic head of the slurry in the wellbore also increases, which leads to the reduction in the surface pressure, but not necessarily in the bottom-hole pressure. When the proppant stage ends, a clean fluid is pumped to displace the slurry from the wellbore into the fracture. As soon as the clean fluid enters the wellbore, the hydrostatic head of the wellbore fluid starts to decrease and as a result the surface pressure starts to increase quickly, which is illustrated between points C and D in the plot. Toward the end of the treatment, the pumping rate quickly drops to zero from the point D to the point E in the plot. The pressure at the point E when the rate drops to zero is called the “instantaneous shut-in



**FIGURE 14.18**

Surface treating pressure responses from a typical fracturing treatment.

pressure” or ISIP for short. At the point E, the friction is gone as there is no fluid flow. From this point forward, the only difference between the surface and bottom-hole pressures is the hydrostatic head of the wellbore fluid. Once the treatment is completed, the fluid pressure continues to decline even after the fracture is closed on the proppant pack.

Nolte and Smith (1981) introduced a technique to interpret the fracture geometry created during pumping by analyzing the pressure response. The technique is based on the expected pressure response from 2D fracture models and then predicts the pressure response when certain types of pressure behavior take place. In the theory of LEFM, the fracture width is directly proportional to net pressure, and vice versa. According to Eqs. (14.48) and (14.53), the PKN model predicts that the net pressure is proportional to the fifth root of time for the propagation of a fracture with constant height or a well confined fracture. This means that on a log-log plot, the relationship between the net pressure and time is a straight line with a slope of  $1/5$ . When the pressure behavior deviates from the ideal case, other types of fracture growth can be identified. Nolte and Smith also defined the pressure response of other fracture propagation behavior. Based on the pressure response behavior, they classified the fracture propagation into four modes, as illustrated in Fig. 14.19 and summarized in Table 14.2. Fig. 14.19 is commonly referred to as the “Nolte-Smith plot.”

The Nolte-Smith pressure analysis technique can be used in real-time during pumping to identify potential problems such as natural fissure opening, near-wellbore screen-out event, and unrestricted height growth (or the fracture growing into low stress zones). Screen-out literally means that the fracture created is bridged or plugged off by proppants. Natural fissures can be important for hydrocarbon recovery in low-permeability reservoirs. However, the opening of natural fissures during the treatment can create a complicated fracture behavior and cause enhanced fluid loss, which can lead to a premature screen-out during proppant injection. The behavior of fracturing pressure during pumping between fissure opening and restricted height growth is similar. A primary diagnostic technique for distinguishing between natural fissure opening and height growth is the analysis of pressure decline data collected after the shut-in. Pressure decline analysis will be described subsequently.

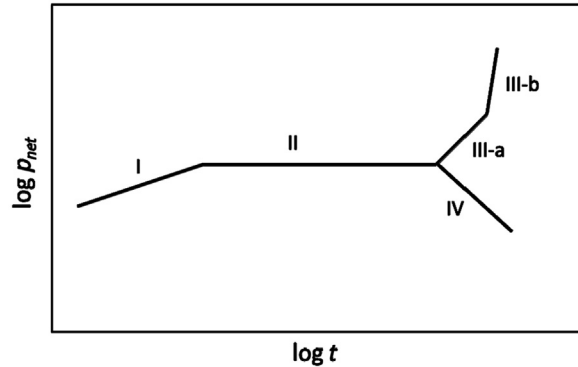


FIGURE 14.19

Net pressure response based on the Nolte-Smith analysis.

**Table 14.2 Net Pressure Response Modes Based on the Nolte-Smith Analysis**

Growth Mode	Slope	Behavior
I	1/5	No height growth. Propagation according to the PKN model.
II	0	Height growth or increased fluid loss possibly due to fissure dilation.
III-a	1	Unit slope. Net pressure is directly proportional to time. This behavior usually indicates tip screen-out associated with width growth.
III-b	$\geq 2$	Screen-out, probably occurring near the wellbore because of a very rapid pressure rise.
IV	Negative	Unrestricted and rapid height growth.

### 14.5.2 OBSERVED NET PRESSURE CALCULATION

Among all the variables measured during a hydraulic treatment, the three parameters that are the most important ones are pressure, rate, and proppant concentration. The proppant concentration is inferred from the slurry density measured with densometers. Net pressure observed from the fracturing treatment is used in all fracturing pressure analysis methods, including the Nolte-Smith pressure analysis just discussed. As defined in Eq. (14.25), net pressure is defined as the pressure inside the fracture minus the rock closure stress. In order to obtain the observed net pressure, the fluid pressure at the fracture initiation point has to be calculated first. The fracture initiation point is literally somewhere along the perforated interval and right beyond the end of all the perforation tunnels. Pressure calculation during the treatment is complicated by fluid friction, which includes wellbore friction and perforation friction, plus another important friction called “near-wellbore fracture tortuosity” or for short, “tortuosity.” When the surface treating pressure is available only, observed net pressure, which is directly related to hydraulic fracture dimensions, can be determined using the following equation:

$$P_{net,obs} = P_{surface} + \Delta P_{hydrostatic} - \Delta P_{wellbore} - \Delta P_{perforation} - \Delta P_{tortuosity} + \sigma_{closure} \quad (14.76)$$

where  $p_{net,obs}$  is the observed net pressure,  $\Delta p_{surface}$  is the surface treatment pressure,  $\Delta p_{hydrostatic}$  is the hydrostatic pressure of the fluid in the wellbore,  $\Delta p_{wellbore}$  is the fluid friction along the wellbore,  $\Delta p_{perforation}$  is the perforation friction,  $\Delta p_{tortuosity}$  is the near-wellbore tortuosity friction, and  $\sigma_{closure}$  is the fracture closure stress or the minimum principal stress.

The hydrostatic pressure of the fluid/slurry column in the wellbore can be easily and accurately calculated from the density of the fluid/slurry. However, the wellbore friction during pumping is difficult to calculate accurately for several reasons. Turbulent flow in the wellbore is almost always encountered during a fracturing treatment. The wellbore friction for gelled fluids, especially crosslinked gels, is more difficult to estimate as the crosslinking process further complicates the fluid friction behavior. When friction reducers (FR) (polymer) is added to plain water, the apparent viscosity of the fluid is typically increased from 1 cp to 1.5–3 cp, but the fluid friction can be by up to 70%. Service companies usually measure the friction of their fluid systems using flow loops in yard testing and provide friction tables for estimating friction at various rates in various wellbore sizes.

In addition to the reasons above, water quality and composition, fluid type and composition, and wellbore temperature are constantly changing during the treatment. All these factors make predicting fluid friction unreliable. There is no predicted pressure data that can replace reliable bottom-hole pressure measurements. However, the following equations can be used to estimate fluid friction. To calculate the fluid friction pressure drop, the Reynolds number must be estimated first to determine the flow regime. For a power law fluid, the Reynolds number is calculated by:

$$N_{Re} = \frac{0.249\rho V^{2-n}(D/96)^n}{K[(3n+1)/4n]^n}, \quad (14.77)$$

$$V = 17.17 \frac{q}{D^2}, \quad (14.78)$$

where  $N_{Re}$  is the Reynolds number,  $\rho$  is the fluid density in lb/ft<sup>3</sup>,  $V$  is the flow velocity in ft/sec,  $D$  is the pipe diameter in inch,  $K$  is the consistency index in lbf-s<sup>*n*</sup>/ft<sup>2</sup>,  $n$  is the flow behavior index (dimensionless), and  $q$  is the pumping rate in bbl/min.

For laminar flow ( $N_{Re} < 2100$ ), the Fanning friction factor for smooth pipes can be calculated by:

$$f_f = \frac{16}{N_{Re}}, \quad (14.79)$$

For turbulent flow ( $N_{Re} > 2100$ ), the Fanning friction factor for smooth pipes can be estimated by:

$$f_f = \frac{(\log(n) + 2.5)/50}{N_{Re}^{(1.4 - \log(n))/7}}, \quad (14.80)$$

The friction pressure drop is given by:

$$\Delta p_f = 0.0052 \frac{f_f \rho L V^2}{D}, \quad (14.81)$$

where  $L$  is the pipe length in ft.

Eqs. (14.77)–(14.81) generally over estimate actual friction values as polymers added in fracturing fluids can dramatically reduce fluid friction. Eqs. (14.77)–(14.81) should also apply to Newtonian fluids, in which  $n$  becomes 1 and  $K$  becomes the fluid viscosity. The friction for proppant laden fluids, especially at higher proppant concentrations, is even more difficult to estimate. Various correlations for estimating the friction of proppant slurry are available (Keck et al., 1992).

In most fracturing operations, surface treating pressures are the only data measured. Bottom-hole pressure data is occasionally measured using a retrievable pressure gauge and the pressure data can only be recovered when the gauge is brought to surface. The fracturing fluids are usually pumped down the casing. However, for smaller treatments in conventional high-permeability reservoirs, a tubing string is available and the fluids can be pumped down through the tubing or the annulus or both. When coiled tubing is used for a fracturing treatment, the fluid and slurry are usually pumped down through the annulus. Whenever there are two flow paths along the wellbore and only one path is used to pump the fluids, the other path is called “dead string.” In this case surface pressures for both the treating string and the dead string can be measured and collected during the treatment. The surface pressures from the dead string can readily reflect and be used to obtain the bottom-hole treating pressure without any complications from the wellbore friction of the fluid and slurry.

In theory, the perforation friction is very easy to calculate, as the calculation is the same as the flow through an orifice or orifices. The calculation takes account of the fluid and fluid conditions, the orifice size and the coefficient of discharge. The equation used to calculate perforation friction is as follows:

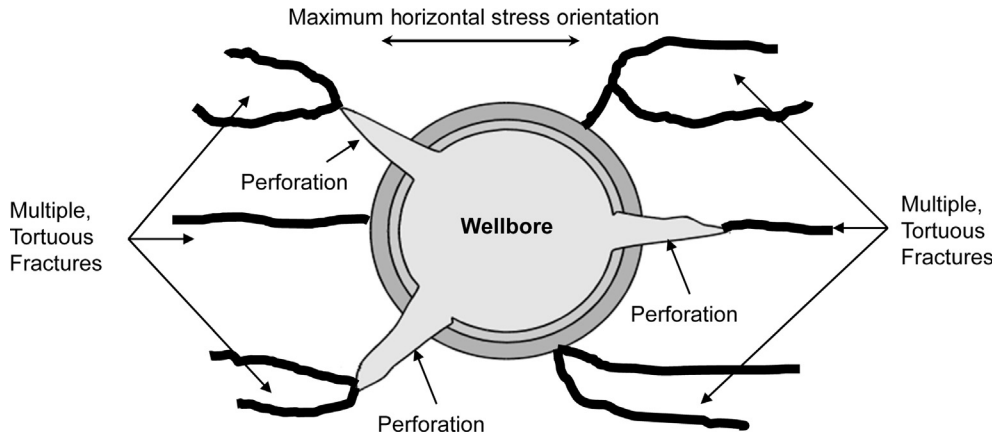
$$\Delta p_{\text{perforation}} = 0.237\rho \frac{(q/N)^2}{C_d^2 D^4}, \quad (14.82)$$

where  $\rho$  is the slurry density in ppg,  $q$  is the flow rate in bbl/min,  $N$  is the number of perforations,  $D$  is the perforation diameter in inches, and  $C_d$  is the discharge coefficient. The value of the discharge coefficient is usually 0.8. In reality, not all the perforations are created equal and the fractures may not initiate from some of the perforations. With the uncertainty with perforation efficiency, the effective perforation friction can be estimated by the following equation:

$$\Delta p_{\text{perforation}} = k_{\text{perf}} q^2, \quad (14.83)$$

where  $k_{\text{perf}}$  is the perforation friction coefficient and has to be determined by a diagnostic test during the treatment.

The near-wellbore tortuosity friction is a flow restriction in the near-wellbore that connects the wellbore with the far-field fracture, which is similar to the skin effect in well production. This near-wellbore friction results in a difference between the fluid pressure at the fracture entry point and the fluid pressure in the main body of the fracture. The “fracture system” in the near wellbore area is complicated because the wellbore and perforations alter the state of stress in this area with a few times the wellbore diameter. A number of fracture propagation phenomena could occur in this area. Fractures may re-orientate from the perforation towards preferred fracture plane. Fractures may interact with and dilate natural fractures. The explosive energy during perforating could induce microcracks and initiate shear cracks. As a result, multiple and tortuous fractures can be created in the near wellbore area, which leads to additional fluid friction or pressure drop. An illustration of fracture tortuosity in the near-wellbore area is illustrated in Fig. 14.20, in which the blue circle



**FIGURE 14.20**

Illustration of fracture tortuosity and multiple fractures in the near-wellbore area.

represents the near-wellbore area where fracture tortuosity occurs. Cleary et al. (1993) first recognized the importance of near-wellbore tortuosity and proposed a diagnostic method to quantify the near-wellbore tortuosity friction. The near-wellbore friction due to fracture tortuosity is related to the pumping rate and can be estimated with the following empirical equation:

$$\Delta p_{\text{tortuosity}} = k_{\text{nw}b} q^\beta, \quad (14.84)$$

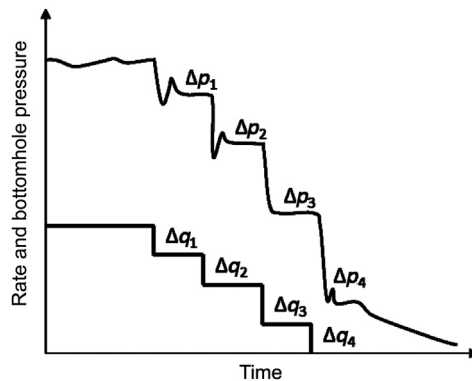
where  $k_{\text{nw}b}$  is the near-wellbore friction coefficient and  $\beta$  is the power-law exponent. The value of  $\beta$  ranges between 0.25 and 1.0, but is typically assumed as 0.5. Since Eq. (14.84) is an empirical equation, both  $k_{\text{nw}b}$  and  $\beta$  have to be determined by a diagnostic test during the treatment.

### 14.5.3 DIAGNOSTIC RATE TEST ANALYSIS

Most fracture diagnostic injection tests are centered on the analysis of the pressure decline data after shut-in. There are basically two types of diagnostic tests that involve the analysis of the changes in rate and pressure during pumping. This section describes these tests and their applications.

#### 14.5.3.1 Rate step-down testing

A rate step-down test is the only appropriate diagnostic test to estimate the perforation and near-wellbore friction during a fracture treatment. To conduct a rate step-down test, the injection rate should be reduced in steps by  $\frac{1}{4}$  to  $\frac{1}{3}$  of the full rate at each step. A rate step-down test can only be performed toward the end of an injection, with the last rate being zero at the shut-in. The rate should be kept steady at each step for 15–20 seconds to obtain a stabilized pressure change. The rate changes are most easily accomplished by simply taking one pump (a couple of pumps if over eight pumps used during the treatment) off line at each step. A rate step-down test should be kept in a short duration. It is important to first create a sizable hydraulic fracture, either with a



**FIGURE 14.21**

Schematic of a typical rate step-down test.

slickwater injection, minifrac, or the main fracture treatment, as a sizable fracture can store a great deal of fluid and energy. During the short duration of a rate step-down test, any changes, such as fracture geometry change, fluid loss and pressure change, are neglected. Therefore, the drop in bottom-hole pressure is caused only by the drop in rate. This assumption is reasonable only for a sizable fracture as it can store a great deal of fluid and energy in the fracture.

The changes in rate and bottom-hole pressure are used to calculate the perforation and near-wellbore friction from a rate step-down test. If only the surface treating pressure is measured, the wellbore friction has to be estimated from the fluid specific correlations in order to calculate the bottom-hole pressure during the rate step-down test. The accuracy of the wellbore friction will affect the accuracy of the calculated bottom-hole pressure. If bottom-hole pressure is measured, this should be used directly. If the dead-string pressure at surface is available, the calculated bottom-hole pressure is as good as the one measured with a bottom-hole pressure gauge.

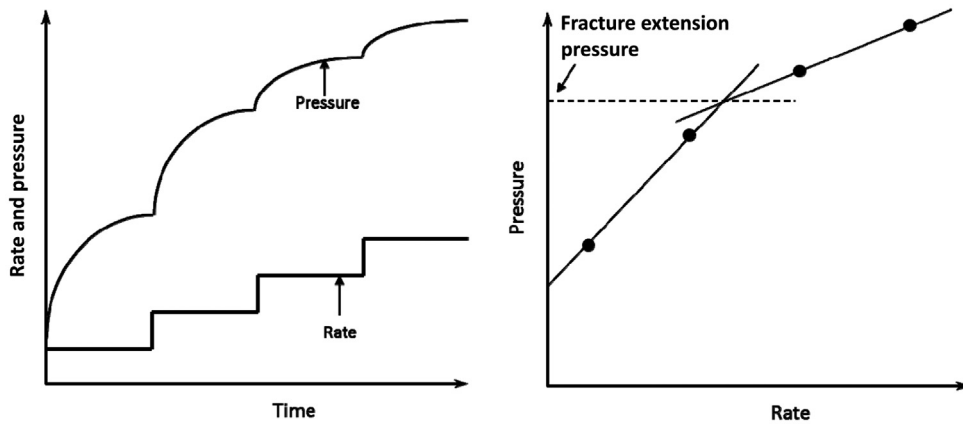
Since there are three knowns,  $k_{perf}$ ,  $k_{nwb}$ , and  $\beta$ , associated with Eqs. (14.83) and (14.84), a rate step-down test involving minimum three different injection rates is required to determine these unknowns. Based on calculated or actual bottom-hole pressure during the step-down test, the perforation and near-wellbore friction can be readily calculated using a typical fracture simulator (Wright et al., 1995). Fig.14.21 shows a typical rate step-down test.

The results of a rate step-down test are very useful to distinguish between the perforation and near-wellbore friction. For a perforation friction dominated case, the largest changes in friction occur at the high rates, whereas for a near-wellbore friction dominated case the largest changes in friction occur at the low flow rates. When proppant laden slurry enters the fracture, near-wellbore friction may increase dramatically due to difficulties in transporting the proppant through the tortuous near-wellbore region, and a result proppant bridging may occur. In fact, most premature screen-outs are caused by tortuosity, but not due to inadequate pad fluid volume.

### 14.5.3.2 Step-rate testing

Step rate testing can be conducted at the beginning of a fracture treatment, either a diagnostic injection or the main treatment, to estimate the fracture extension pressure. The test procedure requires





**FIGURE 14.22**

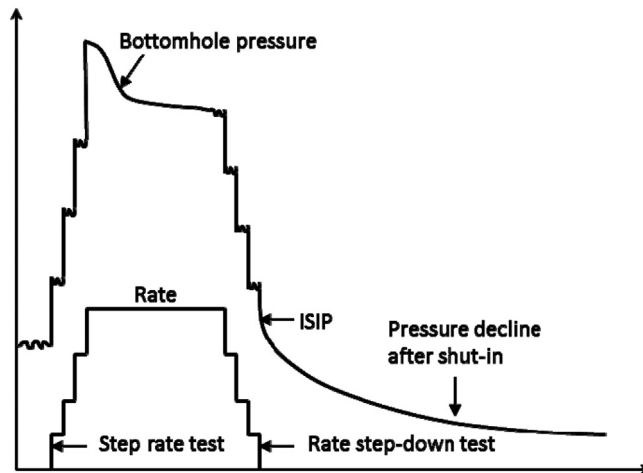
Illustration of a typical step-rate test.

the test well to be shut in prior to the start of the step rate test. The step rate test consists of a series of constant-rate injections with the rate started from zero and increased in each step. The rate incremental in the first few steps should be small to ensure a matrix injection is established before fracturing the formation. The rate at each step should be kept constant for a short duration to achieve a stabilized pressure. The duration of each constant-rate step is typically about the same. As the rate increases, the pressure will also increase. Once a fracture is created, the pressure increase dramatically slows down as the rate continues to increase.

Fig. 14.22 shows the schematic of a typical step-rate test. The plot on the left illustrates the testing procedures. The plot on the right shows a cross plot of the rate versus the pressure. The pressure will start to bend or slow down when a fracture is created. To assist the analysis, two lines can be drawn on the curve, one to follow the rate-pressure trend under the matrix injection and the other to follow the trend under fracturing. The intersecting point between the two lines is supposed to be the fracture extension pressure. The pressure plotted for the analysis can be either surface treating pressure or bottom-hole pressure. However, it is preferable to plot the measured or calculated bottom-hole pressure data versus the so that the fracture extension pressure at bottom-hole can be obtained. The fracture extension pressure is not very useful for fracture design, as the fracture closure stress or the minimum principal stress is really needed as an important input parameter in any fracture model. The fracture extension pressure is measured at the beginning of a treatment while the ISIP is measured at the end of a treatment. Both of the two pressures provide an upper bound for the closure stress.

#### 14.5.4 PRESSURE DECLINE ANALYSIS

All friction terms in Eq. (14.76) disappear at the end of a diagnostic test or a treatment when the injection stops. The quality of the pressure data can be improved significantly when collected during the shut-in period. The pressure continues to decline during the shut-in even after the fracture is closed on the proppant pack. Pressure decline analysis can provide a great deal of information about the fracture created, including the fluid efficiency, the time of fracture closure, and the closure stress, etc. In short, pressure



**FIGURE 14.23**

A typical minifrac test.

decline analysis is the most important one among various fracturing pressure analysis approaches. Testing procedures and several pressure decline analysis techniques are described in this section.

#### **14.5.4.1 DFIT testing**

DFIT stands for diagnostic fracture injection test. The DFIT goes by many names, including minifrac, datafrac, mini falloff, diagnostic injection, or microfrac. They all refer to a test of injecting a small volume of clean fluid above fracture gradient in a specific zone to create a small fracture, shutting in the well to allow the pressure fall-off naturally, and accurately measuring the pressure decline during the injection and the shut-in periods. A clean fluid, such as 2% or 3% KCL water is typically injected during the test.

The name DFIT tends to be used more often for diagnostic injection tests performed for ultra-low permeability shale reservoirs, while the name minifrac tends to be used more often for diagnostic injection tests performed for conventional reservoirs. After the test is completed, it may take days or weeks for the fracture to close in unconventional shale reservoirs, and minutes, but no more than a couple of hours, for the fracture to close in conventional reservoirs. For conventional reservoirs, the test may often be combined with a step rate test at the beginning of a diagnostic injection and a rate step-down test at the end of the injection. However, the step rate and rate step-down tests are seldom combined with the DFIT because the duration of the entire injection is too short to allow other tests and also because it is desirable to keep the injection rate constant. Fig. 14.23 shows illustrative pressure responses during and after the injection for a typical minifrac test with the step rate and rate step-down tests included.

#### **14.5.4.2 Pressure decline analysis techniques**

The pressure decline during shut-in is affected by the total amount of energy (the product of net pressure and fracture volume at shut-in) stored in the fracture and the rate of fluid loss. The pressure decline analysis is based on the assumption that the change in the fracture volume is entirely

contributed by the change in the average fracture width throughout the shut-in period. The change in the fracture width is then related to the change in the net pressure through their compliance with a fracture geometry model. As a result, the fluid efficiency, the time of fracture closure, and the closure stress and other information can be determined by the combination of the compliance and fracture geometry equations. The analysis can be performed conveniently in most fracture design simulators commercially available.

Linear flow regime develops during pumping and after shut-in, and pressure decline depends on fluid leakoff rate and fracture compliance. Closure stress can be determined by identifying the end of the first linear flow regime. A later time linear flow may also develop if shut-in time is long enough. If the later linear flow develops, reservoir pressure can be determined and reservoir permeability can be estimated by the DFIT analysis. As pressure decline continues, pseudo-radial flow may or may not develop, because the rate of pressure decline depends on reservoir diffusivity. Once the radial flow regime is identified, reservoir pressure and permeability can be easily and more accurately determined by the Horner method.

There are three commonly used pressure-against-time plots for analyzing pressure decline data versus time, including the square root time plot, log-log plot, and G-function plot. Among these diagnostic plots, the G-function plot is the most popular one, as it is often used to also identify the opening of natural fractures in addition to calculating closure stress (Barree et al., 2009).

Fig. 14.24 shows pressure decline during the shut-in period on the square root time plot. Since finding fracture closure is to find the point on the pressure decline curve where the gradient changes or where the linear flow ends, it makes sense to also plot the pressure derivative (gradient) versus square root of time on the same plot. The closure stress is then readily determined at the reflection point on the derivative curve. Before the fracture closes, the pressure decline versus time becomes a line with a half slope on log-log scale, as shown in Fig. 14.25.

The G-function was developed by Nolte (1979) on the assumption that both the injection rate and the total leakoff coefficient during fracturing are constant, and was derived based on the fracture growth behavior from 2D fracture models (KGD, PKN and radial). The G-function is a dimensionless time function relating the total elapsed time to the total pumping time. According to Barree et al. (2009), the total elapsed time,  $t$ , should be determined from the start of fracture initiation (but not necessarily from the start of pumping) and that the total pumping time,  $t_p$ , is the elapsed time from fracture initiation to shut-in. The G-function calculations are based on the following equations:

$$\Delta t_D = (t - t_p)/t_p \quad (14.85)$$

$$g(\Delta t_D) = \begin{cases} 4/3((1 + \Delta t_D)^{1.5} - \Delta t_D^{1.5}) & \text{for low-leakoff cases} \\ (1 + \Delta t_D)\sin^{-1}(1 + \Delta t_D)^{-0.5} + \Delta t_D^{0.5} & \text{for high-leakoff cases} \end{cases} \quad (14.86)$$

$$G(\Delta t_D) = \frac{4}{\pi}(g(\Delta t_D) - g_0) \quad (14.87)$$

where  $g_0$  is the dimensionless time at shut-in ( $\Delta t_D = 0$  or  $t = t_p$ ). Note that according to Eq. (14.86),  $g_0 = 4/3$  for the low-leakoff cases and  $g_0 = \pi/2$  for the high-leakoff cases. Although there are different forms of the G-function for the low- and high-leakoff cases, there is little difference between these two limiting cases. As  $\Delta t_D$  increases, the difference in the values of the G-function between the two extreme cases becomes smaller and eventually negligible (Economides and Martin, 2007). One way to avoid the confusion between the two limiting cases is to simply take the average of the upper and lower expressions in Eq. (14.86).

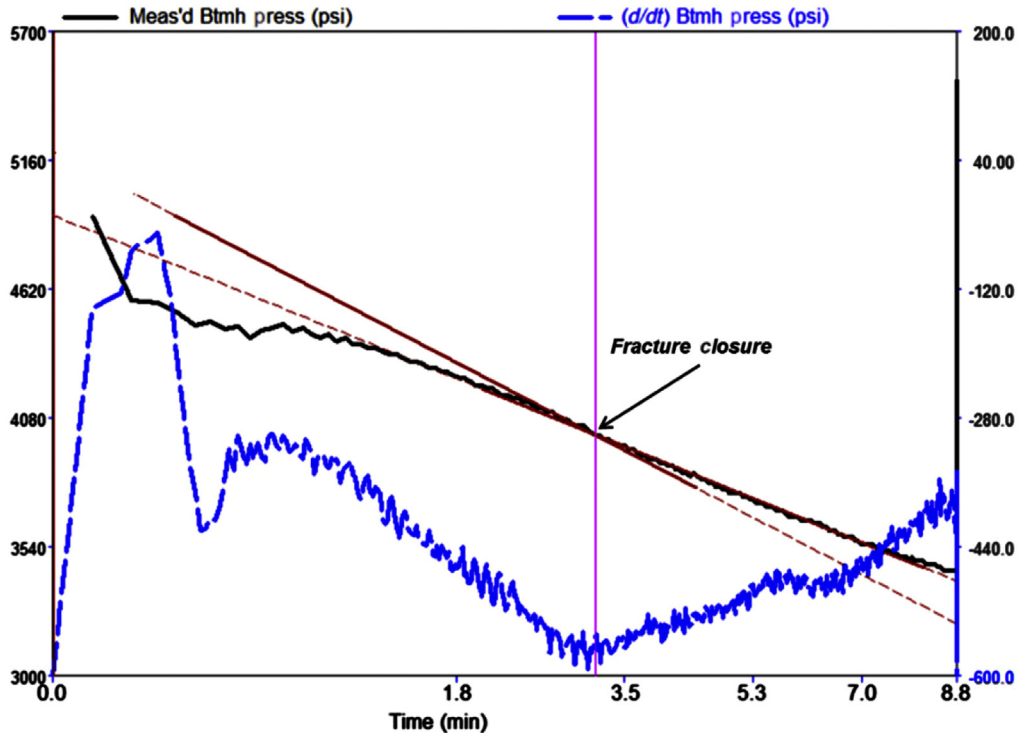


FIGURE 14.24

A sample plot of pressure vs square root of time.

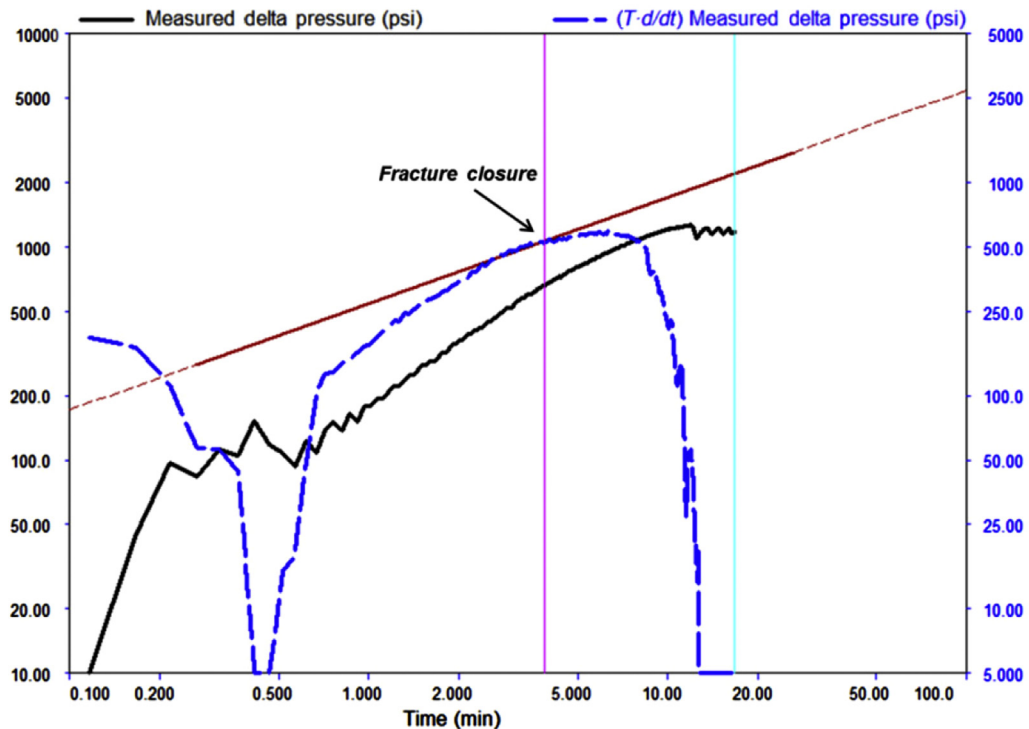
The objective of the G-function derivative analysis is to identify the leakoff type and fracture closure stress. In most cases, the superposition derivative provides a definitive indication of hydraulic fracture closure when the data deviate downward from an extrapolated straight line through the period of normal leakoff. Fig. 14.26 shows a sample plot of pressure vs the G-function time.

## 14.6 FRACTURING MATERIALS AND EQUIPMENT

Hydraulic fracturing is the process of pumping both fluid and a mixture of fluid and proppant into a wellbore to break down the formation, generate a fracture and keep it open after the treatment. Various types of fracturing fluids and proppants, the surface equipment required to execute a fracturing treatment are described in this section.

### 14.6.1 FRACTURING FLUIDS

A fracturing fluid is a critical component to a hydraulic fracturing treatment; and its function is not only to create a fracture, but also to transport and place proppant in the fracture. When selecting a fracturing fluid, one of the main considerations is its viscosity. The fluid viscosity plays a major



**FIGURE 14.25**

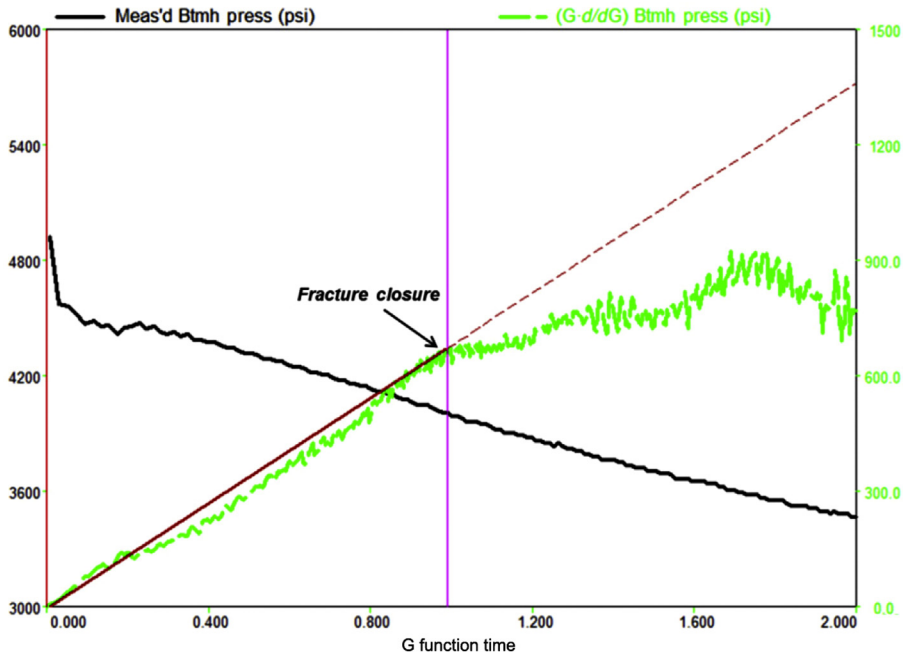
A sample plot of pressure vs time on log-log scale.

role in providing enough viscous forces to transport proppant and in creating sufficient fracture width to allow proppant to travel inside the fracture.

Fracturing fluids can generally be divided into oil based fluids, water based, or multiphase fluids. Multiphase fluids can be further grouped into foams, energized fluids and emulsions. A fracturing fluid does not simply contain a base fluid and viscosifying material. Various additives are generally used to control the fluid properties. Commonly used fracturing fluids and additives are also described.

### 14.6.1.1 Oil based fracturing fluids

Oil based fluids were once commonly used in the early days as fracturing fluids, mainly because these fluids were believed as less damaging to petroleum-bearing formations than water based fluids. Oil based fracturing fluids can be crude oil, gelled crude oil, or gelled refined oil. In the 1960s, aluminum carboxylate salts were commonly used to increase the viscosity of hydrocarbon fracturing fluids (Burnham et al., 1980). By the 1970s, the aluminum carboxylate salts were replaced by aluminum phosphate ester salts. Since then, aluminum phosphate ester salts have remained the preferred method of gelling hydrocarbons for hydraulic fracturing. Oil based fluids work well in water sensitive formations or during wintertime when water freezes. Environmental concerns with oil based fluids are their potential for groundwater contamination.



**FIGURE 14.26**

A sample plot of pressure vs G-function time.

By the early 1970s, the use of metal based crosslinking agents had greatly enhanced the viscosity of gelled water based fracturing fluids for wells with wide temperature ranges. Oil based fluids have gradually fallen out of favor because they are more expensive to use, more difficult to handle, and also exhibit higher wellbore friction than typical water based fluids. Water has since become the base fluid for the majority of hydraulic fracturing fluids.

With the development of unconventional resources, hydraulic fracturing requires huge amounts of water to effectively stimulate these reservoirs using hydraulic fracturing treatments. The demands on water usage for hydraulic fracturing have renewed the interests in seeking alternatives to water based fluids. Calgary-based GasFrac Energy Services Inc. developed a waterless stimulation process to use a propane-butane gel for hydraulic fracturing in horizontal wells (Tudor et al., 2009). The company has since used the process in more than 2000 completions in Canada and the United States. Similar to oil based fluids in the early days, gelled propane-butane fluids are also expensive to use, more difficult to handle, and also exhibit higher wellbore friction than typical water based fluids.

#### **14.6.1.2 Water based fracturing fluids**

At the time of this writing, the vast majority of fracturing fluids used in the industry are water based fluids because of their low cost, high performance and ease of handling. Polymers are the main ingredient in water based fluids. When polymers are added to water, its molecules hydrate and stretch out in the solution and thus increase the fluid viscosity significantly. Guar gum and cellulose derivatives are the most common types of polymers used in fracturing fluids.

Guar gum is the endosperm of guar beans. Guar is a plant grown mainly in India and Pakistan, with the two countries accounting for about 80% of world production. The process used to produce guar powder cannot separate the guar gum from water insoluble materials completely, which leaves as much as 6%–10% insoluble residue in the fluid. Guar can be derivatized with propylene oxide to produce hydroxypropylguar (HPG). The derivatizing process, plus washing and additional processes, can remove much of the plant material from the polymer. HPG contains less insoluble residue (only about 2%–4%), and is more stable at elevated temperatures of >300°F (150°C) than guar. There is another guar derivative named carboxymethylhydroxypropylguar (CMHPG).

Cellulose is a polysaccharide and the most abundant organic polymer on Earth. For example, the cellulose content of cotton fiber is 90%, and that of wood is 40%–50%. Cellulose derivatives used in fracturing fluids include hydroxyethylcellulose (HEC), hydroxypropylcellulose (HPC), and carboxymethylhydroxyethylcellulose (CMHEC). Cellulose derivatives are residue-free and are widely used in Frac-Pack applications as they are perceived as less damaging to the formation. Cellulose derivatives are difficult to disperse because of their rapid rate of hydration, and difficult to break. Strong oxidizing agents are generally required to break the polymer.

Both guar gum and cellulose derivatives can provide most, if not all, of the desired properties of an ideal fracturing fluid. However, the use of cellulose derivatives is complicated, as they are sensitive to environmental conditions such as field grade water compositions and reservoir temperatures. Guar derivatives are currently the main gelling agents used for hydraulic fracturing. However, the main issue with guar derivatives is their insoluble residues that potentially could cause damage to the formation and the proppant pack.

There are several types of water based fracture fluids, including slickwater, linear gel, cross-linked gel, and viscoelastic surfactant (VES) fluid. The difference between them is whether gelling agents (polymers) or crosslinkers are used.

*Slickwater* is mainly composed of water and a FR (friction reducer), plus a clay control agent and bactericide. All FR are basically variants of high molecular weight polyacrylamide copolymers. The viscosity of slickwater depends on the concentration or loading of polyacrylamide used in the fluid, but is generally in the range of a few centipoises (cP) for the purpose of friction reduction. [Motiee et al. \(2016\)](#) demonstrated in field trials that high concentrations of FR have been used as a direct replacement for a guar-based borate crosslinked without modification to the standard treatment and proppant schedule. The field trials proved successful in reducing completions costs and improving operational efficiency while maintaining baseline well productivity.

*Linear Gel* is mainly composed of water, a gelling agent such as Guar, HPG or HEC, plus a clay control agent and bactericide. The viscosity of linear gel strongly depends on the gel concentration, but is generally less than 50 cP. The main advantages of a liner gel are its lower cost and better viscosity characteristics compared to slickwater. The main disadvantage is its relatively low viscosity. Another disadvantage of liner gel is that the flowback water contains residual gel and breaker that makes the water more difficult to reuse.

*Crosslinked Gel* is composed of similar materials as a linear gel, but with the addition of a crosslinker which can increase the viscosity of the linear gel by up to 10 times or more. The benefits of higher viscosity are two folds: (1) to improve proppant transport capability with higher viscous drag forces applied on proppants, and (2) to increase the fracture width that makes proppant travel more easily inside the fracture and allows higher proppant concentrations more acceptable. A description of crosslinkers and other additives are discussed in the section to follow.

*Acid based fluids* are special water based fluids that are commonly used in unconventional fracturing operations and in acid fracturing treatments. For both types of applications, hydrochloric acid (HCl) is the main acid component, in addition to other ingredients.

In high-rate fracturing treatments for unconventional reservoirs, reducing friction can help deliver more horsepower into the formation. A small amount of HCl acid solution is typically pumped at the beginning of each stage to help break down the formation and to reduce perforation friction and near wellbore fracture tortuosity friction by dissolving perforation debris and minerals around the perforation tunnels.

In acid fracturing treatments, HCl solution is usually injected into a carbonate formation to both create a fracture and to react with formation minerals on the fracture walls, thereby creating the etched width needed for production enhancement. Acrylamide copolymers are often used to viscosify acid based fracturing fluids.

VES fluids are another type of water based fluids that are polymer-free, and are prepared using VES (Stewart et al., 1995). These surfactants, typically a quaternary ammonium salt of a long-chain fatty acid, are composed of the head and tail groups. The head group is hydrophilic and the tail group is hydrophobic. When the surfactants are added to water, their molecules are arranged into structures called micelles, in which the hydrophilic head groups are on the outside and in direct contact with the water phase and the hydrophobic tail groups form an inner core.

If the surfactant concentration is sufficient, the micelles associate with one another, making the fluid both viscous and elastic. The micellar structure of VES fluids can be permanently destroyed by contact with hydrocarbons or by dilution with aqueous fluids such as formation water. In both cases, the viscosity of the VES fluid reduces significantly. Because the above scenarios normally occur during posttreatment production, VES fluids do not require any chemical breaker to destroy their systems.

The main advantage of VES fluids is less damage to the proppant pack and fracture face because little residue is left after cleanup. The main disadvantages of VES fluids are that they are more expensive than other water based fluids, and that the surfactants may potentially cause adverse effects on the relative permeability to hydrocarbon phases in the fluid invaded region.

### **14.6.1.3 Foams and energized fluids**

Foam is a multiphase fluid composed of a stable mixture of liquid and gas. The liquid phase is external continuous phase while the gas is the internal discontinuous phase. In foams used for hydraulic fracturing, water is the liquid phase, and nitrogen (N<sub>2</sub>) and/or carbon dioxide (CO<sub>2</sub>) are the gas phase. To make the mixture stable, a surfactant (foaming agent) is needed. The surfactant concentrates at the gas/liquid interface, lowers the interfacial tension, and prevents the cells from coalescing. The thicker the continuous phase, the more difficult it is for the gas bubbles to coalesce. Guar and HPG are generally added to improve system viscosity and to stabilize the foam. Fracturing fluids containing CO<sub>2</sub> or N<sub>2</sub> have been used to stimulate tight gas, coalbed methane, and under-pressured formations for nearly 50 years.

The term “quality” is often used to describe the concentration of CO<sub>2</sub> or N<sub>2</sub> used in the system, which is defined as the ratio of the volume of CO<sub>2</sub> or N<sub>2</sub> to the total fluid volume under bottom-hole pressure and temperature conditions. According to Ward (1986), a fluid system is classified as an energized fluid system if its quality is less than 52% or as a foamed fluid system if its quality equals or is larger than 52%. A fluid system with a quality of 52% or higher is required to maintain



the dispersion of the gas phase and to form stable foam. Energized fluid systems are typically used with a quality between 10% and 30%, and foaming agents are often not needed to modify the fluid system properties.

The main disadvantages of foams or energized fluids are high costs, logistic restrictions and additional operational requirements. Some of the advantages of using foams or energized fluids systems include:

- Eliminating the need of swabbing wells after treatments in low pressure reservoirs
- Rapid cleanup after treatments to reduce fluid damage to the formation
- Removal or prevention of formation damage due to water or emulsion blocks
- Prevention of formation damage due to clay swelling and precipitation of iron and aluminum hydroxides
- Quick return to production

Insufficient fluid clean-up can often hamper stimulation success in tight, under-pressured, and water sensitive reservoirs. Foam fracturing has proved successful in achieving effective stimulation in these types of reservoirs.

#### **14.6.1.4 Emulsions**

An emulsion is a mixture of two immiscible phases such as oil in water or water in oil. Surfactants are required to stabilize the emulsion system. Generally, the higher the percentage of the internal phase is, the more viscous the system becomes. Polyemulsion is the most common type of emulsion fluid and is formed by emulsifying a hydrocarbon such as condensate or diesel with water such that the hydrocarbon is the internal phase. Polymer is added to the aqueous phase to improve the emulsion stability and to significantly reduce friction pressure because the polymer also acts as a FR.

Major disadvantages of polyemulsions include high cost, high friction, and poor stability in high-temperature wells. The main advantages are less water and polymer usage, highly viscous solutions at modest temperature environments, and less damage to the formation and the prop-pack.

#### **14.6.1.5 Additives**

Additives are commonly added to a fracturing fluid system to modify and control its properties. When multiple additives are used, it is important to determine that these additives do not interfere with each other and create any side effects. Commonly used fracturing additives are described below.

*Crosslinkers* are one of the important additives used in fracturing fluids. Instead of increasing the polymer concentration to improve the fluid viscosity, crosslinking agents are commonly used to significantly enhance the fluid viscosity by crosslinking the molecular chains of the polymer, and forming a 3D network of molecular chains. Some metal compounds, such as borate, titanium, zirconium, and aluminum compounds, are frequently used to as crosslinkers in water-soluble polymer fluids (Conway et al., 1983).

All fracturing gels become less viscous with heat or shear, but some can return to their original state once heat or shear is removed. Most polymers generally exhibit thermal degradation to some degree. Borate crosslinking is reversible because crosslinks can form, break, and then form again as shear rates change. Some fluids crosslinked with transition metal, such as titanium, zirconium, and

**Table 14.3 Characteristics of Commonly Used Crosslinkers (Economides and Nolte, 2000)**

Crosslinker	Borate	Titanate	Zirconate	Aluminum
Polymer type	Guar, HPG, CMHPG	Guar, HPG, CMHPG, CMHEC	Guar, HPG, CMHPG, CMHEC	CMHPG, CMHEC
pH range	8–12	3–11	3–11	3–5
Upper temperature limit (°F)	325	325	400	150
Shear degraded	No	Yes	Yes	Yes

aluminum, degrade irreversibly with high shear. Unlike borate crosslinker, once the bond between the transition metal crosslinker and polymer is broken, it does not reform. To avoid the negative effects of high shear occurring in the tubing, the crosslinking process can be delayed for a few minutes to limit viscosity development until the fluid leaves the wellbore and enters the fracture. In addition to minimizing shear degradation, delaying crosslinking also reduces frictional losses and hydraulic horsepower requirements.

Some key characteristics of commonly used crosslinkers are compared and summarized in Table 14.3 (Economides and Nolte, 2000). The pH level of a fluid is important to the crosslinking process. Borate can only crosslink in alkaline environments so it cannot be used in acid based fluids. Aluminum compounds can only crosslink in acidic environments. Titanate and zirconate complexes can crosslink in a wider pH range. Reservoir temperature is another factor when selecting a crosslinker. The temperature limit for aluminum compounds is low (150°F), while zirconate enjoys the highest temperature limit (400°F). Among other crosslinkers, borate is the most commonly used one and can produce extremely viscous gels with guar and HPG that are stable up to 325°F. Borate ions and guar will form a very viscous gel in few seconds when the pH value of the fluid is above 8. However, to improve the stability of the crosslinked gel at higher temperatures, both the pH value and borate concentration must be increased. Fig. 14.27 shows a typical borate crosslinked gel sample.

*Gel stabilizers* can be used in high-temperature environments. Methanol and sodium thiosulfate are typically gel stabilizers. They can extend the temperature range of guar based fluids to over 350°F.

*Gel breakers* are used to reduce the viscosity of a gelled fluid to a low viscosity so that it can flow back easily. Also, leaving a high viscosity fluid in the fracture would damage the proppant pack once the created fracture has closed on proppant after the treatment is completed. Gel breakers reduce viscosity by cleaving the polymer into fragments with smaller molecular weights.

The most widely used breakers in fracturing fluids are oxidizers and enzymes. The most common oxidizers are the ammonium, potassium, and sodium salts of peroxydisulfate ( $S_2O_8^{2-}$ ).

Note that peroxydisulfate is often referred to as persulfate (sometimes known as peroxyulfate) in the literature. In fact, persulfate refers to two groups of ion compounds containing the anions  $SO_5^{2-}$  (peroxomonosulfate) and  $S_2O_8^{2-}$  (peroxydisulfate). These persulfate salts are all strong oxidizers. As temperature increases, oxidative breakers become very reactive and can break down the polymer during the treatment. This high reactivity at elevated temperatures is undesirable. To avoid the problem, encapsulated breakers are manufactured. Encapsulated breakers cannot react with the polymer until the capsules are broken during the fracture closure. The introduction of encapsulated breakers has greatly improved persulfate performance at elevated temperatures.



**FIGURE 14.27**

A typical borate crosslinked gel sample.

*Image Courtesy of Liberty Oilfield Services.*

Certain enzyme breakers are also used to reduce the viscosity of water based fluids. The use of enzymes as breakers is limited to relatively mild environments with pH range between 3.5 and 8 and temperatures less than about 150°F (Economides and Nolte, 2000). Enzymes begin to degrade the polymer immediately upon mixing as they are active at ambient temperatures. Therefore, they can be too reactive under some conditions, like persulfates. Since enzymes are biocatalysts, they are not used up when they react with guar. Enzymes can be used together with persulfates.

*Buffers* are used as a means of keeping the pH of an aqueous fluid at a desirable range or at a nearly constant value. Some crosslinkers and breakers simply do not function outside specific pH ranges. The use of buffers in fracturing fluids can help control the crosslinking process for specific crosslinkers. Commonly used buffers include sodium bicarbonate, fumaric acid, combination of mono- and disodium phosphate, soda ash, sodium acetate, or a combination of these chemicals. Buffers are also used to keep fracture tanks from contamination.

*FR* are the main ingredient in slickwater. Common FR are polyacrylamide based and are used with a typical loading range from 0.25 gal of FR per 1000 gal (gpt) of water to 1 gpt of water. Virtually all polymers act as FR because they can suppress turbulent flow in the presence of low viscosity base fluids (linear gels).

FR can be nonionic, anionic, or cationic. Cationic FR is usually used for applications involving fracturing fluids that utilize cationic additives or systems containing significant levels of divalent

ions (Calcium, Magnesium, etc.) in addition to high levels of chlorides. Anionic FR is usually used for fracturing operations that utilize freshwater as well as light to heavy monovalent brines and are compatible with all anionic and nonionic additives.

*Bactericides*, also called biocides, are used in slickwater, linear, and crosslinked fluids to control bacteria growth, as the gelling agents, such as guar and polysaccharides, are a food source for bacteria. Bactericides commonly used to kill bacteria in fracturing fluids include glutaraldehyde, chlorophenates, quaternary amines and isothiazoline. Bactericides are not necessary in acid-based or oil-base fracturing fluids. In practice, bactericide is also added to fracture tanks before water is added to keep the bacterial enzyme low.

*Clay stabilizers* are used to control clay particles in the formation exposed to fracturing fluids during treatments. As discussed in Chapter 12, Well Problem Identification, clay swelling and fines migration induced by stimulation treatments can cause formation damage. Water containing 1%–3% KCl is commonly used as the base liquid in fracturing fluids to stabilize clays and prevent swelling. Conway et al. (2011) showed that the minimum loading of various salts, including ammonium chloride, methylammonium chloride, dimethylammonium chloride, trimethylammonium chloride and tetramethylammonium chloride, can achieve the same protection as 2% KCl. In addition to inorganic salts, others commonly used clay stabilizers include cationic polymeric and non-polymeric clay stabilizers (Maley et al., 2013).

*Surfactants* adsorb at the interface between two immiscible substances and thus reduce interfacial tension. Surfactants must be used in foam and emulsion fluids. Some clay-control agents are surfactants. Surfactants are commonly used in water based fluids to promote flow back. Surfactants are often used as a relative permeability modifier to reduce interfacial tension and modify contact angle and reservoir wettability (Penny et al., 2012).

*Fluid loss additives* are commonly used in high-permeability and naturally fractured reservoirs to control fluid loss. As discussed on leakoff mechanisms in Section 14.4.1, fluid loss in low-permeability reservoirs is small and controlled by reservoir properties. Polymers used in water based fluids act like fluid loss additives as they form a filtercake during leakoff that helps control fluid loss. Finely ground silica flour is the most commonly used fluid loss additive for water based fluids. Deformable particles such as starches are also good fluid loss additives. Oil-soluble resins can also be used to control fluid loss in oil reservoirs as produced oil will dissolve the resins. Fluids that contain oil-in-water dispersions (for example 5% diesel) exhibit good fluid loss control. Yoshimura et al. (2016) recently found that powder, granular, and fibrous materials made of polyglycolic acid (PGA) or polylactic acid (PLA) are very suitable as fluid loss agents.

*Diverting agents* are used to temporarily block high-permeability paths that are taking most of the fluid, thereby shifting subsequent fluids into the next-most permeable path. All diverting agents are composed of graded materials that are insoluble in fracturing fluids during treatments, but are soluble in formation fluids or dissolvable through thermal degradation process. Traditional diverting agents include benzoic acid flakes, rock salt, and oil-soluble resins, etc. New diverting agents have been introduced in recent years, including biodegradable particulates made of polymer (Allison et al., 2011), and other undisclosed materials (McCartney and Kennedy, 2016). Finely ground granular and fibrous materials made of PGA or PLA discussed by Yoshimura et al. (2016) are also excellent for fluid diverting.

*Scale inhibitors* are often added in hydraulic fracturing fluids as a preventive measure. The most common scales in oilfields are calcium carbonate, calcium sulfate, barium sulfate, and

strontium sulfate. Water based fracturing fluids dissolve the formation minerals as the well is fractured, and some dissolved minerals precipitate to form scales if conditions are right. Most available scale inhibitors are phosphorous compounds such as phosphonates and organophosphonates, which are anionic. Organic polymers are also used as scale inhibitors.

### 14.6.1.6 Fluid rheology

Hydraulic fracturing fluids are generally either Newtonian or nonNewtonian fluids. Newtonian fluids can be characterized by a constant viscosity at a specific temperature. Freshwater, KCl and HCl solution, and slickwater are examples of Newtonian fluids. The flow behavior for a Newtonian fluid can be expressed as:

$$\tau = \mu\gamma, \quad (14.88)$$

where  $\tau$  is the shear stress,  $\mu$  is the fluid viscosity, and  $\gamma$  is the shear rate which is defined as the velocity difference between the planes divided by the distance between the planes.

A fracturing fluid that will have considerably different apparent viscosity values depending on the shear exerted on the fluid is called nonNewtonian fluids. Linear gel, crosslinked gel, and gelled foam fluids are considered nonNewtonian fluids. The power law model is the most widely used model to describe the flow behavior of nonNewtonian fluids:

$$\tau = K\gamma^n, \quad (14.89)$$

$$\mu_a = K/\gamma^{(1-n)}, \quad (14.90)$$

where  $K$  is the consistency index in  $\text{lbf}\cdot\text{s}^n/\text{ft}^2$  or  $\text{kPa}\cdot\text{s}^n$ ,  $n$  is the flow behavior index (dimensionless), and  $\mu_a$  is the apparent fluid viscosity. These relations hold for most fracturing fluids over the range of shear rates in which the fluid displays nonNewtonian behavior. In oilfield units, Eq. (14.79) becomes:

$$\mu_a = 47,879 \frac{K}{\gamma^{(1-n)}}, \quad (14.91)$$

where  $\mu_a$  is in cp,  $K$  in  $(\text{lbf}/\text{ft}^2)/\text{sec}$ ,  $n$  is unitless, and  $\gamma$  is in  $\text{sec}^{-1}$ .

During hydraulic fracturing treatments, the fluid experiences wide variations in shear and temperature. High shear is experienced by the fluid during pumping through the tubulars and perforation tunnels. Once in the fracture, the shear on the fluid is significantly less, but the fluid temperature increases until it eventually reaches formation temperature.

The rheological properties of a fracturing fluid are measured using a viscometer. For example, a rotational speed of 100 RPM represents a shear rate of  $170 \text{ second}^{-1}$  and a speed of 300 RPM represents a shear rate of  $511 \text{ second}^{-1}$  for the Fann 35 viscometer. That is why the apparent viscosities of gelled fracturing fluids are often reported at different shear rates (usually 170 or  $511 \text{ second}^{-1}$ ). However, the shear rate inside a fracture for a typical fracturing treatment can be as low as  $30\text{--}40 \text{ second}^{-1}$ . Fig. 14.28 shows the rheological behavior of a typical borate crosslinked gel over time at three different shear rates, 511, 170, and  $40 \text{ second}^{-1}$ . First, the shear thinning effects are clearly demonstrated in this plot as the shear rate is decreased from  $511 \text{ second}^{-1}$  to  $170 \text{ second}^{-1}$  to  $40 \text{ second}^{-1}$ , the apparent viscosity of the fluid is increased significantly. In this plot, the rapid reduction of apparent viscosity over time is caused mainly by the breaking down of the gel by the breaker and partially due to thermal degradation of the gel as the fluid heats up in

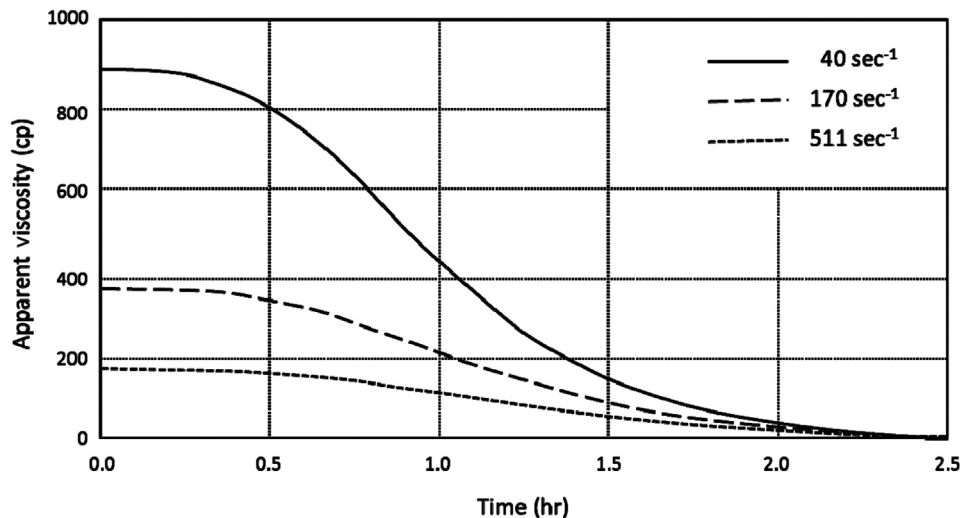


FIGURE 14.28

Apparent viscosity vs time at different shear rates for a typical borate crosslinked gel.

the fracture. For example, if a minimum apparent viscosity of 100 cp at a shear rate of 40 second<sup>-1</sup> inside the fracture is required to suspend proppants in 1.5 hours during the treatment, the viscosity of this fluid is not sufficient for this treatment.

## 14.6.2 PROPPANTS

Proppants are small particles made of a solid material, typically sand, or a man-made ceramic material. During a fracturing treatment, a clean fracturing fluid is pumped first to create a fracture with adequate width, and then a mixture of proppants and fracturing fluids (often called slurry) follows. Proppants are designed to fill in the fracture space and strong enough to hold the walls of the fracture apart so that a conductive path to the wellbore can maintain after the treatment has completed and the fracturing fluid has leaked off.

### 14.6.2.1 Proppant pack conductivity

The only goal of a hydraulic fracturing treatment is to create a conductive path in the formation. The wider and the more permeable a fracture is, the more conductive it becomes. To describe the flow capacity of the fracture or how conductive it is, the term *fracture conductivity* is introduced, which is defined as the product of the width and permeability of the fracture. Fracture conductivity is commonly expressed as md-ft in oilfield units.

For proppant testing in laboratory, the conductive path is not a fracture but a proppant pack placed in a test cell. There are two types of proppant conductivity testing: short-term or long-term testing (Kaufman et al., 2007). As documented in the API/ISO standard testing procedures, such as the ISO 13503-2 “Measurement of Properties of Proppants Used in Hydraulic Fracturing and

Gravel-Packing Operations,” the test cell holds proppants at 2.0 lb/ft<sup>2</sup>, which provides the cross-section area and width of the proppant pack for establishing fluid flow. Proppant conductivity is measured under various stresses applied to the proppant pack. The width of the proppant pack depends on the proppant density and applied stress. The higher the proppant density is the narrower the proppant pack is, simply because the same amount of proppant mass (2.0 lb/ft<sup>2</sup>) is used for testing. Also, the higher is the stress applied, the narrower the proppant pack becomes, because proppant grains will rearrange to tighter packing under stress. The proppant pack permeability depends on the physical properties of proppants and the stress applied. Tighter packing under stress will reduce the permeability. Proppant (pack) conductivity is the most paramount parameter in evaluating proppant performance.

### 14.6.2.2 Proppant properties

Proppants have various physical properties. Some of the properties that commonly tested in laboratory and have impacts on proppant performance include grain size and grain size distribution, sphericity and roundness, crush resistance, density, turbidity, and acid solubility.

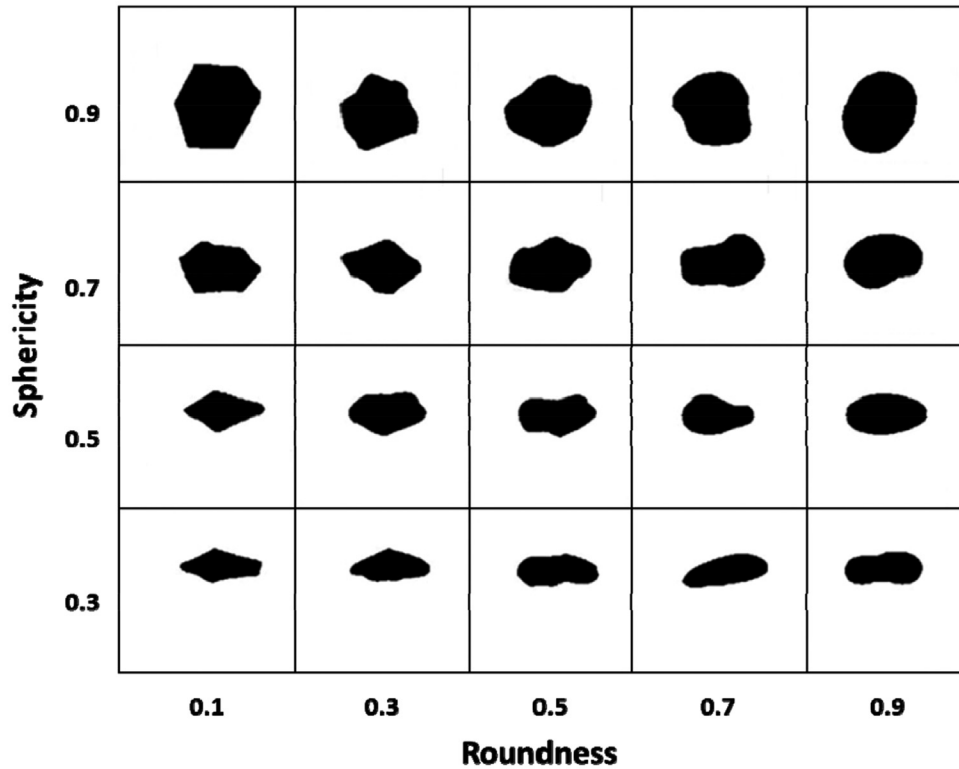
Proppant particle (or grain) size is an important parameter for proppant evaluation and treatment designs, as it affects fracture conductivity and proppant transport. Grain size is measured in mesh size ranges. The mesh size is defined by the number of openings across one linear inch of screen. The smaller the mesh size number is, the larger the particle size is. For example, 20/40-mesh proppants are larger than 30/50-mesh proppants. Larger proppants provide higher fracture conductivity because the pore spaces present in the proppant pack are larger. However, larger proppants may break down or crush more easily under stress because there are fewer contact points or smaller contact areas to distribute the stress applied to the proppant pack. Also, larger proppants are more difficult to transport through the fracture. The range of particle sizes also affects the permeability/conductivity of a proppant pack. A wider range of particle sizes results in a tighter packing arrangement and lower permeability/conductivity. For example, 40/60-mesh proppants will provide better permeability/conductivity than 40/70-mesh proppants. Commonly used proppant sizes include 12/20-mesh, 16/30-mesh, 20/40-mesh, 30/50-mesh, 40/70-mesh, and 70/140-mesh.

Proppant particle shape is measured by its sphericity and roundness. Sphericity is defined as the ratio of the surface area of a sphere to the surface area of the particle. The sphericity is 1 for a sphere and is less than 1 for any particle that is not a sphere. Roundness defines how smooth a grain is, and can be defined mathematically as the ratio of the average radius of curvature of the edges or corners to the radius of curvature of the maximum inscribed sphere. Fig. 14.29 shows a visual chart that can be used for evaluating the sphericity and roundness of proppant grains. There is difference in the shape of proppants. Ceramics typically achieve the roundness and sphericity of 0.9, while sands are typically in the 0.7 range, with some occasionally at 0.8. Proppant particles of higher sphericity and roundness will lead to greater conductivity. Higher sphericity and roundness also improves the crush resistance of the proppants.

The crush resistance test is performed by crushing a sample of proppants under increasing stresses. The highest stress level (rounded down to the nearest 1000 psi) under which the proppants generate no more than 10% crushed material is defined as the crush resistance (sometimes called the *K*-value). The higher the crush resistance is, the better the proppants are.

Density is important for proppant selection, as it affects proppant transport. Proppant density comes with both bulk density and absolute density. The difference between the bulk and absolute





**FIGURE 14.29**

Visual chart for evaluating the roundness and sphericity of particle grains.

densities results from the void spaces present in proppant packs. Typical porosity values of proppant packs are in the range between 0.35 and 0.43. For natural sands, the absolute density usually ranges between 2.62 and 2.65 in specific gravity. For ceramic proppants, the absolute density usually ranges between 2.55 and 3.9 in specific gravity.

Turbidity is basically a measure of clays, silts and other fine particulate present in the proppants. It is measured by a turbidity meter that looks at light refraction in water exposed to the proppants. The presence of clays and silts reduces conductivity. Acid solubility determines the percentage of acid soluble materials present in the proppants. Lower acid solubility indicates a smaller amount of “impurities” present in the proppants. These two specifications are generally provided by proppant suppliers for each type of proppants, but are more relevant for evaluating natural sands for fracturing applications.

### 14.6.2.3 Proppant types

There are basically two types of proppants used for hydraulic fracturing applications: either naturally occurring silica sands or made-made ceramic proppants. Sands represent the majority of



proppants used in the industry. A subclass called resin-coated proppants is manufactured to improve proppant performance. The majority of resin-coated proppants are sands. Proppant type has a significant impact on proppant permeability/conductivity. Fig. 14.30 shows the conductivity versus the effective closure stress for various types of proppants. The data in this figure clearly demonstrates the permeability difference among sand, resin-coated sand, intermediate-strength ceramic proppant, and high-strength ceramic proppant.

Silica sand is comprised of weathered quartz, which is one of the most commonly occurring minerals in the Earth's crust. Sand can be explored from beaches, river beds, and sand mines. The quality of the sand proppants is dependent on the sand deposits and manufacturing processes. Generally speaking, sands from buried sand mines provide better quality as proppants. Commonly used sands for fracturing are explored from sand mines.

Sands from sand mines are not used directly for fracturing without processing. Unlike loose beach or river sand, the sandstone mined for proppant is cemented together as rock. Excavating the sandstone takes place after removing topsoil and unwanted rock layers, and crushing sandstone chunks then follows. The remaining processes include washing, drying, sorting, and final shipment.

In North America, two main types of sand are used for fracturing, namely white sand and brown sand. Most white sand is mined from geological formations found in the Midwest region of the United States, with Wisconsin currently holding about 75% of the fracture sand market in the United States. Texas is the second in supplying the fracture sand, mostly brown sand. Generally, the white sand tends to have fewer impurities and rounder grains than the brown sand, which makes the brown sand cheaper and more prone to crushing at higher stress.

Ceramic proppants are manufactured from ceramic materials, such as bauxite or nonmetallurgical grades or kaolin clay. Bauxite is an aluminum ore that is typically composed of hydrous aluminum

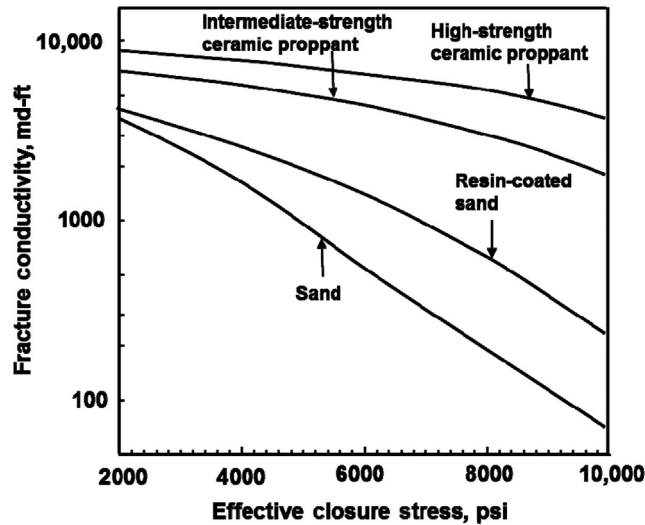


FIGURE 14.30

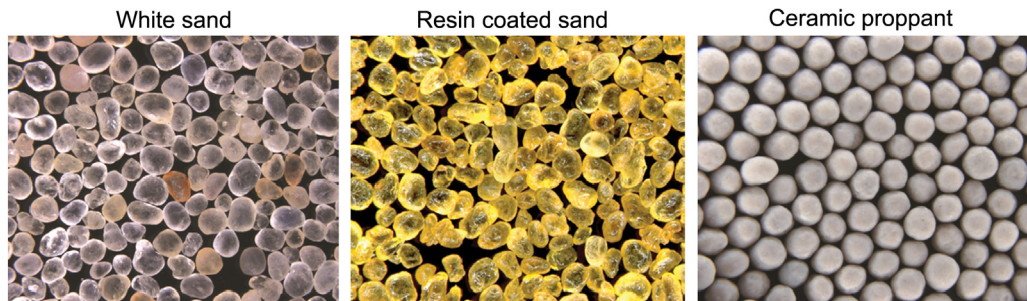
Effect of effective closure stress on proppant pack conductivity for various types of proppants.

oxides, aluminum hydroxides, and clay minerals. Clay minerals are composed of hydrous aluminum silicates. Kaolin is one type of clay minerals that also contains aluminum, but not at ore grade levels. During the ceramic proppant manufacturing process, the ceramic material is crushed, pelletized and sieved into specifically sized particles. Sintering then occurs in high-temperature kilns that bake the sorted particles to change their crystalline structure, so that proppants can withstand very high levels of stresses. Ceramic proppant particles are created during a manufacturing process to ensure that relatively high roundness and sphericity are achieved.

Because bauxite is heavier than kaolin, proppants made from bauxite are heavier than proppants made from kaolin. The ceramic mineral that contains more aluminum produces heavier and stronger proppants. As a result, the conductivity of ceramic proppants generally correlates very well with the proppant density. Based on density, ceramic proppants can be divided into three groups, lightweight ceramics (LWC), intermediate-density ceramics (IDC) or often referred to as intermediate-strength proppant (ISP), and high-density ceramics (HDC) or often referred to as high-strength proppant (HSP).

Resin coatings can be applied to both sand and ceramic proppant, but more commonly to sand. Coating sand or ceramic proppants serves to improve proppant strength and to reduce proppant flowback. Resin coatings provide more contact areas that help distribute the load on proppants more uniformly, and hold together pieces of crushed proppants (fines) to prevent the fines from migrating in the proppant pack, entering the borehole and compromising the well productivity. Resin coatings also help bond individual proppant particles together under the intense pressure and temperature of the fracture in the reservoir to minimize proppant flowback during production. Although resin coatings improve proppant performance, they may contain components that can interfere with common fracturing fluid additives, such as organometallic crosslinkers, buffers, and oxidative breakers.

Fig. 14.31 shows a photo of 20/40-mesh white sand, resin-coated sand, and ceramic proppant samples. Proppant selection is a balance of quality and cost. Sands are cheaper than resin-coated sands, and much cheaper than ceramic proppants. Since proppant cost constitutes a significant portion of the overall stimulation treatment cost, the decision should be based on productivity enhancement and return on investment.



**FIGURE 14.31**

Photo of 20/40-mesh proppant samples.

*Image Courtesy of Carbo Ceramics.*

### 14.6.3 FRACTURING EQUIPMENT

The implementation of a hydraulic fracturing treatment requires an array of specialized equipment. In this section, the equipment necessary to carry out typical hydraulic fracture operations will be described. The equipment required to perform a hydraulic fracturing treatment includes high-pressure pumps, blenders, fluid storage tanks, chemical tanks, proppant storage units, monitor and control equipment, and ancillary equipment such as hoses, pipes, valves, and manifolds, etc. A combination of all the equipment that is capable to implement a typical fracture treatment often called as a “frac spread” or a “frac fleet”. Fig. 14.32 shows the schematic of equipment layout for a typical fracturing treatment.

#### 14.6.3.1 Wellhead equipment

The pressure rating of the production wellhead equipment or Christmas tree is often less than the pressure required to pump a high-pressure fracturing treatment. Frac stacks are used to temporarily replace the production wellhead for protecting it from the effects of high-pressure and abrasion during fracturing operations. Frac stacks are temporary wellhead equipment composed of high-pressure flange, flow tee, and hydraulic and manual valves, etc. Frac stacks rated for 15,000 psi or higher are commonly used in horizontal well applications for unconventional development.

Tree savers are another type of wellhead isolation tools that can protect a Christmas tree at the wellhead during fracturing operations. The tree saver is mounted on the existing Christmas tree. A mandrel is extended through the valves on the tree and into the tubing. The mandrel has a rubber cup assembly that seals to the walls of the tubing and prevents fluid or pressure from directly reaching the tree. Once set, a tree saver can extend the working pressure of a wellhead up to 20,000 psi. Due to the smaller ID (inner diameter) of the mandrel, tree savers are not used often in high-rate horizontal well applications as they dramatically restrict rates and interfere with the operation of pumping down perforation guns and plugs.

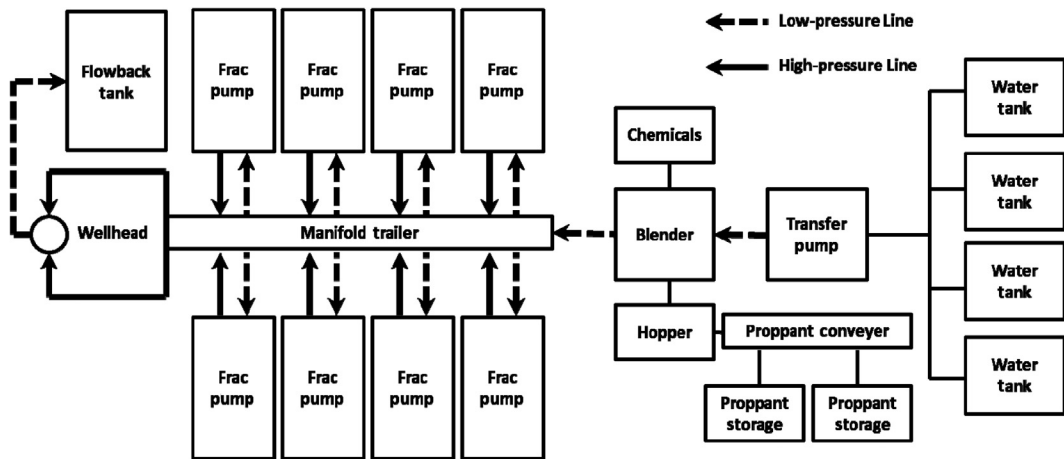


FIGURE 14.32

Schematic of equipment layout for a typical fracturing treatment.

### 14.6.3.2 High-pressure pumps

Pumps used to pressurize the fracturing fluid system in hydraulic fracturing applications are designed to withstand high-pressure conditions. For that reason, these pumps are often called high-pressure pumps or frac pumps to distinguish with other types of pumps used in oilfield applications. As the heart of any fracturing treatment, high-pressure pumps are one of the most important pieces of fracturing equipment as they provide the horsepower necessary to break down the formation and to transmit the fluid and proppant into the fracture. Reciprocating plunger pumps have been used for decades to propel fracturing fluid, proppant and chemicals into a well at pressures as high as 20,000 psi. High-pressure pumps generally come in two types, triplex and quintuplex, and are able to provide hydraulic horsepower up to 3000 hhp. Several or many pumps are used for a typical treatment, and the number of pumps required is determined by the anticipated pumping rates and pressures. The low-pressure suction end of a frac pump pulls the fluid from the blender. The high-pressure discharge end of a frac pump sends the fluid to the wellhead via a high-pressure treating line. Isolation and bleed-off valves are installed and tied into the high-pressure treating line to facilitate taking the pump offline and making minor repairs during pumping operations. High-pressure pumps for onshore hydraulic fracturing applications are typically mounted on trucks. Typically there are always a couple of backup frac pumps on location to ensure enough horsepower is available in case some pumps fail during a treatment.

Shale fracturing treatments have stretched the abilities of legacy pumping systems to the extremes of their performance envelope. Newer equipment has emerged to handle extreme conditions, provide better longer-term performance and reduce NPT (nonproductive time). [Fig. 14.33](#) shows the photo of a high-pressure pump typically used for shale fracturing applications.

### 14.6.3.3 Blenders

There are three important components associated with a blender: suction pump, mixing tub and discharge pump. The suction and discharge pumps are of the centrifugal type. The blending system is



**FIGURE 14.33**

Photo of a typical high-pressure pump.

*Image Courtesy of Halliburton.*

a low pressure unit. Blenders take water from the fluid tanks with a suction pump, which sends the water to a mixing tub. The mixing tub mixes the water with proppant that is delivered by sand screws. Additional chemicals can also be delivered to the mixing tub. Dry chemicals are delivered by a dry additive system mounted on the blender. Liquid additives are delivered by a liquid additive system either mounted on-board or off-board the blender. A discharge pump pulls the mixture from the mixing tub and discharges it to the discharge manifold on the blender. From the discharge manifold, the mixture is sent to the manifold trailer and is transferred to the frac pumps, which discharge the mixture under pressure to the wellhead. Modern blenders are computer controlled, enabling the flow of chemicals and ingredients to be efficiently metered and to achieve good control over the blend quality and delivery rate. Typically, there is one primary blender and one backup blender on location, as the dependability of the blender is critical to the fracturing operation. Fig. 14.34 shows the photo of a typical blender used in hydraulic fracturing treatments.

#### 14.6.3.4 Manifolds

The manifold, often called “missile,” is an arrangement of flow lines, fittings and valves that connect all fracturing equipment to the wellhead. It has both a low-pressure side tied to the blender and a high-pressure side tied to the wellhead, with all the high-pressure pumps in between to pressurize the fluid system. A modular and flexible manifold trailer is often used to help organize both the low-pressure suction hookup and the high-pressure discharge hookup. Fig. 14.35 shows the photo of a typical manifold trailer.

The number of suction hoses between the blender and the high-pressure pumps is determined by the pump rate. As a part of the manifold system, the high-pressure flow line that transmits the fluid discharged from the high-pressure pumps to the wellhead is often called “treating iron” as it is made of metal pipe. The size of the high-pressure pipe is determined by both the anticipated pumping rates and pressures. Lines with smaller sizes (both IDs and ODs) have higher pressure ratings than those with larger ones. The treating iron and associated connections are machined from single pieces of metal without welded seams to withstand the harsh conditions caused by high pressures, abrasive fluids, vibration, and wear and tear.



**FIGURE 14.34**

Photo of a typical blender.

*Image Courtesy of Halliburton.*



**FIGURE 14.35**

Photo of a typical manifold trailer.

*Image Courtesy of Liberty Oilfield Services.*

#### **14.6.3.5 Data van**

The data van is specialized piece of mobile equipment installed with computer programs, larger-screen monitors and control switches on a mobile van for frac engineers to monitor and control a fracturing treatment at the well site. During the treatment, pumping rates, treating pressures, density of the fluid and the slurry, chemical additive rates, etc. are constantly monitored and collected. All aspects of the treatment, from the changing of the pumping rate, to the blending of the fluid and proppant, and to the shutting down of the pumps, and so on, are also controlled on the van. A mobile fluid lab is often installed on the data van. [Fig. 14.36](#) shows an outside photo of a typical data van.

#### **14.6.3.6 Material storage units**

For hydraulic fracturing treatments in conventional reservoirs, fluids are brought to location by trucks and stored in fluid tanks at the treatment site. For unconventional developments, multiple horizontal wells are drilled and stimulated by hydraulic fracturing on a single well pad. Due to the tremendous amount of water required to stimulate these horizontal wells, a temporary water pond is commonly constructed to store water from various sources including ground water, river water or municipal water. A single water pond is often built to provide water for fracturing treatments on multiple well pads.

Similarly, for fracturing applications in conventional reservoirs, a sufficient amount of proppants is brought to location prior to the treatment and stored in proppant storage units, often called “proppant silos,” at the well site. However, for unconventional fracturing treatments, there might not be enough proppant storage units or space at the well site to store all the proppant for the treatment, and the proppant may be brought in by trucks to the treatment site from a nearby proppant distribution center continuously during a multiwell fracturing treatment that could last for weeks. Regardless of treatment sizes, storage tanks for chemicals are generally located at the well site.

Fracturing horizontal wells in unconventional reservoirs is material intensive. Storage of fracturing materials can occupy large amounts of space at well sites. [Fig. 14.37](#) shows one type of proppant silo that is positioned horizontally during transportation but can be oriented vertically on location to save space. This unit has a total working volume of 2500 sacks (250,000 lb). A typical fracture treatment



**FIGURE 14.36**

Photo of a typical data van.

*Image Courtesy of Liberty Oilfield Services.*



**FIGURE 14.37**

Propellant silos.

*Image Courtesy of Halliburton.*

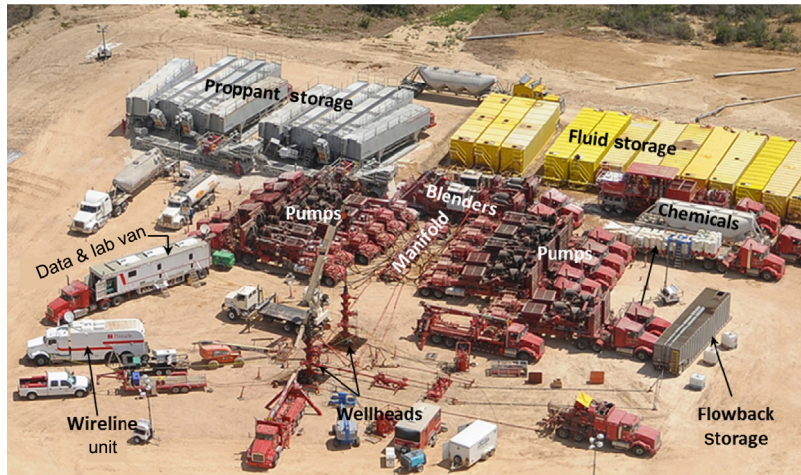
**FIGURE 14.38**

Photo of fracturing equipment layout at well site.

*Image Courtesy of Halliburton.*

**FIGURE 14.39**

Up close view of fracturing equipment layout at well site.

*Image Courtesy of Halliburton.*

for horizontal well completion in unconventional reservoirs calls for 200,000–300,000 lb of proppant per stage. There are typically 20 to 30 stages in each horizontal well. The amount of proppants required to fracture a single horizontal well will require 20 to 30 silos of this type fully loaded with proppants.

Fig. 14.38 shows a bird's-eye view of the fracturing equipment and wellsite during fracture operations. Fracturing horizontal wells in unconventional reservoirs is also equipment intensive. Fig. 14.39 shows an up-close view of high-pressure pumps, blender, manifolds, and chemical units.



## 14.7 FRACTURED WELL PRODUCTIVITY

The objective of a hydraulic fracturing treatment is to enhance well productivity by creating a conductive path that starts from the wellbore and extends deep into the reservoir. The productivity of a fractured is affected by two simultaneous processes: the influx of fluid into the fracture from the reservoir, and the influx of fluid into the wellbore from the fracture. Assuming a steady-state flow condition, the influx of fluid into the fracture from the reservoir obeys Darcy's law:

$$q_r = \frac{2hx_f k_r \Delta p_y}{\mu \Delta y}, \quad (14.92)$$

where  $q_r$  is the flow rate from the reservoir into the fracture,  $h$  is the payzone height (which is typically smaller than the fracture height),  $x_f$  is the fracture half-length,  $k_r$  is the reservoir permeability,  $\mu$  is the viscosity of the reservoir fluid,  $\Delta p_y$  is the pressure drop from the reservoir boundary to the fracture face, and  $\Delta y$  is the distance from the reservoir boundary to the fracture face. Note that two fracture faces are accounted for in Eq. (14.92).

If the fluid influx from the reservoir to the fracture is assumed as uniform flux, the flow rate in the fracture is linearly increased from the fracture tip to the wellbore, with the flow rate being zero at the fracture tip and maximum at the wellbore. With that, the average flow rate in the fracture is one half of the flow rate at the wellbore. Similarly, the average fluid influx from the fracture into the wellbore also obeys Darcy's law:

$$\frac{1}{2}q_f = \frac{hwk_f \Delta p_x}{\mu \Delta x}, \quad (14.93)$$

where  $q_f$  is the flow rate at the wellbore,  $h$  is the payzone height,  $w$  is the fracture width,  $k_f$  is the fracture permeability,  $\mu$  is the viscosity of the reservoir fluid,  $\Delta p_x$  is the pressure drop from the fracture tip to the wellbore, and  $\Delta x$  is the distance from the fracture tip to the wellbore, which is the fracture half-length,  $x_f$ .

Since a steady-state flow condition is assumed and there is no mass accumulation inside the fracture, the total flow rate from the reservoir to the fracture,  $q_r$ , must equal the total flow rate from the fracture to the wellbore,  $q_f$ . The combination of Eqs. (14.92) and (14.93) results in the following expression:

$$\frac{k_f w}{k x_f} = \frac{\Delta p_y / \Delta y}{\Delta p_x / \Delta x}. \quad (14.94)$$

Eq. (14.93) looks familiar to the concept of dimensionless fracture conductivity defined as (Argawal et al., 1979; Cinco-Ley and Samaniego, 1981):

$$F_{CD} = \frac{k_f w}{k x_f}, \quad (14.95)$$

where  $F_{CD}$  is the dimensionless fracture conductivity, which provides a comparison of the flow capacity of the fracture that transmits the fluid into the wellbore with the flow capacity of the reservoir that delivers the fluid into the fracture. Note that the term  $k_f w$  in Eq. (14.95) is the fracture conductivity, which is defined as the product of the fracture permeability and the fracture width.

Both fracture conductivity and dimensionless fracture conductivity are key parameters for fracture treatment designs. Depending on the reservoir permeability and the fracture length and conductivity achieved, the production rate of a fractured well is usually limited by one of the two influxes described above. A fracture with an  $F_{CD}$  value of greater than 30 is generally considered infinitely conductive, as the pressure drop along the fracture during production becomes very small. An  $F_{CD}$  value in the range between 1 and 10 is generally obtained in fracture design. The  $F_{CD}$  value from a typical fracture design can easily exceed 10 in extreme low-permeability reservoirs, but hardly rises above 1 in high-permeability reservoirs.

The transient flow condition can last for a very long time during the production of a hydraulically fractured well, especially when the fracture is long and the reservoir permeability is low. Therefore, the productivity of a fractured well is best to predict using a reservoir simulator. Reservoir models, for a single fractured well and typically in single-phase flow, are usually built in most commercial fracture design simulators. However, in situations where the fracture dimension is much less than the drainage area of the well, the long-term productivity of the fractured well can be estimated assuming pseudo-radial flow in the reservoir. Then the inflow equation can be written as:

$$q = \frac{kh(p_e - p_{wf})}{141.2B\mu \left( \ln \frac{r_e}{r_w} + S_f \right)}, \quad (14.96)$$

where  $S_f$  is the equivalent skin factor. The fold of increase can be expressed as:

$$\frac{J}{J_o} = \frac{\ln \frac{r_e}{r_w}}{\ln \frac{r_e}{r_w} + S_f}, \quad (14.97)$$

where

$J$  = productivity of fractured well, stb/day-psi

$J_o$  = productivity of nonfractured well, stb/day-psi.

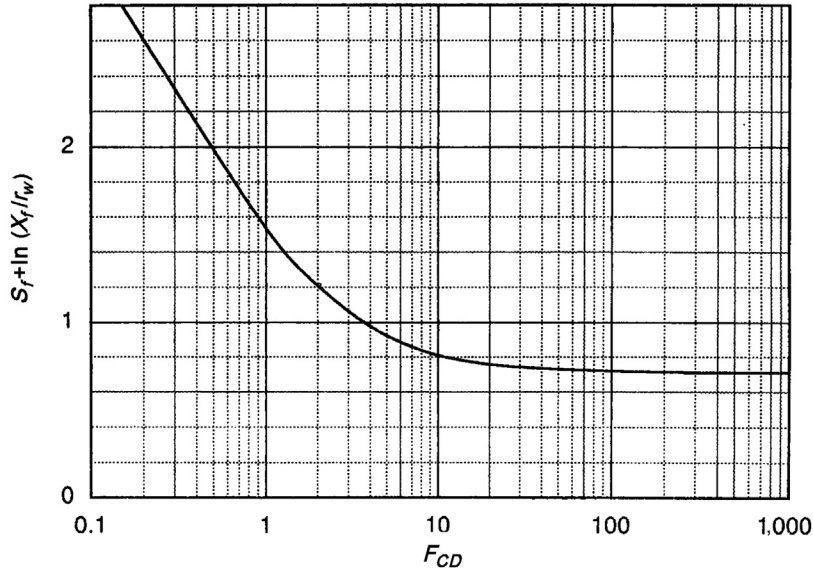
The effective skin factor  $S_f$  can be determined from Fig. 14.40 using the value of  $F_{CD}$  (Cinco-Ley and Samaniego, 1981). It is seen from Fig. 14.40 that the parameter  $S_f + \ln(x_f/r_w)$  approaches a constant value of approximately 0.7 in the range of  $F_{CD} > 100$ , that is,

$$S_f \approx 0.7 - \ln(x_f/r_w), \quad (14.98)$$

which implies that the equivalent skin factor of fractured wells depends only on the fracture half-length, but not on either the fracture conductivity or the reservoir permeability when the value of  $F_{CD}$  is greater than 100. Stimulation effectiveness increases as the fracture half-length increases. This situation occurs in low-permeability reservoirs in which production is limited by the reservoir flow capacity. This analysis indicates that low-permeability reservoirs, naturally leading to a fracture with higher dimensionless fracture conductivity, would benefit greatly from increasing the fracture length,

On the other hand, it can also be seen from Fig. 14.40 that the parameter  $S_f + \ln(x_f/r_w)$  declines linearly with  $\log(F_{CD})$  in the range of  $F_{CD} < 1$ , that is,

$$S_f \approx 1.52 + 2.30 \log(r_w) + 1.55 \log(k) - 1.55 \log(k_f w) - 0.75 \log(x_f). \quad (14.99)$$



**FIGURE 14.40**

Relationship between fracture conductivity and equivalent skin factor (Cinco-Ley and Samaniego, 1981).

The first two terms in this relation are constants for a given well. The third term indicates that the equivalent skin factor increases as the reservoir permeability increases. Note that an increase in the equivalent skin factor means a reduction in production enhancement. Comparing the coefficients of the last two terms in this relation reveals that the equivalent skin factor of a fractured well is more sensitive to the fracture conductivity (i.e., the product of fracture permeability and width) than the fracture half-length when the value of  $F_{CD}$  is less than 1. This situation generally occurs in high-permeability reservoirs, in which the well production rate is limited by the fracture flow capacity. This analysis indicates that high-permeability reservoirs, naturally leading to a fracture with lower dimensionless fracture conductivity, require higher fracture conductivity for more effective stimulation.

**Example Problem 14.4** A gas reservoir has a permeability of 1 md. A vertical well of 0.328-ft radius draws the reservoir from the center of an area of 160 acres. If the well is hydraulically fractured to create a 1500-ft long, 0.12-in. wide fracture of 150,000 md permeability around the center of the drainage area, what would be the fold of increase in well productivity?

**Solution**

Radius of the drainage area:

$$r_e = \sqrt{\frac{A}{\pi}} = \sqrt{\frac{(43,560)(160)}{\pi}} = 1490 \text{ ft}$$

Fracture half-length:  $x_f = 1500/2 = 750 \text{ ft}$

Dimensionless fracture conductivity:

$$F_{CD} = \frac{K_f w}{k x_f} = \frac{(150,000)(0.12/12)}{(1)(750)} = 2$$

Fig. 14.40 reads:

$$S_f + \ln(x_f/r_w) \approx 1.2,$$

which gives:

$$S_f \approx 1.2 - \ln(x_f r_w) = 1.2 - \ln(750/0.328) = -6.53.$$

The fold of increase is:

$$\frac{J}{J_o} = \frac{\ln \frac{r_e}{r_w}}{\ln \frac{r_e}{r_w} + S_f} = \frac{\ln \frac{1490}{0.328}}{\ln \frac{1490}{0.328} - 6.53} = 4.45.$$

In the situations in which the fracture dimension is comparable to the drainage area of the well, significant error may result from using Eq. (14.97), which was derived based on radial flow conditions. In these cases, the long-term productivity of the well may be estimated by assuming bilinear flow (linear flow in the reservoir and linear flow in the fracture). An analytical solution to estimate the ratio of increase in well productivity under bilinear flow conditions was presented by Guo and Schechter (1999) as follows:

$$\frac{J}{J_o} = \frac{0.72 \left( \ln \frac{r_e}{r_w} - \frac{3}{4} + S_o \right)}{(z_e \sqrt{c} + S) \left( \frac{1}{1 - e^{-\sqrt{c} x_f}} - \frac{1}{2 x_f \sqrt{c}} \right)}, \quad (14.100)$$

where  $c = \frac{2k}{z_e w k_f}$  and  $z_e$  are distance between the fracture and the boundary of the drainage area.

## 14.8 FRACTURING TREATMENT DESIGN

Hydraulic fracturing designs are performed on the basis of parametric studies to maximize net present values (NPVs) of the wells to be stimulated. A hydraulic fracturing design should follow a general procedure:

1. Select a candidate well
2. Collect reservoir and rock mechanical properties, and calibrate rock mechanical properties and in-situ stress data
3. Select a fracture design simulator
4. Select fracturing materials (fluids and proppants)
5. Build a base treatment design including the pumping schedule and treating pressure and horsepower estimate, and perform design parameter sensitivity study using the fracture design simulator of choice
6. Perform production forecast and NPV analyses
7. Optimize the treatment design based on economics and data analyses of previous treatments in the area of interest

### 14.8.1 CANDIDATE WELL SELECTION

Hydraulic fracturing is an effective well stimulation technique. There are many applications for hydraulic fracturing, including unconventional development, production enhancement in low- and moderate-permeability reservoirs, bypassing near wellbore damage in high-permeability reservoirs, reducing sand production in loosely consolidated or unconsolidated reservoirs, and connecting the natural fractures in a formation to the wellbore. However, hydraulic fracturing may not be applicable to all types of wells and reservoirs. Candidate selection, treatment design, production forecasting and economic analysis are the keys to success of a hydraulic fracture treatment.

Low-permeability wells are obvious candidates for hydraulic fracturing as these wells can hardly become economic without effective stimulation. However, it is possible that the reservoir permeability is too low to provide economic production even with effective stimulation. Regardless of the reservoir permeability, wells suffering from near-wellbore formation damage are always good candidates for hydraulic fracturing. A short, conductive hydraulic fracture is often a desired solution to stimulate damaged wells. The stimulation of naturally fractured reservoirs can be very successful, though it can be challenging to place an adequate amount of proppants into the fracture due to excessive fluid loss from the dilation of natural fractures during the treatment. Hydraulic fracturing is also commonly used in unconsolidated high-permeability reservoirs to bypass formation damage and to enhance well productivity, and more importantly to mitigate sand production.

Candidate well selection for hydraulic fracturing treatments is determined by reservoir properties. Some of the reservoir characteristics suitable for hydraulic fracturing include:

- Unconventional shale or coalbed methane reservoirs
- Low-permeability formations, or payzones that have been damaged
- Undepleted reservoirs with medium to high reservoir pressure
- Good stress barriers to minimize fracture growth out of payzones
- Relatively thick pay zone(s) with enough hydrocarbons in place

Reservoirs that are poor candidates for hydraulic fracturing are basically those that lack the above characteristics.

### 14.8.2 FRACTURING FLUID SELECTION CONSIDERATIONS

Fracturing fluid plays a vital role in hydraulic fracture treatment because it creates the desired fracture geometry and controls the efficiencies of carrying proppant. The first major variable is fluid viscosity, as it affects a fluid's ability to suspend and transport proppants, and to flowback after treatment. The viscosity should be controlled in a range suitable for the treatment. A fluid viscosity being too high can result in excessive injection pressure during the treatment. Fluid loss is another major fracture design variable. Excessive fluid loss hinders fracture propagation or growth because of insufficient fluid volume accumulation in the fracture.

There are other considerations that can be important for particular cases, including compatibility with reservoir fluids and rock, with other materials (e.g., resin-coated proppant), and with operating pressure and temperature, as well as safety and environmental concerns. The selection of a proper fracturing fluid depends on many considerations, some of which are listed below:

- Whether the fluid is safe to use and friendly to the environment
- Whether the fluid is cost effective

- Whether the fluid requires cross-linking to gel it up during the treatment and can then break easily to a low viscosity fluid once the treatment is over
- Whether the fluid is compatible with reservoir rocks and fluids
- Whether the fluid can break to low viscosity that helps flow back and clean up without leaving residuals to cause damage to the reservoir and proppant pack
- Whether the fluid can provide low wellbore friction and enough hydrostatic head to reduce surface pumping pressures
- Whether the fluid requires additives to help control fluid loss

### 14.8.3 PROPPANT SELECTION CONSIDERATIONS

Since proppant cost constitutes a significant portion of the stimulation treatment cost, the ultimate goal for selecting the right proppant is to optimize the NPV for a given well. Obviously, natural sands are cheaper than resin-coated sands, and much cheaper than ceramic proppants and resin-coated ceramic proppants.

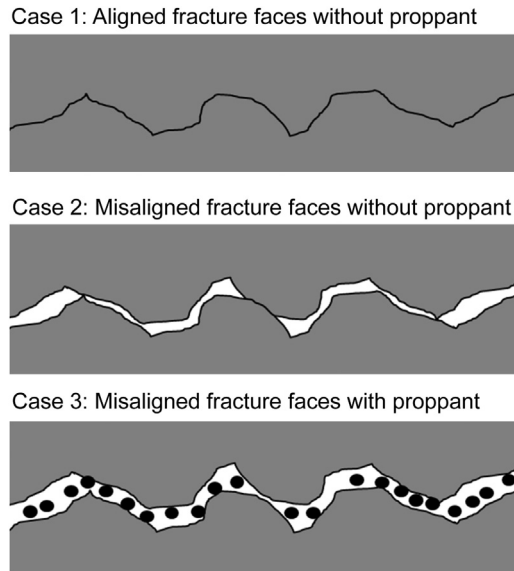
A major consideration in proppant selection is conductivity. As shown in Fig. 14.30, the conductivity of proppants degrades rapidly as the effective stress increases. Therefore, the effective stress applied to the proppant pack must be taken into consideration for selecting proper proppant(s) to use. The concept of effective stress defined in Eq. (14.17) also applies to the proppant pack in the formation. The fracture closure stress (or the minimum horizontal stress) in the fracture is counteracted by the fluid pressure in the fracture. Before the well is put into production after a fracture treatment, the fluid pressure in the fracture should be slightly larger than or similar to the reservoir pressure, depending on the duration of the shut-in period after the treatment. However, the fluid pressure in the fracture reduces significantly during production. The effective stress on proppant increases as the flowing bottom-hole pressure decreases. The worst-case scenario occurs near the wellbore where the fluid pressure becomes the flowing bottom-hole pressure. In contrast to the reservoir rocks, Biot's poroelastic constant for proppant packs is about the same as soils or unconsolidated formations, with a value close to 1. Assuming that Biot's poroelastic constant equal 1 in the proppant pack, Eq. (14.17) thus takes the following form for estimating the effective stress on proppant:

$$\sigma_e = \sigma_{h,\min} - p_{wf}, \quad (14.101)$$

where  $\sigma_e$  is the effective closure stress on proppant,  $\sigma_{h,\min}$  is the minimum horizontal stress in the payzone, and  $p_{wf}$  is the flowing bottom-hole pressure during production.

Proppants in the formation are subject to various types of damage that can significantly impair the fracture conductivity. Main damage mechanisms include proppant crushing, fines generation/plugging, proppant embedment, and gel residue plugging. The proppant pack is also subject to high flow velocity during production, especially for high-rate gas wells. The nonDarcy and multiphase flow effects can further reduce the effective proppant conductivity. These potential damage effects should also be considered for proppant selection. Some fracture design software tools provide an estimate of these damaging factors that impair the proppant conductivity.

On the other hand, it has been well recognized that unproped fractures also provide some conductivity. Hydraulic fracturing generally results in tensile fractures. However, shear displacement at natural discontinuities can occur, which results in misalignment between the two fracture walls once the fracture is closed. The residual fracture opening due to rough fracture surface is the

**FIGURE 14.41**

An illustration of the propped and unpropped fractures.

main mechanism that attributes to the conductivity of unpropped fractures. Laboratory results by [Fredd et al. \(2000\)](#) demonstrated that fracture displacement is required for surface asperities to provide residual fracture width and that the conductivity of unpropped fractures may vary by at least two orders of magnitude depending on formation properties such as the degree of fracture displacement, the size and distribution of asperities, and rock mechanical properties.

In general, rocks with higher Young's modulus and higher rock embedment strength provide higher unpropped fracture conductivity. However, a little bit of proppant placed in the fracture can dramatically improve the fracture conductivity. [Fig. 14.41](#) illustrates how the conductivity in propped and unpropped fractures differs. Slickwater fracture treatments using smaller proppants at low concentrations have been very popular for unconventional development. It has been recognized that an interconnected fracture network with large contact areas and just "enough" conductivity is required to effectively stimulate unconventional tight reservoirs.

The concept of dimensionless fracture conductivity defined in [Eq. \(14.95\)](#) clearly demonstrates the relative importance between the fracture flow capacity and the reservoir flow capacity. It does not take a larger fracture conductivity to create infinitely conductive fractures in nano-Darcy rocks. A fracture will attain its highest conductivity if there is a way to keep it open without packing it with proppants, which occupy space in the fracture and thus reduces its conductivity. The permeability of a perfect crack, analogous to the empty space between two parallel plates, is given by the following equation in a consistent unit system:

$$k_f = \frac{w^2}{12}, \quad (14.102)$$

A crack with a width of 1 mm provides a permeability of 84,400 Darcy and a crack with a width of 1  $\mu\text{m}$  provides a permeability of 84.4 md. Instead of finding ways to improve the proppant pack conductivity, channel fracturing has been introduced and used in the industry to create flow channels without proppants inside the proppant pack to provide infinite conductivity (Samir, 2013).

#### 14.8.4 COLLECTION AND VALIDATION OF RESERVOIR PROPERTIES

A complete and accurate data set that describes formation properties in all layers of interest and well configuration is important for fracture designs, especially for fracture model assisted designs. The best practice is to enter data for as many layers as feasible and let the fracture model determine potential fracture height growth. If data is entered only for a few layers, the fracture dimensions predicted by the model may be subject to data bias. The most critical parameters for hydraulic fracturing are:

- The description of reservoir lithology versus depth
- Basic reservoir properties, including effective reservoir permeability, porosity, pressure, temperature, reservoir fluid viscosity, reservoir rock/fluid compressibility
- Rock mechanical properties such as Young's modulus, Poisson's ratio, and fracture toughness
- The in-situ stress distribution, namely the minimum horizontal stress value in each formation layer
- Well configuration (tubing/casing size and grade, perforations, and wellbore trajectory)
- Wellhead equipment specifications

Reservoir and rock mechanical properties can be inferred from wireline logs and through laboratory fluid and core testing procedures. The reliability of the data inferred from these methods is affected by a number of factors, including the test environment, scale of measurement, data calibration, and variability of samples collected and tested. Bad data quality can lead to a poor fracture design and ultimately a suboptimal stimulation treatment.

The in-situ minimum horizontal stress, and rock mechanical properties, especially the Young's modulus, are very important to hydraulic fracturing as it controls the treating pressure required for a fracture to initiate and propagate, and affects the shape and vertical extent of the fracture. In most fracture design and analysis, a layer-cake reservoir model and a 1D MEM (mechanical earth model) are considered. In models like these, the reservoir and mechanical parameters vary only by layers in the vertical direction.

Essential components to the 1D MEM include Young's modulus, Poisson's ratio, and minimum horizontal stress in each layer. Young's modulus and Poisson's ratio can be measured using core samples in laboratory testing or using sonic logs. Two types of sonic or acoustic waves used to estimate the elastic properties of a formation are compressional waves (P-waves) and shear waves (S-waves). A dipole sonic logging tool measures the characteristic propagation speed of the P- and S-waves. Young's modulus and Poisson's ratio are related to the velocities of the P- and S-waves as follows:

$$E_d = \frac{\rho V_s^2 (3V_p^2 - 4V_s^2)}{V_p^2 - V_s^2}, \quad (14.103)$$

$$\nu_d = \frac{V_p^2 - 2V_s^2}{2(V_p^2 - V_s^2)}, \quad (14.104)$$



where  $E_d$  is the dynamic Young's modulus,  $\nu_d$  is the dynamic Poisson's ratio,  $\rho$  is the rock density,  $V_s$  is the S-wave velocity, and  $V_p$  is the P-wave velocity. Note that Eqs. (14.103) and (14.104) are expressed in a consistent unit system.

There is a difference between the dynamic and static elastic properties (i.e., Young's modulus and Poisson's ratio). The dynamic properties are usually larger than the static properties. The dynamic Young's modulus for some rocks can be as large as twice the static Young's modulus, but the difference between the dynamic and static Poisson's ratios is usually very small and can often be neglected for fracture modeling. The elastic properties measured in laboratory testing are static while the elastic properties measured by sonic log are dynamic. Static elastic properties are required for fracture modeling. Therefore, the dynamic elastic properties have to be calibrated using laboratory testing results or from correlations (Lacy, 1997).

Once the static elastic properties are calibrated or estimated, the minimum horizontal stress for each layer can be estimated from Eq. (14.21). However, the stress model built from sonic log data have to be calibrated using the fracture closure data obtained from minifrac tests described in Section 14.5.4. Fig. 14.42 shows an illustration of a 1D stress model that is calibrated by stress values in two zones obtained from minifrac testing. Usually, minimum horizontal stress increases with depth. Minimum horizontal stress is lithology dependent, and shales usually exhibit higher stresses than sands because shales generally have higher Poisson's ratio values.

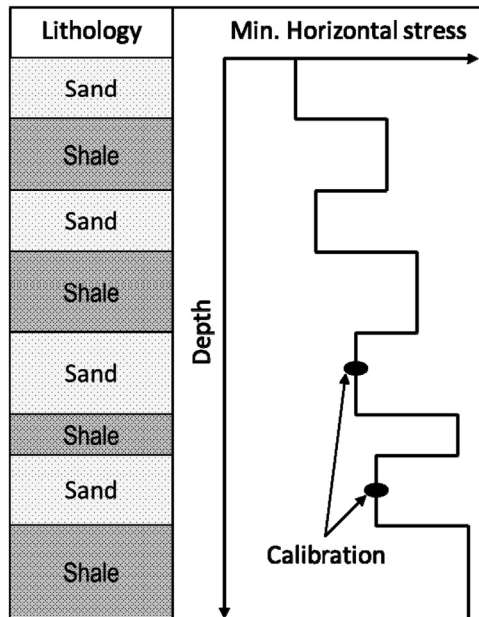


FIGURE 14.42

An illustration of stress calibration.

### 14.8.5 FRACTURE MODEL SELECTION AND CALIBRATION

An appropriate fracture design simulator should be selected to match the level of complexity required for the specific application, quality and quantity of data, allocated time to perform a treatment design, and desired level of output. Modeling with a planar 3D model can be time consuming. Pseudo-3D models provide a compromise solution and are most often used in the industry. Also, governing equations and analytical solutions in 2D models can still be useful to demonstrate the influence of key design parameters.

Most commercial fracture simulators are generally built with some bells and whistles that can be used to adjust fracture growth behavior and to calibrate the fracture propagation model. In addition to rock mechanical property and stress calibration described earlier, fracture model calibration is an important procedure to make the model more relevant to the problem at hand. Model calibration can be carried on several levels depending on the availability and quality of input data. If treatment data from offset wells is available, the first step is to perform net pressure analysis on a few fracture treatments in offset wells in the area of interest in order to understand the leakoff behavior of the reservoir formation and the fracturing fluids used, and to look for pressure anomalies. If posttreatment production or well testing data are available, the propped fracture geometry (mainly propped fracture half-length) must be consistent with the fracture half-length obtained from the production or well testing data analysis. If the results of fracture monitoring, such as using microseismic and tilt monitoring methods, are available, the hydraulic fracture geometry has to be consistent with the monitoring results.

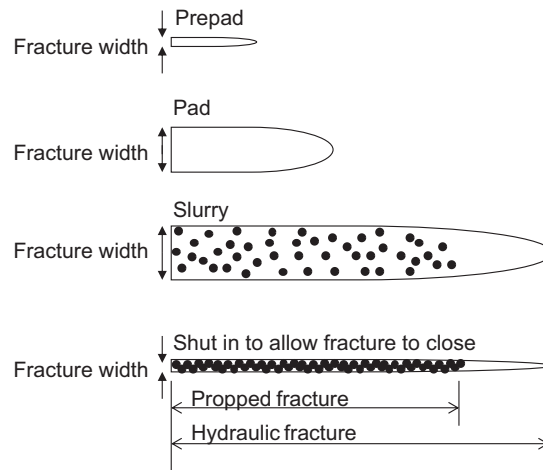
More importantly, a diagnostic testing procedure should be included in the treatment plan. The diagnostic injection test should be conducted prior to the main fracture treatment. The analysis of diagnostic injection testing data performed on-site can help refine the final propped treatment schedule. Ideally, two diagnostic injection tests should be conducted prior to the main fracture treatment. KCl water should be pumped during the first test, and sufficient time after shut-in should be given to allow the fracture to close. The objective of the first test is to obtain the closure stress using the G-function or the square root of time plot, determine the efficiency of KCl water without the filtercake effects, and calibrate the system permeability resulting from fluid leakoff which could be larger than the reservoir permeability. The fracturing fluid used in the main treatment should be pumped during the second diagnostic injection test to reconfirm the closure stress, and to evaluate the leakoff coefficient of the main fracturing fluid.

The diagnostic injection testing prior to the main treatment is necessary to obtain fluid efficiency, to obtain and calibrate the stress model used in the fracture design simulator. In summary, integrated studies are the key to making model assisted design more valuable.

### 14.8.6 TREATMENT PROCEDURE AND SCHEDULE

#### 14.8.6.1 *Treatment procedure*

A typical pumping schedule consists of a number of treatment steps or stages, including prepad, pad, proppant stage(s), displacement, and shut-in. One of the reasons to have these stages in a pumping schedule is to ensure the successful placement of proppant and to achieve the desired fracture conductivity. Fig. 14.43 shows an illustration of fracture width/length growth and proppant placement. The sequence of these stages is described below.

**FIGURE 14.43**

An illustration of fracture growth in width and length and proppant placement.

1. The first fluid pumped into the formation is called “prepad.” The prepapad has low viscosity and does not contain any proppant. A small amount of KCl brine, slickwater, or HCl acid fluid is typically used to break down the formation and to allow fracture initiation. Acid is often used in the prepapad as it dissolves perforation debris and minerals around the perforation tunnels, and thus reduces the formation break down pressure.
2. The fluid that follows the prepapad is called “pad.” The pad can be a more viscous fluid or simply slickwater. From this point forward, the fracture propagates into the formation. Typically, no proppant is pumped during the pad; however, in some cases, very small amounts of proppant may be added in short bursts in order to clean the perforations and to bridge off smaller cracks that provides a chance to allow fewer and larger fractures to propagate away from the near-wellbore region. The goal of pumping a pad is to create a fracture with adequate width to allow proppant to travel deep in the fracture. Another purpose of the pad is to provide enough fluid volume within the fracture to account for fluid loss that occurs throughout the entire treatment.
3. After the pad is pumped, the subsequent stages will contain varying concentrations of proppant. The proppant laden fluid is commonly referred to as “slurry.” During the proppant stages, smaller proppants or lower proppant concentrations are pumped first, and the proppant concentrations are increased gradually, to ensure a successful placement of proppants. As proppant laden slurry travels toward the tip or the outer edge of the fracture, some of the fracturing fluid is lost into the formation due to leakoff, resulting in an increase in proppant concentration. The fracture width also becomes narrower when it gets close to the fracture edge. These are the primary reason why to ramp up proppant concentrations as the treatment

continues. The proppant slurry stage is typically divided into a number of sub-stages to allow the fluid type or the proppant concentration to be specified at each sub-stage. The fluid used in the slurry can be of many types, including slickwater, linear gel, crosslinked gel, viscoelastic fluid, or foamed fluid, depending on the type of the design or the type of the reservoir treated.

4. Once the desired amount of fluids and proppants are pumped, the proppant slurry in the wellbore has to be displaced by a clean fluid. The purpose of the displacement is to flush the previous proppant laden stage to a depth just above the perforations, so that the wellbore is not left full of proppant and most of the proppant pumped is placed in the fractures. The final displacement is commonly called the “flush.” The flush fluid is usually plain water, KCl water, slickwater, or a low gel-loading fluid.
5. Once the treatment is completed, the well is shut down to allow the fracture to close as the fluid inside the fracture continues leaking into the reservoir or flow back to speed up the fracture closing processes. Depending on the pad size and treatment design, there is typically a portion of the fracture near the tip without proppant placed. As a result, there will be two fracture geometries, hydraulic fracture and propped fracture, as illustrated in Fig. 14.43.

Treatment execution can be disrupted by equipment failure or screen-out events. Screen-out refers to a condition during hydraulic fracturing where continued injection of proppant slurry has caused the treatment pressure to exceed the safe limitations of the wellbore or wellhead equipment. Screen-outs can cause severe disruptions in fracturing operations and often require cleaning proppants from the wellbore prior to resumption of operations. In many cases, the treatment may have to be abandoned because the fracture created prior to the screen-out event can no longer take any proppant slurry or even clean fluids. A remedy treatment may be performed after re-perforating at a different zone or interval. As an operational issue, screen-out results in less proppant pumped, but it does not necessarily mean damage to well productivity. The Nolte-Smith plot (net pressure versus time on log-log scales) described in Section 14.5.1 can be used in real-time during pumping to identify signs of premature screen-outs. Screen-outs can often be avoided by identifying the root cause of previous screen-outs in the area and by modifying the treatment schedule accordingly. Pumping a larger pad volume, using more viscous fluids in the pad, lower proppant concentration, higher pumping rates, and even small volumes of proppant slugs can help mitigate screen-out potentials.

#### **14.8.6.2 Treatment schedule generation**

The only objective of hydraulic fracturing is to stimulate well production by creating a conductive path that extends from the wellbore deep into the reservoir. The goal of a treatment design is to provide a pumping schedule, which is composed of fluid type, fluid volume, proppant type, proppant concentration, and pumping rate. A treatment design including the above information should be based on the stimulation objective, reservoir properties, material availability, equipment capability, and economical considerations.

This section demonstrates how to design a treatment schedule using the PKN fracture model for simplicity. Based on the early work from [Nolte \(1986\)](#), and the information from [Economides et al. \(1994\)](#), a summary of treatment design procedures using the PKN model is described as follows:

1. Assume a fracture half-length  $x_f$  to achieve and an injection rate  $q_i$  to pump, calculate the average fracture width  $\bar{w}$  using a selected fracture model.
2. Based on material balance, solve injection fluid volume  $V_{inj}$  from the following equation:

$$V_{inj} = V_{frac} + V_{Leakoff}, \quad (14.105)$$

where

$$V_{inj} = q_i t_i \quad (14.106)$$

$$V_{frac} = A_f \bar{w} \quad (14.107)$$

$$V_{Leakoff} = 2A_f r_p K_L (C_L \sqrt{t_i} + S_p) \quad (14.108)$$

where  $S_p$  is spurt loss.

$$K_L = \frac{1}{2} \left[ \frac{8}{3} \eta + \pi(1 - \eta) \right] \quad (14.109)$$

$$r_p = \frac{h}{h_f} \quad (14.110)$$

$$A_f = 2x_f h_f \quad (14.111)$$

$$\eta = \frac{V_{frac}}{V_{inj}} \quad (14.112)$$

$$V_{pad} = V_{inj} \frac{1 - \eta}{1 + \eta} \quad (14.113)$$

Since  $K_L$  depends on fluid efficiency  $\eta$ , which is not known in the beginning, a numerical iteration procedure is required. The procedure is illustrated in [Fig. 14.44](#).

3. Generate proppant concentration schedule using:

$$c_p(t) = c_f \left( \frac{t - t_{pad}}{t_{inj} - t_{pad}} \right)^\varepsilon, \quad (14.114)$$

where  $c_f$  is the final concentration in ppg. The proppant concentration in pound per gallon of added fluid (ppga) is expressed as

$$c'_p = \frac{c_p}{1 - c_p / \rho_p} \quad (14.115)$$

and

$$\varepsilon = \frac{1 - \eta}{1 + \eta}. \quad (14.116)$$

4. Predict propped fracture width using

$$w_p = \frac{C_p}{(1 - \phi_p) \rho_p}, \quad (14.117)$$

Assume a  $K_L$  value

$$q_i t_i = A_f \bar{w} + 2A_f r_p K_L (C_L \sqrt{t_i} + S_p) \quad \curvearrowright$$

$$\downarrow$$

$$t_i \quad K_L = \frac{1}{2} \left[ \frac{8}{3} \eta + \pi(1-\eta) \right]$$

$$\downarrow$$

$$V_{inj} = q_i t_i$$

$$V_{frac} = A_f \bar{w} \quad \eta = \frac{V_{frac}}{V_{inj}} \quad \curvearrowright$$

$$V_{pad} = V_{inj} \left( \frac{1-\eta}{1+\eta} \right)$$

**FIGURE 14.44**

Iteration procedure to determine the pumping time.

where

$$C_p = \frac{M_p}{2x_f h_f} \tag{14.118}$$

$$M_p = \bar{c}_p (V_{inj} - V_{pad}) \tag{14.119}$$

$$\bar{c}_p = \frac{c_f}{1 + \varepsilon} \tag{14.120}$$

**Example Problem 14.5** The following data is given for a hydraulic fracturing treatment design:

Pay zone thickness:	70 ft
Young's modulus of rock:	$3 \times 10^6$ psi
Poisson's ratio:	0.25
Fluid viscosity:	1.5 cp
Leak-off coefficient:	$0.002 \text{ ft/min}^{1/2}$
Spurt loss:	$0.0 \text{ gal/ft}^2$
Proppant density:	$165 \text{ lb/ft}^3$
Proppant porosity:	0.4
Fracture half-length:	1000 ft
Fracture height:	100 ft
Fluid injection rate:	40 bbl/min or bpm
Final proppant concentration:	3 ppg

Assuming PKN fracture, estimate

1. Fluid volume requirement
2. Proppant mixing schedule
3. Proppant weight requirement
4. Propped fracture width

**Solution**
**1. Fluid volume requirements:**

The average fracture width:

$$\begin{aligned}
 w &= 0.39 \left[ \frac{q_i \mu (1 - \nu) x_f^2}{G h_f} \right]^{1/4} \left( \frac{\pi}{5} \right) \\
 &= 0.39 \left[ \frac{(40)(1.5)(1 - 0.25)(1000)^2}{\frac{(3 \times 10^6)}{2(1 + 0.25)}(70)} \right]^{1/4} \left( \frac{\pi}{5} \right) = 0.21 \text{ in.}
 \end{aligned}$$

Fracture area:

$$A_f = 2x_f h_f = 2(1000)(100) = 2 \times 10^5 \text{ ft}^2$$

Fluid volume is based on volume balance:

$$q_i t_i = A_f \bar{w} + 2A_f r_p K_L (C_L \sqrt{t_i + S_p}).$$

 Assuming  $K_L = 1.5$ ,

$$\begin{aligned}
 (40)(5.615)t_i &= (2 \times 10^5) \left( \frac{0.21}{12} \right) + 2(2 \times 10^5) \left( \frac{70}{100} \right) \\
 &\quad \times (1.5) \left( (2 \times 10^{-3}) \sqrt{t_i} + \left( \frac{5.615}{42} \right) 0 \right)
 \end{aligned}$$

 gives  $t_i = 37$  min.

 Check  $K_L$  value:

$$V_{inj} = q_i t = (40)(42)(37) = 6.216 \times 10^4 \text{ gal}$$

$$V_{frac} = A_f \bar{w} = (2 \times 10^5) \left( \frac{0.21}{12} \right) (7.48) = 2.43 \times 10^4 \text{ gal}$$

$$\eta = \frac{V_{frac}}{V_{inj}} = \frac{2.43 \times 10^4}{6.26 \times 10^4} = 0.3875$$

$$K_L = \frac{1}{2} \left[ \frac{8}{3} \eta + \pi(1 - \eta) \right] = \frac{1}{2} \left[ \frac{8}{3} (0.3875) + \pi(1 - 0.3875) \right]$$

$$= 1.48 \text{ OK}$$

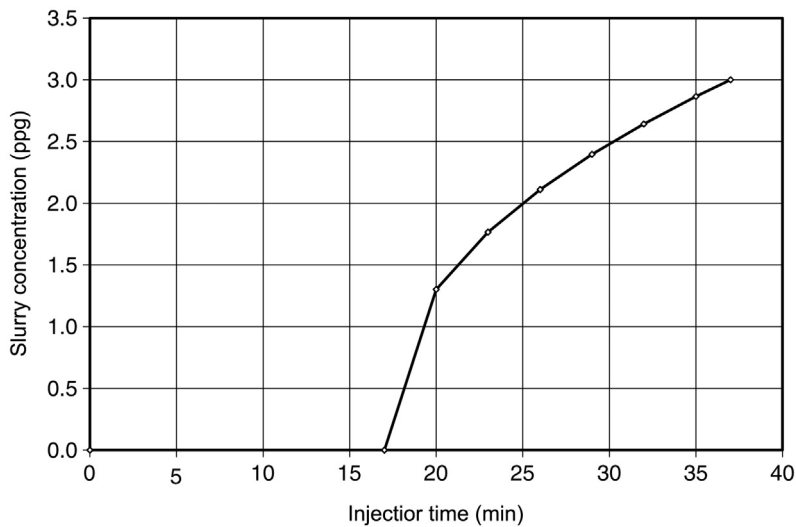
Pad volume:

$$\varepsilon = \frac{1 - \eta}{1 + \eta} = \frac{1 - 0.3875}{1 + 0.3875} = 0.44$$

$$V_{pad} = V_{inj} \varepsilon = (6.216 \times 10^4)(0.44) = 2.735 \times 10^4 \text{ gal}$$

It will take 17 minutes to pump the pad volume at an injection rate of 40 bpm.

$t$ (min)	$c_p$ (ppg)
0	0
17	0.00
20	1.30
23	1.77
26	2.11
29	2.40
32	2.64
35	2.86
37	3.00



**FIGURE 14.45**

Calculated slurry concentration.

**2.** Proppant mixing schedule:

$$c_p(t) = (3) \left( \frac{t-17}{37-17} \right)^{0.44}$$

which results in a proppant concentration schedule as shown in Table 14.4. Slurry concentration schedule is plotted in Fig. 14.45.



3. Proppant weight requirement:

$$\bar{c}_p = \frac{c_f}{1 + \varepsilon} = \frac{3}{1 + 0.44} = 2.08 \text{ ppg}$$

$$\begin{aligned} M_p &= \bar{c}_p(V_{inj} - V_{pad}) = (2.08)(6.216 \times 10^4 - 2.735 \times 10^4) \\ &= 72,404 \text{ lb} \end{aligned}$$

4. Proppant placement concentration and propped fracture width:

$$C_p = \frac{M_p}{2x_f h_f} = \frac{72,404}{2(1000)(100)} = 0.362 \text{ lb/ft}^2,$$

$$w = \frac{C_p}{(1 - \phi_p)\rho_p} = \frac{0.362}{(1 - 0.4)(165)} = 0.00366 \text{ ft} = 0.044 \text{ in.}$$

Example Problem 14.5 can be extended to build a design pumping schedule that a service can readily use to pump the treatment. For that, slickwater is selected for the treatment because the fluid viscosity given in this example is very low at 1.5 cp. Also, due to slickwater's poor transport capability, smaller proppant, 40/70-mesh sand, is selected. Furthermore, this is a vertical well completed and cemented with 5-1/2 in. casing (grade of N-80 and weight of 13 lb/ft) to a target depth (TD) of 4650 ft. The treatment will be pumped down through a 3-1/2 in. tubing (grade of N-80 and weight of 8.68 lb/ft) with the bottom of the tubing string at a depth of 4500 ft. The perforated interval is 10 ft in length and located at depths of 4530–4540 ft. The wellbore volume for fracture treatments is typically calculated from the wellhead to the top depth of the upper most perforation interval. In this case, the wellbore for the treatment is composed of a 3-1/2 in. tubing string of 4500 ft in length and a 5-1/2 in. casing section of 30 ft in length. Based on the weight of the tubular goods, the pipe IDs are 5.044 in. for the casing and 3.00 in. for the tubing. With that, a total wellbore volume of 1684 gal is obtained, which is approximately 40 bbl. Once the wellbore volume is calculated, the displacement or flush volume can also be determined. In treatment designs for conventional reservoirs, “under flush,” meaning that the flush volume is less than the wellbore volume, is desirable. The opposite of under flush is over flush that could leave the fracture filled with less proppant and lead to lower fracture conductivity in the near-wellbore area.

In this example, a flush volume of 40 bbl or 1680 gal, just about the same as the wellbore volume, is selected for simplicity. The flush volume will displace the proppant slurry to the top of the perforated interval and leave little proppant in the wellbore. The proppant concentration schedule shown in Table 14.4 is a “ramped” proppant concentration schedule, which means that the proppant concentration is ramped up continuously during the treatment until the flush stage. Ramped schedules are often used in smaller treatment sizes like “frac-pack” applications as there is usually not enough time in each stage to observe the pressure response when the proppant in the current stage hits the perforation before pumping a subsequent stage. On the other hand, the proppant concentration in each stage is kept constant in “staged” proppant concentration schedules. Staged schedules are commonly used in larger treatments so that the pressure response can be observed when the proppant in the current stage reaches the perforation before pumping a subsequent stage. Table 14.5 shows the treatment design with a staged proppant concentration schedule for this

**Table 14.5 Design Treatment Schedule for Example 14.5**

Stage #	Stage Type	Elapsed Time (min)	Fluid Type	Clean Volume (gal)	Prop Conc (ppg)	Stage Prop. (klbs)	Slurry Rate (bpm)	Proppant Type
1	Pad	17.0	Slickwater	28,560	0.00	0.0	40.00	
2	Slurry	20.0	Slickwater	4734	1.30	6.2	40.00	Sand 40/70
3	Slurry	23.0	Slickwater	4633	1.77	8.2	40.00	Sand 40/70
4	Slurry	26.0	Slickwater	4562	2.11	9.6	40.00	Sand 40/70
5	Slurry	29.0	Slickwater	4503	2.40	10.8	40.00	Sand 40/70
6	Slurry	32.0	Slickwater	4456	2.64	11.8	40.00	Sand 40/70
7	Slurry	35.0	Slickwater	4413	2.86	12.6	40.00	Sand 40/70
8	Slurry	37.0	Slickwater	2924	3.00	8.8	40.00	Sand 40/70
9	Flush	38.0	Slickwater	1680	0.00	0.0	40.00	
10	Shut-in	50.0		0	0.00	0.0	0.00	

example. A “shut-in” stage is added to the end of the treatment schedule in order to obtain an ISIP at the shut-in and to monitor and collect pressure decline data for 12 more minutes. With the wellbore configuration specified, the design in this example can be ready for planning and execution.

A treatment schedule is the last step and the outcome of the treatment design process. More time and effort is generally spent during data collection, model calibration, and fluid and proppant selection. Although some commercial fracture simulators have the capability of guiding a user to automatically generate a pumping schedule, experienced engineers seldom, if never, use a pumping schedule generated by a fracture simulator. A pumping schedule is basically a summary of treatment steps that a service company can use to pump the treatment, which is typically either based on experience or the current treatment practice in the area. Once a base design schedule is determined and entered into the fracture simulator, parameter sensitivity analyses will typically be performed to refine the design schedule and ultimately to obtain an optimized design. Treatment design optimization should be based on production enhancement and economic analyses, which will be described in [Section 14.8.8](#).

### 14.8.7 TREATMENT PRESSURE AND HORSEPOWER ESTIMATION

In most fracturing treatments, the maximum treatment pressure typically occur at the beginning of the treatment when the formation is broken down. However, the maximum treatment pressure generally occurs toward the end of a treatment for “frac-pack” and “tip screen-out (TSO)” treatment applications. Also, when unwanted events such as screen-outs occur, the maximum treatment pressure can occur at any time during the treatment. An estimation of the maximum surface treatment pressure is important for casing design and wellhead selection.

If the maximum bottom-hole treatment pressure is equal to the formation breakdown pressure  $p_{bd}$  that occurs at the beginning of the treatment, the maximum surface treatment pressure can be calculated by:

$$p_{si} = p_{bd} - \Delta p_h + \Delta p_f, \quad (14.121)$$

where

- $p_{st}$  = surface treatment pressure, psi
- $p_{bd}$  = formation breakdown pressure, psi
- $\Delta p_h$  = hydrostatic pressure, psi
- $\Delta p_f$  = frictional pressure drop in the wellbore, psi

The formation breakdown pressure can be estimated from Eq. (14.24). However, as discussed in Section 14.2.7, it is difficult to accurately estimate the formation breakdown pressure. The hydrostatic pressure can be calculated using Eq. (11.93) (see Chapter 11, Transportation Systems).

As discussed in Section 14.5.2, predicting fluid friction in the wellbore is unreliable. If a friction table for the fluid of interest is not available from the service company, Eqs. (14.76)–(14.80) can be used to calculate the fluid friction for nonNewtonian fluids. The fluid flow velocity through tubing or casing in hydraulic fracturing treatments is almost always in turbulent conditions. To avert the procedure of the Reynolds number and the Fanning friction factor determination, the following approximation may be used to calculate the frictional pressure drop of Newtonian fluids:

$$\Delta p_f = \frac{518\gamma^{0.79} q^{1.79} \mu^{0.207}}{1000D^{4.79}} L, \quad (14.122)$$

where

- $\gamma$  = fluid specific gravity, water = 1.0
- $q$  = injection rate, bbl/min
- $\mu$  = fluid viscosity, cp
- $D$  = pipe inner diameter, in.
- $L$  = pipe length, ft.

Note that fracturing fluid friction calculated from Eqs. (14.77)–(14.81) and Eq. (14.122) can over estimate actual friction values significantly as polymers added in fracturing fluids can dramatically reduce fluid friction.

Once the maximum surface treating pressure is estimated and the maximum pumping rate is determined, the horsepower required for the treatment can be estimated. In oilfield units, the horsepower is calculated by:

$$HHP = \frac{qp_{tr}}{40.8}, \quad (14.123)$$

**Example Problem 14.6** For Example Problem 14.1, predict the maximum expected surface injection pressure and the horsepower required using the following additional data:

Fluid specific gravity (water = 1.0):	1.0
Viscosity of fracturing fluid:	1.0 cp
Tubing inner diameter:	3.0 in
Pumping rate:	20 bbl/min

### Solution

Hydrostatic pressure drop:

$$\Delta p_h = (0.433) (1) (10,000) = 4330 \text{ psi}$$

Frictional pressure drop:

$$\begin{aligned}\Delta p_f &= \frac{518 \rho^{0.79} q^{1.79} \mu^{0.207}}{1000 D^{4.79}} L \\ &= \frac{518 (1)^{0.79} (20)^{1.79} (1)^{0.207}}{1000 (3)^{4.79}} (10,000) = 5725 \text{ psi}\end{aligned}$$

Expected surface treatment pressure:

$$p_{si} = p_{bd} - \Delta p_h + \Delta p_f = 7100 - 4330 + 5725 = 8495 \text{ psi}$$

Horsepower required:

$$HHP = \frac{qp_{tr}}{40.8} = \frac{(20)(8495)}{40.8} = 4164 \text{ hhp}$$

### 14.8.8 TREATMENT DESIGN OPTIMIZATION

Fracture treatment design should ultimately be based on production enhancement and economic analyses. Most commercial fracture design simulators have built-in modules for production forecasting and economic analyses. However, if these modules are not sufficient, rigorous reservoir simulation and comprehensive economic analyses should be conducted using other more advanced tools.

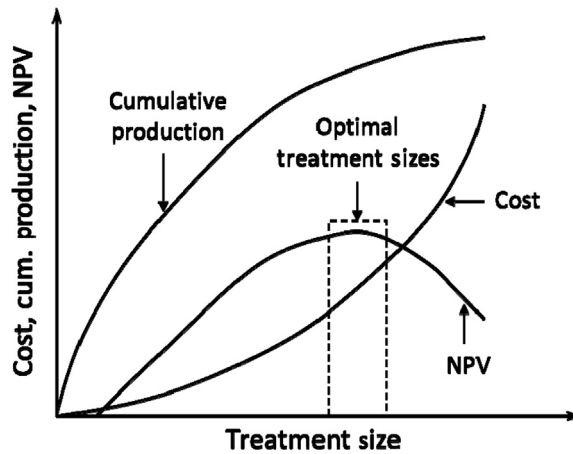
The optimization of treatment design starts with a base treatment design that could have been determined through fracture modeling and parameter sensitivity analysis or based on the current design practice in the area of interest. The base treatment design should include a pumping schedule that is composed of fluid type, fluid volume, proppant type, proppant concentration, proppant volume, and pumping rate. The design optimization process can be performed in the following steps using software tools selected:

- Choose a range of treatment sizes for evaluation
- Estimate treatment costs required for various treatment sizes
- Predict the performance of the well stimulated with various treatment sizes
- Calculate NPV, ROR, and/or other economic indicators using incremental production, which is the difference between the fractured and unfractured cases

As illustrated in Fig. 14.46, both the treatment cost and posttreatment cumulative production increase as the treatment size increases. However, there is a point of diminishing returns in increasing the treatment size. Beyond this point, the return on investment is overtaken by the cost increase. An optimal range of treatment sizes can then be determined.

The NPV can be calculated as follows. A comparison of the production forecast for the fractured unstimulated wells allows for calculations of the annual incremental cumulative production for year  $n$  for an oil well:

$$\Delta N_{p,n} = N_{p,n}^f - N_{p,n}^{nf}, \quad (14.124)$$


**FIGURE 14.46**

An illustration of treatment cost, posttreatment production and NPV vs treatment size.

where

$$\begin{aligned} \Delta N_{p,n} &= \text{predicted annual incremental cumulative production for year } n \\ N_{p,n}^f &= \text{predicted annual cumulative production of fractured well for year } n \\ N_{p,n}^{nf} &= \text{predicted annual cumulative production of unfractured well for year } n. \end{aligned}$$

The annual incremental revenue above the one that the unstimulated well would deliver is expressed as:

$$\Delta R_n = (\$)\Delta N_{p,n}, \quad (14.125)$$

where (\$) is oil price. The present value of the future revenue is then:

$$NPV_R = \sum_{n=1}^m \frac{\Delta R_n}{(1+i)^n}, \quad (14.126)$$

where  $m$  is the remaining life of the well in years and  $i$  is the discount rate. The NPV of the hydraulic fracture project is

$$NPV = NPV_R - \text{cost}. \quad (14.127)$$

The cost should include the expenses for fracturing fluid, proppant, pumping, and the fixed cost for the treatment. Wells without hydraulic fracturing do not produce any hydrocarbons in unconventional shale reservoirs. Therefore, the predicted annual cumulative production of an unfractured well for year  $n$ ,  $N_{p,n}^{nf}$ , is zero.

## 14.9 FRAC-PACK TREATMENTS

Frac-pack, also known as “frac pack,” “frac and pack” or “frac & pack,” is a combination of hydraulic fracturing and gravel packing. Gravel packing is a completion method for sand control.

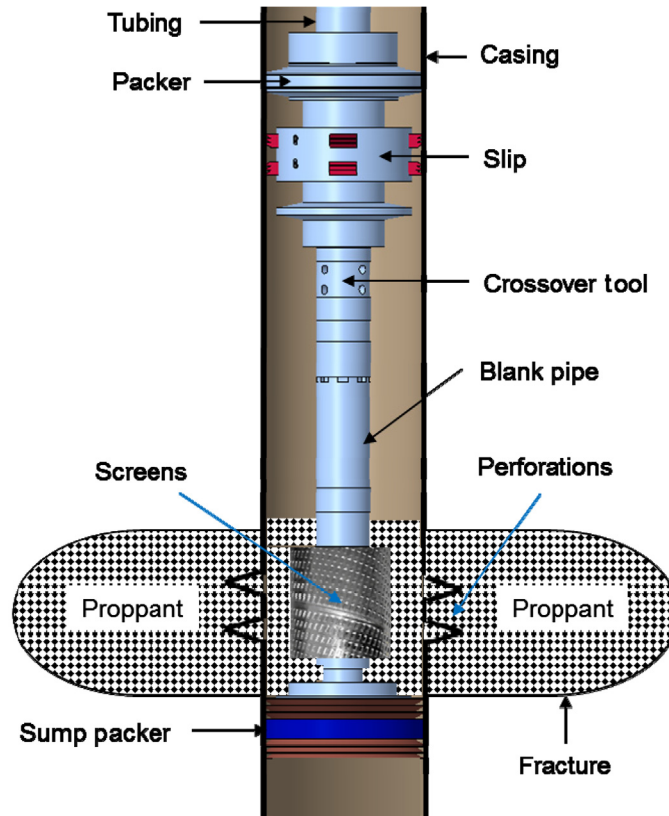
Frac-pack is commonly used to complete wells in unconsolidated reservoirs to achieve both production enhancement from a fracture and sand control from a gravel pack. Even without gravel-pack screens, sand control under some reservoir conditions can be accomplished by hydraulic fracturing using curable-resin-coated proppant. Flow rate and production drawdown are important factors that affect sand production. The presence of a fracture increases the surface area exposed to the formation and reservoir fluids, thus reducing the drawdown around the wellbore and mitigating the potential of sand production. In frac-pack treatments, the proper sizes of gravel and proppant are important as the goal is to stop sand production with the gravel pack and fracture created (Fischer et al., 2016). A number of products (Nguyen and Rickman, 2012; Christanti et al., 2011) are available in the industry that can be used to prevent fines production. These products are either resin or polymer based, and create thin coating layers around the surfaces of formation fines and other particles to make them immobile. There are a number of completion methods for sand control, including stand-alone screens, gravel pack, high-rate water pack, and frac-pack. This section focuses on frac-pack only.

In most frac-pack applications, screens are in place at the time of pumping. The screens serve as a barrier to prevent proppant flowback and formation sand production. Fig. 14.47 illustrates typical components of a frac-pack completion, including tubing string, upper packer, slips, crossover tool, blank pipe, screens, and sump packer (Economides and Martin, 2007).

During a frac-pack treatment, the fluid is pumped down the tubing, enters the annulus between the casing and the blank pipe through the crossover tool, then flows down the annulus between the screens and the casing, and finally leaves the wellbore through the perforations. A fracture is first created by pumping high viscosity fluid above fracturing pressure. Slurry containing high proppant concentrations is then pumped to achieve a high conductivity proppant pack and a sufficient fracture length for the flow of reservoir fluids into the wellbore at lower pressure drawdown. The type of proppants used is based on the reservoir depth and formation closure stress, but sands are commonly used. A frac-pack treatment is designed to screen out at the end of the treatment to ensure that both the fracture and the annulus between the screens and the casing are packed with proppant after the screen-out. In contrast, screen-outs, especially premature screen-outs, should be avoided in conventional fracturing treatments.

The designed fracture length for a typical frac-pack treatment generally ranges from 10 to 50 ft. In order to achieve a high-conductivity proppant pack, the frac-pack treatment is designed to create a propped fracture as wide as possible. As a result, a huge amount of proppant is generally placed in the fracture that can exceed  $20 \text{ lb/ft}^2$  of fracture area, which can be more than 10 times the amount of proppant placed per unit fracture area for a typical fracture treatment in low-permeability reservoirs (not to mention nano-Darcy shale reservoirs). The principle of frac-pack treatments is the same as high-permeability TSO treatments, which is described as follows.

High-permeability and high-porosity are often associated with unconsolidated sand formations. As described in Section 14.7, transmitting the fluid from the high-permeability formation to the fracture is relatively easier than moving the fluid through the fracture to the wellbore. Based on the concept of dimensionless fracture conductivity defined in Eq. (14.95), in order to maintain a desirable  $F_{CD}$  value (an  $F_{CD}$  value of 2 for example), it is required to increase the fracture conductivity (both the fracture width and permeability) and reduce the fracture half-length as the reservoir permeability increases. Therefore, the main objective of hydraulic fracturing in high-permeability reservoirs is to generate more fracture conductivity than length. Techniques used for increasing



**FIGURE 14.47**

Typical components of a frac-pack completion.

fracture conductivity include increasing proppant concentration for all applications and increasing proppant size for cases where the reservoir does not generate formation fines which could plug the proppant pack. However, there is a limit in increasing proppant size and concentration. Another important technique for increasing fracture conductivity is TSO design, which was introduced by [Smith et al. \(1984\)](#). Although each of the above techniques has positive results on increasing fracture conductivity for high-permeability fracture treatments, TSO fracturing has completely transformed well stimulation for high-permeability reservoirs.

The TSO design is based on intentionally screening out the fracture tip or its entire perimeter with proppant when the pad is depleted or the slurry becomes dehydrated. Continuing to pump slurry will then increase the fracture width and pack the fracture with proppant to obtain high conductivity. Because this type of treatments involves the risk of a premature screen-out and/or the failure to achieve the goal of creating TSO, diagnostic inject testing prior to the fracture treatment is generally required to determine fracture design parameters such as fluid efficiency or total leakoff coefficient, and closure stress. TSO treatments are generally designed using an appropriate fracture simulator.

High-permeability reservoirs, especially unconsolidated sand formations, generally exhibit low Young's modulus. With reference to Eq. (14.52) for the PKN model, low Young's modulus formations require low net pressure to achieve the same fracture dimensions (width, length and height) if everything else is equal. In addition, high-permeability reservoirs are usually associated with high fluid loss. These unique properties make TSO fracturing achievable and manageable from an operational point of view. Once TSO occurs, continued injection increases both the net pressure and surface treating pressure. However, the pressure increase is less significant in low Young's modulus formations than high Young's modulus formations. Also, high fluid loss in high-permeability reservoirs can help create TSO and ensure the entire fracture packed with proppants.

---

## 14.10 FRACTURING HORIZONTAL WELLS

Modern horizontal well drilling and completion started in the 1980s, gained acceptance in the industry through the 1990s and early 2000, but did not become indispensable until the recent shale revolution. Commercial developments of unconventional resources would not be possible today without horizontal well drilling and multistage hydraulic fracturing.

### 14.10.1 TRANSVERSE AND LONGITUDINAL FRACTURES

Depending on the intersection angle between the hydraulic fracture and the horizontal section, hydraulic fractures created in horizontal well completion generally fall into two categories:

- Transverse
- Longitudinal

Of course, the intersection between the hydraulic fracture and the horizontal section can occur at other angles, which is less desirable. During well planning, the fracture orientation is given as it is determined by the in-situ stress. However, the horizontal section can be drilled in other directions and cause it to intersect with a hydraulic fracture at an angle other than perpendicular or parallel. This situation occurs due to lease size constraint or the consideration of maximizing the numbers of horizontal wells that can be placed from a single platform offshore or a single well pad onshore.

Horizontal wells are commonly stimulated with multiple fractures in the lateral section. To avoid the communication between the previous and subsequent fractures, the treatment size for each stage is generally limited in the case of longitudinal fractures. Reservoir permeability affects the relative performance of a horizontal well stimulated with longitudinal or transverse fractures. The advantage of transverse fractures becomes apparent in low-permeability reservoirs. In general, longitudinally fractured horizontal wells do not perform as effectively as transversely fractured horizontal wells. Horizontal wells stimulated with longitudinal fractures have been reported to achieve better sweep efficiency for water flooding projects in low-permeability, conventional reservoirs.

Higher fracture density along the horizontal section is generally required for transverse fractures, and smaller treatment sizes are required for longitudinal fractures. One perforation cluster or single-entry point is used in each stage when a longitudinal fracture is expected while multiple perforation clusters are used in each stage for transverse fractures. From treatment design point of



view, there are no other significant differences between longitudinal and transverse fractures. Transverse fractures are used almost exclusively to stimulate unconventional shale reservoirs, as multistage transverse fractures help maximize reservoir exposure and drainage volume. Therefore, the remaining part of this section focuses on design considerations of transverse fractures.

To create transverse fractures, the horizontal wellbore must be drilled in the direction of the minimum horizontal principal stress. The orientation of the minimum horizontal stress can be obtained using a number of methods, including the information of wellbore failure orientation in a vertical pilot hole, seismic anisotropy data, crossed-dipole sonic logs, core-based testing, regional tectonic stress map, and geological indications. Wellbore breakouts occur in vertical wells at the same azimuth as the maximum horizontal stress orientation while drilling-induced tensile failures occur at the same azimuth as the minimum horizontal stress orientation, which is  $90^\circ$  to breakouts at the maximum horizontal stress orientation. Therefore, the orientations of these stress-induced wellbore failures can be used to determine the orientations of the far-field horizontal stresses when using data from vertical wells. Mechanical caliper logs are the most commonly used method in detecting breakouts, and are often used to identify stress orientations although less accurate. Far-field fracture monitoring techniques, such as microseismic and tiltmeter mapping, can be used not only to determine the fracture dimensions, but also to estimate the fracture orientation.

### 14.10.2 HORIZONTAL WELL COMPLETION OPTIONS

In the early days, true “openhole” completion without production casing or liner in the payzone was often used for short horizontal wells landed in competent formations with low risk of borehole collapse or instability problems. Another type of horizontal well completions is also often referred to as “openhole,” which involves running casing into the horizontal section without cementing the annulus between the casing and the borehole. In another word, this type of completions leaves an “open hole” behind the casing. To avoid the confusion between the two types of completions, the first type can be called “barefoot” completions and the second type can be referred to as “uncemented” or “uncemented cased-hole” completions. The third type of horizontal well completions is “cemented” completions, in which the entire well is cemented including the production casing or liner in the horizontal section.

Horizontal wells using the “barefoot” completion are generally not good candidates for hydraulic fracturing as there is no way to control fracture initiation location(s) and determine how many fractures are expected to be created along the openhole section. If a fracturing treatment has to be performed in this type of wells, particulate diverters may be required in hope of creating multiple fractures.

Uncemented cased-hole completions are used to account for borehole stability over the expected long well life and for ease of future well intervention procedures. Fracture treatments can be performed in a single stage to stimulate the entire horizontal section using slotted or preperforated liner. Multiple stage treatments can also be performed using multiple perforation clusters in uncemented casing without isolation between stages behind the casing. These practices were once used often in the early days, but have now been abandoned in unconventional reservoirs. The current industry’s practice to perform multiple stage treatments in uncemented casing is to use mechanical or swellable packers to isolate the annulus between the casing and the borehole, and sliding sleeves to provide fluid entry and fracture initiation points.

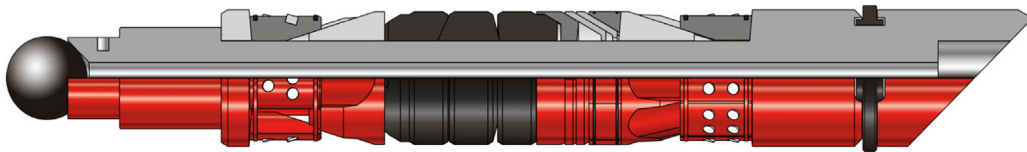
The vast majority of horizontal wells are currently completed using multiple stage fracturing treatments in cemented casing. Multiple stage completion is achieved using cemented sleeves (ball or coiled tubing activated) or the “plug and perf” (PnP) method. The majority of cemented completions in horizontal wells are currently performed using the PnP method, which makes it by far the most commonly used technique for horizontal well completions. Sleeve systems can also be used in combination with packers to achieve multistage horizontal well completion in uncemented casing. There is another type of completion technique, which combines a coiled tubing deployed frac-isolation assembly. These multistage completion options will be described below.

### 14.10.2.1 Plug and perf

In this type of completion, the production casing or liner is fully cemented, and the horizontal well is completed in multiple stages. The treatments for all stages are pumped down the casing. In each stage, the fracture treatment is designed to stimulate the stage interval with multiple perforation clusters. The objective is to allow a fracture to initiate at every perforation cluster. The treatment for the first stage starts from the toe. The fluid entry point(s) on the casing for the first or toe stage is achieved using coiled tubing or tubing conveyed perforating guns or a sleeve system, often called “toe sleeve,” which is placed at the end of the liner. If a toe sleeve is used, the treatment size for the first stage is usually very small.

Once the treatment for the first stage is completed, a wireline-conveyed assembly, consisting of plug, setting tool, perforating guns and firing head plug, is pumped down the casing to the designed location or measured depth. Then set the frac plug to isolate from the previous stage and release the rest of the assembly. The next step is to use the wireline and pull the assembly back to the designed location of the first perforation cluster for the upcoming stage, fire the gun, and pull back further to perforate another cluster, and so on. Once all the clusters are perforated, pull the assembly back to surface. Perform the treatment for the new stage. Repeat this process until all the stages are pumped.

Fig. 14.48 shows a photo of typical plugs used by the PnP method. There are generally three types of plugs. Bridge Plug offers isolation from either above the isolation point or below. Frac Plug is designed to only isolate from above the plug. The ball check valve in the top allows pressure and flow from below to assist in wellbore clean up after stimulation. The ball can either be run in place or dropped from surface after the plug is set. Caged Ball Frac Plug is also designed to only isolate from above the plug. The ball check valve in the top is captured and allows pressure and flow from below to assist in wellbore clean up after stimulation. This tool is specifically



**FIGURE 14.48**

A typical frac plug.

*Image Courtesy of Halliburton.*

designed for deviated wellbores where it may be difficult to obtain a seal with a free floating ball. Isolation plugs are typically milled out with coiled tubing or tubing. Plugs that consist of composite materials give minimal metal content and are easy to drill out.

Fig. 14.49 illustrates the concept of multistage completion using the PnP method. In this example, there are four stages and each stage has four perforation clusters, and a fracture is expected to be created from each perforation cluster. By far, PnP is the most commonly used completion technique in unconventional reservoirs. This technique provides great flexibility for the initiation and placement of multiple fractures. In theory, an “unlimited” number of stages can be performed using this technique. However, when the lateral is too long, due to friction it becomes difficult to pump the PnP assembly to stages near the toe. A hybrid completion is required for long lateral wells: the part of the lateral that is close to the toe is completed using sleeve systems and the rest is completed with the PnP method.

### 14.10.2.2 Sleeve system

A sleeve system can be used in uncemented or cemented cased-hole completions. Sleeves are always run with casing or liner. The number and locations of the sleeves are already determined when the production casing or liner is run into the horizontal section. The number of sleeves that can be run depends on the sleeve type and activation method.

In uncemented cased-hole situations, a sleeve system is run between every two packers. The packers may be swellable or mechanical. As soon as the fluid enters the annulus between the casing and the borehole through the openings in the sleeve, it will find the point(s) of least resistance to break down the formation. Therefore, there is no control over the fracture initiation point(s). The objective of running packers is to isolate the uncemented annulus between stages. However, when packers are set, they create tensile stresses around the borehole where they are set, which provides

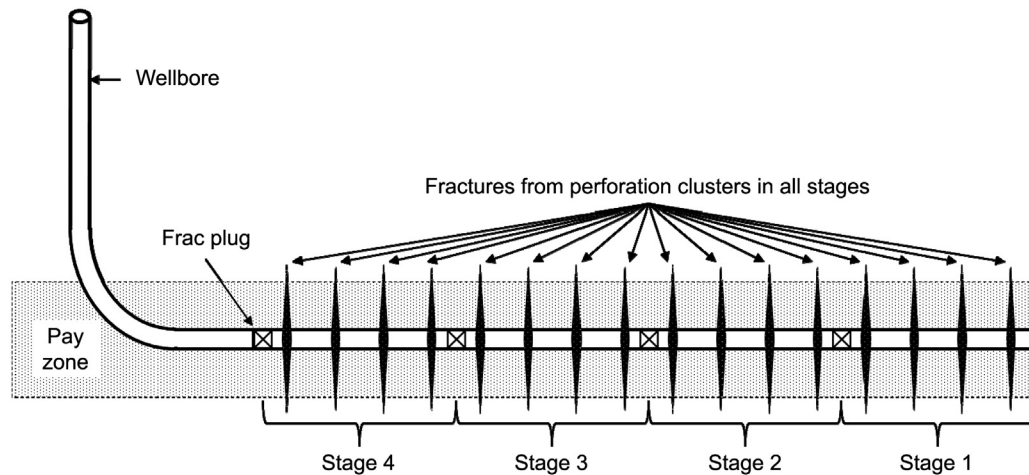


FIGURE 14.49

Illustration of multistage completion using the plug and perf method.



**FIGURE 14.50**

A typical frac sleeve system.

*Image Courtesy of Halliburton.*

a weak point for the fracture initiation. Evidence from fiberoptic and microseismic monitoring results suggests that many fractures initiate at the packers. Unlike openhole or uncemented cased-hole completion in conventional reservoirs, having rocks exposed to the wellbore through an uncemented section does not provide any benefits to production.

In cemented cased-hole situations, sleeves are also run on casing or liner, but cemented in place. Packers are no longer required because cement provides isolation between stages. Sleeve systems in cemented casing or liner can provide control of fracture initiation.

Sliding sleeves are the main components in all sleeve systems and are run as part of the production string (casing or liner). The sleeve system has a number of ports or holes located on the outer layer that are covered and sealed by the inner sliding sleeve. Prior to the fracture treatment, the sliding sleeve is activated to shift and uncover the ports to allow communication between the casing and the formation. Most sleeves are actuated by releasing a ball in sequence (from the smallest to the largest) at surface into the treatment fluid stream, landing it on a baffle in the sleeve, and applying additional hydraulic pressure to shift the sleeve open to expose the ports above the baffle, diverting flow through ports and providing isolation from previous stages. The ball-activated sleeve systems result in restricted IDs on the production casing or liner unless all the inner sliding sleeves and baffles are milled out. The number of sleeves that can be run is limited by the number of balls that are allowed by the system because there must be a minimum size difference between different balls. Although multiple sleeves can be used for each stage in attempt to achieve multiple fractures, the maximum number of sleeves that can be run has limited this type of applications using ball active sleeve systems. Fig. 14.50 shows a photo of a ball activated sleeve system.

Some sleeve systems can be operated by a hydro-mechanical shifting tool run on coiled or jointed tubing for flexibility. When using the mechanical shift sleeve system, there is no limit to the number of sleeves that can be run on a production string (casing or liner). This system allows selective opening and closing for stimulation and production with full wellbore access by using the hydro-mechanical shifting tool.

### **14.10.2.3 Multistage fracturing via coiled tubing**

In vertical well completions, coiled tubing is often used to perform multistage fracturing. A coiled tubing conveyed assembly typically consists of packer and sand-jet perforating sub. Pinpoint (i.e., single perforation cluster) multistage fracturing can be accomplished in a single trip. A typical procedure is as follows: deploy via coiled tubing the assembly across the desired interval for fracturing, set the packer to isolate lower zones, pump sand slurry to perforate the casing and the formation through nozzles on the sand-jet perforating sub, and pump down the treatment down the annulus, unset the packer and move up to the next stage, and repeat the same process until all zones/stages are stimulated. For vertical well stimulation, the packer can sometimes be eliminated

by setting a sand plug to isolate previous stages. The treatments using sand plugs also progress upwards from the deepest zone to the shallowest zone. Sand plug isolation does not work well in horizontal wells.

In horizontal wells, a combination of a coiled tubing deployed isolation assembly with either sliding sleeves or sand-jet perforating sub can also deliver multistage completions in a single trip. The isolation assembly conveyed on coiled tubing can shift the sliding sleeves open and seal the casing below the ports to isolate previous stages. The sleeves have the same ID, collapse and burst strength as the host casing, thus providing full wellbore access and flexibility for future operations.

During the treatment, fluid and slurry are pumped down the annulus between the coiled tubing and the production casing/liner, which makes the coiled tubing as a dead string to monitor real-time, bottom-hole treating pressure. The system can provide quick recovery from screen-outs by reverse-circulating excess proppant out of the well. It also allows the use of sand-jet perforating to add stages as needed, without tripping out of the hole. Once the treatment on the current stage is completed, the coiled tubing can unset the plug on the isolation assembly. The isolation assembly is then moved up to the next sleeve and the sequence is repeated until all stages are completed.

In a fracture treatment involved with multiple perforation clusters or multiple sleeves per stage, there is no control of the placement of fluid and proppant laden slurry into individual fractures. The coiled tubing conveyed system allows a single entry point in each stage in an attempt to provide better fracture coverage along the entire lateral. A major disadvantage is potential expensive work-over operations in case that the coiled tubing gets stuck in the well when failing to clean out a severe screen-out through reverse circulation and other interventions.

### 14.10.3 TREATMENT DESIGN CONSIDERATIONS

Unconventional reservoirs are complex and heterogeneous, and often contain natural fractures and other planes of weakness, which can lead to complex fracture propagation. Stress shadowing effects from previous stages can make treatment design analysis more complicated. All of these have limited the applicability of fracture models to multistage treatment design for horizontal wells in unconventional reservoirs.

It is clear that multiple stages are necessary to stimulate a horizontal well. The number of stages depends on lateral length, completion method, and completion tools. Multiple fracture initiation points in each stage are achieved via sleeves or perforation clusters, but the vast majority of the treatments are performed via multiple perforation clusters. The individual fracture expected to initiate and propagate from each entry point is the building block of stimulation in unconventional wells. The treatment design for a horizontal well should start with the design on a single fracture initiating from one cluster.

In unconventional reservoirs, the majority of fracturing fluids used are slickwater. The main reason to use slickwater in unconventional reservoirs is its low cost. Another reason to use slickwater is that it can penetrate natural fractures and help create more fracture surface area that is required to effectively stimulate unconventional reservoirs. Other advantages of using slickwater include ease of mixing, ability for recovery and reuse, and less damage to the formation. The main disadvantage of slickwater is its low viscosity which results in narrow fracture width and poor proppant transport capability. Because of the low viscosity, proppant transport mainly relies on high flow velocity. Fracturing treatments using slickwater are typically pumped at very high rates ranging from 80 to 130 bbl/min.

In unconventional reservoirs, the vast majority of proppants used are sand. The main reason to use natural sands in unconventional reservoirs is also because of their low cost. Smaller sands are usually used to improve the transport capability of low viscosity fluids through narrow and complex fracture systems. Most commonly used proppant sizes for unconventional developments include 30/50-mesh, 40/70-mesh, and 100-mesh sands. The current trend in the industry is to reduce the proppant sizes, and there are reports that 200-mesh sands are being used to stimulate unconventional reservoirs.

The technique of limited-entry perforating is used to create a large frictional pressure drop across all the perforation clusters in each stage in an attempt to divert the fracturing fluid into every perforation. Generally, a minimum 300 psi pressure differential is considered necessary to provide adequate control over fluid placement in low-permeability reservoirs. The most commonly used perforation design includes 6 shots per foot (spf), 60° phase angle, and 3/8 in. perforating hole size. The perforating interval length per cluster typically ranges from 1 to 2 ft. According to Eq. (14.82), a minimum rate of  $\sim 1.5$  bbl/min is required in order to achieve a minimum 300 psi pressure differential. For example, if a perforation cluster with a length of 2 ft, a shot density of 6 per foot and 3/8 in. perforating hole size is designed, there will be 12 perforation holes, which translates to a design pumping rate of 18 bbl/min per cluster. As a rule of thumb, a pumping rate of  $\sim 20$  bbl/min per cluster is typically required for slickwater fracturing and  $\sim 15$  bbl/min is required for hybrid (slickwater + gelled fluid) fracturing. Once the cluster based treatment design is completed, the number of clusters per stage is then determined by the design pumping rate per cluster and the pumping capacity available. Depending on the perforated interval length in each cluster, the number of clusters per stage typically ranges from 3 to 6, but up to 8 clusters per stage have been used. The treatment volumes for each stage are then determined by the number of clusters per stage.

The stage spacing is determined by the number of clusters and the cluster spacing. There are two approaches to determining cluster and stage locations. In a “geometric” design, all clusters are equally spaced. In an “engineered” design, log-based rock mechanical properties and in-situ stress data are used to determine individual stage locations and corresponding stage spacing to ensure that rocks with similar properties and stresses are stimulated in each stage. The geometric design is the most common method used in the industry, because it is simple, cheap, and streamlines operations in a factory mode. Due to reservoir heterogeneity, rock properties obtained from logging in an 8” borehole cannot warrant similar rock properties far-field. The extra logging cost and concerns about reservoir heterogeneity have limited the application of engineered fracture design.

The fluid and proppant volumes are generally based on the current industry’s best practice. The current trend in the industry favors “high-density” fracturing designs in unconventional reservoirs. The high-density design means tighter cluster spacing, and higher fluid and proppant loading per unit length of completed lateral. Over the past few years, the cluster spacing has been reduced by some operators from 100 ft used initially to 30 ft or even smaller by now. Similarly, the proppant loading per unit length of completed lateral has also been increased significantly from 500–750 lb/ft to 2000 lb/ft or higher. At the time of this writing, the industrial record was over 30 million pounds of sand pumped in a Haynesville well with a lateral length of 10,000 ft (Chesapeake Energy, 2016), which translates to a proppant loading of 3000 lb/ft. The average proppant concentration (including the pad volume) is slightly less than 1.0 lb/gal (ppg) for slickwater treatments, 1.0–2.0 lb/gal for hybrid treatments using slickwater and gelled fluids (linear or crosslinked gels), and 1.5–3.0 lb/gal for gel fracturing.

Multistage fracturing treatment designs for horizontal wells in unconventional reservoirs still evolve rapidly. There is no typical design that can apply to all reservoir conditions. Hundreds of thousands of horizontal wells have been drilled and completed in unconventional plays in North America. Data mining is another way to select fluids, proppants, and treatment volumes.

---

## 14.11 FRACTURING TREATMENT EVALUATION

Various techniques have been developed to evaluate hydraulic fracturing treatments. These fracture diagnostic tools can generally be divided into three categories: indirect, near-wellbore, and far-field diagnostic methods. The indirect method includes net pressure analysis, well testing, back-pressure and Nodal analysis, and production analysis, etc. The near-wellbore diagnostic method includes radioactive proppant tracers, fluid tracers, temperature logging, PLT, DTS and DAS, etc. The far-field diagnostic method includes tiltmeter monitoring, microseismic monitoring, and electromagnetic imaging. These diagnostic technologies are often employed to gain insight into the geometry and complexity of hydraulic fractures. A few fracture diagnostic techniques are described in this section.

### 14.11.1 NET PRESSURE ANALYSIS

Net pressure is the driving force of the fracture propagation. Net pressure matching using a fracture simulator is the first step to evaluate the fracturing treatment. Pseudo-3D models developed for processing speed of pressure-matching applications are widely used. It is well understood that the more accurate the input data is, the more valuable the fracture parameters obtained from the net pressure matching become. Most commercial fracture simulators are generally built with some bells and whistles that can be used to adjust fracture growth behavior and to calibrate the fracture propagation model. However, these options should be left as the last resort, and any changes to these default options are only warranted by calibrating the model using the fracture geometry measured from far-field diagnostics technologies such as microseismic and tiltmeter monitoring methods.

It is important to understand the key parameters that affect the fracture propagation. Closure stress profile determines the fracture shape: excessive height growth occurs if the stress differences between the target zone and bounding layers are small; and confined height growth occurs if significant stress “barriers” are present. The effectiveness of a stress “barrier” is determined by the stress contrast and the magnitude of net pressure obtained from the treatment data. Attention should be paid to the evolution and the magnitude of net pressure and signs of pressure anomalies during pumping. The evolution of net pressure versus time on the Nolte-Smith log-log plot can help identify various types of fracture growth behavior and provide indication of the degree or lack of fracture confinement. A positive slope is an indication of confinement, a negative slope an indication of height growth, and a zero slope an indication of height growth or increased fluid loss possibly due to the dilation of natural fractures.

The magnitude of net pressure is affected by fracture entry friction, stress barrier, Young’s modulus, and tip effect, etc. Fracture entry friction adjustments can be obtained by changing the parameters that



control the near-wellbore effects. Example parameters include the number of perforations open during the treatment, the relative erosion rate of perforation with proppant, and the characteristics of near-wellbore tortuosity. These parameters have a major impact on the bottom-hole pressure response and the net pressure calculated from measured data during pumping. The net pressure curve should be smooth and continuous at the moment of shut-in. A net pressure spike at the shut-in indicates that the wellbore and/or fracture entry friction is not calculated correctly. If pressure decline data for a long shut-in period is available, the net pressure analysis should be focused on the pressure decline data as the data is clean without all friction effects.

#### ***14.11.1.1 Analyzing the net pressure from diagnostic injection tests***

Matching the net pressure of a main fracture treatment without diagnostic injection data offers little value. The analysis of diagnostic injection data can provide the closure stress, fluid efficiency, leak-off coefficient, and the system permeability resulting from fluid leakoff which could be larger than the reservoir permeability. Net pressure match of the diagnostic injection data should also be conducted. This match should be reviewed before proceeding with the analysis of the main treatment itself. Consistency between the parameters obtained from both matches should be maintained and deviation recognized. The first estimate of efficiency and leakoff is obtained from the diagnostic injection or calibration treatment decline analysis. The calibration treatment provides a direct measurement of the efficiency using the graphical G-plot analysis. Then calibration with a model that estimates the geometry of the fracture provides the corresponding leakoff coefficient (Meyer and Jacot, 2000). This leakoff coefficient determination is model dependent.

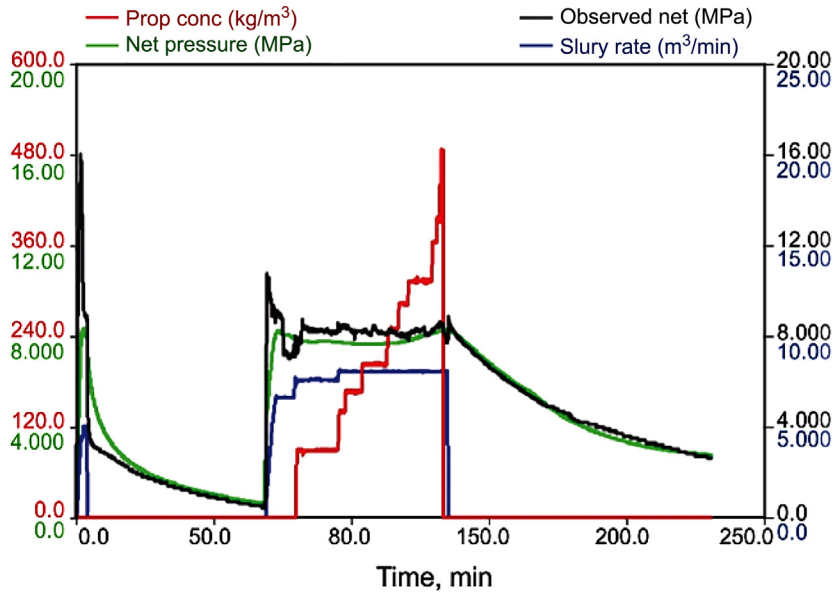
#### ***14.11.1.2 Using pseudo-3D models***

Height constraint is adjusted by increasing the stress difference between the pay-zone and the bounding layer. Stiffness can be increased with an increase of the Young modulus of all the layers that are fractured or to some extent by adding a small shale layer with high stress in the middle of the zone (pinch-point effect). Tip effect can also be adjusted by changing toughness (Meyer et al., 1990). For some simulators, the users have no direct control of this effect, as an apparent toughness is recalculated from the rock toughness and fluid-lag effect.

The final result of the net pressure-matching process should ideally be an exact superposition of the simulation on the pumping record. A perfect match is obtainable by adjusting controlling parameters of a fracture simulator, but this procedure is quite time consuming and is not the goal of the exercise. A typical pressure matching with a pseudo-3D fracturing model is shown in Fig. 14.51 (Sun et al., 2013). The pressure matching can be performed using data from real-time measurements (Wright et al., 1996; Burton et al., 2002). Computer simulation of fracturing operations with recorded treatment data can yield the following fracture parameters:

- Hydraulic fracture half-length
- Propped fracture half-length
- Fracture conductivity
- Fracture height
- Fracture width





**FIGURE 14.51**

Typical net pressure matching with a pseudo-3D fracture model.

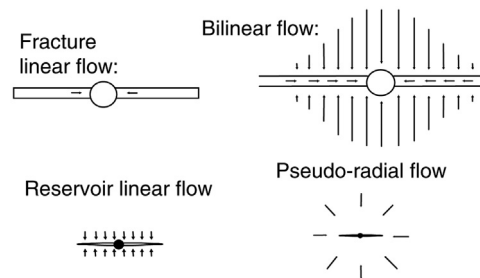
### 14.11.2 PRESSURE TRANSIENT ANALYSIS

Fracture and reservoir parameters can be estimated using data from pressure transient well tests (Cinco-Ley and Samaniego, 1981; Lee and Holditch, 1981). In the pressure transient well-test analysis, the log-log plot of pressure derivative versus time is called a *diagnostic plot*. Special slope values of the derivative curve usually are used for identification of reservoir and boundary models. The transient behavior of a well with a finite-conductivity fracture includes several flow periods. Initially, there is a fracture linear flow characterized by a half-slope straight line; after a transition flow period, the system may or may not exhibit a bilinear flow period, indicated by a one-fourth-slope straight line. As time increases, a reservoir linear flow period might develop. Eventually, the system reaches a pseudo-radial flow period if the drainage area is significantly larger than the fracture dimension, as shown in Fig. 14.52.

During the fracture linear flow period, most of the fluid entering the wellbore comes from the expansion of the system within the fracture. The behavior in the period occurs at very small amounts of time, normally a few seconds for the fractures created during frac-packing operations. Thus, the data in this period, even if not distorted by wellbore storage effect, are still not of practical use.

The bilinear flow regime means two linear flows occur simultaneously. One flow is a linear flow within the fracture and the other is a linear flow in the formation toward the fracture. Bilinear flow analysis gives an estimate of fracture length and conductivity. A calculated pressure distribution during a bilinear flow is illustrated in Fig. 14.52 (Guo and Schechter, 1999).

The reservoir linear flow toward the fracture occurs after the bilinear flow. Linear flow analysis yields an estimate of the reservoir flow capacity (i.e., the product of reservoir permeability and



**FIGURE 14.52**

Four flow regimes that can occur in hydraulically fractured reservoirs.

fracture half-length). Prior to the fracture treatment, a pressure buildup test of the unfractured well should be conducted and analyzed to first obtain the reservoir permeability in order to estimate the fracture half-length (Liu et al., 2003). Unfortunately, unconventional wells do not produce prior to hydraulic fracturing treatments. In this situation, rate transient analysis can provide useful information about the performance of fractured wells (Anderson et al., 2012). If the test time is long enough and there is no boundary effect, a system pseudo-radial flow will eventually occur. Pseudo-radial flow analysis provides an estimate of formation permeability and pressure. The reader is referred to Chapter 12, Well Problem Identification for analysis and interpretation of pressure transient data.

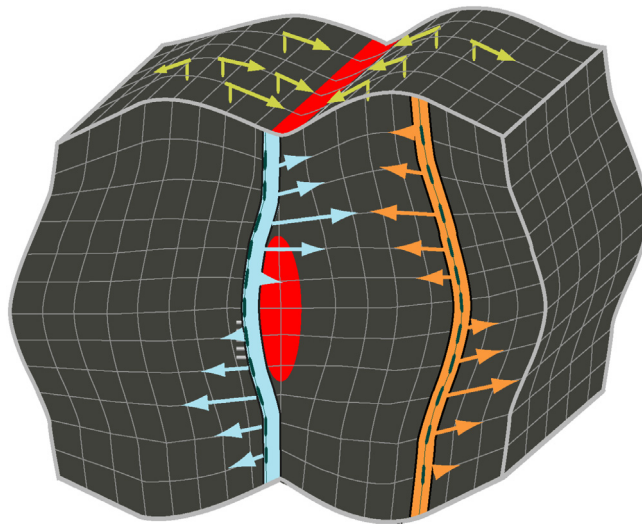
It is important to note that by no means does the pressure transient data analysis give details of the fracture geometry such as fracture width conductivity near the wellbore, which can dominate the posttreatment well performance in modest or high-permeability reservoirs. The fracture conductivity near the wellbore can be significantly lower than that in the region away from the wellbore. This can occur because of a number of mishaps. Over displacement of proppant leads to the fracture unsupported near the wellbore, resulting in fracture closure. Flowback reduces the amount of proppant near the wellbore, which results in less fracture width supported by the proppant. If the proppant grains are not strong enough to withstand the stress concentration in the near-wellbore region, they will be crushed during production, resulting in tight fracture near the wellbore. The reduced fracture width near the wellbore affects well productivity because of the fracture choking effect. Posttreatment flow tests should be run to verify well performance. The effect of near-wellbore fracture geometry on posttreatment well production is of special significance in deviated and horizontal wells (Chen and Economides, 1999). This is because a fracture from an arbitrarily oriented well “cuts” the wellbore at an angle, thereby limiting the communication between the wellbore and the reservoir. This feature of fluid entry to the wellbore itself causes the fracture-choking effect, even though the near-wellbore fracture is perfectly propped.

### 14.11.3 FAR-FIELD DIAGNOSTIC TECHNIQUES

The far-field fracture diagnostic technologies such as microseismic and tiltmeter monitoring methods are often used to gain insight into the geometry and complexity of hydraulic fractures. This section briefly describes these two techniques.

Creation of a hydraulic fracture involves parting of the rock and displacing the fracture faces to create fracture width. The principle of tiltmeter fracture mapping is simply to infer hydraulic fracture geometry by measuring this fracture-induced rock deformation (Wright et al., 1998; Griffin et al., 2000). As shown in Fig. 14.53, the induced deformation field radiates in all directions and can be measured from the surface using surface tiltmeter arrays and from downhole using wireline-conveyed downhole tiltmeter arrays. At the surface, the induced deformation magnitudes are so small, typically in the order of one ten-thousandth of a centimeter, that they are impossible to measure. Fortunately, measuring the gradient of the displacement field, or the tilt field, is far easier. Tiltmeters are highly sensitive instruments with a maximum resolution of up to one nano-radian. Surface tiltmeter arrays can be used to obtain fracture azimuth, dip, depth to fracture center, and total fracture volume, vertical or horizontal fracture, identify complex fractures such as T-shaped fractures, transverse and longitudinal fractures, characterize the stimulated reservoir volume, and measure surface deformation due to production, water and steam flooding processes. Downhole tiltmeter arrays can be used to measure the fracture height, and the length if the monitor well is in the right location.

Microseismic monitoring is a technique to measure the locations of microseisms created during a hydraulic fracture treatment (Warpinski et al., 2001; Liu et al., 2006). The formation around the fracture undergoes significant stress increases and large changes in the pore pressure during a fracture treatment. Both of these changes affect the stability of planes of weakness adjacent to the hydraulic fracture and cause them to undergo shear slippage. The shear slippages are similar to earthquakes along faults, but with much lower magnitude. The name “microseism” or “microseismic” is thus often used to describe this phenomenon. Fig. 14.54 illustrates microseisms induced during hydraulic fracturing. Microseisms generated during a hydraulic fracture treatment emit



**FIGURE 14.53**

Earth deformation created from a hydraulic fracture.

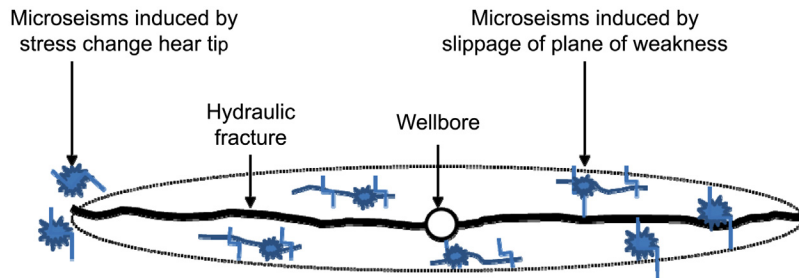
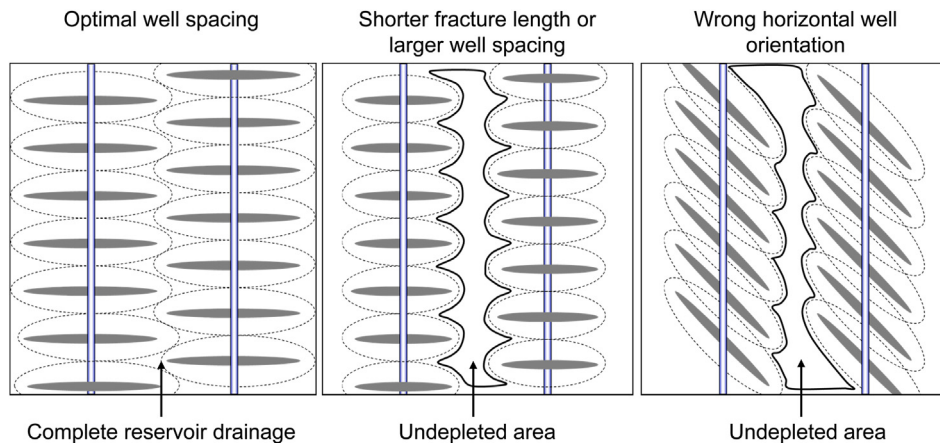
**FIGURE 14.54**

Illustration of microseisms induced during hydraulic fracturing.

**FIGURE 14.55**

Effects of horizontal well spacing and orientation on reservoir drainage.

elastic waves, shear and compressional waves, at frequencies that generally fall within the acoustic frequency range. These acoustic signals can be detected using appropriate receivers and processed to determine the locations of these microseismic events. Once the microseisms are located, the actual fracture is interpreted within the envelope of microseisms mapped. Microseismic monitoring can be used not only to provide fracture geometry and azimuth, but also to improve reservoir development and avoid risks of fracture growth into water zones or geological hazards.

Far-field fracture diagnostics can provide useful insights for optimizing well spacing, well placement, and completion design. Reservoir drainage in tight rock formations is limited by the extent that hydraulic fractures can reach. Fig. 14.55 illustrates the effects of horizontal well spacing and orientation on reservoir drainage. Poor reservoir drainage can result from short fracture length, large well spacing, wrong horizontal well orientation, or wrong well pattern.

---

## 14.12 SUMMARY

This chapter presents various aspects of hydraulic fracturing. Topics covered in this chapter include basic rock mechanics, hydraulic fracture geometry overview, hydraulic fracture models, fracturing pressure analysis, fracturing materials and equipment, fractured well productivity, fracturing treatment design, frac-pack treatments, fracturing horizontal wells, and fracturing treatment evaluation.

---

## REFERENCES

- Ahmed, U., 1984. A practical hydraulic fracturing model simulating necessary fracture geometry, fluid flow and leakoff, and proppant transport. In: SPE Unconventional Gas Recovery Symposium, 13–15 May, Pittsburgh, PA. doi:10.2118/12880-MS.
- Allison, D.B., Curry, S.S., Todd, B.L., 2011. Restimulation of wells using biodegradable particulates as temporary diverting agents. In: Canadian Unconventional Resources Conference, 15–17 November, Calgary, Alberta, Canada. doi:10.2118/149221-MS.
- Anderson, D.M., Liang, P., Okouma Mangha, V., 2012. Probabilistic forecasting of unconventional resources using rate transient analysis: case studies. In: SPE Americas Unconventional Resources Conference, 5–7 June, Pittsburgh, PA. doi:10.2118/155737-MS.
- Anderson, E.M., 1951. *The Dynamics of Faulting and Dyke Formation with Application to Britain*. second ed. Oliver and Boyd, Edinburgh.
- Argawal, R.G., Carter, R.D., Pollock, C.B., 1979. Evaluation and prediction of performance of lowerpermeability gas wells stimulated by massive hydraulic fracturing, *JPT* March 1979 .Trans. AIME 267, 362–372
- Barenblatt, G.I., 1962. Mathematical theory of equilibrium cracks. *Adv. Appl. Mech* 7, 56–131.
- Barree, R.D., A practical numerical simulator for three dimensional fracture propagation in heterogeneous media. In: Proceedings of the Reservoir Simulation Symposium, San Francisco, CA, 403–411 november 1983. SPE 12273.
- Barree, R.D., Barree, V.L., Craig, D., 2009. Holistic fracture diagnostics: consistent interpretation of prefracture injection tests using multiple analysis methods. *Soc. Pet. Eng.* 24 (03), 396–406. Available from: <http://dx.doi.org/10.2118/107877-PA>.
- Blyton, C.A.J., Gala, D.P., Sharma, M.M., 2015. A comprehensive study of proppant transport in a hydraulic fracture. In: SPE Annual Technical Conference and Exhibition, 28–30 September, Houston, TX. doi:10.2118/174973-MS.
- Burnham, J.W., Harris, L.E., McDaniel, B.W., 1980. Developments in hydrocarbon fluids for high-temperature fracturing. *Soc. Pet. Eng.* 32 (02), 217–220. Available from: <http://dx.doi.org/10.2118/7564-PA>.
- Burton, R.C., Davis, E.R., Hodge, R.M., Stomp, R.J., Palthe, P.W., Saldungaray, P., Innovative completion design and well performance evaluation for effective Frac-packing of long intervals: a case study from the West Natuna Sea, Indonesia. In: Presented at the SPE International Petroleum Conference and Exhibition held 10–12 February 2002, in Villahermosa, Mexico. Paper SPE 74351.
- Carter, R.D., 1957. Derivation of the general equation for estimating the extent of the fractured area, Appendix I of optimum fluid characteristics for fracture extension. In: Howard, G.C., Fast, C.R. (Eds.), *Drilling and Production Practice*. American Petroleum Institute, New York, pp. 261–269.
- Chen, Z., Economides, M.J., 1999. Effect of near-wellbore fracture geometry on fracture execution and post-treatment well production of deviated and horizontal wells. *SPE Prod. Facil.* 14 (03), 177–186.
- Chesapeake Energy. 2016. Q2 2016 chesapeake energy earnings conference call transcript. <<http://www.chk.com/investors/earnings-calls-archive>> .

- Cinco-Ley, H., Samaniego, F., 1981. Transient pressure analysis for fractured wells. *J. Pet. Technol.* 33 (09), 1749–1766.
- Cleary, M.P., 1980. Comprehensive design formulae for hydraulic fracturing. In: Presented at the SPE Annual Technology Conference held in Dallas, TX, September 1980. SPE 9259.
- Cleary, M.P., Kavvas, M., Lam, K.Y., 1983. Development of a fully three-dimensional simulator for analysis and design of hydraulic fracturing. In: SPE/DOE Low Permeability Gas Reservoirs Symposium, 14–16 March, Denver, CO. doi:10.2118/11631-MS.
- Cleary, M.P., Johnson, D.E., Kogsbøll, H.-H., Owens, K.A., Perry, K.F., de Pater, C.J., et al., 1993. Field implementation of proppant slugs to avoid premature screen-out of hydraulic fractures with adequate proppant concentration. In: Low Permeability Reservoirs Symposium, 26–28 April, Denver, CO. doi:10.2118/25892-MS.
- Clifton, R.J., Abou-sayed, A.S., 1979. On the computation of the three-dimensional geometry of hydraulic fractures. In: Presented at the SPE/DOE Low Perm. Gas Res. Symposium, held in Denver, CO, May 1979. SPE 7943.
- Clifton, R.J., Abou-Sayed, A.S., A variational approach to the prediction of the three-dimensional geometry of hydraulic fractures. In: Paper SPE 9879, presented at the SPE Low Permeability Symposium, Denver, CO, 27–29 May, 1981.
- Conway, M.W., Almond, S.W., Briscoe, J.E., Harris, L.E., 1983. Chemical model for the rheological behavior of crosslinked fluid systems. *Soc. Pet. Eng.* 35 (02), 315–320. Available from: <http://dx.doi.org/10.2118/9334-PA>.
- Conway, M.W., Venditto, J.J.J., Reilly, P.B., Smith, K.W., 2011. An examination of clay stabilization and flow stability in various North American gas shales. In: SPE Annual Technical Conference and Exhibition, 30 October–2 November, Denver, CO. doi:10.2118/147266-MS.
- Cottrell, M., Hosseinpour, H., Dershowitz, W., 2013. Rapid discrete fracture analysis of hydraulic fracture development in naturally fractured reservoirs. In: Unconventional Resources Technology Conference, 12–14 August, Denver, CO. doi:10.1190/URTEC2013-245.
- Christanti, Y., Ferrara, G., Ritz, T., Busby, B., Jeanpert, J., Abad, C., et al., A new technique to control fines migration in poorly consolidated sandstones - laboratory development and case histories. In: SPE European Formation Damage Conference, 7–10 June, Noordwijk, The Netherlands. doi:10.2118/143947-MS, June 2011.
- Dean, R.H., Schmidt, J.H., 2009. Hydraulic-fracture predictions with a fully coupled geomechanical reservoir simulator. *Soc. Pet. Eng.* 14 (04), 707–714. Available from: <http://dx.doi.org/10.2118/116470-PA>.
- Deng, J., Mou, J., Hill, A.D., Zhu, D., 2012. A new correlation of acid-fracture conductivity subject to closure stress. *SPE Prod. Oper.* 27 (02), 158–169.
- Economides, M.J., Martin, T., 2007. *Modern Fracturing - Enhancing Natural Gas Production*. ET Publishing, Houston, TX.
- Economides, M.J., Nolte, K.G., 2000. *Reservoir Stimulation*. third ed. John Wiley & Sons, New York.
- Economides, M.J., Hill, A.D., Ehlig-Economides, C., 1994. *Petroleum Production Systems*. Prentice Hall PTR, Upper Saddle River, NJ.
- Fischer, C., Constien, V., Vining, C., 2016. Gravel pack sizing criteria - It's time to re-evaluate. In: SPE International Conference and Exhibition on Formation Damage Control, 24–26 February, Lafayette, LA. doi:10.2118/179023-MS.
- Fredd, C.N., McConnell, S.B., Boney, C.L., England, K.W., 2000. Experimental study of hydraulic fracture conductivity demonstrates the benefits of using proppants. In: SPE Rocky Mountain Regional/Low-Permeability Reservoirs Symposium and Exhibition, 12–15 March, Denver, Colorado. Available from: <http://dx.doi.org/10.2118/60326-MS>.
- Fung, R.L., Vilajakumar, S., Cormack, D.E., 1987. Calculation of vertical fracture containment in layered formations. *SPE Form. Eval.* 2 (4), 518–523. Available from: <http://dx.doi.org/10.2118/14707-PA>

- Geertsma, J., de Klerk, F., 1969. A rapid method of predicting width and extent of hydraulic induced fractures. *J. Pet. Technol* 21, 1571–1581.
- Gidley, J.L., Holditch, S.A., Nierode, D.E., Veatch Jr., R.W., 1989. Recent Advances in Hydraulic Fracturing, J.L., Monograph Series. Society of Petroleum Engineers, Richardson, TX.
- Guo, B., Schechter, D.S., 1999. A simple and rigorous IPR equation for vertical and horizontal wells intersecting long fractures. *J. Can. Pet.* 38 (7), 46–54.
- Griffith, A.A., 1921. The phenomena of rupture and flow in solids. *Phil. Trans. Roy. Soc.* 221, 163–198.
- Griffith, A.A., 1924. The theory of rupture. In: *Proceeding of the 1st International Congress for Applied Mechanics*, Delft, Netherlands, pp. 55–63.
- Griffin, L.G., Wright, C.A., Davis, E.J., Wolhart, S.L., Moschovidis, Z.A., 2000. Surface and downhole tiltmeter mapping: an effective tool for monitoring downhole drill cuttings disposal. In: *SPE Annual Technical Conference and Exhibition*, 1-4 October, Dallas, TX. doi:10.2118/63032-MS.
- Gu, H., Weng, X., Lund, J.B., Mack, M.G., Ganguly, U., Suarez-Rivera, R., 2012. Hydraulic fracture crossing natural fracture at nonorthogonal angles: a criterion and its validation. *Soc. Pet. Eng.* 27 (01), 20–26. Available from: <http://dx.doi.org/10.2118/139984-PA>.
- Howard, G.C., Fast, C.R., 1957. Optimum fluid characteristics for fracture extension. *Drilling and Production Practice*. American Petroleum Institute, New York, pp. 261–269.
- Hubbert, M.K., Willis, D.G., Mechanics of hydraulic fracturing. In: Paper 686-G, presented at the SPE Annual Meeting, Los Angeles, CA, 14–17 October 1956; also in *J. Pet. Technol.* (September 1957) 9, (6), 153–168 and *Trans. AIME* (1957) 210.
- Inui, S., Ishida, T., Nagaya, Y., Nara, Y., Chen, Y., Chen, Q., 2014. AE Monitoring of Hydraulic Fracturing Experiments in Granite Blocks Using supercritical CO<sub>2</sub>, Water and Viscous Oil. 48th U.S. Rock Mechanics/Geomechanics Symposium, 1–4 June, Minneapolis, Minnesota, American Rock Mechanics Association. ISBN: 978-0-9894844-1-1.
- Irwin, G., 1957. Analysis of stresses and strains near the end of a crack traversing a plate. *J. Appl. Mech.* 24, 361–364.
- Kaufman, P.B., Anderson, R.W., Parker, M.A., Brannon, H.D., Neves, A.R., Abney, K.L., et al., 2007. Introducing new API/ISO procedures for proppant testing. In: *SPE Annual Technical Conference and Exhibition*, 11–14 November, Anaheim, CA. doi:10.2118/110697-MS.
- Keck, R.G., Nehmer, W.L., Strumolo, G.S., 1992. A new method for predicting friction pressures and rheology of proppant-laden fracturing fluids. *Soc. Pet. Eng.* 07 (01), 21–28. Available from: <http://dx.doi.org/10.2118/19771-PA>.
- Khristianovich, S.A., Zheltov, Y.P., 1955. Formation of vertical fractures by means of highly viscous liquid. In: *Proceedings of the SPE Fourth World Petroleum Congress held in Rome*, Section II. 1955, pp. 579–586.
- Kresse, O., Weng, X., Chuprakov, D., Romain, R., Cohen, C., 2013. Effect of flow rate and viscosity on complex fracture development in ufm model. doi: 10.5772/56406, in *Effective and sustainable hydraulic fracturing*, ISBN: 978-953-51-1137-5, book edited by Bungler, A.P., McLennan, J., and Jeffrey, R., published InTech on May 17, 2013 under CC BY 3.0 license.
- Lacy, L.L., 1997. Dynamic rock mechanics testing for optimized fracture designs. In: *SPE Annual Technical Conference and Exhibition*, 5–8 October, San Antonio, TX. doi:10.2118/38716-MS.
- Lee, M.H., Roberts, L.D., 1980. Effect of heat of reaction on temperature distribution and acid penetration in a fracture. *Soc. Pet. Eng.* 20 (06), 501–507. Available from: <http://dx.doi.org/10.2118/7893-PA>.
- Lee, W.J., Holditch, S.A., 1981. Fracture evaluation with pressure transient testing in low-permeability gas reservoirs. *J. Pet. Technol* 33 (9), 1776–1792.
- Liu, X., Cipolla, C.L., Mayerhofer, M., 2003. Case history of hydraulic fracture performance in a channel reservoir. In: *SPE Annual Technical Conference and Exhibition*, 5–8 October, Denver, CO. doi:10.2118/84396-MS.



- Liu, X., Xu, Y., Zhao, Z., Mu, L., Liu, J., Alcott, J., 2006. Application of microseismic mapping and modeling analysis to understand hydraulic fracture growth behavior. In: SPE International Symposium and Exhibition on Formation Damage Control, 15–17 February, Lafayette, LA. doi:10.2118/98219-MS.
- Lo, K.K., Dean, R.H., 1989. Modeling of acid fracturing. *Soc. Pet. Eng.* 4 (02), 194–200. Available from: <http://dx.doi.org/10.2118/17110-PA>.
- Maley, D., Farion, G., Giurea-Bica, G., O’Neil, B., 2013. Non-polymeric permanent clay stabilizer for shale completions. In: SPE European Formation Damage Conference & Exhibition, 5–7 June, Noordwijk, The Netherlands. doi:10.2118/165168-MS.
- McCartney, E.S., Kennedy, R.L., 2016. A family of unique diverting technologies increases unconventional production and recovery in multiple applications—Initial fracturing, refracturing, and acidizing. In: SPE Hydraulic Fracturing Technology Conference, 9–11 February, The Woodlands, TX. doi:10.2118/179115-MS.
- McClure, M.W., Babazadeh, M., Shiozawa, S., Huang, J., 2016. Fully coupled hydromechanical simulation of hydraulic fracturing in 3D discrete-fracture networks. *Soc. Pet. Eng.* 21 (04), 1302–1320. Available from: <http://dx.doi.org/10.2118/173354-PA>.
- Meyer, B.R., 1986. Design formulae for 2-D and 3-D vertical hydraulic fractures: model comparison and parametric studies. In: Paper SPE 15240, presented at the SPE Unconventional Gas Technology Symposium, Louisville, KY, 18–21 May 1986.
- Meyer, B.R., Jacot, R.H., 2000. Implementation of fracture calibration equations for pressure dependent leak-off. In: Presented at the 2000 SPE/AAPG Western Regional Meeting, held in Long Beach, CA, 19–23 June 2000. Paper SPE 62545.
- Meyer, B.R., Cooper, G.D., Nelson, S.O., 1990. Real-time 3-D hydraulic fracturing simulation: theory and field case studies. In: Presented at the 65th Annual Technical Conference and Exhibition of the Society of Petroleum Engineers, held in New Orleans, LA, 23–26 September 1990. Paper SPE 20658.
- Motiee, M., Johnson, M., Ward, B., Gradl, C., McKimmy, M., Meeheib, J., 2016. High concentration polyacrylamide-based friction reducer used as a direct substitute for guar-based borate crosslinked fluid in fracturing operations. In: SPE Hydraulic Fracturing Technology Conference, 9-11 February, The Woodlands, TX. doi:10.2118/179154-MS.
- Nguyen, P.D., Rickman, R.D., 2012. Foaming aqueous-based curable treatment fluids enhances placement and consolidation performance. In: SPE International Symposium and Exhibition on Formation Damage Control, 15-17 February, Lafayette, LA. doi:10.2118/151002-MS.
- Nierode, D.D., Kruk, K.F., 1973. An evaluation of acid fluid loss additives, retarded acids, and acidized fracture conductivity. In: Paper SPE 4549 presented at the Fall Meeting of the SPE of AIME, Las Vegas, NV, 30 September–3 October, 1973.
- Nierode, D.E., Williams, B.B., 1971. Characteristics of acid reaction in limestone formations. *Soc. Pet. Eng.* 11 (04), 406–418. Available from: <http://dx.doi.org/10.2118/3101-PA>.
- Nolte, K.G., Determination of fracture parameters from fracturing pressure decline. In: Paper SPE 8341, presented at the SPE Annual Technical Conference and Exhibition, Las Vegas, NV, 23–26 September, 1979.
- Nolte, K.G., 1986. Determination of proppant and fluid schedules from fracturing-pressure decline. *Soc. Pet. Eng.* 1 (04), 255–265. Available from: <http://dx.doi.org/10.2118/13278-PA>.
- Nolte, K.G., Smith, M.B., 1981. Interpretation of fracturing pressures. *J. Pet. Technol.* 03 (09), 1767–1775.
- Nordgren, R.P., 1972. Propagation of vertical hydraulic fracture. *SPE J.* 12 (04), 306–314.
- Penny, G.S., Zelenev, A., Lett, N., Paktinat, J., Neil, B.J., 2012. Nano surfactant system improves post frac oil and gas recovery in hydrocarbon rich gas reservoirs. In: SPE Improved Oil Recovery Symposium, 14–18 April, Tulsa, OK. doi:10.2118/154308-MS.
- Perkins, T.K., Kern, L.R., 1961. Width of hydraulic fracture. *J. Pet. Technol* 13 (09), 937–949.



- Profit, M.L., Dutko, M., Yu, J., 2015. Developing a framework to simulate the hydraulic fracturing of tight gas reservoirs based on integrative adaptive remeshing and combined finite/discrete element approach. In: 49th U.S. Rock Mechanics/Geomechanics Symposium, 28 June–1 July, San Francisco, CA.
- Roberts, L.D., Guin, J.A., 1975. A new method for predicting acid penetration distance. *Soc. Pet. Eng.* 15 (04), 277–286. Available from: <http://dx.doi.org/10.2118/5155-PA>.
- Roussel, N.P., Sharma, M.M., 2011. Optimizing fracture spacing and sequencing in horizontal-well fracturing. *Soc. Pet. Eng.* 26 (02), 173–184. Available from: <http://dx.doi.org/10.2118/127986-PA>.
- Samir, M., 2013. Novel technique to increase production from tight reservoirs using Hi-Way Frac technique for the first time at Middle East and North Africa. In: North Africa Technical Conference and Exhibition, 15–17 April, Cairo, Egypt. doi:10.2118/164655-MS.
- Settari, A., 1993. Modeling of acid-fracturing treatments. *Soc. Pet. Eng.* 08 (01), 30–38. Available from: <http://dx.doi.org/10.2118/21870-PA>.
- Settari, A., Cleary, M.P., 1984. Three-dimensional simulation of hydraulic fracturing. In: Paper SPE 10504, presented at the SPE Symposium on Reservoir Simulation, New Orleans, LA, January 31–February 3 1982; also in *J. Pet. Technol.* (July 1984) 36 (7), 1177–1190.
- Settari, A., Sullivan, R.B., Hansen, C., 2001. A new two-dimensional model for acid-fracturing design. *Soc. Pet. Eng.* 16 (04), 200–209. Available from: <http://dx.doi.org/10.2118/73002-PA>.
- Simonson, E.R., Abou-Sayed, A.S., Clifton, R.J., 1978. Containment of massive hydraulic fractures. *Soc. Pet. Eng. J.* 18 (1), 27–32. Available from: <http://dx.doi.org/10.2118/6089-PA>.
- Smith, M.B., Miller, W.K., Haga, J., Tip screen-out fracturing: a technique for soft, unstable formations. In: Paper SPE 13273, presented at the SPE Annual Technical Conference and Exhibition, Houston, TX, 16–19 September 1984.
- Sneddon, I.N., 1946. The distribution of stress in the neighbourhood of a crack in an elastic solid. *Proc. Royal Soc. Lond.* 187 (Ser. A.), 229–260.
- Sneddon, I.N., Elliott, A.A., 1946. The opening of a Griffith crack under internal pressure. *Quart. Appl. Math.* IV, 262.
- Stewart, B.R., Mullen, M.E., Howard, W.J., Norman, W.D., 1995. Use of a solids-free viscous carrying fluid in fracturing applications: an economic and productivity comparison in shallow completions. In: SPE European Formation Damage Conference, 15–16 May, The Hague, Netherlands. doi:10.2118/30114-MS.
- Sun, H., Zuo, J., Liu, X., Mayerhofer, M.J., Wu, J., Zhang, P., et al., 2013. CBM development in the qinshui basin: hydraulic fracture complexities revealed by modeling analysis and microseismic monitoring. In: SPE Unconventional Resources Conference and Exhibition-Asia Pacific, 11–13 November, Brisbane, Australia. doi:10.2118/167045-M.
- Tudor, E.H., Nevison, G.W., Allen, S., Pike, B., 2009. 100% gelled LPG fracturing process: an alternative to conventional water-based fracturing techniques. In: SPE Eastern Regional Meeting, 23–25 September, Charleston, WV. doi:10.2118/124495-MS.
- Ward, V.L., 1986. N<sub>2</sub> and CO<sub>2</sub> in the oil field: stimulation and completion applications. *Soc. Pet. Eng.* 1 (4), 275–278. Available from: <http://dx.doi.org/10.2118/12594-PA>.
- Warpinski, N.R., Wolhart, S.L., Wright, C.A., 2001. Analysis and prediction of microseismicity induced by hydraulic fracturing. *Soc. Pet. Eng.* 9 (1), 24–33. Available from: <http://dx.doi.org/10.2118/71649-MS>.
- Warpinski, N., Kramm, R.C., Heinze, J.R., Waltman, C.K., 2005. Comparison of single- and dual-array microseismic mapping techniques in the barnett shale. In: SPE Annual Technical Conference and Exhibition, 9–12 October, Dallas, Texas. doi.org/10.2118/95568-MS.
- Warpinski, N.R., Mayerhofer, M.J., Vincent, M.C., Cipolla, C.L., Lolon, E., 2008. Stimulating unconventional reservoirs: maximizing network growth while optimizing fracture conductivity. In: Paper SPE 114173 presented at the SPE Unconventional Reservoirs Conference, Keystone, CO, 10–12 February 2008. doi:10.2118/114173-MS.

- Weng, X., Kresse, O., Cohen, C.E., Wu, R., Gu, H., 2011. Modeling of hydraulic fracture network propagation in a naturally fractured formation. *Soc. Pet. Eng.* 26 (4), 368–380. Available from: <http://dx.doi.org/10.2118/140253-MS>.
- Williams, B.B., Gidley, J.L., Schechter, R.S., 1979. *Acidizing Fundamentals*. Society of Petroleum Engineers, Richardson, TX.
- Wright, C.A., Tanigawa, J.J., Shixin, M., Li, Z., 1995. Enhanced hydraulic fracture technology for a coal seam reservoir in central china. In: *International Meeting on Petroleum Engineering*, 14–17 November, Beijing, China. doi:10.2118/29989-MS.
- Wright, C.A., Weijers, L., Germani, G.A., MacIvor, K.H., Wilson, M.K., Whitman, B.A., 1996. Fracture treatment design and evaluation in the pakenham field: a real-data approach. in: *SPE Annual Technical Conference and Exhibition*, 6-9 October, Denver, CO. doi:10.2118/36471-MS.
- Wright, C.A., Davis, E.J., Minner, W.A., Ward, J.F., Weijers, L., Schell, E.J., et al., 1998. Surface tiltmeter fracture mapping reaches new depths - 10,000 feet and beyond? In: *SPE Rocky Mountain Regional/Low-Permeability Reservoirs Symposium*, 5-8 April, Denver, CO. doi:10.2118/39919-MS.
- Wu, K., Olson, J.E., 2015. Simultaneous multifracture treatments: fully coupled fluid flow and fracture mechanics for horizontal wells. *Soc. Pet. Eng.* 20 (02), 337–346. Available from: <http://dx.doi.org/10.2118/167626-PA>.
- Xu, G., Wong, S.-W., 2013. Interaction of multiple non-planar hydraulic fractures in horizontal wells. In: *International Petroleum Technology Conference*, 26–28 March, Beijing, China. doi:10.2523/IPTC-17043-MS.
- Yoshimura, K., Matsui, H., Morita, N., 2016. Development of polyglycolic- and polylactic-acid fluid-loss-control materials for fracturing fluids. *Soc. Pet. Eng.* 30 (4), 295–309. Available from: <http://dx.doi.org/10.2118/168179-PA>.
- Zhu, D., Oeth, C.V., Hill, A.D., 2013. Acid fracturing: fully 3D simulation and performance prediction. *society of petroleum engineers*. In: *SPE Hydraulic Fracturing Technology Conference*, 4–6 February, The Woodlands, TX. doi:10.2118/163840-MS.

---

## PROBLEMS

- 14.1.** A sandstone at a depth of 8000 ft has a Poisson's ratio of 0.275 and a poro elastic constant of 0.70. The average density of the overburden formation is 162 lb/ft<sup>3</sup>. The pore–pressure gradient in the sandstone is 0.46 psi/ft. Assuming a tectonic stress of 500 psi and a tensile strength of the sandstone of 800 psi, predict the breakdown pressure for the sandstone.
- 14.2.** A carbonate rock at a depth of 12,000 ft has a Poisson's ratio of 0.3 and a poro elastic constant of 0.75. The average density of the overburden formation is 178 lb/ft<sup>3</sup>. The pore–pressure gradient in the sandstone is 0.45 psi/ft. Assuming a tectonic stress of 1000 psi and a tensile strength of the rock of 1000 psi, predict the breakdown pressure for the sandstone.
- 14.3.** A gas reservoir has a permeability of 5 md. A vertical well of 0.328-ft radius draws the reservoir from the center of an area of 320 acres. If the well is hydraulically fractured to create a 2000-ft long, 0.15-in. wide fracture of 150,000-md permeability around the center of the drainage area, what would be the fold of increase in well productivity?
- 14.4.** A reservoir has a permeability of 100 md. A vertical well of 0.328-ft radius draws the reservoir from the center of an area of 160 acres. If the well is hydraulically fractured to create an 800-ft long, 0.24-in. wide fracture of 240,000-md permeability around the center of the drainage area, what would be the fold of increase in well productivity?

- 14.5.** For the following situation, estimate the minimum required compressive strength of proppant. If HSP is used, estimate the proppant pack conductivity:

Formation depth:	12,000 ft
Overburden density:	165 lb/ft <sup>3</sup>
Poisson's ratio:	0.25
Biot constant:	0.72
Reservoir pressure:	6800 psi
Production drawdown:	3000 psi

- 14.6.** For the Problem 14.5, predict the maximum expected surface injection pressure using the following additional data:

Specific gravity of fracturing fluid:	1.1
Viscosity of fracturing fluid:	1.5 cp
Tubing inner diameter:	3.0 in.
Fluid injection rate:	20 bpm

- 14.7.** The following data are given for a hydraulic fracturing treatment design:

Pay zone thickness:	50 ft
Young's modulus of rock:	$4 \times 10^6$ psi
Poisson's ratio:	0.25
Fluid viscosity:	1.25 cp
Leakoff coefficient:	0.003 ft/min <sup>1/2</sup>
Proppant density:	185 lb/ft <sup>3</sup>
Proppant porosity:	0.4
Fracture half-length:	1000 ft
Fracture height:	70 ft
Fluid injection rate:	35 bpm
Final proppant concentration:	5 ppg

Assuming PKN fracture, estimate

- a. Fluid volume requirement
  - b. Proppant mixing schedule
  - c. Proppant weight requirement
  - d. Propped fracture width
- 14.8.** Predict the productivity index of the fractured well described in Problem 14.7.

## WELL WORKOVER

## 15

---

## 15.1 INTRODUCTION

Well workover refers to any kind of oil and gas well intervention involving invasive techniques, such as wireline, coiled tubing, or snubbing. It is an expensive process of pulling and replacing a well completion to repair an existing production well for the purpose of restoring, prolonging, or enhancing the production of hydrocarbons. Well workover can be employed for different reasons, including: (1) production tubing is damaged due to operational factors like corrosion to the point where well integrity is threatened; (2) downhole components such as tubing, retrievable downhole safety valves, or electrical submersible pumps may have malfunctioned, needing replacement; (3) completion itself is in a bad condition; and (4) there is a need of new completion suitable for deteriorated reservoir conditions. This chapter provides fundamentals that are essential for planning successful workover operations.

---

## 15.2 TYPES OF WORKOVERS

Workovers are classified, to some degree, on the basis of the reasons for them. Another way to describe types of workovers is to divide them into (1) jobs performed primarily to influence the reservoir and (2) jobs applied to the wellbore (including the cement) and its associated equipment. Workovers done primarily to influence the reservoir can be subdivided into (1) work done for the zone already open, and (2) work done to shut off the existing zone in favor of opening a new zone, termed a *recompletion*. Operations typically done in an existing zone may include stimulation, reperforating, perforating additional intervals, and plugging off unwanted perforations (because of high gas or water production). Recompletion work varies depending on whether the new zone is above or below the currently open zone. If above, the lower zone will be abandoned via squeeze cementing, a cement plug, or a mechanical bridge plug, and the zone of interest will be perforated and stimulated. Appropriate outflow equipment will then be installed. If the new zone is below, the existing zone will probably be squeeze cemented (in the same manner as repairing casing). The cement in the wellbore is drilled out, the lower zone perforated and stimulated, and production equipment run. Some wells have had sufficient well work done upon initial completion to permit recompletion by simply using a wireline to run plugs and open sleeves.

Wellbore workovers can include casing or equipment repair, but may also simply involve cleaning out fill over the producing zone or circulating chemicals to remove scale or paraffin. Many workovers involve the installation, maintenance, and repair of artificial lift equipment in the wellbore. About 85% of the oil wells in the United States are on some form of artificial lift.

Approximately 85% of those wells are on rod pump, 10% on gas lift, and 5% on submersible or hydraulic pumps. Rigs are required for most artificial lift workovers; however, many gas lift wells can be serviced with a wireline.

---

## 15.3 WORKOVER CONSIDERATIONS

Although the considerations necessary to design a workover are virtually the same as those for standard well completion, some special issues are mentioned here. They are:

- Safety must receive special attention. The tendency to consider a workover as “routine” sometimes reduces the level of safety attentiveness.
- Well pressure may be a primary consideration. If the open zone has experienced significant depletion, the circulation of fluids becomes difficult or even impossible. The well killing process will introduce significant amounts of fluids into the reservoir with the potential for formation damage. If the wellbore is now open to high pressure, safety is of paramount importance. If existing well equipment has been in the well for a long time, it may not be capable of containing high shut-in pressure.
- In thermal projects, the elevated temperatures create special needs for doing a workover safely.
- The condition of the well equipment may be a major factor in what and how much is done in a particular workover. The toll taken by corrosion, erosion, and mechanical wear may be significant, particularly if the casing is involved. Extra funds and time may need to be allocated to cover potential squeeze cement jobs, fishing operations, and equipment replacement.

The procedure of well workover depends on well condition. In general the well must first be killed before any workover. Reverse circulation is very common in killing wells. The intense nature of this operation often requires no less than the capabilities of a drilling rig. The workover begins by removing the wellhead and possibly the flow line, then lifting the tubing hanger from the casing head, thus beginning to pull the completion out of the well. The string will almost always be fixed in place by at least one production packer. If the packer is retrievable it can be released easily enough and pulled out with the completion string. If it is permanent, then it is common to cut the tubing just above it and pull out the upper portion of the string. If necessary, the packer and the tubing left in hole can be milled out, though more commonly, the new completion will make use of it by setting a new packer just above it and running new tubing down to the top of the old.

---

## 15.4 WORKOVER EQUIPMENT

Workovers can be done with conventional rigs (smaller but similar to drilling rigs) or nonconventional systems. Conventional rigs can be equipped to handle almost all types of work that may be required. Nonconventional systems allow specific types of work to be done without pulling the tubing, disassembling the Christmas tree, or even killing the well. This is accomplished by using lubricators and packoff equipment at the surface and by running the required equipment inside the production tubing. Common types of nonconventional systems are wireline units,

coiled tubing units, and snubbing units. Generally, these systems are designed to do a relatively narrow scope of work.

Wireline units use special equipment on a solid wireline to gather data (pressure, temperature, and depth) and to set, manipulate, and/or retrieve tubing plugs, sliding sleeves, flow regulators, gas lift valves, safety valves, and wireline fishing tools. Wireline equipment can also be used to cut paraffin and remove wellbore fill. Prior planning, good operators, good equipment, and reasonable well conditions are prerequisites to the success of this method.

Coiled tubing units find application in cleanout work, stimulation, plugback jobs, and unloading wells with nitrogen. Coiled tubing units can have 10,000–15,000 ft of pipe (usually 1-in. outside diameter) that can be reeled continuously into the wellbore. The pipe can be used to pump into the well and circulate fluids such as water, acid, or cement. The use of a dynadrill permits some drilling with coiled tubing. Limitations of coiled tubing include the reduced strength of the tubing and low pumping rates (high friction pressure because of the diameter and length). Coiled tubing can be run into wells against pressures of up to 5000 psi.

Snubbing units use hydraulic pressure and rams to introduce small, coupled tubing into the well, if necessary, against pressures above 5000 psi. The tubing is stronger and can be rotated so that tougher cleanout or fishing jobs can be accomplished. Snubbing units are used for the same type of jobs as are coiled tubing units, but their compactness is an advantage in offshore work. They are slow and expensive, but in the right applications, they are the more economical way to accomplish the task.

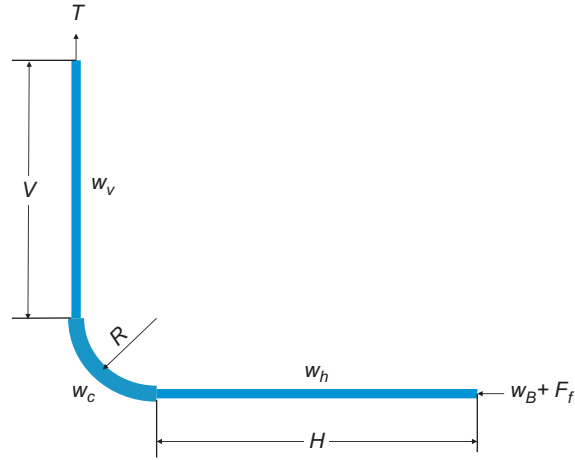
## 15.5 ENGINEERING CALCULATIONS

Success of workover operations requires careful engineering of work tools and work fluids. Typical engineering tasks involve calculations of required hook load of work string, dynamic pressure, and flow rate for hole cleaning. The tubing mechanics presented in Chapter 9, Well Tubing and Packers can be used for designing workover operations involving tubing string for well stimulations. The fluid mechanics described in Chapter 4, Wellbore Flow Performance can be utilized for hydraulics calculations. This section presents mathematical models that can be employed for analyzing axial force transfer in working string and determining the hydraulics requirement for hole cleaning.

### 15.5.1 FORCE TRANSFER IN WORKOVER STRINGS

Tubing strings are often used in workover operations to convey work tools. While the issue of force transfer in tubing string in vertical wells is straight forward for most engineers, the issue in horizontal wells is problematic for many field personnel. This is essentially due to the friction between wellbore wall and the tubing string.

Fig. 15.1 shows the configuration of a work string in a horizontal well, where  $V$  is the vertical depth of the kick off point,  $R$  is the radius of curvature of the curve section, where  $H$  is the length of the horizontal wellbore,  $T$  is the tension at the surface (hook load),  $\mu$  is the average friction coefficient,  $W_B$  is the contact force from the bottom hole (weight on bit for hole extending operations or additional force to set a packer), and  $F_f$  is the fluid pressure force acting on the cross-sectional


**FIGURE 15.1**

Nomenclature of a tubing string in a horizontal well.

area of the string. The unit weight  $w_v$ ,  $w_c$ , and  $w_h$  are the buoyant weights per unit length of the string in the vertical, curve, and horizontal sections. The proportion of the string in tension depends on the direction of motion, i.e., upward pull or downward slack-off.

### 15.5.1.1 Workover strings in slack-off

If the string is not buckled locked-up, in a downward motion, the compressive force at the kick off point (zero inclination angle) is expressed as:

$$F_0 = w_v V - T \quad (15.1)$$

The compressive force at any point with an inclination angle  $\theta$  in the curve section is expressed as:

$$F_\theta = F_0 + w_c R [\sin(\theta) - \mu(1 - \cos(\theta))] \quad (15.2)$$

The compressive force at the end point of the curve section ( $\pi/2$  inclination angle) is expressed as:

$$F_{\pi/2} = F_0 + w_c R(1 - \mu) \quad (15.3)$$

The compressive force at the end point of the curve section is also found based on the condition at the lower end of string:

$$F_{\pi/2} = \mu w_h H + W_B + F_f \quad (15.4)$$

Combing Eqs. (15.1), (15.3), and (15.4) gives the following equation:

$$T = w_v V + w_c R(1 - \mu) - \mu w_h H - F_f - W_B \quad (15.5)$$

which gives the contact force in the form of

$$W_B = w_v V - T + w_c R(1 - \mu) - \mu w_h H - F_f \quad (15.6)$$

One of the applications of this equation is to predict the maximum reachable length of the horizontal wellbore in well extending operations:

$$H_{\max} = \frac{w_v V + w_c R(1 - \mu) - W_{B\min} - F_f}{\mu w_h} \quad (15.7)$$

where  $W_{B\min}$  is the minimum weight on bit required to drill in a given pay zone.

### 15.5.1.2 Workover strings in pull

In an upward motion, the compression force at the kick off point (zero inclination angle) is expressed as:

$$F_0 = w_v V - T \quad (15.8)$$

The compressive force at any point with an inclination angle  $\theta$  in the curve section is expressed as:

$$F_\theta = F_0 + w_c R[\sin(\theta) + \mu(1 - \cos(\theta))] \quad (15.9)$$

The compressive force at the end point of the curve section ( $\pi/2$  inclination angle) is expressed as:

$$F_{\pi/2} = F_0 + w_c R(1 + \mu) \quad (15.10)$$

The compressive force at the end point of the curve section is also found based on the condition at the lower end of string:

$$F_{\pi/2} = -\mu w_h H - F_p + F_f \quad (15.11)$$

where  $F_p$  is the anchor force from packer. Combining Eqs. (15.8), (15.10), and (15.11) gives

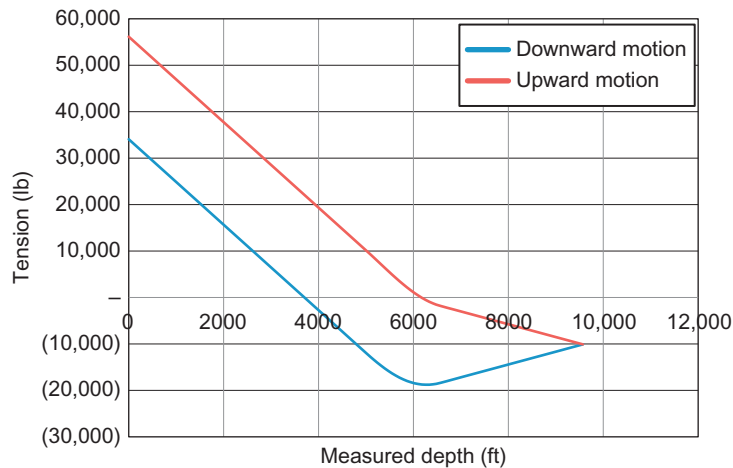
$$T = w_v V + w_c R(1 + \mu) + \mu w_h H - F_f + F_p \quad (15.12)$$

This equation can be used for estimating the expected tension required to set the tubing string on the tubing head with the bottom end anchored to a packer.

**Example Problem 15.1** For the horizontal well described below, assuming zero contact force from bottom hole or packer, plot tension force profile in the string during (1) downward motion and (2) upward motion.

String OD	3.500 in.
String ID	2.992 in.
Horizontal section length	3000 ft
Radius of curvature	1000 ft
Vertical section length	5000 ft
Friction coefficient	0.30
Density of workover fluid	12.50 ppg



**FIGURE 15.2**

Calculated tension profiles in the workover string for Example Problem 15.1.

**Solution** Example Problem 15.1 can be solved using computer spreadsheet String Tension in Horizontal Wells.xls. The result is shown in Fig. 15.2.

### 15.5.2 WORKOVER FLUID FLOW RATE REQUIREMENT

Workover for extending well by drilling through existing wellbore requires a minimum fluid flow rate to clean the hole. Workover for cleaning sanded wells requires a minimum flow rate to remove sand/debris from the well. This minimum flow rate can be estimated based on the minimum required fluid velocity expressed by:

$$\nu_{\min} = \nu_{sl} + \nu_{tr} \quad (15.13)$$

where  $\nu_{sl}$  and  $\nu_{tr}$  are called particle slip velocity and particle transport velocity, respectively.

Because of the complex geometry and boundary conditions involved, analytical expressions describing particle slip velocity have been obtained only for very idealized conditions. For a solid particle falling in a Newtonian fluid, its terminal slip velocity can be expressed as:

$$\nu_{sl} = 1.89 \sqrt{\frac{d_s}{f_p} \left( \frac{\rho_s - 7.48\rho_f}{7.48\rho_f} \right)} \quad (15.14)$$

where  $\nu_{sl}$  = particle slip velocity, ft/s

$d_s$  = equivalent particle diameter, in.

$\rho_s$  = particle density, lb/ft<sup>3</sup>

$\rho_f$  = fluid density, ppg

$f_p$  = particle friction factor, dimensionless.

The particle friction factor  $f_p$  is a function of the Reynolds number  $N_{Re}$  and particle sphericity  $\psi$ . The sphericity is defined as the surface area of a sphere containing the same volume as the particle divided by the surface area of the particle. A conservative value for cuttings' sphericity is 0.8. Engineering charts are available for finding the values of the friction factor (Bourgoyne et al., 1986). Fang et al. (2008) developed the following correlation to replace the charts:

$$f_p = 10 \left( A' + B' \log(N_{ReP}) + C' [\log(N_{ReP})]^2 \right) \quad (15.15)$$

where

$$A' = 2.2954 - 2.2626\psi + 4.4395\psi^2 - 2.9825\psi^3 \quad (15.16)$$

$$B' = -0.4193 - 1.9014\psi + 3.3416\psi^2 - 2.0409\psi^3 \quad (15.17)$$

$$C' = 0.1117 + 0.0553\psi - 0.1468\psi^2 + 0.1145\psi^3 \quad (15.18)$$

where the particle Reynolds number is defined as

$$N_{ReP} = \frac{928\rho_f v_{sl} d_s}{\mu} \quad (15.19)$$

where  $\mu$  is viscosity of Newtonian fluid in cp. Because the slip velocity is implicitly involved in Eqs. (15.14) and (15.19), the slip velocity can only be solved numerically (trial and error). A computer program called *Minimum Flow.xls* is attached to this book for easy calculations.

The particle transport velocity can be calculated based on rate of penetration and solid particle concentration in the stream:

$$v_{tr} = \frac{\pi d_b^2}{4c_s A_a} \left( \frac{R_p}{3600} \right) \quad (15.20)$$

where  $d_b$  is drill bit diameter,  $c_s$  is the permissible solid particle concentration in the annulus,  $A_a$  is the cross-sectional area of annulus, and  $R_p$  is rate of penetration.

Once the required minimum flow velocity is computed, the required minimum flow rate can be calculated based on the cross-sectional area of the annulus. In a vertical wellbore the minimum required flow rate is expressed as:

$$q_{\min V} = v_{\min} A_a \quad (15.21)$$

In a deviated wellbore with an inclination angle  $\alpha$ , the minimum required flow rate is expressed as:

$$q_{\min \alpha} = (1 + 0.005556\alpha)[1 + 0.4\sin(2\alpha)]q_{\min V} \quad (15.22)$$

where the inclination angle  $\alpha$  is in degree. It is seen from this equation that the wellbore section with inclination angle  $55^\circ$  requires the highest flow rate.

**Example Problem 15.2** For the horizontal well described below, estimate the required minimum workover fluid flow rate for hole cleaning:

Critical inclination angle:	55°
Solid specific gravity:	2.75 water = 1
Particle Sphericity:	0.85 ball = 1
Fluid viscosity:	10 cp
Fluid density:	85 lb/ft <sup>3</sup>
Annulus OD:	4.89 in.
Annulus ID:	3.5 in.
Equivalent diameter of particle:	0.2 in.
Bit size:	4.5 in.
Permissible solid concentration:	2%
Rate of penetration:	30 ft/hr

**Solution** Example Problem 15.2 can be solved using computer spreadsheet Minimum Flow Rate.xls. The result is 62 gpm.

---

## 15.6 SUMMARY

Well workover refers to any kind of oil and gas well intervention involving invasive techniques, such as wireline, coiled tubing, or snubbing. It is an expensive process of pulling and replacing a well completion to repair an existing production well for the purpose of restoring, prolonging, or enhancing the production of hydrocarbons. This chapter describes the types of workovers, summarizes workover considerations, and discusses workover equipment. Engineering calculations are briefly outlined and illustrated with computer programs.

---

## REFERENCES

- Bourgoyne Jr., A.T., Millheim, K.K., Chenevert, M.E., Young Jr., F.S., 1986. Applied drilling engineering, SPE Textbook Series, Dallas, TX.
- Fang, Q, Guo, B., Ghalambor, A., 2008. Formation of underwater cuttings piles in offshore drilling. SPE Drill. Compl. J. Vol. 23, No. 1.

---

**PROBLEMS**

- 15.1.** For the horizontal well described below, assuming zero contact force from bottom hole or packer, plot tension force profile in the string during (1) downward motion and (2) upward motion.

String OD	2.875 in.
String ID	2.441 in.
Horizontal section length	2500 ft
Radius of curvature	750 ft
Vertical section length	4000 ft
Friction coefficient	0.30
Density of workover fluid	11.50 ppg

- 15.2.** For the horizontal well described below, estimate the required minimum workover fluid flow rate for hole cleaning:

Critical inclination angle:	55°
Solid specific gravity:	2.75 water = 1
Particle Sphericity:	0.80 ball = 1
Fluid viscosity:	5 cp
Fluid density:	85 lb/ft <sup>3</sup>
Annulus OD:	4.89 in.
Annulus ID:	3.0 in.
Equivalent diameter of particle:	0.2 in.
Bit size:	4.5 in.
Permissible solid concentration:	1%
Rate of penetration:	60 ft/hr

# ARTIFICIAL LIFT METHODS

# IV

*Most oil reservoirs are of the volumetric type where the driving mechanism is the expansion of solution gas when reservoir pressure declines because of fluid production. Oil reservoirs will eventually not be able to produce fluids at economical rates unless natural driving mechanisms (e.g., aquifer and/or gas cap) or pressure maintenance mechanisms (e.g., water flooding or gas injection) are present to maintain reservoir energy. The only way to obtain a high production rate of a well is to increase production pressure drawdown by reducing the bottom-hole pressure with artificial lift methods.*

*Approximately 50% of wells worldwide need artificial lift systems. The commonly used artificial lift methods include the following:*

- Sucker rod pumping
- Gas lift
- Electrical submersible pumping
- Hydraulic piston pumping

- Hydraulic jet pumping
- Plunger lift
- Progressing cavity pumping

*Each method has applications for which it is the optimum installation. Proper selection of an artificial lift method for a given production system (reservoir and fluid properties, wellbore configuration, and surface facility restraints) requires a thorough understanding of the system. Economics analysis is always performed. Relative advantages and disadvantages of artificial lift systems are discussed at the beginning of each chapter in this part of the book. The chapters in this part provide production engineers with fundamentals of sucker rod pumping and gas lifts, as well as an introduction to other artificial lift systems. The following three chapters are included in this part of the book:*

Chapter 16: Sucker Rod Pumping 16/515

Chapter 17: Gas Lift 17/549

Chapter 18: Other Artificial Lift Methods 18/603

## SUCKER ROD PUMPING

## 16

---

## 16.1 INTRODUCTION

Sucker rod pumping is also referred to as “beam pumping.” It provides mechanical energy to lift oil from bottom-hole to surface. It is efficient, simple, and easy for field people to operate. It can pump a well down to very low pressure to maximize oil production rate. It is applicable to slim holes, multiple completions, and high-temperature and viscous oils. The system is also easy to change to other wells with minimum cost. The major disadvantages of beam pumping include excessive friction in crooked/deviated holes, solid-sensitive problems, low efficiency in gassy wells, limited depth due to rod capacity, and bulky in offshore operations. Beam pumping trends include improved pump-off controllers, better gas separation, gas handling pumps, and optimization using surface and bottom-hole cards.

---

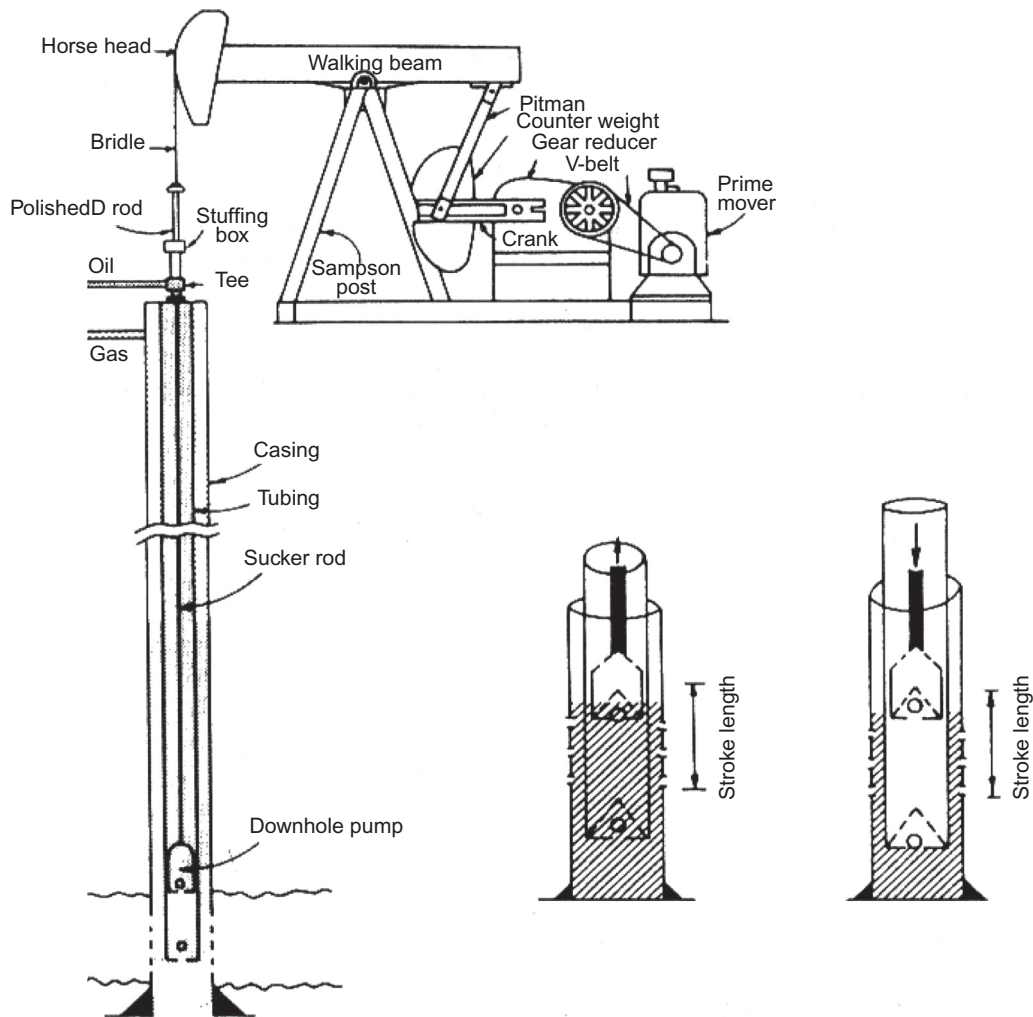
## 16.2 PUMPING SYSTEM

As shown in Fig. 16.1, a sucker rod pumping system consists of a pumping unit at surface and a plunger pump submerged in the production liquid in the well.

The *prime mover* is either an electric motor or an internal combustion engine. The modern method is to supply each well with its own motor or engine. Electric motors are most desirable because they can easily be automated. The power from the prime mover is transmitted to the input shaft of a gear reducer by a *V-belt drive*. The output shaft of the gear reducer drives the *crank arm* at a lower speed ( $\sim 4\text{--}40$  revolutions per minute [rpm] depending on well characteristics and fluid properties). The rotary motion of the crank arm is converted to an oscillatory motion by means of the *walking beam* through a *pitman arm*. The *horse's head* and the *hanger cable* arrangement is used to ensure that the upward pull on the sucker rod string is vertical at all times (thus, no bending moment is applied to the *stuffing box*). The *polished rod* and stuffing box combine to maintain a good liquid seal at the surface and, thus, force fluid to flow into the “T” connection just below the stuffing box.

Conventional pumping units are available in a wide range of sizes, with stroke lengths varying from 12 to almost 200 in. The strokes for any pumping unit type are available in increments (unit size). Within each unit size, the stroke length can be varied within limits (about six different lengths being possible). These different lengths are achieved by varying the position of the pitman arm connection on the crank arm.

Walking beam ratings are expressed in allowable polished rod loads (PRLs) and vary from approximately 3000–35,000 lb. Counterbalance for conventional pumping units is accomplished by



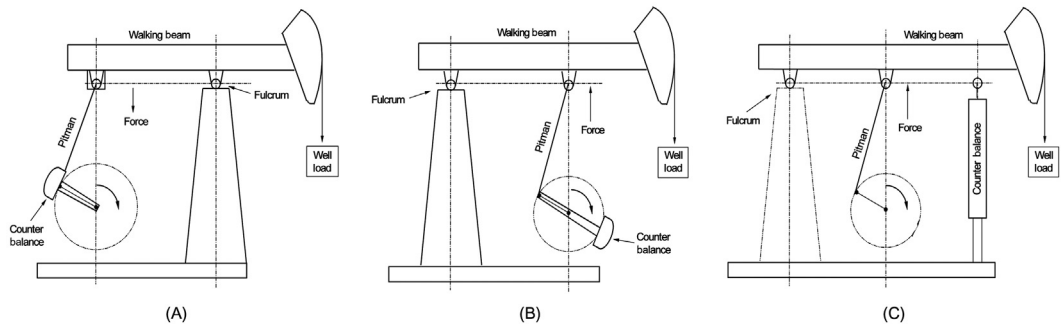
**FIGURE 16.1**

A diagrammatic drawing of a sucker rod pumping system (Golan and Whitson, 1991).

placing weights directly on the beam (in smaller units) or by attaching weights to the rotating crank arm (or a combination of the two methods for larger units). In more recent designs, the rotary counterbalance can be adjusted by shifting the position of the weight on the crank by a jackscrew or rack and pinion mechanism.

There are two other major types of pumping units. These are the Lufkin Mark II and the Air-Balanced Units (Fig. 16.2). The pitman arm and horse's head are in the same side of the walking beam in these two types of units (Class III lever system). Instead of using counterweights in Lufkin





**FIGURE 16.2**

Sketch of three types of pumping units: (A) conventional unit; (B) Lufkin Mark II Unit; (C) air-balanced unit.

Mark II type units, air cylinders are used in the air-balanced units to balance the torque on the crankshaft.

The American Petroleum Institute (API) has established designations for sucker rod pumping units using a string of characters containing four fields. For example,

C-228D-200-74.

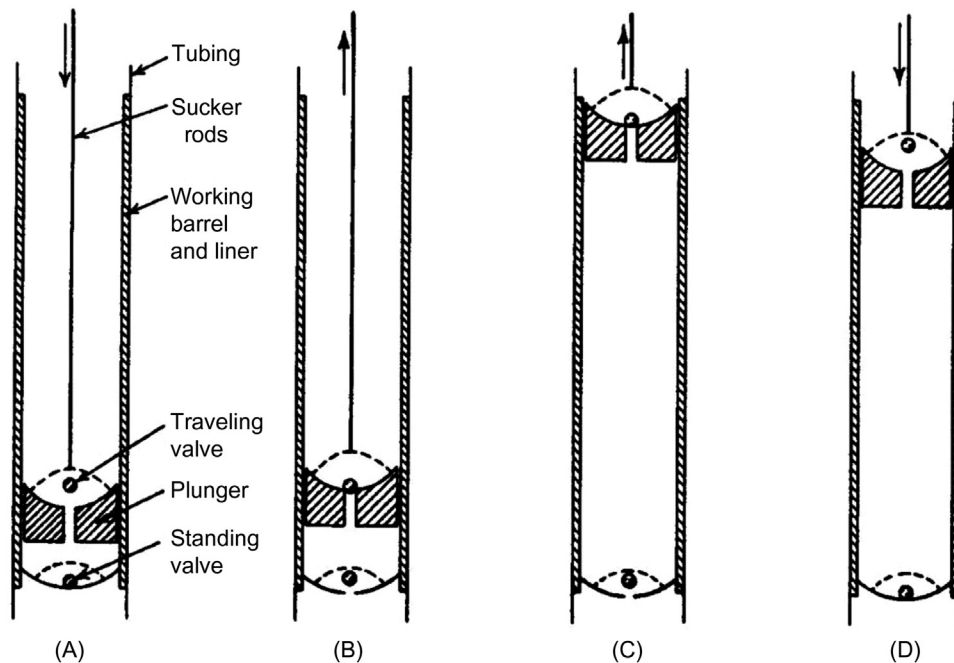
The first field is the code for type of pumping unit. *C* is for conventional units, *A* is for air-balanced units, *B* is for beam counterbalance units, and *M* is for Mark II units. The second field is the code for peak torque rating in thousands of inch-pounds and gear reducer. *D* stands for double-reduction gear reducer. The third field is the code for PRL rating in hundreds of pounds. The last field is the code for stroke length in inches.

Fig. 16.3 illustrates the working principle of a plunger pump. The pump is installed in the tubing string below the dynamic liquid level. It consists of a *working barrel* and *liner*, *standing valve* (SV), and *traveling valve* (TV) at the bottom of the *plunger*, which is connected to *sucker rods*.

As the plunger is moved downward by the sucker rod string, the TV is open, which allows the fluid to pass through the valve, which lets the plunger move to a position just above the SV. During this downward motion of the plunger, the SV is closed; thus, the fluid is forced to pass through the TV.

When the plunger is at the bottom of the stroke and starts an upward stroke, the TV closes and the SV opens. As upward motion continues, the fluid in the well below the SV is drawn into the volume above the SV (fluid passing through the open SV). The fluid continues to fill the volume above the SV until the plunger reaches the top of its stroke.

There are two basic types of plunger pumps: tubing pump and rod pump (Fig. 16.4). For the tubing pump, the working barrel or liner (with the SV) is made up (i.e., attached) to the bottom of the production tubing string and must be run into the well with the tubing. The plunger (with the TV) is run into the well (inside the tubing) on the sucker rod string. Once the plunger is seated in the working barrel, pumping can be initiated. A rod pump (both working barrel and plunger) is run into the well on the sucker rod string and is seated on a wedged type seat that is fixed to the bottom joint of the production tubing. Plunger diameters vary from  $\frac{3}{8}$  to  $4\frac{3}{8}$  in. Plunger area varies from 0.307 in.<sup>2</sup> to 17.721 in.<sup>2</sup>.



**FIGURE 16.3**

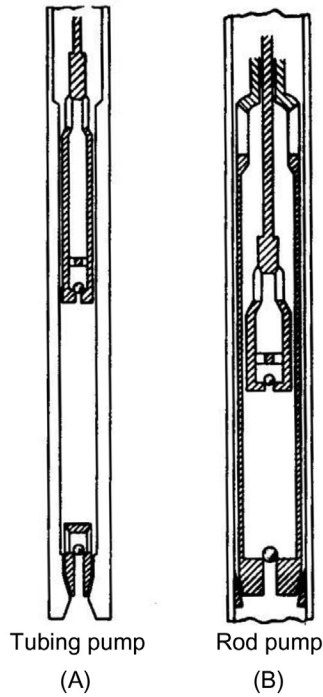
The pumping cycle: (A) plunger moving down, near the bottom of the stroke; (B) plunger moving up, near the bottom of the stroke; (C) plunger moving up, near the top of the stroke; (D) plunger moving down, near the top of the stroke (Nind, 1964).

## 16.3 POLISHED ROD MOTION

The theory of polished rod motion has been established since the 1950s (Nind, 1964). Fig. 16.5 shows the cyclic motion of a polished rod in its movements through the stuffing box of the conventional pumping unit and the air-balanced pumping unit.

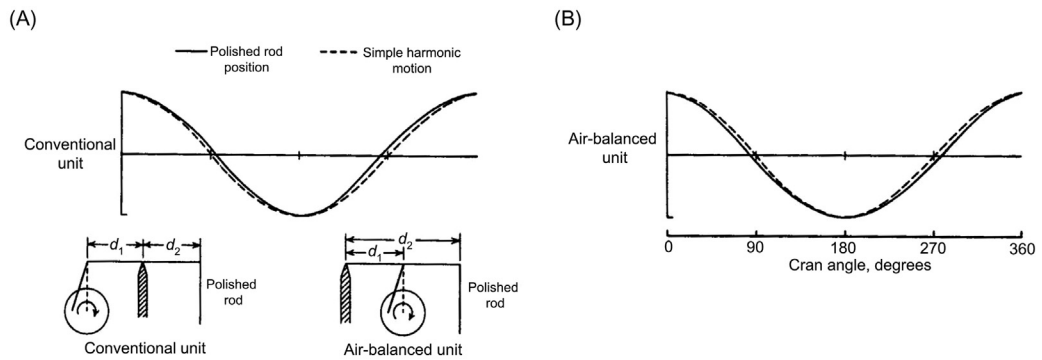
### 16.3.1 CONVENTIONAL PUMPING UNIT

For this type of unit, the acceleration at the bottom of the stroke is somewhat greater than true simple harmonic acceleration. At the top of the stroke, it is less. This is a major drawback for the conventional unit. Just at the time the TV is closing and the fluid load is being transferred to the rods, the acceleration for the rods is at its maximum. These two factors combine to create a maximum stress on the rods that becomes one of the limiting factors in designing an installation. Table 16.1 shows dimensions of some API conventional pumping units. Parameters are defined in Fig. 16.6.



**FIGURE 16.4**

Two types of plunger pumps (Nind, 1964). (A) Tubing pump and (B) Rod pump.



**FIGURE 16.5**

Polished rod motion for (A) conventional pumping unit and (B) air-balanced unit (Nind, 1964).

**Table 16.1 Conventional Pumping Unit API Geometry Dimensions**

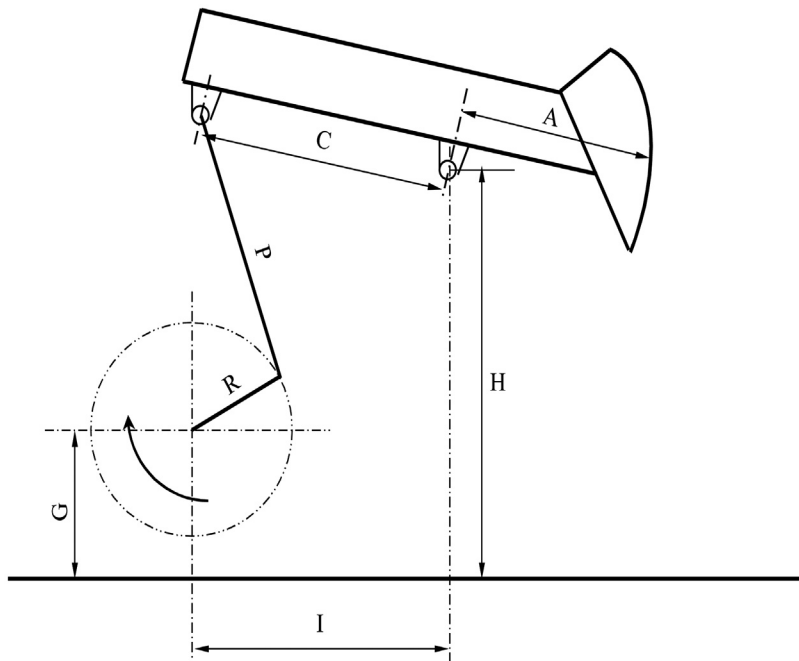
API Unit Designation	A (in.)	C (in)	I (in.)	P (in.)	H (in.)	G (in.)	R1, R2, R3 (in.)	C <sub>s</sub> (lb)	Torque Factor
C-912D-365-168	210	120.03	120	148.5	237.88	86.88	47, 41, 35	-1500	80.32
C-912D-305-168	210	120.03	120	148.5	237.88	86.88	47, 41, 35	-1500	80.32
C-640D-365-168	210	120.03	120	148.5	237.88	86.88	47, 41, 35	-1500	80.32
C-640D-305-168	210	120.03	120	148.5	237.88	86.88	47, 41, 35	-1500	80.32
C-456D-305-168	210	120.03	120	148.5	237.88	86.88	47, 41, 35	-1500	80.32
C-912D-427-144	180	120.03	120	148.5	237.88	86.88	47, 41, 35	-650	68.82
C-912D-365-144	180	120.03	120	148.5	237.88	86.88	47, 41, 35	-650	68.82
C-640D-365-144	180	120.03	120	148.5	238.88	89.88	47, 41, 35	-650	68.82
C-640D-305-144	180	120.08	120	144.5	238.88	89.88	47, 41, 35	-520	68.45
C-456D-305-144	180	120.08	120	144.5	238.88	89.88	47, 41, 35	-520	68.45
C-640D-256-144	180	120.08	120	144.5	238.88	89.88	47, 41, 35	-400	68.45
C-456D-256-144	180	120.08	120	144.5	238.88	89.88	47, 41, 35	-400	68.45
C-320D-256-144	180	120.08	120	144.5	238.88	89.88	47, 41, 35	-400	68.45
C-456D-365-120	152	120.03	120	148.5	238.88	89.88	47, 41, 35	570	58.12
C-640D-305-120	155	111.09	111	133.5	213	75	42, 36, 30	-120	57.02
C-456D-305-120	155	111.09	111	133.5	213	75	42, 36, 30	-120	57.02
C-320D-256-120	155	111.07	111	132	211	75	42, 36, 30	55	57.05
C-456D-256-120	155	111.07	111	132	211	75	42, 36, 30	55	57.05
C-456D-213-120	155	111.07	111	132	211	75	42, 36, 30	0	57.05
C-320D-213-120	155	111.07	111	132	211	75	42, 36, 30	0	57.05
C-228D-213-120	155	111.07	111	132	211	75	42, 36, 30	0	57.05
C-456D-265-100	129	111.07	111	132	211	75	42, 36, 30	550	47.48
C-320D-265-100	129	111.07	111	132	211	75	42, 36, 30	550	47.48
C-320D-305-100	129	111.07	111	132	211	75	42, 36, 30	550	47.48
C-228D-213-100	129	96.08	96	113	180	63	37, 32, 27	0	48.37
C-228D-173-100	129	96.05	96	114	180	63	37, 32, 27	0	48.37
C-160D-173-100	129	96.05	96	114	180	63	37, 32, 27	0	48.37
C-320D-246-86	111	111.04	111	133	211	75	42, 36, 30	800	40.96
C-228D-246-86	111	111.04	111	133	211	75	42, 36, 30	800	40.96
C-320D-213-86	111	96.05	96	114	180	63	37, 32, 27	450	41.61
C-228D-213-86	111	96.05	96	114	180	63	37, 32, 27	450	41.61
C-160D-173-86	111	96.05	96	114	180	63	37, 32, 27	450	41.61
C-114D-119-86	111	84.05	84	93.75	150.13	53.38	32, 27, 22	115	40.98
C-320D-245-74	96	96.05	96	114	180	63	37, 32, 27	800	35.99
C-228D-200-74	96	96.05	96	114	180	63	37, 32, 27	800	35.99
C-160D-200-74	96	96.05	96	114	180	63	37, 32, 27	800	35.99
C-228D-173-74	96	84.05	84	96	152.38	53.38	32, 27, 22	450	35.49
C-160D-173-74	96	84.05	84	96	152.38	53.38	32, 27, 22	450	35.49
C-160D-143-74	96	84.05	84	93.75	150.13	53.38	32, 27, 22	300	35.49

**Table 16.1 Conventional Pumping Unit API Geometry Dimensions *Continued***

API Unit Designation	A (in.)	C (in)	I (in.)	P (in.)	H (in.)	G (in.)	R1, R2, R3 (in.)	C <sub>s</sub> (lb)	Torque Factor
C-114D-143-74	96	84.05	84	93.75	150.13	53.38	32, 27, 22	300	35.49
C-160D-173-64	84	84.05	84	93.75	150.13	53.38	32, 27, 22	550	31.02
C-114D-173-64	84	84.05	84	93.75	150.13	53.38	32, 27, 22	550	31.02
C-160D-143-64	84	72.06	72	84	132	45	27, 22, 17	360	30.59
C-114D-143-64	84	72.06	72	84	132	45	27, 22, 17	360	30.59
C-80D-119-64	84	64	64	74.5	116	41	24, 20, 16	0	30.85
C-160D-173-54	72	72.06	72	84	132	45	27, 22, 17	500	26.22
C-114D-133-54	72	64	64	74.5	116	41	24, 20, 16	330	26.45
C-80D-133-54	72	64	64	74.5	116	41	24, 20, 16	330	26.45
C-80D-119-54	72	64	64	74.5	116	41	24, 20, 16	330	26.45
C-P57D-76-54	64	51	51	64	103	39	21, 16, 11	105	25.8
C-P57D-89-54	64	51	51	64	103	39	21, 16, 11	105	25.8
C-80D-133-48	64	64	64	74.5	116	41	24, 20, 16	440	23.51
C-80D-109-48	64	56.05	56	65.63	105	37	21, 16, 11	320	23.3
C-57D-109-48	64	56.05	56	65.63	105	37	21, 16, 11	320	23.3
C-57D-95-48	64	56.05	56	65.63	105	37	21, 16, 11	320	23.3
C-P57D-109-48	57	51	51	64	103	39	21, 16, 11	180	22.98
C-P57D-95-48	57	51	51	64	103	39	21, 16, 11	180	22.98
C-40D-76-48	64	48.17	48	57.5	98.5	37	18, 14, 10	0	23.1
C-P40D-76-48	61	47	47	56	95	39	18, 14, 10	190	22.92
C-P57D-89-42	51	51	51	64	103	39	21, 16, 11	280	20.56
C-P57D-76-42	51	51	51	64	103	39	21, 16, 11	280	20.56
C-P40D-89-42	53	47	47	56	95	39	18, 14, 10	280	19.92
C-P40D-76-42	53	47	47	56	95	39	18, 14, 10	280	19.92
C-57D-89-42	56	48.17	48	57.5	98.5	37	18, 14, 10	150	20.27
C-57D-76-42	56	48.17	48	57.5	98.5	37	18, 14, 10	150	20.27
C-40D-89-42	56	48.17	48	57.5	98.5	37	18, 14, 10	150	20.27
C-40D-76-42	56	48.17	48	57.5	98.5	37	18, 14, 10	150	20.27
C-40D-89-36	48	48.17	48	57.5	98.5	37	18, 14, 10	275	17.37
C-P40D-89-36	47	47	47	56	95	39	18, 14, 10	375	17.66
C-25D-67-36	48	48.17	48	57.5	98.5	37	18, 14, 10	275	17.37
C-25D-56-36	48	48.17	48	57.5	98.5	37	18, 14, 10	275	17.37
C-25D-67-30	45	36.22	36	49.5	84.5	31	12, 8	150	14.53
C-25D-53-30	45	36.22	36	49.5	84.5	31	12, 9	150	14.53

**16.3.2 AIR-BALANCED PUMPING UNIT**

For this type of unit, the maximum acceleration occurs at the top of the stroke (the acceleration at the bottom of the stroke is less than simple harmonic motion). Thus, a lower maximum stress is set up in the rod system during transfer of the fluid load to the rods.

**FIGURE 16.6**

Definitions of conventional pumping unit API geometry dimensions.

The following analyses of polished rod motion apply to conventional units. Fig. 16.7 illustrates an approximate motion of the connection point between pitman arm and walking beam.

If  $x$  denotes the distance of  $B$  below its top position  $C$  and is measured from the instant at which the crank arm and pitman arm are in the vertical position with the crank arm vertically upward, the law of cosine gives

$$(AB)^2 = (OA)^2 + (OB)^2 - 2(OA)(OB)\cos AOB,$$

that is,

$$h^2 = c^2 + (h+c-x)^2 - 2c(h+c-x)\cos \omega t,$$

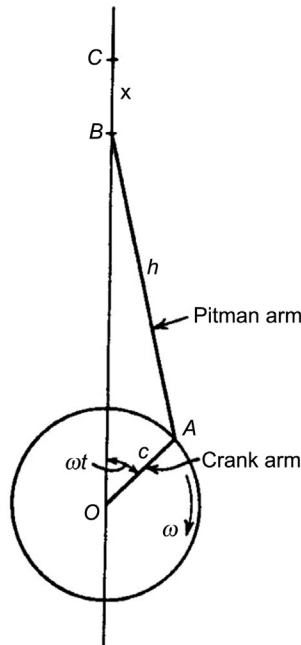
where  $\omega$  is the angular velocity of the crank. The equation reduces to

$$x^2 - 2x[h+c(1-\cos \omega t)] + 2c(h+c)(1-\cos \omega t) = 0$$

so that

$$x = h + c(1 - \cos \omega t) \pm \sqrt{c^2 \cos^2 \omega t + (h^2 - c^2)}.$$

When  $\omega t$  is zero,  $x$  is also zero, which means that the negative root sign must be taken. Therefore,



$AB$  = length of pitman arm ( $h$ )  
 $OA$  = length of crank arm ( $c$ )  
 $OB$  = distance from center  $O$  to pitman arm - walking beam connection at  $B$

**FIGURE 16.7**

Approximate motion of connection point between pitman arm and walking beam (Nind, 1964).

$$x = h + c(1 - \cos \omega t) - \sqrt{c^2 \cos^2 \omega t + (h^2 + c^2)}.$$

Acceleration is

$$a = \frac{d^2 x}{dt^2}.$$

Carrying out the differentiation for acceleration, it is found that the maximum acceleration occurs when  $\omega t$  is equal to zero (or an even multiple of  $\pi$  radians) and that this maximum value is

$$a_{\max} = \omega^2 c \left(1 + \frac{c}{h}\right). \quad (16.1)$$

It also appears that the minimum value of acceleration is

$$a_{\min} = \omega^2 c \left(1 - \frac{c}{h}\right). \quad (16.2)$$

If  $N$  is the number of pumping strokes per minute, then

$$\omega = \frac{2\pi N}{60} \text{ (rad/sec)}. \quad (16.3)$$

The maximum downward acceleration of point  $B$  (which occurs when the crank arm is vertically upward) is

$$a_{\max} = \frac{cN^2}{91.2} \left(1 + \frac{c}{h}\right) \text{ (ft/sec}^2\text{)} \quad (16.4)$$

or

$$a_{\max} = \frac{cN^2g}{2936.3} \left(1 + \frac{c}{h}\right) \text{ (ft/sec}^2\text{)}. \quad (16.5)$$

Likewise the minimum upward ( $a_{\min}$ ) acceleration of point  $B$  (which occurs when the crank arm is vertically downward) is

$$a_{\max} = \frac{cN^2g}{2936.3} \left(1 - \frac{c}{h}\right) \text{ (ft/sec}^2\text{)}. \quad (16.6)$$

It follows that in a conventional pumping unit, the maximum upward acceleration of the horse's head occurs at the bottom of the stroke (polished rod) and is equal to

$$a_{\max} = \frac{d_1}{d_2} \frac{cN^2g}{2936.3} \left(1 + \frac{c}{h}\right) \text{ (ft/sec}^2\text{)}, \quad (16.7)$$

where  $d_1$  and  $d_2$  are shown in Fig. 16.5. However,

$$\frac{2cd_2}{d_1} = S,$$

where  $S$  is the polished rod stroke length. So if  $S$  is measured in inches, then

$$\frac{2cd_2}{d_1} = \frac{S}{12}$$

or

$$\frac{cd_2}{d_1} = \frac{S}{24}. \quad (16.8)$$

So substituting Eq. (16.8) into Eq. (16.7) yields

$$a_{\max} = \frac{SN^2g}{70471.2} \left(1 + \frac{c}{h}\right) \text{ (ft/sec}^2\text{)}, \quad (16.9)$$

or we can write Eq. (16.9) as

$$a_{\max} = \frac{SN^2g}{70,471.2} M \text{ (ft/sec}^2\text{)}, \quad (16.10)$$

where  $M$  is the machinery factor and is defined as

$$M = 1 + \frac{c}{h}. \quad (16.11)$$

Similarly,

$$a_{\min} = \frac{SN^2g}{70471.2} \left(1 - \frac{c}{h}\right) \text{ (ft/sec}^2\text{)}. \quad (16.12)$$



For air-balanced units, because of the arrangements of the levers, the acceleration defined in Eq. (16.12) occurs at the bottom of the stroke, and the acceleration defined in Eq. (16.9) occurs at the top. With the lever system of an air-balanced unit, the polished rod is at the top of its stroke when the crank arm is vertically upward (Fig. 16.5B).

## 16.4 LOAD TO THE PUMPING UNIT

The load exerted to the pumping unit depends on well depth, rod size, fluid properties, and system dynamics. The maximum PRL and peak torque are major concerns for pumping unit.

### 16.4.1 MAXIMUM PRL

The PRL is the sum of weight of fluid being lifted, weight of plunger, weight of sucker rods string, dynamic load due to acceleration, friction force, and the up-thrust from below on plunger. In practice, no force attributable to fluid acceleration is required, so the acceleration term involves only acceleration of the rods. Also, the friction term and the weight of the plunger are neglected. We ignore the reflective forces, which will tend to underestimate the maximum PRL. To compensate for this, we set the up-thrust force to zero. Also, we assume the TV is closed at the instant at which the acceleration term reaches its maximum. With these assumptions, the  $PRL_{\max}$  becomes

$$PRL_{\max} = S_f(62.4)D \left( \frac{A_p - A_r}{144} \right) + \frac{\gamma_s DA_r}{144} + \frac{\gamma_s DA_r}{144} \left( \frac{SN^2 M}{70,471.2} \right), \quad (16.13)$$

where

$S_f$  = specific gravity of fluid in tubing

$D$  = length of sucker rod string, ft

$A_p$  = gross plunger cross-sectional area, in.<sup>2</sup>

$A_r$  = sucker rod cross-sectional area, in.<sup>2</sup>

$\gamma_s$  = specific weight of steel, 490 lb/ft<sup>3</sup>

$M$  = Eq. (16.11).

Note that for the air-balanced unit,  $M$  in Eq. (16.13) is replaced by  $1-c/h$ . Eq. (16.13) can be rewritten as

$$PRL_{\max} = S_f(62.4) \frac{DA_p}{144} - S_f(62.4) \frac{DA_r}{144} + \frac{\gamma_s DA_r}{144} + \frac{\gamma_s DA_r}{144} \left( \frac{SN^2 M}{70,471.2} \right). \quad (16.14)$$

If the weight of the rod string in air is

$$W_r = \frac{\gamma_s DA_r}{144}, \quad (16.15)$$

which can be solved for  $A_r$ , which is

$$A_r = \frac{144W_r}{\gamma_s D}. \quad (16.16)$$

Substituting Eq. (16.16) into Eq. (16.14) yields

$$\begin{aligned} \text{PRL}_{\max} = S_f(62.4) \frac{DA_p}{144} - S_f(62.4) \frac{W_r}{\gamma_s} + W_r \\ + W_r \left( \frac{SN^2M}{70,471.2} \right). \end{aligned} \quad (16.17)$$

The above equation is often further reduced by taking the fluid in the second term (the subtractive term) as a 50 °API with  $S_f = 0.78$ . Thus, Eq. (16.17) becomes (where  $\gamma_s = 490$ )

$$\text{PRL}_{\max} = S_f(62.4) \frac{DA_p}{144} - 0.1W_r + W_r + W_r \left( \frac{SN^2M}{70,471.2} \right)$$

or

$$\text{PRL}_{\max} = W_f + 0.9W_r + W_r \left( \frac{SN^2M}{70,471.2} \right), \quad (16.18)$$

where  $W_f = S_f(62.4) \frac{DA_p}{144}$  and is called the fluid load (not to be confused with the actual fluid weight on the rod string). Thus, Eq. (16.18) can be rewritten as

$$\text{PRL}_{\max} = W_f + (0.9 + F_1)W_r, \quad (16.19)$$

where for conventional units

$$F_1 = \frac{SN^2 \left( 1 + \frac{c}{h} \right)}{70,471.2} \quad (16.20)$$

and for air-balanced units

$$F_1 = \frac{SN^2 \left( 1 - \frac{c}{h} \right)}{70,471.2}. \quad (16.21)$$

### 16.4.2 MINIMUM PRL

The minimum PRL occurs while the TV is open so that the fluid column weight is carried by the tubing and not the rods. The minimum load is at or near the top of the stroke. Neglecting the weight of the plunger and friction term, the minimum PRL is

$$\text{PRL}_{\min} = -S_f(62.4) \frac{W_r}{\gamma_s} + W_r - W_r F_2,$$

which, for 50 °API oil, reduces to

$$\text{PRL}_{\min} = 0.9W_r - F_2W_r = (0.9 - F_2)W_r, \quad (16.22)$$

where for the conventional units

$$F_2 = \frac{SN^2 \left(1 - \frac{c}{h}\right)}{70,471.2} \quad (16.23)$$

and for air-balanced units

$$F_2 = \frac{SN^2 \left(1 + \frac{c}{h}\right)}{70,471.2}. \quad (16.24)$$

### 16.4.3 COUNTERWEIGHTS

To reduce the power requirements for the prime mover, a counterbalance load is used on the walking beam (small units) or the rotary crank. The ideal counterbalance load  $C$  is the average PRL. Therefore,

$$C = \frac{1}{2}(\text{PRL}_{\max} + \text{PRL}_{\min}).$$

Using Eqs. (16.19) and (16.22) in the above, we get

$$C = \frac{1}{2}W_f + 0.9W_r + \frac{1}{2}(F_1 - F_2)W_r \quad (16.25)$$

or for conventional units

$$C = \frac{1}{2}W_f + W_r \left(0.9 + \frac{SN^2}{70,471.2} \frac{c}{h}\right) \quad (16.26)$$

and for air-balanced units

$$C = \frac{1}{2}W_f + W_r \left(0.9 - \frac{SN^2}{70,471.2} \frac{c}{h}\right). \quad (16.27)$$

The counterbalance load should be provided by structure unbalance and counterweights placed at walking beam (small units) or the rotary crank. The counterweights can be selected from manufacturer's catalog based on the calculated  $C$  value. The relationship between the counterbalance load  $C$  and the total weight of the counterweights is

$$C = C_s + W_c \frac{r d_1}{c d_2},$$

where

$C_s$  = structure unbalance, lb

$W_c$  = total weight of counterweights, lb

$r$  = distance between the mass center of counterweights and the crank shaft center, in.

### 16.4.4 PEAK TORQUE AND SPEED LIMIT

The peak torque exerted is usually calculated on the most severe possible assumption, which is that the peak load (polished rod less counterbalance) occurs when the effective crank length is also a maximum (when the crank arm is horizontal). Thus, peak torque  $T$  is (Fig. 16.5)

$$T = c[C - (0.9 - F_2)W_r] \frac{d_2}{d_1}. \quad (16.28)$$

Substituting Eq. (16.8) into Eq. (16.28) gives

$$T = \frac{1}{2}S[C - (0.9 - F_2)W_r] \quad (16.29)$$

or

$$T = \frac{1}{2}S \left[ \frac{1}{2}W_f + \frac{1}{2}(F_1 + F_2)W_r \right]$$

or

$$T = \frac{1}{4}S \left( W_f + \frac{2SN^2W_r}{70,471.2} \right) \text{ (in.-lb)}. \quad (16.30)$$

Because the pumping unit itself is usually not perfectly balanced ( $C_s \neq 0$ ), the peak torque is also affected by structure unbalance. Torque factors are used for correction:

$$T = \frac{\frac{1}{2}[\text{PRL}_{\max}(TF_1) + \text{PRL}_{\min}(TF_2)]}{0.93}, \quad (16.31)$$

where

- $TF_1$  = maximum upstroke torque factor
- $TF_2$  = maximum downstroke torque factor
- 0.93 = system efficiency.

For symmetrical conventional and air-balanced units,  $TF = TF_1 = TF_2$ .

There is a limiting relationship between stroke length and cycles per minute. As given earlier, the maximum value of the downward acceleration (which occurs at the top of the stroke) is equal to

$$a_{\max/\min} = \frac{SN^2g \left( 1 \pm \frac{c}{h} \right)}{70,471.2}, \quad (16.32)$$

(the  $\pm$  refers to conventional units or air-balanced units, see Eqs. (16.9) and (16.12)). If this maximum acceleration divided by  $g$  exceeds unity, the downward acceleration of the hanger is greater than the free-fall acceleration of the rods at the top of the stroke. This leads to severe pounding when the polished rod shoulder falls onto the hanger (leading to failure of the rod at the shoulder). Thus, a limit of the above downward acceleration term divided by  $g$  is limited to approximately 0.5 (or where  $L$  is determined by experience in a particular field). Thus,

$$\frac{SN^2 \left( 1 \pm \frac{c}{h} \right)}{70,471.2} \leq L \quad (16.33)$$

or

$$N_{\text{limit}} = \sqrt{\frac{70,471.2L}{S\left(1 \mp \frac{c}{h}\right)}} \quad (16.34)$$

For  $L = 0.5$ ,

$$N_{\text{limit}} = \frac{187.7}{\sqrt{S\left(1 \mp \frac{c}{h}\right)}} \quad (16.35)$$

The minus sign is for conventional units and the plus sign for air-balanced units.

### 16.4.5 TAPERED ROD STRINGS

For deep well applications, it is necessary to use tapered sucker rod strings to reduce the PRL at the surface. The larger diameter rod is placed at the top of the rod string, then the next largest, and then the least largest. Usually these are in sequences up to four different rod sizes. The tapered rod strings are designated by 1/8-in. (in diameter) increments. Tapered rod strings can be identified by their numbers, such as:

1. No. 88 is a non-tapered 8/8 - or 1-in. diameter rod string
2. No. 76 is a tapered string with 7/8-in. diameter rod at the top, then a 6/8-in. diameter rod at the bottom.
3. No. 75 is a three-way tapered string consisting of
  - a. 7/8-in. diameter rod at top
  - b. 6/8-in. diameter rod at middle
  - c. 5/8-in. diameter rod at bottom
4. No. 107 is a four-way tapered string consisting of
  - a. 10/8-in. (or 1¼-in.) diameter rod at top
  - b. 9/8-in. (or 1½-in.) diameter rod below 10/8-in. diameter rod
  - c. 8/8-in. (or 1-in.) diameter rod below 9/8-in. diameter rod
  - d. 7/8-in. diameter rod below 8/8-in. diameter rod

Tapered rod strings are designed for static (quasi-static) loads with a sufficient factor of safety to allow for random low-level dynamic loads. Two criteria are used in the design of tapered rod strings:

1. Stress at the top rod of each rod size is the same throughout the string.
2. Stress in the top rod of the smallest (deepest) set of rods should be the highest (~30,000 psi) and the stress progressively decreases in the top rods of the higher sets of rods.

The reason for the second criterion is that it is preferable that any rod breaks occur near the bottom of the string (otherwise macaroni).

**ExampleProblem 16.1** The following geometric dimensions are for the pumping unit C-320D-213-86:

$$\begin{aligned} d_1 &= 96.05 \text{ in.} \\ d_2 &= 111 \text{ in.} \\ c &= 37 \text{ in.} \\ c/h &= 0.33. \end{aligned}$$

If this unit is used with a 2½-in. plunger and ⅞-in. rods to lift 25 °API gravity crude (formation volume factor 1.2 rb/stb) at depth of 3000 ft, answer the following questions:

1. What is the maximum allowable pumping speed if  $L = 0.4$  is used?
2. What is the expected maximum PRL?
3. What is the expected peak torque?
4. What is the desired counterbalance weight to be placed at the maximum position on the crank?

**Solution** The pumping unit C-320D-213-86 has a peak torque of gearbox rating of 320,000 in.-lb, a polished rod rating of 21,300 lb, and a maximum polished rod stroke of 86 in.

1. Based on the configuration for conventional unit shown in Fig. 16.5A and Table 16.1, the polished rod stroke length can be estimated as

$$S = 2c \frac{d_2}{d_1} = (2)(37) \frac{111}{96.05} = 85.52 \text{ in.}$$

The maximum allowable pumping speed is

$$N = \sqrt{\frac{70,471.2L}{S\left(1 - \frac{c}{h}\right)}} = \sqrt{\frac{(70,471.2)(0.4)}{(85.52)(1 - 0.33)}} = 22 \text{ SPM.}$$

2. The maximum PRL can be calculated with Eq. (16.17). The 25 °API gravity has an  $S_f = 0.9042$ . The area of the 2½-in. plunger is  $A_p = 4.91 \text{ in.}^2$ . The area of the ⅞-in. rod is  $A_r = 0.60 \text{ in.}^2$ . Then

$$\begin{aligned} W_f &= S_f(62.4) \frac{DA_p}{144} = (0.9042)(62.4) \frac{(3000)(4.91)}{144} \\ &= 5770 \text{ lbs} \\ W_r &= \frac{\gamma_s DA_r}{144} = \frac{(490)(3000)(0.60)}{144} = 6138 \text{ lbs} \\ F_1 &= \frac{SN^2 \left(1 + \frac{c}{h}\right)}{70,471.2} = \frac{(85.52)(22)^2(1 + 0.33)}{70,471.2} = 0.7940. \end{aligned}$$

Then the expected maximum PRL is

$$\begin{aligned} \text{PRL}_{\max} &= W_f - S_f(62.4) \frac{W_r}{\gamma_s} + W_r + W_r F_1 \\ &= 5770 - (0.9042)(62.4)(6138)/(490) \\ &\quad + 6138 + (6138)(0.794) \\ &= 16,076 \text{ lbs} < 21,300 \text{ lb} \end{aligned}$$

3. The peak torque is calculated by Eq. (16.30):

$$\begin{aligned} T &= \frac{1}{4} S \left( W_f + \frac{2SN^2 W_r}{70,471.2} \right) \\ &= \frac{1}{4} (85.52) \left( 5770 + \frac{2(85.52)(22)^2(6138)}{70,471.2} \right) \\ &= 280,056 \text{ lb-in.} < 320,000 \text{ lb-in.} \end{aligned}$$

4. Accurate calculation of counterbalance load requires the minimum PRL:

$$F_2 = \frac{SN^2 \left(1 - \frac{c}{h}\right)}{70,471.2} = \frac{(85.52)(22)^2(1 - 0.33)}{70,471.2} = 0.4$$

$$\begin{aligned} \text{PRL}_{\min} &= -S_f(62.4) \frac{W_r}{\gamma_s} + W_r - W_r F_2 \\ &= -(0.9042)(62.4) \frac{6138}{490} + 6138 - (6138)(0.4) \\ &= 2976 \text{ lb} \\ C &= \frac{1}{2}(\text{PRL}_{\max} + \text{PRL}_{\min}) = \frac{1}{2}(16,076 + 2976) = 9526 \text{ lb.} \end{aligned}$$

A product catalog of LUFKIN Industries indicates that the structure unbalance is 450 lb and 4 No. 5ARO counterweights placed at the maximum position ( $c$  in this case) on the crank will produce an effective counterbalance load of 10,160 lb, that is,

$$W_c \frac{(37)(96.05)}{(37)(111)} + 450 = 10,160,$$

which gives  $W_c = 11,221$  lb. To generate the ideal counterbalance load of  $C = 9526$  lb, the counterweights should be placed on the crank at

$$r = \frac{(9526)(111)}{(11,221)(96.05)}(37) = 36.30 \text{ in.}$$

The computer program *SuckerRodPumpingLoad.xls* can be used for quickly seeking solutions to similar problems. It is available from the publisher with this book. The solution is shown in [Table 16.2](#).

## 16.5 PUMP DELIVERABILITY AND POWER REQUIREMENTS

Liquid flow rate delivered by the plunger pump can be expressed as

$$q = \frac{A_p}{144} N \frac{S_p E_v}{12 B_o} \frac{(24)(60)}{5.615} \text{ (bbl/day)}$$

or

$$q = 0.1484 \frac{A_p N S_p E_v}{B_o} \text{ (stb/day),}$$

where  $S_p$  is the effective plunger stroke length (in.),  $E_v$  is the volumetric efficiency of the plunger, and  $B_o$  formation volume factor of the fluid.

### 16.5.1 EFFECTIVE PLUNGER STROKE LENGTH

The motion of the plunger at the pump setting depth and the motion of the polished rod do not coincide in time and in magnitude because sucker rods and tubing strings are elastic. Plunger

**Table 16.2 Solution Given by Computer Program SuckerRodPumpingLoad.xls**

*SuckerRodPumpingLoad.xls*

*Description:* This spreadsheet calculates the maximum allowable pumping speed, the maximum PRL, the minimum PRL, peak torque, and counterbalance load.

*Instruction:* (1) Update parameter values in the Input section; and (2) view result in the Solution section.

**Input Data**

Pump setting depth ( $D$ ):	3000 ft
Plunger diameter ( $d_p$ ):	2.5 in.
Rod section 1, diameter ( $d_{r1}$ ):	1 in.
Length ( $L_1$ ):	0 ft
Rod section 2, diameter ( $d_{r2}$ ):	0.875 in.
Length ( $L_2$ ):	3000 ft
Rod section 3, diameter ( $d_{r3}$ ):	0.75 in.
Length ( $L_3$ ):	0 ft
Rod section 4, diameter ( $d_{r4}$ ):	0.5 in.
Length ( $L_4$ ):	0 ft
Type of pumping unit (1 = conventional; -1 = Mark II or Air-balanced):	1
Beam dimension 1 ( $d_1$ )	96.05 in.
Beam dimension 2 ( $d_2$ )	111 in.
Crank length ( $c$ ):	37 in.
Crank to pitman ratio ( $c/h$ ):	0.33
Oil gravity (API):	25 °API
Maximum allowable acceleration factor ( $L$ ):	0.4

**Solution**

$S = 2c \frac{d_p}{d_1}$	= 85.52 in.
$N = \sqrt{\frac{70471.2L}{S(1 - \frac{c}{h})}}$	= 22 spm
$A_p = \frac{\pi d_p^2}{4}$	= 4.91 in. <sup>2</sup>
$A_r = \frac{\pi d_r^2}{4}$	= 0.60 in.
$W_f = S_f(62.4) \frac{DA_p}{144}$	= 5770 lb
$W_r = \frac{\gamma_s DA_r}{144}$	= 6138 lb
$F_1 = \frac{SN^2(1 \pm \frac{c}{h})}{70,471.2}$	= 0.7940°
$PRL_{max} = W_f - S_f(62.4) \frac{W_r}{\gamma_s} + W_r + W_r F_1$	= 16,076 lb
$T = \frac{1}{4} S \left( W_f + \frac{2SN^2 W_r}{70,471.2} \right)$	= 280,056 lb
$F_2 = \frac{SN^2(1 \mp \frac{c}{h})}{70,471.2}$	= 0.40
$PRL_{min} = -S_f(62.4) \frac{W_r}{\gamma_s} + W_r - W_r F_2$	= 2976 lb
$C = \frac{1}{2}(PRL_{max} + PRL_{min})$	= 9526 lb



motion depends on a number of factors including polished rod motion, sucker rod stretch, and tubing stretch. The theory in this subject has been well established (Nind, 1964).

Two major sources of difference in the motion of the polished rod and the plunger are elastic stretch (elongation) of the rod string and overtravel. Stretch is caused by the periodic transfer of the fluid load from the SV to the TV and back again. The result is a function of the stretch of the rod string and the tubing string. Rod string stretch is caused by the weight of the fluid column in the tubing coming on to the rod string at the bottom of the stroke when the TV closes (this load is removed from the rod string at the top of the stroke when the TV opens). It is apparent that the plunger stroke will be less than the polished rod stroke length  $S$  by an amount equal to the rod stretch. The magnitude of the rod stretch is

$$\delta l_r = \frac{W_f D_r}{A_r E}, \quad (16.36)$$

where

$W_f$  = weight of fluid, lb

$D_r$  = length of rod string, ft

$A_r$  = cross-sectional area of rods, in.<sup>2</sup>

$E$  = modulus of elasticity of steel,  $30 \times 10^6$  lb/in.<sup>2</sup>.

Tubing stretch can be expressed by a similar equation:

$$\delta l_t = \frac{W_f D_t}{A_t E} \quad (16.37)$$

But because the tubing cross-sectional area  $A_t$  is greater than the rod cross-sectional area  $A_r$ , the stretch of the tubing is small and is usually neglected. However, the tubing stretch can cause problems with wear on the casing. Thus, for this reason a tubing anchor is almost always used.

Plunger overtravel at the bottom of the stroke is a result of the upward acceleration imposed on the downward-moving sucker rod elastic system. An approximation to the extent of the overtravel may be obtained by considering a sucker rod string being accelerated vertically upward at a rate  $n$  times the acceleration of gravity. The vertical force required to supply this acceleration is  $nW_r$ . The magnitude of the rod stretch due to this force is

$$\delta l_o = n \frac{W_r D_r}{A_r E} \text{ (ft)}. \quad (16.38)$$

But the maximum acceleration term  $n$  can be written as

$$n = \frac{SN^2 \left(1 \pm \frac{c}{h}\right)}{70,471.2}$$

so that Eq. (16.38) becomes

$$\delta l_o = \frac{W_r D_r}{A_r E} \frac{SN^2 \left(1 \pm \frac{c}{h}\right)}{70,471.2} \text{ (ft)}, \quad (16.39)$$

where again the plus sign applies to conventional units and the minus sign to air-balanced units.

Let us restrict our discussion to conventional units. Then Eq. (16.39) becomes

$$\delta l_o = \frac{W_r D_r}{A_r E} \frac{SN^2 M}{70,471.2} \quad (\text{ft}). \quad (16.40)$$

Eq. (16.40) can be rewritten to yield  $\delta l_o$  in inches.  $W_r$  is

$$W_r = \gamma_s A_r D_r$$

and  $\gamma_s = 490 \text{ lb/ft}^3$  with  $E = 30 \times 10^6 \text{ lb/m}^2$ . Eq. (16.40) becomes

$$\delta l_o = 1.93 \times 10^{-11} D_r^2 SN^2 M \quad (\text{in.}), \quad (16.41)$$

which is the familiar Coberly expression for overtravel (Coberly, 1938).

Plunger stroke is approximated using the above expressions as

$$S_p = S - \delta l_r - \delta l_t + \delta l_o$$

or

$$S_p = S - \frac{12D}{E} \times \left[ W_f \left( \frac{1}{A_r} + \frac{1}{A_t} \right) - \frac{SN^2 M}{70,471.2} \frac{W_r}{A_r} \right] \quad (\text{in.}). \quad (16.42)$$

If pumping is carried out at the maximum permissible speed limited by Eq. (16.34), the plunger stroke becomes

$$S_p = S - \frac{12D}{E} \times \left[ W_f \left( \frac{1}{A_r} + \frac{1}{A_t} \right) - \frac{1 + \frac{c}{h} L W_r}{1 - \frac{c}{h} A_r} \right] \quad (\text{in.}). \quad (16.43)$$

For the air-balanced unit, the term is replaced by its reciprocal.

## 16.5.2 VOLUMETRIC EFFICIENCY

Volumetric efficiency of the plunger mainly depends on the rate of slippage of oil past the pump plunger and the solution–gas ratio under pump condition.

Metal-to-metal plungers are commonly available with plunger-to-barrel clearance on the diameter of  $-0.001$ ,  $-0.002$ ,  $-0.003$ ,  $-0.004$ , and  $-0.005$  in. Such fits are referred to as  $-1$ ,  $-2$ ,  $-3$ ,  $-4$ , and  $-5$ , meaning the plunger outside diameter is 0.001 in. smaller than the barrel inside diameter. In selecting a plunger, one must consider the viscosity of the oil to be pumped. A loose fit may be acceptable for a well with high-viscosity oil (low °API gravity). But such a loose fit in a well with low-viscosity oil may be very inefficient. Guidelines are as follows:

1. Low-viscosity oils (1–20 cps) can be pumped with a plunger to barrel fit of  $-0.001$  in.
2. High-viscosity oils (7400 cps) will probably carry sand in suspension so a plunger-to-barrel fit of approximately 0.005 in. can be used.

An empirical formula has been developed that can be used to calculate the slippage rate,  $q_s$  (bbl/day), through the annulus between the plunger and the barrel:

$$q_s = \frac{k_p (d_b - d_p)^{2.9} (d_b + d_p) \Delta p}{\mu d_b^{0.1} L_p}, \quad (16.44)$$

where

$k_p$  = a constant

$d_p$  = plunger outside diameter, in.

$d_b$  = barrel inside diameter, in.

$\Delta p$  = differential pressure drop across plunger, psi

$L_p$  = length of plunger, in.

$\mu$  = viscosity of oil, cp.

The value of  $k_p$  is  $2.77 \times 10^6$ – $6.36 \times 10^6$  depending on field conditions. An average value is  $4.17 \times 10^6$ . The value of  $\Delta p$  may be estimated on the basis of well productivity index and production rate. A reasonable estimate may be a value that is twice the production drawdown.

Volumetric efficiency can decrease significantly due to the presence of free gas below the plunger. As the fluid is elevated and gas breaks out of solution, there is a significant difference between the volumetric displacement of the bottom-hole pump and the volume of the fluid delivered to the surface. This effect is denoted by the shrinkage factor greater than 1.0, indicating that the bottom-hole pump must displace more fluid by some additional percentage than the volume delivered to the surface (Brown, 1980). The effect of gas on volumetric efficiency depends on solution–gas ratio and bottom-hole pressure. Down-hole devices, called “gas anchors,” are usually installed on pumps to separate the gas from the liquid.

In summary, volumetric efficiency is mainly affected by the slippage of oil and free gas volume below plunger. Both effects are difficult to quantify. Pump efficiency can vary over a wide range but are commonly 70%–80%.

### 16.5.3 POWER REQUIREMENTS

The prime mover should be properly sized to provide adequate power to lift the production fluid, to overcome friction loss in the pump, in the rod string and polished rod, and in the pumping unit. The power required for lifting fluid is called “hydraulic power.” It is usually expressed in terms of net lift:

$$P_h = 7.36 \times 10^{-6} q \gamma_l L_N, \quad (16.45)$$

where

$P_h$  = hydraulic power, hp

$q$  = liquid production rate, bbl/day

$\gamma_l$  = liquid specific gravity, water = 1

$L_N$  = net lift, ft

and

$$L_N = H + \frac{P_{tf}}{0.433\gamma_l}, \quad (16.46)$$

where

$H$  = depth to the average fluid level in the annulus, ft

$p_{tf}$  = flowing tubing head pressure, psig.

The power required to overcome friction losses can be empirically estimated as

$$P_f = 6.31 \times 10^{-7} W_r S N. \quad (16.47)$$

Thus, the required prime mover power can be expressed as

$$P_{pm} = F_s (P_h + P_f), \quad (16.48)$$

where  $F_s$  is a safety factor of 1.25–1.50.

**Example Problem 16.2** A well is pumped off (fluid level is the pump depth) with a rod pump described in Example Problem 16.1. A 3-in. tubing string (3.5-in. OD, 2.995 ID) in the well is not anchored. Calculate (1) expected liquid production rate (use pump volumetric efficiency 0.8), and (2) required prime mover power (use safety factor 1.35).

**Solution** This problem can be quickly solved using the program *SuckerRodPumping Flowrate&Power.xls*. The solution is shown in [Table 16.3](#).

## 16.6 PROCEDURE FOR PUMPING UNIT SELECTION

The following procedure can be used for selecting a pumping unit:

1. From the maximum anticipated fluid production (based on inflow performance relationship (IPR)) and estimated volumetric efficiency, calculate required pump displacement.
2. Based on well depth and pump displacement, determine API rating and stroke length of the pumping unit to be used. This can be done using either [Fig. 16.8](#) or [Table 16.4](#).
3. Select tubing size, plunger size, rod sizes, and pumping speed from [Table 16.4](#).
4. Calculate the fractional length of each section of the rod string.
5. Calculate the length of each section of the rod string to the nearest 25 ft.
6. Calculate the acceleration factor.
7. Determine the effective plunger stroke length.
8. Using the estimated volumetric efficiency, determine the probable production rate and check it against the desired production rate.
9. Calculate the dead weight of the rod string.
10. Calculate the fluid load.
11. Determine peak PRL and check it against the maximum beam load for the unit selected.
12. Calculate the maximum stress at the top of each rod size and check it against the maximum permissible working stress for the rods to be used.

**Table 16.3 Solution Given by SuckerRodPumpingFlowrate&Power.xls**

*SuckerRodPumpingFlowRate&Power.xls*

*Description:* This spreadsheet calculates expected deliverability and required prime mover power for a given sucker rod pumping system.

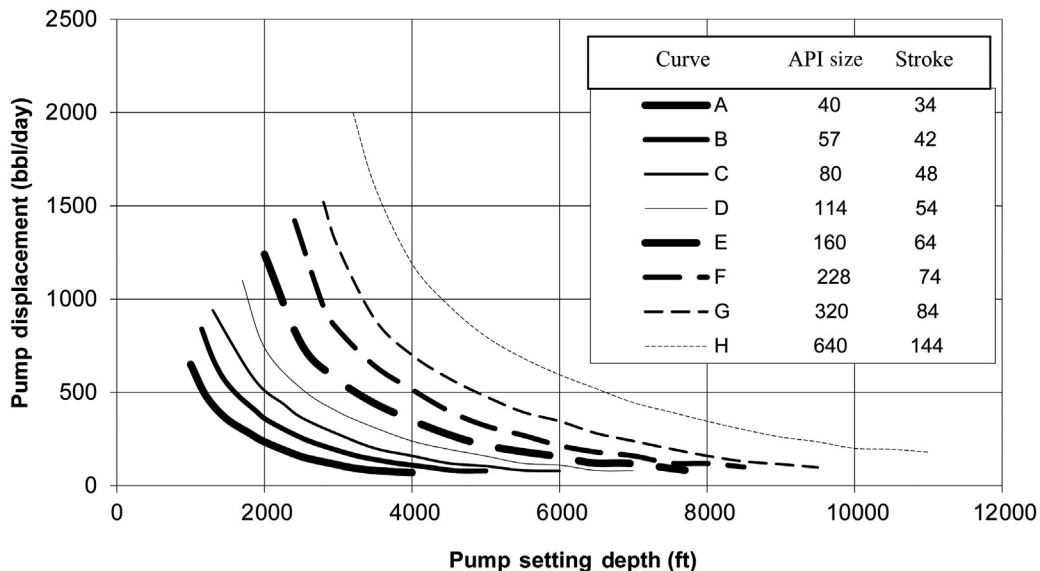
*Instruction:* (1) Update parameter values in the Input section; and (2) view result in the Solution section.

**Input Data**

Pump setting depth ( $D$ ):	4000 ft
Depth to the liquid level in annulus ( $H$ ):	4000 ft
Flowing tubing head pressure ( $p_{tf}$ ):	100 psi
Tubing outer diameter ( $d_{to}$ ):	3.5 in.
Tubing inner diameter ( $d_{ti}$ ):	2.995 in.
Tubing anchor (1 = yes; 0 = no):	0
Plunger diameter ( $d_p$ ):	2.5 in.
Rod section 1, diameter ( $d_{r1}$ ):	1 in.
Length ( $L_1$ ):	0 ft
Rod section 2, diameter ( $d_{r2}$ ):	0.875 in.
Length ( $L_2$ ):	0 ft
Rod section 3, diameter ( $d_{r3}$ ):	0.75 in.
Length ( $L_3$ ):	4000 ft
Rod section 4, diameter ( $d_{r4}$ ):	0.5 in.
Length ( $L_4$ ):	0 ft
Type of pumping unit (1 = conventional; -1 = Mark II or Air-balanced):	1
Polished rod stroke length ( $S$ ):	86 in.
Pumping speed ( $N$ ):	22 spm
Crank to pitman ratio ( $c/h$ ):	0.33°
Oil gravity (API):	25 °API
Fluid formation volume factor ( $B_o$ ):	1.2 rb/stb
Pump volumetric efficiency ( $E_v$ ):	0.8
Safety factor to prime mover power ( $F_s$ ):	1.35

**Solution**

$A_t = \frac{\pi d_t^2}{4}$	= 2.58 in. <sup>2</sup>
$A_p = \frac{\pi d_p^2}{4}$	= 4.91 in. <sup>2</sup>
$A_r = \frac{\pi d_r^2}{4}$	= 0.44 in.
$W_f = S_f(62.4) \frac{DA_p}{144}$	= 7693 lb
$W_r = \frac{\gamma_s DA_r}{144}$	= 6013 lb
$M = 1 \pm \frac{c}{h}$	= 1.33
$S_p = S - \frac{12D}{E} \left[ W_f \left( \frac{1}{A_r} + \frac{1}{A_t} \right) - \frac{SN^2 M}{70471.2} \frac{W_r}{A_r} \right]$	= 70 in.
$q = 0.1484 \frac{A_p NS_p E_v}{B_o}$	= 753 sbt/day
$L_N = H + \frac{P_{tf}}{0.433 \gamma_l}$	= 4255 ft
$P_h = 7.36 \times 10^{-6} q \gamma_l L_N$	= 25.58 hp
$P_f = 6.31 \times 10^{-7} W_r SN$	= 7.2 hp
$P_{pm} = F_s(P_h + P_f)$	= 44.2 hp



**FIGURE 16.8**

Sucker rod pumping unit selection chart (Kelly and Willis, 1954).

13. Calculate the ideal counterbalance effect and check it against the counterbalance available for the unit selected.
14. From the manufacturer's literature, determine the position of the counterweight to obtain the ideal counterbalance effect.
15. On the assumption that the unit will be no more than 5% out of counterbalance, calculate the peak torque on the gear reducer and check it against the API rating of the unit selected.
16. Calculate hydraulic horsepower, friction horsepower, and brake horsepower of the prime mover. Select the prime mover.
17. From the manufacturer's literature, obtain the gear reduction ratio and unit sheave size for the unit selected, and the speed of the prime mover. From this, determine the engine sheave size to obtain the desired pumping speed.

**Example Problem 16.3** A well is to be put on a sucker rod pump. The proposed pump setting depth is 3500 ft. The anticipated production rate is 600 bbl/day oil of 0.8 specific gravity against wellhead pressure 100 psig. It is assumed that the working liquid level is low, and a sucker rod string having a working stress of 30,000 psi is to be used. Select surface and subsurface equipment for the installation. Use a safety factor of 1.35 for the prime mover power.

**Solution**

1. Assuming volumetric efficiency of 0.8, the required pump displacement is

$$(600)/(0.8) = 750 \text{ bbl/day.}$$

<b>Table 16.4 Design Data for API Sucker Rod Pumping Units</b>				
<b>Pump Depth (ft)</b>	<b>Plunger Size (in.)</b>	<b>Tubing Size (in.)</b>	<b>Rod Sizes (in.)</b>	<b>Pumping Speed (stroke/min)</b>
<b>(a) Size 40 Unit with 34-in. Stroke</b>				
1000–1100	2¾	3	7/8	24–19
1100–1250	2½	3	7/8	24–19
1250–1650	2¼	2½	3/4	24–19
1650–1900	2	2½	3/4	24–19
1900–2150	1¾	2½	3/4	24–19
2150–3000	1½	2	5/8–3/4	24–19
3000–3700	1¼	2	5/8–3/5	22–18
3700–4000	1	2	5/8–3/6	21–18
<b>(b) Size 57 Unit with 42-in. Stroke</b>				
1150–1300	2¾	3	7/8	24–19
1300–1450	2½	3	7/8	24–19
1450–1850	2¼	2½	3/4	24–19
1850–2200	2	2½	3/4	24–19
2200–2500	1¾	2½	3/4	24–19
2500–3400	1½	2	5/8–3/4	23–18
3400–4200	1¼	2	5/8–3/5	22–17
4200–5000	1	2	5/8–3/6	21–17
<b>(c) Size 80 Unit with 48-in. Stroke</b>				
1400–1500	2¾	3	7/8	24–19
1550–1700	2½	3	7/8	24–19
1700–2200	2½	2½	3/4	24–19
2200–2600	2	2½	3/4	24–19
2600–3000	1¾	2½	3/4	23–18
3000–4100	1½	2	5/8–3/4	23–19
4100–5000	1¼	2	5/8–3/5	21–17
5000–6000	1	2	5/8–3/6	19–17
<b>(d) Size 114 Unit with 54-in. Stroke</b>				
1700–1900	2¾	3	7/8	24–19
1900–2100	2½	3	7/8	24–19
2100–2700	1¾	2½	3/4	24–19
2700–3300	2	2½	3/4	23–18
3300–3900	1¾	2½	3/4	22–17
3900–5100	1½	2	5/8–3/4	21–17
5100–6300	1¼	2	5/8–3/5	19–16
6300–7000	1	2	5/8–3/6	17–16
<b>(e) Size 160 Unit with 64-in. Stroke</b>				
2000–2200	2¾	3	7/8	24–19
2200–2400	2½	3	7/8	24–19

(Continued)

<b>Table 16.4 Design Data for API Sucker Rod Pumping Units <i>Continued</i></b>				
<b>Pump Depth (ft)</b>	<b>Plunger Size (in.)</b>	<b>Tubing Size (in.)</b>	<b>Rod Sizes (in.)</b>	<b>Pumping Speed (stroke/min)</b>
2400–3000	2¼	2½	3/4 –7/8	24–19
3000–3600	2	2½	3/4 –7/8	23–18
3600–4200	1¾	2½	3/4 –7/8	22–17
4200–5400	1½	2	5/8–3/4–7/8	21–17
5400–6700	1¼	2	5/8–3/4–7/8	19–15
6700–7700	1	2	5/8–3/4–7/8	17–15
<b>(f) Size 228 Unit with 74-in. Stroke</b>				
2400–2600	2¾	3	7/8	24–20
2600–3000	2½	3	7/8	23–18
3000–3700	2¼	2½	3/4 –7/8	22–17
3700–4500	2	2½	3/4 –7/8	21–16
4500–5200	1¾	2½	3/4 –7/8	19–15
5200–6800	1½	2	5/8–3/4–7/8	18–14
6800–8000	1¼	2	5/8–3/4–7/8	16–13
8000–8500	11/16	2	5/8–3/4–7/8	14–13
<b>(g) Size 320 Unit with 84-in. Stroke</b>				
2800–3200	2¾	3	7/8	23–18
3200–3600	2½	3	7/8	21–17
3600–4100	2¼	2½	3/4 –7/8 – 1	21–17
4100–4800	2	2½	3/4 –7/8 – 1	20–16
4800–5600	1¾	2½	3/4 –7/8 – 1	19–16
5600–6700	1½	2½	3/4 –7/8 – 1	18–15
6700–8000	1¼	2½	3/4 –7/8 – 1	17–13
8000–9500	11/16	2½	3/4 –7/8 – 1	14–11
<b>(h) Size 640 Unit with 144-in. Stroke</b>				
3200–3500	2¾	3	7/8–1	18–14
3500–4000	2½	3	7/8–1	17–13
4000–4700	2¼	2½	3/4 –7/8 – 1	16–13
4700–5700	2	2½	3/4 –7/8 – 1	15–12
5700–6600	1¾	2½	3/4 –7/8 – 1	14–12
6600–8000	1½	2½	3/4 –7/8 – 1	14–11
8000–9600	1¼	2½	3/4 –7/8 – 1	13–10
9600–11,000	11/16	2½	3/4 –7/8 – 1	12–10

2. Based on well depth 3500 ft and pump displacement 750 bbl/day, Fig. 16.8 suggests API pump size 320 unit with 84 in. stroke, that is, a pump is selected with the following designation:



3. Table 16.4(g) suggests the following:

Tubing size:	3 in. OD, 2.992 in. ID
Plunger size:	2½ in.
Rod size:	7/8 in.
Pumping speed:	18 spm

4. Table 16.1 gives  $d_1 = 96.05$  in.,  $d_2 = 111$  in.,  $c = 37$  in., and  $h = 114$  in., thus  $c/h = 0.3246$ . The spreadsheet program *SuckerRodPumpingFlowRate&Power.xls* gives

$$q_o = 687 \text{ bbl/day} > 600 \text{ bbl/day}$$

$$P_{pm} = 30.2 \text{ hp}$$

5. The spreadsheet program *SuckerRodPumpingLoad.xls* gives

$$PRL_{\max} = 16,121 \text{ lb}$$

$$PRL_{\min} = 4533 \text{ lb}$$

$$T = 247,755 \text{ in.-lb} < 320,000 \text{ in.-lb}$$

$$C = 10,327 \text{ lb}$$

6. The cross-sectional area of the 7/8-in. rod is  $0.60 \text{ in.}^2$ . Thus, the maximum possible stress in the sucker rod is

$$\sigma_{\max} = (16,121)/(0.60) = 26,809 \text{ psi} < 30,000 \text{ psi.}$$

Therefore, the selected pumping unit and rod meet well load and volume requirements.

7. If a LUFKIN Industries C-320D-213-86 unit is chosen, the structure unbalance is 450 lb and 4 No. 5 ARO counterweights placed at the maximum position ( $c$  in this case) on the crank will produce an effective counterbalance load of 12,630 lb, that is,

$$W_c \frac{(37)(96.05)}{(37)(111)} + 450 = 12,630 \text{ lb,}$$

which gives  $W_c = 14,075$  lb. To generate the ideal counterbalance load of  $C = 10,327$  lb, the counterweights should be placed on the crank at

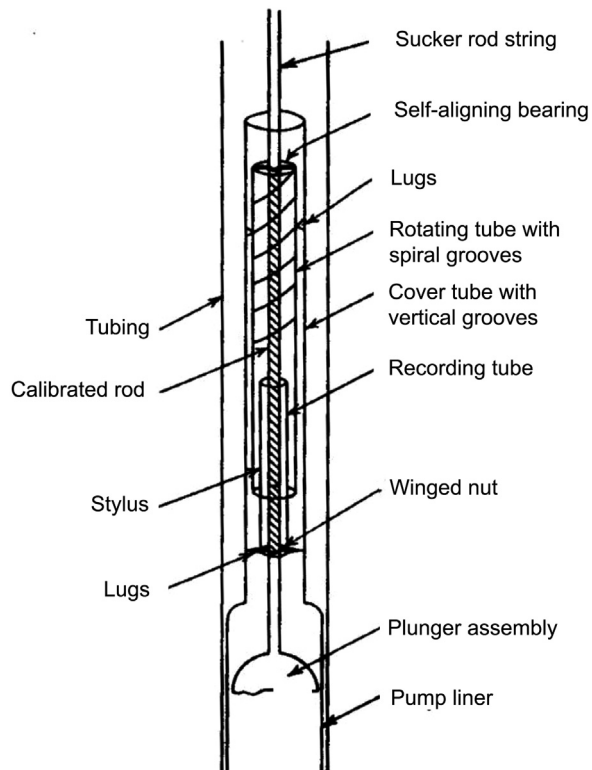
$$r = \frac{(10,327)(111)}{(14,076)(96.05)}(37) = 31.4 \text{ in.}$$

8. The LUFKIN Industries C-320D-213-86 unit has a gear ratio of 30.12 and unit sheave sizes of 24, 30, and 44 in. are available. If a 24-in. unit sheave and a 750-rpm electric motor are chosen, the diameter of the motor sheave is

$$d_e = \frac{(18)(30.12)(24)}{(750)} = 17.3 \text{ in.}$$

## 16.7 PRINCIPLES OF PUMP PERFORMANCE ANALYSIS

The efficiency of sucker rod pumping units is usually analyzed using the information from a pump dynagraph and polisher rod dynamometer cards. Fig. 16.9 shows a schematic of a pump dynagraph.



**FIGURE 16.9**

A sketch of pump dynagraph (Nind, 1964).

This instrument is installed immediately above the plunger to record the plunger stroke and the loads carried by the plunger during the pump cycle.

The relative motion between the cover tube (which is attached to the pump barrel and hence anchored to the tubing) and the calibrated rod (which is an integral part of the sucker rod string) is recorded as a horizontal line on the recording tube. This is achieved by having the recording tube mounted on a winged nut threaded onto the calibrated rod and prevented from rotating by means of two lugs, which are attached to the winged nut, which run in vertical grooves in the cover tube. The stylus is mounted on a third tube, which is free to rotate and is connected by a self-aligning bearing to the upper end of the calibrated rod. Lugs attached to the cover tube run in spiral grooves cut in the outer surface of the rotating tube. Consequently, vertical motion of the plunger assembly relative to the barrel results in rotation of the third tube, and the stylus cuts a horizontal line on a recording tube.

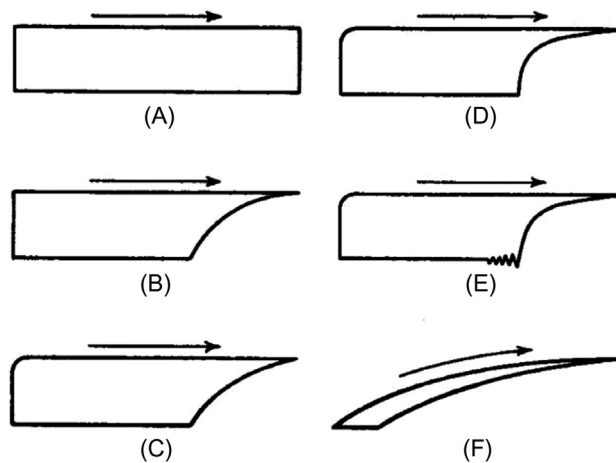
Any change in plunger loading causes a change in length of the section of the calibrated rod between the winged nut supporting the recording tube and the self-aligning bearing supporting the rotating tube (so that a vertical line is cut on the recording tube by the stylus). When the pump is in operation, the stylus traces a series of cards, one on top of the other. To obtain a new series of

cards, the polished rod at the well head is rotated. This rotation is transmitted to the plunger in a few pump strokes. Because the recording tube is prevented from rotating by the winged nut lugs that run in the cover tube grooves, the rotation of the sucker rod string causes the winged nut to travel—upward or downward depending on the direction of rotation—on the threaded calibrated rod. Upon the completion of a series of tests, the recording tube (which is 36 in. long) is removed.

It is important to note that although the bottom-hole dynamograph records the plunger stroke and variations in plunger loading, no zero line is obtained. Thus, quantitative interpretation of the cards requires some speculation unless a pressure element is run with the dynamograph.

Fig. 16.10 shows some typical dynamograph card results. Card (A) shows an ideal case where instantaneous valve actions at the top and bottom of the stroke are indicated. In general, however, some free gas is drawn into the pump on the upstroke, so a period of gas compression can occur on the down-stroke before the TV opens. This is shown in card (B). Card (C) shows gas expansion during the upstroke giving a rounding of the card just as the upstroke begins. Card (D) shows fluid pounding that occurs when the well is almost pumped off (the pump displacement rate is higher than the formation of potential liquid production rate). This fluid pounding results in a rapid fall off in stress in the rod string and the sudden imposed shock to the system. Card (E) shows that the fluid pounding has progressed so that the mechanical shock causes oscillations in the system. Card (F) shows that the pump is operating at a very low volumetric efficiency where almost all the pump stroke is being lost in gas compression and expansion (no liquid is being pumped). This results in no valve action and the area between the card nearly disappears (thus, is gas locked). Usually, this gas-locked condition is only temporary, and as liquid leaks past the plunger, the volume of liquid in the pump barrel increases until the TV opens and pumping recommences.

The use of the pump dynamograph involves pulling the rods and pump from the well bath to install the instrument and to recover the recording tube. Also, the dynamograph cannot be used in a well that



**FIGURE 16.10**

Pump dynamograph cards: (A) ideal card; (B) gas compression on down-stroke; (C) gas expansion on upstroke; (D) fluid pound; (E) vibration due to fluid pound; (F) gas lock (Nind, 1964).

is equipped with a tubing pump. Thus, the dynagraph is more a research instrument than an operational device. Once there is knowledge from a dynagraph, surface dynamometer cards can be interpreted.

The surface, or polished rod, dynamometer is a device that records the motion (and its history) of the polished rod during the pumping cycle. The rod string is forced by the pumping unit to follow a regular time versus position pattern. However, the polished rod reacts with the loadings (on the rod string) that are imposed by the well.

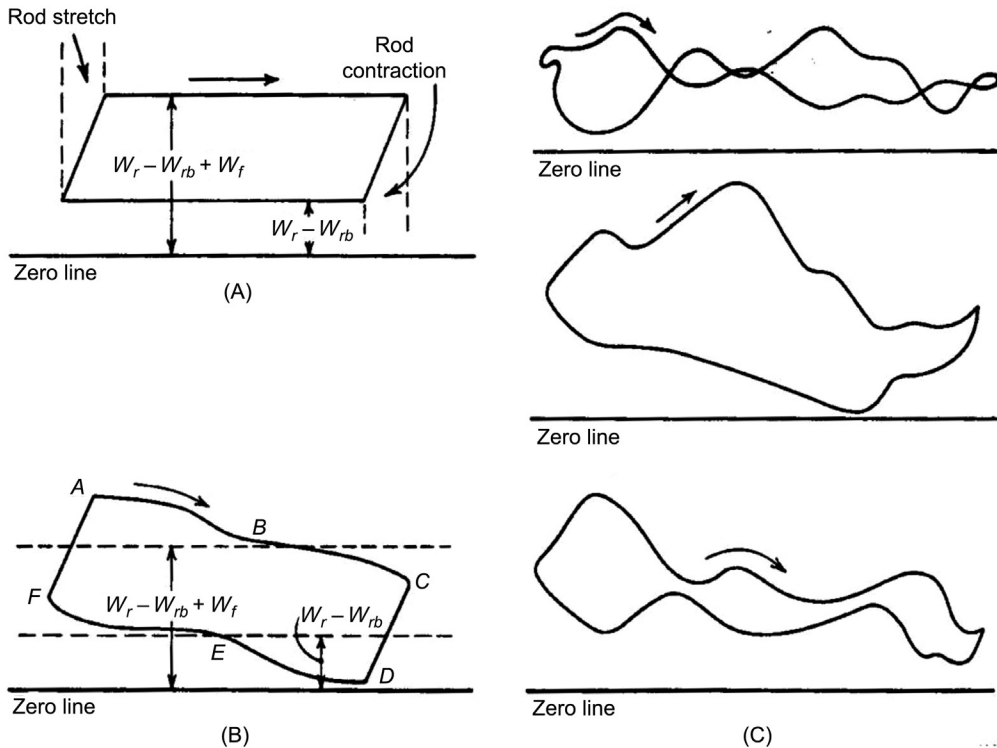
The surface dynamometer cards record the history of the variations in loading on the polished rod during a cycle. The cards have three principal uses:

1. To obtain information that can be used to determine load, torque, and horsepower changes required of the pump equipment
2. To improve pump operating conditions such as pump speed and stroke length
3. To check well conditions after installation of equipment to prevent or diagnose various operating problems (like pounding, etc.)

Surface instruments can be mechanical, hydraulic, and electrical. One of the most common mechanical instruments is a ring dynamometer installed between the hanger bar and the polished rod clamp in such a manner as the ring may carry the entire well load. The deflection of the ring is proportional to the load, and this deflection is amplified and transmitted to the recording arm by a series of levers. A stylus on the recording arm traces a record of the imposed loads on a waxed (or via an ink pen) paper card located on a drum. The loads are obtained in terms of polished rod displacements by having the drum oscillate back and forth to reflect the polished rod motion. Correct interpretation of surface dynamometer card leads to estimate of various parameter values.

- Maximum and minimum PRLs can be read directly from the surface card (with the use of instrument calibration). These data then allow for the determination of the torque, counterbalance, and horsepower requirements for the surface unit.
- Rod stretch and contraction is shown on the surface dynamometer card. This phenomenon is reflected in the surface unit dynamometer card and is shown in [Fig. 16.11A](#) for an ideal case.
- Acceleration forces cause the ideal card to rotate clockwise. The PRL is higher at the bottom of the stroke and lower at the top of the stroke. Thus, in [Fig. 16.11B](#), Point A is at the bottom of the stroke.
- Rod vibration causes a serious complication in the interpretation of the surface card. This is result of the closing of the TV and the “pickup” of the fluid load by the rod string. This is, of course, the fluid pounding. This phenomenon sets up damped oscillation (longitudinal and bending) in the rod string. These oscillations result in waves moving from one end of the rod string to the other. Because the polished rod moves slower near the top and bottom of the strokes, these stress (or load) fluctuations due to vibrations tend to show up more prominently at those locations on the cards. [Fig. 16.11C](#) shows typical dynamometer card with vibrations of the rod string.

[Fig. 16.12](#) presents a typical chart from a strain-gage type of dynamometer measured for a conventional unit operated with a 74-in. stroke at 15.4 strokes per minute. It shows the history of the load on the polished rod as a function of time (this is for a well 825 ft in depth with a No. 86 three-tapered rod string). [Fig. 16.13](#) reproduces the data in [Fig. 16.12](#) in a load versus displacement

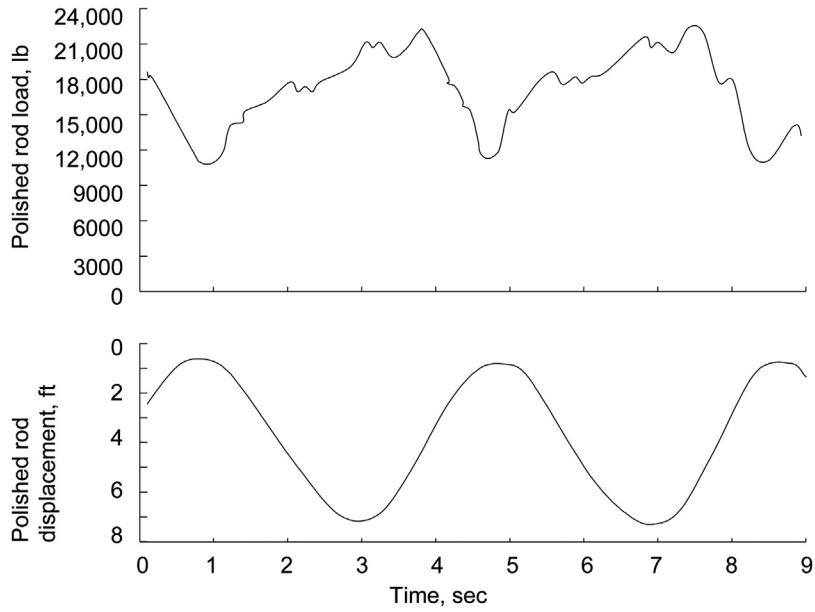


**FIGURE 16.11**

Surface dynamometer card: (A) ideal card (stretch and contraction); (B) ideal card (acceleration); (C) three typical cards (Nind, 1964).

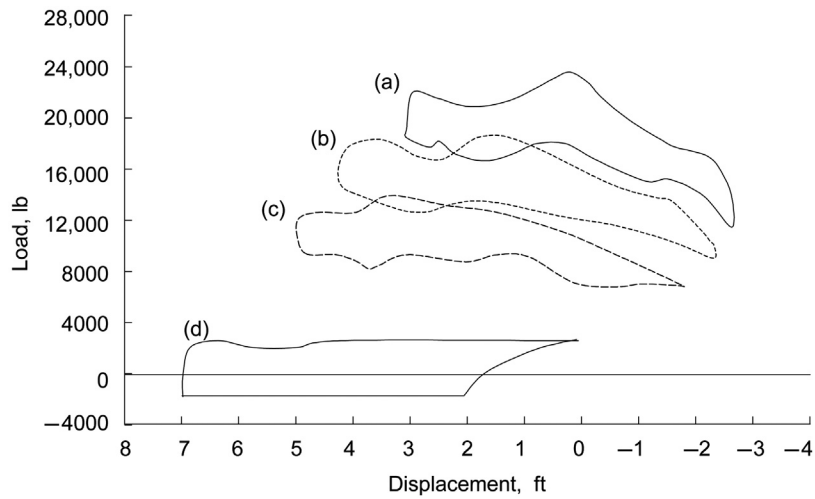
diagram. In the surface chart, we can see the peak load of 22,649 lb (which is 28,800 psi at the top of the 1-in. rod) in Fig. 16.13a. In Fig. 16.13b, we see the peak load of 17,800 lb (which is 29,600 psi at the top of the  $\frac{7}{8}$ -in. rod). In Fig. 16.13c, we see the peak load of 13,400 lb (which is 30,300 psi at the top of the  $\frac{3}{4}$ -in. rod). In Fig. 16.13d is the dynamometer card at the plunger itself. This card indicates gross pump stroke of 7.1 ft, a net liquid stroke of 4.6 ft, and a fluid load of  $W_f = 3200$  lb. The shape of the pump card, Fig. 16.13d, indicates some down-hole gas compression. The shape also indicates that the tubing anchor is holding properly. A liquid displacement rate of 200 bbl/day is calculated and, compared to the surface measured production of 184 bbl/day, indicated no serious tubing flowing leak. The negative in Fig. 16.13d is the buoyancy of the rod string.

The information derived from the dynamometer card (dynagraph) can be used for evaluation of pump performance and troubleshooting of pumping systems. This subject is thoroughly addressed by Brown (1980).



**FIGURE 16.12**

Strain-gage-type dynamometer chart.



**FIGURE 16.13**

Surface to down hole cards derived from surface dynamometer card.

---

## 16.8 SUMMARY

This chapter presents the principles of sucker rod pumping systems and illustrates a procedure for selecting components of rod pumping systems. Major tasks include calculations of PRL, peak torque, stresses in the rod string, pump deliverability, and counterweight placement.

---

## REFERENCES

- Brown, K.E., 1980. *The Technology of Artificial Lift Methods*, vol. 2a. Petroleum Publishing Co., Tulsa, OK.
- Coberly, C.J., 1938. Problems in modern deep-well pumping. *Oil Gas J* 36, 33–39.
- Golan, M., Whitson, C.H., 1991. *Well Performance*. second ed. Prentice Hall, Englewood Cliffs, NJ.
- Kelly, H.L. and Willis, R.M. 1954. Manual for selection of beam pumping equipment—part 3. *Pet. Eng.*, Sept. B77–B97.
- Nind, T.E.W., 1964. *Principles of Oil Well Production*. McGraw-Hill Book Co, New York.

---

## PROBLEMS

- 16.1.** If the dimensions  $d_1$ ,  $d_2$ , and  $c$  take the same values for both conventional unit (Class I lever system) and air-balanced unit (Class III lever system), how different will their polished rod strokes length be?
- 16.2.** What are the advantages of the Lufkin Mark II and air-balanced units in comparison with conventional units?
- 16.3.** Use your knowledge of kinematics to prove that for Class I lever systems,
- the polished rod will travel faster in down stroke than in upstroke if the distance between crankshaft and the center of Sampson post is less than dimension  $d_1$ .
  - the polished rod will travel faster in upstroke than in down stroke if the distance between crankshaft and the center of Sampson post is greater than dimension  $d_1$ .
- 16.4.** Derive a formula for calculating the effective diameter of a tapered rod string.
- 16.5.** Derive formulas for calculating length fractions of equal-top-rod-stress tapered rod strings for (1) two-sized rod strings, (2) three-sized rod strings, and (3) four-sized rod strings. Plot size fractions for each case as a function of plunger area.
- 16.6.** A tapered rod string consists of sections of  $\frac{5}{8}$ - and  $\frac{1}{2}$ - in. rods and a 2-in. plunger. Use the formulas from Problem 16.5 to calculate length fraction of each size of rod.
- 16.7.** A tapered rod string consists of sections of  $\frac{3}{4}$ -,  $\frac{5}{8}$ -, and  $\frac{1}{2}$ -in. rods and a  $1\frac{3}{4}$ -in. plunger. Use the formulas from Problem 16.5 to calculate length fraction of each size of rod.
- 16.8.** The following geometry dimensions are for the pumping unit C–80D–133–48:

$$d_1 = 64 \text{ in.}$$

$$d_2 = 64 \text{ in.}$$

$$c = 24 \text{ in.}$$

$$h = 74.5 \text{ in.}$$

Can this unit be used with a 2-in. plunger and  $\frac{3}{4}$ -in. rods to lift 30 °API gravity crude (formation volume factor 1.25 rb/stb) at depth of 2,000 ft? If yes, what is the required counterbalance load?

- 16.9.** The following geometry dimensions are for the pumping unit C–320D–256–120:

$$d_1 = 111.07\text{in.}$$

$$d_2 = 155\text{in.}$$

$$c = 42\text{in.}$$

$$h = 132\text{in.}$$

Can this unit be used with a 2½-in. plunger and  $\frac{3}{4}$ -,  $\frac{7}{8}$ -, 1-in. tapered rod string to lift 22° API gravity crude (formation volume factor 1.22 rb/stb) at a depth of 3000 ft? If yes, what is the required counterbalance load?

- 16.10.** A well is pumped off with a rod pump described in Problem 16.8. A 2½-in. tubing string (2.875-in. OD, 2.441 ID) in the well is not anchored. Calculate (1) expected liquid production rate (use pump volumetric efficiency 0.80) and (2) required prime mover power (use safety factor 1.3).
- 16.11.** A well is pumped with a rod pump described in Problem 16.9 to a liquid level of 2800 ft. A 3-in. tubing string (3½-in. OD, 2.995-in. ID) in the well is anchored. Calculate (1) expected liquid production rate (use pump volumetric efficiency 0.85) and (2) required prime mover power (use safety factor 1.4).
- 16.12.** A well is to be put on a sucker rod pump. The proposed pump setting depth is 4500 ft. The anticipated production rate is 500 bbl/day oil of 40 °API gravity against wellhead pressure 150 psig. It is assumed that the working liquid level is low, and a sucker rod string having a working stress of 30,000 psi is to be used. Select surface and subsurface equipment for the installation. Use a safety factor of 1.40 for prime mover power.
- 16.13.** A well is to be put on a sucker rod pump. The proposed pump setting depth is 4000 ft. The anticipated production rate is 550 bbl/day oil of 35 °API gravity against wellhead pressure 120 psig. It is assumed that working liquid level will be about 3000 ft, and a sucker rod string having a working stress of 30,000 psi is to be used. Select surface and subsurface equipment for the installation. Use a safety factor of 1.30 for prime mover power.



---

# GAS LIFT

# 17

---

## 17.1 INTRODUCTION

Gas lift technology increases oil production rate by injection of compressed gas into the lower section of tubing through the casing–tubing annulus and an orifice installed in the tubing string. Upon entering the tubing, the compressed gas affects liquid flow in two ways: (1) the energy of expansion propels (pushes) the oil to the surface and (2) the gas aerates the oil so that the effective density of the fluid is less and, thus, easier to get to the surface.

There are four categories of wells in which a gas lift can be considered:

1. High productivity index (PI), high bottom-hole pressure wells
2. High PI, low bottom-hole pressure wells
3. Low PI, high bottom-hole pressure wells
4. Low PI, low bottom-hole pressure wells

Wells having a PI of 0.50 or less are classified as low productivity wells. Wells having a PI greater than 0.50 are classified as high productivity wells. High bottom-hole pressures will support a fluid column equal to 70% of the well depth. Low bottom-hole pressures will support a fluid column less than 40% of the well depth.

Gas lift technology has been widely used in the oil fields that produce sandy and gassy oils. Crooked/deviated holes present no problem. Well depth is not a limitation. It is also applicable to off-shore operations. Lifting costs for a large number of wells are generally very low. However, it requires lift gas within or near the oil fields. It is usually not efficient in lifting small fields with a small number of wells if gas compression equipment is required. Gas lift advancements in pressure control and automation systems have enabled the optimization of individual wells and gas lift systems.

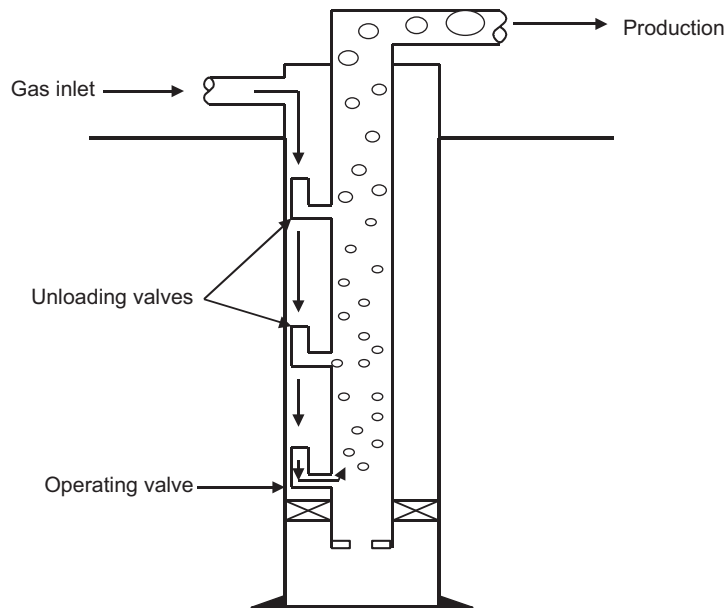
---

## 17.2 GAS LIFT SYSTEM

A complete gas lift system consists of a gas compression station, a gas injection manifold with injection chokes and time cycle surface controllers, a tubing string with installations of unloading valves and operating valve, and a down-hole chamber.

Fig. 17.1 depicts a configuration of a gas lifted well with installations of unloading valves and operating valve on the tubing string. There are four principal advantages to be gained by the use of multiple valves in a well:

1. Deeper gas injection depths can be achieved by using valves for wells with fixed surface injection pressures.
2. Variation in the well's productivity can be obtained by selectively injecting gas valves set at depths "higher" or "lower" in the tubing string.



**FIGURE 17.1**

Configuration of a typical gas lift well.

3. Gas volumes injected into the well can be “metered” into the well by the valves.
4. Intermittent gas injection at progressively deeper set valves can be carried out to “kick off” a well to either continuous or intermittent flow.

A continuous gas lift operation is a steady-state flow of the aerated fluid from the bottom (or near bottom) of the well to the surface. Intermittent gas lift operation is characterized by a start-and-stop flow from the bottom (or near bottom) of the well to the surface. This is *unsteady state flow*.

In continuous gas lift, a small volume of high-pressure gas is introduced into the tubing to aerate or lighten the fluid column. This allows the flowing bottom-hole pressure with the aid of the expanding injection gas to deliver liquid to the surface. To accomplish this efficiently, it is desirable to design a system that will permit injection through a single valve at the greatest depth possible with the available injection pressure.

Continuous gas lift method is used in wells with a high PI ( $\geq 0.5$  stb/day/psi) and a reasonably high reservoir pressure relative to well depth. Intermittent gas lift method is suitable to wells with (1) high PI and low reservoir pressure or (2) low PI and low reservoir pressure.

The type of gas lift operation used, continuous or intermittent, is also governed by the volume of fluids to be produced, the available lift gas as to both volume and pressure, and the well reservoir's conditions such as the case when the high instantaneous bottom hole pressure (BHP) draw-down encountered with intermittent flow would cause excessive sand production, or coning, and/or gas into the wellbore.

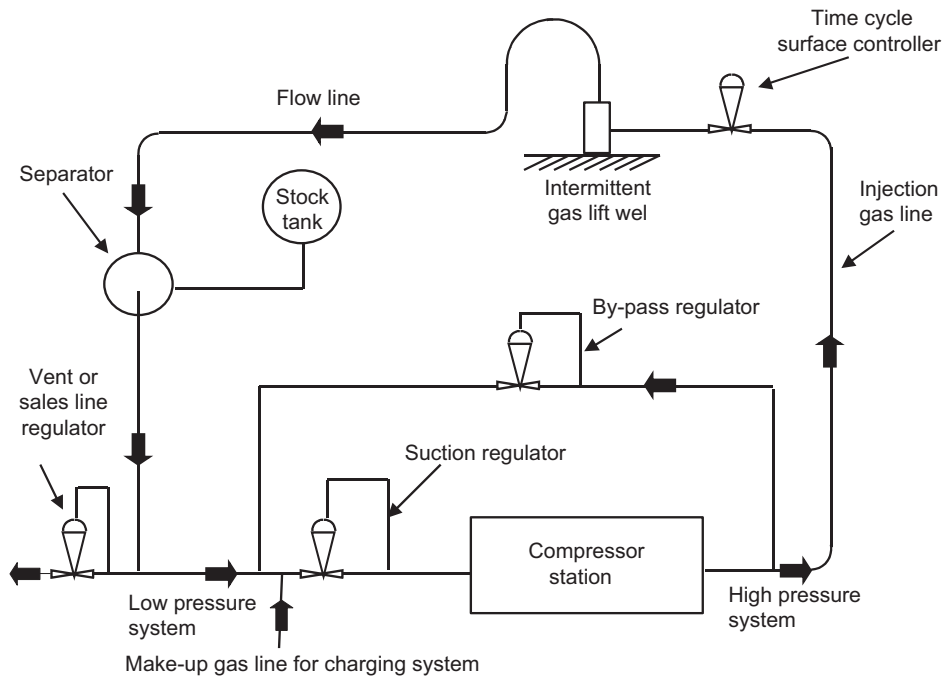
Fig. 17.2 illustrates a simplified flow diagram of a closed rotary gas lift system for a single well in an intermittent gas lift operation. The time cycle surface controller regulates the start-and-stop injection of lift gas to the well.

For proper selection, installation, and operations of gas lift systems, the operator must know the equipment and the fundamentals of gas lift technology. The basic equipment for gas lift technology includes the following:

1. Main operating valves
2. Wire-line adaptations
3. Check valves
4. Mandrels
5. Surface control equipment
6. Compressors

This chapter covers basic system engineering design fundamentals for gas lift operations. Relevant topics include the following:

1. Liquid flow analysis for evaluation of gas lift potential
2. Gas flow analysis for determination of lift gas compression requirements



**FIGURE 17.2**

A simplified flow diagram of a closed rotary gas lift system for single intermittent well.

3. Unloading process analysis for spacing subsurface valves
4. Valve characteristics analysis for subsurface valve selection
5. Installation design for continuous and intermittent lift systems.

---

### 17.3 EVALUATION OF GAS LIFT POTENTIAL

Continuous gas lift can be satisfactorily applied to most wells having a reasonable degree of bottom-hole maintenance and a PI of approximately 0.5 bbl/day/psi or greater. A PI as low as 0.2 bbl/day/psi can be used for a continuous gas lift operation if injection gas is available at a sufficiently high pressure. An intermittent gas lift is usually applied to wells having a PI less than 0.5 bbl/day/psi.

Continuous gas lift wells are changed to intermittent gas lift wells after reservoir pressures drop to below a certain level. Therefore, intermittent gas lift wells usually give lower production rates than continuous gas lift wells. The decision of whether to use gas lift technology for oil well production starts from evaluating gas lift potential with continuous gas injection.

Evaluation of gas lift potential requires system analyses to determine well operating points for various lift gas availabilities. The principle is based on the fact that there is only one pressure at a given point (node) in any system; no matter, the pressure is estimated based on the information from upstream (inflow) or downstream (outflow). The node of analysis is usually chosen to be the gas injection point inside the tubing, although bottom-hole is often used as a solution node.

The potential of gas lift wells is controlled by gas injection rate or gas liquid ratio (GLR). Four gas injection rates are significant in the operation of gas lift installations:

1. Injection rates of gas that result in no liquid (oil or water) flow up the tubing. The gas amount is insufficient to lift the liquid. If the gas enters the tubing at an extremely low rate, it will rise to the surface in small semi-spheres (bubbly flow).
2. Injection rates of maximum efficiency where a minimum volume of gas is required to lift a given amount of liquid.
3. Injection rate for maximum liquid flow rate at the “optimum GLR.”
4. Injection rate of no liquid flow because of excessive gas injection. This occurs when the friction (pipe) produced by the gas prevents liquid from entering the tubing.

Fig. 17.3 depicts a continuous gas lift operation. The tubing is filled with reservoir fluid below the injection point and with the mixture of reservoir fluid and injected gas above the injection point. The pressure relationship is shown in Fig. 17.4.

The inflow performance curve for the node at the gas injection point inside the tubing is well IPR curve minus the pressure drop from bottom-hole to the node. The outflow performance curve is the vertical lift performance curve, with total GLR being the sum of formation GLR and injected GLR. Intersection of the two curves defines the operation point, that is, the well production potential.

In a field-scale evaluation, if an unlimited amount of lift gas is available for a given gas lift project, the injection rate of gas to individual wells should be optimized to maximize oil production of each well. If only a limited amount of gas is available for the gas lift, the gas should be

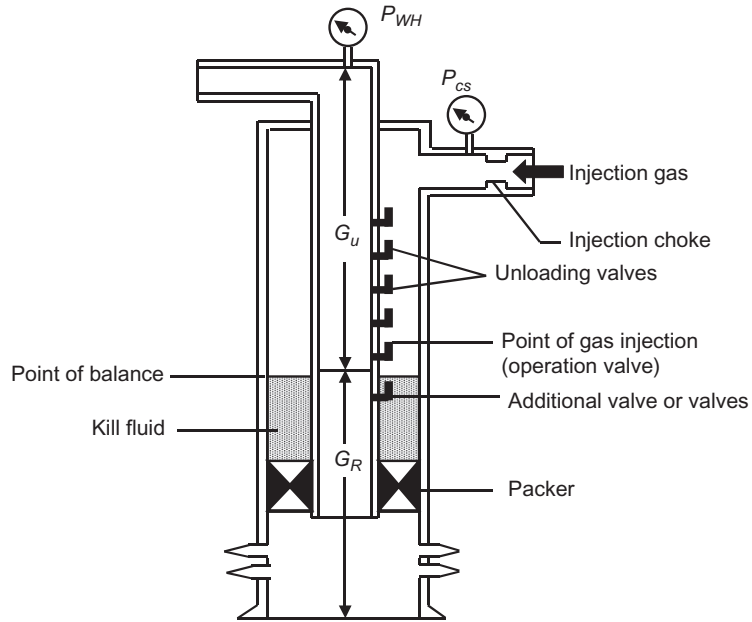


FIGURE 17.3

A sketch of continuous gas lift.

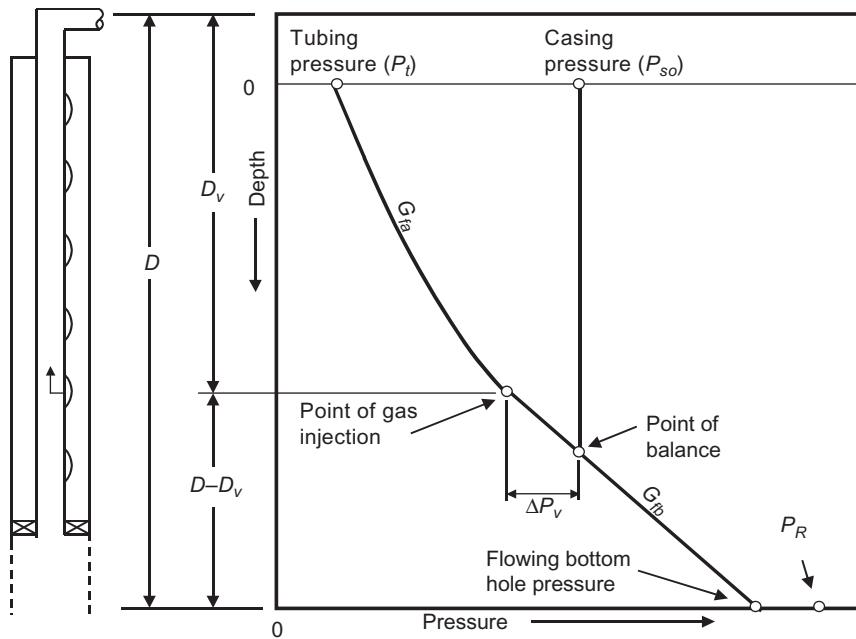


FIGURE 17.4

Pressure relationship in a continuous gas lift.

distributed to individual wells based on predicted well lifting performance, that is, the wells that will produce oil at higher rates at a given amount of lift gas are preferably chosen to receive more lift gas.

If an unlimited amount of gas lift gas is available for a well, the well should receive a lift gas injection rate that yields the optimum GLR in the tubing so that the flowing bottom-hole pressure is minimized, and thus, oil production is maximized. The optimum GLR is liquid flow rate dependent and can be found from traditional gradient curves such as those generated by Gilbert (1954). Similar curves can be generated with modern computer programs using various multiphase correlations. The computer program *OptimumGLR.xls* in the CD attached to this book was developed based on modified Hagedorn and Brown method (Brown, 1977) for multiphase flow calculations and the Chen method (1979) for friction factor determination. It can be used for predicting the optimum GLR in tubing at a given tubing head pressure and liquid flow rate.

After the system analysis is completed with the optimum GLRs in the tubing above the injection point, the expected liquid production rate (well potential) is known. The required injection GLR to the well can be calculated by

$$\text{GLR}_{inj} = \text{GLR}_{opt,o} - \text{GLR}_{fm}, \quad (17.1)$$

where

$\text{GLR}_{inj}$  = injection GLR, scf/stb

$\text{GLR}_{opt,o}$  = optimum GLR at operating flow rate, scf/stb

$\text{GLR}_{fm}$  = formation oil GLR, scf/stb.

Then the required gas injection rate to the well can be calculated by

$$q_g, inj = \text{GLR}_{inj} q_o, \quad (17.2)$$

where  $q_o$  is the expected operating liquid flow rate.

If a limited amount of gas lift gas is available for a well, the well potential should be estimated based on GLR expressed as

$$\text{GLR} = \text{GLR}_{fm} + \frac{q_g, inj}{q}, \quad (17.3)$$

where  $q_g$  is the lift gas injection rate (scf/day) available to the well.

**Example Problem 17.1** An oil well has a pay zone around the mid-perf depth of 5200 ft. The formation oil has a gravity of 26 °API and GLR of 300 scf/stb. Water cut remains 0%. The IPR of the well is expressed as where

$$q = q_{\max} \left[ 1 - 0.2 \frac{P_{wf}}{\bar{p}} - 0.8 \left( \frac{P_{wf}}{\bar{p}} \right)^2 \right],$$

where

$$q_{\max} = 800 \text{ stb/day}$$

$$\bar{p} = 2000 \text{ psia.}$$

A 2½-in. tubing (2.259 in. inside diameter [ID]) can be set with a packer at 200 ft above the mid-perf. What is the maximum expected oil production rate from the well with continuous gas lift at a wellhead pressure of 200 psia if

1. an unlimited amount of lift gas is available for the well?
2. only 1 MMscf/day of lift gas is available for the well?

**Solution** The maximum oil production rate is expected when the gas injection point is set right above the packer. Assuming that the pressure losses due to friction below the injection point are negligible, the inflow-performance curve for the gas injection point (inside tubing) can be expressed as

$$p_{vf} = 0.125\bar{p}[\sqrt{81 - 80(q/q_{\max})} - 1] - G_R(D - D_v),$$

where  $p_{vf}$  is the pressure at the gas injection point,  $G_R$  is the pressure gradient of the reservoir fluid,  $D$  is the pay zone depth, and  $D_v$  is the depth of the gas injection point. Based on the oil gravity of 26 °API,  $G_R$  is calculated to be 0.39 psi/ft.  $D$  and  $D_v$  are equal to 5200 ft and 5000 ft, respectively in this problem.

The outflow performance curve for the gas injection point can be determined based on 2.259-in. tubing ID, 200 psia wellhead pressure, and the GLRs.

1. Spreadsheet *OptimumGLR.xls* gives the following:

$q$ (stb/day)	GLR <sub>opt</sub> (scf/stb)
400	4500
600	3200
800	2400

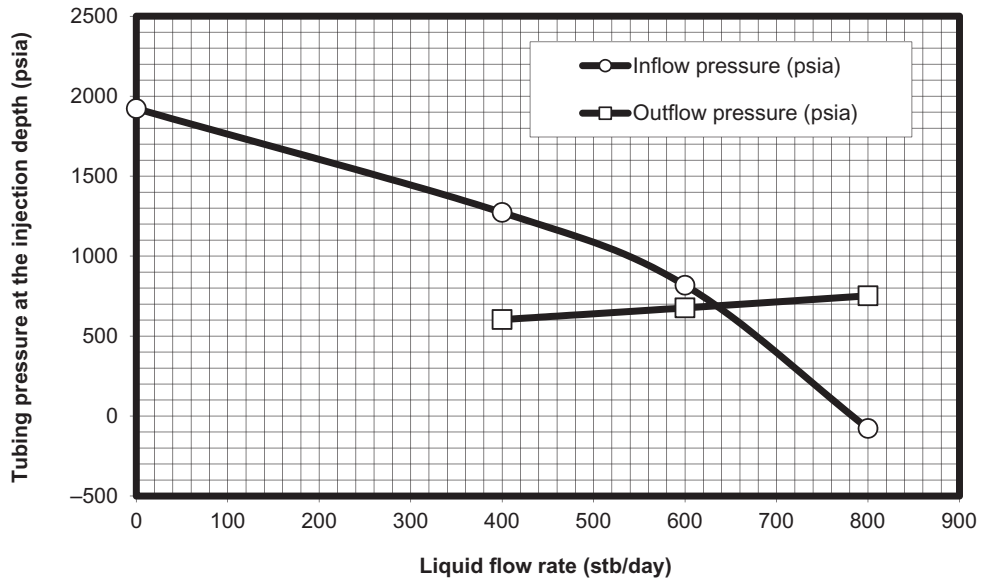
Using these data to run computer program *HagedornBrownCorrelation.xls* (on the CD attached to this book) gives

$q$ (stb/day)	$p_t$ (psia)
400	603
600	676
800	752

Fig. 17.5 shows the system analysis plot given by the computer program *GasLiftPotential.xls*. It indicates an operating point of  $q = 632$  stb/day and  $p_{t,v} = 698$  psia tubing pressure at the depth of injection.

The optimum GLR at the operating point is calculated with interpolation as

$$\begin{aligned} \text{GLR}_{opt,o} &= 2400 + \frac{3200 - 2400}{800 - 600}(800 - 632) \\ &= 3072 \text{ scf/stb.} \end{aligned}$$



**FIGURE 17.5**

System analysis plot given by GasLiftPotential.xls for the unlimited gas injection case.

The injection GLR is

$$GLR_{inj} = 3072 - 300 = 2772 \text{ scf/stb.}$$

Then the required gas injection rate to the well can be calculated:

$$q_{g, inj} = (2772)(632) = 1,720,000 \text{ scf/day}$$

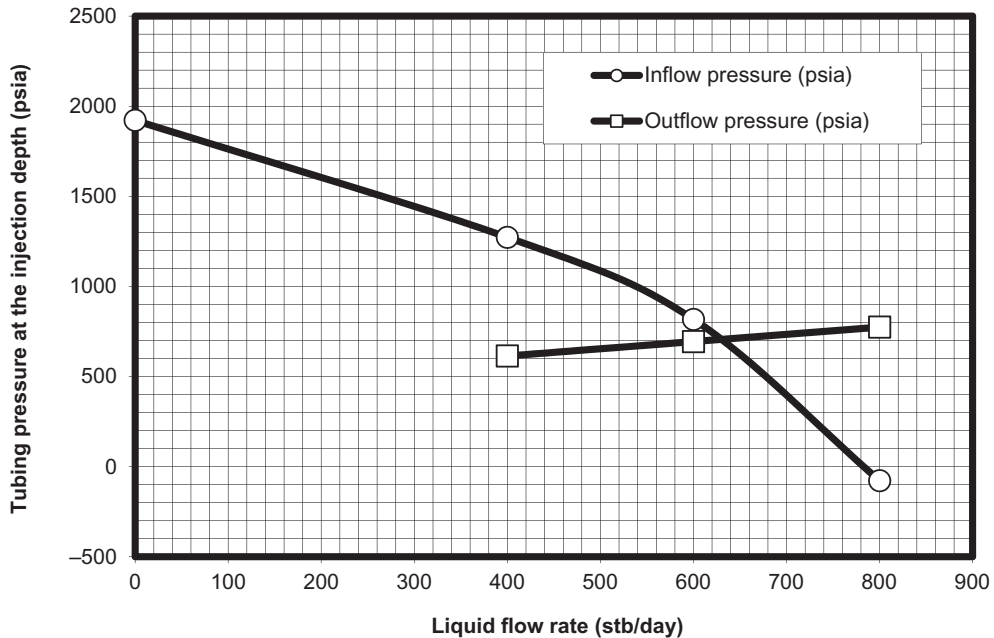
- For a given amount of lift gas 1 MMscf/day, the GLR can be calculated with Eq. (17.3) as

$q$ (stb/day)	GLR (scf/stb)
400	2800
600	1967
800	1550

Using these data to run computer program *HagedornBrownCorrelation.xls* gives

$q$ (stb/day)	$p_t$ (psia)
400	614
600	694
800	774





**FIGURE 17.6**

System analysis plot given by GasLiftPotential.xls for the limited gas injection case.

Fig. 17.6 shows the system analysis plot given by the computer program *GasLiftPotential.xls*. It indicates an operating point of  $q = 620$  stb/day and  $p_t = 702$  psia tubing pressure at the depth of injection.

This example shows that increasing the gas injection rate from 1 to 1.58 MMscf/day will not make a significant difference in the oil production rate.

## 17.4 GAS LIFT GAS COMPRESSION REQUIREMENTS

The gas compression station should be designed to provide an adequate gas lift gas flow rate at sufficiently high pressure. These gas flow rates and output pressures determine the required power of the compression station.

### 17.4.1 GAS FLOW RATE REQUIREMENT

The total gas flow rate of the compression station should be designed on the basis of gas lift at peak operating condition for all the wells with a safety factor for system leak consideration, that is,

$$q_{g,total} = S_f \sum_{i=1}^{N_w} (q_{g,inj})_i, \quad (17.4)$$

where

$q_g$  = total output gas flow rate of the compression station, scf/day

$S_f$  = safety factor, 1.05 or higher

$N_w$  = number of wells.

The procedure for determination of lift gas injection rate  $q_{g,inj}$  to each well has been illustrated in Example Problem 17.1.

## 17.4.2 OUTPUT GAS PRESSURE REQUIREMENT

Kickoff of a dead well (non-natural flowing) requires much higher compressor output pressures than the ultimate goal of steady production (either by continuous gas lift or by intermittent gas lift operations). Mobil compressor trailers are used for the kickoff operations. The output pressure of the compression station should be designed on the basis of the gas distribution pressure under normal flow conditions, not the kickoff conditions. It can be expressed as

$$p_{out} = S_f p_L, \quad (17.5)$$

where

$p_{out}$  = output pressure of the compression station, psia

$S_f$  = safety factor

$p_L$  = pressure at the inlet of the gas distribution line, psia.

Starting from the tubing pressure at the valve ( $p_{t,v}$ ), the pressure at the inlet of the gas distribution line can be estimated based on the relationships of pressures along the injection path. These relationships are discussed in the following subsections.

### 17.4.2.1 Injection pressure at valve depth

The injection pressure at valve depth in the casing side can be expressed as

$$p_{c,v} = p_{t,v} + \Delta p_v, \quad (17.6)$$

where

$p_{c,v}$  = casing pressure at valve depth, psia

$\Delta p_v$  = pressure differential across the operating valve (orifice).

It is a common practice to use  $\Delta p_v = 100$  psi. The required size of the orifice can be determined using the choke flow equations presented in [Subsection 17.4.2.3](#).

### 17.4.2.2 Injection pressure at surface

Accurate determination of the surface injection pressure  $p_{c,s}$  requires rigorous methods such as the Cullender and Smith method ([Katz et al., 1959](#)). The average temperature and compressibility factor method also gives results with acceptable accuracy. In both methods, the frictional pressure

losses in the annulus are considered. However, because of the large cross-sectional area of the annular space, the frictional pressure losses are often negligible. Then the average temperature and compressibility factor model degenerates to (Economides et al., 1994)

$$p_{c,v} = p_{c,s} e^{0.01875 \frac{\gamma_g D_v}{\bar{z} T}}, \quad (17.7)$$

where

$p_{c,v}$  = casing pressure at valve depth, psia

$p_{c,s}$  = casing pressure at surface, psia

$\gamma_g$  = gas-specific gravity, air = 1.0

$\bar{z}$  = the average gas compressibility factor

$\bar{T}$  = the average temperature, °R.

Eq. (17.7) can be rearranged to be

$$p_{c,s} = p_{c,v} e^{-0.01875 \frac{\gamma_g D_v}{\bar{z} T}}. \quad (17.8)$$

Since the  $z$  factor also depends on  $p_{c,s}$ , this equation can be solved for  $p_{c,s}$  with a trial-and-error approach. Because Eq. (17.8) involves exponential function that is difficult to handle without a calculator, an approximation to the equation has been used traditionally. In fact, when Eq. (17.7) is expanded as a Taylor series, and if common fluid properties for a natural gas and reservoir are considered such as  $\gamma_g = 0.7$ ,  $\bar{z} = 0.9$ , and  $\bar{T} = 600$  °R, it can be approximated as

$$p_{c,v} = p_{c,s} \left( 1 + \frac{D_v}{40,000} \right), \quad (17.9)$$

which gives

$$p_{c,s} = \frac{p_{c,v}}{1 + \frac{D_v}{40,000}}. \quad (17.10)$$

Neglecting the pressure losses between injection choke and the casing head, the pressure downstream of the choke ( $p_{dn}$ ) can be assumed to be the casing surface injection pressure, that is,

$$p_{dn} = p_{c,s}.$$

### 17.4.2.3 Pressure upstream of the choke

The pressure upstream of the injection choke depends on flow condition at the choke, that is, sonic or subsonic flow. Whether a sonic flow exists depends on a downstream-to-upstream pressure ratio. If this pressure ratio is less than a critical pressure ratio, sonic (critical) flow exists. If this pressure ratio is greater than or equal to the critical pressure ratio, subsonic (subcritical) flow exists. The critical pressure ratio through chokes is expressed as

$$R_c = \left( \frac{2}{k+1} \right)^{\frac{k}{k-1}}, \quad (17.11)$$

where  $k = C_p/C_v$  is the gas-specific heat ratio. The value of the  $k$  is about 1.28 for natural gas. Thus, the critical pressure ratio is about 0.55.

Pressure equations for choke flow are derived based on an isentropic process. This is because there is no time for heat to transfer (adiabatic) and the friction loss is negligible (assuming reversible) at choke.

#### 17.4.2.3.1 Sonic flow

Under sonic flow conditions, the gas passage rate reaches and remains at its maximum value. The gas passage rate is expressed in the following equation for ideal gases:

$$q_{gM} = 879C_c A p_{up} \sqrt{\left(\frac{k}{\gamma_g T_{up}}\right) \left(\frac{2}{k+1}\right)^{\frac{k+1}{k-1}}} \quad (17.12)$$

where

- $q_{gM}$  = gas flow rate, Mscf/day
- $p_{up}$  = pressure upstream the choke, psia
- $A$  = cross-sectional area of choke, in.<sup>2</sup>
- $T_{up}$  = upstream temperature, °R
- $\gamma_g$  = gas-specific gravity related to air
- $C_c$  = choke flow coefficient.

The choke flow coefficient  $C_c$  can be determined using charts in Figs. 5.2 and 5.3 (see Chapter 5: Choke Performance) for nozzle- and orifice-type chokes, respectively. The following correlation has been found to give reasonable accuracy for Reynolds numbers between  $10^4$  and  $10^6$  for nozzle-type chokes (Guo and Ghaleb, 2005):

$$C = \frac{d}{D} + \frac{0.3167}{\left(\frac{d}{D}\right)^{0.6}} + 0.025[\log(N_{Re}) - 4], \quad (17.13)$$

where

- $d$  = choke diameter, in.
- $D$  = pipe diameter, in.
- $N_{Re}$  = Reynolds number

and the Reynolds number is given by

$$N_{Re} = \frac{20q_{gM}\gamma_g}{\mu d}, \quad (17.14)$$

where

- $\mu$  = gas viscosity at *in situ* temperature and pressure, cp.

Eq. (17.12) indicates that the upstream pressure is independent of downstream pressure under sonic flow conditions. If it is desirable to make a choke work under sonic flow conditions, the upstream pressure should meet the following condition:

$$p_{up} \geq \frac{p_{dn}}{0.55} = 1.82p_{dn} \quad (17.15)$$

Once the pressure upstream of the choke/orifice is determined by Eq. (17.15), the required choke/orifice diameter can be calculated with Eq. (17.12) using a trial-and-error approach.

#### 17.4.2.3.2 Subsonic flow

Under subsonic flow conditions, gas passage through a choke can be expressed as

$$q_{gM} = 1248 C_c A p_{up} \times \sqrt{\frac{k}{(k-1)\gamma_g T_{up}} \left[ \left( \frac{p_{dn}}{p_{up}} \right)^{\frac{2}{k}} - \left( \frac{p_{dn}}{p_{up}} \right)^{\frac{k+1}{k}} \right]} \quad (17.16)$$

If it is desirable to make a choke work under subsonic flow conditions, the upstream pressure should be determined from Eq. (17.16) with a trial-and-error method.

#### 17.4.2.4 Pressure of the gas distribution line

The pressure at the inlet of gas distribution line can be calculated using the Weymouth equation for horizontal flow (Weymouth, 1912):

$$q_{gM} = \frac{0.433 T_b}{p_b} \sqrt{\frac{(p_L^2 - p_{up}^2) D^{16/3}}{\gamma_g \bar{T} \bar{z} L_g}} \quad (17.17)$$

where

$T_b$  = base temperature, °R

$p_b$  = base pressure, psi

$p_L$  = pressure at the inlet of gas distribution line, psia

$L_g$  = length of distribution line, mile

Eq. (17.17) can be rearranged to solve for pressure:

$$p_L = \sqrt{p_{up}^2 + \left( \frac{q_{gM} p_b}{0.433 T_b} \right)^2 \frac{\gamma_g \bar{T} \bar{z} L_g}{D^{16/3}}} \quad (17.18)$$

**Example Problem 17.2** An oil field has 16 oil wells to be gas lifted. The gas lift gas at the central compressor station is first pumped to two injection manifolds with 4-in. ID, 1-mile lines and then is distributed to the wellheads with 4-in. ID, 0.2-mile lines. Given the following data, calculate the required output pressure of compression station:

Gas-specific gravity ( $\gamma_g$ ):	0.65
Valve depth ( $D_v$ ):	5000 ft
Maximum tubing pressure at valve depth ( $p_v$ ):	500 psia
Required lift gas injection rate per well:	2 MMscf/day
Pressure safety factor ( $S_f$ ):	1.1
Base temperature ( $T_b$ ):	60°F
Base pressure ( $p_b$ ):	14.7 psia

**Solution** Using  $\Delta p_v = 100$  psi, the injection pressure at valve depth is then 600 psi. Eq. (17.10) gives

$$p_{c,s} = \frac{p_{c,v}}{1 + \frac{D_v}{40,000}} = \frac{600}{1 + \frac{5000}{40,000}} = 533 \text{ psia.}$$

Neglecting the pressure losses between the injection choke and the casing head, pressure downstream of the choke ( $p_{dn}$ ) can be assumed to be the surface injection pressure, that is,

$$p_{dn} = p_{c,s} = 533 \text{ psia.}$$

Assuming minimum sonic flow at the injection choke, the pressure upstream of the choke is calculated as

$$p_{up} \geq \frac{p_{dn}}{0.55} = 1.82p_{dn} = (1.82)(533) = 972 \text{ psia.}$$

The gas flow rate in each of the two gas distribution lines is  $(2)(16)/(2)$ , or 16 MMscf/day. Using the trial-and-error method, Eq. (17.18) gives

$$\begin{aligned} p_L &= \sqrt{(972)^2 + \left( \frac{(16,000)(14.7)}{0.433(60+460)} \right)^2 \frac{(0.65)(530)(0.97)(1)}{(4)^{16/3}}} \\ &= 1056 \text{ psia.} \end{aligned}$$

The required output pressure of the compressor is determined to be

$$p_{out} = S_f p_L = (1.1)(1056) = 1162 \text{ psia.}$$

The computer program *CompressorPressure.xls* can be used for solving similar problems. The solution given by the program to this example problem is shown in Table 17.1.

### 17.4.3 COMPRESSION POWER REQUIREMENT

The compressors used in the petroleum industry fall into two distinct categories: reciprocating and rotary compressors. Reciprocating compressors are built for practically all pressures and volumetric capacities. Reciprocating compressors have more moving parts and, therefore, lower mechanical efficiencies than rotary compressors. Each cylinder assembly of a reciprocating compressor consists of a piston, cylinder, cylinder heads, suction and discharge valves, and other parts necessary to convert rotary motion to reciprocating motion. A reciprocating compressor is designed for a certain range of compression ratios through the selection of proper piston displacement and clearance volume within the cylinder. This clearance volume can be either fixed or variable, depending on the extent of the operation range and the percent of load variation desired. A typical reciprocating compressor can deliver a volumetric gas flow rate up to 30,000 cubic feet per minute (cfm) at a discharge pressure up to 10,000 psig.

<b>Table 17.1 Result Given by Computer Program CompressorPressure.xls</b>		
<i>CompressorPressure.xls</i>		
<i>Description:</i> This spreadsheet calculates required pressure from compressor.		
<i>Instruction:</i> (1) Select a unit system; (2) click "Solution" button; and (3) view result.		
<i>Input Data</i>	<i>U.S. Units</i>	<i>SI Units</i>
Depth of operating valve ( $D_v$ ):	5000 ft	
Length of the main distribution line ( $L_g$ ):	1 mi	
ID of the main distribution line ( $D$ ):	4.00 in.	
Gas flow rate in main distribution line ( $q_{g,i}$ ):	16 MMscf/day	
Surface temperature ( $T_s$ ):	70°F	
Temperature at valve depth ( $T_v$ ):	120°F	
Gas-specific gravity ( $\gamma_g$ ):	0.65 (air = 1)	
Gas-specific heat ratio ( $k$ ):	1.25	
Tubing pressure at valve depth ( $p_t$ ):	500 psia	
Valve pressure differential ( $\Delta p_v$ ):	100 psia	
Base temperature ( $T_b$ ):	60°F	
Base pressure ( $p_b$ ):	14.7 psia	
Pressure safety factor ( $S_f$ ):	1.1	
<b>Solution</b>		
$p_{c,v} = p_{t,v} + \Delta p_v$	600 psia	
Average $z$ -factor in annulus:	0.9189?	
$p_{c,s} - p_{c,v} e^{h - 0.01875 \frac{\gamma_g D_v}{zF}} = 0$ gives $p_{c,s}$	532 psia	
$p_{dn} = p_{c,s}$	532 psia	
$p_{up} \geq \frac{p_{dn}}{0.55} = 1.82 p_{dn}$	969 psia	
Average $z$ -factor at surface:	0.8278	
$p_L - \sqrt{p_{up}^2 + \left(\frac{q_g M P b}{0.433 T_b}\right)^2 \frac{\gamma_g \bar{T} z L_g}{D^{16/3}}} = 0$ gives $p_L$	1063 psia	
$p_{out} = S_f p_L$	1170 psia	

Rotary compressors are divided into two classes: the centrifugal compressor and the rotary blower. A centrifugal compressor consists of a housing with flow passages, a rotating shaft on which the impeller is mounted, bearings, and seals to prevent gas from escaping along the shaft. Centrifugal compressors have few moving parts because only the impeller and shaft rotate. Thus, its efficiency is high and lubrication oil consumption and maintenance costs are low. Cooling water is normally unnecessary because of lower compression ratio and lower friction loss. Compression rates of centrifugal compressors are lower because of the absence of positive displacement. Centrifugal compressors compress gas using centrifugal force. Work is done on the gas by an impeller. Gas is then discharged at a high velocity into a diffuser where the velocity is reduced and its kinetic energy is converted to static pressure. Unlike reciprocating compressors, all this is done without confinement and physical squeezing. Centrifugal compressors with relatively unrestricted

passages and continuous flow are inherently high-capacity, low-pressure ratio machines that adapt easily to series arrangements within a station. In this way, each compressor is required to develop only part of the station compression ratio. Typically, the volume is more than 100,000 cfm and discharge pressure is up to 100 psig.

When selecting a compressor, the pressure-volume characteristics and the type of driver must be considered. Small rotary compressors (vane or impeller type) are generally driven by electric motors. Large-volume positive compressors operate at lower speeds and are usually driven by steam or gas engines. They may be driven through reduction gearing by steam turbines or an electric motor. Reciprocation compressors driven by steam turbines or electric motors are most widely used in the petroleum industry as the conventional high-speed compression machine. Selection of compressors requires considerations of volumetric gas deliverability, pressure, compression ratio, and horsepower.

### 17.4.3.1 Reciprocating compressors

Two basic approaches are used to calculate the horsepower theoretically required to compress natural gas. One is to use analytical expressions. In the case of adiabatic compression, the relationships are complicated and are usually based on the ideal-gas equation. When used for real gases where deviation from ideal-gas law is appreciable, they are empirically modified to take into consideration the gas deviation factor. The second approach is the enthalpy-entropy or Mollier diagram for real gases. This diagram provides a simple, direct, and rigorous procedure for determining the horsepower theoretically necessary to compress the gas.

Even though in practice the cylinders in the reciprocating compressors may be water-cooled, it is customary to consider the compression process as fundamentally adiabatic—that is, to idealize the compression as one in which there is no cooling of the gas. Furthermore, the process is usually considered to be essentially a perfectly reversible adiabatic, that is, an isentropic process. Thus, in analyzing the performance of a typical reciprocating compressor, one may look upon the compression path following the general law

$$pV^k = \text{a constant.} \quad (17.19)$$

For real natural gases in the gravity range  $0.55 < \gamma_g < 1$ , the following relationship can be used at approximately 150°F:

$$k^{150^\circ\text{F}} \approx \frac{2.738 - \log \gamma_g}{2.328} \quad (17.20)$$

When a real gas is compressed in a single-stage compression, the compression is polytropic tending to approach adiabatic or constant-entropy conditions. Adiabatic compression calculations give the maximum theoretical work or *horsepower* necessary to compress a gas between any two pressure limits, whereas isothermal compression calculations give the minimum theoretical work or horsepower necessary to compress a gas. Adiabatic and isothermal work of compression, thus, give the upper and lower limits, respectively, of work or horsepower requirements to compress a gas. One purpose of intercoolers between multistage compressors is to reduce the horsepower necessary to compress the gas. The more intercoolers and stages, the closer the horsepower requirement approaches the isothermal value.



## 17.4.3.1.1 Volumetric efficiency

The volumetric efficiency represents the efficiency of a compressor cylinder to compress gas. It may be defined as the ratio of the volume of gas actually delivered to the piston displacement, corrected to suction temperature and pressure. The principal reasons that the cylinder will not deliver the piston displacement capacity are wire-drawing, a throttling effect on the valves; heating of the gas during admission to the cylinder; leakage past valves and piston rings; and re-expansion of the gas trapped in the clearance-volume space from the previous stroke. Re-expansion has by far the greatest effect on volumetric efficiency.

The theoretical formula for volumetric efficiency is

$$E_v = 1 - (r^{1/k} - 1)C_l, \quad (17.21)$$

where

$E_v$  = volumetric efficiency, fraction

$r$  = cylinder compression ratio

$C_l$  = clearance, fraction.

In practice, adjustments are made to the theoretical formula in computing compressor performance:

$$E_v = 0.97 - \left[ \left( \frac{z_s}{z_d} \right) r^{1/k} - 1 \right] C_l - e_v, \quad (17.22)$$

where

$z_s$  = gas deviation factor at suction of the cylinder

$z_d$  = gas deviation factor at discharge of the cylinder

$e_v$  = correction factor.

In this equation, the constant 0.97 is a reduction of 1 to correct for minor inefficiencies such as incomplete filling of the cylinder during the intake stroke. The correction factor  $e_v$  is to correct for the conditions in a particular application that affect the volumetric efficiency and for which the theoretical formula is inadequate.

## 17.4.3.1.2 Stage compression

The ratio of the discharge pressure to the inlet pressure is called the *pressure ratio*. The volumetric efficiency becomes less, and mechanical stress limitation becomes more, pronounced as pressure ratio increases. Natural gas is usually compressed in stages, with the pressure ratio per stage being less than 6. In field practice, the pressure ratio seldom exceeds 4 when boosting gas from low pressure for processing or sale. When the total compression ratio is greater than this, more stages of compression are used to reach high pressures.

The total power requirement is a minimum when the pressure ratio in each stage is the same. This may be expressed in equation form as

$$r = \left( \frac{p_d}{p_s} \right)^{1/N}, \quad (17.23)$$

where

$p_d$  = final discharge pressure, absolute

$p_s$  = suction pressure, absolute

$N_s$  = number of stages required.

As large compression ratios result in gas being heated to undesirably high temperatures, it is common practice to cool the gas between stages and, if possible, after the final stage of compression.

### 17.4.3.1.3 Isentropic horsepower

The computation is based on the assumption that the process is ideal isentropic or perfectly reversible adiabatic. The total ideal horsepower for a given compression is the sum of the ideal work computed for each stage of compression. The ideal isentropic work can be determined for each stage of compression in a number of ways. One way to solve a compression problem is by using the Mollier diagram. This method is not used in this book because it is not easily computerized. Another approach commonly used is to calculate the horsepower for each stage from the isentropic work formula:

$$w = \frac{k}{k-1} \frac{53.241 T_1}{\gamma_g} \left[ \left( \frac{p_2}{p_1} \right)^{(k-1)/k} - 1 \right], \quad (17.24)$$

where

$w$  = theoretical shaft work required to compress the gas, ft-lb<sub>f</sub>/lb<sub>m</sub>

$T_1$  = suction temperature of the gas, °R

$\gamma_g$  = gas-specific gravity, air = 1

$p_1$  = suction pressure of the gas, psia

$p_2$  = pressure of the gas at discharge point, psia.

When the deviation from ideal gas behavior is appreciable, Eq. (17.24) is empirically modified. One such modification is

$$w = \frac{k}{k-1} \frac{53.241 T_1}{\gamma_g} \left[ \left( \frac{p_2}{p_1} \right)^{z_1(k-1)/k} - 1 \right] \quad (17.25)$$

or, in terms of power,

$$HP_{MM} = \frac{k}{k-1} \frac{3.027 p_b}{T_b} T_1 \left[ \left( \frac{p_2}{p_1} \right)^{z_1(k-1)/k} - 1 \right], \quad (17.26)$$

where

$H_{pMM}$  = required theoretical compression power, hp/MMcfd

$z_1$  = compressibility factor at suction conditions.

The theoretical adiabatic horsepower obtained by the proceeding equations can be converted to brake horsepower ( $Hp_b$ ) required at the end of prime mover of the compressor using an overall efficiency factor,  $E_o$ . The brake horsepower is the horsepower input into the compressor. The efficiency factor  $E_o$  consists of two components: compression efficiency (compressor-valve losses) and the mechanical efficiency of the compressor. The overall efficiency of a compressor depends on a number of factors, including design details of the compressor, suction pressure, speed of the compressor, compression ratio, loading, and general mechanical condition of the unit. In most modern compressors, the compression efficiency ranges from 83% to 93%. The mechanical efficiency of most modern compressors ranges from 88% to 95%. Thus, most modern compressors have an overall efficiency ranging from 75% to 85%, based on the ideal isentropic compression process as a standard. The actual efficiency curves can be obtained from the manufacturer. Applying these factors to the theoretical horsepower gives

$$Hp_b = \frac{q_{MM}Hp_{MM}}{E_o}, \quad (17.27)$$

where  $q_{MM}$  is the gas flow rate in MMscfd.

The discharge temperature for real gases can be calculated by

$$T_2 = T_1 \left( \frac{p_2}{p_1} \right)^{z_1(k-1)/k}. \quad (17.28)$$

Calculation of the heat removed by intercoolers and after-coolers can be accomplished using constant pressure-specific heat data:

$$\Delta H = n_G \bar{C}_p \Delta T, \quad (17.29)$$

where

$n_G$  = number of lb-mole of gas

$\bar{C}_p$  = specific heat under constant pressure evaluated at cooler operating pressure and the average temperature, btu/lb-mol-°F.

**Example Problem 17.3** For data given in Example Problem 17.2, assuming the overall efficiency is 0.80, calculate the theoretical and brake horsepower required to compress the 32 MMscfd of a 0.65-specific gravity natural gas from 100 psia and 70°F to 1165 psia. If intercoolers cool the gas to 70 °F, what is the heat load on the intercoolers and what is the final gas temperature?

**Solution** The overall compression ratio is

$$r_{ov} = \frac{1165}{100} = 11.65.$$

Because this is greater than 6, more than one-stage compression is required. Using two stages of compression gives

$$r = \left( \frac{1165}{100} \right)^{1/2} = 3.41.$$

The gas is compressed from 100 to 341 psia in the first stage, and from 341 to 1165 psia in the second stage. Based on gas-specific gravity, the following gas property data can be obtained:

$$T_c = 358 \text{ }^\circ\text{R}$$

$$p_c = 671 \text{ psia}$$

$$T_r = 1.42$$

$$p_{r,1} = 0.149 \text{ at 100 psia}$$

$$p_{r,2} = 0.595 \text{ at 341 psia}$$

$$z_1 = 0.97 \text{ at } 70^\circ\text{F and 100 psia}$$

$$z_2 = 0.95 \text{ at } 70^\circ\text{F and 341 psia.}$$

First stage:

$$\begin{aligned} Hp_{MM} &= \frac{1.25}{0.25} \left( 3.027 \times \frac{14.7}{520} \right) 530 \left[ (3.41)^{0.97(0.25/1.25)} - 1 \right] \\ &= 61 \text{ hp/MMcfd} \end{aligned}$$

Second stage:

$$\begin{aligned} Hp_{MM} &= \frac{1.25}{0.25} \left( 3.027 \times \frac{14.7}{520} \right) 530 \left[ (3.41)^{0.95(0.25/1.25)} - 1 \right] \\ &= 59 \text{ hp/MMcfd} \end{aligned}$$

Total theoretical compression work = 61 + 59 = 120 hp/MMcfd.

Required brake horsepower is

$$Hp_b = \frac{(32)(120)}{(0.8)} = 4800 \text{ hp.}$$

Number of moles of gas is

$$\begin{aligned} n_G &= \frac{1,000,000}{378.6} (32) = 2.640 \times 10^3 (32) \\ &= 84 \times 10^3 \text{ lb-mole/day.} \end{aligned}$$

Gas temperature after the first stage of compression is

$$T_2 = (530)(3.41)^{0.97(0.25/1.25)} = 670 \text{ }^\circ\text{R} = 210 \text{ }^\circ\text{F.}$$

The average cooler temperature is  $\frac{210+70}{2} = 140 \text{ }^\circ\text{F.}$

$$\bar{C}_p \text{ at } 140^\circ\text{F and 341 psia} = 9.5 \frac{\text{btu}}{\text{lb-mol}^\circ\text{F}}$$

$$\begin{aligned} \text{Intercooler load} &= 2.640 \times 10^3 (32)(9.5)(210 - 70) \\ &= 55.67 \times 10^6 \text{ btu/day} \end{aligned}$$

Final gas temperature:

$$T_d = (530)(3.41)^{0.95(0.25/1.25)} = 669^\circ\text{R} = 209^\circ\text{F}$$

It can be shown that the results obtained using the analytical expressions compare very well to those obtained from the Mollier diagram.

The computer program *ReciprocatingCompressor Power.xls* can be used for computing power requirement of each stage of compression. The solution given by the program for the first stage of compression in this example problem is shown in [Table 17.2](#).

<b>Table 17.2 Result Given by Computer Program ReciprocatingCompressorPower.xls for the First-Stage Compression</b>	
<i>ReciprocatingCompressorPower.xls</i>	
<i>Description:</i> This spreadsheet calculates stage power of reciprocating compressor.	
<i>Instruction:</i> (1) Update parameter values in the “Input data” in blue; (2) click “Solution” button; (3) view result in the Solution section.	
<b>Input Data</b>	
Gas flow rate ( $q_g$ ):	32 MMscf/day
Stage inlet temperature ( $T_1$ ):	70°F
Stage inlet pressure ( $p_1$ ):	100 psia
Gas-specific gravity ( $\gamma_g$ ):	0.65 (air = 1)
Stage outlet pressure ( $p_2$ ):	341 psia
Gas-specific heat ratio ( $k$ ):	1.25
Overall efficiency ( $E_o$ ):	0.8
Base temperature ( $T_b$ ):	60°F
Base pressure ( $p_b$ ):	14.7 psia
<b>Solution</b>	
$z = \text{Hall-Yarborough Method}$	= 0.9574
$r = \frac{p_2}{p_1}$	= 3.41
$HP_{MM} = \frac{k}{k-1} \frac{3.027 p_b}{T_b} T_1 \left[ \left( \frac{p_2}{p_1} \right)^{z_1(k-1)/k} - 1 \right]$	= 60 hp
$HP_b = \frac{q_{MM} HP_{MM}}{E_o}$	= 2401 hp
$T_2 = T_1 \left( \frac{p_2}{p_1} \right)^{z_1(k-1)/k}$	= 210.33°F
$T_{avg} = \frac{T_1 + T_2}{2}$	= 140.16°F
$\bar{C}_p$	= 9.50 btu/lbm-mol°F
Cooler load = $2.640 \times 10^3 q_{MM} \bar{C}_p (T_2 - T_1)$	= 56,319,606 btu/day

### 17.4.3.2 Centrifugal compressors

Although the adiabatic compression process can be assumed in centrifugal compression, polytropic compression process is commonly considered as the basis for comparing centrifugal compressor performance. The process is expressed as

$$pV^n = \text{constant}, \quad (17.30)$$

where  $n$  denotes the polytropic exponent. The isentropic exponent  $k$  applies to the ideal frictionless adiabatic process, while the polytropic exponent  $n$  applies to the actual process with heat transfer and friction. The  $n$  is related to  $k$  through polytropic efficiency  $E_p$ :

$$\frac{n-1}{n} = \frac{k-1}{k} \times \frac{1}{E_p} \quad (17.31)$$

The polytropic efficiency of centrifugal compressors is nearly proportional to the logarithm of gas flow rate in the range of efficiency between 0.7 and 0.75. The polytropic efficiency can be represented by the following correlation (Guo and Ghalambor, 2005):\*\*

$$E_p = 0.61 + 0.03 \log(q_1), \quad (17.32)$$

where  $q_1$  = gas capacity at the inlet condition, cfm.

There is a lower limit of gas flow rate below which severe gas surge occurs in the compressor. This limit is called *surge limit*. The upper limit of gas flow rate is called *stone-wall limit*, which is controlled by compressor horsepower.

The procedure of preliminary calculations for selection of centrifugal compressors is summarized as follows:

1. Calculate compression ratio based on the inlet and discharge pressures:

$$r = \frac{p_2}{p_1} \quad (17.33)$$

2. Based on the required gas flow rate under standard condition ( $q$ ), estimate the gas capacity at inlet condition ( $q_1$ ) by ideal gas law:

$$q_1 = \frac{p_b T_1}{p_1 T_b} q \quad (17.34)$$

3. Find a value for the polytropic efficiency  $E_p$  from the manufacturer's manual based on  $q_1$ .
4. Calculate polytropic ratio  $(n-1)/n$ :

$$R_p = \frac{n-1}{n} = \frac{k-1}{k} \times \frac{1}{E_p} \quad (17.35)$$

5. Calculate discharge temperature by

$$T_2 = T_1 r^{R_p}. \quad (17.36)$$

6. Estimate gas compressibility factor values at inlet and discharge conditions.
7. Calculate gas capacity at the inlet condition ( $q_1$ ) by real gas law:

$$q_1 = \frac{z_1 p_b T_1}{z_2 p_1 T_b} q \quad (17.37)$$

8. Repeat steps 2–7 until the value of  $q_1$  converges within an acceptable deviation.

9. Calculate gas horsepower by

$$Hp_g = \frac{q_1 p_1}{229 E_p} \left( \frac{z_1 + z_2}{2 z_1} \right) \left( \frac{r^{R_p} - 1}{R_p} \right). \quad (17.38)$$

Some manufacturers present compressor specifications using polytropic head in lbf-ft/lbm defined as

$$H_g = RT_1 \left( \frac{z_1 + z_2}{2} \right) \left( \frac{r^{R_p} - 1}{R_p} \right), \quad (17.39)$$

where  $R$  is the gas constant given by  $1544/MW_a$  in psia-ft<sup>3</sup>/lb<sub>m</sub>-°R. The polytropic head relates to the gas horsepower by

$$Hp_g = \frac{M_F H_g}{33,000 E_p}, \quad (17.40)$$

where  $M_F$  is mass flow rate in lb<sub>m</sub>/min.

10. Calculate gas horsepower by

$$Hp_b = Hp_g + \Delta Hp_m, \quad (17.41)$$

where  $\Delta Hp_m$  is mechanical power losses, which is usually taken as 20 horsepower for bearing and 30 horsepower for seals.

The proceeding equations have been coded in the computer program *CnetriComp.xls* (on the CD attached to this book) for quick calculation.

**Example Problem 17.4** Assuming two centrifugal compressors in series are used to compress gas for a gas lift operation. Size the first compressor using the formation given in Example Problem 17.3.

**Solution** Calculate compression ratio based on the inlet and discharge pressures:

$$r = \sqrt{\frac{1165}{100}} = 3.41$$

Calculate gas flow rate in scfm:

$$q = \frac{32,000,000}{(24)(60)} = 22,22 \text{ scfm}$$

Based on the required gas flow rate under standard condition ( $q$ ), estimate the gas capacity at inlet condition ( $q_1$ ) by ideal gas law:

$$q_1 = \frac{(14.7)(530)}{(100)(520)} (22,222) = 3329 \text{ cfm}$$

Find a value for the polytropic efficiency based on  $q_1$ :

$$E_p = 0.61 + 0.03 \log (3329) = 0.719$$

Calculate polytropic ratio  $(n-1)/n$ :

$$R_p = \frac{1.25 - 1}{1.25} \times \frac{1}{0.719} = 0.278$$

Calculate discharge temperature by

$$T_2 = (530)(3.41)^{0.278} = 745^\circ\text{R} = 285^\circ\text{F}.$$

Estimate gas compressibility factor values at inlet and discharge conditions:

$$\begin{aligned}z_1 &= 1.09 \text{ at } 100 \text{ psia and } 70^\circ\text{F} \\z_2 &= 0.99 \text{ at } 341 \text{ psia and } 285^\circ\text{F}\end{aligned}$$

Calculate gas capacity at the inlet condition ( $q_1$ ) by real gas law:

$$q_1 = \frac{(1.09)(14.7)(530)}{(0.99)(100)(520)}(22,222) = 3674 \text{ cfm}$$

Use the new value of  $q_1$  to calculate  $E_p$ :

$$E_p = 0.61 + 0.03 \log(3674) = 0.721$$

Calculate the new polytropic ratio  $(n-1)/n$ :

$$R_p = \frac{1.25 - 1}{1.25} \times \frac{1}{0.721} = 0.277$$

Calculate the new discharge temperature:

$$T_2 = (530)(3.41)^{0.277} = 746^\circ\text{R} = 286^\circ\text{F}$$

Estimate the new gas compressibility factor value:

$$z_2 = 0.99 \text{ at } 341 \text{ psia and } 286^\circ\text{F}$$

Because  $z_2$  did not change,  $q_1$  remains the same value of 3674 cfm.

Calculate gas horsepower:

$$\begin{aligned}Hp_g &= \frac{(3674)(100)}{(229)(0.721)} \left( \frac{1.09 + 0.99}{2(1.09)} \right) \left( \frac{3.41^{0.277} - 1}{0.277} \right) \\ &= 3100 \text{ hp}\end{aligned}$$

Calculate gas apparent molecular weight:

$$MW_a = (0.65)(29) = 18.85$$

Calculated gas constant:

$$R = \frac{1544}{18.85} = 81.91 \text{ psia-ft}^3/\text{lb}_m\text{-}^\circ\text{R}$$

Calculate polytropic head:

$$\begin{aligned}H_g &= (81.91)(530) \left( \frac{1.09 + 0.99}{2} \right) \left( \frac{3.41^{0.277} - 1}{0.277} \right) \\ &= 65,850 \text{ lb}_f\text{-ft}/\text{lb}_m\end{aligned}$$

Calculate gas horsepower:

$$Hp_b = 3100 + 50 = 3150 \text{ hp}$$

The computer program *CentrifugalCompressorPower.xls* can be used for solving similar problems. The solution given by the program to this example problem is shown in [Table 17.3](#).



<b>Table 17.3 Result Given by the Computer Program CentrifugalCompressorPower.xls</b>	
<i>CentrifugalCompressorPower.xls</i>	
<i>Description:</i> This spreadsheet calculates stage power of reciprocating compressor.	
<i>Instruction:</i> (1) Update parameter values in the “Input data” in blue; (2) click “Solution” button; (3) view result in the Solution section.	
<b>Input Data</b>	
Gas flow rate ( $q_g$ ):	32 MMscf/day
Inlet temperature ( $T_1$ ):	70°F
Inlet pressure ( $p_1$ ):	100 psia
Gas-specific gravity ( $\gamma_g$ ):	0.65 (air = 1)
Discharge pressure ( $p_2$ ):	341 psia
Gas-specific heat ratio ( $k$ ):	1.25
Base temperature ( $T_b$ ):	60°F
Base pressure ( $p_b$ ):	14.7 psia
<b>Solution</b>	
$r = \frac{p_2}{p_1}$	= 3.41
$q = \frac{q_{MM}}{(24)(60)}$	= 22,222 scfm
$q_1 = \frac{p_b T_1}{p_1 T_b} q$	= 3329 scfm
$E_p = 0.61 + 0.03 \log(q_1)$	= 0.7192
$R_p = \frac{n-1}{n} = \frac{k-1}{k} \times \frac{1}{E_p}$	= 0.2781
$T_2 = T_1 r^{R_p}$	= 285°F
$z_1$ by Hall–Yarborough Method	= 1.0891
$z_2$ by Hall–Yarborough Method	= 0.9869
$q_1 = \frac{z_1 p_b T_1}{z_2 p_1 T_b} q$	= 3674
$E_p = 0.61 + 0.03 \log(q_1)$	= 0.7205
$R_p = \frac{n-1}{n} = \frac{k-1}{k} \frac{1}{E_p}$	= 0.2776
$T_2 = T_1 r^{R_p}$	= 285°F
$HP_g = \frac{q_1 p_1}{229 E_p} \left( \frac{z_1 + z_2}{2 z_1} \right) \left( \frac{r^{R_p} - 1}{R_p} \right)$	= 3102 hp
$HP_b = HP_g + 50$	= 3152 hp
$MW_a = 29 \gamma_g$	= 18.85
$R = \frac{1544}{MW_a}$	= 81.91
$H_g = RT_1 \left( \frac{z_1 + z_2}{2} \right) \left( \frac{r^{R_p} - 1}{R_p} \right)$	= 65,853 lbf-ft/lbm

## 17.5 SELECTION OF GAS LIFT VALVES

Kickoff of a dead well requires a much higher gas pressure than the ultimate operating pressure. Because of the kickoff problem, gas lift valves have been developed and are run as part of the overall tubing string. These valves permit the introduction of gas (which is usually injected down the annulus) into the fluid column in tubing at intermediate depths to unload the well and initiate well flow. Proper design of these valve depths to ensure unloading requires a thorough understanding of the unloading process and valve characteristics.

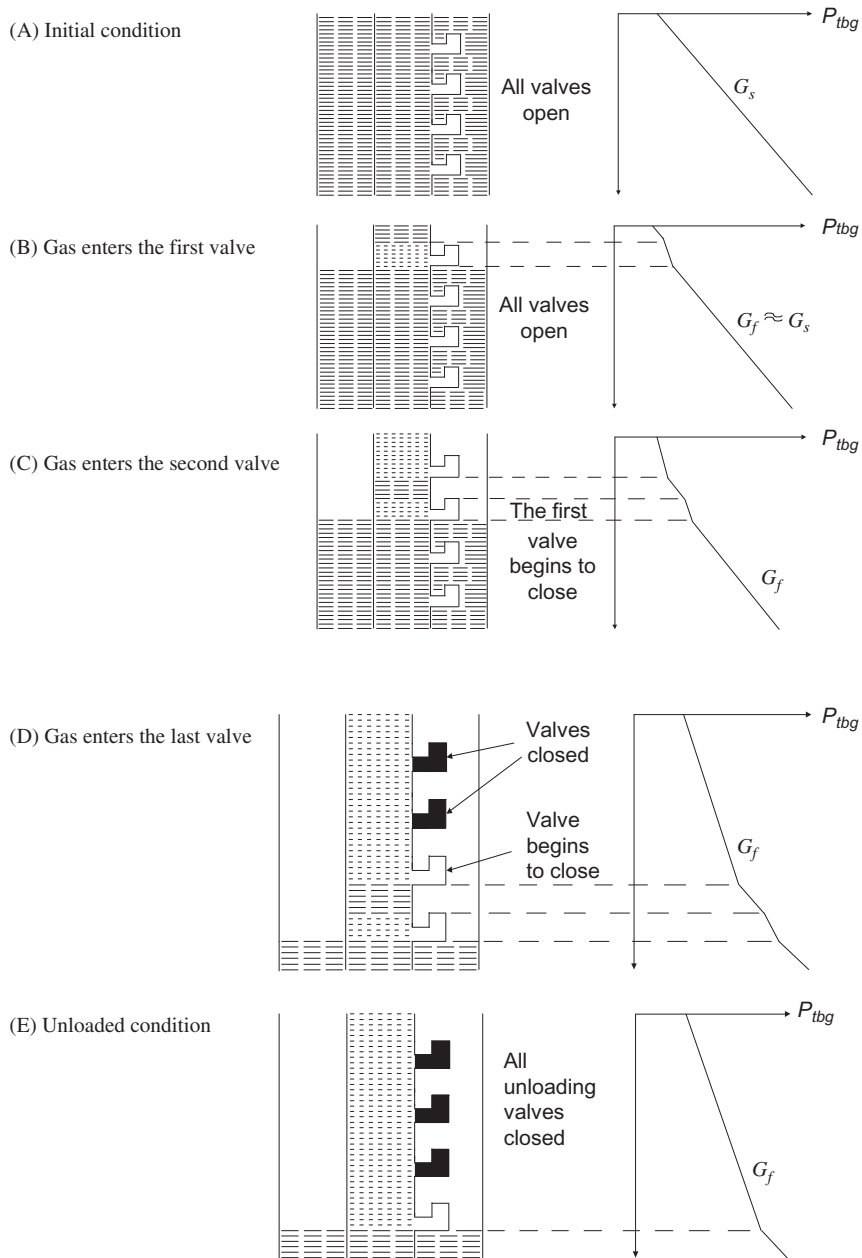
### 17.5.1 UNLOADING SEQUENCE

Fig. 17.7 shows a well unloading process. Usually all valves are open at the initial condition, as depicted in Fig. 17.7A, due to high tubing pressures. The fluid in tubing has a pressure gradient  $G_s$  of static liquid column. When the gas enters the first (top) valve as shown in Fig. 17.7B, it creates a slug of liquid–gas mixture of less density in the tubing above the valve depth. Expansion of the slug pushes the liquid column above it to flow to the surface. It can also cause the liquid in the bottom-hole to flow back to reservoir if no check valve is installed at the end of the tubing string. However, as the length of the light slug grows due to gas injection, the bottom-hole pressure will eventually decrease to below reservoir pressure, which causes inflow of reservoir fluid. When the tubing pressure at the depth of the first valve is low enough, the first valve should begin to close and the gas should be forced to the second valve as shown in Fig. 17.7C. Gas injection to the second valve will gasify the liquid in the tubing between the first and the second valve. This will further reduce bottom-hole pressure and cause more inflow. By the time the slug reaches the depth of the first valve, the first valve should be closed, allowing more gas to be injected to the second valve. The same process should occur until the gas enters the main valve (Fig. 17.7D). The main valve (sometimes called the *master valve* or *operating valve*) is usually the lower most valve in the tubing string. It is an orifice type of valve that never closes. In continuous gas lift operations, once the well is fully unloaded and a steady-state flow is established, the main valve is the only valve open and in operation (Fig. 17.7E).

### 17.5.2 VALVE CHARACTERISTICS

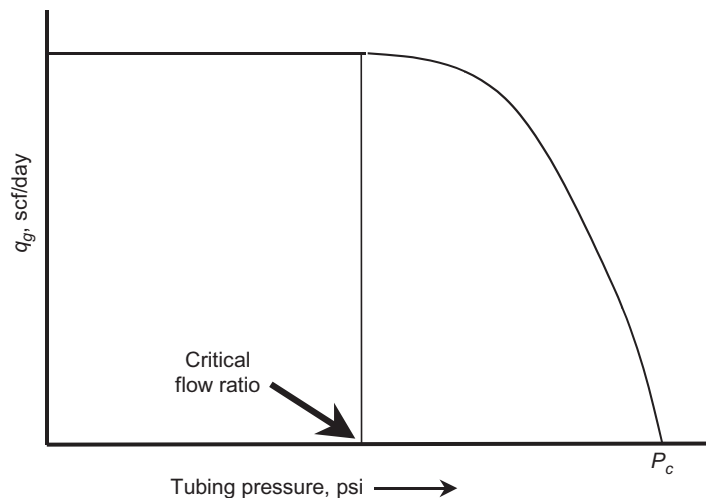
Eqs. (17.12) and (17.16) describing choke flow are also applicable to the main valve of orifice type. Flow characteristics of this type of valve are depicted in Fig. 17.8. Under sonic flow conditions, the gas passage is independent of tubing pressure but not casing pressure.

There are different types of unloading valves, namely casing pressure-operated valve (usually called a *pressure valve*), throttling pressure valve (also called a *proportional valve* or *continuous flow valve*), fluid-operated valve (also called a *fluid valve*), and combination valve (also called a *fluid open-pressure closed valve*). Different gas lift design methods have been developed and used in the oil industry for applications of these valves.



**FIGURE 17.7**

Well unloading sequence. (A) initial condition, (B) gas enters the first valve, (C) gas enters the second valve, (D) gas enters the last valve, and (E) unloaded condition.



**FIGURE 17.8**

Flow characteristics of orifice-type valves.

### 17.5.2.1 Pressure valve

Pressure valves are further classified as unbalanced bellow valves, balanced pressure valves, and pilot valves. Tubing pressure affects the opening action of the unbalanced valves, but it does not affect the opening or closing of balanced valves. Pilot valves were developed for intermittent gas lift with large ports.

#### 17.5.2.1.1 Unbalanced bellow valve

As shown in Fig. 17.9, an unbalanced bellow valve has a pressure-charged nitrogen dome and an optional spring loading element. While the forces from the dome pressure and spring act to cause closing of the valve, the forces due to casing and tubing pressures act to cause opening of the valve. Detailed discussions of valve mechanics can be found in Brown (1980). When a valve is at its closed condition (as shown in Fig. 17.9), the minimum casing pressure required to open the valve is called the *valve opening pressure* and is expressed as

$$P_{vo} = \frac{1}{1-R}P_d + S_t - \frac{R}{1-R}P_t, \quad (17.42)$$

where

$P_{vo}$  = valve opening pressure, psig

$P_d$  = pressure in the dome, psig

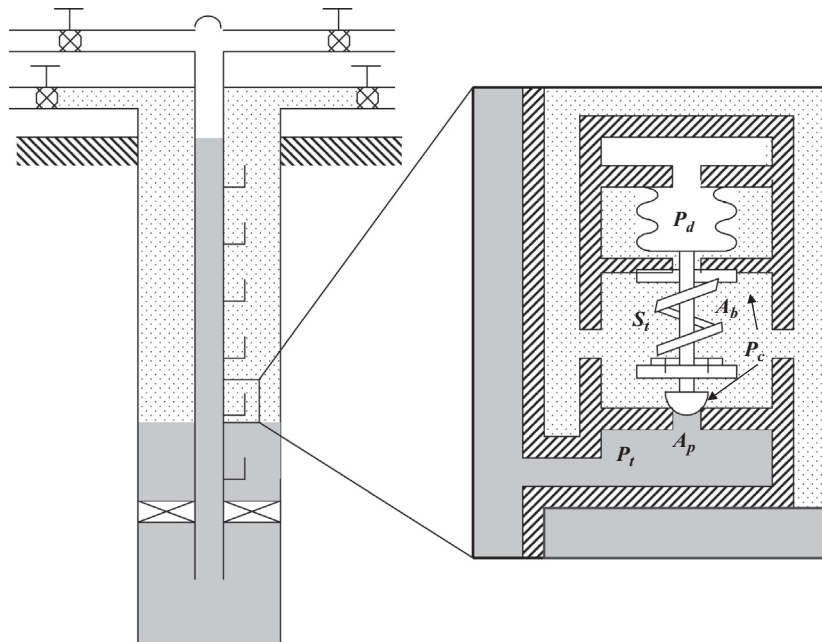
$S_t$  = equivalent pressure caused by spring tension, psig

$P_t$  = tubing pressure at valve depth when the valve opens, psi

$R$  = area ratio  $A_p/A_b$

$A_p$  = valve seat area, in.<sup>2</sup>

$A_b$  = total effective bellows area, in.<sup>2</sup>.


**FIGURE 17.9**

Unbalanced bellow valve at its closed condition.

The term  $\frac{R}{1-R}P_t$  is called *tubing effect* (T.E.) and  $\frac{R}{1-R}$  is called *tubing effect factor* (T.E.F.). With other parameters given, Eq. (17.42) is used for determining the required dome pressure at depth, that is,  $P_d = (1 - R)(P_{vo} - S_t) + RP_t$  in valve selection.

When a valve is at its open condition (as shown in Fig. 17.10), the maximum pressure under the ball (assumed to be casing pressure) required to close the valve is called the *valve closing pressure* and is expressed as

$$P_{vc} = P_d + S_t(1 - R), \quad (17.43)$$

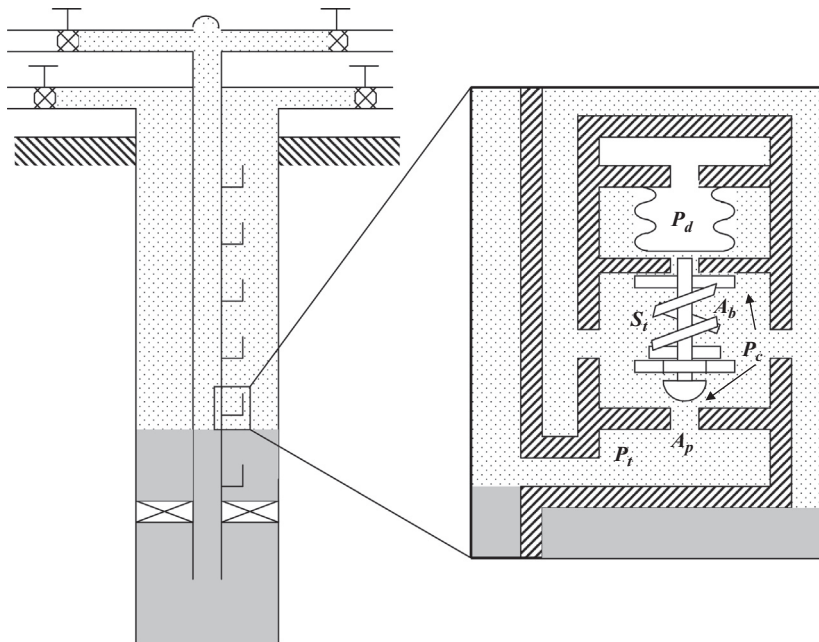
where  $P_{vc}$  = valve closing pressure, psig.

The difference between the valve opening and closing pressures,  $P_{vo} - P_{vc}$ , is called *spread*. Spread can be important in continuous flow installations but is particularly important in intermittent gas lift installations where unbalanced valves are used. The spread controls the minimum amount of gas used for each cycle. As the spread increases, the amount of gas injected during the cycle increases.

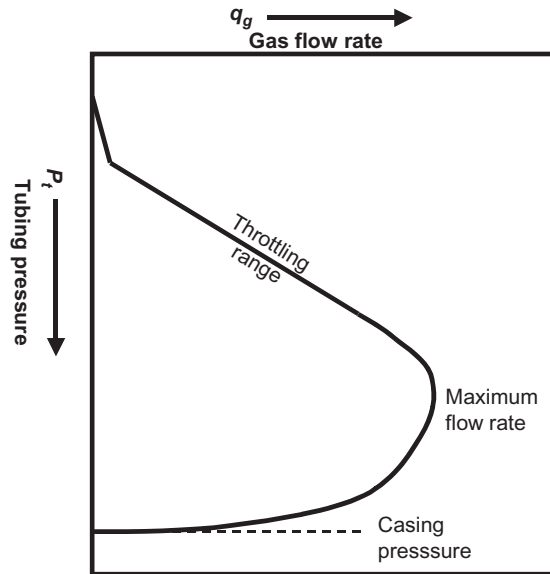
Gas passage of unbalanced valves are tubing pressure dependent due to partial travel of the valve stem. Fig. 17.11 illustrates flow characteristics of unbalanced valves.

#### 17.5.2.1.2 Balanced pressure valve

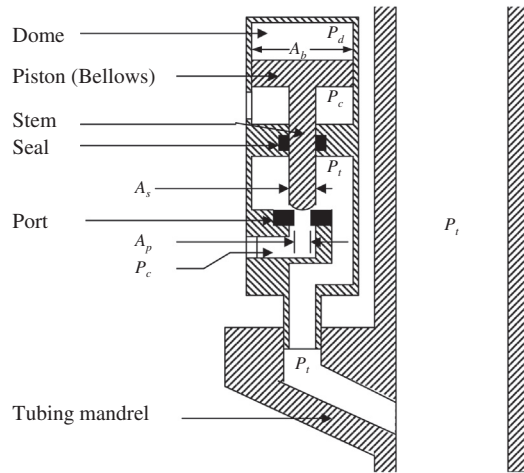
Fig. 17.12 depicts a balanced pressure valve. Tubing pressure does not influence valve status when in the closed or open condition. The valve opens and closes at the same pressure—dome pressure. Balanced pressure valves act as expanding orifice regulators, opening to pass any amount of gas injected from the surface and partial closing to control the lower gas flow rate.



**FIGURE 17.10**  
Unbalanced bellow valve at its open condition.



**FIGURE 17.11**  
Flow characteristics of unbalanced valves.

**FIGURE 17.12**

A sketch of a balanced pressure valve.

### 17.5.2.1.3 Pilot valve

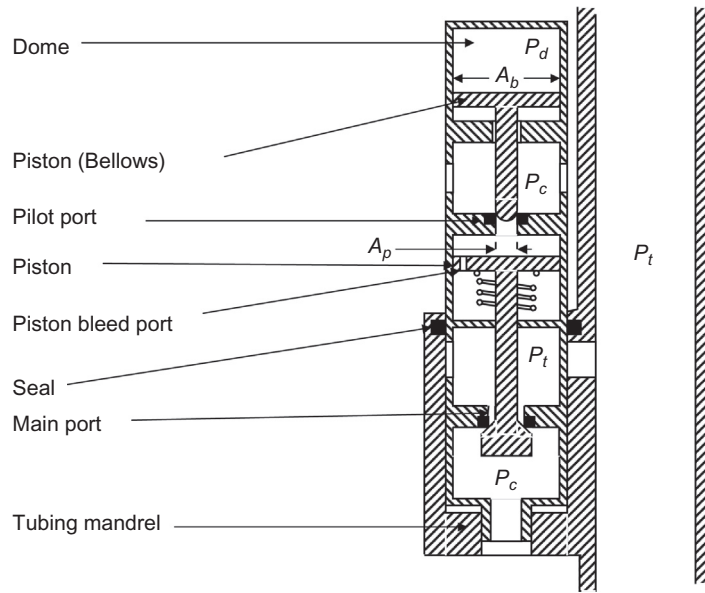
Fig. 17.13 shows a sketch of a pilot valve used for intermittent gas lift where a large port for gas passage and a close control over the spread characteristics are desirable. It has two ports. The smaller port (control port) is used for opening calculations and the large port (power port) is used for gas passage calculations. The equations derived from unbalanced valves are also valid for pilot valves.

### 17.5.2.2 Throttling pressure valve

Throttling pressure valves are also called *continuous flow valves*. As shown in Fig. 17.14, the basic elements of a throttling valve are the same as the pressure-operated valve except that the entrance port of the valve is choked to drop the casing pressure to tubing pressure by using a tapered stem or seat, which allows the port area to sense tubing pressure when the valve is open. Unlike pressure-operated valves where the casing pressure must drop to a pressure set by dome pressure and spring for the valve to close, a throttling pressure valve will close on a reduction in tubing pressure with the casing pressure held constant. The equations derived from pressure-operated valves are also to be applied to throttling valves for opening pressure calculations.

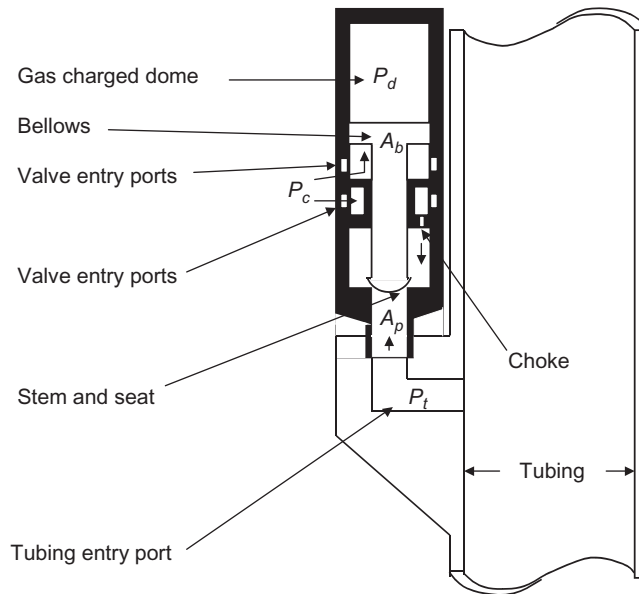
### 17.5.2.3 Fluid-operated valve

As shown in Fig. 17.15, the basic elements of a fluid-operated valve are identical to those in a pressure-operated valve except that tubing pressure now acts on the larger area of the bellows and casing pressure acts on the area of the port. This configuration makes the valve



**FIGURE 17.13**

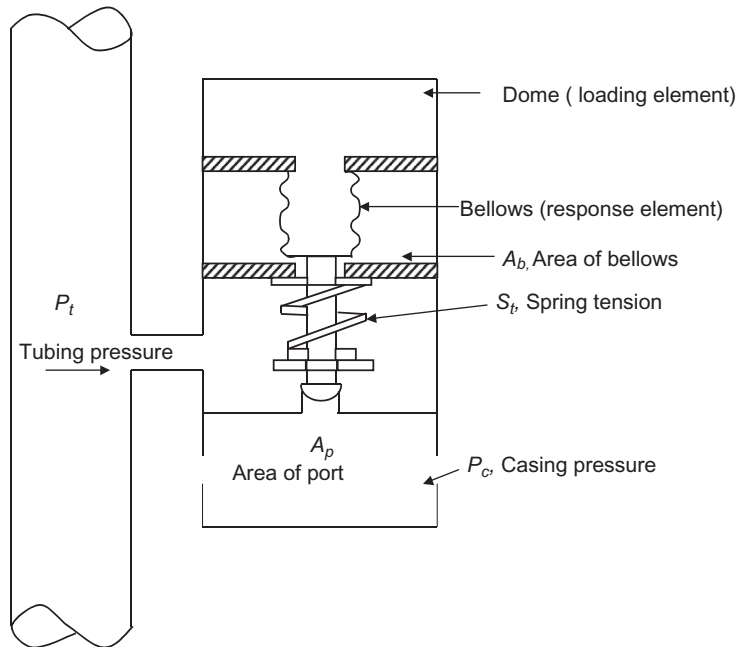
A sketch of a pilot valve.



**FIGURE 17.14**

A sketch of a throttling pressure valve.




**FIGURE 17.15**

A sketch of a fluid-operated valve.

mostly sensitive to the tubing fluid pressure. Therefore, the opening pressure is defined as the tubing pressure required to open the valve under actual operating conditions. Force balance gives

$$P_{vo} = \frac{1}{1-R}P_d + S_t - \frac{R}{1-R}P_c, \quad (17.44)$$

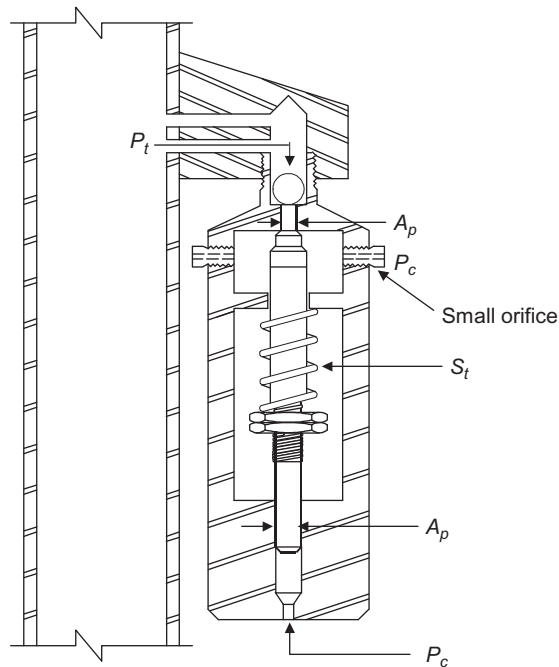
where  $P_c$  = casing pressure, psig.

The term  $\frac{R}{1-R}P_c$  is called the C.E. and  $\frac{R}{1-R}$  is called T.E.F. for fluid valves. With other parameters given, Eq. (17.44) is used for determining required dome pressure at depth, that is,  $P_d = (1-R)(P_{vo} - S_t) + RP_c$  in valve selection.

When a fluid valve is in its open position under operating conditions, the maximum pressure under the ball (assumed to be tubing pressure) required to close the valve is called the *valve closing pressure* and is expressed as

$$P_{vc} = P_d + S_t(1-R), \quad (17.45)$$

which is identical to that for a pressure-operated valve.



**FIGURE 17.16**

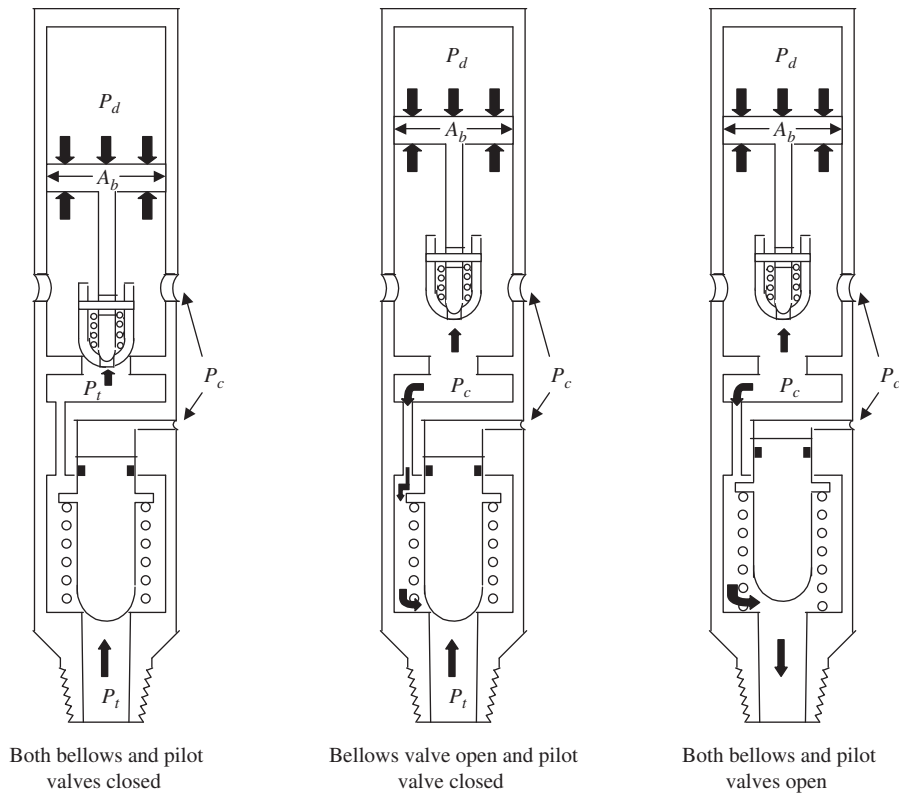
A sketch of a differential valve.

The first generation of fluid valves is a differential valve. As illustrated in Fig. 17.16, a differential valve relies on the difference between the casing pressure and the spring pressure effect to open and close. The opening and closing pressures are the same tubing pressure defined as

$$P_{vo} = P_{vc} = P_c - S_t. \quad (17.46)$$

#### 17.5.2.4 Combination valves

Fig. 17.17 shows that a combination valve consists of two portions. The upper portion is essentially the same as that found in pressure-operated valves, and the lower portion is a fluid pilot, or a differential pressure device incorporating a stem and a spring. Holes in the pilot housing allow the casing pressure to act on the area of the stem at the upper end. The spring acts to hold the stem in the upward position. This is the open position for the pilot. The casing pressure acts to move the stem to the closed position. The fluid pilot will only open when tubing pressure acting on the pilot area is sufficient to overcome the casing pressure force and move the stem up to the open position. At the instant of opening, the pilot opens completely, providing instantaneous operation for intermittent lift.



**FIGURE 17.17**

A sketch of combination valve.

### 17.5.3 VALVE SPACING

Various methods are being used in the industry for designing depths of valves of different types. They are the universal design method, the API-recommended method, the fallback method, and the percent load method. However, the basic objective should be the same:

1. To be able to open unloading valves with kickoff and injection operating pressures
2. To ensure single-point injection during unloading and normal operating conditions
3. To inject gas as deep as possible

No matter which method is used, the following principles apply:

- The design tubing pressure at valve depth is between gas injection pressure (loaded condition) and the minimum tubing pressure (fully unloaded condition).
- Depth of the first valve is designed on the basis of kickoff pressure from a special compressor for well kickoff operations.
- Depths of other valves are designed on the basis of injection operating pressure.

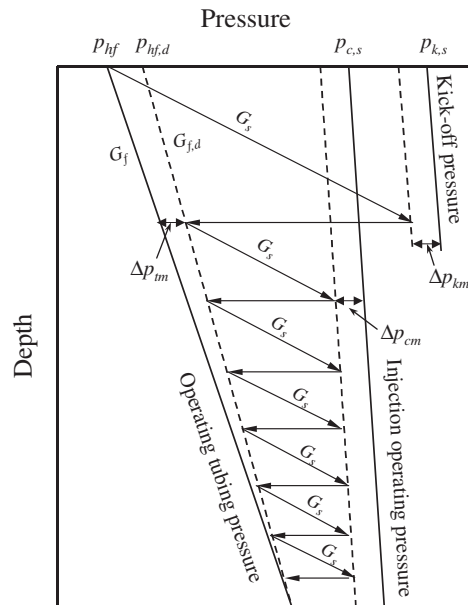
- Kickoff casing pressure margin, injection operating casing pressure margin, and tubing transfer pressure margin are used to consider the following effects:
  - Pressure drop across the valve
  - Tubing pressure effect of the upper valve
  - Nonlinearity of the tubing flow gradient curve.

The universal design method explained in this section is valid for all types of continuous-flow gas lift valves. Still, different procedures are used with the universal design method, including the following:

1. Design procedure using constant surface opening pressure for pressure-operated valves.
2. Design procedure using 10–20-psi drop in surface closing pressures between valves for pressure-operated valves.
3. Design procedure for fluid-operated valves.
4. Design procedure for combination of pressure-closed fluid-opened valves.

Detailed descriptions of these procedures are given by [Brown \(1980\)](#). Only the design procedure using constant surface opening pressure for pressure-operated valves is illustrated in this section.

[Fig. 17.18](#) illustrates a graphical solution procedure of valve spacing using constant surface opening pressure for pressure-operated valves. The arrows in the figure depict the sequence of line drawing.



**FIGURE 17.18**

A flow diagram to illustrate procedure of valve spacing.

For a continuous-flow gas lift, the analytical solution procedure is outlined as follows:

1. Starting from a desired wellhead pressure  $p_{hf}$  surface, compute a flowing tubing pressure traverse under fully unloaded condition. This can be done using various two-phase flow correlations such as the modified Hagedorn–Brown correlation (*HagedornBrownCorrelation.xls*).
2. Starting from a design wellhead pressure  $p_{hf,d} = p_{hf} + \Delta p_{hf,d}$  at surface, where  $\Delta p_{hf}$  can be taken as  $0.25 p_{c,s}$  establish a design tubing line meeting the flowing tubing pressure traverse at tubing shoe. Pressures in this line, denoted by  $p_{td}$ , represent tubing pressure after adjustment for tubing pressure margin. Gradient of this line is denoted by  $G_{fd}$ . Set  $\Delta p_{hf} = 0$  if tubing pressure margin is not required.
3. Starting from a desired injection operating pressure  $p_c$  at surface, compute a injection operating pressure line. This can be done using Eq. (17.7) or Eq. (17.9).
4. Starting from  $p_{cs} - \Delta p_{cm}$  at surface, where the casing pressure margin  $\Delta p_{cm}$  can be taken as 50 psi, establish a design casing line parallel to the injection operating pressure line. Pressures in this line, denoted by  $p_{cd}$ , represent injection pressure after adjustment for casing pressure margin. Set  $\Delta p_{cm} = 0$  if the casing pressure margin is not required as in the case of using the universal design method.
5. Starting from available kickoff surface pressure  $p_{k,s}$ , establish kickoff casing pressure line. This can be done using Eq. (17.7) or Eq. (17.9).
6. Starting from  $p_k - \Delta p_{km}$  at surface, where the kickoff pressure margin  $\Delta p_{km}$  can be taken as 50 psi, establish a design kickoff line parallel to the kickoff casing pressure line. Pressures in this line, denoted  $p_{kd}$ , represent kickoff pressure after adjustment for kickoff pressure margin. Set  $\Delta p_{km} = 0$  if kickoff casing pressure margin is not required.
7. Calculate depth of the first valve. Based on the fact that  $p_{hf} + G_s D_1 = p_{kd1}$ , the depth of the top valve is expressed as

$$D_1 = \frac{p_{kd1} - p_{hf}}{G_s}, \quad (17.47)$$

where

$p_{kd1}$  = kickoff pressure opposite the first valve, psia

$G_s$  = static (dead liquid) gradient; psi/ft

Applying Eq. (17.9) gives

$$p_{kd1} = (p_{k,s} - \Delta p_{km}) \left( 1 + \frac{D_1}{40,000} \right). \quad (17.48)$$

Solving Eqs. (17.47) and (17.48) yields

$$D_1 = \frac{p_{k,s} - \Delta p_{km} - p_{hf}}{G_s - \frac{p_k - \Delta p_{km}}{40,000}}. \quad (17.49)$$

When the static liquid level is below the depth calculated by use of Eq. (17.49), the first valve is placed at a depth slightly deeper than the static level. If the static liquid level is known, then

$$D_1 = D_s + S_1, \quad (17.50)$$

where  $D_s$  is the static level and  $S_1$  is the submergence of the valve below the static level.

8. Calculate the depths to other valves. Based on the fact that  $p_{hf} + G_{fd}D_1 + G_s(D_2 - D_1) = p_{cd2}$ , the depth of valve 2 is expressed as

$$D_2 = \frac{p_{cd2} - G_{fd}D_1 - p_{hf}}{G_s} + D_1, \quad (17.51)$$

where

$p_{cd2}$  = design injection pressure at valve 2, psig

$G_{fd}$  = design unloading gradient, psi/ft.

Applying Eq. (17.9) gives

$$p_{cd2} = (p_{c,s} - \Delta p_{cm}) \left( 1 + \frac{D_2}{40,000} \right). \quad (17.52)$$

Solving Eqs. (17.51) and (17.52) yields

$$D_2 = \frac{p_{c,s} - \Delta p_{cm} - p_{hf,d} + (G_s - G_{fd})D_1}{G_s - \frac{p_c - \Delta p_{cm}}{40,000}}. \quad (17.53)$$

Similarly, the depth to the third valve is

$$D_3 = \frac{p_{c,s} - \Delta p_{cm} - p_{hf,d} + (G_s - G_{fd})D_2}{G_s - \frac{p_c - \Delta p_{cm}}{40,000}}. \quad (17.54)$$

Thus, a general equation for depth of valve  $i$  is

$$D_i = \frac{p_{c,s} - \Delta p_{cm} - p_{hf,d} + (G_s - G_{fd})D_{i-1}}{G_s - \frac{p_c - \Delta p_{cm}}{40,000}}. \quad (17.55)$$

Depths of all valves can be calculated in a similar manner until the minimum valve spacing ( $\sim 400$  ft) is reached.

**Example Problem 17.5** Only 1 MMscf/day of lift gas is available for the well described in the Example Problem 17.1. If 1000 psia is available to kick off the well and then a steady injection pressure of 800 psia is maintained for gas lift operation against a wellhead pressure of 130 psia, design locations of unloading and operating valves. Assume a casing pressure margin of 50 psi.

**Solution** The hydrostatic pressure of well fluid (26 °API oil) is (0.39 psi/ft) (5200 ft), or 2028 psig, which is greater than the given reservoir pressure of 2000 psia. Therefore, the well does not flow naturally. The static liquid level depth is estimated to be

$$5200 - (2000 - 14.7)/(0.39) = 110 \text{ ft}$$

Depth of the top valve is calculated with Eq. (17.49):

$$D_1 = \frac{1000 - 50 - 130}{0.39 - \frac{1000 - 50}{40,000}} = 2245 \text{ ft} > 110 \text{ ft}$$

Tubing pressure margin at surface is  $(0.25)(800)$ , or 200 psi. The modified Hagedorn–Brown correlation gives tubing pressure of 591 psia at depth of 5000 ft. The design tubing flowing gradient is  $G_{fd} = [591 - (130 + 200)] / (5000)$  or 0.052 psi/ft. Depth of the second valve is calculated with Eq. (17.53):

$$D_2 = \frac{800 - 50 - 330 + (0.39 - 0.052)(2245)}{0.39 - \frac{800 - 50}{40,000}} = 3004 \text{ ft}$$

Similarly,

$$D_3 = \frac{800 - 50 - 330 + (0.39 - 0.052)(3004)}{0.39 - \frac{800 - 50}{40,000}} = 3676 \text{ ft}$$

$$D_4 = \frac{800 - 50 - 330 + (0.39 - 0.052)(3676)}{0.39 - \frac{800 - 50}{40,000}} = 4269 \text{ ft}$$

$$D_5 = \frac{800 - 50 - 330 + (0.39 - 0.052)(4269)}{0.39 - \frac{800 - 50}{40,000}} = 4792 \text{ ft}$$

which is the depth of the operating valve.

Similar problems can be quickly solved with the computer spreadsheet *GasLiftValveSpacing.xls*.

## 17.5.4 VALVE SELECTION AND TESTING

Valve selection starts from sizing of valves to determine required proper port size  $A_p$  and area ratio  $R$ . Valve testing sets dome pressure  $P_d$  and/or string load  $S_r$ . Both of the processes are valve-type dependent.

### 17.5.4.1 Valve sizing

Gas lift valves are sized on the basis of required gas passage through the valve. All the equations presented in Section 17.4.2.3 for choke flow are applicable to valve port area calculations. Unloading and operating valves (orifices) are sized on the basis of subcritical (subsonic flow) that occurs when the pressure ratio  $P/P_c$  is greater than the critical pressure ratio defined in the right-hand side of Eq. (17.11). The value of the  $k$  is about 1.28 for natural gas. Thus, the critical pressure ratio is about 0.55. Rearranging Eq. (17.12) gives

$$A_p = \frac{q_{gM}}{1248Cp_{up} \sqrt{\frac{k}{(k-1)\gamma_g T_{up}} \left[ \left( \frac{p_{dn}}{p_{up}} \right)^{\frac{2}{k}} - \left( \frac{p_{dn}}{p_{up}} \right)^{\frac{k+1}{k}} \right]}}. \quad (17.56)$$

Since the flow coefficient  $C$  is port-diameter dependent, a trial-and-error method is required to get a solution. A conservative  $C$  value is 0.6 for orifice-type valve ports. Once the required port area is determined, the port diameter can then be calculated by  $d_p = 1.1284\sqrt{A_p}$  and up-rounded off to the nearest 1/16 in.

The values of the port area to bellows area ratio  $R$  are fixed for given valve sizes and port diameters by valve manufacturers. Table 17.4 presents  $R$  values for Otis Spreadmaster Valves.

**Table 17.4 R Values for Otis Spreadmaster Valves**

Port Diameter (in.)		9/16 in. OD Valves			1-in. OD Valves			1½-in. OD Valves		
		R	1-R	T.E.F.	R	1-R	T.E.F.	R	1-R	T.E.F.
(⅙)	0.1250	0.1016	0.8984	0.1130	0.0383	0.9617	0.0398			
	0.1520	0.8429	0.1775							
	0.1730	0.8042	0.2434							
	3/16	0.1875			0.0863	0.9137	0.0945	0.0359	0.9641	0.0372
		0.1960	0.2508	0.7492	0.3347					
	13/64	0.2031			0.1013	0.8987	0.1127			
		0.2130	0.2966	0.7034	0.4216					
		0.2460	0.3958	0.6042	0.6550					
(¼)	0.2500				0.1534	0.8466	0.1812	0.0638	0.9362	0.0681
	9/32	0.2812			0.1942	0.8058	0.2410			
	5/16	0.3125			0.2397	0.7603	0.3153	0.0996	0.9004	0.1106
	1 ⅛	0.3437			0.2900	0.7100	0.4085			
(⅜)	0.3750				0.3450	0.6550	0.5267	0.1434	0.8566	0.1674
	7/16	0.4375			0.4697	0.5303	0.8857	0.1952	0.8048	0.2425
(½)	0.5000							0.2562	0.7438	0.3444
	9/16	0.5625						0.3227	0.6773	0.4765
(⅝)	0.6250							0.3984	0.6016	0.6622
(¾)	0.7500							0.5738	0.4262	1.3463

**Example Problem 17.6** Size port for the data given below:

Upstream pressure:	900 psia
Downstream pressure for subsonic flow:	600 psia
Tubing ID:	2.259 in.
Gas rate:	2500 Mscf/day
Gas-specific gravity:	0.75 (1 for air)
Gas-specific heat ratio:	1.3
Upstream temperature:	110°F
Gas viscosity:	0.02 cp
Choke discharge coefficient:	0.6
Use Otis Spreadmaster Valve	

**Solution**

$$A_p = \frac{2500}{1248(0.6)(900) \sqrt{\frac{1.3}{(1.3-1)(0.75)(110+460)} \left[ \left( \frac{600}{900} \right)^{\frac{2}{k}} - \left( \frac{600}{900} \right)^{\frac{1.3+1}{1.3}} \right]}}$$

$$A_p = 0.1684 \text{ in.}^2$$

$$d_p = 1.1284 \sqrt{1.684} = 0.4631 \text{ in.}$$



Table 17.1 shows that an Otis 1½-in. outside diameter (OD) valve with ½-in. diameter seat will meet the requirement. It has an  $R$  value of 0.2562.

#### 17.5.4.2 Valve testing

Before sending to field for installation, every gas lift valve should be set and tested at an opening pressure in the shop that corresponds to the desired opening pressure in the well. The pressure is called *test rack opening pressure* ( $P_{tro}$ ). The test is run with zero tubing pressure for pressure-operated valves and zero casing pressure for fluid-operated valves at a standard temperature (60°F in the U.S. petroleum industry). For pressure-operated unbalanced bellows valves at zero tubing pressure, Eq. (17.42) becomes

$$P_{tro} = \frac{P_d \text{ at } 60^\circ\text{F}}{1 - R} + S_t. \quad (17.57)$$

For fluid-operated valves at zero casing pressure, Eq. (17.44) also reduces to Eq. (17.57) at zero casing pressure and 60°F.

To set  $P_d$  at 60°F to a value representing  $P_d$  at valve depth condition, real gas law must be used for correction:

$$P_d \text{ at } 60^\circ\text{F} = \frac{520z_{60^\circ\text{F}}P_d}{T_d z_d}, \quad (17.58)$$

where

$T_d$  = temperature at valve depth, °R

$z_d$  = gas compressibility factor at valve depth condition.

The  $z$  factors in Eq. (17.58) can be determined using the Hall–Yarborough correlation. Computer spreadsheet *Hall-Yarborough-z.xls* is for this purpose.

Eq. (17.57) indicates that the  $P_{tro}$  also depends on the optional string load  $S_t$  for double-element valves. The  $S_t$  value can be determined on the basis of manufacturer's literature.

The procedure for setting and testing valves in a shop is as follows:

- Install valve in test rack.
- Adjust spring setting until the valve opens with  $S_t$  psig applied pressure. This sets  $S_t$  value in the valve.
- Pressure up the dome with nitrogen gas. Cool valve to 60°F.
- Bleed pressure off of dome until valve opens with  $P_{tro}$  psig applied pressure.

**Example Problem 17.7** Design gas lift valves using the following data:

Pay zone depth:	6500 ft
Casing size and weight:	7 in., 23 lb.
Tubing 2⅝ in., 4.7 lb. (1.995 in. ID)	
Liquid level surface:	
Kill fluid gradient:	0.4 psi/ft
Gas gravity:	0.75
Bottom-hole temperature:	170°F

Temperature surface flowing:	100°F
Injection depth:	6300 ft
Minimum tubing pressure at injection point:	600 psi
Pressure kickoff:	1000 psi
Pressure surface operating:	900 psi
Pressure of wellhead:	120 psi
Tubing pressure margin at surface:	200 psi
Casing pressure margin:	0 psi

Valve specifications given by Example Problem 17.6

**Solution** Design tubing pressure at surface ( $p_{hfd}$ ):

$$120 + 200 = 320 \text{ psia}$$

Design tubing pressure gradient ( $G_{fd}$ ):

$$(600 - 320)/6300 = 0.044 \text{ psi/ft}$$

Temperature gradient ( $G_t$ ):

$$(170 - 100) = 6300 = 0.011 \text{ F/ft}$$

$$1 - R = 1.0 - 0.2562 = 0.7438$$

$$\text{T.E.F.} = R/(1 - R) = 0.2562/0.7438 = 0.3444$$

Depth of the top valve is calculated with Eq. (17.49):

$$D_1 = \frac{1000 - 0 - 120}{0.40 - \frac{1000 - 0}{40,000}} = 2347 \text{ ft}$$

Temperature at the top valve:  $100 + (0.011)(2347) = 126^\circ\text{F}$

Design tubing pressure at the top valve:  $320 + (0.044)(2347) = 424 \text{ psia}$

For constant surface opening pressure of 900 psia, the valve opening pressure is calculated with Eq. (17.9):

$$p_{vol} = (900) \left( 1 + \frac{2347}{40,000} \right) = 953 \text{ psia}$$

The dome pressure at the valve depth is calculated on the basis of Eq. (17.42):

$$P_d = 0.7438(953) - 0 + (0.2562)(424) = 817 \text{ psia}$$

The valve closing pressure at the valve depth is calculated with Eq. (17.43):

$$P_{vc} = 817 + (0)(0.7438) = 817 \text{ psia}$$

The dome pressure at  $60^\circ\text{F}$  can be calculated with a trial-and-error method. The first estimate is given by idea gas law:

$$P_d \text{ at } 60^\circ\text{F} = \frac{520P_d}{T_d} = \frac{(520)(817)}{(126 + 460)} = 725 \text{ psia}$$

**Table 17.5 Summary of Results for Example Problem 17.7**

Valve No.	Valve Depth (ft)	Temperature (°F)	Design Tubing Pressure (psia)	Surface Opening Pressure (psia)	Valve Opening Pressure (psia)	Dome Pressure at Depth (psia)	Valve Closing Pressure (psia)	Dome Pressure at 60°F (psia)	Test Rack Opening (psia)
1	2347	126	424	900	953	817	817	683	918
2	3747	142	487	900	984	857	857	707	950
3	5065	156	545	900	1014	894	894	702	944
4	6300	170	600	900	1042	929	929	708	952

Spreadsheet programs give  $z_{60°F} = 0.80$  at 725 psia and 60°F. The same spreadsheet gives  $z_d = 0.85$  at 817 psia and 126°F. Then Eq. (17.58) gives

$$P_d \text{ at } 60^\circ\text{F} = \frac{(520)(0.80)P_d}{(126 + 460)(0.85)}(817) = 683 \text{ psia.}$$

Test rack opening pressure is given by Eq. (17.57) as

$$P_{tro} = \frac{683}{0.7438} + 0 = 918 \text{ psia.}$$

Following the same procedure, parameters for other valves are calculated. The results are summarized in Table 17.5.

The spreadsheet program *GasLiftValveDesign.xls* can be used to seek solutions to similar problems.

## 17.6 SPECIAL ISSUES IN INTERMITTENT-FLOW GAS LIFT

The intermittent-flow mechanism is very different from that of the continuous-flow gas lift. It is normally applicable in either high-BHP–low PI or low-BHP–low PI reservoirs. In these two reservoir cases, an excessive high drawdown is needed, which results in a prohibitively high GLR to produce the desired quantity of oil (liquid) by continuous gas lift. In many instances, the reservoir simply is not capable of giving up the desired liquid regardless of drawdown.

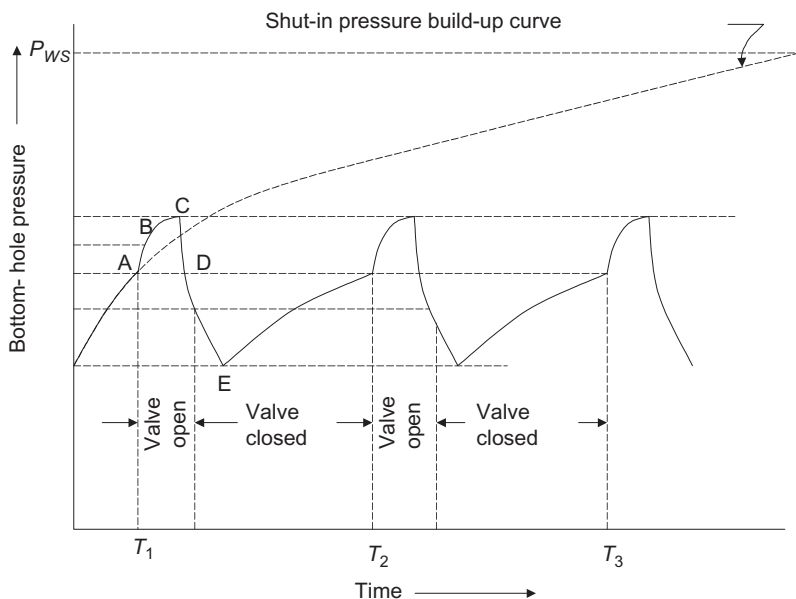
The flow from a well using intermittent gas lift techniques is called “ballistic” or “slug” flow. Two major factors that define the intermittent-gas lift process must be understood:

1. Complex flowing gradient of the gas lifted liquids from the well.
2. Contribution of the PI of the well to the actual deliverability of liquid to the surface.

Fig. 17.19 shows the BHP of a well being produced by intermittent-flow gas lift.

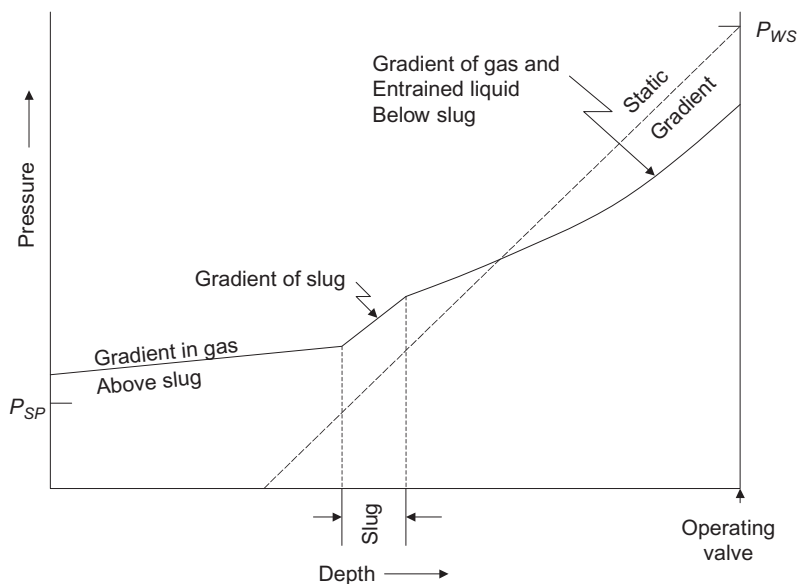
The BHP at the instant the valve opens is indicated by Point A. The pressure impulse results in an instantaneous pressure buildup at Point B, which reaches a maximum at C after the initial acceleration of the oil column.

Fig. 17.20 shows the intermittent-flowing gradient, which is a summation of the gradient of gas above the slug, the gradient of the slug, and the gradient of the lift gas and entrained liquids below the slug.



**FIGURE 17.19**

Illustrative plot of BHP of an intermittent flow.



**FIGURE 17.20**

Intermittent flow gradient at midpoint of tubing.

**Example Problem 17.8** Determine the depth to the operating (master) valve and the minimum GLR ratio for the following well data:

$$\begin{aligned} \text{Depth} &= 8000 \text{ ft} \\ p_{so} &= 800 \text{ psig} \\ 2\frac{3}{8} \text{-in. tubing} &= 1.995 \text{ in. ID} \\ 5\frac{1}{2} \text{-in., 20 lb/ft casing} & \end{aligned}$$

No water production

$$\begin{aligned} \gamma_o &= 0.8762, 30^\circ \text{ API} \\ \text{BHP (SI)} &= 2000 \text{ psig} \\ \text{PI} &= 0.10 \text{ bbl/day/psi} \\ p_{if} &= 50 \text{ psig} \\ t_{av} &= 127^\circ \text{ F} \end{aligned}$$

Cycle time: 45 minutes

Desired production: 100 bbl/day

$$\gamma_g = 0.80$$

**Solution** The static gradient is

$$G_s = 0.8762(0.433) = 0.379 \text{ psi/ft.}$$

Thus, the average flowing BHP is

$$P_{bhfave} = 2000 - 1000 = 1000 \text{ psig.}$$

The depth to the static fluid level with the  $p_{if} = 50$  psig, is

$$D_s = 8000 - \left( \frac{2000 - 50}{0.379} \right) = 2855 \text{ ft.}$$

The hydrostatic head after a 1000 psi drawdown is

$$D_{dds} = \frac{1000}{0.379} = 2639 \text{ ft.}$$

Thus, the depth to the working fluid level (WFL) is

$$\text{WFL} = D_s + D_{dds} = 2855 + 2639 = 5494 \text{ ft.}$$

Fig. 17.21 shows the example well and the WFL.

The number of cycles per day is approximately  $\frac{24(60)}{45} = 32$  cycles/day.

The number of bbls per cycle is  $\frac{100}{32} \approx 3$  bbl/cycle.

Intermittent-gas lift operating experience shows that depending on depth, 30%–60% of the total liquid slug is lost due to slippage or fallback.

If a 40% loss of starting slug is assumed, the volume of the starting slug is  $\frac{3}{0.60} \approx 5.0$  bbl/cycle.

Because the capacity of our tubing is 0.00387 bbl/ft, the length of the starting slug is  $\frac{5.0}{0.00387} \approx 1292$  ft.

This means that the operating valve should be located  $\frac{1292}{2} = 646$  ft below the working fluid level. Therefore, the depth to the operating valve is  $5494 + 646 = 6140$  ft.

The pressure in the tubing opposite the operating valve with the 50 psig surface back-pressure (neglecting the weight of the gas column) is

$$p_i = 50 + (1292)(0.379) = 540 \text{ psig.}$$

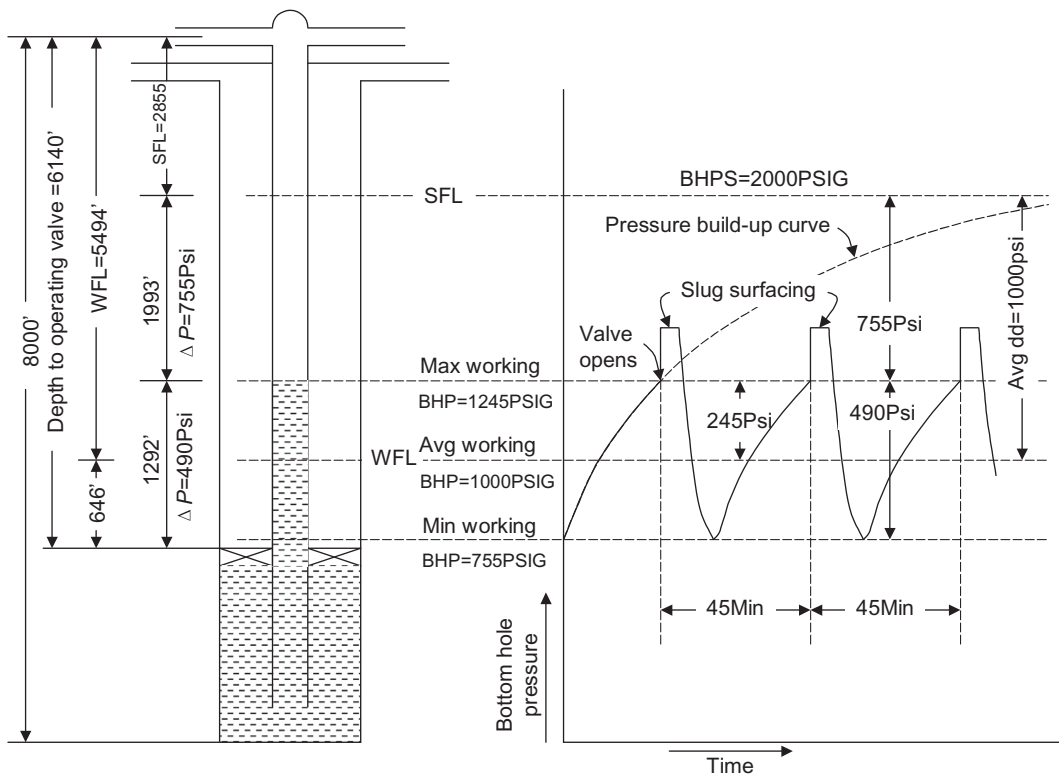


FIGURE 17.21

Example Problem 17.8 schematic and BHP buildup for slug flow.

For minimum slippage and fallback, a minimum velocity of the slug up the tubing should be 100 ft/min. This is accomplished by having the pressure in the casing opposite the operating valve at the instant the valve opens to be at least 50% greater than the tubing pressure with a minimum differential of 200 psi. Therefore, for a tubing pressure at the valve depth of 540 psig, at the instant the valve opens, the minimum casing pressure at 6140 ft is

$$p_{\min c} = 540 + 540/2 = 810 \text{ psig.}$$

Eq. (17.10) gives a  $p_{so} = 707$  psig.

The minimum volume of gas required to lift the slug to the surface will be that required to fill the tubing from injection depth to surface, less the volume occupied by the slug. Thus, this volume is  $(6140 + 1292) 0.00387 = 18.8$  bbls, which converts to  $105.5 \text{ ft}^3$ .

The approximate pressure in the tubing immediately under a liquid slug at the instant the slug surfaces is equal to the pressure due to the slug length plus the tubing backpressure. This is

$$p_{ts} = 50 + \left[ \frac{3.0}{0.00387} \right] (0.379) = 344 \text{ psig.}$$

Thus, the average pressure in the tubing is

$$p_{ave} = \frac{810 + 344}{2} = 577 \text{ psig} = 591.7 \text{ psia.}$$

The average temperature in the tubing is 127°F or 587°R. This gives  $z = 0.886$ . The volume of gas at standard conditions (API 60°F, 14.695 psia) is

$$V_{sc} = 105.5 \left( \frac{591.7}{14.695} \right) \left( \frac{520}{587} \right) \frac{1}{0.886} = 4246 \text{ scf/cycle.}$$

## 17.7 DESIGN OF GAS LIFT INSTALLATIONS

Different types of gas lift installations are used in the industry depending on well conditions. They fall into four categories: (1) open installation, (2) semiclosed installation, (3) closed installation, and (4) chamber installation.

As shown in Fig. 17.22A, no packer is set in open installations. This type of installation is suitable for continuous flow gas lift in wells with good fluid seal. Although this type of installation is simple, it exposes all gas lift valves beneath the point of gas injection to severe fluid erosion due to the dynamic changing of liquid level in the annulus. Open installation is not recommended unless setting packer is not an option.

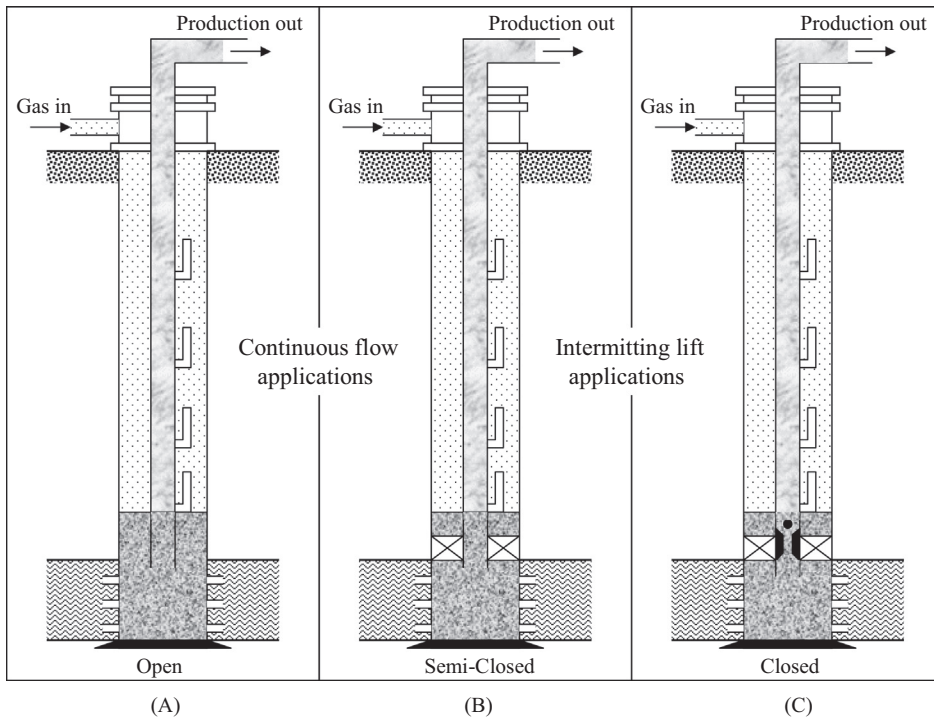


FIGURE 17.22

Three types of gas lift installations. (A) open installation, (B) semi-closed installation, and (C) closed installation.

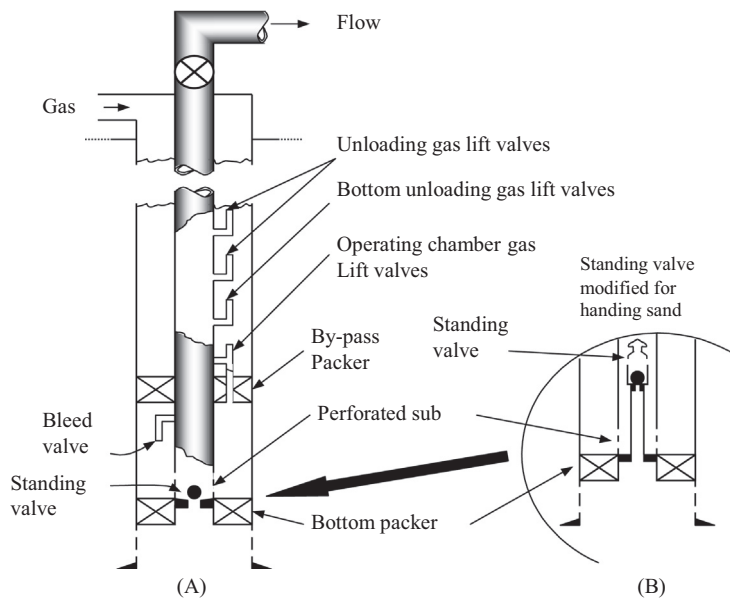
Fig. 17.22B demonstrates a semiclosed installation. It is identical to the open installation except that a packer is set between the tubing and casing. This type of installation can be used for both continuous- and intermittent-flow gas lift operations. It avoids all the problems associated with the open installations. However, it still does not prevent flow of well fluids back to formation during unloading processes, which is especially important for intermittent operating.

Illustrated in Fig. 17.22C is a closed installation where a standing valve is placed in the tubing string or below the bottom gas lift valve. The standing valve effectively prevents the gas pressure from acting on the formation, which increases the daily production rate from a well of the intermittent type.

Chamber installations are used for accumulating liquid volume at bottom-hole of intermittent-flow gas lift wells. A chamber is an ideal installation for a low BHP and high PI well. The chambers can be configured in various ways including using two packers, insert chamber, and reverse flow chamber. Fig. 17.23 shows a standard two-packer chamber. This type of chamber is installed to ensure a large storage volume of liquids with a minimum amount of backpressure on the formation so that the liquid production rate is not hindered.

Fig. 17.24 illustrates an insert chamber. It is normally used in a long open hole or perforated interval where squeezing of fluids back to formation by gas pressure is a concern. It takes the advantage of existing bottom-hole pressure. The disadvantage of the installation is that the chamber size is limited by casing diameter.

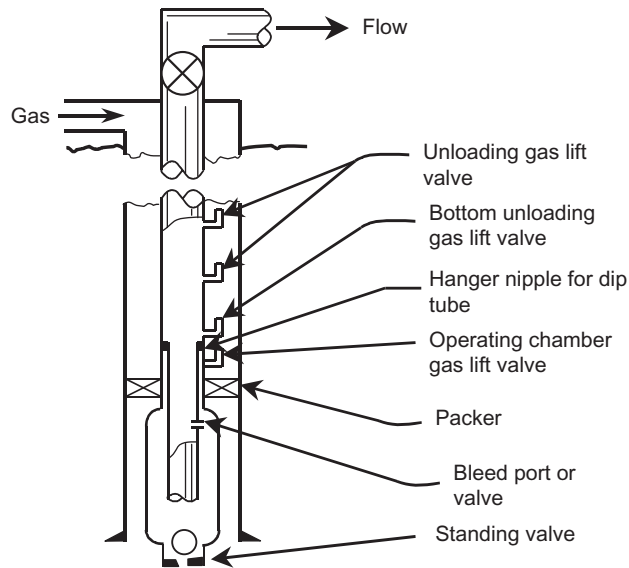
Shown in Fig. 17.25 is a reverse flow chamber. It ensures venting of all formation gas into the tubing string to empty the chamber for liquid accumulation. For wells with high formation GLR, this option appears to be an excellent choice.



**FIGURE 17.23**

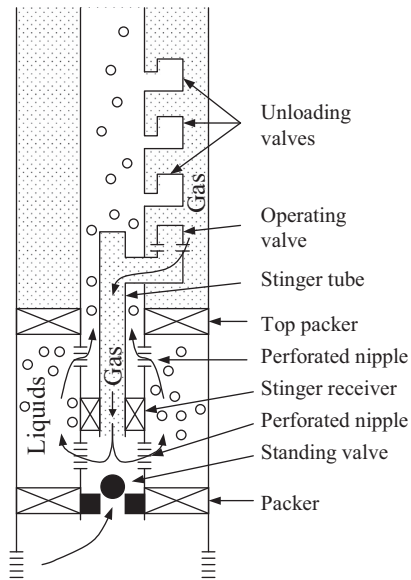
Sketch of a standard two-packer chamber. (A) full system sketch, and (B) sketch of standing valve.





**FIGURE 17.24**

A sketch of an insert chamber.



**FIGURE 17.25**

A sketch of a reserve flow chamber.

## 17.8 SUMMARY

This chapter presents the principles of gas lift systems and illustrates a procedure for designing gas lift operations. Major tasks include calculations of well deliverability, pressure and horsepower requirements for gas lift gas compression, gas lift valve selection and spacing, and selection of installation methods. Optimization of existing gas lift systems is left to Chapter 18, Other Artificial Lift Methods.

## REFERENCES

- Brown, K.E., 1977. The Technology of Artificial Lift Methods, vol. 1. PennWell Books, Tulsa, OK.  
 Brown, K.E., 1980. The Technology of Artificial Lift Methods, vol. 2a. Petroleum Publishing Co., Tulsa, OK.  
 Chen, N.H., 1979. An explicit equation for friction factor in pipe. *Ind. Eng. Chem. Fund* 18, 296.  
 Economides, M.J., Hill, A.D., Ehig-Economides, C., 1994. *Petroleum Production Systems*. Prentice Hall PTR, Upper Saddle River, NJ.  
 Gilbert, W.E., 1954. Flowing and gas-lift well performance. *API Drill. Prod. Practice* 20, 126–157.  
 Guo, B., Ghalambor, A., 2005. *Natural Gas Engineering Handbook*. Gulf Publishing Co, Houston, TX.  
 Katz, D.L., Cornell, D., Kobayashi, R., Poettmann, F.H., Vary, J.A., Elenbaas, J.R., et al., 1959. *Handbook of Natural Gas Engineering*. McGraw-Hill Publishing Company, New York.  
 Weymouth, T.R., 1912. Problems in natural gas engineering. *Trans. ASME* 34, 185.

## PROBLEMS

- 17.1. An oil well has a pay zone around the mid-perf depth of 5200 ft. The formation oil has a gravity of 30°API and GLR of 500 scf/stb. Water cut remains 10%. The IPR of the well is expressed as

$$q = J[\bar{p} - p_{wf}]$$

where

$$J = 0.5 \text{ stb/day/psi}$$

$$p = 2000 \text{ psia.}$$

A 2-in. tubing (1.995-in. ID) can be set with a packer at 200 ft above the mid-perf. What is the maximum expected oil production rate from the well with continuous gas lift at a wellhead pressure of 200 psia if

- a. unlimited amount of lift gas is available for the well?
  - b. only 1.2 MMscf/day of lift gas is available for the well?
- 17.2. An oil well has a pay zone around the mid-perf depth of 6200 ft. The formation oil has a gravity of 30°API and GLR of 500 scf/stb. Water cut remains 10%. The IPR of the well is expressed as

$$q = q_{\max} \left[ 1 - 0.2 \frac{p_{wf}}{\bar{p}} - 0.8 \left( \frac{p_{wf}}{\bar{p}} \right)^2 \right]$$

where

$$q_{\max} = 2000 \text{ stb/day}$$

$$\bar{p} = 2500 \text{ psia.}$$

A 2½-in. tubing (2.259-in. ID) can be set with a packer at 200 ft above the mid-perf.

What is the maximum expected oil production rate from the well with continuous gas lift at a wellhead pressure of 150 psia if

- a. unlimited amount of lift gas is available for the well?
- b. only 1.0 MMscf/day of lift gas is available for the well?

- 17.3.** An oil field has 24 oil wells defined in Problem 17.1. The gas lift gas at the central compressor station is first pumped to three injection manifolds with 6-in. ID, 2-mile lines and then distributed to the well heads with 4 in. ID, 0.5-mile lines. Given the following data, calculate the required output pressure of the compression station:

Gas-specific gravity ( $\gamma_g$ ):	0.75
Base temperature ( $T_b$ ):	60°F
Base pressure ( $p_b$ ):	14.7 psia.

- 17.4.** An oil field has 32 oil wells defined in Problem 17.2. The gas lift gas at the central compressor station is first pumped to four injection manifolds with 4-in. ID, 1.5-mile lines and then distributed to the wellheads with 4-in. ID, 0.4-mile lines. Given the following data, calculate the required output pressure of compression station:

Gas-specific gravity ( $\gamma_g$ ):	0.70
Base temperature ( $T_b$ ):	60°F
Base pressure ( $p_b$ ):	14.7 psia

- 17.5.** For a reciprocating compressor, calculate the theoretical and brake horsepower required to compress 50 MMcfd of a 0.7-gravity natural gas from 200 psia and 70°F to 2500 psia. If intercoolers cool the gas to 90°F, what is the heat load on the intercoolers and what is the final gas temperature? Assuming the overall efficiency is 0.75.
- 17.6.** For a reciprocating compressor, calculate the theoretical and brake horsepower required to compress 30 MMcfd of a 0.65-gravity natural gas from 100 psia and 70°F to 2000 psia. If intercoolers and endcoolers cool the gas to 90°F, what is the heat load on the coolers? Assuming the overall efficiency is 0.80.
- 17.7.** For a centrifugal compressor, use the following data to calculate required input horsepower and polytropic head:

Gas-specific gravity:	0.70
Gas-specific heat ratio:	1.30
Gas flow rate:	50 MMscfd at 14.7 psia and 60°F
Inlet pressure:	200 psia
Inlet temperature:	70°F
Discharge pressure:	500 psia
Polytropic efficiency:	$E_p = 0.61 + 0.03 \log(q_1)$

- 17.8.** For the data given in Problem 17.7, calculate the required brake horsepower if a reciprocating compressor is used.
- 17.9.** Only 1 MMscf/day of lift gas is available for the well described in Problem 17.3. If 1000 psia is available to kick off the well and then a steady injection pressure of 800 psia is maintained for gas lift operation against a wellhead pressure of 130 psia, design locations of unloading and operating valves. Assume a casing pressure margin of 0 psi.
- 17.10.** An unlimited amount of lift gas is available for the well described in Problem 17.4. If 1100 psia is available to kick off the well and then a steady injection pressure of 900 psia is maintained for gas lift operation against a wellhead pressure of 150 psia, design locations of unloading and operating valves. Assume a casing pressure margin of 50 psi.
- 17.11.** Size port for the data given below:

Upstream pressure:	950 psia
Downstream pressure for subsonic flow:	650 psia
Tubing ID:	2.259 in.
Gas rate:	2000 Mscf/day
Gas-specific gravity:	0.70 (1 for air)
Gas-specific heat ratio:	1.3
Upstream temperature:	100°F
Gas viscosity:	0.02 cp
Choke discharge coefficient:	0.6
Use Otis Spreadmaster Valve	

- 17.12.** Size port for the data given below:

Upstream pressure:	950 psia
Downstream pressure for subsonic flow:	550 psia
Tubing ID:	1.995 in.
Gas rate:	1500 Mscf/day
Gas-specific gravity:	0.70 (1 for air)
Gas-specific heat ratio:	1.3
Upstream temperature:	80°F
Gas viscosity:	0.03 cp
Choke discharge coefficient:	0.6
Use Otis Spreadmaster Valve	

- 17.13.** Design gas lift valves using the following data:

Pay zone depth:	5500 ft
Casing size and weight:	7 in., 23 lb
Tubing 2½ in.,	4.7 lb (1.995-in. ID):
Liquid level surface:	
Kill fluid gradient:	0.4 psi/ft
Gas gravity:	0.65
Bottom-hole temperature:	150°F

Temperature surface flowing:	80°F
Injection depth:	5300 ft
The minimum tubing pressure at injection point:	550 psi
Pressure kickoff:	950 psi
Pressure surface operating:	900 psi
Pressure of wellhead:	150 psi
Tubing pressure margin at surface:	200 psi
Casing pressure margin:	0 psi
Otis 1½-in. OD valve with ½-in. diameter seat:	$R = 0.2562$

**17.14.** Design gas lift valves using the following data:

Pay zone depth:	7500 ft
Casing size and weight:	7 in., 23 lb
Tubing 2⅞-in.,	4.7 lb (1.995 in. ID):
Liquid level surface:	
Kill fluid gradient:	0.4 psi/ft
Gas gravity:	0.70
Bottom-hole temperature:	160°F
Temperature surface flowing:	90°F
Injection depth:	7300 ft
The minimum tubing pressure at injection point:	650 psi
Pressure kickoff:	1050 psi
Pressure surface operating:	950 psi
Pressure of wellhead:	150 psi
Tubing pressure margin at surface:	200 psi
Casing pressure margin:	10 psi
Otis 1-in. OD valve with ½-in. diameter seat:	$R = 0.1942$

**17.15.** Determine the gas lift gas requirement for the following well data:

Depth	= 7500 ft
$P_{so}$	= 800 psig
2⅞-in. tubing	= 1.995 in. ID
5½-in., 20-lb/ft casing	
No water production	
$\gamma_o$	= 0.8762, 30° API
BHP (SI)	= 1800 psig
PI	= 0.125 bbl/day/psi
$P_{tf}$	= 50 psig
$t_{av}$	= 120°F
Cycle time:	45 minutes
Desired production:	150 bbl/day
$\gamma_g$	= 0.70

# OTHER ARTIFICIAL LIFT METHODS 18

## 18.1 INTRODUCTION

In addition to beam pumping and gas lift systems, other artificial lift systems are used in the oil industry. They are electrical submersible pumping (ESP), hydraulic piston pumping, hydraulic jet pumping, progressive cavity pumping, and plunger lift systems. All these systems are continuous pumping systems except the plunger lift, which is very similar to intermittent gas lift systems.

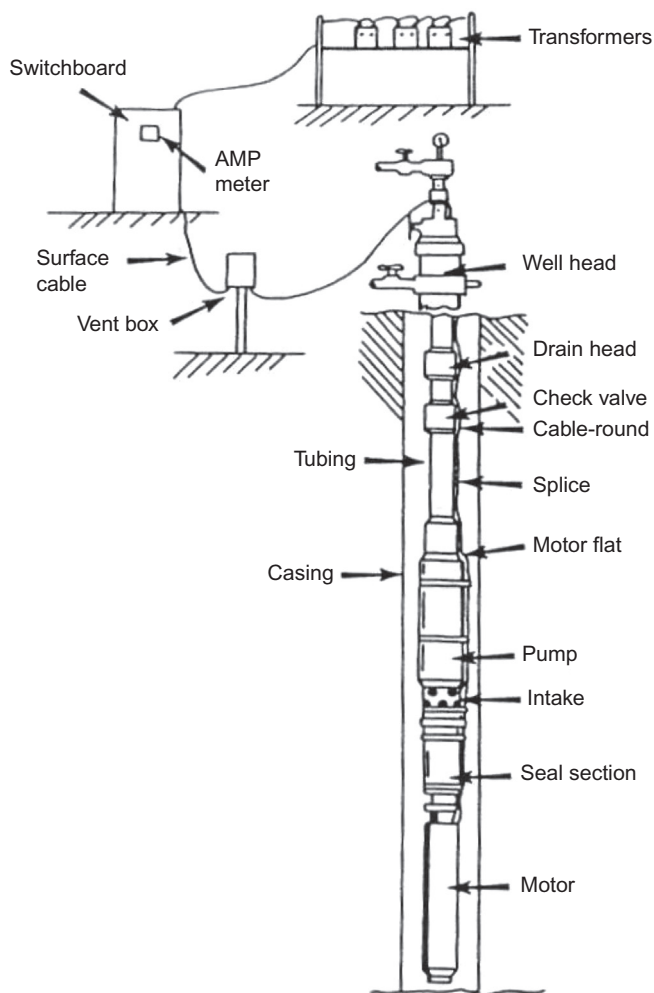
## 18.2 ELECTRICAL SUBMERSIBLE PUMP

Electrical submersible pumps (ESPs) are easy to install and operate. They can lift extremely high volumes from highly productive oil reservoirs. Crooked/deviated holes present no problem. ESPs are applicable to offshore operations. Lifting costs for high volumes are generally very low. Limitations to ESP applications include high-voltage electricity availability, non-applicable to multiple completions, unsuitable for deep and high-temperature oil reservoirs, troublesome gas and solids production, and costly installation and repair. ESP systems have higher horsepower, operate in hotter applications, are used in dual installations and as spare down-hole units, and include down-hole oil/water separation. Sand and gas problems have led to new products. Automation of the systems includes monitoring, analysis, and control.

The ESP is a relatively efficient artificial lift. Under certain conditions, it is even more efficient than sucker rod beam pumping. As shown in Fig. 18.1, an ESP consists of subsurface and surface components.

- Subsurface components
  - Pump
  - Motor
  - Seal electric cable
  - Gas separator
- Surface components
  - Motor controller (or variable speed controller)
  - Transformer
  - Surface electric cable

The overall ESP system operates like any electric pump commonly used in other industrial applications. In ESP operations, electric energy is transported to the down-hole electric motor via the electric cables. These electric cables are run on the side of (and are attached to) the production

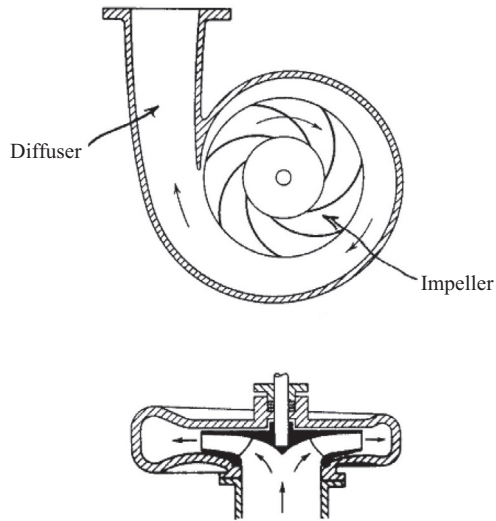
**FIGURE 18.1**

A sketch of an ESP installation (Centrilift-Hughes, Inc., 1998).

tubing. The electric cable provides the electrical energy needed to actuate the down-hole electric motor. The electric motor drives the pump and the pump imparts energy to the fluid in the form of hydraulic power, which lifts the fluid to the surface.

### 18.2.1 PRINCIPLE

ESPs are pumps made of dynamic pump stages or centrifugal pump stages. Fig. 18.2 gives the internal schematic of a single-stage centrifugal pump. Fig. 18.3 shows a cutaway of a multistage centrifugal pump.



**FIGURE 18.2**

An internal schematic of centrifugal pump.



**FIGURE 18.3**

A sketch of a multistage centrifugal pump.



The electric motor connects directly to the centrifugal pump module in an ESP. This means that the electric motor shaft connects directly to the pump shaft. Thus, the pump rotates at the same speed as the electric motor. Like most down-hole tools in the oil field, ESPs are classified by their outside diameter (from 3.5 to 10.0 in.). The number of stages to be used in a particular outside diameter sized pump is determined by the volumetric flow rate and the lift (height) required. Thus, the length of a pump module can be 40–344 in. in length. Electric motors are three-phase (AC), squirrel cage, induction type. They can vary from 10 to 750 hp at 60 Hz or 50 Hz (and range from 3 $\frac{3}{8}$  to 7 $\frac{1}{4}$  in. in diameter). Their voltage requirements vary from 420–4200 V.

The seal system (the protector) separates the well fluids from the electric motor lubrication fluids and the electrical wiring. The electric controller (surface) serves to energize the ESP, sensing such conditions as overload, well pump-off, short in cable, and so on. It also shuts down or starts up in response to down-hole pressure switches, tank levels, or remote commands. These controllers are available in conventional electromechanical or solid-state devices. Conventional electromechanical controllers give a fixed-speed, fixed flow rate pumping. To overcome this limitation, the variable speed controller has been developed (solid state). These controllers allow the frequency of the electric current to vary. This results in a variation in speed (rpm) and, thus, flow rate. Such a device allows changes to be made (on the fly) whenever a well changes volume (static level), pressure, gas liquid ratio (GLR), or water/oil ratio (WOR). It also allows flexibility for operations in wells where the PI is not well known. The transformer (at surface) changes the voltage of the distribution system to a voltage required by the ESP system.

Unlike positive-displacement pumps, centrifugal pumps do not displace a fixed amount of fluid but create a relatively constant amount of pressure increase to the flow system. The output flow rate depends on backpressure. The pressure increase is usually expressed as pumping head, the equivalent height of freshwater that the pressure differential can support (pumps are tested with freshwater by the manufacturer). In U.S. field units, the pumping head is expressed as

$$h = \frac{\Delta p}{0.433}, \quad (18.1)$$

where

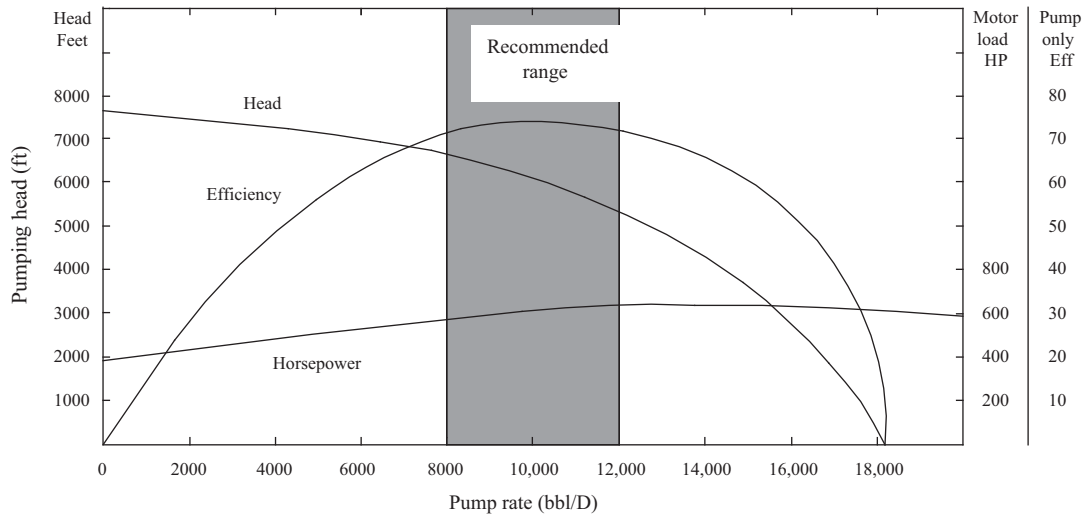
$h$  = pumping head, ft

$\Delta p$  = pump pressure differential, psi.

As the volumetric throughput increases, the pumping head of a centrifugal pump decreases and power slightly increases. However, there exists an optimal range of flow rate where the pump efficiency is maximal. A typical ESP characteristic chart is shown in Fig. 18.4.

ESPs can operate over a wide range of parameters (depths and volumes), to depths over 12,000 ft and volumetric flow rates of up to 45,000 bbl/day. Certain operating variables can severely limit ESP applications, including the following:

- Free gas in oil
- Temperature at depth
- Viscosity of oil
- Sand content fluid
- Paraffin content of fluid



**FIGURE 18.4**

A typical characteristic chart for a 100-stage ESP.

Excessive free gas results in pump cavitation that leads to motor fluctuations that ultimately reduces run life and reliability. High temperature at depth will limit the life of the thrust bearing, the epoxy encapsulations (of electronics, etc.), insulation, and elastomers. Increased viscosity of the fluid to be pumped reduces the total head that the pump system can generate, which leads to an increased number of pump stages and increased horsepower requirements. Sand and paraffin content in the fluid will lead to wear and choking conditions inside the pump.

### 18.2.2 ESP APPLICATIONS

The following factors are important in designing ESP applications:

- PI of the well
- Casing and tubing sizes
- Static liquid level

ESPs are usually for high PI wells. More and more ESP applications are found in offshore wells. The outside diameter of the ESP down-hole equipment is determined by the inside diameter (ID) of the borehole. There must be clearance around the outside of the pump down-hole equipment to allow the free flow of oil/water to the pump intake. The desired flow rate and tubing size will determine the total dynamic head (TDH) requirements for the ESP system. The “TDH” is defined as the pressure head immediately above the pump (in the tubing). This is converted to feet of head (or meters of head). This TDH is usually given in water equivalent. Thus,  $TDH = \text{static column of fluid (net) head} + \text{friction loss head} + \text{backpressure head}$ .

The following procedure can be used for selecting an ESP:

1. Starting from well inflow performance relationship (IPR), determine a desirable liquid production rate  $q_{Ld}$ . Then select a pump size from the manufacturer's specification that has a minimum delivering flow rate  $q_{Lp}$ , that is,  $q_{Lp} > q_{Ld}$ .
2. From the IPR, determine the flowing bottom-hole pressure  $p_{wf}$  at the pump-delivering flow rate  $q_{Lp}$ , not the  $q_{Ld}$ .
3. Assuming zero casing pressure and neglecting gas weight in the annulus, calculate the minimum pump depth by

$$D_{pump} = D - \frac{p_{wf} - p_{suction}}{0.433\gamma_L}, \quad (18.2)$$

where

$D_{pump}$  = minimum pump depth, ft

$D$  = depth of production interval, ft

$p_{wf}$  = flowing bottom-hole pressure, psia

$p_{suction}$  = required suction pressure of pump, 150–300 psi

$\gamma_L$  = specific gravity of production fluid, 1.0 for freshwater.

4. Determine the required pump discharge pressure based on wellhead pressure, tubing size, flow rate  $q_{Lp}$ , and fluid properties. This can be carried out quickly using the computer spreadsheet *HagedornBrownCorrelation.xls*.
5. Calculate the required pump pressure differential  $\Delta p = p_{discharge} - p_{suction}$  and then required pumping head by Eq. (18.1).
6. From the manufacturer's pump characteristics curve, read pump head or head per stage. Then calculate the required number of stages.
7. Determine the total power required for the pump by multiplying the power per stage by the number of stages.

**Example Problem 18.1** A 10,000-ft-deep well produces 32°API oil with gas-oil ratio (GOR) 50 scf/stb and zero water cut through a 3-in. (2.992-in. ID) tubing in a 7-in. casing. The oil has a formation volume factor of 1.25 and average viscosity of 5 cp. Gas-specific gravity is 0.7. The surface and bottom-hole temperatures are 70°F and 170°F, respectively. The IPR of the well can be described by the Vogel model with a reservoir pressure 4350 psia and absolute open flow (AOF) 15,000 stb/day. If the well is to be put in production with an ESP to produce liquid at 8000 stb/day against a flowing wellhead pressure of 100 psia, determine the required specifications for an ESP for this application. Assume the minimum pump suction pressure is 200 psia.

#### Solution

1. Required liquid throughput at pump is

$$q_{Ld} = (1.25)(8000) = 10,000 \text{ bbl/day.}$$

Select an ESP that delivers liquid flow rate  $q_{Lp} = q_{Ld} = 10,000$  bbl/day in the neighborhood of its maximum efficiency (Fig. 18.4).

2. Well IPR gives

$$\begin{aligned} p_{wfd} &= 0.125\bar{p} \left[ \sqrt{81 - 80(q_o/q_{\max})} - 1 \right] \\ &= 0.25(4350) \left[ \sqrt{81 - 80(8000/15000)} - 1 \right] \\ &= 2823 \text{ psia.} \end{aligned}$$

3. The minimum pump depth is

$$\begin{aligned} D_{\text{pump}} &= D - \frac{p_{wf} - p_{\text{suction}}}{0.433\gamma_L} \\ &= 10,000 - \frac{2823 - 200}{0.433(0.865)} \\ &= 2997 \text{ ft.} \end{aligned}$$

Use pump depth of  $10,000 - 200 = 9800$  ft. The pump suction pressure is

$$\begin{aligned} p_{\text{suction}} &= 2823 - 0.433(0.865)(10,000 - 9800) \\ &= 2748 \text{ psia.} \end{aligned}$$

4. Computer spreadsheet *HagedornBrownCorrelation.xls* gives the required pump discharge pressure of 4452 psia.  
5. The required pump pressure differential is

$$\Delta p = p_{\text{discharge}} - p_{\text{suction}} = 4452 - 2748 = 1704 \text{ psi.}$$

The required pumping head is

$$h = \frac{\Delta p}{0.433} = \frac{1704}{0.433} = 3935 \text{ feet of freshwater.}$$

6. At throughput 10,000 bbl/day, Fig. 18.4 gives a pumping head of 6000 ft for the 100-stage pump, which yields 60 ft pumping head per stage. The required number of stages is  $(3935)/(60) = 66$  stages.  
7. At throughput 10,000 bbl/day, Fig. 18.4 gives the power of the 100-stage pump of 600 hp, which yields 6 hp/stage. The required power for a 66-stage pump is then  $(6)(66) = 394$  hp.

The solution given by the computer spreadsheet *ESPdesign.xls* is shown in Table 18.1.

---

## 18.3 HYDRAULIC PISTON PUMPING

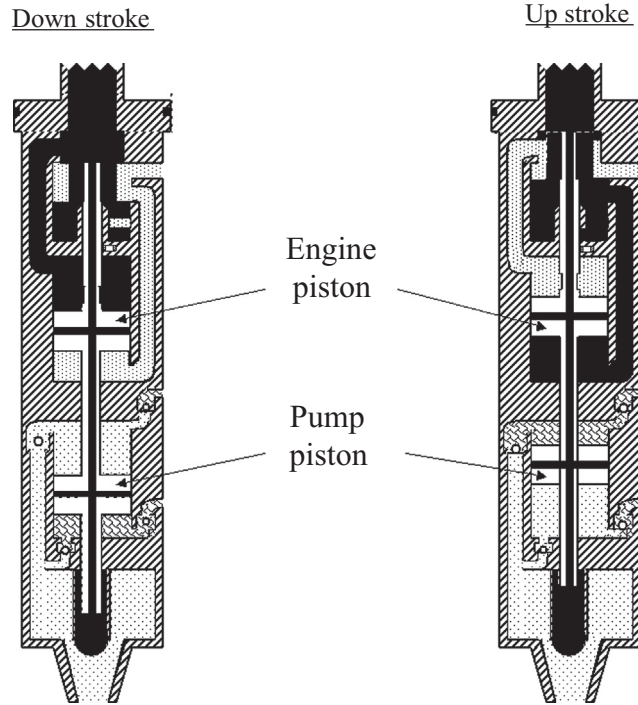
Hydraulic piston pumping systems can lift large volumes of liquid from great depth by pumping wells down to fairly low pressures. Crooked holes present minimal problems. Both natural gas and electricity can be used as the power source. They are also applicable to multiple completions and offshore operations. Their major disadvantages include power oil systems being fire hazards and costly, power water treatment problems, and high solids production being troublesome.

As shown in Fig. 18.5, a hydraulic piston pump (HPP) consists of an engine with a reciprocating piston driven by a power fluid connected by a short shaft to a piston in the pump end. HPPs are

<b>Table 18.1 Result Given by the Computer Spreadsheet ESPdesign.xls</b>	
<i>ESPdesign.xls</i>	
<i>Description:</i> This spreadsheet calculates parameters for ESP selection.	
<i>Instruction:</i> (1) Update parameter values in the Input data and Solution sections; and (2) view result in the Solution section.	
<b>Input Data</b>	
Reservoir depth ( $D$ ):	10,000 ft
Reservoir pressure ( $p_{bar}$ ):	4350 psia
AOF in Vogel equation for IPR ( $q_{max}$ ):	15,000 stb/day
Production fluid gravity ( $\gamma_L$ ):	0.865 1 for H <sub>2</sub> O
Formation volume factor of production liquid ( $B_L$ ):	1.25 rb/stb
Tubing inner diameter ( $d_{ti}$ ):	2.992 in.
Well head pressure ( $p_{wh}$ ):	100 psia
Required pump suction pressure ( $p_{suction}$ ):	200 psia
Desired production rate ( $q_{Ld}$ ):	8000 stb/day
<b>Solution</b>	
Desired bottom-hole pressure from IPR ( $p_{wfd}$ )	= 2823 psia
Desired production rate at pump ( $q_{Ld}$ )	= 10,000 bbl/day
Input here the minimum capacity of selected pump ( $q_{Lp}$ ):	10,000 bbl/day
Minimum pump setting depth ( $D_{pump}$ )	= 2997 ft
Input pump setting depth ( $D_{pump}$ ):	9800 ft
Pump suction pressure ( $p_{suction}$ )	= 2748 psia
Input pump discharge pressure ( $p_{discharge}$ ):	4452 psia
Required pump pressure differential ( $\Delta p$ )	= 1704 psia
Required pumping head ( $h$ )	= 3935 ft H <sub>2</sub> O
Input pumping head per stage of the selected pump ( $h_s$ ):	60.00 ft/stage
Input horsepower per stage of the selected pump ( $hp_s$ ):	6.00 hp/stage
Input efficiency of the selected pump ( $E_p$ ):	0.72
Required number of stages ( $N_s$ )	= 66
Total motor power requirement ( $hp_{motor}$ )	= 394 hp

usually double-acting, that is, fluid is being displaced from the pump on both the upstroke and the downstroke. The power fluid is injected down a tubing string from the surface and is either returned to the surface through another tubing (closed power fluid) or commingled with the produced fluid in the production string (open power fluid). Because the pump and engine pistons are directly connected, the volumetric flow rates in the pump and engine are related through a simple equation (Cholet, 2000):

$$q_{pump} = q_{eng} \frac{A_{pump}}{A_{eng}}, \quad (18.3)$$


**FIGURE 18.5**

A sketch of a hydraulic piston pump.

where

$q_{pump}$  = flow rate of the produced fluid in the pump, bbl/day

$q_{eng}$  = flow rate of the power fluid, bbl/day

$A_{pump}$  = net cross-sectional area of pump piston, in.<sup>2</sup>

$A_{eng}$  = net cross-sectional area of engine piston, in.<sup>2</sup>.

Eq. (18.3) implies that liquid production rate is proportional to the power fluid injection rate. The proportionality factor  $A_{pump}/A_{eng}$  is called the “P/E ratio.” By adjusting the power fluid injection rate, the liquid production rate can be proportionally changed. Although the P/E ratio magnifies production rate, a larger P/E ratio means higher injection pressure of the power fluid.

The following pressure relation can be derived from force balance in the HPP:

$$p_{eng,i} - p_{eng,d} = (p_{pump,d} - p_{pump,i}) (P/E) + F_{pump}, \quad (18.4)$$

where

$p_{eng,i}$  = pressure at engine inlet, psia

$p_{eng,d}$  = engine discharge pressure, psia

$p_{pump,d}$  = pump discharge pressure, psia  
 $P_{pump,i}$  = pump intake pressure, psia  
 $F_{pump}$  = pump friction-induced pressure loss, psia.

Eq. (18.4) is also valid for open power fluid system where  $p_{eng,d} = p_{pump,d}$ .

The pump friction-induced pressure loss  $F_{pump}$  depends on pump type, pumping speed, and power fluid viscosity. Its value can be estimated with the following empirical equation:

$$F_{pump} = 50\gamma_L(0.99 + 0.01\nu_{pf}) (7.1e^{Bq_{total}})^{N/N_{max}}, \quad (18.5)$$

where

$\gamma_L$  = specific gravity of production liquid, 1.0 for H<sub>2</sub>O  
 $\nu_{pf}$  = viscosity of power fluid, centistokes  
 $q_{total}$  = total liquid flow rate, bbl/day  
 $N$  = pump speed, spm  
 $N_{max}$  = maximum pump speed, spm  
 $B = 0.000514$  for 23/8-in. tubing  
 $= 0.000278$  for 27/8-in. tubing  
 $= 0.000167$  for 31/2-in. tubing  
 $= 0.000078$  for 41/2-in. tubing

The pump intake pressure  $p_{pump,i}$  can be determined on the basis of well IPR and desired liquid production rate  $q_{Ld}$ . If the IPR follows Vogel's model, then for an HPP installed close to bottom-hole,  $p_{pump,i}$  can be estimated using

$$p_{pump,i} = 0.125\bar{p} \left[ \sqrt{81 - 80(q_{Ld}/q_{max})} - 1 \right] - G_b \times (D - D_p), \quad (18.6)$$

where

$G_b$  = pressure gradient below the pump, psi/ft  
 $D$  = reservoir depth, ft  
 $D_p$  = pump setting depth, ft.

The pump discharge pressure  $p_{pump,d}$  can be calculated based on wellhead pressure and production tubing performance. The engine discharge pressure  $p_{eng,d}$  can be calculated based on the flow performance of the power fluid returning tubing. With all these parameter values known, the engine inlet pressure  $p_{eng,i}$  can be calculated by Eq. (18.6). Then the surface operating pressure can be estimated by

$$p_s = p_{eng,i} - p_h + p_f, \quad (18.7)$$

where

$p_s$  = surface operating pressure, psia  
 $p_h$  = hydrostatic pressure of the power fluid at pump depth, psia  
 $p_f$  = frictional pressure loss in the power fluid injection tubing, psi.

The required input power can be estimated from the following equation:

$$HP = 1.7 \times 10^{-5} q_{eng} P_s \quad (18.8)$$

Selection of HPP is based on the net lift defined by

$$L_N = D_p - \frac{P_{pump,i}}{G_b} \quad (18.9)$$

and empirical value of  $P/E$  defined by

$$P/E = \frac{10,000}{G_b} \quad (18.10)$$

The following procedure is used for selecting an HPP:

1. Starting from well IPR, determine a desirable liquid production rate  $q_{Ld}$ . Then calculate pump intake pressure with Eq. (18.6).
2. Calculate net lift with Eq. (18.9) and  $P/E$  ratio with Eq. (18.10).
3. Calculate flow rate at pump suction point by  $q_{Ls} = B_o q_{Ld}$ , where  $B_o$  is formation volume factor of oil. Then estimate pump efficiency  $E_p$ .
4. Select a pump rate ratio  $N/N_{max}$  between 0.2 and 0.8. Calculate the design flow rate of pump by

$$q_{pd} = \frac{q_{Ls}}{E_p(N/N_{max})}$$

5. Based on  $q_{pd}$  and  $P/E$  values, select a pump from the manufacturer's literature and get rated displacement values  $q_{pump}$ ,  $q_{eng}$ , and  $N_{max}$ . If not provided, calculate flow rates per stroke by

$$q'_{pump} = \frac{q_{pump}}{N_{max}}$$

and

$$q'_{eng} = \frac{q_{eng}}{N_{max}}$$

6. Calculate pump speed by

$$N = \left( \frac{N}{N_{max}} \right) N_{max}$$

7. Calculate power fluid rate by

$$q_{pf} = \left( \frac{N}{N_{max}} \right) \frac{q_{eng}}{E_{eng}}$$

8. Determine the return production flow rate by

$$q_{total} = q_{pf} + q_{Ls}$$

for open power fluid system or

$$q_{total} = q_{Ls}$$

for closed power fluid system.

9. Calculate pump and engine discharge pressure  $p_{pump,d}$  and  $p_{eng,d}$  based on tubing performance.



10. Calculate pump friction-induced pressure loss using Eq. (18.5).
11. Calculate required engine pressure using Eq. (18.4).
12. Calculate pressure change  $\Delta p_{inj}$  from surface to engine depth in the power fluid injection tubing based on single-phase flow. It has two components:

$$\Delta p_{inj} = p_{potential} - p_{friction}$$

13. Calculate required surface operating pressure by

$$p_{so} = p_{eng,i} - \Delta p_{inj}$$

14. Calculate required surface operating horsepower by

$$HP_{so} = 1/7 \times 10^{-5} \frac{q_{pf} p_{so}}{E_s},$$

where  $E_s$  is the efficiency of surface pump.

**Example Problem 18.2** A 10,000-ft-deep well has a potential to produce 40°API oil with GOR 150 scf/stb and 10% water cut through a 2-in. (1.995-in. ID) tubing in a 7-in. casing with a pump installation. The oil has a formation volume factor of 1.25 and average viscosity of 5 cp. Gas- and water-specific gravities are 0.7 and 1.05, respectively. The surface and bottom-hole temperatures are 80 and 180°F, respectively. The IPR of the well can be described by Vogel's model with a reservoir pressure 2000 psia and AOF 300 stb/day. If the well is to be put in production with an HPP at a depth of 9700 ft in an open power fluid system to produce liquid at 200 stb/day against a flowing wellhead pressure of 75 psia, determine the required specifications for the HPP for this application. Assume the overall efficiencies of the engine, HHP, and surface pump to be 0.90, 0.80, and 0.85, respectively.

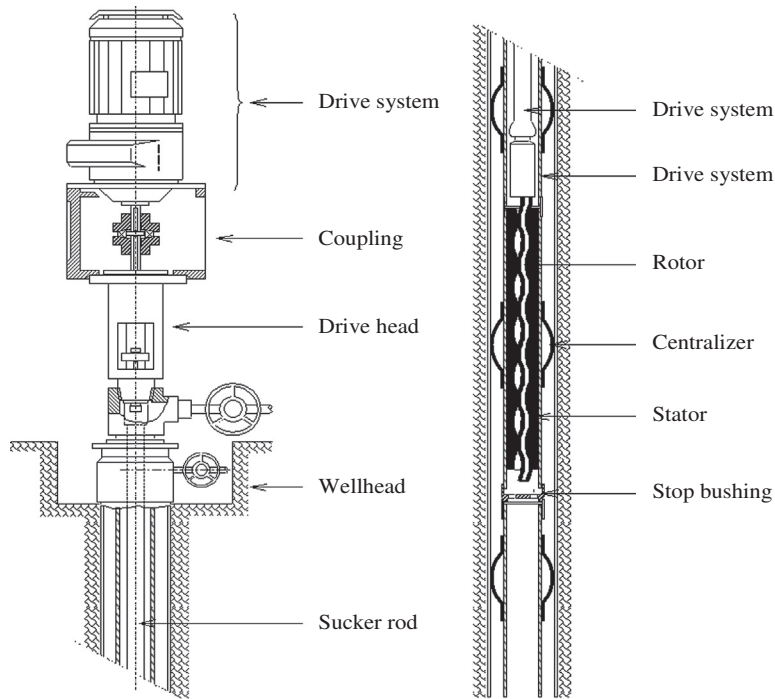
**Solution** This problem is solved by computer spreadsheet *HydraulicPistonPump.xls*, as shown in Table 18.2.

## 18.4 PROGRESSIVE CAVITY PUMPING

The progressive cavity pump (PCP) is a positive displacement pump, using an eccentrically rotating single-helical rotor, turning inside a stator. The rotor is usually constructed of a high-strength steel rod, typically double-chrome plated. The stator is a resilient elastomer in a double-helical configuration molded inside a steel casing. A sketch of a PCP system is shown in Fig. 18.6.

Progressive cavity pumping systems can be used for lifting heavy oils at a variable flow rate. Solids and free gas production present minimal problems. They can be installed in deviated and horizontal wells. With its ability to move large volumes of water, the progressing cavity pump is also used for coal bed methane, dewatering, and water source wells. The PCP reduces overall operating costs by increasing operating efficiency while reducing energy requirements. The major disadvantages of PCPs include short operating life (2–5 years) and high cost.

<b>Table 18.2 Solution Given by HydraulicPistonPump.xls</b>	
<i>HydraulicPistonPump.xls</i>	
<i>Description:</i> This spreadsheet calculates parameters for HPP selection.	
<i>Instruction:</i> (1) Update parameter values in the Input data and Solution sections; and (2) view result in the Solution section.	
<b>Input Data</b>	
Reservoir depth ( $D$ ):	10,000 ft
Reservoir pressure ( $p_{bar}$ ):	2000 psia
AOF in Vogel equation for IPR ( $q_{max}$ ):	300 stb/day
Production fluid gravity ( $\gamma_L$ ):	0.8251 1 for H <sub>2</sub> O
Formation volume factor of production liquid ( $B_L$ ):	1.25 rb/stb
Tubing inner diameter ( $d_{ti}$ ):	1.995 in.
$B$ value:	0.000514
Power fluid viscosity ( $v_{pf}$ ):	1 cs
Well head pressure ( $p_{wh}$ ):	100 psia
Pump setting depth ( $D_p$ ):	9700 ft
Desired production rate ( $q_{Ld}$ ):	200 stb/day
HPP efficiency ( $E_p$ ):	0.80
Surface pump efficiency ( $E_s$ ):	0.85
Engine efficiency ( $E_e$ ):	0.90
Pump speed ratio ( $N/N_{max}$ ):	0.80
Power fluid flow system (1 = OPFS, 0 = CPFS):	1
<b>Solution</b>	
Desired bottom-hole pressure from IPR ( $p_{wfd}$ )	= 1065 psia
Pump intake pressure ( $p_{pump}$ )	= 958 psia
Net lift ( $L_N$ )	= 7019 ft
Design pump to engine area ratio ( $P/E$ )	= 1.42
Flow rate at pump suction point ( $q_{Ls}$ )	= 250 bbl/day
Design flow rate of pump ( $q_{pd}$ )	= 391 bbl/day
Input from manufacturer's literature:	
Pump $P/E$ :	1.13
$q_{p,max}$ :	502 bbl/day
$q_{e,max}$ :	572 bbl/day
$N_{max}$ :	27
Flow rate per stroke/min in pump ( $q'_p$ )	= 18.59 bbl/day
Flow rate per stroke/min in engine ( $q'_e$ )	= 21.19 bbl/day
Pump speed ( $N$ )	= 21.60 spm
Power fluid rate ( $q_{pp}$ )	= 508 bbl/day
Return production flow rate ( $q_{total}$ )	= 758 bbl/day
Input pump discharge pressure by mHB correlation ( $p_{pump,d}$ ):	2914 psia
Input engine discharge pressure by mHB correlation ( $p_{eng,d}$ ):	2914 psia
Pump friction-induced pressure loss ( $F_{pump}$ )	= 270 psi
Required engine pressure ( $p_{eng,i}$ )	= 5395 psia
Input pressure change in the injection tubing ( $\Delta p_{inj}$ ):	= 3450 psi
Required surface operating pressure ( $p_{so}$ )	= 1945 psia
Required surface horsepower ( $HP_{so}$ )	= 20 hp



**FIGURE 18.6**

Sketch of a PCP system.

### 18.4.1 DOWN-HOLE PCP CHARACTERISTICS

Proper selection of a PCP requires knowledge of PCP geometry, displacement, head, and torque requirements. Fig. 18.7 (Cholet, 2000) illustrates rotor and stator geometry of PCP

where

$D$  = rotor diameter, in.

$E$  = rotor/stator eccentricity, in.

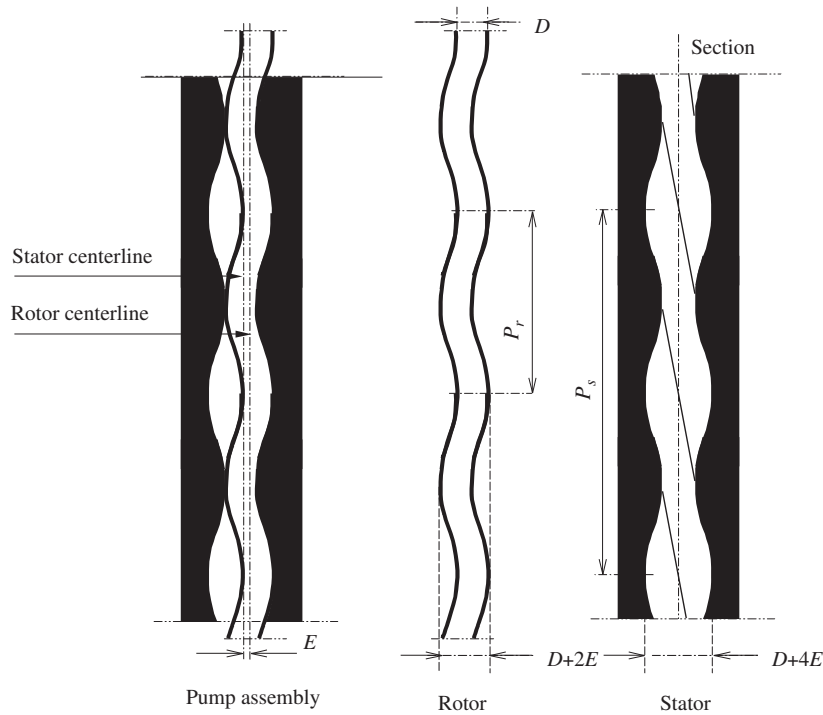
$P_r$  = pitch length of rotor, ft.

$P_s$  = pitch length of stator, ft.

Two numbers define the geometry of the PCP: the number of lobes of rotor and the number of lobes of the stator. A pump with a single helical rotor and double-helical stator is described as a “1-2 pump” where  $P_s = 2P_r$ . For a multilobe pump,

$$P_s = \frac{L_r + 1}{L_r} P_r, \quad (18.11)$$

where  $L_r$  is the number of rotor lobes. The ratio  $P_r/P_s$  is called the “kinematics ratio.”


**FIGURE 18.7**

Rotor and stator geometry of PCP.

Pump displacement is defined by the fluid volume produced in one revolution of the rotor:

$$V_0 = 0.028DEP_s, \quad (18.12)$$

where  $V_0$  = pump displacement,  $\text{ft}^3$ .

Pump flow rate is expressed as

$$Q_c = 7.12DEP_s N - Q_s, \quad (18.13)$$

where

$Q_c$  = pump flow rate, bbl/day

$N$  = rotary speed, rpm

$Q_s$  = leak rate, bbl/day.

The PCP head rating is defined by

$$\Delta P = (2n_p - 1)\delta p, \quad (18.14)$$

where

$\Delta P$  = pump head rating, psi

$n_p$  = number of pitches of stator

$\delta p$  = head rating developed into an elementary cavity, psi.

PCP mechanical resistant torque is expressed as

$$T_m = \frac{144V_0\Delta P}{e_p}, \quad (18.15)$$

where

$T_m$  = mechanical resistant torque, lb<sub>f</sub>-ft

$e_p$  = efficiency.

The load on thrust bearing through the drive string is expressed as

$$F_b = \frac{\pi}{4}(2E+D)^2\Delta P, \quad (18.16)$$

where  $F_b$  = axial load, lb<sub>f</sub>.

### 18.4.2 SELECTION OF DOWN-HOLE PCP

The following procedure can be used in the selection of a PCP:

1. Starting from well IPR, select a desirable liquid flow rate  $q_{Lp}$  at pump depth and the corresponding pump intake pressure below the pump  $p_{pi}$ .
2. Based on manufacturer's literature, select a PCP that can deliver liquid rate  $Q_{Lp}$ , where  $Q_{Lp} > q_{Lp}$ . Obtain the value of head rating for an elementary cavity  $\delta_p$ .
3. Determine the required pump discharge pressure  $p_{pd}$  based on wellhead pressure, tubing size, flow rate  $Q_{Lp}$ , and fluid properties. This can be carried out quickly using the computer spreadsheet *HagedornBrownCorrelation.xls*.
4. Calculate required pump head by

$$\Delta P = p_{pd} - p_{pi}. \quad (18.17)$$

5. Calculate the required number of pitches  $n_p$  using Eq. (18.14).
6. Calculate mechanical resistant torque with Eq. (18.15).
7. Calculate the load on thrust bearing with Eq. (18.16).

### 18.4.3 SELECTION OF DRIVE STRING

Sucker rod strings used in beam pumping are also used in the PCP systems as drive strings. The string diameter should be properly chosen so that the tensile stress in the string times the rod cross-sectional area does not exceed the maximum allowable strength of the string. The following procedure can be used in selecting a drive string:

1. Calculate the weight of the selected rod string  $W_r$  in the effluent fluid (liquid level in annulus should be considered to adjust the effect of buoyancy).
2. Calculate the thrust generated by the head rating of the pump  $F_b$  with Eq. (18.16).
3. Calculate mechanical resistant torque  $T_m$  with Eq. (18.15).
4. Calculate the torque generated by the viscosity of the effluent in the tubing by

$$T_v = 2.4 \times 10^{-6} \mu_f L N \frac{d^3}{(D-d)} \frac{1}{\ln \frac{\mu_s}{\mu_f}} \left( \frac{\mu_s}{\mu_f} - 1 \right), \quad (18.18)$$

where

$T_v$  = viscosity-resistant torque, lb<sub>f</sub>-ft

$\mu_f$  = viscosity of the effluent at the inlet temperature, cp

$\mu_s$  = viscosity of the effluent at the surface temperature, cp

$L$  = depth of tubing, ft

$d$  = drive string diameter, in.

5. Calculate total axial load to the drive string by

$$F = F_b + W_r. \quad (18.19)$$

6. Calculate total torque by

$$T = T_m + T_v. \quad (18.20)$$

7. Calculate the axial stress in the string by

$$\sigma_t = \frac{4}{\pi d^3} \sqrt{F^2 d^2 + 64 T^2 \times 144}, \quad (18.21)$$

where the tensile stress  $s_t$  is in pound per square inch. This stress value should be compared with the strength of the rod with a safety factor.

#### 18.4.4 SELECTION OF SURFACE DRIVER

The prime mover for PCP can be an electrical motor, hydraulic drive, or internal-combustion engine. The minimum required power from the driver depends on the total resistant torque requirement from the PCP, that is,

$$P_h = 1.92 \times 10^{-4} T N. \quad (18.22)$$

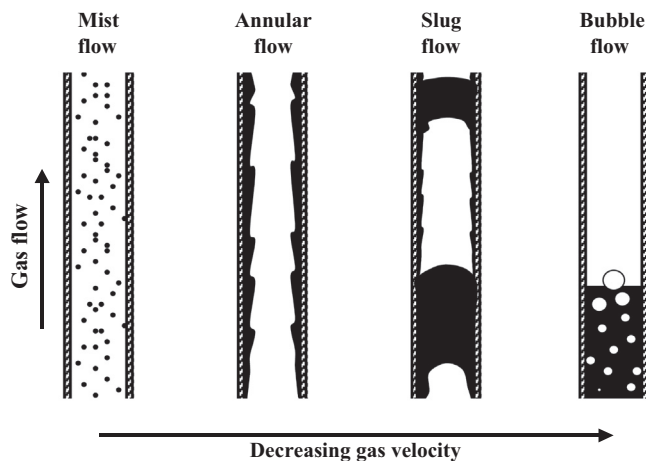
where the hydraulic power  $P_h$  is in hp. Driver efficiency and a safety factor should be used in driver selection from manufacturer's literature.

---

## 18.5 PLUNGER LIFT

Plunger lift systems are applicable to high gas–liquid ratio wells. They are very inexpensive installations. Plunger automatically keeps tubing clean of paraffin and scale. But they are good for low-rate wells normally less than 200 B/D. [Listiak \(2006\)](#) presents a thorough discussion of this technology.

Traditionally, plunger lift was used on oil wells. Recently, plunger lift has become more common on gas wells for de-watering purposes. As shown in [Fig. 18.8](#), high-pressure gas wells produce gas carrying liquid water and/or condensate in the form of mist. As the gas flow velocity in the well drops as a result of the reservoir pressure depletion, the carrying capacity of the gas decreases. When the gas velocity drops to a critical level, liquid begins to accumulate in the well and the well

**FIGURE 18.8**

Four flow regimes commonly encountered in gas wells.

flow can undergo annular flow regime followed by a slug flow regime. The accumulation of liquids (liquid loading) increases bottom-hole pressure that reduces gas production rate. Low gas production rate will cause gas velocity to drop further. Eventually the well will undergo bubbly flow regime and cease producing.

Liquid loading is not always obvious, and recognizing the liquid-loading problem is not an easy task. A thorough diagnostic analysis of well data needs to be performed. The symptoms to look for include onset of liquid slugs at the surface of well, increasing difference between the tubing and casing pressures with time, sharp changes in gradient on a flowing pressure survey, sharp drops in a production decline curve, and prediction with analytical methods.

Accurate prediction of the problem is vital for taking timely measures to solve the problem. Previous investigators have suggested several methods to predict the problem. Results from these methods often show discrepancies. Also, some of these methods are not easy to use because of the difficulties with prediction of bottom-hole pressure in multiphase flow.

Turner et al. (1969) were the pioneer investigators who analyzed and predicted the minimum gas flow rate capable of removing liquids from the gas production wells. They presented two mathematical models to describe the liquid-loading problem: the film movement model and entrained drop movement model. On the basis of analyses on field data they had, they concluded that the film movement model does not represent the controlling liquid transport mechanism.

The Turner et al. entrained drop movement model was derived on the basis of the terminal-free settling velocity of liquid drops and the maximum drop diameter corresponding to the critical Weber number of 30. According to Turner et al. (1969), gas will continuously remove liquids from the well until its velocity drops to below the terminal velocity. The minimum gas flow rate for a particular set of conditions (pressure and conduit geometry) can be calculated using a mathematical model. Turner et al. (1969) found that this entrained drop movement model gives underestimates of the minimum gas flow rates. They recommended the equation-derived values be adjusted upward

by approximately 20% to ensure removal of all drops. Turner et al. (1969) believed that the discrepancy was attributed to several facts including the use of drag coefficients for solid spheres, the assumption of stagnation velocity, and the critical Weber number established for drops falling in air, not in compressed gas.

The main problem that hinders the application of the Turner et al. entrained drop model to gas wells comes from the difficulties of estimating the values of gas density and pressure. Using an average value of gas-specific gravity (0.6) and gas temperature (120°F), Turner et al. derived an expression for gas density as 0.0031 times the pressure. However, they did not present a method for calculating the gas pressure in a multiphase flow wellbore.

Starting from the Turner et al. entrained drop model, Guo and Ghalambor (2005) determined the minimum kinetic energy of gas that is required to lift liquids. A four-phase (gas, oil, water, and solid particles) mist-flow model was developed. Applying the minimum kinetic energy criterion to the four-phase flow model resulted in a closed-form analytical equation for predicting the minimum gas flow rate. Through case studies, Guo and Ghalambor demonstrated that this new method is more conservative and accurate. Their analysis also indicates that the controlling conditions are bottom-hole conditions where gas has higher pressure and lower kinetic energy. This analysis is consistent with the observations from airdrilling operations where solid particles accumulate at bottom-hole rather than top-hole (Guo and Ghalambor, 2002). However, this analysis contradicts the results by Turner et al. (1969) that indicated that the wellhead conditions are, in most instances, controlling.

### 18.5.1 WORKING PRINCIPLE

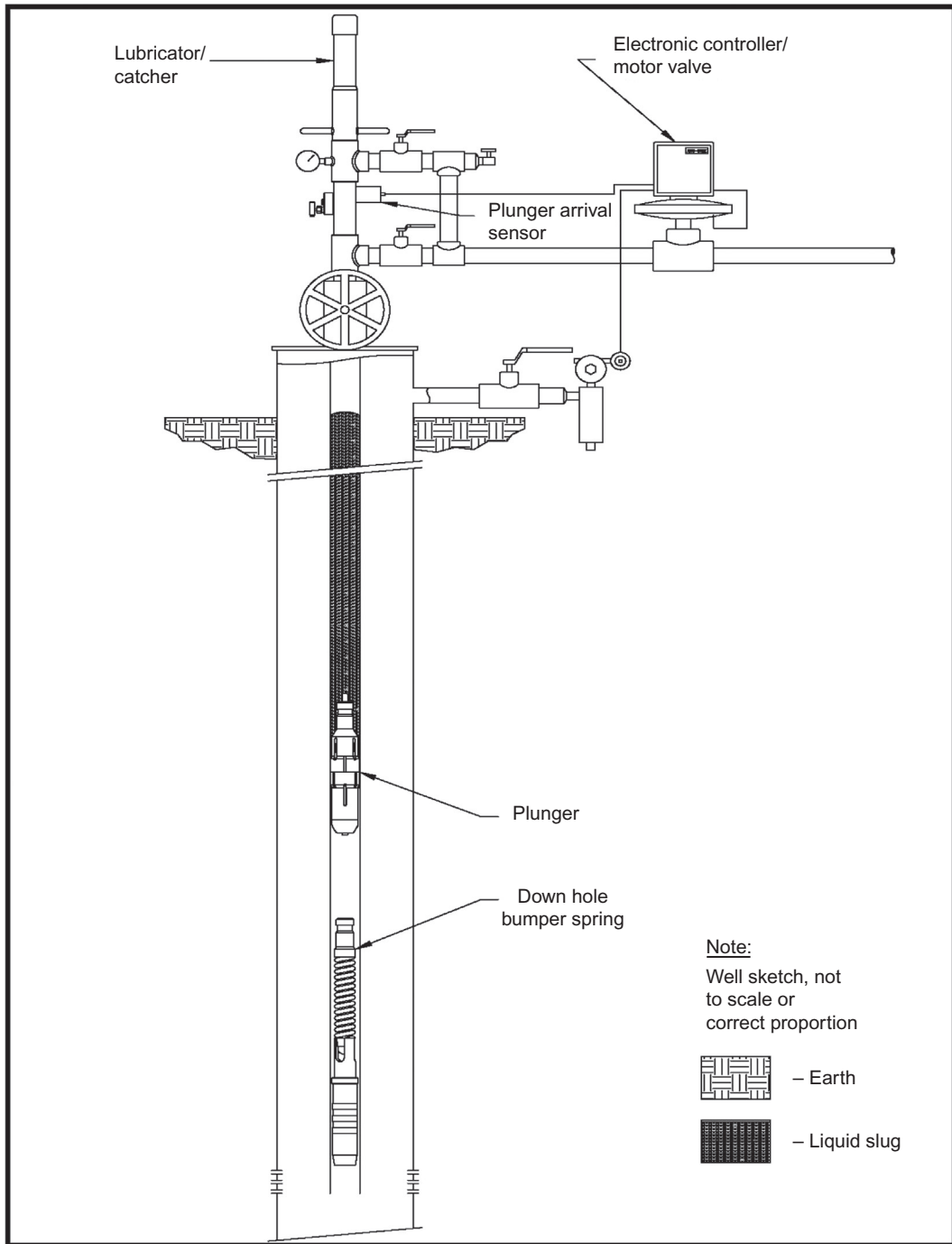
Fig. 18.9 illustrates a plunger lift system. Plunger lift uses a free piston that travels up and down in the well's tubing string. It minimizes liquid fallback and uses the well's energy more efficiently than in slug or bubble flow.

The purpose of plunger lift is like that of other artificial lift methods: to remove liquids from the wellbore so that the well can be produced at the lowest bottom-hole pressures. Whether in a gas well, oil well, or gas lift well, the mechanics of a plunger lift system are the same. The plunger, a length of steel, is dropped down the tubing to the bottom of the well and allowed to travel back to the surface. It provides a piston-like interface between liquids and gas in the wellbore and prevents liquid fallback. By providing a "seal" between the liquid and gas, a well's own energy can be used to efficiently lift liquids out of the wellbore. A plunger changes the rules for liquid removal. However, in a well without a plunger, gas velocity must be high to remove liquids. With a plunger, gas velocity can be very low. Unloading relies much more on the well's ability to store enough gas pressure to lift the plunger and a liquid slug to surface, and less on critical flow rates.

Plunger operation consists of shut-in and flow periods. The flow period is further divided into an unloading period and flow after plunger arrival. Lengths of these periods will vary depending on the application, producing capability of the well, and pressures.

A plunger cycle starts with the shut-in period that allows the plunger to drop from the surface to the bottom of the well. At the same time, the well builds gas pressure stored either in the casing, in the fracture, or in the near wellbore region of the reservoir. The well must be shut-in long enough to build reservoir pressure that will provide energy to lift both the plunger and the liquid slug to the surface against line pressure and friction. When this time and pressure have been





**FIGURE 18.9**

A sketch of a plunger lift system.

*Courtesy Ferguson Beauregard.*

reached, the flow period is started and unloading begins. In the initial stages of the flow period, the plunger and liquid slug begin traveling to the surface. Gas above the plunger quickly flows from the tubing into the flowline, and the plunger and liquid slug follow up the hole. The plunger arrives at the surface, unloading the liquid. Initially, high rates prevail (often three to four times the average daily rate) while the stored pressure is blown down. The well can now produce free of liquids, while the plunger remains at the surface, held by the well's pressure and flow. As rates drop, velocities eventually drop below the critical rate, and liquids begin to accumulate in the tubing. The well is shut-in and the plunger falls back to the bottom to repeat the cycle.

At the end of the shut-in period, the well has built pressure. The casing pressure is at its maximum, and the tubing pressure is lower than the casing pressure. The difference is equivalent to the hydrostatic pressure of the liquid in the tubing.

When the well is opened, the tubing pressure quickly drops down to line pressure, while the casing pressure slowly decreases until the plunger reaches the surface. As the plunger nears the surface, the liquid on top of the plunger may surge through the system, causing spikes in line pressure and flow rate. This continues until the plunger reaches the surface. After the plunger surfaces, a large increase in flow rate will produce higher tubing pressures and an increase in flowline pressure. Tubing pressure will then drop very close to line pressure. Casing pressure will reach its minimum either on plunger arrival or after, as the casing blows down and the well produces with minimal liquids in the tubing. If the well stays above the critical unloading rate, the casing pressure will remain fairly constant or may decrease further. As the gas rate drops, liquids become held up in the tubing and casing pressure will increase.

Upon shut-in, the casing pressure builds more rapidly. How fast depends on the inflow performance and reservoir pressure of the well. The tubing pressure will increase quickly from line pressure, as the flowing gas friction ceases. It will eventually track casing pressure (less the liquid slug). Casing pressure will continue to increase to maximum pressure until the well is opened again.

As with most wells, maximum plunger lift production occurs when the well produces against the lowest possible bottom-hole pressure. On plunger lift, the lowest average bottom-hole pressures are almost always obtained by shutting the well in the minimum amount of time. Practical experience and plunger lift models demonstrate that lifting large liquid slugs requires higher average bottom-hole pressure. Lengthy shut-in periods also increase average bottom-hole pressure. So the goal of plunger lift should be to shut the well in the minimum amount of time and produce only enough liquids that can be lifted at this minimum buildup pressure.

What is the minimum shut-in time? The absolute minimum amount of time for shut-in is the time it takes the plunger to reach the bottom. The well must be shut-in in this length of time regardless of what other operating conditions exist. Plungers typically fall between 200 and 1000 ft/min in dry gas and 20 and 250 ft/min in liquids. Total fall time varies and is affected by plunger type, amount of liquids in the tubing, the condition of the tubing (crimped, corkscrewed, corroded, etc.), and the deviation of the tubing or wellbore.

The flow period during and after plunger arrival is used to control liquid loads. In general, a short flow period brings in a small liquid load, and a long flow period brings in a larger liquid load. By controlling this flow time, the liquid load is controlled. So the well can be flowed until the desired liquid load has entered the tubing. A well with a high GLR may be capable of long flow periods without requiring more than minimum shut-in times. In this case, the plunger could

operate as few as 1 or 2 cycles/day. Conversely, a well with a low GLR may never be able to flow after plunger arrival and may require 25 cycles/day or more. In practice, if the well is shutting in for only the minimum amount of time, it can be flowed as long as possible to maintain target plunger rise velocities. If the well is shutting in longer than the minimum shut-in time, there should be little or no flow after the plunger arrives at the surface.

## 18.5.2 DESIGN GUIDELINE

Plunger lift systems can be evaluated using rules of thumb in conjunction with historic well production or with a mathematical plunger model. Because plunger lift installations are typically inexpensive, easy to install, and easy to test, most evaluations are performed by rules of thumb.

### 18.5.2.1 Estimate of production rates with plunger lift

The simplest and sometimes most accurate method of determining production increases from plunger lift is from decline curve analysis. Gas and oil reservoirs typically have predictable declines, either exponential, harmonic, or hyperbolic. Initial production rates are usually high enough to produce the well above critical rates (unloaded) and establish a decline curve. When liquid loading occurs, a marked decrease and deviation from normal decline can be seen. By unloading the well with plunger lift, a normal decline can be reestablished. Production increases from plunger lift will be somewhere between the rates of the well when it started loading and the rate of an extended decline curve to the present time. Ideally, decline curves would be used in concert with critical velocity curves to predetermine when plunger lift should be installed. In this manner, plunger lift will maintain production on a steady decline and never allow the well to begin loading.

Another method to estimate production is to build an inflow performance curve based on the backpressure equation. This is especially helpful if the well has an open annulus and casing pressure is known. The casing pressure gives a good approximation of bottom-hole pressure. The IPR curve can be built based on the estimated reservoir pressure, casing pressure, and current flow rate. Because the job of plunger lift is to lower the bottom-hole pressure by removing liquids, the bottom-hole pressure can be estimated with no liquids. This new pressure can be used to estimate a production rate with lower bottom-hole pressures.

### 18.5.2.2 GLR and buildup pressure requirements

There are two minimum requirements for plunger lift operation: minimum GLR and buildup pressure. For the plunger lift to operate, there must be available gas to provide the lifting force, in sufficient quantity per barrel of liquid for a given well depth.

#### 18.5.2.2.1 Rules of thumb

As a rule of thumb, the minimum GLR requirement is considered to be about 400 scf/bbl/1000 ft of well depth, that is,

$$\text{GLR}_{\min} = 400 \frac{D}{1000}, \quad (18.23)$$

where

GLR<sub>min</sub> = minimum required GLR for plunger lift, scf/bbl  
 D = depth to plunger, ft.

Eq. (18.23) is based on the energy stored in a compressed volume of 400 scf of gas expanding under the hydrostatic head of a barrel of liquid. The drawback is that no consideration is given to line pressures. Excessively high line pressures, relative to buildup pressure may increase the requirement. The rule of thumb also assumes that the gas expansion can be applied from a large open annulus without restriction. Slim-hole wells and wells with packers that require gas to travel through the reservoir or through small perforations in the tubing will cause a greater restriction and energy loss. This increases the minimum requirements to as much as 800–1200 scf/bbl/1000 ft.

Well buildup pressure is the second requirement for plunger operation. This buildup pressure is the bottom-hole pressure just before the plunger begins its ascent (equivalent to surface casing pressure in a well with an open annulus). In practice, the minimum shut-in pressure requirement for plunger lift is equivalent to  $P_{1/2}$  times maximum sales line pressure. The actual requirement may be higher. The rule works well in intermediate-depth wells (2000–8000 ft) with slug sizes of 0.1–0.5 barrels/cycle. It breaks down for higher liquid volumes, deeper wells (due to increasing friction), and excessive pressure restrictions at the surface or in the wellbore.

An improved rule for minimum pressure is that a well can lift a slug of liquid equal to about 50%–60% of the difference between shut-in casing pressure and maximum sales line pressure. This rule gives

$$p_c = p_{Lmax} + \frac{p_{sh}}{f_{sl}}, \quad (18.24)$$

where

$p_c$  = required casing pressure, psia  
 $p_{Lmax}$  = maximum line pressure, psia  
 $p_{sh}$  = slug hydrostatic pressure, psia  
 $f_{sl}$  = slug factor, 0.5–0.6.

This rule takes liquid production into account and can be used for wells with higher liquid production that require more than 1–2 barrels/cycle. It is considered as a conservative estimate of minimum pressure requirements. To use Eq. (18.24), first the total liquid production on plunger lift and number of cycles possible per day should be estimated. Then the amount of liquid that can be lifted per cycle should be determined. That volume of liquid per cycle is converted into the slug hydrostatic pressure using the well tubing size. Finally, the equation is used to estimate required casing pressure to operate the system.

It should be noted that a well that does not meet minimum GLR and pressure requirements could still be plunger lifted with the addition of an external gas source. Design at this point becomes more a matter of the economics of providing the added gas to the well at desired pressures.

#### 18.5.2.2.2 Analytical method

Analytical plunger lift design methods have been developed on the basis of force balance. Several studies in the literature address the addition of makeup gas to a plunger installation through either

existing gas lift operations, the installation of a field gas supply system, or the use of wellhead compression. Some of the studies were presented by [Beeson et al. \(1955\)](#), [Lebeaux and Sudduth \(1955\)](#), [Foss and Gaul \(1965\)](#), [Abercrombie \(1980\)](#), [Rosina \(1983\)](#), [Mower et al. \(1985\)](#), and [Lea \(1981, 1999\)](#).

The forces acting on the plunger at any given point in the tubing include the following:

1. Stored casing pressure acting on the cross-section of the plunger
2. Stored reservoir pressure acting on the cross-section of the plunger
3. Weight of the fluid
4. Weight of the plunger
5. Friction of the fluid with the tubing
6. Friction of the plunger with the tubing
7. Gas friction in the tubing
8. Gas slippage upward past the plunger
9. Liquid slippage downward past the plunger
10. Surface pressure (line pressure and restrictions) acting against the plunger travel

Several publications have been written dealing with this approach. [Beeson et al. \(1955\)](#) first presented equations for high GLR wells based on an empirically derived analysis. [Foss and Gaul \(1965\)](#) derived a force balance equation for use on oil wells in the Ventura Avenue field. [Mower et al. \(1985\)](#) presented a dynamic analysis of plunger lift that added gas slippage and reservoir inflow and mathematically described the entire cycle (not just plunger ascent) for tight-gas/very high GLR wells.

The methodology used by [Foss and Gaul \(1965\)](#) was to calculate a casing pressure required to move the plunger and liquid slug just before it reached the surface, called  $P_{C_{min}}$ . Since  $P_{C_{min}}$  is at the end of the plunger cycle, the energy of the expanding gas from the casing to the tubing is at its minimum. Adjusting  $P_{C_{min}}$  for gas expansion from the casing to the tubing during the full plunger cycle results in the pressure required to start the plunger at the beginning of the plunger cycle, or  $P_{C_{max}}$ .

The equations below are essentially the same equations presented by [Foss and Gaul \(1965\)](#) but are summarized here as presented by [Mower et al. \(1985\)](#). The Foss and Gaul model is not rigorous, because it assumes constant friction associated with plunger rise velocities of 1000 ft/min, does not calculate reservoir inflow, assumes a value for gas slippage past the plunger, assumes an open unrestricted annulus, and assumes the user can determine unloaded gas and liquid rates independently of the model. Also, this model was originally designed for oil well operation that assumed the well would be shut-in on plunger arrival, so the average casing pressure,  $P_{C_{avg}}$ , is only an average during plunger travel. The net result of these assumptions is an overprediction of required casing pressure. If a well meets the Foss and Gaul (1956) criteria, it is almost certainly a candidate for plunger lift.

### 18.5.2.3 Plunger lift models

#### 18.5.2.3.1 Basic Foss and Gaul equations (modified by Mower et al.)

The required minimum casing pressure is expressed as

$$P_{cmin} = [P_p + 14.7 + P_t + (P_{th} + P_{lf}) \times V_{slug}] \times \left(1 + \frac{D}{K}\right), \quad (18.25)$$

where

$P_{cmin}$  = required minimum casing pressure, psia

$P_p = W_p/A_t$ , psia

$W_p$  = plunger weight, lbf

$A_t$  = tubing inner cross-sectional area, in.<sup>2</sup>

$P_{lh}$  = hydrostatic liquid gradient, psi/bbl slug

$P_{lf}$  = flowing liquid gradient, psi/bbl slug

$P_t$  = tubing head pressure, psia

$V_{slug}$  = slug volume, bbl

$D$  = depth to plunger, ft

$K$  = characteristic length for gas flow in tubing, ft.

Foss and Gaul suggested an approximation where  $K$  and  $P_{lh} + P_{lf}$  are constant for a given tubing size and a plunger velocity of 1000 ft/min:

Tubing Size (in.)	$K$ (ft)	$P_{lh} + P_{lf}$ (psi/bbl)
2 $\frac{7}{8}$	33,500	165
2 $\frac{7}{8}$	45,000	102
3 $\frac{1}{2}$	57,600	63

To successfully operate the plunger, casing pressure must build to  $P_{cmax}$  given by

$$P_{cmax} = P_{cmin} \left( \frac{A_a + A_t}{A_a} \right). \tag{18.26}$$

The average casing pressure can then be expressed as

$$P_{cavg} = P_{cmin} \left( 1 + \frac{A_t}{2A_a} \right), \tag{18.27}$$

where  $A_a$  is annulus cross-sectional area in squared inch.

The gas required per cycle is formulated as

$$V_g = \frac{37.14 F_{gs} P_{cavg} V_t}{Z(T_{avg} + 460)}, \tag{18.28}$$

where

$V_g$  = required gas per cycle, Mscf

$F_{gs} = 1 + 0.02 (D/1000)$ , modified Foss and Gaul slippage factor

$V_t = A_t(D - V_{slug}L)$ , gas volume in tubing, Mcf

$L$  = tubing inner capacity, ft/bbl

$Z$  = gas compressibility factor in average tubing condition

$T_{avg}$  = average temperature in tubing, °F

The maximum number of cycles can be expressed as

$$N_{Cmax} = \frac{1440}{\frac{D}{V_r} + \frac{D - V_{slug}L}{V_{fg}} + \frac{V_{slug}L}{V_{fl}}}, \tag{18.29}$$

where

$N_{C_{\max}}$  = the maximum number of cycles per day

$V_{fg}$  = plunger falling velocity in gas, ft/min

$V_{fl}$  = plunger falling velocity in liquid, ft/min

$V_r$  = plunger rising velocity, ft/min

The maximum liquid production rate can be expressed as

$$q_{L_{\max}} = N_{C_{\max}} V_{slug}. \quad (18.30)$$

The required GLR can be expressed as

$$\text{GLR}_{\min} = \frac{V_g}{V_{slug}}. \quad (18.31)$$

### Example Problem 18.3 Plunger Lift Calculations

Calculate required GLR, casing pressure, and plunger lift operating range for the following given well data:

Gas rate:	200 Mcfd expected when unloaded
Liquid rate:	10 bbl/day expected when unloaded
Liquid gradient:	0.45 psi/ft
Tubing, ID:	1.995 in.
Tubing, OD:	2.375 in.
Casing, ID:	4.56 in.
Depth to plunger:	7000 ft
Line pressure:	100 psi
Available casing pressure:	800 psi
Reservoir pressure:	1200 psi
Average Z-factor:	0.99
Average temperature:	140°F
Plunger weight:	10 lb
Plunger fall in gas:	750 fpm
Plunger fall in liquid:	150 fpm
Plunger rise velocity:	1000 fpm

**Solution** The minimum required GLR by a rule of thumb is

$$\text{GLR}_{\min} = 400 \frac{D}{1000} = 400 \frac{7000}{1000} = 2800 \text{ scf/bbl.}$$

The well's GLR of  $200/10 = 20$  Mscf/bbl is above 2800 scf/bbl and is, therefore, considered adequate for plunger lift.

The minimum required casing pressure can be estimated using two rules of thumb. The simple rule of thumb gives

$$p_c = 1.5p_{L_{\max}} = (1.5)(100) = 150 \text{ psi.}$$

To calculate the minimum required casing pressure with the improved rule of thumb, the slug hydrostatic pressure needs to be known. For this case, assuming 10 cycles/day, equivalent to a plunger trip every 2.4 hours, and 10 bbls of liquid, the plunger will lift 1 bbl/cycle. The hydrostatic pressure of 1 bbl of liquid in 2<sup>3</sup>/<sub>8</sub>-in. tubing with a 0.45-psi/ft liquid gradient is about 120 psi. Then

$$P_c = P_{Lmax} + \frac{P_{sh}}{f_{sl}} = 100 \frac{120}{0.5 \text{ to } 0.6} = 300 \text{ to } 340 \text{ psi.}$$

Since the well has 800 psi of available casing pressure, it meets the pressure requirements for plunger lift.

The Foss and Gaul-type method can be used to determine plunger lift operating range. Basic parameters are given in Table 18.3.

Since the Foss and Gaul-type calculations involve determination of Z-factor values in Eq. (18.28) at different pressures, a spreadsheet program *PlungerLift.xls* was developed to speed up the calculation procedure. The solution is given in Table 18.4.

It was given that the estimated production when unloaded is 200 Mcfd with 10 bbl/day of liquid (GLR = 200/10 = 20 Mscf/bbl), and the maximum casing pressure buildup is 800 psi. From the Table 18.4, find casing pressure of about 800 psi, GLR of 20 Mscf/bbl, and production rates of 10 bbl/day. This occurs at slug sizes between about 0.25 and 3 bbl. The well will operate on plunger lift.

Table 18.3 Summary of Calculated Parameters	
Tubing inner cross-sectional area ( $A_t$ ) =	3.12 in. <sup>2</sup>
Annulus cross-sectional area ( $A_a$ ) =	11.90 in. <sup>2</sup>
Plunger-weight pressure ( $P_p$ ) =	3.20 psi
Slippage factor ( $F_{gs}$ ) =	1.14
Tubing inner capacity ( $L$ ) =	258.80 ft/bbl
The average temperature ( $T_{avg}$ ) =	600°R

Table 18.4 Solution Given by Spreadsheet Program PlungerLift.xls									
$V_{slug}$ (bbl)	$P_{Cmin}$ (psia)	$P_{Cmax}$ (psia)	$P_{Cavg}$ (psia)	Z	$V_l$ (Mcf)	$V_g$ (Mscf)	$N_{Cmax}$ (cycles/day)	$q_{Lmax}$ (bbl/day)	GLR <sub>min</sub> (Mscf/bbl)
0.05	153	193	173	0.9602	0.1516	1.92	88	4.4	38.44
0.1	162	205	184	0.9624	0.1513	2.04	87	8.7	20.39
0.25	192	243	218	0.9744	0.1505	2.37	86	21.6	9.49
0.5	242	306	274	0.9689	0.1491	2.98	85	42.3	5.95
1	342	432	387	0.9499	0.1463	4.20	81	81.3	4.20
2	541	684	613	0.9194	0.1406	6.61	75	150.8	3.31
3	741	936	838	0.8929	0.1350	8.95	70	211.0	2.98
4	940	1187	1064	0.8666	0.1294	11.21	66	263.6	2.80
5	1140	1439	1290	0.8457	0.1238	13.32	62	309.9	2.66

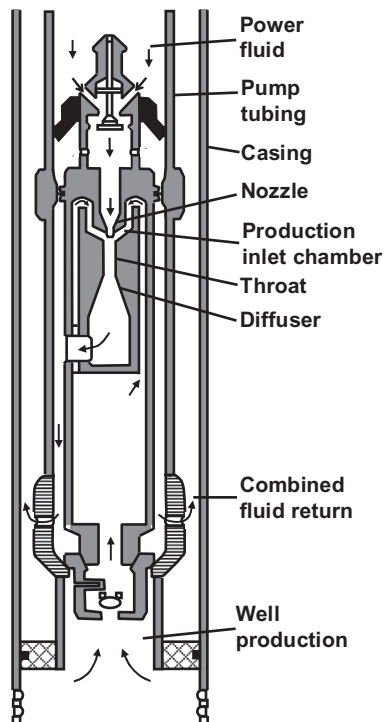


## 18.6 HYDRAULIC JET PUMPING

Fig. 18.10 shows a hydraulic jet pump installation. The pump converts the energy from the injected power fluid (water or oil) to pressure that lifts production fluids. Because there are no moving parts involved, dirty and gassy fluids present no problem to the pump. The jet pumps can be set at any depth as long as the suction pressure is sufficient to prevent pump cavitation problem. The disadvantage of hydraulic jet pumps is their low efficiency (20%–30%).

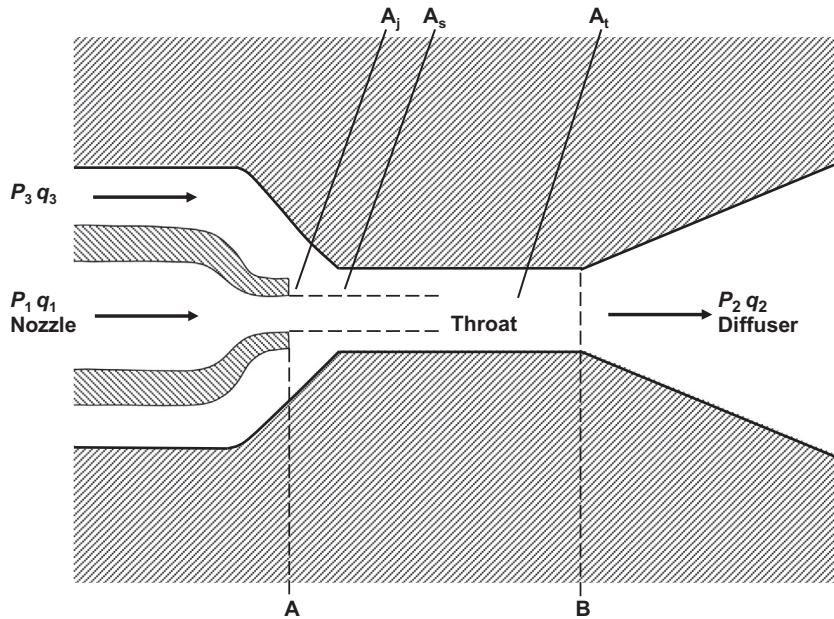
### 18.6.1 WORKING PRINCIPLE

Fig. 18.11 illustrates the working principle of a hydraulic jet pump. It is a dynamic-displacement pump that differs from a HPP in the manner in which it increases the pressure of the pumped fluid with a jet nozzle. The power fluid enters the top of the pump from an injection tubing. The power fluid is then accelerated through the nozzle and mixed with the produced fluid in the throat of the pump. As the fluids mix, the momentum of the power fluid is partially transferred to the produced fluid and increases its kinetic energy (velocity head). Some of the kinetic energy of the mixed



**FIGURE 18.10**

Sketch of a hydraulic jet pump installation.



**FIGURE 18.11**

Working principle of a hydraulic jet pump.

stream is converted to static pressure head in a carefully shaped diffuser section of expanding area. If the static pressure head is greater than the static column head in the annulus, the fluid mixture in the annulus is lifted to the surface.

### 18.6.2 TECHNICAL PARAMETERS

The nomenclatures in Fig. 18.11 are defined as

- $p_1$  = power fluid pressure, psia
- $q_1$  = power fluid rate, bbl/day
- $p_2$  = discharge pressure, psia
- $q_2$  =  $q_1 + q_3$ , total fluid rate in return column, bbl/day
- $p_3$  = intake pressure, psia
- $q_3$  = intake (produced) fluid rate, bbl/day
- $A_j$  = jet nozzle area, in.<sup>2</sup>
- $A_s$  = net throat area, in.<sup>2</sup>
- $A_t$  = total throat area, in.<sup>2</sup>

The following dimensionless variables are also used in jet pump literature (Cholet, 2000):

$$R = \frac{A_j}{A_t} \quad (18.32)$$

$$M = \frac{q_3}{q_1} \quad (18.33)$$

$$H = \frac{P_2 - P_3}{P_1 - P_2} \quad (18.34)$$

$$\eta = MH, \quad (18.35)$$

where

$R$  = dimensionless nozzle area

$M$  = dimensionless flow rate

$H$  = dimensionless head

$\eta$  = pump efficiency.

### 18.6.3 SELECTION OF JET PUMPS

Selection of jet pumps is made on the basis of manufacturer's literatures where pump performance charts are usually available. Fig. 18.12 presents an example chart. It shows the effect of  $M$  on  $H$  and  $\eta$ . For a given jet pump specified by  $R$  value, there exists a peak efficiency  $\eta_p$ . It is good field

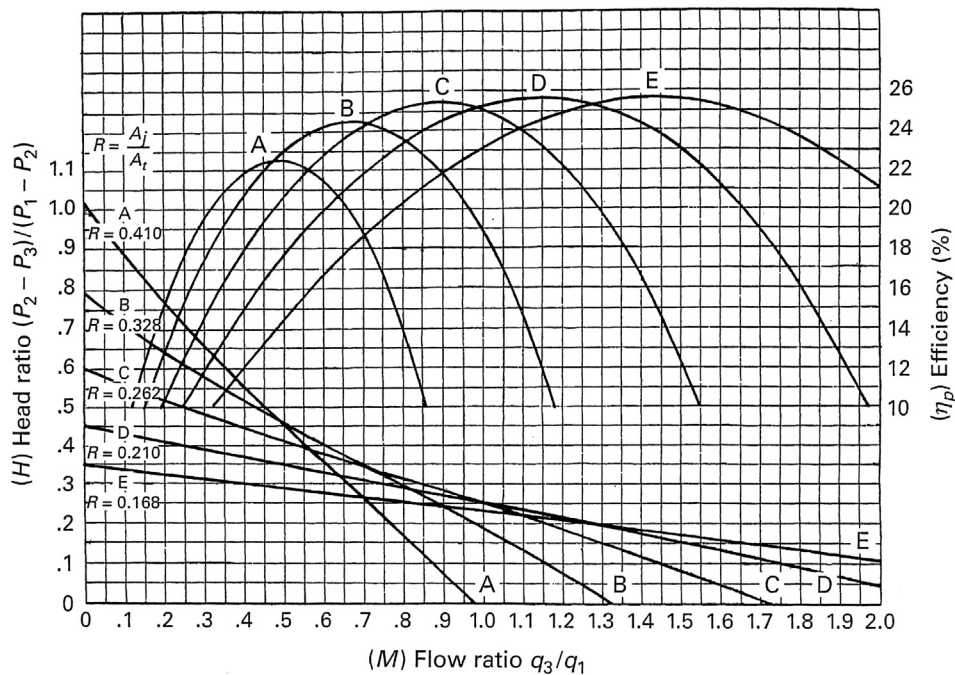


FIGURE 18.12

Example jet pump performance chart.

practice to attempt to operate the pump at its peak efficiency. If  $M_p$  and  $H_p$  are used to denote  $M$  and  $H$  at the peak efficiency, respectively, pump parameters should be designed using

$$M_p = \frac{q_3}{q_1} \quad (18.36)$$

and

$$H_p = \frac{p_2 - p_3}{p_1 - p_2}, \quad (18.37)$$

where  $M_p$  and  $H_p$  values can be determined from the given performance chart. If the  $H$  scale is not provided in the chart,  $H_p$  can be determined by

$$H_p = \frac{\eta_p}{M_p}. \quad (18.38)$$

The power fluid flow rate and pump pressure differential are related through jet nozzle size by

$$q_1 = 1214.5A_j \sqrt{\frac{p_1 - p_3}{\gamma_1}}, \quad (18.39)$$

where  $\gamma_1$  is the specific gravity of the power fluid,  $q_1$  is in bbl/day, and  $p_1$  and  $p_3$  are both in psi.

The following procedure can be taken to select a jet pump:

1. Select a desired production rate of reservoir fluid  $q_3$  based on well IPR. Determine the required bottom-hole pressure  $p_{wf}$ .
2. Design a pump setting depth  $D$  and estimate required pump intake pressure  $p_3$  based on  $p_{wf}$  and flow gradient below the pump.
3. From manufacturer's literature, choose a pump with  $R$  value and determine  $M_p$  and  $H_p$  values for the pump based on pump performance curves.
4. Calculate power fluid rate  $q_1$  by

$$q_1 = \frac{q_3}{M_p}.$$

5. Based on tubing flow performance, calculate the required discharge pressure  $p_{2,r}$  using production rate  $q_2 = q_1 + q_3$ . This step can be performed with the spreadsheet program *HagedornBrownCorrelation.xls*.
6. Determine the power fluid pressure  $p_1$  required to provide power fluid rate  $q_1$  with Eq. (18.39), that is,

$$p_1 = p_3 + \gamma_1 \left( \frac{q_1}{1214.5A_j} \right)^2.$$

7. Determine the available discharge pressure  $p_2$  from the pump with Eq. (18.37), that is,

$$p_2 = \frac{p_3 + H_p p_1}{1 + H_p}.$$

8. If the  $p_2$  value is greater than  $p_{2,r}$  value with a reasonable safety factor, the chosen pump is okay to use, and go to Step 9. Otherwise, go to Step 3 to choose a different pump. If no pump meets the requirements for the desired production rate  $q_3$  and/or lifting pressure  $p_{2,r}$ , go to Step 2 to change pump setting depth or reduce the value of the desired fluid production rate  $q_3$ .

9. Calculate the required surface operating pressure  $p_s$  based on the values of  $p_1$  and  $q_1$  and single-phase flow in tubing.
10. Calculate input power requirement by where

$$HP = 1.7 \times 10^{-5} q_1 p_s,$$

where

$HP$  = required input power, hp

$p_s$  = required surface operating pressure, psia

## 18.7 SUMMARY

This chapter provides a brief introduction to the principles of ESP, hydraulic piston pumping, hydraulic jet pumping, progressive cavity pumping, and plunger lift systems. Design guidelines are also presented. Example calculations are illustrated with spreadsheet programs.

## REFERENCES

- Abercrombie, B., 1980. Plunger lift. In: Brown, K.E. (Ed.), *The Technology of Artificial Lift Methods*, vol. 2b. PennWell Publishing Co, Tulsa, OK, pp. 483–518.
- Beeson, C.M., Knox, D.G., Stoddard, J.H., 1955. Plunger lift correlation equations and nomographs. In: Presented at AIME Petroleum Branch Annual meeting, 2–5 October 1955, New Orleans, LA. Paper 501-G.
- Cholet, H., 2000. *Well Production Practical Handbook*. Editions TECHNIP, Paris.
- Foss, D.L., Gaul, R.B., 1965. Plunger lift performance criteria with operating experience: Ventura Avenue field. In: *Drilling Production Practices API*, 1 January, New York, pp. 124–140.
- Guo, B., Ghalambor, A., 2002. *Gas Volume Requirements for Underbalanced Drilling Deviated Holes*. PennWell Books Tulsa, OK.
- Guo, B., Ghalambor, A., 2005. *Natural Gas Engineering Handbook*. Gulf Publishing Co, Houston, TX.
- Lea, J.F., 1981. Dynamic analysis of plunger lift operations. In: Presented at the 56th Annual Fall Technical Conference and Exhibition, 5–7 October 1981, San Antonio, TX. Paper SPE 10253.
- Lea, J.F., 1999. Plunger lift vs velocity strings. In: *Energy Sources Technology Conference & Exhibition (ETCE '99)*, 1–2 February 1999, Houston Sheraton Astrodome Hotel in Houston, TX.
- Lebeaux, J.M., Sudduth, L.F., 1955. Theoretical and practical aspects of free piston operation. *JPT* 07 (9), 33–35.
- Listiak, S.D., 2006. Plunger lift. In: Lake, L. (Ed.), *Petroleum Engineering Handbook*. Society of Petroleum Engineers, Dallas, TX.
- Mower, L.N., Lea, J.F., Beauregard, E., Ferguson, P.L., 1985. Defining the characteristics and performance of gas-lift plungers. In: Presented at the SPE Annual Technical Conference and Exhibition held in 22–26 September 1985, Las Vegas, NV. SPE Paper 14344.
- Rosina, L., 1983. *A Study of Plunger Lift Dynamics [Masters Thesis]*. University of Tulsa, Tulsa, OK.
- Turner, R.G., Hubbard, M.G., Dukler, A.E., 1969. Analysis and prediction of minimum flow rate for the continuous removal of liquids from gas wells. *J. Petroleum Technol* 21, 1475–1482.

---

**PROBLEMS**

- 18.1.** A 9000-ft-deep well produces 26°API oil with GOR 50 scf/stb and zero water cut through a 3-in. (2.992-in. ID) tubing in a 7-in. casing. The oil has a formation volume factor of 1.20 and average viscosity of 8 cp. Gas-specific gravity is 0.75. The surface and bottom-hole temperatures are 70 and 160°F, respectively. The IPR of the well can be described by Vogel's model with a reservoir pressure 4050 psia and AOF 12,000 stb/day. If the well is put in production with an ESP to produce liquid at 7000 stb/day against a flowing well head pressure of 150 psia, determine the required specifications for an ESP for this application. Assume the minimum pump suction pressure is 220 psia.
- 18.2.** A 9000-ft-deep well has a potential to produce 35°API oil with GOR 120 scf/stb and 10% water cut through a 2-in. (1.995-in. ID) tubing in a 7-in. casing with a pump installation. The oil has a formation volume factor of 1.25 and average viscosity of 5 cp. Gas- and water-specific gravities are 0.75 and 1.05, respectively. The surface and bottom-hole temperatures are 70 and 170°F, respectively. The IPR of the well can be described by Vogel's model with a reservoir pressure 2000 psia and AOF 400 stb/day. If the well is to put in production with a HPP at depth of 8500 ft in an open power fluid system to produce liquid at 210 stb/day against a flowing well head pressure of 65 psia, determine the required specifications for the HPP for this application. Assume the overall efficiencies of the engine, HHP, and surface pump to be 0.90, 0.80, and 0.85, respectively.
- 18.3.** Calculate required GLR, casing pressure, and plunger lift operating range for the following given well data:

Gas rate:	250 Mcfd expected when unloaded
Liquid rate:	12 bbl/day expected when unloaded
Liquid gradient:	0.40 psi/ft
Tubing, ID:	1.995 in.
Tubing, OD:	2.375 in.
Casing, ID:	4.56 in.
Depth to plunger:	7000 ft
Line pressure:	120 psi
Available casing pressure:	850 psi
Reservoir pressure:	1250 psi
Average Z-factor:	0.99
Average temperature:	150°F
Plunger weight:	10 lb
Plunger fall in gas:	750 fpm
Plunger fall in liquid:	150 fpm
Plunger rise velocity:	1000 fpm

# PIPELINE FLOW ASSURANCE



*The most severe operational hazards of pipelines are the risks associated with the transportation of multiphase fluids. When water, oil, and gas are flowing simultaneously inside the pipeline, there are quite a few potential problems that can occur: Water and hydrocarbon fluids can form hydrate and block the pipeline; Wax and asphaltene can deposit on the wall and may eventually block the pipeline; With high enough water cut, corrosion may occur; With the pressure and temperature changes along the pipeline and/or with incompatible water mixing, scales may form and deposit inside the pipeline and restrict the flow; And severe slugging may form inside the pipeline and cause operational problems to downstream processing facilities. The challenge that engineers will face is thus how to design the pipeline and transmission system to assure the multiphase fluids will be safely and economically transported from the bottom of the wells all the way to the downstream*

*processing plant. The practice of identifying, quantifying, and mitigating all of the flow risks associated with offshore pipelines and subsea systems is called flow assurance. The following four chapters are included in this part of the book:*

Chapter 19: Pipeline Precommissioning and Testing 19/639

Chapter 20: Gas Hydrate Control 20/649

Chapter 21: Other Flow Assurance Issues 21/663

Chapter 22: Pipeline Pigging 22/701



# PIPELINE PRECOMMISSIONING AND TESTING

# 19

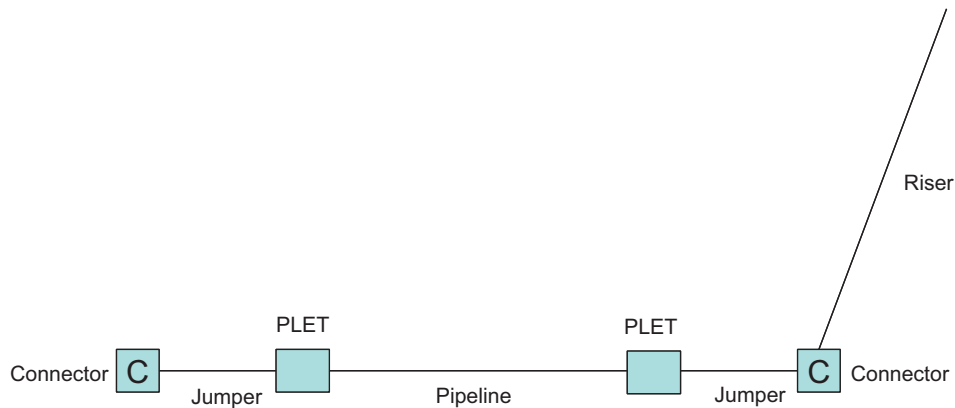
## 19.1 INTRODUCTION

From its fabrication to startup, a pipeline system has to pass a series of tests. Some of the tests, such as the Factory Acceptance Test (FAT), are done onshore on the fabrication yards and are done with individual components. The FAT mainly consists of the inspection, testing, and reporting of the system according to the drawings, specifications, and requirements of the contract. Pipe sections have to pass the FAT before they are accepted. Some of the tests, such as pipeline hydrotest, are mainly done offshore and are done with either a portion of the whole pipeline system or the whole pipeline system. The hydrotests are conducted to check the mechanical strength of the pipeline system and the integrity of the connections. The pipeline hydrotest is one of the pipeline precommissioning activities. Precommissioning is performed after the pipeline system is installed and all the tie-ins are completed to assess the global integrity, qualify the system as ready for commissioning and startup, confirm the safety to personnel and environment, and confirm the operational control of the pipeline system.

Subsea pipeline systems typically consist of pipeline and riser. A jumper is usually used to connect the pipeline and the riser, as shown in Fig. 19.1. Pipeline jumper is a short section of pipe which can be either rigid or flexible. The jumper is tied with the riser and the pipeline with connectors and PLET (Pipe Line End Termination). The PLET is used to support a pipeline connector and/or a pipeline valve. At the subsea end, the pipeline is tied to a manifold or a well through a jumper which is installed between one connector at the PLET and one connector on the manifold or on the tree, as shown in Fig. 19.1.

When the subsea pipeline system is installed, because of the various connections along the pipeline system, it is necessary to make sure the pipe sections are leak proof and have the required mechanical strength to withstand the designed pressure with the specified level of safety. Pipeline may get damaged during the transportation and installation process and its mechanical strength may thus be reduced. The various connections along the pipeline system may not be tied-in properly and leaks may occur under high-pressure conditions. All of the above mentioned potential problems have to be detected by performing pressure testing, and corrected properly before the pipeline is put in service, to prevent any operational accidents (environmental and safety impacts) from happening (Guo et al., 2004).

Before the pipeline system can be used, it also has to be cleaned and gauged. During the fabrication and installation, debris may be left inside the pipeline. If the debris is not removed, they can plug and damage valves and chokes. Pipeline internal dimensions and internal integrity also need to be checked for proper operations. For example, the pipeline has to be checked to make sure that no deformations have occurred during the installation and no internal restrictions exist. Otherwise, operational pigs may not pass the deformed pipe sections.

**FIGURE 19.1**

Schematic of a typical subsea pipeline system (Guo et al., 2004).

This chapter will cover the main activities associated with subsea pipeline testing and precommissioning.

## 19.2 PIPELINE FLOODING, CLEANING, AND GAUGING OPERATIONS

The pipeline precommissioning consists of the following activities:

- Flooding
- Cleaning and gauging
- Hydrotesting
- Leak tests

After the pipeline is laid, it will have to be verified that the pipeline is internally clean and free from restrictions or debris, and will withstand its design pressure. This verification process generally involves flooding the line with treated fluids and sending a cleaning pig down the line to clear out any accumulated debris followed by a gauging pig to prove it is of full bore over the entire length. The cleaning and gauging can be carried out with a single pig. Thus, the main objectives of the flooding, cleaning, and gauging operation are to:

- Fill the pipeline with a suitable pressure testing medium
- Verify the cleanliness of the pipeline
- Verify the pipeline integrity by gauging to make sure no buckles or obstructions exist.

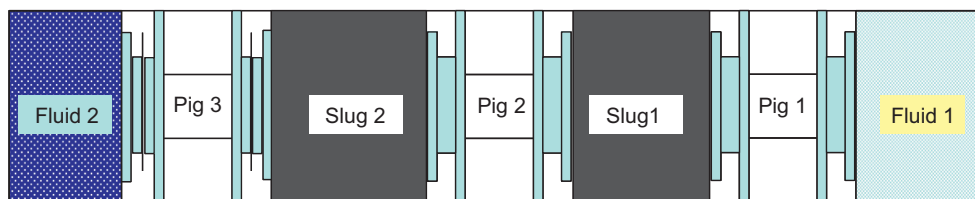
The pipeline should be filled with clean filtered water. The suspended material in the water should be removed by a filter that is capable of removing all particles larger than a specified size (50–100 microns). A meter with sufficient accuracy should be used to measure the quantity of water injected into each pipe section. Knowing the quantity of water injected is critical for leak detection. Chemicals, like biocide, are usually injected into the test water with a certain

concentration, which will depend upon the test conditions. If the test water will stay in the pipeline for a relatively long time, corrosion inhibitor will also need to be injected into the pipeline to protect the pipeline from excessive corrosion. All the chemicals injected have to be compatible with the water so no solids will form inside the line (Guo et al., 2004).

While filling the pipeline, a series of pigs (pig train), which are separated by slug of fluids, shall be passed through the pipeline at a specified minimum velocity. The pig train consists of cleaning pigs and gauging pigs. The best choices for cleaning pigs are pigs with discs, conical cups, spring-mounted brushes, and bypass ports. Discs are effective at pushing out solids while also providing good support for the pig. Conical cups provide excellent sealing characteristics and long wear. Spring mounted brushes provide continuous forceful scraping for removal of rust and other build-ups on the pipe wall. Bypass ports allow some of the flow to bypass through the pig and helps minimize solids build-up in front of the pig. The pig should also include a magnetic cleaning assembly to clean any metal debris. Some application may use a bidirectional disc pig when the water used to fill the line has to be pushed back to its source after completion of the test. Bidirectional pigs may be used if there is a fear of the pig getting stuck and there is an option to reverse flow and bring the pig back to the launch point.

Gauging pigs are used to determine if there are unacceptable reductions/obstructions in a line. These reductions can be caused by ovality due to overburden, by dents, and by buckles. A conventional gauging pig is a cup type pig with a slotted aluminum gauging plate. The slotted aluminum plate will bend out of the way when it encounters an excessive reduction. If the pig comes out with a damaged plate, it is usually run again, and if the plate is damaged again, it is assumed there is an unacceptable reduction in the line. The restriction shall need to be located and removed. After removing the restriction, the gauging pigs should be run again to verify that the repairs are done properly and the line is indeed free of obstructions (Guo et al., 2004).

A typical pipeline flooding, cleaning, and gauging pig train is shown in Fig. 19.2. Two cleaning pigs and one gauging pig are shown. Depending upon the individual cases, more cleaning and gauging pigs can be used. For hydrotesting and precommissioning the Yacheng pipeline, four cleaning pigs and two gauging pigs were used (Karklis et al., 1996).



Pig 1: Cleaning pig  
Pig 2: Cleaning pig  
Pig 3: Gauging pig

Fluid 1: Filtered sea water  
Fluid 2: Chemically treated, filtered seawater  
Slug 1: Chemically treated seawater  
Slug 2: Chemically treated seawater

**FIGURE 19.2**

Typical flooding, cleaning, and gauging pig train (Guo et al., 2004).

There are two key issues associated with the flooding, cleaning, and gauging operations. One is the control of the pig train velocity at the downhill section. The other is the cleanliness of the pipeline. For the pig train, there are recommended traveling velocity by the manufacturers, normally 3–6 miles per hour. But at the downhill sections, due to the gravity effect, the pig train will travel at higher than recommended velocity. To help control the velocity, if the pipeline is not very long, it is possible to pressurize the whole pipeline with air. But if the pipeline is too long, this option can be quite expensive. The biggest concern of the flooding, cleaning, and gauging operations is that the pig train may get stuck because of the debris. To mitigate this risk, it is very critical to have stringent controls of the pipe cleanliness at every stage, from pipe manufacture to installation.

---

### 19.3 PIPELINE HYDROTESTING AND LEAK TESTING

The hydrotests are mainly conducted to verify the mechanical strength of pipeline or pipeline sections. The hydrotesting is carried out by pressurizing the system to a specified internal pressure and holding it for a certain period of time to check whether or not there is a pressure drop. If the pressure drops within the hold period, it is assumed that a leak or leaks may exist somewhere in the system. After the holding period is over, the pressure will be released and a complete visual inspection will follow. Standard codes, such as [ASME B31.4](#), [ASME B31.8](#), and [API RP 1110](#), provide guidance on how to perform pressure tests of gas and liquid pipelines.

Before conducting the tests, it is necessary to establish the specifications for the test procedures and equipment. The procedure specifications should include the following ([Guo et al., 2004](#)):

- A description of the pipe sections to be tested (lengths, elevation, tie-ins, etc.)
- Test medium (seawater is used for subsea pipelines)
- Chemicals to be mixed with the test medium (biocide and corrosion inhibitors)
- Mixing process of the chemicals with the test medium including the chemical concentrations
- Test pressures
- Test holding time
- Process of pressurizing
- Description of all testing equipment
- Description of testing instrument
- Monitoring and recording of test pressure
- Procedure for depressurizing and discharge of test medium

The test pressure is recommended to be set at no less than 1.25 times of the internal design pressure for both hydrostatic testing and leak testing. The holding time is recommended to be at least 4 hours for hydrostatic testing and at least 1 hour for leak testing.

A complete description of the test equipment and instrument is very important for the success of the tests. The following is a partial list of the devices needed for the tests ([Guo et al., 2004](#)):

- A high-volume pump that can fill the line at high enough velocity to remove debris and to push the pigs
- A filter that would remove all particles larger than a certain size to ensure the test fluid is clean
- A meter to measure the quantity of water filled

- Injection pumps for chemical injections
- A variable speed, positive displacement pump to pressurize the line. The pump should have a known volume per stroke and should have a stroke counter
- A pressure recorder that would continuously record the test pressure for the whole test period. The pressure measuring equipment should have an accuracy and repeatability of  $\pm 0.1\%$
- A temperature measurement device that is properly calibrated and should continuously measure the fluid temperature. The device should be able to read in increments of no less than  $0.1^{\circ}\text{F}$  ( $0.05^{\circ}\text{C}$ )
- A temperature device to measure the ambient temperature
- Pressure relief valves
- Pig transmitter device or remote pig signaling system

When planning the hydrotesting and leak testing, a few issues have to be taken into account. The tests should be planned so that nowhere in the test segment the pressure level will produce hoop stress near or above the specified minimum yield stress (SMYS). This will require the test pressure shall be determined by taking into full account the effect of the pipeline profile and external conditions. If the test pressure is relatively high because of the high design pressure, the pressure relief valves have to be properly checked and set at the right pressure to protect the pipeline and the involved personnel. When launching a suite of pigs from a test-head launcher and receiving into a similar receiver, there is always concern that not all the launched pigs have been successfully launched or received into the terminal. It is necessary to install a pig transmitter device or some kind of remote pig signaling system on the final pig to confirm the pig launch and reception.

How the test results will be reported and what will be reported should be defined before performing the tests. The test records should include the details of the test operations and details of any failures. The failure report should include the exact location of each failure, the types of failure, the causes for the failure, and the recommended repair methods. When the tests are finished, all waste should be disposed of in the correct manner, which should be defined in company's waste management and disposal policy.

---

## 19.4 PIPELINE DEWATERING, DRYING, AND PURGING

For offshore gas transmission pipelines, after a successful hydrotesting and leak testing and before introducing gas, the pipelines have to be dewatered, dried, and purged. For offshore liquid pipeline, the water is usually displaced by diesel or dead oil and it is not necessary to dry the pipeline. The process of dewatering, drying, and purging can be quite complicated depending upon the application. This is because after the tests, the pipeline is full of seawater and the water has to be sufficiently displaced from the pipeline. Otherwise hydrate may form inside the pipeline when the hydrocarbon is introduced. Another reason for displacing the water is that many products react with water to form acids and other corrosive compounds which would corrode the pipeline. This is especially true if the gases contain carbon dioxide. Thus, displacing the water from the pipeline, which is also called dewatering, is a necessary step for pipeline precommissioning. If the pipeline is very short, it may be economical to just inject enough methanol or glycol to treat the water to mitigate hydrate without the need for displacing the water (Guo et al., 2004).

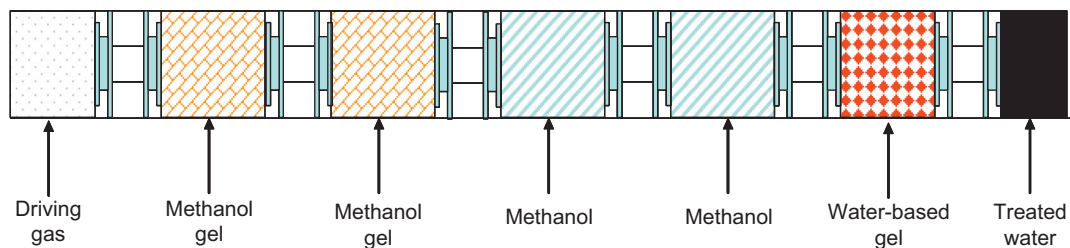
The primary function of a dewatering pig train is to displace water efficiently, leaving behind a minimum quantity of fluids for subsequent drying. A typical dewatering system involves a displacement fluid supply, a dewatering pig train, and a valve for water flowrate control. For relatively short pipelines, the pig train may consist of a small number of mechanical pigs which can be driven with nitrogen or air. Sometimes produced gas may be used to push the pig train. Nitrogen is also used for dewatering the stainless steel pipelines. For long pipelines, a typical dewatering pig train may include a number of pigs and fluid slugs. The fluid slugs serve different functions, like providing lubrication of the pig seals and preventing forward slippage of the driving gas. The speed of the pig train is controlled by adjusting the water flowrate at the outlet while the pressure is controlled at the inlet by the gas. A typical dewatering pig train is shown in Fig. 19.3.

The dewatering train for the Zeepipe system (Falk et al., 1994) consisted of 10 mechanical pigs which were separated by slugs of various liquids. Two slugs of water-based gel were at the front of the train. The purpose of the gel slugs was to lubricate the first pigs to decrease wear. Behind the gel slugs were four batches of methanol which were used to coat the pipe wall to inhibit the water that was left behind. Three batches of methanol gel were at the rear of the train to prevent gas bypassing forward into the train due to imperfect sealing.

The performance of the gel slugs in the pig train will impact the efficiency of the dewatering operation. There are a couple of gel systems available (Schreure et al. 1994). One is the water-based gel systems which is a mixture of polymers and crosslinkers. The other is methanol or hydrocarbon gel systems. The gel slugs should satisfy the following functions requirements (Schreure et al. 1994):

- The gel slugs should minimize fluid bypass across pig seals. The slugs should prevent water from backward bypassing and prevent gas from forward bypassing
- The fluids in the gel slugs should be compatible with the pigs and the pipeline materials
- Gels should be strong enough to sustain any shearing and dilution, thereby preserving their rheological properties through the whole operations
- Gels should be chemically stable at the operating conditions for the whole operations which can last for weeks.

After dewatering operations, the pipeline may still have enough water that may cause problems during startup and drying operation is required to further remove the residual amount of water in



**FIGURE 19.3**

Typical dewatering pig train (Guo et al., 2004).

the pipeline. Of course, if the pipeline is going to transport water-wet gas, there is no need to dry the pipeline. If the pipeline is stainless steel, the dewatering operations are normally carried out with nitrogen and thus, no need to dry the pipeline.

There are two common methods for drying pipeline: air drying and vacuum drying. Air drying techniques have extensively been discussed in literature. The main advantages of air drying are:

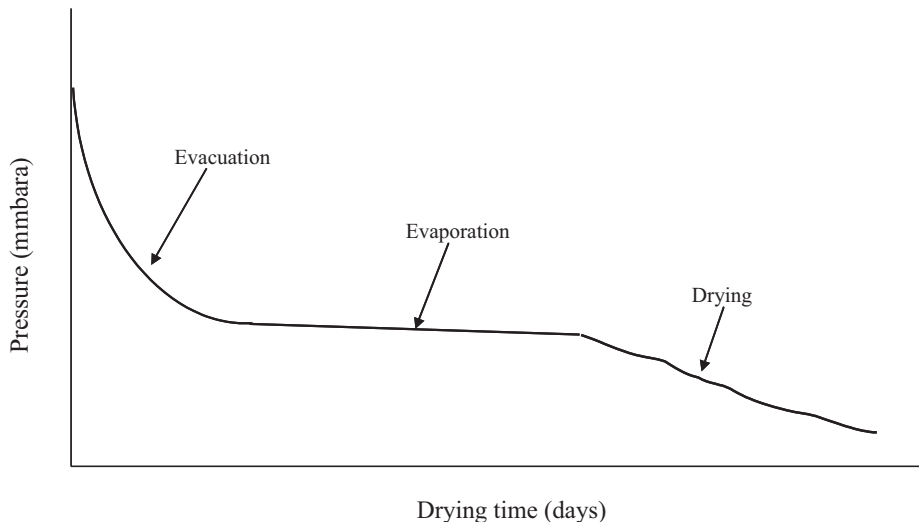
- All free water can be removed from the pipeline
- Very low dew points can be achieved down to as low as  $-90^{\circ}\text{F}$
- The drying process is relatively short

Unfortunately, the air drying techniques are not well suited for offshore pipelines because it requires a large area for equipments.

Vacuum drying is based upon the fact that the water will boil at low temperatures if the pipeline pressure is reduced down to the saturated vapor pressure for the ambient temperature. Thus, by reducing the system pressure, it is possible to cause the water to boil and be removed from the pipeline as a gas with a vacuum pump. A typical vacuum drying pressure curve is shown in Fig. 19.4.

The vacuum drying process can be divided into three stages. The first stage is the evacuation phase in which the pipeline pressure is drawn down from atmospheric to the saturated vapor pressure by removing the air from the pipeline. The saturated vapor pressure is a function of the pipeline temperature. This phase is also called drawdown phase.

As the pressure approaches the saturated vapor pressure, water starts to evaporate and the pressure is more or less maintained as a constant. As the pressure tries to fall, more water evaporates and as such the pressure stays constant. This vapor is sucked out of the pipeline by the vacuum pump. This process continues until all the free water in the pipeline has evaporated. This phase is also called boiling phase.



**FIGURE 19.4**

Typical vacuum drying pressure plot (Guo et al., 2004).

When all the free water in the pipeline has evaporated, the pressure in the pipeline will start to fall as there is no more water to evaporate and maintain the equilibrium. All the air in the pipeline has been evacuated and the pipeline pressure can be directly correlated to the dew point. This phase is called final drying phase.

Water evaporation requires heat input. In subsea pipeline, the heat has to come from the surrounding water. If the pipeline is insulated, the heat transfer process from the surrounding water to the pipeline can be quite slow. Thus, the vacuum pump has to be properly sized so that the water will not be forced to evaporate faster than the pipeline can absorb the heat of evaporation from the surroundings. Otherwise, ice can form inside the pipeline.

The main advantages of the vacuum drying method are (Guo et al., 2004):

- All free water can be removed from the pipeline
- Very low dew points can be achieved
- No large space is needed for equipments
- No significant amount of waste will be produced

The main disadvantages of vacuum drying are that the drying process can be quite long and the method is not suitable for very long or small bore pipelines.

After drying and before gas-up, the pipeline may need to be purged using nitrogen for the following reasons:

- To further verify the line dryness
- To provide a barrier before the introduction of hydrocarbons

Even though hydrocarbon can be directly introduced after vacuum drying without the risk of achieving an explosive mixture, the nitrogen purging operations provide an extra safety margin. After the precommissioning, the pipeline is ready for commissioning and startup.

---

## 19.5 SUMMARY

This chapter outlines major procedures of pipeline precommissioning and testing, including pipeline flooding, cleaning, gauging operations, pipeline hydrotesting, leak testing, pipeline dewatering, drying, and purging. More details are given in references Guo et al. (2004) and Guo et al. (2013).

---

## REFERENCES

- API RP 1110, 1997. *Pressure Testing of Liquid Petroleum Pipelines*. forth ed American Petroleum Institute, Washington, DC.
- ASME B31.4, *Liquid Transportation System for Hydrocarbons, Liquid Petroleum Gas, Anhydrous Ammonia, and Alcohols*, 1989 Edition.
- ASME B31.8, *Gas Transmission and Distribution Piping Systems*, 1992 Edition.
- Falk, C., Maribu, J., Eide, L.O., 1994. "Commissioning the zeepipe system sets new standards". *Pipeline & Gas J.* 221 (8), 24–33.
- Guo, B., Song, S., Chacko, J., Ghalambor, A., 2004. *Offshore Pipelines*. Elsevier, Oxford.



Guo, B., Song, S., Ghalambor, A., Lin, T., 2013. *Offshore Pipelines*. second ed. Elsevier, Oxford.

Karklis, P., et al., 1995—The year of the Pig: hydrotesting and precommissioning the Yacheng pipeline. In: Proceedings of the 1996 Pipeline Pigging Conference, Jakarta, Indonesia, 1996.

Schreure, G., Burman, P., Hamid, S., Falck, C., Maribu, J., Ashwell, C., Development of gel system for pipeline dewatering and drying applications. In: Presented at the 26th annual OTC in Houston, TX, 1994.

---

## PROBLEMS

- 19.1. What activities does a pipeline precommissioning consist of?
- 19.2. What components does a typical flooding, cleaning, and gauging pig train include?
- 19.3. What is the primary function of a dewatering pig train? What does a typical dewatering system involve?

## GAS HYDRATE CONTROL

## 20

**20.1 INTRODUCTION**

Formation of gas hydrates in offshore pipelines presents a threat to the transportation of oil and gas in the subsea environment. This chapter describes hydrate forming conditions and methods employed in the petroleum industry to effectively mitigate gas hydrate problems in offshore pipeline operations. These methods include chemical inhibition, thermal insulation, heating, and system depressurization.

**20.2 HYDRATE FORMING CONDITION**

Gas hydrates are solid crystalline compounds formed by the chemical combination of natural gas and water under pressure at temperatures considerably higher than the freezing point of water. In the presence of free water, hydrates form when the temperature is below a certain degree (hydrate temperature). The hydrate temperature would be less than or equal to the dew point temperature of the hydrate forming gas. The chemical formulas of some natural gas hydrates are:

Methane hydrates:	$\text{CH}_4 \cdot 7\text{H}_2\text{O}$
Ethane hydrates:	$\text{C}_2\text{H}_6 \cdot 8\text{H}_2\text{O}$
Propane hydrates:	$\text{C}_3\text{H}_8 \cdot 18\text{H}_2\text{O}$
$\text{CO}_2$ hydrates:	$\text{CO}_2 \cdot 7\text{H}_2\text{O}$

During the flow of natural gas, it becomes necessary to define, and thereby avoid, conditions that promote the formation of hydrates. This is essential because hydrates may choke the flow string, surface lines, and other equipment, resulting in lower flow rates of gas. The conditions that tend to promote the formation of natural gas hydrates are:

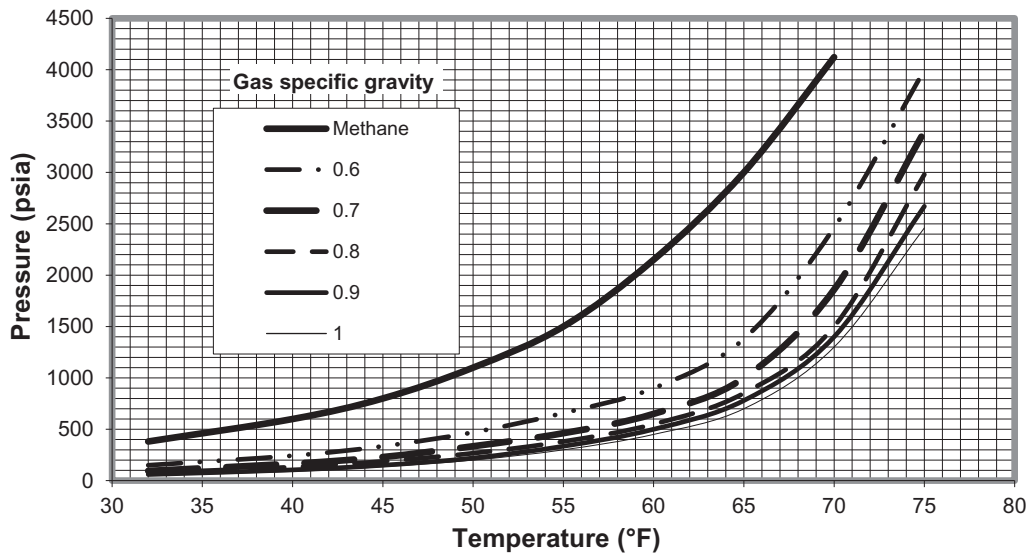
- Presence of liquid water
- Low-temperature
- High-pressure
- High velocity or agitation
- Presence of “seed” crystals of hydrate
- Presence of highly soluble gas in water, such as  $\text{H}_2\text{S}$  or  $\text{CO}_2$

It is convenient to divide hydrate formation into two categories: (1) hydrate formation due to a decrease in temperature with no sudden pressure drop, such as in the flow string or pipelines, and (2) hydrate formation where a sudden expansions occurs, such as in the flow provers, orifices,

back-pressure regulators, or chokes. For problems in category (1), Table 20.1 and Fig. 20.1 give approximate values of the hydrate temperature as a function of pressure and specific gravity. Hydrates will form whenever temperature and pressure plot to the left of the hydrate formation line for the gas in question. The problems in category (2) do not occur often in offshore pipeline operations and thus are not addressed in this chapter.

Temperature °F	Gas-Specific Gravity (air = 1)					
	Methane	0.6	0.7	0.8	0.9	1
32	381	150	95	76	60	50
40	600	243	165	132	105	90
45	800	335	230	188	150	136
50	1100	470	335	267	220	200
55	1500	658	462	381	335	300
60	2150	900	650	550	500	450
65	3000	1380	1000	851	780	700
70	4122	2463	1860	1500	1400	1300
75		4000	3400	2980	2670	2460

*Courtesy of SPE-AIME.*



**FIGURE 20.1**

Hydrate forming conditions of natural gases.

*Courtesy of SPE-AIME.*

Keeping in mind that the presence of  $\text{H}_2\text{S}$  and  $\text{CO}_2$  will increase the hydrate temperature and reduce the pressure above which hydrates will form. In other words, the presence of  $\text{H}_2\text{S}$  and  $\text{CO}_2$  increases the possibility of hydrate formation. A rigorous technique for predicting conditions for hydrate formation involves the use of vapor/solid equilibrium constants such as that given by Katz (1945). The calculations are analogous to a dew point calculation for multicomponent mixtures. This method of hydrate prediction has proved to be rather reliable. A number of computer packages are available in the industry for prediction of hydrate forming conditions.

## 20.3 HYDRATE PREVENTION AND MITIGATION

Several methods have been employed in the petroleum industry to effectively mitigate gas hydrate problems in offshore pipeline operations. These methods include water removal, chemical inhibition, heating by electricity or hot oil circulation, and system depressurization.

### 20.3.1 WATER REMOVAL

The most effective way to mitigate hydrate is to get rid of water. If there is no liquid water in the pipeline, there will be no hydrate risk. But getting rid of water completely may not be the most practical or most economical way. Some other methods such as chemical inhibition have to be utilized. However, reducing water content in the pipeline can significantly cut down the usage of chemical inhibitors. This method is widely used for preventing hydrates in natural gas pipelines.

Solubility of water in natural gas is called water content of natural gas. It increases with temperature and decreases with pressure. Water content data for a typical natural gas are presented in Table 20.2 and Fig. 20.2. Salt's presence in the liquid water reduces the water content of the gas. Water content of untreated natural gases is normally in the magnitude of a few hundred pounds of water per million standard cubic foot of gas ( $\text{lb}_m/\text{MMscf}$ ); while gas pipelines normally require water content to be in the range of 6–8  $\text{lb}_m/\text{MMscf}$  and even lower for pipelines in deepwater.

The water content of natural gas is indirectly indicated by the dew point defined as the temperature at which the natural gas is saturated with water vapor at a given pressure. At the dew point, natural gas is in equilibrium with liquid water; any decrease in temperature or increase in pressure will cause the water vapor to begin condensing. The difference between the dew point temperature of a water-saturated gas stream and the same stream after it has been dehydrated is called dew point depression.

**Example Problem 20.1** Estimate water content of a natural gas at a pressure of 3000 psia and temperature of 150°F.

**Solution:**

The chart in Fig. 20.2 gives water contents of:

$$C_{w140\text{ F}} = 84 \text{ lb}_m/\text{MMcf}$$

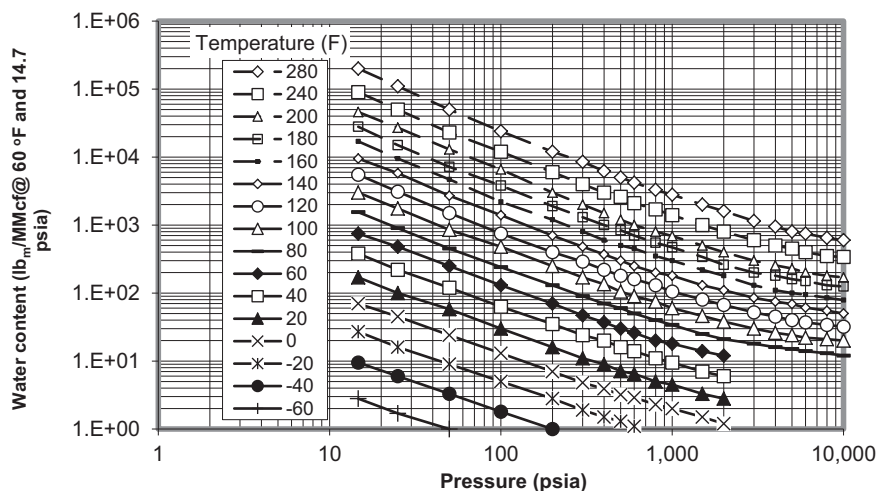
$$C_{w160\text{ F}} = 130 \text{ lb}_m/\text{MMcf}.$$

Linear interpolation yields:

$$C_{w150\text{ F}} = 107 \text{ lb}_m/\text{MMcf}.$$

**Table 20.2 Water Content of Typical Natural Gas (lb<sub>m</sub> H<sub>2</sub>O/MMcf @60°F, 14.7 psia)**

<i>p</i>	<i>t</i> (°F)															
(psia)	-60	-40	-20	0	20	40	60	80	100	120	140	160	180	200	240	280
15	3	10	27	70	170	380	750	1550	3000	5500	9500	17,000	28,000	46,000	90,000	200,000
25	2	6	16	45	100	220	480	900	1750	3100	5800	9500	15,000	27,000	50,000	110,000
50	1	3	9	24	58	120	250	450	850	1500	2700	4700	7200	13,000	23,000	50,000
100		2	5	13	30	63	130	240	480	750	1400	2200	3800	6600	12,000	24,000
200		1	3	7	16	35	70	130	250	400	700	1200	1900	3000	6000	12,000
300			2	5	11	24	47	90	170	290	480	800	1300	2000	4000	8500
400			2	4	9	20	37	70	135	220	370	600	1000	1500	3000	6200
500			1	3	7	16	30	60	105	180	300	500	840	1200	2600	5000
600			1	3	7	14	26	50	90	160	250	450	700	1000	2100	4200
800				2	5	11	20	40	75	130	200	350	550	800	1700	3300
1000				2	5	10	18	34	60	105	180	300	470	690	1400	2800
1500				2	3	7	14	25	46	80	130	220	340	500	1000	2000
2000				1	3	6	12	21	38	67	110	180	260	400	800	1600
3000								18	30	52	85	130	200	300	600	1150
4000								16	26	45	75	110	180	255	500	950
5000								15	24	40	69	100	160	230	450	800
6000								14	22	37	61	95	150	200	400	750
8000								13	21	34	55	85	130	180	350	650
10,000								12	20	32	50	79	125	170	340	600



**FIGURE 20.2**

Water content of natural gases (Guo and Ghaleb, 2005).

Dehydration systems used in the natural gas industry fall into four categories in principle: (1) direct cooling, (2) compression followed by cooling, (3) absorption, and (4) adsorption. Dehydration in the first two methods does not result in sufficiently low water contents to permit injection into a pipeline for hydrate control. Further dehydration by absorption or adsorption is often required.

The ability of natural gas to contain water vapor decreases as the temperature is lowered at constant pressure. During the cooling process, the excess water in the vapor state becomes liquid and is removed from the system. Natural gas containing less water vapor at low-temperature is output from the cooling unit. The gas dehydrated by cooling is still at its water dew point unless the temperature is raised again or the pressure is decreased. Cooling for the purpose of gas dehydration is sometimes economical if the gas temperature is unusually high. It is often a good practice that cooling is used in conjunction with other dehydration processes.

Gas compressors can be used partially as dehydrators. Because the saturation water content of gases decreases at higher pressure, some water is condensed and removed from gas at compressor stations by the compressor discharge coolers. Modern lean oil absorption gas plants use mechanical refrigeration to chill the inlet gas stream. Ethylene glycol (EG) is usually injected into the gas chilling section of the plant, which simultaneously dehydrates the gas and recovers liquid hydrocarbons, in a manner similar to the low-temperature separators.

Absorption is a process where water vapor is removed from natural gas by bubbling the gas counter-currently through certain liquids that have a special attraction or affinity for water. Water vapor in the gas bubbles is entrained in the liquid and carried away by the liquid. Adsorption is a process where gas flows through a bed of granular solids that have an affinity for water. The water is retained on the surface of the particles of the solid material. The vessel that allows either the absorption or adsorption process to take place is called the contactor or sorber. The liquid or solid that has affinity for water and is used in the contactor in connection with either of the processes is called the desiccant. Two major types of dehydration equipment in use today are the liquid

desiccant dehydrator and the solid-desiccant dehydrator. Each type of dehydrator has its advantages and disadvantages. These two types of dehydrators practically dehydrate all the natural gas moved through transmission lines.

Adsorption is defined as the ability of a substance to hold gases or liquids on its surface. In adsorption dehydration, the water vapor from the gas is concentrated and held at the surface of the solid-desiccant by forces caused by residual valiancy. Solid desiccants have very large surface areas per unit weight to take advantage of these surface forces. The most common solid adsorbents used today are silica, alumina, and certain silicates known as molecular sieves. Dehydration plants can remove practically all water from natural gas using solid desiccants. Because of their great drying ability, solid desiccants are employed where higher efficiencies are required. The advantages of solid-desiccant dehydration include (Guo and Ghalambor, 2005):

- Lower dew point, essentially dry gas (water content <20.0 lb/MMcf) can be produced.
- Higher contact temperatures can be tolerated with some adsorbents.
- Higher tolerance to sudden load changes, especially on startup.
- Quick start up after a shutdown.
- High adaptability for recovery of certain liquid hydrocarbons in addition to dehydration functions.

Operating problems with the solid-desiccant dehydration include:

- Space adsorbents degenerate with use and require replacement.
- Dehydrating tower must be regenerated and cooled for operation before another tower approaches exhaustion. The maximum allowable time on dehydration gradually shortens because desiccant loses capacity with use.

Although this type of dehydrator has high adaptability to sudden load changes, sudden pressure surges should be avoided because they may upset the desiccant bed and channel the gas stream resulting in poor dehydration. If a plant is operated above its rated capacity, high-pressure loss may cause some attrition to occur. Attrition causes fines, which may in turn cause excessive pressure loss and result in loss of capacity. Replacing the desiccant should be scheduled and completed ahead of the operating season. To maintain continuous operation, this may require discarding the desiccant before its normal operating life is reached. To cut operating costs, the inlet part of the tower can be recharged and the remainder of the desiccant retained because it may still possess some useful life. Additional service life of the desiccant may be obtained if the direction of gas flow is reversed at a time when the tower would normally be recharged.

Water vapor is removed from the gas by intimate contact with a hygroscopic liquid desiccant in absorption dehydration. The contacting is usually achieved in packed or trayed towers. Glycols have been widely used as effective liquid desiccants. Dehydration by absorption with glycol is usually economically more attractive than dehydration by solid-desiccant when both processes are capable of meeting the required dew point.

Glycols used for dehydrating natural gas are EG, diethylene glycol (DEG), triethylene glycol (TEG), and tetraethylene glycol (T<sub>4</sub>EG). Normally a single type of pure glycol is used in a dehydrator. But sometimes a glycol blend is economically attractive. TEG has gained nearly universal acceptance as the most cost effective of the glycols due to its superior dew point depression, operating cost, and operation reliability. TEG has been successfully used to dehydrate sweet and sour natural gases over wide ranges of operating conditions. Dew point depression of 40°F–140°F can

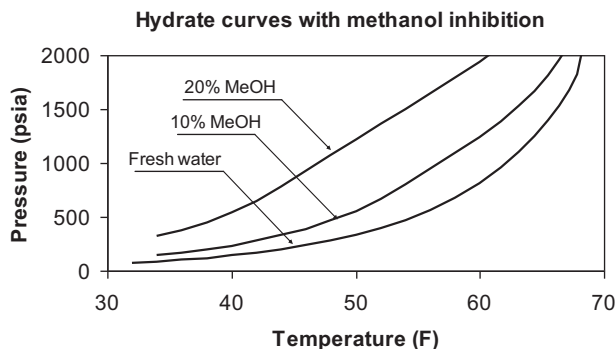
be achieved at a gas pressure ranging from 25 to 2500 psig and gas temperature between 40°F and 160°F. The dew point depression obtained depends on the equilibrium dew point temperature for a given TEG concentration and contact temperature. Increased glycol viscosity may cause problems at lower contact temperature. Thus heating of the natural gas may be desirable. Very hot gas streams are often cooled prior to dehydration to prevent vaporization of TEG.

The feeding-in gas must be cleaned to remove all liquid water and hydrocarbons, wax, sand, drilling muds, and other impurities. These substances can cause severe foaming, flooding, higher glycol losses, poor efficiency, and increased maintenance in the dehydration tower or absorber. These impurities can be removed using an efficient scrubber, separator, or even a filter separator for very contaminated gases. Methanol, injected at the wellhead as hydrate inhibitor, can cause several problems for glycol dehydration plants. It increases the heat requirements of the glycol regeneration system. Slugs of liquid methanol can cause flooding in the absorber. Methanol vapor vented to the atmosphere with the water vapor from the regeneration system is hazardous and should be recovered or vented at nonhazardous concentrations.

### 20.3.2 CHEMICAL INHIBITION

Salt can affect the hydrate formation conditions. By adding more salt into the water, the hydrate formation curve will shift to the left in Fig. 20.1. The impact of salt on hydrate curve can be significant. By adding 2 mole % NaCl into the fresh water, the hydrate formation temperature will be 4–5°F lower. If the salt concentration is increased to 8 mole %, the hydrate formation temperature will be more than 25°F lower. However even though salt solution can be used for hydrate inhibition, too much salt can cause salt deposition and scale deposits in the process facilities. Salt solution is also corrosive and can cause corrosion problems to equipment.

Methanol, EG, and DEG are commonly injected into gas pipelines to depress the freezing point. All of these inhibitors can be recovered and recycled; however, the recovery of methanol is often uneconomical. Hydrate inhibitor injection does not always provide the ultimate degree of dehydration specified by the purchaser or required by the process conditions. Fig. 20.3 shows a typical gas hydrate curve with different amount of methanol inhibition (Guo et al., 2004). It indicates that a significant concentration of methanol is required to inhibit hydrate formation.



**FIGURE 20.3**

Gas hydrate curve with different amount of methanol inhibition.



Methanol injection systems are frequently installed at facilities where low gas volumes prohibit dehydration. They are also temporarily used for situations where hydrate inhibition requires high capital investment equipment before a decision regarding a permanent facility is made. These systems have been utilized in fields where hydrate problems are relatively mild, infrequent, seasonal, or expected during start-up. The EG and DEG are injected primarily at low-temperature processing plants for extracting natural gas liquids. The glycol prevents freezing in these plants during the condensation of water and hydrocarbons. The water phase of the process liquid contains the EG or DEG, which is always recovered and regenerated.

The minimum amount of hydrate inhibitor required can be calculated using [Hammerschmidt's \(1939\)](#) method:

$$W_h = \frac{(MW)_{inh} \Delta t_h}{(MW)_{inh} \Delta t_h + K_H} \times 100 \quad (20.1)$$

where  $W_h$  = weight of pure inhibitor in liquid water phase, %

$(MW)_{inh}$  = molecular weight of inhibitor

$\Delta t_h$  = depression of hydrate formation temperature, °F

$K_H$  = Hammerschmidt constant for inhibitor, 2335 for methanol, 4000 for EG and DEG

If glycol is used as the inhibitor at an operating temperature of below 20°F, the freezing point of the glycol must be considered. It is a common practice to keep the glycol concentrations ( $W_h$ ) between 60 and 80 wt% to avoid “mushy” glycol in the system ([Kohl and Riesenfeld, 1985](#)). If the calculated  $W_h$  value from [Eq. \(20.1\)](#) is less than 60%, the quantity of inhibitor required should be calculated by a material balance:

$$W_G = I_{100} \left( \frac{100}{W_{out}} - \frac{100}{W_{in}} \right) \quad (20.2)$$

or

$$I_{100} = \frac{W_G}{\left( \frac{100}{W_{out}} - \frac{100}{W_{in}} \right)} \quad (20.3)$$

where  $W_G$  = water removed from gas stream, lb<sub>m</sub>/MMscf

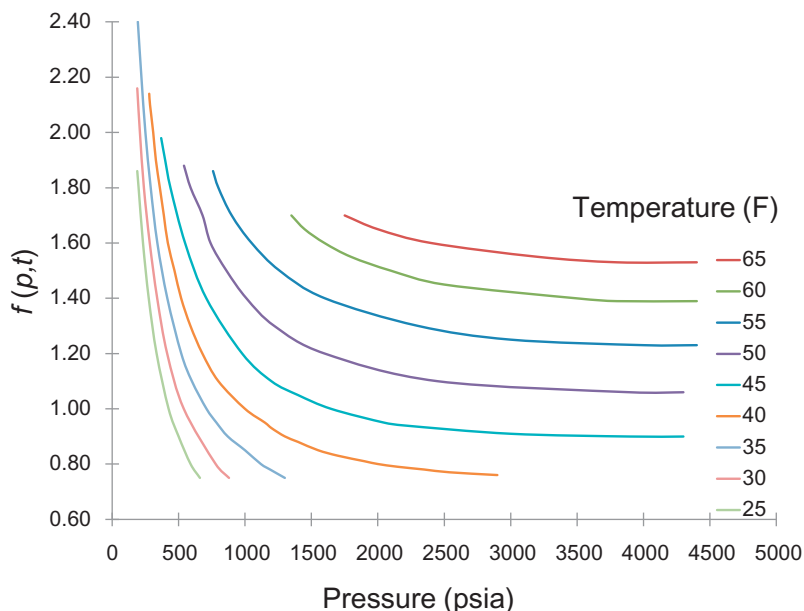
$I_{100}$  = pure inhibitor required, lb<sub>m</sub>/MMscf

$W_{out}$  = concentration of inhibitor in outlet inhibitor stream, wt%

$W_{in}$  = concentration of inhibitor in inlet inhibitor stream, wt%.

Combining [Eqs. \(20.1\) and \(20.3\)](#) to eliminate  $W_{out}$  gives:

$$I_{100} = \frac{W_G}{1 + \frac{K_H}{(MW)_{inh} \Delta t_h} - \frac{100}{W_{in}}} \quad (20.4)$$



**FIGURE 20.4**

Methanol in gas phase as a function of methanol in liquid phase.

If methanol is used as the inhibitor, the vapor-phase inhibitor losses should also be considered. The following correlation has been obtained based on [Jacoby's \(1955\)](#) data:

$$\frac{\text{lb}_m \text{ MeOH/MMscf}}{\text{wt}\% \text{ MeOH in Water}} = f(p, t) \quad (20.5)$$

where  $p$  = pressure, psia

$t$  = temperature, °F

The function can be expressed in [Fig. 20.4](#) or correlation in [Eq. \(20.6\)](#):

$$f(p, t) = a_0 + a_1p + a_2p^2 + a_3p^3 + a_4p^4 + a_5p^5 \quad (20.6)$$

where the correlation coefficients are given in [Table 20.3](#).

**Example Problem 20.2** Ten MMscfd of a 0.7 specific gravity natural gas cools down to 40°F in a buried pipeline. The minimum pipeline pressure is 900 psia. Concentration of commercially available glycol and methanol inhibitors is 75% and 100% by weight, respectively. What volume of inhibitor solution must be added daily if the gas enters line saturated at 90 °F? Consider both DEG and MeOH inhibitors.

**Solution:**

[Fig. 20.1](#) shows that the hydrate temperature at 900 psia is 64°F, which is higher than the working temperature of 40°F. Therefore, the formation of gas hydrates will be likely a problem in the

**Table 20.3 Correlation Coefficients in Eq. (20.6)**

Temperature (F)	$a_0$	$a_1$	$a_2$	$a_3$	$a_4$	$a_5$
25	3.9078	-0.0151	2.00E-05	3.00E-09	-4.00E-11	3.00E-14
30	5.409	-0.03	9.00E-05	-2.00E-07	20.00E-10	-4.00E-14
35	4.8559	-0.0192	4.00E-05	-5.00E-08	3.00E-11	-6.00E-15
40	3.8309	-0.0086	20.00E-05	-6.00E-09	2.00E-12	-2.00E-16
45	3.1025	-0.0041	3.00E-06	-20.00E-09	2.00E-13	-2.00E-17
50	3.3181	-0.004	3.00E-06	-20.00E-09	2.00E-13	-2.00E-17
55	3.5711	-0.0038	3.00E-06	-20.00E-09	2.00E-13	-20.00E-17
60	2.4814	-0.0009	2.00E-07	-2.00E-11	0	0
65	2.3502	-0.0006	20.00E-07	-20.00E-11	0	0

operation. The depression of hydrate temperature is 24°F. Based on Fig. 20.2, the water content of the input gas at 900 psia is 48 lb/MMscf. The water content of the output gas at 900 psia and 40°F is 9.6 lb/MMscf. The water flow (to be removed from gas phase) is therefore 38.4 lb/MMscf.

If the glycol solution is used to absorb water from the gas phase, Eq. (20.1) gives a glycol concentration of 27.11 wt%, which is lower than 60 wt%. Using a design value of 65 wt% glycol concentration at outlet, Eq. (20.3) yields a required dosage of pure glycol of 187.2 lb/MMscf, or a dosage of 75% glycol solution of 249.6 lb/MMscf. This corresponds to 274.89 gal/day of 75% glycol solution for the 10 MMscfd of gas flow rate.

If the methanol is used to as a hydrate inhibitor, Eq. (20.1) gives a methanol concentration of 24.75 wt%, which is lower than 60 wt%. Using a design value of 65 wt% methanol concentration at outlet, Eq. (20.3) yields a required dosage of pure methanol of 12.63 lb/MMscf in the liquid phase. Fig. 2.4 gives  $f(p,t) = 20.05$ . Then Eq. (20.5) yields a methanol concentration in vapor phase of 13.26 lb/MMscf. Therefore, the total required methanol dosage of 25.89 lb/MMscf. This corresponds to 58 gal/day of methanol for the 10 MMscfd of gas flow rate.

The above example shows that high water flow will require large amounts of methanol or monoethylene glycol (MEG) for hydrate inhibition, resulting in high operating expense (OPEX). To mitigate the high dosage problems, more effective hydrate inhibitors than methanol and MEG are needed for high water flow. The inhibition mechanisms of the new chemicals have to be different from the traditional thermodynamic inhibitors to be more effective at low dosage. The chemicals that would effectively inhibit hydrate at low dose rate are called low dosage hydrate inhibitors (LDHI). Two kinds of LDHI are most popular in oil industry: one is kinetic hydrate inhibitor and the other is anti-agglomerant (AA) (Fu, 2002, Mehta et al., 2003, Kelland et al., 1995).

The kinetic hydrate inhibitors tend to slow down the hydrate nucleation process and delay the formation and growth of hydrate crystals for an extended period of time (Fu, 2002). But kinetic inhibitors can only delay the kinetics and cannot completely prevent the nucleation process. Thus, kinetic inhibitors can only prevent hydrate from forming for a finite time. Once this period of time has lapsed, there is a very rapid conversion of the remaining water into large hydrate and blockage may occur (Mehta et al., 2003). Thus, when designing the hydrate mitigation strategies for subsea system, it is very critical to make sure the fluid residence time in the pipeline during steady-state

flow is less than the “hold-time” which is the time before hydrates start to form rapidly. The “hold-time” of some kinetic inhibitors can be about 24–48 hours. Another important parameter for kinetic inhibitors is the sub-cooling. It is reported that kinetic inhibitors can only work up to 15–23°F sub-cooling (Fu, 2002). For deepwater applications, the sub-cooling is normally larger than 25°F and the applications of kinetic inhibitors are severely limited.

The AA are polymers and surfactants that tend to prevent the formation and accumulation of large hydrate crystals into a hydrate blockage so that a transportable slurry can be maintained. It will not delay the nucleation of hydrate crystals but keep the crystals in hydrocarbon phase by reducing the growth rate of the crystals. The hydrate crystals will be transported with hydrocarbon as slurry flow. AA has no sub-cooling limitation as kinetic inhibitors and can be effective at sub-coolings of greater than 40°F (Mehta et al., 2003). Since the crystals have to be carried out of flowline, a liquid hydrocarbon phase is required to suspend the crystals.

### 20.3.3 THERMAL INSULATION AND HEATING

Based on the hydrate formation curve, as long as the fluid temperature is above the hydrate formation temperature, no hydrate will form. Thus, a meaningful way to mitigate the hydrate risk is to maintain the fluid temperature inside the pipeline to be above the hydrate formation temperature. However, for pipelines in offshore, the water temperature can be as low as the water freezing point, depending upon the water depth. Because the pipeline steel is a good conductor of heat, it is necessary to put thermal insulation material around the pipeline to prevent the heat from losing to the seawater.

Different insulation methods are used in the petroleum industry. One of them is to directly cast insulation materials onto the outer surface of the pipeline (cast-in-place). The insulation materials for this application may be a layer of homogeneous material or may consist of multiple layers with each layer being a different material. Single layer insulation is most used for cases where the insulation thickness is not excessive. For the large insulation thickness cases, multiple layer insulation is required due to the mechanical and installation reasons.

Pipe-in-pipe is another insulation method where the hydrocarbon pipeline is put into another concentric pipeline. The annulus between the two pipelines is either completely or partially filled with insulation material. Pipe-in-pipe thermal insulations normally provide better insulation than cast-in-place methods. But pipe-in-pipe methods are also normally more costly. Among many computer models, Guo et al.’s (2006) simple analytical solution can be used for designing pipeline insulations.

Pipe bundles are also used for thermal insulation. Hydrocarbon pipelines and some other pipelines which flow hot water are bundled together. The heat is transferred from the hot water to the hydrocarbon fluids. Thus, the fluid temperature is kept above the hydrate formation temperature.

Some offshore pipelines were intentionally buried under the seabed to use soil as a thermal insulation material. But due to the burial process, excessive water will exist in the covering soil and convection may be significant. Burying the pipeline alone may not be enough for thermal insulation. Some extra insulation may be needed.

For gas pipelines, thermal insulation may not be very effective in mitigating the hydrate risks. This is mainly due to the low density and heat capacity of gas plus the Joule-Thomson cooling effect during gas expansion in the pipeline. For oil pipelines, thermal insulation is a very good

hydrate mitigation strategy, especially when the pipeline is in the operation condition. By using insulation, it is easy to have fluid flowing temperature everywhere along the pipeline to be above the hydrate temperature. But no matter how much insulation is put on the pipeline, after a long pipeline shutdown, the fluid temperature will fall below the hydrate formation temperature and eventually cool down to the sea water temperature. Thus, thermal insulation itself is not enough for hydrate mitigation for long pipeline shutdowns. Other mitigation strategies, like pipeline depressurization or dead oil displacement, will be needed. But thermal insulations do provide a certain period of cool down time before another mitigation measure is taken. Cool down time is defined as the time, after pipeline shutdown, before the fluid temperature drops down to the hydrate formation temperature for a given pipeline shutdown pressure. Thus, operations, like pipeline depressurization or dead oil displacement would have to finish within the cool down time. Otherwise, hydrate will form inside the shutdown pipeline.

There is a time period called “no-touch” time or “hand-free” time. “No-touch” time is defined as the time within which no action needs to take place after a pipeline shutdown. That is why it is also called “hand-free” time. “No-touch” time is always shorter than the cool down time. It is the difference between the cool down time and the time needs to perform the operations, like pipeline depressurization. This “no-touch” time provides a very valuable period for the operator to diagnose the problems that cause pipeline shutdown. If the problems are found and fixed within the “no-touch” time, the pipeline can be re-started up with no need to use other hydrate mitigation operations. If the problems cannot be fixed within the “no-touch” time period, the operators will need to perform operations to mitigate hydrate. The longer the “no-touch” time, the longer the time available for the operator to fix the problems and the less chance to perform extra operations. But the longer the “no-touch” time, the thicker the needed insulation layer. Among several mathematical and computerized models for estimating the “no-touch” time, [Guo et al.’s \(2006\)](#) simple analytical solution can be used for the purpose.

Some studies have been conducted on hydrate mitigation using electric heating ([Lervik et al., 1997](#)). Electric heating can be divided into two categories: direct electric heating and indirect electric heating. With direct electric heating, electric current flows axially through the pipe wall and directly heats the flowline. With the indirect heating, electric current flows through a heating element on the pipe surface and the flowline is then heated through thermal conduction. After operation shutdown, electric heating can be used to keep the pipeline fluid temperature above the hydrate formation temperature to prevent hydrate formation. Electric heating can also be used as an intervention/remediation strategy for hydrate problem. Once a hydrate plug is formed, electric heating can be used to melt the hydrate. In this way, the hydrate will be melted much faster than using pipeline depressurization. Shell’s Na Kika project in the Gulf of Mexico used electric heating as hydrate remediation method ([March et al., 2003](#)). Among the several numerical models, [Guo et al.’s \(2006\)](#) simple analytical solution can be used for calculating the power requirement of electric heating.

Hot oil circulation is also a popular strategy for hydrate mitigation during system re-startup. After a long shutdown, the fluid in the pipeline is cold (sea water temperature). If the pipeline is re-started up with cold fluid in it, hydrate risk is very high. To reduce the hydrate risk, hot oil is first circulated through the pipelines (looped pipelines are required) to displace the cold fluid out and also warm up the pipelines. The time required to warm up the pipelines depends upon the hot oil discharge temperature, hot oil circulation flowrates, and pipeline length. Usually it would take up to 5–10 hours to warm up the subsea pipeline.

### 20.3.4 SYSTEM DEPRESSURIZATION

System depressurization is used to mitigate hydrate plug after a long shutdown. From the hydrate formation curve, for a given temperature, non-hydrate region can be reached by reducing the pressure. After a long shutdown, the fluid temperature will eventually reach the sea water temperature. Based upon the hydrate curve, the hydrate formation pressure at the sea water temperature can be determined. Thus, the pipelines can be depressurized (also called pipeline blowdown) below the hydrate formation pressure. Once the pipeline pressure is below the hydrate formation pressure, no hydrate will form and the system can be continued to be shutdown.

Pipeline depressurization is also often used to dissociate a hydrate plug formed in pipeline. When the system pressure is below the hydrate formation pressure, the hydrate plug would start to decompose. The hydrate plug dissociate process is a fairly slow process. It can take up to weeks or even months to completely melt a long hydrate plug. That is why it is very important to design and operate subsea pipeline out of hydrate region. For safety reasons, it is always better to be able to depressurize the pipeline from both sides of the hydrate plug.

---

## 20.4 SUMMARY

This chapter describes hydrate forming conditions and methods employed in the petroleum industry to effectively mitigate gas hydrate problems in pipeline operations. These methods include water removal, chemical inhibition, thermal insulation, heating and system depressurization. More details are given in reference [Guo et al. \(2013\)](#).

---

## REFERENCES

- Fu, B., 2002. *The Development of Advanced Kinetic Hydrate Inhibitors*. Royal Society of Chemistry, Chemistry in the Oil Industry VII, Manchester.
- Guo, B., Ghalambor, A., 2005. *Natural Gas Engineering Handbook*. Gulf Publishing Company, Houston, TX.
- Guo, B., Song, S., Chacko, J., Ghalambor, A., 2004. *Offshore Pipelines*. Elsevier, Oxford.
- Guo, B., Duan, S., Ghalambor, A., 2006. A simple model for predicting heat loss and temperature profiles in insulated pipelines. *SPE Prod. Facil. J.* 21, 107–113.
- Guo, B., Song, S., Ghalambor, A., Lin, T., 2013. *Offshore Pipelines*. second ed. Elsevier, Oxford.
- Hammerschmidt, E.G., 1939. Preventing and removing gas hydrate formations in natural gas pipelines. *Oil Gas J.* 37 (52), 66–72.
- Jacoby, R.S., 1955. Calculation of methanol requirements to prevent formation of gas hydrates. *Gas* 31 (2), 114.
- Katz, D.L., 1945. Prediction of conditions for hydrate formation in natural gas. *Trans. AIME* 160, 140.
- Kelland, M.A., Svartaas, T.M., Dybvik, L.A., 1995. Studies on new gas hydrate inhibitors. In: Presented at the 1995 SPE Offshore Europe Conference, Aberdeen, 5–8 September.
- Kohl, A.L., Riesenfeld, F.C., 1985. *Gas Purification*. fourth ed. Gulf Publishing Co, Houston, TX.
- Lervik, J.K., Kulbotten, H., Klevjer, G., 1997. Prevention of hydrate formation in pipelines by electrical methods. In: *Proceedings of the Seventh International Offshore and Polar Engineering Conference*, Honolulu, 1997.

March, D.M., Bass, R.M., Phillips, D.K., 2003. Robust technology implementation process applied to a first deepwater electrical heating ready system. In: Presented at the 2003 Offshore Technology Conference, Houston, TX, 2003.

Mehta, A.P., Hebert, P.B., Cadena, E.R., Weatherman, J.P., 2003. Fulfilling the promise of low-dosage hydrate inhibitors; journey from academic curiosity to successful field implementation. SPE Prod. Facil. 18, 73–79.

---

## PROBLEMS

- 20.1. Estimate water contents of a natural gas at pressures of 1000 psia, 2000 psia, and 3000 psia at a temperature of 50°F.
- 20.2. Twenty MMscfd of a 0.75 specific gravity natural gas cools down to 50°F in a buried pipeline. The minimum pipeline pressure is 1000 psia. Concentration of commercially available glycol and methanol inhibitors is 75% and 100% by weight, respectively. What volume of inhibitor solution must be added daily if the gas enters line saturated at 70°F? Consider both DEG and MeOH inhibitors.

# OTHER FLOW ASSURANCE ISSUES

# 21

## 21.1 INTRODUCTION

In addition to the gas hydrate problems described in the last chapter, there are other flow assurance issues in oil and gas pipeline operations. Wax and asphaltene can deposit on the wall and may eventually block the pipeline. Corrosion may occur. Scales may form and deposit inside the pipeline and restrict the flow. And severe slugging may form inside the pipeline and cause operational problems to downstream processing facilities. Pipelines should be operated under engineering protection to assure that the oil and gas will be safely and economically transported from wells all the way to the downstream processing plant. Attacking these problems requires fundamental knowledge of composition and chemistry of fluids being transported.

## 21.2 FLUID SAMPLING AND CHARACTERIZATIONS

One of the most critical steps in identifying and quantifying the flow assurance risks is fluid sampling. Whether or not there will have any flow assurance risks in subsea pipeline has to be determined from the fluid sample analysis: What is the fluid composition? Is there a potential for wax deposition? Is the potential for asphaltene deposition high, medium, or low? Will the fluid gel when the temperature is low enough after system shutdown? How much energy will be required to re-mobilize the fluid once it is gelled? All these questions can only be answered by lab or flowloop measurements of the fluid samples. Thus, it is very important to sample the representative fluid that will be transported by pipeline. No matter how accurate the lab measurements and interpretations are, but if the fluids do not represent the real production fluids, wrong conclusions may be drawn. Any flow assurance mitigation strategies based upon the wrong conclusions will not work properly and the pipeline and subsea system will encounter severe operational risks.

Water samples are also very critical in establishing flow assurance risks. These include scaling, hydrate formation tendencies, corrosivity, compatibility with other water (injected water or water from different production zones), material metallurgy, and design of the water handling equipment. One special challenge associated with flow assurance risk assessment is that there is no water available for sampling because the exploration wells may never reach the aquifer zones. Without water samples makes it very difficult for accurate flow assurance risk assessments. A lot of times, water samples from nearby fields have to be used, resulting in high uncertainty in the developments of the flow assurance mitigation strategies.



### 21.2.1 FLUID SAMPLING

There are a lot of discussions in the literature on fluid sampling and handling (API RP 44, API RP 45, 1968, Ostrof, 1979, Chancey, 1987). Fluid samples can be obtained from downhole and/or from surface separator. The downhole samples are the primary sample for pressure-volume-temperature (PVT) measurements, and the surface separator samples are usually treated as back-up and can be used as bulk samples for process or reservoir design. It is a good practice to collect at least two downhole samples with one serving as a back-up and collect at least three one-gallon samples from separator. A certain amount of stock tank oil samples are needed for other crude oil analyses (geochemical and crude assay).

For fluid sampling plan, it is important to know the pros and cons of all the available fluid sampling tools. Will drillstem testers (DST) or wireline testers be used? For wireline testers, will RCI (reservoir characterization instrument) or MDT (modular formation dynamics tester) be used? The key is how can we obtain the most representative fluid samples from downhole and transport it unaltered to surface and to the lab for measurements and analysis. To achieve this, it is important to obtain fluid samples from the main production zone.

Once zone or zones to be sampled is determined, the next question is how to make sure the formation fluids will be sampled with the least mud contamination. During the drilling, with over-balanced drilling, the drilling fluids will penetrate into the formation to form a damaged zone just outside the wellbore. The fluid sampling tool needs to be able to penetrate through the damaged zone to get to the virgin formation fluids. Since it is very difficult to completely avoid mud filtrate contamination during the sampling, it is important that the tool can monitor the mud contamination level and thus whether or not the samples are acceptable can be determined. When the fluids are flowing into the tool, the pressure drop between the formation pressure and the pressure in the sample chamber should be kept low so that the fluids will not change phases during the sampling. Gas can come out oil when the fluid pressure is below the bubble point. Gas may leak out the tool during the transportation. It is also important to make sure there is no solid—like asphaltene—deposition, which may stick onto the chamber wall and not completely be recovered. Otherwise the sampled fluids may not accurately represent those in the formation.

When the sampled fluids are transported from downhole to surface, the pressure in fluids may drop due to the temperature drop. Whether or not this pressure drop would cause the pressure to be below the bubble point will need to be checked out.

### 21.2.2 PVT MEASUREMENTS

Once the fluid samples are in lab, numerous tests will be performed to measure the fluid properties. Compositional analysis of the downhole sample would be performed through at least C36+, including density and molecular weight of the Heptanes plus. Pressure—Volume Relations are determined at reservoir temperature by constant mass expansion. This measurement provides oil compressibility, saturation pressure, single-phase oil density, and phase volumes. The compositions and gas formation volume factors for the equilibrium reservoir gas during primary depletion can be obtained by performing differential vaporization at reservoir temperature. Gas viscosities are then calculated from the composition. Undersaturated and depleted oil viscosity at reservoir temperature can be measured by using capillary tube viscometry.

The following parameters will normally be measured for black oil:

- Stock tank oil density (API gravity)
- Bubble point pressure
- Flash gas-oil ratio (GOR)
- Live oil compressibility
- Fluid density at bubble point
- Reservoir oil viscosity
- Flash gas composition
- Flash gas specific gravity
- Reservoir fluid composition

For gas condensate:

- Condensate density (API gravity)
- Dew point pressure
- Flash GOR
- Flash gas specific gravity
- Flash gas composition
- Stock tank oil composition
- Reservoir fluid composition
- Z factor at dew point

---

## 21.3 FLOW ASSURANCE ANALYSIS

Other than the PVT measurements, the fluid samples are also used for specific flow assurance measurements. For wax deposition evaluation: the compositional analysis through C70+ will be performed. Measurements, such as, wax appearance temperature (WAT) for the dead oils, shear rate, pour point, molecular weight, and total acid number (TAN) would normally be done. For asphaltene analysis, asphaltene titration would be done to determine the stability of asphaltenes. Titration of stock tank oil is normally done with n-heptane or n-pentane while monitoring the percent of asphaltenes precipitates to determine stability. If light oil and heavy oil will mix together for the transportation, tests would be required to determine the tendency of asphaltene precipitation for the mixed oil. Even though the hydrate curves of reservoir fluids are usually modeled by software, it is also desirable to confirm the models by performing lab measurements.

Crude oils have also to be tested for foaming tendency and emulsion forming tendency. It is also necessary to evaluate how the water oil emulsion stability can be affected by shearing resulted from pumping and lifting mechanisms. It is also very desirable to measure the live oil water emulsion viscosity at both operating and seabed conditions with water cut ranging between 0 and 100%. The existing public emulsion viscosity models are not universal and different oil most likely will form emulsions with quite different reology behavior. Thus, it is important to measure the emulsion viscosity in the lab. The measurements of live oil water emulsion viscosity is quite expensive and only a few labs available to do the tests. There are also chemical screening tests with water samples for corrosion and scale analysis.

### 21.3.1 FLUID CHARACTERIZATIONS

Fluid characterizations have been discussed extensively over the last few decades and excellent papers are available in literature for reference (Katz and Firoozabadi, 1998; Pedersen et al., 1985, 1989, 1992, 2001; Riazi and Daubert, 1980; Huron and Vidal, 1979; Mathias and Copeman, 1983; Peneloux et al., 1982; Peng and Robinson, 1976, 1978; Reid et al., 1977; Soave, 1972; Sorensen et al., 2002; Tsonopoulos and Heidman, 1986).

No matter how many tests we do, the measured parameters will not be able to cover all the application ranges we need. Thus, fluid models (equation of state) that can predict the fluid PVT behavior at different pressure and temperature conditions will be needed in pipeline design. Normally cubic equation of state models are used, like the SRK (Soave-Redlich-Kwong) (Soave, 1972), PR (Peng-Robinson) (Peng and Robinson, 1976), and modified PR (Peng and Robinson, 1978) models. The preferred models would be able to accurately predict the fluid behavior at conditions that cover the whole pressure range of reservoir and topsides processing pressures and the whole temperature range of reservoir and seabed temperatures.

To develop a model to predict the PVT behavior of oil and gas condensate mixture using a cubic equation of state, the critical temperature, the critical pressure, and the acentric factor must be known for each component of the mixture. Unfortunately, oil or gas condensate mixtures may contain thousands of different components. It is thus not practical to develop a model that would cover all the individual components. Some of the components must be grouped together and represented as pseudo-components. A common approach is to characterize the fluids using C7+ which consists of representing the hydrocarbons with seven and more carbon atoms as a reasonable number of pseudo-components. For each pseudo-component, the parameters of critical pressure, critical temperature, and acentric factor have to be determined (Pedersen et al., 1992). The characterized models are then fine-tuned using the PVT parameters obtained from lab measurements.

It is difficult to tune the model that will match all the lab-measured PVT parameters accurately. One or a few parameters can be tuned to match the lab data well and the rest of the parameters may not match the lab data well enough. Judgment may be needed to decide which the critical PVT parameters for the applications are. Effort should be made to try to tune the critical parameters to match the lab data well.

### 21.3.2 IMPACTS OF PRODUCED WATER ON FLOW ASSURANCE

In offshore production pipeline, there usually exists water together with oil and gas. Water is produced from reservoir and because water is an excellent solvent, it has dissolved plenty of chemical compounds and gases inside the formation. Water also contains suspended solids and impurities. Inside the reservoir formation, water and the chemical compounds are usually in equilibrium. As water is produced from the formation into pipeline, because of the changes of pressure and temperature, the equilibrium is destroyed and some compounds would become insoluble and start to precipitate from water and form all kinds of scales. When free water directly contacts the pipeline wall of carbon steel, water would dissolve metal and cause corrosion problems to the pipeline. When water and gases flow together in the pipeline, at certain pressure and temperature conditions, they would form hydrate which can potentially block the pipeline. Produced water presents major flow assurance problems for deep, subsea pipelines.

Proper water sampling, handling, and analysis are very critical for flow assurance risk assessment. Many of the water properties, like dissolved gases, suspended solids, and pH values would change with time and would change with pressure and temperature. Both lab and on-site analysis are necessary to get accurate water analysis (API RP 45, 1968, Ostrof, 1979). The main ions in water that are of importance for flow assurance are listed below.

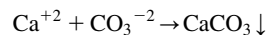
The main negative charged ions (anions) in water are:

Chloride	$\text{Cl}^-$
Sulfide	$\text{HS}^-$
Sulfate	$\text{SO}_4^{-2}$
Bromide	$\text{Br}^-$
Bicarbonate	$\text{HCO}_3^-$
Carbonate	$\text{CO}_3^{-2}$

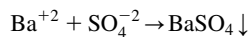
And the main positive charged ions (cations) in water are:

Sodium	$\text{Na}^+$
Potassium	$\text{K}^+$
Calcium	$\text{Ca}^{+2}$
Magnesium	$\text{Mg}^{+2}$
Strontium	$\text{Sr}^{+2}$
Barium	$\text{Ba}^{+2}$
Iron	$\text{Fe}^{+2}$ and $\text{Fe}^{+3}$
Aluminium	$\text{Al}^{+3}$

The cations and anions can combine and form different substances. When pressure and temperature change, the solubility of each ion will change. The excessive ions will precipitate from water and form solids, like scales. For example, calcium and carbonate would form calcium carbonate scale.



Similarly, barium and sulfate can form barium sulfate scale.



Water with dissolved salts is also an excellent electrolyte which is required for corrosion to occur. When free water is high enough to wet the inner pipe wall, corrosion may occur. The more salts or ions in the water, the more conductive the water is and the severer the corrosion will be.

It is well known that when free gas and water are mixed together at a certain pressure and temperature, hydrate will form. Hydrates are solids that are similar to ice. Hydrocarbon and free water often co-exist inside the offshore pipelines. When the pipeline pressure is high enough and/or fluids temperature is low enough, hydrates will form. If hydrates form inside the offshore pipeline, the pipeline flow can be blocked by the hydrates. Once the pipeline is blocked by hydrates, it can take weeks or months to dissociate the hydrates. Hydrate plugging is one of the major flow assurance risks in deep water production systems.

Water can significantly change the multiphase flow characteristics inside the pipeline and cause severe slugs to occur. For example, for the same total liquid flowrate and the same gas-oil ratio, the total amount of gas inside the pipeline will be much less with water cut of 90% than with water cut of 0%. With less gas flow, the liquid inventory inside the pipeline will be higher and it is harder for the gas to carry the liquid out of riser due to less gas energy. Thus, it is easier to form severe slugs.

More detailed descriptions on scales, corrosion, hydrates, and severe slugging will be given in sections below. But based upon the above brief discussions, it is obvious that produced water has significant impacts on flow assurance risks. The most effective way to mitigate flow assurance risks in production pipelines is to dispose the water subsea and make sure no water will get into pipeline. Unfortunately, most effective way may not be the most economical way, nor the most practical way. Currently, the most common ways to mitigate the flow assurance risks in offshore pipelines are thermal insulation and chemical inhibitions. But if the amount of water flowing inside the pipeline can be reduced (downhole separation and/or seafloor processing), the amount of chemicals needed for inhibition will also be less, resulting in less operation costs.

### 21.3.3 WAX DEPOSITIONS

Crude oil is a complex mixture of hydrocarbons which consist of aromatics, paraffins, naphthenic, resins, asphaltenes, diamondoids, mercaptans, etc. When the temperature of crude oil is reduced, the heavy components of oil, like paraffin/wax (C18–C60), will precipitate and deposit on the pipe wall. The pipe internal diameter will be reduced with wax deposition, resulting higher pressure drop. Wax deposition problem can become so severe that the whole pipeline can be completely blocked. It would cost millions of dollars to remediate an offshore pipeline that is blocked by wax.

The wax solubility in aromatic and naphthenic is low and it decreases drastically with decreasing temperatures. Thus, it is easy for wax to precipitate at low temperature. The highest temperature below which the paraffins start to precipitate as wax crystals is defined as crude cloud point or WAT. Since light ends can stabilize the paraffin molecules (Meray et al., 1993), the cloud point of live oil with pressure below the bubble point is usually lower than the cloud point of the dead oil or stock tank oil. The cloud point of live oil is more difficult to measure than that of dead oil. Thus, the cloud point of dead oil sample is often used in offshore pipeline thermal insulation design. This approach is conservative and can practically result in millions of dollars of extra cost in thermal insulation.

When measuring the cloud point, the key is to preheat the oil sample to high enough temperature to solubilize all the preexisting wax crystals. There are quite a few techniques available for cloud point measurement: viscometry, cold finger, differential scanning calorimetry, cross polarization microscopy, filter plugging, and Fourier transform infrared energy scattering, etc. The cloud points measured using different techniques may differ by up to more than 10 degrees (Monger-McClure et al., 1999; Hammami and Raines, 1997).

When the waxy crude is cooled, paraffins or waxes will precipitate out of the crude oil once the crude temperature is below the cloud point. The precipitated wax may deposit on the pipe wall in the form of a wax-oil gel (Venkatesan et al., 2002). The gel deposit consists of wax crystals that trap some amount of oil. As temperature gets cooler, more wax will precipitate and the thickness of the wax gel will increase, causing gradual solidification of the crude. When the wax precipitates so

much and forms the wax gel, the oil will eventually stop moving. The temperature at which the oil sample movement stops is defined as the crude pour point. When crude gets so cold that it stops moving inside the offshore pipeline after shutdown, depending upon the characteristics of the gel, crude oil may not be able to be re-mobilized during re-startup. Thus, it is very important to check the re-start up pressure of the crude by cooling the crude down to below the pour point. Because the seawater temperature can be below the pour point of the crude, wax gel may form after long pipeline shutdown. It is critical to make sure the pipeline will be able to be re-started up after long shutdown.

Extensive researches have been conducted to try to understand and model the wax deposition process which is a complex problem involving fluid dynamics, mass and heat transfers, and thermodynamics (Burger et al., 1981; Brown et al., 1993; Creek et al., 1999; Hsu et al., 1999; Singh et al., 1999). It is widely accepted that molecular diffusion of paraffin is one of the dominant deposition mechanisms. Whether or not Brownian motion, gravity settling, and shear dispersion play a significant role in wax deposition is still a research topic.

When waxy crude is flowing in offshore pipeline, the temperature at the center of the pipeline is the hottest while the temperature at the pipe wall is the coldest, resulting in a radial temperature profile. Since the wax solubility in the oil is a decreasing function of temperature. When the temperature is lower than the cloud point, wax crystals will come out of solution. Thus, the radial temperature gradient will produce a concentration gradient of wax in oil with the wax concentration in the oil lowest close to the pipe wall. The concentration gradient would thus result in mass transfer of wax from the center of the pipe to the pipe wall by molecular diffusion. The wax mass transfer can be described by the Fick's law as:

$$\frac{dm_w}{dt_w} = \rho_w D_w A_d \frac{dC_w}{dr} \quad (21.1)$$

where

- $m_w$  = mass of the deposited wax on the pipe wall
- $t_w$  = time
- $\rho_w$  = density of the solid wax
- $D_w$  = diffusion coefficient of liquid wax
- $A_d$  = deposition area
- $C_w$  = volume fraction concentration of wax in liquid oil
- $r$  = radial coordinate

The diffusion coefficient is expressed by Burger et al. (1981) as a function of oil viscosity:

$$D_w = \frac{K_w}{\nu} \quad (21.2)$$

where

- $K_w$  = constant
- $\nu$  = oil dynamic viscosity

The constant in Eq. (21.2) is often adjusted to match modeled deposition rates with experimental ones.

There are a few wax deposition mechanisms that are not widely accepted, like Brownian diffusion, shear dispersion, and gravity settling. Once the temperature is below the cloud point, wax crystals will precipitate out of solution and be suspended in the oil. The suspended wax crystals will collide with each other and with oil molecules due to Brownian motion. Because of the wax concentration gradient, it is possible that net effect of the Brownian motions is to transport the wax crystals in the direction of decreasing concentration. It is thus suggested that wax deposition can be potentially due to the Brownian diffusion of wax crystals. But quite a few existing wax deposition models do not take into account the Brownian diffusion.

Gravity settling as one of the possible wax deposition mechanisms is based upon the argument that the wax crystals tend to be denser than the oil and they would thus settle in a gravity field and deposit on the bottom of the pipelines. But experiments with horizontal and vertical flows showed that there was no difference in the amount of wax deposited for the two flow configurations. Thus, it is not clear yet how significant a role that gravity would play for wax deposition.

Burger et al. (1981) and Weingarten and Euchner (1986) reported possible wax deposition by shear dispersion. They claimed that the shear dispersion played a role in wax deposition mainly in laminar flow and proposed the following equation for the deposition rate.

$$\frac{dm_s}{dt} = k_w C_s A_d \gamma \quad (21.3)$$

where

$m_s$  = mass of the deposited wax due to shear dispersion

$k_w$  = constant

$C_s$  = the concentration of solid wax at the pipe wall

$A_d$  = deposition area

$\gamma$  = shear rate

Brown et al. (1993) performed experiments with zero heat flux across the pipe wall (thus no molecular diffusion) and showed no wax deposition due to shear dispersion. Brown et al. concluded that shear dispersion does not contribute to wax deposition.

For subsea production pipeline, the most widely used wax mitigation method is to put enough thermal insulation to maintain the fluid temperature everywhere along the pipeline above the WAT during normal or “steady-state” operations. For transient operations, like shutdown, the fluid temperature inside the pipeline will cool down with time and eventually will reach the seawater temperature within a transient time that is about 12–36 hours depending upon the insulation design. Once the pipeline cools down to the seawater temperature, there is no temperature gradient between the bulk fluid and the pipe wall and no wax will deposit. During the cool down transient time, the fluid temperature can be lower than the WAT and some wax will deposit onto the pipe wall. Since the transient time is relatively short, the amount of wax deposited will be very small because wax deposition is a slow process. Furthermore the wax deposited during shutdown will be re-melted once the pipeline reaches normal operation again.

To be conservative for the insulation design, the WAT of dead oil is normally used. But for subsea pipeline insulation design, the most important drivers are hydrate mitigation and system cool down time. If the subsea pipeline insulation design satisfies the hydrate mitigation and cool down

time requirements, it will normally also satisfy the requirement that fluid temperature to be above the WAT during steady-state flow. Details on subsea thermal insulation are provided in Chapter 11 of this book.

Another popular wax mitigation method is to regularly pig the pipeline to remove the deposited wax from pipe wall. For some subsea pipelines, especially the export lines where hydrate is not a concern, pigging would normally be the main wax management strategy. There are numerous types of pigs, like simple spheres, foam pigs, and smart pigs.

The pig is sent down into the pipeline from pig launcher and is pushed by the production crude or any other fluids, like dead oil or gas. The pig would mechanically scrape off the wax from the pipe wall and re-deposit it back into the crude in front of the pig. A regularly scheduled pigging program is very critical for the success of pigging operations. If the pigging operation is not scheduled frequently enough, too much wax may have deposited onto the pipe wall. During the pigging operation, pig may get stuck inside the pipe due to the excessive amount of wax in front of it. The pigging schedule program will be developed based upon wax deposition modeling and will be fine-tuned as more on the wax deposition rate is understood in field operations.

Wax chemical inhibitors can be divided into two different types: one is to prevent/delay the formation of wax crystals and thus reduce the WAT and also prevent the wax from depositing onto the pipe wall; the other is to decrease the wax pour point and thus delay the waxy crude solidification when the crude cools down.

The mechanisms that chemicals inhibit the wax formation and deposition with are not well understood. It seems that it is accepted that with absorption of polymers and additives onto the surface of wax crystals, it is possible to keep them from agglomerating and to keep the wax crystals dispersed and thus reduce the wax deposition rate. Groffe et al. (2001) performed lab and field studies on wax chemical inhibition. They developed novel chemicals that would have an ability to interfere with the wax crystal growth mechanism and were capable of keeping or making the crystals smaller so that they may cause the settling process to be much slower. The chemical, if possible, would also be able to absorb onto the metal surfaces and make them oleophobic. They claimed, based upon their lab work, the chemical they developed was able to lower the WAT of a waxy crude by almost 10°C. It was also noticed that the chemical has anti-sticking properties and was able to reduce the amount of wax deposited onto adhering metal surface.

Wang et al. (2003) tested eight different commercial wax inhibitors and found that all the inhibitors reduced the total amount of wax deposited. They noticed that the inhibitors that depress the WAT the most also are most effective in reducing the wax deposition. But the inhibitors could only effectively decrease the deposition of low molecular weight wax ( $C_{34}$  and below) and had little effect on the deposition of high molecular weight wax ( $C_{35}$ – $C_{44}$ ). They claimed that although the total amount of wax formed is reduced, the absolute amount of high molecular wax was increased. Thus, the net effect of many the commercial wax inhibitors is to form harder wax which will be more difficult to be removed.

With waxy crudes, when the temperature is lowered the wax crystallizes gradually in the form of needles and thin plates. With further crystallization, these needles and thin plates turn into 3-dimensional networks and cause solidification of crude (Groffe et al., 2001). Chemicals of specific polymers and surfactants can prevent the formation of these networks by retarding the



growth of waxy crystals, resulting in many tiny crystals. Thus, by changing the crystal structure, the ability of wax crystals to intergrow and interlock is reduced, making the pour point of the crude lower.

### 21.3.4 ASPHALTENE DEPOSITIONS

Asphaltenes are defined as the compounds in oil that are insoluble in n-pentane or n-hexane, but soluble in toluene or benzene. That is, asphaltene solids would precipitate when excess n-pentane or n-hexane is added to the crude oil. Asphaltene solids are dark brown or black and will not melt, unlike waxes. But like waxes, with changes in pressure, temperature, and composition, asphaltenes tend to flocculate and deposit inside reservoir formation, well tubing, and production flowlines. Mixing reservoir fluids with a different gas (injected gas or gas-lift gas) or mixing two oil streams can also induce asphaltene precipitations (Wang et al., 2003).

The saturation of asphaltenes in crude oil is a key parameter to determine whether or not asphaltene would cause any problems. If asphaltenes are always under-saturated in crude oil, that is, asphaltenes are stable and no precipitation will occur. On the other hand, asphaltenes precipitation will occur if they are highly super-saturated in crude oil. The saturation of asphaltenes in crude oil can change from under-saturated to super-saturated if the pressure, temperature, and composition change. During oil production, the temperature and pressure changes between reservoir and production pipeline can be quite significant. Similarly the fluid composition can also change significantly during the production: gas can separate from the oil when the oil pressure drops below the bubble point or gas-lift gas can be injected into the oil stream. Thus, during oil production and transportation, asphaltene precipitation inside the production system is a potential risk.

A parameter that is closely related to the asphaltene stability in oil is the solubility parameter. Solubility parameters of oil and asphaltenes are key input data for most of the thermodynamic models for asphaltene phase behavior. The solubility parameter is defined as

$$\delta_s^2 = \frac{\Delta u^v}{v_m} \quad (21.4)$$

where

$\delta_s$  = solubility parameter

$\Delta u$  = cohesive energy per mole (the energy change upon isothermal vaporization of one mole of liquid to the ideal gas state).

$v_m$  = molar volume

Solubility parameter is a measure of the cohesive energy density or the internal pressure that is exerted by molecules within a solution. When two liquids with quite different molecules are mixed together, the liquid with higher solubility parameter will tend to “squeeze” the molecules of the liquid with a lower solubility parameter out of the solution matrix, resulting in two immiscible phases. On the other hand, if two liquids with similar solubility parameters are mixed, it is more likely for the two liquids to be miscible to one another (Burke et al., 1990).

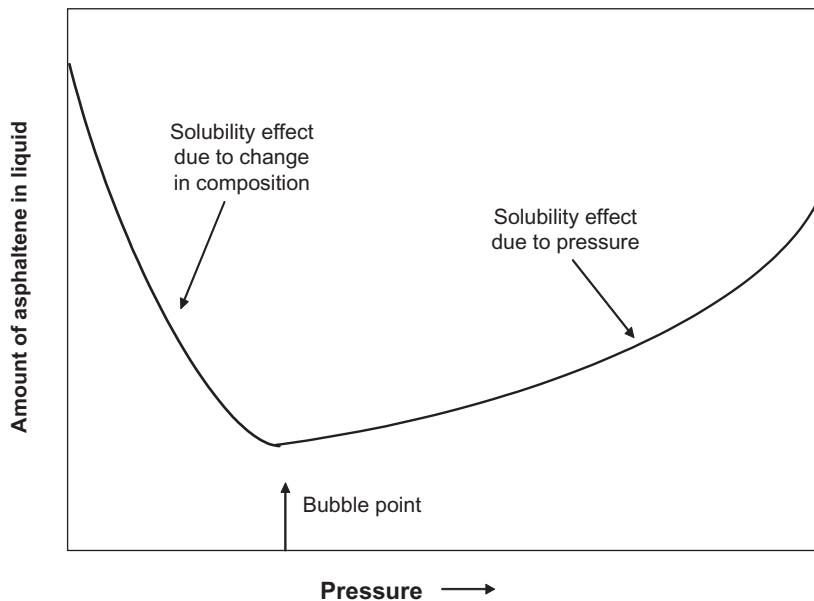
The solubility parameter of asphaltene and the solubility parameter of crude oil will strongly affect how much asphaltene will be soluble in the crude oil. If the solubility parameter of the crude

oil is similar to the solubility parameter of asphaltene, more asphaltene will be soluble in the crude. Solubility parameter is a function of temperature (Barton, 1991). Increasing the temperature tends to decrease the asphaltene solubility parameter (Hirschberg et al., 1984; Buckley et al., 1998).

The pressure effect on asphaltene solubility depends upon the pressure is above the bubble point or below the bubble point. de Boer et al. (1992) and Hirschberg et al. (1984) studied the pressure dependence of asphaltene solubility and presented similar plots of asphaltene soluble in oil as a function of pressure. When the pressure is above the bubble point, the fluid composition is constant, but with decreasing pressure, the density of crude decreases due to oil expansion and so does the asphaltene solubility as shown in Fig. 21.1. The asphaltene solubility reduces to a minimum when the pressure is approaching the bubble point. Below the bubble point, gases start to evolve from the live oil and the oil density increases. The asphaltene solubility also increases with decreasing pressure. The loss of light ends improves the asphaltene stability in crude oil.

The solubility parameter of a mixed system, like crude oil that consists of many components, can be calculated based upon the solubility parameter of the individual component (de Boer et al., 1992):

$$\delta_m = \sum_{i=1}^{n_c} f_i \delta_i \quad (21.5)$$



**FIGURE 21.1**

Pressure dependence of asphaltene solubility in crude oil.

where

- $\delta_m$  = solubility parameter of mixed system
- $f_i$  = the volume fraction of  $i^{\text{th}}$  component
- $\delta_i$  = solubility parameter of  $i^{\text{th}}$  component
- $n_c$  = total number of components in the system

During the production, fluid composition will change as a function of pressure and temperature. Especially when the pressure is below the bubble point, gas starts to come out of solution. Similarly, gases like  $\text{CO}_2$  can be added to crude for enhanced oil recovery and gases can also be added into crude through gas-lift operations. All those operations can change crude oil compositions and the crude oil solubility parameters, and thus may potentially induce asphaltene precipitation.

Assuming the asphaltene and crude oil are in equilibrium (no asphaltene precipitation), the maximum volume fraction of asphaltenes soluble in the crude is given by the Flory-Huggins theory (Hirschberg et al., 1984; Burke et al., 1990) as the following:

$$(\phi_a)_{\max} = \exp \left\{ \frac{V_a}{V_L} \left[ 1 - \frac{V_L}{V_a} - \frac{V_L}{RT} (\delta_a - \delta_L)^2 \right] \right\} \quad (21.6)$$

where

- $\varphi_a$  = volume fraction of asphaltenes in oil
- $V_a, V_L$  = molar volume of asphaltenes and liquid oil phase, respectively
- $\delta_a, \delta_L$  = solubility parameter of asphaltenes and liquid oil, respectively
- $T$  = temperature
- $R$  = ideal gas constant

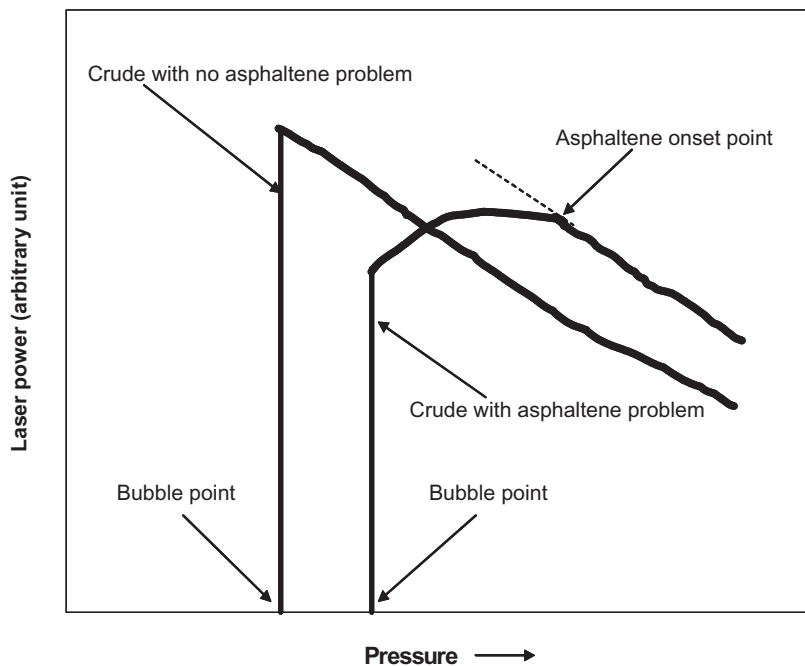
The properties of liquid oil (molar volume and solubility parameter) can be calculated from proper equation of state while the properties of asphaltenes have to be estimated from experimental data.

Asphaltene solubility parameter can also be affected by the other components in the oil, like resins (Hirschberg et al., 1984). Asphaltenes and resins are heterocompounds and form the most polar fraction of crude oil. Resins have a strong tendency to associate with asphaltenes and they help reduce the asphaltene aggregation. On the other hand, if normal alkane (pentane or heptane) liquids are added to crude oil, the crude oil becomes lighter and resin molecules desorb from the surface of asphaltenes in an attempt to re-establish the thermodynamic equilibrium that existed in the oil before the addition of the normal alkane liquids. Because of the desorption of resins, asphaltene micelles start to agglomerate to reduce the overall surface free energy (Hammami et al., 1999). If sufficient quantities of normal alkane are added to the oil, the asphaltene molecules aggregate to such an extent that the particles would overcome the Brownian forces of suspension and begin to precipitate.

Hammami et al. (1999) performed experimental studies on the onset of asphaltene precipitation using a solids detection system (SDS) which consists of a visual PVT cell and fiber optic light transmission probes. The sample oil is first charged into the PVT cell and the pressure of the cell is then lowered isothermally at programmable rates. At each equilibrium pressure, the sample volume is measured and the corresponding density is calculated. The power of the transmitted light is

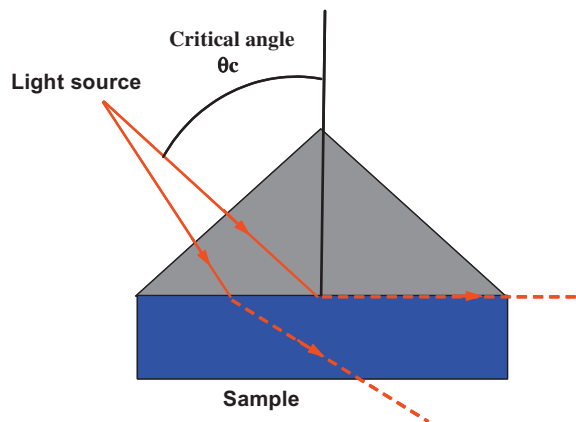
continuously measured. The power of transmitted light is inversely proportional to the oil density. When the pressure is above the bubble point, decreasing pressure would result in reduced oil density and thus increased power of transmitted light. The power of transmitted light is also inversely proportional to the particle sizes. If particle sizes increase, as asphaltenes flocculate, the power of transmitted light will decrease. If sufficient gas bubbles exist in the oil, the power of transmitted light will decrease dramatically. Thus, the experiments would stop at the bubble point.

If the crude oil has no asphaltene precipitation and deposition problems, Hammami et al. claimed that the power of transmitted light would more or less linearly increase as the pressure is decreased isothermally from above the bubble point. This is due to the decrease in fluid density with decreasing pressure when the pressure is above the bubble point. When the bubble point is approached, the power of transmitted light would drop dramatically to noise level, as shown in Fig. 21.2. If the crude oil has asphaltene precipitation and deposition problems, the trend of the power of the transmitted light as pressure is reduced is quite different from that of oils without asphaltene deposition problems. As the pressure is reduced from above the bubble point, the power of transmitted light would initially increase more or less linearly and then it would reach a plateau with further pressure reduction. After the plateau, the power of transmitted light would gradually decrease and eventually drop to the noise level when the bubble point is reached, as shown in Fig. 21.2. The pressure at which the power of transmitted light is deviated from the straight line is defined as the onset point of asphaltene precipitation.



**FIGURE 21.2**

Laser power as a function of pressure.



**FIGURE 21.3**

Schematic diagram of refractometer.

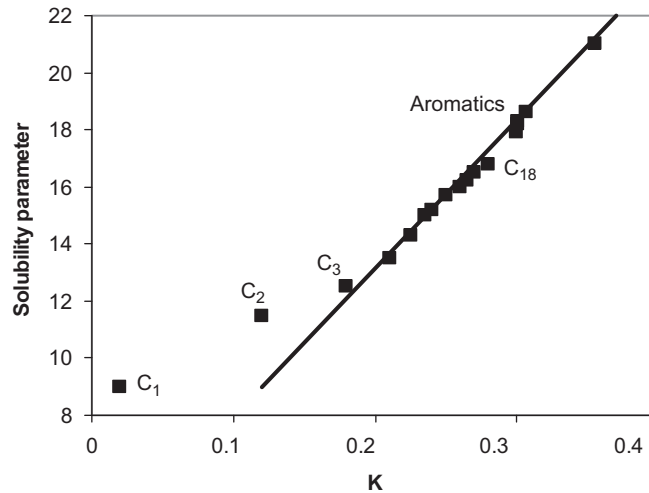
Improved prediction of the onset of asphaltene precipitation may be achieved using refractive index (RI) to characterize crude oils and their mixtures with precipitates and solvents (Buckley et al., 1998; Wang et al., 2003). The RI is calculated based upon the measurement of the total internal reflection angle (critical angle) as shown in Fig. 21.3, and is expressed as:

$$RI = \frac{1}{\sin \theta_c} \quad (21.7)$$

RI is a function of fluid composition and density. For different fluid, the RI will be different. Based upon experimental studies, Buckley et al. (1998) noticed that the onset of asphaltene precipitation occurred at a characteristic RI and the RI can be correlated with the solubility parameter as shown in Fig. 21.4. Based upon Fig. 21.4, for most of the normal alkanes and some aromatics, the relationship between solubility parameters and  $\frac{RI^2 - 1}{RI^2 + 2}$  is more or less linear.

For a mixture of crude oil and precipitant (like, n-alkane), the RI of the mixture is in between the RI of the crude oil and the RI of the precipitant and can be determined based on the RIs and the volume fractions of the crude oil and the precipitant. The precipitation of asphaltenes will only occur when the mixture RI is below a critical RI called  $P_{RI}$ . By studying the mixtures of crude oil and n-Heptane for ten different oils, Buckley et al. found that the mixture RI ranged between 1.47 and 1.57 while the  $P_{RI}$  was more or less a constant of about 1.44. The asphaltene content in those sample oils ranged between 1.2 and 10.9 wt% and no correlations between the asphaltene content and either RI or  $P_{RI}$  was found.

With the asphaltene onset RI ( $P_{RI}$ ) known, whether or not a crude oil would have asphaltene precipitation problem at a given pressure and temperature condition can be determined by measuring the corresponding RI. If the measured RI is larger than  $P_{RI}$ , there will be no precipitation risk. On the other hand, if the measured RI is smaller than  $P_{RI}$ , asphaltene precipitation is possible. Unfortunately, the RI of live oil under pressure and temperature cannot be easily measured.



**FIGURE 21.4**

Relationship between solubility parameter and RI ( $K = \frac{RI^2 - 1}{RI^2 + 2}$ ) for n-alkanes and aromatics.

From Buckley, J.S., Hirasaki, G.J., Liu, Y., Von Drasek, S., Wang, J.X., Gill, B.S., 1998. *Asphaltene precipitation and solvent properties of crude oils*, *Pet. Sci. Technol.*, 16 (3&4), 251–285.

The RI of live crude oils under pressure can be estimated from the RI of stock tank oil and gas-oil ratio (Buckley et al., 1998) as

$$\left(\frac{RI^2 - 1}{RI^2 + 2}\right)(p) = \frac{1}{B_o} \left(\frac{RI^2 - 1}{RI^2 + 2}\right)_{STO} + 7.52 \times 10^{-6} \frac{R_s}{B_o} \sum_{i=1}^m x_i R_i \quad (21.8)$$

where

STO = stock tank oil

$B_o$  = formation volume factor

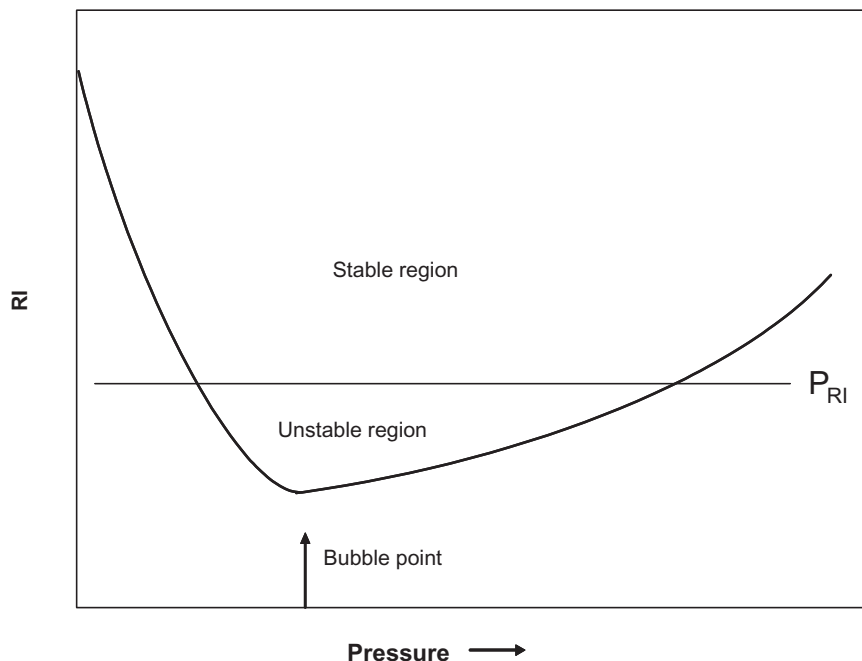
$R_s$  = gas-oil ratio

$x_i$  = mole fraction of  $i^{\text{th}}$  component in the gas

$R_i$  = molar refraction of  $i^{\text{th}}$  component in the gas

Fig. 21.5 shows how the RI of a live oil may change with pressure. For pressure above the bubble point, the RI of live oil decreases with pressure. The RI of live oil will reach a minimum around the bubble point. Below the bubble point, the RI increases with decreasing pressure. When the RI is below the  $P_{RI}$ , asphaltenes become unstable and flocculation may occur.

The above mentioned RI measurement and transmitted light power measurement are sound experimental methods for detecting the onset of asphaltenes precipitation. But these tests take time. In 1992, de Boer et al. published a simple method for screening crude oils on their tendency for asphaltene precipitation (de Boer et al., 1992). By correlating crude properties, like solubility parameter, molar volume, and asphaltene solubility in oil, with the density of the crude at in-situ conditions, de Boer et al. was able to develop an asphaltene supersaturation plot, called de Boer



**FIGURE 21.5**

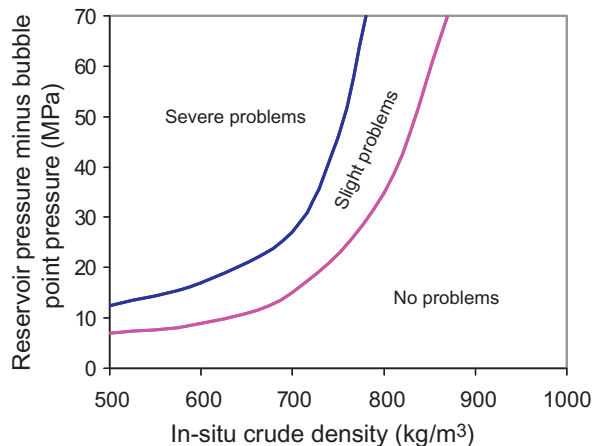
Live oil RI changes as a function of pressure.

plot which has the difference of reservoir pressure and bubble point pressure as the y axis and the in-situ crude density as the x-axis. A simplified de Boer plot is shown in Fig. 21.6. For a given crude and given reservoir conditions, the difference of reservoir pressure and bubble point pressure and the crude densities at reservoir conditions can be calculated. Then, Fig. 21.6 can be used to quickly assess the risk level of asphaltene precipitation during production.

Based upon field experiences, de Boer et al. (1992) concluded that asphaltene deposition problems are encountered with light crude oils that are high in C1–C3 (>37 mole%) and have a relatively low C7<sup>+</sup> content (<46 mole%), with high bubble point pressure (>10 MPa) and a large difference between reservoir and bubble point pressures. The asphaltene content in those light oils is low (<0.5 wt%). The heavy crude oils which have high asphaltene content tend to have fewer problems with asphaltene deposition. This is especially true if the reservoir pressure is close to the bubble point pressure.

There are two kinds of methods that are currently being used for asphaltene remediation. One is the mechanical method which includes pigging, coiled tubing operations, and wireline cutting. The other is to use chemical solvents to dissolve the deposited asphaltenes. Chemical inhibitors are used to prevent asphaltenes from deposition in production system includes pipelines.

Pigging can be used to remove asphaltenes inside manifolds and pipelines, provided the manifold and pipeline system can handle pigs. Compared to waxes, asphaltenes are brittle and hard and thus special pigs are required. Pigs with disks and cups should be used and spheres and foam pigs



**FIGURE 21.6**

de Boer crude oil supersaturation plot.

*Based upon De Boer, R.B., Leerlooyer, K., Eigner, M.R.P., van Bergen, A.R.D., 1992. Screening of crude oils for asphalt precipitation: theory, practice, and the selection of inhibitors. In: Presented at the European Petroleum Conference held in Cannes, France, November 1992.*

will not be efficient for removing asphaltene solids. For successful pigging operation, the pigging frequency is important. If the time between pigging operations is too long, too much asphaltene depositions can occur inside the pipeline. Excessive asphaltene deposition can cause pig get stuck. On the other hand, pigging operations often require production shutdown and unnecessary pigging operations will result in production loss. Since there is no reliable way to predict how much asphaltenes will deposit with time inside a pipeline, the pigging frequency can only be optimized by learning the system behavior. It is safe to start at high pigging frequency and monitor the amount of asphaltene solids removed. Once the system behavior is better understood, the pigging frequency can be optimized.

Wireline cutting can be used to remove asphaltene solids inside wellbore provided the wellbore can be easily accessed. Coiled tubing systems can be used to remove asphaltene solids inside wellbore and inside pipelines. The limitation with coiled tubing is that if the solid deposition is too far away from the coiled tubing deployment point, coiled tubing cannot be used.

Even though asphaltenes are not soluble in alkanes, they are very soluble in aromatics solvents, like benzene. Products of aromatics and alcohols mixtures are available from chemical companies that can be used to remove asphaltene deposits. It is always critical to test the chemicals first to assess the effectiveness of the products for a specific deposit. Chemical solvents are often squeezed into formation to fight the asphaltene deposit problems near wellbore region which cannot be easily accessed by mechanical means.

Chemicals, like blend of aromatics, surfactants, and oil and water soluble alcohols, are developed to inhibit asphaltene precipitation. Some of the chemicals would increase the surface tension of the crude oils and thus help keep asphaltenes from precipitating in the treated hydrocarbon.



Some of the chemicals would help supply resins in the oil to stabilize the asphaltene molecules. Again, whether or not an inhibitor is effective for a specific asphaltene problem can only be determined by testing. It is often true that a product is effective for dissolving deposits may not be a good inhibitor.

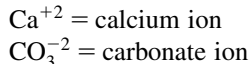
### 21.3.5 INORGANIC PRECIPITATES—SCALES

Waxes and asphaltenes are precipitates from crude oils. In this section, the potential precipitates from water (inorganic precipitates—called scales) will be discussed. Like wax and asphaltene depositions, scales can potentially cause serious flow assurance concerns by plugging production facilities and topsides processing devices, jamming control valves, and restricting flows in tubing and in pipelines. Scales can also form inside the formation and can potentially reduce the productivity by plugging the formation. Thus, it is important to understand how the scales are formed and how to mitigate the scale problems.

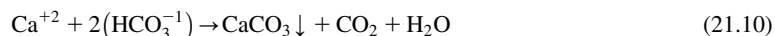
The most common scales occurring in the oil industry are calcium carbonate, barium sulfate, strontium sulfate, and calcium sulfate. Calcium carbonate ( $\text{CaCO}_3$ ) is also called calcite scale. Calcite scale is formed when the calcium ion is combined with carbonate ion.



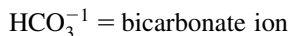
where



Calcium carbonate is a solid and can potentially precipitate from solution to form scale. Similarly when calcium ion is combined with bicarbonate ion, calcium carbonate will also be formed.



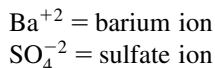
where



Barium sulfate is formed when barium ion is combined with sulfate ion:



where



Like calcium carbonate, barium sulfate is a solid and can potentially precipitate from solution to form scale.

Strontium sulfate is formed when strontium ion is combined with sulfate ion:



where

$\text{Sr}^{+2}$  = strontium ion

Calcium sulfate can precipitate from water if calcium ion is combined with sulfate ion:



Calcium sulfate scales include anhydrite ( $\text{CaSO}_4$ ) and gypsum ( $\text{CaSO}_4 \cdot 2\text{H}_2\text{O}$ ). Carbonate scales tend to form from formation waters with reduced pressure, increased temperature, and/or increased pH value. Sulfate scales tend to form when formation waters mix with seawater because seawaters normally have high sulfate concentrations.

There are some less common scales, like calcium fluoride ( $\text{CaF}_2$ ), reported in the literature (Yuan et al., 2003). Calcium fluoride is extremely insoluble and there are currently not many chemicals available to effectively treat it.

Solubility is a parameter used to assess how much a substance can stay in a solution without precipitation and is defined as the maximum amount of a solute that can be dissolved in a solvent under given physical conditions (pressure, temperature, pH, etc.). The higher the solubility of a compound, the larger amount of the compound can dissolve in a solution. The solubility of a compound can change when pressure, temperature, and/or compositions change. Different compounds have different solubilities. It is well known that the solubility of calcium carbonate, barium sulfate, strontium sulfate, or calcium sulfate in water is relatively small. That is why these compounds tend to precipitate from water to form scales.

Saturation Ratio (SR) is defined as the ratio of the ion product to the ion product at saturation conditions. For example, for calcium carbonate ( $\text{CaCO}_3$ ),

$$\text{SR} = \frac{C_{\text{Ca}^{+2}} \times C_{\text{CO}_3^{-2}}}{\left(C_{\text{Ca}^{+2}} \times C_{\text{CO}_3^{-2}}\right)_{\text{saturation}}} \quad (21.14)$$

where

$C_{\text{Ca}^{+2}}$  = concentration of  $\text{Ca}^{+2}$  in solution

$C_{\text{CO}_3^{-2}}$  = concentration of  $\text{CO}_3^{-2}$  in solution

For a given solution:

- SR = 1      the solution is saturated with  $\text{CaCO}_3$
- SR < 1     the solution is undersaturated with  $\text{CaCO}_3$  and precipitation will not occur
- SR > 1     the solution is supersaturated with  $\text{CaCO}_3$  and precipitation can potentially occur

A concept that is used more often than SR is called saturation index (SI) which is defined as:

$$\text{SI} = \log_{10}(\text{SR}) \quad (21.15)$$

And if

- SI < 0      the scaling ions are undersaturated in the solution at the given condition and no scale precipitation
- SI = 0      the scaling ions are at equilibrium in the solution
- SI > 0      the scaling ions are supersaturated in the solution at the given condition and scale precipitation is possible

**Table 21.1 Summary of Major Factors Impacting Scale Precipitations**

Scales	Temperature Effects	Pressure Effects	pH value Effects	Dissolved Solids Effects
Calcium carbonate	Less soluble with increased temperature  More likely scale will form with hotter water	Less soluble with reduced pressure  If waters go through the bubble point, CO <sub>2</sub> would evolve from solution and scale likely to form	Less soluble with increased pH value	Less soluble with reduced total dissolved solids in water Adding salts into distilled water can increase the solubility
Barium sulfate	For common temperature range, solubility increase with increased temperature	Less soluble with reduced pressure	Little impact	More soluble with increased dissolved salt
Strontium sulfate	Less soluble with increased temperature	Less soluble in NaCl brines with reduced pressure	Little impact	More soluble with increased NaCl content
Calcium sulfate	Less soluble with increased temperature for the common reservoir temperature range	Less soluble with reduced pressure	Little impact	More soluble with increased water salinity

As shown in [Table 21.1](#), the major factors affecting the scale precipitation from water are pressure, temperature, pH value, and the dissolved solids in water. The following table summarizes the impacts of these factors for the common scales in oil industry ([Jacues and Bourland, 1983](#); [Carlberg and Matches, 1973](#); [Kan et al., 2001](#); [Rosario and Bezerra, 2001](#)).

Even though the main reasons for carbonate scales to form inside wellbore are pressure drop inside tubing (increased pH due to the escape of CO<sub>2</sub>) and the high downhole temperature, the main cause for sulfate scales to form is the mixing of different waters. Mixing waters from different fields, from different wells at the same field, from different laterals in the same well, and mixing of formation water and seawater can potentially induce scales to form in the production facilities.

Scale is one of the major flow assurance concerns in deep water production. There are large pressure and temperature changes through the production system (from reservoir to topsides). These pressure and temperature changes may induce scales. Fluids with formation water from different formations and wells are normally mixed in the production pipeline system. Different formation waters may have different compositions and scales may form when these waters are mixed. For fields where seawater is injected for pressure maintenance, scales may become serious when different seawater fractions are being produced into the production system.

The main means for scale control is chemical inhibition which includes both continuous chemical injection and periodic scale squeeze into formation. Scale inhibitors prevent scale deposition and they do not normally re-dissolve the deposits that have already formed. So the key function of a scale inhibitor is prevention not remedy. The scale control strategies can be different at different stages of field life ([Jordan et al., 2001](#)). At early life, only connate water or aquifer water breaks through. The most likely scales will be carbonate scales which will be the main focus for scale

control strategy. The scale severity will increase with increased water cut. If seawater is injected, at later field life, sulfate scales can be formed when the injected seawater breaks through and mixes with formation water. The strategies at this stage would include controlling both carbonate and sulfate scales. With production, the seawater fraction in the produced water will increase with time and the severity of sulfate scales will change accordingly.

When chemical inhibitors are used for scale control, inhibitors will work with one or more of the following three main mechanisms (Yuan et al., 2003; Graham et al., 1997):

- Crystal nucleation inhibition
- Crystal growth retardation
- Dispersion of small scale crystals in the flowing fluid

An inhibitor molecule works against crystal nucleation by interacting directly with the scaling ions in the brine and thus prevents the ions from agglomerating into nuclei. Inhibitor molecules can also retard crystal growth by either adsorbing onto the crystal surface (the growth sites) or fitting into the crystal lattice to replace one of the scaling ions (usually the anion). By doing so, it distorts the crystal lattice or the growth steps thus preventing the crystal from growing rapidly in a regular morphology.

If small scale crystals have already formed in solution, an inhibitor may also prevent the crystals from adhering to each other and to other surfaces by dispersing them in the fluid. The small crystals are hence carried along with the fluid and scale deposition is minimized. A particular inhibitor often inhibits scale formation with a primary inhibition mode. Some are better at exhibiting one particular inhibition mechanism than the other.

Testing and selecting the right inhibitor for a given scale problem is very critical for successful scale control (Yuan et al., 2003; Rosario and Bezerra, 2001; Graham et al. (2002); Jordan et al., 2001). The most important step for screening an inhibitor is water sampling. With representative samples available, the water chemistry data which is the most important information needed to diagnose and analyze the scaling potential of produced waters can be obtained. Water chemistry data include concentrations of ions (anions and cations, like calcium, barium, strontium, bicarbonate and sulfate) and pH. Accurate chemistry data of the produced water under the system conditions (in-situ), along with system information such as production data, temperature and pressure as well as gas composition are essential for assessing scale risks and for testing inhibitors.

Obtaining representative water samples requires good practices. For a new oil/gas field, original formation water samples should be collected. Water samples need to be preserved and stabilized at the time of sampling. Samples without preservation often go through changes including precipitation of scaling ions, evolution of carbon dioxide (CO<sub>2</sub>) and pH drift. If a sample is collected without using a pressurized container, pH and bicarbonate should be determined immediately on-site. This is because both will drift rapidly, resulting from CO<sub>2</sub> evolution from the solution. It is also important to determine whether or not the samples have been contaminated by drilling muds and completion fluids before performing analysis. Finally, the water chemistry data should be reviewed by experts to ensure the quality.

Once water chemistry data is available, the scale prediction can be performed using simulation packages. There are a few commercial simulation packages available (Kan et al., 2001; Rosario and Bezerra, 2001; Yuan et al., 2003). Based upon the simulations, the nature of scale and potential

amount of scale that will precipitate can be assessed. And proper scale control technologies/strategies can be eventually developed. A very successful story on how to develop a new scale inhibitor for a specific field problem in the Gulf of Mexico was reported by [Yuan et al. \(2003\)](#).

A successful scale inhibitor has to have the following properties:

- It must inhibit scale formation at threshold inhibitor levels under a range of brine, temperature, and pressure conditions.
- It should have good compatibility with the produced water to avoid the formation of solids and or suspensions. Some scale inhibitors will react with calcium, magnesium or barium ions to form insoluble compounds which can precipitate to form scales, thus creating new problems.
- It should have good compatibility with the valves, wellbore, and flowline materials, e.g., low corrosivity on metals. Thus, corrosivity test is necessary.
- It should be compatible with other chemicals, like corrosion inhibitors, wax inhibitors, and hydrate inhibitors. The scale inhibitor should be physically compatible with other chemicals so no solids will form. The scale inhibitor should also be compatible with other chemicals so their individual performance will not be significantly interfered. It was reported by [Kan et al. \(2001\)](#) that hydrate inhibitors (methanol and glycols) would impact the solubility of sulfate minerals and the effectiveness of scale inhibitors may be impacted.
- It must be thermally stable under the application temperature and within the residence time. This can be challenging for some fields with high formation temperatures.
- Its residuals in a produced brine must be detectable for monitoring purposes.

For controlling the scales in wellbore and in pipelines, scale inhibitor is required to be injected continuously so it can inhibit the growth of each scale crystal as it precipitates from the water. Scale inhibitor must be present in the water upstream of the point that scale precipitation occurs to have the maximum effectiveness for inhibiting further growth. That is why in a lot of cases scale inhibitor is injected at the bottom of wellbore.

If scale is a risk in formation, especially near wellbore region, it is not practical to continuously inject inhibitor into formation. Scale squeeze operations to bullhead inhibitor into formation are required. Scale squeeze has been used extensively in North Sea fields for quite a long time ([Graham et al., 2002](#)) and is relative new in South Africa and Gulf of Mexico operations. An extensive literature is available on scale squeeze operations ([Lynn and Nasr-El-Din, 2003](#); [Collins et al., 1999](#); [Bourne et al., 2000](#); [Graham et al., 2002](#); [Jordan et al., 2001](#)).

If sulfate scales are due to the seawater injection, an alternative scale control strategy is to partially remove the sulfate ions from the injected seawater. Sulfate removal can be achieved by using a desulfation plant ([Davis and McElhiney, 2002](#); [Vu et al., 2000](#); [Graham et al., 2002](#)). Sulfate removal plant can reduce the sulfate content from the typical level of 2700–3000 ppm to a value in the range of 40–120 ppm. With the much reduced sulfate ions in the seawater, the tendency for sulfate scale formation will be significantly reduced. However, even with sulfate removal operation, scale squeeze and/or scale control in production stream may still be required. But the squeeze frequency will be reduced.

Once scales are formed in the production facilities, they can be removed either by mechanical means, such as pigging, or by dissolving using chemicals. When brush or scraper pigs are run through the pipeline, they can mechanical remove some of the scale deposits on the pipe wall. But if the deposits which may contain scales, waxes, and/or asphaltenes are too hard, pigging may not be very effective.

Acids can react with scales and dissolve the scale deposits on pipe wall. For calcium carbonate scales, either hydrochloric acid or chelating agents can be used. Calcium sulfate scale is not soluble to hydrochloric acid, inorganic converters, like ammonium carbonate ((NH<sub>4</sub>)<sub>2</sub>CO<sub>3</sub>), can be used to convert it into calcium carbonate which can then be dissolved using hydrochloric acid. Since it is quite possible that hydrocarbons can deposit on the surface of the scales and hydrocarbons can interfere with the acid reaction with the scales, it is necessary to prewash the scales using hydrocarbon solvents. Furthermore, to keep the acid from dissolving the pipe wall, a corrosive inhibitor is also necessary to be added to the acid.

### 21.3.6 CORROSION

With gas, oil, and water flowing through offshore pipeline, one of the important flow assurance issues is corrosion. This is because an aqueous phase is almost always present in the oil and gas fluids. When enough water is flowing through the pipeline, the water would wet the pipe inner surface and corrosion can occur. The corrosivity of the liquid phase depends upon the concentrations of CO<sub>2</sub> and H<sub>2</sub>S, temperature, pressure, flow regime, and flowrates. Corrosion can occur in a subsea production system with different forms: galvanic corrosion, pitting, cavitation, stress corrosion cracking, hydrogen embrittlement, corrosion fatigue, etc. Corrosion can result in millions of dollars loss if a subsea pipeline is not properly protected. Pipeline engineers need to understand the corrosion fundamentals to design sound strategies that will effectively control corrosion and protect the pipelines.

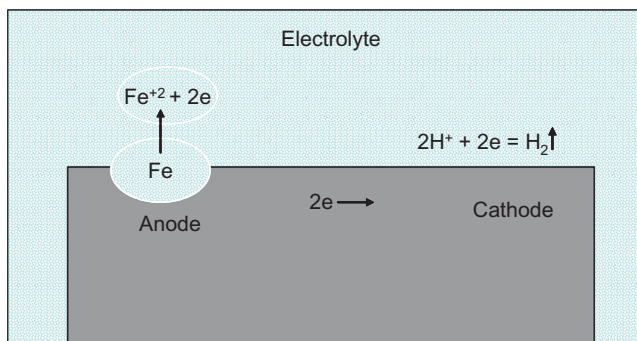
The phenomena associated with corrosion in gas, oil, and water multiphase flow is very complex, involving the chemistry of the produced fluids, the metallurgy of the pipeline material, and the multiphase flow hydraulics. During their refining process, metals absorbed quite a significant amount of extra energy. Because of the extra energy, metals are unstable in aqueous environments. With the right chemical process, the metals would corrode and return to their original lower energy, stable states. Different metals have different energy stored and thus have different corrosion tendency. The metals used for subsea pipeline and well tubulars are not homogeneous and the potential differences of these inhomogeneous materials are the primary cause of corrosion (Cramer and Covino, 1987; Fontana and Greene, 1967).

Corrosion that involves conductive water is called wet corrosion and is an electrochemical process. There are four basic fundamental elements in a corrosion process:

- An anode
- A cathode
- An electrolyte
- A conducting circuit

Fig. 21.7 shows the corrosion process. When a piece of metal is put in a conductive fluid, like water, due to the potential difference among different materials, a portion of the metal surface is easier to corrode than the rest. This portion of metal is called anode where metal dissolves into the conductive fluid. Thus, during corrosion, metal is lost by dissolving into solution. The chemical reaction is described as:



**FIGURE 21.7**

Schematic of the corrosion process.

where

$e$  = electron

$Fe$  = iron atom

$Fe^{+2}$  = iron ion

By losing 2 electrons, iron atom becomes iron ion which is positively charged. The electrons left behind would travel to another area on the metal surface which is called cathode where the electrons are consumed by reaction with ions in the electrolyte. For example, if the electrolyte is conductive water:



where

$H^{+}$  = hydrogen ion

$H_2$  = hydrogen gas

To complete the electric circuit, a conductive solution to conduct the current from the anode to the cathode is needed. The conductive solution is called electrolyte. Water with dissolved solids is a good electrolyte. A path is also needed to conduct the current from the cathode to the anode. The metal itself provides the path and completes the electric circuit. Thus, the anode, the cathode, the electrolyte, and the electron conductor form the essential elements (corrosion cell) for metal corrosion.

The environment for subsea pipeline system provides favoring formation of corrosion cell. The metals used for the pipeline system can serve as anode, cathode, and the metallic conductor between the two. The water, either produced or injected seawater, provides the electrolyte required to complete the electron circuit. Pipeline consists of dissimilar metals that may have different tendency to corrode with the higher tendency metal to be the anode and the lower tendency metal to be the cathode. Even with the same metal, due to the inhomogeneity, one local metal area (anode) can be more corrosive than the other (cathode).

The amount of gas dissolved in water greatly impacts its corrosivity. For water with no dissolved gases, the water will normally cause no corrosion problems. On the other hand, if gases, like

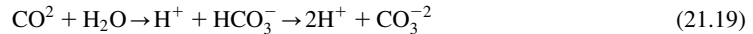
oxygen, carbon dioxide, and hydrogen sulfide, are dissolved in water, the water would be very corrosive. The corrosion reactions involved with the three gases can be expressed as the following:

For carbon dioxide:

At the anode



At the cathode



Combining the above two equations, we have



For oxygen:

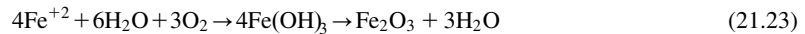
At the anode



At the cathode



Combining the two equations:

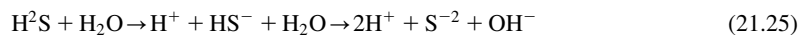


For hydrogen sulfide

At the anode



At the cathode



By combining the above two equations, we have:



From the above discussions, it is clear that there are a few parameters that would control the corrosion reactions: the reactions at the cathode and anode, the flow of electrons from the anode to the cathode, and the conductivity of the electrolyte. These controlling factors are the main parameters dealt in almost all the corrosion prediction models (de Waard and Lotz, 1993; Nescic et al., 1995). If the reactions at both anode and cathode can be reduced, for example, by using corrosion inhibitors to slow down the ion transport in the electrolyte, the corrosion rate will be slowed down. Similarly, if the electrolyte is less conductive due to the removal of dissolved oxygen, carbon dioxide, or hydrogen sulfide, the corrosion rate will also be reduced. The conductivity of the electrolyte can be reduced by adding chemicals to increase the pH value of the electrolyte. These are the methods that are widely used in industry for corrosion control (Strommen, 2002; Kolts et al., 1999).



Corrosions can occur in different forms and can be caused by a variety of different reasons. Pitting corrosion is formed when localized holes or cavities are created in the material due to metal loss. Pitting corrosion can occur if the protective film is not uniformly applied to the metal surface. Poorly applied film areas are easier to be corroded. Pitting corrosion is very disastrous because it is difficult to detect. One single pit can cause material fatigue and stress corrosion cracking, and may even cause catastrophic failure of subsea pipelines. Galvanic corrosion is referred as the corrosion due to two dissimilar materials coupled in a conductive electrolyte. With galvanic corrosion, one metal which is generally more corrosive becomes the anode while the less corrosive one becomes the cathode. The anode metal in galvanic corrosion will corrode more rapidly than it would do alone, and the cathode metal will corrode slower than it would do alone. The larger the potential difference between the two metals, the more rapidly the anode will corrode. A very important factor that would impact the galvanic corrosion is the ratio of the exposed area of the cathode to the exposed area of the anode. A small anode to cathode area ratio is highly undesirable. Under this condition, the current is concentrated in a small anodic area and the rapid loss of the dissolving anode will occur. Galvanic corrosion principle can be used favorably to protect the important system by scarifying a dedicated system that will corrode away. This principle is used in so-called cathodic protection systems where steel is connected to a more corrosive metal, like zinc, and is protected. The steel is the cathode and the zinc is the anode. Cavitation occurs when vapor bubbles are repeatedly formed and subsequently collapsed in a liquid on a metal surface. The explosive forces associated with the bubble collapses can damage any protective films and result in increased local corrosion. Cavitation can also cause mechanical damages to the system parts, like pump impellers. Cavitation is less likely to occur in offshore pipelines.

In sour systems, hydrogen can diffuse into metal to fill any voids that may exist in the material. As corrosion continues, hydrogen atoms continue to diffuse into the voids to form hydrogen molecules, increasing the pressure in the voids. Depending upon the hardness of the material, the voids would develop into a blister which is called hydrogen blistering or into cracks which is called sulfide stress cracking. Due to the stress cracking, materials can fail at stress levels below their yield strength. If materials contain elongated defects that are parallel to the surface, hydrogen can get into the defects and create cracks. Once the cracks on different planes inside the metal are connected, the effective wall thickness is reduced. This kind of hydrogen attacks is called hydrogen-induced cracking. [Crolet and Adam \(2000\)](#) reported a form of hydrogen cracking called stress-oriented, hydrogen-induced cracking (SOHIC). SOHIC, which is a hybrid of sulfide stress cracking and hydrogen-induced cracking, is found to be associated with refining in the vicinity of welds that are not stress-relieved. After shutdown, subsea pipelines would experience much colder temperature compared to the normal operation temperatures. The reduced temperature cause thermal contraction and result in increased tensile stress. If the welds were done with imperfections, the welds tend to experience localized corrosion.

There are a few methods available for the corrosion control of subsea pipelines: using CRAs (corrosion resistant alloy) instead of carbon steel, applying corrosion inhibitors, isolating the metal from the electrolyte, and using cathodic protection. One or more of these methods may be used together. Cathodic protection and chemical inhibition can both be used to protect a subsea pipeline.

CRA steel is often used to replace carbon steel for corrosive applications. But CRAs are normally more expensive than carbon steel. Thus, whether or not CRAs should be used depends upon

the overall economics. In subsea applications, the very critical, high impact components, like trees, jumpers, and manifolds, are often made of CRAs. Subsea pipelines, especially long pipelines are often made of carbon steel, continuous corrosion inhibitor injection is utilized to protect the pipeline.

Corrosion inhibitors are chemicals that when added to an environment would affectively reduce the corrosion rate of a metal that is exposed to that environment. Corrosion inhibitors would react with metal surface and adhere to the inner surface of the pipeline and prevent the pipe from corrosion. The surface active compounds in the inhibitor help form a film layer of inhibitor on the surface and prevent the water from touching the pipe wall. A minimum inhibitor concentration is required to provide high inhibition efficiency. But inhibitor concentration that is significantly higher than the minimum required concentration provides little or no additional benefits. Some inhibitors can also slow down the diffusion process of ions to the metal surface and increase the electrical resistance of the metal surface. For example, some specific inhibitors can help slow down the reaction at cathode by forming a deposit layer on cathode area to increase the resistance and limit the ion diffusion process.

In order for the inhibitor to be distributed evenly around the inner pipe wall perimeter, the fluids inside the pipeline have to have a certain high flowing velocity. If the fluid velocity is too low, the inhibitor may not be able to reach the upper portion of the pipe wall and the inhibitor will only form a protective film around the lower portion of pipe wall. On the other hand, if the velocity is too high and causes high near wall shear stress, the protective film may be removed from the pipe wall. For smooth pipeline, the efficiency of corrosion inhibitors can be as high as 85%–95%, but can drop if the shear stress increases drastically at locations such as fittings, valves, chokes, bends, and weld beads. These irregular geometries cause flow separation and reattachment of the flow boundary and increase the rates of turbulence.

In gas/condensate pipeline, adding the hydrate inhibitors, like glycol or methanol, can also help reduce the corrosion rate (Strommen, 2002). This is because the hydrate inhibitors absorb free water and make the water phase less corrosive.

The protective layer to isolate the pipe wall from water can also be achieved by using plastic coating and plastic liners. Water injection pipelines and well tubings often use plastic liners to control corrosion problems.

As we discussed in the previous section, one element of the corrosion cell is the current flow. If we stop the current flow from the anode to the cathode, the corrosion is stopped. This is the principle of cathodic protection, which is one of the widely used corrosion control methods in subsea pipeline. The key for the cathodic protection to work is to provide enough current from an external source to overpower the natural current flow. As long as there is no net current flow from the pipeline, there is no pipeline corrosion.

It is well known that different metals have different tendencies for corrosion in seawater. By connecting more corrosive metal to the subsea pipeline, the pipeline metal is forced to be the cathode while the more corrosive metal is the anode which will be corroded away. In this way, the pipeline corrosion is significantly reduced. The galvanic anodes used in cathodic protection are usually made of alloys of magnesium, zinc, or aluminum, which are much more active in seawater than steel pipeline. With proper design, cathodic protection is one of the most reliable corrosion control methods.

### 21.3.7 SEVERE SLUGGING

One of the flow assurance issues in subsea pipeline is related to production delivery. From the processing point of view, it is always desirable that the fluids coming from the pipeline are stable in compositions and in flow. If the flow arriving the processing is not stable, the processing system may experience upsets that often result in the whole subsea production system shutdown (Song and Peoples, 2003).

A typical subsea production system usually consists of subsea pipeline and production riser. Depending upon the water depth, the riser length ranges from less than one hundred feet, as in shallow water production systems, to a few thousand feet, as in deep water production systems. With a longer production riser, more energy will be required to deliver stable flow to the processing system. For deep water production fields, especially at the late field life stage when the reservoir pressure is low and the total production rate is reduced, the gas and liquid velocities in the pipeline are not high enough to continuously carry the fluids out of the riser, resulting in intermittent (unstable) fluid delivery to the processing devices.

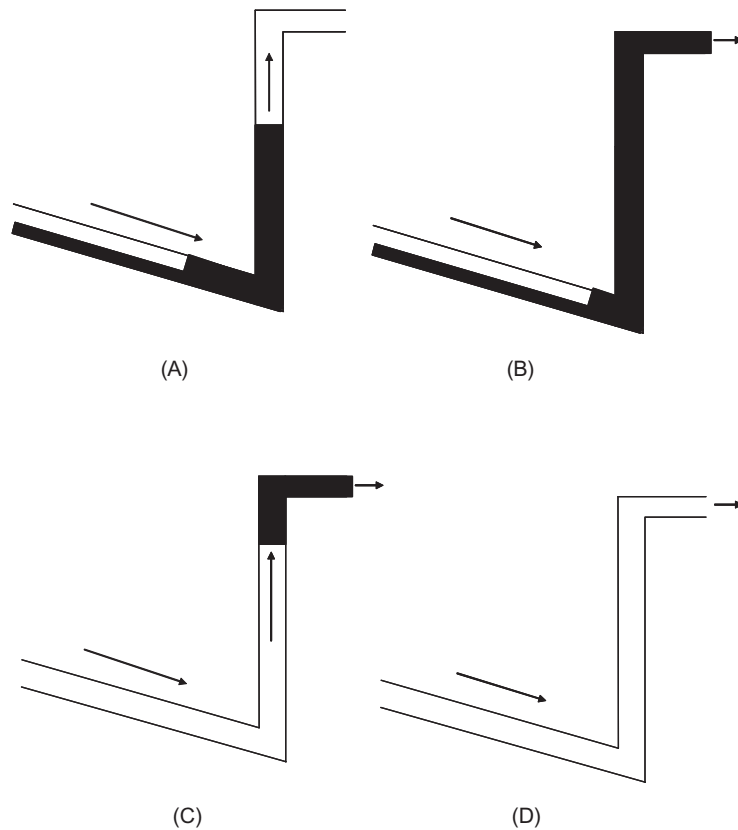
When the liquid cannot be continuously produced out of the riser, the liquid would accumulate at the riser base to form a liquid column, called liquid slug. The liquid slug would completely block the gas flow. When the gas pressure behind the slug is high enough, the liquid slug will be pushed out of the riser, resulting in a huge amount of liquid flowing into processing separator. This phenomenon is called severe slugging. The liquid slug with little or no gas in it would often cause upsets (like high liquid level) in the separator if the separator and its control system are not adequately designed. When liquid slug is being produced, there is little or no gas flowing to the compressors. This can cause compression system problems.

Typical severe slugging would occur in a pipeline riser configuration showing in Fig. 21.8. The pipeline section that is coupled with the riser is normally inclined downward. The pipeline sections upstream from the downward inclined section may be upward inclined, horizontal, or downward inclined.

When the gas and liquid flowrates are low, the liquid cannot continuously flow out of the riser and start to fall back from the riser and accumulate at the riser base, as shown in Fig. 21.8A. This stage is called severe slugging formation or severe slugging generation. During this stage, there is almost no liquid and gas production and no fluid flowing into the separator. While liquid is accumulating at the riser base, gas and liquids are continuously flowing into the riser base from the pipeline inlet. Thus, the liquid column or slug formed at the riser base would continue to grow into the riser and also grow against the flow direction into the pipeline. Depending upon the GOR and other parameters, like system pressure and temperature, the slug inside the pipeline can be a few times longer than the riser height. Since the liquid slug prevents the gas from entering the riser, the pressure behind the slug is building up by the gas flow.

As more and more liquid accumulates at the riser base, the liquid slug would eventually reach the riser top and start to produce the liquid slug, as shown in Fig. 21.8B. This stage is called slug production. During this phase, the liquid is producing into the separator at high velocity and little or no gas is being produced. Because of the high velocity liquid flow and huge amount of liquid associated with the slug, the separator may reach high liquid levels and cause trips or upsets.

When the liquid slug is being produced, the gas would eventually enter the riser, as shown in Fig. 21.8C. When gas enters the riser, the difference between the separator pressure and the gas

**FIGURE 21.8**

Schematic of classical severe slugging formation process. (A) Liquid fall back, (B) liquid slug accumulation and production, (C) gas enters the riser, and (D) gas blowdown.

pressure behind the slug becomes higher and higher as the liquid slug becomes shorter and shorter inside the riser. The liquid slug is being produced or being pushed by the gas at higher and higher velocity. This stage is called liquid blowout.

After the liquid slug is produced, the huge gas packet behind the slug will be blown out of the riser and charge into the separator. This stage is called gas blowdown as depicted in Fig. 21.8D. During this stage, little or no liquid would flow into the separator and low liquid levels may be reached that would eventually cause system upsets and shutdown. The gas blowdown stage in the severe slugging can cause as big a problem as the slug production stage.

Once the gas is blown out of the riser, the pipeline system pressure is reduced. The liquid would again fall back from the riser upper portion and start to accumulate at the riser base. This is the start of the next severe slugging circle. In summary, severe slugging is undesirable because it would cause a period of no liquid and gas production followed by high liquid and gas flows, resulting in large pressure and flow fluctuations which would often cause processing device shutdown. Once the processing system is shutdown, the subsea production system, including trees and pipelines, will have to be shutdown.

Since severe slugging can cause production system shutdown, it is very critical to be able to correctly predict the onset of severe slugging. For a proper design of a subsea pipeline system, the multiphase flow characteristics inside the pipeline has to be checked for the whole field life and the processing devices and their control systems have to be designed to be able to handle the delivered flow from the pipeline. Whether or not severe slugging is a risk will significantly impact the design philosophy of the processing and control system.

Pots et al. (1987) presented a model to predict the onset of severe slugging:

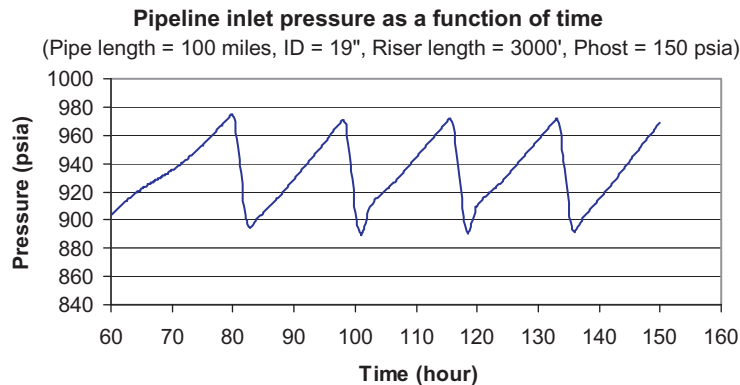
$$\pi_{ss} = \frac{W_g}{W_l} \frac{ZRT}{M_g g L (1 - H_l)} \leq 1 \quad (21.27)$$

where

- $\pi_{ss}$  = Pots' number, dimensionless
- $W_g, W_l$  = gas and liquid mass flowrate, respectively
- $Z$  = gas compressibility factor
- $R$  = gas universal constant
- $T$  = pipeline temperature
- $M_g$  = gas molecular weight
- $L$  = pipeline length
- $g$  = accelerational gravity
- $H_l$  = average liquid holdup inside the pipeline

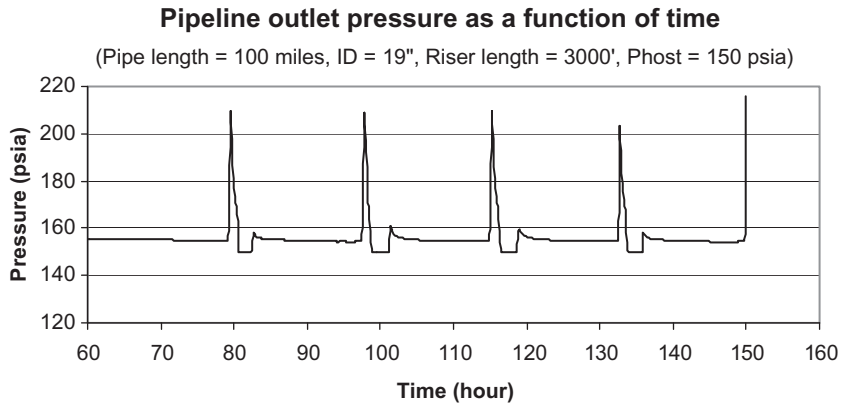
Severe slugging is expected when the Pot's number is equal to or less than unity. Pots' model can be used to determine the onset of severe slugging, but the model cannot predict how long the severe slugs will be and how fast the severe slugs will be produced into separator. For subsea pipeline design, transient multiphase flow simulators are often used to determine the important flow parameters, like pressure, temperature, flow velocity, flow regime, slug frequency, and slug size.

Figs. 21.9–21.11 show typical pipeline inlet pressure, outlet pressure, and outlet gas flowrate as function of time during severe slugging flow (from Song and Kouba, 2000). Those are simulation

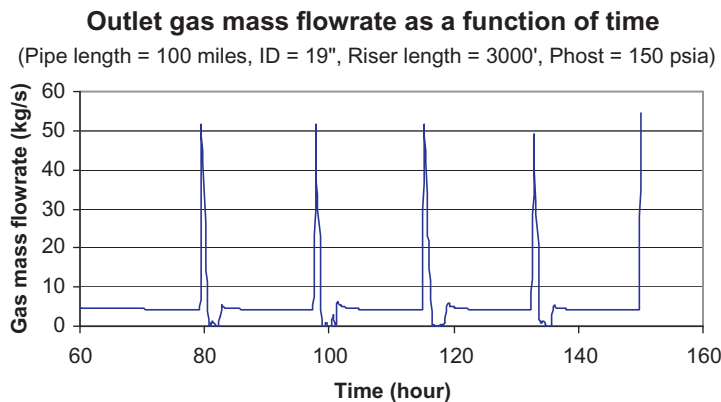


**FIGURE 21.9**

Pipeline inlet pressure as a function of time for severe slugging flow (Song and Kouba, 2000).

**FIGURE 21.10**

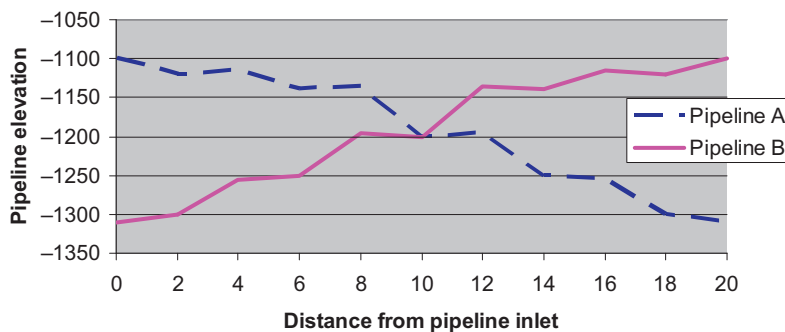
Pipeline outlet pressure as a function of time for severe slugging flow (Song and Kouba, 2000).

**FIGURE 21.11**

Outlet gas mass flowrate as a function of time for severe slugging flow (Song and Kouba, 2000).

results for a pipeline of 19" ID with flowrate of 50 mb/day and GOR of 500 scf/stb. Fig. 21.9 shows how the pipeline inlet pressure changes with time during severe slugging. The inlet pressure fluctuates between 890 psia and 970 psia. The severe slugging occurs once every 20 hours. When the severe slugs are being pushed out from the pipeline outlet, the pipeline outlet pressure also increases as shown in Fig. 21.10. Before the severe slugs are produced, the pipeline outlet pressure is about 150 psia, which equals to the platform pressure.

Fig. 21.11 shows how the outlet gas mass flowrates change with time during severe slug flow. Before the slug is pushed out of the pipeline, the gas mass flow is a constant and the gas flowrate equals to the steady-state flowrate. Once the liquid slug is pushed out, the huge gas pocket behind



**FIGURE 21.12**

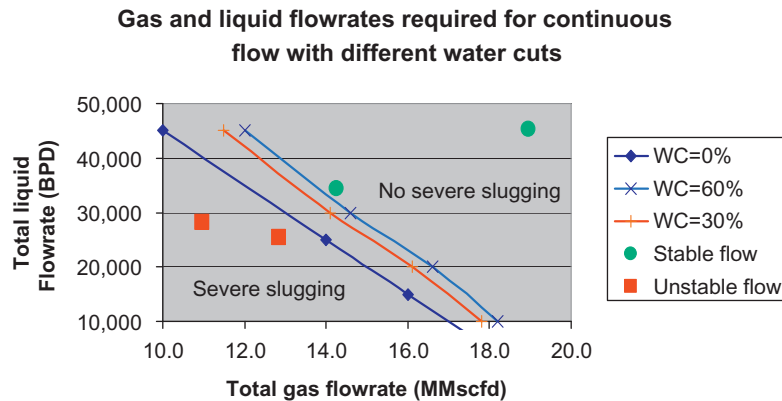
Upwards and downwards inclined pipeline profiles (Song and Kouba, 2000).

the liquid slug is produced, resulting in a much higher gas mass flowrate, as shown in the figure. Once the gas pocket is produced, for a period of time, no gas is flowing out. The same behavior can be expected for the outlet liquid flow.

There are a few methods that can be used to effectively mitigate the severe slugging problems. A pipeline bathymetry is preferred if the pipeline flow is going upwards. In other words, the water depth at the pipeline outlet is preferred to be shallower than that at the inlet. This is because that the multiphase slug flow is much less severe with an upwards inclined pipeline than with a downwards inclined pipeline. The pipeline A shown in Fig. 21.12 will tend to have more severe slugging problems than pipeline B. Thus, it is important that, at the pipeline design stage, the favorable pipeline routing is chosen, if possible, to eliminate severe slugging risks.

One of the main reasons that severe slugging occurs is that the gas velocity is too low to carry the liquid out of the riser. If more gas can be introduced into the pipeline riser system, the gas velocity will be increased and the gas will also help lift the liquid out of the riser by reducing the fluid mixture density. Song and Peoples (2003) reported that a West Africa subsea field, when a well is pulled out of the pipeline for testing, the flow inside the pipeline would change to severe slugging flow due to the reduced production. But if enough extra gas is added into the flowline before the well is shifted out for well testing, the gas can help stabilize the flow inside the pipeline and no severe slugging will occur. They developed a plot showing the required total liquid and total gas flowrates for continuous stable flow for different water cut, as shown in Fig. 21.13. For a given liquid flowrate, if the total gas flowrate is high enough that the flowing condition is above the curve, no severe slugging will occur. Otherwise, severe slugging will occur. The individual points in the figure are field measurements. This information, together with well test data, was used by operations personnel to estimate when severe slug flow was likely. The primary mitigating measure that the operations personnel undertook to avoid slugging was to increase gas flow inside the pipeline.

If enough gas can be injected at the riser base to change the flow inside the riser to hydrodynamic slug flow, churn flow, or annular flow (Song and Kouba, 2000), the severe slugging problem can be mitigated. With hydrodynamic slug flow or churn flow, the slugs are much shorter than the slugs in

**FIGURE 21.13**

Required total gas flow for stable flow in flowline for different water cut (Song and Kouba, 2000).

the severe slugging flow. Topside separators normally are sized to handle the hydrodynamic this kind of slugs and no system shutdown is likely. If sufficient gas is injected at the riser base to change the flow to annular flow, the flow will even be more stable. But to reach annular flow, a significant amount of gas will be needed and may not be practical.

Severe slugging can be mitigated by choking the flow at the top of the riser. Choking the flow would increase the system pressure and make the system “stiffer.” With increased system pressure, the gas becomes less compressible. Thus, when the liquid slug formed at the riser base blocks the gas flow, the gas pressure behind the liquid slug would increase quicker and be able to push the liquid slug out of riser quicker. In this way, the liquid accumulation time is shorter and the liquid slugs will consequently be smaller. So the severe slugs are minimized. But choking would increase the system back pressure and thus reduce the overall production.

Song and Kouba (2000) performed studies on severe slugging elimination using subsea separation. It is understood that the favorable condition for severe slugs to form is that gas and liquid simultaneously flow through a long riser at low velocities. It is very difficulty to change the fluid velocity that is controlled by the production rates and pipe size. But, it is possible to separate the gas from the liquid and let the gas and the liquid flow through two different pipelines or risers. In this way, the gas and the liquid will not be flowing simultaneously through the riser and severe slugging can, thus, be avoided. Seafloor separation becomes one of the methods that can potentially solve the severe slugging problems associated with deep water production. Based upon their studies, Song and Kouba concluded:

- Subsea separation can help mitigate severe slugging. By separating the gas from the liquid, it is possible to eliminate severe slugs. This is especially true for riser base separation.
- Subsea separation can boost the production by reducing the back pressure assuming single-phase liquid pump is used to boost the liquid.
- There is an optimum separator location for subsea applications. For certain flowrates and pipe sizes, it is more effective to put the separator at the riser base than at the wellhead.



- For the purpose of eliminating the severe slugs, the requirement for the subsea separation efficiency is not very high. Based on the study, for the riser base separation, as long as the separation efficiency is higher than 75%, severe slugs can be eliminated.

One disadvantage associated with riser base separation is that two risers will be required.

---

## 21.4 SUMMARY

This chapter describes several flow assurance issues in oil and gas pipeline operations including wax and asphaltene, corrosion, scales, and severe slugging. They all attribute to operational problems in oil and gas transportation in pipelines. In-depth analyses are found in references (Guo et al., 2004, 2013).

---

## REFERENCES

- API RP 44, 1966. API Recommended Practice for Sampling Petroleum Reservoir Fluids. American Petroleum Institute, Washington, DC.
- API RP 45, 1968. API Recommended Practice for Analysis of Oil-Field Waters. American Petroleum Institute, Dallas, TX.
- Barton, A.F.M., 1991. CRC Handbook of Solubility Parameters and Other Cohesive Parameters. second ed. CRC Press, Boca Raton, FL.
- Bourne, H.M., Heath, S.M., McKay, S., Fraser, J., Muller, S., 2000. Effective treatment of subsea wells with a solid scale inhibitor system. In: Presented at the 2000 International Symposium on Oilfield Scales held in Aberdeen, 2000.
- Brown, T.S., Niesen, V.G., Erickson, D.D., 1993. Measurement and prediction of the kinetics of paraffin deposition. In: Presented at the SPE Annual Technical Conference and Exhibition, 1993.
- Buckley, J.S., Hirasaki, G.J., Liu, Y., Von Drasek, S., Wang, J.X., Gill, B.S., 1998. Asphaltene precipitation and solvent properties of crude oils. *Pet. Sci. Technol.* 16 (3&4), 251–285.
- Burger, E.D., Perkins, T.K., Striegler, J.H., 1981. Studies of wax deposition in the trans alaska pipeline. *J. Pet. Technol.* 33, 1075–1086.
- Burke, N.E., Hobbs, R.E., Kashou, S., 1990. Measurement and modeling of asphaltene precipitation. *J. Pet. Technol.* 42, 1440–1446.
- Carlberg, B.L., Matches, R.R., 1973. Solubility of calcium sulfate in brine. In: SPE paper presented at the Oilfield Chemistry Symposium of the SPE, Denver, TX, 1973.
- Chancey, D.G., 1987. Measuring, sampling, and testing crude oil, chapter 17. In: Bradley, H.B. (Ed.), *Petroleum Engineering Handbook*. Society of Petroleum Engineers, Richardson, TX.
- Collins, I.R., Cowie, L.G., Nicol, M., Stewart, N.J., 1999. Field application of a scale inhibitor squeeze enhancing additive. *SPE Prod. Facil.* 14, 21–29.
- Cramer, S.D., Covino, B.S., 1987. *ASM Handbook Volume 13A: Corrosion: Fundamentals, Testing, and Protection*. ASM International, Materials Park, OH.
- Creek, J.L., Matzain, A., Apte, M.S., Brill, J.P., Volk, M., Delle Case, E., et al., 1999. Mechanisms for wax deposition. In: Presented at the AIChE National Spring Meeting, Houston, TX, 1999.
- Crolet, J.L., Adam, C., 2000. SOHIC without H<sub>2</sub>S. *Mater. Performance* 39, 86–90.

- Davis, R.A., McElhiney, J.E., 2002. The advancement of sulfate removal from seawater in offshore waterflood operations. In: Presented at the NACE Corrosion 2002, Denver, TX, 2002.
- De Boer, R.B., Leerlooyer, K., Eigner, M.R.P., van Bergen, A.R.D., 1992. Screening of crude oils for asphalt precipitation: theory, practice, and the selection of inhibitors. In: Presented at the European Petroleum Conference held in Cannes, France, November 1992.
- De Waard, C. Lotz, U., 1993. Prediction of CO<sub>2</sub> corrosion of carbon steel. In: Paper No. 69, Corrosion 93.
- [Fontana, M.G., Greene, N.D., 1967. Corrosion Engineering. McGraw-Hill, New York.](#)
- Graham, G.M., Sorbie, K.S., Jordan, M.M., 1997. How scale inhibitors work and how this affects test methodology. In: Presented at the 3rd International Conference on Advances in Solving Oilfield Scaling, Aberdeen, 1997.
- Graham, G.M., Mackay, E.J., Dyer, S.J., Bourne, H.M., 2002. The challenges for scale control in deepwater production systems: chemical inhibition and placement. In: Presented at the NACE Corrosion 2002, Denver, TX, 2002.
- [Groffe, D., Groffe, P., Takhar, S., Andersen, S.I., Stenby, E.H., Lindeloff, N., et al., 2001. A wax inhibition solution to problematic fields: a chemical remediation process. \*Pet. Sci. Technol.\* 19 \(1–2\), 205–217.](#)
- [Guo, B., Song, S., Chacko, J., Ghalambor, A., 2004. Offshore Pipelines. Elsevier, Oxford.](#)
- [Guo, B., Song, S., Ghalambor, A., Lin, T., 2013. Offshore Pipelines. second ed. Elsevier, Oxford.](#)
- Hammami, A., Raines, M., 1997. Paraffin deposition from crude oils: comparison of laboratory results to field data. In: Presented at the SPE Annual Technical Conference and Exhibition, 1997.
- Hammami, A., Phelps, C.H., Monger-McClure, T., Mitch Little, T., 1999. Asphaltene precipitation from live oils: an experimental investigation of the onset conditions and reversibility. In: Presented at the AIChE 1999 Spring National Meeting, Houston, TX, 1999.
- [Hirschberg, A., deJong, L.N.J., Schipper, B.A., Meijer, J.G., 1984. Influence of temperature and pressure on asphaltene flocculation. \*SPE J.\* 24, 283–293.](#)
- Hsu, J.C., Elphinstone, G.M., Greenhill, K.L., 1999. Modeling of multiphase wax deposition. *J. Energy Res, Technol, Trans. ASME* 121, 81–85.
- Huron, M.J., Vidal, J., 1979. New mixing rules in simple equations of state for representing vapor-liquid equilibria of strongly non-ideal mixtures. *Fluid Phase Equilib.* 3, 255–271.
- [Jacues, D.F., Bourland, B.I., 1983. A study of solubility of strontium sulfate. \*J. Pet. Technol.\* 23, 292–300.](#)
- Jordan, M.M., Sjuraether, K., Collins, I.R., Feasey, N.D., Emmons, D., 2001. Life cycle management of scale control within subsea fields and its effect on flow assurance. Gulf of Mexico and the North Sea Basin. SPE paper 71557. In: Proceedings of the SPE Annual Technical Conference and Exhibition. Louisiana, New Orleans, 30 September–3 October 2001.
- Kan, A.T., Fu, G. and Tomson, M.B., 2001. Mineral-scale control in subsea completion. In: Presented at the 2001 Offshore Technology Conference held in Houston, 2001.
- [Katz, D.L., Firoozabadi, A., 1998. Predicting phase behavior of condensate/crude-oil systems using methane interaction coefficients. \*J. Pet. Technology.\* 20.](#)
- Kolts, J., Joosten, M., Salama, M., Danielson, T.J., Humble, P., Belmear, C., et al. 1999. Overview of britannia subsea corrosion-control philosophy. In: Presented at the 1999 Offshore Technology Conference held in Houston, TX, 1999.
- Lynn, J.D., Nasr-El-Din, H.A., 2003. A novel low-temperature, forced precipitation phosphonate squeeze for water sensitive, non-carbonate bearing formations. In: Presented at the SPE Annual Technology Conference and Exhibition held in Denver, TX, 2003.
- [Mathias, P.M., Copeman, T.W., 1983. Extension of the Peng-Robinson equation of state to complex mixtures: evaluation of the various forms of the local composition concept. \*Fluid Phase Equilib.\* 13, 91–108.](#)
- Meray, V.R., Volle, J.L., Schranz, C.J.P., Marechal, P.L., Behar, E., 1993. Influence of light ends on the onset crystallization temperature of waxy crudes within the frame of multiphase transport. In: Presented at the 68th Annual Technical Conference and Exhibition of the Society of Petroleum Engineers, 1993.

- Monger-McClure, T.G., Tackett, J.E., Merrill, L.S., 1999. Comparisons of cloud point measurement and paraffin prediction methods. *SPE Prod. Facil.* 14 (1), 4–16.
- Nesic, S., Postlethwaite, J., Olsen, S., 1995. An electrochemical model for prediction of CO<sub>2</sub> corrosion. In: Paper No. 131, Corrosion 95.
- Ostrof, A.G., 1979. *Introduction to Oilfield Water Technology*. second ed. National Association of Corrosion Engineers, Houston, TX.
- Pedersen, K.S., Bliilie, A., Meisingset, K.K., 1992. PVT calculations of petroleum reservoir fluids using measured and estimated compositional data for the plus fraction. *Ind. Eng. Chem. Res.* 31, 1378–1384.
- Pedersen, K.S., Fredenslund, A., Thomassen, P., 1989. *Properties of Oils and Natural Gases*. Gulf Publishing Inc, Houston, TX.
- Pedersen, K.S., Milter, J., Rasmussen, C.P., 2001. Mutual solubility of water and reservoir fluids at high temperatures and pressures, experimental and simulated phase equilibrium data. *Fluid Phase Equilibria* 189, 85–97.
- Peneloux, A., Rauzy, E., Fréze, R., 1982. A consistent correlation for Redlich-Kwong-Soave volumes. *Fluid Phase Equilib.* 8, 7–23.
- Pedersen, K.S., Thomassen, P., Fredenslund, A., 1985. Thermodynamics of petroleum mixtures containing heavy hydrocarbons. 3. efficient flash calculation procedures using the SRK equation of state. *Ind. Eng. Chem. Process Des. Dev.* 24, 163–170.
- Peng, D.-Y., Robinson, D.B., 1976. A new two-constant equation of state. *Ind. Eng. Chem. Fundam.* 15, 59–64.
- Peng, D.-Y., Robinson, D.B., The characterization of the heptanes and heavier fractions for the GPA Peng-Robinson programs, GPA Research Report RR-28, 1978.
- Pots, B.F.M., Bromilov, I.G., Konijn, M.J.W.F., 1987. Severe slug flow in offshore flowline/riser system. *SPE Prod. Eng.* 2, 319–324.
- Reid, R.C., Prausnitz, J.M., Sherwood, J.K., 1977. *The Properties of Gases and Liquids*. McGraw-Hill, New-York.
- Riazi, M.R., Daubert, T.E., 1980. Prediction of the Composition of Petroleum Fractions. *Ind. Eng. Chem. Process Des. Dev.* 19, 289–294.
- Rosario, F.F., Bezerra, M.C., 2001. Scale potential of a deep water field—Water characterisation and scaling assessment. In: Presented at the 2001 SPE 3rd International Symposium on Oilfield Scale in Aberdeen, 2001.
- Singh, P., Gogler, H.S., Nagarajan, N., 1999. Prediction of the wax content of the incipient wax-oil gel in a flowloop: an application of the controlled-stress rheometer. *J. Rheol.* 43, 1437.
- Soave, G., 1972. Equilibrium constants from a modified Redlich-Kwong equation of state. *Chem. Eng. Sci.* 27, 1197–1203.
- Song, S., Kouba, G., 2000. Fluid transport optimization using seabed separation. In: Presented at the Energy Sources Technology Conference & Exhibition, 14–17 February in New Orleans, 2000.
- Song, S., Peoples, K., 2003. Impacts of transient analysis on kuito production operations. In: Presented at the 2003 Offshore Technology Conference held in Houston, TX, 2003.
- Sorensen, H., Pedersen, K.S., Christensen, P.L., 2002. Modeling of Gas Solubility in Brine, *Org. Geochem.* 33, 635–642.
- Strommen, R.D., 2002. Seven years experience from subsea, deepwater pipeline internal corrosion monitoring. In: Paper No. 2251, Corrosion 2002.
- Tsonopoulos, C., Heidman, J.L., 1986. High-pressure vapor-liquid equilibria with cubic equations of state. *Fluid Phase Equilib.* 29, 391.
- Venkatesan, R., Singh, P., Fogler, H.S., 2002. Delineating the pour point and gelation temperature of waxy crude oils. *SPE J.* 7, 349–352.

- Vu, V.K., Hurtevent, C., Davis, R.A., 2000. Eliminating the need for scale inhibition treatments for Elf exploration Angola's Girassol field. In: Presented at 2000 International Symposium on Oilfield Scale held in Aberdeen, 2000.
- Wang, J.X., Buckley, J.S., Burke, N.A., Creek, J.L., 2003. Anticipating asphaltene problems offshore—A practical approach. In: Presented at the 2003 Offshore Technology Conference, Houston, TX, 2003.
- Wang, K.S., Wu, C.H., Creek, J.F., Shuler, P.J., Tang, Y.C., 2003. Evaluation of effects of selected wax inhibitors on paraffin deposition. *Pet. Sci. Technol.* 21 (3–4), 369–379.
- Weingarten., J.S., Euchner, J.A., 1986. Methods for predicting wax precipitation and deposition. In: Presented at the SPE Annual Technical Conference and Exhibition, 1986.
- Yuan, M., Williamson, D.A., Smith, J.K., Lopez, T.H., 2003. Effective control of exotic mineral scales under harsh system conditions. In: Presented at the SPE International Symposium on Oilfield Chemistry held in Houston, TX, 2003.

---

## PROBLEMS

- 21.1. What is the difference between wax and scales? How to remove them?
- 21.2. What is the difference between wax and asphaltene? How to reduce asphaltene?
- 21.3. How do corrosion inhibitors work? How to reduce corrosion?
- 21.4. What is the reason for severe slugging? How to reduce the severity of slugging?

---

# PIPELINE PIGGING

# 22

---

## 22.1 INTRODUCTION

The term pig was originally referred to Go-Devil scrapers driven through the pipeline by the flowing fluid trailing spring-loaded rakes to scrape wax off the internal walls. One of the tales about the origin of the name pig is that the rakes made a characteristic loud squealing noise. Pipeline operators now describe any device made to pass through a pipeline for cleaning and other purposes with the word pig. The process of driving the pig through a pipeline by fluid is called a pigging operation (Kennedy, 1993).

Although pigs were originally developed to remove deposits, which could obstruct or retard flow through a pipeline, today pigs are used during all phases in the life of a pipeline for many different reasons. During pipeline construction, pigging is used for debris removing, gauging, cleaning, flooding, and dewatering. During fluid production operations, pigging is utilized for removing wax in oil pipelines, removing liquids in gas pipelines, and meter proving. Pigging is widely employed for pipeline inspection purposes such as wall thickness measurement and detection of spanning and burial. Pigging is also run for coating the inside surface of pipeline with inhibitor and providing pressure resistance during other pipeline maintenance operations. Fig. 22.1 shows pipeline deposits displaced by a pig. This chapter describes how to apply different pigging techniques to solve various problems in the pipeline operations.

---

## 22.2 PIGGING SYSTEM

A pigging system includes pigs, a launcher, and a receiver. It also includes pumps and compressors, which are not discussed here because they have to be available for transporting the product fluids anyway. Obviously pigs are the most essential equipment. Although each pipeline has its own set of characteristics that affects how and why pigging is utilized, there are basically three reasons to pig a pipeline: (1) to batch or separate dissimilar products; (2) to displace undesirable materials; and (3) to perform internal inspections. The pigs used to accomplish these tasks fall into three categories (Mare, 1985):

1. Utility Pigs, which are used to perform functions such as cleaning, separating, or dewatering.
2. In-Line Inspection Tools, which provide information on the condition of the line, as well as the extent and location of any problems.
3. Gel Pigs, which are used in conjunction with conventional pigs to optimize pipeline dewatering, cleaning, and drying tasks.

**FIGURE 22.1**

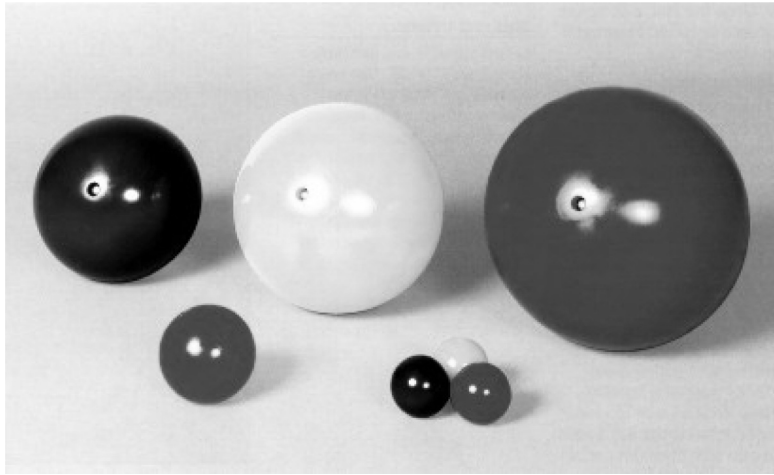
Pipeline deposits that could obstruct or retard flow through a pipeline.

*Courtesy of Pigging Products & Services Association.*

### 22.2.1 UTILITY PIGS

Utility pigs can be divided into two groups based upon their fundamental purpose: (1) cleaning pigs used to remove solid or semi-solid deposits or debris from the pipeline, and (2) sealing pigs used to provide a good seal in order to either sweep liquids from the line, or provide an interface between two dissimilar products within the pipeline. Within these two groups, a further subdivision can be made to differentiate among the various types or forms of pigs: Spherical Pigs, Foam Pigs, Mandrel Pigs, and Solid Cast Pigs.

Spherical pigs, or spheres, are of either a solid composition or inflated to their optimum diameter with glycol and/or water. Fig. 22.2 shows some spheres. Spheres have been used for many years as a sealing pig. There are four basic types of spheres: inflatable, solid, foam, and soluble. Soluble spheres are usually used in crude oil pipelines containing microcrystalline wax and paraffin inhibitor. Spheres normally dissolve in a few hours. The dissolving rate depends on fluid temperature, fluid movement, friction, and absorbability of the crude. If the line has never been pigged, it is a good idea to run the soluble pig. If it hangs up in the line, it will not obstruct the flow. Inflatable spheres are manufactured of various elastomers (polyurethane, neoprene, nitrile and Viton) depending on their applications. An inflatable sphere has a hollow center with filling valves that are used to inflate the sphere with liquid. Spheres are filled with water, or water and glycol, and inflated to the desired size. Spheres should never be inflated with air. Depending on the application and material, the sphere is inflated 1%–2% over the pipe inside diameter. As the sphere wears from service, it is resized, extending its life. In small sizes the sphere can be manufactured



**FIGURE 22.2**

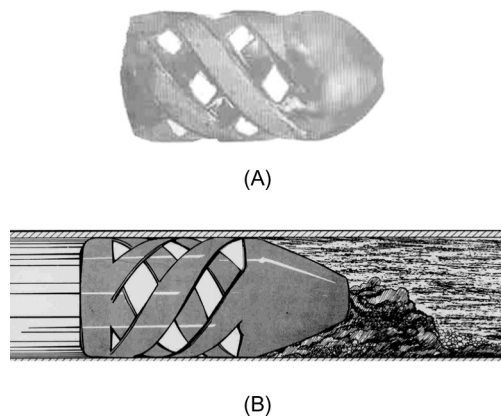
Some spheres used in the pipeline pigging operations.

*Courtesy of Girard Industries, Inc.*

solid, eliminating the need to inflate it. The solid sphere does not have the life of an inflatable sphere because it cannot be resized. Spheres can also be manufactured from open cell polyurethane foam. They can be coated with a polyurethane material to give better wear. For cleaning purposes they can have wire brushes on the surface. The advantages of the foam sphere are that they are lightweight, economical, and do not need to be inflated. Spheres in general are easy to handle, negotiate short radius, 90° angles, irregular turns and bends. They go from smaller lateral lines to larger main lines and are easier to automate than other styles of pigs. Spheres are commonly used to remove liquids from wet gas systems, serve to prove fluid meters, control paraffin in crude oil pipelines, flood pipeline to conduct hydrostatic test, and de-water after pipeline rehabilitation or new construction. Special design considerations for the pipeline should be considered when using spheres. They should never be run in lines that do not have special flow tees installed.

Foam pigs, also known as Polly-Pigs, are molded from polyurethane foam with various configurations of solid polyurethane strips and/or abrasive materials permanently bonded to them. Fig. 22.3 demonstrates a foam pig and how it works.

Foam pigs are molded from open cell polyurethane foams of various densities ranging from light density (2 lbs/ft<sup>3</sup>), through medium density (5–8 lbs/ft<sup>3</sup>), to heavy density (9–10 lbs/ft<sup>3</sup>). They are normally manufactured in a bullet shape. They can be bare foam or coated with a 90-durometer polyurethane material. The coated pigs may have a spiral coating of polyurethane, various brush materials or silicon carbide coating. If the pig is of bare foam, it will have the base coated. The standard foam pig length is twice the diameter. Foam pigs are compressible, expandable, lightweight, and flexible. They travel through multiple diameter pipelines, go around mitered bends, and short radius 90° bends. They make abrupt turns in tees so laterals can be cleaned. They also go through valves with as little as 65% opening. The disadvantages of foam pigs are that they

**FIGURE 22.3**

(A) A foam pig (B) An ideal foam pig cleaning the pipeline.

*Courtesy of Montauk Service, Inc.*

are one-time use products; shorter length of runs, and high concentrations of some acids will shorten life. Foam pigs are also inexpensive. Foam pigs are used for pipeline proving, drying and wiping, removal of thick soft deposits, condensate removal in wet gas pipelines and pigging multiple diameter lines. Foam pigs coated with a wire brush or silicon carbide are used for scraping and mild abrasion of the pipeline.

A mandrel pig has a central body tube, or mandrel, and various components can be assembled onto the mandrel to configure a pig for a specific duty. Fig. 22.4 demonstrates some mandrel pigs.

The pig is equipped with wire brushes or polyurethane blades for cleaning the line. The mandrel pig can be either a cleaning pig, or a sealing pig, or a combination of both. The seals and brushes can be replaced to make the pig reusable. Cleaning pigs are designed for heavy scraping and can be equipped with wire brushes or polyurethane blades. These pigs are designed for long runs. Bypass holes in the nose of the pig control the speed or act as jet ports to keep debris suspended in front of the pig. The cost of redressing the pig is high, and larger pigs require special handling equipment to load and unload the pig. Occasionally the wire brush bristles break off and get into instrumentation and other unwanted places. Smaller size mandrel pigs do not negotiate 1.5D bends.

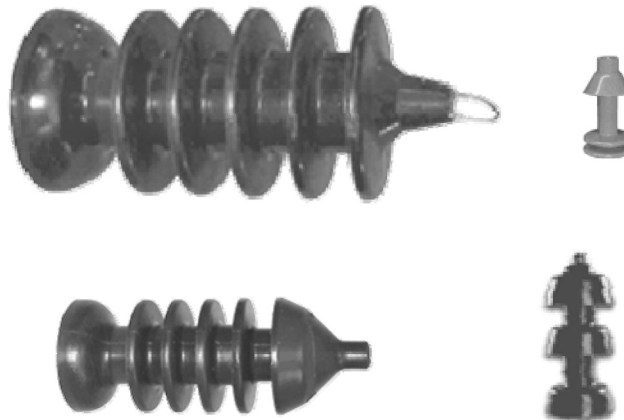
Solid cast pigs are usually molded in one piece, usually from polyurethane, however neoprene, nitrile, Viton, and other rubber elastomers are available in smaller size pigs. Fig. 22.5 demonstrates some solid cast pigs. Solid cast pigs are considered sealing pigs although some solid cast pigs are available with wrap-around brushes and can be used for cleaning purposes. The solid cast pig is available in the cup, disc, or a combination cup/disc design. Most of the pigs are of one-piece construction but several manufacturers have all urethane pigs with replaceable sealing elements. Because of the cost to redress a mandrel pig, many companies use the solid cast pig up through 14" or 22". Some solid cast designs are available in sizes up to 36". Solid cast pigs are extremely effective in removing liquids from product pipelines, removing condensate and water from wet gas systems, and controlling paraffin build-up in crude oil systems.



**FIGURE 22.4**

Some mandrel pigs used in pipeline pigging operations.

*Courtesy of Girard Industries, Inc.*

**FIGURE 22.5**

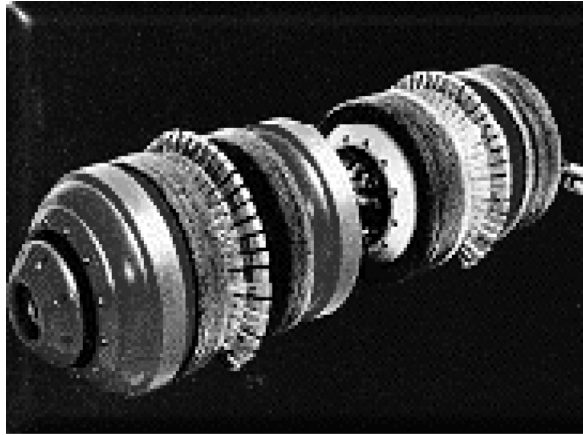
Some solid cast pigs used in pipeline pigging operations.

*Courtesy of Apache Pipeline Products, Inc.*

### 22.2.2 IN-LINE INSPECTION TOOLS

In-line inspection tools are used to carry out various types of tasks including:

- Measuring pipe diameter/geometry
- Monitoring pipeline curvature
- Determining pipeline profile
- Recording temperature/pressure

**FIGURE 22.6**

An ultrasonic inspection tool.

*Courtesy of Pigging Products and Services Association.*

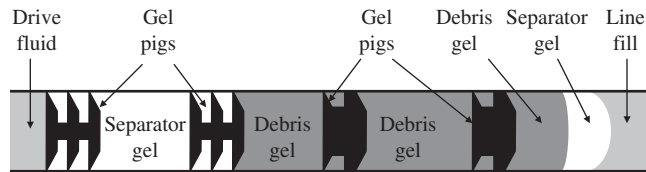
- Measuring bend
- Detecting metal-loss/corrosion
- Performing photographic inspection
- Detecting crack
- Measuring wax deposition
- Detecting leak
- Taking product samples
- Mapping

A typical in-line inspection tool is an ultrasonic tool shown in [Fig. 22.6](#). Ultrasonic in-line inspection tools are used for measuring metal loss and detecting crack of pipelines. Ultrasonic tools are especially suitable if there are high requirements regarding sensitivity and accuracy, which is especially relevant in offshore pipelines. Ultrasound tools are also well suited with regard to the range of wall thicknesses usually experienced in offshore lines.

### 22.2.3 GEL PIGS

Gel pigs have been developed for use in pipeline operations, either during initial commissioning, or as a part of a continuing maintenance program. [Fig. 22.7](#) shows how gel pigs work. The principle pipeline applications for gel pigs are as follows:

- Product separation
- Debris removal
- Line filling/hydrotesting
- Dewatering and drying



**FIGURE 22.7**

Application of gel pigs in pipeline pigging operations.

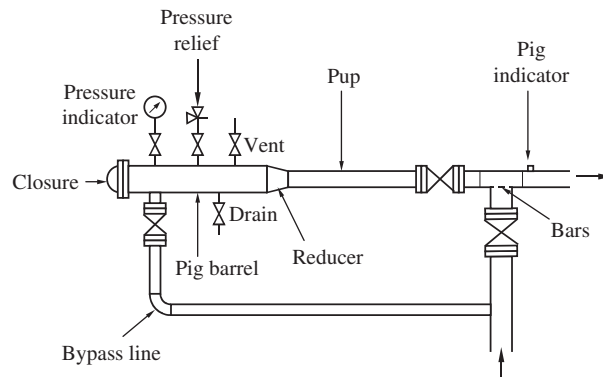
- Condensate removal from gas lines
- Inhibitor and biocide laydown
- Special chemical treatment
- Removal of stuck pigs

Most pipeline gels are water-based, but a range of chemicals, solvents, and even acids can be gelled. Some chemicals can be gelled as the bulk liquid and others only diluted in a carrier. Gelled diesel is commonly used as a carrier of corrosion inhibitor in gas lines. The four main types of gel used in pipeline applications are: batching, or separator gel; debris pickup gel; hydrocarbon gel; and dehydrating gel. The gel can be pumped through any line accepting liquids. Gel pigs can be used alone (in liquid lines), in place of batching pigs, or in conjunction with various types of conventional pigs. When used with conventional pigs, gelled pigs can improve overall performance while almost eliminating the risk of sticking a pig. Gel pigs do not wear out in service like conventional pigs. They can, however, be susceptible to dilution and gas cutting. Care must be taken when designing a pig train that incorporates gel pigs to minimize fluid bypass of the pigs, and to place a conventional pig at the back of the train when displacing with gas. Specially formulated gels have also been used to seal gate valves during hydrostatic testing. Gels have been developed with a controlled gelation time and a controlled viscosity for temporary pipeline isolation purposes.

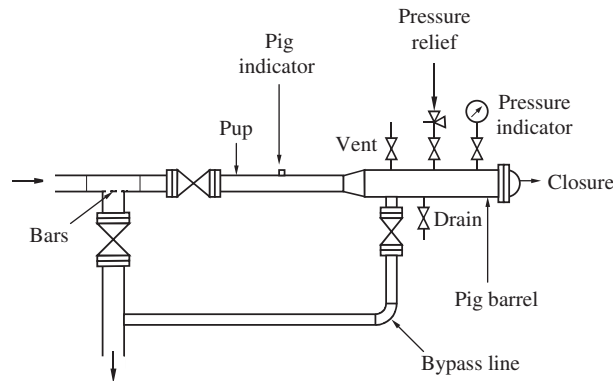
#### 22.2.4 LAUNCHER AND RECEIVER

Pigs generally need specially designed launching and receiving vessels (launcher and receiver) to introduce them into the pipeline. The launcher and receiver are installed at the upstream and downstream of the pipeline section being pigged, respectively. The distance between the launcher and receiver depends on the service, location of pump (liquid product) or compressor (gas product) stations, operating procedures, and the materials used in the pig. In crude oil pipeline systems, the distance between launcher and receiver can be as long as 500 miles for spheres and 300 miles for pigs. The amount of sand, wax, and other materials carried along the pig can affect the proper distance. In gas transmission service, the distance between the launcher and receiver can be as long as 200 miles for spheres and 100 miles for pigs, depending on the amount of lubrication used.

The launcher and receiver consist of a quick opening closure for access, an oversized barrel, a reducer and a neck pipe for connection to the pipeline. Pigs can be located using fixed signalers along the pipe or electronic tracking systems mounted inside the pig. A typical configuration of pig

**FIGURE 22.8**

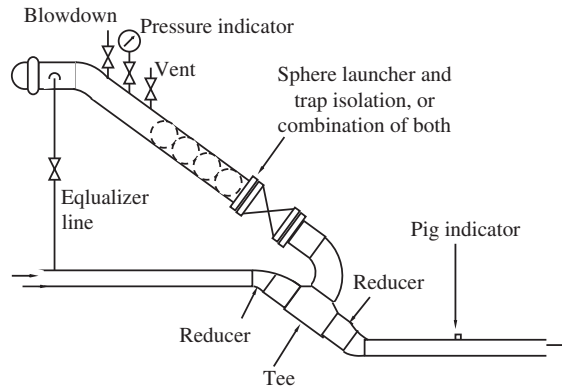
A typical configuration of pig launcher for liquid services.

**FIGURE 22.9**

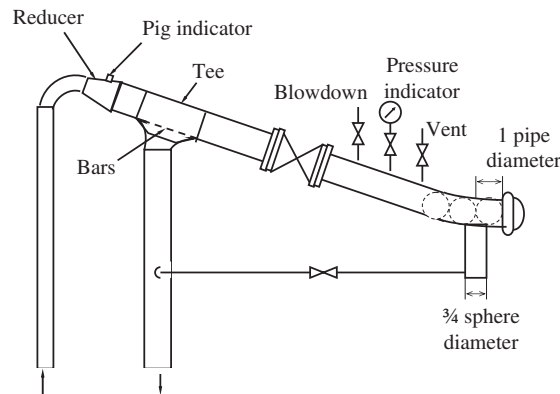
A typical configuration of pig receiver for liquid services.

launcher for liquid service is illustrated [Fig. 22.8](#). The horizontal barrel holds the pig for loading. [Fig. 22.9](#) shows a typical configuration of pig receiver for liquid service. The horizontal barrel holds the pig for unloading. A barrel diameter 2 in. larger than the diameter of pipeline has been recommended for both launchers and receivers. The barrel length should be 1.5 times the pig length and long enough to hold 10 or more spheres.

Typical configurations of pig launchers and receivers for gas service are depicted in [Figs. 22.10 and 22.11](#), respectively. The inclined barrels should be long enough to hold 10 or more spheres. In large-diameter gas pipelines, the barrel diameter can be 1 in. larger than the pipeline.

**FIGURE 22.10**

A typical configuration of pig launcher for gas services.

**FIGURE 22.11**

A typical configuration of pig receiver for gas services.

## 22.3 SELECTION OF PIGS

The purpose of operational pigging is to obtain and maintain efficiency of the pipeline to be pigged. The pipeline's efficiency depends on two things: first, it must operate continuously, and second, the required throughput must be obtained at the lowest operating cost. The type of pig to be used and its optimum configuration for a particular task in a particular pipeline should be determined based upon several criteria, including:

- Purpose of pigging
  - type, location, and volume of the substance to be removed or displaced
  - type of information to be gathered from an intelligent pig run
  - objectives and goals for the pig run

- Line contents
  - contents of the line while pigging
  - available vs required driving pressure
  - velocity of the pig
- Characteristics of the pipeline
  - the minimum and maximum internal line sizes
  - the maximum distance the pig must travel
  - the minimum bend radius, and bend angles
  - additional features such as valve types, branch connections, and the elevation profile

### 22.3.1 CLEANING PIGS

Cleaning pigs are designed to remove solids or accumulated debris in the pipeline. This increases the efficiency and lowers the operating cost. They have wire brushes to scrape the walls of the pipe to remove the solids. Pigs of 14" and smaller normally use rotary wire wheel brushes. These brushes are easy to replace and inexpensive. Special rotary brushes are used on some larger pigs. Larger pigs have wear-compensating brushes. These brushes can be individually replaced as needed and are mounted on either leaf springs, cantilever springs, or coil springs. The springs push the brushes against the pipe wall. As the wire brushes wear, the force of the spring keeps it in contact with the pipe wall, compensating for the brush wear. There are many different brush materials available. The standard brushes are made of fine or coarse carbon steel wire. For pipelines with internal coatings, Prostran is the material of choice. Some service requires a stainless steel brush. Special brush designs such as the pit cleaning brush are also available. When soft deposits of paraffin, mud, etc., need to be removed, the urethane blade is an excellent choice. The blade design is interchangeable with the brushes. Bypass ports are installed in the nose of the pig or on the body. These ports are used to control fluid bypass. If the ports are on the body of the pig, the flow will also flow through the brushes and keep them clean. As the fluid passes through the ports on the nose of the pig, it helps keep the debris in front of the pig stirred up and moving. Plugs are used to regulate the bypass. The sealing elements are either elastomer cups or discs. They are used as a combination cleaning and sealing element to remove soft deposits. Cups are of standard or conical design. Specialty cups are available for some applications. The cup and disc material is normally manufactured from a polyurethane material, which gives outstanding abrasion and tear resistance, but is limited in temperature range. Neoprene, nitrile, ethylene-propylene diene monomer (EPDM), and Viton are available for higher temperature applications.

The best choice for cleaning applications are normally pigs with discs, conical cups, spring mounted brushes and bypass ports. Fig. 22.12 shows details of two pigs of this type. Discs are effective for pushing out solids and providing good support for the pig. Conical cups provide sealing characteristics, good support, and long wear. Spring mounted brushes provide continuous forceful scraping for removal of rust, scale and other build-ups on the pipe wall. Instead of brushes, polyurethane scraper blades can also be selected for cleaning waxy crude oil lines because the scraper blades are easier to clean than brushes. Bypass ports allow some of the flow to bypass through the pig. This can help minimizing solids build-up in front of the pig. For a new pipeline construction, it is a good practice to include a magnetic cleaning assembly in the pig.



**FIGURE 22.12**

Some mandrel pigs used in pipeline pigging operations.

*Courtesy of T. D. Williamson, Inc.*

### 22.3.2 GAUGING PIGS

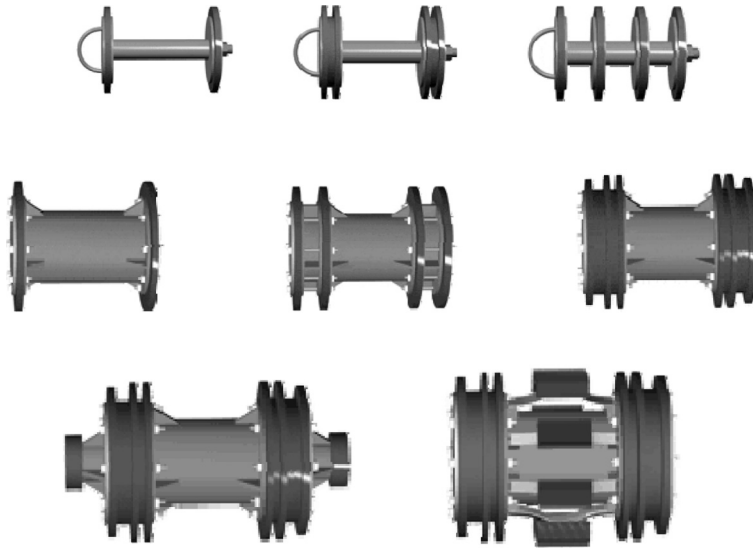
Gauging pigs are used after constructing the pipeline to determine if there are any obstructions in the pipeline. These obstructions can be caused by partially closed valves, wrinkle bends, ovality caused by overburden, dents caused by rocks underneath the pipe, third party damage, buckles caused by flooding, earthquakes, etc. Gauging pig assures that the ovality of the line is within accepted tolerance. The gauging plate may be mounted on the front or rear of the pig and is made of a mild steel or aluminum. The plate may be slotted or solid. The outside diameter of the plate is 90%–95% of the pipe's inside diameter. Gauging runs are normally done during new construction and prior to running a corrosion inspection pig. The best practice is to choose inspection tools that can provide critical information about the line such as determining the location (distance), o'clock position and severity of a reduction ([Muhlbauer, 1992](#)).

### 22.3.3 CALIPER PIGS

Caliper pigs are used to measure pipe internal geometry. They have an array of levers mounted in one of the pig cups. The levers are connected to a recording device in the pig body. The body is normally compact, about 60% of the internal diameter, which combined with flexible cups allows the pig to pass constrictions up to 15% of bore. Caliper pigs can be used as gauging pigs. The ability of caliper pig to pass constrictions means minimum risk of jamming. This is very important for subsea pipelines where it would be very difficult and expensive to locate a stuck pig.

### 22.3.4 DISPLACEMENT PIGS

Displacement pigs displace one fluid with another based on sealing mechanism. They can be bidirectional or unidirectional in design. They are used in the testing and commissioning phase of the



**FIGURE 22.13**

Some bi-directional pigs used in pipeline pigging operations.

*Courtesy of Apache Pipeline Products, Inc.*

pipeline, i.e., hydrostatic testing, line fills and de-watering, etc. Line evacuation and abandonment is another application for the displacement pig. Bi-directional (Fig. 22.13) pigs can be sent back to the launch sight by reversing flow should they encounter an obstacle. They are also used in filling and dewatering associated with hydrostatic testing when the water used to fill the line has to be pushed back to its source after completion of test.

The best choice of displacement pigs are normally pigs with multilipped conical cups (Fig. 22.14). Conical cups can maintain contact with the pipe wall even in out-of-round pipe, which is more common in large-diameter pipelines. Conventional cups and discs usually cannot maintain a seal in the out-of-round pipe. Multilipped cups have numerous, independent sealing lips on each cup, which significantly improves its ability to maintain a seal.

### 22.3.5 PROFILE PIG

A profile pig is a gauging pig with multiple gauging plates, usually three plates. One plate is mounted on the front, one in the middle, and one on the rear of the pig. It is normally used before running an ILI (In-Line Inspection) tool to assure the tool's passage around bends and through the pipeline.





**FIGURE 22.14**

Pig with multilipped conical cups.

*Courtesy of T. D. Williamson, Inc.*

### 22.3.6 TRANSMITTER PIGS

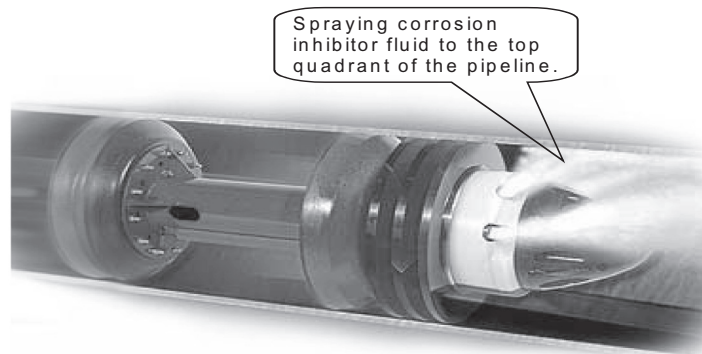
Occasionally pigs will get stuck in a line. The location of the stuck pig can be found by using a detector pig with a transmitter in its body. The transmitter emits a signal so it can be located with a receiver. Transmitters are normally mounted into a mandrel, solid cast, or Polly-Pig.

### 22.3.7 SPECIAL PIGS

Many applications require special pigs. Manufacturers in the pigging industry have made special pigs for many applications. Fig. 22.15 illustrates that a special pig can be used for spraying corrosion inhibitor to the upper side of pipe interior. Dual Diameter Pigs are designed for pigging dual diameter pipelines. They are usually mandrel pigs fitted with solid discs for the smaller line and slotted discs for the larger line. If it is a cleaning pig, the brushes will support it in the line and keep the pig centered. The Polly-Pig is also widely used in this application.

Other special pigs include pinwheel pigs, which use steel pins with hardened tips. They were developed to remove wax and scale from a pipeline. Magnetic cleaning pigs were developed to pick up ferrous debris left in the pipeline.

There are many pig configurations to choose from but some configurations will not work in some pipelines. It is very important to compare pipeline information to the pig specifications. The best way to stay out of trouble is to provide the pipeline specifications to the pig manufacturer and ask them to recommend a pig.

**FIGURE 22.15**

A special pig for spraying corrosion inhibitor.

*Courtesy of T. D. Williamson, Inc.*

## 22.4 MAJOR APPLICATIONS

Major applications of pigging are found during pipeline construction, operation, inspection, and maintenance. Depending on application type and pipeline conditions, different kinds of pigs are chosen to minimize the cost of pigging operations. [Tiratsoo \(1992\)](#) presents a comprehensive description of applications of pigging in the pipeline industry.

### 22.4.1 CONSTRUCTION

During pipeline construction, it is quite possible for construction debris to get inside the pipeline. The debris could harm downstream equipment such filters and pumps. The only way to remove possible debris is to run a pig through the pipeline. Typically, debris removal is done section by section as the lay barge moves forward. An air-driven cleaning pig is usually sent through the pipeline section to sweep out the debris. Features of the cleaning pig should be selected based on anticipated pipeline conditions. The most effective way to clear debris is by the use of a magnetic cleaning assembly which can be mounted on conventional pigs. The removal of this type of debris is a must before attempting to run corrosion inspection pigs.

Pipelines subjected to subsea conditions may buckle in certain sections. The place for a buckle to occur during pipe laying is most likely the sag bend just before the touchdown on the seabed. To detect the buckle, a gauging pig is pulled along behind the touchdown point. If the pig encounters a buckle, the towing line goes taut indicating that it is necessary to retrieve and replace the buckled section of the pipeline. Features of the gauging pig should be selected based on anticipated pipeline conditions. Caliper pigs can be used as gauging pigs after completion of construction. The ability of caliper pig to pass constrictions can reduce the possibility of jamming, which is vitally important for subsea pipelines where it would be very difficult and expensive to locate a stuck pig.

Upon completion of construction, the pipeline should be cleaned to remove rust, dirt, and mill-scale that contaminate product fluids. These contaminants also reduce the effectiveness of corrosion inhibitor. A typical cleaning operation would consist of sending through a train of displacement pigs with different features suitable to the pipeline conditions. Gel slugs are used to pick up the debris into suspension, clearing the pipeline more efficiently. Corrosion inhibitor can also be added to the interior of the pipeline in the trip of cleaning pigging.

After cleaning, the pipeline is flooded with water for hydrotesting. Air must be completely removed so that the pipeline can be pressurized efficiently. Pigging with displacement pigs is normally the best solution for flooding a pipeline. Use of bi-directional batching pigs is favorable for the afterward-dewatering operation.

Upon a successful hydrotest, water is usually displaced with air, nitrogen, or the product fluid. Since dewatering is the reverse process of flooding, a bi-directional batching pig used to flood the pipeline, left during the hydrotest, can be used to dewater the pipeline. In cases of gas service pipelines, it is necessary to dry the pipeline to prevent formation of hydrates and waxy solids. For this purpose, methanol or glycol slugs can be sent through the pipeline between batching pigs. An alternative means of drying the pipeline is to vacuum the pipeline with vacuum pumps.

### 22.4.2 OPERATION

During fluid production operations, pigging is utilized to maintain efficiency of pipelines by removing wax in oil pipelines and liquids (water and condensate) in gas pipelines. Sometimes pigging operations are for meter proving. Pipeline wax is characterized as long-chain paraffin formed and deposited in pipelines due to changes in pressure and temperature. Accumulation of wax in pipeline reduces the effective pipeline hydraulic diameter and hence efficiency of the pipeline. A variety of cleaning pigs are available to remove wax. Most of them work on the principle of causing a bypass flow through the body of the pig over the brushes or scrapers and out to front. The pigs used for removing wax should be selected to have features of inducing the bypass flow. The action of the pig also polishes wax remaining on the pipe wall, leaving a surface for low flow resistance of product fluids. To remove hard scale deposits, aggressive and progressive pigs are the best choice. They can be used with cleaning fluids that help to attack the deposits and/or help to keep the deposits in suspension while being pushed out of the line. This is a very special application that would normally be provided by a pipeline cleaning service company. Samples of the deposits are usually required for chemical analysis and to see what cleaning fluids are best suited. Sometimes chemical cleaning is used for removal of specific types of pipe deposits. Chemical cleaning is a process of using pigs in conjunction with environmentally friendly detergent-based cleaning fluids and is almost always done by pipeline cleaning service companies. The detergents help to suspend solid particles and keep them in a slurry thus allowing removal of large volumes of solids in one pig run. Samples of the material to be removed from the line are required in order to select the best cleaning fluid. The cleaning fluids are captured between batching and cleaning pigs and normally a slug of the fluid is introduced in front of the first pig.

In gas service pipelines, liquid water and/or gas condensate can form and accumulate on the bottom of the pipeline. The liquid accumulation reduces flow efficiency of the pipeline. It can also develop slug flow causing problems with the processing facilities. Different types of displacement and cleaning pigs are available to remove the liquids. Because gas is the drive fluid, the pigs used

for removing the liquids in the gas pipeline should be selected to have features of good sealing. Spheres are usually the preferred choice for liquid removal from wet gas systems. Most of these systems are designed to automatically (remotely) launch and receive spheres. A large number of spheres can be loaded into the automatic launcher and launched at predetermined frequencies. At the receiving end of the line is a slug catcher to capture all the liquid pushed in by a sphere. If more liquid is brought in than the slug catcher can handle, the plant normally shuts down. Thus spheres are launched at a frequency that prevents exceeding the capacity of the slug catcher. Pipeline systems are normally designed for use with spheres or pigs but not both. Pipelines designed for spheres may require modifications of launchers and receivers in order to run conventional pigs.

To clean pipelines with known internal corrosion, special pigs are available that have independent scraping wires that will go into a pit to break up and remove deposits that prevent corrosion inhibitors from getting to the corroding area. Brushes on conventional pigs will not extend into a pit. To clean internally coated pipelines, the preferred choice is a pig with discs and cups as these will normally remove deposits from the coating due to the “teflon like” characteristics of epoxy coatings. Conventional cleaning pigs with “prostran” brushes or polyurethane blades can also be used on internally coated pipelines.

### 22.4.3 INSPECTION

A variety of intelligent pigs have been employed for pipeline inspection purposes including detection of not only dents and buckles but also corrosion pitting, cracks, spanning and burial, and measurement of wall thickness. The information obtained from the pigging operations is used for assessment of pipeline safety and integrity.

Magnetic-flux leakage pigs have been used for detection of dents and buckles, and measurement of pipe ovality and wall thickness over the entire pipe surface. The principle of magnetic-flux leakage detection relies on measurement of metal loss, and hence the size of defect. Usually a series of survey runs over years are required to establish trends. Magnetic-flux leakage pigging can be utilized in liquid and gas pipelines.

Ultrasonic intelligent pig is used to make direct measurement of wall thickness of the entire pipe surface. They are better suited to liquid pipelines and cannot be used in gas pipelines without a liquid couplant.

Pipeline spans have traditionally been found by external inspection using side-scan sonar or remotely operated vehicles (ROVs). In recent years, neutron-scatter pigs have been employed to detect spanning and burial in subsea pipelines with lower cost and better accuracy.

### 22.4.4 MAINTENANCE

Pigging is also run for maintenance of pipelines for coating the inside surface of pipeline, providing pressure resistance, installing barrier valves. Traditionally the internal surfaces of pipe joints are precoated with a smooth epoxy liner and leave the welds uncoated. Recently a pigging system has been developed to coat the entire pipeline internal surface by first cleaning the surface and then pushing through a number of slugs of epoxy paint.

Shutting down offshore, especially deepwater, pipelines for maintenance is very expensive. With advanced technology, it is possible to carry out some maintenance jobs without shutting down the pipeline. In cases where there are not enough isolation valves, a pressure-resisting plug may be pigged into the pipeline to seal off downstream operation.

Corrosion inhibitors are normally injected into the line on a continuous basis and carried through the line with the product flow. Sometimes inhibitors are batched between two pigs but there is no way to guarantee the effectiveness of this method especially at the 12 o'clock position. Special pigs have been developed that spray inhibitor to the top of the pipe as they travel through the pipe. This is done by using a siphoning effect created by bypass flow through an orifice specifically designed to pick up inhibitor from the bottom of the pipe.

---

## 22.5 PIGGING PROCEDURE

### 22.5.1 PRESSURE AND FLOW RATE

Any pigging operation should follow a safe procedure that is suitable to the given pipeline conditions. Operating pigging pressures and fluid flow rates should be controlled carefully. Velocity of driving fluid is usually between 3 ft per second to 5 ft per second during pigging. Recommended ranges of operating pressures and flow rates are presented in [Table 22.1 \(McAllister, 2002\)](#).

### 22.5.2 PRERUN INSPECTION

The pig must be in good condition if it is to do the job it was selected to do. If the pig has been run before, it should be inspected to assure it will run again without stopping in the pipeline. Measure the outside diameter of the pig's sealing surface. This diameter must be larger than the inside pipe diameter to maintain a good seal. Inspect the sealing surfaces to assure there are no cuts, tears, punctures or other damage that will affect the pig's ability to run in the pipeline. The unrestrained diameter of brush pigs should also be measured to assure that the brushes will maintain contact with the pipe wall during the complete run. When using brush type mandrel cleaning pigs, the brushes should be inspected for corrosion or breakage. Every precaution should be taken to prevent these brushes from breaking in the pipeline. Loose bristles can damage valves, instrumentation, and other pipeline equipment. All components of brush type mandrel pigs should be checked to be certain that they are tight and in good condition.

### 22.5.3 PIG LAUNCHING AND RECEIVING

Pig launchers are used to launch the pig into the pipeline, and pig receivers are used to receive the pigs after they have made a successful run. The design of these pig traps will depend on the type of pig to be run and pipeline design conditions. Provisions in the station design should include handling equipment for pigs of 20" and larger. Caution should be taken for liquid spillage from the pig traps.

**Table 22.1 Recommended Pigging Pressures and Flow Rates**

Pipe Inner Diameter (in)	Typical Pigging Pressure (psig)		Liquid Flow Rate (GPM)		Gas Flow Rate (SCFM)	
	Launching	Running	3 FPS	5 FPS	5 FPS	10 FPS
2	100–200	40–100	20	40	30	60
3	100–150	35–85	60	100	70	140
4	75–125	30–80	110	190	120	240
6	50–100	30–75	260	430	270	540
8	30–80	25–70	460	770	440	880
10	30–60	25–50	720	1200	580	1200
12	30–50	20–45	1040	1700	760	1500
14	20–50	15–40	1400	2300	930	1900
22	15–45	10–40	1800	3100	1100	2200
18	15–40	10–30	2300	3900	1200	2400
20	10–25	5–20	2900	4800	1200	2400
24	10–25	5–20	4100	6900	1700	3400
30	10–20	5–15	6500	10,900	2400	4800
36	10–20	5–10	9400	15,700	3200	6400
40	10–20	5–10	11,600	19,400	4000	8000
42	10–20	5–10	12,800	21,400	4400	8800
48	10–20	5–10	22,700	27,900	5800	11,600
54	10–20	5–10	21,200	35,300	7300	14,600
60	10–20	5–10	26,200	43,600	9000	18,000
72	10–20	5–10	37,700	62,900	13,000	26,000

The following pig-launching procedures can be used as a guideline for developing operating procedures. Since company policies vary regarding whether the pig launcher is left on stream or isolated from the pipeline after the pig is launched, the operator should verify that the trap is isolated from the pipeline and depressurized before commencing any part of the launch procedure.

To launch pigs, make sure that the isolation valve and the kicker valves are closed. In liquid systems, open the drain valve and allow air to displace the liquid by opening the vent valve. In natural gas systems, open the vent and vent the launcher to atmospheric pressure. When the pig launcher is completely drained (no pressure left), with the vent and drain valves still open, open the trap (closure) door. Install the pig with the nose firmly in contact with the reducer between the barrel and the nominal bore section of the launcher. Clean the closure seal and other sealing surfaces, lubricate if necessary, and close and secure the closure door. Close the drain valve. Slowly fill the trap by gradually opening the kicker valve and venting through the vent valve. When the filling is completed, close the vent valve to allow pressure to equalize across the isolation valve. Open the isolation valve. The pig is ready for launching. Partially close the main line valve. This will increase the flow through the kicker valve and behind the pig. Continue to close the main line valve until the pig leaves the trap into the main line as indicated by the pig signaler. After the pig leaves

the trap and enters the main line, fully open the main line valve. Close the isolation valve and the kicker valve. The pig launching is complete.

To receive pigs, make sure the receiver is pressurized. Fully open the bypass valve. Fully open the isolation valve and partially close the main line valve. Monitor the pig signaler for pig arrival. Close the isolation valve and bypass valve. Open the drain valve and the vent valve. Check the pressure gauge on the receiver to assure the trap is completely depressurized. Open the trap closure and remove the pig from the receiver. Clean the closure seal and other sealing surfaces, lubricate if necessary, and close and secure the trap (closure) door. Return the receiver to the original condition.

#### 22.5.4 FREEING A “STUCK” PIG

The goals of “pigging” a pipeline include not only running pigs to remove a product or to clean the line, but to do the work without sticking the pig. Getting the pig stuck rarely happens in pipeline that is pigged routinely, but can happen when pigging a pipeline that has been neglected or never pigged before. It is a good practice to run a low density ( $2 \text{ lb/ft}^3$ ) foam pig in any “suspect” pipeline and examine the foam pig for wear patterns, tears, gouges, etc. The pigging project should be continued only after feeling comfortable that the line is piggable. If a pig becomes stuck, it is important to identify the cause. Retrieving the pig is the first priority. When bi-directional pigs are used, the stuck pigs may be recovered with reverse flow.

Pig tracking is normally done on critical projects and when attempting to locate stuck pigs. A pig tracking system consists of a transmitter mounted on the pig, an antenna, and a receiver that records and stores each pig passage. In addition, the operator can see and hear the signal of the pig passing under the antenna. The antenna and receiver are simply laid on the ground above and in line with the pipe and the passage of the pig is heard, seen and recorded. Inexpensive audible pig tracking systems are also available, however, they cannot be used to find a stuck pig as they rely on the noise the pig makes as it travels through the line. Sometimes a pig without a transmitter fails to come in to the receiver because it gets stuck somewhere in the line. When this happens, the pig cups usually flip forward and flow continues around the stuck pig. In order to find the stuck pig, another pig with a transmitter is launched and tracked closely at all points that are readily accessible. When the transmitter pig passes one tracking point but never reaches the next point, it is assumed the transmitter pig has reached the stuck pig and they are both stuck. The line is then walked carrying the antenna and receiver until the transmitter pig is pinpointed. Both pigs and the debris ahead of the pigs are then removed by cutting the pipe behind and well ahead of the stuck pig.

---

## 22.6 SUMMARY

This chapter provides a description of pipeline pigging systems. Utility pigs, in-line inspection tools, and gel pigs are used for pipeline cleaning and inspection operations. Pigs are selected based on applications. Different launchers and receivers are employed for oil and gas pipeline systems. Pigging pressures and flow rates are recommended based on pipeline size.

---

## REFERENCES

- Kennedy, J.L., 1993. Oil and Gas Pipeline Fundamentals. PennWell Books, Tulsa, OK.
- Mare, R.F.D., 1985. Advances in Offshore Oil & Gas Pipeline Technology. Gulf Publishing Company, Boston, MA.
- McAllister, E.W., 2002. Pipeline Rules of Thumb Handbook. Gulf Publishing Company, Boston, MA.
- Muhlbauer, W.K., 1992. Pipeline Risk Management Manual. Gulf Publishing Company, Houston, TX.
- Tiratsoo, J.N.H., 1992. Pipeline Pigging Technology. second ed. Gulf Publishing Company, Accrington.

---

## PROBLEMS

- 22.1. What types of pigs are used for pipeline commissioning?
- 22.2. What type of pig is used for pipeline inspection?
- 22.3. How to free a stuck pig?



# Appendix A: Unit Conversion Factors

Quantity	U.S. Field Unit	To SI Unit	To U.S. Field Unit	SI Unit
Length ( <i>L</i> )	feet (ft)	0.3084	3.2808	meter (m)
	mile (mi)	1.609	0.6214	kilometer (km)
	inch (in.)	25.4	0.03937	millimeter (mm)
Mass ( <i>M</i> )	ounce (oz)	28.3495	0.03527	gram (g)
	pound (lb)	0.4536	2.205	kilogram (kg)
	Lbm	0.0311	32.17	slug
Volume ( <i>V</i> )	gallon (gal)	0.003785	264.172	meter <sup>3</sup> (m <sup>3</sup> )
	cu. ft. (ft <sup>3</sup> )	0.028317	35.3147	meter <sup>3</sup> (m <sup>3</sup> )
	barrel (bbl)	0.15899	6.2898	meter <sup>3</sup> (m <sup>3</sup> )
	Mcf (1000 ft <sup>3</sup> , 60°F, 14.7 psia)	28.317	0.0353	Nm <sup>3</sup> (15°C, 101.325 kPa)
Area ( <i>A</i> )	sq. ft (ft <sup>2</sup> )	$9.29 \times 10^{-2}$	10.764	meter <sup>2</sup> (m <sup>2</sup> )
	Acre	$4.0469 \times 10^3$	$2.471 \times 10^{-4}$	meter <sup>2</sup> (m <sup>2</sup> )
	sq. mile	2.59	0.386	(km) <sup>2</sup>
Pressure ( <i>P</i> )	lb/in. <sup>2</sup> (psi)	6.8948	0.145	kPa (1000 Pa)
	Psi	0.0680	14.696	atm
	psi/ft	22.62	0.0442	kPa/m
	inch Hg	$3.3864 \times 10^3$	$0.2953 \times 10^{-3}$	Pa
Temperature ( <i>t</i> )	F	$0.5556(F-32)$	$1.8 C + 32$	C
	Rankine (°R)	0.5556	1.8	Kelvin (K)
Energy/work ( <i>w</i> )	Btu	252.16	$3.966 \times 10^{-3}$	cal
	Btu	1.0551	0.9478	kilojoule (kJ)
	ft-lbf	1.3558	0.73766	joule (J)
	hp-hr	0.7457	1.341	kW-hr
Viscosity ( $\mu$ )	Cp	0.001	1,000	Pa · s
	lb/ft-sec	1.4882	0.672	kg/(m-sec) or (Pa · s)
	lbf-s/ft <sup>2</sup>	479	0.0021	dyne-s/cm <sup>2</sup> (poise)
Thermal conductivity ( <i>k</i> )	Btu-ft/hr-ft <sup>2</sup> -F	1.7307	0.578	W/(m · K)
Specific heat ( <i>C<sub>p</sub></i> )	Btu/(lbm°F)	1	1	cal/(g°C)
	Btu/(lbm°F)	$4.184 \times 10^3$	$2.39 \times 10^{-4}$	J. (kg · K)
Density ( $\rho$ )	lbm/ft <sup>3</sup>	16.02	0.0624	kg/m <sup>3</sup>
Permeability ( <i>k</i> )	Md	0.9862	1.0133	mD (=10 <sup>-15</sup> m <sup>2</sup> )
	md (=10 <sup>-3</sup> darcy)	$9.8692 \times 10^{-16}$	$1.0133 \times 10^{15}$	m <sup>2</sup>

# Appendix B: The Minimum Performance Properties of API Tubing

Nom. (in.)	O.D. (in.)	Grade	Wt per ft with Couplings (lb)		Inside Diameter (in.)	Drift Diameter (in.)	O.D. of Upset (in.)	O.D. of Cplg. (in.)		Collapse Resistance (psi)	Internal Yield Pressure (psi)	Joint Yield Strength (lb)	
			Nonupset	Upset				Nonupset	Upset			Nonupset	Upset
¾	1.050	F-25		1.20	0.824	0.730	1.315		1.660	5960	4710		8320
		H-40		1.20	0.824	0.730	1.315		1.660	7680	7530		13,300
		J-55		1.20	0.824	0.730	1.315		1.660	10,560	10,360		18,290
		C-75	1.14	1.20	0.824	0.730	1.315	1.313	1.660	14,410	14,120	11,920	24,950
		N-80		1.20	0.824	0.730	1.315		1.660	15,370	15,070		26,610
1	1.315	F-25		1.80	1.049	0.955	1.469		1.900	5540	4430		12,350
		H-40		1.80	1.049	0.955	1.469		1.900	7270	7080		19,760
		J-55		1.80	1.049	0.955	1.469		1.900	10,000	9730		27,160
		C-75	1.70	1.80	1.049	0.955	1.469	1.660	1.900	13,640	13,270	20,540	37,040
		N-80		1.80	1.049	0.955	1.469		1.900	14,650	14,160		39,510
1¼	1.660	F-25		2.40	1.380	1.286	1.812		2.200	4400	3690		16,710
		H-40		2.40	1.380	1.286	1.812		2.200	6180	5910		26,740
		J-55		2.40	1.380	1.286	1.812		2.200	8490	8120		36,770
		C-75	2.30	2.40	1.380	1.286	1.812	2.054	2.200	11,580	11,070	29,120	50,140
		N-80		2.40	1.380	1.286	1.812		2.200	12,360	11,800		53,480
1½	1.900	F-25	2.75	2.90	1.610	1.516	2.094	2.200	2.500	3920	3340	11,930	19,900
		H-40	2.75	2.90	1.610	1.516	2.094	2.200	2.500	5640	5350	19,090	31,980
		J-55	2.75	2.90	1.610	1.516	2.094	2.200	2.500	7750	7350	26,250	43,970
		C-75	2.75	2.90	1.610	1.516	2.094	2.200	2.500	10,570	10,020	35,800	59,960
		N-80	2.75	2.90	1.610	1.516	2.094	2.200	2.500	11,280	10,680	38,180	63,960
2	2.375	F-25	4.00		2.041	1.947		2.875		3530	3080	18,830	
		F-25	4.60	4.70	1.995	1.901	2.594	2.875	3.063	4160	3500	22,480	32,600
		H-40	4.00		2.041	1.947		2.875		5230	4930	30,130	
		H-40	4.60	4.70	1.995	1.901	2.594	2.875	3.063	5890	5600	35,960	52,170
		J-55	4.00		2.041	1.947		2.875		7190	6770	41,430	
		J-55	4.60	4.70	1.995	1.901	2.594	2.875	3.063	8100	7700	49,440	71,730
		C-75	4.00		2.041	1.947		2.875		9520	9230	56,500	
		C-75	4.60	4.70	1.995	1.901	2.594	2.875	3.063	11,040	10,500	67,430	97,820
		C-75	5.80	5.95	1.867	1.773	2.594	2.875	3.063	14,330	14,040	96,560	126,940
		N-80	4.00		2.041	1.947		2.875		9980	9840	60,260	
		N-80	4.60	4.70	1.995	1.901	2.594	2.875	3.063	11,780	11,200	71,920	104,340
		N-80	5.80	5.95	1.867	1.773	2.594	2.875	3.063	15,280	14,970	102,980	135,400

2½	2.875	P-105	4.60	4.70	1.995	1.901	2.594	2.875	3.063	15,460	14,700	94,400	136,940
		P-105	5.80	5.95	1.867	1.773	2.594	2.875	3.063	20,060	19,650	135,170	177,710
		F-25	6.40	6.50	2.441	2.347	3.094	3.500	3.668	3870	3300	32,990	45,300
		H-40	6.40	6.50	2.441	2.347	3.094	3.500	3.668	5580	5280	52,780	72,480
		J-55	6.40	6.50	2.441	2.347	3.094	3.500	3.668	7680	7260	72,570	99,660
		C-75	6.40	6.50	2.441	2.347	3.094	3.500	3.668	10,470	9910	98,970	135,900
		C-75	8.60	8.70	2.259	2.165	3.094	3.500	3.668	14,350	14,060	149,360	186,290
		N-80	6.40	6.50	2.441	2.347	3.094	3.500	3.668	11,160	10,570	105,560	144,960
		N-80	8.60	8.70	2.259	2.165	3.094	3.500	3.668	15,300	15,000	159,310	198,710
		P-105	6.40	6.50	2.441	2.347	3.094	3.500	3.668	14,010	13,870	138,550	190,260
3	3.500	P-105	8.60	8.70	2.259	2.165	3.094	3.500	3.668	20,090	19,690	209,100	260,810
		F-25	7.70		3.068	2.943		4.250		2970	2700	40,670	
		F-25	9.20	9.3	2.992	2.867	3.750	4.250	4.500	3680	3180	49,710	64,760
		F-25	10.20		2.922	2.797		4.250		4330	3610	57,840	
		H-40	7.70		3.068	2.943		4.250		4630	4320	65,070	
		H-40	9.20	9.3	2.992	2.867	3.750	4.250	4.500	5380	5080	79,540	103,610
		H-40	10.20		2.922	2.797		4.250		6060	5780	92,550	
		J-55	7.70		3.068	2.943		4.250		5970	5940	89,470	
		J-55	9.20	9.3	2.992	2.867	3.750	4.250	4.500	7400	6980	109,370	142,460
		J-55	10.20		2.922	2.797		4.250		8330	7940	127,250	
3½	4.000	C-75	7.70		3.068	2.943		4.250		7540	8100	122,010	
		C-75	9.20	9.3	2.992	2.867	3.750	4.250	4.500	10,040	9520	149,140	194,260
		C-75	10.20		2.922	2.797		4.250		11,360	10,840	173,530	
		C-75	12.70	12.95	2.750	2.625	3.750	4.250	4.500	14,350	14,060	230,990	276,120
		N-80	7.70		3.068	2.943		4.250		7870	8640	130,140	
		N-80	9.20	9.3	2.992	2.867	3.750	4.250	4.500	10,530	10,160	159,080	207,220
		N-80	10.20		2.922	2.797		4.250		12,120	11,560	185,100	
		N-80	12.70	12.95	2.750	2.625	3.750	4.250	4.500	15,310	15,000	246,390	294,530
		P-105	9.20	9.3	2.992	2.867	3.750	4.250	4.500	13,050	13,340	208,790	271,970
		P-105	12.70	12.95	2.750	2.625	3.750	4.250	4.500	20,090	19,690	323,390	386,570
3½	4.000	F-25	9.50		3.548	3.423		4.750		2630	2470	15,000	
		F-25		11.00	3.476	3.351	4.250		5.000	3220	2870		76,920
		H-40	9.50		3.548	3.423		4.750		4060	3960	72,000	
		H-40		11.00	3.476	3.351	4.250		5.000	4900	4580		123,070
		J-55	9.50		3.548	3.423		4.750		5110	5440	99,010	
J-55		11.00	3.476	3.351	4.250		5.000	6590	6300		169,220		

Nom. (in.)	O.D. (in.)	Grade	Wt per ft with Couplings (lb)		Inside Diameter (in.)	Drift Diameter (in.)	O.D. of Upset (in.)	O.D. of Cplg. (in.)		Collapse Resistance (psi)	Internal Yield Pressure (psi)	Joint Yield Strength (lb)	
			Nonupset	Upset				Nonupset	Upset			Nonupset	Upset
4	4.500	C-75	9.50		3.548	3.423		4.750		6350	7420	135,010	
		C-75		11.00	3.476	3.351	4.250		5.000	8410	8600		230,760
		N-80	9.50		3.548	3.423		4.750		6590	7910	144,010	
		N-80		11.00	3.476	3.351	4.250		5.000	8800	9170		246,140
		F-25	12.60	12.75	3.958	3.833	4.750	5.200	5.563	2870	2630	65,230	90,010
		H-40	12.60	12.75	3.958	3.833	4.750	5.200	5.563	4500	4220	104,360	144,020
		J-55	12.60	12.75	3.958	3.833	4.750	5.200	5.563	5720	5790	143,500	198,030
		C-75	12.60	12.75	3.958	3.833	4.750	5.200	5.563	7200	7900	195,680	270,030
N-80	12.60	12.75	3.958	3.833	4.750	5.200	5.563	7500	8440	208,730	288,040		

# Index

*Note:* Page numbers followed by “*f*” and “*t*” refer to figure and tables, respectively.

## A

Absolute open flow (AOF), 54  
Absorption, 653–654  
Acid(s), 367–369, 685  
    capacity number, 379  
    dissolving power of, 370  
    diversion, 383–384  
    fluids, 442  
    fracturing, 367, 382–383, 382*f*, 424–426  
    injection rate and pressure, 374–376  
    matrix treatment. *See* Matrix acidizing  
    placement diagnosis, 384–385  
    selection, 371, 372*f*, 376–378  
    volume, 371–374  
Acidizing, 367  
    acid diversion, 383–384  
    acid placement diagnosis, 384–385  
    acid–rock interaction, 369–370  
    candidate selection, 369  
    carbonate acidizing design, 376–383  
    sandstone acidizing design, 371–376, 371*t*  
Acid–rock interaction, 369–370  
Additives, 443–447  
Adiabatic compression, 293, 564  
Adsorption, 261, 654  
Air drying techniques, 645  
Air-balanced pumping unit, 521–525  
Air-balanced units, 516–517, 517*f*, 525–529, 533  
Alkaline flooding, 359  
American Petroleum Institute (API), 3–4, 219–220, 517  
    gravity, 20  
    tubing, 00035#APP0002  
        tensile requirements, 220*t*  
Analytical method, 625–626  
Analytical plunger lift design methods, 625–626  
Anode, 685–686  
Anti-agglomerant (AA), 658–659  
Artificial lift methods, 603. *See also* Gas lift technology  
    ESP, 603–609  
    HPP, 609–614, 611*f*, 615*t*  
    hydraulic jet pumping, 630–634  
    PCP, 614–619, 616*f*  
    plunger lift system, 619–629  
Asphaltene depositions, 672–680  
Authigenic clays, 354  
Average compressibility factor method, 88–89  
Average temperature factor method, 88–89

## B

Bactericides, 446  
Balanced pressure valve, 577–578  
“Ballistic” flow, 591  
Ballooning effect, 231  
“Barefoot” completions, 483  
Barium ion ( $\text{Ba}^{+2}$ ), 680  
Barium sulfate, 680  
Barnett shale, 401–402  
Bauxite, 451–452  
Beam pumping systems, 603  
Bicarbonate ion ( $\text{HCO}_3^{-1}$ ), 680  
Bidirectional disc pig, 641  
Bidirectional pigs, 641, 711–712, 712*f*  
Bidirectional slip system, 237  
Bilinear flow regime, 491, 492*f*  
Biocide, 640–641  
Biot’s poroelastic constant, 464  
Blenders, 454–455, 455*f*  
Bottom-hole node, analysis with, 131–137  
    gas well, 131–132, 133*t*  
    oil well, 132–137, 136*t*  
Brake horsepower (*Hpb*), 567  
Bridge Plug, 484–485  
Brownian motion, 670  
Bubble-point pressure, 53–54, 57–59, 83  
Buckling prevention during production, 225–226  
Buildup pressure requirements, 624–626  
Burial process, 659  
Burst design, 224–225

## C

Caged Ball Frac Plug, 484–485  
Calcite scale, 680  
Calcium carbonate ( $\text{CaCO}_3$ ), 680–681  
Calcium fluoride ( $\text{CaF}_2$ ), 368, 681  
Calcium ion ( $\text{Ca}^{+2}$ ), 680  
Calcium sulfate, 681  
Calgary-based GasFrac Energy Services Inc, 440  
Calibrated rod, 542–543  
Caliper pigs, 711  
Candidate selection, acidizing treatments, 369  
Candidate well selection, 463  
Cane mist eliminators, 244  
Carbon dioxide ( $\text{CO}_2$ ), 239, 313, 442, 683

- Carbonate acidizing design, 376–383, 377*t*. *See also*  
 Sandstone acidizing design  
 acid fracturing, 382–383  
 selection of acid, 376–378  
 wormhole penetration and growth, 378–380  
 wormholes created by acid dissolution of  
 limestone, 377*f*
- Carbonate ion ( $\text{CO}_3^{-2}$ ), 680  
 rock types, 367  
 scales, 363
- Carboxymethylhydroxyethylcellulose (CMHEC), 441  
 Carboxymethylhydroxypropylguar (CMHPG), 441
- Carter 1D leakoff model, 406
- Casing head, 4–6, 6*f*
- Casing pressure, 623
- Casing pressure-operated valve, 574
- Cathode, 686–687
- Cathodic protection, 688–689
- Cavitation, 685, 688
- Cemented cased-hole situations, 486
- Cemented completions, 483
- Cemented sleeves method, 484
- Centrifugal compressors, 281–282, 282*f*, 293–296,  
 563–564, 570–573, 573*t*. *See also* Reciprocating  
 compressors
- Centrifugal inlet device, 243–244
- Chamber installations, gas lift installations, 596, 596*f*
- Chemical cleaning process, 715
- Chemical diversion methods, 384
- Chemical inhibition, 651, 655–659, 655*f*, 688
- Chemical inhibitors, 678, 683
- Chemical reactions, 369–370, 369*t*
- Choke, pressure upstream of, 559–561  
 sonic flow conditions, 560–561  
 subsonic flow conditions, 561
- Choke performance. *See also* Wellbore flow performance  
 curve, 112*f*  
 multiphase flow, 120–125  
 single-phase gas flow, 114–119  
 single-phase liquid flow, 112–113  
 sonic and subsonic flow, 111–112
- Choke performance relationship (CPR), 137
- “Christmas tree” equipment, 6, 7*f*
- Clay  
 minerals, 354–355, 451–452  
 stabilizers, 446
- Cleaning  
 operations, 640–642, 641*f*  
 pigs, 710, 711*f*
- Clinedinst equation for horizontal flow, 307–308
- Closed installation, gas lift installations, 595*f*, 596
- Coberly expression, 534
- Coiled tubing, 486–487, 505, 679
- Colebrook correlation, 300
- Colebrook–White equation, 85
- Collapse criterion, 312–313
- Collapse design, 224–225
- Composite IPR models, 68–72
- Compression packer, 233–235, 234*f*
- Compression power requirement, 562–573
- Compression-set versatile landing packer, 236, 236*f*
- Compressional force, 391, 506
- Compressional waves (P-waves), 466–467
- Compressors, 280–296. *See also* Pipelines  
 centrifugal, 293–296  
 reciprocating, 283–293
- Computational Fluid Dynamics/Discrete Element Method  
 (CFD-DEM), 423
- Constant-pressure boundary, 39, 39*f*
- Continuous flow valve. *See* Throttling pressure valve
- Continuous gas lift method, 550, 552, 553*f*
- Conventional pumping units, 515, 517*f*, 518–520
- Conventional rigs, 504–505
- Cool down time, 659–660
- Cooling process, 653
- Corrosion, 685–689, 686*f*
- Corrosion resistant alloy (CRA), 688–689
- Counterbalance, 515–516  
 load, 527–528
- Counterweights, 527
- Cover tube, 542
- Critical flow. *See* Sonic flow
- Critical stress intensity factor, 394
- Crosslinked Gel, 441
- Crosslinkers, 443, 444*t*
- Crude oils, 275, 300–301, 665, 668
- Crush resistance, 449
- Crystal growth retardation, 683
- Crystal nucleation inhibition, 683
- Cubic feet per minute (cfm), 562
- Cullender and Smith method, 89–92, 91*f*, 92*t*, 558–559
- Cumulative oil production, 198
- Cumulative productions, 179, 182, 199–200
- Curved sections, well data for, 165*t*

## D

- Dalton’s law of partial pressures, 260
- Darcy-Wiesbach friction factor chart, 299*f*
- Darcy’s law, 39, 404, 459
- Darcy–Wiesbach friction factor, 85, 86*f*, 88–89, 94
- Data mining, 489
- Data van, 456, 457*f*
- de Boer plot, 677–678
- Dead string, 432
- Decline rate, 197–202
- Degradation, 262
- Dehydrating tower, 262

- Dehydration, 259–272, 262*f*, 653  
 by cooling, 261  
 glycol, 263–265, 264*f*  
 plants, 261  
 water content of natural gas streams, 259–260, 260*f*
- Density  
 of gas, 29–30, 30*r*  
 of oil, 20  
 produced water, 32
- Desiccant process, 653–654
- Detrital clays, 354
- Deviation factor. *See* Gas compressibility factor
- Dew point, 651  
 depression, 260, 263
- Dewatering, 643–646, 644*f*, 715
- Diagnostic fracture injection test (DFIT), 436, 436*f*
- Diagnostic injection testing, 468
- Diagnostic plot, 491
- Diagnostic rate test analysis, 433–435
- Diesel prime mover, 290–292
- Diethylene glycol (DEG), 263, 654–655
- Dimensionless fracture conductivity, 459, 465–466
- Direct electric heating process, 660
- Discharge pump, 454–455
- Discrete-fracture networks (DFNs), 422–423
- Displacement pigs, 711–712, 712*f*, 713*f*
- Distortion Energy Criteria, 221
- Distributed temperature sensing tools (DTS tools), 384, 428
- Double-action piston stroke, 275, 276*f*
- Double-reduction gear reducer, 517
- Down-hole PCP, 616–618, 617*f*
- Drilling induced damage, 357–358
- Drilling mud pressure, 357
- Drillstem testers (DST), 664
- Drive string, selection of, 618–619
- Drying, 643–646
- Dual Diameter Pigs, 713
- Duplex pumps, 275, 278–280
- Dynamic viscosity, 25
- Dynamometer, 544
- E**
- Elastic deformation, 392, 418
- Elastomers, 702–703
- Electric heating process, 660
- Electric motors, 515
- Electric resistance welded (ERW), 309
- Electric wireline setting tool, 235–236, 235*f*
- Electrical submersible pumping (ESP), 603–609. *See also*  
 Hydraulic jet pumping  
 application, 607–609, 610*r*  
 installation, 604*f*  
 principle, 604–607
- Electrolyte, 686–687
- Emulsified acid, 368–369
- Emulsions, 443
- Energized fluids, 442–443
- Engineering calculations, 505–510
- Enhanced oil recovery (EOR), 357, 359
- Enthalpy-entropy diagram, 564
- Entrained drop movement model, 345, 620–621
- Envelope, 239–240, 240*f*  
 rating, 240
- Equation of State (EoS), 250, 666, 674
- Equivalent stress, 221–222
- Ethylene glycol (EG), 261, 263, 653, 655
- Ethylenediaminetetraacetic acid (EDTA), 363
- Exponential decline, 197–202, 204*f*, 205*f*, 208*f*
- External pressure, design for, 312–313
- F**
- Factory Acceptance Test (FAT), 639
- Fanning friction factor ( $f_F$ ), 84–85
- Far-field  
 diagnostic techniques, 489, 492–494  
 fracture monitoring techniques, 483
- Faults stresses, 397–398, 398*f*
- Fetkovich's equation, 58, 67
- Fetkovich's method, 76–77
- Fibers, 384
- Fick's law, 669
- Field separation processes, 243
- Field-scale evaluation, 552–554
- Film-movement model, 345
- Filtercake, 404–405
- Filtrate invaded zone, 405
- Fines migration, 353–354, 353*f*
- First law of thermodynamics, 87, 297, 306
- “Fishbone wells”, 50, 51*f*
- Flash calculation, 249–252
- Flooding operations, 640–642, 641*f*
- Flow assurance, 663, 666–668  
 analysis, 665–696  
 fluid sampling and characterizations, 663–665  
 mitigation strategies, 663
- Flow in pipelines, 297–308
- Flow rate change, transient temperature during, 318–323
- Flow rates, 352, 352*f*, 355–356, 479–480
- Flow regimes, 95–97, 96*f*
- Flowing gradient survey (FGS), 330
- Flowline, 9, 10*f*, 14*f*, 15*f*, 296, 311, 623
- Fluid leakoff models, 403–406, 403*f*  
 combined leakoff effects, 406  
 filtercake, 404–405  
 filtrate invaded zone, 405  
 reservoir region, 405–406



- Fluid sampling, 663–664
    - and characterizations, 663–665
    - PVT measurements, 664–665
  - Fluid-operated valve, 574, 579–582, 581*f*, 582*f*
  - Fluid-swellable packers, 232
  - Fluids, 47*f*, 504–505
    - characterizations, 666
    - density logs, 342–343
    - flow, 415
      - rate, 508
    - load, 526
    - loss, 463
      - additives, 446
    - property data, 165*t*
    - rheology, 447–448
    - valve. *See* Fluid-operated valve
    - velocity, 86–87
    - viscosity, 438–439
    - volume, 182, 404, 442–443, 473, 617
  - Flush fluid, 470
  - Foam pigs, 703, 704*f*
  - Foams fluids, 442–443
  - Force transfer in workover strings, 505–508
  - Formation breakdown around wellbore, 399–401
  - Formation damage, 352–364
    - evaluation, 359–361
    - from oilfield operations, 357–359
    - prevention and control, 361–364
    - sources, 353–357
  - Formation volume factor, 20–21, 31–32, 190, 530, 547–548, 608, 613
  - Formic acids, 368
  - Foss and Gaul equations, 626–629, 629*t*
  - Four-phase flow model, 348–349
  - Frac Plug, 484–485, 484*f*
  - Frac-pack, 362, 475–476, 479–482, 481*f*
  - Fracture, 46–48, 432–433, 453, 453*f*
    - conductivity, 448, 459
    - horizontal wells, 46
    - longitudinal, 482–483
    - modes, 393–394, 468
    - pressure, 400
    - simulators, 468
    - toughness, 393–394
    - well, 43
  - Fracturing fluids, 438–448
    - selection considerations, 463–464
  - Fracturing horizontal wells, 458
  - Fracturing pressure analysis, 428–438, 429*f*
  - Friction factor, 85, 98–99, 104, 297–300, 303
  - Friction reducers (FR), 431
  - Fuel consumption curves for prime movers, 290, 290*f*
- ## G
- Galvanic corrosion, 688
  - Gas, 685
    - anchors, 535
    - capacity, 253–254
    - compressibility, 31
      - factor, 27–29, 29*t*
    - compressibility factor, 27–29, 29*t*
    - compression requirements, 557–573
    - compressors, 261, 653
    - flow, 302–308
      - rate, 287–288, 346, 557–558
    - formation volume factor, 31
    - gas-condensate separation systems, 249
    - hydrate control, 649
      - hydrate forming condition, 649–651
      - hydrate prevention and mitigation, 651–661
    - mass flow, 693–694
    - pipelines, 659–660
    - pressure of gas distribution line, 561–562, 563*t*
    - properties, 22
    - pseudo-critical pressure and temperature, 23–25, 24*t*
    - service pipelines, 715–716
    - specific gravity of, 22
    - velocity number, 102
    - viscosity, 25–26, 27*t*
    - wellbores, 3
    - wells, 3, 131–132, 133*t*, 138*t*, 140–141
  - Gas lift technology, 549, 603. *See also* Artificial lift methods
    - evaluation, 552–557
    - gas compression requirements, 557–573
    - installations design, 595–597, 595*f*
    - special issues in intermittent-flow gas lift, 591–595
    - system, 549–552, 550*f*
    - valves selection, 574–591
  - Gas liquid ratio (GLR), 552, 606, 624–626
  - Gas production, 339. *See also* Water—production
    - to channeling behind casing, 340*f*
    - to gas coning, 341*f*
    - nodes in, 130*f*
    - to preferential flow through high-permeability zones, 340*f*
    - during pseudo-steady-state flow period, 188–191, 191*t*, 192*f*
    - temperature and fluid density logs identifying gas entry zone, 342*f*
    - temperature and noise logs, 341*f*
    - during transient flow period, 187, 188*t*
  - Gas–liquid ratio (GLR), 180
  - Gas–oil ratio (GOR), 3, 19, 244
  - Gauging
    - operations, 640–642, 641*f*
    - pigs, 641, 711

- Gel  
 breakers, 444  
 gelled acid systems, 368  
 pigs, 701, 706–707  
 slugs, 644  
 stabilizers, 444  
 “Geometric” design, 488  
 Glycol-gas contactor, 266–271, 269*f*, 270*f*, 271*f*  
 Glycol/water ratio (GWR), 266  
 Glycol(s), 263, 654–656  
 circulating pump, 272  
 dehydration, 263–265, 264*f*  
 dehydrators, 265–266  
 flash separator, 272  
 glycol-powered pumps, 272  
 lines, 266  
 re-concentrator, 271–272  
 viscosity, 263  
 Gravel packing method, 479–480  
 Gravimetric dissolving power, 370  
 Gravity settling mechanisms, 670  
 Guar gum, 441  
 Guo et al. method, 347–352. *See also* Turner et al. method  
 four-phase flow model, 348–349  
 minimum kinetic energy, 347–348  
 minimum required gas production rate, 350–351  
 Guo–Ghalambor model, 93–94, 95*t*, 135  
 TPR by, 145
- H**
- Hagedorn–Brown correlation, 100, 105*t*, 106*f*  
 Hagen–Poiseuille equation for laminar flow, 298  
 Halite scale, 363  
 Hammerschmidt’s method, 656  
 “Hand-free” time, 660  
 Hanger cable arrangement, 515  
 Harmonic decline, 203, 205*f*, 206*f*, 211*f*  
 Heat transfer models, 317–323  
 Heating, 659–660  
 High-density ceramics (HDC), 452  
 High-permeability reservoirs, 482  
 High-pressure pumps, 454, 454*f*  
 High-pressure separators  
 standard horizontal, 256*t*  
 standard spherical, 258*t*  
 standard vertical, 255*t*  
 High-pressure separators, 255  
 High-strength proppant (HSP). *See* High-density ceramics (HDC)  
 High-viscosity oils, 534  
 Homogeneous-flow models, 97–100  
 Hooke’s law, 392, 396
- Horizontal flow  
 Clinedinst equation for, 307–308  
 linear flow, 332  
 Panhandle-A equation for, 307  
 Panhandle-B equation for, 307  
 pseudo-linear flow, 333  
 pseudo-radial flow, 333–335  
 radial flow, 331–332  
 Weymouth equation for, 303–306  
 Horizontal sections, well data for, 166*t*  
 Horizontal separators, 245–246, 246*f*, 247*f*  
 Horizontal stress, 396–399  
 Horizontal wells, 45–50, 482–489. *See also* Vertical wells  
 completion options, 483–487  
 deliverability of, 149–158  
 multi-stage-fractured, 154–158, 156*f*, 158*f*  
 multistage fractured wells, 46–50  
 non-fractured, 149–153  
 nonfractured wells, 45–46  
 single-fractured, 152*f*, 153*f*, 154  
 single-fractured wells, 46  
 treatment design considerations, 487–489  
 “Horse’s head” arrangement, 515  
 Horsepower equation, 278–279  
 Horsepower estimation, 476–478  
 Hot oil circulation strategy, 660  
 Hydrate  
 forming condition, 649–651  
 natural gases, 650*f*, 650*t*  
 plug dissociate process, 661  
 prevention and mitigation, 651–661  
 temperature, 649–650  
 Hydraulic fracturing, 369, 389, 390*f*, 427*t*, 459, 463  
 damage control by, 362–363  
 frac-pack treatments, 479–482  
 fractured well productivity, 459–462, 461*f*  
 geometry, 401–402, 401*f*  
 horizontal wells, 482–489  
 hydraulic fracture geometry, 401–402, 401*f*  
 materials and equipment, 438–458  
 models, 402–428  
 pressure analysis, 428–438  
 rock mechanics, 390–401  
 treatment, 462–479, 489–494  
 Hydraulic jet pumping, 603, 630–634, 630*f*. *See also*  
 Electrical submersible pumping (ESP)  
 selection, 632–634  
 technical parameters, 631–632  
 working principle, 630–631, 631*f*  
 Hydraulic piston pumping (HPP), 603, 609–614, 611*f*, 615*t*  
 Hydraulic power, 535–536  
 Hydraulic-fractured wells, 42–45  
 Hydraulic-set packer, 237

Hydraulic-set single-string packer, 237–238  
 Hydro-mechanical shifting tool, 486  
 Hydrocarbon gel systems, 644  
 Hydrocarbon pipelines, 659  
 Hydrocarbons, Coefficients of Correlations for Parachors of, 33*t*  
 Hydrochloric acid (HCl), 239, 359, 362, 367, 442, 685  
 Hydrofluoric acid (HF), 359, 362, 368, 424  
 Hydrogen, 686, 688  
 Hydrogen sulfide (H<sub>2</sub>S), 239, 262, 313  
 Hydrogen-induced cracking, 688  
 Hydrostatic pressure, 431  
 Hydrotest condition, check for, 314  
 Hydrotesting process, 642–643  
 Hydroxyethylcellulose (HEC), 441  
 Hydroxypropylcellulose (HPC), 441  
 Hydroxypropylguar (HPG), 441  
 Hyperbolic decline, 203–204, 213*f*

## I

Ideal gas law, 284–285, 348  
 Ideal-gas equation, 564  
 Illite clay minerals, 355  
 Impure gas, flow of, 92–94  
 In-line inspection tools (ILI tools), 701, 705–706, 712  
   ultrasonic inspection tool, 706*f*  
 Incompressible fluids, 423–424  
 Indirect electric heating process, 660  
 Indirect heater, 248  
 Individual separators, 245–246  
 Inflatable sphere, 702–703  
 Inflow control devices (ICDs), 239  
 Inflow performance curve, 131  
 Inflow performance relationship (IPR), 31, 37, 53–62, 56*f*, 111, 131, 179, 536, 608  
   curve for oil well, 54*f*  
   curves construction using test points, 62–67, 64*f*, 67*f*  
   Fetkovich's method, 76–77  
   for partial two-phase oil reservoirs, 59–62, 60*f*  
   for single-phase reservoirs, 53–57  
   for two-phase reservoirs, 57–59  
   Vogel's method, 74–75  
 Injection pressure  
   at surface, 558–559  
   at valve depth, 558  
 Injection rate, 374  
 Inlet scrubber, 266, 267*f*  
 Inorganic precipitates, 680–685  
 Inorganic scales, 358–359  
 Insert chamber, 596, 597*f*  
 Inside diameter (ID), 351, 555, 607  
 Inspection, pipeline, 716  
 Instantaneous shut-in pressure (ISIP), 428–429

Insulation design, 314–323, 319*t*  
   heat transfer models, 317–323  
   insulation materials, 315–317, 315*t*, 316*t*  
 Interfacial tension (IFT), 33–34  
 Intermediate-density ceramics (IDC), 452  
 Intermediate-strength proppant (ISP). *See* Intermediate-density ceramics (IDC)  
 Intermittent gas lift method, 550  
 Intermittent-flow gas lift, special issues in, 591–595  
 Internal pressure, design for, 309–311, 310*f*  
   gas lines, 311*t*  
   oil lines, 311*t*  
 Interstitial acid velocity in radial geometry, 380  
 Iron, 686  
 Isentropic  
   horsepower, 566–569, 569*t*  
   process, 284, 564  
 Isolation plugs, 484–485  
 Isothermal compressibility, 182

## J

Joule–Thomson cooling effect, 115, 659–660  
 Jumper, 639, 688–689

## K

*K*-value. *See* Crush resistance  
 Kaolinite clay minerals, 354–355  
 Kinematics ratio, 616  
 Kinetic energy, minimum, 347–348  
 Kinetic energy per unit volume of gas, 347  
 Kinetic hydrate inhibitor, 658  
 Klerk fracture model model (KGD model), 406, 412–414, 412*f*

## L

Laminar flow, 85, 226, 297–298  
 Lateral and well production rates, 166*t*, 167*t*, 168*t*, 169*t*  
 Leak testing process, 642–643  
 Leakoff velocity, 405  
 Lightweight ceramics (LWC), 452  
 Limited-entry perforating technique, 488  
 Linear Elastic Fracture Mechanics (LEFM), 393–394  
 Linear flow, 334, 437, 491–492  
 Linear gel, 441  
 Linear-radial flow model, 48  
 Liquid  
   capacity, 254–259  
   flow rate, 531  
   holdup, 97  
   hydrocarbon, 272  
   liquid-loading problem, 344–345  
   load, 272

loading, 344–352, 620  
 overflow, 11  
 slug, 690  
 velocity number, 102  
 viscosity number, 102  
 volume fraction, 347–348

Logging production, 339

Low dosage hydrate inhibitors (LDHI), 658

Low productivity, well problem identification, 329–338

Low-pressure separators, 255  
 standard horizontal, 257*t*  
 standard spherical, 258*t*  
 standard vertical, 256*t*

Low-viscosity oils, 534

Lumped-parameter models, 415

**M**

Magnetic cleaning pigs, 713

Magnetic-flux leakage pigs, 716

Maintenance of pipelines, 716–717

Mandrel pig, 704, 705*f*, 711*f*

Manifolds, 455, 456*f*

Mass transfer coefficient, 426

Master valve, 574

Material balance, principle of, 179

Material storage units, 456–458  
 photo of fracturing equipment layout at well site, 458*f*  
 up close view of fracturing equipment layout at well site, 458*f*

Matrix acidizing, 362, 367

Maximum allowable operating pressure (MAOP), 311

Mechanical diversion methods, 383–384

Mechanical type packers, 232, 233*f*

Metal-to-metal plungers, 534–535

Methanol, 263, 655, 657*f*  
 gel systems, 644  
 injection systems, 656

Micelles, 442

Microseismic mapping, 483

Microseismic monitoring technique, 493–494

Mineral acids, 367–368

Minimum required gas production rate, 350–351

Missile. *See* Manifolds

Mist eliminator, 244

Mixing rule, 25–26

Mobil compressor trailers, 558

Mode I fracture. *See* Opening mode

Mode II fracture. *See* Sliding mode

Mode III fracture. *See* Tearing mode

Modern lean oil absorption gas plants, 261

Modified Hagedorn–Brown method (mH-B method), 100, 103–104

Modular formation dynamics tester (MDT), 664

Molecular sieves, 261

Molecular weights of compounds (*MWi*), 22

Mollier diagram, 564, 566

Moody friction factor (*fM*). *See* Darcy–Wiesbach friction factor

Multi-stage-fractured horizontal wells, 154–158, 156*f*, 158*f*

Multilateral wells, 50–53  
 deliverability of, 159–170  
 fishbone wells, 159–161, 160*f*  
 fluid property data, 165*t*  
 reservoir property data, 164*t*  
 root wells, 161–170, 162*f*  
 well data, 165*t*, 166*t*, 167*t*, 168*t*, 169*t*

Multiphase flow, 94–104, 120–125

Multiphase fluids, 439

Multiphase oil wells, 94

Multistage fracturing via coiled tubing, 486–487  
 horizontal wells, 46, 47*f*  
 wells, 46–50

**N**

Natural gas, 275  
 production industry, 280–281  
 properties of, 22–31  
 water content, 259–260, 260*f*, 651, 652*t*, 653*f*

Near-wellbore  
 diagnostic method, 489  
 fracture tortuosity, 430–431, 433*f*  
 tortuosity friction, 432–433

Net present values (NPVs), 462–463

Net pressure, 403  
 analysis, 489–490  
 analyzing, 490  
 pseudo-3D models, 490, 491*f*

Net pressure, maximum, 409

Newton and Raphson iteration method, 29

Newtonian fluids, 447, 477

Newton–Raphson iteration, 89, 299–300, 350

Nikuradse friction factor correlation, 89

Nitrogen (N<sub>2</sub>), 442, 644, 646

“No-touch” time, 660

Nodal analysis, 129, 131, 179

Nolte-Smith plot, 429, 470

Nolte-Smith pressure analysis  
 technique, 429, 430*f*, 430*t*

Nominal pipeline wall thickness, 311

Non-fractured horizontal wells, 149–153

Nonconventional systems, 504–505

Nonfractured wells, 45–46

Nonhorizontal flow, Weymouth equation for, 306–307

Nonproductive time (NPT), 454

Nordgren model, 410

Normal stresses, 394

**O**

Observed net pressure calculation, 430–433

Oil, 83, 685

- compressibility, 22
- flow, 300–302
- fracturing fluids, 439–440
- pipelines, 659–660
- production, 180–186, 187*t*
  - nodes in, 130*f*
    - during single-phase flow period, 182–183, 184*f*, 184*t*, 188*t*
    - during transient flow period, 179–180, 181*f*, 181*t*
    - during two-phase flow period, 183–186, 189*f*
- properties, 19–22
  - density of oil, 20
  - formation volume factor of oil, 20–21
  - oil compressibility, 22
  - solution GOR, 19
  - viscosity of oil, 21
- wellbores, 3
- wells, 94–104, 132–137, 136*t*, 141–149, 142*t*, 144*t*, 147*t*

Oil-swellable packer, 238–239, 238*f*

Oilfield operations, formation damage from, 357–359

- completion/workover induced damage, 358
- drilling induced damage, 357–358
- production induced damage, 358–359
- stimulation induced damage, 359

Waterflooding and EOR induced damage, 359

Oil–gas–water three-phase separator, 246

1D stress model, 467, 467*f*

Open installations, 595, 595*f*

“Openhole” completion, 483

Opening mode, 393

Operating valve, 574

Optimum injection rate, 374

Organic acids, 368

Organic precipitation, 356, 363

Organic scaling, 358–359

Orifice type valve, 574, 576*f*

Orifice-type chokes, choke flow coefficient for, 114*f*

Original oil in place (OOIP), 182

Outer diameter (OD), 219–220

Outflow performance curve, 131

Output gas pressure requirement, 558–562

Overall heat-transfer coefficient (OHTC), 315

Overburden stress, 396–397

**P**

Packed glycol contactors, 268*t*, 269*t*

Packers, 232–240, 234*f*, 236*f*

Panhandle equations, 302–303
 

- Panhandle-A equation for horizontal flow, 307
- Panhandle-B equation for horizontal flow, 307

Paraffin, 356–357, 363, 607, 668–669

Partial two-phase flow, 70–72

Partial two-phase oil reservoirs, IPR for, 59–62, 60*f*

Particle friction factor, 509

Particle Reynolds number, 509

Particle slip velocity, 508

Particle transport velocity, 508–509

Peak load, 528

Peak torque, 528–529

Peng-Robinson model (PR model), 666

Perforation, 358

Perkins-Kern-Nordgren model (PKN model), 406, 408–412, 409*f*, 471–473

Permanent packers, 233

Permeability anisotropy, 52–53

Peroxydisulfate, 444

Peroxyulfate. *See* Peroxydisulfate

Persulfate. *See* Peroxydisulfate

Petroleum
 

- fluid properties
  - IFT, 33–34
  - natural gas properties, 22–31
  - oil properties, 19–22
  - produced water properties, 31–32
- production system, 4*f*
- reservoirs, 354

Petroleum engineers, 253

Pig, 701–702
 

- pinwheel, 713
- selection, 709–713
- tracking system, 719
- train, 641

Pigging, 678–679, 701–708, 716
 

- gel pigs, 706–707, 707*f*
- in-line inspection tools, 705–706
- launcher, 707–708, 708*f*, 709*f*
- procedure, 717–719
- receiver, 707–708, 708*f*, 709*f*
- utility pigs, 701–704

Pilot valves, 576, 579, 580*f*

Pinwheel pigs, 713

Pipe bundles insulation, 659

Pipe diameter number, 102

Pipe Line End Termination (PLET), 639

Pipe-in-pipe (PIP), 315
 

- insulation methods, 659

Pipeline pigging, 701–708
 

- construction, 714–715
- freeing “stuck” pig, 719
- inspection, 716
- maintenance, 716–717
- operation, 715–716
- pig launching and receiving, 717–719
- prerun inspection, 717

- pressure and flow rate, 717, 718*t*
- selection of pigs, 709–713
- Pipelines, 9, 10*f*, 296–323, 639, 663. *See also* Compressors
  - bathymetry, 694
  - blowdown, 661
  - construction, 714
  - deposits, 702*f*
  - depressurization, 661
  - design, 275, 308–323
  - efficiency, 308
  - flow in pipelines, 297–308
  - hydrottest, 639, 642–643
  - jumper, 639
  - leak testing, 642–643
  - precommissioning
    - pipeline dewatering, drying, and purging, 643–646
    - pipeline flooding, cleaning, and gauging operations, 640–642, 641*f*
  - spans, 716
  - steel, 659
  - subsea pipeline system, 640*f*
  - values of pipeline efficiency factors, 308*t*
  - wax, 715
- Planar 3D models, 418
- Plastic deformation, 392
- “Plug and perf” method (PnP method), 484–485, 485*f*
- Plunger lift systems, 603, 619–629, 622*f*
  - design guideline, 624–629
  - flow regimes, 620*f*
  - Foss and Gaul equations, 626–629, 629*t*
  - working principle, 621–624
- Plunger pump, 517, 519*f*
- Plunger stroke length, 531–534
- Poettmann–Carpenter’s model, 97–98, 101*t*, 132
- Poisson’s ratio, 391–392, 396, 399, 410, 466–467
- Polished rod, 515
  - motion, 518–525, 519*f*, 520*t*
    - air-balanced pumping unit, 521–525, 523*f*
    - conventional pumping unit, 518–520, 522*f*
  - polisher rod dynamometer cards, 541–542
- Polished rod loads (PRLs), 515–516, 525–527, 544
- Polly-Pigs. *See* Foam pigs
- Polyemulsion, 443
- Polyglycolic acid (PGA), 446
- Polylactic acid (PLA), 446
- Polymers, 440, 443
  - flooding, 359
- Polypropylene, 316
- Polypropylene layer, 320, 321*f*
- Polytropic efficiency of centrifugal compressors, 293
- Polyurethane, 316, 322*f*
- Poroeleastic constant, 396–397
- Poroeleastic effects, 400
- “Power pumps”. *See* Reciprocating piston pumps
- Power requirements, 535–536, 537*t*
- Power-operated valves, 261
- Precommissioning, pipeline, 639
  - pipeline dewatering, drying, and purging, 643–646
  - pipeline flooding, cleaning, and gauging operations, 640–642, 641*f*
- Prepad, 469
- Prerun inspection, 717
- Pressure, 243, 248–250
  - decline analysis, 435–438
    - DFIT testing, 436
    - techniques, 436–438
  - dehydrator, 654
  - dew point, 651
  - distribution, 418
  - drop across choke, 111–113
  - effect, 227–232
  - equations for gas flow, 114
  - hydrate formation, 649–650, 661
  - natural gas, 653
  - ratio, 565
  - transient analysis, 491–492, 492*f*
  - waves, 111, 574, 576–579
    - balanced pressure valve, 577–578
    - pilot valve, 579
    - unbalanced bellow valve, 576–577
- Pressure transient data analysis, 330–338
  - effective permeability, 331
  - horizontal linear flow, 332
  - horizontal pseudo-linear flow, 333
  - horizontal pseudo-radial flow, 333–335
  - horizontal radial flow, 331–332
  - reservoir pressure, 331
  - skin factor, 335–338
  - vertical radial flow, 332
- Prime mover, 515
  - power ratio, 290, 291*f*
- Principal stresses, 394–396, 399, 437, 489
- Produced water, properties of, 31–32
  - density, specific gravity, and salinity, 32
  - water compressibility, 32
  - water formation volume factor, 32
  - water viscosity, 32
- Production
  - casing, 3
  - data, 204
  - decline analysis, 197, 207–213, 208*t*, 210*t*, 211*t*
    - determination of model parameters, 206–207, 207*f*
    - exponential decline, 197–202, 208*f*
    - harmonic decline, 203, 205*f*, 206*f*
    - hyperbolic decline, 203–204
    - model identification, 204–205
  - drawdown, 479–480
  - engineer, 3

Production (*Continued*)

- forecast through reservoir simulation, 192–193, 193*f*
- liner, 3
- packers, 232–240
- plant, 656
- rate decline, 199
- Production logging tools (PLT), 384, 385*f*, 428, 489
- Productivity index (PI), 53–54, 549
- Profile pig, 712
- Progressive cavity pump (PCP), 614–619, 616*f*
  - down-hole PCP, 616–618
  - drive string selection, 618–619
  - surface driver selection, 619
- Progressive cavity pumping, 603
- Propagation criterion, 312
- Proportional valve. *See* Throttling pressure valve
- Proppants, 448–452, 451*f*
  - laden fluid, 469–470
  - pack conductivity, 448–449
  - selection considerations, 464–466, 465*f*
  - silos, 456, 457*f*
  - storage units, 456
  - transport models, 423–424
- Prostran, 701
- Pseudo-3D models (P3D models), 415–417, 416*f*, 417*f*, 468, 489–490, 491*f*
- Pseudo-linear flow, 334
- Pseudo-linear-radial-combined model, 51
- Pseudo-radial flow analysis, 491–492
- Pseudo-steady flow period, oil production during, 180–186, 187*t*
  - oil production
    - during single-phase flow period, 182–183, 184*f*, 184*t*, 188*t*
    - during two-phase flow period, 183–186
- Pseudo-steady-state flow, 40–41
  - gas production during, 188–191, 191*t*, 192*f*
- Pumping
  - schedule, 468–470
  - system, 515–517, 517*f*, 518*f*, 519*f*
- Pumping unit, load to, 525–531
  - counterweights, 527
  - maximum PRL, 525–526
  - minimum PRL, 526–527
  - peak torque and speed limit, 528–529
  - tapered rod strings, 529–531, 532*t*
- Pumping unit selection, procedure for, 536–541, 538*f*, 539*t*
- Pumps, 275–280
  - deliverability, 531–536
  - duplex, 278–280
  - dynagraph, 541–544, 542*f*, 543*f*
  - efficiency, 535
  - performance analysis principles, 541–546
  - triplex, 275–278
- Purging process, 643–646
- PVT measurements, 19, 21, 664–666, 674–675

**R**

- Radial models, 407–408
- “Ramped” proppant concentration schedule, 475–476
- Rate step-down testing, 433–434, 434*f*
- Rate transient analysis, 491–492
- Reaction kinetics, 370
- Real gas law, 570, 572
- Reboiler, 271–272
- Reciprocating compressors, 281, 281*f*, 283–293, 562, 564–569
- Reciprocating piston pumps, 275
- Recompletion work, 503
- Refractive index (RI), 676
- Relative decline rate, 197–199, 206*f*, 209*f*, 210*f*, 212*f*
- Repair, 503
  - casing or equipment, 503–504
- Required fluid velocity, minimum, 508–509
- Reservoir characterization instrument (RCI), 664
- Reservoir deliverability, 37, 188–190. *See also* Well deliverability
  - factors, 37
  - horizontal wells, 45–50
  - IPR, 53–77, 64*f*, 67*f*
  - multilateral wells, 50–53
  - vertical wells, 37–45
- Reservoirs, 6–9
  - collection and validation of reservoir properties, 466–467
  - pressure, 331
  - production forecast through reservoir simulation, 192–193, 193*f*
  - property data, 164*t*
  - region, 405–406
  - reservoir-fracture cross-flow model, 48
  - simulators, 192
- Resin-coated proppants, 450–451
- Retarded acids, 368–369
- Retention time, 254, 254*t*
- Retrievable packer, 233, 235
- Reverse flow chamber, 596, 597*f*
- Reynolds number, 84–85, 87, 297–298, 301
- Rock mechanics, 390–392
  - faults and tectonic stresses, 397–398, 398*f*
  - formation breakdown around wellbore, 399–401
  - fracture modes and fracture toughness, 393–394
  - minimum horizontal stress, 398–399
  - overburden, horizontal and effective stresses, 396–397
  - principal stresses, 394–396
  - rock deformation under uniaxial loading, 391*f*
- Rock wettability, 356–357
- Rod
  - magnitude of rod stretch, 533
  - pump, 517
  - stretch and contraction, 544
  - string stretch, 533
  - vibration, 544

- “Root wells”, 50, 50*f*
  - Rotary blower, 281–282
  - Rotary compressors, 281–282, 563–564
  - Rough fracture surface, 464–465
  - Roundness, 449, 450*f*
  - Rules of thumb, 488, 624–625
- S**
- Sachdeva’s multiphase choke flow mode, 122, 124*t*
  - Safety control system, 10–11, 12*f*, 14*f*, 15*f*, 16*f*
  - Salinity, 32
  - Salt, 355, 655
  - Sand-jet perforating technique, 487
  - Sandstone acidizing design, 371–376, 371*t*. *See also*
    - Carbonate acidizing design
    - acid injection rate and pressure, 374–376
    - acid volume requirement, 371–374
    - selection of acid, 371
  - Sandstone pores, 369
  - Saturated vapor pressure, 645
  - Saturation index (SI), 681
  - Saturation ratio (SR), 681
  - Scale(s), 680–685, 682*t*
    - control, 363
    - inhibitors, 446–447
    - precipitation, 356
    - squeeze, 684
  - Screen-out event, 470
  - Separated-flow models, 97, 100–104
  - Separation efficiency, 247
  - Separation systems, 243–259
    - dehydration systems, 259–272
    - factors affecting separation, 247–252
    - flash calculation, 249–252
    - principles of, 243–244
    - stage separation, 248–249
    - types of separators, 244–247
  - Separators, 243–247
    - horizontal, 245–246, 246*f*, 247*f*
    - selection of, 253–259
    - spherical, 247, 248*f*
    - vertical, 244, 245*f*
  - Severe slugging, 690–696
    - formation process, 691*f*
    - outlet gas mass flowrate, 693*f*
    - pipeline inlet pressure, 692*f*, 693*f*
    - total gas flow, 695*f*
    - upwards and downwards inclined pipeline profiles, 694*f*
  - Shear dispersion, 670
  - Shear strain, 392
  - Shear stress, 392, 394
  - Shear waves (S-waves), 466–467
  - Silica sand, 451
  - Silicate minerals, 369–370
  - Single layer insulation methods, 659
  - Single-action piston stroke, 275, 276*f*
  - Single-fractured wells, 46
    - horizontal wells, 152*f*, 153*f*, 154
  - Single-phase flow period, oil production during, 182–183, 184*f*, 184*t*, 188*t*
  - Single-phase gas flow, 87–94, 114–119
    - applications, 116–119
    - average temperature and compressibility factor method, 88–89
    - Cullender and Smith method, 89–92, 91*f*, 92*t*
    - flow of impure gas, 92–94
    - sonic flow, 115
    - subsonic flow, 114–115
    - temperature at choke, 115
  - Single-phase liquid flow, 69, 83–87, 112–113
  - Single-phase reservoirs, IPR for, 53–57
  - Sizing glycol dehydrator unit, 266–272
    - glycol circulating pump, 272
    - glycol flash separator, 272
    - glycol re-concentrator, 271
    - glycol-gas contactor, 266–271, 268*t*, 269*f*, 269*t*, 270*f*, 271*f*
    - inlet scrubber, 266
    - reboiler, 271–272
    - stripping still, 272
  - Skin, 367
    - factor, 335–338, 360–361, 375–376
    - low permeability or high damage, 384
  - Slack-off, workover strings in, 506–507
  - Sleeve system, 484–486, 486*f*
  - Slickwater, 441, 487
    - fracture treatments, 465
  - Sliding
    - mode, 393
    - sleeves, 486
  - Slip swellable slip-on packers, 239
  - “Slug” flow, 591
  - “Slurry”. *See* Proppant laden fluid
  - “Slush pumps”. *See* Reciprocating piston pumps
  - Small scale crystals, 683
  - Smectite clay minerals, 355
  - Snubbing units, 505
  - Soave-Redlich-Kwong model (SRK model), 666
  - Sodium chloride (NaCl), 363
  - Solid cast pigs, 704
  - Solid desiccants, 654
  - Solids detection system (SDS), 674–675
  - Solubility parameter, 672, 681
  - Soluble spheres, 702–703
  - Solution gas–oil ratio (solution GOR), 19
  - Sonic flow, 111–112, 115, 120–121, 560–561
  - Sound waves, 111
  - Sour systems, 688
  - Space adsorbents, 262
  - Special pigs, 713



- Specific gravity
    - of gas, 22
    - produced water, 32
  - Specified minimum yield stress (SMYS), 643
  - Speed limit, 528–529
  - Spheres, 702–703, 703*f*
  - Spherical pigs, 702–703
  - Spherical separators, 247, 248*f*
  - Sphericity, 449, 450*f*
  - Spread, 577, 579
  - Spurt loss, 404–406
  - Stage compression, 565–566
  - Stage separation, 248–249
  - Standing valve (SV), 517
  - Stator, 614
  - Steady fluid flow, temperature and heat transfer for, 317–318
  - Steady-flow temperature profiles, 320, 320*f*
  - Steady-state flow, 39, 459
  - Steady-state operations, 670
  - Step-rate testing, 434–435, 435*f*
  - Stone-wall limit, 293, 570
  - Strain, 391
  - Strain-gage dynamometer, 544–545, 546*f*
  - Stratified reservoirs, composite IPR of, 68–72
  - Stress-oriented, hydrogen-induced cracking (SOHIC), 688
  - Stress(es), 390, 396–397, 397*f*
    - cracking, 688
    - faults and tectonic stresses, 397–398
    - intensity factor, 394
    - minimum horizontal stress, 398–399
    - overburden, horizontal and effective stresses, 396–397
    - perturbation, 419–421
    - shadowing effects, 419–421
      - potential stress shadowing effects, 420*f*
      - stress variation vs. distance away from semi-infinite crack, 420*f*
  - Stretch, 533, 545*f*
  - String, 504–505
    - tubing, 505
  - Stripping still, 272
  - Strontium ion ( $\text{Sr}^{+2}$ ), 681
  - Strontium sulfate, 680–681
  - “Stuck” pig, freeing, 719
  - Stuffing box, 515
  - Stylus, 542–544
  - Subcritical flow. *See* Subsonic flow
  - Submerged arc welded (SAW), 309
  - Subsonic flow, 111–112, 114–115, 121–125, 561
  - Sucker rod pumping, 515, 516*f*
    - load to pumping unit, 525–531
    - polished rod motion, 518–525, 519*f*, 520*t*
    - principles of pump performance analysis, 541–546, 542*f*, 543*f*, 545*f*, 546*f*
    - procedure for pumping unit selection, 536–541, 538*f*, 539*t*
    - pump deliverability and power requirements, 531–536
    - pumping system, 515–517, 517*f*, 518*f*, 519*f*
  - Sucker rod strings, 618–619
  - Suction pump, 454–455
  - Sulfate ion ( $\text{SO}_4^{-2}$ ), 680
  - Sulfate scales, 363, 684
  - Sulfide stress cracking, 688
  - Surface choke, 6–9
  - Surface driver selection, 619
  - Surface dynamometer cards, 544, 545*f*, 546*f*
  - Surface instruments, 544
  - Surface tiltmeter arrays, 493
  - Surfactants, 446
  - Surge limit, 293, 570
  - Swellable packers, 232, 238–239
  - Symmetric bi-wing fracture, 408
  - System depressurization, 661
- ## T
- Tapered rod strings, 529–531, 532*t*
  - Target depth (TD), 475
  - Taylor series, 559
  - Tearing mode, 393
  - Tectonic stresses, 397–398, 398*f*
  - Temperature, 115, 227, 230–232, 247, 254, 259–261, 267, 317–323
  - Tension
    - design, 224–225
    - packers, 233, 234*f*
    - tension-set versatile landing packer, 236, 236*f*
  - Terminal slip velocity, 508–509
  - Tetraethylene glycol ( $\text{T}_4\text{EG}$ ), 263, 654–655
  - Thermal insulation method, 659–660
  - Three-dimensional fracture models (3D fracture models), 415–418
    - planar 3D models, 418
    - pseudo 3D models, 415–417
  - Three-phase flash separators, 272
  - Three-phase glycol flash separator, 272
  - Throttling pressure valve, 574, 579, 580*f*
  - Tiltmeters, 483, 493
  - Tip screen-out treatment (TSO treatment), 476, 481
  - “Toe sleeve” system, 484
  - Torque factors, 528
  - Total acid number (TAN), 665
  - Total dynamic head (TDH), 607
  - Transient flow, 37–39
    - gas production during, 187, 188*t*
    - oil production during, 179–180, 181*f*, 181*t*
  - Transient temperature
    - during flow rate change, 318–323
    - during startup, 318
  - Transmission factor, 303
  - Transmitter pigs, 713
  - Transportation systems
    - compressors, 280–296
    - pipelines, 296–323
    - pumps, 275–280

- Transverse fractures, 482–483
  - Traveling valve (TV), 517
  - Trayed glycol contactors, 268*t*
  - Trial-and-error approach, 559
  - Triethylene glycol (TEG), 263, 654–655
  - Triplex pumps, 275–278
  - Tubing
    - pressure, 623
    - pump, 517
    - stretch, 533
    - strings, 219, 226, 228, 505
      - buckles, 229–230
      - nomenclature of tubing string in horizontal well, 506*f*
    - tubing–packer relation, 228*f*
  - Tubing effect (T.E), 577
  - Tubing effect factor (T.E.F), 577
  - Tubing performance relationship (TPR), 83, 131, 179
    - homogeneous-flow models, 97–100
    - models, 97–104
    - separated-flow models, 100–104
  - Turbulent flow region, 299
  - Turner et al. method, 345–347, 346*f*, 352. *See also* Guo et al. method
  - Two-dimensional fracture models (2D fracture models), 406–414
    - KGD model, 412–414, 412*f*
    - PKN model, 408–412, 409*f*
    - radial models, 407–408
  - Two-mineral model, 374
  - Two-phase flow, 69–70, 183–186, 189*f*
  - Two-phase friction factor ( $f_{2F}$ ), 99
  - Two-phase reservoirs, IPR for, 57–59
  - Two-stage compression unit, 288, 288*f*
  - Two-stage compressor, 289
- U**
- Ultrasonic in-line inspection tools, 706, 706*f*
  - Ultrasonic intelligent pig, 716
  - Unbalanced bellows valve, 576–577
    - closed condition, 577*f*
    - flow characteristics, 578*f*
    - open condition, 578*f*
  - Uncemented cased-hole completions, 483
    - situations, 485–486
  - Unconventional fracture models, 418–423
    - complex fracture network, 421*f*
    - nonplanar fracture geometry, 422*f*
    - stress shadowing effects, 419–421
  - Unconventional reservoirs, 487
  - Uniaxial compressive strength (UCS), 392
  - Uniaxial stress testing, 392
  - Unit conversion factors, 00034#APP0001
  - Unloading sequence process, 574, 575*f*
  - Unsteady state flow, 550
  - Utility pigs, 701–704
    - foam pig, 704*f*
    - mandrel pig, 705*f*
    - solid cast pigs, 705*f*
    - spheres, 703*f*
- V**
- V-belt drive, 515
  - Vacuum drying process, 645–646, 645*f*
  - Valve(s)
    - closing pressure, 577, 581
    - injection pressure at valve depth, 574–591
    - opening pressure, 576–577
    - selection, 574–591
      - characteristics, 574–582
      - combination valves, 582, 583*f*
      - fluid-operated valve, 579–582
      - pressure valve, 576–579
      - spacing, 583–587, 584*f*
      - throttling pressure valve, 579
      - unloading sequence process, 574
      - sizing, 587–589, 588*t*
      - testing, 587, 589–591, 591*t*
  - Vapor load, 272
  - Vertical lift performance, 83
  - Vertical radial flow, 332
  - Vertical separators, 244, 245*f*
  - Vertical wells, 37–45. *See also* Horizontal wells
    - deliverability of, 131–149
      - analysis with bottom-hole node, 131–137
      - analysis with wellhead node, 137–149
    - hydraulic-fractured wells, 42–45
    - pseudo-steady-state flow, 40–41
    - steady-state flow, 39
    - transient flow, 37–39
  - Viscoelastic surfactant fluid (VES fluid), 441
  - Viscosity, 21, 25–26
  - Vogel’s method, 58, 74–75
  - Volumetric dissolving power, 370
  - Volumetric efficiency, 277, 534–535, 565
  - Volumetric model, 380–381
- W**
- Walking beam, 515–516
  - Wall roughness, 300
  - Wall thickness design, 308–314
    - check for hydrotest condition, 314
    - corrosion allowance, 313–314
    - for external pressure, 312–313
    - for internal pressure, 309–311, 310*f*
    - procedure, 309

- Water, 685  
 compressibility, 32  
 content of natural gas, 259–260, 260f, 652t, 653f  
 formation volume factor, 32  
 fracturing fluids, 440–442  
 impacts of producing water on flow assurance, 666–668  
 production, 339–343, 342f, 343f, 344f, 345f. *See also* Gas production  
 removal, 651–655  
 samples, 663  
 specific gravity, 32  
 vapor, 259, 263  
 viscosity, 32  
 water-based gel systems, 644
- Water-swellable packers, 239
- Waterflooding, 359
- Wax appearance temperature (WAT), 665
- Wax chemical inhibitors, 671
- Wax crystals, 668
- Wax depositions process, 668–672
- Wax mitigation method, 670
- Well components  
 flowline, 9, 10f  
 safety control system, 10–11, 12f, 14f, 15f, 16f  
 well data, 167t, 168t, 169t  
 wellbore, 3–4  
 wellhead, 4–9, 5f, 8f
- Well deliverability, 129. *See also* Reservoir deliverability  
 horizontal wells, deliverability of, 149–158  
 multilateral wells, deliverability of, 159–170  
 principle of nodal analysis, 129–131  
 vertical wells, deliverability of, 131–149
- Well problem identification  
 excessive gas production, 339  
 excessive water production, 339–343  
 formation damage, 352–364  
 liquid loading of gas wells, 344–352  
 low productivity, 329–338  
 oil and gas production rates, 329
- Well production  
 gas production  
 during pseudo–steady-state flow period, 188–191, 191t, 192f  
 during transient flow period, 187, 188t  
 oil production  
 during pseudo–steady flow period, 180–186  
 during transient flow period, 179–180, 181f, 181t  
 principle of material balance, 179  
 production forecast through reservoir simulation, 192–193, 193f
- Well testing, 329, 361
- Well treatment and stimulation, considerations for, 226–232  
 pressure effect, 227–229  
 temperature effect, 227  
 total effect of temperature and pressure, 230–232
- Well tubing  
 tubing design, 219–232  
 buckling prevention during production, 225–226  
 considerations for well treatment and stimulation, 226–232  
 tension, collapse, and burst design, 224–225  
 wellhead-tubing-packer relation, 219, 220f
- Well workover, 503  
 engineering calculations, 505–510  
 types of workovers, 503–504  
 workover considerations, 504  
 workover equipment, 504–505
- Wellbore, 401–402, 428–429  
 formation breakdown around, 399–401
- Wellbore flow performance. *See also* Choke performance  
 multiphase flow in oil wells, 94–104  
 single-phase gas flow, 87–94  
 single-phase liquid flow, 83–87
- Wellhead  
 analysis with wellhead node, 137–149  
 gas well, 138t, 140–141  
 oil well, 141–149, 142t, 144t, 147t  
 chokes, 111  
 equipment, 453
- Wellhead performance relationship (WPR), 137
- Wellhead shut-in pressure (WSIP), 311
- Wet corrosion, 685
- Wettability alteration, 356–357, 363–364
- Weymouth equation, 302–303, 561  
 for horizontal flow, 303–306  
 for nonhorizontal flow, 306–307
- Wireline  
 cutting process, 679  
 units, 505  
 wireline-conveyed downhole tiltmeter arrays, 493
- Work per stroke cycle, 278
- Work per stroke for single piston, 275
- Workover, 503–504  
 equipment, 504–505  
 fluid flow rate requirement, 508–510  
 strings, 505–508
- Wormhole penetration and growth, 378–380
- Y**  
 Young's modulus, 392, 399, 401–402, 407, 409, 465–467, 482, 489–490, 640, 642
- Z**  
 Z-factor, 27–28, 29t, 92, 123–125  
 Zeepipe system, 644